Transactions of the ASME®

Transactions of the ASME, Journal of Heat Transfer (ISSN 0022-1481) is published quarterly (Feb., May, Aug., Nov.) for $210.00 per year by The American Society of Mechanical Engineers, 345 East 47th Street, New York, NY 10017. Second class postage paid at New York, NY and additional mailing offices. POSTMASTER: Send address changes to Transactions of the ASME, Journal of Heat Transfer, c/o THE AMERICAN SOCIETY OF MECHANICAL ENGINEERS, 22 Law Drive, Box 2300, Fairfield, NJ 07007-2300.
CHANGES OF ADDRESS must be received at Society headquarters seven weeks before they are to be effective. Please send old label and new address. **PRICES:** To members, $40.00, annually: to nonmembers, $210.00. Add $30.00 for postage to countries outside the United States and Canada.

Journal of Heat Transfer

Published Quarterly by The American Society of Mechanical Engineers

VOLUME 118 • NUMBER 1 • FEBRUARY 1996

TECHNICAL PAPERS

(Contents continued on page 268)

Phase-Change Heat Transfer

Transport Phenomena in Microgravity

TECHNICAL NOTES

(Contents continued)

ANNOUNCEMENTS

Journal of Heat Transfer

Obituary

John Gordon Collier

John Gordon Collier passed away on November 18, 1995.

He was Chairman of Nuclear Electric plc, England's state-owned nuclear power utility. Previously he held the posts of Chairman of the UKAEA (United Kingdom Atomic Energy Authority); Director-General of the Generating and Construction Development Division of the Central Electricity Generating Board; Head of the Atomic Energy Technical Unit at Harwell; Head of the Chemical Engineering Division, also at Harwell; and earlier held responsible positions with Atomic Energy of Canada, Ltd., and Atomic Power Constructions, Ltd.

John Collier was born on January 22, 1935. He received a First Class Honors Degree B.Sc. (Chemical Engineering) from University College, London in 1956. After graduating, he began his work on reactor heat transfer systems at AERE, Harwell, notably for steam and gas-cooled, heavy water moderated reactors. From there, John joined the reactor heat transfer team designing the CANDU reactor system in Canada. He later returned to Harwell to lead the research on use of liquid metals as reactor coolants.

John Collier was one of the world's leading authorities on two-phase flow and boiling, as evidenced by his authoritative book *Convective Boiling and Condensation,* first published in 1972 and rewritten in its third edition in 1994. The book is used as a textbook and reference in leading universities and nuclear research laboratories throughout the world. Notably, he played a key role in establishing two-phase flow as a scientific discipline. John Collier also played a leading role in the development of Great Britain's nuclear power industry.

John Collier was a Fellow of the Royal Society, the Royal Academy of Engineering, the Institutions of Chemical, Mechanical, and Nuclear Engineering, and the Institute of Energy. He held an honorary Doctorate of Science from Cranfield Institute of Technology and an honorary Doctorate of Engineering from Briston University. John was a Calvin Rice Lecturer and an honorary lifetime member of the American Society of Mechanical Engineers.

The international heat transfer community wishes to extend this tribute to John G. Collier for his dedication to two-phase flow and heat transfer engineering and his leadership in the safe use of nuclear power.

Journal of Heat Transfer

Editorial

The editors of the journals publishing in the field of heat transfer are very concerned about several items that are occurring more frequently. These involve simultaneous submission of a single article to multiple journals for review, publication of articles with only incremental advancement of previously established knowledge, and the publication of articles that are essentially identical in multiple journals. We take this opportunity to remind the heat transfer community of their moral and legal responsibility to insure that the work that they submit for publication is both original and technically significant. As editors in a common field of research, we are all working together to make available to our readers the highest quality publications and to do so in a timely and efficient manner. Multiple submission of the same article for review in different journals taxes the already overburdened review system, and is in direct violation of the editorial policy of virtually all journals. While recognizing the pressure placed on many individuals to publish, the submission of manuscripts containing only small or incremental improvements over existing work, particularly when published by the same author, is clearly not in the best interest of the heat transfer community, authors, reviewers, or editors. We all have a responsibility to ensure that the work published is of significant value and cannot be obtained directly from previously published work. Finally, the submission of articles that are identical in content to separate journals, aside from being unethical, is in violation of the copyright statutes and is prohibited by law.

As a group, we remind the heat transfer community that it has a responsibility to act in an ethical and professional manner. Further, it must do everything possible to ensure that publications that bear our name and represent our institutions are of the highest quality and present original research results not previously reported in the archival literature.

This editorial was developed by the editors of the following journals and will appear in an upcoming issue of each:

AIAA *Journal of Thermophysics and Heat Transfer*
ASME *Journal of Heat Transfer*
Enhanced Heat Transfer
Experimental Heat Transfer
Experimental Thermal and Fluid Science
International Journal of Heat and Mass Transfer
International Journal of Heat and Fluid Flow
Journal of Heat Transfer Technology Education
Numerical Heat Transfer

Elastoplastic Contact Conductance Model for Isotropic Conforming Rough Surfaces and Comparison With Experiments

M. R. Sridhar
Post-Doctoral Fellow.
Assoc. Mem. ASME

M. M. Yovanovich
Professor and Director.
Fellow ASME

Microelectronics Heat Transfer Laboratory,
Department of Mechanical Engineering,
University of Waterloo,
Waterloo, Ontario, Canada N2L 3G1

A new thermal elastoplastic contact conductance model for isotropic conforming rough surfaces is proposed. This model is based on surface and thermal models used in the Cooper, Mikic, and Yovanovich plastic model, but it differs in the deformation aspects of the thermal contact conductance model. The model incorporates the recently developed simple elastoplastic model for sphere-flat contacts, and it covers the entire range of material behavior, i.e., elastic, elastoplastic, and fully plastic deformation. Previously data were either compared with the elastic model or the plastic model assuming a type of deformation a priori. The model is used to reduce previously obtained isotropic contact conductance data, which cover a wide range of surface characteristics and material properties. For the first time data can be compared with both the elastic and plastic models on the same plot. This model explains the observed discrepancies noted by previous workers between data and the predictions of the elastic or plastic models.

Introduction

The thermal contact conductance models for two conforming rough surfaces consist of three basic models: the thermal model, the surface model, and the deformation model. The essential difference between the different contact conductance models is found in the surface model. Most of the contact conductance models for isotropic surfaces assume circular contact spots and use either the Hertz elastic model (Johnson, 1985) or the geometric plastic deformation model. Depending on the type of deformation model used, the contact conductance model for conforming rough surfaces becomes an elastic or a plastic model.

There is considerable confusion regarding the type of deformation associated with a pair of contacting conforming rough surfaces under static load. In order to predict experimental results with the present contact conductance models, a type of deformation must be assumed a priori. A plasticity index has been used to assess the type of deformation (elastic or plastic). This index requires a value of plastic hardness. Since only a single value of hardness for a particular material has been used in the past (for, e.g., Aikawa and Winer, 1994) instead of an appropriate microhardness (see Yovanovich et al., 1982) it did not necessarily point to the right deformation mode.

There is a need to be able to reduce data without assuming a type of deformation. This is because most of the rough surfaces in contact under load undergo elastic or elastoplastic deformation. This can be achieved by incorporating an elastoplastic deformation model into the present thermal contact conductance model.

Recently a simple elastoplastic model for sphere-flat contacts has been proposed by Sridhar (1994). This model predicts the contact radius or displacement for all three regimes of deformation: elastic, elastoplastic, and fully plastic.

The aim of the present paper is to develop a novel thermal contact conductance model for conforming rough isotropic surfaces using the recently proposed elastoplastic model for sphere-flat contacts and then reduce experimental data (Antonetti, 1983; Hegazy, 1985; McWaid, 1990; Maddren, 1994) obtained for similar isotropic metal pairs to dimensionless form. Data reduced using the elastic or elastoplastic model can be compared with both the elastic and plastic models on the same plot.

There are a number of thermal contact conductance models available in the literature. The important models that use statistical analysis are: (*i*) Greenwood and Williamson (1966) (GW) model, (*ii*) Cooper, Mikic, and Yovanovich (1969) (CMY) and Mikic (1974) model, (*iii*) Bush, Gibson, and Thomas (1975) (BGT) asymptotic model, and (*iv*) Whitehouse and Archard (1970) (WA) model. A detailed review of these contact conductance models can be found in Sridhar and Yovanovich (1994).

Elastic-plastic models for contacting rough surfaces have been proposed in the past by Ishigaki et al. (1979), Chang et al. (1987), and Majumdar and Bhushan (1991). The Ishigaki et al. (1979) model assumes that the total deformation is the sum of elastic and plastic deformations. Chang et al. (1987) have improved upon the previous models by considering volume conservation of an asperity control volume during plastic deformation. The Majumdar and Bhushan (1991) model is based on the contact mechanics of two fractal surfaces in contact. In the Chang et al. (1987) and Majumdar and Bhushan (1991) models the asperity deformation is purely elastic or purely plastic and the model switches between these two modes. The problem of switching has been circumvented in the Sridhar (1994) model and predicts contact size or displacement for the elastic, the elastoplastic, and the plastic regimes with a single expression.

There is a choice of converting any of the surface models (CMY/Mikic, GW, WA, and BGT) into an elastoplastic model. We know that the GW model and the WA model require an additional surface parameter (see Sridhar and Yovanovich, 1994) and the BGT model is only an approximate model, which does not compare well with the other models. Hence the present work of developing an elastoplastic model for isotropic conforming rough surfaces will be based on the existing, well-established, CMY plastic model and the Mikic elastic model.

Contributed by the Heat Transfer Division for publication in the JOURNAL OF HEAT TRANSFER. Manuscript received by the Heat Transfer Division May 1994; revision received January 1995. Keywords: Conduction, Electronic Equipment, Thermal Packing. Associate Technical Editor: L. S. Fletcher.

The main results from the analyses of the CMY plastic model and the Mikic elastic model are given in Table 1. The thermal model used in these contact conductance models was first presented by Cooper et al. (1969) and in a convenient form by Yovanovich (1982), where the contact conductance h_c is given by:

$$h_c = \frac{2k_s n a}{(1 - \sqrt{A_r/A_a})^{1.5}} \tag{1}$$

where $k_s \equiv$ harmonic mean thermal conductivity, $n \equiv$ contact spot density, $a \equiv$ mean contact spot radius, and $A_r/A_a \equiv$ ratio of real area to apparent area of contact. The relationship in the denominator of Eq. (1) accounts for the "crowding" of adjacent microcontacts and it is important for large relative contact pressures.

In Table 1, λ is the dimensionless mean plane separation, σ and m are the surface asperity roughness and slope parameters for the surface pair, P is the applied pressure, and E' the equivalent elastic modulus.

The elastoplastic model developed here will take into account the differences between the elastic and plastic models and will move smoothly from the elastic model to the fully plastic model.

Table 1 Mikic/CMY elastic and plastic model

Deformation	Results
Elastic or Plastic	$\frac{A_r}{A_a} = \frac{\kappa^*}{4} erfc(\lambda/\sqrt{2})$ $n = \frac{1}{16}\left(\frac{m}{\sigma}\right)^2 \frac{exp(-\lambda^2)}{erfc(\lambda/\sqrt{2})}$ $a = \frac{2\sqrt{\kappa^*}}{\sqrt{\pi}} \frac{\sigma}{m} exp(\lambda^2/2) erfc(\lambda/\sqrt{2})$ $h_c = \frac{\sqrt{\kappa^*} k_s m}{4\sqrt{\pi}\sigma} \frac{exp(-\lambda^2/2)}{\left[1 - \sqrt{\frac{\kappa^*}{4} erfc(\lambda/\sqrt{2})}\right]^{1.5}}$
Elastic	$\lambda = \sqrt{2} erfc^{-1}\left(\frac{4\sqrt{2}P}{E'm}\right)$
Plastic	$\lambda = \sqrt{2} erfc^{-1}\left(\frac{2P}{H_c}\right)$

* $\kappa = 1$ for elastic, $\kappa = 2$ for plastic

Brief Review of Deformation Models for Sphere-Flat Contacts

In this section results of the three deformation models for sphere-flat contacts are presented. The models will be based on two methods of defining surface hardness: (*i*) hardness based on contact radius: $H_{d,a} = \tilde{F}/(\pi a^2)$, and (*ii*) hardness based on contact displacement: $H_{d,\delta} = \tilde{F}/(\pi\beta\delta)$, where the subscript d refers to the type of deformation: elastic (e), plastic (p), and elastoplastic (ep).

1 Elastic Model of Hertz. A sphere in contact with a flat produces a circular contact. Hertz (see Johnson, 1985) solved the problem for an elliptical contact. The circular contact is a special case of the elliptical contact problem. Hertz simplified the problem by assuming that each body is regarded as an elastic half-space loaded over a small elliptical or circular (in this case) region of its plane surface. A detailed review is available from Sridhar (1994).

Nondimensional elastic hardness based on contact radius a is given by (see Sridhar, 1994):

$$C_{e,a} = \frac{H_{e,a}}{S_f} = \frac{4}{3\pi} \cdot \frac{E'}{S_f} \cdot \frac{a}{\beta} = \frac{4}{3\pi} \cdot \epsilon^*_{c,a} \tag{2}$$

where $\epsilon^*_{c,a} = E'/S_f \cdot a/\beta \equiv$ nondimensional contact strain based on the circular contact spot radius.

Nondimensional elastic hardness based on contact displacement δ is given by (see Sridhar, 1994):

Nomenclature

A_a = apparent contact area, m^2
$\tilde{A}$ = contact area for a single circular contact, m^2
A_r = real contact area, m^2
a = mean circular contact radius, m
C_e, C_p, C_{ep} = elastic, plastic and elastoplastic constraint parameters
c_1, c_2 = Vickers correlation coefficients, c_1, MPa
d_V = Vickers indentation diagonal, μm
E = elastic modulus, MPa
E' = equivalent elastic modulus, MPa $\equiv [(1 - \nu_A^2)/E_A + (1 - \nu_B^2)/E_B]^{-1}$
$\tilde{F}$ = load on a single circular contact (sphere-flat), N
$f_{ep}(\epsilon_c^*)$ = function used in the elastoplastic model, Eq. (18)
H_e, H_{corp}, H_{ep} = elastic, plastic and elastoplastic hardness, MPa
h_c = contact conductance, $W/m^2 \cdot K$
k_s = harmonic mean thermal conductivity $\equiv 2k_Ak_B/(k_A + k_B)$, $W/m \cdot K$
m = effective mean absolute surface slope $\equiv \sqrt{m_A^2 + m_B^2}$, rad
n = contact spot density, m^{-2}, or blending parameter
n_1, n_2 = interpolation indices
P = nominal contact pressure, MPa
Q = heat transfer rate, W
S_f = material yield or flow stress, MPa
T_c = mean interface temperature, °C
β = radius of curvature of asperity summits or sphere, m
ΔT_c = effective temperature drop across the interface, °C
δ = contact displacement, m
ϵ_c^* = nondimensional contact strain $\equiv (E'/S_f) \cdot (a/\beta)$ or $(E'/S_f) \cdot \sqrt{\delta/\beta}$ or $1.67 \cdot (E'/S_f) \cdot m$
λ = dimensionless surface mean plane separation
ν = Poisson ratio
σ = rms surface roughness heights for given surface or surface pair $\equiv \sqrt{\sigma_A^2 + \sigma_B^2}$, m

Subscripts

A, B = surfaces A and B
a = apparent area or based on contact radius a
c = contact or plastic
e, p, ep = elastic, plastic, elastoplastic
r = real

Abbreviations

Al = aluminum
BGT = Bush, Gibson, and Thomas
CMY = Cooper, Mikic, and Yovanovich
GW = Greenwood and Williamson
Ni = Nickel
SS = stainless steel
WA = Whitehouse and Archard
Zr-Nb = zirconium alloy with niobium
Zr-4 = zirconium alloy

$$C_{e,\delta} = \frac{H_{e,\delta}}{S_f} = \frac{4}{3\pi} \cdot \frac{E'}{S_f} \cdot \sqrt{\frac{\delta}{\beta}} = \frac{4}{3\pi} \cdot \epsilon^*_{c,\delta} \tag{3}$$

where $\epsilon^*_{c,\delta} = E'/S_f \cdot \sqrt{\delta/\beta} \equiv$ nondimensional contact strain based on the contact displacement.

From the Hertz analysis we also have the important geometric relationship:

$$a = \sqrt{\beta\delta} \tag{4}$$

With this result one can obtain the very important relationship between the dimensionless contact strains based on the contact radius or the contact displacement:

$$\epsilon^*_{c,a} = \epsilon^*_{c,\delta} = \epsilon^*_c \tag{5}$$

This result will be used in the development of the elastoplastic model.

2 Geometric Plastic Model for Sphere-Flat Contact. This simple deformation model assumes that the sphere and the flat interact geometrically under fully plastic deformation.

Nondimensional plastic hardness based on contact radius a is given by (see Sridhar, 1994):

$$C_{p,a} = \frac{H_{p,a}}{S_f} = 2.76 \tag{6}$$

Nondimensional plastic hardness based on contact displacement δ is given by (see Sridhar, 1994):

$$C_{p,\delta} = \frac{H_{p,\delta}}{S_f} = 5.52 \tag{7}$$

3 Elastoplastic Model for Sphere-Flat Contact. The expression for the elastoplastic hardness was obtained by Sridhar (1994) by "patching" or "blending" the two asymptotic solutions (i.e., elastic and plastic). The technique was first introduced into convection heat transfer by Churchill and Usagi (1972).

An implicit model between the unknown geometric constraint parameter and the known nondimensional contact strain was developed by Sridhar (1994) based on the assumption that the relative elastoplastic constraint parameter C_{ep} can be related to the two asymptotic results valid for pure elastic contact C_e and for fully plastic flow C_p in the following blended form:

$$C_{ep} = [(C_e)^{-n} + (C_p)^{-n}]^{-1/n} \tag{8}$$

where the index n is called the "blending" parameter, which is to be determined from analysis, experimental results, or numerical results.

Implicit Elastoplastic Model Based on Contact Size a. The model written in terms of the dimensionless contact strain is

$$C_{ep,a} = \frac{2.76}{\left[1 + \left(\frac{6.51}{\epsilon^*_{c,a}}\right)^{n_1}\right]^{1/n_1}} \tag{9}$$

to reveal its characteristics. The elastoplastic model, Eq. (9), has interesting features. It goes smoothly to the two asymptotes that form the basis of the elastoplastic model independent of the numerical value of the "blending" index.

We can rewrite the Eq. (9) in the following form:

$$\frac{\tilde{F}}{\tilde{A}_{ep} S_f} = \frac{2.76}{\left[1 + \left(\frac{6.5}{\epsilon^*_c}\right)^{n_1}\right]^{1/n_1}} \tag{10}$$

where $\tilde{A}_{ep}$ is elastoplastic contact area of a single contact spot. Implicit elastoplastic model based on contact deflection δ:

The constraint parameter is given by:

$$C_{ep,\delta} = \frac{5.52}{\left[1 + \left(\frac{13.02}{\epsilon^*_{c,\delta}}\right)^{n_2}\right]^{1/n_2}} \tag{11}$$

Similarly we have:

$$\frac{\tilde{F}}{\pi\beta\delta S_f} = \frac{5.52}{\left[1 + \left(\frac{13.0}{\epsilon^*_c}\right)^{n_2}\right]^{1/n_2}} \tag{12}$$

In Eq. (10) and Eq. (12) $\epsilon^*_{c,a}$ and $\epsilon^*_{c,\delta}$ have been replaced by ϵ^*_c because we know that they are equal to each other from Eq. (5).

There are two interpolation indices (n_1 and n_2) that have to be determined through analysis or numerical or experimental results. For the implicit models presented above the interpolation indices were determined from the explicit models presented by Sridhar (1994). The explicit and implicit models are two forms of the same model (see Sridhar, 1994). Hence if the interpolation index for the explicit model is known, the index for the implicit model can be derived. If the applied load $\tilde{F}$ is characterized as the *input* and the resulting size (a or δ) as the *output* then it can be seen that the size appears on both sides of the implicit model. Hence the comparison with data with the implicit model would lead to larger errors as the size appears twice. This is the reason the interpolation indices were determined using the explicit model. The indices for the explicit model were in turn determined by comparing the models with classical experiments of Tabor (1951) and Foss and Brumfield (1922) in dimensionless forms (see Sridhar, 1994). When the implicit models were cast in appropriate forms and compared with the corresponding explicit models they yielded values of $n_1 = 2$ and $n_2 = 1.2$.

Present Elastoplastic Model for Conforming Rough Surfaces

From the comparison of the two asymptotic models (Table 1) it is clear that the ratio of real area to apparent area of contact A_r/A_a, size of average contact spot a, and the relationship between the applied pressure P and dimensionless mean plane separation λ depend upon the type of deformation. In this section these parameters will be examined and the corresponding expressions for the new elastoplastic model will be derived.

Ratio of Real Area to the Apparent Area of Contact A_r/A_a. Examining the results of the analyses of the CMY plastic model and the Mikic elastic model we find:

$$4\left(\frac{A_r}{A_a}\right)_{\text{elastic}} = 2\left(\frac{A_r}{A_a}\right)_{\text{plastic}} = \text{erfc}(\lambda/\sqrt{2}) \tag{13}$$

Similarly for a single sphere-flat contact:

$$\tilde{A}_e = \tfrac{1}{2}\tilde{A}_p = \pi\beta\delta \tag{14}$$

Therefore

$$\frac{\tilde{A}_e}{\tilde{A}_p} = \frac{1}{2} \tag{15}$$

Mikic (1974) derived the ratio A_r/A_a for elastic contact based on Eq. (15), which indicates that the elastic contact area is half that of the plastic contact area.

Elastoplastic Contact Area for a Single Contact Spot. From Eq. (10) we have

$$\tilde{A}_{ep} = \frac{\tilde{F}\left[1 + \left(\frac{6.5}{\epsilon_c^*}\right)^2\right]^{1/2}}{2.76 S_f} \tag{16}$$

Also from Eq. (12) we find

$$\tilde{F} = \frac{5.52\pi S_f \beta \delta}{\left[1 + \left(\frac{13.0}{\epsilon_c^*}\right)^{1.2}\right]^{1/1.2}} \tag{17}$$

Substituting for $\tilde{F}$ in Eq. (16) we get:

$$\frac{\tilde{A}_{ep}}{\tilde{A}_p} = \frac{\left[1 + \left(\frac{6.5}{\epsilon_c^*}\right)^2\right]^{1/2}}{\left[1 + \left(\frac{13.0}{\epsilon_c^*}\right)^{1.2}\right]^{1/1.2}} = f_{ep}(\epsilon_c^*) \tag{18}$$

It will be shown later that ϵ_c^* for conforming rough surfaces in contact is independent of size (a) or displacement (δ) and dependent only on the material properties (E', S_f) and the mean absolute surface slope (m) for a surface pair.

Therefore the elastoplastic ratio of real area to apparent area is given by:

$$\frac{A_r}{A_a} = \frac{f_{ep}(\epsilon_c^*)}{2} \operatorname{erfc}(\lambda/\sqrt{2}) \tag{19}$$

It can seen that as $\epsilon_c^* \to 0$, $f_{ep}(\epsilon_c^*) \to 0.5$ and as $\epsilon_c^* \to \infty$, $f_{ep}(\epsilon_c^*) \to 1$. As ϵ_c^* ranges from 0 to ∞, $f_{ep}(\epsilon_c^*)$ moves smoothly from 0.5 to 1.0 as seen in Fig. 1.

Contact Spot Density n. It can be seen from Table 1 that the contact spot density is predicted with the same expression for both elastic or plastic deformation.

Therefore for elastoplastic deformation:

$$n = \frac{1}{16}\left(\frac{m}{\sigma}\right)^2 \frac{\exp(-\lambda^2)}{\operatorname{erfc}(\lambda/\sqrt{2})} \tag{20}$$

Force Balance. We know from the CMY plastic model that:

$$\frac{A_r}{A_a} = \frac{P}{H_c} \tag{21}$$

where $P \equiv$ applied pressure and $H_c \equiv$ appropriate contact hardness (plastic) of the softer material.

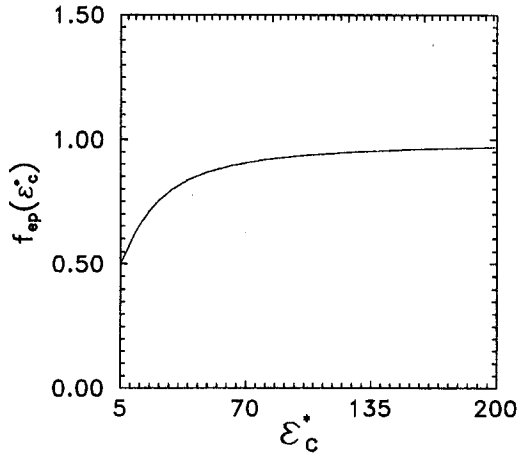

Fig. 1 Plot of the function $f_{ep}(\epsilon_c^*)$ versus ϵ_c^*

It was shown by Mikic and Roca (1993) for conforming surfaces undergoing elastic deformation that:

$$\frac{A_r}{A_a} = \frac{P}{\frac{E'}{\sqrt{2}} m} = \frac{P}{H_e} \tag{22}$$

Therefore

$$H_e = \frac{E'}{\sqrt{2}} \cdot m \tag{23}$$

where H_e is defined as the elastic hardness of the softer material in contact and m is the mean absolute slope for a surface pair. The elastic hardness H_e refers to the mean pressure on a single mean asperity as it is pressed against a rigid, smooth flat.

Hence we make the assumption that

$$H_e = \frac{E'}{\sqrt{2}} \cdot m = \frac{4}{3\pi} \cdot E' \cdot \frac{a}{\beta} \tag{24}$$

Therefore we find the relationship between the ratio a/β and m:

$$\frac{a}{\beta} = 1.67 \cdot m \tag{25}$$

With this we rewrite ϵ_c^* as:

$$\epsilon_c^* = \frac{E'}{S_f} \cdot \frac{a}{\beta} = 1.67 \cdot \frac{E'}{S_f} \cdot m \tag{26}$$

Finally, we assume for elastoplastic deformation of two conforming rough surfaces in contact that:

$$\frac{A_r}{A_a} = \frac{P}{H_{ep}} \tag{27}$$

where H_{ep} is the elastoplastic hardness given by:

$$H_{ep} = \frac{2.76 S_f}{\left[1 + \left(\frac{6.5}{\epsilon_c^*}\right)^2\right]^{1/2}} \tag{28}$$

Therefore we have

$$\frac{A_r}{A_a} = \frac{f_{ep}(\epsilon_c^*)}{2} \operatorname{erfc}(\lambda/\sqrt{2}) = \frac{P}{H_{ep}} \tag{29}$$

and

$$\lambda = \sqrt{2}\, \operatorname{erfc}^{-1}\left(\frac{2}{f_{ep}(\epsilon_c^*)} \frac{P}{H_{ep}}\right) \tag{30}$$

Table 2 summarizes the important results of the new elastoplastic model. It should be noted that the present elastoplastic model assumes Gaussian distribution profile heights and slopes.

Comparison of Thermal Contact Conductance Models With Experimental Data

In order to compare the models with themselves as well as with experimental data, they must be cast in dimensionless form. It has been found that the most suitable dimensionless form for contact conductance is: $C_c = \sigma/m \cdot h_c/k_s$, where k_s is the mean harmonic thermal conductivity, and σ and m are the equivalent rms surface roughness and mean absolute slope, respectively, for a surface pair.

The dimensionless contact pressures used in this work for the three different models are P/H_e, $P/H_{c\,or\,p}$, and P/H_{ep}, respectively, where H_e, H_c or H_p, and H_{ep} refer to the elastic, the plastic, and the elastoplastic hardness, respectively.

Table 2 Elastoplastic model

Results
$\frac{A_r}{A_a} = \frac{f_{ep}(\epsilon_c^*)}{2} erfc(\lambda/\sqrt{2})$
$n = \frac{1}{16}\left(\frac{m}{\sigma}\right)^2 \frac{exp(-\lambda^2)}{erfc(\lambda/\sqrt{2})}$
$a = \sqrt{\frac{8}{\pi}} \cdot \sqrt{f_{ep}(\epsilon_c^*)} \cdot \frac{\sigma}{m} exp(\lambda^2/2) erfc(\lambda/\sqrt{2})$
$h_c = \frac{k_s}{2\sqrt{2\pi}} \frac{m}{\sigma} \frac{\sqrt{f_{ep}(\epsilon_c^*)} \cdot exp(-\lambda^2/2)}{\left[1 - \sqrt{\frac{f_{ep}(\epsilon_c^*)}{2}} erfc(\lambda/\sqrt{2})\right]^{1.5}}$
$\lambda = \sqrt{2} erfc^{-1}\left(\frac{1}{f_{ep}(\epsilon_c^*)} \cdot \frac{2P}{H_{ep}}\right)$

Figure 2 shows a plot of the new elastoplastic model for different values of the nondimensional contact strain ϵ_c^*. For $\epsilon_c^* = 0$, the elastoplastic model reduces to the elastic model (Mikic). As ϵ_c^* is increased, the elastoplastic model moves downward. The plots of $\epsilon_c^* = 15$ and 60 are seen to lie below the elastic model but parallel to it. A value of $\epsilon_c^* = \infty$ reduces the elastoplastic model to the plastic model (CMY). It can be seen from Fig. 3 that a single model is able to handle all three regimes of loading, i.e., the elastic, the elastoplastic, and the fully plastic.

Data Reduction. Experimental contact conductance h_c is determined as follows: $h_c = Q/(A_a \Delta T_c)$, where Q is the heat flow rate, A_a is the apparent contact area, and ΔT_c interface temperature drop. This is nondimensionalized by multiplying it by $(\sigma/m)/k_s$. The surface parameters $\sigma = \sqrt{\sigma_A^2 + \sigma_B^2}$ and $m = \sqrt{m_A^2 + m_B^2}$, where A and B refer to the upper and lower surfaces. The harmonic mean thermal conductivity k_s is defined as: $k_s = (2k_A k_B)/(k_A + k_B)$, where k_A and k_B are thermal conductivities of the upper and lower specimens. The thermal conductivities k_A and k_B for a test pair were determined at the mean interface temperature T_c.

Microhardness is the most important property in the thermal contact conductance data reduction. It has been known for the last 50 years that microhardness is a size-dependent property.

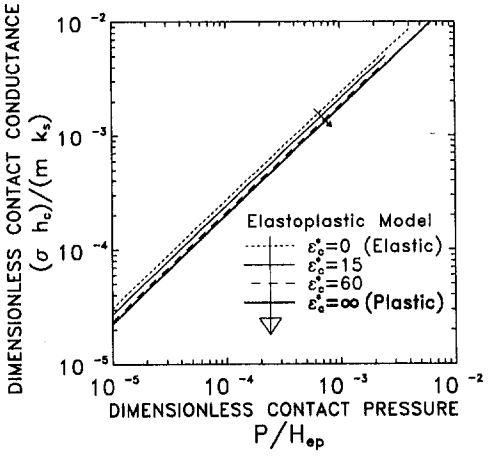

Fig. 2 Plot of the present elastoplastic model for different values of ϵ_c^*

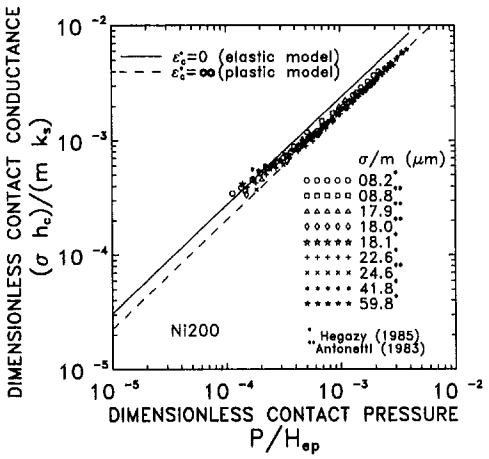

Fig. 3 Comparison of elastic and plastic asymptotic models with Ni200 data (Hegazy, 1985; Antonetti, 1983) reduced using the proposed elastoplastic model

Since Hegazy (1985), Vickers microhardness (H_V) and indentation size (d_V) have been correlated. Experimental correlations between Vickers microhardness and indentation diagonal ($H_V = c_1 d_V^{c_2}$) were available for Antonetti (1983) and Hegazy (1985) isotropic data.

Iterative Procedure to Determine P/H_{ep}. In order to determine the dimensionless contact pressure P/H_{ep} for each experimental point one has to know the appropriate value of elastoplastic contact microhardness H_{ep}. An iterative technique was required to determine this appropriate elastoplastic contact microhardness. The technique used in the present work is similar to the one developed by Yovanovich et al. (1982, 1983) and Yovanovich and Hegazy (1983). The only difference is that the elastoplastic model is used instead of the fully plastic model (CMY).

Examining the expression for the elastoplastic hardness, Eqs. (26) and (28), it can be seen that the value of yield/flow stress S_f is unknown. Hence an appropriate value of S_f has to be chosen in order to determine the elastoplastic hardness H_{ep}. The iterative procedure developed calculates the appropriate value of S_f and thus the elastoplastic hardness H_{ep}.

Equations (31)–(37) constitute the present model for predicting P/H_{ep} for a particular applied pressure P on a conforming rough surface pair. The expression for S_f in Eq. (37) was obtained by solving for S_f using Eq. (28).

$$H_{ep} = \frac{H_V}{0.9272} = \frac{c_1}{0.9272} \cdot d_V^{c_2} \tag{31}$$

$$d_V = \sqrt{2\pi} \cdot a \tag{32}$$

$$a = \sqrt{\frac{8}{\pi}} \cdot \sqrt{f_{ep}(\epsilon_c^*)} \cdot \frac{\sigma}{m} \exp(\lambda^2/2)\ \text{erfc}\ (\lambda/\sqrt{2}) \tag{33}$$

$$\lambda = \sqrt{2}\ \text{erfc}^{-1}\left(\frac{1}{f_{ep}(\epsilon_c^*)} \cdot \frac{2P}{H_{ep}}\right) \tag{34}$$

$$f_{ep}(\epsilon_c^*) = \frac{\left[1 + \left(\frac{6.5}{\epsilon_c^*}\right)^2\right]^{1/2}}{\left[1 + \left(\frac{13.0}{\epsilon_c^*}\right)^{1.2}\right]^{1/1.2}} \tag{35}$$

$$\epsilon_c^* = 1.67 \frac{E'}{S_f} \cdot m \tag{36}$$

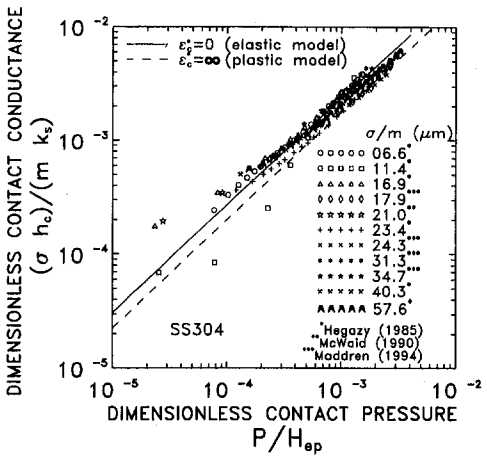

Fig. 4 Comparison of elastic and plastic asymptotic models with SS304 data (Hegazy, 1985) reduced using the elastic and the proposed elastoplastic model

$$S_f = \frac{1}{2.76\sqrt{\frac{1}{H_{ep}^2} - \frac{1}{H_e^2}}} \tag{37}$$

In Eq. (31) the Vickers microhardness H_V is divided by 0.9272 to convert the Vickers hardness, which is based on total surface area of indentation to a hardness based on the projected area. This is because hardness is defined based on the projected area of indentation.

Equations (31)–(37) were solved iteratively using *Mathematica* (1988–91) until the assumed value of H_{ep} in Eq. (37) and the calculated value of H_{ep}, Eq. (31), coincided. The numerical "FindRoot" was used to achieve this. The "FindRoot" command in *Mathematica* (1988–91) required two guesses around the actual root. If the elastoplastic hardness is equal to the elastic hardness, then the iterative procedure appears to fail. This problem can be avoided by using the elastic model to reduce data whenever the iterative procedure fails.

Comparison of Experimental Data With the Proposed Models. It was clear from the iterative procedure that each surface pair, depending upon its surface and material characteristics, will have different values of ϵ_c^*. It was found that the value of ϵ_c^* was almost invariant for a single surface pair and as load was increased it remained more or less constant. The nondimensional strain ϵ_c^* used in the elastoplastic model is strongly dependent on the value of surface slope m. It is known that this quantity (m) is difficult to measure without errors. The extent of care taken during the measurement of surface slope m by previous researchers is not clear. Hence at this stage the experimental data from Antonetti (1983), Hegazy (1985), McWaid (1990), and Maddren (1994) will be reduced to a dimensionless form and compared with the two asymptotes, i.e., the elastic ($\epsilon_c^* = 0$) and plastic models ($\epsilon_c^* = \infty$).

The iterative procedure appears to fail if the data sets are below the elastic model in dimensionless form (i.e., when data are reduced assuming elastic deformation and compared with the elastic model). To circumvent this problem data sets were first compared with the elastic model, and only sets that showed significant plastic deformation (i.e., data well above the elastic model) were reduced using the elastoplastic model. A rms error of the order 25 percent (i.e., between data and elastic model) and greater was considered a good measure for significant plastic deformation. This rule was applied after removing the first few data points, which normally have large low-load deviation. Ideally data should lie between these two bounds, i.e., the Mikic elastic model and CMY plastic model. The asymptotes run parallel to each other and are quite close (difference $\simeq$ 30 percent). It should be noted that in the past data could not be compared with both the elastic and plastic models because a type of deformation had to be assumed a priori.

Figure 3 shows the comparison of experimental data from Antonetti (1983) and Hegazy (1985) for Ni200 conforming rough surface pairs with the elastic model and the plastic models. The data set covers a wide range surface roughness with the roughness parameter σ/m varying from 8.2 μm to 59.8 μm. Even though the light load data points show some scatter, the data lie well within the bounds set by the elastic and plastic models. It should be noted that all Ni200 data underwent elastoplastic deformation.

Figure 4 shows the comparison between the SS304 data from Hegazy (1985), McWaid (1990), and Maddren (1994) with the elastic and the plastic models. The 11 surface pairs covered a range of roughness values with σ/m varying from 6.6 to 57.6 μm. Most of the data lie between the two bounds set by the elastic and plastic models. All McWaid (1990) and Maddren (1994) data underwent fully elastic deformation, whereas only the smoothest pair from Hegazy (1985) underwent fully elastic deformation. The rougher surfaces from Hegazy (1985) (σ/m = 11.4, 16.9, 23.4, 40.3, and 57.6 μm) had to be reduced using the elastoplastic model.

Figure 5 shows the comparison between the Zr–Nb data from Hegazy (1985) with the elastic and plastic models. The low load data points lie outside the bounds of the elastic and plastic

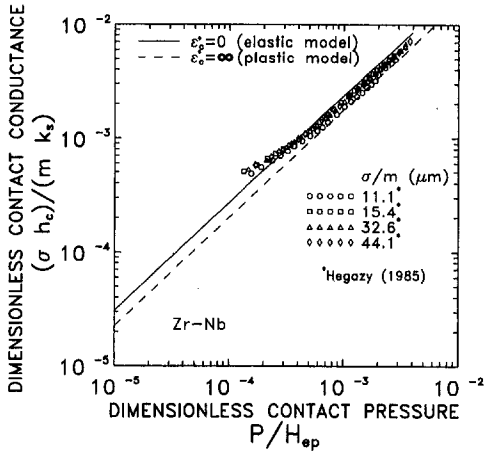

Fig. 5 Comparison of elastic and plastic asymptotic models with Zr–Nb data (Hegazy, 1985) reduced using the elastic and the proposed elastoplastic model

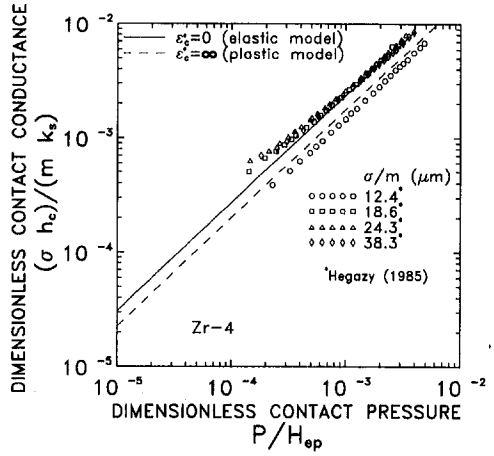

Fig. 6 Comparison of elastic and plastic asymptotic models with Zr–4 data (Hegazy, 1985) reduced using the elastic and the proposed elastoplastic model

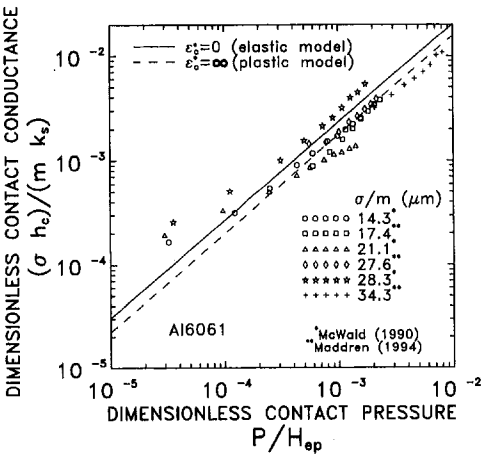

Fig. 7 Comparison of elastic and plastic asymptotic models with Al6061 data (McWaid, 1990; Maddren, 1994) reduced using the elastic and the proposed elastoplastic model

models. However, the data points at higher loads lie within the bounds. This material was found to be quite elastic in comparison to Ni200. The smoothest pair underwent fully elastic deformation.

Figure 6 shows another zirconium alloy Zr-4 compared with the elastic and the plastic models. The smoothest pair underwent predominantly elastic deformation. This data set lies outside the lower bound, i.e., the plastic model, whereas the other pairs underwent elastoplastic deformation. The rougher surface (σ/m = 18.6, 24.3, and 38.3) data sets lie slightly outside the bounds closer to the elastic model.

Figure 7 shows the comparison of Al6061 data from McWaid (1990) and Maddren (1994) reduced to dimensionless form and compared with elastic and plastic models. Except for the Maddren (1994) data set with σ/m = 34.3 μm, which underwent elastoplastic deformation, all the others underwent fully elastic deformation. It should be noted that the Nho (1990) Vickers hardness correlation was used to reduce the Maddren (1994) data set, which underwent elastoplastic deformation. One isotropic pair data from Maddren (1994) could not be reduced for comparison in this work because the corresponding microhardness correlations at cryogenic temperatures were unavailable.

Discussion and Concluding Remarks

The nondimensional strain $\epsilon_c^* = 1.67(E'/S_f)\cdot m$ is similar to the plasticity index proposed by Mikic (1974) except that the hardness H is replaced by a yield/flow stress S_f and a constant (1.67) appears here. This nondimensional strain is a combination of both the material and surface properties of a particular pair.

The comparisons of the two asymptotic models (elastic and plastic) with Ni200, SS304, and Zr–Nb data from Antonetti (1983), Hegazy (1985), McWaid (1990), and Maddren (1994) are excellent. The Ni200 data show significant plastic deformation. Only five out of eleven pairs of SS304 data underwent elastoplastic deformation, whereas the rest of them underwent fully plastic deformation.

The smoothest pairs of zirconium alloys Zr–Nb and Zr-4 show significant elastic deformation. The comparison of the Zr-4 data of the smoothest pair with the models is not satisfactory. This may be due to the errors in surface slope or hardness measurements. The McWaid (1990) and Maddren (1994) data obtained for isotropic similar metal pairs of Al6061 show considerable scatter.

For the first time thermal contact conductance data have been reduced using both the elastic and elastoplastic model. This new procedure for data reduction eliminates the dilemma of assuming a type of deformation a priori.

Surface slope m is an important parameter of the elastoplastic model and there is a need to determine this accurately. At this stage it is believed that the discrepancies between some data and the model are due to errors in the value of the surface slope. Future work should be aimed at obtaining a better estimate of the surface slope m.

Acknowledgments

The authors acknowledge the support of the Natural Science and Engineering Research Council of Canada under grant No. A7445.

References

Aikawa, T., and Winer, W. O., 1994, "Thermal Contact Conductance Across Si_3N_4–Si_3N_4 Contact," *Wear,* Vol. 177, pp. 25–32.

Antonetti, V. W., 1983, "On the Use of Metallic Coatings to Enhance Thermal Contact Conductance," Ph.D. Thesis, University of Waterloo, Canada.

Bush, A. W., Gibson, R. D., and Thomas, T. R., 1975, "The Elastic Contact of a Rough Surface," *Wear,* Vol. 35, pp. 87–111.

Chang, W. R., Etsion, I., and Bogy, D. B., 1987, "An Elastic-Plastic Model for the Contact of Rough Surfaces," ASME *Journal of Tribology*, Vol. 109, pp. 257–263.

Churchill, S. W., and Usagi, R., 1972, "A General Expression for the Correlations of Rates and Other Phenomena," *AIChE Journal,* Vol. 18, pp. 1121–1132.

Cooper, M. G., Mikic, B. B., and Yovanovich, M. M., 1969, "Thermal Contact Conductance," *Int. J. Heat Mass Transfer,* Vol. 12, pp. 279–300.

Foss, F. E., and Brumfield, R. C., 1922, "Some Measurements of the Shape of Brinell Ball Indentation," *Proceedings ASTM,* Vol. 22, p. 312.

Greenwood, J. A., and Williamson, J. B. P., 1966, "Contact of Nominally Flat Surfaces," *Proc. Roy. Soc. Lond.,* A295, pp. 300–319.

Hegazy, A. A., 1985, "Thermal Joint Conductance of Conforming Rough Surfaces," Ph.D. Thesis, University of Waterloo, Canada.

Ishigaki, H., Kawaguchi, I., and Mizuta, S., 1979, "A Simple Estimation of the Elastic-Plastic Deformation of Contacting Asperities," *Wear,* Vol. 54, pp. 157–164.

Johnson, K. L., 1985, *Contact Mechanics,* Cambridge University Press, Cambridge, United Kingdom.

Maddren, J., 1994, "Thermal Contact Resistance of Bolted Joints at Cryogenic Temperatures," Ph.D. Thesis, University of California, Santa Barbara.

Majumdar, A., and Bhushan, B., 1991, "Fractal Model of Elastic-Plastic Contact Between Rough Surfaces," ASME *Journal of Tribology,* Vol. 113, pp. 1–11.

McWaid, T. H., 1990, "Thermal Contact Resistance Across Pressed Metal Contact in a Vacuum Environment," Ph.D. Thesis, University of California, Santa Barbara.

Mikic, B. B., 1974, "Thermal Contact Conductance; Theoretical Considerations," *Int. J. Heat Mass Transfer,* Vol. 17, pp. 205–214.

Mikic, B. B., and Roca, R. T., 1993, "On Elastic Deformation of Rough Surfaces in Contact," personal communication from B. B. Mikic to M. M. Yovanovich.

Mathematica, 1988–91, A System for Doing Mathematics by Computer, Version 2.2 for DOS, Wolfram Research, Inc., Champaign, IL.

Nho, K. M., 1990, "Experimental Investigation of Heat Flow Rate and Directional Effect on Contact Conductance of Anisotropic Ground/Lapped Interfaces," Ph.D. Thesis, University of Waterloo, Canada.

Sridhar, M. R., and Yovanovich, M. M., 1994, "Review of Elastic and Plastic Contact Conductance Models: Comparison With Experiment," *Journal of Thermophysics and Heat Transfer,* Vol. 8, No. 4, Oct.–Dec., pp. 633–640.

Sridhar, M. R., 1994, "Elastoplastic Contact Models for Sphere-Flat and Conforming Rough Surface Applications," Ph.D. Thesis, University of Waterloo, Canada.

Tabor, D., 1951, *The Hardness of Metals,* Oxford University Press, London.

Whitehouse, D. J., and Archard, J. F., 1970, "The Properties of Random Surfaces of Significance in their Contact," *Proc. Roy. Soc. Lond.,* Vol. A316, pp. 97–121.

Yovanovich, M. M., 1982, "Thermal Contact Correlations, Spacecraft Radiative Transfer and Temperature Control," T. E. Horton, ed., Vol. 83 of Progress in Astronautics and Aeronautics, New York.

Yovanovich, M. M., Hegazy, A. A., and De Vaal, J., 1982, "Surface Hardness Distribution Effects Upon Contact, Gap and Joint Conductances," AIAA Paper No. 82-0887.

Yovanovich, M. M., Hegazy, A. A., and Antonetti, V. W., 1983, "Experimental Verification of Contact Conductance Models Based Upon Distributed Surface Micro-hardness," AIAA Paper No. 83-0532.

Yovanovich, M. M., and Hegazy, A. A., 1983, "An Accurate Universal Contact Conductance Correlation for Conforming Rough Surfaces With Different Microhardness Profiles," AIAA Paper No. 83-1434.

N. J. Ruperti, Jr.

M. Raynaud

J. F. Sacadura

Centre de Thermique-URA CNRS 1372,
Institut National des Sciences
Appliquées de Lyon,
69621-Villeurbanne Cedex, France

A Method for the Solution of the Coupled Inverse Heat Conduction-Radiation Problem

The inverse problem of estimating surface temperatures and fluxes from simulated transient temperatures measured within a semitransparent slab is studied. A space-marching technique, whose performance is already known for the solution of the inverse heat conduction problem (IHCP), is adapted to solve an inverse heat conduction-radiation problem (IHCRP). An iterative algorithm is proposed. Different values of the conduction-to-radiation parameter are considered in order to show, with benchmark test cases, the effects of the radiative heat transfer mode on the performance of the inverse method.

Introduction

Semitransparent materials are widely used in buildings, solar energy installations, and high-temperature systems. In such thermal systems it is often necessary to know the surface temperature or the temperature profile within the semitransparent medium. At elevated temperatures the energy transfer is dominated by radiation, which makes it more difficult to predict the internal temperature distribution due to the nonlinear behavior of the problem. This nonlinear characteristic increases the time of numerical simulations, giving results that are strongly dependent on the temperature range. There are two ways to determine the temperature distribution within a semitransparent medium. The first one is by the solution of a direct problem, when the properties of the medium and the boundary conditions are known, then the temperature profile and the radiation intensities can be calculated. In the second one, the boundary conditions are to be estimated from the knowledge of the internal temperature readings or from the measured exit radiation data. The problem is called an inverse radiation problem (IRP) when the temperature profile or the boundary conditions are to be estimated from external radiation data. When the temperature distribution in a semitransparent solid is estimated from transient temperature measurements within the solid, the inverse problem is called an inverse heat conduction-radiation problem (IHCRP). In the IHCRP the energy equation with a radiative source term is used, while the IRP just involves the equation of radiative transfer.

The literature review shows that inverse methods have been used for the analysis of the three different modes of heat transfer: conduction, convection, and radiation. The use of inverse methods allows for the determination of thermophysical properties and for the estimation of the temperature distribution and unknown boundary conditions by internal or external measurements. Some examples of inverse solutions will be briefly shown in the following paragraphs.

A considerable amount of work has been done in the past three decades for the study of inverse problems in heat conduction. The inverse heat conduction problem (IHCP) is the estimation of surface heat flux and temperature histories from transient temperatures measured within an opaque solid (Beck et al., 1985). Another type of time-dependent inverse problem in heat conduction deals with the determination of thermal properties from transient temperature measurements (Beck and Arnold, 1977). The main difference between these inverse problems is that in the IHCP, the unknown surface heat flux histories can be arbitrary or adjustable by humans making this problem more involved than the parameter estimation problem. The IHCP is an ill-posed problem, so small inaccuracies in the measured interior temperatures can cause large oscillations in the calculated surface conditions. Several numerical procedures have been proposed to reduce the sensitivity to measurement errors. Unfortunately, in all of the inverse techniques, it has been shown (Hills et al., 1986; Raynaud and Beck, 1988) that greater stability is only achieved with a loss of resolving power. A recent review in the IHCP can be found in Hensel (1991) and Murio (1993).

An example of inverse problem in heat convection was presented by Huang and Özişik (1992) where a combination of the regular and modified conjugate gradient method was used to determine the unknown wall heat flux in a parallel plate duct. The spacewise variation of the wall heat flux was obtained from the temperature variations inside the fluid at several different locations.

In inverse radiation problems, the radiative properties or the internal temperatures are determined from internal or external measurements. Remote measurements of exit radiative intensities have been used for determining radiative properties such as optical thickness and phase function (Nicolau et al., 1994; Matthews et al., 1984; Sakami and Lallemand, 1993). Remote sensing was also employed for the estimation of the temperature profile in atmospheres, or in semitransparent solids (Viskanta et al., 1975; Sakami and Lallemand, 1993; Mann and Viskanta, 1995). Li and Özişik (1993) used the conjugate gradient technique for simultaneous estimation of temperature profile and surface reflectivity in an absorbing, emitting, and isotropically scattering gray medium. The estimation was based on simulated exit radiation intensities.

Some attempts have been made to estimate the thermal properties in inverse problems involving combined conduction and radiation heat transfer. Andre and Degiovanni (1992) have used an extension of the flash technique for measuring the diffusivity of glass at temperatures up to 800 K. Direct techniques have been applied to determine thermal properties in semitransparent materials. Matthews et al. (1984) determined the thermal capacity and the thermal conductivity of zirconia samples from temperature measurements obtained within a semitransparent medium. These techniques, as was noted by Field and Viskanta (1993), are the only ones presently available for obtaining reliable internal temperature data. The difficulty of obtaining time-dependent internal temperature measurements in sheets of glass was minimized in that work. A new thermocouple installation

Contributed by the Heat Transfer Division for publication in the JOURNAL OF HEAT TRANSFER. Manuscript received by the Heat Transfer Division April 1995; revision received August 1995. Keywords: Numerical Methods, Radiation Interactions, Transient and Unsteady Heat Transfer. Associate Technical Editor: M. F. Modest.

method was developed to allow the placement of thermocouples throughout the interior of glass test plates and assured excellent thermal contact.

The purpose of this paper is to present a thorough discussion of the solution of a IHCRP (Ruperti et al., 1995). A space-marching technique (Raynaud and Bransier, 1986a, b) is adapted to consider inverse problems where radiative transfer must be taken into account. The use of this inverse technique allows for the estimation of the internal radiation fluxes, temperature distribution, and the surface heat flux histories, from transient temperature measurements within the semitransparent solid. Some test cases initially employed to measure the performance of different inverse methods for the IHCP (Raynaud and Beck, 1988) are used to evaluate the behavior of this method for the IHCRP. The present analysis considers a semitransparent gray slab bounded by infinite black walls and various initial temperature profiles to show the influence of radiation on the inverse solution. All the results are compared with benchmark solutions available for the IHCP.

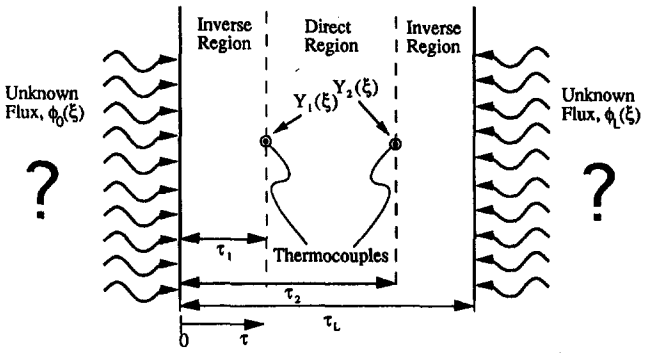

Fig. 1 Surface heat flux estimation in a semitransparent slab

Inverse Problem Formulation

The physical model of the one-dimensional plane-parallel slab considers simultaneous radiation and conduction heat transfer as illustrated in Fig. 1. The IHCRP consists of estimating the two surface heat fluxes $\phi_0(\xi)$, $\phi_L(\xi)$ and the temperature histories in the whole domain from internal temperature measurements. A more tedious problem would be to estimate simultaneously the radiative boundary conditions. The feasibility of such an estimation has not yet been studied. This work is limited to the case of a homogeneous, gray, nonscattering semitransparent medium with constant thermophysical properties bounded by two infinite black surfaces.

The objective is to quantify, by numerical simulations, the accuracy with which the unknown boundary conditions can be determined. The input data for the IHCRP, instead of being measured temperatures, are predicted from the solution of a direct problem for a given set of boundary conditions.

Direct Problem Formulation

The governing equation for the coupled conductive and radiative heat transfer in the semitransparent slab is in dimensionless form:

$$\frac{\partial\theta(\tau,\xi)}{\partial\xi}=\frac{\partial^2\theta(\tau,\xi)}{\partial\tau^2}-\frac{1}{N}\frac{\partial Q^r(\tau,\xi)}{\partial\tau},\qquad \xi>0,\quad 0\le\tau\le\tau_L \quad (1a)$$

with the initial and boundary conditions:

$$\theta(\tau,\xi)=\theta_0,\quad \xi=0,\quad 0\le\tau\le\tau_L \quad (1b)$$

$$-\frac{\partial\theta(\tau,\xi)}{\partial\tau}+\frac{Q^r(\tau,\xi)}{N}=\phi_0(\xi),\quad \tau=0,\quad \xi>0 \quad (1c)$$

Nomenclature

k = thermal conductivity
L = slab thickness
q_0 = incident heat flux density at $\tau = 0$
q_L = incident heat flux density at $\tau = \tau_L$
q_{max} = maximum value of the surface heat flux density
q^c = conductive heat flux density
q^r = radiative heat flux density
T_0 = initial temperature
T_r = reference temperature
t = time
x = distance from heated surface
κ = absorption coefficient
$\bar{\sigma}$ = Stefan–Boltzmann constant = 5.6699×10^{-8} W/m^{2}K^4

Dimensionless Groups and Parameters

B_1 = first measure of the bias (Eq. (14))
B_2 = second measure of the bias (Eq. (15))
M = total number of grid points
N = conduction-to-radiation parameter = $k\kappa/4n^2\bar{\sigma}T_r^3$
n = refraction index
Q_0 = estimated heat flux at $\tau = 0$ (Eq. (12))
Q^c = conductive heat flux; $Q^c(\tau, \xi) = q^c(x, t)/k\kappa T_r$
Q^r = radiative heat flux; $Q^r(\tau, \xi) = q^r(x, t)/4n^2\bar{\sigma}T_r^4$
S = standard deviation (Eq. (20))
w = weights of Gauss–Legendre quadrature (Eq. (9)) and width of the gaussian filter (Eq. (21))
Y_1, Y_2 = temperature histories at the first and second thermocouple locations
Y_1^*, Y_2^* = filtered temperatures at the first and second thermocouple locations (Eq. (21))
α = thermal diffusivity
$\Delta\tau$ = space step
$\Delta\xi$ = time step
ϵ = random variable
ϕ_0 = incident heat flux at $\tau = 0$; $\phi_0(\xi) = q_0(t)/k\kappa T_r$
ϕ_L = incident heat flux at $\tau = \tau_L$; $\phi_L(\xi) = q_L(t)/k\kappa T_r$
ϕ_{max} = maximum value of the surface heat flux = $q_{max}/k\kappa T_r$
Φ^r = radiative heat fluxes calculated by the solution of the direct problem (Eq. (9))
θ = temperature; $\theta(\tau, \xi) = T(x, t)/T_r$
θ_0 = initial temperature = T_0/T_r
σ = standard deviation (Eq. (17))
τ = space coordinate = κx
τ_1 = first thermocouple location
τ_2 = second thermocouple location
τ_L = optical thickness = κL
ξ = time = $\alpha\kappa^2 t$
ξ_0 = instant of the impulse
Ψ = temperatures calculated by the solution of the direct problem (Eq. (10a))

Subscripts

0 = initial condition
i = grid space index
j = node number at $\tau = \tau_1$

Superscripts

c = conductive flux
m = final time
n = time index
r = radiative flux

$$-\frac{\partial\theta(\tau,\xi)}{\partial\tau}+\frac{Q^r(\tau,\xi)}{N}=\phi_L(\xi),\quad \tau=\tau_L,\quad \xi>0 \quad (1d)$$

where the dimensionless quantities are defined in the nomenclature. Note that N, the conduction-to-radiation parameter, indicates the relative magnitude of the two heat transfer modes. The smaller N, the larger is the radiation mode.

The hypothesis made for the formulation of the radiative problem allows one to obtain an exact solution of the equation of radiative transfer (Özişik, 1973). The radiative source term, $Q^r(\tau,\xi)$, can be calculated when the slab temperature profile, $\theta(\tau,\xi)$, is known:

$$Q^r(\tau,\xi)=\frac{1}{2}\left[\theta^4(0,\xi)E_3(\tau)+\int_0^\tau\theta^4(\tau',\xi)E_2(\tau-\tau')d\tau'\right]-\frac{1}{2}\left[\int_\tau^{\tau_L}\theta^4(\tau',\xi)E_2(\tau'-\tau)d\tau'+\theta^4(\tau_L,\xi)E_3(\tau_L-\tau)\right],\quad 0\le\tau\le\tau_L \quad (2)$$

where $E_i(\tau)$ are the exponential integrals. This is equivalent to Eq. (8-84) in Özişik (1973) for the special case of black wall radiative boundary conditions.

Solution of the Nonlinear Inverse Problem

The space-marching technique proposed by Raynaud and Bransier (1986a, b) is adapted to consider the radiative heat source of Eq. (1a). In fact three distinct problems can be studied. The first one is for two internal temperature measurements as shown in Fig. 1, which leads to two inverse regions. The second case occurs when one of the temperature measurements is done on one surface, thus only one inverse region arises. The last possibility is to have known temperature and heat flux histories at one point. These three cases are very similar and the technique developed to solve one of these problems can be easily adapted for the solution of the other ones. Herein to facilitate the comparison with previous works (Raynaud and Beck, 1988), the case of measurements at $\tau_1=\tau_L/2$ and $\tau_2=\tau_L$ is chosen. For this IHCRP the set of equations is Eqs. (1a) and (1b) along with:

$$-\frac{\partial\theta(\tau,\xi)}{\partial\tau}+\frac{Q^r(\tau,\xi)}{N}=?,\quad \tau=0,\quad \xi>0 \quad (3a)$$

$$\theta(\tau,\xi)=Y_1(\xi),\quad \tau=\tau_L/2,\quad \xi>0 \quad (3b)$$

$$\theta(\tau,\xi)=Y_2(\xi),\quad \tau=\tau_L,\quad \xi>0 \quad (3c)$$

The slab thickness is divided into a direct and an inverse region as shown in Fig. 1. The problem in the direct region $\tau_1\le\tau\le\tau_2$ is a boundary value problem with boundary conditions of the first kind given by the simulated temperature measurements Y_1 and Y_2.

The space marching method uses finite differences to approximate the energy equation. Central difference approximations for the three derivatives of Eq. (1a) lead to:

$$\frac{\theta_i^{n+1}-\theta_i^{n-1}}{2\Delta\xi}=\frac{Q_{i-1/2}^{c^n}-Q_{i+1/2}^{c^n}}{\Delta\tau}-\frac{1}{N}\frac{Q_{i+1}^{r^n}-Q_{i-1}^{r^n}}{2\Delta\tau} \quad (4)$$

In all stable inverse methods a bias must be introduced to decrease the sensitivity to measurement errors (Beck et al., 1982; Hensel and Hills, 1986; Raynaud and Beck, 1988). For this space-marching method the bias is obtained as follows:

$$Q_{i+1/2}^{c^n}=\frac{Q_{i+1/2}^{c^{n+1}}+Q_{i+1/2}^{c^{n-1}}}{2} \quad (5)$$

This time averaging accounts for the time lag due to the diffusion of heat in solids. On the other hand, the radiative heat transfer being almost instantaneous, it is not necessary to make such an approximation for the radiative source terms.

Using central differences to evaluate the conductive heat flux densities:

$$Q_{i+1/2}^{c^n}=-\frac{1}{2}\left[\frac{\theta_{i+1}^{n+1}-\theta_i^{n+1}}{\Delta\tau}+\frac{\theta_{i+1}^{n-1}-\theta_i^{n-1}}{\Delta\tau}\right] \quad (6a)$$

$$Q_{i-1/2}^{c^n}=-\frac{\theta_i^n-\theta_{i-1}^n}{\Delta\tau} \quad (6b)$$

The substitution of Eqs. (6) into Eq. (4) leads to an explicit relation to estimate the temperature in the inverse region:

$$\theta_{i-1}^n=\theta_i^n+\frac{\Delta\tau^2}{2\Delta\xi}(\theta_i^{n+1}-\theta_i^{n-1})+\frac{1}{2}(\theta_i^{n+1}-\theta_{i+1}^{n+1}+\theta_i^{n-1}-\theta_{i+1}^{n-1})+\frac{\Delta\tau}{2N}(Q_{i+1}^{r^n}-Q_{i-1}^{r^n}) \quad (7)$$

In this method, the stability increases with the number of grid points since the bias is introduced by Eq. (5) at each step. Consequently, the larger the number of steps, the larger is the bias. The computational molecule is shown in Fig. 2. The temperature at node $i-1$ and time n is calculated from temperatures at times $n+1$ and $n-1$, called future and past temperatures, respectively. However, it is necessary to know the radiative source terms to estimate the temperature field from Eq. (7) but the calculation of the former requires the knowledge of the later. Thus an iterative process must be used. The following iterative algorithm is proposed to solve the nonlinear inverse heat conduction-radiation problem:

Step 1—Solve the energy equation in the direct region without considering the radiative source terms. This is a linear direct heat conduction problem that can be solved by any stable technique.

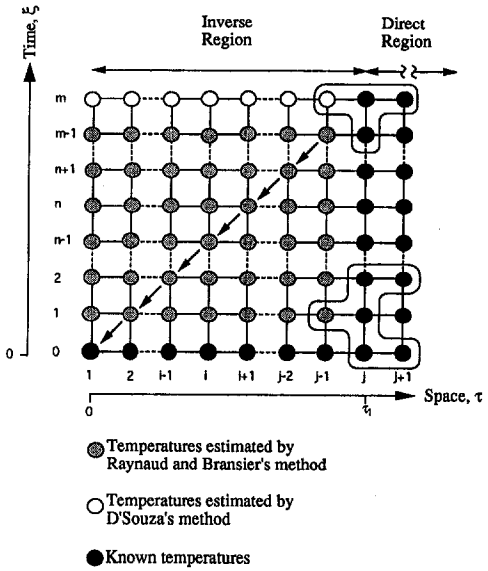

Fig. 2 Computational molecules used to march in space

Step 2—Solve the energy equation in the inverse region (Eq. (7)) without considering the radiative source terms. The unknown surface temperature history is then broadly estimated.

Step 3—Compute the radiative source terms from the solution of the energy equation combined to the radiative transfer formal solution (Eqs. (1) and (2)) in the whole domain, with the boundary conditions given by the temperatures measured at $\tau = \tau_L$ and the surface temperatures ($\tau = 0$) computed in Step 2 for the first iteration, and Step 5 for the other iterations.

Step 4—Solve the energy equation in the direct region with the radiative flux profiles computed in Step 3.

Step 5—Solve the energy equation in the inverse region with the source terms computed in Step 3 and the temperatures at node j (simulated measurements) and node $j + 1$ (calculated in Step 4).

Step 6—Continue the iteration (Steps 3 to 5) until the convergence of the temperatures at $\tau = 0$, then calculate the unknown surface heat flux. Otherwise, under-relax the surface temperatures and go to Step 3.

Each of the steps is now briefly presented.

Step 3. The energy equation, Eq. (1a), with the boundary conditions given by the surface temperatures computed in Step 5 and the temperatures measured at $\tau = \tau_L$ is solved by a finite difference method. Central differences are used to approximate the partial derivatives of the right-hand side:

$$\frac{d\psi_i^n}{d\xi} = \frac{(\psi_{i+1}^n - \psi_i^n)/\Delta\tau_{i+1} - (\psi_i^n - \psi_{i-1}^n)/\Delta\tau_i}{(\Delta\tau_{i+1} + \Delta\tau_i)/2} - \frac{1}{N}\frac{(\Phi_{i+1}^{r^n} - \Phi_{i-1}^{r^n})}{\Delta\tau_{i+1} + \Delta\tau_i}, \quad \xi > 0 \quad (8)$$

The exact solution of the radiative fluxes is used to express the source term of Eq. (8) in terms of temperatures. The integrals of Eq. (2) are computed with a Gauss–Legendre quadrature rule:

$$\Phi_i^{r^n}(\xi) = \frac{1}{2}\theta_1^{n^4}E_3(\tau_i) - \frac{1}{2}Y_2^{n^4}E_3(\tau_L - \tau_i) + \frac{1}{2}\sum_{k=1}^{60} w_k \frac{(\tau_i - \tau_k)}{|\tau_i - \tau_k|}\psi_k^{n^4}E_2(|\tau_i - \tau_k|) \quad (9)$$

Thus a nonuniform computational grid, coincident with the quadrature points, is used. To obtain accurate results, 60 quadrature points are required. It results in a system of 60 nonlinear first-order differential equations. A backward second-order approximation (Tseng and Chu, 1992) of the time derivative is used to transform the system of nonlinear differential equations into a system of nonlinear algebraic equations:

$$\frac{1}{2\Delta\xi}(3\psi_i^n - 4\psi_i^{n-1} + \psi_i^{n-2}) - \frac{(\psi_{i+1}^n - \psi_i^n)/\Delta\tau_{i+1} - (\psi_i^n - \psi_{i-1}^n)/\Delta\tau_i}{(\Delta\tau_{i+1} + \Delta\tau_i)/2} + \frac{1}{N}\frac{(\Phi_{i+1}^{r^n} - \Phi_{i-1}^{r^n})}{\Delta\tau_{i+1} + \Delta\tau_i} = 0 \quad \text{for} \quad i = 1, 2, \ldots, 60, \quad \text{and} \quad n = 2, 3, \ldots, m \quad (10a)$$

where

$$\psi_i^0 = \theta_0, \quad \xi = 0, \quad i = 1, 2, \ldots, 60 \quad (10b)$$

$$\psi_0^n = \theta_1^n, \quad \xi > 0, \quad n = 2, 3, \ldots, m \quad (10c)$$

$$\psi_{61}^n = Y_2^n, \quad \xi > 0, \quad n = 2, 3, \ldots, m \quad (10d)$$

The results given by this backward second-order approximation were compared and validated with the ones obtained with the ISML routine DIVPAG (Gear's method). However, in the inverse solution, the later routine cannot be used because the time step must be constant and moreover the former method is quicker.

The nature of the radiative source terms requires iterations to be performed at each time interval to satisfy the local thermodynamic equilibrium condition. Newton–Raphson's method is used to solve the nonlinear system of algebraic equations, where the Jacobians are numerically computed by a finite difference approximation. The temperature profile computed in the previous time step is used as the initial guess to start the iterative process at each time step. For each time step the converged temperature profile is used to calculate the radiative flux profile that is used as input in Steps 4 and 5.

Step 4. The computations in the direct region are performed using a uniform node distribution and central finite difference approximations of the energy equation. The boundary conditions in this case are the measured temperatures at $\tau_L/2$ and at τ_L. The implicit time-marching scheme used in Eq. (10a) is employed, leading to a tridiagonal system of linear equations that can be solved by a standard routine. However, due to the incompatibility between the computational grid used in radiative heat source calculations (Step 3) and the one used in the direct and inverse regions (Steps 4 and 5), the radiative heat sources must be interpolated. The routine DQDVAL from the IMSL math library, which evaluates a function defined on a set of points using quadratic interpolation, is used to perform the interpolations.

Step 5. The calculation of the temperature field in the inverse region proceeds from the measurement node $i = j$ to the surface node $i = 1$. Since Eq. (7) involves one future temperature, it only allows one to estimate the temperature at any spatial node i from the initial time $n = 0$ up to the time $n = m - j + i$ as indicated by the arrows in Fig. (2) (see Raynaud and Bransier, 1986a). But the calculations of the radiative source terms, Step 3, require that the temperature must be known over the complete spatial domain. Thus it is necessary to calculate the temperatures at the nodes located above the arrows. One solution is to use a less stable relation that does not introduce future temperatures. The explicit relation, proposed by D'Souza (1975) for the IHCP, which corresponds to the classical pure implicit scheme for heat conduction has been chosen. The computational molecule of D'Souza, modified to consider the radiative source terms, is shown in Fig. (2) and is expressed as:

$$\theta_{i-1}^m = 2\theta_i^m - \theta_{i+1}^m + \frac{\Delta\tau^2}{\Delta\xi}(\theta_i^m - \theta_i^{m-1}) + \frac{\Delta\tau}{2N}(Q_{i+1}^{r^m} - Q_{i-1}^{r^m}) \quad (11)$$

Thus at each step toward the surface, Eq. (7) is used for $n = 1$ to $m - 1$ while Eq. (11) is used for $n = m$. Consequently the four-point computational molecule is only employed to determine the temperature for the last time step as indicated by the open circle in Fig. 2.

Step 6. The total surface heat flux is calculated from the converged temperature field, using an energy balance at the surface node. Central finite-difference approximations are used to derive, from the energy equation, the following expression:

$$Q_0^n = \frac{(\theta_1^n - \theta_2^n)}{\Delta\tau} + \frac{\Delta\tau}{4\Delta\xi}(\theta_1^{n+1} - \theta_1^{n-1}) + \frac{1}{2N}(Q_2^{r^n} + Q_1^{r^n}) \quad (12)$$

Test Cases

Some test problems were selected to analyze the performance of the inverse solution in situations where radiation and conduc-

tion are of the same order of magnitude. These test cases were initially defined to evaluate the performance of inverse methods for the IHCP. Hence, all the results that are obtained for the IHCRP can be compared with available benchmark solutions for the IHCP. These test cases correspond to a slab insulated on the surface $\tau = \tau_L$, $\phi_L(\xi) = 0$, with an imposed time-dependent heat flux, $\phi_0(\xi)$, on the other surface.

Some assumptions have been made in the problem formulation, for example the hypothesis of a gray semitransparent medium, which has limited real applications. However, the thermophysical properties and other input data were chosen so as to correspond to average values of a semitransparent material. The chosen input data are:

$$\kappa = 100\ \mathrm{m}^{-1};\quad k = 0.1\ \mathrm{W/mK};\quad n = 1;$$

$$q_{\max} = 1000\ \mathrm{W/m}^2;\quad L = 0.01\ \mathrm{m};\quad \alpha = 10^{-6}\ \mathrm{m}^2/\mathrm{s}$$

where $q_{\max}$ is the maximum value of the total heat flux.

The first test cases considered are those introduced by Raynaud and Beck (1988). Their purpose is to show the tradeoff that exists between the deterministic bias, i.e., the resolving power, and the sensitivity to measurement errors. The first test case estimates the deterministic error for a heat impulse that is constant over just one time step, where $q_{\max} = 1000\ \mathrm{W/m}^2$, and zero at other times:

$$\phi_0(\xi) = \begin{cases} 0, & \xi < \xi_0 - \Delta\xi/2 \text{ or } \xi > \xi_0 + \Delta\xi/2 \\ \phi_{\max}, & \xi_0 - \Delta\xi/2 \le \xi \le \xi_0 + \Delta\xi/2 \end{cases} \tag{13}$$

This impulse flux is the smallest temporal fluctuation that can be estimated. The better the estimation of the impulse flux, the higher is the resolving power of the method or the lower the deterministic bias. One measure of the deterministic bias is the relative difference between the exact heat flux and the heat flux estimated at the time of the impulse:

$$B_1 = 1 - Q_0(\xi_0)/\phi_{\max} \tag{14}$$

Another measure of the deterministic bias is the normalized square root of the sum of the squares of the deviations of the estimated heat fluxes, $Q_0(\xi_n)$, from the exact heat fluxes, $\phi_0(\xi_n)$:

$$B_2 = \frac{1}{\phi_{\max}} \left[\sum_{n=1}^{m} (\phi_0^n - Q_0^n)^2 \right]^{1/2} \tag{15}$$

where m is the number of time steps. Notice that the values of B_1 and B_2 have been normalized with regard to $\phi_{\max}$ to allow comparisons with the IHCP benchmark solutions.

The second test case gives the sensitivity to measurement errors of the inverse algorithm. In practical applications the temperature histories at the measurement locations are known as discrete functions of time. In any realistic experiment these discrete temperatures are contaminated by noise. The case where the temperature measured at the first thermocouple location equals the initial temperature, except for the temperature at time ξ_0, which is equal to the initial temperature increased by 1 K is considered:

$$Y_1(\xi) = \begin{cases} \theta_0 + 1/T_r, & \xi = \xi_0 \\ \theta_0, & \xi \ne \xi_0 \end{cases} \tag{16}$$

If this error were absent, all of the input temperatures would not change from the initial values and the estimated surface heat flux would be zero. Hence, the standard deviation of the estimated surface flux (Hills et al., 1986) can be evaluated by:

$$\sigma = \left(\sum_{n=1}^{m} Q_0^{n^2} \right)^{1/2} \tag{17}$$

For a linear problem, a 2 K single error would produce a standard deviation twice as large (Hills et al., 1986). For a nonlinear problem, such as the IHCRP, this property is not valid anymore but the case of a 1 K single error has been chosen.

The dimensionless time $\xi_0 = 10\Delta\xi$ was selected for the heat impulse and the standard deviation test cases (Raynaud and Beck, 1988). The values of σ and B_2 will depend on the end time if the values of the heat flux estimates are not given adequate time to approach zero, or if the method produces oscillatory results or is unstable. For a well-behaved estimation, the test case must be long enough to ensure that the estimates have returned to zero; herein, the test cases were performed with 25 time steps, i.e., $m = 25$.

Although these two test cases enable the comparison of inverse methods and give insights into their behavior when the introduced bias varies, it is also interesting to study a classical problem. An incident flux that varies in a triangular fashion is studied. The surface heat flux has a linear stepwise variation between zero and $q_{\max} = 1000\ \mathrm{W/m}^2$:

$$\phi_0(\xi) = \begin{cases} 0, & \xi < 0.1 \text{ or } \xi > 0.3 \\ 10\phi_{\max}(\xi - 0.1), & 0.1 \le \xi \le 0.2 \\ 10\phi_{\max}(0.3 - \xi), & 0.2 \le \xi \le 0.3 \end{cases} \tag{18}$$

Three situations are considered for the estimation of the surface heat flux histories from the temperature histories at $\tau = \tau_L/2$ and $\tau = \tau_L$: exact data (predicted values), simulated experimental data, and noisy filtered data. In order to simulate experimental data, the following procedure was used. A thermocouple was immersed in icy water. The signal was recorded at a 100 Hz frequency during 20 seconds with a 16-bit Keithley 500 data acquisition system. The mean value was calculated and subtracted from the signal. Finally, this noise was normalized between -1 and 1. The contaminated input data are then calculated with the following relations:

$$Y_1(\xi) = \theta(\tau_L/2, \xi) + \epsilon/T_r, \quad \tau = \tau_L/2$$
$$Y_2(\xi) = \theta(\tau_L, \xi) + \epsilon/T_r, \quad \tau = \tau_L \tag{19}$$

where ϵ represents successive data points of this experimental noise. The first 80 points are used to contaminate the temperature at $\tau = \tau_L/2$ and the following 80 points for $\tau = \tau_L$. The mean value, the standard deviation, and the correlation coefficient are -0.042, 0.350, and 0.24×10^{-7}, respectively, for the first 80 points and -0.019, 0.310, and 0.33×10^{-7} for the next 80 points. We believe that it is preferable to use such a procedure, based on a real experimental noise, rather than a random noise generated by a numerical routine. The standard deviation of the estimated heat flux is, in this case, evaluated by:

$$S = \frac{1}{\phi_{\max}} \left[\frac{1}{m} \sum_{n=1}^{m} (\phi_0^n - Q_0^n)^2 \right]^{1/2} \tag{20}$$

It has been shown (Raynaud, 1986) that better results can be obtained if the data are smoothed prior to the inversion. The measured temperature is replaced by a linear combination of past and future measurements. The filtered temperatures are evaluated by the following expression:

$$Y_k^*(\xi_i) = \sum_{s=1}^{w} Z_s Y_k(\xi_{i+s-(w+1)/2}), \quad k = 1, 2 \tag{21}$$

where w, the width of the filter, is an odd integer and Z_s are the weighting coefficients. The coefficients for the gaussian filter used to smooth the contaminated data are:

$$Z_s = \frac{e^{-2\pi \left(\frac{w + 1 - 2s}{w - 1} \right)^2}}{\sum_{i=1}^{w} Z_i}, \quad s = 1, 2, \ldots, w \tag{22}$$

This filtering technique is equivalent to the mollification procedure used by Murio to stabilize some inverse problems (Murio, 1993).

Numerical Results

The performance of the proposed inverse method for a given time step with different values of the conduction-to-radiation parameter, N, is studied first. Three values of N were chosen to show the influence of the radiative transfer on the inverse solution: $N \rightarrow \infty$ (pure conduction), $N = 0.1$, and $N = 0.05$. For the purely conductive case, the initial temperature $T_0 = 773$ K is chosen. The same initial condition, $T_0 = 773$ K, is considered for $N = 0.1$, while $T_0 = 973.93$ K is used in the most radiative case, $N = 0.05$.

The performance of the method is evaluated, Fig. 3, for each value of N by plotting on the same graph the standard deviation of the estimates, σ, versus the deterministic bias, B_2, both functions of the number of grid points, M. Several values of M were used to plot each curve; see the numbers on the curves. Figure 3 shows the tradeoff that exists between the resolving power and the sensitivity to measurement errors. In all situations, the sensitivity to measurement errors can only be decreased by increasing the bias. For this inverse method the introduced bias increases with M. For a given number of grid points, the inverse solutions for the radiative cases are more accurate and more sensitive to measurement errors than the inverse solution for the pure conductive case. This is due to the separation of the total heat flux in two components: a radiative and a conductive part. At $\tau = 0$ and $\xi = \xi_0$, the radiative flux represents 44 and 61 percent of the total heat flux for $N = 0.1$ and 0.05, respectively. As the bias is only introduced in the conductive part of the heat flux, for small values of N the inverse method will be less sensitive to changes in M. This implies, as shown by Fig. 3, that more nodes must be used for highly radiative cases to obtain a weak sensitivity to measurement noises. For example, the three curves almost cross for $B_2 = 0.9$ but only 31 nodes are used for the pure conductive case, while 71 are necessary for the most radiative case.

The quantitative tradeoff between the standard deviation and the bias shown by Fig. 3 is only valid for a particular time step, $\Delta\xi = 0.01$. The influence of the time step for the three situations is now quantified. The two measures of the bias B_1 and B_2, given by Eqs. (14) and (15), depends very weakly on the time steps and N. B_1 ranges from 0.84 to 0.87 while B_2 ranges from 0.88 to 0.91 when $\Delta\xi$ is varied from 0.005 to 0.05. On the other hand, the standard deviation σ, Eq. (17), depends greatly on these two parameters as shown in Table 1 for $\Delta\xi = 0.005$, 0.01, and 0.05. Table 1 clearly shows that the sensitivity to measurement errors increases when the time step decreases. This is particularly true for the pure conductive case for which σ increases more than 20 times when $\Delta\xi$ is decreased from 0.05 to 0.005. This phenomenon is well known (Beck et al., 1985; Hensel, 1991): It is due to the fact that in heat diffusion the high frequencies are largely attenuated contrary to the low frequencies. In the inverse analysis, the use of small time step means that high frequencies are sought, which evidently is the most difficult task since they are the most attenuated. On the contrary, since radiation is instantaneous, a semitransparent slab does not attenuate high frequencies as much as an opaque slab. That explains why S decreases when N decreases. In the algorithm, the bias is only introduced on the conduction flux. When N decreases, the conduction flux decreases; thus, in order to maintain the same bias, it is necessary to increase the number of grid points. As an example, for $\Delta\xi = 0.01$, a constant bias is obtained with $M = 31$, 61, and 71 for $N \rightarrow \infty$, 0.1, and 0.05, respectively.

Table 1 Standard deviation of the estimates σ for different values of $\Delta\xi$ and N

N \ $\Delta\xi$	0.005	0.01	0.05
N →∞ (M=31)	0.084	0.021	0.004
N=0.1 (M=61)	0.050	0.021	0.012
N=0.05 (M=71)	0.042	0.023	0.017

The results obtained for the triangular pulse test case are now studied. The estimated heat flux with exact and noisy data are shown Fig. 4 by the line with open triangles and black triangles, respectively. Similar results are obtained for other N values. The estimated and exact heat fluxes at $\tau = 0$ for the pure conductive case and for $N = 0.05$ with noisy filtered data are shown Fig. 5. The conductive and the radiative parts of the estimated heat flux are also shown; the radiative flux dominates. It demonstrates that the radiative transfer does not make the problem more ill posed. Table 2 summarizes the standard deviation of the estimated flux for exact, noisy, and noisy filtered data. The noisy input data were smoothed with a gaussian filter, Eqs. (21) and (22), of bandwidth $w = 5$. Table 2 indicates that

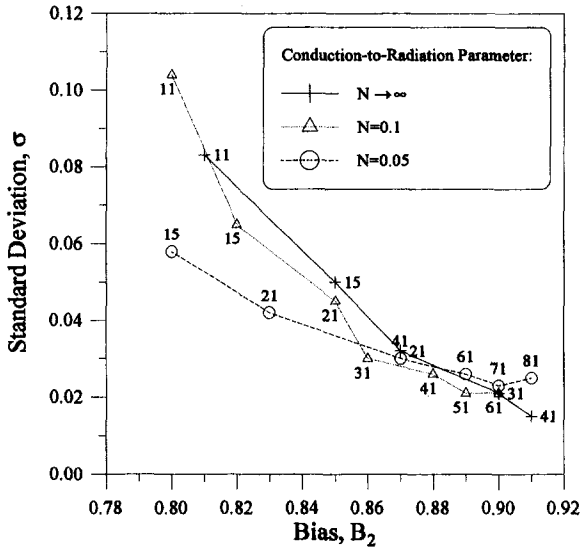

Fig. 3 Tradeoff between random error sensitivity and bias of the inverse solution for the three values of the conduction-to-radiation parameter, N; $\Delta\xi = 0.01$

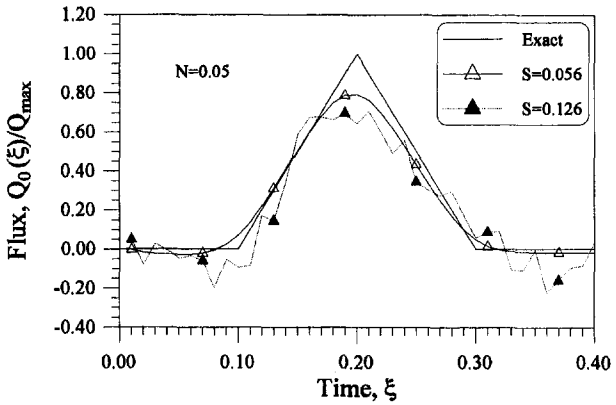

Fig. 4 Comparison between true heat flux and estimated heat flux at $\tau = 0$ for $N = 0.05$, $M = 71$, and $\Delta\xi = 0.01$, using exact (open triangles) and noisy input data (dotted line)

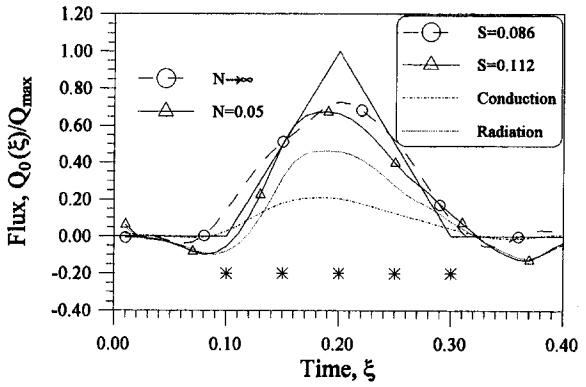

Fig. 5 Comparison between true heat flux and estimated heat flux at $\tau = 0$ for $N \to \infty$, $M = 31$ (open circles), and $N = 0.05$, $M = 71$ (open triangles), using noisy filtered input data. The asterisks correspond to the times chosen to plot the temperature profiles in Figs. 6 and 7. The dashed and dotted lines represent the contribution of conduction and radiation to the total heat flux.

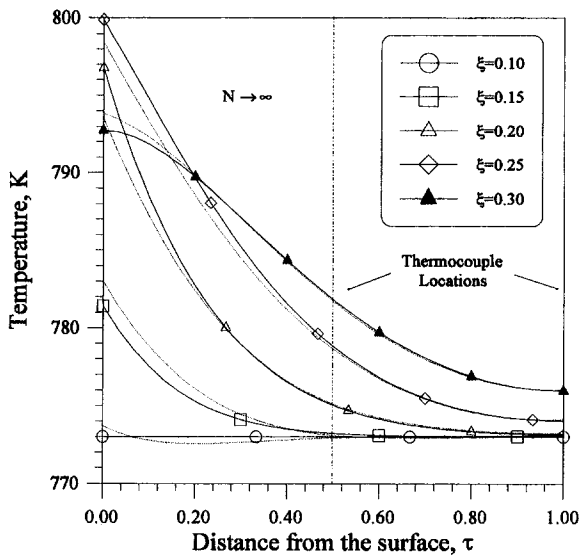

Fig. 6 Comparison between true (solid lines) and estimated (dotted lines) temperature profiles for the pure conductive case ($N \to \infty$) with $M = 31$ and $\Delta\xi = 0.01$, using filtered input data

the worst cases correspond to the noisy unfiltered data. It shows that the inverse method is slightly more accurate for lower values of N when exact data are used. With noisy data the results present an opposite trend: The most radiative case is the least accurate. This triangular heat flux case confirms the information provided by Fig. 3. This is interesting since the two test cases were previously designed for a linear IHCP whereas the IHCRP is highly nonlinear.

Figures 6 and 7 show the true and estimated temperature profiles within the slab, which correspond to the times indicated by asterisks in Fig. 5, for $N \to \infty$ and $N = 0.05$. The temperature profiles are quite flat for the radiative case but the differences between true and estimated temperature are comparable for the two N values, showing that the inverse method conserves the same characteristic from the purely conductive to the most radiative case. It is interesting to see that it is possible to recover the main trends of the surface heat flux variations even with such a flat temperature profile in the semitransparent slab.

The radiative part of the total heat flux inside the semitransparent slab is presented in Fig. 8, for $N = 0.05$. Now, the differences between true and estimated fluxes are larger. It is always more difficult to estimate a flux than a temperature (Beck et al., 1985). The larger discrepancies are observed at time $\xi = 0.2$, which corresponds to the abrupt change of the surface heat flux. It is important to note that only 40 time steps have been used to describe such sharp heat flux variations.

All the calculations were performed in double precision with a RISC 6000/340 workstation. The computational time to solve the inverse problem is approximately the number of iterations multiplied by the time required to solve the direct problem. When filtered data are used 21 iterations are needed for $N = 0.1$ and $M = 61$, resulting in 1072 seconds of CPU time. For $N = 0.05$ and $M = 71$, 80 iterations are necessary, and the inverse code will run in 5071 seconds. This is several orders of magnitude higher than the pure conductive inverse problem (0.5 second). The iterative process was stopped when the dimensionless temperature variations at the surface for any time steps were less than 10^{-5}. The relaxation coefficient was equal to 0.5 and 0.1 for $N = 0.1$ and 0.05, respectively.

Table 2 Standard deviation of the estimates S for different values of N using: exact data (predicted values), simulated experimental data, and filtered data

N \ Δξ	Exact Data (no filter)	Noisy Data (no filter)	Noisy Data (filter)
N →∞ (M=31)	0.062	0.086	0.086
N=0.1 (M=61)	0.059	0.094	0.091
N=0.05 (M=71)	0.056	0.126	0.112

Conclusions

This work showed that it is possible to estimate the surface flux and temperature histories of a gray semitransparent medium from two internal temperature measurements. One is used as a boundary condition, and the other one is used to determine the unknown boundary condition. An iterative algorithm based on a space-marching method has been proposed. Such a method has been chosen because, for the pure conductive case, the computational time is one order of magnitude smaller than other type of methods (Raynaud and Bransier, 1986a). One weakness of the method is that the inversion can only be done with the

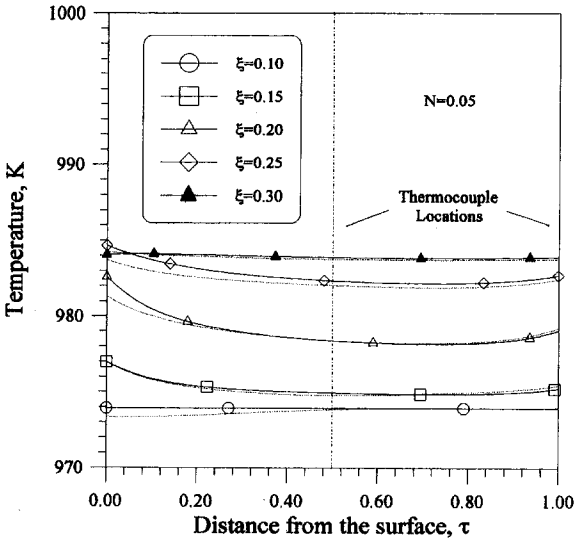

Fig. 7 Comparison between true (solid lines) and estimated (dotted lines) temperature profiles for $N = 0.05$, $M = 71$ and $\Delta\xi = 0.01$, using filtered input data

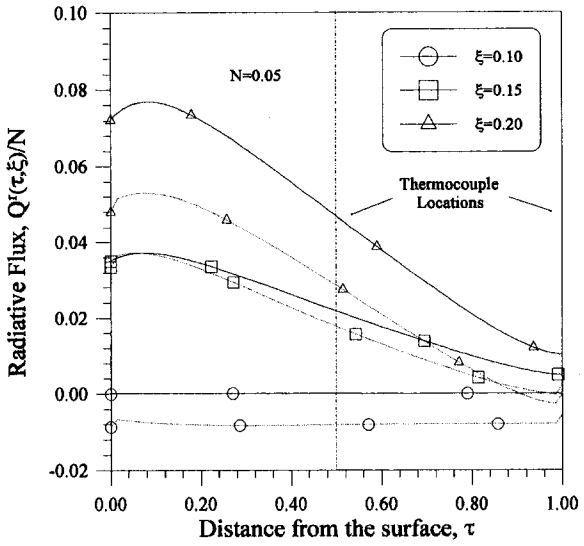

Fig. 8 Comparison between true (solid lines) and estimated (dotted lines) radiative heat flux profiles for $N = 0.05$, $M = 71$ and $\Delta\xi = 0.01$, using filtered input data

information given by the sensor closest to the unknown boundary conditions. The simultaneous treatment of sensors placed at different locations is not possible. For other types of boundary conditions, such as semitransparent walls, it should be possible to include external radiation measurements in the inversion technique.

The two test cases proposed to show the tradeoff between deterministic bias (or resolving power) and sensitivity to measurement errors of inverse heat conduction methods were used to study the effects of the radiative transfer on the inverse solution. A comparison between the results for the radiative cases with those already known for the pure conductive case showed that, as in the IHCP, the sensitivity to measurement errors can only be decreased by decreasing the resolving power, i.e., for the proposed method by increasing the number of grid points, M. For the same value of M, the inverse solutions for the radiative cases are more accurate, hence more sensitive to measurement errors than the inverse solution for the pure conductive case. This implies that more nodes must be used for highly radiative cases to obtain a stable solution. The influence of the time step was also studied and showed that, for the same bias, the sensitivity to measurement errors increases when the time step decreases. But the time step has a much smaller influence for semitransparent slabs than for opaque slabs.

A triangular heat flux pertubation was also investigated. The results confirmed the trends given by the two test cases: the radiative part of the heat transfer in the semitransparent solid complicates the numerical solution and therefore increases the computational time but does not significantly change the accuracy of the surface temperature and heat flux estimates.

This work will be extended in order to consider nongray media with any type of known radiative boundary conditions. It will require the use of a numerical method to solve the equation of radiative transfer.

Acknowledgments

The first author would like to acknowledge the financial support of Conselho Nacional de Desenvolvimento Científico e Tecnológico—CNPq (Brasil), under grant No. 200888/91-9, and the facilities provided by the Centre de Thermique de l'INSA de Lyon.

References

Andre, S., and Degiovanni, A., 1992, "An Extension of the Flash Technique in the 300 K to 800 K Temperature Range: Application to Thermal Diffusivity Measurement of Semi-transparent Materials," *Proceedings of the Third UK National Heat Transfer Conference,* Rugby, United Kingdom, Paper No. 153, Vol. 2, pp. 1197–1203.

Beck, J. V., and Arnold, K. J., 1977, *Parameter Estimation in Engineering and Science,* Wiley, New York.

Beck, J. V., Litkouhi, B., and St. Clair, C. R., Jr., 1982, "Efficient Sequential Solution of the Nonlinear Inverse Heat Conduction Problem," *Numerical Heat Transfer,* Vol. 5, pp. 275–286.

Beck, J. V., Blackwell, B., and St. Clair, C. R., Jr., 1985, *Inverse Heat Conduction: Ill-Posed Problems,* Wiley, New York.

D'Souza, N., 1975, "Numerical Solution of One-Dimensional Inverse Transient Heat Conduction by Finite Difference Method," ASME Paper No. 75-WA/HT-81.

Field, R. E., and Viskanta, R., 1993, "Measurement and Prediction of Dynamic Temperatures in Unsymmetrically Cooled Glass Windows," *AIAA Journal of Thermophysics and Heat Transfer,* Vol. 7, No. 4, pp. 616–623.

Hensel, E. H., and Hills, R. G., 1986, "An Initial Value Approach to the Inverse Heat Conduction Problem," ASME JOURNAL OF HEAT TRANSFER, Vol. 108, pp. 248–256.

Hensel, E. H., 1991, *Inverse Theory and Applications for Engineers,* Prentice-Hall, Englewood Cliffs, NJ.

Hills, R. G., Raynaud, M., and Hensel, E., 1986, "Surface Variance Estimates Using an Adjoint Formulation for a One-Dimensional Nonlinear Inverse Heat Conduction Technique," *Numerical Heat Transfer,* Vol. 10, pp. 441–461.

Huang, C. H., and Özişik, M. N., 1992, "Inverse Problem of Determining Unknown Wall Heat Flux in Laminar Flow Through a Parallel Plate Duct," *Numerical Heat Transfer,* Part A, Vol. 21, pp. 55–70.

Li, H. Y., and Özişik, M. N., 1993, "Inverse Radiation Problem for Simultaneous Estimation of Temperature Profile and Surface Reflectivity," *AIAA Journal of Thermophysics and Heat Transfer,* Vol. 7, No. 1, pp. 88–93.

Mann, D., and Viskanta, R., 1995, "An Inverse Method for Determining Transient Temperature Distribution in Glass Plates," *Inverse Problems in Engineering,* Vol. 1, pp. 273–291.

Matthews, L. K., Viskanta, R., and Incropera, F. P., 1984, "Development of Inverse Methods for Determining Thermophysical and Radiative Properties of High-Temperature Fibrous Materials," *International Journal of Heat and Mass Transfer,* Vol. 27, No. 4, pp. 487–495.

Murio, D. A., 1993, *The Mollification Method and the Numerical Solution of Ill-Posed Problems,* Wiley, New York.

Nicolau, V. P., Raynaud, M., and Sacadura, J. F., 1994, "Spectral Radiative Properties Identification of Fiber Insulating Materials," *International Journal of Heat and Mass Transfer,* Vol. 37, Suppl. 1, pp. 311–324.

Özişik, M. N., 1973, *Radiative Transfer and Interactions With Conduction and Convection,* Wiley, New York.

Raynaud, M., 1986, "Combination of Methods for the Inverse Heat Conduction Problem With Smoothing Filters," AIAA Paper No. 86-1243.

Raynaud, M., and Bransier, J., 1986a, "A New Finite Difference Method for the Nonlinear Inverse Heat Conduction Problem," *Numerical Heat Transfer,* Vol. 9, No. 1, pp. 27–42.

Raynaud, M., and Bransier, J., 1986b, "Experimental Validation of a New Space Marching Finite Difference Algorithm for the Inverse Heat Conduction Problem," *Proceedings of the Eighth International Heat Transfer Conference,* San Francisco, CA.

Raynaud, M., and Beck, J. V., 1988, "Methodology for Comparison of Inverse Heat Conduction Methods," ASME JOURNAL OF HEAT TRANSFER, Vol. 110, pp. 30–37.

Ruperti, N. J., Jr., Raynaud, M., and Sacadura, J. F., 1995, "Influence of Radiation on the Coupled Inverse Heat Conduction-Radiation Problem," ASME HTD-Vol. 312, pp. 79–86.

Sakami, M., and Lallemand, M., 1993, "Retrieval of Absorption and Temperature Profiles in Axisymmetric and Non-axisymmetric Emitting-Absorbing Media by Inverse Radiative Methods," *Proceedings of the First International Conference on Inverse Problems in Engineering: Theory and Practice,* Palm Coast, FL, pp. 259–266.

Tseng, C. J., and Chu, H. S., 1992, "Transient Combined Conduction and Radiation in an Absorbing, Emitting and Anisotropically-Scattering Medium With Variable Thermal Conductivity," *International Journal of Heat and Mass Transfer,* Vol. 35, No. 7, pp. 1844–1847.

Viskanta, R., Hommert, P. J., and Groninger, G. L., 1975, "Spectral Remote Sensing of Temperature Distribution in Semitransparent Solids Heated by an External Radiation Source," *Journal of Applied Optics,* Vol. 14, No. 2, pp. 428–437.

Advanced Calculation Method for the Surface Temperature Distribution of Turbine Blades

A. S. Dorfman
Ann Arbor, MI 48109

A method of solution of the thermal boundary layer equation for a gas, together with the heat conduction equation for the turbine blade, using the boundary condition of the fourth kind (conjugate problem), is presented. The effect of the surface temperature distribution on the heat transfer coefficient (the effect of thermal history) is considered. This effect is important for gas turbine blades because the difference in temperatures between the blade's surface and gas usually varies considerably along the blade's surface; hence, the effect of thermal history can be significant. It is shown that the results, obtained accounting for thermal history, can differ substantially from results calculated with the assumption that the blade's surface is isothermal. This might be one of the reasons why there is a marked difference between the actual temperature distribution of the turbine blade and the calculated one. It is important to consider the effect of thermal history since it is a fact that the major unknown in the design of turbine blade cooling systems is in the estimation of external heat transfer coefficient (Hannis and Smith, 1989).

Introduction

It is known that the heat transfer coefficient depends on the temperature distribution along the surface (the effect of thermal history). On the other hand, the temperature distribution depends on the heat transfer coefficient distribution. Therefore, the effect of thermal history can be calculated only by using the boundary condition of the fourth kind (by solving a conjugate problem). Years ago, the effect of thermal history was not taken into account, and the heat transfer coefficient was calculated with the assumption that the surface is isothermal. This approximate approach is often used today as well.

At the present time, conjugate heat transfer problems are considered in a variety of cases, particularly with flow past bodies. However, in most cases it is assumed that the free-stream velocity is constant, and the pressure gradient is zero. One of the earliest solutions of the heat transfer conjugate problem was given by Viskanta and Abrams (1971). They considered heat transfer between two streams separated by a thin plate. Later, solutions of more complicated conjugate problems were published. For instance, many authors studied conjugate heat transfer from fins. Forced convention from vertical fins in air was considered by Garg and Velusamy (1986). Huang and Chen (1987) studied this case for fins in power law fluid. Mixed convection from fins in air was studied by Sunden (1983). The same conjugate problem for fins embedded in a porous medium was solved by Lin et al. (1986). Corla (1988) analyzed the radiative effect on forced convection. Many other cases for plates and fins were considered. These were reviewed by Dorfman (1989). Most of the conjugate problems were solved numerically by using the finite difference method. Some authors employed the superposition method (for example, Karvinen, 1983), the integral method (Sarma et al., 1988), and the Laplace transformation (Sucec, 1987).

An advanced superposition method proposed by Dorfman (1973) makes it possible to consider the effect of pressure gradient in the case of nonseparated flow past a curvilinear body. That effect is considerable in many important cases, for instance, for turbine blades or vanes. In the present paper, the heat transfer conjugate problem for turbine blades is solved by using that advanced superposition method. The effect of thermal history is studied by comparing the results obtained by solving the conjugate problem with the results determined by using the boundary condition of the third kind and the assumption that the blade's surface is isothermal.

The purpose of the present work is to find out how significant is the effect of thermal history, but not to predict exactly the temperature distribution. Therefore, the same relatively simple well-known boundary layer model is employed for both calculations. However, the method of solving a conjugate problem, which is presented here, can be applied by using a more complicated modern boundary layer model.

Theoretical Development

The boundary conditions of the fourth kind are represented in the form of equalities of temperatures and heat fluxes on the body surface calculated from the gas side (+0) and from the body side (−0):

$$T_w(+0) = T_w(-0) \quad q_w(+0) = q_w(-0)$$

Since the temperatures are unknown, one should employ the method applicable to an arbitrary temperature distribution. The superposition method is used to solve the boundary layer equation. The surface heat flux is given by expression (Dorfman, 1973)

$$q_w = h_T[T_\infty - T_w(0) - \int_0^\phi f(\xi/\phi)(dT_w/d\xi)d\xi];$$

$$\phi = \int_0^s V(\xi)d\xi \tag{1}$$

This expression is applicable to the general case of variable free-stream velocity over a body with arbitrary surface temperature distribution. In Eq. (1)

$$f(\xi/\phi) = [1 - (\xi/\phi)^{c_1}]^{-c_2} \tag{2}$$

is the influence function of the unheated zone that describes the changes in heat transfer coefficient in the case when the surface is heated not from $x = 0$ but from $x = \xi$ (from $\phi = \xi$ for the

Contributed by the Heat Transfer Division for publication in the JOURNAL OF HEAT TRANSFER. Manuscript received by the Heat Transfer Division September 1993; revision received September 1995. Keywords: Conjugate Heat Transfer, Forced Convection, Turbines. Associate Technical Editor: Y. Bayazitoglu.

case of curvilinear body when the pressure gradient is not zero). The exponents are dependent on Prandtl number and pressure gradient (Dorfman, 1973). Since the effect of the pressure gradient is almost completely contained in the variable ϕ, the exponents c_1 and c_2 are only slightly dependent on the pressure gradient. When pressure gradient changes from its value at the stagnation point ($m = 1$) to the one in the flow near separation ($m = -0.075$), the exponents vary from its mean value (for each Prandtl number) by only a few percent. If the solution were exact, the exponents would be independent on the pressure gradient. Since they are practically independent on the pressure gradient, Eqs. (1) and (2) describe quite accurately the effect of variable surface temperature in a general case when the pressure gradient is not zero. Solutions (1) and (2) generalize the well-known superposition method, which in its usual form can be used only in the case of zero pressure gradient ($V = 1$; $\phi = S = x$). For gases (Pr $\sim$ 1) the exponents are $c_1 = \frac{3}{4}$ and $c_2 = \frac{1}{3}$ (Dorfman, 1973). For turbulent boundary layer for gases $c_1 = 1$, $c_2 = 0.18$ at Re $= 5 \times 10^5$; $c_1 = 0.85$, $c_2 = 0.1$ at Re $= 10^8$ (Dorfman and Lipovetskaya, 1976).

The Green's function method is used to solve the heat conduction equation for the blade. The solution can be presented in the form (Courant and Hilbert, 1962)

$$\pi T_{wk} = \int_S (1/r_{ki}) T_{wi} \cos(n_i, r_{ki}) dS - \int_S \ln r_{ki} (q_{wi}/K_w) dS \quad (3)$$

This expression determines the temperature T_{wk} at any blade contour point k in terms of the temperatures T_{wi} and the heat fluxes q_{wi} at the other contour points i.

If the blade is cooled on the inside, one needs to solve the conjugate problem for the interior side too. However, the effect of thermal history for turbulent flow in the long narrow cooling channels is comparatively small. Thus, the heat flux for the inside of the blade can be defined by Newton's law

$$q_w = h_a (T_w - T_a) \quad (4)$$

Substituting into Eq. (3) for q_{wi}, Eq. (1) at the outside and Eq. (4) at the inside, one gets

$$\pi T_{wk} = \int_S (1/r_{ki}) T_{wi} \cos(n_i, r_{ki}) dS - (h_T/K_w) \int_{S_1} \ln r_{ki} [T_\infty - T_w(0) - \int_0^{\phi_i} f(\xi/\phi_i)(dT_w/d\xi) d\xi] dS - (h_a/K_w) \int_{S_2} \ln r_{ki} (T_{wi} - T_{ai}) dS \quad (5)$$

Two unknowns, T_{wi} and T_{ai}, are determined by Eq. (5) and the energy balance Eq. (6) for cooling air

$$h_a (T_{wi} - T_{ai}) = (Gc_p/H)(dT_a/dS)_i \quad (6)$$

When the temperatures T_{wi} and T_{ai} are known, one can calculate the surface heat flux from Eq. (1). Then, the local heat transfer coefficient at the outside of the blade accounting for thermal history can be determined by the formula

$$h = q_w/(T_\infty - T_w)$$

If the blade wall is considered to be thin, the longitudinal thermal conduction is negligible. In that case, the heat flux for the interior side of the blade can be determined as usual by using the overall heat transfer coefficient h_{ov}. This heat flux must be equal to that from the gas, determined by Eq. (1). Thus, one obtains in the case of the thin wall, instead of Eq. (5), the following relatively simple equation:

$$h_{ov}(T_w - T_a) = h_T [T_\infty - T_w(0) - \int_0^\phi f(\xi/\phi)(dT_w/d\xi) d\xi]; \quad h_{ov} = 1/h_a + \delta/K_w \quad (7)$$

Numerical Formulation

The unknown temperature distribution $T_w(S)$ can be approximated by a piecewise function with constant derivatives dT_w/dS at each interval. Assuming that free-stream velocity V is constant at each interval ΔS, one gets that $dT_w/d\phi$ is also constant at each interval. Then, one can substitute sums for integrals. If there are N and M points at the outside and at the inside of the blade, respectively, instead of Eqs. (5) and (6) one would get

$$\pi T_{wk} = \{ \sum_{i=0}^{N+M} (1/r_{ki}) T_{wi} \cos(n_i, r_{ki}) - (h_T/K_w) \times \sum_{i=0}^{N} \ln r_{ki} [T_\infty - T_w(0) - \sum_{j=1}^{i} (T_{wj} - T_{w(j-1)})(\Delta I_j/\Delta\phi_j)] - (h_a/K_w) \sum_{i=0}^{M} \ln r_{ki} (T_{wi} - T_{ai}) \} \Delta S_i; \quad (8)$$

$$\Delta I_j = \int_{\phi_{j-1}}^{\phi_j} f(\xi/\phi_i) d\xi$$

$$T_{ai} - T_{a(i-1)} = b_a (T_{wi} - T_{ai}); \quad b_a = h_a H \Delta S/Gc_p \quad (9)$$

The integral ΔI_j can be calculated numerically from 0 to ϕ_{i-1}. However, the point $\xi = \phi$ is singular. For that reason, it is convenient to calculate the integral ΔI_i from ϕ_{i-1} to ϕ_i for each point i analytically. The formula, given below, can be also used for analytical calculation ΔI_j in each other interval (ϕ_{j-1}, ϕ_j)

Nomenclature

c_1, c_2 = exponents, Eq. (2)
c_p = specific heat at constant pressure
$f(\xi/\phi)$ = influence function of unheated zone
G = cooling air flow rate
h = heat transfer coefficient
H = blade height
K = thermal conductivity
m = exponent in the free-stream velocity distribution; $V \sim x^m$
n = external normal to the blade cross section contour
Pr, Re = Prandtl and Reynolds numbers
r_{ki} = radius vector from point k to point i
S = longitudinal coordinate measured along the blade cross section contour referred to analogously defined contour length
S_1, S_2 = dimensionless length of outside and inside of the blade contour
$T, T(0)$ = temperature at any point and stagnation point temperature
$V(S)$ = potential flow velocity referred to the free-stream velocity
x = longitudinal coordinate referred to plate length
δ = blade wall thickness
$\zeta = (T_\infty - T_w)/[T_\infty - T_a(0)]$ = cooling effectiveness
ξ, ϕ = integration and Gortler's variables, Eq. (1)

Subscripts

a, ov, w, T, ∞ = cooling air, overall, wall, isothermal, free stream

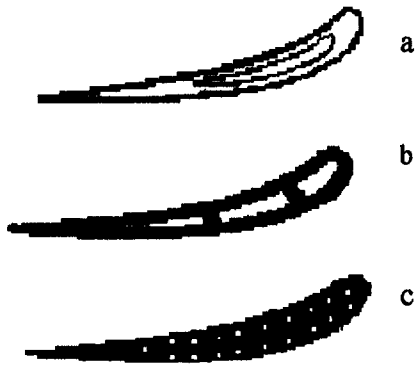

Fig. 1 Schematic drawing of the blade cross sections; blade with deflector (*a*) and with radial cooling channels over the whole blade cross section (*b*) and over the part of the blade cross section near the surface (*c*)

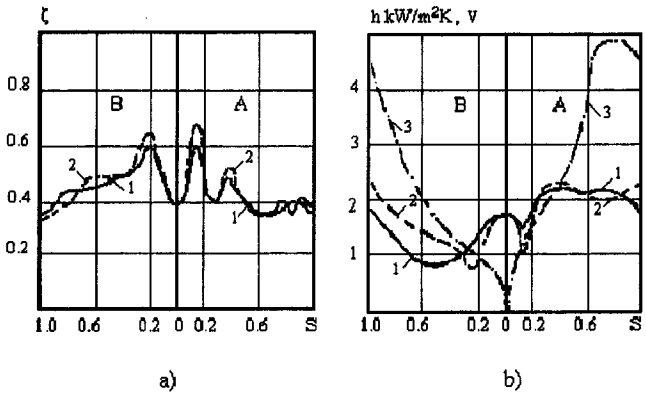

Fig. 3 Results of calculation for the blade with deflector (the wall is considered to be thin). (*A*), (*B*) and (*a*), (*b*): see Fig. 2. (3) Velocity of flow around blade referred to free-stream velocity.

instead of numerical calculation. Using an inequality $\phi_i \gg (\phi_j - \phi_{j-1})$, that is correct everywhere, except a small domain near stagnation point, one obtains for the integral (8)

$$\Delta I_j = (1 - c_2)^{-1}(\phi_i/c_1)^{c_2}[(\phi_i - \phi_{j-1})^{1-c_2} - (\phi_i - \phi_j)^{1-c_2}]$$

Equation (8) can be written for all $N + M$ points at the outside and at the inside of the blade. Equation (9) can be written for all M points at the inside of the blade. Thus, one gets system of $N + 2M$ algebraic equations that determines $N + 2M$ unknown temperatures T_{wi} and T_{ai}. An analogous system is used if thermal history is ignored, and the boundary condition of the third kind is applied. In this case, the heat flux at the outside of the blade is also determined by Newton's law (4), and the second term of Eq. (8) becomes the form of the third one. Thus, instead of Eq. (8), one gets

$$\pi T_{wk} = \{\sum_{i=0}^{N+M} (1/r_{ki}) T_{wi} \cos(n_i, r_{ki}) - (h_T/K_w) \times \sum_{i=0}^{N} \ln r_{ki}(T_\infty - T_{wi}) - (h_a/K_w) \sum_{i=0}^{M} \ln r_{ki}(T_{wi} - T_{ai})\}\Delta S_i$$

The second equation is the same Eq. (9) in this case.

If the wall is considered to be thin, the temperatures are then determined by the system of Eqs. (6) and (7). In that case, the temperatures can be calculated in consecutive order. Let the temperatures of $(i - 1)$ points be known. For next point i, the integral in Eq. (7) can be presented as

$$I_i = \int_0^{\phi_i} f(\xi/\phi_i)(dT_w/d\xi)d\xi = \int_0^{\phi_{i-1}} f(\xi/\phi_i)(dT_w/d\xi)d\xi + (\Delta I_i/\Delta\phi)[T_{wi} - T_{w(i-1)}]$$

Since the temperatures of $(i - 1)$ points are known, the integral I_{i-1} from 0 to ϕ_{i-1} can be calculated numerically. The integral ΔI_i from ϕ_{i-1} to ϕ_i is defined by Eq. (8). Substituting the air temperature T_{ai} from Eq. (9), that is the finite difference form of Eq. (6), into Eq. (7) and solving this equation for the wall temperature T_{wi}, one obtains

$$T_{wi} = [h_T(\Delta I_i/\Delta\phi_i)(1 + b_{ov}) + h_{ov}]^{-1}\{h_T(1 + b_{ov}) \times [T_\infty - T_w(0) - I_{i-1} + T_{w(i-1)}(\Delta I_i/\Delta\phi_i)] + +h_{ov}T_{a(i-1)}\};$$

$$b_{ov} = h_{ov}H\Delta S/Gc_p \qquad (10)$$

Since the integral in Eq. (7) equals zero at the stagnation point, it is easy to find out the temperature at that point, $T_w(0) = [h_T T_\infty + h_{ov}T_a(0)]/(h_T + h_{ov})$. Then, since the temperature of cooling air at the stagnation point $T_a(0)$ is known, one can calculate T_{w1} by Eq. (10) and T_{a1} by Eq. (9) at point 1, and so on.

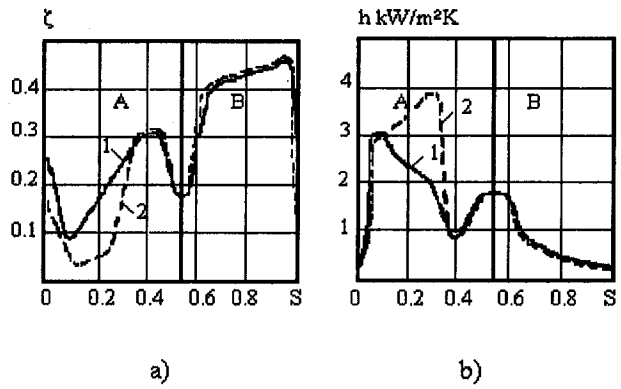

Fig. 2 Results of calculation for the blade with deflector (the wall is considered to be thick): (*A*) pressure side; (*B*) suction side; cooling effectiveness (*a*) and heat transfer coefficient (*b*) calculated with (1) and without (2) thermal history

Effect of Thermal History

A schematic drawing of the cross sections of the considered blades is given in Fig. 1. Figures 2 and 3 present the surface temperature (in terms of cooling effectiveness ξ) and the heat transfer coefficient distributions on the blade with deflector (Fig. 1(*a*)). The results are obtained from the following data: T_∞ = 1070 K; $T_a(0)$ = 340 K (Fig. 2), and T_∞ = 1460 K; $T_a(0)$ = 560 K (Fig. 3); δ = 0.0025 m; Gc_p/H = 3330 W/mK. The blade is considered to be thick in the first case (Fig. 2), and it is considered to be thin in the second one (Fig. 3). Hence, Eqs. (8) and (9) are applied in the calculation in the first case, and Eqs. (9) and (10) are used in the second one. It is assumed that the boundary layer is laminar on the leading part of the blade, before the heat transfer coefficient becomes minimum, and it is turbulent on the remainder of the blade.

It can be shown that the effect of thermal history depends generally on the nature of the changes in the absolute value of the temperature difference $|T_\infty - T_w|$. The heat transfer coefficient, obtained accounting for thermal history, is higher than that for an isothermal surface if the difference $|T_\infty - T_w|$ increases along the surface, and lower than the isothermal one if that difference decreases along the surface. For a turbine blade, this leads to the higher surface temperature, in the case of increasing the temperature difference, and to the lower surface temperature, in the case of decreasing the temperature differ-

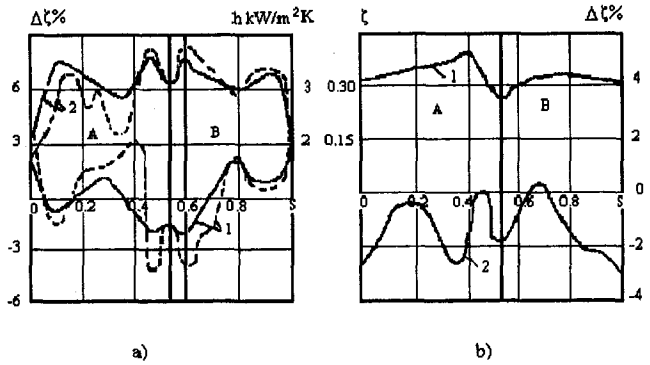

Fig. 4 Results of calculation for the blade with radial cooling channels distributed over the whole blade cross section (*a*) (Fig. 1 (*b*)) and near the blade surface (*b*) (Fig. 1 (*c*)). (*a*) 1: Difference of the cooling effectiveness calculated with and without thermal history, 2: heat transfer coefficient calculated taking thermal history into account; Re = 6×10^6, and Re = 3×10^6 (dashed curves). (*b*) 1: Cooling effectiveness calculated taking thermal history into account, 2: difference of the cooling effectiveness calculated with and without thermal history. (*A*), (*B*): see Fig. 2.

ence, in comparison with those obtained without accounting for thermal history. For example, in the case of a thick blade (Fig. 2), the surface temperature increases (the effectiveness ζ decreases) along the blade on the pressure side at the section with turbulent boundary layer. Hence, the difference $|T_\infty - T_w|$ on this section decreases. For that reason, the heat transfer coefficient is lower than that for an isothermal surface; hence, the surface temperature, obtained accounting for thermal history, is lower (the effectiveness is higher) than the one calculated by using the boundary condition of the third kind and isothermal heat transfer coefficient (Fig. 2). In this case, the largest differences between both calculations are on the pressure side of the blade. There at some points, the value of the heat transfer coefficient for the isothermal surface is twice that obtained accounting for thermal history. The maximum value of the surface temperature, obtained with thermal history, is more than 100 K ($\zeta = 0.15$) lower than that calculated without considering thermal history. The temperature distribution accounting for thermal history is usually more uniform. The highest temperature decreases (ζ increases), while the lowest temperature increases (ζ decreases), in comparison with those calculated by using the boundary condition of the third kind. Thus, the difference between the highest and the lowest temperatures is smaller, when thermal history is taken into account ($\Delta T_{wth} < \Delta T_{woth}$). In this case, the difference between ΔT_{wth} and ΔT_{woth} is equal to that between the highest temperatures because the lowest temperatures, obtained in both calculations, are almost the same. So in this case, ΔT is more than 100 K smaller when thermal history is taken into account.

The results, presented in Fig. 3, are similar. The temperature distribution, obtained accounting for thermal history, is also more uniform. In some of the blade sections, the heat transfer coefficients, obtained with and without thermal history, differ by 30 to 40 percent. The corresponding surface temperature difference is 50 K to 60 K ($\zeta = 0.07 \div 0.08$), but for the most part of the blade surface it is 15 K to 25 K ($\zeta = 0.02 \div 0.03$). The difference between the highest and the lowest temperatures ΔT, calculated with thermal history, is smaller by 45 K (0.06) and by 75 K (0.09) for the suction and pressure sides, respectively.

Figure 4 presents the surface temperature distribution for two blades with different systems of radial cooling channels (Fig. 1) calculated for $T_\infty = 1500$ K and $T_a(0) = 660$ K. The procedure for calculation is similar to the one used for the blade with deflector. However, in that case, the temperature of the cooling air T_a coming into each cooling channel from the neighboring part of the blade is considered to be known. Since these temperatures are known, the $N + M$ unknown blade temperatures T_{wi} are determined by solving the system of $N + M$ algebraic Eqs. (8). The effect of thermal history for the blades with radial cooling channels is generally smaller than that for the blades with deflector. This is so because the temperature distribution on the blades with radial cooling channels is more uniform. The surface temperature distribution on the blade with channels near the blade surface (Fig. 1(*c*)) is more uniform than the one with channels over the whole blade section (Fig. 1(*b*)). In accordance with that, the effect of thermal history is smallest for this blade (Fig. 4). The effect of Reynolds number and of free-stream velocity distribution along the blade was studied for the blade with channels over the whole blade section. It was found that the effect of thermal history is more significant for a larger Reynolds number (Fig. 4(*a*)) and for an unfavorable pressure gradient.

Uncertainties in Numerical Results

The present method is simpler, more reliable, and more accurate than a numerical solution of the thermal boundary layer equation, together with the heat conduction equation usually employed to solve the conjugate problems. The reasons for that are: (*a*) Equation (3) is an exact solution of the heat conduction equation, and Eqs. (1) and (2) are a quite accurate solution of the thermal boundary layer equation; (*b*) there are no problems with stability, convergence, or truncation errors; (*c*) the accuracy of the numerical calculation of the integrals in Eqs. (5) and (7) is higher than that of the derivatives in the thermal boundary layer and heat conduction equations. The magnitudes of the errors are (James et al., 1985): $\sim\Delta S^3$ for the integrals, and $\sim\Delta S^2$ or $\sim\Delta S$ for the derivatives.

No more than 25 to 30 segments in the longitudinal direction of the blade surface were used because it is known that the magnitude of the errors depends on the number of simultaneously solved algebraic equations. The system of Eqs. (8) and (9) was solved by Gauss' method. The magnitudes of the errors were estimated by error equations (James et al., 1985). If there was less than a three-digit accuracy, the results were refined by increasing of the number of segments. In this case, no more than 25 to 30 simultaneous solved algebraic equation were used. However, the system of Eqs. (8) and system of Eqs. (9) were solved separately in consecutive order using iterations. Those iterations were repeated until the magnitude of the errors became ∓ 0.5 K.

Conclusion

A method of solving the heat transfer conjugate problem (using the boundary condition of the fourth kind) for the turbine blade is presented. The problem is reduced to solving the system of algebraic equations. The effect of thermal history (the effect of the surface temperature distribution on the heat transfer coefficient) is studied by comparing the results, obtained by solving the conjugate problem, with the results calculated by using the boundary condition of the third kind and an assumption that the blade surface is isothermal. Since the physical models of boundary layer and everything else (except the boundary conditions) are the same in both cases, one can see when the effect of thermal history is important; hence, there is the necessity of solving the conjugate problem, and when the simpler boundary condition of the third kind can be used. That is important to know since the uncertainty in external heat transfer coefficient is prevalent in the design of the turbine blade cooling systems (Hannis and Smith, 1989).

Two cooling systems are considered (Fig. 1): (*a*) the blade with deflector, (*b*), (*c*) the blades with radial cooling channels. The comparison shows that the effect of thermal history can be considerable. The surface temperature distribution, obtained accounting for thermal history, is more uniform than the one

calculated using the boundary condition of the third kind. The maximum values of the temperatures decrease, while the minimum values increase in comparison with similar values calculated without accounting for thermal history. The value of the difference between both results of calculation depends on the uniformity of the surface temperature distribution. The most significant distinctions are for the blades with deflector. In this case at some points, the heat transfer coefficient for isothermal surface is twice that obtained accounting for thermal history. The highest temperature is more than 100 K less than the one obtained using the boundary condition of the third kind and heat transfer coefficient for the isothermal blade surface. The most uniform surface temperature distribution is achieved by the blade that has the radial cooling channels distributed near the blade surface (Fig. 1(*c*)). The effect of thermal history is usually small in such cases (Fig. 4).

References

Corla, Rama Subba Reddy, 1988, "Radiative Effect on Conjugate Forced Convection and Conductive Heat Transfer in a Circular Pin," *Int. J. Heat Fluid Flow,* Vol. 9, pp. 49–52.

Courant, R., and Hilbert D., 1965, *Methods of Mathematical Physics,* Vol. 2, Interscience Publishers, Inc., New York.

Dorfman, A. S., 1973, "Influence Function for an Unheated Section and Relation Between the Superposition Method and Series Expansion With Respect to Form Parameters," *Teplofizika Vysokikh Temperatur,* Vol. 11, pp. 99–105 (translation, *High Temperature,* Vol. 11, 1973, pp. 84–89).

Dorfman, A. S., and Lipovetskaya, O. D., 1976, "Heat Transfer of Arbitrarily Nonisothermic Surfaces With Gradient Turbulent Flow of an Incompressible Liquid Within a Wide Range of Prandtl and Reynolds Numbers," *Teplofizika Vysokikh Temperatur,* Vol. 14, pp. 98–105 (translation, *High Temperature,* Vol. 14, 1976, pp. 86–92).

Dorfman, A. S., 1989, "Heat Transfer Conjugate Problems for Fins (Review)," *Promyshlennaya Teplotekhnika,* Vol. 11, pp. 3–18.

Garg, V. K., and Velusamy, K., 1986, "Heat Transfer Characteristics for a Plate Fin," ASME JOURNAL OF HEAT TRANSFER, Vol. 108, pp. 224–226.

Hannis, J. M., and Smith, M. K. D., 1989, "A Comparison Between Engine Test Results and Design Prediction of Turbine Blade Cooling Performance," ASME Paper No. 89-GT-169.

Huang, Ming-Jer, and Chen, Cha'o-Kuang, 1987, "Conjugate Forced Convection-Conduction Plate Fin in Power Law Fluids," *Int. Commun. Heat Mass Transfer,* Vol. 14, pp. 371–380.

James, M. L., Smith, G. M., and Wolford, J. C., 1985, *Applied Numerical Methods for Digital Computation,* Harper & Row Publisher, Inc., New York.

Karvinen, R., 1983, "Efficiency of Straight Fins Cooled by Natural or Forced Convection," *Int. J. Heat Mass Transfer,* Vol. 26, pp. 635–638.

Lin, Jin-Yuan, Minkowycz, W. I., and Cheng, P., 1986, "Conjugate Mixed Convection Heat Transfer Analysis of a Plate Fin Embedded in a Porous Medium," *Numerical Heat Transfer,* Vol. 9, pp. 575–590.

Sarma, P. K., Subrahmanyat, T., and Dharma Rao, V., 1988, "Natural Convection From a Vertical Heat Generating Fin—A Conjugate Problem," ASME JOURNAL OF HEAT TRANSFER, Vol. 110, pp. 99–102.

Sucec, J., 1987, "Exact Solution for Unsteady Conjugated Heat Transfer in the Thermal Entrance Region of Duct," ASME JOURNAL OF HEAT TRANSFER, Vol. 109, pp. 295–299.

Sunden, B., 1983, "Conjugate Mixed Convection Heat Transfer From a Rectangular Fin," *Int. Commun. Heat Mass Transfer,* Vol. 4, pp. 267–276.

Viskanta, R., and Abrams, M. A., 1971, "Thermal Interaction of Two Streams in Boundary-Layer Flow Separated by a Plate," *Int. J. Heat Mass Transfer,* Vol. 14, pp. 1311–1321.

Experimental Studies and Correlations of Radially Outward and Inward Air-Flow Heat Transfer in a Rotating Square Duct

C. R. Kuo

G. J. Hwang
Mem. ASME

Department of Power Mechanical Engineering,
National Tsing Hua University,
Hsinchu 30043, Taiwan

Experiments were conducted to investigate the convective heat transfer of radially outward and inward air flows in a uniformly heated rotating square duct. The interior duct surfaces, constructed by fiberglass-reinforced plastic, were plated with separated film heaters for distinguishing the local wall heat transfer rate. The duct hydraulic diameter, the actively heated length, and the mean rotation radius are 4, 120, and 180 mm, respectively. In the experiments, the parameters were the throughflow Reynolds number, Re = 1,000~15,000; the rotation number, Ro = 0~0.32; and the rotational buoyancy parameter, Ra = 0~0.5. For the outward flow the Coriolis-induced cross-stream secondary flow strongly enhanced the heat transfer on the leading edge. But for the radially inward flow the trend was reversed. When the throughflow Reynolds number was increased, the rotating-buoyancy decreased, then increased the heat transfer for the outward flow; however, the rotating-buoyancy always increased the heat transfer for the inward flow. The heat transfer data are correlated for the outward and inward flows for the ranges of parameters under study.*

Introduction

The study of convective heat transfer in rotating ducts is significant for engineers because of its potential applications in industry, e.g., the cooling of turbine blades and electrical machinery. Increasing the turbine entry temperature is especially required for improving the thermodynamic efficiency and reducing the specific fuel consumption of advanced gas turbine engines. On the other hand, the torque output of electrical machinery is increased via increases in the electrical and magnetic loadings, and consequently, more heat is generated in the stators and rotors of the machine. Since high operating temperature environments can potentially cause material degradation in insulation and rotating components, and excess ohm loss in electrical conductors, investigations to obtain effective convective cooling systems by channeling compressor-bled air into a rotating component for removing the excess heat are increasingly important.

Inside a radially rotating heated duct, the flow structure is simultaneously influenced by the cross-stream secondary flow induced by the Coriolis force and the radial secondary flow induced by the centrifugal-buoyancy force. As a result, the flow heat transfer can be affected not only by the main flow strength and direction, the rotational speed, and geometry of the duct, but also by differences over the leading edge, trailing edge, and side walls. Predicting the rotating effects on heat transfer remains challenging as the complexity of flow expands and the interaction of the flow variables mingles.

Obtaining an approximate perturbation series solution, Barua (1955) showed that two counterrotating vortices induced by the Coriolis acceleration appear symmetrically in a rotating duct. Johnston et al. (1972) used both the dye and the hydrogen-bubble visualization methods to investigate the effects of rotation on the fully developed turbulent channel water flow. The results demonstrated that rotation may induce the instability of the flow to large-scale disturbances on the trailing edge but suppress turbulent transition on the leading edge for the outward flow. Morris and Ayhan (1979, 1982) reported that the centrifugal buoyancy increases the heat transfer rate for the inward flow but decreases it for the outward flow in a radially rotating circular passage. Clifford et al. (1984) experimentally observed that the Coriolis acceleration has a beneficial influence on the mean heat transfer of low Re turbulent range in an isosceles triangular channel. Also, increasing buoyancy reduces the heat transfer for the radially outward flow when Re $<$ 30,000. Harasgama and Morris (1988) experimentally studied the heat transfer characteristics of circular, triangular, and square-sectioned coolant passages. The results indicated that the increasing buoyancy decreases the mean heat transfer for radially outward flow, but it generally increases the mean heat transfer for the radially inward flow. Guidez (1989) reported that the Coriolis force induced secondary flow causes a global augmentation of the heat transfer coefficient for the radially outward turbulent flow. Locally, along the trailing edge the heat transfer increases strongly; on the contrary, along the leading edge it decreases slightly.

Hwang and Soong (1989), and Soong et al. (1991) performed heat transfer measurements on radially outward flows in rotating isothermal rectangular ducts for aspect ratios of 0.2, 0.5, 1.0, 2.0, and 5.0, and Re = 700 ~ 20,000. The heat transfer enhancement due to rotation was found, especially for the aspect ratio of 1.0. Wagner et al. (1991a, b) investigated the local heat transfer of radially outward and inward flows in rotating serpentine passages with uniform wall temperature. The buoyant flow is found to be favorable for the heat transfer on both the trailing and leading edges. However, the increase in the heat transfer for the inward flow was relatively less than that for the outward flow. Morris and Ghavami-Nasr (1991) observed that centrifugal buoyancy improves the heat transfer on trailing and leading edges for radially outward flows in a rotating rectangular

Contributed by the Heat Transfer Division for publication in the JOURNAL OF HEAT TRANSFER. Manuscript received by the Heat Transfer Division September 1994; revision received September 1995. Keywords: Forced Convection, Mixed Convection, Rotating Flows. Associate Technical Editor: T. W. Simon.

duct for Re = 10,000 ~ 25,000. Han and Zhang (1992) and Han et al. (1993) revealed the effects of uneven wall temperature on heat transfer in a rotating two-pass square channel with smooth walls. The results suggested that the effect of uneven wall temperatures on local heat transfer coefficients in the second channel (inward flow) is greater than that in the first channel (outward flow).

There are significant discrepancies of these measurement results. The different experimental conditions, including rotational speeds, flow regimes, channel dimensions, and temperature differences may be responsible for the scattering of these results. Generally speaking, the results show that the Coriolis force generates a pair of vortices formed as cross-stream secondary flows, which give additional mixing to the main flow and consequently enhance the convective heat transfer. In a radially outward flow the Coriolis force strongly enhances the heat transfer on the trailing edge. But this trend is reversed in a radially inward flow because of the reverse direction of the Coriolis-induced cross-stream secondary flow. Since in a radially rotating heated passage, significant density gradients of flow can arise due to high rotational speeds and high wall-to-coolant temperature differences, the rotating buoyancy is present under these operating conditions. The direction of this buoyancy free convection flow is opposite to the main flow direction in a radially outward-flowing passage but is the same as the main flow direction in a radially inward-flowing one. The rotating buoyancy on heat transfer obviously depends on the main flow direction.

The objectives of this study were to investigate the rotation effects with varying throughflow Reynolds numbers and the influence of flow direction on the local heat transfer in a radially rotating square duct. The test sections with light weight and high strength were built to obtain higher rotational speed and, as a result, to manifest the rotation effect on the convective heat transfer. The channel with small hydraulic diameter, $D_h = 4$ mm, was constructed in the experiments to meet the cooling channel size requirement in a real engine, and for easily obtaining a higher wall-to-coolant temperature difference when the centrifugal-buoyancy effect was concerned. The four duct walls were made of low-conductivity material and heated separately with stainless-steel film heaters in order to suppress the circumferential wall heat conduction and measure the local heat transfer coefficients along the leading edge, trailing edge, and two side walls. An attempt to correlate the heat transfer results will be made. The discrepancies of the heat transfer data in literature are also explained and clarified.

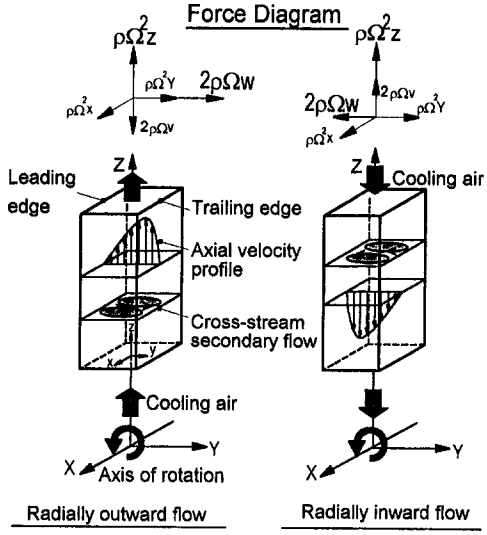

Fig. 1 Physical notations and coordinate system

Governing Parameters

The velocity profiles and coordinates, shown in Fig. 1, illustrate the effects of the rotation-induced secondary flow on the forced convection for outward and inward air flows in a radially rotating heated square duct. From the force diagram, the dominant forces due to rotation are the force vectors of $2\rho\Omega W$ and $\rho\Omega^2 Z$ because of $W \gg V$ and $Z \gg X$ and Y. The Coriolis force $2\rho\Omega W$, which induces a cross-stream secondary flow, distorts the axial velocity profile and moves the point of maximum velocity toward the trailing edge for the outward flow but toward the leading edge for the inward flow. On the other hand, the centrifugal buoyancy force $\rho\Omega^2 Z$ accelerates the less dense air near the heated wall toward the rotation axis for both the outward and the inward flows.

A dimensional analysis of the flow governing equations reveals that the heat transfer coefficient of the radially rotating duct is influenced by the operating parameters (Morris and Ayhan, 1979) as shown in the following form:

$$\mathrm{Nu}_\Omega = f(\mathrm{Re}, \mathrm{Re}_\Omega, \mathrm{Ra}, \mathrm{Pr}, L/D_h, R/D_h, z/D_h) \quad (1)$$

where the definitions of these dimensionless parameters are

Nomenclature

c_p = specific heat of air, J/kg · °C
D_h = hydraulic diameter, mm
h = heat transfer coefficient = $q_{\mathrm{net}}/(T_w - T_b)$, W/m² · °C
k_{air} = thermal conductivity of air, W/m · °C
K_p = wall conduction parameter based on channel air pure heat conduction
K_p' = wall conduction parameter based on channel air mixed convection
k_w = thermal conductivity of wall, W/m · °C
L = actively heated length of duct, mm
M = Mach number
Nu = Nusselt number = hD_h/k_{air}
Nu_0 = Nusselt number for nonrotating condition
Nu_Ω = Nusselt number for rotating condition
Pr = Prandtl number = $c_p\,\mu/k_{\mathrm{air}}$
q_{net} = net wall heat flux, W/m²
R = mean rotation radius = $Z_0 + L/2$, mm
Ra = rotational Rayleigh number = $\mathrm{Ro}^2\mathrm{Re}^2(\epsilon + z/D_h)[(T_w - T_b)/T_w]\mathrm{Pr}$
Ra* = rotational buoyancy parameter = $\mathrm{Ra}/\mathrm{Re}^2$
Re = throughflow Reynolds number = $\rho W_0 D_h/\mu$
Re_Ω = rotational Reynolds number = $\rho\Omega D_h^2/\mu$
Ro = rotation number = $\mathrm{Re}_\Omega/\mathrm{Re} = \Omega D_h/W_0$
t = duct wall thickness, mm
T_b = bulk temperature of air, °C
$T_{b,i}$ = bulk temperature of inlet air, °C
$T_{b,0}$ = bulk temperature of outlet air, °C
T_r = recovery temperature of air, °C
T_w = duct wall temperature, °C
U, V, W = velocity components in x, y, and z directions, respectively, m/s
W_0 = mean air velocity, m/s
X, Y, Z = system coordinates, mm
x, y, z = local coordinates for outward flow passage, mm
$\bar{x}, \bar{y}, \bar{z}$ = local coordinates for inward flow passage, mm
Z_0 = distance between rotating axis and heated duct, mm
γ = temperature recovery factor
ϵ = eccentricity = Z_0/D_h
μ = air dynamic viscosity, kg/m · s
ρ = air density, kg/m³
Ω = rotational speed, rad/s

Table 1 Ranges of the experimental variables and the nondimensional parameters

VARIABLES	RANGES	RANGES
FLOW DIRECTION	RADIALLY OUTWARD FLOW	RADIALLY INWARD FLOW
rpm	0, 500, 1000, 1500, 2000, 3000	0, 500, 1000, 1500, 2000
$T_{b,o} - T_{b,i}$ (°C)	15, 30, 45	15, 30
T_w (°C)	40 - 130	40 - 120
z/D_h (or $\bar{z}/D_h$)	2.5, 10.0, 17.5, 25.0	5.0, 12.5, 20.0, 27.5
Pr	0.72	0.72
Re	1000, 2300, 4000, 8200, 10000, 15500	1000, 2300, 3000, 4000, 7000, 10000
Re_Ω	53.4, 106.8, 162.2, 214.0, 320.4	56.6, 120.0, 164.5, 217.2
Ro	0 - 0.32	0 - 0.19
Ra^*	0 - 0.5	0 - 0.12

listed in the nomenclature. In the present study, air with Pr = 0.72 was chosen as the coolant fluid. The ratio of the heated length to hydraulic diameter L/D_h of 30 and the ratio of the mean rotation radius to hydraulic diameter R/D_h of 45 were also fixed. In addition, the value $L/D_h = 30$ is large enough to neglect both the axial viscous and conduction effects, and $R/D_h = 45$ is also large enough to omit the effect of radius which appears only near the center of rotation. It is expected that the results obtained here may be applicable generally to the other cases for large L/D_h and R/D_h. Thus Eq. (1) is reduced to

$$\mathrm{Nu}_\Omega/\mathrm{Nu}_0 = f(\mathrm{Re}, \mathrm{Ro}, \mathrm{Ra}^*, z/D_h) \quad (2)$$

where the heat transfer results due to rotation are presented by the ratio of the rotating Nusselt number Nu_Ω to the nonrotating Nusselt number Nu_0. The Reynolds number Re indicates the forced convection effect; the rotation number $\mathrm{Ro} = \mathrm{Re}\,\mathrm{Re}_\Omega/\mathrm{Re}^2$, a ratio of the relative strength of the Coriolis force to the inertia force, represents the effect of the Coriolis force on the main flow forced convection; the rotational buoyancy parameter $\mathrm{Ra}^* = \mathrm{Ra}/\mathrm{Re}^2$, a ratio of relative strength of centrifugal buoyancy force to the inertia force, denotes the effect of centrifugal-buoyancy force on the forced convection. All the thermophysical properties needed in calculating these parameters were evaluated at the corresponding bulk temperature T_b.

For scaling the effects of rotation and deducing the heat transfer from the experimental data, nondimensional parameter groups were applied. Table 1 depicts the ranges of the experimental variables and the nondimensional parameters used in the present study. Due to the limitation of the pressure difference between the atmosphere and the centrifugal pump, it was difficult to obtain the same range of flow for a high rotation speed. Therefore, for the inward flow cases, compared with the outward flow cases, the Reynolds number was limited to 10,000 with rotational speed of 2000 rpm.

Experimental Facilities and Test Procedure

The experimental setup, also shown in previous work (Kuo et al., 1993), consists of four major parts: an air compressor or a centrifugal pump, two test sections, one electric motor with speed controller, and a data acquisition system. For the outward flow experiment, air was supplied from a compressor through flow meters, ranging from 0.2 to 8.0 m^3/h for indicating the air flow rate, and a rotary seal assembly to the test section. For the inward flow experiment, a centrifugal pump instead of a compressor was used to draw coolant from the atmosphere to the test section. Note that a bell-mouth entrance was designed for the outward flow passage, but a sharp-edged entry was employed for the inward flow passage.

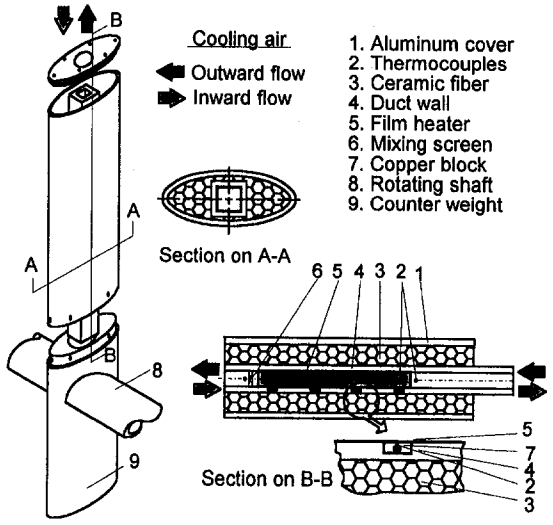

Fig. 2 Details of the test section

For deliberately suppressing the circumferential wall heat conduction and distinguishing the local heat transfer rate on each duct wall, low thermal conductivity material of fiberglass-reinforced plastic was employed to construct the duct wall with smooth interior surfaces. Four pieces of 0.01-mm-thick stainless-steel film heaters with dimensions of 4×120 mm^2, heated by electrical power supplies through slip-rings, were plated separately on the four duct wall surfaces. A T-type thermocouple was located at the duct inlet for measuring the inlet bulk temperature of air. A mixing chamber installed with staggered rod bundles for providing a well-mixed condition was attached to the exit plane for monitoring the outlet bulk temperature. At a certain location, the local regional average temperature on each wall was read by a thermocouple firmly soldered to a 0.5-mm-thick copper block with dimensions of 3.8×2 mm^2. The copper block was directly glued to the back of a film heater. Note that the copper blocks are electrically isolated from the film heater. Further constructional details of the test section are shown in Fig. 2.

Morcos and Bergles (1975), Hwang and Chou (1987), and Chen and Hwang (1989) proposed the wall heat conduction parameters K_p and K_p' to analyze the duct wall thermal boundary conditions, i.e.,

$$K_p = (k_w t)/(k_{\mathrm{air}} D_h) \quad (3)$$

is the ratio of wall heat conduction and air pure conduction inside a duct; and

$$K_p' = (k_w t)/(h D_h^2) \quad (4)$$

is the ratio of wall heat conduction and air mixed convection inside a duct.

Table 2 gives the estimated K_p and K_p' values for the fiberglass duct wall, the film heater, and the copper block. Because

Table 2 Estimation of the values of the wall conduction parameters

MATERIAL	k_w (W/m°C)	t (mm)	K_p (Based on air pure conduction)*	K_p' (Based on air mixed convection)**	REMARKS
FIBER GLASS	0.048	3.0	1.199	0.1199	WALL INSULATION
STAINLESS FILM HEATER	16.3	0.01	1.357	0.1357	WALL INSULATION
COPPER BLOCK	111.0	0.5	462.0	46.2	REGIONAL AVERAGE WALL TEMPERATURE

*Air thermal conductivity $k_{air} = 0.03003$ W/m°C.

**The Nusselt number assumed for mixed convection is 10.

$K_p' \ll 1.0$ for the fiberglass-reinforced plastic and the film heater, both of them can be treated as a material similar to the insulator. When the heater is supplied with electrical power, a boundary condition of nearly uniform heat flux can be achieved. On the other hand, the high K_p and K_p' of the copper block make the thermocouple readings in the block the regional average ones.

The test section had an actively heated length of 120 mm, a mean rotation radius of 180 mm, and a relatively small hydraulic diameter of 4 mm. This gave a relatively large ratio of actively heated length to hydraulic diameter of 30, which covered most of the laminar flow entrance region and both the turbulent flow entrance and the fully developed regions. The ratio of mean rotation radius to hydraulic diameter was 45, which was also reasonably large as compared with the value in a gas turbine and an electrical machine.

The test section assembly was encased in an oval aluminum tube for reducing the aerodynamic drag in the rotating condition. The internal void space was filled with insulating ceramic fiber, and the assembly was subsequently bolted perpendicular to the rotating shaft. The whole model, which was driven by an electric motor controlled by adjusting the electric current frequency from an inverter, was installed in a test cell enclosed by a support frame with three safety glass plates and two ventilation openings. The rotational speed was detected by a photo-electric tachometer. At the other end of the shaft, another slip-ring was applied for transmitting the detected data from the thermocouples to a recorder.

Data Reduction

In an experiment with either a large flow rate or a large rotational speed, a compressibility correction for the measured temperature of coolant flow was performed. By denoting T_r as the measured recovery temperature and T_w' is the measured wall temperature, the fluid temperature and the wall temperature may be corrected by both the effects of flow speed and the rotational potential:

$$T = T_r/(1 + \frac{k-1}{2}\gamma M^2) - \frac{(Z\Omega)^2}{2c_p} \quad (5)$$

$$T_w = T_w' - \frac{(Z\Omega)^2}{2c_p} \quad (6)$$

where c_p is the constant-pressure specific heat, k the specific heat ratio, and γ the temperature recovery factor. The values of γ for different flow regimes are (Schlichting, 1979):

$$\gamma = \mathrm{Pr}^{1/2} \quad \text{for laminar flow}$$

$$\gamma = \mathrm{Pr}^{1/3} \quad \text{for turbulent flow}$$

For instance, a maximum temperature correction of 2.5°C was found for Re = 15,500 (M ≈ 0.15) and 1.5°C for Ω = 315 rad/s (3000 rpm) in the outward flow case. In calculating the Nusselt number, the term $(Z\Omega)^2/2c_p$ is canceled between the fluid and wall temperature. But this correction does affect the thermal energy gain of the air flow passing through the channel, or the thermal energy transferred through the wall. Although the rotational potential is just a small correction in temperature measurement for rotation speed of 3000 rpm, it may be 100 times larger for rotation speed of 30,000 rpm in a real engine.

At a certain axial location, the heat transfer coefficient h_z was evaluated as the ratio of the net wall heat flux $q_{\mathrm{net},z}$ to the temperature difference between the wall temperature $T_{w,z}$ and the coolant bulk temperature $T_{b,z}$, i.e., $h_z = q_{\mathrm{net},z}/(T_{w,z} - T_{b,z})$. The net wall heat flux from the duct walls to the air flow was obtained by subtracting the external heat loss from the electric power supplied to the film heaters. The external heat loss including the axial conduction and radiation, estimated by means of measuring wall temperature over ranges of heater power setting and rotational speed under no-flow condition, was attributed to both conduction from the heated test section to the model support structure and convection to the ambient air in the test cell. The no-flow condition was achieved by filling insulation material inside the square duct of the test section. Based on an energy balance, the coolant bulk temperature along the main flow direction was determined by marching from the inlet value to the downstream direction by calculating the net heat flux added to the coolant. Note that when the marching procedure was executed at the outlet the accumulation effect of the term $(Z\Omega)^2/2c_p$ in Eq. (5) should be taken to compare the calculated and measured exit temperature.

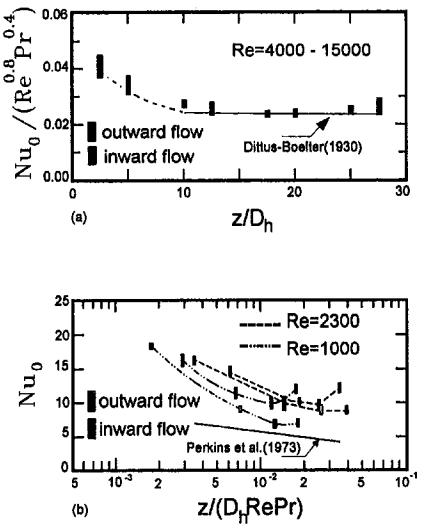

Fig. 3 Heat transfer distributions in nonrotating experiments: (*a*) turbulent flow regimes and (*b*) laminar regime

The root-sum-square method introduced by Kline and McClintock (1953) for uncertainty analysis showed in the present study that the estimated uncertainties in the rotational Nusselt number were mainly attributed to the local wall-to-coolant temperature difference (~75 percent) and the net heat flux added to coolant (~20 percent) from each wall. Uncertainty in the Nusselt number increases with the decrease in either the wall-to-coolant temperature difference or the net heat flux. The measured raw variable and its uncertainty can be expressed as $X_i = X_i$ (measured) $\pm \delta X_i$ where the best estimate of X_i is X_i (measured), and an uncertainty in X_i may be as large as δX_i. It is found that the uncertainties in the Nusselt number were less than 15 percent for ranges of parameters under study. When the Reynolds numbers were greater than 10,000, the values of the uncertainties were all less than 9 percent.

Results and Discussion

For simplifying the construction of the test section, the thermocouples were only installed on two adjacent walls of the duct. By rotating the radial duct in clockwise and counterclockwise directions, the temperature data on the four duct walls were obtained. The experiments without rotation were first conducted to determine the nonrotating Nusselt number Nu_0 distributions along the four duct sides for both the outward and the inward flows. Figure 3 gives the results, which are compared with the Dittus–Boelter (1930) correlation for the turbulent flow regime and the Perkins et al. (1973) correlation for the laminar flow regime. These corresponding correlations are:

Dittus–Boelter (1930)

$$\mathrm{Nu}_0 = \mathrm{Nu}_{TFD}[1.0 + 2.0/(z/D_h)] \quad (7)$$

for $z/D_h \geq 10.0$, where $\mathrm{Nu}_{TFD} = 0.023\,\mathrm{Re}^{0.8}\mathrm{Pr}^{0.4}$ is for the fully

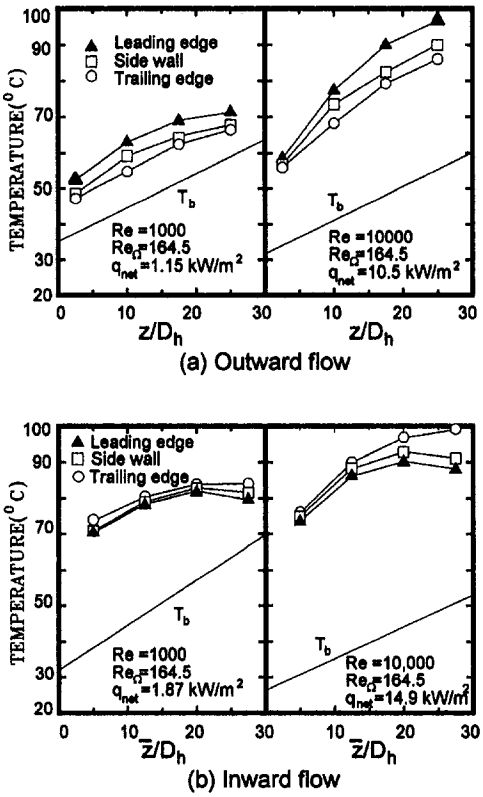

Fig. 4 Wall and coolant-bulk temperature distributions in rotating cases

developed turbulent flow in a circular duct with uniform wall temperature.

Perkins et al. (1973)

$$\mathrm{Nu}_0 = 1/[0.277 - 0.152 \exp(-38.6\delta)] \qquad (8)$$

where $\delta = z/D_h\mathrm{RePr} \geq 0.005$ for a square duct with a uniform wall heat flux.

For higher Reynolds numbers, Fig. 3(a) shows that the values of Nu_0 along the streamwise direction are approximately 10 percent within the results of Dittus–Boelter (1930). Near the duct exit, the measured wall temperature was lower in the experiment than that with the ideal thermal boundary condition of uniform heat flux; therefore, a higher Nu_0 was observed. This is affected by the discontinuity of the uniform heat flux thermal boundary condition at the exit. For low Reynolds numbers, Re = 1000 and 2300, Fig. 3(b) indicates that the inward flow Nu_0 is relatively higher than that of the outward flow Nu_0, and the measured values are higher than the laminar correlation. This is because: (1) the entry flow effect—the outward flow having a 90 deg turn before the bell-mouth entrance and a leading length, which may result in a swirl flow motion and a higher Nu_0 than that of a pure laminar flow in the entrance region—is observed. However, the inward flow with a sharp-edged entry could create flow separation and causes more disturbed flow over the entire duct length. As a result, the inward flow heat transfers are higher than the outward flow heat transfers. (2) The higher heat transfer results are also attributed to the axial conduction of heat on the duct walls. In addition, a higher Nu_0 near the exit for the laminar inward flow is due to a larger axial conduction heat loss near the rotation axis for the inward flow than the axial conduction heat loss near the outer end region for the outward flow. Note that the error bars of the measured data are within 10 percent.

When the flow passage is rotating, the typical distributions of local wall-to-bulk temperature along the test section for the inward and the outward flows are illustrated in Fig. 4. It is revealed that for the outward flow the temperature on the leading edge is relatively higher than that on the trailing edge; on the other hand, for the inward flow this trend is reversed. It is also found that the variations of the wall temperatures on the side walls are always between the values on the leading and trailing edges for both the outward and inward flows. Due to the extra heat loss at both ends of the channels for both the outward and the inward flows, the curves of temperature distributions bend at both ends. A greater temperature drop near exit for the inward flow is observed due to the larger conduction heat loss near the rotation axis, as mentioned previously. It is also observed in this figure that the heat flux increases the difference between the wall temperature and the bulk temperature.

Using the Nusselt number ratio $\mathrm{Nu}_\Omega/\mathrm{Nu}_0$, Fig. 5 depicts the heat transfer variations for the outward and the inward flows with different throughflow Reynolds numbers and rotational Reynolds numbers. The effects of the Coriolis and the centrifugal buoyancy forces on the heat transfer for the outward and the inward flows on the leading and the trailing edges are rather complex, and an attempt is made here to explain the heat transfer mechanism. The cross-stream secondary flow induced by the parameter ReRe_Ω may generally enhance the heat transfer on the four duct walls. But the secondary flow moving toward or away from the duct wall may further enhance or suppress the wall heat transfer. The radial secondary flow induced by the centrifugal buoyancy near the heated duct wall accelerates the main flow in the inward flow but decelerates the main flow in the outward flow. Therefore, the heat transfer ratio may be expressed qualitatively as follows:

$$\frac{\mathrm{Nu}_\Omega}{\mathrm{Nu}_0} = 1 + c_1 \frac{\mathrm{Re}\,\mathrm{Re}_\Omega}{\mathrm{Re}^2} \pm c_2 \frac{\mathrm{Re}\,\mathrm{Re}_\Omega}{\mathrm{Re}^2} \pm c_3 \frac{\mathrm{Ra}}{\mathrm{Re}^2} \qquad (9)$$

where c_1, c_2, and c_3 are some positive values, which should be functions of z/D_h and may vary for different parameters. c_1 signifies the general heat transfer enhancement on the four duct walls. $\pm c_2$ are for the duct wall facing and opposing the secondary flow, respectively. $\pm c_3$ are for the effect of centrifugal buoyancy for the inward and outward flows, respectively. Since the trailing edge for the outward flow and the leading edge for the inward flow are the walls facing the cross-stream secondary flow, they have the largest heat transfer enhancement among those on the four duct walls. Because of $+c_3\ \mathrm{Ra}/\mathrm{Re}^2$ for the

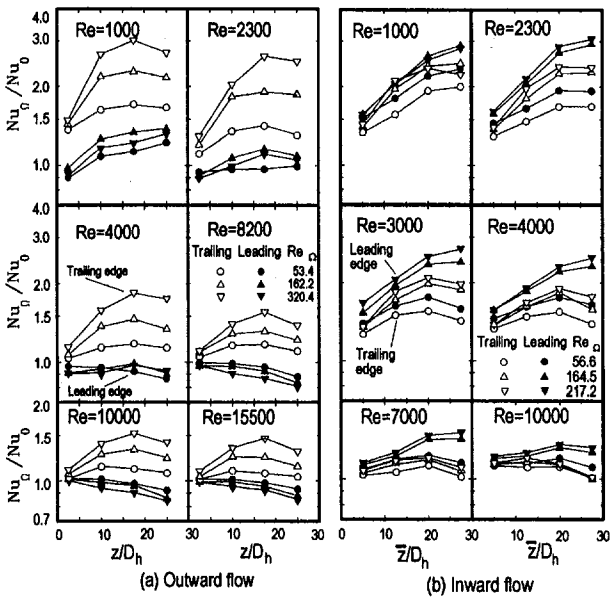

Fig. 5 Variations of heat transfer results along streamwise direction with varying Re

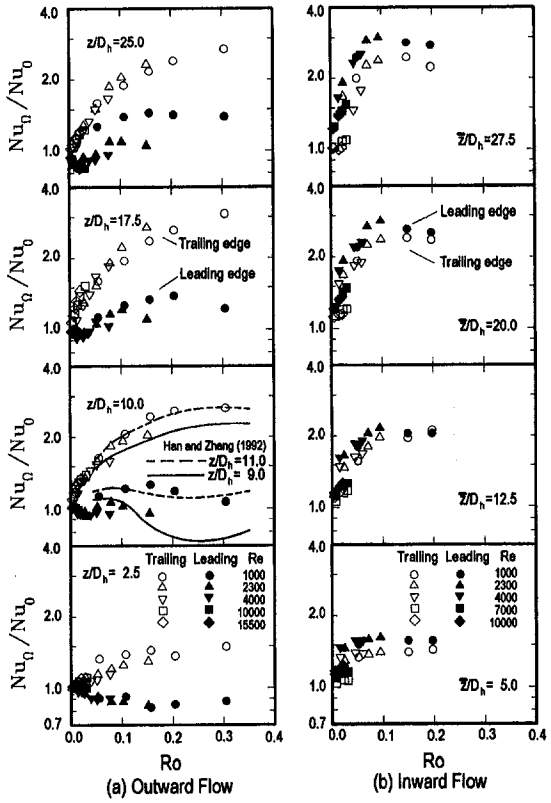

Fig. 6 Ro effects on heat transfer along streamwise direction

inward flow, all the heat transfer on the four walls is enhanced, i.e., $Nu_\Omega/Nu_0 > 1.0$ as shown in Fig. 5(b), regardless of $-c_2$ $ReRe_\Omega/Re^2$ for the trailing edge. The terms $(c_1 - c_2)$ Re $Re_\Omega/Re^2 - c_3Ra/Re^2$ for the outward flows and the leading edge give only a little heat transfer enhancement for Re = 1000 and 2300 and $z/D_h \geq 10$ or even suppress the Nu_Ω/Nu_0 for Re $\geq$ 4000. This yields a larger difference between the Nu_Ω/Nu_0 of the trailing and leading edge for the outward flow than that for the inward flow. At large Reynolds number, the rotation number was too low to have a substantial effect on heat transfer as shown in Fig. 5 and Eq. (8). Note that all the curves of Nu_Ω/Nu_0 bend near the exit because of a higher stationary Nu_0 observed in that region.

To examine the effect of the Coriolis-induced cross-stream secondary flow on the heat transfer at selected local positions, Fig. 6 discloses the variations of the Nusselt number ratio with the rotation number along with a comparison with the experimental results of radially outward flow from Han and Zhang (1992). The results of outward flow show that both the trailing edge and leading edge Nusselt number ratios of the present study at $z/D_h = 10.0$ agree fairly well with those of Han and Zhang (1992) at $z/D_h = 9.0$ and 11.0 under the following conditions: Ro calculated at rotational speeds of 400 and 800 rpm, Re between 2500 and 25,000, $R/D_h = 30$, and $D_h = 12.7$ mm. The present data are based on: Ro calculated at rotational speeds of 500, 1000, 1500, 2000, and 3000 rpm, Re between 1000 and 15,500, $R/D_h = 45$, and $D_h = 4.0$ mm. This indicates that Ro is indeed an important parameter in rotating heat transfer and a higher value can be obtained by either increasing the rotational speed or decreasing the Reynolds number. The results in Fig. 6 also reveal that for a higher rotation number, the heat transfer enhancement is considerably greater than that for a low rotation number because of the corresponding higher strength of the Coriolis-induced cross-stream secondary flow for the case of high rotation number. In the entry region the observed enhancement in heat transfer for the present developing flow is less than that of larger z/D_h. These results are consistent with the experimental data of Metzger and Stan (1977) for entry region heat transfer in rotating radial tube. For the inward flow, as expected, the leading edge shows the largest heat transfer enhancement because of the combined positive effects of Coriolis and centrifugal buoyancy forces. The data on the trailing edge are also higher than 1.0 at all positions and close to those of leading edge, as observed in Fig. 6 of Han et al. (1993). This is not the same as that for the outward flow. In the outward flow Nusselt number ratios less than 1.0 are observed at $z/D_h = 2.5$ on the leading edge due to both the negative centrifugal-buoyancy effect and the negative cross-stream secondary flow effect.

By definition the rotational buoyancy parameter is affected by the rotation number, the wall-to-coolant temperature, the eccentricity, and the local positions. In the heated rotating duct the centrifugal acceleration causes less dense fluid to move toward the axis of rotation, and generates radial secondary flows, which have a significant influence on the heat transfer. To highlight the salient feature of the centrifugal-buoyancy radial secondary flow, the outlet-to-inlet bulk temperature differences $T_{b,0} - T_{b,i}$ = 15.0, 30.0, and 45.0°C for the outward-flowing passage and $T_{b,0} - T_{b,i}$ = 15.0 and 30.0°C for the inward-flowing passage were selected while the other operating parameters were held constant during the measurement. Figure 7 illustrates the variations of Nusselt number ratio with the rotational buoyancy parameter at an axial location of $z/D_h = 17.5$. In the outward-flowing passage the increasing outlet-to-inlet bulk temperature differences made the Nusselt number ratios decrease at both the trailing edge and leading edge for low Reynolds number flows Re = 1000 and 2300, but for Re $\geq$ 4000 the trend is reversed. This may be due to the introduction of turbulence in the transitional flow regime by the retarded centrifugal buoyancy force. Then, the heat transfer variation is gradually diminished for higher Reynolds numbers.

In the inward-flowing passage the heat transfer coefficients always increase as the outlet-to-inlet bulk temperature differences increase. This is because the radial secondary flow induced is in the same direction as the inward flow. These phenomena can be found by analyzing mixed convection of the

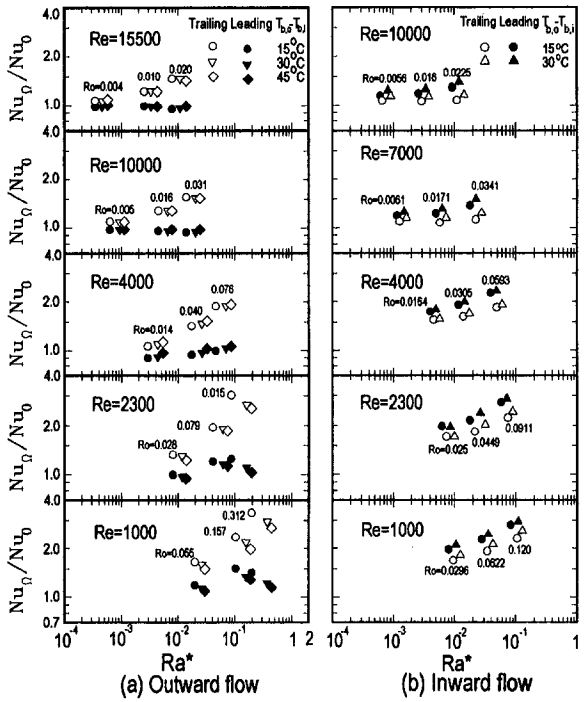

Fig. 7 Ra* effects on heat transfer with varying Re

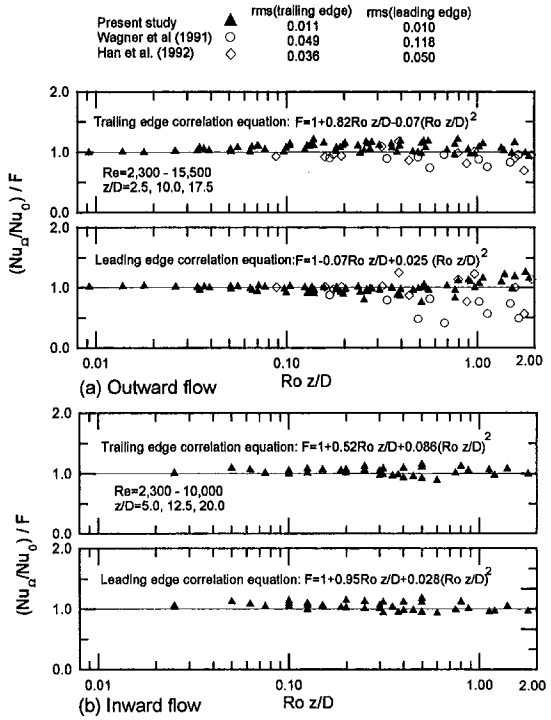

Fig. 8 Correlation of heat transfer data for: (*a*) outward flow and (*b*) inward flow

buoyancy-induced opposing and aiding flows in a vertical heated tube with either constant wall temperature or uniform wall heat flux (Abdelmeguid and Spalding, 1979; Buhr et al., 1974). As the rotational buoyancy parameter in the outward flowing passage increased, suppression of heat transfer was observed by Morris and Ayhan (1979), Clifford et al. (1984), Harasgama and Morris (1988), and Soong et al. (1991); on the other hand, increased tendencies toward heat transfer were found by Wagner et al. (1991a, b), Morris and Ghavami-Nasr (1991), and Han and Zhang (1992). The opposite trend may be due to the increase of turbulent shear stresses near the duct wall by flow deceleration, as explained previously.

It is extremely difficult to correlate the complex behavior of the heat transfer characteristics of the four duct walls with varying Re, Ro, Ra*, and z/D_h as shown in Eq. (2). As seen in Fig. 6 that the dependence of Re on the Nusselt number in the range of Re = $O(10^3 \sim 10^4)$ is only 5 percent difference in rms, and the dependence of Ra* on the Nusselt number is also 7 percent in rms, as shown in Fig. 7. Therefore, one may drastically simplify the correlation to the form $Nu_\Omega/Nu_0 = f$ (Ro, z/D_h). Furthermore, on closer examination of Nu_Ω/Nu_0 in Figs. 5 and 6, it may be seen that Ro and z/D_h show similar effects on the enhancement of the Nusselt number ratios. Thus, one may try to use the product $Ro \cdot z/D_h$ for the correlation. The results are shown in Fig. 8. Four second-order polynomials with the variable $Ro \cdot z/D_h$ are used for the leading and trailing edges of the outward and inward flows. The ranges of the variables used for the correlations and the maximum rms errors of the correlating and test data to the correlations are also described in the figure. The maximum rms differences between the correlation and the present data are quite small in both outward and inward flow. The differences compared with the data of Wagner et al. (1991a, b) may be due to the different thermal boundary condition used.

Concluding Remarks

The investigation has presented the rotation effects with varying throughflow Reynolds numbers of radially outward and inward flows on the local heat transfer in a rotating square duct. A high rotational speed test section with light weight and high strength was built for measuring the effects of rotation on the convective heat transfer in laminar, transitional, and turbulent flow regimes. The duct walls were constructed of low-conductivity material and heated by film heaters of 0.01 mm thickness for distinguishing the local average heat transfer performance on each wall and for achieving the required uniform wall heat flux boundary condition. The results obtained in the experiments are as follows.

1 Near the duct exit, the measured wall temperature was lower in experiment than that with the ideal thermal boundary condition of uniform heat flux; therefore, a higher Nu_0 was observed. This is affected by the discontinuity of the uniform heat flux thermal boundary condition at the exit.

2 The rotation effect can be expressed by

$$\frac{Nu_\Omega}{Nu_0} = 1 + c_1 \frac{Re\ Re_\Omega}{Re^2} \pm c_2 \frac{Re\ Re_\Omega}{Re^2} \pm c_3 \frac{Ra}{Re^2}$$

where c_1, c_2, and c_3 are some positive values that should be functions of z/D_h and may be varying for different parameters. c_1 signifies the general heat transfer enhancement on the four duct walls. $\pm c_2$ are for the duct wall facing and opposing the secondary flow, respectively. $\pm c_3$ are for the effect of centrifugal buoyancy for the inward and outward flows, respectively.

3 The heat transfer ratios were correlated to second-order polynomials with the variable $Ro \cdot z/D_h$ for the leading and the trailing edges of the outward and the inward flows. The ranges of the variables used for the correlations and the maximum rms errors of the correlating and test data to the correlations are also described.

Acknowledgments

The authors wish to express their appreciation to the National Science Council, Taiwan (Grant No. NSC-81-0401-E007-04), for their encouragement and financial support of this work.

References

Abdelmeguid, A. M., and Spalding, D. B., 1979, "Turbulent Flow and Heat Transfer in Pipes With Buoyancy Effects," *Journal of Fluid Mechanics,* Vol. 94, pp. 383–400.

Barua, S. N., 1955, "Secondary Flow in a Rotating Straight Pipe," *Proc. Royal Soc. London,* Vol. 227 A, pp. 133–139.

Buhr, H. O., Horsten, E. A., and Carr, A. D., 1974, "The Distortion of Turbulent Velocity and Temperature Profiles on Heating for Mercury in a Vertical Pipe," ASME JOURNAL OF HEAT TRANSFER, Vol. 96, pp. 152–158.

Chen, R. S., and Hwang, G. J., 1989, "Effect of Wall Conduction on Combined Free and Forced Laminar Convection in Horizontal Tubes," ASME JOURNAL OF HEAT TRANSFER, Vol. 111, pp. 581–585.

Clifford, R. J., Harasgama, S. P., and Morris, W. D., 1984, "An Experimental Study of Local and Mean Heat Transfer in a Triangular-Sectioned Duct Rotating in the Orthogonal Mode," ASME *Journal of Engineering for Gas Turbines and Power,* Vol. 106, pp. 661–667.

Dittus, F. W., and Boelter, L. M. K., 1930, "Heat Transfer in Automobile Radiators of the Tubular Type," University of California Publications in Engineering, Vol. 2, No. 13, pp. 443–461, reprinted in *Int. Comm. Heat Mass Transfer,* Vol. 12, 1985, pp. 3–22.

Guidez, J., 1989, "Study of the Convective Heat Transfer in a Rotating Coolant Channel," ASME *Journal of Turbomachinery,* Vol. 111, pp. 43–50.

Han, J. C., and Zhang, Y. M., 1992, "Effect of Uneven Wall Temperature on Local Heat Transfer in a Rotating Square Channel With Smooth Walls and Radial Outward Flow," ASME JOURNAL OF HEAT TRANSFER, Vol. 114, pp. 850–858.

Han, J. C., Zhang, Y. M., and Kalkuehler, K., 1993, "Uneven Wall Temperature Effect on Local Heat Transfer in a Rotating Two-Pass Square Channel With Smooth Walls," ASME JOURNAL OF HEAT TRANSFER, Vol. 115, pp. 912–920.

Harasgama, S. P., and Morris, W. D., 1988, "The Influence of Rotation on the Heat Transfer Characteristics of Circular, Triangular, and Square-Sectioned Coolant Passage of Gas Turbine Rotor Blades," ASME *Journal of Turbomachinery,* Vol. 110, pp. 44–50.

Hwang, G. J., and Chou, F. C., 1987, "Effect of Wall Conduction on Combined Free and Forced Laminar Convection in Horizontal Rectangular Channels," ASME JOURNAL OF HEAT TRANSFER, Vol. 109, pp. 936–942.

Hwang, G. J., and Soong, C. Y., 1989, "Experimental Automation and Heat Transfer Measurement on a Rotating Thermal System," *Transport Phenomena*

in Thermal Control, G. J. Hwang, ed., Hemisphere Publishing Corp., New York, pp. 375–388.

Johnston, J. P., Halleen, R. M., and Lezius, D. K., 1972, "Effects of Spanwise Rotation on the Structure of Two-Dimensional Fully Developed Turbulent Channel Flow," *Journal of Fluid Mechanics,* Vol. 56, Part 3, pp. 533–557.

Kline, S. J., and McClintock, F. A., 1953, "Describing Uncertainties in Single Sample Experiments," *Mechanical Engineering,* Vol. 75, Jan., pp. 3–8.

Kuo, C. R., Chen, J. L., and Hwang, G. J., 1993, "Experimental Study of Convective Heat Transfer in a Radially Rotating Square Duct With Uniform Wall Heat Flux and Inward Flow," ASME Paper No. 93-WA/HT-54.

Metzger, D. E., and Stan, R. L., 1977, "Entry Region Heat Transfer in Rotating Radial Tubes," AIAA Paper No. 77-189.

Morcos, S. M., and Bergles, A. E., 1975, "Experimental Investigation of Combined Forced and Free Laminar Convection in Horizontal Tubes," ASME JOURNAL OF HEAT TRANSFER, Vol. 97, pp. 212–219.

Morris, W. D., and Ayhan, T., 1979, "Observation on the Influence of Rotation on Heat Transfer in the Coolant Channels of Gas Turbine Rotor Blades," *Proc. Inst. Mech. Eng.,* Vol. 193, pp. 303–311.

Morris, W. D., and Ayhan, T., 1982, "An Experimental Study of Turbulent Heat Transfer in the Tube Which Rotates About an Orthogonal Axis," presented at the XIVth ICHMT Symposium on Heat and Mass Transfer in Rotating Machinery, Dubrovnik, Yugoslavia, Aug. 30–Sep. 3.

Morris, W. D., and Ghavami-Nasr, G., 1991, "Heat Transfer Measurements in Rectangular Channels With Orthogonal Mode Rotation," ASME *Journal of Turbomachinery,* Vol. 113, pp. 339–345.

Perkins, K. R., Shade, K. W., and McEligot, D. M., 1973. "Heat Laminarizing Gas Flow in a Square Duct," *International Journal of Heat and Mass Transfer,* Vol. 16, pp. 897–976.

Schlichting, H., 1979, *Boundary Layer Theory,* 7th ed., McGraw-Hill, New York, pp. 335, 714.

Soong, C. Y., Lin, S. T., and Hwang, G. J., 1991, "An Experimental Study of Convective Heat Transfer in Radially Rotating Rectangular Ducts," ASME JOURNAL OF HEAT TRANSFER, Vol. 113, pp. 604–611.

Wagner, J. H., Johnson, B. V., and Hajek, T. J., 1991a, "Heat Transfer in Rotating Passages With Smooth Walls and Radial Outward Flow," ASME *Journal of Turbomachinery,* Vol. 113, pp. 42–51.

Wagner, J. H., Johnson, B. V., and Kopper, F. C., 1991b, "Heat Transfer in Rotating Serpentine Passages With Smooth Walls," ASME *Journal of Turbomachinery,* Vol. 113, pp. 321–330.

Experimental Investigation of Natural Convection Heat Transfer in Volumetrically Heated Spherical Segments[1]

F. J. Asfia

B. Frantz

V. K. Dhir

Mechanical, Aerospace, and Nuclear Engineering Department,
School of Engineering and Applied Science,
University of California, Los Angeles,
Los Angeles, CA 90024

External cooling of a light water reactor vessel by flooding of the concrete cavity with subcooled water is one of several management strategies currently being considered for accidents in which significant relocation of core material is predicted to occur. At present, uncertainty exists with respect to natural convection heat transfer coefficients between the pool of molten core material and the reactor vessel wall. In the present work, experiments were conducted to examine natural convection heat transfer in internally heated partially filled spherical pools with external cooling. In the experiments, Freon-113 was contained in a Pyrex bell jar, which was cooled externally with subcooled water. The pool was heated using a 750 W magnetron taken from a conventional microwave. The pool had a nearly adiabatic free surface. The vessel wall temperature was not uniform and varied from the stagnation point to the free surface. A series of chromel–alumel thermocouples was used to measure temperatures in both steady-state and transient conditions. Each thermocouple was placed in a specific vertical and radial location in order to determine the temperature distribution throughout the pool and along the inner and outer walls of the vessel. In the experiments, pool depth and radius were varied parametrically. Both local and average heat transfer coefficients based on maximum pool temperature were obtained. Rayleigh numbers based on pool height were varied from 2×10^{10} to 1.1×10^{14}. Correlations for the local heat transfer coefficient dependence on pool angle and for the dependence of average Nusselt number on Rayleigh number and pool depth have been developed.

1 Introduction

The study of natural convection in volumetrically heated fluids is of interest in many engineering applications. The particular area of interest in this study is that of post-accident heat removal in nuclear reactors. Recently it has been suggested that flooding of the cavity of a Pressurized Water Reactor (PWR) or drywell of a Boiling Water Reactor (BWR) can be used as a mitigating procedure to prevent reactor vessel melt through. Thermal analyses carried out by Park and Dhir (1991) show that significant deviations in the predicted temperatures of the vessel head containing molten material can occur because of uncertainties in the reported natural convection heat transfer results obtained from numerical models and correlations. At present, no data are available at high Rayleigh numbers of interest for the calculation of natural convection heat transfer in the molten pool.

The earliest study of natural convection in volumetrically heated layers is that of Kulacki and Goldstein (1972). In their experiments, the fluid layer was bounded by two isothermal upper and lower plates held at a constant temperature and four insulated side walls. The Rayleigh numbers covered a range of $1.28 \times 10^4 \leq \mathrm{Ra} \leq 2.42 \times 10^7$. Heat transfer data were obtained using interferograms and included the laminar, transition, and turbulent regimes of natural convection. Upon examination of the temperature field, they discovered the existence of cellular structures in the upper portion for the laminar regime ($\mathrm{Ra} \leq 6.4 \times 10^5$). The area occupied by the cells decreased with increasing Rayleigh numbers until the cells were nonexistent in the turbulent regime. In this regime, the temperature field consisted of an isothermal central region bounded by a thin, unstable upper boundary layer and a wider, more stable lower boundary layer. The energy transport at the upper bounding surface was found to be much higher than that on the lower surface.

Subsequently, Kulacki and Emara (1975) conducted natural convection experiments in a horizontal fluid layer bounded from above by a plate held at constant temperature and from below by an insulated plate. For this set of boundary conditions, heat transfer data were obtained for Rayleigh numbers up to about 2×10^{12}. For Prandtl numbers varying from 2.75 to 6.85 the data were correlated as

$$\mathrm{Nu}_{\text{upper surface}} = 0.403\ \mathrm{Ra}^{0.226} \tag{1}$$

However, when explicit dependence of Nusselt number on Prandtl number was considered, the data were correlated as

$$\mathrm{Nu}_{\text{upper surface}} = 0.233\ \mathrm{Ra}^{0.233}\ \mathrm{Pr}^{0.239} \tag{2}$$

Nusselt and Rayleigh numbers were defined based on the height of the rectangular cavity.

Later, Min and Kulacki (1978) performed the same type of experiment but with the exception that the fluid layer was bounded from below by a spherical segment rather than a horizontal plate. Aspect ratio, defined as L/D, where L is the depth of the fluid layer and D is the diameter, was found to play an important role in determining the relationship between Nusselt and Rayleigh numbers. At low aspect ratios, the dependence of Nusselt number on Rayleigh number was much weaker, which corresponds to the theory that conduction is the primary source of heat transfer. However, when they increased the aspect ratio,

[1] This work received support from EPRI.

Contributed by the Heat Transfer Division for publication in the JOURNAL OF HEAT TRANSFER. Manuscript received by the Heat Transfer Division July 1994; revision received November 1994. Keywords: Enclosure Flows, Natural Convection. Associate Technical Editor: R. Viskanta.

the Nusselt number versus Rayleigh number results approached those for a horizontal fluid layer. This is due to the fact that as the volume of fluid increases, the effects of the spherical boundary diminish.

An experimental and numerical study of natural convection in internally heated pools contained in rectangular and semicircular cavities (trough) have been performed by Jahn and Reineke (1974). In the experiments, holographic interferometry was used to record the temperature field. The range of Rayleigh numbers for the computed data was $5 \times 10^5 \leq \mathrm{Ra} \leq 5 \times 10^8$. Jahn and Reineke found that for the rectangular cavity, the temperature field showed the presence of nonuniform eddies in the upper region of the pool with a stable and calm liquid layer in the lower region. They concluded that for this particular geometry, heat was transferred more effectively in the upper region as opposed to the bottom portion. The results for the semicircular cavity were similar to those for the rectangular container in that the temperature fields in the upper and lower regions exhibited almost the same type of behavior. The isotherm pattern for the curved region resembled that characteristic of a cooled vertical wall. This pattern led to the conclusion that the Nusselt number varied greatly along the cooled surface. Nusselt number was highest at the equator and lowest at the bottom. Numerical results were found to compare favorably with the data.

Mayinger et al. (1976) numerically and experimentally obtained the average heat transfer coefficient on the wall of a rectangular and a semicircular cavity. They also used numerical analysis to determine the average heat transfer coefficient on the wall of a hemispherical and a vertical cylinder cavity. In their numerical calculations, the wall temperatures were kept constant. According to their work, for $7 \times 10^6 \leq \mathrm{Ra} \leq 5 \times 10^{14}$, the average heat transfer coefficients on the upper surface and on the lower curved surface of the hemispherical pool were found to be

$$\mathrm{Nu}_{\text{upper surface}} = 0.4\ \mathrm{Ra}^{0.2} \tag{3}$$

$$\mathrm{Nu}_{\text{lower surface}} = 0.55\ \mathrm{Ra}^{0.2} \tag{4}$$

where $\mathrm{Ra} = g\beta\dot{Q}_v R^5/k_p\nu\alpha$ and Nusselt numbers are based on the radius of curvature and the maximum temperature difference within the cavity. It is somewhat surprising that according to Eqs. (3) and (4), the average heat transfer coefficient on the upper rigid surface is smaller than that on the lower curved surface.

Very recently, Sonnenkalb (1994) has presented a report on previous German research activities on natural convection in volumetrically heated fluids. According to this report, Reineke (1979) used numerical analysis to determine the average heat transfer coefficient on the wall of a partially filled hemispherical cavity with constant wall temperatures and obtained the following correlations:

$$\mathrm{Nu}_{\text{lower surface}} = 0.49\ \mathrm{Ra}^{0.18}(H/R)^{0.29} \quad H/R \geq 0.2 \tag{5}$$

$$\mathrm{Nu}_{\text{lower surface}} = 0.64\ \mathrm{Ra}^{0.18}(H/R)^{0.29} \quad H/R < 0.2 \tag{6}$$

where $10^7 \leq \mathrm{Ra} \leq 10^{10}$. Both Nusselt and Rayleigh numbers were defined in terms of maximum fluid level. It should be noted that when for $H/R = 1.0$ Eq. (5) is extrapolated to $\mathrm{Ra} = 10^{17}$ (Rayleigh number of interest in nuclear reactor applications), Nusselt numbers calculated from Eq. (4) are about two times higher than those obtained from Eq. (5).

Gabor et al. (1980) present the only previous experimental study in which natural convection in internally heated pools has been studied experimentally for a spherical geometry. The surface of the spherical containers was cooled and the surface also served as one of the electrodes. A disk in the center, placed near the pool free surface, served as the second electrode. This arrangement of electrodes led to nonuniformity in the heating process. In the experiments, Z_nSO_4–H_2O pools were formed in three sizes of hemispherical copper containers and pool depth was varied parametrically. No attempt was made in the experiments to calculate the variation of heat transfer coefficient along the curved surface. The average heat transfer coefficient data for $2 \times 10^{10} \leq \mathrm{Ra} \leq 2 \times 10^{11}$ were correlated as

$$\mathrm{Nu} = 0.55\ \mathrm{Ra}^{0.15}(H/R)^{1.1} \tag{7}$$

The Nusselt and Rayleigh numbers were defined based on the radius of curvature. It was noted that the highest temperature occurred in the middle of the upper pool surface, which was open to the atmosphere.

Although obtained under slightly different boundary conditions, comparisons from predictions from Eq. (4) of Mayinger et al. with Eq. (7) of Gabor et al. for $H/R = 1.0$ show that the difference between heat transfer coefficients predicted from the two correlations increases as the Rayleigh number becomes large. For Rayleigh number of 10^{17} (which is beyond the range of the data for which the two sets of correlations were developed), the average heat transfer coefficient predicted from the correlation of the Mayinger et al. is about ten times higher than that obtained from the extension of the correlation of Gabor et al. Also Eq. (7) gives a much different dependence of Nusselt number on the pool height than that given by Reineke (1979), Eqs. (5) and (6).

From this discussion, it is clear that significant uncertainty exists in the magnitudes of heat transfer coefficients predicted

Nomenclature

A = wetted surface area, m^2
c_p = specific heat, kJ/kg K
g = gravitational acceleration, m/s^2
H = pool depth, m
$\bar{h}(\theta)$ = time-averaged local heat transfer coefficient, W/m^2 K
$\bar{h}$ = time-averaged heat transfer coefficient, W/m^2 K
$\bar{h}_{av}$ = time and area-averaged heat coefficient, W/m^2 K
k = wall thermal conductivity, W/m K
k_p = thermal conductivity of fluid, W/m K
Nu = Nusselt number = $(Q_{\text{gen}}H)/(Ak_p\Delta T) = \bar{h}_{av}H/k_p$
Pr = Prandtl number
Q = rate of heat transfer, W
$\dot{Q}_v$ = volumetric heat generation rate, W/m^3
Ra = Rayleigh number = $g\beta\dot{Q}_vH^5/k_p\nu\alpha$
R = inner radius, m
R_e = equivalent radius corresponding to pool volume, m
r = radial distance, m
T = temperature, K
t = time, s
V = volume
z = vertical distance from free surface
α = thermal diffusivity of fluid
β = coefficient of thermal expansion, 1/K
θ = angle along the vessel wall, deg
$\Theta = (\theta/\phi)(\pi/2)$, rad
ν = kinematic viscosity of fluid
ρ = density
ϕ = pool angle, deg
ΔT = temperature difference

Subscripts

av = average
j = indices
max = maximum
p = pool
wi = inside wall
wo = outside wall
W = water

Superscripts

$-$ = time average

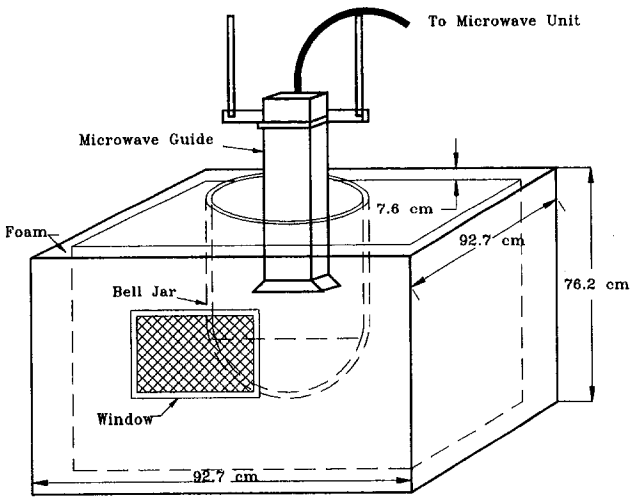

Fig. 1 Experimental apparatus

from various correlations. Thus experimental data are needed to resolve the following issues:

(*i*) Can existing correlations be extended to higher Rayleigh numbers with confidence?
(*ii*) What is the effect of ratio of the fluid layer depth to hemispherical cavity radius on the heat transfer coefficient?
(*iii*) How does the heat transfer coefficient vary along the surface of the hemispherical cavity?

The purpose of the present work is to shed light on the above-listed issues.

2 Experimental Procedure

The apparatus used in this work consists of a rigid box, which serves as a tank for subcooled water, as well as a support for a glass bell jar containing the test fluid. Figure 1 shows the test setup. The box is a three-layer water-tight container made of plywood and polyurethane foam. The outer and inner layers are made of 0.635-cm-thick plywood. The outer and inner dimensions of the box are 0.927 m × 0.927 m × 0.762 m and 0.762 m × 0.762 m × 0.686 m, respectively. The middle is a 7.62-cm-thick layer of Hathane 1680-11 (11 lb/ft^3 density) polyurethane foam. On the top of the box a plywood sheet with sixteen 2.54-cm-dia vent-holes and a larger hole cut in the middle is placed. The middle hole is cut so that a bell jar can pass through it and can rest on the sheet. Four different sizes of Pyrex bell jars were used in the experiments. Bell jar 1 is 59.55 cm in length (from the top edge down to the center of the spherical bottom), 60.1 cm in diameter (inner), and has a wall thickness of 1.17 cm. Bell jar 2 is 59.44 cm in length, 43.65 cm in diameter, and has a wall thickness of 1.1 cm. Two smaller bell jars 3 and 4 are 21 cm and 15.2 cm in diameter, respectively. The wall thickness of bell jar 3 in the hemispherical section varies from 1.0 cm in the bottom to 0.8 cm in the remainder of the hemisphere; bell jar 4 has 0.95 cm wall thickness. Two double-paned 0.25 m × 0.18 m wooden picture windows are built into the opposite sides of the box to allow viewing of the lower portion of the vessel.

The fluid inside the vessel is heated uniformly with a 750 W magnetron, the power to which is controlled with a conventional microwave oven. The magnetron is attached to a 10.2-cm-dia copper tube serving as a waveguide for the microwaves. This device is suspended by steel rods and aluminum clamps above the vessel. To control radiation from the microwave, bronze screens were placed along each inner wall of the large plywood box prior to pouring of the polyurethane foam. The screen is set to ground in order to short out the electromagnetic charge. A lucite lid is made to cover the opening of the vessel. A square opening with dimensions 11.4 cm × 11.4 cm was cut in the center of the lid to allow the waveguide to be lowered into the bell jar. Twenty-eight holes 5 mm in diameter were also drilled into the lid. Through these holes, twenty-eight 4 mm ID Pyrex tubes, each containing a chromel–alumel thermocouple wire, are placed and held in position by brass compression fittings. Thermocouples are located in two perpendicular planes. The location of thermocouples in one half of each plane is shown in Fig. 2. Details of thermocouple locations are given by Asfia (1995). Seven additional thermocouples are attached to the inner wall and seven more are placed on the outer wall of the vessel using Omegabond 101 epoxy. Each thermocouple wire is shrouded in a meshed steel braid for interference reduction. To ensure that the thermocouples return to their precise position whenever the lid is removed for cleaning and layer depth adjustment, the lid is equipped with four tabs, which fit into notches placed on the vessel. Readings from the thermocouples are taken with an Acro 900 Data Acquisition System. The data are stored and later plotted using computer graphics.

A water cooling system is used to maintain the temperature of water surrounding the vessel nearly constant with time. A 2.5 cm hole was drilled into the bottom of the box and fitted with a copper pipe and flange to serve both as a water inlet and a drain when a particular experiment is completed. A coil made of 1.27 cm copper tubing is used as a heat exchanger for the apparatus. Through a series of flexible plastic tubing, copper valves, and a 1/25 H.P. pump, water is removed from the upper surface of the pool. It is then passed through the copper coil, around which there is a continuous flow of cold water. Water exiting the heat exchanger is returned back to the bottom of the pool. Over the period of five hours, the maximum variation of water temperature in the outer pool was less than 1.25°C. In the experiments, the free surface of water was generally kept 6–9 cm above the free surface of R-113.

Before the actual experiment was run, each thermocouple was calibrated. All thermocouples were individually submerged sequentially in an ice bath, a pool of boiling Freon-113, and a pool of boiling water. The thermocouple outputs were compared with the temperature reading from a separate mercury thermometer. Using these data, calibration curves were drawn for each thermocouple. From these curves, relative error in reading from a particular thermocouple could be determined. Once every thermocouple was properly calibrated, all of the thermocouples were placed in their designated spots. With the lid in place and all of the thermocouples checked, the waveguide was lowered and fastened in place.

Prior to every test run, the test liquid was pumped into the vessel to the desired pool volume. Before adding water to the tank, a calibration run for heat generation rate in the fluid (lasting approximately 25–30 min.) was made. This was done in

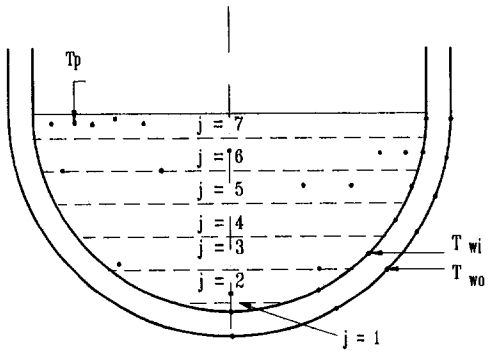

Fig. 2 Location of thermocouples in the pool and on the wall for bell jar 2, H/R_o = 1.0

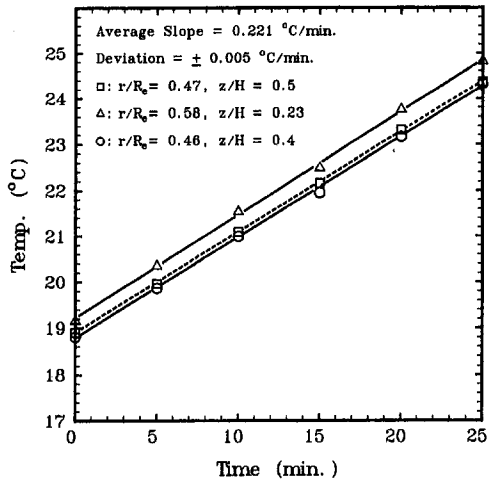

Fig. 3 Heat generation rate at different locations in the pool

order to calculate the power output from the microwave and to determine the uniformity of heat generation rate in the test liquid. The data from these runs were plotted and the slopes of the temperature versus time plots were used to calculate the heat input into the pool. Figure 3 shows a typical rate of rise of fluid temperature at three locations in a single plane of the pool when R-113 was used as the test liquid. The heat generation rate at different locations in the pool for all experiments was found to be within ±7 percent.

After the calibration for heat input to the test liquid was performed, the tank was filled with water and the cooling system was started. After assuring that everything was properly running, the microwave was turned on again, and the pool was allowed to heat up. After approximately one hour, the pool acquired a nearly steady-state temperature. The entire test run was carried out for about six hours. Since R-113 vapor is heavier than air, evaporation from the pool free surface is expected not to contribute in any significant way to the heat loss over long periods of time. The Acro Acquisition System was adjusted to record the temperatures every 15 seconds. It takes almost 50 ms for the system to read the input of each thermocouple. Because of the inevitable interference from the microwave, proper thermocouple readings could not be obtained unless power was shut off. To avoid this problem, thermocouple readings were taken at 10 min. intervals. Thus, after every 575 seconds, power was cut off for 25 seconds and two sets of thermocouple readings were taken (at 585 seconds and at 600 seconds). After recording the second set, power was immediately restored. These short power interruptions appeared to have no effect on the temperature behavior of the pool over the duration of the experiment.

3 Results and Discussion

One of the important considerations in the experiments conducted with internally heated pools is uniformity of the heat generation rate. Heating rates in various liquids, such as water, ethanol, olive oil, silicone oil, and R-113, using the microwave guide arrangement as shown in Fig. 1, were determined. A large difference in the heating rates near the pool free surface and at the bottom of the pool was found to exist in all liquids except R-113. As noted earlier with R-113, the rate of temperature rise at any location in the pool did not differ by more than ±7 percent from the mean value. Our lack of success in finding other liquids that could be heated uniformly with microwaves limited the number of data points that could be obtained.

Prior to conducting the experiments, the equivalent radii, R_e, of the vessels were obtained by noting the volume of liquid needed to fill the jar to a certain height. Table 1 gives the equivalent radii along with other data. The volume of liquid was measured before and after the experiments to obtain the rate of evaporation. The heat loss from evaporation at the free surface was calculated to be less than 5 percent of input heat during the duration of the experiments.

Because of the spherical geometry of the pool, the heat transfer area changes significantly with the angular position measured from the lower stagnation point. To determine the area associated with each of the thermocouples located discretely on the bell jar surface, the angle between any two neighboring thermocouples was determined. Half of this angle on either side of a given thermocouple was assigned to that thermocouple. By knowing the total subtended angle and the equivalent radius, the surface area and pool volume assigned to a given surface thermocouple could be determined. Figure 2 shows how the pool was divided into strips.

Knowing the vessel wall thickness, δ, the thermal conductivity, k, of the bell jar, the surface area for each strip, ΔA_j, the heat transfer rate for each section could be determined as:

$$Q_j = (\Delta A_j)k/\delta(T_{wi} - T_{wo}). \quad (8)$$

It should be noted that the temperature was not constant along the curved wall. For example, when bell jar 2 was used with $H/R_e = 0.72$, the inner wall temperature near the pool free surface was 20.7°C while at the lower stagnation point it was 17.6°C. The variation in wall temperature for other cases is given by Asfia (1995). Equation (8) is written under the assumption that heat transfer across the vessel wall is one dimensional. The assumption is realistic everywhere except for two locations, near the pool free surface and the lower stagnation point. Two-dimensional conduction analyses were performed to calculate the heat losses through the vessel wall at the top and bottom portions. The total heat transfer rate, ΣQ_j, to water is the sum of heat transfer rate for each section. Table 1 lists all the tests and gives the heat generation rate, Q_{in}, heat loss by evaporation, $Q_{l,\text{evap}}$, and heat transferred, Q_{out}, across the curved surface. A satisfactory balance is found to exist between the energy input rate in the pool and the total energy loss rate from the pool. For bell jars 3 and 4, smaller H/R_e ratios were not studied because for shallow pools sufficient energy could not be deposited into the pools.

The time-averaged heat transfer coefficient at a given location was determined by knowing the maximum temperature, $T_{p\max}$, in the pool as:

$$\bar{h}_j = \frac{k(T_{wi} - T_{wo})}{\delta(T_{p\max} - T_{wi})} \quad (9)$$

Uncertainty in $\bar{h}_j$ is determined from the expression

$$\Delta\bar{h}_j/\bar{h}_j = [(\Delta k/k)^2 + (\Delta(T_{wi} - T_{wo})/(T_{wi} - T_{wo}))^2 + (\Delta\delta/\delta)^2 + (\Delta(T_{p\max} - T_{wi})/(T_{p\max} - T_{wi}))^2]^{1/2} \quad (10)$$

Table 1 Heat transfer rates for each experiment

	R_e cm	H/R_e	Ra	dT/dt °C/sec	Q_{in} W	$Q_{l,\text{evap}}$ W	Q_{out} W
Bell jar 1	30.8	1.0	1.1×10^{14}	$2.5 \times 10^{-3} \pm 5\%$	216.9	4.6	189
	30.8	0.55	4.54×10^{12}	$2.45 \times 10^{-3} \pm 7\%$	81.8	3.6	77
Bell jar 2	21.83	1.0	2.8×10^{13}	$3.72 \times 10^{-3} \pm 1.2\%$	123.4	3.9	116.9
	23.3	0.72	6.2×10^{12}	$3.22 \times 10^{-3} \pm 2\%$	72	2.4	65
	23.5	0.55	2×10^{12}	$3.4 \times 10^{-3} \pm 2.1\%$	53.5	1.0	52.7
	22.7	0.4	3.95×10^{11}	$4.4 \times 10^{-3} \pm 2.3\%$	37	0.7	37
	24.3	0.26	1.01×10^{11}	$5.7 \times 10^{-3} \pm 1\%$	30.1	0.5	29.5
Bell jar 3	11.9	0.53	6.3×10^{10}	$4.23 \times 10^{-3} \pm 0.7\%$	10.1	0	10.9
Bell jar 4	8.7	0.9	2.2×10^{11}	$5.5 \times 10^{-3} \pm 0.1\%$	9	0	8.4
	8.46	0.63	3.5×10^{10}	$4.64 \times 10^{-3} \pm 2.1\%$	3.8	0	3.1

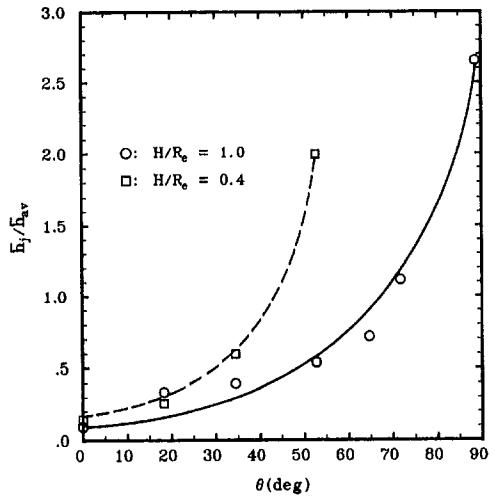

Fig. 4 Ratio of local to average heat transfer coefficient with respect to angle for bell jar 2

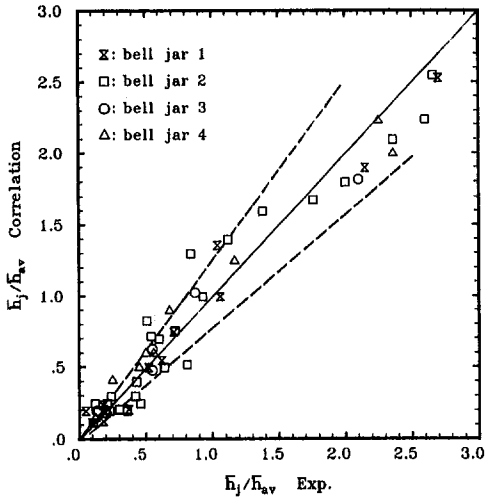

Fig. 5 Comparison of obtained data with developed correlation (Eq. (12))

The maximum pool temperature occurred in the upper section of the pool almost between the pool center and the vessel wall. Uncertainty in measurement of maximum pool temperature is considered to be less than 0.6 percent. Maximum uncertainties in thermocouple readings and thermal conductivity of glass are ±5 and ±3 percent, respectively. Uncertainties in measurements of glass thickness are ±9 percent for bell jars 1 and 2 and ±20 percent for bell jars 3 and 4. From Eq. (10), the uncertainty in heat transfer coefficient is found to range from ±9 to ±16 percent for bell jars 1 and 2 and ±20 to ±40 percent for bell jars 3 and 4. The highest uncertainty in the heat transfer coefficient occurred at the lower portions of the bell jars 3 and 4 where the difference between the inside and outside wall temperatures had the smallest value.

Average heat transfer coefficient for the spherical segment is obtained as

$$\bar{h}_{av} = \frac{\sum_{j=1}^{j=N} \bar{h}_j \Delta A_j}{\sum_{j=1}^{j=N} \Delta A_j} \tag{11}$$

Figure 4 shows the ratio of the local to average heat transfer coefficient as a function of angular position measured from the lower stagnation point. The plotted data are for $H/R_e = 0.4$ and $H/R_e = 1.0$ for bell jar 2. Heat transfer coefficient is highest near the free surface and decreases along the periphery of the spherical segment. The decrease in the heat transfer coefficient along the periphery is due to thickening of the thermal layer caused by the wall drag and reduction of the flow area. The maximum heat transfer coefficient is found to be 2.5 times larger than the average heat transfer coefficient. The ratio of maximum to minimum heat transfer coefficient is as high as 20. Similar behavior in the ratio of local to average heat transfer coefficient has been observed for other pool heights. Generally the heat transfer coefficient near the free surface decreased while that at the stagnation point increased when pool height was decreased. Local heat transfer coefficient is a function of the angular position measured from the lower stagnation point, θ, and the height of the pool or pool angle, ϕ, and is correlated as:

$$\frac{\bar{h}(\theta)}{\bar{h}_{(av)}} = C_1 \sin \Theta - C_2 \cos \Theta \quad \text{for} \quad 0.73 < \theta/\phi \leq 1$$

$$C_1 = -1.2 \cos \phi + 2.6$$

$$C_2 = -2.65 \cos \phi + 3.6 \tag{12}$$

and

$$\frac{\bar{h}(\theta)}{\bar{h}_{(av)}} = C_3 \sin^4 \Theta + C_4 \quad \text{for} \quad 0 \leq \theta/\phi \leq 0.73$$

$$C_3 = -0.31 \cos \phi + 1.06$$

$$C_4 = 0.24 \cos \phi + 0.15$$

where $\Theta = (\theta/\phi)(\pi/2)$. All of the data obtained in this study are compared with the correlation in Fig. 5. Most of the data are seen to lie within ±20 percent of predictions from correlation.

Figure 6 shows the isotherms obtained by linear interpolation of temperatures obtained from thermocouples placed at different locations in the pool. Isotherms are not exactly symmetric about a plane passing through the center of the spherical section. Stratification in the lower part of the middle section of the pool is much stronger than in the upper part. The isotherm pattern shown on the left-hand side of Fig. 6 is indicative of the existence of a recirculatory zone in the corner formed by the pool free surface and the vessel wall. From the isotherm pattern shown in Fig. 6, it is clear that the uncertainty in measurement of the maximum pool temperature cannot be greater than 0.2°C or 0.6 percent, which is considered for the evaluation of the heat transfer coefficient uncertainties in Eq. (10). After initial heating of the pool, liquid and wall temperatures were observed to oscillate with time. The period, amplitude, and time for onset of oscillations for pools of different radii for bell jar 1 is given in Table 2. For a given H/R_e, the time at which oscillations begin is observed to depend on the location within the pool. In the lower portion of the pool, the temperatures generally begin

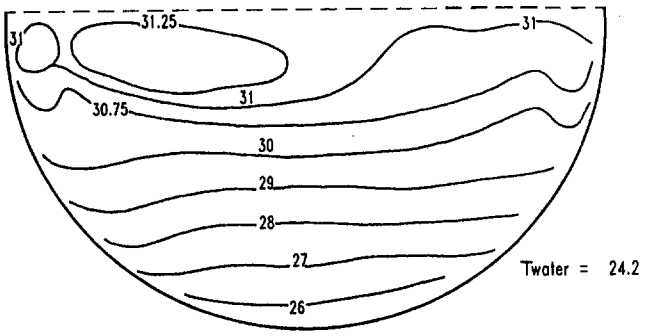

Fig. 6 Isotherm patterns for bell jar 2, $H/R_e = 1.0$ (all temperatures are in °C)

Table 2 Temperature oscillations: bell jar 2

H/R_e	Position	$\dot{Q}_v(W/m^3)$, $T_{pmax} - T_W$	Onset of osci.(min)	Period min	Most Prob. Period(min)	Amplitude $\pm°C$
1.0	r/R_e=0.94, z/H=0.1	5342,	130	20-50	20	0.04-0.06
1.0	r/R_e=0.62,z/H=0.14	5.8	130	30-60	-	0.02-0.04
1.0	r/R_e=0.44,z/H=0.14		130	20-50	30	0.02-0.04
1.0	r/R_e=0.55,z/H=0.75		100	20-50	-	0.02-0.06
1.0	r/R_e=0.86,z/H=0.27		130	40-50	-	0.04
1.0	r/R_e=0.34,z/H=0.27		130	30-60	50	0.02
1.0	T_{wi},z/H=0.05		130	30-40	-	0.04-0.08
1.0	T_{wi},z/H=0.22		150	30-40	30	0.02-0.07
0.40	r/R_e=0.0,z/H=0.75	6672.7,	80	20-50	40	0.075-0.15
0.40	r/R_e=0.44,z/H=0.33	8.0	120	20-50	40	0.02-0.15
0.40	r/R_e=0.56,z/H=0.16		120	20-60	30	0.01-0.30
0.40	r/R_e=0.56,z/H=0.16		120	30-60	30	0.02-0.19
0.40	T_{wi},z/H=0.044		90	40-60	40	0.025-0.15
0.40	T_{wi},z/H=0.57		80	20-60	30	0.015-0.15

to oscillate somewhat earlier than in the upper portion. Close to the pool surface, the values of amplitude and frequency of the oscillations are larger than those in the interior of the pool. In the middle region, the largest values of amplitude and frequency of oscillations occur near the walls. These values decrease as one approaches the center. It was observed that the temperature oscillations for symmetric locations across the pool are not symmetric, even though the values for their time period and their amplitude are almost similar. The difference between the maximum pool temperature and the water temperature is also given in Table 2. The amplitude of oscillations is found to be almost 1 percent of the total temperature difference. Generally, oscillation time periods varying from 20 to 70 minutes were found. No clear effect of change in pool height on the behavior of oscillations is noted. The temperature oscillations probably are a reflection of disruptions in the internal circulatory flow. The disruptions are caused by the imbalance that develops between buoyancy and viscous forces. From the temperature data, it is clear that the magnitude of wall heat transfer coefficients also oscillates with time.

The data for the Nusselt number based on the heat transfer coefficient averaged over the wetted surface of the pool are plotted in Fig. 7 as a function of Rayleigh number. The plotted data are for H/R_e = 0.26, 0.4, 0.55, 0.72, and 1.0, when bell jar 2 was used. In this figure, H/R_e = 1.0 and 0.55 data for bell jar 1 and H/R_e = 0.53 for bell jar 3 and H/R_e = 0.9 and 0.63 for bell jar 4 are also plotted. The Nusselt and Rayleigh number are defined as

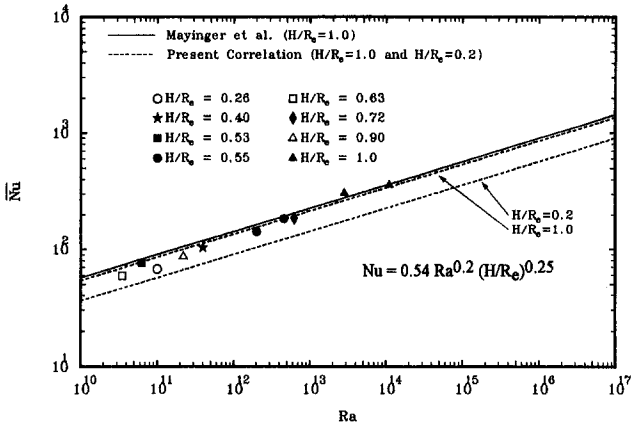

Fig. 7 Comparison of the present date with Mayinger's numerical results and present correlation

$$\mathrm{Nu} = \frac{\bar{h}_{av} H}{k_p} \tag{13}$$

$$\mathrm{Ra} = \frac{g\beta \dot{Q}_v H^5}{k_p \nu_p \alpha_p} \tag{14}$$

From the data obtained in this study, a correlation for the dependence of Nusselt number on Rayleigh number and pool depth has been developed. This correlation can be expressed as

$$\mathrm{Nu} = 0.54(\mathrm{Ra})^{0.2}(H/R_e)^{0.25} \tag{15}$$

The heat transfer data have been correlated within ±15 percent with this correlation. In Fig. 7 the results of numerical calculations of Mayinger et al. for a hemisphere with no-slip boundary condition at the pool surface and isothermal boundaries (Eq. (4)), and the present correlation for two different pool heights, H/R_e = 1.0 and 0.2, are also plotted. The data for H/R_e = 1.0 appear to lie very close to the numerical calculations of Mayinger et al. (Eq. (4)). Thus, it can be concluded that heat transfer coefficients predicted from the numerical work of Mayinger et al. for a hemispherical cavity are almost representative of the present data. This is despite the fact that in the present experiments, the pool surface was free and nearly adiabatic and the curved wall bounding the pool was nonisothermal. A rather good agreement of the present data for the average heat transfer coefficient with the numerical prediction of Mayinger et al. for a hemispherical pool suggests that changes in boundary conditions had a weaker role to play. The present correlation covers a range of $2 \times 10^{10} \leq \mathrm{Ra} \leq 1.1 \times 10^{14}$, when pool height, H, is used as the characteristic length in Nusselt and Rayleigh numbers. Since $\mathrm{Nu} \sim \mathrm{Ra}^{0.2}$, average heat transfer coefficient for H/R_e = 1.0 is independent of pool height. Also, the same form of correlation will be realized if equivalent radius of the vessel instead of height was used as the characteristic length. For shallower pools the heat transfer coefficient depends very weakly on the ratio of pool height to pool radius. Because the Nusselt number depends very weakly on H or R_e, it is believed that the results of the present study can be extended with little uncertainty to a reactor situation where Rayleigh numbers of interest are on the order of 10^{17}. To confirm this conclusion, further experimental or numerical studies will be required. It should also be noted that the molten pool in a reactor vessel will be at a very high temperature. As a result, in comparison to present work, the radiative heat transfer from the pool top surface will be nonnegligible.

Conclusions

1 Microwave heating has been successfully used in this work to produce uniform internal heating in pools contained in spherical segments. However, this is true only for R-113 as tests with other liquids showed significant nonuniformities.

2 Using R-113 as the test liquid, natural convection heat transfer data in internally heated pools contained in spherical segments cooled from outside have been obtained. The data have been obtained for H/R_e varying from 0.26 to 1.0.

3 Although in the present study the pool curved wall was not isothermal, Nusselt numbers obtained from the numerical results of Mayinger et al. for a hemispherical cavity with isothermal boundaries appear to compare favorably with the present data.

4 The heat transfer coefficient is lowest at the stagnation point and increases along the spherical segment. The ratio of maximum to minimum heat transfer coefficient can be as high as 20, while the ratio of maximum to average heat transfer coefficient can be as high as 2.5.

5 From the data for different pool radii and pool depths, a correlation for the dependence of Nusselt number based

on average heat transfer coefficient on Rayleigh number and pool depth has been found to be

$$\mathrm{Nu} = 0.54\ \mathrm{Ra}^{0.2}(H/R_e)^{0.25}$$

$$2 \times 10^{10} \leq \mathrm{Ra} \leq 1.1 \times 10^{14}$$

6 From the data at different pool heights a correlation for the dependence of local heat transfer coefficient on the angular position and the height of the pool or the pool angle has also been developed.

References

Asfia, F. J., 1995, "Experimental Study of Natural Convection in a Volumetrically Heated Hemispherical Pool," Ph.D. Dissertation, UCLA, Los Angeles, CA.

Gabor, J. D., Ellison, P. G., and Cassulo, J. C., 1980, "Heat Transfer From Internally Heated Hemispherical Pools," presented at the 19th National Heat Transfer Conference, Orlando, FL.

Jahn, M., and Reineke, H. H., 1974, "Free Convection Heat Transfer With Internal Heat Sources," *Proceedings of the Fifth International Heat Transfer Conference,* Vol. 3, p. 74.

Kulacki, F. A., and Goldstein, R. J., 1972, "Thermal Convection in a Horizontal Fluid Layer With Uniform Volumetric Energy Sources," *Journal of Fluid Mechanics,* Vol. 55, Part 2, pp. 271–287.

Kulacki, F. A., and Emara, A. A., 1975, "High Rayleigh Number Convection in Enclosed Fluid Layers With Internal Heat Sources," U.S. Nuclear Regulatory Commission Report NUREG-75/065.

Kulacki, F. A., 1976, "Review and Evaluation of 'Examination of Thermohydraulic Processes and Heat Transfer in a Core Melt,' by Mayinger, Jahn, Reineke, and Steinbrenner," letter report prepared for the U.S. NRC under contract AT(49-24)-0149).

Mayinger, F., Jahn, M., Reineke, H., and Steinbrenner, V., 1976, "Examination of Thermohydraulic Processes and Heat Transfer in a Core Melt," BMFT RS 48/1, Institut für Verfanhrenstechnic der T.U., Hanover, Germany.

Min, J. H., and Kulacki, F. A., 1978, "An Experimental Study of Thermal Convection With Volumetric Energy Sources in a Fluid Layer Bounded From Below by a Segment of a Sphere," presented at the 6th International Heat Transfer Conference, Toronto, Canada.

Park, H., and Dhir, V. K., 1991, "Steady State Analysis of External Cooling of a PWR Vessel Lower Head," *AIChE Symposium Series,* No. 283, Vol. 87, pp. 1–12.

Reineke, H. H., 1979, "Numerische Untersuchung der thermohydraulischen Vorgange und des Warmeuberganges in einer Kernschmeize bei kugelsegmentförmiger Geometrie und bei zuflie βendem Material von oben," BMFT RS 166-79-05, Band II A1.

Sonnenkalb, M., 1994, "Summary of Previous German Research Activities and Status of GRS Program on In-Vessel Molten Pool Behaviour and Ex-Vessel Coolability," presented at the OECD Conference on Large Molten Pool Heat Transfer, Grenoble, France.

Flow and Heat Transfer Due to a Buoyant Ceiling Jet Turning Downward at a Corner

K. Kapoor

Y. Jaluria
Fellow ASME

Department of Mechanical and Aerospace Engineering, Rutgers—The State University of New Jersey, New Brunswick, NJ 08903

An experimental investigation has been carried out on the flow and heat transfer characteristics of a horizontal buoyant ceiling jet that turns downward at a corner to yield a vertical negatively buoyant wall flow. Such flow situations are frequently encountered in thermal energy storage, in electronic systems, and in room fires. However, not much work has been done to understand the basic mechanisms governing such flows, particularly the flow near the corner. In this study, a two-dimensional jet of heated air is discharged adjacent to the lower surface of an isothermal horizontal plate. An isothermal vertical plate is attached at the other end of the horizontal surface, making a right angle corner. The vertical penetration distance of the resulting downward flow is measured and is related to the inflow conditions, particularly to the temperature and velocity at the jet discharge. This penetration distance is found to increase as the distance between the discharge location and the corner is reduced and also as the relative buoyancy level in the inlet flow is decreased. Velocity and temperature measurements are also carried out over the flow region. These indicate that the ceiling flow separates from the horizontal surface just before reaching the corner and then reattaches itself to the vertical wall at a finite distance vertically below the corner. The local surface heat flux measurements show a minimum in the heat transfer rate before the turn, along with a recovery in the heat transfer rate after the turn and the existence of a small recirculation zone near the corner. The net entrainment into the flow and heat transfer rate to the solid boundaries are also measured and correlated with the jet discharge conditions.

Introduction

Buoyant jets are important in meteorological, oceanographic, and environmental studies. Heat rejection to the atmosphere and to water bodies involves turbulent buoyant jets. Solar energy heat extraction and energy storage systems are also concerned with buoyant jet flows. Similarly, a fire in an enclosure generates a fire plume, which impinges on the ceiling and gives rise to a ceiling jet. This ceiling jet spreads outward from the point of impingement and turns downward at the corners of the room. This generates a downward wall flow with an opposing buoyancy force, since this force is directed upward. Although the vertical buoyant jet and ceiling jet have been considered separately, very little work has been done on negatively buoyant wall flows and on the flow characteristics of a downward-turning buoyant ceiling jet. In the present paper, an experimental investigation is reported on such mixed convection flows and the effect of buoyancy on the transport.

Laminar buoyant jets have been studied by several investigators, as reviewed by Jaluria (1986). Turbulent jets, which are of much greater practical interest, have been studied more extensively; see, for instance, Morton (1959), Chen and Rodi (1979), Turner (1979) and List (1982). Jets with opposing buoyancy have been considered by Turner (1966), Seban et al. (1978), and Baines et al. (1990). Goldman and Jaluria (1986) carried out a detailed experimental investigation of negatively buoyant jets. The flow characteristics of a two-dimensional wall jet, with opposing buoyancy force, in an isothermal medium were studied. It was found that the penetration distance δ_p decreases with an increase in the Richardson number Ri, which indicates the relative buoyancy level. The net entrainment into the flow was found to increase with Ri over the investigated range. Jaluria and Kapoor (1988) extended this range and found that large flow rates are generated in the wall flow due to entrainment.

Kapoor and Jaluria (1989) investigated the heat transfer characteristics of a two-dimensional negatively buoyant wall jet in an isothermal environment. The heat transfer rate to an isothermal surface was measured and was found to decrease with an increase in Ri, mainly because of the reduction in the penetration distance, which reduces the heat transfer area. It was also found that the penetration distance decreases with an increase in the wall temperature. This is due to a decrease in the heat transfer, since an increase in surface temperature reduces the temperature difference between the jet inlet and the surface. This, in turn, results in a higher opposing local buoyancy level in the flow and thus a smaller penetration distance.

The transport in a horizontal buoyant ceiling jet has been considered by a few investigators. The flow generated by a ceiling jet, which is driven by the fire plume, has been studied by Alpert (1975). The characteristics of a ceiling jet were investigated by Cooper (1982, 1989). He developed analytical estimates to predict the depth of penetration and entrainment into negatively buoyant, ceiling jet-driven wall flows at the early stages of the fire. You (1985) measured steady-state velocity and temperature profiles in the ceiling jet. Veldman et al. (1975) and Motevalli and Marks (1990) measured the temperature and velocity profiles in ceiling jets driven by a fire plume impinging on a ceiling for different thermal conditions. Baines and Turner (1969) studied the turbulent convection from a source in an enclosed space, simulating the physical circumstance outlined above and indicating different flow regimes that arise.

It is seen from this review of the relevant literature that, although separate studies on vertical and ceiling jets are available, no detailed effort has been directed at the flow and

Contributed by the Heat Transfer Division for publication in the JOURNAL OF HEAT TRANSFER. Manuscript received by the Heat Transfer Division March 1995; revision received August 1995. Keywords: Fire/Flames, Jets, Mixed Convection. Associate Technical Editor: R. Viskanta.

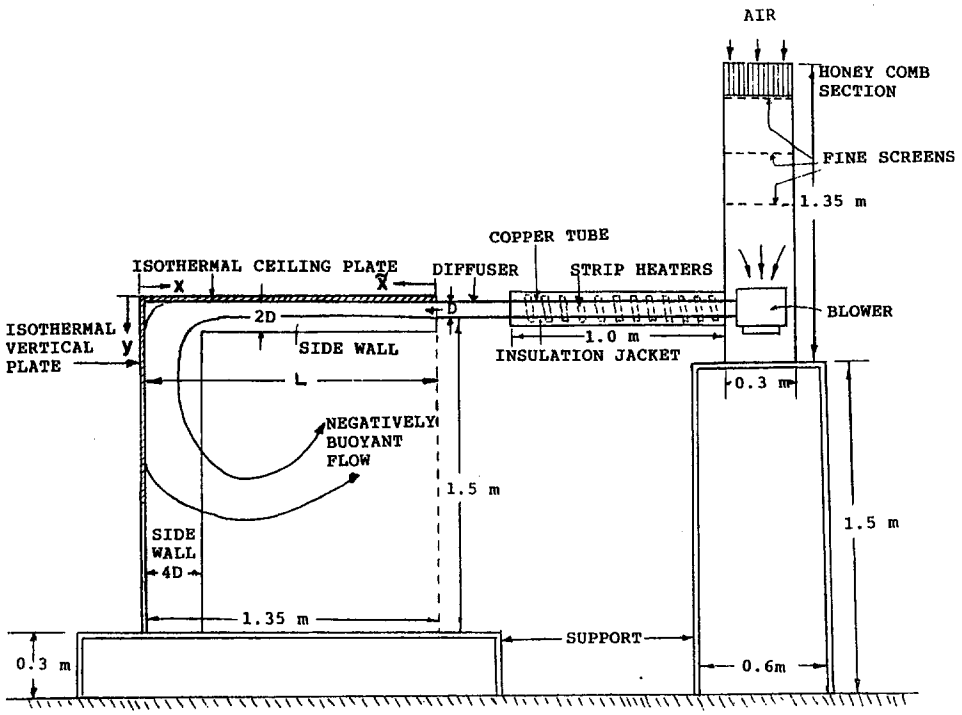

Fig. 1 Experimental arrangement and coordinate system for the study of a heated, two-dimensional ceiling jet discharged horizontally and turning downward at a corner with a vertical surface

heat transfer characteristics of a downward-turning horizontal buoyant ceiling jet or at the flow near a corner. In this paper, an experimental study is carried out on this flow circumstance.

Experimental System

Figure 1 shows a sketch of the experimental arrangement employed for the study of a downward-turning heated, two-dimensional, horizontal ceiling jet in an isothermal medium. The coordinate system used is also shown. A blower is installed at the bottom of a vertical channel, which is 1.35 m high, 0.3 m × 0.3 m in cross section, and placed on a metal frame. A honeycomb section and three very fine screens are employed at the entrance to the channel. Two very fine screens, which are 0.3 m apart, are located in the middle portion of the channel. This arrangement gives rise to a very low level of turbulence (with the measured intensities less than about 0.5 percent) and a fairly uniform flow across the channel (with a variation in the dimensionless velocity of less than ±3 percent of the mean value). The blower sends ambient air, over a wide range of flow rates, through a heated copper tube. The copper tube is 5

Nomenclature

A_0 = cross-sectional area of the slot through which the heated air jet is discharged
C_p = specific heat of the fluid at constant pressure
D = height of the slot for jet discharge
g = magnitude of gravitational acceleration
Gr = Grashof number = $g\beta \times (T_0 - T_\infty)D^3/\nu^2$
h = local heat transfer coefficient = $q/(T_0 - T_s)$
k = thermal conductivity of air
L = horizontal distance between ceiling jet discharge and corner
$\dot{m}$ = mass flow rate
$\dot{m}_{in}$ = mass flow rate at jet discharge
Nu_D, $\overline{\mathrm{Nu}}_D$ = local and average Nusselt numbers, respectively, based on D
q = local heat transfer flux to the surface
Q = total net heat transfer to the isothermal surface from the heated jet flow
Q_{in} = total thermal energy input by the ceiling jet = $\rho_0 U_0 A_0 C_p \times (T_0 - T_\infty)$
Re = Reynolds number = $U_0 D/\nu$
Ri = Richardson number = $\mathrm{Gr}/\mathrm{Re}^2$
T = local temperature
U_0 = discharge velocity of the ceiling jet
u, v = horizontal and vertical velocity components, respectively
u^*, v^* = dimensionless horizontal and vertical velocity components, respectively, $u^* = u/U_0$, $v^* = v/U_0$
W = width of the horizontal and vertical plates
x = horizontal coordinate distance, measured from the vertical surface
$\tilde{x}$ = distance along the two surfaces from the slot, around the corner
y = vertical coordinate distance measured downward from the horizontal surface
z = transverse coordinate distance
β = coefficient of thermal expansion of fluid
δ_p = penetration distance of jet flow, measured downward from horizontal surface
θ = dimensionless temperature = $(T - T_\infty)/(T_0 - T_\infty)$
ν = kinematic viscosity of fluid
ρ = density of fluid

Subscripts

0 = at jet discharge
∞ = ambient medium

cm in diameter and 1 m in length. It is heated by means of three fiberglass insulated heaters, which are wrapped around it. The energy input to each of the heaters is varied by means of individual power controllers. A diffuser at the end of the copper tube is employed to discharge the heated air as a two-dimensional jet, whose height could be varied. Several diffuser designs were considered to ensure uniform two-dimensional flow at the entrance. The heat loss from the copper tube and the diffuser to the environment was minimized by employing an insulated jacket, which has an inner layer of fiber glass and an outer layer of glass wool.

The discharge velocity of the jet U_0 could be varied from about 0.3 m/s to 2.5 m/s and the discharge temperature T_0 from room temperature to about 150°C. Thus, the arrangement could be used for studying fairly wide ranges of the governing parameters, which are the Reynolds number Re and the Grashof number Gr, both being based on the inlet conditions and defined later. The values for Re and Gr employed in the present experiments range from 2000 to 4000 and 0 to 10^6, respectively. The discharge velocity of the jet was determined by measuring the velocity distribution at the jet discharge and taking the average value. A calibrated DANTEC constant-temperature hot-wire anemometer was used, with the sensor positioned horizontally and normal to the x-axis. The hot wire was calibrated using a special calibration facility, designed for velocity levels in the range 0–0.5 m/s and for arbitrary flow direction (Tewari and Jaluria, 1990). Flow visualization was also carried out with smoke to confirm the results interpreted from temperature and velocity data. Though not shown here for conciseness, visualization results supported the trends indicated by the local measurements.

The discharge temperature of the jet was measured by using a rake of five thermocouples, located across the jet discharge slot. The average of the five temperatures measured was taken as the jet discharge temperature T_0. Again, the discharge temperature was found to be fairly uniform, within ±2°C across the slot cross section, giving a variation of less than ±3 percent of the mean values considered in this study.

The heated, two-dimensional air jet is discharged horizontally into a flow region 1.5 m high and 1.35 m × 0.3 m in cross section; see Fig. 1. At the top of the region, a water-cooled aluminum plate, 1.25 cm thick, which represents the ceiling of the enclosure, is attached. Another water-cooled aluminum plate is located vertically on one side, thus forming a 90 deg corner with the ceiling plate. The two-dimensional diffuser is placed horizontally, adjacent to the ceiling plate, as shown in Fig. 1. The horizontal distance L between the corner and the jet discharge location can be varied from about 0.60 m to 0.95 m by moving the jet discharge slot along the ceiling plate. Isothermal conditions are used at the boundaries to simulate the initially cold walls at the early stages of a room fire.

The sides of the enclosure are kept partially open to ensure that the enclosure is not stratified. However, it is necessary to minimize edge flows in order to maintain the two dimensionality of the flow. Extensive experimental data were taken without any side walls and it was found that the discharged jet flow was largely confined to regions near the ceiling and the vertical wall. The velocity and temperature measurements suggested that the jet flow was confined to a maximum value of 2D from the ceiling and of 4D from the vertical wall. Based on these experimental observations, sidewalls of width 2D and 4D were used for the ceiling and the vertical wall, respectively. However, it was ascertained that the measurements near the midplane were largely unaffected by the presence of side walls. The bottom was kept open to allow entrainment from below and the vertical dimension of the tank was large enough to avoid any significant effect on the flow due to this open boundary.

The water-cooled ceiling and vertical plates have the same design. Four rectangular copper tubes, each 2.5 cm × 1.25 cm in cross section, run along the length of the plate. Water from an outside source enters at the top of the vertical plate and the water coming out from this plate is allowed to enter at one end of the ceiling plate and the water coming out at the other end of the ceiling plate is allowed to drain into a sink. The temperature of the water entering the plate is maintained at a desired value by mixing hot and cold water streams from two separate sources. Twelve thermocouples were embedded in the plate close to the surface to monitor the temperature. For further details of the plate assembly, see Kapoor and Jaluria (1989). The maximum dimensionless temperature difference measured between any two embedded thermocouples on the two plates was found to be less than 5 percent of the mean values in most cases.

The heat transfer from the hot jet to the ceiling and vertical plate was measured by means of microfoil heat flow sensors (RdF type 20472-3) flush with the surface. Each heat flow sensor was 15 mm × 6 mm in surface area and 0.3 mm in thickness, and could be attached easily to the plate surface. The typical distance between two heat flux sensors along the ceiling and vertical plate was approximately 5.0 cm except near the corner where the sensors were placed 1 cm from each other. It was ensured that the heat flux gages did not significantly affect the local temperature and heat flux by estimating the additional thermal resistance introduced and by comparison with independent measurements of these quantities. The electric output (in millivolts) from the heat flux sensor was converted into heat flux (in W/m^2) with the help of individual calibration curves supplied by the manufacturer and verified in the laboratory by employing surfaces with known heat flux inputs. The accuracy of the measured heat flux was estimated to be high, with an estimated error of less than 5 percent in the present experiments. The outputs of the heat flux sensors were constantly monitored on a strip chart recorder and all the heat flux data were collected by using a Keithley data acquisition system. Thus, the errors in the reported Nusselt and Richardson numbers were estimated to be less than 5 and 3 percent, respectively. Considerable care had to be exercised to obtain accurate and repeatable data. In general, the repeatability was very high, being within 5 percent of the measured values for most measurements reported here.

Results and Discussion

The height D of the two-dimensional slot through which the hot jet is discharged is taken as the characteristic dimension in order to quantify the inlet conditions of the flow, as discussed by Goldman and Jaluria (1986). Thus, the governing parameters are obtained as the Reynolds number Re and the Grashof number Gr. The Richardson number $\mathrm{Ri} = \mathrm{Gr}/\mathrm{Re}^2$, which is also known as the mixed convection parameter, is frequently employed in the literature to indicate the relative buoyancy level. These parameters, along with the Nusselt number Nu_D, which gives the dimensionless heat transfer rate, are defined as

$$\mathrm{Re} = \frac{U_0 D}{\nu}, \quad \mathrm{Gr} = \frac{g\beta(T_0 - T_\infty)D^3}{\nu^2} \tag{1}$$

$$\mathrm{Ri} = \frac{\mathrm{Gr}}{\mathrm{Re}^2}, \quad \mathrm{Nu}_D = \frac{hD}{k} \tag{2}$$

Also, the dimensionless velocities u^* and v^* and temperature θ are defined as

$$u^* = \frac{u}{U_0}, \quad v^* = \frac{v}{U_0}, \quad \theta = \frac{T - T_\infty}{T_0 - T_\infty} \tag{3}$$

All the symbols are defined in the nomenclature. It has been shown in several earlier papers, mentioned here, that the dominant parameter in these flows is the Richardson number Ri and, even though the Reynolds number Re is obviously important in characterizing the flow, particularly near the boundaries, the results are well correlated in terms of Ri alone. The effect of Re, over the range considered in the experiments, was indeed

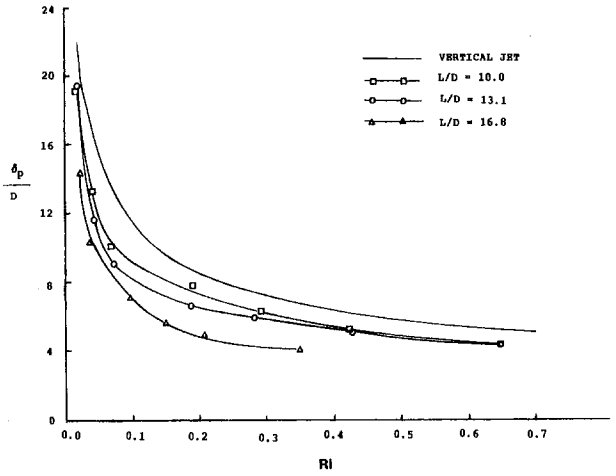

Fig. 2 Variation of the penetration depth δ_p with Ri at various values of L/D

found to be small compared to that of Ri and, thus, the results are largely presented in terms of Ri and other variables arising from the geometry and the thermal conditions.

Downward Turning of the Ceiling Jet. The buoyant horizontal ceiling jet, after losing some of its momentum and thermal energy to the ceiling, reaches the corner and turns downward along the vertical wall and behaves like a negatively buoyant wall jet, a flow that has been studied in detail by Goldman and Jaluria (1986) and Kapoor and Jaluria (1989). The heated wall jet flow penetrates downward to a finite distance due to its buoyancy, then turns upward and finally flows out of the enclosure.

The penetration distance δ_p, which represents the penetration of the thermal effects in the flow, is quantitatively taken as the location where 99 percent of the temperature drop has occurred, i.e., $\theta = 0.01$, indicating negligible thermal effects beyond this point. It was repeatedly found that this location was fairly well defined, within 1–2 cm. Similar results have been found earlier by Goldman and Jaluria (1986) and Kapoor and Jaluria (1989), for vertical heated jets discharged downward adjacent to vertical surfaces. The variations of the penetration distance δ_p with the mixed convection parameter Ri for $L/D = 10$, 13.1, and 16.8 are shown in Fig. 2. In all the cases shown, the ceiling and the vertical wall temperatures are essentially the same and are kept close to the ambient temperature (within ±1.0°C). It is seen that the penetration distance decreases with an increase in the mixed convection parameter Ri. These results are similar to those of a negatively buoyant wall jet. The penetration distance is found to be smaller at higher values of L/D, for a constant value of Ri. It was found from the detailed boundary layer measurements close to the ceiling plate that the momentum level decreases at a faster rate than the thermal buoyancy along the horizontal plate as the flow approaches the corner. Hence, for larger values of L/D, the momentum at the corner is smaller, resulting in smaller penetration distance.

The variation of the nondimensional penetration distance δ_p/D with Ri was measured over the range $0.02 \leq \text{Ri} \leq 0.65$. These results may be expressed in terms of the following correlations:

$$\frac{\delta_p}{D} = 3.65(\text{Ri})^{-0.41}, \quad \text{for} \quad L/D = 10 \tag{4a}$$

$$\frac{\delta_p}{D} = 3.51(\text{Ri})^{-0.41}, \quad \text{for} \quad L/D = 13.1 \tag{4b}$$

$$\frac{\delta_p}{D} = 2.77(\text{Ri})^{-0.41}, \quad \text{for} \quad L/D = 16.5 \tag{4c}$$

The corresponding correlation for a vertical negatively buoyant wall jet, as obtained by Kapoor and Jaluria (1989) and shown in Fig. 2, is

$$\frac{\delta_p}{D} = 4.45(\text{Ri})^{-0.41} \tag{5}$$

These correlations were found to be very accurate, with the correlation coefficients larger than 0.99. It is interesting to note that the exponents obtained for all cases are the same. The multiplication constant for the ceiling jet depends on the distance L between the corner and the location of the jet discharge. An attempt was made to obtain a general correlating equation incorporating the effects of both L/D and Ri. The correlation thus obtained was

$$\frac{\delta_p}{D} = 13.07(L/D)^{-0.54}(\text{Ri})^{-0.41} \tag{6}$$

However, this correlation equation was found to be not as accurate as the earlier ones, the correlation coefficient being about 0.9.

In order to understand the basic physics of the flow field, detailed measurements of the thermal field, across the enclosure, were carried out. Only a few typical results are presented here for brevity. The thermal field was mapped very closely by using a rake of thermocouples at the middle of the width (z direction) of the enclosure. From these extensive temperature measurements, the corresponding isotherms were determined by interpo-

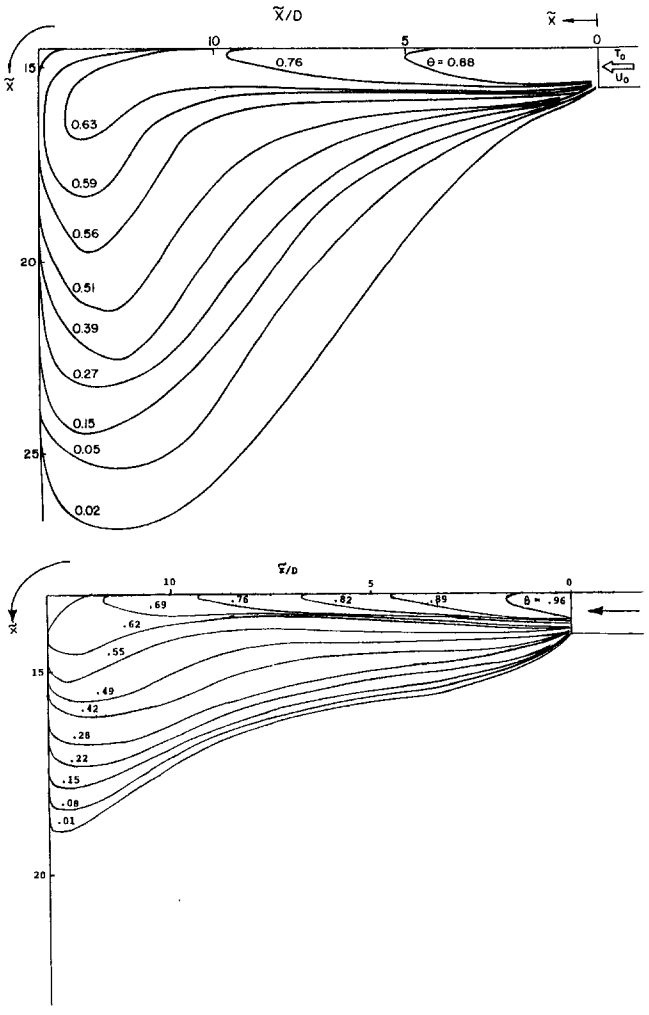

Fig. 3 Isotherms obtained from the temperature data at (*a*) Ri = 0.042 and (*b*) Ri = 0.303, for L/D = 13.1

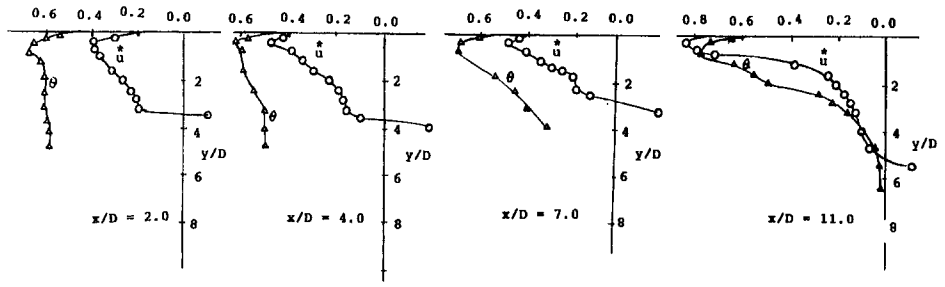

Fig. 4 Measured profiles of the horizontal component of the velocity and of the temperature near the ceiling at Ri = 0.043 and L/D = 13.1

lation. Figure 3 shows typical sets of such isotherms at Ri = 0.042 and 0.303. It is seen from the figure that the horizontal jet loses thermal energy as it flows toward the corner and then turns downward along the vertical wall. The jet flow penetrates downward up to a finite distance δ_p, as discussed earlier, and then stagnates before rising vertically upward due to its buoyancy and finally escaping out of the enclosure. The downward penetration is much less at the larger Ri. It is seen from the isotherms that the horizontal jet flow starts turning downward some distance before the corner. This indicates that the jet flow separates from the ceiling before reaching the corner and reattaches to the vertical wall at a certain distance downstream from the corner. This shows the presence of a small recirculation zone in the corner. The flow separation at the corner is further confirmed by the corresponding velocity profiles and heat flux measurements at the ceiling and the vertical walls, as discussed later in this paper.

Characteristics of the Flow Along the Ceiling and the Vertical Wall. Velocity measurements were carried out near the horizontal and vertical surfaces to characterize the flow field before and after the mixed convection flow turns at the corner. A constant-temperature hot-wire anemometer was used for the velocity measurements. It was ensured that the disturbance to the local flow due to the probe was small. Both the horizontal and the vertical components of velocity were measured. To measure the horizontal component u, the hot-wire sensor was kept vertical along the y direction, so that in the present two-dimensional flow, essentially the horizontal component of the flow velocity is measured. The vertical component v is measured by keeping the hot-wire sensor horizontal along the x direction so that essentially the vertical component of the flow velocity is measured (Jaluria, 1980).

Figure 4 shows the typical horizontal velocity and temperature distributions near the horizontal boundary at four stations between the jet discharge and the corner. It is seen from this figure that the velocity field decreases in both magnitude and thickness as the flow approaches the corner. However, as mentioned in the last section, the thermal field remains almost unchanged. It shows that the ceiling jet flow loses a significant amount of its momentum, but retains much of its thermal energy, as it moves toward the corner. It is interesting to observe from the figure that the slope of the velocity profile near the ceiling gradually decreases and becomes quite sharp near the corner (see Fig. 4(d)). This confirms the tendency of the jet flow to separate near the corner, as discussed in the last section. The jet flow reattaches to the vertical wall at a certain distance below the corner as seen in the next figure.

Figure 5 is the continuation of the flow described by Fig. 4 and shows the vertical velocity and temperature distributions near the vertical wall at four stations. It is seen from this figure that the magnitude and outward spread of the vertical velocity decrease as the jet flow penetrates downward. As expected, this trend is similar to the velocity and temperature fields obtained in the case of the penetration of a negatively buoyant vertical wall jet in an isothermal medium (Goldman and Jaluria, 1986) and in a thermally stratified medium (Kapoor and Jaluria, 1993). It is also seen from this figure that the velocity field decreases more rapidly than its temperature level. The slope of the velocity profile at the wall also decreases as the jet flow penetrates downward along the vertical wall. As mentioned ear-

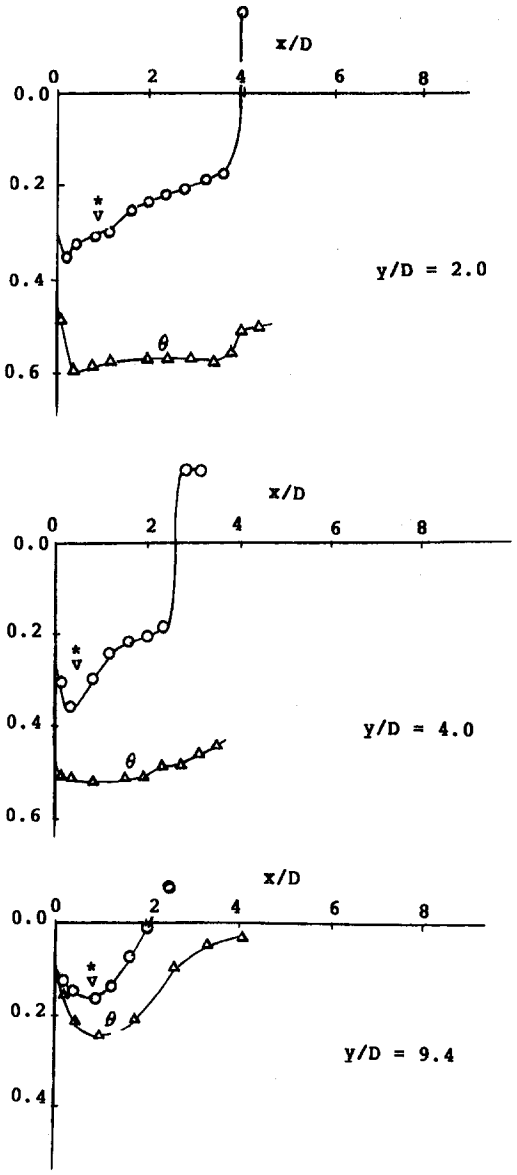

Fig. 5 Measured vertical velocity and temperature profiles near the vertical wall at Ri = 0.043 and L/D = 13.1

lier, this trend confirms the flow reattachment to the vertical wall at a certain distance below the corner. Also, as shown in Fig. 5(*a*), the jet flow tries to separate from the wall before becoming stagnant and then rising upward due to buoyancy, yielding a finite penetration distance δ_p.

From Figs. 4 and 5, the local mass flow rate can be obtained by integrating the corresponding product of the velocity and the density (as obtained from the measured temperature distributions) over the flow region. The mass flow rate $\dot{m}$ is nondimensionalized with the corresponding jet discharge mass flow rate $\dot{m}_{in}$. The variation of $\dot{m}/\dot{m}_{in}$ along the ceiling and the vertical wall for Ri = 0.0435 is shown in Fig. 6. It is seen from this figure that the ceiling jet entrains a significant amount of fluid from the surroundings as it flows along the ceiling wall. The mass flow rate first increases and then gradually decreases as the jet flow moves along the ceiling plate. After crossing approximately half of the length of ceiling plate, the flow rate remains almost constant over the rest of the boundary. This is an expected behavior for strongly stratified flows, for which the entrainment drops to zero as the local Richardson number becomes larger than about 1.0 (Koh, 1971). It is also seen from the figure that the mass flow rate remains almost constant as the flow turns downward at the corner. The flow rate gradually decreases along the vertical wall and finally becomes zero at the penetration distance. The corresponding penetration distance δ_p has also been shown in the figure. These results thus indicate the basic nature of such a downward-turning ceiling jet, of the resulting negatively buoyant wall flow, and of the flow in the neighborhood of the corner.

Net Mass Flow Entrainment by the Flow. As mentioned earlier, the negatively buoyant vertical wall jet entrains a significant amount of air from its surroundings (Goldman and Jaluria, 1986; Jaluria and Kapoor, 1988). The net mass flow entrainment was found to be dependent on the value of Ri of the discharged jet. It was found that the entrainment increases with an increase in Ri up to a value of around 0.4 and then it becomes almost constant in the range of $0.4 \leq \text{Ri} \leq 0.5$. These trends are due to decreasing δ_p and increasing vigor of the buoyancy-driven flow as Ri increases. The mass flow rate was obtained at different locations within the jet flow. Figure 7 shows the net flow rate near the horizontal surface at a distance of 4D from the corner for L/D = 10, 13.1, and 16.5. This flow rate is called $\dot{m}_1$ in the present experiments and is nondimensionalized with the corresponding discharge jet flow rate $\dot{m}_{in}$. It is seen from the figure that the ceiling jet entrains a significant amount of air up to a Ri value of around 0.2. The entrained mass flow was found to be higher at higher values of L/D. This is expected since a larger value of L/D implies greater length of the ceiling at constant D. This permits more surrounding air to be entrained by the ceiling jet. However, at higher values of Ri, there is very little flow entrainment into the ceiling jet flow,

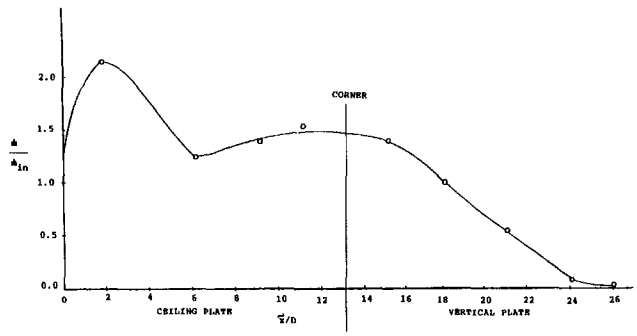

Fig. 6 The variation of the mass flow rate in the ceiling and the wall jets with distance $\bar{x}$ from the slot along the two surfaces at Ri = 0.043 and L/D = 13.1

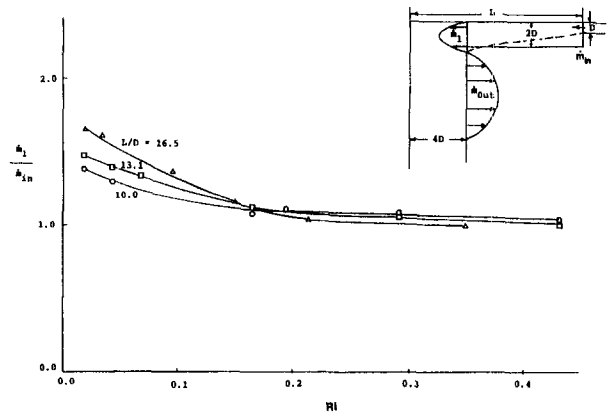

Fig. 7 Variation of the mass flow rate in the ceiling jet $\dot{m}_1/\dot{m}_{in}$ with Ri at different values of L/D

as mentioned above. In some cases, the mass flow rate was also measured at a distance of 2D below the corner near the vertical wall and it was found that this mass flow rate was almost the same as the corresponding mass flow $\dot{m}_1$. This suggests that the jet flow essentially does not entrain fluid while turning downward at the corner.

The net mass flow rate, $\dot{m}_{out}$ leaving the vertical flow region was measured at a distance of 4D from the vertical wall, using the corresponding horizontal velocity and temperature profiles. This mass flow rate represents the total entrainment into the downward turning ceiling jet, i.e., the sum of the mass flow entrained by the ceiling and the vertical wall flows, from the surroundings. Figure 8 shows the variation of $\dot{m}_{out}/\dot{m}_{in}$ with Ri. It is seen from this figure that the wall jet flow entails a significant amount of fluid after turning at the corner. As discussed earlier, the jet flow rate remains almost constant during the turn at the corner and most of the fluid is entrained when the jet flow penetrates downward along the vertical wall and when it rises upward due to buoyancy. It is seen from this figure that the entrained mass flow decreases with an increase in Ri. This is again an expected result because at a higher value of Ri, the flow penetration is decreased, resulting in smaller flow entrainment. These trends are similar to those found in the earlier investigations by Goldman and Jaluria (1986) and Jaluria and Kapoor (1988) for a negatively buoyant vertical wall jet. It is seen from Fig. 8 that the entrainment is smaller for a larger value of L/D. This is due to the fact that, in case of a larger L/D, the

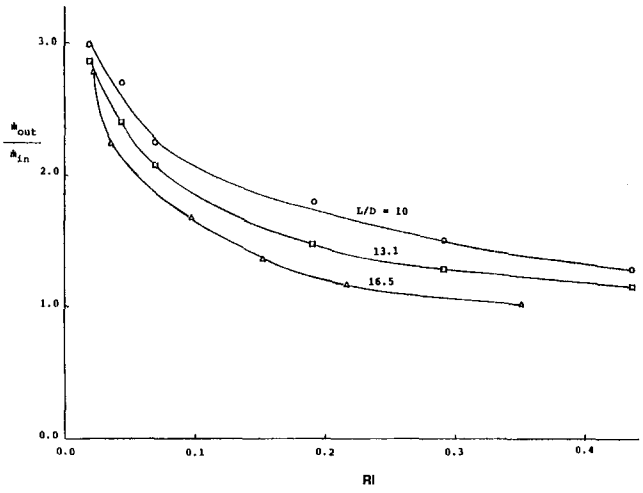

Fig. 8 Variation of the dimensionless total mass flow rate $\dot{m}_{out}/\dot{m}_{in}$ with Ri at different values of L/D

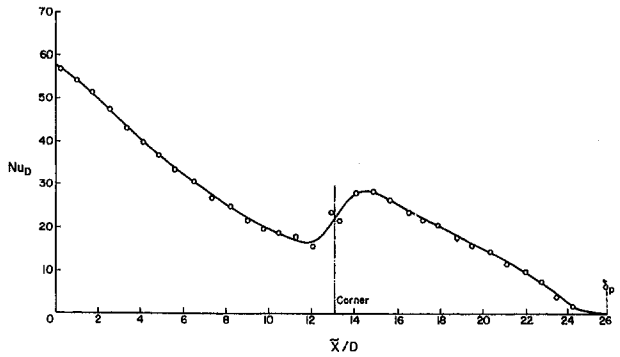

Fig. 9 Variation of the local Nusselt number Nu_D with distance $\bar{x}$ from the slot along the two surfaces at Ri = 0.042 and L/D = 13.1

penetration distance δ_p is smaller, as discussed earlier, resulting in smaller fluid entrainment.

Heat Transfer From the Ceiling Jet to the Isothermal Surfaces. Figure 9 shows the variation of the local Nusselt number Nu_D along the horizontal and the vertical plate at Ri = 0.042 and L/D = 13.1. It is seen that the local Nusselt number decreases along the ceiling and reaches its smallest value just before the corner. As the ceiling jet turns at the corner, the local heat transfer rate is seen to increase sharply downstream and to reach its maximum value just below the corner indicating the point of flow reattachment to the vertical wall. From this point, the heat transfer rate decreases gradually along the vertical wall and becomes almost zero at a location close to the penetration distance δ_p, which has also been shown in the figure. These results clearly show that a minimum and a maximum arise in the heat transfer rate on either side of the corner. This figure also confirms the earlier results that the flow separates from the horizontal plate before the corner and reattaches itself to the vertical wall just below the corner. All these results indicate the existence of a small recirculation zone in the corner.

Figure 10 shows the variation of the local Nusselt number Nu_D along the ceiling and the vertical plate for four values of Ri and for L/D = 10. The basic trends are similar to those observed in Fig. 9. The dimensionless local heat transfer rates, in terms of the Nusselt number, are seen to be higher for the smaller values of Ri. It should be mentioned here that the measured value of local heat flux q is actually smaller at the lower value of Ri. Higher values of Nu_D are obtained because of still smaller value of $(T_0 - T_s)$. It is seen from the figure that, in general, the local heat transfer rate first decreases along the ceiling plate, then increases at the corner and again decreases along the vertical plate, becoming almost zero at some location downstream. The penetration distance δ_p has also been marked on the figure. The decrease in Nu_D along the ceiling and the wall is obviously due to the increasing boundary layer thickness of the flow (Jaluria, 1980).

It is seen in Fig. 10 that the recovery in the local heat transfer rate at the corner depends upon the value of Ri. The recovery in the local heat flux was found to be larger for the smaller values of Ri. At the lower value of Ri, the ceiling jet flow has relatively larger momentum before it turns downward at the corner. Therefore, it separates from the ceiling plate at a larger distance from the corner and reattaches itself to the vertical wall at a larger distance below the corner. This suggests that at the smaller value of Ri, the size of recirculation region at the corner is larger than that found at the higher values of Ri. Hence, at the smaller value of Ri, the separated ceiling jet flow has to travel a larger distance at the corner before it reattaches itself to the vertical wall, resulting in a higher heat transfer recovery factor.

The variation of the average Nusselt number $\overline{Nu}_D$ for the ceiling plate with Ri for L/D = 10, 13.1, and 16.5 is shown in Fig. 11. The total net heat transfer rate to the ceiling $Q_{ceiling}$ was obtained by integrating the measured heat flux over the length of the ceiling plate. It is seen from this figure that the average Nusselt number decreases with an increase in Ri. This is due to the fact that, while the net heat transfer to the ceiling plate $Q_{ceiling}$ increases with Ri, the jet temperature difference $(T_0 - T_s)$ increases more rapidly than $Q_{ceiling}$. This results in a lower average heat transfer coefficient and hence a lower value of $\overline{Nu}_D$ at higher Ri. Figure 11 shows that the average Nusselt number was also found to be larger for the lower value of L/D due to the average film thickness being lower.

The variation of the average Nusselt number $\overline{Nu}_D$ for the vertical plate was also obtained. The basic trends of the results were similar to those discussed in the case of the ceiling plate. The variation of the average Nusselt number $\overline{Nu}_D$ for both the ceiling and the vertical wall with Ri is shown in Fig. 12. The results show the average heat transfer rate from the jet flow to the ceiling and the vertical wall. The basic trends, as expected, are a combination of individual results for the ceiling and the vertical wall.

All these results may also be expressed in terms of correlating equations to indicate the dependence of $\overline{Nu}_D$ on Ri and L/D. There is also a weak additional dependence on Re. However, for such turbulent mixed convection flows, the dependence on Ri is found to be much stronger than that on either Gr or Re and the results may be expressed fairly accurately in terms of

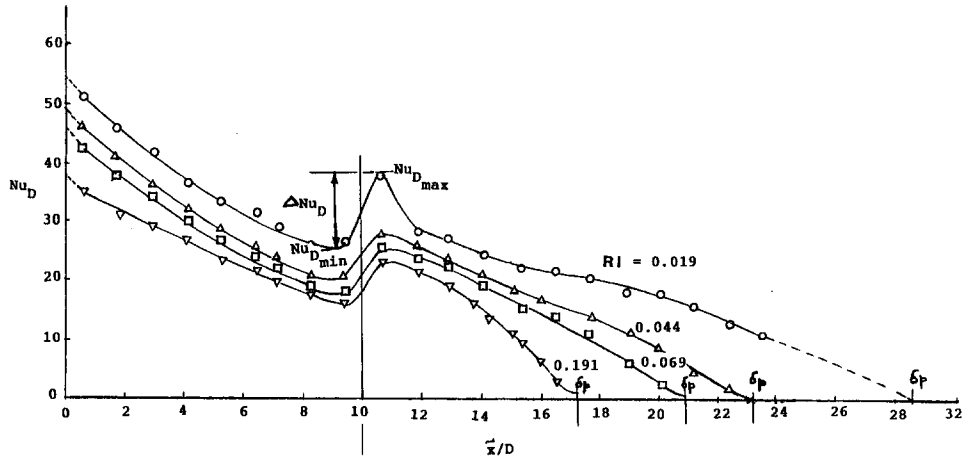

Fig. 10 Distribution of the local Nusselt number Nu_D over the ceiling and the vertical wall for Ri = 0.019, 0.044, 0.069, and 0.191 at L/D = 10.0

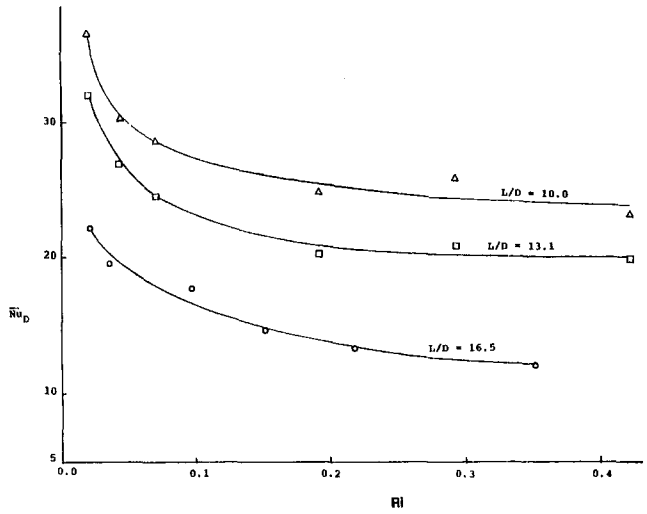

Fig. 11 Variation of the average Nusselt number $\overline{Nu}_D$ with Ri for the ceiling plate at different values of L/D

the mixed convection parameter. Thus, over the ranges $0.02 < Ri < 0.65$ and $10 < L/D < 20$, the experimental results are well correlated by the equations:

$$(\overline{Nu}_D)_{ceiling} = 250.47(Ri)^{-0.15}(L/D)^{-1.0} \quad (7)$$

$$(\overline{Nu}_D)_{wall} = 82.77(Ri)^{-0.25}(L/D)^{-0.8} \quad (8)$$

$$(\overline{Nu}_D)_{ceiling+wall} = 61.35(Ri)^{-0.09}(L/D)^{-0.5} \quad (9)$$

The correlation coefficients for these equations are larger than 0.95, indicating a fairly close approximation of the data with these equations.

Conclusions

A detailed experimental study has been carried out to investigate the basic flow characteristics of a heated horizontal ceiling jet, which turns downward at a corner. A heated two-dimensional jet is discharged horizontally adjacent to the underside of an isothermal horizontal surface in a large enclosure. An isothermal vertical plate was fixed at the other end of this surface, making a right angle corner. The following are the major findings of the present study:

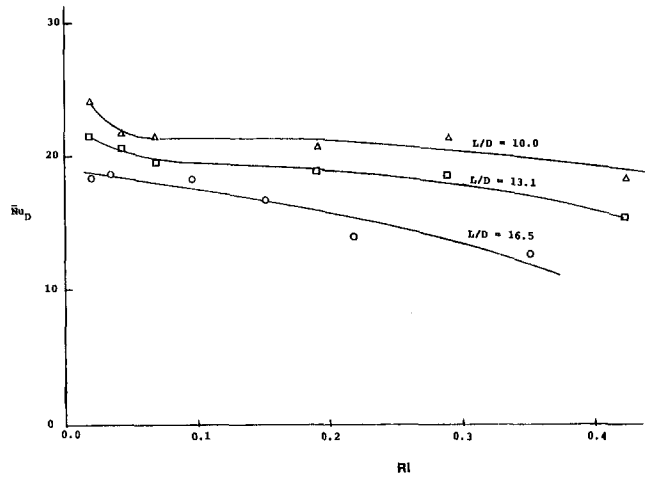

Fig. 12 Variation of the average Nusselt $\overline{Nu}_D$ with Ri for the total heat transfer to the ceiling and the vertical wall

1 The penetration distance δ_p was found to decrease with an increase in Ri. The penetration distance was also found to be smaller for higher values of L/D at a constant value of Ri. These trends are explained in terms of the underlying physical mechanisms and correlating equations for δ_p in terms of these parameters are derived from the data.

2 The detailed velocity and temperature measurements near the ceiling and the vertical wall show that the flow separates from the ceiling just before the corner and reattaches itself to the vertical wall at some distance below the corner.

3 The isotherms indicate the basic nature of the corner flow. The local heat flux measurements on the ceiling and vertical wall show that a minimum arises just before the turn and a recovery in the local heat transfer rate occurs after the turn due to reattachment of the flow.

4 The ceiling jet entrains some fluid from the surroundings as it flows along the ceiling. The flow rate remains almost unchanged as the flow turns at the corner. After turning at the corner, the flow again entrains a large amount of ambient air as it penetrates along the vertical wall and rises as an upward buoyant plume. This results in a large flow rate generated by the downward-turning ceiling jet. The net flow entrainment at different locations was obtained and correlated in terms of the mixed convection parameter Ri of the discharge jet. It was found that the overall net mass flow rate decreases with an increase in Ri.

5 The heat transfer recovery at the corner, i.e., the difference between the maximum and minimum Nu_D on either side of the corner, was found to decrease with the mixed convection parameter Ri of the discharged ceiling jet. This suggests that at a lower value of Ri, the jet flow separation from the ceiling and reattachment to the vertical wall occur at larger distances from the corner. This indicates that the size of the recirculation zone at the corner decreases with an increase in Ri of the discharged ceiling jet.

6 The average Nusselt number $\overline{Nu}_D$ for the ceiling and the vertical wall, put together, was found to decrease with Ri and to be smaller for a larger value of L/D at a constant Ri. These trends are explained in terms of the underlying physical mechanisms and the area over which heat transfer occurs.

Acknowledgments

This research was carried out with support from the Building and Fire Research Laboratory of the National Institute of Standards and Technology, United States Department of Commerce, under grant number 60NANB7D0743. The several interactions with Dr. L. Y. Cooper during the course of this work are also acknowledged.

References

Alpert, R. L., 1975, "Turbulent Ceiling Jet Induced by Large Scale Fires," *Combustion Science and Technology,* Vol. 11, pp. 197–213.

Baines, W. D., and Turner, J. S., 1969, "Turbulent Buoyant Convection From a Source in a Confined Region," *J. Fluid Mech.,* Vol. 37, pp. 51–80.

Baines, W. D., Turner, J. S., and Campbell, I. H., 1990, "Turbulent Fountains in an Open Chamber," *J. Fluid Mech.,* Vol. 212, pp. 557–592.

Chen, C. J., and Rodi, W. A., 1979, *Vertical Turbulent Buoyant Jets: A Review of Experimental Data,* Pergamon Press, Oxford, United Kingdom.

Cooper, L. Y., 1982, "Heat Transfer From a Buoyant Plume to an Unconfined Ceiling," ASME JOURNAL OF HEAT TRANSFER, Vol. 104, pp. 446–451.

Cooper, L. Y., 1989, "Heat Transfer in Compartment Fires Near Regions of Ceiling-Jet Impingement on a Wall," ASME JOURNAL OF HEAT TRANSFER, Vol. 111, pp. 455–460.

Goldman, D., and Jaluria, Y., 1986, "Effect of Opposing Buoyancy on the Flow in Free and Wall Jets," *J. Fluid Mech.,* Vol. 166, pp. 41–56.

Jaluria, Y., 1980, *Natural Convection and Mass Transfer,* Pergamon Press, Oxford, United Kingdom.

Jaluria, Y., 1986, "Hydrodynamics of Laminar Buoyant Jets," in: *Encyclopedia of Fluid Mechanics,* N. P. Chereminoff, ed., Gulf, Houston, TX, Vol. 2, pp. 317–348.

Jaluria, Y., and Kapoor, K., 1988, "Importance of Wall Flows at the Early Stages of Fire Growth in the Mathematical Modeling of Enclosure Fires," *Combustion Science and Technology,* Vol. 59, pp. 355–369.

Kapoor, K., and Jaluria, Y., 1989, "Heat Transfer From a Negatively Buoyant Wall Jet," *Int. J. Heat Mass Transfer,* Vol. 32, pp. 697–709.

Kapoor, K., and Jaluria, Y., 1993, "Penetrative Convection of a Plane Turbulent Wall Jet in a Two-Layer Thermally Stable Environment," *Int. J. Heat Mass Transfer,* Vol. 36, pp. 155–167.

Koh, R. C. Y., 1971, "Two-Dimensional Surface Warm Jets," *J. Hyd. Div.,* Vol. 97, pp. 819–836.

List, E. J., 1982, "Turbulent Jets and Plumes," *Ann. Rev. Fluid Mech.,* Vol. 14, pp. 189–212.

Morton, B. R., 1959, "Forced Plumes," *J. Fluid Mech.,* Vol. 5, pp. 151–163.

Motevalli, V., and Marks, C. H., 1990, "Transient and Steady State Study of Small-Scale Unconfined Ceiling Jets," in: *Heat and Mass Transfer in Fires,* J. G. Quintiere and L. Y. Cooper, eds., ASME HTD-Vol. 141, pp. 49–61.

Seban, R. A., Behnia, M. M., and Abreu, J. E., 1978, "Temperatures in a Heated Jet Discharged Downward," *Int. J. Heat Mass Transfer,* Vol. 21, pp. 1453–1458.

Tewari, S. S., and Jaluria, Y., 1990, "Calibration of Constant-Temperature Hot-Wire Anemometers for Very Low Velocities in Air," *Rev. Sci. Instrum.,* Vol. 61, pp. 3834–3845.

Turner, J. S., 1966, "Jets and Plumes With Negative or Reversing Buoyancy," *J. Fluid Mech.,* Vol. 26, pp. 779–792.

Turner, J. S., 1979, *Buoyancy Effects in Fluids,* Cambridge Univ. Press, Cambridge, United Kingdom.

Veldman, C. C., Kubota, T., and Zukoski, E. E., 1975, "An Experimental Investigation of Heat Transfer From a Buoyant Gas Plume to a Horizontal Ceiling—Part 1—Unobstructed Ceiling," National Bureau of Standards, Rep. No. NBS-GCR-77-97.

You, H. Z., 1985, "An Investigation of Fire-Plume Impingement on a Horizontal Ceiling: 2—Impingement and Ceiling Jet Regions," *Fire and Materials,* Vol. 9, pp. 46–55.

Unstable Aiding and Opposing Mixed Convection of Air in a Bottom-Heated Rectangular Duct Slightly Inclined From the Horizontal

W. L. Lin

T. F. Lin

Department of Mechanical Engineering,
National Chiao Tung University,
Hsinchu, Taiwan

Buoyancy-induced secondary vortex and reverse flows, flow transition, and the associated heat transfer processes in mixed convection of air through a bottom heated inclined rectangular duct were investigated experimentally. The local spanwise-averaged heat transfer coefficient and air temperature variations with time at selected locations were measured and the cross plane secondary flow was visualized for the Reynolds number ranging from 35 to 186, Grashof number up to 5×10^6, and $-20° \leq \phi \leq 26°$. The results indicated that the heat transfer enhancement is due to the presence of the buoyancy-driven secondary vortex flow and/or reverse flow. The onset of thermal instability was found to move upstream for a larger negative inclined angle (opposing convection) and/or a higher Grashof number and to be delayed for a larger positive inclined angle (aiding convection) and/or a higher Reynolds number. At increasing Grashof number, the instantaneous flow visualizations clearly showed the changes of the vortex flow and/or reverse flow structures in the downstream section of the duct. At slightly supercritical Grashof numbers the secondary flow is in the form of two pairs of longitudinal rolls with the vortex flow ascending along the side walls. For higher Grashof numbers the vortex rolls rotate in the opposite direction with the secondary flow descending near the side walls and the flow was found to be time periodic. At even higher Grashof numbers in opposing convection the buoyancy induced reverse flow exists and the flow is quasi-periodic. Further raising the Grashof number or lowering the Reynolds number causes the flow to change from a transitional quasi-periodic state to a chaotic turbulent state.

1 Introduction

Buoyancy-induced secondary flow and heat transfer in a forced flow through a heated duct are known to be relatively sensitive to the duct orientation. In a bottom-heated horizontal rectangular duct, the buoyancy is normal to the forced flow direction and the longitudinal and transverse vortex rolls can be induced at supercritical Grashof numbers. When the duct is inclined from the horizontal the secondary vortex flow is expected to be weaker due to the smaller normal buoyancy component. The forced flow will be accelerated in the aiding situation and decelerated in the opposing situation by the tangential buoyancy component. At high buoyancy, the resulting flow will be rather complex and can undergo transition to a time-dependent state. These complicated processes are often encountered in a low-Reynolds-number flow. Detailed understanding of these buoyancy-induced flow transition processes is important in fundamental fluid mechanics and heat transfer study and in various technological processes, such as the cooling of microelectronic equipments (Incropera, 1988), heat transfer in compact heat exchangers (Kays and London, 1984), growth of a single crystal through chemical vapor deposition (Evan and Grief, 1989) and many others. The literature on the mixed convection in horizontal rectangular ducts has already been reviewed by Huang and Lin (1994). In the following only the literature on the flow in inclined ducts is briefly reviewed.

Fukui et al. (1983) experimentally and numerically investigated steady fully developed mixed convective flow in an inclined duct with the Rayleigh number $Ra < 9300$ and inclined angle measured from the horizontal $\phi \leq 32.1$ deg. In the horizontal flow, the interaction between vortices was found to be rather small. However, in the inclined flow the neighboring vortices tend to form a vortex pair with a single velocity peak. Experimental data for the local and average Nusselt numbers were provided by Morcos et al. (1986) and Maughan and Incropera (1987). Visualization of recirculating flow in steady aiding and opposing mixed convection at low buoyancy in inclined ducts was recently conducted by Morton et al. (1989), Lavine et al. (1989), and Ingham et al. (1990). The corresponding numerical analysis was performed by Heggs et al. (1990), including heat conduction in the wall. This literature review clearly indicates that the detailed characteristics of the buoyancy-induced vortex flow structure and its transition from steady laminar to unsteady irregular, turbulent state in inclined ducts are still poorly understood.

The present experiment aims to measure the characteristics of the flow transition and the associated changes in the secondary flow structure and heat transfer in the mixed convective air flow in a bottom-heated inclined rectangular duct of a finite aspect ratio ($A = 4$). Attention is focused on the effects of the inclined angle, Grashof, and Reynolds numbers on the flow characteristics. Specifically, the inclination angle were limited to -20 deg $\leq \phi \leq 26$ deg. The experiment is designed to detect the flow transition by tracing the air temperature variations with time at selected detection points and to visualize the flow structure at a relatively large Gr/Re^2.

Contributed by the Heat Transfer Division for publication in the JOURNAL OF HEAT TRANSFER. Manuscript received by the Heat Transfer Division March 1995; revision received October 1995. Keywords: Flow Instability, Flow Visualization, Mixed Convection. Associate Technical Editor: Y. Jaluria.

2 Experimental Apparatus and Procedures

2.1 Experimental Apparatus. Figure 1 shows a schematic view of the mixed convection experimental apparatus established in this study. The apparatus consists of three parts: the wind tunnel, the test section, and the measuring probes along with the data acquisition system. The test section is a bottom-heated rectangular duct and is constructed of 9-mm-thick plexiglass top and side walls to facilitate flow visualization. The cross section of the duct is 30 mm in height and 120 mm in width, providing an aspect ratio of $A = 4$; it has a total length of $L = 800$ mm. Its bottom wall was made of 0.25-mm-thick SS301 stainless steel heater plate, and is bonded onto a sheet of 12-mm-thick plexiglass plate. Direct electric current was provided from a 30 V–50 A D.C. power supply and transferred to the heater plate through several copper bus-bars firmly attached at the ends of the heater, intending to produce a nearly uniform heat flux boundary condition. Power dissipation was determined by measuring the current and voltage drop across the heater plate. The uniformity of the energy dissipation was checked by measuring the voltage distribution on the plate. Specifically, the longitudinal measurements in the forced flow direction yield a linear voltage drop and the spanwise measurements resolve variations no larger than 0.3 mV for a voltage drop of 0.418 V across the heater plate. The total heat dissipation in the plate is $Q_{tot} = I \times V$, where I is the electric current and V is the electric voltage drop across the plate. To measure the D.C. current passing through the heater plate, a D.C. ammeter (Yokogawa model 201137) is arranged in series connection with the plate. The accuracy of the ammeter is within 0.1 A. To determine the voltage drop across the heater plate, a digital multimeter (Chung 6005) with an accuracy of 0.01 mV is employed to measure the voltage difference between two ends of the heater plate. The entire channel, including the test section and the upstream and downstream flow straighteners, was insulated with a Superlon insulator 150 mm thick and was mounted on a rigid supporting frame.

Air was driven by a blower and sent into the long rectangular duct downstream of a diffuser buffer section, as shown in Fig. 1. The flow rate is controlled by a variable speed blower. The volume flow rate of air upstream of the diffuser buffer section was measured by a float-area-type flowmeter with an accuracy of 1.6 percent. To reduce the influence of the vibration from the blower, a flexible connection made of cloth is used to connect the blower and a diffuser buffer section. The purpose of installing the diffuser buffer section and a series of three additional fine-mesh screens is to reduce turbulence from the blower blades. In the inlet section, turbulence was further suppressed

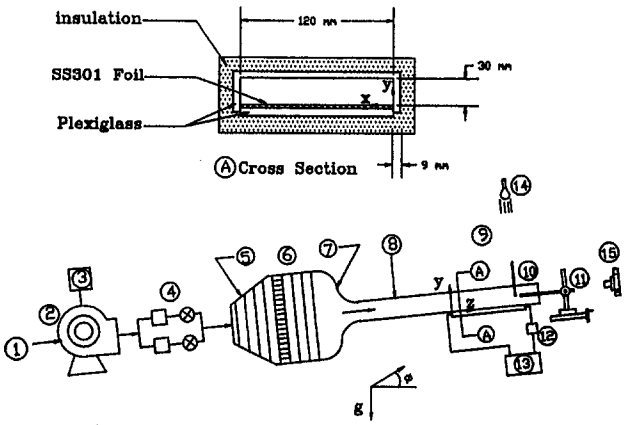

Schematic Diagram of Experimental Apparatus.

1.air flow ; 2.blower ; 3.frequency regulator ; 4.flowmeters and valves ; 5.diffuser with screens ; 6.straightener with honeycomb and screens ; 7.nozzle ; 8.developping channel ; 9.test section ; 10.probes ; 11.three-way traversing device ; 12.ammeter ; 13. D.C. power supply ; 14.lamp ; 15.camera.

Fig. 1 Schematic diagram of the experimental apparatus

by passing the air through a section packed with plastic straws 3 mm in diameter and bounded on each side by two fine mesh screens and then followed by a nozzle and a developing channel, before entering the test section. The nozzle is made of 5-mm-thick acrylic plate with a contraction ratio of 10:1 and has been designed to eliminate flow separation, minimize turbulence, and provide a nearly uniform velocity profile at the inlet of the developing section. The developing section is 1000 mm in full length, approximately 33 times the duct height. This insures the flow being fully developed at the inlet of the test section for $Re \leq 200$. An outlet section was added to the test section to reduce the effects of the disturbances from the ambient surrounding of the open-loop wind tunnel on the flow in the test section. The optical observations of the flow structure were performed using smoke tracers. A thin sheet of smoke was injected into the test section along the bottom of the channel through a slot across the width of the heater plate just in front of the test section. When illuminated through the top wall by lamps and viewed from the exit end of the channel, a sharp contrast could be achieved between the channel walls and the smoke.

Nomenclature

A = aspect ratio = b/d
b, d = width and height of the duct
g = gravitational acceleration
Gr = modified Grashof number = $g\beta q''_{conv} d^4/k\nu^2$
h = local convection heat transfer coefficient
I = electric current
k = thermal conductivity
L = length of the heated plate
Nu = Nusselt number = hd/k
Pr = Prandtl number = ν/α
Q_{tot} = the total heat dissipation in the plate
q''_{conv} = local convective heat flux
q''_{insul} = local conduction heat loss through the insulation
q''_{loss} = local heat loss = $q''_{rad} + q''_{insul}$
q''_{rad} = local radiation heat loss from the surface
q''_{tot} = total heat flux in the plate
Ra = Rayleigh number
Ra^*_c = critical Rayleigh number
Re = Reynolds number = $\bar{w}_{in} d/\nu$
T = temperature
u, v, w = velocity components in x, y, z directions
V = voltage
x, y, z = Cartesian coordinates
X, Y, Z = dimensionless Cartesian coordinates = x/d, y/d, z/d
Z^* = modified axial coordinate = $z/d \cdot \mathrm{Re} \cdot \mathrm{Pr}$
α = thermal diffusivity
β = thermal expansion coefficient
ν = kinematic viscosity
ρ = density
σ = Stefan–Boltzmann constant
τ = time
τ_p = period of flow oscillation
ϕ = inclined angle

Subscripts

c = values at the onset of thermal instability
in = values at the inlet of the test section
side = of side wall quantities
t = of top wall quantities
w = of heated wall quantities

Superscripts

$\bar{}$ = average value

In order to obtain adequate resolution of the temperature distributions on the bottom wall, the heater plate was instrumented with 57 (placed at 19 longitudinal stations) calibrated copper-constantan (T-type) thermocouples and their signals were recorded by the Hewlett-Packard 3852A data acquisition system with a resolution of ±0.05°C. Additional thermocouples were used to measure the temperatures of the inlet and outlet air flow and the top and side plates and to determine the temperature differences across the Superlon insulation underneath the heater plate. A T-type thermocouple having a bead of 70 μm diameter was used to measure the air temperature in the duct, which was equipped in the flow so as to have its sensing point 5 mm upstream of the supporting stainless steel pipe of 1 mm outer diameter. This probe was inserted into the flow through the top wall or from the exit end of the channel and can be traversed in the flow to measure the time-averaged temperature field and the instantaneous temperature. The temperature data are recorded when the system reaches steady or statistical state, usually 5–6 hours after starting the test. The experiment was performed mainly at Grashof numbers ranging from 10^4 to 5×10^6 and for Reynolds numbers below 200. The resulting Gr/Re^2 ratio was above 2.

2.2 Data Reduction for Heat Transfer Coefficient. The spanwise-average Nusselt number, defined as

$$\mathrm{Nu}_z = \frac{hd}{k} = \frac{q''_{\mathrm{conv}} d}{(\bar{T}_w - T_{in})k}, \tag{1}$$

is obtained from measuring the local spanwise mean bottom wall temperature $\bar{T}_w$ and local convective heat flux q''_{conv}. The surface energy balance relating the total energy dissipated in the heater plate q''_{tot} to the heat fluxes for the convection from the surface to the flow q''_{conv}, radiation heat loss from the surface q''_{rad}, and conduction loss through the insulation q''_{insul} is

$$q''_{\mathrm{tot}} = q''_{\mathrm{conv}} + q''_{\mathrm{rad}} + q''_{\mathrm{insul}} \tag{2}$$

The convective heat flux is therefore determined by measuring q''_{tot} and applying appropriate correlations for the nonconvective components. An implication of the expression in Eq. (2) is that although a uniform heat generation q''_{tot} can be approximately achieved in the heated plate, variations in the radiation and conduction losses with location induce spatial nonuniformities in the convective heat flux.

Considering the shape factor and surface resistances for thermal radiation from the heated bottom surface to the top surface in a rectangular duct, and that from the bottom surface to the two side plates (Holman, 1986), the net radiation loss from the bottom surface is estimated as

$$q''_{\mathrm{rad}} = 0.331\ \sigma(\bar{T}_w^4 - \bar{T}_t^4) + 2 \times 0.082\ \sigma(\bar{T}_w^4 - \bar{T}_{\mathrm{side}}^4) \tag{3}$$

with $\bar{T}_w$ measured directly and the mean top and side plate temperatures $\bar{T}_t$ and $\bar{T}_{\mathrm{side}}$ obtained by interpolation between the measured values.

Conduction losses through the insulation q''_{insul} were calculated by assuming one-dimensional conductive transfer and by measuring the temperature difference across the first 9 mm of the insulation ($k_{\mathrm{insul}} = 0.21$ W/m°C) beneath the heater plate,

$$q''_{\mathrm{insul}} = -k_{\mathrm{insul}} \left.\frac{\Delta T}{\Delta y}\right|_{\mathrm{insul}} \tag{4}$$

2.3 Analysis of Temperature Fluctuation. The time-averaged temperature and the intensity of the temperature fluctuation of the air flow were obtained by averaging 1000 sampled data at each detection point. In the tests the detection points are distributed at 24 equispaced spanwise positions in the horizontal planes at y = 5, 15, and 25 mm. Also, the power spectrum densities of the temperature fluctuation were obtained by analyzing the output of the thermocouple using a FFT analyzer. The response time of the thermocouple is about 0.13 s, which is much shorter than the period of the flow oscillation considered here.

3 Results and Discussion

In what follows only a small sample of the results are presented to illustrate the buoyancy-induced flow characteristics and heat transfer in the duct. More detailed results are available from our technical report (Lin and Lin, 1994).

3.1 Preliminary Investigation of Flow Field. In order to confirm the fully developed laminar flow at the inlet of the test section, the cross-sectional velocity distributions were measured at the inlet using a hot-wire probe, which was operated by a constant-temperature anemometer (Dantec Probe Type 55P11 with 56C17 CTA Bridge). For calibrating the hot wires, the pipe-flow method, in which the probe is placed in the center of a fully developed laminar flow in a circular pipe, was used. The total flow rate is measured and the pipe center velocity is calculated from the parabolic distribution. The measured inlet velocity profiles are in good agreement with the analytical results given by Shah and London (1978). The turbulence level of the inlet stream is all within 1 percent, implying that the effects of the free-stream turbulence on the mixed convective flow characteristics are moderate.

3.2 Heat Transfer Coefficient. Uncertainties in the Nusselt number and other parameters were estimated according to the standard procedures proposed by Kline and McClintock (1953). Our analysis indicated that the combination of many measurements together with the uncertainties in the predicted quantities (radiation and conduction losses) yields the spanwise average Nusselt number uncertainties ranging from 4 to 7 percent. Uncertainty in the Grashof number ranges from 10 to 25 percent, which primarily reflects the uncertainty in the convective heat flux. The estimated uncertainty in the Reynolds number was 2 percent. Because of the fluid property variations with the temperature, the Reynolds and Grashof numbers vary with the axial distance. Although the variations in the Reynolds number were small, the Grashof number could vary by as much as 25 percent. It is also important to note that the thermal conductivity of the plexiglass side and top walls is much higher than that of air, so the side wall thermal boundary condition deviates greatly from the perfect thermal insulation condition, which can substantially affect the secondary flow structures. A detailed account of this influence requires a complicated conjugate heat transfer analysis including convection in the flow and conduction in the walls, which will be attempted in a separate study. For convenience, experiments are identified according to the Reynolds and Grashof numbers based on the inlet conditions and averaged convection heat flux.

The reliability of the data of the spanwise-averaged Nusselt number was established through various tests and comparison with some appropriate standard conditions. The most relevant comparison is to compare the measured data for small Grashof numbers with the numerical solution for the corresponding forced convection. This comparison showed that the measured data were in excellent agreement with the numerical prediction (Huang and Lin, 1994).

As the heat flux is increased beyond certain critical value depending on the Reynolds number Re and inclined angle ϕ, the Nusselt number exhibits a discernible departure from the forced convection limit indicating the onset of the longitudinal vortex rolls. This is shown in Fig. 2 for the case with ϕ = 0 deg, Gr = 1.1×10^5, and Re = 102 and the data are also compared to the numerical solution and the forced convection results based on the numerical method from Huang and Lin (1994). The

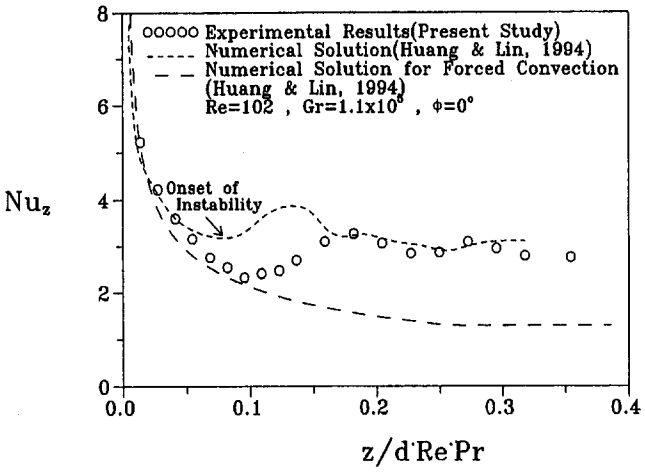

Fig. 2 Comparison of the predicted spanwise-averaged Nusselt number distribution (Huang and Lin, 1994) with the measured data for Re = 102, Gr = 1.1 × 10^5, and A = 4

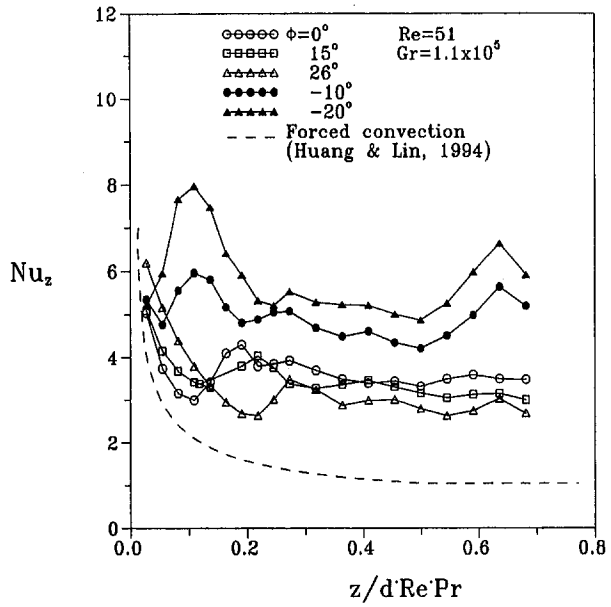

Fig. 3 Spanwise-averaged Nusselt number distributions for various inclined angles for Re = 51 and Gr = 1.5 × 10^5

agreement is also good except that earlier appearance of the vortex rolls is predicted in the numerical study. Note that the monotonic decay in the Nusselt number, which is associated with the laminar forced convection dominated region, ends when the buoyancy force becomes strong enough to destabilize the boundary layer on the bottom plate. This result is relatively similar to that from Maughan and Incropera (1987). To be specific, the onset of thermal instability is defined herein at the location where the local spanwise-averaged Nusselt number is 5 percent larger than the corresponding forced convection value at the same location. Beyond the onset of instability, plumes of warm fluid rise from the heated surface, ascending along the side walls, resulting in a developing secondary vortex flow and the bottom-heated plate temperature is reduced by the cold fluid descending from the duct core. Thus, the secondary flow circulation provides an effective mechanism for heat transfer enhancement. As the secondary flow strengthens, the Nusselt number rises well above the forced convection limit. Note that the secondary flow can enhance the heat transfer by as much as 110 percent as the Nusselt number rises to its maximum at $Z^* \approx 0.17$ or $z \approx 0.4$ m, where z is the axial distance measured from the inlet of the test section. Downstream of this location the fluid in the core region has been warmed up by the secondary flow and the descending fluid is no longer at the inlet temperature. Thus the reduction in the surface temperature is less pronounced and the Nusselt number begins to decline.

The expected wavy spanwise temperature variations on the heated bottom plate caused by the three-dimensional nature of the secondary vortex flow were justified by the present measurements. The local Nusselt number distributions were uniform at a given axial position prior to the onset of instability, but certain spanwise variations (±10 percent) occurred after the formation of the secondary flow. Since a much larger axial change in the Nusselt number following the onset of thermal instability was always accompanied by some spanwise variations, the axial distribution of the local Nusselt number can be well represented by its spanwise average.

The effects of the duct inclination on the convective heat transfer coefficient are now examined. In an inclined channel the buoyancy force is no longer exclusively perpendicular to the heated surface, since a component also exists in the streamwise direction. The influences of this component on the local spanwise average Nusselt number are given in Figs. 3 and 4, where the data for -20 deg $\leq \phi \leq 26$ deg with Re = 51 are plotted. It is evident from Fig. 3 that the aiding buoyancy for $\phi > 0$ deg causes a delay in the onset of thermal instability but enhances heat transfer prior to the onset of secondary flow. Both effects are due to the flow acceleration by the aiding buoyancy component in the flow direction, which increases with the duct inclination. When the forced air flows downward for negative inclination angles, the parallel component of the thermal buoyancy tends to retard the primary flow near the lower heated plate. Meanwhile it assists the forced flow near the upper unheated plate to maintain the overall mass balance at every cross section for a flow of a Boussinesq fluid. This retarding buoyancy force thickens and hence destablizes the boundary layer on the heated plate. As a result, earlier appearance of the onset of thermal instability is found. The critical axial distance for the onset of instability is shorter for a larger negative inclination angle. It is important to point out that the opposing buoyancy is so large that the flow is highly unstable and heat transfer is significantly augmented. The Nusselt numbers for $\phi = -10$ and -20 deg are higher than that for $\phi = 0$ deg and obviously are much higher than the forced convection limit. Larger Nusselt number results for a larger negative inclination angle. Furthermore, the effects of the Grashof number on the Nusselt number are shown in Fig. 4 for $\phi = -20$ deg. The results indicate that the critical axial distance for the onset of thermal instability is shorter for a larger Grashof number. Note that the presence of

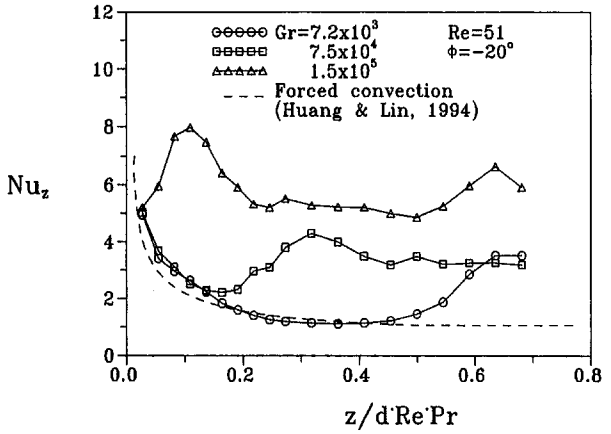

Fig. 4 Spanwise-averaged Nusselt number distributions for various Grashof numbers for Re = 51 and $\phi = -20$ deg

the strong reverse flow causes the large rise in the local Nusselt number in the exit region for Gr = 1.5×10^5. This strong flow reversal by the large opposing buoyancy, in turn, substantially strengthens the vortex flow and enhances the heat transfer, while the reverse is the case for the aiding buoyancy. Thus at a given high Grashof number, beyond the onset of thermal instability the Nusselt number for $\phi = -10$ deg is larger than that for $\phi = 0$ deg, which in turn is higher than that for $\phi = 26$ deg. Data for the onset of thermal instability from the present study for both aiding and opposing convection can be empirically correlated as

$$\mathrm{Ra}_c^* = 5320(1 + 2\sin\phi)(Z_c^*)^{-0.75/\cos\phi}, \quad \phi > 0$$

or (5)

$$= 7980(1 + 2\sin\phi)(Z_c^*)^{-0.53/\cos\phi}, \quad \phi < 0$$

3.3 Flow Visualization. As mentioned earlier, the normal buoyancy component can induce longitudinal rolls, but the parallel component can accelerate or decelerate the flow depending on its relative orientation to the forced flow, which, in turn, may cause flow reversal at a high Grashof number. Thus, the longitudinal rolls and flow reversal can be simultaneously present in the inclined duct at a high opposing buoyancy.

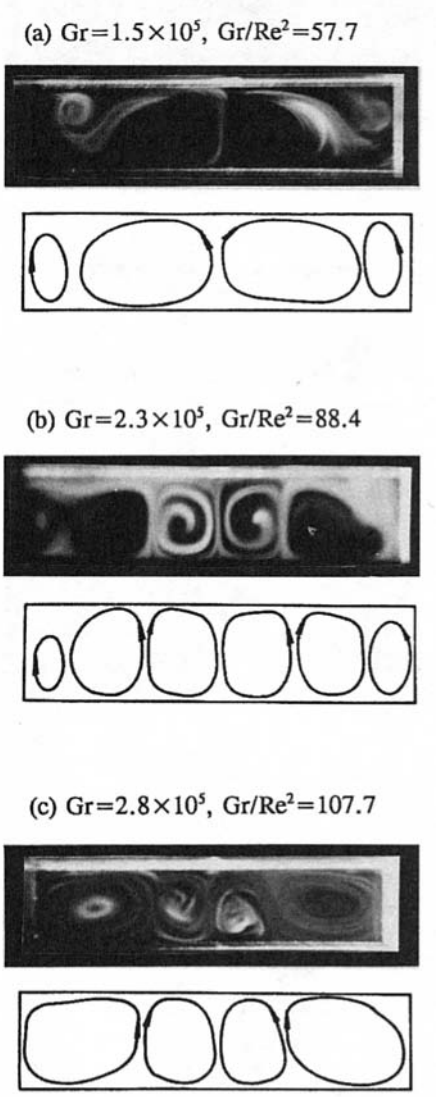

Fig. 5 Instantaneous flow photos and schematically sketched vortex flow for various Grashof numbers for Re = 51 and ϕ = 26 deg at $Z^* \approx$ 0.64 or z = 0.7 m

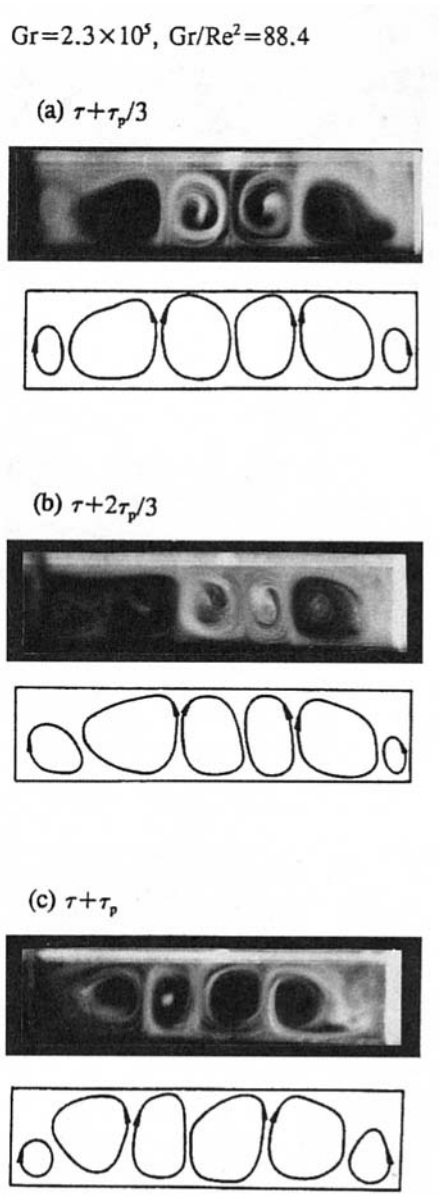

Fig. 6 Instantaneous flow photos and schematically sketched vortex flow in a typical period of $\tau_p \approx$ 13.3 seconds for Re = 51, ϕ = 26 deg, and Gr = 2.3×10^5 at $Z^* \approx$ 0.64 or z = 0.7 m

In the first case to be discussed, the air flows upward in the duct ($\phi > 0$ deg). To understand the buoyancy-induced secondary flow, the cross-plane flow was visualized at a cross section selected at $Z^* \approx 0.64$ or $z = 0.7$ m. Figure 5 shows the instantaneously pictured and schematically drawn secondary flow at long time at which the flow already reaches steady state or statistical state for several Grashof numbers with the Reynolds number fixed at 51 and ϕ at 26 deg. At a low Grashof number ($\approx 1.5 \times 10^5$), two pairs of steady longitudinal vortex rolls were observed in the cross section with the secondary flow ascending along the vertical middle plane (x = 60 mm) and the side walls. As the Grashof number is raised to 2.3×10^5, another pair of vortices is induced in the duct core around the vertical middle plane. These new vortices grow gradually and squeeze the existing ones (Fig. 5(b)). The flow was found to oscillate periodically with time, which will become evident later when the time histories of the air temperature at selected detection points are examined. As the Grashof number is further raised to 2.8×10^5, the disappearance of the vortices near the

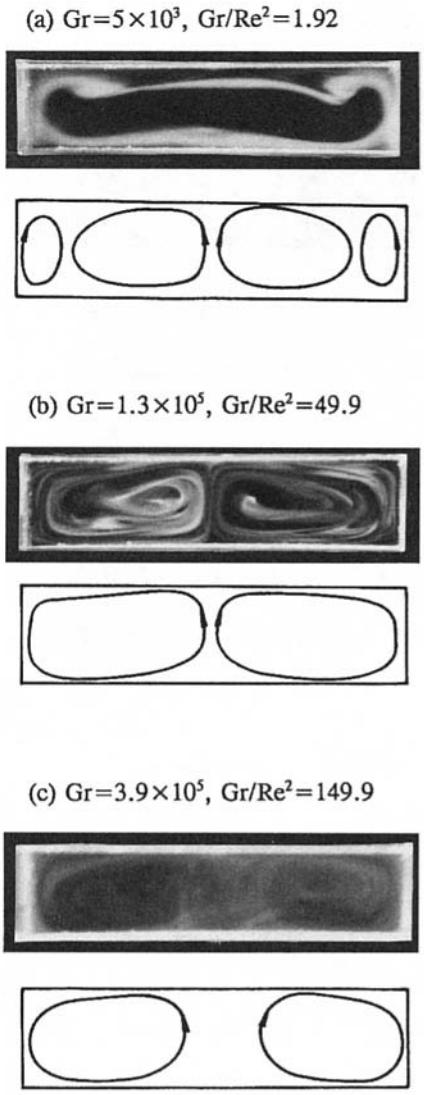

Fig. 7 Instantaneous flow photos and schematically sketched vortex flow for various Grashof numbers for Re = 51 and $\phi = -10$ deg at $Z^* \approx 0.64$ or $z = 0.7$ m

side walls is noted. Thus only two pairs of vortices are seen in Fig. 5(*c*). The corresponding flow is highly unsteady. To illustrate the time periodic secondary flow characteristics, Fig. 6 presents the snapshots of the roll structures at three time instants in a typical period for the case with Gr = 2.3×10^5. The period of the oscillation τ_p is about 13.3 seconds. The results suggest that there are three pairs of vortices induced at the cross section for the entire period and the vortices near the vertical middle plane are much stronger than those near the side walls, which are also smaller in size. Besides, the vortices were found to swing back and forth in the spanwise direction. Thus, the vortex flow is not always symmetric with respect to the vertical middle plane (Fig. 6(*b*)). It is worthwhile to mention that for the aiding buoyancy considered here the buoyancy-induced secondary flow for all cases is mainly in the form of longitudinal vortex rolls with the Grashof number up to 2.8×10^5.

When the air flows downward in the duct ($\phi < 0$ deg), the tangential component of the opposing buoyancy may reverse the forced flow at high Gr and a flow recirculating zone is formed. The secondary flow structure simultaneously induced by the tangential and normal components of the buoyancy force and the stability of the flow are of major concern in the following discussion.

Figure 7 shows the snapshots of the cross-plane secondary flow at long time again at $Z^* \approx 0.64$ or $z = 0.7$ m for several Grashof numbers with ϕ fixed at -10 deg and Re at 51. The results indicate that for Gr up to 5×10^3 the flow is forced convection dominated with the weak upwelling secondary flow along the side walls. As Gr is raised to 1.3×10^5, one pair of vortices is induced. Note that at this Gr the vortex flow descends near the side walls. This can be attributed to the significant heat conduction in the plexiglass side walls. Additionally, the flow was found to be time periodic. As Gr is further raised to 3.9×10^5, the parallel component of the buoyancy was large enough to reverse the forced flow. The direct observation of the reverse flow will be discussed later. The reverse flow was found to weaken the longitudinal vortices. Note that the reverse flow mainly appears in the duct core around the vertical central plane ($x = 60$ mm) and the longitudinal vortices are squeezed toward the side walls to a smaller size and are weaker. Meanwhile, the

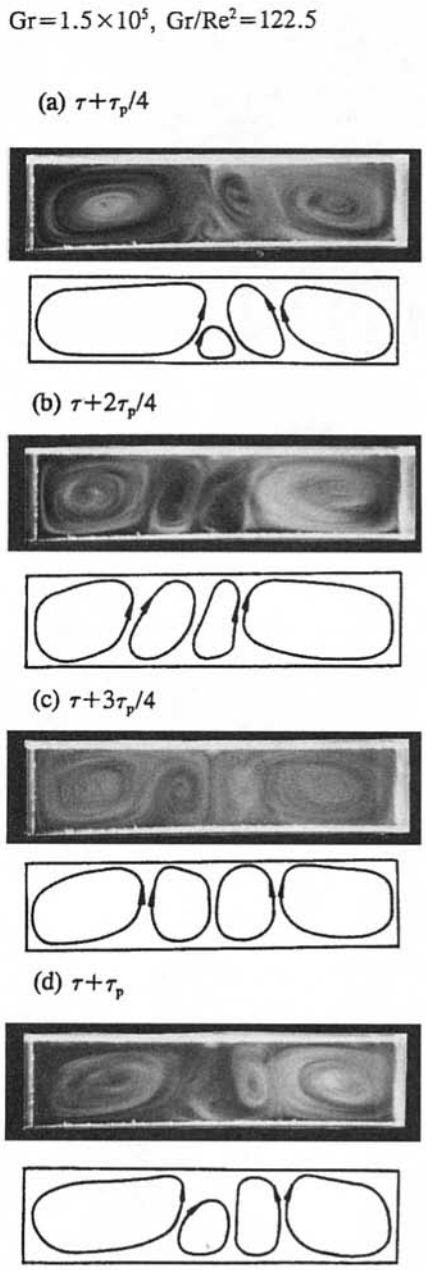

Fig. 8 Instantaneous flow photos and schematically sketched vortex flow in a typical period of $\tau_p \approx 55$ seconds for Re = 35, $\phi = -20$ deg and Gr = 1.5×10^5 at $Z^* \approx 0.93$ or $z = 0.7$ m

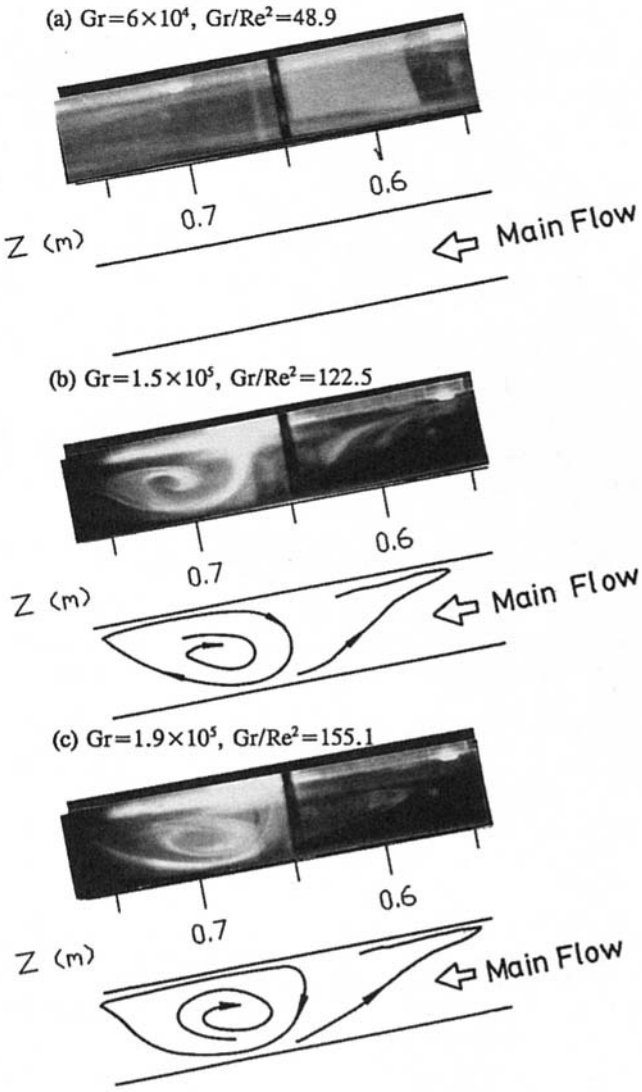

Fig. 9 Sideview of the instantaneous flow photos and schematically sketched reverse flow for various Grashof numbers for Re = 35 and ϕ = −20 deg at X = 2 or x = 60 mm

flow is also time periodic. When Re is reduced from 51 to 35, the parallel component of the buoyancy force can overwhelm the inertia force at a lower Grashof number. The observed periodic cross-plane flow for Re = 35 and Gr = 2.1×10^5 ($\tau_p \approx$ 15 seconds) showed that the reverse flow in the duct is stronger than that for Re = 51 and Gr = 3.9×10^5 and the reverse flow zone swings back and forth in the axial direction, squeezing the longitudinal rolls and causing temporal oscillation of the flow. The flow was also found to be highly asymmetric in certain part of the period.

When the duct is further inclined to −20 deg, the parallel component of the buoyancy force is even larger. As those for ϕ = −10 deg, the buoyancy-induced secondary flow for ϕ = −20 deg is also characterized by the longitudinal vortex rolls adjacent to the side walls and flow reversal in the duct core (Figs. 8 and 9). Obviously, the reverse flow begins to appear at a lower Grashof number for ϕ = −20 deg. Moreover, the reverse flow is stronger and its zone is larger. The periodic cross-plane secondary flow patterns displayed in Fig. 8 for Gr = 1.5×10^5 and Re = 35 suggest that the longitudinal vortices in the core region exist in the entire period and are larger in size and stronger in intensity than those for ϕ = −10 deg. Note that the two pairs of longitudinal vortex rolls are counterrotating and move axially in opposite directions. The interaction of these two vortex pairs causes the flow to be time periodic with a period $\tau_p \approx$ 55 seconds. Figure 9 shows the flow on the vertical middle plane (x = 60 mm) around the axial station $Z^* \approx 0.93$ or z = 0.7 m at various Grashof numbers by viewing the flow from the duct side. As Gr is increased gradually, the increasing opposing buoyancy drives the reverse flow in the exit end of the test section slightly upstream. It was noted that the normal extent of the reverse flow is comparable with the duct height. Its spanwise extent can be inferred from the cross-plane flow just discussed. Also it was noted that the reverse flow moves axially back and forth periodically with time.

3.4 Time Records of Air Temperature and the Associated Power Spectrum Densities. Several important flow characteristics can be identified in the mixed convective flow through the bottom-heated inclined duct. The appearance of the secondary vortex flow and/or the reverse flow as the buoyancy force exceeds the critical level is already discussed above. The transition of the steady to the time periodic flow, the so-called "Hopf bifurcation," at even higher buoyancies is also an important feature to be examined in the following. Only the traced air temperature for the detection point at z = 0.7 m, x = 60 mm, and y = 25 mm is presented here.

Results for the buoyancy-aiding cases for various Re, Gr, and ϕ indicate that at a very low Grashof number steady temperature was recorded. As the Grashof number exceeds a certain critical value, depending on Re and ϕ, a time periodic temperature oscillation was seen. The associated power spectrum densities imply that the temperature oscillation is mainly dominated by a single fundamental frequency f_1 and its harmonics. The results given in Fig. 10 for Re fixed at 51 suggest that at ϕ = 26 deg the flow oscillates periodically at $f_1 \approx$ 0.1 Hz, which is

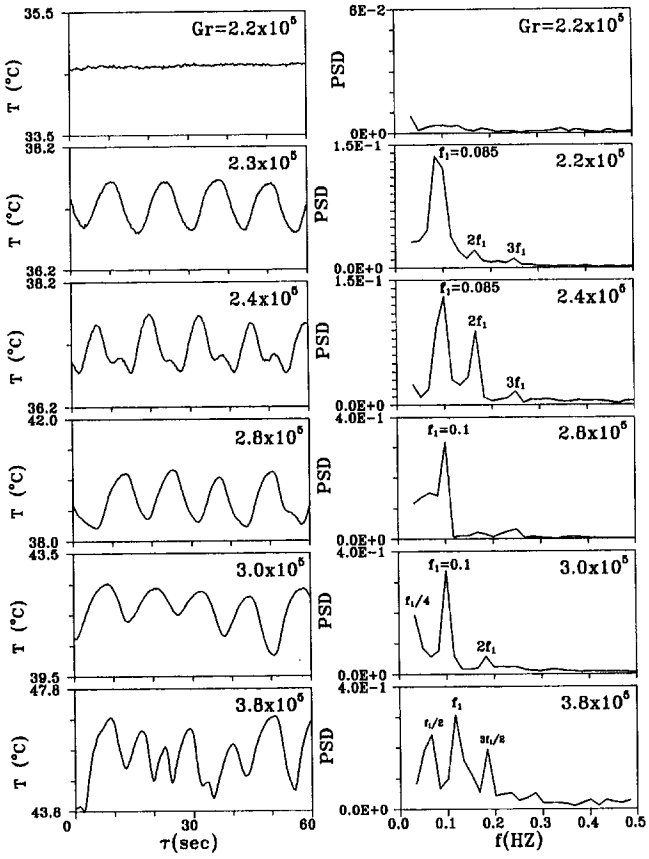

Fig. 10 Time records of the air temperature and the corresponding power spectrum densities for Re = 51 and ϕ = 26 deg at Z^* ≈ 0.64 or z = 0.7 m, X = 2, and Y ≈ 0.83 at increasing Gr

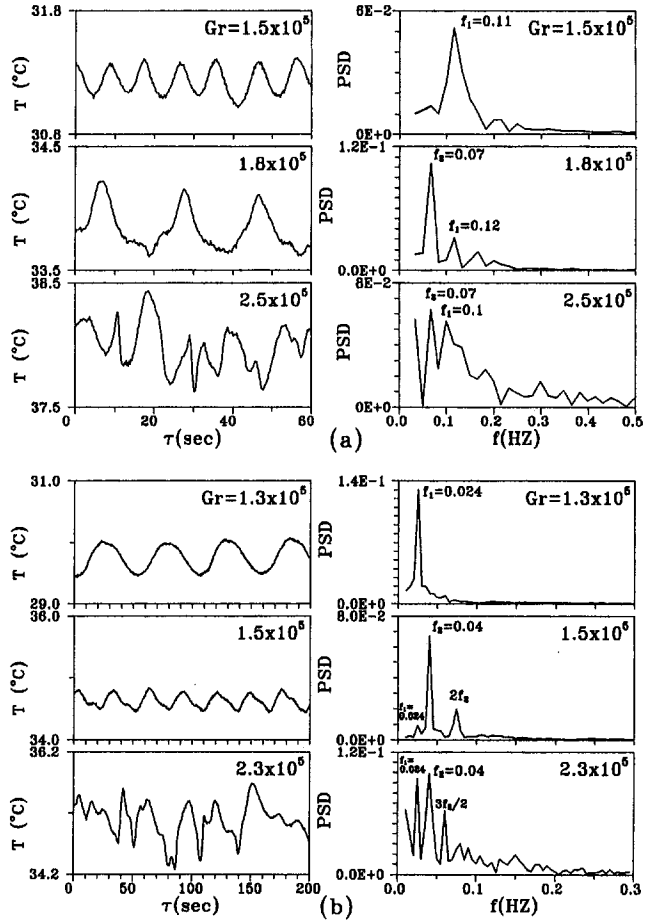

Fig. 11 Time records of the air temperature and the corresponding power spectrum densities for various Grashof numbers for (*a*) Re = 51 and (*b*) Re = 35 for $\phi = -20$ deg at $z = 0.7$ m, $X = 2$, and $Y \approx 0.83$

much lower than that for $\phi = 15$ deg ($f_1 \approx 0.5$ Hz). The amplitude of the temperature oscillation increases slightly with the Grashof number. For ϕ fixed at the same value and the Reynolds number increased from 51 to 102, the flow was found to oscillate in a smaller amplitude but at a much higher frequency.

To illustrate the stability of the opposing mixed convective flow, the time histories of the temperature for various Gr for $\phi = -10$ and -20 deg were examined. The results again suggest that at a given Re the flow is steady for a very low Grashof number. As the Grashof number exceeds a certain critical value, the temperature oscillation is time periodic. The oscillation amplitude does not always increase with Gr. The time records of the air temperature for various Gr for Re = 51 and 35 for $\phi = -20$ deg are presented in Fig. 11 to substantiate these statements. It is noted from Fig. 11(b) that the periodic temperature oscillation is characterized by a single fundamental frequency f_1 ($\approx$0.024 Hz for Re = 35) and its harmonics. For a higher Grashof number, a second fundamental frequency f_2 ($\approx$0.04 Hz for Re = 35) appears in the temperature fluctuation, indicating that the flow is quasi-periodic. This can be seen in the curves for Re = 51 with Gr $\geq 1.8 \times 10^5$ (Fig. 11(a)) and for Re = 35 with Gr $\geq 1.5 \times 10^5$ (Fig. 11(b)). These results also suggest that the reverse flow (as shown in Fig. 9) and the second fundamental frequency f_2 appear nearly at the same Gr. At an even higher Gr irregular temperature oscillations prevail in the flow at the cross section $z = 0.7$ m, as evident from the temperature traces for Re = 51 with Gr $\geq 2.5 \times 10^5$ and for Re = 35 with Gr $\geq 2.3 \times 10^5$.

Based on the results for various Re, Gr, and ϕ, the critical Grashof number for the onset of the Hopf bifurcation at the cross section $z = 0.7$ m is found to be higher for a larger inclined angle for the aiding flow. Obviously, a smaller Reynolds number and/or a larger inclined angle for the opposing flow cause an earlier appearance of the time periodic oscillation.

4 Concluding Remarks

We have performed an experimental investigation concerning the effects of the Reynolds and Grashof numbers and duct inclination on the flow transition in the mixed convective air flow of a bottom-heated rectangular duct by systematic measurement of the heat transfer coefficient and time records of air temperature. Additionally, the flow visualization was also conducted.

The major conclusions obtained are summarized as follows:

1 The buoyancy force increases the thermal boundary layer thickness prior to the onset of the thermal instability and the Nusselt number shows a rapid decline with the downstream distance. Subsequent heat transfer enhancement was attributed to the formation and development of the buoyancy driven secondary flow.

2 The onset of thermal instability was found to move upstream for increasing Gr and negative inclined angle ϕ. The reverse is the case for increasing Re and positive inclination angle ϕ.

3 Results from the flow visualization reflect the complicate changes in the vortex and reverse flow structures at high Gr/Re^2.

4 As the Grashof number is high enough, the transition of the steady vortex flow to the time periodic one could occur. Further raising the Grashof number causes the flow to change to a quasi-periodic one and even to a chaotic state.

During the course of this study it is realized that the complete picture of the buoyancy-induced secondary flow and its spatial-temporal transition can only be more clearly delineated by probing and visualizing the vortex and reverse flow in the entire duct. This will be carried out in the near future.

Acknowledgments

Financial support of this study by the engineering division of National Science Council of Taiwan, through contract No. NSC83-0404-E-009-054, is greatly appreciated.

References

Evan, G., and Grief, R., 1989, "A Study of Traveling Wave Instabilities in a Horizontal Channel Flow With Applications to Chemical Vapor Deposition," *International Journal of Heat and Mass Transfer*, Vol. 32, pp. 895–911.

Fukui, K., Nakajima, M., and Ueda, H., 1983, "The Longitudinal Vortex and Its Effects on the Transport Processes in Combined Free and Force Laminar Convection Between Horizontal and Inclined Parallel Plates," *International Journal of Heat and Mass Transfer*, Vol. 26, pp. 109–120.

Heggs, P. J., Ingham, D. B., and Keen, D. J., 1990, "The Effects of Heat Conduction in the Wall on the Development of Recirculating Combined Convection Flows in Vertical Tubes," *International Journal of Heat and Mass Transfer*, Vol. 33, pp. 517–528.

Holman, J. P., 1986, *Heat Transfer*, McGraw-Hill, New York, Chap. 8.

Huang, C. C., and Lin, T. F., 1994, "Buoyancy Induced Flow Transition in Mixed Convective Flow of Air Through a Bottom Heated Horizontal Rectangular Duct," *International Journal of Heat and Mass Transfer*, Vol. 37, pp. 1235–1255.

Incropera, F. P., 1988, "Convective Heat Transfer in Electronic Equipment Cooling," ASME JOURNAL OF HEAT TRANSFER, Vol. 110, pp. 1097–1111.

Ingham, D. B., Heggs, D. J., and Morton, B. R., 1990, "Recirculating Pipe Flows," *J. Fluid Mech.*, Vol. 213, pp. 443–464.

Kays, W. M., and London, A. L., 1984, *Compact Heat Exchangers*, 3rd ed., McGraw-Hill, New York.

Kline, S. J., and McClintock, F. A., 1953, "Describing Uncertainties in Single-Sample Experiments," *Mechanical Engineering*, Vol. 75, Jan., pp. 3–12.

Lavine, A. S., Kim, M. Y., and Shores, C. N., 1989, "Flow Reversal in Opposing Mixed Convection Flow in Inclined Pipes," ASME JOURNAL OF HEAT TRANSFER, Vol. 111, pp. 114–120.

Lin, T. F., and Lin, W. L., 1994, "Thermal Control of Microelectronic Equipment—Buoyancy Driven Unstable Mixed Convection in Rectangular Channel (III)," Report for National Science Council of Taiwan, Chap. 5.

Maughan, J. R., and Incropera, F. P., 1987, "Experiments on Mixed Convection Heat Transfer for Airflow in a Horizontal and Inclined Channel," *International Journal of Heat and Mass Transfer,* Vol. 30, pp. 1307–1318.

Morcos, S. M., Hilal, M. M., Kamel, M. M., and Soliman, M. S., 1986, "Experimental Investigation of Mixed Laminar Convection in the Entrance Region of Inclined Rectangular Channels," ASME JOURNAL OF HEAT TRANSFER, Vol. 108, pp. 574–579.

Morton, B. R., Ingham, D. B., Keen, D. J., and Heggs, P. J., 1989, "Recirculating Combined Convection in Laminar Pipe Flow," ASME JOURNAL OF HEAT TRANSFER, Vol. 111, pp. 106–113.

Shah, R. K., and London, A. L., 1978, *Laminar Flow Force Convection in Ducts,* Academic Press, New York, pp. 196–198.

Combined Natural Convection–Conduction and Radiation Heat Transfer in a Discretely Heated Open Cavity

A. A. Dehghan[1]

M. Behnia

School of Mechanical and Manufacturing Engineering, The University of New South Wales, Sydney, 2052, Australia

Combined natural convection, conduction, and radiation heat transfer in an open-top upright cavity containing a discrete heat source has been modeled numerically. The surface emissivity has been varied and its effects on the flow and thermal fields have been determined for different values of Rayleigh number. The complex interaction of the three modes of heat transfer mechanisms is explored by solving the coupled convection, conduction, and radiation equations. It is noted that the inclusion of radiation has a significant effect on the flow, resulting in the formation of a recirculation zone within the cavity. Comparison of the local heat transfer coefficients for the conjugate analysis and no radiation case reveals that the inclusion of radiation has a negligible effect on the heat transfer performance of the heat source. However, comparison of the numerical results with experimental observations shows that accurate prediction of the flow and thermal fields is strongly dependent on the consideration of radiation heat transfer in the numerical case.

1 Introduction

Air cooling has been and will likely remain a promising option in the cooling of electronic equipment. This is due to its simplicity in design and low installation and maintenance cost (Incropera, 1987). In systems employing low heat generating electronic devices such as microchips, natural convection cooling is the most favorable alternative and is frequently employed, mainly because it is noise free and highly reliable. Electronic components are usually mounted on the vertical boards, which form channels or cavities, and the heat generated by the components is removed by a naturally induced flow of air.

The natural convection of air in enclosures or channels either uniformly heated and cooled or discretely heated has received much attention (e.g., Chu et al., 1976; Cesini et al., 1988; Chadwick et al., 1991; Refai and Yovanovich, 1991). In most of these investigations, the heated section of the cavity is treated either as a uniform temperature or uniform heat flux, and natural convection has been considered to be responsible for the cooling process.

In applications employing natural convection as a heat transfer mechanism, the range of temperatures is normally low, and therefore it may be justifiable to neglect radiation effects for both simplicity and computational economy. However, there are some limited studies in which the problem of conjugate natural convection and radiation has been investigated. One of the first studies in this area is the investigation of Carpenter et al. (1976) in which combined radiation and free convection from a vertical channel with constant isoflux heating conditions over the plates was considered. Both symmetric and asymmetric heating boundary conditions were examined. They showed that for the asymmetric case, consideration of the radiation heat transfer between the heated and adiabatic vertical walls of the channel changes the calculated flow and velocity patterns inside the channel. Hence, they concluded that for the asymmetric heating, radiation has an important effect and cannot be neglected.

Larson and Viskanta (1976) investigated the problem of transient laminar free convection and radiation in a rectangular enclosure, aimed at simulating the rate of fire spread in buildings. They showed that radiation heat transfer had a considerable influence on the flow and thermal fields inside the cavity, and was the predominant mechanism of heat transfer in both this application, and other applications involving high-temperature heat sources in enclosures. Sparrow et al. (1980) considered the interaction of natural convection and radiation between vertical plates that formed a channel. For an asymmetric heated channel with one isothermal wall with the other wall insulated, they concluded that radiation generally enhanced heat transfer relative to the pure natural convection case.

In the numerical and experimental study of Yamada (1988), the configuration of Carpenter et al. (1976) was considered. The working fluid was assumed to be a participating medium and two models for gas radiation were examined. It was concluded that in the asymmetric heating condition, radiation heat exchange between the vertical plates was important and could increase the heat transfer rate from the heated plate up to 30 percent, a finding in agreement with those of Carpenter et al. (1976) and Sparrow et al. (1980). However, in Yamada's study the radiation heat exchange between the plates was simplified using a one-dimensional model.

The importance of the radiation heat transfer in the problems dealing with the natural convection in asymmetrically heated channels was also shown by Webb and Hill (1989) and Manca and Naso (1990). Recently Behnia et al. (1990) considered combined natural convection and radiation in a rectangular enclosure. One wall of the cavity was isothermal while the opposite wall exchanged heat by convection from its external surface to the surroundings and was also semitransparent, permitting radiation exchange between the cavity and surroundings. A two-band radiation model was used in conjunction with natural convection equations in the cavity. Their computations showed that radiation strengthens the internal circulation. The brief survey presented here shows that most of these investigations have emphasized the importance of radiation in asymmetric channel

[1] Present address: School of Mechanical Engineering, Yazd University, Yazd, Iran.

Contributed by the Heat Transfer Division for publication in the JOURNAL OF HEAT TRANSFER. Manuscript received by the Heat Transfer Division September 1994; revision received July 1995. Keywords: Conjugate Heat Transfer, Electronic Equipment, Natural Convection. Associate Technical Editor: Y. Jaluria.

flows employing natural convection. In most of these studies, the isoflux or isothermal boundary conditions were applied over the entire length of the heated plate, and almost uniform or near-uniform wall temperature distributions over the heated plates were calculated. In geometries using discrete heating boundary conditions, which are more practical and relevant to the electronic cooling applications, the temperature distribution over the vertical walls is not normally uniform. This nonuniformity intensifies in channels or cavities employing low conductive vertical walls. Therefore, in circumstances in which nonuniformity in the temperature distribution along the solid boundaries is encountered, radiation may have a substantial contribution and its effect is worth examining.

This study is a continuation of the work of Dehghan et al. (1992) in which natural convection in the cavity, conduction in the vertical walls, and radiation heat exchange between all surfaces of the cavity have all been included. It aims to explore the complex interaction of these three modes of heat transfer, especially the effect of radiation.

2 Problem Description and Governing Equations

The schematic diagram of the geometry under investigation is shown in Fig. 1. A constant heat flux heat source is mounted on the middle of the left vertical wall of an open top vertical cavity, simulating a discrete heating condition. The heat generated is dissipated via convection to the fluid, by conduction to the vertical wall, and by radiation heat exchange with other surfaces. The prime motivation for considering the fully conjugate problem has originated primarily from the concurrent analysis of our experimental results for the same geometry, in which the results suggested that there was radiation heat exchange across the slot between the vertical walls.

The full set of governing flow equations is nondimensionalized by using the following variables:

$$X = x/d, \quad Y = y/d, \quad \tau = t\nu/d^2$$

$$U = ud/\alpha_f, \quad \theta = (T - T_0)/(q''d/k_f\lambda)$$

$$\mathrm{Pr} = \frac{\nu}{\alpha_f}, \quad \mathrm{Ra}^* = \frac{g\beta q'' d^4}{k_f \nu}\frac{\mathrm{Pr}}{\lambda}$$

The flow is assumed to be laminar, two-dimensional, and incompressible, with constant properties except density in the buoyancy term of the momentum equation, which is assumed to follow the Boussinesq approximation. The vorticity-stream function formulations of the governing equations are used in the fluid region (in nondimensional form):

$$\frac{\partial \xi}{\partial \tau} + \frac{1}{\mathrm{Pr}}\left(U\frac{\partial \xi}{\partial X} + V\frac{\partial \xi}{\partial Y}\right) = \nabla^2\xi + \mathrm{Ra}^*\frac{\partial \theta}{\partial Y} \tag{1}$$

$$\frac{\partial \theta}{\partial \tau} + \frac{1}{\mathrm{Pr}}\left(U\frac{\partial \theta}{\partial X} + V\frac{\partial \theta}{\partial Y}\right) = \frac{1}{\mathrm{Pr}}\nabla^2\theta \tag{2}$$

$$\nabla^2\Psi = -\xi \tag{3}$$

in which Ψ (stream function) and ξ (vorticity) have their conventional definitions:

$$U = \frac{\partial \Psi}{\partial Y}, \quad V = -\frac{\partial \Psi}{\partial X} \tag{4}$$

$$\xi = \frac{\partial V}{\partial X} - \frac{\partial U}{\partial Y} \tag{5}$$

2.1 Boundary Conditions. The outside of each vertical wall is adiabatic, as shown in Fig. 1. An energy balance for an element of each of the vertical walls yields the appropriate equations coupling the temperature in the fluid to that in the solid. All the solid boundaries of the cavity are assumed to be impermeable and nonslip, so that both Ψ and the fluid velocities are set to zero on these surfaces.

The computational domain is restricted to the cavity for both economy and simplicity. Therefore, appropriate boundary conditions are required for the open top. Here, it is assumed that the incoming flow is at the ambient temperature, $\theta_{in} = 0$, and the outgoing flow is assumed to have zero axial temperature gradient, i.e., $\partial\theta/\partial X = 0$. For the case of a single heat source mounted on a vertical wall, Jaluria (1985) has shown that the flow is a boundary layer type and this is a valid assumption at downstream locations from the heat source, especially for higher

Nomenclature

d = width of the cavity
F_{i-j} = view factor between segments i and j
H = height of the cavity
k = thermal conductivity
k_r = thermal conductivity ratio (solid to fluid) = k_s/k_f
NS = number of subdivisions (see Fig. 2)
Nu = Nusselt number
Nu_s = average heat source Nusselt number
$\mathrm{Nu}(X)$ = local Nusselt number
$\mathrm{Nu}_r(X)$ = local radiation Nusselt number
p = vertical position of the heat source
Pr = Prandtl number = ν/α_f
q'' = input heat flux
Q_{con} = interface heat flux
q''_{conv} = dimensional convective heat flux
q''_{cond} = dimensional conduction heat flux
q''_{rj} = net radiation heat flux from surface j
Q_c = local nondimensional convective heat flux
Q_{rj} = nondimensional surface net radiation heat flux = $q''_{rj}/\sigma T^4_{\mathrm{ref}}$
Ra^* = $(g\beta q'' d^4/k_f\nu)\,(\mathrm{Pr}/\lambda)$ = heat flux based Rayleigh number
R_{cof} = radiation coefficient = $q''/\sigma T^4_{\mathrm{ref}}$
s = height of the heat source
S = dimensionless height of the heat source = s/d
t = dimensional time
T = dimensional temperature
T_O = ambient temperature, K
T_{ref} = reference temperature = $q''d/k_f\lambda$
u, v = vertical and horizontal velocities
U, V = dimensionless vertical and horizontal velocities
w = thickness of the vertical walls
w_r = wall thickness ratio = w/d
x, y = dimensional coordinates (see Fig. 1)
X, Y = dimensionless coordinates
α_r = thermal diffusivity ratio (solid to fluid) = α_s/α_f
δ_{kj} = $\begin{cases} 1 & \text{when } k = j \\ 0 & \text{when } k \neq j \end{cases}$
$\partial/\partial n$ = outward normal derivative
ϵ = surface radiation emissivity
θ = nondimensional vorticity
$\overline{\theta_j}$ = average nondimensional temperature of the segment j
λ = cavity aspect ratio = H/d
ξ = nondimensional vorticity
σ = Stefan–Boltzmann constant = 5.67×10^{-8} W/m^{2}K^4
τ = nondimensional time
Ψ = nondimensional stream function

Subscripts

f = fluid
j = subdivision j on the left or right wall of the cavity
n = normal outward direction
s = heat source
w = surface of the wall

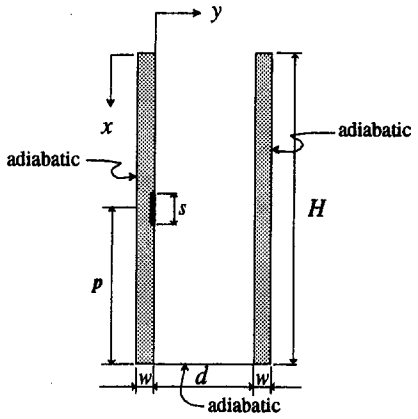

Fig. 1 Schematic diagram of the open cavity

Grashof numbers. Therefore, the horizontal component of the velocity, V, is assumed to be zero at the open boundary. The boundary condition for the vertical velocity, U, is obtained from continuity equation which gives $\partial U/\partial X = 0$. The hydrodynamic boundary conditions at the open top, when translated to the vorticity stream function form, yield $\partial \Psi/\partial X = \partial \xi/\partial X = 0$. In summary, the boundary conditions applied to the open boundary are as follows:

$$\theta_{in} = 0 \quad \text{for incoming flow} \tag{6}$$

$$\left(\frac{\partial \theta}{\partial X}\right)_{\text{out}} = 0 \quad \text{for outgoing flow} \tag{7}$$

$$V = \frac{\partial U}{\partial X} = \frac{\partial \Psi}{\partial X} = \frac{\partial \xi}{\partial X} = 0 \quad \text{for both flows} \tag{8}$$

The same approximate boundary conditions were used by Gosman et al. (1971) in their numerical study of heat transfer within an open thermosyphon. For shallow open cavities Chan and Tien (1985) have shown both numerically and experimentally that the basic flow pattern and heat transfer characteristic of the cavity can be adequately predicted by employing the approximate open boundary conditions as described above. They also showed that even for square cavities at moderate to high Rayleigh numbers, the flow and heat transfer were identical with those obtained from extending the computational domain outside the cavities. Abib and Jaluria (1988) employed the same boundary conditions as Gosman et al. (1971) for predicting buoyancy-driven flow generated by a discrete isothermal heat source inside a partially open enclosure. More recently Lage et al. (1992) and Jones and Cai (1993) adopted this approach and used the same boundary conditions, which are used in this study in their numerical study of natural convection heat transfer from open top cavities.

2.2 Radiation Equations. For an enclosure having NS surfaces, the net radiation heat fluxes from each surface can be related to its temperatures by the following nondimensional equation:

$$\sum_{j=1}^{NS} \left(\frac{\delta_{kj}}{\epsilon_j} - F_{k-j}\frac{1-\epsilon_j}{\epsilon_j}\right) Q_{rj} = \sum_{j=1}^{NS} (\delta_{kj} - F_{k-j})\sigma\theta_j^4 \quad 1 \le k \le NS \tag{9}$$

in which:

$$\theta_j = \overline{\theta_j} + \frac{T_0}{T_{\text{ref}}}.$$

The average temperature of each subdivision surface j (i.e., $\overline{\theta_j}$) is obtained by numerically integrating the temperature profile over the subsurface using Simpson's rule. The open boundary (i.e., subdivision NS) is assumed to be a black surface at ambient temperature. All other surfaces are assumed to be diffuse and gray.

In order to use this equation, each vertical wall must be divided into subsurfaces, since the temperature distribution along the walls is assumed to be nonuniform. In each subdivision a nearly isothermal condition can be assumed. The subdivision of the enclosure for this purpose is shown in Fig. 2.

2.3 Conduction Equation. In our previous study (Dehghan et al., 1992) in developing the one-dimensional conduction equation in the solid regions, the radiation heat exchange between the surfaces of the cavity was neglected. However, the general form of conduction equation for the walls can be obtained by writing an energy balance for an element of the wall, considering all modes of heat transfer. Results are also obtained using a two-dimensional conduction model in the vertical walls for the no-radiation case and for the values of wall conductivity and wall thickness used in this study. Differences of 1.4 and 0.6 percent between the heat source temperature and its Nusselt number were observed, respectively (Dehghan, 1994). Hence, the one-dimensional model, which needs less computational time, is used in this study. The one-dimensional dimensionless form of the conduction equation in the vertical walls is given by:

$$\frac{\text{Pr}}{\alpha_r}\frac{\partial \theta}{\partial \tau} = \frac{\partial^2 \theta}{\partial X^2} + Q_{\text{con}} - \frac{\lambda Q_{rj}}{k_r w_r R_{\text{cof}}} \tag{10}$$

where R_{cof} and Q_{con} are defined as follows:

$$R_{\text{cof}} = q''/\sigma T_{\text{ref}}^4$$

$$Q_{\text{con}} = \frac{1}{k_r w_r}\left[\lambda + \left.\frac{\partial \theta}{\partial n}\right|_f\right] \quad \text{on the heated sections} \tag{11}$$

$$Q_{\text{con}} = \frac{1}{k_r w_r}\left.\frac{\partial \theta}{\partial n}\right|_f \quad \text{on the nonheated sections.} \tag{12}$$

The thermal boundary condition on the bottom wall is derived from the energy balance in this wall. The bottom wall is considered to be adiabatic. Hence, conduction of heat to the fluid in the vicinity of this wall must be balanced by the net radiative heat exchange with other surfaces of the cavity. The required boundary condition for the bottom wall in the dimensionless form is:

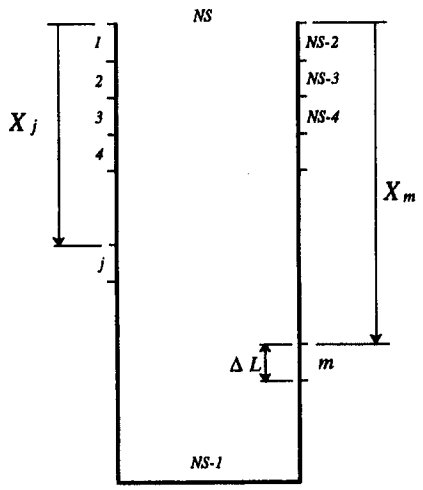

Fig. 2 Subdivision of enclosure walls to the subsurfaces for radiation heat exchange calculation

$$\frac{\partial\theta}{\partial X} + \frac{\lambda}{R_{cof}} Q_{rj} = 0 \quad (13)$$

The coefficients in the system of Eqs. (9) contains elements that are a function of view factors between each segment of the cavity. These view factors must be first determined prior to any attempt to solve the system of Eqs. (9). The view factors between each segment j on the left wall and segment m on the right wall (see Fig. 2), between each segment j on the left wall and the top boundary (i.e., segment NS) and between the bottom and top boundaries are obtained from the following relationships, respectively:

$$F_{j-m} = \frac{1}{2\Delta L}\{[(X_m - X_j + \Delta L)^2 + 1]^{1/2} + [(X_m - X_j - \Delta L)^2 + 1]^{1/2} - 2[(X_m - X_j)^2 + 1]^{1/2}\} \quad (14)$$

$$F_{j-NS} = j \cdot F_{(1,2,\ldots,j)-NS} - (j-1) \cdot F_{(1,2,\ldots,j-1)-NS} \quad (15)$$

$$F_{(NS-1)-(NS)} = \sqrt{1+\lambda^2} - \lambda \quad (16)$$

Once all the view factors are determined, they are constant for a fixed geometry and the calculation of view factors is accomplished at the first time step and does not appear in the main iteration procedure.

2.4 Computation of Different Modes of Heat Dissipation. Due to the conjugate nature of the problem, different heat transfer mechanisms such as convection to the fluid, conduction in the wall, and radiation to the other surfaces are involved in dissipating the input energy at the heat source location. Each mode of heat transfer may be calculated after the steady-state solution is obtained. The local nondimensional convective heat transfer coefficient, $\mathrm{Nu}(X)$, along each wall can be defined as:

$$\mathrm{Nu}(X) = -\frac{1}{\theta_w(X)}\left(\frac{\partial\theta}{\partial n}\right)_w \quad (17)$$

The ratio of the convective heat flux, q_{conv}, to input heat flux, q'', can be determined from the following equation:

$$\frac{q''_{con}}{q''} = \frac{\mathrm{Nu}(X)\cdot\theta_w(X)}{\lambda} \quad (18)$$

Hence Eqs. (17) and (18) can be used to determine the contribution of the convection mode. Integration of Eq. (17) over the heat source length, and the left and right walls gives the average heat source Nusselt number, Nu_s, and the average hot and cold wall Nusselt numbers, respectively.

A nondimensional local radiation heat transfer coefficient, $\mathrm{Nu}_r(X)$, may be defined in the same fashion as:

$$\mathrm{Nu}_r(X) = \frac{\lambda}{R_{cof}}\frac{Q_{rj}}{\theta_w(X)} \quad j = 1, 2, \ldots, NS-1 \quad (19)$$

in which Q_{rj} is the outcome of the system of Eqs. (9). The ratio of radiation heat flux, q''_{rj} to the imposed heat flux can be calculated from:

$$\frac{q''_r}{q''} = \frac{Q_{rj}}{R_{cof}} \quad (20)$$

The contribution of conduction heat transfer to the vertical walls from the back face of the heated patch can be obtained by implementing an energy balance between all three modes of heat transfer and input energy to the heat source at the solid–fluid interface. This yields:

$$\frac{q''_{cond}}{q''} = 1 - \left\{-\frac{1}{\lambda}\frac{\partial\theta}{\partial n}\bigg|_f + \frac{Q_{rj}}{R_{cof}}\right\}$$

at the heat source location (21)

The contribution of each mode of heat transfer in dissipating the imposed heat into the heat source can be obtained by integrating Eqs. (18), (20), and (21) over the heat source.

2.5 Solution Procedure. Equations (1)–(5), (9), and (10) are coupled and must be solved simultaneously. The false transient technique proposed by Mallinson and de Vahl Davis (1973) is employed for solving Eqs. (1), (2), and (3).

The governing flow Eqs. (1), (2), and (3) and the solid conduction Eq. (10) are approximated by finite differences. First-order finite differences in time and second-order central differences in space are employed. The resulting finite difference form of the governing flow equations is solved by the ADI scheme proposed by Samarskii and Andreyev (1963), and a fully implicit scheme is employed for the solution of the one-dimensional conduction equation.

The unknown in the system of equations given in Eq. (9) is Q_{rj}, which represents the net nondimensional radiation heat flux from each subdivision shown in Fig. 2. The right-hand side of this system of equations is a function of the average temperature of subdivisions, their view factors, and surface radiation properties. The average temperature of each segment can be used from the previous time step solution. The LU decomposition scheme is used for solving this system of equations. The outcome of the solution is Q_{rj}, which is then used in the conduction Eq. (10).

3 Results

The results presented here are for a cavity with an aspect ratio of 5 and with bakelite as the vertical walls, leading to a thermal conductivity ratio to the air (k_r) of 8.8. The heat source is located in the middle of the left vertical wall. The ratio of the heat source length to the wall height is 0.11. The other geometric parameters are $w/d = 0.1$ and $p/H = 0.5$. Because the influence of radiation is the prime objective of this study, all the geometric parameters are considered to be fixed and only the surface emissivity and the heat flux or Ra* have been varied. Both vertical plates are assumed to be homogeneous, gray, and diffuse emitters and have the same thermal conductivity, emissivity, and thickness. The working fluid is air and is considered as a nonparticipant media. Results have been obtained for a range of input heat fluxes corresponding to the variation of Ra* from 1.148×10^4 to 8.03×10^4 for different values of surface emissivity. However, only a selection of results obtained will be presented and discussed here.

A uniform 41×101 mesh was used in all the computations as a compromise between computational effort and the accuracy required. Further decreasing the mesh size resulted less than 1 percent difference between the temperature and heat transfer coefficient of the heat source. The calculations were performed on an IBM RS/6000-320 computer. On this machine the CPU time required for 1000 iterations was approximately 150 seconds, with around 8×10^5 iterations being typically required to obtain a steady-state solution. The run times were shortened by using the converged solution of a previously computed similar case as a starting solution.

In Fig. 3 the predicted streamlines and isotherms are presented for Ra* of 5.74×10^4 for different values of surface emissivity. Significant changes in the flow and thermal fields are observed. When there is no radiation heat transfer between the surfaces of the cavity, the isotherms are confined to the left vertical wall, producing a thermal boundary layer. The rest of the enclosure is occupied by the cold flow and only the left wall participates in the heat transfer process. The right vertical wall is affected by the presence of the heat source primarily

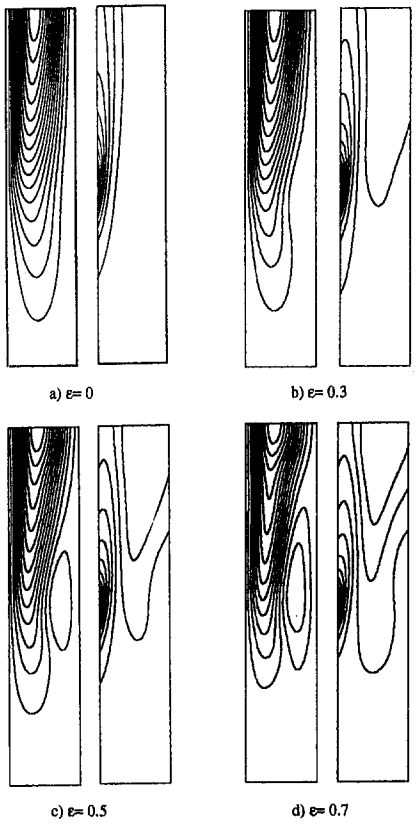

Fig. 3 Streamlines and isotherms for Ra* = 5.74 × 10⁴

due to the diffusion of heat across the slot, which, in this case, is negligible. When radiation is taken into account the right wall of the cavity becomes a separate active convective heat transfer region and part of the input heat into the heat source is convected to the fluid from this wall. This causes the temperature of the incoming flow to be gradually increased as it descends along the right wall. Increasing the surface emissivity increases the radiation heat exchange between the vertical plates, resulting in more of the area of the cavity being occupied by the warm fluid.

In the case of pure convection heat transfer from the surfaces of the cavity (see Fig. 3*a*) there is little bending of the incoming streamlines toward the hot plate. The slight bending is due to the effect of flow entrainment into the rising plume along the left wall. As surface emissivity is increased, the bending of the streamlines becomes more pronounced. The deformation of the flow in this manner is the direct effect of radiation heat exchange

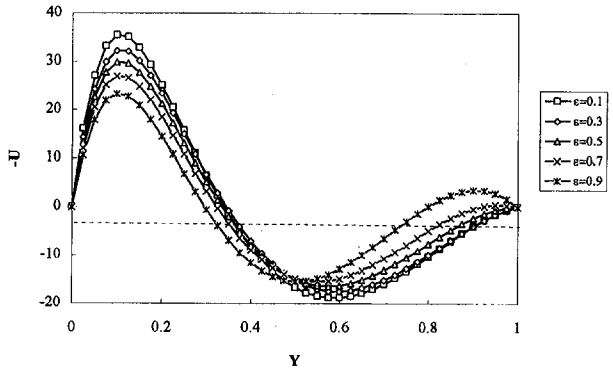

Fig. 4 Vertical velocity profiles at the midheight of the cavity for Ra* = 5.74 × 10⁴ for various surface emissivities

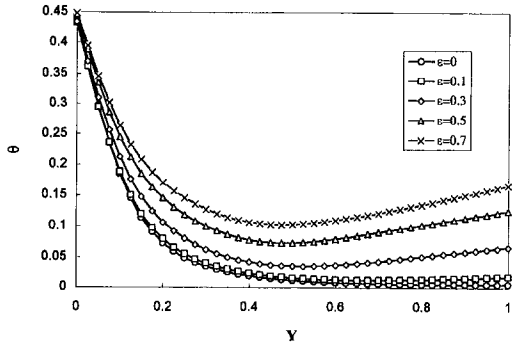

Fig. 5 Fluid temperature distribution at the midheight of the cavity for different values of surface emissivity at Ra* = 5.74 × 10⁴

between the vertical walls. As the incoming fluid proceeds downward, it loses its momentum while its buoyancy force increases due to the convective heat flux from the right wall. Increasing the surface emissivity decreases the momentum of the downcoming fluid while increasing its buoyancy force. At some location along the right wall, the incoming flow no longer posseses sufficient momentum to adhere to the wall, and flow separation occurs. Increasing the surface emissivity results in a higher heat exchange between the heat source and the right wall and an increase in the buoyancy force along the right wall. This causes an increase in the size of the recirculation region and the point of the flow separation to move upward. Its growth in size also prevents deeper penetration of the incoming flow.

The effect of radiation in generating this flow reversal and its effect on the velocity profiles is also shown in Fig. 4 where the vertical velocity profiles at the midheight of the cavity are presented for Ra* = 5.74 × 10⁴ for different values of surface emissivity. The flow recirculation in the neighborhood of the right plate can be observed in this figure, where the vertical velocities become upward along the right wall. For lower input heat flux values, the formation of counterclockwise cell is observed to occur at higher surface emissivities. The velocities of the rising fluid at the heat source location are reduced by enhancing the radiation heat transfer, resulting in a weaker convection.

The fluid temperature profiles at the midheight of the cavity (i.e., middle of the heat source) and at $X = 1.25$, downstream of the heat source, are shown in Figs. 5 and 6. At the heat source location, the gradient of the temperature profiles is reduced at the left plate, while it increases on the opposing plate as the emissivity is increased. The overall fluid temperature in the core region of the cavity is increased with the presence of radiation. For the case of pure convection or low surface emissivities, no temperature inversion inside the cavity occurs and a thermal boundary layer exists along the left wall. Increasing the surface emissivity causes a stronger temperature inversion within the

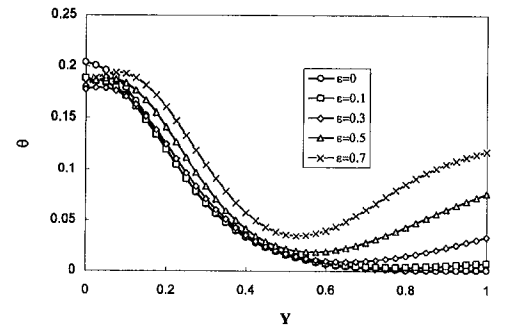

Fig. 6 Fluid temperature distribution at $X = 1.25$, downstream of the heat source for different values of surface emissivity at Ra* = 5.74 × 10⁴

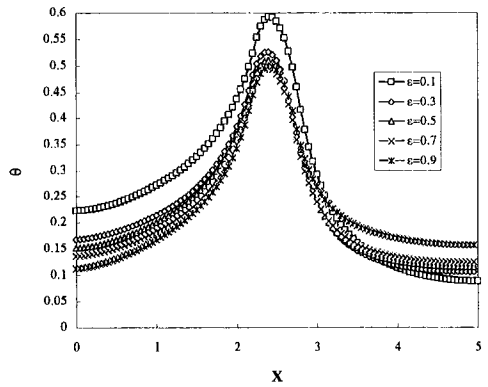

Fig. 7 Temperature distribution along the left wall for different values of surface emissivities at Ra* = 2.296 × 10^4

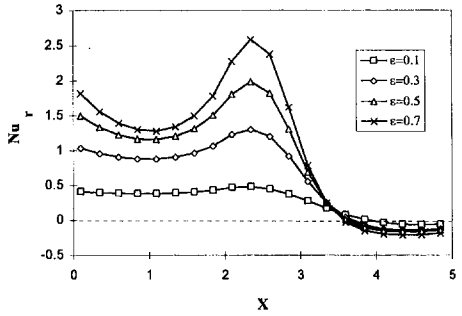

Fig. 9 Variation of local nondimensional radiative heat transfer coefficient along the left wall for Ra* = 5.746 × 10^4

flow, which is responsible for the separation phenomenon discussed earlier.

A continuous increase in the downcoming fluid temperature is also observed on the right-hand side of this figure where the curves shift upward when the surface emissivity is increased. At the downstream location considerable changes in the temperature profiles occur as the emissivity is increased (see Fig. 6). For the present case and conductivity ratio, it is seen that for pure convection, the direction of heat transfer is always from the left vertical wall to the fluid over its entire length. When the radiation is included, the direction of heat transfer is reversed from the rising fluid to the left vertical wall at downstream locations once emissivity is increased beyond a certain value. This may be seen in Fig. 6 where a change in the temperature gradient is observed from a negative to a positive value in the proximity of the left wall for $\epsilon \geq 0.3$. Hence, part of the heat convected away from the heat source by the rising plume is transferred back to the left vertical wall before the hot fluid leaves the cavity.

The temperature distribution along the left wall containing the heat source is presented in Fig. 7 for Ra* = 2.296 × 10^4, and Fig. 8 for Ra* = 5.74 × 10^4, for various surface emissivities. As would be expected, the maximum temperature is generally located in the vicinity of the heat source for all cases. For pure convection, the temperatures are lower at the upstream locations of the heat source since at these locations the surface of the wall is in close contact with the cold flow (see Fig. 3*a*). When radiation is considered and the emissivity of the surface is increased, the temperature increases at the upstream locations, and decreases at downstream points for both Rayleigh numbers. The decrease in temperature of the downstream location is attributed to a higher radiation heat loss to the cold ambient through the opening. As the surface emissivity is increased, the temperature of the fluid near the bottom of the cavity increases, due to a higher convective heat transfer from the right wall. Hence, the bottom of the left wall is no longer in close contact with the cold fluid and the convective heat transfer becomes lower than in the case of pure convection. Therefore, higher temperatures are observed in these locations for the case of conjugate radiation and convection. Near the heat source location, the temperatures are slightly reduced for the case of Ra* = 2.296 × 10^4 when the emissivity is increased. However, the effect of radiation on the temperatures at this location is negligible for higher Rayleigh numbers. At low values of Ra*, the flow is predominantly in the conduction regime and convection heat transfer is not very significant. Hence, inclusion of radiation enhances the total heat transfer around the heat source. For higher Rayleigh numbers, increasing the surface emissivity causes the convective flow to become weaker with the lower flow velocities around the heat source, even though there is an increase in the radiation heat transfer around the heat source. Hence, the increased heat transfer by radiation is compensated by the decrease in convection heat transfer, resulting in a negligible variation in the temperatures around the heat source.

The influence of radiation on the total heat transfer process may be seen in Fig. 9 where the distribution of the local radiative Nusselt number defined by Eq. (19) is plotted over the left wall for different values of the surface emissivity for Ra* = 5.74 × 10^4. The maximum radiation heat transfer is seen to occur around the heat source due to the maximum temperature at this location. The radiation heat transfer coefficient peaks near the heat source location, and this effect is especially pronounced when the surface emissivity is increased. In the downstream regions of the heat source, the local radiative Nusselt numbers are higher than the upstream regions. This is because the downstream regions of the left wall see more of the cold, black environment through the opening. Furthermore, this section of the left vertical wall is in front of the lowest temperature regions

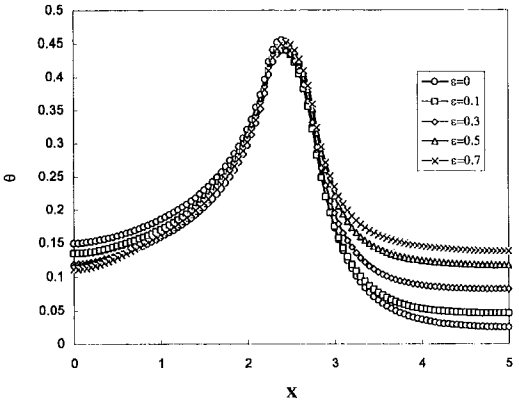

Fig. 8 Temperature distribution along the left wall for different values of surface emissivities at Ra* = 5.746 × 10^4

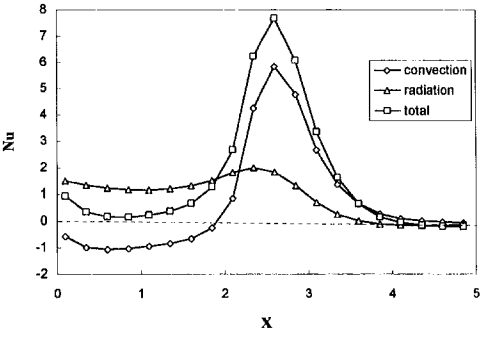

Fig. 10 Variation of local convective, radiative, and total Nusselt numbers along the left wall for Ra* = 5.746 × 10^4 and ϵ = 0.5

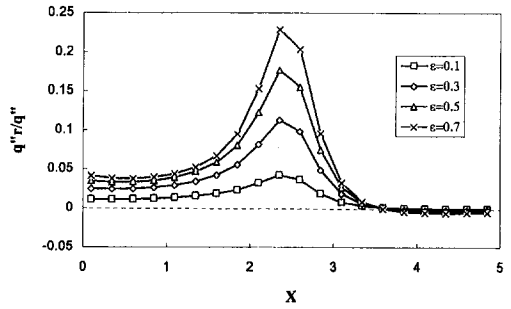

Fig. 11 Variation of relative local radiative heat transfer rate along the left wall at Ra* = 5.746 × 10⁴

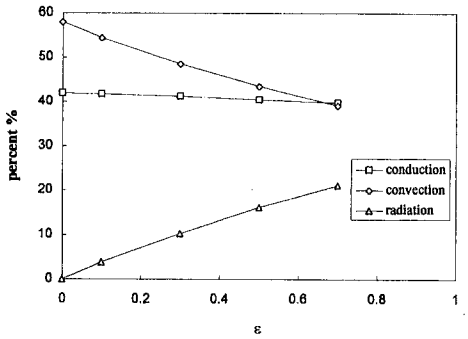

Fig. 13 Contribution of each mode of heat transfer at the heat source location as a function of surface emissivity for Ra* = 5.746 × 10⁴

of the right wall and there is direct radiation heat exchange across the cavity between these locations. In the bottom section of the walls, there is a net radiative heat transfer into the left wall as indicated by the negative values of radiative Nusselt number in these locations. This is due to the possible radiative heat transfer from the horizontal bottom boundary to the far upstream location of the left plate. The temperatures at the bottom boundary of the cavity were observed to be slightly higher than at the base of the left vertical wall.

In order to compare the relative importance and magnitude of each mode of heat transfer from the left wall, both the local radiative and convective nondimensional heat transfer coefficients for Ra* = 5.746×10^4 and $\epsilon = 0.5$ are presented in Fig. 10. The distribution of the overall local heat transfer coefficient, which is in fact the sum of the local radiative and convective Nusselt numbers, is also presented. It is seen that around the heat source area, the convective heat transfer is dominant, while at the downstream location, the radiation heat transfer is the governing mode. At this location, reversed heat transfer from the fluid to the solid wall, indicated by the negative convective Nusselt number, is compensated by radiation heat transfer. The total heat transfer coefficient reveals that most of the input energy to the heat source is dissipated in the vicinity of the heat source either by convection to the fluid or radiation to the other surfaces of the cavity.

In Figure 11 the variation of nondimensional parameter q_r''/q'', which is the local radiation heat flux scaled with the input heat flux, is presented for Ra* = 5.74×10^4, for various surface emissivities. The importance of radiation heat transfer increases with increasing surface emissivity for a fixed input heat flux as expected. However, it is interesting to note that for a fixed surface emissivity, its relative importance decreases when the Rayleigh number or input heat flux increases, as shown in Fig. 12, due to the strengthening of the convection, which can be expected for higher values of Rayleigh number.

In a physical situation, the input energy to the heat source is partly conducted to the left plate from the backface of the heated strip, partly radiated to the other surfaces of the cavity and the rest is transported away by the convective fluid. The relative magnitude of each of these three modes of heat transfer mechanisms depends on various nondimensional parameters such as Ra*, Pr, k_r, w_r, λ, and ϵ. The effects of Ra*, k_r, and λ were discussed for the case of conjugate convection and conduction in our previous investigations (Dehghan et al., 1992; Dehghan and Behnia, 1994a). In Fig. 13, the effect of the surface emissivity on the contribution of the different mechanisms of heat transfer involved in dissipating the energy generated at the heat source is illustrated for a typical case of Ra* = 5.74×10^4. An increase in the emissivity increases the contribution of the radiation while it decreases the convection heat transfer from the heat source. The conduction heat transfer to the substrate is almost unchanged. For the range of Ra* and surface emissivity investigated, it is found that natural convection is still the dominant mode of heat transfer.

In Fig. 14, the local total Nusselt number for combined radiation and convection is presented and compared with the convective Nusselt number for the case of pure convection. For the case of combined radiation and convection heat transfer from the cavity, the total Nusselt number is lower than the case of pure convection at most locations over the plate, although the difference between them is negligible downstream of the heat source. The presence of radiation in conjunction with the convection in the fluid and conduction in the vertical plates slightly reduces the total heat transfer coefficient in this particular geometry, due to the weakening of the dominant convection mechanism. In the studies of Carpenter et al. (1976), Sparrow et al. (1980), and Yamada (1988), enhancement of the total heat transfer rates relative to the pure convection was reported by the introduction of radiation. However, the geometry considered in these studies was an open-ended channel in which the presence of radiation allowed the participation of the opposing adiabatic wall in heat exchange. However, in the present study, the channel is open to the ambient at one boundary and although inclusion of radiation activates the right wall, this increases the

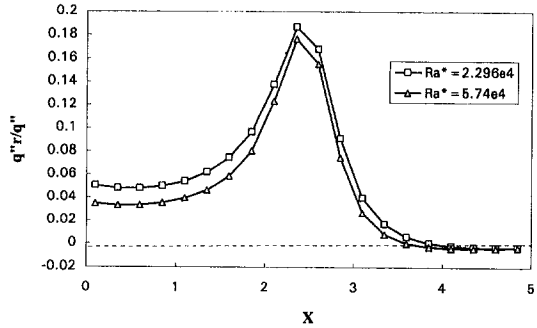

Fig. 12 Relative local radiative heat transfer rate along the left wall for $\epsilon = 0.5$

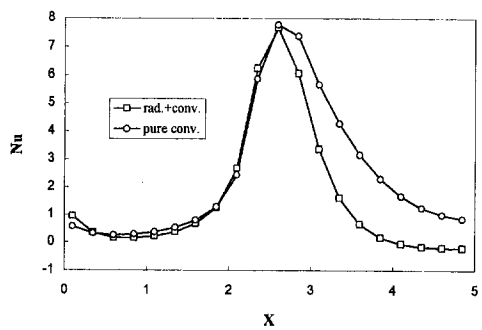

Fig. 14 Distribution of local Nusselt number over the left wall for Ra* = 5.746×10^4 and $\epsilon = 0.5$

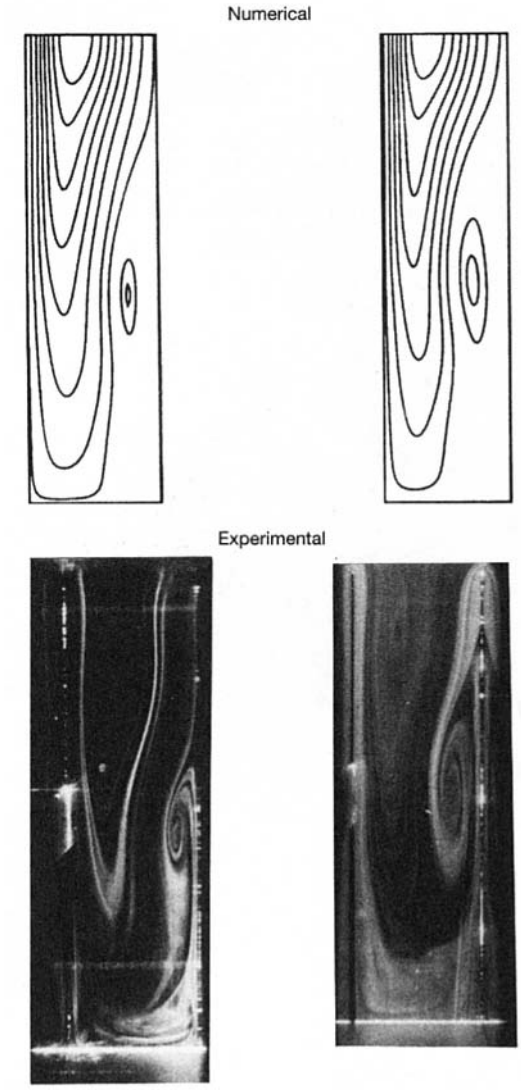

Fig. 15 Comparisons between the predicted and observed flow patterns for cavity of aspect ratio 3.57 with bakelite plate: (*a*) $Ra^* = 2.08 \times 10^5$; (*b*) $Ra^* = 3.0 \times 10^5$

temperature of the downward flow (which would have been near ambient temperature if there was no radiation) before it reaches the left wall and the heat source. This, when combined with the weaker flow for combined radiation and convection, reduces the total heat transfer coefficient.

In Fig. 15 the numerically predicted flow is compared with experimentally observed flows for different values of input heat flux. The experimental flow visualization procedure is described in Dehghan and Behnia (1994b). Favorable agreement is observed between the numerical prediction and the experiment. From these figures and other experimental results, it can be concluded that the detail of the flow pattern can be accurately predicted by numerical computation, when conjugate convection, radiation, and conduction are considered. The prediction of the flow recirculation further endorses the validity of the numerical procedure.

4 Conclusion

The problem of natural convection in a discretely heated open-top vertical cavity has been investigated numerically. Heat conduction in the vertical walls and radiation heat exchange in the cavity were accounted for. The radiation heat exchange was found to have a significant influence on the thermal and flow fields. A recirculation cell was noted in the vicinity of the right vertical wall due to the interaction of the momentum of the downward flow and the buoyancy force generated by this wall. The size and strength of this recirculation zone were increased by increasing the thermal emissivity of the surface. The inclusion of radiation was found to weaken the strength of convection within the cavity. The enhancement of the heat transfer by radiation was compensated by a weaker convective heat transfer, resulting a negligible variation in the maximum temperature of the heat source. It was found that most of the heat generated by the heat source is dissipated in the vicinity of the heat source either by convection or radiation mechanisms. The contribution of the radiation in total heat transfer was found to increase with the surface emissivity and to decrease with Rayleigh number. For the range of Rayleigh number and surface emissivity considered in this study, it was found that natural convection is the major mode of heat transfer from the heated device. For the geometry investigated here, it was determined that inclusion of radiation does not enhance the total heat transfer coefficient in comparison with the case of pure natural convection, due to the weakening of the dominant convection mode. However, it was revealed that the accurate prediction of the flow and thermal fields necessitates the consideration of radiation in the numerical model.

References

Abib, A. H., and Jaluria, Y., 1988, "Numerical Simulation of the Buoyancy-Induced Flow in a Partially Open Enclosure," *Num. Heat Transfer,* Vol. 14, pp. 235–254.

Behnia, M., Reizes, J. A., and de Vahl Davis, G., 1990, "Combined Radiation and Natural Convection in a Rectangular Cavity With a Transparent Wall and Containing a Non-participating Fluid," *Int. J. Num. Methods in Fluids,* Vol. 10, pp. 305–325.

Carpenter, J. R., Briggs, D. G., and Sernas, V., 1976, "Combined Radiation and Developing Laminar Free Convection Between Vertical Flat Plates With Asymmetric Heating," ASME JOURNAL OF HEAT TRANSFER, Vol. 98, pp. 95–100.

Cesini, G., Paroncini, M., and Ricci, R., 1988, "Experimental and Numerical Investigation on Natural Convection in Square Enclosures With a Non-uniformly Heated Vertical Surface," presented at the ICHMT XXth International Symposium, Dubrovnik, Yugoslavia.

Chadwick, M. L., Webb, B. W., and Heaton, H. S., 1991, "Natural Convection From Two-Dimensional Discrete Heat Sources in a Rectangular Enclosure," *Int. J. Heat Mass Transfer,* Vol. 34, pp. 1679–1693.

Chan, Y. L., and Tien, C. L., 1985, "A Numerical Study of Two-Dimensional Laminar Natural Convection in Shallow Open Cavities," *Int. J. Heat Mass Transfer,* Vol. 28, pp. 603–612.

Chu, H. H., Churchill, S. W., and Patterson, C. V. S., 1976, "The Effect of Heater Size, Location, Aspect Ratio and Boundary Conditions on Two-Dimensional, Laminar Natural Convection in Rectangular Channels," ASME JOURNAL OF HEAT TRANSFER, Vol. 98, pp. 194–201.

Dehghan, A. A., Behnia, M., and de Vahl Davis, G., 1992, "Combined Natural Convection–Conduction in an Open-Top Cavity Containing a Discrete Heat Source," *Proc. 5th Int. Symp. on Transport Phenomena,* Beijing, pp. 117–122.

Dehghan, A. A., and Behnia, M., 1994a, "Natural Convection in a Discretely Heated Open Top Cavity," *Proceeding of the 10th Int. Heat Transfer Conference,* Vol. 7, Paper No. NC-9, Brighton, United Kingdom.

Dehghan, A. A., and Behnia, M., 1994b, "Experimental Flow Visualization of Natural Convection in Discretely Heated Open Cavities," to appear in *J. of Flow Visualization and Image Processing.*

Dehghan, A. A., 1994, "Natural Convection in Discretely Heated Open Cavities," PhD Thesis, University of New South Wales, Sydney, Australia.

Gosman, A. D., Lockwood, F. C., and Tatchell, G., 1971, "A Numerical Study of The Heat-Transfer Performance of the Open Thermosyphon," *Int. J. Heat Mass Transfer,* Vol. 14, pp. 1717–1730.

Incropera, F. P., 1987, *Future Research Directions, Cooling Technology for Electronic Equipment,* W. Aung, ed., International Symposium on Cooling Technology for Electronic Equipment, Honolulu, HI, pp. 809–821.

Jaluria, Y., 1985, "Interaction of Natural Convection Wakes Arising From Thermal Sources on a Vertical Surface," ASME JOURNAL OF HEAT TRANSFER, Vol. 107, pp. 883–892.

Jones, G. F., and Cai, J., 1993, "Analysis of a Transient Asymmetrically Heated/Cooled Open Thermosyphon," ASME JOURNAL OF HEAT TRANSFER, Vol. 115, pp. 621–630.

Lage, J. L., Lim, J. S., and Bejan, A., 1992, "Natural Convection With Radiation in a Cavity With Open Top End," ASME JOURNAL OF HEAT TRANSFER, Vol. 114, pp. 479–486.

Larson, D. W., and Viskanta, R., 1976, "Transient Combined Laminar Free Convection and Radiation in a Rectangular Enclosure," *J. Fluid Mech.,* Vol. 78, Part 1, pp. 65–85.

Mallinson, G. D., and de Vahl Davis, G., 1973, "The Method of False Transient for the Solution of Coupled Elliptic Equations," *J. Computational Physics,* Vol. 12, pp. 435–461.

Manca, O., and Naso, V., 1990, "Experimental Analysis of Natural Convection and Thermal Radiation in Vertical Channels, Single and Multiphase Convective Heat Transfer," ASME HTD-145, pp. 13–21.

Refai Ahmed, G., and Yovanovich, M. M., 1991, "Influence of Discrete Heat Source Location on Natural Convection Heat Transfer in a Vertical Square Enclosure," ASME *Journal of Electronic Packaging,* Vol. 113, pp. 268–274.

Samaraskii, A. A., and Andreyev, V. B., 1963, "On a High Accuracy Difference Scheme for Elliptic Equations With Several Space Variables," *USSR Comput. Math. & Math. Phys.,* Vol. 3, pp. 1373–1382.

Sparrow, E. M., Shah, S., and Prakash, C., 1980, "Natural Convection in a Vertical Channel: I. Interacting Convection and Radiation. II. The Vertical Plate With and Without Shrouding," *Numerical Heat Transfer,* Vol. 3, pp. 297–314.

Webb, B. W., and Hill, D. P., 1989, "High Rayleigh Number Laminar Natural Convection in an Asymmetrically Heated Vertical Channel," ASME JOURNAL OF HEAT TRANSFER, Vol. 111, pp. 649–656.

Woods, L. C., 1954, "A Note on the Numerical Solution of Fourth Order Differential Equations," *Aero. Quart.,* Vol. 5, pp. 176–184.

Yamada, Y., 1988, "Combined Radiation and Free Convection Heat Transfer in a Vertical Channel With Arbitrary Wall Emissivities," *Int. J. Heat Transfer,* Vol. 31, No. 2, pp. 429–440.

Evidence of a Convective Instability Allowing Warm Water to Freeze in Less Time Than Cold Water

P. K. Maciejewski
Mechanical Engineering Department,
University of Pittsburgh,
Pittsburgh, PA 15261

This experimental study explores the possibility that warm water may freeze in less time than cold water due to natural convection alone, i.e., in the absence of significant cooling by evaporation. This possibility is rooted in the following two hypotheses: (1) The Rayleigh number associated with a sample of warm water may exceed a critical value above which the convective motions within the water sample may become turbulent and enhance the rate of convective cooling, and (2) the inversion of the flow field that is expected to occur in the vicinity of maximum density, i.e., at 4°C, will occur at different points in the cooling process for identical samples of water at different levels of initial temperature and result in an enhanced rate of convective cooling after the flow field inversion for those cases at higher levels of initial temperature that enter the flow field inversion with higher kinetic energy. The results of this study establish that, under certain circumstances, a sample of water that is initially warm will freeze in less time than an identical sample of water that is initially cold due to natural convection alone.

Introduction

Since the work of Kell (1969), it has generally been accepted that, in the absence of cooling by evaporation, a sample of warm water will take a longer time to freeze than an identical sample of cold water. Indeed, there is not a single study that claims to have established that, under any circumstances, warm water will freeze in less time than cold water in the absence of significant cooling by evaporation. The primary aim of the present study will be to answer one simple question: Are there circumstances in which warm water will freeze in less time than cold water due to natural convection alone, i.e., in the absence of significant cooling by evaporation?

Arguments against the possibility that warm water may freeze in less time than cold water due to natural convection alone appear to rest on a single argument—an argument of similarity. In its purest form, this argument of similarity might be stated as follows: The solution for the temperature field within the water as a function of time is scaled by the initial temperature of the water, but its form is not determined by the initial temperature of the water. If the problem is posed and solved in terms of an appropriate set of nondimensional variables, then it would be found that, in these nondimensional terms, every sample of water (for a given geometry) must pass through the same series of states as it first cools and then solidifies.

Arguments in favor of the possibility that warm water may freeze in less time than cold water can be developed on the grounds that the problem is not similar for different levels of initial temperature. For example, the density of water varies with temperature on the domain 0°C to 100°C. If one defines a nondimensional temperature variable, $\theta = (T - T_o)/(T_i - T_o)$, and a nondimensional density variable, $\rho^* = \rho/\rho_i$, then $\rho^*(\theta)$ will depend on the initial temperature, T_i. Corresponding arguments could be made for other temperature-dependent fluid properties that influence the physics of the problem.

The density of water has a maximum value in the vicinity of 4°C. This peculiar feature of water opens the possibility that some unusual flow physics may occur within the flow field as a sample of water within an enclosure passes through a series of states in the vicinity of 4°C during a cooling process. For example, as a sample of water in an enclosure passes through the region of 4°C, one would expect a complete inversion of the sample identified by a rush of warmer water from the top of the enclosure to the bottom of the enclosure, and a corresponding rush of cooler water from bottom to top. Since the nondimensional temperature of the water corresponding to the physical temperature of 4°C depends on the initial temperature of the water, one would expect the effect of this inversion of the flow field near 4°C to vary with T_i.

One might expect that the physics of the buoyancy-induced flow field will depend on some parameter, e.g., Rayleigh number, whose value depends on the initial temperature of the water. For example, the Rayleigh number for water in a vertical cylindrical container varies nearly three orders of magnitude on the domain 10°C to 100°C. It is possible that somewhere on this domain there exists some critical value for Rayleigh number, $\mathrm{Ra}_c = \mathrm{Ra}(T_{i,c})$, above which the buoyancy-induced fluid motion becomes turbulent. If a critical value for Rayleigh number does fall on this domain, then one might expect a dramatic increase in the convective heat transfer rate for cases with initial temperatures above $T_{i,c}$ as compared with the convective heat transfer rate for cases with initial temperatures below $T_{i,c}$. If this does occur, then water that is initially warmer, e.g., $T_i > T_{i,c}$, may freeze in less time than water that is initially cooler, e.g., $T_i < T_{i,c}$, due to convective heat transfer alone.

On the grounds that there is no similarity for the problem of freezing water (i.e., that the form of the solution for the temperature field depends on the initial temperature), it is at least possible, if not likely, that under certain circumstances water that is initially warmer will freeze in less time than water that is initially cooler.

There are a number of studies which, although they do not address the issue of whether warm water may freeze in less time than cold water, touch upon aspects of natural convection

Contributed by the Heat Transfer Division for publication in the JOURNAL OF HEAT TRANSFER. Manuscript received by the Heat Transfer Division May 1995; revision received October 1995. Keywords: Flow Instability, Natural Convection, Phase-Change Phenomena. Associate Technical Editor: A. Faghri.

in water and the freezing of water that are relevant to the present study. Schechter and Isbin (1958), Tien (1968), and Forbes and Cooper (1975) have considered the stability and the flow patterns in the region of the maximum water density, i.e., in the region of 4°C. Boger and Westwater (1967), Heitz and Westwater (1971), and Tankin and Farhadieh (1971), have considered transitions in convective domain more generally, either the transition from a conduction-dominated domain to a convection-dominated domain, or the transition from a laminar convective domain to a turbulent convective domain. Chen et al. (1992) studied the effects of natural convection on ice formation inside an isothermal, horizontal cylinder for levels of initial water temperature between 1.0°C and 21.7°C. These authors conclude that the "density inversion effect" in the neighborhood of 4°C plays a significant role in the solidification process, including an influence on the shape of the ice–water interface. Although these authors do report that there is a minimum in mean Nusselt number for initial water temperature near 6°C, they do not address the question as to whether warm water will freeze in less time than cold water.

The physical phenomena involved in the present investigation of the freezing of water are complicated by both natural convection and solidification. Gebhart et al. (1988) present a comprehensive treatment of buoyancy-induced flows and transport, including topics specific to water. An introduction to the fundamentals of solidification is provided by Lock (1994).

The time required for water to freeze is relevant to the design of many devices of interest to engineers, including the design of commercial and industrial freezers, ice makers, and water storage tanks for use in cold climates.

Design of the Experiment

The design of the experimental facility and the design of the experiment are tailored to determine whether, under some circumstances, warm water will freeze in less time than cold water due to natural convection alone.

Test Facility. A schematic of the test facility is provided in Fig. 1. A thermally conductive cylindrical container holds a fixed sample of distilled, deaerated water that can be heated to any desired initial temperature on the domain 0°C to 100°C. During test runs, the test cell is sealed to prevent loss of mass of the water sample due to evaporation. For every value of initial temperature, the cylinder containing the sample is submerged, at a time designated $t = 0$, in a cold bath maintained at a temperature T_b set on the domain $-15°C < T_b < -5°C$. Prior to being submerged in the cold bath, the cylinder containing the water sample is handled such that there is minimal initial motion in the water. As the sample of water cools and eventually freezes, the temperature at various locations within the water is monitored. At any given time, points in the water at a temperature above 0°C are presumed to be liquid, while points in the water below 0°C are taken to be solid. The entire sample of water is taken to be completely frozen when every point within the water falls below 0°C. When this occurs, the total time for the sample to freeze is recorded.

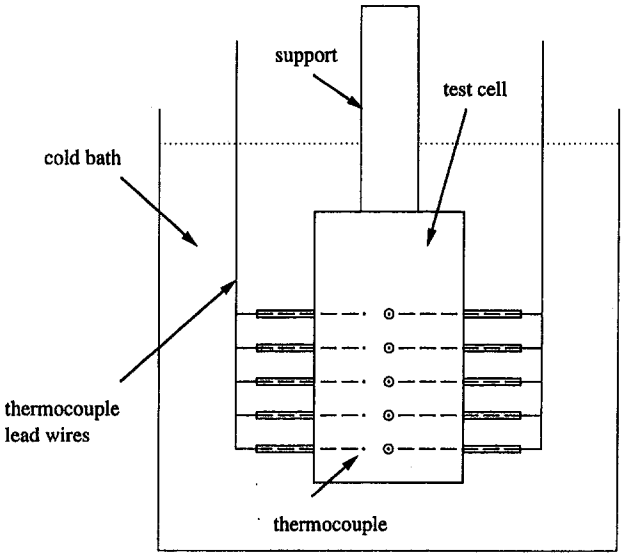

Fig. 1 Schematic of the test facility

The copper test cell has a height $H = 10.16$ cm and an inner radius $R = 2.475$ cm. (The dimensions of the test cell were selected so that the domain of the planned experiment would be expected to contain a critical value of Rayleigh number.) The core of the cylindrical container is instrumented with 15 type-T thermocouples with insulated leads. The thermocouples are located at the center of the cylinder, at one third the radius of the cylinder, and at two thirds the radius of the cylinder for each of five elevations within the cylinder, $y/H = \frac{1}{8}, \frac{1}{4}, \frac{3}{8}, \frac{1}{2}$, and $\frac{5}{8}$. In addition to the 15 thermocouples within the cylindrical container, there are four other type-T thermocouples attached to the outside of the container to detect the moment at which

Nomenclature

A = aspect ratio of the water sample in the test cell = h/R
A_s = test cell wetted surface area
C_p = specific heat
g = gravitational acceleration
Gr = Grashof number based on test cell radius = $g\beta_i(T_i - T_o)R^3/\nu_i^2$
H = height of cylindrical test cell
h = height of water level within the test cell
$\mathbf{h}$ = convective heat transfer coefficient = $(Q/A_s)/T_{\text{avg}}$
h_{sf} = enthalpy of melting
k = thermal conductivity
Nu = Nusselt number based on test cell radius = hR/k
Pr = Prandtl number = $\rho_i\nu_i C_{pi}/k_i$
Q = heat transfer rate
r = radial coordinate
R = inner radius of the cylindrical test cell
Ra = Rayleigh number based on test cell radius = Gr Pr
t = time
t_f = time to freeze
T = temperature
U = internal energy
V = volume
X = nondimensional time to freeze = $t_f[Cp_i(T_o - T_b)/hR]^{1/2}$
X_1 = nondimensional time to reach 4°C; $X_1 = X(t_4/t_f)$
X_2 = nondimensional time between 4°C and completely frozen = $X(t_f - t_4)/t_f$
y = coordinate parallel to the axis of the test cell
β = volumetric thermal expansion coefficient
ν = kinematic viscosity
Π_Q = nondimensional heat transfer rate below 4°C; $\Pi_Q = Q\rho^2C_p^3R/k^3$
θ = nondimensional temperature variable = $(T - T_o)/(T_i - T_o)$
Θ_b = nondimensional cold bath temperature = $(T_o - T_b)\rho_i^2C_{pi}^3R^2/k_i^2$
ρ = density
ρ^* = nondimensional density = ρ/ρ_i

Subscripts

avg = average
b = evaluated in the cold bath
c = critical value
i = initial, evaluated at time $t = 0$
0 = evaluated at 0°C
4 = evaluated at 4°C

the container is lowered into the cold bath. All thermocouple voltages (relative to an external reference ice bath) are measured using an HP 44701A High-Resolution Voltmeter that is housed in an HP 3852A Data Acquisition and Control System that is accessed by means of a personal computer.

The cold bath consisted of a mixture of 80 percent water and 20 percent ethylene glycol (by volume). This mixture is nearly all solid at −15°C and all liquid at −5°C. For all of the test cases, the water/ethylene glycol mixture of the cold bath existed in two phases. The solid phase of this mixture, which appeared as a "slush," was observed to be in direct contact with the container holding the test sample. For the coldest bath temperatures, this solid-phase "slush" filled the entire cold bath volume. For the warmer cold bath temperatures, this "slush" would float on the top of the liquid phase, surrounding the container holding the sample. The presence of the solid-phase "slush" serves to inhibit convective currents in the cold bath, so that the characteristics of the heat transfer process from the container to the cold bath are similar in all cases. The total volume of the cold bath was approximately 16 liters, or 200 times the volume of the cylindrical container.

The primary variables of interest are the total time required for the sample of water to freeze, t_f, the time required for some point within the sample of water to reach 4°C, t_4, and the difference between these two times, $t_f - t_4$. Temperatures within the water sample are determined and stored every 2 seconds. The total time required for the sample of water to freeze, t_f, corresponds to the time at which all 15 thermocouples submerged within the water sample first indicate a temperature of less than 0°C. The time required for some point within the sample of water to reach 4°C, t_4, corresponds to the time at which one of the 15 thermocouples submerged within the water sample first indicates a temperature of less than 4°C. For each run in this experiment, time $t = 0$ corresponds to the time at which one of the thermocouples attached to the outside bottom of the cylinder indicates a temperature below 0°C, indicating that the test cell has been inserted into the cold bath.

There are three independent factors that are varied in this experiment. The initial temperature of the water, T_i, is set to 16 different levels, from 5°C to 80°C in increments of 5°C. The temperature of the cold bath, T_b, is set to one of two nominal levels, either −7°C or −13.5°C. The height of the water level within the cylinder relative to the radius, h/R, is set to one of two levels, either 3.08 or 3.86. For $T_b = -7$°C, T_i is set to 10 different levels, $T_i = 10$, 15, 20, 25, 30, 35, 40, 50, 60, and 70°C, for each level of h/R (for a total of 20 operating points at $T_b = -7$°C). For $T_b = -13.5$°C, T_i is set to 16 different levels, from 5°C to 80°C in increments of 5°C, for one level of h/R (for a total of 16 operating points at $T_b = -13.5$°C). Every test condition is replicated three times. The total number of runs in the design of the experiment is 108.

Nondimensional Variables. For the sake of the analysis of the present data, the following four nondimensional variables, one to represent each of the dimensional variables expected to vary during the study, were constructed:

$$\Pi_1 \equiv t_f[C_{pi}(T_o - T_b)/hR]^{1/2}$$

$$\Pi_2 \equiv h/R$$

$$\Pi_3 \equiv (T_o - T_b)\rho_i^2 C_{pi}^3 R^2/k_i^2$$

$$\Pi_4 \equiv g\beta_i(T_i - T_o)\nu_i\rho_i^3 C_{pi}^3 R^3/k_i^3$$

The first of these variables, Π_1, which will be given the interpretation of the nondimensional time to freeze, will be designated by the symbol X. The second of these variables, Π_2, which is simply the aspect ratio of the cylindrical volume of the water sample, will be designated by the symbol A. The third of these variables, Π_3, which will be given the interpretation of the nondimensional cold bath temperature, will be designated by the symbol Θ_b. The last of these variables, Π_4, which can be recognized as the product of the Grashof number based on the radius of the cylinder and the cube of the Prandtl number, will be designated by either $GrPr^3$ or $RaPr^2$.

Table 1 presents the design of the experiment expressed in terms of the nominal values assigned to the nondimensional independent variables A, Θ_b, and $GrPr^3$ for each test run. Once again, each test condition is replicated three times for a total of 108 test cases. Table 1 also provides the shape of the plotting symbol employed in Figs. 2–6, identifying the result of each test run with its nominal values for A and Θ_b.

Assessment of Experimental Uncertainty. There are only three types of measurement associated with the present experiments that contribute significantly to the uncertainty in the overall results. These are thermocouple (temperature) measurements, time measurements, and water-sample mass measurements. For fluid temperatures above 0°C, thermocouple voltage is interpreted through a polynomial model to the NIST *Thermocouple Reference Tables* (1979), and the uncertainty in temperature measurement is estimated at 0.37°C at 95 percent confidence. At 0°C, thermocouple voltage is interpreted directly through the NIST *Thermocouple Reference Tables,* and the uncertainty in temperature measurement at 0°C is estimated at 0.20°C at 95 percent confidence. The uncertainty in time measurement differs for each test run, depending on the uncertainty in locating the termination of each particular test, and is estimated to be between 12 s and 120 s at 95 percent confidence. The uncertainty in the mass of the water sample is estimated at 0.005 kg at 95 percent confidence.

The uncertainties associated with each of the quantities derived from these directly measured variables, including the uncertainties in the nondimensional variables employed to interpret the results of the experiment, are calculated using the standard methods described in ANSI/ASME PTC 19.1 (1985). Thermodynamic properties are derived from data presented in the *CRC Handbook of Chemistry and Physics.* Uncertainty estimates are represented in Figs. 2–6 by the uncertainty bounds associated with each of the individual data points.

Time to Freeze

A preliminary analysis of the results from this study revealed that the data for the nondimensional time to freeze, X, fall into two distinct categories. For the data falling within the first of these two categories, the nondimensional time to freeze, controlling for each of the three factors investigated in this study, is approximately twice the nondimensional time to freeze for the data falling within the second of these two categories.

In order to investigate the possibility that the difference in the behavior of the data between these two categories is related to the peculiarity of the density as a function of temperature in the neighborhood of 4°C, the total time to freeze for each test run was partitioned into two parts: the nondimensional time for the sample to reach 4°C, $X_1 = X(t_4/t_f)$, and the nondimensional time for the sample to freeze once it has reached 4°C, $X_2 = X(t_f - t_4)/t_f$. The results in terms of these two variables were then modeled in terms of the three factors under investigation in the present study.

Results for Total Time to Freeze. The results for the total time for a sample of water to freeze are presented in Fig. 2. The data fall in two distinct clusters, and the data in each cluster

Table 1 Experimental design

symbol	$\Theta_b \times 10^{-15}$	A	$GrPr^3 \times 10^{-8}$														
◇	1.53	3.08	0.04	0.58	1.29	2.01	2.69	3.31	3.85	4.32	4.73	5.08	5.39	5.66	5.88	6.09	6.26	6.42
□	0.84	3.08		0.58	1.29	2.01	2.69	3.31	3.85	4.32		5.08		5.66		6.09		
△	0.84	3.86		0.58	1.29	2.01	2.69	3.31	3.85	4.32		5.08		5.66		6.09		

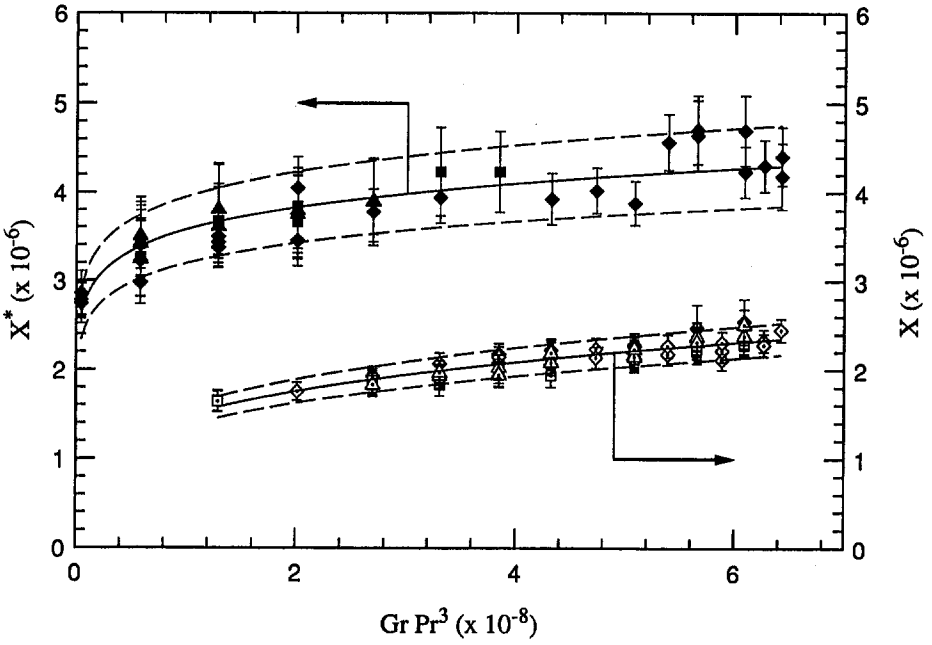

Fig. 2 Nondimensional time to freeze as a function of initial $GrPr^3$

have been scaled in slightly different terms. For the data in the cluster representing a shorter nondimensional time to freeze, the ordinate in Fig. 2 is simply the nondimensional time to freeze, X. The empirical model representing this cluster of data in Fig. 2 is given by the following correlation:

$$X = 1.47 \times 10^4 (GrPr^3)^{0.25}$$

The pair of dashed lines about this correlation in Fig. 2 represent a 95 percent confidence interval for the data falling within this cluster. For the data in the cluster representing a longer nondimensional time to freeze, the ordinate in Fig. 2 is given by the variable $X^* = X[A\Theta_b/(A\Theta_b)_{mean}]^{-0.25}$, where $(A\Theta_b)_{mean} = 4.15 \times 10^{15}$ is the mean value of the product of the aspect ratio and the nondimensional temperature of the cold bath for the data falling within this cluster. The empirical model representing this cluster of data in Fig. 2 is given by the following correlation:

$$X^* = 5.66 \times 10^5 (GrPr^3)^{0.1}$$

The pair of dashed lines about this correlation in Fig. 2 represent a 95 percent confidence interval for the data falling within this second cluster. The nondimensional time to freeze for the data within this second cluster depends on the product of the aspect ratio and the nondimensional temperature of the cold bath. The variable X^* has been constructed to allow a direct comparison between X for the first data cluster and X^* for the second data cluster. (The value of X^* in Fig. 2 may be interpreted as the value of X in the second cluster of data controlling for $A\Theta_b$.)

The data, as presented in Fig. 2, confirm that the data from this experiment fall into two distinct clusters. Within the first cluster of data, the cluster representing the shorter nondimensional time to freeze, X depends only on the variable $GrPr^3$. All of the data within this first cluster fall on the domain $1.29 \times 10^8 < GrPr^3 < 6.42 \times 10^8$. In terms of Rayleigh number, all of the data within this first cluster fall above $Ra \approx 2 \times 10^6$. Within the second cluster of data, X depends on both the variable $GrPr^3$ and the product of the variables A and Θ_b. The data within this second cluster fall on the entire domain of $GrPr^3$ for the present study. On the domain of $GrPr^3$ for which the two clusters overlap, the nondimensional time to freeze for the data within the second cluster is approximately twice the nondimensional time to freeze for the data within the first cluster.

Table 2 presents the operating conditions (expressed both in terms of the dimensional variables T_i, T_b and h, and in terms of the nondimensional variables $GrPr^3$, Θ_b, and A) and the results for total time to freeze (expressed both in terms of the dimensional variable t_f and the nondimensional variable X) for selected test cases. The number in the first column of Table 2 represents the order in which these test cases where executed, relative to the entire test plan of 108 test cases. The cases presented in Table 2 for T_i = 30°C and T_i = 60°C may be divided into two clusters, one cluster (given by runs 6, 28, and 34) for which the test cases at T_i = 30°C and T_i = 60°C take a shorter time to freeze than the test cases presented in Table 2 for T_i = 10°C and another cluster (given by runs 17, 39, and 44) for which the test cases at T_i = 30°C and T_i = 60°C take a longer time to freeze than the test cases presented in Table 2 for T_i = 10°C.

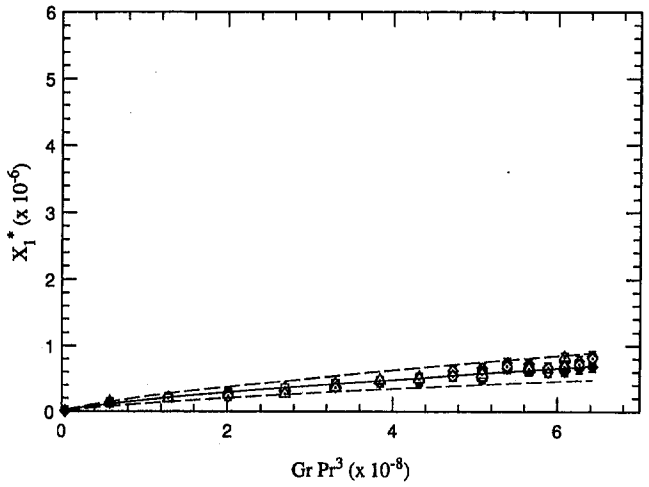

Fig. 3 Nondimensional time to reach 4°C as a function of initial $GrPr^3$

Results for Time to Reach 4°C. Figure 3 presents the nondimensional time for the sample to reach 4°C, X_1, for all of the test runs in the present study. The ordinate in Fig. 3 is given

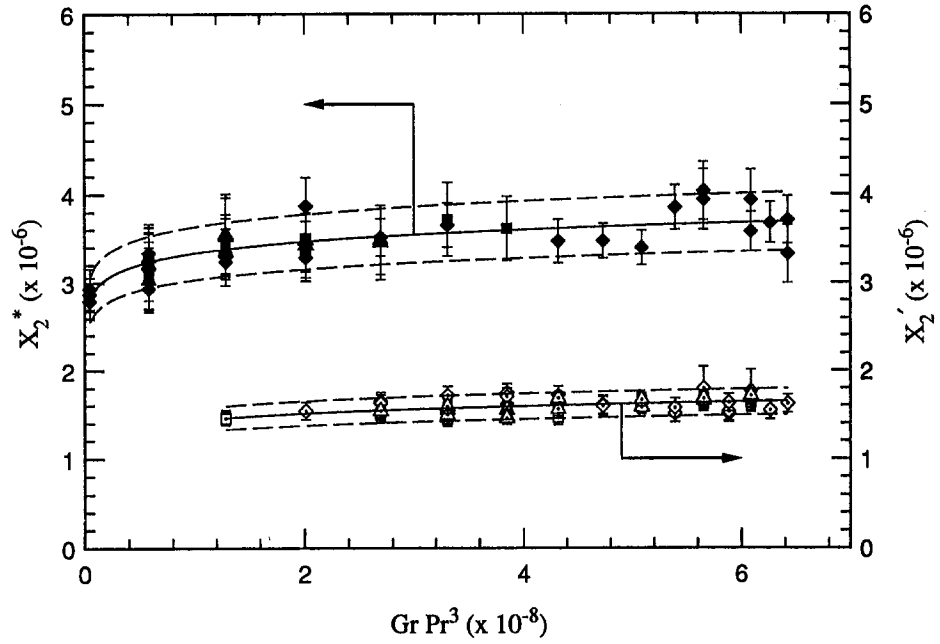

Fig. 4 Nondimensional time between 4°C and completely frozen as a function of initial $GrPr^3$

by the variable $X_1^* = X_1(A/A_{mean})^{0.8}$, where $A_{mean} = 3.295$ is the mean value of aspect ratio for all of the data within this study. The empirical model representing the data in Fig. 3 is given by the following correlation:

$$X_1^* = 0.171(GrPr^3)^{0.75}$$

The pair of dashed lines about this correlation in Fig. 3 represent a 95 percent confidence interval for the data within this study. Note that all of the data for X_1 for this study can be represented by a single correlation. The results from this study given in terms of X_1 are not divided into two distinct clusters as were the results from this study given in terms of X.

Results for $t_f - t_4$. Figure 4 presents the nondimensional time for the sample to freeze once it has reached 4°C, X_2, for all of the test runs in the present study. Once again, the data fall in two distinct clusters, and the data in each cluster have been scaled in slightly different terms. For the data in the cluster representing a shorter nondimensional time to freeze, the ordinate in Fig. 4 is given by the variable $X_2' = X_2(A/A_{mean})^{-0.25}$, where $A_{mean} = 3.310$ is the mean value of the aspect ratio for

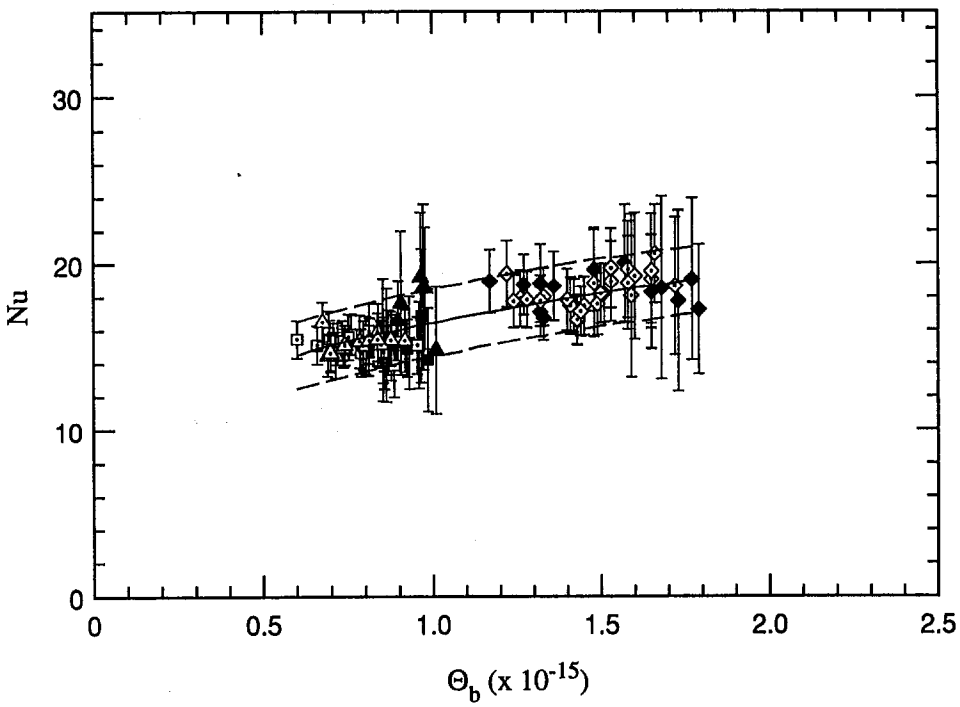

Fig. 5 Nusselt number as a function of nondimensional cold bath temperature for $\frac{1}{3} < t/t_4 < \frac{2}{3}$

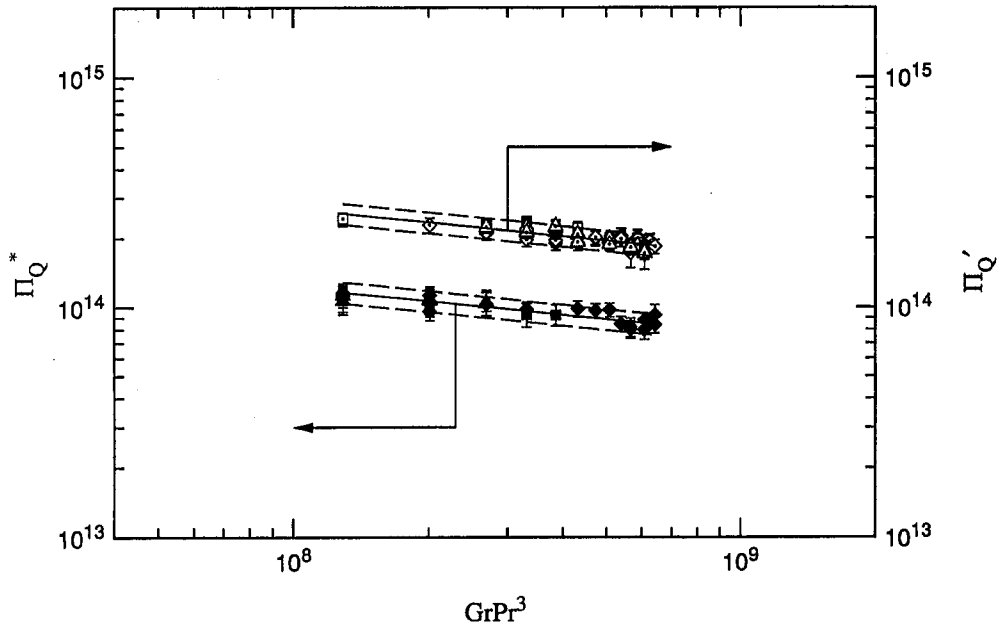

Fig. 6 Nondimensional heat transfer rate below 4°C as a function of initial $GrPr^3$

the data falling within this cluster. The empirical model representing this cluster of data in Fig. 4 is given by the following correlation:

$$X_2' = 3.60 \times 10^5 (GrPr^3)^{0.075}$$

The pair of dashed lines about this correlation in Fig. 4 represent a 95 percent confidence interval for the data falling within this cluster. The nondimensional time to freeze for the data within this first cluster depends on the aspect ratio. For the data in the cluster representing a longer nondimensional time to freeze, the ordinate in Fig. 4 is given by the variable $X_2^* = X_2(A/A_{mean})^{-0.33}[\Theta_b/(\Theta_b)_{mean}]^{-0.25}$, where $A_{mean} = 3.274$ is the mean value of the aspect ratio and $(\Theta_b)_{mean} = 1.29 \times 10^{15}$ is the mean value of the nondimensional temperature of the cold bath for the data falling within this cluster. The empirical model representing this second cluster of data in Fig. 4 is given by the following correlation:

$$X_2^* = 1.21 \times 10^6 (GrPr^3)^{0.055}$$

The pair of dashed lines about this correlation in Fig. 4 represent a 95 percent confidence interval for the data falling within this second cluster. The nondimensional time to freeze for the data within this second cluster depends on both the aspect ratio and the nondimensional temperature of the cold bath. The variables X_2' and X_2^* have been constructed to allow a direct comparison between X_2 for the first data cluster and X_2 for the second data cluster. (The value of X_2' in Fig. 4 may be interpreted as the value of X_2 in the first cluster of data controlling for A, and the value X_2^* in Fig. 4 may be interpreted as the value of X_2 in the second cluster of data controlling for A and Θ_b.)

Estimates of Heat Transfer Rate

The time required to freeze a sample of water falls in two distinct clusters, and the difference in the behavior of the data between these two clusters can be attributed to some phenomenon that occurs only after the water sample has reached 4°C. This finding suggests that the convective heat transfer rate from the water sample prior to time $t/t_4 = 1$ may be correlated by means of a single empirical relation, and that the heat transfer rate from the water sample after time $t/t_4 = 1$ may be correlated by means of two distinct empirical relations. The aim of the present section is to establish a single correlation for the convective heat transfer rate for a time prior to $t/t_4 = 1$, and to establish two distinct correlations for the heat transfer rate after $t/t_4 = 1$.

The temperature data gathered in the present study permit one to estimate the temperature of the water sample within the test cell as a function of position and time, $T(h, r, t)$, which in turn permits one to estimate the internal energy of the water sample as a function of time, $U(t)$. In all cases, the heat transfer rate, Q, can be estimated by means of an energy balance on the sample of water, either on an instantaneous basis by means of $Q = -dU/dt$ or on a time interval basis by means of $Q = -\Delta U/\Delta t$.

Estimating the Convective Heat Transfer Rate Above 4°C. At times prior to $t/t_4 = 1$, the internal energy of the water sample can be estimated by means of $U = \rho V C_p T_{avg}$, where T_{avg} is an estimate of the average water temperature. Assuming that the water density and specific heat are constant for the purpose of evaluating U, an empirically based estimate for $T_{avg}(t)$ can be used to estimate the convective heat transfer coefficient, $\mathbf{h} = Q/A_s T_{avg}$ (A_s is the wetted surface area of the cylindrical container), provided that $T_{avg}(t)$ decays exponentially.

Table 2 Operating conditions and results for selected test cases

run	T_i	T_b	h	t_f	$GrPr^3$	Θ_b	A	X
	°C	°C	cm	sec	x 10^{-8}	x 10^{-15}		x 10^{-6}
2	10	-13.8	7.62	579	0.58	1.85	3.08	3.22
13	10	-12.8	7.62	674	0.58	1.71	3.08	3.60
24	10	-12.9	7.62	639	0.58	1.72	3.08	3.42
6	30	-12.6	7.62	356	3.31	1.48	3.08	1.89
17	30	-13.4	7.62	751	3.31	1.57	3.08	4.10
28	30	-14.0	7.62	370	3.31	1.65	3.08	2.07
34	60	-14.2	7.62	439	5.66	1.45	3.08	2.48
39	60	-13.9	7.62	844	5.66	1.42	3.08	4.70
44	60	-14.8	7.62	842	5.66	1.51	3.08	4.84

For each test run, T_{avg} was estimated at each time step prior to $t/t_4 = 1$, and an empirical model for $T_{avg}(t/t_4)$ of exponential form was fit on the domain $1/3 < t/t_4 < 2/3$ by means of a least-squares linear regression procedure. (These models were fit on the domain $1/3 < t/t_4 < 2/3$ to avoid the effects associated with the initiation of each test and to avoid the effects associated with the behavior of the gross fluid motions near 4°C.) In each case, the fitted model was compared to the data to ensure that the exponential form of the fitted model is appropriate, which ensures that T_{avg} decays exponentially with t/t_4 on the specified domain, which in turn ensures that the convective heat transfer coefficient may be taken to be constant on the specified domain. The heat transfer coefficient, **h**, was estimated by means of the time constant associated the exponential decay of T_{avg}.

Figure 5 presents the results for Nusselt number, $\mathrm{Nu} = \mathbf{h}R/k$, for 91 of the 108 test cases run for the present study, including estimates for experimental uncertainty. (The data for T_{avg} versus t/t_4 for all three cases corresponding to $T_i = 5$°C and all nine cases corresponding to $T_i = 10$°C did not decay in a strictly exponential fashion on the domain $1/3 < t/t_4 < 2/3$ as required by the method for estimating **h** described above. The data from five other cases also did not meet this criterion, apparently due to "noise" in some of the temperature data on this domain.) The solid line in Fig. 5 represents the following correlation:

$$\mathrm{Nu} = 0.00293\Theta_b^{1/4}$$

The pair of dashed lines about this correlation in Fig. 5 represent a 95 percent confidence interval for estimates of Nu. The Nusselt number on this domain was found to be independent of A and GrPr^3. The primary conclusion to be drawn from Fig. 5 is that the convective heat transfer rate within the water sample prior to time $t/t_4 = 1$ may be correlated by means of a single empirical relation for the test cases within the present study without regard to the ultimate time required for the entire sample of water to freeze in each case. This is consistent with the finding that the nondimensional time required for the water sample to reach 4°C is uniquely determined by A and GrPr^3.

Estimating the Heat Transfer Rate Below 4°C. For the period of time beginning when the water sample reaches 4°C, $t = t_4$, and ending when the water sample is completely frozen, $t = t_f$, the change in the internal energy of the water sample, ΔU, can be estimated by means of $\Delta U = -\rho V[C_p T_{avg}(t_4) + h_{sf}]$, where h_{sf} is the enthalpy of melting. [Note that this estimate of ΔU assumes that $T_{avg}(t_f) = 0$°C. However, this estimate of ΔU is dominated by h_{sf}, so that if, for example, $T_{avg}(t_f) = -1$°C, then the estimate of ΔU as given would differ from a more precise estimate of ΔU, one accounting for the change in internal energy of the sample below 0°C, by approximately 1 percent.] Estimates of the heat transfer rate below 4°C can be expressed in terms of the nondimensional variable $\Pi_Q \equiv Q\rho^2 C_p^3 R/k^3$.

Figure 6 presents the nondimensional heat transfer rate below 4°C, Π_Q, for 96 of the 108 test cases for the present study, including estimates for experimental uncertainty. (All three cases corresponding to $T_i = 5$°C and all nine cases corresponding to $T_i = 10$°C were not included.) As anticipated, the data fall in two distinct clusters. Note that the data in each cluster have been scaled in slightly different terms. For the data within the cluster corresponding to a lower heat transfer rate (and a longer time to freeze), the ordinate in Fig. 6 is given by the variable $\Pi_Q^* = \Pi_Q \Theta_b^{-1/4}$. The empirical model representing this cluster of data in Fig. 6 is given by the following correlation:

$$\Pi_Q^* = 4.87 \times 10^{15}(\mathrm{GrPr}^3)^{-1/5}$$

The pair of dashed lines about this correlation in Fig. 6 represent a 95 percent confidence interval for the data falling within this cluster. The nondimensional heat transfer rate, Π_Q, for the data within this first cluster depends on both Θ_b and GrPr^3, but is independent of A. For the data within the cluster corresponding to a higher heat transfer rate (and a shorter time to freeze), the ordinate in Fig. 6 is given by the variable $\Pi_Q' = \Pi_Q^*[A\Theta_b/(A\Theta_b)_{mean}]^{-1/4}$, where $(A\Theta_b)_{mean} = 3.397 \times 10^{15}$ is the mean value of the product of the aspect ratio and the nondimensional temperature of the cold bath for the data falling within this cluster. The empirical model representing this cluster of data in Fig. 6 is given by the following correlation:

$$\Pi_Q' = 1.07 \times 10^{16}(\mathrm{GrPr}^3)^{-1/5}$$

The pair of dashed lines about this correlation in Fig. 6 represent a 95 percent confidence interval for the data falling within this cluster. The nondimensional heat transfer rate, Π_Q, for the data within this second cluster depends not only on Θ_b and GrPr^3, but also on A. (The value of Π_Q' in Fig. 6 may be interpreted as the value of Π_Q^* in the second cluster of data controlling for $A\Theta_b$.)

The primary conclusion to be drawn from Fig. 6 is that the heat transfer rate from the water sample after $t/t_4 = 1$ may be correlated by means of two distinct empirical relations for the test cases within the present study. Indeed, on the domain of the present investigation, the nondimensional heat transfer rate after $t/t_4 = 1$ for one cluster of data is approximately equal to one-half the nondimensional heat transfer rate after $t/t_4 = 1$ for the second cluster of data. This is consistent with the finding that the nondimensional time required for the water sample to freeze after it has reached 4°C is not uniquely determined by A, Θ_b, and GrPr^3, but rather the data for the nondimensional time between 4°C and 0°C are divided into two distinct clusters, with the nondimensional time between 4°C and 0°C for one cluster of data approximately equal to twice the nondimensional time between 4°C and 0°C for the second cluster of data.

Discussion

The results of the present experiments reveal that there are circumstances in which warm water will freeze in less time than cold water due to natural convection in the absence of significant cooling by evaporation. For the purpose of these experiments, the product GrPr^3 is only a function of the initial temperature of the water sample and may safely be interpreted as the nondimensional initial temperature of the water sample. Below $\mathrm{GrPr}^3 \approx 1.29 \times 10^8$ (corresponding to $\mathrm{Ra} \approx 2 \times 10^6$), all of the observed data for time to freeze fall within a single cluster designated "longer time to freeze." Above $\mathrm{GrPr}^3 \approx 1.29 \times 10^8$ (corresponding to $\mathrm{Ra} \approx 2 \times 10^6$), the data for time to freeze fall within two distinct clusters, designated either "shorter time to freeze" or "longer time to freeze," in a manner that is not determined by GrPr^3 (or Ra). These observations suggest that there exists some critical value for Rayleigh number, $\mathrm{Ra}_c \approx 2 \times 10^6$, below which the sample of water will take a longer time to freeze and above which the sample of water may take either a longer or a shorter time to freeze depending on the manifestation of some instability that affects the cooling and freezing process. Furthermore, the present results reveal that the time required for the sample of water to reach 4°C falls under a single description, while the time required for the sample of water to freeze once it has reached 4°C falls under two distinct descriptions, suggesting that the instability associated with the process is related in some manner to the "density inversion effect" in the neighborhood of 4°C.

In the absence of further information, the most plausible explanation of the observed phenomena is as follows: During the entire cooling and freezing process, the rate at which energy leaves the water in its liquid phase depends on the buoyancy-driven motions that develop within the liquid water. The nondimensional parameter associated with the strength of these convective motions, the Rayleigh number, is an increasing function of the initial temperature of the water sample. While it is not

sufficient, the value of the Rayleigh number is necessary to explain the observed phenomenon. If the Rayleigh number is above a certain critical value, then the flow within the sample develops the potential to "jump" from a laminar to a turbulent regime, but it will not actually become turbulent unless there is a disturbance to trigger the instability in the flow field. The convective motions for warm water have the potential to become turbulent, while the convective motions for cold water do not. However, the fact that warm water has the potential to become turbulent does not ensure that it actually becomes turbulent. Because the substance is water, which has a maximum liquid density at a temperature above its freezing point, there is a complete inversion of the flow field as the liquid passes through a range of temperature near 4°C (the cooler water that has been sitting near the bottom of the container suddenly rushes to the top). For 64 of the 108 test cases within this study, this inversion of the flow field near 4°C serves as the mechanism to trigger a transition to turbulence, resulting in a higher freezing rate and a significant reduction in the time to freeze.

Not every aspect of the proposed explanation of the observed phenomenon, that warm water will freeze in less time than cold water, can be justified directly from the temperature–time data gathered in the present study. Since there is no measurement of fluid velocity within the present study, there is also no direct evidence of any transition to turbulence for any test run. Of course, this does not mean there is no transition to turbulence for some cases. It only means that a transition to turbulence must be inferred from the behavior of the temperature field.

The proposed explanation of the observed phenomenon places an emphasis on the convective motions that are established within the liquid phase of the water sample during the cooling and freezing process. These convective phenomena occur within the context of a solidification process in which the volume of the liquid phase and the geometry of the boundary between the solid phase and the liquid phase change with time. In fact, the water sample is partially frozen at the point in the process at which the instability in the process appears. It seems plausible that, as the process advances, there is some interaction between the geometry of the boundary between the solid phase and the liquid phase and the convective motions within the liquid phase. This interaction may warrant further investigation.

The nondimensional variables adopted in the context of this study have been introduced for the purpose of facilitating the construction of the correlations presented and for the purpose of presenting meaningful graphical comparisons between the two clusters of data. Unraveling the correlations developed for the total time for the sample of water to freeze, the following conclusions may be drawn about the relationship between t_f and the dimensional variables that were altered during the course of this investigation, i.e., h, $(T_o - T_b)$, and $(T_i - T_o)$:

1 Within the cluster of data representing a "longer time to freeze,"

$$t_f \propto h^{3/4}(T_o - T_b)^{-1/4}(T_i - T_o)^{1/10}$$

2 Within the cluster of data representing a "shorter time to freeze,"

$$t_f \propto h^{1/2}(T_o - T_b)^{-1/2}(T_i - T_o)^{1/4}$$

3 At fixed values for h, $(T_o - T_b)$, and $(T_i - T_o)$, the value of t_f for the data within the cluster representing a "longer time to freeze" is approximately twice the value of t_f for the data within the cluster representing a "shorter time to freeze."

The conclusion that warm water may freeze in less time than cold water and the conclusion that there exists some instability in the cooling and freezing process do not rest in any essential way on the present choice of nondimensional variables. Both of these conclusions could be drawn from the present data expressed in terms of the dimensional variables investigated (see Table 2).

Conclusion

Under certain circumstances, a sample of water that is initially warm will freeze in less time than an identical sample of water that is initially cold due to natural convection alone, i.e., in the absence of significant cooling by evaporation.

Acknowledgments

I acknowledge the group of undergraduate students in the Mechanical Engineering Department at the University of Pittsburgh—Dave Toocheck, Phillip Claditis, Joe DeLouis, and Sam Zeli—who introduced me to the problem of the freezing of water, who assisted me in the design and the development of the test facilities employed in the present study, and who conducted a preliminary investigation of the time to freeze a sample of water as a function of its initial temperature.

References

ANSI/ASME, 1985, *Measurement Uncertainty, Part 1, Instruments and Apparatus,* PTC 19.1.

Boger, D. V., and Westwater, J. W., 1967, "Effect of Buoyancy on the Melting and Freezing Process," ASME JOURNAL OF HEAT TRANSFER, Vol. 89, pp. 81–89.

Chen, S. L., Liang, S. S., and Hong, J. T., 1992, "Effects of Natural Convection on Ice Formation Inside a Horizontal Cylinder," *Experimental Heat Transfer,* Vol. 5, pp. 131–145.

Forbes, R. E., and Cooper, J. W., 1975, "Natural Convection in a Horizontal Layer of Water Cooled From Above Near Freezing," ASME JOURNAL OF HEAT TRANSFER, Vol. 97, pp. 47–53.

Gebhart, B., Jaluria, Y., Mahajan, R. L., and Sammakia, B., 1988, *Buoyancy-Induced Flows and Transport,* Hemisphere Publishing Corporation, New York.

Heitz, W. L., and Westwater, J. W., 1971, "Critical Rayleigh Numbers for Natural Convection of Water Confined in Square Cells With L/D From 0.5 to 8," ASME JOURNAL OF HEAT TRANSFER, Vol. 93, pp. 188–196.

Kell, G. S., 1969, "The Freezing of Hot and Cold Water," *American Journal of Physics,* Vol. 37, pp. 564–565.

Lide, D. R., 1991, *CRC Handbook of Chemistry and Physics,* 72nd ed., CRC Press Inc.

Lock, G. S. H., 1994, *Latent Heat Transfer: An Introduction to Fundamentals,* Oxford University Press, New York.

NIST, 1979, *Thermocouple Reference Tables,* NBS Monograph 125, National Bureau of Standards, Washington, DC.

Schechter, R. S., and Isbin, H. S., 1958, "Natural-Convection Heat Transfer in Regions of Maximum Fluid Density," *AIChE Journal,* Vol. 4, No. 1, pp. 81–89.

Tankin, R. S., and Farhadieh, R., 1971, "Effects of Thermal Convection on Formation of Ice," *Int. J. Heat Mass Transfer,* Vol. 14, pp. 953–961.

Tien, C., 1968, "Thermal Instability of a Horizontal Layer of Water Near 4°C," *AIChE Journal,* Vol. 14, No. 4, pp. 652–653.

Surface Temperature Measurement Using Infrared Radiometer by Applying a Pseudo-Gray-Body Approximation: Estimation of Radiative Property for Metal Surface

T. Inagaki
Research Associate,
Department of Mechanical Engineering,
University of Ibaraki,
12-1 Nakanarusawa 4 Chome, Hitachi,
Ibaraki, 316 Japan

Y. Okamoto
Professor,
Department of Mechanical Engineering,
University of Ibaraki,
12-1 Nakanarusawa 4 Chome, Hitachi,
Ibaraki, 316 Japan

The visualization technique using an infrared radiometer has been widely used to estimate a two-dimensional temperature distribution on a surface. We have previously proposed various characteristics of the radiative properties for nonmetal surfaces on which the gray-body approximation can be used. However, the gray-body approximation can not be applied to glossy metal surfaces, because the influence of the reflected energy on the temperature measurement becomes severe. A pseudo-gray-body approximation is therefore proposed to estimate a temperature field on metal surfaces and its applicability is confirmed using an infrared radiometer with three detection wavelength bands.

1 Introduction

Recently, nondestructive evaluation using an infrared radiometry method has become more attractive. If we can establish a quantitative infrared radiometry method near ambient conditions, it will be useful to a wide variety of engineering applications, such as heat transfer measurement and invisible flaw diagnosis. The radiative properties should therefore be analyzed for various material surfaces, and their characteristics should be discussed under near-ambient conditions. Okamoto et al. (1991, 1993) have previously proposed various radiative characteristics of the radiative properties for nonmetal surfaces on which the gray-body approximation can be used. The wavelength dependence of the radiative properties has also been estimated on nonmetal surfaces. However, the gray-body approximation cannot be applied to glossy metal surfaces, because the influence of the reflected energy on the temperature measurement becomes severe.

We should learn more about an infrared radiometry method for metal surfaces in addition to nonmetal surfaces. The pseudo-gray-body approximation is proposed to estimate quantitatively a temperature field on metal surfaces in a limited temperature (293 $\sim$ 373 K) and detection wavelength (2 $\sim$ 13 μm) range. Its applicability is confirmed using an infrared radiometer with three detection wavelength bands. In the same way as in our previous studies (1991, 1993), various characteristics for metal surfaces are suggested. Furthermore, the variation of the radiative properties is discussed. If the pseudo-gray-body approximation is applied, the radiative properties for metal surfaces having a directional property can be treated in a way similar to those for nonmetal surfaces under the gray-body approximation.

Contributed by the Heat Transfer Division for publication in the JOURNAL OF HEAT TRANSFER. Manuscript received by the Heat Transfer Division May 1994; revision received April 1995. Keywords: Measurement Techniques, Radiation. Associate Technical Editor: R. Viskanta.

2 Experimental Apparatus and Measurement

2.1 Optical Configuration and Test Piece. Figure 1 illustrates the fundamental optical configuration of the infrared radiometer, which is an imaging device. Energy radiated from a surface is collected at the focus lens through the germanium window, and the two-dimensional thermal image representing radiation temperature then appears on the color monitor. Noted that each scanning line is previously calibrated by a standard blackbody furnace. The infrared radiometer can detect an area-averaged surface radiation temperature for an area of 0.5 mm $\times$ 0.5 mm when the distance between a target and a sensor is at least 150 mm. However, a constant square area of 10 mm $\times$ 10 mm is scanned in the present study.

Materials for the test piece are stainless steel (SUS304), steel (S35C), aluminum, and brass (Cu–30Zn). The size of test pieces is 20 mm long, 20 mm wide, and 15 mm thick. Its surface is cleaned up by an ultrasonic cleaner after polishing. The surface roughness is estimated about 0.1 μm using an electric micrometer. The measurement field is covered by blackbody surfaces, which are maintained at a constant temperature to eliminate the multiple reflection. The test piece and the optical device are installed in an enclosure, which is covered by black-colored velvet texture to attain an ideal measurement field. Moreover, the measurement space between the target and the sensor is also surrounded by the water-cooled pyramid-shaped hood to maintain a constant ambient temperature throughout all experiments. The emissivity for the inside surface of the pyramid-shaped hood colored by matting black becomes greater than 0.99, and the enclosure surfaces can thus be treated as a blackbody. The sample surface can be treated as a blackbody if its temperature is consistent with that of the enclosure. The true surface temperature of the test piece is measured by the thermocouple of 100 μm diameter mounted 0.5 mm deep from its central surface. A series of measurements are started under thermal equilibrium when the surface temperature of the test piece becomes constant. Under a constant temperature, individ-

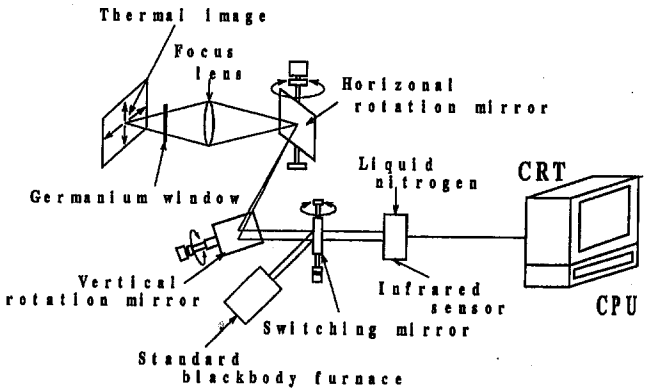

Fig. 1 Fundamental optical configuration of the present infrared radiometer

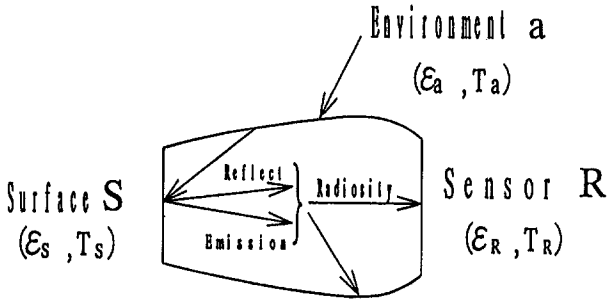

Fig. 2 Concept model of the measurement field

ual experiments are repeated eight times and twelve temperature data sets are obtained individually. The temperature data are then ensemble-averaged after eliminating unusual values using the modified Tompson-τ technique. The sensor is cooled by liquid nitrogen, and the test piece is inclined at 15 deg toward the vertical line. In general, the directional property of the emissivity has a significant influence in the measurement under larger inclination angle when using a narrow band infrared radiometer.

2.2 Radiative Characteristics of the Infrared Radiometer. As shown in Fig. 2, we consider that the test piece surface, S, is surrounded by blackbody surfaces, which are maintained at ambient temperature, T_a, to simplify the measurement field as a standard measurement system. The test surface is heated at temperature T_S. Radiosity, Q_{SR}, is a quantity that is leaving the surface, S, and is the summation of the emitted and reflected energies. The reflected energy is incident from the surroundings at T_a to S and is transferred to the sensor, R. The sensor is cooled at temperature T_R. Since the test piece is surrounded by blackbody surfaces, the effect of multiple reflections between a and S is negligible. Q_{SR} transferred from S to R is expressed in the following form using emissivity, ϵ_S, and reflectivity, ρ_S:

$$Q_{SR} = \sigma\epsilon_S(T_S^n - T_R^n) + \sigma\rho_S(T_a^n - T_R^n) \quad (1)$$

The hypothesis that T_S and T_a are much larger than T_R is usually true when the sensor is cooled by liquid nitrogen. Equation (1) is therefore rewritten in the following form:

$$Q_{SR} = \sigma\epsilon_S T_S^n + \sigma\rho_S T_a^n = \sigma a_S T_S^n = \sigma t_S^n \quad (2)$$

where the radiosity coefficient, a_S, can be described in the following form using T_S and t_s:

$$a_S = \left(\frac{t_s}{T_S}\right)^n \quad (3)$$

where T_S is the true temperature measured by the thermocouple, which was previously calibrated using a normal thermometer. t_S is the indicated value of the infrared radiometer and is the radiation temperature. The power index, n, for the total radiation energy becomes 4.0. However, n for the narrow band infrared radiometer is not consistent with 4.0 and varies according to detection wavelength, λ, as shown in Fig. 4.

The infrared sensor, which has an adequate sensitivity, is usually utilized in the wavelength range of 2 ~ 13 μm. These infrared sensors with three wavelength bands, such as In–Sb (2 ~ 5 μm), Hg–Cd–Te (6 ~ 9 μm), and Hg–Cd–Te (8 ~ 13 μm) sensors, are used to measure the surface radiation temperature. Detection sensitivities, Φ_λ (percent), for three kinds of sensors are illustrated in Fig. 3. It is clear from this figure that the respective sensors have a selective wavelength of several μm in width in the range of 2 ~ 13 μm.

Figure 4 illustrates the distributions of detection energy, Q_{bS}, versus T_S. Q_{bS} for the respective sensors are derived from the integration of $Q_{b\lambda}\cdot\Phi_\lambda$ with λ. Noted that $Q_{b\lambda}$ is the energy described by Planck's law. The blackbody emission, Q_b, denoted by Stefan–Boltzmann's law is also included in this figure. It is obvious from this figure that the Hg–Cd–Te (8 ~ 13 μm) sensor having the longest wavelength has the largest detection energy for T_S = 300 K, and that energy decreases with decreasing λ. However, Q_{bS} for the In–Sb (2 ~ 5 μm) sensor having the shortest wavelength has the largest detection energy for T_S = 450 K. The logarithmic form, $\overline{Q_{bS}} = CT_S^n$, in this figure shows the linear-approximated detection energy for the respective sensors. Noted that the values of n are shown in this figure.

2.3 Radiative Properties for Metal Surfaces. In measuring radiation energy, the measurement field generally becomes complicated owing to the influence of reflection from the surroundings. It is difficult to determine the reflected energy

Nomenclature

a_s = radiosity coefficient
B = bias limit
b_s = radiative quantity under pseudo-gray-body approximation
n = power index for respective sensors
Q_b = radiation energy radiated from blackbody surface, W/m^2
Q_{bS} = detection energy for sensor, W/m^2
$\overline{Q_{bS}}$ = linear-approximated detection energy for sensor, W/m^2
$Q_{b\lambda}$ = energy described by Planck's law, W/m^2
Q_{SR} = energy incident upon the sensor or radiosity, W/m^2
S = precision index
SEE = standard error of estimate
T_a = ambient temperature, K
T_R = surface temperature of sensor, K
T_S = surface temperature of test piece, K
t_S = surface radiation temperature of test piece, K
t_{S0} = surface radiation temperature without reflectivity, K
U_{ADD} = measurement uncertainty level based on the 99 percent coverage
U_{RSS} = measurement uncertainty level based on the 95 percent coverage
Δ = variation of radiative quantity
δ = radiation temperature difference, K
ϵ_S = emissivity of test piece surface
λ = detection wavelength of sensor, μm
ν = degree of freedom
ρ_S = reflectivity of test piece surface
σ = Stefan–Boltzmann constant, W/(m^{2}K^4)
Φ_λ = detection sensitivity of sensor, percent

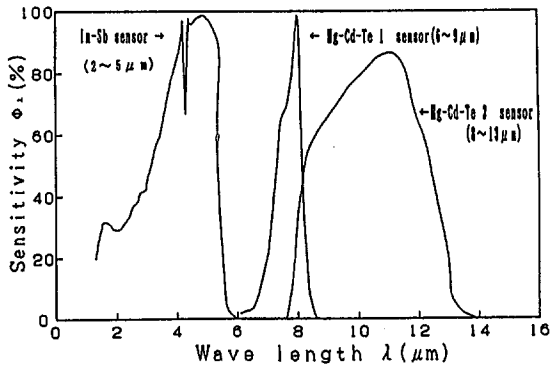

Fig. 3 Detection sensitivity for three kinds of infrared sensors

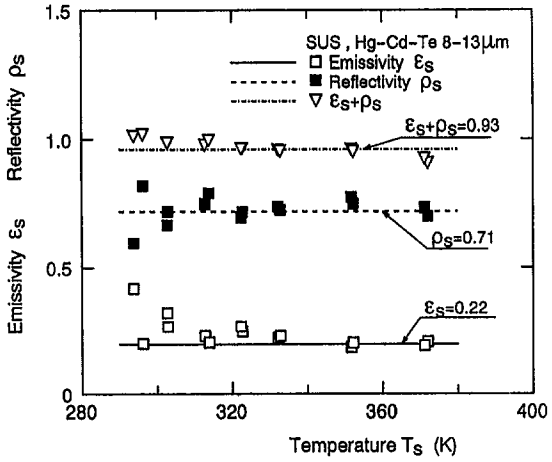

Fig. 5 Radiative properties on stainless steel surface measured by the Hg–Cd–Te sensor (8 ~ 13 μm) at T_a = 293 K

quantitatively. Furthermore, if the measurement field is surrounded by non-blackbody surfaces whose emissivity and reflectivity are not specified, the complicated effect of multiple reflections between surfaces will occur. Therefore, it is necessary to clarify the physical characteristics of a_S, which is representative of the radiosity.

A sample surface, whose emissivity is not given, can be estimated by a two-color method (for example, Chen et al., 1990). But its accuracy and applicability has not been discussed in a practical use for near ambient condition. Iuchi (1992) tried to enhance a measurement accuracy near ambient temperature by changing observation angle. We estimate the sample surface in a different way. Under a constant surface temperature, two radiosity coefficients, a_{S1} and a_{S2}, corresponding to two ambient temperatures, T_{a1} and T_{a2}, are shown in the following equations using Eqs. (2) and (3),

$$a_{S1} = \epsilon_S + \rho_S\left(\frac{T_{a1}}{T_S}\right)^n = \left(\frac{t_{S1}}{T_S}\right)^n \tag{4}$$

$$a_{S2} = \epsilon_S + \rho_S\left(\frac{T_{a2}}{T_S}\right)^n = \left(\frac{t_{S2}}{T_S}\right)^n \tag{5}$$

where the radiation temperatures, t_{S1} and t_{S2}, are the indicated values of the infrared radiometer. ϵ_S and ρ_S can be expressed as follows using Eqs. (4) and (5):

$$\epsilon_S = \frac{a_{S2}T_{a1}^n - a_{S1}T_{a2}^n}{T_{a1}^n - T_{a2}^n} \tag{6}$$

$$\rho_S = \frac{a_{S1} - a_{S2}}{T_{a1}^n - T_{a2}^n}\,T_S^n \tag{7}$$

The summation of both ϵ_S and ρ_S, represented by b_S term, is given by the following form:

$$b_S = \epsilon_S + \rho_S = \frac{a_{S1}(T_S^n - T_{a2}^n) - a_{S2}(T_S^n - T_{a1}^n)}{T_{a1}^n - T_{a2}^n} \tag{8}$$

ϵ_S for an inclined glossy metal surface has a directional property if its temperature is measured by a narrow band infrared radiometer. The summation of both ϵ_S and ρ_S does not become unity in this case. The authors define the summation, b_S, as the pseudo-gray-body approximation in a way similar to the gray-body approximation. b_S is the characteristic value for various metal surfaces. a_S is also given by the following form by transforming Eq. (2) using b_S:

$$a_S = \epsilon_S + (b_S - \epsilon_S)\left(\frac{T_a}{T_S}\right)^n \tag{9}$$

ϵ_S can be also derived by transforming Eq. (9),

$$\epsilon_S = \frac{a_S - b_S(T_a/T_S)^n}{1 - (T_a/T_S)^n} \tag{10}$$

Finally, t_S is also defined in the following form by substituting Eq. (3) into Eq. (10):

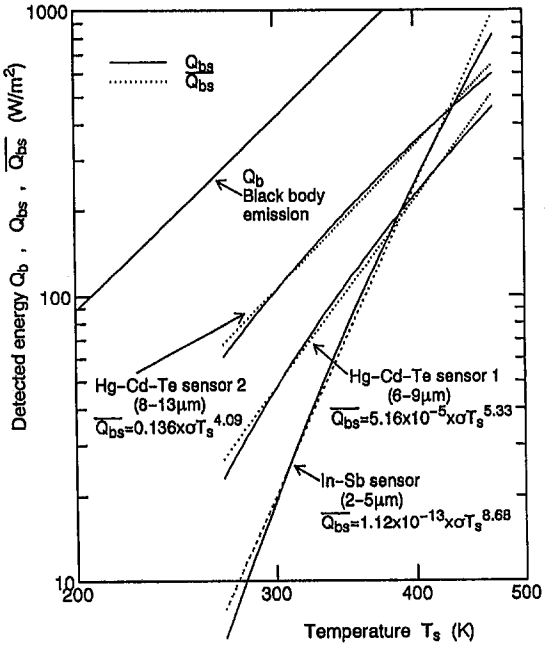

Fig. 4 Distribution of detection energy for three kinds of infrared sensors

Table 1 Averaged radiative properties on various material surfaces measured by three kinds of sensors

T_a=293~373(K)		Hg-Cd-Te(6~9 μm)	Hg-Cd-Te(8~13 μm)	In-Sb(2~5 μm)
SUS	ε_s	0.39	0.22	0.30
	ρ_s	0.59	0.71	0.60
	$b_s=\varepsilon_s+\rho_s$	0.98	0.93	0.90
Brass	ε_s	0.25	0.22	0.22
	ρ_s	0.65	0.71	0.61
	$b_s=\varepsilon_s+\rho_s$	0.90	0.93	0.83
Al	ε_s	0.14	0.15	0.15
	ρ_s	0.76	0.83	0.75
	$b_s=\varepsilon_s+\rho_s$	0.90	0.98	0.90
SS	ε_s	0.40	0.35	0.40
	ρ_s	0.47	0.63	0.50
	$b_s=\varepsilon_s+\rho_s$	0.87	0.98	0.90

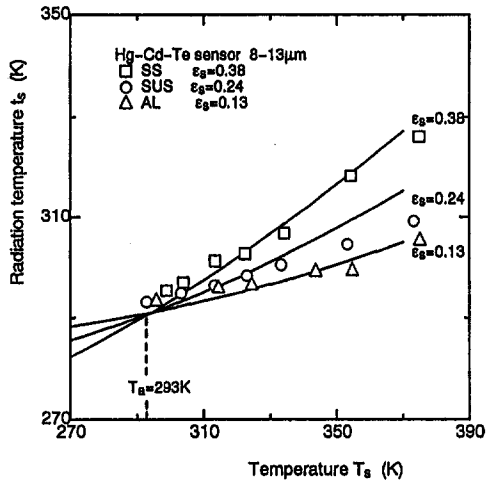

Fig. 6 Surface radiation temperatures on various material surfaces measured by the Hg–Cd–Te sensor (8 ~ 13 μm) at T_a = 293 K

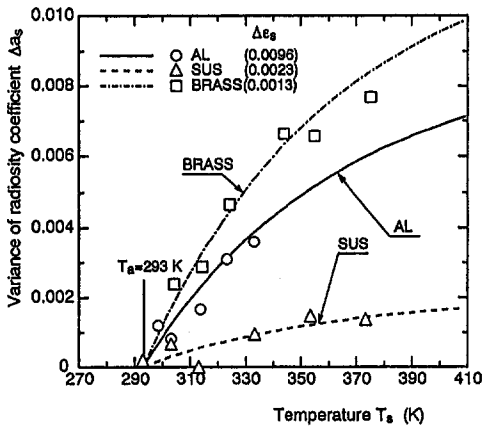

Fig. 7 Variation of radiosity coefficients on various material surfaces measured by the Hg–Cd–Te sensor (8 ~ 13 μm) at T_a = 293 K

$$t_S = T_S[\epsilon_S\{1 - (T_a/T_S)^n\} + b_S(T_a/T_S)^n]^{1/n} \quad (11)$$

Noted that t_S can also be calculated from Eq. (11) after estimating b_S and ϵ_S. The calculated value of t_S is merely to allow a parametric study of how it varies for different values of ϵ_S.

2.4 Variations of Radiative Properties for Metal Surfaces. It is important to estimate the detection sensitivity of the infrared radiometer in analyzing a minute radiation temperature difference. Therefore, we introduce a variation of the measured radiative properties for the sample surfaces.

Since a_S is a function of t_S and ϵ_S as shown in Eqs. (3) and (9), we differentiate Eqs. (3) and (9) with respect to independent variables to obtain its variation. The differentiated form using ϵ_S is the following form:

$$\frac{\partial a_S}{\partial \epsilon_S} = 1 - \left(\frac{T_a}{T_S}\right)^n \quad (12)$$

The variation for emissivity, $\Delta\epsilon_S$, derived from Eq. (12) is then

$$\Delta\epsilon_S = \frac{\Delta a_S}{1 - (T_a/T_S)^n} \quad (13)$$

The differentiated form using t_S is the following form:

$$\frac{\partial a_S}{\partial t_S} = n\left(\frac{t_S}{T_S}\right)^{n-1}\left(\frac{1}{T_S}\right) \quad (14)$$

The variation for radiosity coefficient, Δa_S, derived from Eq. (14) is then,

$$\Delta a_S = n\left(\frac{t_S}{T_S}\right)^{n-1}\left(\frac{\Delta t_S}{T_S}\right) \quad (15)$$

The variation for radiation temperature, Δt_S, in Eq. (15) is empirically determined from the indicated value of the infrared radiometer. Δt_S can be also obtained as the following form by substituting Eq. (11) into Eq. (15), and using Eq. (13):

$$\Delta t_S = \frac{\Delta\epsilon_S[1 - (T_a/T_S)^n]T_S}{n[\epsilon_S + (b_S - \epsilon_S)(T_a/T_S)^n]^{(n-1)/n}} \quad (16)$$

Δt_S defined as Eq. (16) is merely to allow a parametric study of how it varies for different values of ϵ_S.

3 Experimental Results and Discussion

3.1 Radiative Properties for Metal Surfaces. Figure 5 measured by the 8 ~ 13 μm sensor indicates the radiative properties of the test piece surface of stainless steel. The experiment is performed when T_a = 293 K. These data are obtained by Eqs. (4)–(8) using the measured T_a, T_S, and t_S. The respective points are ensemble-averaged as mentioned in section 2.1. It is obvious from this figure that ϵ_S and ρ_S are independent of T_S in the range of the present experiment and that their summations, b_S, are constant and below unity. We can treat the radia-

Table 2 Variations of radiative properties on various material surfaces measured by three kinds of sensors at T_a = 293 K

T_a =293(K)	T_s (K)	In-Sb (2-5 μm)			Hg-Cd-Te (6-9 μm)			Hg-Cd-Te (8-13 μm)		
		$\Delta\varepsilon_s$	Δa_s	Δt_s	$\Delta\varepsilon_s$	Δa_s	Δt_s	$\Delta\varepsilon_s$	Δa_s	Δt_s
BRASS	303	0.0217	0.0060	0.2699	0.0026	0.0047	0.3168	0.0166	0.0024	0.1958
	323	0.0010	0.0055	0.4026	0.0214	0.0089	0.7814	0.0138	0.0047	0.4856
	353	0.0132	0.0107	1.1478	0.0123	0.0079	0.9797	0.0121	0.0066	0.9483
SUS	303	0.0053	0.0013	0.0576	0.0139	0.0023	0.1474	0.0052	0.0007	0.0532
	323	0.0022	0.0012	0.0688	0.0053	0.0022	0.1806	0.0027	0.0009	0.0878
	353	0.0049	0.0040	0.3795	0.0035	0.0022	0.2656	0.0028	0.0015	0.2018
AL	303	0.0086	0.0022	0.0991	0.0206	0.0034	0.2181	0.0055	0.0007	0.0575
	323	0.0043	0.0025	0.1845	0.0092	0.0037	0.3381	0.0094	0.0031	0.3243
	353	0.0043	0.0034	0.4547	0.0018	0.0011	0.1505	0.0028	0.0015	0.2095

Table 3 Stratum of calibration error

	Thermocouple			Infrared radiometer		
Error element	B	S	ν	B	S	ν
Scattering of thermocouple	0.1	-	>30	0.4	0.3	>30
Standard error of estimate(SEE)	-	0.399	>30	-	0.289	>30
Calibration error of thermocouple	-	-	-	0.172	0.413	>30
Total value	0.1	0.399	>30	0.435	0.586	>30

Table 4 Stratum of data acquisition error

	Thermocouple			Infrared radiometer		
Error element	B	S	ν	B	S	ν
Time variation of data	-	0.00348	>30	-	0.0532	>30
Time change & Error of data reading	0.1	0.1	>30	0.0125	0.0125	>30
Error of zero compensation	0.1	-	>30	-	-	-
Spatial non-uniformity	-	-	-	0.0075	-	>30
Total value	0.14	0.108	>30	0.0146	0.0546	>30

tive properties as a constant value for individual materials. However, they are dependent on λ. It is presumed that the narrow band sensors cannot detect omnidirectional information on an inclined sample surface. A series of tendencies of the measured radiative properties for brass, aluminum, and steel surfaces are the same as the results for stainless steel. Therefore, the radiative properties can be averaged in the range of 293 K–373 K and are then shown in Table 1. ϵ_S, ρ_S, and b_S in terms of T_S are summarized in this table, in which the data are measured by the infrared radiometers with three detection wavelength bands. If the sensor could detect total radiation energy, the wavelength dependence would not appear on a gray-body or pseudo-gray-body surface. However, since the range of the present detection wavelength is in a narrow band, as mentioned earlier, the radiative properties vary with λ.

The relation between T_S and t_S for three materials is shown in Fig. 6, in which the data are measured by the Hg–Cd–Te sensor (8 ~ 13 μm). The experiment is performed when T_a = 293 K. The lines shown in this figure indicate the values calculated from Eq. (11) with ϵ_S as a parameter. b_S is previously determined from Table 1. The open symbols represent the empirical data, which are the indicated values of the infrared radiometer. It is obvious that the calculated values are well correlated with the empirical data. The comparison between calculated and empirical data supports the availability of the proposed equations. t_S becomes lower than T_S when $\epsilon_S < 1.0$ and increases with increasing ϵ_S when $T_S > 293$ K. In particular, the rate of increase of t_S for $\epsilon_S = 0.13$ is lowest among the cases. It is assumed that the influence of reflection becomes severe under smaller ϵ_S. That is, the radiation temperature difference, $\delta t_S (= t_S - t_{S0})$, described as $T_S\ [=[\epsilon_S + (b_S - \epsilon_S)(T_a/T_S)^n]^{1/n} - \epsilon_S^{1/n}]$ increases with decreasing ϵ_S under the same T_a and T_S conditions, because b_S is nearly equal to unity. It should be noted that t_{S0}, in which reflectivity is not included, can be obtained using Eq. (11) with $\rho_S = 0$. δt_S means the intensity of the reflected energy in other words. In general, t_S is equal to T_S on a blackbody surface, because ϵ_S becomes unity. We can obtain an equation for metal surfaces, $t_S = T_S b_S^{1/n}$, by evaluating Eq. (11) with $T_S = T_a$. t_S is nearly equal to T_S for metal surfaces when $T_S = T_a$, because the measured b_S is about unity as shown in Table 1.

Table 1 shows the measured radiative properties for three kinds of sensors. It is obvious from this table that b_S terms vary by the detection wavelength of sensor.

3.2 Variations of Radiative Properties for Metal Surfaces. The variation analysis applying the pseudo-gray-body approximation is performed when T_a = 293 K. ϵ_S and b_S included in Eqs. (13), (15), and (16) are those of the measured results. b_S is referred to Table 1 and is defined as a fixed value. ϵ_S is previously determined by Eqs. (3) and (10) using the measured T_a, T_S, t_S, and b_S.

Figure 7 indicates the variations of a_S measured by the Hg–Cd–Te (8 ~ 13 μm) sensor. It is obvious from this figure that the lines calculated from Eq. (15) using the measured T_S, t_S, and Δt_S are well correlated with the empirical results presented by the symbols. The empirical values are determined by the variation of measured a_S. The respective variations are comparatively small. Noted that the variation of a_S theoretically becomes zero when $T_S = T_a$, because Δt_S calculated by Eq. (16) becomes zero. Moreover, the measured variations of the radiative properties are listed in Table 2. It is obvious from this table that the variations are dependent on λ and T_S. Their variations become larger with increasing T_S in the range of the present experiment.

4 Uncertainty Analysis

We estimate the confidence levels of the empirical data by applying uncertainty analysis based on ANSI/ASME PTC 19.1–1985 (1985). The final uncertainty levels when T_S = 55°C are shown in Tables 3 and 4 for the thermocouple and infrared radiometer. The relative uncertainty levels, U_{ADD} and U_{RSS}, for a_S are 3.21 and 2.73 percent. U_{ADD} and U_{RSS} for ϵ_S are 8.14 and 6.19 percent. U_{ADD} and U_{RSS} for ρ_S are 5.55 and 4.01 percent. U_{ADD} and U_{RSS} for b_S are 6.81 and 5.34 percent. They are total averaged values among the measured data for various materials and surface temperatures when the infrared radiometers with three detection wavelength bands are used. It is confirmed that the measured data are useful in discussing the characteristics of the radiative properties.

5 Concluding Remarks

We clarify the physical characteristics of the radiative properties using the infrared radiometers with three detection wavelength bands ($2 \sim 5$, $6 \sim 9$, and $8 \sim 13$ μm). Radiosity coefficient, radiation temperature, emissivity and their variations are measured on various metal surfaces, where the pseudo-gray-body approximation can be applied. It is obvious from a series of studies that the experimental results can be expressed by the pseudo-gray-body approximation theory. That is, the result that the emissivity and reflectivity are independent of surface temperature indicates that their summation, b_S, also becomes constant in the range of the measured temperatures ($293 \sim 373$ K). Therefore, we confirm that the radiative properties for metal surfaces can be treated in a way similar to those for nonmetal surfaces under the gray-body approximation. Moreover, we find the wavelength dependence of the radiative properties for metal surfaces. We can discuss various quantitative temperature data nondestructively after estimating the characteristics of the present infrared radiometry. It will be necessary to develop this method further for various engineering applications to establish a practical method of temperature measurement near ambient conditions. This method may be applied to heat transfer measurement and invisible flaw diagnosis.

References

ASME, 1985, Performance Test Codes, Supplement on Instructions and Apparatus, Part 1, Measurement Uncertainty, published by the American Society of Mechanical Engineers.

Chen, L., Yang, B. T., and Hu, X. R., 1990, "Design Principle for Simultaneous Emissivity and Temperature Measurements," *Optical Engineering,* Vol. 29, No. 12, pp. 1445–1448.

Iuchi, T., 1992, "Radiation Thermometry of Low Emissivity Metals Near Room Temperature," *Temperature, Its Measurement and Control in Science and Industry,* J. F., Vol. 6, Pt. 2, pp. 865–869.

Okamoto, Y., Ishii, T., Kaminaga, F., Sato, K., and Kurokawa, K., 1991, "Clarification of Radiation Temperature and Radiosity Coefficient by Means of Infrared Radiometer," *Transactions of the Japan Society of Mechanical Engineers,* Vol. 57-544, pp. 270–275.

Okamoto, Y., Inagaki, T., and Sekiya, M., 1993, "Surface Temperature Measurement Using Infrared Radiometer (1st Report, Radiosity Coefficient and Radiation Temperature)," *Transactions of the Japan Society of Mechanical Engineers,* Vol. 59-568, pp. 232–237.

Absorption/Scattering Coefficients and Scattering Phase Functions in Reticulated Porous Ceramics

T. J. Hendricks
Video & Networking Division,
Tektronix, Inc.,
Beaverton, OR 97077
Mem. ASME

J. R. Howell
Department of Mechanical Engineering,
University of Texas at Austin,
Austin, TX 78712
Fellow ASME

Spectral absorption and scattering coefficients and spectral scattering phase functions have been derived for partially stabilized zirconia (PS ZrO_2) and oxide-bonded silicon carbide (OB SiC) reticulated porous ceramics (RPCs) *across the wavelength range 0.4–5.0 μm. These spectral radiative properties were investigated and quantified for 10 ppi (pores/inch), 20 ppi, and 65 ppi materials. Radiative properties were recovered from spectral hemispherical reflectance and transmittance measurements using inverse analysis techniques based upon discrete ordinates radiative models. Two dual-parameter phase functions were investigated for these materials: one based on the physical structure of reticulated porous ceramics and the other a modified Henyey-Greenstein phase function. The modified Henyey–Greenstein phase function provided the most consistent spectral radiative properties. PS ZrO_2 radiative properties exhibited strongly spectrally dependent behavior across the wavelength range studied. OB SiC radiative properties exhibited radiative behavior that was relatively independent of wavelength across the wavelength spectrum studied. OB SiC also demonstrated consistently higher absorption coefficients than PS ZrO_2 at all wavelengths. Spectral scattering albedos of PS ZrO_2 were discovered to be in the range 0.81–0.999 and increased as ppi rating increased, while those for OB SiC were lower in the range 0.55–0.888 and decreased as ppi rating increased. The average extinction efficiencies for 0.4–5.0 μm were discovered to be 1.45 for PS ZrO_2 and 1.70 for OB SiC. Extinction coefficients were discovered to correlate well with geometric optics theoretical models and electromagnetic wave/fiber interaction models based on independent scattering and absorption mechanisms.*

Introduction

Radiative processes within reticulated porous ceramics (RPCs) are fundamentally important in many energy system applications currently envisioned for these materials. Reticulated porous ceramics will be applied in advanced energy and combustion systems, such as low NO_x combustion burners, next-generation jet engines, and ceramic automobile engines. Solar thermal energy systems for fuel and chemical processing are other applications where reticulated porous ceramics (RPCs) are envisioned to exchange absorbed radiative energy with a gas flowing through the porous structure. Bohn and Mehos (1990), Hale and Bohn (1993), and Couch (1989) discuss solar thermal systems using ceramic solar receivers/reactors to destroy hazardous wastes, detoxify organics in water streams, absorb and transfer process heat, process carbon fibers, and drive solar thermal chemical reactions. Space vehicle applications also exist, involving radiating aerobraking structures and spacecraft radiator systems, where RPCs could be exploited.

Radiative processes within RPCs will be dominant mechanisms in each of these future applications. Knowledge of the spectral absorption coefficient, spectral scattering coefficient, and spectrally dependent phase function of RPCs is critical to successful implementation and efficient utilization in these systems. It is also important to understanding basic radiative behavior within these materials, and ultimately designing methods and systems for enhancing or diminishing radiative coupling to the RPCs. The radiative properties are essential for predicting: (1) volumetric energy absorption, (2) volumetric energy scattering, and (3) temperature distributions within the materials, coolants, and adjacent system components in system performance simulations. Unfortunately, radiative properties of RPCs are difficult to quantify analytically because of their complex dodecahedral structure and high porosity (≈80–85 percent).

Prior work on RPC radiative properties has been limited. McCarthy (1989) performed some experimental scattering work investigating the multiple scattering phase function of partially stabilized zirconia (PS ZrO_2) and silicon carbide (SiC). McCarthy also estimated the total extinction coefficient and scattering albedo for 10 pores/inch (ppi) PS ZrO_2 and SiC for wavelengths 2.5–14.0 μm from emittance and transmittance measurements. These extinction coefficient estimates were not spectrally dependent and were low because of multiple scattering effects. McCarthy was unsuccessful at determining single-scattering phase function information. Skocypec et al. (1991) determined effective extinction coefficients and scattering albedos of 5 ppi, 10 ppi, and 20 ppi rhodium-impregnated reticulated alumina ceramics by comparing experimental reflectances and transmittances with predictions from a three-flux radiative model assuming isotropic scattering. Hsu and Howell (1992) recovered estimates of extinction coefficients for 10 ppi, 20 ppi, 30 ppi, and 65 ppi PS ZrO_2 from heat transfer experiments and inverse analysis techniques using a combined thermal conduction/radiative diffusion model. Their extinction coefficients were not spectral quantities, and they did not determine phase function characteristics. Hale and Bohn (1993) determined the extinction coefficient and scattering albedo of 10 ppi, 20 ppi,

Contributed by the Heat Transfer Division for publication in the JOURNAL OF HEAT TRANSFER. Manuscript received by the Heat Transfer Division April 1995; revision received October 1995. Keywords: Porous Media, Radiation, Radiation Interactions. Associate Technical Editor: M. Modest.

30 ppi, and 65 ppi reticulated alumina at 0.49 μm assuming an isotropic phase function and constant albedo across the ppi range.

This paper describes new experimental findings on spectral radiative properties of partially stabilized zirconium oxide (PS ZrO_2) and oxide-bonded silicon carbide (OB SiC) in the wavelength range 0.4–5.0 μm. Material categories of 10 ppi, 20 ppi, and 65 ppi were investigated to determine effective absorption coefficients, effective scattering coefficients, and scattering phase function characteristics as a function of wavelength. The porosity of PS ZrO_2 ceramics was approximately 85 percent, while that for OB SiC ceramics was approximately 80 percent. The internal filament (or strut) diameters in the interconnected, spider-web-like, dodecahedral cell structure were: (*a*) 508 μm and 356 μm for 10 ppi and 20 ppi PS ZrO_2, respectively, (*b*) 686 μm and 508 μm for 10 ppi and 20 ppi OB SiC, respectively, and (*c*) approximately 100 μm for both 65 ppi materials. Internal spectral radiative properties were determined from spectral hemispherical reflectance and transmittance measurements on test specimens of differing thickness using inverse analysis techniques.

Reflectance and Transmittance Measurements

Spectral hemispherical reflectance/transmittance measurements were obtained using a computer-automated Model 746 infrared spectroradiometer system from Optronic Laboratories, Inc., Orlando, FL. This system created unidirectional, monochromatic incident radiation (1.2 cm beam diameter) impinging on cylindrical, 2.5 cm diameter test samples of varying thickness. Incident radiation was centered on the cylinder axis and directed approximately along the cylinder axis (10° off-normal angle per system design specifications). Test sample external boundaries were nonreflective. All measurements were taken at room temperature as this research and experimental configuration were not designed to study temperature-dependent effects. Measurement uncertainties in reflectances and transmittances were ±10 percent. This was determined by measurement repeatability on a variety of samples, measurement repeatability upon sample rotation, and using different spectroradiometer configurations in overlapping wavelength bands.

Voluminous spectral reflectance and transmittance measurements for PS ZrO_2 and OB SiC were obtained for test samples of 1–2 cm depth and wavelengths 0.4–5.0 μm. The reader is referred to Hendricks (1993) for a complete presentation and discussion of the spectral reflectance and transmittance measurements used in the inverse analyses to retrieve the spectral radiative properties presented here. In general, PS ZrO_2 exhibited very spectrally dependent reflectance. PS ZrO_2 reflectance typically started at intermediate values (i.e., ≈0.4–0.5) at 0.4 μm, then increased sharply to high values (i.e., ≥0.7) at 0.6 μm, then remained at relatively high values at λ = 0.6–2.4 μm, then decreased abruptly at λ = 2.6–3.0 μm to characteristic reflectance minimums (i.e., 0.1–0.2) at 3.0 μm, and finally increased gradually to slightly higher values (i.e., 0.25–0.4) at λ = 3.2–5.0 μm. PS ZrO_2 reflectance generally showed very little depth dependence for test sample depths of 1–2 cm. PS ZrO_2 transmittance also exhibited very spectrally dependent behavior. It typically started at low values (i.e., 0.01–0.05) at 0.4 μm, increased rapidly to maximums at 1.3 μm, then gradually decayed for λ = 1.3–2.4 μm, then decreased sharply at λ = 2.6–2.8 μm to nearly its starting values at 0.4 μm, and finally remained nearly constant at λ = 3.0–5.0 μm. PS ZrO_2 transmittance generally demonstrated strong depth dependence for test sample depths of 1–2 cm.

In general, OB SiC exhibited low spectral reflectances and transmittances and relatively small variations with wavelength across the wavelength range. OB SiC reflectances typically started at 0.10–0.15 at 0.4 μm, then increased to a slight maximum (i.e., 0.15–0.17) at 0.5 μm, and then gradually decayed for λ = 0.6–5.0 μm to low values (i.e., 0.05) at 5.0 μm. OB SiC reflectances were generally depth-insensitive for test sample depths of 1–2 cm. OB SiC transmittances remained nearly constant at all wavelengths, but were very sensitive to depth for 1–2 cm sample depths. OB SiC transmittances were typically below 0.08, and sometimes so low (i.e., ≈0.001) that they were difficult to measure.

Two-Parameter Phase Functions

Two dual-parameter scattering phase functions were investigated to determine which was more accurate and consistent in predicting the reflectance and transmittance test data. The first phase function was developed from investigations into the physical structure of the RPC matrix and physical reasoning about the nature of radiative scattering off the RPC structure. This produced the linear combination of a diffraction-dominated phase function, an isotropic phase function, and a back scattering phase function, taking the mathematical form:

$$\Phi(\lambda, \theta) = f_{is,\lambda} + (1 - f_{is,\lambda} - f_{bck,\lambda})\Phi_{\text{DIFF}}(\theta) + f_{bck,\lambda}\Phi_{\text{DIF REF}}(\theta) \quad (1)$$

This phase function was termed the DRIFD phase function (i.e., Diffuse-Reflectance, Isotropic, Forward-Diffraction scattering). This function could simulate a variety of forward-peaked, isotropic, and back-scattering combinations simply by adjusting the two parameters, $f_{is,\lambda}$ and $f_{bck,\lambda}$. The diffraction-dominated phase function, Φ_{DIFF}, was given by (Siegel and Howell, 1992):

$$\Phi_{\text{DIFF}}(\chi, \theta) = \chi^2 \left[\frac{2J_1[\chi \sin(\theta)]}{\chi \sin(\theta)}\right]^2 \quad (2)$$

The backscatter-dominated phase function, $\Phi_{\text{DIF REF}}$, was that for large, diffusely reflecting spheres given by (Siegel and Howell, 1992):

Nomenclature

a_λ = spectral absorption coefficient, m^{-1}
D = effective particle diameter, μm
D_f, D_p = fiber or filament diameter and pore diameter, respectively, μm
$f_{is,\lambda}$ = fraction of incident energy isotropically scattered
$f_{bck,\lambda}$ = fraction of incident energy back scattered
$f_{fwd,\lambda}$ = fraction of incident energy forward scattered = $1 - f_{is,\lambda} - f_{bck,\lambda}$
$g_{hg,\lambda}$ = spectral Henyey–Greenstein asymmetry factor
J_1 = Bessel function of the first kind and order 1
p = porosity
$Q_{e,\lambda}$ = spectral extinction efficiency
θ = angle between incident and scattering directions, rad
λ = wavelength, μm
K_λ = spectral extinction coefficient = $a_\lambda + \sigma_\lambda$, m^{-1}
σ_λ = spectral scattering coefficient, m^{-1}
Φ = single-scattering phase function
Φ_{DIFF} = diffraction-dominated phase function [Eq. (2)]
$\Phi_{\text{DIF REF}}$ = diffusely reflective phase function [Eq. (3)]
Φ_{hg} = modified Henyey–Greenstein phase function
χ = particle size parameter = $\pi D/\lambda$
Ψ = empirical geometry parameter in Eq. (6)

$$\Phi_{\text{DIF REF}}(\theta) = \frac{8}{3\pi}[\sin(\theta) - \theta\cos(\theta)] \quad (3)$$

When using this two-parameter phase function, energy conservation considerations created the constraint condition:

$$f_{is,\lambda} + f_{bck,\lambda} \leq 1 \quad (4)$$

McCarthy (1989) proposed a similar linear combination of Φ_{DIFF} and $\Phi_{\text{DIF REF}}$, but used a different interpretation of the linear coefficients and did not incorporate an isotropic scattering component.

The second phase function was a modified Henyey–Greenstein phase function (Prahl, 1988) given by the mathematical expression:

$$\Phi_{hg}(\lambda, \theta) = f_{is,\lambda} + (1 - f_{is,\lambda})\frac{(1 - g_{hg,\lambda}^2)}{(1 + g_{hg,\lambda}^2 - 2\,g_{hg,\lambda}\cos\theta)^{1.5}} \quad (5)$$

where $-1 \leq g_{hg,\lambda} \leq 1$. A variety of forward, isotropic, and back-scattering combinations could again be modeled simply by adjusting the two parameters, $f_{is,\lambda}$ and $g_{hg,\lambda}$. When using this function the constraint condition of Eq. (4) did not apply, thereby simplifying the inverse analysis process.

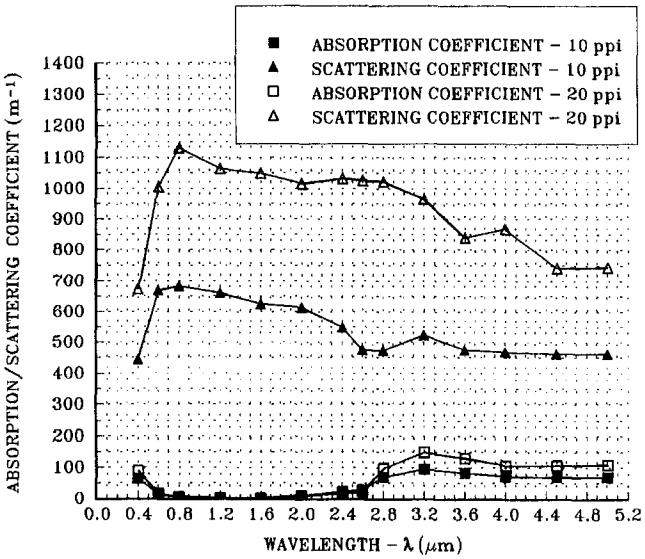

Fig. 1 Spectral absorption and scattering coefficients for PS ZrO_2 (DRIFD phase function)

Inverse Radiative Analysis Technique

The inverse analysis technique (Hendricks and Howell, 1994) essentially compared experimental reflectances and transmittances with radiative model predictions for two different sample thicknesses at each wavelength. Deviations between model predictions and experimental data were then minimized using a nonlinear, least-squares minimization algorithm based on a modified Levenberg–Marquardt method, active set strategy, and special numerical optimization techniques to incorporate constraint conditions. Two-dimensional, circumferentially symmetric S_6 discrete ordinates models, implementing a "diamond-difference" computation scheme and the LSH quadrature set (Fiveland, 1991), were used in the predictive analysis to calculate reflectances and transmittances under test conditions. These models incorporated the two-parameter phase functions discussed above, which introduced two additional parameters into the radiative models and inverse analysis. There were then a total of four variables to determine in the inverse radiative analysis; absorption coefficient, scattering coefficient, and two phase function parameters. This required multiple independent measurements (four as a minimum) on multiple sample thicknesses to provide enough information to retrieve the four variables simultaneously.

Discrete ordinates radiative methods were implemented in the predictive phase because they were easily integrated into the inverse analysis, are relatively straightforward to implement compared to other high-order radiative analysis methods, easily incorporate spectrally dependent properties, and higher-order models (i.e., S_6 and higher) have shown very accurate predictive capability. Direct transmittance of radiative energy was also possible with these RPCs. Hendricks and Howell (1995) discuss how this was quantified, the resulting modifications to the basic radiative transfer equation for RPCs, and the different modeling approaches possible with RPCs. The one serious defect of discrete ordinates, ray effects, was not a problem because ray effects are exacerbated by isolated radiative sources, purely absorbing media, and reflecting boundaries, and none of these characteristics existed in the analyses of our test conditions. Furthermore, highly scattering sources, which was a characteristic of our test analyses, tend to mitigate ray effects in discrete ordinates.

Experimental spectral reflectance and transmittance data were obtained for three different sample thicknesses of each material. Each sample thickness for a given material category provided a reflectance and transmittance test measurement at each wavelength; therefore two sample thicknesses were required as a minimum for the inverse analysis. The third set of spectral reflectances and transmittances could have been used in performing the inverse analysis to recover the spectral radiative properties. However, this significantly increased computational time in the inverse analysis because it required an additional S_6 model execution at each iteration. The third set of spectral reflectances and transmittances was used, instead, as verification on the coefficients and phase function parameters obtained in the inverse analysis. The recovered radiative properties were used to *predict* the third set of reflectances and transmittances using the same S_6 models as in the inverse analysis, thereby confirming the validity of the coefficients and phase function parameters recovered in the inverse analysis (Hendricks and Howell, 1994).

PS ZrO_2 Radiative Properties

DRIFD Phase Function. Figure 1 illustrates the spectral absorption and scattering coefficients (a_λ, σ_λ) recovered from the 10 ppi/20 ppi ZrO_2 reflectance and transmittance data using the DRIFD phase function. The spectral absorption coefficient for 10 ppi/20 ppi PS ZrO_2 exhibited very spectrally dependent behavior. The low absorption coefficients in the visible wavelengths (i.e., 0.4–0.7 μm) explain why PS ZrO_2 appears "white" on visual inspection. Spectral scattering coefficients for 10 ppi/20 ppi PS ZrO_2 were generally much higher than the absorption coefficients, and also demonstrated spectrally dependent behavior, which was smaller on a percentage basis than for the absorption coefficient.

The primary difference in radiative coefficients between 10 ppi and 20 ppi materials was that the scattering coefficients were much larger in the 20 ppi materials. The 20 ppi absorption coefficients were of approximately the same magnitude as for 10 ppi materials at short wavelengths $\leq$ 2.6 μm, but then increased to higher values than for 10 ppi absorption coefficients at longer wavelengths 2.8–5.0 μm. The 20 ppi absorption coefficients were expected to be larger than 10 ppi coefficients at shorter wavelengths also, but the inverse analysis technique was unable to resolve the differences at such low absolute magnitudes (i.e., 1 m^{-1}). Larger scattering and absorption coefficients were expected for 20 ppi materials because of smaller pore size, and correspondingly higher density of scattering and absorption sites, in the 20 ppi porous ceramic structure.

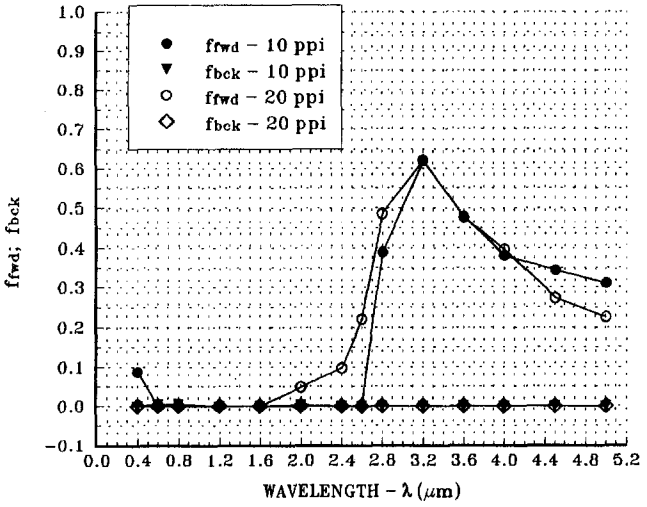

Fig. 2 Spectral DRIFD phase function parameters for PS ZrO_2

Figure 2 displays the spectral phase function parameters, $f_{fwd,\lambda}$ and $f_{bck,\lambda}$, recovered simultaneously in the DRIFD inverse analyses. A noteworthy finding was that the spectral phase function parameters produced an isotropic or nearly isotropic phase function ($f_{is,\lambda} = 1.0$) for wavelengths 0.4–2.4 μm, with at most only a small forward scattering component. Hale and Bohn (1993) *assumed* the phase function for reticulated porous alumina was isotropic in their work at 0.488 μm. This work substantiated their assumption at this particular wavelength. The wavelength range 2.6–3.2 μm was where some rather dramatic changes took place in the PS ZrO_2 scattering phase function. The scattering phase function changed abruptly from completely or nearly isotropic behavior at 2.4 μm to strongly forward-directed scattering behavior with a small isotropic contribution at 3.2 μm. This strong forward-scattering behavior caused sharp decreases in spectral reflectance to minimum values at 3.0–3.2 μm. It was noteworthy that the sharp reflectance changes in this region were caused by sharp changes in phase function character, rather than by significant scattering coefficient variations. One remarkable and surprising result was throughout the wavelength range the backscatter fraction, $f_{bck,\lambda}$, was found to be zero by the inverse analysis for both 10 ppi and 20 ppi ZrO_2. This means that no strong backscattering contribution was necessary in the scattering phase function to match the PS ZrO_2 spectral reflectance/transmittance test data. This result indicated that the strong backscatter component in McCarthy's scattering phase function data for PS ZrO_2 (1989) was caused by strong multiple scattering effects, rather than a specific single-scattering phase function contribution.

Figure 2 shows the spectral phase function behavior to be approximately equivalent in 10 ppi and 20 ppi PS ZrO_2 materials. Some optimum solution data suggested that the 10 ppi $f_{fwd,\lambda}$ curve might be slightly more rounded at 2.6 μm, but the data were inconclusive because the optimum solutions were not as good in minimizing the prediction/test deviation function as the optimum $f_{fwd,\lambda}$ shown in Fig. 2. One might expect that the 20 ppi $f_{fwd,\lambda}$ data should be closer to completely isotropic scattering conditions ($\approx$0.0) at 2.0–2.4 μm, but the inverse analysis technique was unable to resolve the small phase function difference represented by $f_{fwd,\lambda} = 0.1$ versus $f_{fwd,\lambda} = 0.0$. The important point was that the 20 ppi phase function exhibited highly isotropic behavior up to 2.4 μm, and then showed a sharp change toward forward-directed scattering at 2.6–3.2 μm. This behavior mirrored the 10 ppi phase function behavior. The decreasing behavior of $f_{fwd,\lambda}$ for 20 ppi materials at wavelengths 3.6–5.0 μm was also similar to 10 ppi materials. The smaller $f_{fwd,\lambda}$ factors for 20 ppi materials at 4.5 μm and 5.0 μm were actually consistent with what one would expect for the less "open" structure of 20 ppi PS ZrO_2; the less "open" structure reducing the forward-directed scattering in favor of more isotropic scattering behavior.

Modified Henyey–Greenstein Phase Function. In order to determine if better reflectance and transmittance prediction accuracy was possible, the modified Henyey–Greenstein (H-G) phase function was also investigated to recover the radiative properties through inverse analysis. This phase function was studied because it has the capability to model not only a very forward-peaked phase function behavior, but also a broader, more rounded behavior in the forward-directed angles simply by changing $g_{hg,\lambda}$ in Eq. (5).

Figure 3 illustrates the spectral absorption and scattering coefficients recovered by inverse analysis for 10 ppi/20 ppi PS ZrO_2. PS ZrO_2 absorption coefficients exhibited exactly the same behavior (i.e., spectral trends and magnitudes) in the short wavelengths 0.4–2.6 μm as in the DRIFD analysis. The 20 ppi absorption coefficients were expected to be larger at all wavelengths; but again, as discussed above, absorption coefficients for 10 ppi/20 ppi PS ZrO_2 were so low at $\lambda \leq 2.6$ μm it was difficult to discern any differences between the 10 ppi and 20 ppi materials. In the 2.8–5.0 μm range, absorption coefficients also exhibited spectral behavior similar to the DRIFD analysis and did show higher magnitudes for 20 ppi materials compared to 10 ppi materials. Scattering coefficients exhibited relatively small spectral variations on a percentage basis, and showed slightly different spectral behavior and different magnitudes using the H-G phase function compared to the DRIFD function. The reason for this was the modified H-G function produced a much flatter, more rounded, and continuous phase function behavior, which was a distinct contrast to the sharply forward-peaked DRIFD phase functions that were difficult to model in the discrete ordinates formulation. The combined effect of the slightly different scattering coefficients and phase function behavior produced significantly better transmittance prediction accuracy during the inverse analysis. The predominant difference in scattering coefficients between 10 ppi and 20 ppi materials was again that scattering coefficients were much larger in the 20 ppi materials due to higher scattering site number densities.

Figure 4 presents the spectral phase function parameters, $f_{is,\lambda}$ and $g_{hg,\lambda}$, simultaneously determined by inverse analysis with this phase function. The 20 ppi phase function exhibited the same spectral behavior as in 10 ppi materials, but with slightly

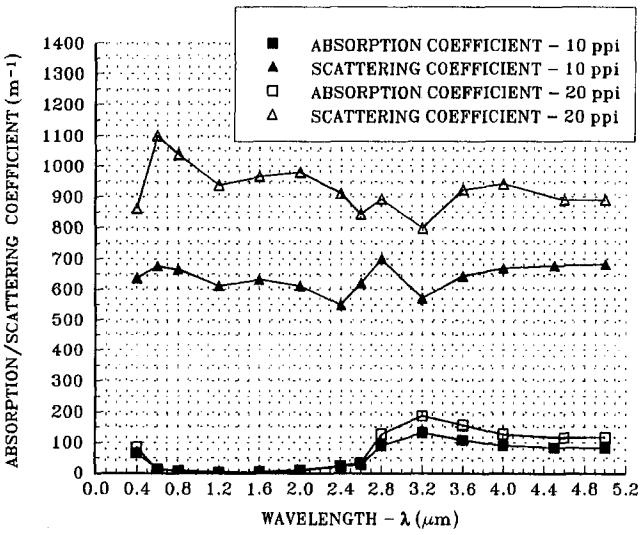

Fig. 3 Spectral absorption and scattering coefficients for PS ZrO_2 (H-G phase function)

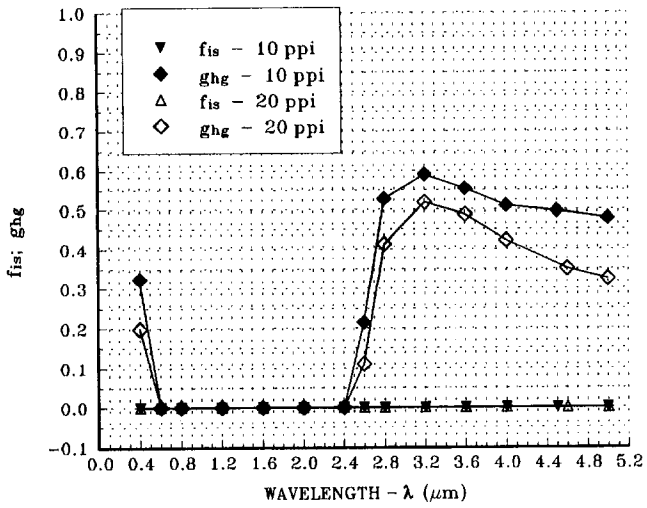

Fig. 4 Spectral H-G phase function parameters for PS ZrO_2

less forward-directed scattering character at the long wavelengths 2.6–5.0 μm. This was consistent with the less "open" structure of 20 ppi materials, which would decrease the forward-directed scattering in lieu of more isotropic scattering behavior. This effect was shown more consistently in modified H-G analysis results, probably due to more consistently accurate integration of the scattering contributions using the H-G phase function. Figure 4 also shows the phase function again abruptly transformed from isotropic behavior to distinctly forward-directed scattering behavior at 2.6–3.2 μm in both 10 ppi and 20 ppi materials. As in the DRIFD results, this phase function behavior was the major cause for the sharp decrease in PS ZrO_2 reflectance at these wavelengths. The scattering coefficient variations in this wavelength range, although certainly noticeable, were relatively small on a percentage basis compared to the dramatic phase function changes.

It was interesting and significant that similar changes in phase function behavior were detected at 2.6–2.8 μm in PS ZrO_2 by performing the inverse analysis with two different phase functions. It was not likely that modeling idiosyncrasies associated with either of the phase function models could have caused exactly the same observed behavior. The phase function changes in this wavelength region warrant further study to determine what radiative interaction within PS ZrO_2 is responsible for this behavior.

One remarkable and interesting result was that $f_{is,\lambda}$ was found to be zero throughout the entire wavelength spectrum in the inverse analysis. The single-parameter Henyey–Greenstein phase function was able to model the phase function characteristics quite adequately in predicting the reflectance and transmittance test data. Equally important was the fact that $g_{hg,\lambda} \geq 0$ for the optimum phase functions, which indicates either isotropic scattering or forward-directed scattering. This again supports the conclusion that strong back scattering in RPCs is due to strong multiple scattering effects, rather than a specific single-scattering phase function component.

In general, the set of optimum spectral radiative properties with the Henyey–Greenstein phase function in the discrete ordinates models did a more consistent and better job of predicting the 10 ppi/20 ppi ZrO_2 reflectance and transmittance test data than the radiative properties from the DRIFD inverse analyses. The modified Henyey–Greenstein function was the better performing phase function for 10 ppi/20 ppi PS ZrO_2 both in predicting test data and detecting phase function characteristics and differences. The reason was the Henyey–Greenstein function is a smoother, more continuous function with no sharp peaks or discontinuities to accommodate in the radiative modeling. Therefore, the discrete ordinates models, with only a limited number of discrete intensities in specific directions, could more accurately integrate the scattering contributions in the RTE.

Table 1 shows the spectral radiative properties recovered for 65 ppi PS ZrO_2 using the H-G phase function in the inverse analysis. Absorption coefficients showed the same general trends observed in 10 ppi and 20 ppi materials. In general, 65 ppi absorption coefficients were significantly larger than those for 20 ppi materials as expected. Scattering coefficients for 65 ppi PS ZrO_2 were also discovered to be extremely high compared to those for 10 ppi and 20 ppi materials. The extremely high scattering coefficients resulted directly from the high reflectances measured for 65 ppi materials (i.e., highest reflectances measured in this study). The expected increasing trend in absorption and scattering coefficients from 10 ppi to 65 ppi materials was again because of increasing number density of absorbing and scattering sites in higher ppi materials.

Another very interesting result exhibited in Table 1 was that optimum or near-optimum phase functions throughout the wavelength spectrum were either completely or nearly isotropic. This was consistent with the general pattern toward more isotropic scattering behavior exhibited from 10 ppi to 20 ppi materials. This phase function behavior was caused by: (1) the increasing number density of scattering sites, which are more randomly oriented in the higher ppi materials, and (2) the corresponding significant decrease in direct forward transmittance in higher ppi materials.

The very high scattering coefficients here created very severe computational stability and accuracy requirements in the discrete ordinates models, which limited the number of optimum solutions found for 65 ppi PS ZrO_2. Hendricks and Howell (1994) discuss the computational problems in the inverse analysis technique associated with these extremely high scattering coefficients. Despite the computational problems, Table 1 was created from: (1) the few successfully converged optimum solu-

Table 1 Spectral radiative properties of 65 ppi partially stabilized ZrO_2 (modified Henyey–Greenstein phase function)

Wavelength (μm)	Absorption Coefficient (m^{-1})	Scattering Coefficient (m^{-1})	$f_{is,\lambda}$	$g_{hg,\lambda}$	Remarks
0.4	163±10%	3149±15%	0.0	0.0	Converged Optimum
0.6	30±100%	3600±20%	0.0	0.0	Non-Converged
1.2	10±100%	3300±20%	0.0	0.0	Non-Converged
2.0	20±100%	3324±20%	0.0	0.0	Non-Converged
2.8	250±10%	2300±15%	0.0	0.0	Converged Optimum
4.0	289±10%	1712±15%	0.0	-0.14	Converged Optimum
4.5	225±10%	2273±15%	0.0	0.050	Converged Optimum
5.0	215±10%	2345±15%	0.0	0.079	Converged Optimum

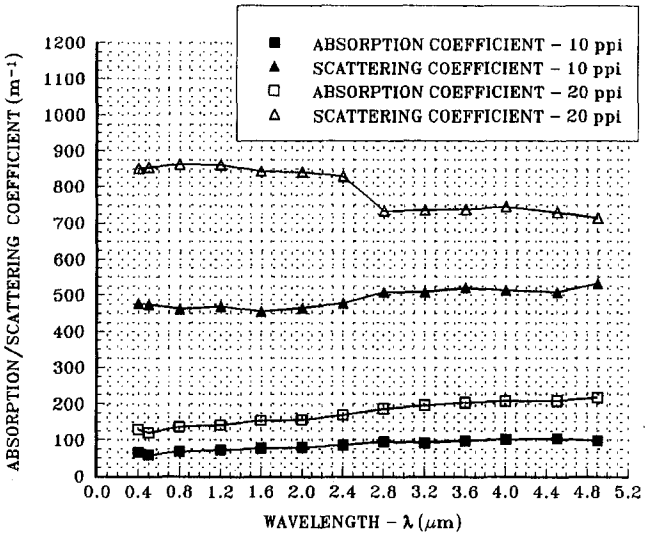

Fig. 5 Spectral absorption and scattering coefficients for OB SiC (DRIFD phase function)

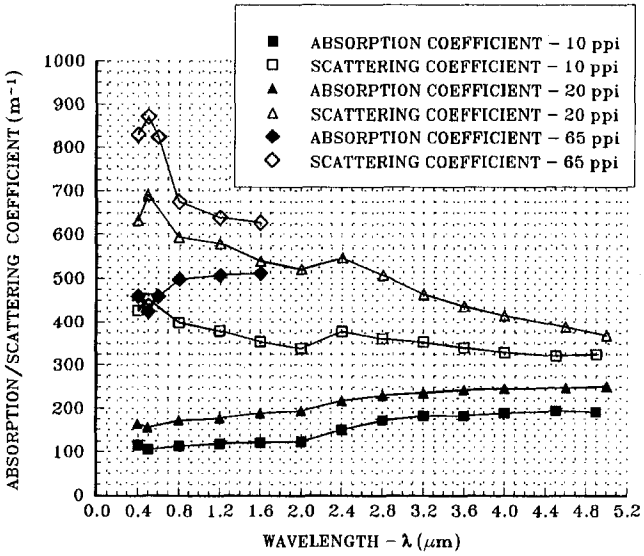

Fig. 7 Spectral absorption and scattering coefficients for OB SiC (H-G phase function)

tions determined by the inverse analyses, and (2) observing the many interim computations performed during the nonconverging analyses to at least determine estimates of optimum solutions.

OB SiC Radiative Properties

DRIFD Phase Function. Figure 5 shows the absorption and scattering coefficients recovered for 10 ppi/20 ppi OB SiC using the DRIFD phase function in the inverse analysis. The absorption and scattering coefficients both exhibited only small spectral variations for these materials, a sharp contrast to PS ZrO_2 spectral behavior. OB SiC absorption coefficients were also much higher than corresponding PS ZrO_2 absorption coefficients (Fig. 1) at all wavelengths, particularly at the short wavelengths 0.4–2.6 μm where the OB SiC absorption coefficient were 5–10 times higher than in PS ZrO_2. The higher absorption coefficients in the visible wavelengths (0.4–0.7 μm) explains why OB SiC appears "gray" upon visual inspection.

Radiative properties for 10 ppi and 20 ppi materials showed the same spectral behavior, only at different magnitudes for the absorption and scattering coefficients and phase function parameters. Figure 5 shows the 20 ppi absorption and scattering coefficients were significantly larger than for 10 ppi materials as expected, again consistent with the larger number density of absorption and scattering sites in the 20 ppi structure. The noticeable dip in scattering coefficient at about 2.6 μm was believed to be an artifact of transmittance and reflectance measurement uncertainties in the 20 ppi materials.

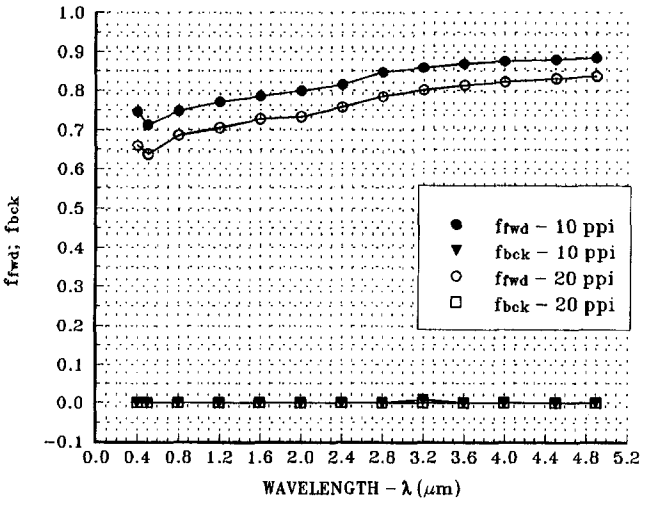

Fig. 6 Spectral DRIFD phase function parameters for OB SiC

Figure 6 illustrates the phase function parameters, $f_{fwd,\lambda}$ and $f_{bck,\lambda}$, simultaneously retrieved in the inverse analyses. These phase function parameters represented a relatively strong forward-directed scattering component in the phase function for 10 ppi and 20 ppi materials and showed little change across the wavelength range. Remarkably, $f_{bck,\lambda}$, was again found to be zero at all wavelengths, indicating no specific back-scattering component to the phase function; again showing the strong back scatter in the McCarthy SiC scattering data (1989) was due to strong multiple scattering effects rather than a specific phase function component. The slight decrease in $f_{fwd,\lambda}$ at 0.5 μm was due to the reflectance maximum at 0.5 μm for OB SiC, the phase function becoming slightly more isotropic and less forward-directed to accommodate the reflectance increase. The steady increase in $f_{fwd,\lambda}$ for 0.6–5.0 μm represents a gradual shifting of phase function behavior toward less isotropic behavior and more forward-directed scattering behavior. This effect, and an increasing absorption coefficient, explained the gradually decreasing reflectance with wavelength exhibited by OB SiC after 0.5 μm. Figure 6 also shows the expected behavior of lower $f_{fwd,\lambda}$ in 20 ppi materials compared to 10 ppi materials, indicating more isotropic scattering behavior in 20 ppi materials as expected.

Modified Henyey–Greenstein Phase Function. The OB SiC inverse analysis was also performed using the modified H-G phase function to again determine whether better reflectance and transmittance prediction accuracy was possible.

Figure 7 displays the spectral absorption and scattering coefficients for 10 ppi/20 ppi/65 ppi OB SiC discovered using the H-G phase function. The 10 ppi/20 ppi/65 ppi absorption coefficients all exhibited the same characteristic gradual increase with wavelength. The relatively high absorption coefficients for OB SiC confirmed its superior absorption capabilities relative to PS ZrO_2. The 10 ppi/20 ppi/65 ppi scattering coefficients exhibited gradually decreasing behavior with increasing wavelength, after an initial peak at 0.5 μm due to the characteristic reflectance maximum of OB SiC at 0.5 μm. It was the combined effect of decreasing scattering coefficients and in-

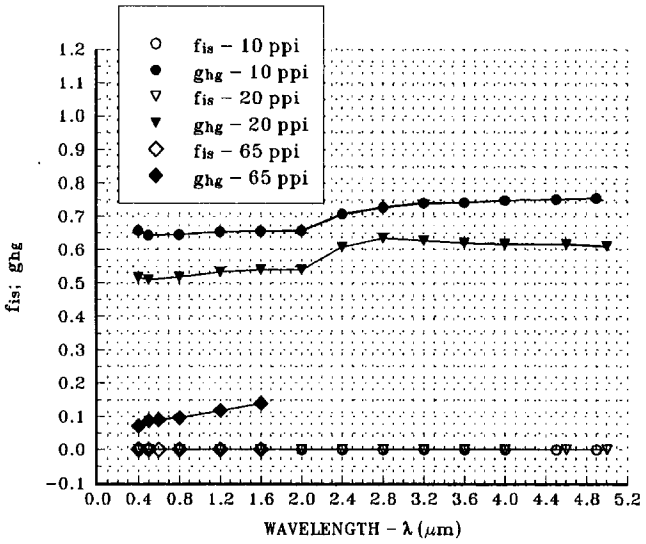

Fig. 8 Spectral H-G phase function parameters for OB SiC

creasing absorption coefficients with wavelength that caused the decreasing reflectance and nearly constant transmittance with wavelength for OB SiC.

The basic difference in 10 ppi/20 ppi/65 ppi absorption and scattering coefficients was again that higher ppi materials demonstrated higher coefficient magnitudes as expected. In particular, Fig. 7 reveals a large increase in absorption coefficients for 65 ppi OB SiC compared to 10 ppi and 20 ppi materials, absorption processes definitely being more dominant in 65 ppi OB SiC materials than in 10 ppi materials. Figure 7 also shows a significant increase in scattering coefficient for 65 ppi OB SiC relative to 20 ppi and 10 ppi materials. Scattering coefficient spectral variations were still consistent among the 10 ppi, 20 ppi, and 65 ppi materials.

The spectral absorption and scattering coefficients demonstrated much different spectral behavior and magnitudes using the H-G phase function compared to the DRIFD phase function (compare Figs. 5 and 7). These scattering coefficient differences are attributable to the much different directional scattering behavior represented by these two phase functions. The very different coefficient behavior in Figs. 5 and 7 highlights the importance of what phase function representation is chosen and its directional behavior in the radiative models used in inverse analyses. It emphasizes the need to use compatible sets of radiative coefficients and phase functions, and to determine radiative coefficients and phase functions simultaneously in an inverse analysis process.

Figure 8 shows the spectral phase function parameters for 10 ppi/20 ppi/65 ppi OB SiC simultaneously recovered in the inverse analysis using the H-G phase function. The phase function parameter, $f_{is,\lambda}$, was again found to be zero at all wavelengths for all three materials. The phase function parameter, $g_{hg,\lambda}$, displayed a small gradual shift as wavelength increased from 0.4 μm to 4.9 μm in 10 ppi and 20 ppi materials, representing a generally forward scattering phase function across the wavelength range. The scattering phase function characteristics of 20 ppi OB SiC showed the expected trend toward more isotropic and less forward-directed scattering, with 20 ppi materials having $f_{is,\lambda} = 0$ and lower $g_{hg,\lambda}$ compared to 10 ppi phase functions. More isotropic scattering in 20 ppi materials was again consistent with the less "open" structure and higher density of randomly scattering sites in 20 ppi materials. It was interesting to note that 10 ppi and 20 ppi OB SiC had a more forward scattering phase function than was found in 10 ppi and 20 ppi PS ZrO_2 using the modified H-G function (compare Figs. 4 and 8). This was compatible with the fact that 10 ppi/20 ppi OB SiC has a more "open" structure compared to 10 ppi/20 ppi PS ZrO_2, causing more forward scattering of energy when treating the SiC/ZrO_2 structures as homogeneous materials.

Figure 8 also displays some very significant changes in phase function behavior for 65 ppi OB SiC relative to 20 ppi and 10 ppi materials. The Henyey–Greenstein coefficient, $g_{hg,\lambda}$, was discovered to be approximately 0.1, with the parameter, $f_{is,\lambda}$, again being zero. This combination of $f_{is,\lambda}$ and $g_{hg,\lambda}$ represents a very nearly isotropic phase function for 65 ppi materials. This was not surprising as 65 ppi SiC materials have much smaller pore sizes and much higher scattering site number densities than 20 ppi and 10 ppi materials. The direct transmittance through 65 ppi OB SiC was also very small; therefore, one would expect less forward-directed scattering behavior.

Table 2 Scattering albedo for different ppi ratings of PS ZrO_2 and OB SiC

ppi Rating	PS ZrO_2 DRIFD P.F.	PS ZrO_2 H-G P.F.	OB SiC DRIFD P.F.	OB SiC H-G P.F.
10 ppi	0.85-0.998	0.81-0.999	0.83-0.888	0.62-0.81
20 ppi	0.87-0.999	0.81-0.998	0.76-0.877	0.60-0.80
65 ppi	---	0.90-0.997	---	0.55-0.67

Parameter Sensitivity Studies

Measurement uncertainties in the spectral reflectances and transmittances ($\pm$10 percent) necessarily created an uncertainty in the radiative coefficients and phase function parameters recovered in the inverse analysis. Coefficient/parameter sensitivities were evaluated at some wavelengths for PS ZrO_2 and OB SiC by introducing a $\pm$10 percent error into the reflectance/transmittance measurements and re-performing the inverse analysis. The recovered radiative coefficients showed the following sensitivities or uncertainties due to the re-inversion process: (*a*) for ZrO_2, $\pm$18 percent variation in absorption coefficients and $\pm$20 percent variation in scattering coefficients; (*b*) for OB SiC, $\pm$11 percent variation in absorption coefficients and $\pm$7 percent variation in scattering coefficients. The phase function parameters were found not to vary as much in this process; in isotropic scattering cases no change in phase function parameters occurred, and in anisotropic cases only a $\pm$10 percent variation (uncertainty) occurred. These sensitivity investigations established that the inverse analysis method is robust and reliable, and quantified just how accurately the recovered coefficients/parameters are really known.

Other sensitivity studies were done by keeping reflectance/transmittance measurements the same and varying the coefficient and parameter initial guesses in the inverse analysis. Variations in recovered coefficients and phase function parameters in these cases were typically small in the range of 3–5 percent. The inverse analysis method was generally quite good at reproducing results.

Scattering Albedo Variations

Scattering albedos (σ_λ/K_λ) were also calculated from the absorption and scattering coefficient data for PS ZrO_2 and OB SiC. Table 2 summarizes the spectral scattering albedo variations discovered using the DRIFD phase function and H-G phase function.

One important result from the DRIFD scattering albedo data for 10 ppi and 20 ppi PS ZrO_2 was that the scattering albedo generally increased for 20 ppi materials relative to 10 ppi materials at all wavelengths. The DRIFD scattering albedo data for 10 ppi and 20 ppi OB SiC revealed the albedo for 20 ppi OB

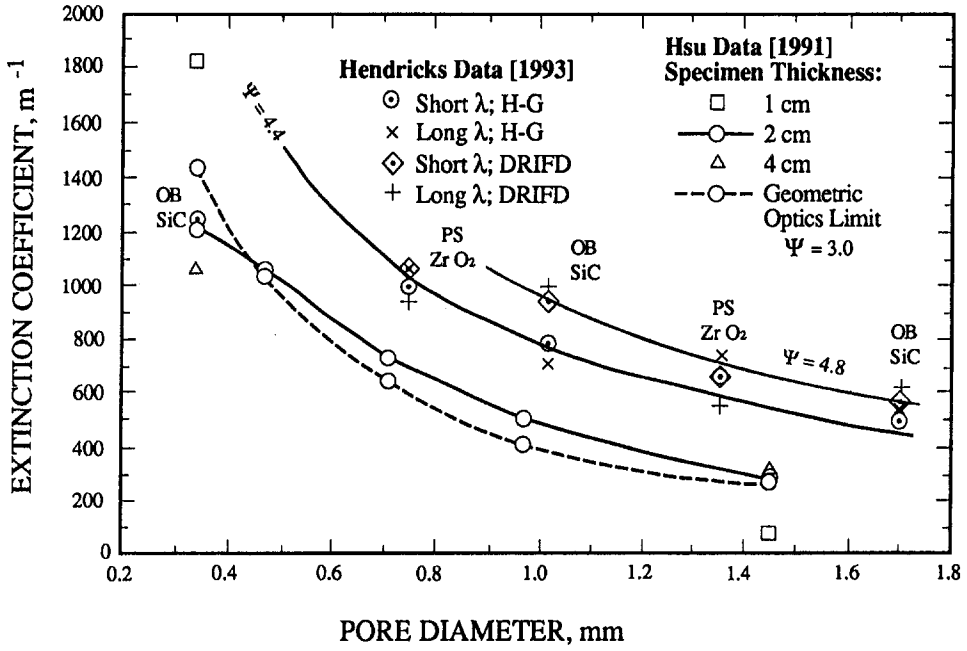

Fig. 9 Comparisons with geometric optics extinction model

SiC generally decreased compared to 10 ppi materials at all wavelengths. These results contradicted the assumption of Hale and Bohn (1993) in their radiative property work on reticulated alumina, in which they assumed that the scattering albedo was constant between 10 ppi, 20 ppi, 30 ppi, and 65 ppi materials. Table 2 also shows the OB SiC albedos were generally lower than PS ZrO_2 scattering albedos in the DRIFD phase function case.

The H-G scattering albedo data for PS ZrO_2 did show some anomalies in the albedo trends. At some of the wavelengths, the scattering albedo was higher in 20 ppi PS ZrO_2 than in 10 ppi materials. However, at the other wavelengths, the albedo for 20 ppi PS ZrO_2 was actually approximately the same or slightly lower than in 10 ppi materials. The H-G scattering albedo for 65 ppi PS ZrO_2 did again demonstrate the increasing trend compared to 20 ppi and 10 ppi materials at wavelengths for which optimum solutions were achieved; this helped to alleviate the uncertainty created by the inconclusive 20 ppi PS ZrO_2 albedo data. This points out how precarious it is to assume anything about the albedo between these different ppi categories for RPCs. The phase function choice plays a large role in the albedo behavior. The advantage of this inverse analysis technique was it allowed simulation of a wide variety of phase function behaviors in determining the optimum combination of absorption and scattering coefficients and phase function which satisfied the experimental data.

The H-G scattering albedos for 20 ppi and 65 ppi OB SiC repeated the generally decreasing trend as ppi rating increased at most wavelengths. 20 ppi OB SiC had lower scattering albedos than 10 ppi materials and 65 ppi OB SiC scattering albedos were much lower than in 20 ppi materials. The H-G scattering albedos for OB SiC were also much lower than corresponding albedos in PS ZrO_2, thereby supporting the same observations using the DRIFD phase function.

Geometric Optics Extinction Model

Hsu and Howell (1992) developed an extinction coefficient model for RPCs based on geometric optics theory, in which pore diameter, D_p, and porosity, p, were the major empirical parameters:

$$K\ [mm^{-1}] = \frac{\Psi}{D_p\ [mm]}(1 - p) \tag{6}$$

and $\Psi = 3$. Hsu developed this equation by considering the porous ceramic as a suspension of monodispersed, independently scattering spherical particles of pore diameter, D_p. This model was shown to work well in predicting measured total extinction coefficients in PS ZrO_2 for pore diameters larger than 0.6 mm (Hsu and Howell, 1992), which essentially applies to 10 ppi and 20 ppi materials here.

Extinction coefficients determined from the absorption and scattering coefficients of this research were also compared with values predicted by Eq. (6) for PS ZrO_2 ($p \approx 0.85$) and OB SiC ($p \approx 0.80$). Figure 9 illustrates the comparison between the extinction coefficients determined here and predicted values from Eq. (6). Extinction coefficients at long wavelengths (Long λ) and short wavelengths (Short λ), which represent upper and lower bounds on the wavelength-integrated extinction coefficients, are shown in Fig. 9. Experimental extinction coefficients for OB SiC and PS ZrO_2 were generally higher than predicted by Eq. (6) with $\Psi = 3$, but correlated well with Eq. (6) if the parameter Ψ was adjusted to $\Psi = 4.4$ for PS ZrO_2 and $\Psi = 4.8$ for OB SiC.

Tong and Li (1995) show that the extinction coefficient and extinction efficiency in porous media are theoretically related by:

$$\overline{K_\lambda} = \left(\frac{4\overline{Q_{e,\lambda}}}{\pi D_f}\right)(1 - p) \tag{7}$$

where D_f is the fiber or filament diameter. If one uses appropriate OB SiC filament diameters given earlier, Eq. (7) indicates the extinction coefficient for a porous media of SiC fibers or filaments corresponding to 10 ppi and 20 ppi OB SiC (1.7 mm and 1.0 mm pore diameters, respectively) should be approximately 742–835 m^{-1} and 1000–1125 m^{-1}, respectively. This theoretical estimate agrees well with experimentally derived OB SiC extinction coefficients shown in Fig. 9. In addition, relating D_f to D_p for RPCs in Eq. (6) and then comparing Eqs. (6) and (7), the average extinction efficiencies of PS ZrO_2 and OB SiC fibers or filaments for $\lambda = 0.4$–5.0 μm were found to be 1.45 and 1.70, respectively. Tong and Li (1995) determined the

theoretical extinction efficiency of SiC fibers for 0.4–5.0 μm to be about 2.0 $\pm$ 10 percent, thus showing good agreement with this work considering the differences in SiC fibers in the two studies. This research therefore shows that radiative processes in RPCs are governed by the laws of geometric optics, with minor adjustments to the resulting relationships, and by independent scattering and absorption radiative mechanisms.

Conclusions

This research has revealed several conclusions concerning the spectral radiative properties of PS ZrO_2 and OB SiC reticulated porous ceramics (RPCs) in the wavelength range 0.4–5.0 μm. PS ZrO_2 spectral radiative properties were discovered to be strongly dependent on wavelength, particularly the absorption coefficient and phase function. In contrast, OB SiC spectral radiative properties were found relatively independent of wavelength, showing only slow changes with wavelength. OB SiC demonstrated superior absorption characteristics, with absorption coefficients that were much higher than those for PS ZrO_2 at all wavelengths. PS ZrO_2 generally demonstrated very high scattering albedos in the range 0.85–0.999, while OB SiC showed much lower scattering albedos in the range 0.55–0.888. The scattering albedo in PS ZrO_2 increased with increasing ppi rating (i.e., smaller pore diameters), while the scattering albedo in OB SiC decreased with increasing ppi rating.

DRIFD and Henyey–Greenstein phase functions both were successful in recovering useful radiative property information for PS ZrO_2 and OB SiC. Henyey–Greenstein phase function results were found slightly superior to DRIFD phase function results in predicting reflectance and transmittance test data, and consistently detecting proper phase function behavior and differences among various ppi materials.

Total extinction coefficients based on experimental absorption and scattering coefficients from this research correlated well with a geometric optics theoretical model, and an electromagnetic wave/fiber interaction model based on independent scattering and absorption radiative mechanisms. The average extinction efficiency at wavelengths 0.4–5.0 μm was found to be 1.45 for PS ZrO_2 and 1.70 for OB SiC.

Acknowledgments

The authors gratefully acknowledge the State of Texas Higher Education Coordinating Board under Energy Research Applications Program Grant No. ERAP-19889 for funding to support this work.

References

Bohn, M. S., and Mehos, M. S., 1990, "Radiative Transport Models for Solar Thermal Receiver/Reactors," *Proceedings, 12th ASME International Solar Energy Conf.*, J. T. Beard and M. A. Ebadian, eds., ASME, New York, pp. 175–182.

Couch, W. A., ed., 1989, *Proceedings, Annual Solar Thermal Technology Research and Development Conference,* SAND89-0463, Sandia National Laboratories, Albuquerque, NM.

Fiveland, W. A., 1991, "The Selection of Discrete Ordinates Quadrature Sets for Anisotropic Scattering," *Fundamentals of Radiation Heat Transfer,* ASME HTD-Vol. 160, pp. 89–96.

Hale, M. J., and Bohn, M. S., 1993, "Measurement of the Radiative Transport Properties of Reticulated Alumina Foams," *Proceedings, ASME/ASES Joint Solar Energy Conf.*, A. Kirkpatrick and W. Worek, eds., ASME, New York, pp. 507–515.

Hendricks, T. J., 1993, "Thermal Radiative Properties and Modelling of Reticulated Porous Ceramics," Ph.D. Dissertation, University of Texas at Austin.

Hendricks, T. J., and Howell, J. R., 1994, "Inverse Radiative Analysis to Determine Spectral Radiative Properties Using Discrete Ordinates Techniques," *Proceedings, 10th International Heat Transfer Conf.*, G. F. Hewitt et al., eds., Institution of Chemical Engineers, United Kingdom, Vol. 2, pp. 75–80.

Hendricks, T. J., and Howell, J. R., 1995, "Novel Discrete Ordinates Radiative Modeling in Reticulated Porous Ceramics," *Proceedings, 30th National Heat Transfer Conference,* ASME HTD-Vol. 315, pp. 21–27.

Hsu, P.-F., and Howell, J. R., 1992, "Measurements of Thermal Conductivity and Optical Properties of Porous Partially Stabilized Zirconia," *Experimental Heat Transfer,* Vol. 5, pp. 293–313.

McCarthy, T. A., 1989, "Measurements of Infrared Radiative Transfer for Porous Ceramic Materials," Master's Thesis, University of Illinois at Urbana–Champaign.

Prahl, S. A., 1988, "Light Transport in Tissue," Ph.D. Dissertation, University of Texas at Austin.

Siegel, R., and Howell, J. R., 1992, *Thermal Radiation Heat Transfer,* 3rd ed., Hemisphere Publishing Corp., Washington, DC.

Skocypec, R. D., Hogan, R. E., Jr., and Muir, J. F., 1991, "Solar Reforming of Methane in a Direct Absorption Catalytic Reactor on a Parabolic Dish: II—Modeling and Analysis," *Proceedings, 1991 ASME–ISME 2nd International Solar Energy Conf.*, T. R. Mancini et al., eds., ASME, pp. 303–310.

Tong, T. W., and Li, W., 1995, "Enhancement of Thermal Emission From Porous Radiant Burners," *Journal of Quantitative Spectroscopy & Radiative Transfer,* Vol. 53, No. 2, pp. 235–248.

Heat Transfer in Open Cell Foam Insulation

D. Doermann

J. F. Sacadura

Centre de Thermique-URA CNRS 1372,
Institut National des Sciences
Appliquées de Lyon,
69621-Villeurbanne Cedex, France

Heat transfer in open cell foam insulation occurs by conduction through the solid material and through the gas in the cell interior and by thermal radiation, which propagates through the structure. The conductive process within these media is described using a simple parallel-series model. Spectral volumetric absorption and scattering coefficients as well as the spectral phase function are predicted using a combination of geometric optics laws and diffraction theory to model the interaction of radiation with the particles forming the foam. The particles considered are both struts formed at the juncture of three cells and strut junctures. The radiative properties can then be utilized to obtain a weighted extinction coefficient, which can be used in the Rosseland equation to obtain the radiative flux. The innovative part of the work lies in the radiative properties predictive model. This new model is compared with simpler ones.

1 Introduction

Open cell carbon foam can be used as efficient thermal insulation for high-temperature applications. Insulating foam consists of a highly porous solid material. Foam cell appears to resemble closely a pentagonal dodecahedron (Fig. 1) (Glicksman and Torpey, 1987b; Glicksman et al., 1992; Kuhn et al., 1992). In open cell foam insulation, heat transfer occurs by conduction through the solid phase consisting of struts (Fig. 1) and conduction through the gas phase and by thermal radiation. Attenuation of thermal radiation occurs via scattering and absorption by struts formed at the junction of three cells.

This paper presents a predictive model for thermal transfer in open cell foam insulation as a function of foam morphology, porosity, thermal properties of solid and gas phases, and optical properties of the solid phase. Previous works on prediction of thermal transfer in foam insulation are recalled here. In recent papers (Glicksman and Torpey, 1987b; Glicksman et al., 1992; Kuhn et al., 1992) the conductive process within this kind of structure is commonly described by using a simple parallel-series model and the Rosseland weighting function is used to determine the radiative conductivity. These models have been proved to provide good results for foam insulation (Glicksman et al., 1987). The main difficulty remains the prediction of radiative properties of these complex materials. Two different models have been adopted to determine radiative properties of foam insulation:

- Glicksman and Torpey (1987b), and Glicksman et al. (1992) considered foam as a set of randomly oriented blackbody struts and used an efficiency factor of one. They neglected scattering by struts. The strut cross section was constant and occupied two thirds of the area of an equilateral triangle formed at the vertices (Fig. 1). The resulting extinction coefficient is a function of the cell diameter and the foam porosity.
- Kuhn et al. (1992) used infinitely long randomly oriented cylinders to describe the struts. The triangular cross sections were converted into circular ones with the same geometric mean cross section. Then they used Mie scattering calculations to predict the radiative properties.

Glicksman's model seems to be interesting because it is applicable to the strut shape (the struts are not very long and their cross section is not circular but roughly triangular). However, the particle modeling is very simple and does not account for strut juncture. Moreover, this model does not account for the scattering phenomena by the particles. In this paper a more realistic representation of foam particles is adopted and scattering phenomena are taken into account.

First of all the usual equations governing heat transfer in foam are recalled.

Then the new predictive model for the foam radiative properties will be described.

Finally, an application to a carbon foam insulation will enable us to compare the improved model to simpler ones.

2 Usual Model Equations Governing Heat Transfer in Foam Insulation

The radiative flux q_r can be added to the flux due to conduction through the gas and the solid phases forming the cell to yield the total heat flux q. For one-dimensional steady heat transfer the energy equation is given by:

$$\frac{dq}{dx} = 0 \tag{1}$$

with

$$q = -k_c \frac{dT}{dx} + q_r \tag{2}$$

Foam insulation is usually thick enough to be considered as optically thick. So the radiative flux can be approximated by the Rosseland equation (Glicksman and Torpey, 1987a, b; Glicksman et al., 1987, 1992):

$$q_r = -k_r \frac{dT}{dx}$$

$$k_r = \frac{16\sigma T^3}{3K_R} \tag{3}$$

where K_R is the Rosseland mean extinction coefficient defined by the following relation:

$$\frac{1}{K_R} = \int_0^\infty \frac{1}{K_\lambda} \frac{\partial e_{b\lambda}}{\partial e_b} d\lambda \tag{4}$$

The Rosseland equation is valid when the medium absorbs and scatters isotropically (Hottel and Sarofim, 1967). Scattering measurements have shown that scattering by foam is highly

Contributed by the Heat Transfer Division for publication in the JOURNAL OF HEAT TRANSFER. Manuscript received by the Heat Transfer Division October 1994; revision received July 1995. Keywords: Modeling and Scaling, Porous Media, Radiation. Associate Technical Editor: M. F. Modest.

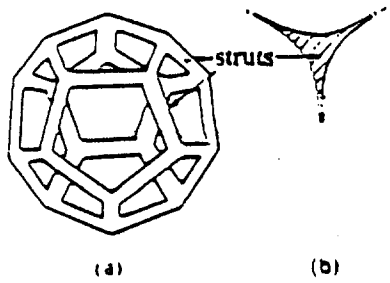

Fig. 1 Dodecaeder model for a foam cell: (*a*) perspective view; (*b*) cross section through struts

anisotropic (Glicksman et al., 1987). If the Rosseland equation is used for this case with the extinction coefficient, there will be considerable inaccuracy on the predicted flux.

A weighted scattering coefficient has been suggested to account for anisotropic scattering (Hottel and Sarofim, 1967; Lee and Buckius, 1982):

$$\sigma_{s\lambda}^{*} = \sigma_{s\lambda}(1 - \langle \cos\theta \rangle_{\lambda}) \tag{5}$$

with

$$\langle \cos\theta \rangle_{\lambda} = 0.5 \int_{-1}^{1} \Phi_{\lambda}(\theta) \cos\theta d(\cos\theta) \tag{6}$$

where $\Phi_{\lambda}(\theta)$ is the spectral volumetric phase function, $\sigma_{s\lambda}$ is the spectral volumetric scattering coefficient.

A weighted spectral extinction coefficient can be deduced:

$$K_{\lambda}^{*} = \alpha_{\lambda} + \sigma_{s\lambda}^{*} \tag{7}$$

where α_{λ} is the spectral volumetric absorption coefficient. K_{λ}^{*} is then used in the solution for isotropic scattering media.

According to Glicksman et al. (1987), the use of the weighted extinction coefficient in the diffusion equation would be valid for insulations of moderate or large optical thicknesses. Glicksman et al. (1987) and Kuhn et al. (1992) have adopted this weighted coefficient for foam insulation.

To evaluate heat transfer it is necessary to determine both the conductivity in the absence of radiation, k_c, and the radiative properties of open cell foam used to determine the weighted spectral extinction coefficient K_{λ}^{*} (Eqs. (5) to (7)). A model equation (Schuetz and Glicksman, 1984), which predicts the phonic thermal conductivity of an isotropic open cell foam sample, has been developed based upon the physical properties and the porosity of foam insulation. Equation (8) includes the two independent mechanisms of conduction heat transfer: conduction through the gas and through the solid material forming the cell:

$$k_c = k_{\text{gas}} + \tfrac{1}{3}(1 - \delta)k_{\text{solid}} \tag{8}$$

where δ is the void fraction or porosity of the foam.

This equation has been proved to lead to a satisfactory representation of the foam conductivity and it was used in recent works (Glicksman and Torpey, 1987b; Glicksman et al., 1992; Kuhn et al., 1992). Therefore this equation was adopted in the present work.

In the next part the model developed to predict the radiative properties of open cell foams is presented.

3 Prediction of the Radiative Properties

The radiative properties of foam are required in Eqs. (5) to (7) to determine the weighted extinction coefficient used in the Rosseland equation. They are the spectral volumetric scattering and absorption coefficients and the spectral volumetric phase function. They can be obtained from the radiative properties of particles forming foam by adding up the effects of all the particles of different sizes (Brewster, 1992). These particle properties are dependent on particle shape and size.

3.1 Particle Modeling. The representation of the particles adopted in this work is somewhat different from Glicksman's one. Particle modeling is closer to reality. It is deduced from microscopic analysis. Two types of particle are considered to make up foams: struts with thickness varying along them (struts are thicker near their extremities, Fig. 2) and the strut junctures (Fig. 3) formed from four struts intersecting. If N_v is the number of struts per unit volume, there are:

- N_v particles of type 1, which are the struts;
- $N_v/2$ particles of type 2, which are the strut junctures.

The other considerations are the same as those of Glicksman:

- the particles have a random orientation;
- the particles are thick enough to be considered as opaque;
- the strut cross-sectional area is on average 2/3 of the area inscribed in a triangle defined by the strut vertices;
- the foam cells are taken as regular pentagonal dodecahedrons.

In this work combination of geometric optics and diffraction theory is applied to determine the complete radiative properties, accounting for the scattering phenomena. It can be noticed that this theory has never been considered for foam in any previous work.

Nomenclature

b = dimension of the strut defined in Fig. 5
$b_{\max}$ = dimension of the strut defined in Fig. 5
e = radiative emissive power
G = particle cross-sectional area projected onto a plane perpendicular to the incident beam
$\bar{G}$ = average geometric cross section of a particle
k_c = conductivity in absence of radiation
k_{gas} = conductivity of gas phase
k_r = radiative conductivity
k_{solid} = conductivity of solid phase
K = volumetric extinction coefficient
K^{*} = weighted extinction coefficient, Eq. (7)
K_R = Rosseland mean absorption coefficient
l = thickness sample
N_v = number of struts per unit volume
q = heat flux
T = temperature
x = coordinate
α = absorption coefficient
δ = foam void fraction (porosity)
θ = polar angle
ρ = particle hemispherical reflectivity
σ = Stefan–Boltzmann constant
σ_s = volumetric scattering coefficient
σ_s^{*} = weighted volumetric scattering coefficient, Eq. (5)
Φ = phase function
Φ_d = phase function of particles due to diffraction
Φ_r = phase function corresponding to reflection
$\langle \cos\theta \rangle$ = asymmetry factor, Eq. (6)

Subscripts

b = blackbody
c = conductive
j = particle of type j (j = 1, 2)
r = radiative
λ = monochromatic wavelength λ

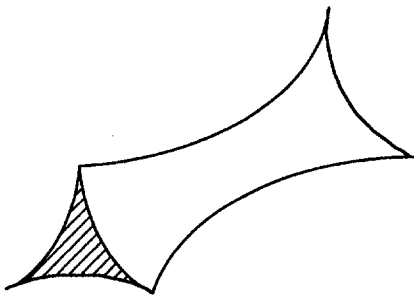

Fig. 2 Strut in perspective view; thickness is not constant

3.2 Results of the Combination of Geometric Optics With Diffraction Theory. Some limiting regions of validity for the scattering predictive models are defined by the magnitudes of the particle optical constants ($\tilde{n} = n - ik$) relative to the surrounding medium and of the size parameter, x (Brewster, 1992):

$$x = \frac{\pi d}{\lambda} \tag{9}$$

where d is the particle diameter and λ is the wavelength.

In these limiting regions it is possible to apply simpler analytical results than the full Mie solution (Brewster, 1992). When the particle is much larger than the wavelength ($x \gg 1$) and the refractive index not very small ($x|\tilde{n} - 1| \gg 1$), which is the case of the studied carbon foam, the series expansions used to evaluate the expressions in the Mie theory converge very slowly and geometric optics combined with diffraction theory can be used to predict the scattering behavior.

According to Brewster (1992), for opaque particles, $x = 5$ is approximately the lowest value for which the phase function predicted by geometric optics combined to diffraction theory can reasonably approximate the phase function derived from Mie theory. Carbon foams studied are used as insulation for high-temperature conditions (3000°C) and the wavelengths considered are less than 15 μm. In these conditions these materials have a value of $x > 5$. The carbon foam sample studied in this paper has a value of $x \approx 13.7$ for $\lambda = 8$ μm.

For most situations involving multiple scattering, the diffraction contribution can be ignored and a total extinction efficiency of unity used. But in order to obtain an accurate model all the scattering phenomena are taken into account. Geometric optics laws plus diffraction theory are applied and an extinction efficiency of two is deduced. This theory is applied to the large type 1 and 2 particles with random orientation. Expressions for foam radiative properties are obtained from the work of Van De Hulst (1957) and Brewster (1992). Van de Hulst (1957) studied scattering due to reflection and scattering due to diffraction by large particles with random orientation. Brewster (1992) provided results of the geometric optics laws combined with diffraction theory but the case of randomly oriented particles was not considered; the phase functions due to reflection and diffraction were given for spherical particles. Using the Van de Hulst and Brewster results, the application of the combination of geometric optics laws and diffraction theory to the particles of the two types considered in this study leads to the following results:

$$K_\lambda = 2N_v\left(\bar{G}_1 + \frac{\bar{G}_2}{2}\right) \tag{10}$$

$$\sigma_{s\lambda} = (\rho_\lambda + 1)N_v\left(\bar{G}_1 + \frac{\bar{G}_2}{2}\right) \tag{11}$$

$$\alpha_\lambda = (1 - \rho_\lambda)N_v\left(\bar{G}_1 + \frac{\bar{G}_2}{2}\right) \tag{12}$$

where: $\bar{G}_j$ is the average geometric cross section of the particles of type j ($j = 1, 2$) and ρ_λ is the spectral hemispherical reflectivity of particles, defined as the ratio of energy reflected into all solid angles to the incident energy arriving from all directions over the hemispherical space.

The phase function obtained by adding up the effects of the two types of particle is:

$$\Phi_\lambda(\theta) = \frac{\bar{G}_1\Phi_{1\lambda}(\theta) + \left(\frac{\bar{G}_2}{2}\right)\Phi_{2\lambda}(\theta)}{\bar{G}_1 + \frac{\bar{G}_2}{2}} \tag{13}$$

where: θ is the angle formed by the scattered beam with the direction of propagation before scattering; $\Phi_{j\lambda}$ is the spectral phase function of particles of type j.

This phase function $\Phi_{j\lambda}$ resulting from the combination of geometric optics and diffraction theories can be expressed by the following relation:

$$\Phi_{j\lambda}(\theta) = \frac{\rho_\lambda\Phi_r(\theta) + \Phi_{dj\lambda}(\theta)}{1 + \rho_\lambda} \tag{14}$$

where: $\Phi_{dj\lambda}$ is the spectral phase function due to the diffraction of particles of type j; Φ_r is the spectral phase function corresponding to reflection.

These radiative coefficients, expressions (10)–(13), are functions of N_v, $\bar{G}_j$, Φ_r, $\Phi_{dj\lambda}$, ρ_λ. The spectral hemispherical reflectivity ρ_λ of the particle solid material can be found from the literature but the other parameters still need to be determined.

3.3 Expression of the Phase Function Due to Particle Diffraction, $\Phi_{dj\lambda}$. From Bohren and Huffman's calculations (1983), the phase function due to diffraction by one particle can be obtained. Moreover Van de Hulst (1957) has studied diffraction by particles with random orientation. Bohren and Huffman's calculations and Van de Hulst's theory can be applied to the two types of particle considered in the current work. The result is given by the following expression:

$$\Phi_{dj\lambda}(\theta, \phi) = \frac{k^2}{4\pi}(1 + \cos\theta)\frac{\overline{G_j^2|D_j|^2(\theta, \phi)}}{\bar{G}_j} \tag{15}$$

where: k is the wavenumber defined by $k = (2\pi/\lambda)$, λ is the wavelength in the surrounding medium; θ, ϕ are the polar angles

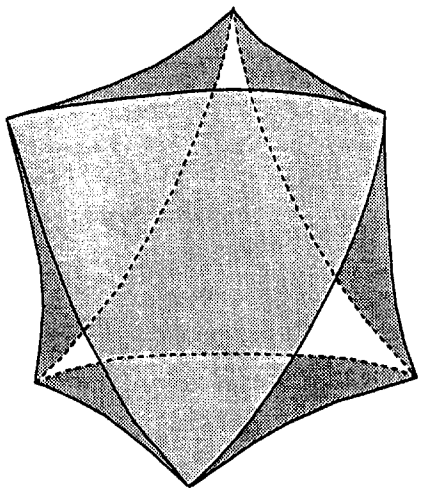

Fig. 3 Strut juncture; faces are curved

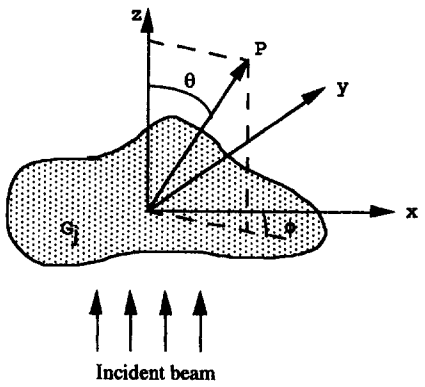

Fig. 4 Diffraction by a large body with a geometric shadow area G_j

of the scattered radiation direction (Fig. 4); G_j is the particle of type j, $j = 1, 2$, cross-sectional area projected onto a plane perpendicular to the incident beam; D_j is a complex function:

$$D_j(\theta, \phi) = \frac{1}{G_j} \iint_{G_j} e^{-ik\sin\theta(x\cos\phi + y\sin\phi)} dxdy \qquad (16)$$

$\overline{G_j^2 \mid D_j \mid^2}$ is the average of $G_j^2 \mid D_j \mid^2$ over all possible angular positions with respect to the direction of propagation.

A rigorous computation of the average value $\overline{G_j^2 \mid D_j \mid^2}$, requires the knowledge of the particle geometric cross section for all potential angular positions with respect to the direction of propagation, which is difficult due to the complex particle shapes, especially for particles of type 2. Moreover this rigorous calculation consumes much time (triple integration for three angular position). So $\overline{G_j^2 \mid D_j \mid^2}$ is approximated by $\bar{G}_j^2 \mid D_j \mid^2$, D_j being calculated from $\bar{G}_j$ for the two types of particle. The difference between radiative fluxes obtained from the two expressions $\overline{G_1^2 \mid D_1 \mid^2}$ and $\bar{G}_1^2 \mid D_1 \mid^2$ (for the strut geometry) is lower than 1 percent for data given in section 4. This approximation was then adopted.

The azimuthal symmetry is assumed. Equation (6) requires the knowledge of the phase function $\Phi_\lambda(\theta)$, which is independent of the azimuthal angle ϕ. Then $\Phi_{dj\lambda}(\theta)$ is approximated by the following expression:

$$\Phi_{dj\lambda}(\theta) = \frac{1}{2\pi} \int_0^{2\pi} \Phi_{dj\lambda}(\theta, \phi) d\phi \qquad (17)$$

3.4 Expression of the Phase Function Due to Reflection, $\Phi_r(\theta)$. To determine the phase function $\Phi_r(\theta)$ corresponding to reflection, the following theorem is applied (Van de Hulst, 1957):

Theorem: The scattering pattern caused by reflection on a very large convex particle with random orientation is identical to the scattering pattern by reflection on a very large sphere of the same material and surface condition.

The particles are considered as convex to apply this theorem and reflection is supposed diffuse. The phase function corresponding to reflection from large opaque diffusely reflecting, diffusely absorbing spheres is (Van de Hulst, 1957, Brewster, 1992):

$$\Phi_r(\theta) = \frac{8}{3\pi} (\sin\theta - \theta\cos\theta) \qquad (18)$$

So the phase function is determined from Eqs. (13)–(18). Consequently radiative properties (expressions (10)–(13)) are functions of ρ_λ, $\bar{G}_j$ and N_v.

Doermann (1995) has determined $\bar{G}_j$ and N_v as function of the foam porosity δ and the strut dimensions b and b_{max} defined in Fig. 5. b is the strut minimum thickness and b_{max} the strut maximum thickness. The calculations are long, so they are not given here. They take into account geometric considerations. It can be noted that b and b_{max} may be obtained from microscopic analysis (Fig. 5) more easily than a mean cell diameter (which is required in Glicksman's model). This is an advantage of the new model taking into account a modeling particle closer to reality. The porosity δ (which is required in the current model and in Glicksman's model) can also be determined from microscopic analysis. On the other hand the hemispherical reflectivity of the solid material ρ_λ can be obtained from literature (Touloukian and Dewitt, 1970).

As a conclusion, the model allows us to predict the radiative parameters K_λ, σ_λ, α_λ, Φ_λ (Eqs. (10) to (13)) from b, b_{max}, δ, ρ_λ, which values are easy to obtain.

Remark: The assumptions of this radiative properties prediction model have been verified by comparing theoretical and experimental results of bidirectional spectral transmittances by using a Fourier transform infrared spectrometer (Doermann, 1995).

4 Application to a Carbon Foam and Comparison Between Different Models

4.1 Data Used. The carbon foam sample data and the boundary conditions used in this study are reported below.

Carbon Foam Sample Data. Microscopic analysis on open cell carbon foam gave the following morphologic data:

$$b = 35\ 10^{-6}\ \text{m}$$

$$b_{max} = 64\ 10^{-6}\ \text{m}$$

$$\delta = 0.975$$

N_v is calculated from b, b_{max}, δ by Doermann (1995) calculations. The value is:

$$N_v = 0.2178 \times 10^{12}$$

Temperature boundary conditions:

- hot temperature, $T_h = 3000$ K,
- cold temperature, $T_c = 600$ K.

Sample thickness: $l = 10 \times 10^{-3}$ m

The carbon hemispherical reflectivity is obtained from the literature (Fig. 6, curve A).

In Fig. 6 three curves of different graphite normal spectral reflectivity are presented. The reflectivity from curve A is taken as the hemispherical graphite reflectivity. It is assumed that

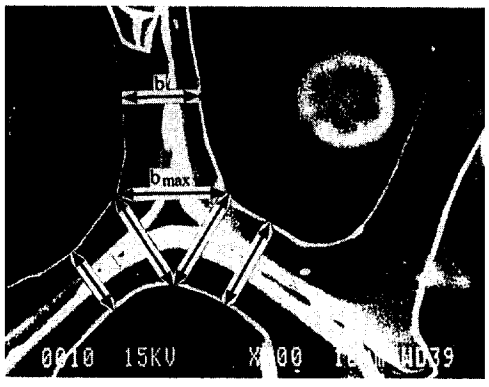

Fig. 5 Microscopic analysis obtained from carbon foam sample (magnification ×400); determination of dimensions b and b_{max}

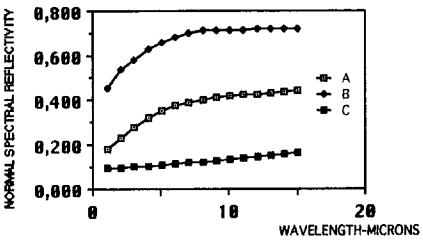

Fig. 6 Reflectivity comparison data. Key: (A) Autio and Scala pyrolytic graphite A-face emissivity measurement (Autio and Scala, 1966); (B) Ichikawa and Kobayashi C-face single crystal graphite, theoretical calculations (Autio and Scala, 1966); (C) Willis, carbon reflectivity calculated from optical constants (Boulet, 1992).

hemispherical spectral reflectivities have nearly the same value as normal spectral reflectivities.

The weighted extinction coefficient obtained from Eqs. (5) to (7) and from the combination of geometric optics and diffraction theory is: $K_R^* = 1319.1\ \mathrm{m}^{-1}$.

The optical thickness is: 13.19.

So this sample can be in fact considered as optically thick.

The gas in the foam is nitrogen. Its conductivity is calculated from the following expression:

$$k_{gas} = k_0 \left(1 + \frac{C}{273} \frac{\sqrt{\frac{T}{273}}}{\left(1 + \frac{C}{T}\right)} \right) (\mathrm{Wm^{-1}K^{-1}})$$

where:

$$k_0 = 0.0242\ (\mathrm{Wm^{-1}K^{-1}})$$

$$C = 161\ (\mathrm{K})$$

$$T \text{ in K}$$

The conductivity of carbon is calculated from:

$$k_{solid} = -1.309\ 10^{-3}T + 7.463\ (\mathrm{Wm^{-1}K^{-1}})$$

In what follows when parameters are not specified, they will take the values given above.

4.2 Numerical Calculations. Radiative properties are predicted from the combination of geometric optics with diffraction theory applied to the two types of particles (struts and strut junctures). The phase function obtained is highly anisotropic. It is due essentially to the contribution of the diffraction phase function. To determine the weighted extinction coefficient used in the Rosseland equation, it is necessary to calculate the integral required in Eq. (6). This integral is numerically calculated and a fine angular resolution is employed: a Gauss quadrature of 24 directions is used (Nicolau et al., 1994b).

The coupling between thermal conduction and radiative transfer is taken into consideration by using Eqs. (1)–(4). The control-volume method (Patankar, 1980) is used to solve the energy equation and find the temperature field across the sample (25 nodes are used and the grid is uniform). The averages over the sample thickness of the radiative and conductive heat flux

Table 1 Comparison between the model results

Models	kc ($\mathrm{Wm^{-1}K^{-1}}$)	kr ($\mathrm{Wm^{-1}K^{-1}}$)	kr relative difference / model 0 (%)
model 0	0.130	1.921	
model 1	0.130	2.103	9.5%
model 2	0.130	1.909	0.6%

Table 2 Comparison between model 0 and model 1 results for different hemispherical reflectivity used

Hemispherical reflectivity ρ_λ	kr ($\mathrm{Wm^{-1}K^{-1}}$) model 0	kr ($\mathrm{Wm^{-1}K^{-1}}$) model 1	kr relative difference / model 0 (%)
A	1.921	2.103	9.5
B	1.730	2.103	21.5
C	2.012	2.103	4.5

can be deducted and a radiative (photonic) or conductive (phonic) conductivity can be calculated:

$$k_r = q_r \frac{l}{(T_h - T_c)}$$

$$k_c = q_c \frac{l}{(T_h - T_c)}$$

In the next step, three models (called models 0, 1, 2) are compared. The conductive part of these models is the same. In these three models particles of two types (struts and strut junctures) are considered. However, the predictive model of radiative properties is different for each of these three models.

4.3 Description of the Radiative Property Prediction of the Three Models.

Model 0: the radiative prediction of this model accounts for scattering due to reflection and diffraction by the type 1 and 2 particles. An extinction efficiency of two is used (current model).

Model 1: in this model scattering is neglected and an efficiency factor of one is used.

Model 2: in this model diffraction is neglected and an efficiency factor of one is used.

The radiative and conductive contributions to the total conductivity obtained from these three models are compared in Table 1. From this table, it can be noticed that, for the boundary conditions (given above), radiative conductivity accounts for roughly 94 percent of the total conductivity. The radiative conductivity difference obtained from model 0 and model 1 is 9.5 percent. The difference between radiative conductivities obtained with model 0 and model 2 is very small (0.6 percent). These results are only valid for data described above. In the next step the radiative conductivities obtained from these three models are compared for different hemispherical reflectivity and different particle dimension values. The emphasis is put on a comparison between models 0 and 1 or models 0 and 2, respectively, aiming to study the influence of neglecting scattering effects or diffraction effects respectively.

4.4 Comparison Between Model 0 and Model 1 Results

Influence of the Hemispherical Reflectivity, ρ_λ. The radiative conductivities obtained from models 0 and 1 are compared for the different considered hemispherical reflectivities. The various reflectivities A, B, C are presented in Fig. 6. When the hemispherical reflectivity increases, the difference between radiative conductivities quickly increases (Table 2). For the hemispherical reflectivity of curve B, the percentage difference is 21.5 percent and neglecting or not the scattering has an important influence on the result.

Table 3 Comparison between model 0 and model 1 results for different strut dimensions used

$b, b_{max}(10^{-6}m)$	kr ($\mathrm{Wm^{-1}K^{-1}}$) model 0	kr ($\mathrm{Wm^{-1}K^{-1}}$) model 1	kr relative difference / model 0 (%)
$b = 32, b_{max} = 60$	1.791	1.961	9.5
$b = 38, b_{max} = 68$	2.052	2.245	9.4

Table 4 Comparison between models 0 and 2 results for different strut dimensions

$b, b_{max}(10^{-6}m)$	kr($Wm^{-1}K^{-1}$) model 0	kr($Wm^{-1}K^{-1}$) model 2	kr relative difference / model 0 (%)
$b = 32, b_{max} = 60$	1.791	1.780	0.6
$b = 38, b_{max} = 68$	2.052	2.038	0.7

Moreover, it can be noticed that when the hemispherical reflectivity increases, the radiative conductivity decreases.

Influence of the Particle Dimensions. The radiative conductivities obtained from models 0 and 1 are compared for various particle dimensions. From Table 3 it can be observed that the percentage difference is nearly independent of the particles dimension; the value is of about 9.5 percent.

Moreover, it can be noticed that when δ is fixed and N_v is calculated from the parameters δ, b, b_{max}, if particle dimensions increase, radiative conductivity increases.

4.5 Comparison Between Model 0 and 2 Results. Radiative conductivities obtained from models 0 and 2 are compared. In model 2, diffraction effects are neglected. The radiative conductivity percentage difference obtained from the two models is very small, about 0.7 percent (Table 4) and this result is independent of particle dimensions. So the diffraction contribution can be neglected and it is admissible to use a total efficiency factor of unity. This can be explained by the sharply forward peaked values of the phase function due to diffraction ($\theta = 0$ to 6 deg depending on the particle dimensions).

5 Conclusions

A predictive model for thermal transfer in open cell foam insulation is presented. The conductive process within these kinds of structure is commonly described using a simple parallel-series model. Common commercial foam insulation can be treated as optically thick, enabling the use of the Rosseland approximation to predict the radiative heat transfer. To account for the foam anisotropic scattering, the weighted extinction calculated from the foam radiative properties is used in the Rosseland's equation. The main difficulty in predicting heat transfer in open cell foam insulations is the determination of radiative properties. In this paper a new model of radiative properties prediction is adopted. Particle modeling is very close to reality; struts and strut junctures are considered. Particle dimensions of carbon foam studied here are located in the limit region where geometric optics and diffraction theory can be used to predict radiative properties taking into account scattering behavior ($\pi d/\lambda \gg 1$ for the wavelength range of this study, 2 μm $\leq \lambda \leq$ 15 μm).

The model described in the current paper is applied to a carbon foam and a comparison with simpler models is carried out. It can be summarized that:

- There is a substantial fraction of heat transfer through foam insulation due to radiation and especially for high temperature boundary conditions (94 percent (Table 1)).
- Neglecting scattering is valid only for low reflecting material. When the material hemispherical reflectivity increases, the radiative conductivity difference between the complete model and the model neglecting scattering increases quickly up to 21.5 percent (Table 2).
- For the particle dimensions used in this study, diffraction can be neglected (0.7 percent, Table 4).
- The influence of particle dimensions and material reflectivity on foam conductivity was also studied. It can be deduced that using a material with higher reflectivity would lead to a decrease in foam conductivity. If porosity δ is fixed and N_v is calculated, when particle dimensions increase, foam radiative conductivity simultaneously increases.

This new model represents a real improvement of the previous work on radiative properties prediction of foam insulations for the following reasons:

- the input data (b, b_{max}, δ, ρ_λ) are easier to obtain and can be more precisely measured than those in previous work. This represents a considerable advantage.
- the scattering is taken into account and it permits to study the influence of solid reflectivity;
- the more realistic model results in an improvement in the accuracy of the results.

Acknowledgments

This project was supported by the Aerospatiale Etablissement d'Aquitaine, under the technical management of Mrs. Colette Acket. The research work of one of the authors (D. Doermann) has been made possible under a fellowship of the French Ministère de la Recherche et de l'Enseignement Supérieur. The authors would like to thank them.

References

Autio, G. W., and Scala, E., 1966, *Carbon,* Vol. 4, pp. 13–28.

Bohren, C. F., and Huffman, D. R., 1983, *Absorption and Scattering of Light by Small Particles,* Wiley, New York.

Boulet, P., 1992, "Etude du Transfert par Rayonnement à Travers les Milieux Fibreux," Doctoral Thesis, Université de Nancy I, France.

Brewster, M. Q., 1992, *Thermal Radiative Transfer and Properties,* Wiley, New York, pp. 301–336.

Doermann, D., 1995, "Modélisation des transferts thermiques dans des matériaux semi-transparents de type mousse à pores ouverts et prédiction des propriétés radiatives," Doctoral Thesis, INSA-Lyon France, No. order 95ISAL0010.

Glicksman, L. R., and Torpey, M. R., 1987a, "Factors Governing Heat Transfer Through Closed Cell Foam Insulation," ASTM Symposium, FL.

Glicksman, L. R., and Torpey, M., 1987b, "Radiation in Foam Insulation," *Proceedings of Polyurethane World Congress,* Aachen, Germany.

Glicksman, L., Schuetz, M., and Sinofsky, M., 1987, "Radiation Heat Transfer in Foam Insulation," *Int. J. Heat Mass Transfer,* Vol. 30, No. 1, pp. 187–197.

Glicksman, L. R., and Torpey, M. R., 1988, "A Study of Radiative Heat Transfer Through Foam Insulation," report prepared by Massachusetts Institute of Technology under Subcontract No. 19X-09099C.

Glicksman, R., Marge, A. L., and Moreno, J. D., 1992, "Radiation Heat Transfer in Cellular Foam Insulation," *Developments in Radiative Heat Transfer,* ASME HTD-Vol. 203.

Hottel, H. C., and Sarofim, A. F., 1967, *Radiative Transfer,* McGraw-Hill, New York, pp. 378–407.

Kuhn, J., et al., 1992, "Thermal Transport in Polystyrene and Polyurethane Foam Insulations," *Int. J. Heat Mass Transfer,* Vol. 35, No. 7, pp. 1795–1801.

Lee, H., and Buckius, R. O., 1982, "Scaling Anisotropic Scattering in Radiation Heat Transfer for a Planar Medium," ASME JOURNAL OF HEAT TRANSFER, Vol. 104, pp. 68–75.

Nicolau, V. P., Raynaud, M., and Sacadura, J. F., 1994a, "Spectral Radiative Properties Identification of Fibber Insulating Materials," *Int. J. Heat Mass Transfer,* Vol. 37, pp. 311–324.

Nicolau, V. P., 1994b, "Identification des Propriétés Radiatives des Matériaux Semi-Transparents Diffusants," Doctoral Thesis, INSA-Lyon France, No. order 94ISAL0001.

Patankar, S. V., 1980, *Numerical Heat Transfer and Fluid Flow,* Hemisphere Publishing Corporation, U.S.A.

Reitz, D. W., 1983, "A Basic Study of Gas Diffusion in Foam Insulation," Master of Science in Mechanical Engineering, Massachusetts Institute of Technology, pp. 34–34.

Schuetz, M. A., and Glicksman, L. R., 1984, "A Basic Study of Heat Transfer Through Foam Insulation," *Journal of Cellular Plastics,* Vol. 20, No. 2, pp. 114–121.

Touloukian, Y. S., and Dewitt, D. P., 1970, *Thermophysical Properties of Matter,* Plenum, New York, Vol. 8.

Van De Hulst, H. C., 1957, *Light Scattering by Small Particles,* Wiley, New York, pp. 103–113.

Correlation of Measured and Computed Radiation Intensity Exiting a Packed Bed

P. D. Jones

D. G. McLeod

D. E. Dorai-Raj

Mechanical Engineering Department,
Auburn University,
Auburn, AL

The spectral and directional distribution of radiation intensity is measured, using a direct radiometric technique, at the exposed boundary of a packed bed of stainless steel spheres. The purpose of these measurements is to provide an experimental data base of radiation intensity with which to correlate intensity field solutions of the radiative transfer equation in participating media. The bed is considered to be one-dimensional, is optically thick, and has measured constant-temperature boundary conditions. Intensity exiting the bed is numerically simulated using a discrete ordinates solution to the radiative transfer equation, with combined mode radiation-conduction solution of the coupled energy conservation equation. Radiative properties for the bed are computed using the large size parameter correlated scattering theory derived by Kamiuto from the general theory of dependent scattering by Tien and others. The measured intensity results show good agreement with computed results in near-normal directions, though agreement in near-grazing directions is poor. This suggests that either radiative transfer near the boundaries of this medium might not be adequately represented by a continuous form of the radiative transfer equation, or that the properties derived from correlated scattering theory are insufficient. In either case, development of a more detailed radiation model for spherical packed beds appears warranted.

Introduction

Radiative heat transfer through radiatively participating media (such as absorbing-emitting gases, particle suspensions, semi-transparent liquids, or solid matrices) is governed by the Radiative Transfer Equation (RTE). The RTE is stated in terms of radiation intensity, a scalar that varies with spatial location, direction, and wavelength, and is coupled through temperature to the energy conservation equation. The RTE is a difficult integrodifferential equation with relatively few analytical solutions, and these are generally restricted in range of application. A wide variety of approximate and computational techniques have therefore been developed to solve unrestricted forms of the RTE (Viskanta and Mengüç, 1987; Howell, 1988). One of these, the Monte Carlo method (cf. Siegel and Howell, 1992; Modest, 1993), is even widely considered to be exact, provided that enough random energy paths are simulated to constitute a statistical continuum, and the medium is defined in sufficient detail. However, it is still necessary to rely on experimental correlation in order to verify the ultimate correctness of modeling assumptions and simplifications, constitutive mechanics, and radiative material properties.

The RTE is written in terms of the radiation intensity, which must be the quantity measured for RTE solution correlation. Intensity itself can be a difficult quantity to measure, and so the heat flux or temperature fields that result from radiation-dominated situations have often been measured instead. Such experiments provide a general measure of the accuracy of overall heat transfer modeling, including radiation, but cannot provide the level of detail necessary to guide improvements in intensity field modeling. For this purpose, it is necessary to measure spectral and directional distributions of radiation intensity, in addition to spatial variations.

Radiative heat transfer prediction depends upon accurate material property information in addition to accurate RTE modeling techniques, and the properties themselves continue to be a source of uncertainty. To this end, most measurements of spectral-directional radiation intensity in participating media involve relatively simple geometries and boundary conditions, so that there will be little doubt about the RTE modeling, and radiative properties may be inferred. For example, Kamiuto et al. (1991a, b), and Kamiuto (1992) investigate cold planar packed beds of spheres (monodisperse and polydisperse), where a monochromatic laser beam impinges on one side of the bed, and the beam's intensity exiting the bed is measured as a function of angle. The exiting intensity data may be correlated with quasi-analytical solutions of the RTE (normal, collimated intensity propagating through cold one-dimensional media) to yield the extinction coefficient, the scattering albedo, and a scattering phase function distribution parameter. The RTE modeling complexities of noncollimated boundary conditions and nonisothermal media, which would cloud the property identification issue, are thus avoided. Similar work is reported for foam insulation by Glicksman et al. (1987), using a CO_2 laser source, for fibrous insulation by Saboonchi et al. (1988), using a blackbody source, and for particle suspensions by Menart et al. (1989), using a graybody source. Hendricks and Howell (1994) examine reticulated porous ceramics using a commercial spectroradiometer system, reducing spectral radiative property data with a discrete ordinates technique. Nicolau et al. (1994) examine several insulation materials using a blackbody source and a wavelength discrimination system to determine spectral property distributions, and apply a formal parameter identification analysis.

Given a radiatively participating material with known properties, apparatus similar to those cited above may be turned toward the question of accuracy in RTE modeling. Nelson and Satish (1987) address the attenuation and directional redistribution of a normally incident laser beam propagating through a cold disperse-particle medium, whose properties are known to correlate well with Mie theory. By measuring the exiting normal intensity as a function of spatial displacement from the axis of

Contributed by the Heat Transfer Division for publication in the JOURNAL OF HEAT TRANSFER. Manuscript received by the Heat Transfer Division September 1995; revision received November 1995. Keywords: Packed and Fluidized Beds, Radiation. Associate Technical Editor: M. Modest.

incidence, they were able to correlate a measured monochromatic intensity with the predictions of an approximate two-dimensional version of an exact one-dimensional single scattering RTE solution. Skocypec et al. (1987) and Walters and Buckius (1991) report measurements of the normal direction, spectral intensity exiting a hot, disperse gas-particle flow of nonuniform temperature profile. Radiative properties are taken from experimental data. Correlation is made with a commercial radiative transfer code. These data are of particular interest as the intensity source is the nonuniform thermal emission of the medium itself, and thus intensity measurements are correlated with RTE modeling in a more general application than in experiments whose goal is property determination.

The object of the present work is to measure the directional and spectral distributions of radiation intensity exiting the boundary of a radiatively participating medium, for present and future correlation of these measurements with the predictions of overall heat transfer and radiation modeling. The goal is to provide measured spectral-directional intensity data for correlating RTE solutions in a nonisothermal medium with boundary emission and reflection; such information is extremely rare in the present literature. A one-dimensional (plane parallel) medium is chosen in order to simplify and clarify correlation. A spherical packed bed is chosen as its radiative properties are relatively broad-banded (as opposed to the high spectral dependence of properties of gases), it has inherent spatial stability (unlike suspensions of particles), and it has a clearly defined geometry (more so than porous or fibrous materials). Because a packed bed might be modeled using either a simple continuous radiation model, or a more complex discrete model (Tien, 1988), the packed bed medium itself might be considered to be a somewhat demanding application. Spectral, directional intensity exiting this medium is measured by adapting the spectral, directional radiative surface property apparatus presented by Jones et al. (1995) for use with a 9-mm-deep continuous medium. The discrete ordinates numerical method is applied to RTE modeling for use in correlating computations. This technique is favored for many applications for its flexibility and ease of coding (Fiveland and Jessee, 1995). Properties for computations are drawn from the literature, using measured radiative surface properties for final specification of the effective bed properties.

Experiment

Apparatus. The participating medium is comprised of a 75 mm × 75 mm × 9.0 mm bed of type 316 stainless steel bearing balls (of the type supplied for manufacture of ball point pens), 1 mm in diameter, laid into an enclosure of the dimensions given above, and shaken and tamped to achieve stable packing. It is assumed that the packing geometry is random. The porosity is determined by weight to be 0.3713. The bed is kept horizontal, and is open to the atmosphere on its top surface. The bottom surface of the bed rests on a heater block (75 mm cube of high grade copper with embedded cartridge heaters and control thermocouples). The enclosure sides are formed by 316 stainless steel plates, 6 mm thick, and all are packed on five sides in ceramic wool insulation blanket 75 mm thick (no material extends above the medium's open top surface). This packing is held in a casing, which is suspended by trunnions from a slotted arc rack (Fig. 1). Setting the trunnions into different slots in the rack and rotating the optical path's collecting reflector allows the intensity to be measured at different angles relative to the surface normal. The medium temperature is sensed by two 1-mm-dia high-temperature thermocouple probes, laid into the top and bottom ball layers. When heated, the steel and copper both oxidize. A thick (~0.4 mm), crusty, black oxide forms on the copper boundary surface. Bright colors are observed through the stainless steel oxide, indicating the possibility of only first-order interference by the oxide in the underlying optical behavior of the steel, and an oxide thickness of less than 100 nm. In order to ensure that oxide growth does not continue during measurements, the bed is heated with the heater block set at 900 K for 200 h. Transient intensity measurements through this period demonstrate that steady state is achieved. Examination of the oxidized balls following measurement runs shows no discernable variation in the oxide thickness on the balls with location in the medium.

The rest of the radiation intensity measurement system (Fig. 2) is essentially that employed by Jones et al. (1995), which measures radiative flux within a finite cell of solid angle and band of wavelength. Design details are described in McLeod (1995). Radiation exiting the medium is reflected and collimated by the collecting reflector (an off-axis parabolic segment). The collecting reflector is on a rotating mount, so that it can be rotated to view either the calibrating blackbody (shown to the right of the reflector in Fig. 2) or the packed bed (shown in plan view underneath the reflector in Fig. 2, and in elevation in Fig. 1). The measurement spot size, as indicated by diode lasers used for optical path alignment, appears to be a little less than 3 mm, or three ball diameters. The collimated beam is trimmed to 19 mm diameter and chopped to allow comparative noise filtering. The beam is transmitted through one of a battery of optical edge filters and refocused into a $\frac{1}{8}$ m grating monochromator. The output of the monochromator is focused onto

Nomenclature

a, b, c = quadrature weight adjustment parameters
C = calibration factor for radiometer reading
d_p = spherical bed particle diameter, m
g_λ = Henyey–Goldstein anisotropic parameter
I_λ = spectral intensity, W/(m^{2}sr μm)
$I_{\lambda b}$ = spectral blackbody intensity, W/(m^{2}sr μm)
k = thermal conductivity, W/mK
m = directional mesh index
M = directional mesh size (twice quadrature order)
N = spherical bed particle number density, m^{-3}
p = scattering phase function
Q_{ex} = extinction efficiency
R = radiometer reading, W/m^2
S = sample standard deviation
$t_{2,90}$ = Student-t parameter, 2 d.o.f., 90 percent confidence
T = temperature, K
u = uncertainty, units of subscript
w_m = quadrature integration weight
y = spatial coordinate, m
y_o = bed depth, m
β = extinction coefficient, m^{-1}
γ_2 = bed extinction parameter
$\delta\lambda$ = monochromator wavelength interval, μm
$\delta\Omega$ = optical path acceptance solid angle, sr
ϵ_λ = spectral emittance (directional or hemispherical)
θ = polar angle, rad
λ = wavelength, μm
σ_b = Stefan–Boltzmann constant = 5.67 × 10^{-8} W/m^{2}K^4
ϕ = bed porosity
ω_λ = scattering albedo

Subscripts

b = bed
co = oxidized copper
ss = oxidized stainless steel
1 = bed bottom boundary
2 = bed top boundary
∞ = surroundings

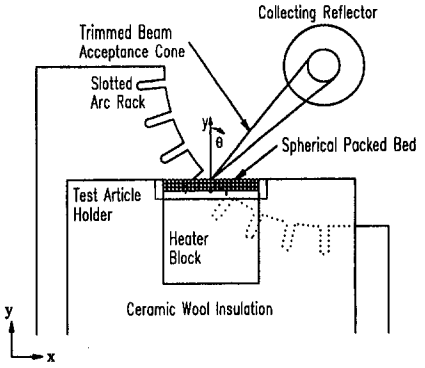

Fig. 1 One-dimensional spherical packed bed, heated from below; elevation view (actual bed is 10 ball rows deep)

a pyroelectric detector (electrically polarized lithium tantalate crystalline chip with a black overlay), whose output is amplified and taken to a radiometer (Oriel Merlin). The total optical path is 1.1 m long, and entirely through atmospheric air (manual adjustments are required to change wavelength and direction; resources for automating these functions and enclosing the apparatus in a vacuum chamber are unavailable). The acceptance solid angle of the intensity measurement system optical path is 0.020 sr (maximum polar variation 9.2 deg), while the monochromator passes a wavelength band that varies between 0.026 μm in width at a wavelength of 1.5 μm and 0.16 μm in width at 10 μm. The radiometer display may then be taken as proportional to the radiative intensity, averaged over this solid angle and wavelength band. A radiating cavity (*hohlraum*) blackbody is chosen as a calibration source, in consideration of the moderately diffuse, randomly polarized, broad band intensity expected from the packed bed medium. The cavity, which has an effective exit aperture emittance of 0.9992, is described in detail by Jones et al. (1995). The intensity measurement system (present apparatus less participating medium arrangement) yields spectral data in surface radiation applications (as opposed to the present radiation-in-depth application) which compare well with the available literature, and directional data that compare well with the Fresnel relations.

Procedure. The intensity measurement system is calibrated in advance of packed bed measurements by measuring the correlation of measurement signal to blackbody intensity as a function of wavelength. Repeated measurements of the blackbody correlation over a range of temperature between 600 K and 1000 K demonstrate an uncertainty of 1 to 2 percent for most readings, and as high as 3 percent for some. Higher uncertainties occur at lower temperatures and at both very high and very low wavelengths, where the signal strength is lower (system response to cold media is unmeasurably small). For this reason, measurements are limited to temperatures above approximately 700 K, and wavelengths between 1.5 and 10 μm.

The blackbody and all other apparatus in view of the packed bed surface are kept cold during measurement of the medium intensity in order to preclude incident radiation on the medium. Some items of support structure become slightly warm to the touch during measurement runs, and these are coated with carefully smoothed aluminum foil to reduce their emittance, and oriented so that specular reflections of intensity exiting the packed bed cannot become reincident on the bed.

After the oxide film growth period, spectral series (18 wavelength points) are measured at each polar angle (8 directional points). Some measurements are repeated to ensure repeatability. A reduced measurement set is taken for a series of bed location shifts (1, 2, and 3 mm in each of two directions) to ensure that there is no measurement point bias. Since copper oxide is a brittle material which cracks when cooled to room temperature, the medium is kept heated continuously until all measurements are complete.

Data Reduction. A calibration factor is determined as

$$C(\lambda) = \frac{1}{R_c(\lambda, T_c)} \left[\int_{\lambda-\delta\lambda/2}^{\lambda+\delta\lambda/2} I_{\lambda b}(T_c) d\lambda \right] \delta\Omega \qquad (1)$$

where R_c is the radiometer measurement taken from the calibration blackbody set at T_c (the expected functional dependence of R_c upon $I_{\lambda b}$ is derived by McLeod, 1995). $C(\lambda)$ is found to have a detectable sensitivity to T_c over a range of temperatures between 100 K below the lowest bed temperature and 100 K above the highest bed temperature. However, this effect is an order of magnitude smaller than the random scatter of $C(\lambda)$, and therefore by including this additional uncertainty the measurement system may be considered to have a linear response over the reported intensity range. The spectral intensity is determined by

$$I_\lambda(\lambda, \theta) = \frac{R_I(\lambda, \theta) C(\lambda)}{\delta\lambda\delta\Omega} \qquad (2)$$

where R_I is the radiometer measurement taken from the top surface of the bed and I_λ is considered to be constant over $\delta\lambda$ and $\delta\Omega$.

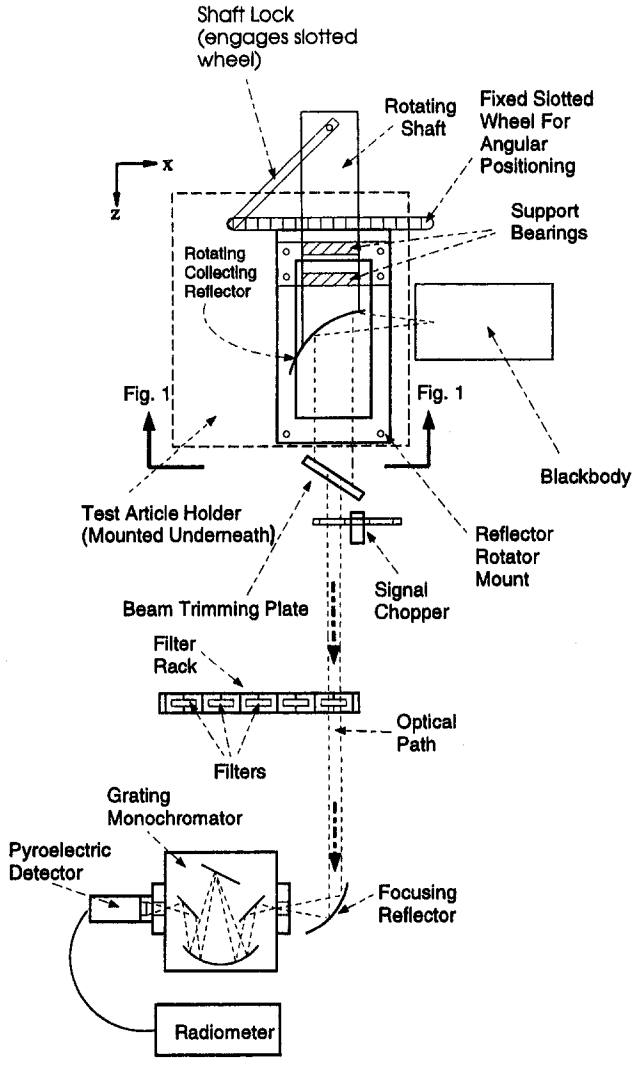

Fig. 2 Intensity measurement system; plan view

Uncertainty. Combining Eqs. (1) and (2), the measured uncertainty in the spectral intensity may be stated

$$u_{I_\lambda}^2 = \left(\frac{\partial I_\lambda}{\partial R_I} u_{R_I}\right)^2 + \left(\frac{\partial I_\lambda}{\partial R_c} u_{R_c}\right)^2 + \left(\frac{\partial I_\lambda}{\partial I_{\lambda b}} \frac{\partial I_{\lambda b}}{\partial T_c} u_{T_c}\right)^2 \quad (3)$$

where $\delta\Omega$ and $\delta\lambda$ are considered to be perfectly repeatable (further low-order errors are considered by McLeod, 1995, where it is shown the uncertainty due to background radiation at T_∞ is insignificant). Considering R_c and R_I to have similar uncertainties, this may be reduced to

$$u_{I_\lambda}^2 = \left[1 + \left(\frac{R_I}{R_c}\right)^2\right]\left(\frac{C}{\delta\lambda\delta\Omega} t_{2,90} S_{R_c}\right)^2 + \left(\frac{R_I}{R_c} \frac{\partial I_{\lambda b}}{\partial T_c} u_{T_c}\right)^2 \quad (4)$$

for three complete calibration spectra and a 90 percent confidence level. With the uncertainty in the calibration temperature taken as its control uncertainty, the second term in Eq. (4) is found to have a negligible influence on the uncertainty in intensity. The total uncertainty in spectral intensity varies between 4 and 7 percent of its value, with some uncertainties (typically for wavelengths at the high and low extremes) as high as 11 percent. This magnitude of uncertainty is similar to that found by Jones et al. (1995) for surface radiation using the same intensity measurement system.

Results. The reduced spectral intensity data, measured exiting the center of the top surface of the optically thick spherical packed bed, are shown in Figs. 3(*a*) and 3(*b*). Figure 3(*a*) shows spectra for a range of intensity directions. The general spectral shape is similar to that of a graybody. Comparing the measured spectral-normal intensity to that of a blackbody at the top surface temperature shows a relatively constant effective normal emittance for the bed, varying from ~0.77 at 3 μm to ~0.72 at 9 μm. This is somewhat higher than the actual emittance of the bed material (as discussed in the following section), indicating significant radiative transfer from within the bed. Although the extinction coefficient of the medium is considered to be independent of wavelength, the scattering albedo and the boundary emittance of the bottom heating surface have significant spectral variation (see following). It appears that the bed is optically thick enough to mask the spectral effect of the nongray scattering albedo and boundary emittance, as the overall character of the bed's exiting intensity is relatively gray. (Note the slight irregularity of the results around $\lambda = 6.5$ μm. The magnitude of this anomaly is within the experimental uncertainty of the measured intensity. It is possible that this effect is deterministic, and related to an air absorption band on the open optical measurement path. Adjustment for such absorption would require a more involved and much less straightforward calibration procedure than that reported here.)

Figure 3(*b*) shows a polar plot of the directional distribution of measured intensity for a range of wavelengths. For polar angles up to 36 deg there is little directional variation in intensity, although the intensity attenuates with further increases in polar angle, and is reduced by nearly half its normal direction value at an angle of 84 deg. It appears that radiative transfer from within the bed has a broadly normal orientation. Intensity exiting the bed cannot be considered to be diffuse.

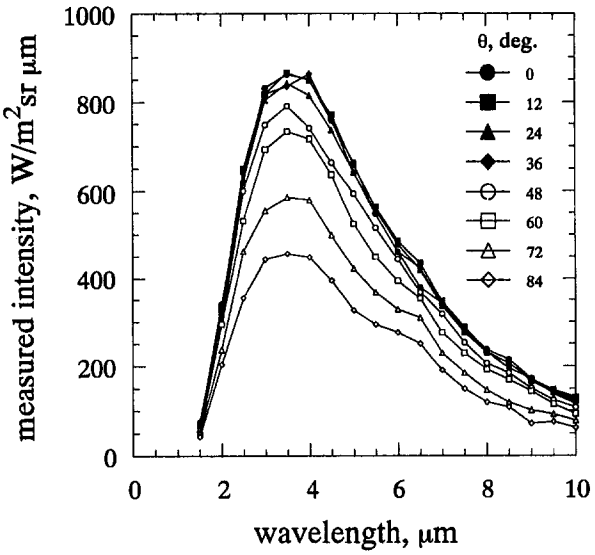

Fig. 3(*a*) Measured intensity spectra for a range of polar angles, exiting a nonisothermal packed bed of monodisperse, opaque, optically large, spherical particles

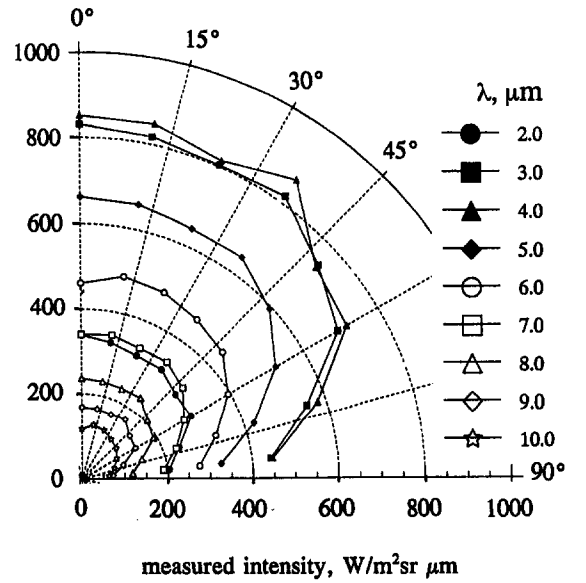

Fig. 3(*b*) Measured intensity polar distributions for a range of wavelengths

Numerical Analysis

Governing Equations. Since the temperature of the bed is only measured in two places, it is necessary to solve the energy conservation equation to determine the complete temperature field for use in the RTE. The oxidized stainless steel spherical packed bed used in the experiment is a finite plane parallel square slab with a vertical aspect ratio of 8.3 and insulated vertical boundaries, and the spatial intensity measurement point is on its vertical centerline. The medium is therefore treated as one dimensional. The Rayleigh number of the medium geometry treated as an unobstructed closed cavity is an order of magnitude less than that minimum Rayleigh number for advective flow (Incropera and DeWitt, 1990). There is a free advection from the open surface of the bed, although this flow is assumed not to penetrate into the bed. The medium is therefore treated using combined radiation and conduction heat transfer, without advection. The one-dimensional, radiation/conduction energy equation is written

$$-\frac{\partial}{\partial y}\left(k_b \frac{\partial T}{\partial y}\right) + 4\pi\beta \int_0^\infty (1 - \omega_\lambda) I_{\lambda b} d\lambda$$

$$-2\pi\beta \int_{\lambda=0}^\infty (1 - \omega_\lambda) \int_{\theta=0}^\pi I_\lambda \sin\theta d\theta d\lambda = 0 \quad (5)$$

on the coordinate system shown in Fig. 1. The ratio between the thermal conductivity of the bed particles and that of the interstitial medium (air) is on the order of 300. The analysis

of Batchelor and O'Brien (1977), as extended by Sangani and Acrivos (1983), yields an effective thermal conductivity for a random array of monodisperse spheres that is 17.2 times the thermal conductivity of the interstitial medium for this conductivity ratio. A least-squares linear fit over the operating temperature range is applied to the air thermal conductivity data of Incropera and DeWitt (1990) to complete the expression of the bed thermal conductivity. Equation (5) is solved with measured temperature boundary conditions just above the $y = 0$ surface and just below the $y = y_o$ surface.

For spatially one-dimensional media the radiation intensity is independent of the azimuthal component of direction (presuming that the directional polar axis is aligned with the axis of the spatial variable), and the RTE is written

$$\cos\theta \frac{\partial I_\lambda}{\partial y} + \beta I_\lambda = \beta(1 - \omega_\lambda) I_{\lambda b} + \frac{\beta\omega_\lambda}{2} \int_0^\pi I_\lambda p_\lambda(\theta, \theta') \sin\theta' d\theta'. \quad (6)$$

On the bed's open top surface, the incoming boundary condition intensity is taken to be blackbody radiation at the temperature of the surroundings. On the bottom surface, resting on the heater block, intensity results from directional emission and hemispherical-directional reflection

$$I_\lambda(0, \theta < \pi/2) = \epsilon_{\lambda,co}(\theta) I_{\lambda b}(T_1) + 2[(1 - \epsilon_{\lambda,co}(\theta)] \int_{\pi/2}^\pi I_\lambda \cos\theta \sin\theta d\theta \quad (7)$$

where $\epsilon_{\lambda,co}(\theta)$ is a spectral-directional quantity. The emittances in Eq. (7) are measured data for the spectral-directional emittance of fully oxidized copper, reported by Jones et al. (1995), and abstracted here as Fig. 4.

The spherical bed of 1-mm-dia balls has a minimum size parameter $\pi d_p/\lambda$ of 314 for the measured wavelength range, and a solid volume fraction of 0.6287. Kamiuto (1990) offers a correlated scattering theory for packed beds of spheres with large size parameters based on the general size parameter dependent scattering analyses of Tien and others (as cited by Kamiuto). This theory is verified by experiment for cold beds, also comprised of randomly packed type 316 stainless steel (nonoxidized) balls of 1 mm diameter, in which the attenuation and scattering of a collimated incident intensity is measured (Kamiuto, 1991a, b). For Kamiuto's correlated scattering theory, the radiative properties are expressed

$$\gamma_2 = 1 + 1.5(1 - \phi) - 0.75(1 - \phi)^2$$

$$Q_{ex} = 2\gamma_2$$

$$\omega_\lambda = \frac{2\gamma_2 - \epsilon_{\lambda,ss}}{2\gamma_2}. \quad (8)$$

where $\beta = Q_{ex}\pi d_p^2 N/4$, $N = 6(1 - \phi)/\pi d_p^3$, and $\epsilon_{\lambda,ss}$ is the spectral-hemispherical emittance of the bed particle material. Note that the extinction coefficient is taken to be independent of wavelength, though the albedo is not. The size parameter and volume fraction of the bed may place it in the regime of independent scattering regime (Tien, 1988), for which $Q_{ex} = 1$, $\omega_\lambda = 1 - \epsilon_{\lambda,ss}$ (assuming that the bed particles are opaque and that diffraction scattering is uniquely forward). The results of Eqs. (8) indicate a much larger extinction efficiency than those of independent scattering theory (a factor of 3.3), and also a larger albedo, though some of this is due to the inclusion of the effects of extinction by diffraction in Eqs. (8).

In order to establish the spectral-hemispherical emittance of the lightly oxidized 316 stainless steel balls, a plate of this material is prepared by polishing to a #8 lathe finish (polished smooth, but not mirrorlike, with small scratches and imperfections plainly visible), thoroughly cleaned to remove foreign films and particles, and held at 900 K for 200 h. A light oxide film develops, similar in appearance to that on the 1-mm-dia balls. The spectral-directional emittance of this sample is measured using the same apparatus and procedure as used for the oxidized copper bottom boundary, and the result numerically integrated to obtain the spectral-hemispherical emittance. The result is shown in Fig. 5.

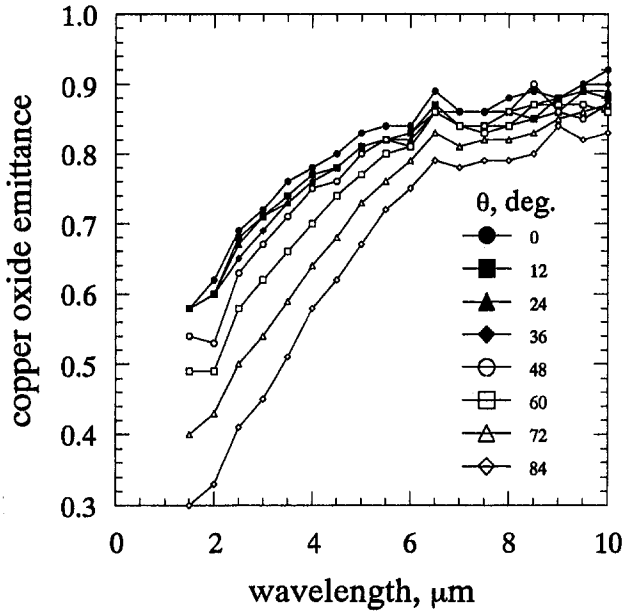

Fig. 4 Measured spectral-directional emittance of heavily oxidized copper

Large opaque spheres may have scattering phase functions that are either forward scattering if the sphere surface is specular, or backward scattering if the surface is diffuse. Since the surface of the lightly oxidized stainless steel balls is neither completely specular nor completely diffuse, the general scattering phase function of Henyey and Greenstein (1940, op. cit. Siegel and Howell, 1992) is employed:

$$p_\lambda(\theta, \theta') = \frac{(1 - g_\lambda^2)}{(1 + g_\lambda^2 - 2g_\lambda \cos\theta \cos\theta')^{3/2}}$$

$$g_\lambda = \frac{1 - 0.48(2\gamma_2 - 1)(1 - \epsilon_{\lambda,ss})}{1 + (2\gamma_2 - 1)(1 - \epsilon_{\lambda,ss})} \quad (9)$$

where the second of Eqs. (9) represents Kamiuto's (1992) model, fit to experimental measurements on the same type of bed as considered here.

Discretization. The spatial terms in Eqs. (5) and (6) are discretized in a cell-integrated manner, using a uniform mesh. (A power law variable mesh is found to bring no advantage, as the conduction to radiation ratio or Stark number, $\beta k/4\sigma_b T_1^3 = 25$, is large, indicating that conduction is dominant and a near-linear temperature profile is expected). The temperature boundary conditions are centered at the temperature measurement probes (1 mm diameter) in the second layer of balls above the bottom boundary and in the top layer of balls, rather than at the computational boundaries of the bed. The discrete expression of the temperature derivatives in Eq. (5) is modified accordingly.

The directional terms in Eqs. (5) and (6) are discretized for application of the discrete ordinates method using an ad hoc quadrature, which allows consideration of directions near the polar axis and also meets zeroth (incidence), first (flux), and second (diffusion) moment criteria. Conventional quadratures

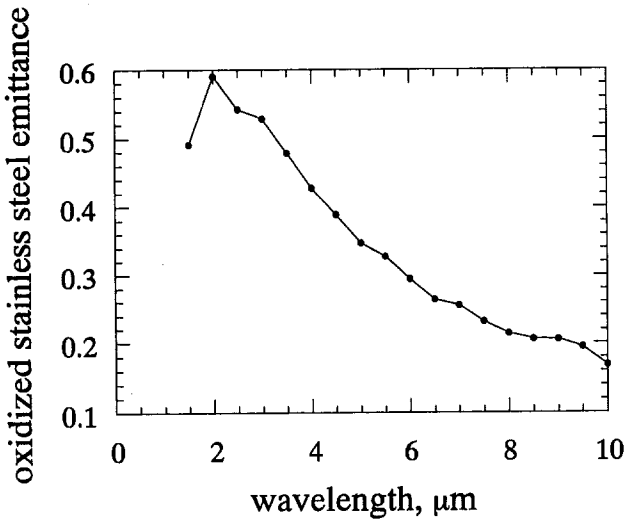

Fig. 5 Measured spectral-hemispherical emittance of lightly oxidized stainless steel

for plane-parallel media (cf. Fiveland, 1987) correctly recover the first $n-1$ moments of an n-order (one quadrant) directional mesh with equal integration weights. The equal weight feature tends to skew the quadrature direction distribution away from the polar axis. However, intensity measurements are most conveniently made at an even distribution of polar angles, and more direct comparisons may be made between measured and computed intensities if the computational and measurement directional meshes correspond. Therefore, an unequal weight quadrature is adopted with equally distributed ordinates, $\theta_m = \pi(m - \frac{1}{2})/M$, and moderately unequal weights, $w_m^* = \pi \sin \theta_m / M$, where the weights are slightly adjusted so that the zeroth, first, and second moments are satisfied:

$$a \sum_{1}^{M/6} w_m^* + b \sum_{(M/6)+1}^{M/3} w_m^* + c \sum_{(M/3)+1}^{M/2} w_m^* = 1$$

$$a \sum_{1}^{M/6} \cos\theta_m w_m^* + b \sum_{(M/6)+1}^{M/3} \cos\theta_m w_m^* + c \sum_{(M/3)+1}^{M/2} \cos\theta_m w_m^* = \tfrac{1}{2}$$

$$a \sum_{1}^{M/6} \cos^2\theta_m w_m^* + b \sum_{(M/6)+1}^{M/3} \cos^2\theta_m w_m^* + c \sum_{(M/3)+1}^{M/2} \cos^2\theta_m w_m^* = \tfrac{1}{3} \quad (10)$$

and then $w_m = a w_m^*$ for $m \le M/6$, $w_m = b w_m^*$ for $M/6 < m \le M/3$, and $w_m = c w_m^*$ for $m > M/3$. The limits of summation in Eqs. (10) are adjusted for mesh sizes not evenly divisible by six. For an eighth-order quadrature ($M = 16$) with $\theta_1 = 0$ ($w_1^* = \pi \sin(\theta_2/2)/2M$), $a = 1.0531$, $b = 1.0330$, and $c = 1.0902$.

The spectral integrations in Eq. (5) are computed by solving Eq. (6) for constant spectral band intensities between 1.5 μm and 10 μm, and completing the integration outside this range using the range limit intensity and a scaling based on the blackbody spectral distribution.

Solution. The general solution algorithm is nested iteration, with a temperature-linearized form of Eq. (5) in the outer loop and Eq. (6) in the inner loop. The temperature profile is solved with the tridiagonal Thomas algorithm for each linearization point, and successive overrelaxation with an acceleration coefficient of 1.5 is used to update the linearization point. Each temperature profile iteration includes a complete RTE solution. The RTE is solved using a marching algorithm starting from the top boundary facing down, with successive intensity update for the in-scattering term. Projection across each spatial cell follows the exponential scheme of Chai et al. (1994). Two methods for RTE solution acceleration are employed. The first is the partially implicit method also described by Chai et al. (1994), in which for a given direction the discretized in-scattering term self-contribution in Eq. (6) is removed from the right side and grouped with the linear term on the left. This method is most useful in low-order quadratures, but still has some use even at eighth order. The second is simply successive over relaxation, using an acceleration coefficient of 1.5. Using both acceleration methods together generally results in a roughly 50 percent reduction in run time, as compared to a simple updating technique.

Mesh Sensitivity. Mesh sensitivity studies are based on the total radiative flux at the top surface of the medium. Variation of spatial mesh size shows the flux discretization error to be approximately related to the square of the mesh interval (second order error), although not uniformly so through all mesh variations. A mesh size of 16 results in a deviation of <0.1 percent as related to a mesh size 64 result, and the mesh size 16 is therefore chosen for results generation.

Top surface flux sensitivity to directional mesh size does not appear to follow a smooth power law relation. In general, any directional mesh size ≥12 (sixth-order quadrature) produces a discretization uncertainty <0.1 percent, as compared to mesh size 48 results. A mesh size of 16 is chosen for results generation for the convenience of direct comparison to experimental results.

Sensitivity to spectral mesh is similar to that for the directional mesh, with uncertainty <0.1 percent for 8 spectral bands, as compared to the 32 band results, and an 18 band mesh is chosen for the convenience of direct experimental comparison.

Uncertainty. Uncertainty in the computed intensity is a function of uncertainty in the boundary values and the thermophysical properties, in addition to mesh sensitivity. The uncertainty in intensity is expressed $u_I^2 = \Sigma\, (\partial I/\partial x)^2 u_x^2$ where the eight primary uncertain parameters are listed in Table 1. The sensitivities of the exiting intensity to each parameter ($\partial I/\partial x_i$) are themselves functions of wavelength and direction. In order to illustrate the relative contributions of the uncertainty in each parameter, Table 1 lists the sensitivities for the normal direction and for $\lambda = 3.5$ μm, at which the highest intensity value is measured. Table 1 shows that while the top surface temperature and bed thickness uncertainties have a significant effect on the total uncertainty in intensity, the dominant uncertainty is that of the ball emittance. Computation of the uncertainty in exiting intensity for each wavelength and direction results in an uncertainty due to property uncertainty that varies between 2.5 and 3.5 percent, with greater uncertainty at directions further from the surface normal. In order to reduce the possibility of uncertainty due to programming error, two of the authors wrote independent programs to implement the computation scheme.

Results. Figure 6 shows the computed temperature profile, which is nearly linear, with only a small deviation near the low-temperature (top, open) surface. This nonlinearity is caused by the low incident intensity resulting from blackbody emission from the surroundings at $T_\infty = 300$ K. Since the profile is already nearly linear, further increases in the effective Stark number would have an insignificant effect on the temperature distribution, and therefore also on the intensity.

Figure 7 shows the computed exiting intensity for the measurement wavelengths and directions, which clearly shows a much more diffuse behavior than the measured intensity (Fig. 3(*a*)). Figure 8 shows a spectral comparison between measurement and computation for the normal ($\theta = 0$ deg) and grazing ($\theta = 84$ deg) directions. Comparison between measured and computed intensities is very good for $0 \le \theta \le 48$ deg, and is well within the calculated uncertainties for these quantities. For

Table 1 Computational intensity uncertainty due to property and boundary condition uncertainty

x	$\frac{\partial I_\lambda}{\partial x}$	u_x	$\frac{\partial I_\lambda}{\partial x} u_x$, $W/m^2 sr\,\mu m$
T_1	0.472 $W/m^2 sr\,\mu m\,K$	1 K	0.472
T_2	5.03 $W/m^2 sr\,\mu m\,K$	1 K	5.03
T_∞	0.00722 $W/m^2 sr\,\mu m\,K$	10 K	0.0722
y_o	5760 $W/m^2 sr\,\mu m\,m$	0.001 m	5.76
k_b	11.9 $K/m\,sr\,\mu m$	0.075 W/mK	0.889
ϵ_{co}	0.0988 $W/m^2 sr\,\mu m$	0.035	0.0035
ϕ	9.41 $W/m^2 sr\,\mu m$	0.02	0.188
ϵ_{ss}	778 $W/m^2 sr\,\mu m$	0.025	19.5

$\theta > 48$ deg there is increasing disagreement as the measured intensity shows a strong directional character while the computed intensity remains relatively diffuse. At grazing angles, computed intensity is on the order of 80 percent higher than

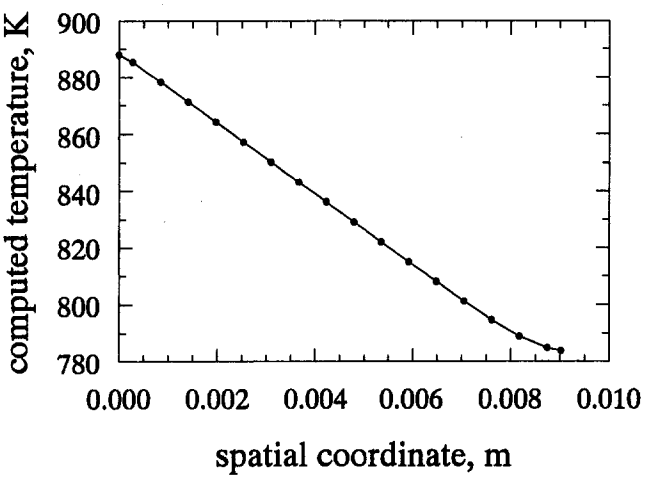

Fig. 6 Computed temperature profile (with measured boundary values)

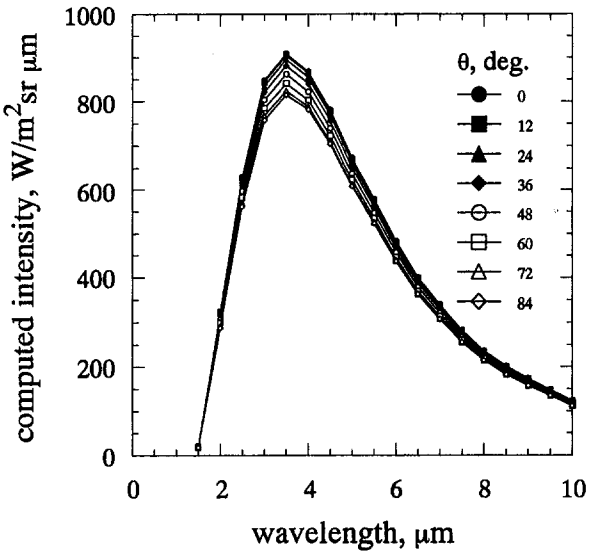

Fig. 7 Computed intensity spectra for a range of polar angles

measured intensity. The measured intensities are integrated to yield a radiative heat flux of 12.42 kW/m^2, as compared to 13.36 kW/m^2 for the computed results (computation is 7.6 percent high). Since the smaller polar angles have a greater influence on normal flux, discrepancies in intensity in the grazing angles do not lead to equivalent flux errors.

Results are also computed for independent scattering radiative properties. These results are similar in spectral and directional character to Fig. 7, showing perhaps slightly more directional attenuation in the grazing angles, though the intensity magnitudes are on the order of 25 percent higher than those computed with correlated scattering properties. Since the magnitudes of the computed intensities using correlated scattering properties compare much more closely to the measured results than those computed with independent scattering properties, it seems clear that independent scattering theory is not appropriate for the large sphere packed bed.

It is not clear why the measured and computed intensity results should fail to agree directionally. The intensity measurement system calibrates well with a blackbody, and has shown no tendency to fail to predict diffuse behavior (Jones et al.,

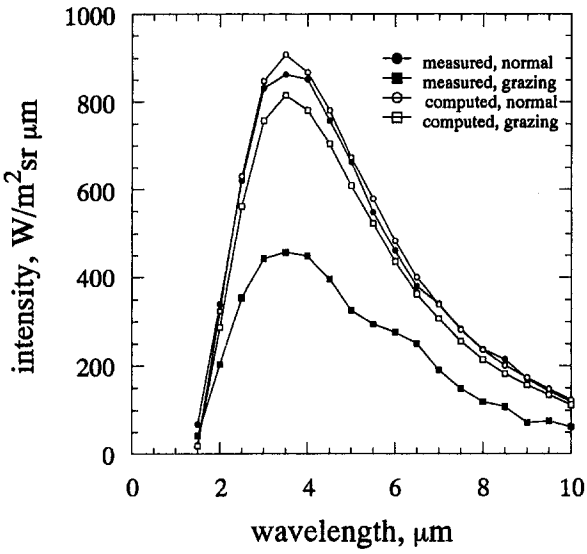

Fig. 8 Comparison of measured and computed intensity at normal and grazing angles

1995, measure higher than expected intensity at grazing angles in a surface radiation application, rather than lower as found here). Continuum considerations might suggest better behavior at higher angles, as the number of ball rows on a directional path is higher. The numerical program compares well with results of Özişik (1973) for both radiative and combined mode cases in continuous media. Considering the history of correlating radiative intensity with RTE modeling, Walters and Buckius (1991) found good correlation using a thermally emissive, disperse particulate medium in the normal direction, although off-normal directions were not measured. Other workers who have examined scattered transmission of a single collimated beam through cold media have derived radiative properties that correlate well with continuous RTE-based theories (as, indeed, the correlated scattering radiative properties used here, which are verified by Kamiuto, 1992, in experiments also on a similar randomly packed bed of 1-mm-dia stainless steel balls).

It is interesting to note in Fig. 3(a) that the off-normal intensities at the grazing angles bear a strong resemblance to surface emission at the top surface temperature and an emittance as indicated in Fig. 5 (for the oxidized stainless steel bed material). It might be reasonable to say that while the continuous form of the RTE is reasonable deep in the packed bed, its use is suspect near the boundaries off the bed. Better correlation between measurement and computation may result from development of a discrete radiation model (as in Tien, 1988, accounting for the detailed structure of the packed bed geometry) for use near the boundaries. In the past, discrete bed methods have focused on normal transmission through and reflection from packed beds, and have been correlated with experiments configured to respond to normal direction transfer. Further development is necessary to produce a discrete radiation model for a packed bed that yields off-normal intensity distributions.

On the other hand, numerical experiments conducted to find a combination of radiative properties that might mimic Fig. 3(a) successfully identified lower values of extinction efficiency ($Q_{ex} \approx 2$, including diffraction), higher scattering albedos ($\omega \approx 0.99$), and more forward scattering phase functions ($g \sim 0.6$). That numerical experiments can identify a possible combination of radiative properties that will satisfy the data suggests a potential improvement from that quarter. However, such lower extinction efficiencies require use of independent scattering theory, while higher albedos, given the emittance values in Fig. 5, can only be obtained through correlated scattering theory. Since the identified parameters are of inconsistent origin, the numerical experiments should be expanded into a detailed system identification analysis to identify the complete range of suitable parameters before undertaking to piece together a rationale supporting an alternate radiative property derivation. Further experimentation using simpler radiative boundary conditions would aid system identification of radiative properties.

Conclusions

The radiation intensity exiting a heated, nonisothermal packed bed of monodisperse, opaque, large spherical particles, bounded by opaque, nondiffuse surfaces, is measured spectrally and directionally using a radiometric technique. The bed is modeled using a one-dimensional continuous radiative transfer equation, arranged for solution using the discrete ordinates method, with radiative properties estimated using correlated (dependent) scattering theory. Material emittances to which the bed properties are related are measured experimentally. Bed boundary temperatures are measured, and the remainder of the temperature profile is computed.

It is found that measured and computed intensities agree quite well in near-normal directions. However, the values of measured and computed intensities diverge as the polar angle is increased beyond about 48 deg, with the measured result showing a strong directional character, while the computed results are nearly diffuse. Intensities computed with independent scattering theory radiative properties are about 25 percent higher than measured intensities, demonstrating that independent scattering does not hold in this case.

It is concluded that the nonisothermal large sphere packed bed is not appropriately modeled by the continuous radiative transfer equation and radiative properties as presented; although since it is only higher polar angles that fail to correlate, there is only a small discrepancy in radiative flux. Further investigation is necessary to distinguish whether the deficiency is due to the form of the radiation model, the solution technique, or the effective bed properties. It is suggested that a noncontinuous radiation model, accounting for spatial features in detail, may be necessary to model radiation intensity near the medium boundaries. Such a model might be used to match boundary behavior to the RTE at some depth within the medium. Further investigation is also appropriate to identify formally the radiative properties that give rise to the measured behavior, in the framework of both the continuous RTE, and for a more complicated boundary model matched to the RTE.

Acknowledgments

Funding for this work was provided by the National Science Foundation, under grant No. CTS-9209926, whose support is gratefully acknowledged. Measurements of the emittance of oxidized stainless steel were provided by Mr. Eugen Nisipeanu.

References

Batchelor, G. K., and O'Brien, R. W., 1977, "Thermal or Electrical Conduction Through a Granular Material," *Proceedings of the Royal Society of London, Series A,* Vol. 355, No. 1682, pp. 313–333.

Chai, J. C., Lee, H. S., and Patankar, S. V., 1994, "Improved Treatment of Scattering Using the Discrete Ordinates Method," ASME JOURNAL OF HEAT TRANSFER, Vol. 116, pp. 260–263.

Fiveland, W. A., 1987, "Discrete Ordinates Method for Radiative Heat Transfer in Isotropically and Anisotropically Scattering Media," ASME JOURNAL OF HEAT TRANSFER, Vol. 109, pp. 809–812.

Fiveland, W. A., and Jessee, J. P., 1995, "Comparison of Discrete Ordinates Formulations for Radiative Heat Transfer in Multidimensional Geometries," *Journal of Thermophysics and Heat Transfer,* Vol. 9, No. 1, pp. 47–54.

Glicksman, L., Schuetz, M., and Sinofsky, M., 1987, "Radiation Heat Transfer in Foam Insulation," *International Journal of Heat and Mass Transfer,* Vol. 30, No. 1, pp. 187–197.

Hendricks, T. J., and Howell, J. R., 1994, "Absorption/Scattering Coefficients and Scattering Phase Functions in Reticulated Porous Ceramics," in: *Radiative Heat Transfer: Current Research,* Y. Bayazitoğlu et al., eds., ASME HTD-Vol. 276, pp. 105–114.

Howell, J. R., 1988, "Thermal Radiation in Participating Media: the Past, the Present, and Some Possible Futures," ASME JOURNAL OF HEAT TRANSFER, Vol. 110, pp. 1220–1229.

Incropera, F. P., and DeWitt, D. P., 1990, *Fundamentals of Heat and Mass Transfer,* 3rd ed., Wiley, New York.

Jones, P. D., Dorai-Raj, D. E., and McLeod, D. G., 1995, "Spectral-Directional Emittance of Fully Oxidized Copper," AIAA Paper No. 95-3521.

Kamiuto, K., 1990, "Correlated Radiative Transfer in Packed-Sphere Systems," *Journal of Quantitative Spectroscopy and Radiative Transfer,* Vol. 43, No. 1, pp. 39–43.

Kamiuto, K., Iwamoto, M., Sato, M., and Nishimura, T., 1991a, "Radiation-Extinction Coefficients of Packed-Sphere Systems," *Journal of Quantitative Spectroscopy and Radiative Transfer,* Vol. 45, No. 2, pp. 93–96.

Kamiuto, K., Iwamoto, M., Nishimura, T., and Sato, M., 1991b, "Albedos and Asymmetry Factors of the Phase Functions for Packed-Sphere Systems," *Journal of Quantitative Spectroscopy and Radiative Transfer,* Vol. 46, No. 4, pp. 309–316.

Kamiuto, K., 1992, "Radiative Properties of Packed-Sphere Systems Estimated by the Extended Emerging-Intensity Fitting Method," *Journal of Quantitative Spectroscopy and Radiative Transfer,* Vol. 47, No. 4, pp. 257–261.

McLeod, D. G., 1995, "Determination of Radiative Properties of a Spherical Packed Bed Through Direct Intensity Measurements," M.S. Thesis, Auburn University, Auburn, AL.

Menart, J. A., Lee, H. S., and Buckius, R. O., 1989, "Experimental Determination of Radiative Properties for Scattering Particulate," *Experimental Heat Transfer,* Vol. 2, pp. 309–322.

Modest, M. F., 1993, *Radiative Heat Transfer,* McGraw-Hill, New York.

Nelson, H. F., and Satish, B. V., 1987, "Transmission of a Laser Beam Through Anisotropic Scattering Media," *Journal of Thermophysics and Heat Transfer,* Vol. 1, No. 3, pp. 233–239.

Nicolau, V. P., Raynaud, M., and Sacadura, J. F., 1994, "Spectral Radiative Properties Identification of Fiber Insulating Materials," *International Journal of Heat and Mass Transfer,* Vol. 37, suppl. 1, pp. 311–324.

Özişik, M. N., 1973, *Radiative Transfer and Interactions With Conduction and Convection,* Wiley, New York (reprinted by Werbel & Peck, New York, 1985).

Saboonchi, A., Sutton, W. H., and Love, T. J., 1988, "Direct Determination of Gray Participating Thermal Radiation Properties of Insulating Materials," *Journal of Thermophysics and Heat Transfer,* Vol. 2, No. 2, pp. 97–103.

Sangani, A. S., and Acrivos, A., 1983, "The Effective Conductivity of a Periodic Array of Spheres," *Proceedings of the Royal Society of London, Series A,* Vol. 386, No. 1791, pp. 263–275.

Siegel, R., and Howell, J. R., 1992, *Thermal Radiation Heat Transfer,* 3rd ed., Hemisphere Publishing Corp., Washington, DC.

Skocypec, R. D., Walters, D. V., and Buckius, R. O., 1987, "Spectral Emission Measurements From Planar Mixtures of Gas and Particulates," ASME JOURNAL OF HEAT TRANSFER, Vol. 109, pp. 151–158.

Tien, C. L., 1988, "Thermal Radiation in Packed and Fluidized Beds," ASME JOURNAL OF HEAT TRANSFER, Vol. 110, pp. 1230–1242.

Viskanta, R., and Mengüç, M. P., 1987, "Radiation Heat Transfer in Combustion Systems," *Progress in Energy and Combustion Science,* Vol. 13, pp. 97–160.

Walters, D. V., and Buckius, R. O., 1991, "Normal Spectral Emission From Nonhomogeneous Mixtures of CO_2 Gas and Al_2O_3 Particulate," ASME JOURNAL OF HEAT TRANSFER, Vol. 113, pp. 174–184.

On the Role of Marangoni Effects on the Critical Heat Flux for Pool Boiling of Binary Mixtures

W. R. McGillis

V. P. Carey

Department of Mechanical Engineering,
University of California,
Berkeley, CA 94720

The Marangoni effect on the critical heat flux (CHF) condition in pool boiling of binary mixtures has been identified and its effect has been quantitatively estimated with a modified model derived from hydrodynamics. The physical process of CHF in binary mixtures, and models used to describe it, are examined in the light of recent experimental evidence, accurate mixture properties, and phase equilibrium revealing a correlation to surface tension gradients and volatility. A correlation is developed from a heuristic model including the additional liquid restoring force caused by surface tension gradients. The CHF condition was determined experimentally for saturated methanol/water, 2-propanol/water, and ethylene glycol/water mixtures, over the full range of concentrations, and compared to the model. The evidence in this study demonstrates that in a mixture with large differences in surface tension, there is an additional hydrodynamic restoring force affecting the CHF condition.

Introduction

A number of investigations have examined the CHF for pool boiling of binary mixtures. Thome and Shock (1984) provide an extensive review of the literature on binary mixtures. As early as 1941, Bonilla and Perry experimentally investigated boiling binary mixtures of aqueous and organic mixtures from a flat horizontal plate. In numerous studies, Van Stralen and co-authors (1956; 1969) extensively studied pool boiling in binary mixtures. The most interesting finding of these studies was that the CHF for mixtures may significantly exceed the CHF for either of the pure components.

Reddy and Lienhard (1989) investigated the CHF mechanism for ethanol/water mixtures on small horizontal cylinders. They provided a brief summary of binary mixture CHF studies since 1941. Reddy and Lienhard (1989) emphasized that the prediction of the CHF condition should account for heater size variations and that the overall trends in these previous CHF studies were almost impossible to identify at the time data were obtained. They stated that the interpretation offered in previous studies may have suffered because the influence of the role of geometry on the CHF was not identified.

Previous interpretations of the CHF mechanism in binary liquids focus on the observation that the liquid near the interface where vaporization occurs is effectively subcooled (McEligot, 1964). The evaporation from the liquid–vapor interface in a binary system leaves the liquid phase at a higher concentration of the less volatile component. The less volatile component has the higher saturation temperature. Correlations to predict the CHF in binary liquid mixtures based on the induced subcooling have been proposed by Kutateladze et al. (1966), Matorin (1973), and Reddy and Lienhard (1989).

Kutateladze et al. (1966) correlated the CHF condition to the shape of the phase equilibrium diagram. Maxima in the CHF condition were correlated to maxima in the liquid–vapor composition difference $(x - y)$. Figure 1 shows the composition difference on the phase diagram.

Reddy and Lienhard (1989) discussed how the amount of subcooling is not known. One approximation for the amount of subcooling is $(x - y)\partial T/\partial x$. Reddy and Lienhard (1989) quantitatively evaluated the effective subcooling in a boiling binary mixture. Using a well-tested pure component CHF correlation that accounts for size effects, dimensional analysis, and a least-squares fit to their data, Reddy and Lienhard (1989) successfully correlated the CHF in their ethanol/water mixture system with an effective Jakob number.

$$q''_{m,\mathrm{RL}} = \frac{q''_{m,\mathrm{SL}}}{(1 + 0.1x)}\left(1 - 0.170\, Ja_e^{0.308}\right)^{-1} \tag{1}$$

where Ja_e is defined as

$$Ja_e = \frac{\rho_l c_{pl}[T_{s,v}(x_b) - T_{s,l}(x_b)]}{\rho_v h_{lv}} \tag{2}$$

and $q''_{m,\mathrm{SL}}$ is the Sun–Lienhard (1970) prediction for saturated critical heat flux from horizontal cylinders. Although the agreement with their ethanol/water data is quite good (see Fig. 10), Reddy and Lienhard (1989) acknowledged that additional research is needed to examine the effects of heat diffusion, heater geometry, and heater boundary condition on the CHF condition.

It has been occasionally mentioned in binary mixture CHF papers that there is another possible mechanism responsible for the nonmonotonic CHF behavior in some binary mixtures. In boiling mixtures, the influence of surface tension differences, known as the Marangoni effect, may be acting on the evaporating liquid film. It is well known that surface tension gradients exist on the liquid–vapor interface of an evaporating film containing a mixture of liquids with different volatility. Hovestreijdt (1963) provided CHF measurements on binary organic mixtures with differences in surface tension. The experimental results show differences in CHF values for a platinum heated wire. Hovestreijdt (1963) speculated that the influence of the surface tension difference was to stabilize the bubbles on the wire. In this study, the effects of heater geometry and mixture property variations were not known or understood, so no decisive conclusions were made.

Contributed by the Heat Transfer Division for publication in the JOURNAL OF HEAT TRANSFER. Manuscript received by the Heat Transfer Division September 1994; revision received October 1995. Keywords: Boiling, Phase-Change Phenomena. Associate Technical Editor: R. A. Nelson, Jr.

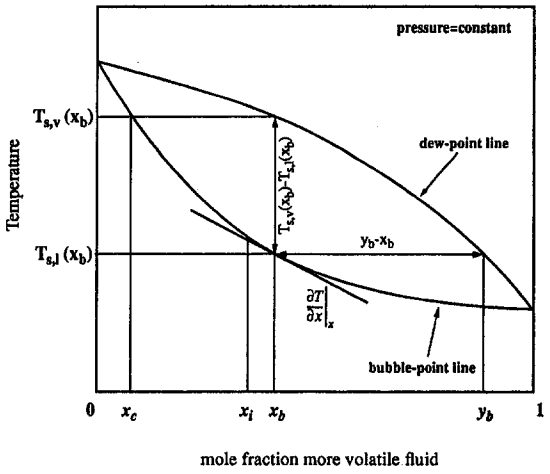

Fig. 1 Liquid–vapor phase-equilibrium diagram

Due to differences in fluid volatility, preferential evaporation of one component occurs along the liquid–vapor interface of a binary mixture. The variations in concentration along, and normal to, the liquid–vapor interface result in physical property gradients. This investigation uses the most up-to-date mixture property prediction methods. Most predictions are determined from Prausnitz (1992) and Reid et al. (1987). Knowledge of accurate mixture properties is necessary because of the large nonlinear variations with concentration, which can significantly affect CHF predictions.

The prior investigations noted above have not produced a method that accurately predicts the CHF for a wide range of fluids, geometries, configurations, and pressures. Also, it is not apparent that the correct binary mixture CHF mechanism has been identified. The hypotheses used for correlation have been based on subcooling and limited data. Observing the highly nonlinear experimental CHF data and property variations has motivated a second look at the phenomena associated with the binary mixture CHF mechanism. Surface tension gradients due to a composition gradient cause shear stresses that can enhance the flow and might significantly affect the CHF condition.

This study specifically explores the effective subcooling theories versus the Marangoni effect theories on the CHF mechanism. A full comparison is done on a broad range of operating fluids. A proven test facility is used to measure the CHF condition experimentally. Accurate mixture thermodynamic property models are used in a hydrodynamic model developed, which assesses which mechanism is important.

Phase Equilibrium

Accurate determination of thermophysical properties of the fluid mixture is critical to accurate prediction of boiling heat transfer performance. Approximate methods are necessary to investigate a wide range of conditions accurately (concentrations and pressures). Methods for predicting binary mixture boiling phenomena require interpretations of the mixture properties and the mixture phase equilibrium characteristics. The calculation of phase equilibrium and thermodynamic properties of binary mixtures usually requires pure component property data.

Mixtures of water and ethylene glycol and water and alcohol are not ideal mixtures. Physical properties can be predicted by techniques provided by Prausnitz (1992) and Reid et al. (1987). In binary mixtures, the fugacity (or equivalently, the chemical potential) of component i in the liquid must be equal to that of component i in the vapor, $f_i^v = f_i^l$. The fugacity of component i in the vapor is related to the total pressure by $f_i^v = \phi_i y_i P$, and the fugacity of component i in the liquid is related to the saturation pressure of pure component i by $f_i^l = \gamma_i x_i P_i^S$. Using the fact that $y_1 + y_2 = 1$ and $x_1 + x_2 = 1$, the saturation pressure of the mixtures used in this investigation at low pressure can be expressed as

$$P = x_2\gamma_2 P_2^S + (1 - x_2)\gamma_1 P_1^S \tag{3}$$

The fugacity coefficient, ϕ_i, is an indication of the nonideal behavior of the mixture from ideal gas behavior. For low pressure, $\phi_i = 1$ is a very good approximation. However, the activity coefficient, γ_i, is not unity for most liquid mixtures with strong molecular interactions, such as polar liquids. For such liquids, the assumption of a simple mixing rule is not accurate. For real liquids, the activity coefficients of a binary mixture can be determined from the two-parameter Margules equations,

$$\ln \gamma_i = [A_{ij} + 2(A_{ji} - A_{ij})x_i]x_j^2 \tag{4}$$

The constants A_{ij} and A_{ji} can be determined from experimental data for mixtures and are independent of temperature over the range of interest in this investigation.

Figure 2 shows a phase diagram for the 2-propanol/water mixture with a pressure equal to 101 kPa. To the left of the azeotrope, water is less volatile than 2-propanol. To the right of the azeotrope, water is slightly more volatile than 2-propanol. At the azeotropic point, water and 2-propanol have the same volatility.

Knowledge of accurate phase equilibrium characteristics are known for any mixture and pressure for the fluids used in this investigation. The equations of phase equilibrium can then be used to solve for vapor and liquid mole fractions used in model

Nomenclature

A_v = cross-sectional area of vapor stem
A_w = area of heated surface
Az = azeotrope
A_{ij}, A_{ji} = activity coefficient constants
c_m = constant in correlation
c_{pl} = liquid specific heat
f = fugacity in the liquid
f^v = fugacity in the vapor
g = gravity
h_{lv} = heat of vaporization
Ja_e = effective Jakob number
P = system pressure
P^s = saturation pressure
q''_m = critical or maximum heat flux
$q''_{m,\mathrm{HK}}$ = Haramura–Katto CHF
$q''_{m,\mathrm{SL}}$ = Sun–Lienhard CHF
$q''_{m,\mathrm{RL}}$ = Reddy–Lienhard CHF
$q''_{m,\mathrm{MC}}$ = McGillis–Carey CHF
$q''_{m,sf}$ = single-fluid CHF
$q''_{m,Zuber}$ = Zuber CHF
R = radius of cylinder
T = temperature
T_s = liquid saturation temperature
x = liquid mole fraction
x_c = interfacial depleted liquid mole fraction
y = vapor mole fraction
γ = activity coefficient
$\Delta\psi_r$ = available liquid return energy
λ_D = Taylor wavelength
ρ_l = liquid density
ρ_v = vapor density
σ = liquid surface tension
ϕ = fugacity coefficient

Subscripts

b = bulk
f = body force
l = liquid
v = vapor
w = water
τ = mixture or total

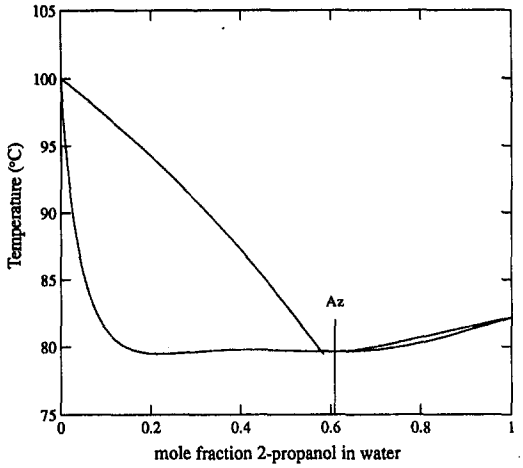

Fig. 2 Phase equilibrium diagram for the mixture of 2-propanol and water at a pressure of 101 kPa; 2-propanol and water exhibit azeotropy

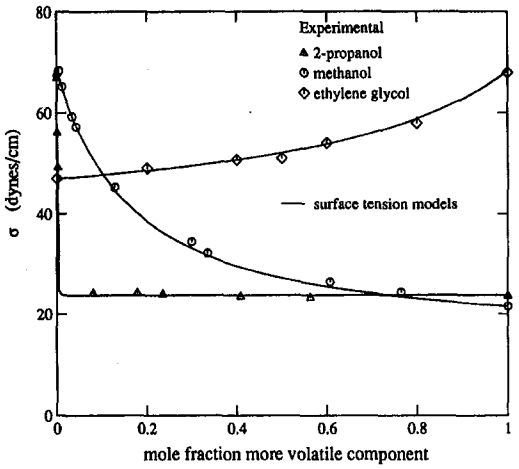

Fig. 3 Comparison of measured and calculated surface tension of aqueous mixtures at 25°C

calculations. Once phase equilibrium is known, physical properties can be estimated using some of the following models.

Mixture Properties

The vapor density of water and ethylene glycol at subatmospheric pressure is predicted by the ideal gas equation of state (EOS). If the ideal gas EOS is not an accurate prediction for the pure component vapor density, then more sophisticated models may be used. The virial EOS is often accurate for many substances and can be extended to binary mixtures. Because no new large molecular forces are created when the mixtures of this investigation are combined, the mixture vapor density is accurately predicted by the partial vapor density. Because of phase equilibrium characteristics, the mixture vapor density can be highly nonlinear.

Differential heat of vaporization for a mixture, h_{lv}, is the enthalpy difference between the liquid and vapor at the same concentration. The differential heat of vaporization for the mixture can be determined from the Clausius–Clapeyron equation. The mixture properties used to calculate the differential heat of vaporization are highly nonlinear.

In almost all cases, the surface tension in liquid mixtures is usually less than a mole-weighted average surface tension of the pure components at the same temperature. This is because the concentration at the surface may become different than what is in the bulk liquid. This is often the case for aqueous/organic mixtures. Prausnitz (1993) recently stated that most accurate surface tension models are empirical. No single model accurately predicts the surface tensions of the mixtures used in this investigation. Consequently, different surface tension mixing models must be used for almost every different liquid mixture combination.

Figure 3 shows calculated and measured surface tension data. The surface tension gradient in a binary mixture is important to the phenomenological understanding of transport mechanisms in phase-change processes. In a mixture, the composition at the surface is not the same as what is in the bulk. Mole-dependent surface tension gradients, $\partial\sigma_t/\partial x$, can be calculated by differentiating equations for surface tension with respect to mole fraction.

Theory of Surface Tension Effects

The hydrodynamic model of Zuber (1959) assumed the CHF is attained when the large vapor columns leaving the surface become Helmholtz unstable. As heat flux on a surface is increased, the bubbles generated coalesce. These joined bubbles form large columns of vapor (Fig. 4). In Zuber's model, the CHF is postulated to occur when a Helmholtz instability of the vapor columns leaving the surface distorts and blocks liquid flow to the heated surface. As vaporization continues, the surface becomes deprived of liquid and a stable vapor film covers portions or all of the surface. The Helmholtz unstable wavelength is assumed to be equal to the Taylor wave node spacing λ_D. As shown in Fig. 4, the classic Zuber model postulates that the vapor column radius is equal to $\lambda_D/4$, and the spacing of the vapor columns is λ_D.

In this model of the CHF mechanism, at any instant, the available gravitational energy to return liquid to the surface per unit cell resulting from body forces is given by:

$$\Delta\psi_{r,f} = (\rho_l - \rho_v)\lambda_D\left(\pi\frac{\lambda_D^2}{16}\right)g\frac{\lambda_D}{2} \tag{5}$$

where λ_D is defined as:

$$\lambda_D = 2\pi\left[\frac{3\sigma}{(\rho_l - \rho_v)g}\right]^{1/2} \tag{6}$$

However, when vapor forms rapidly in liquid mixtures, the

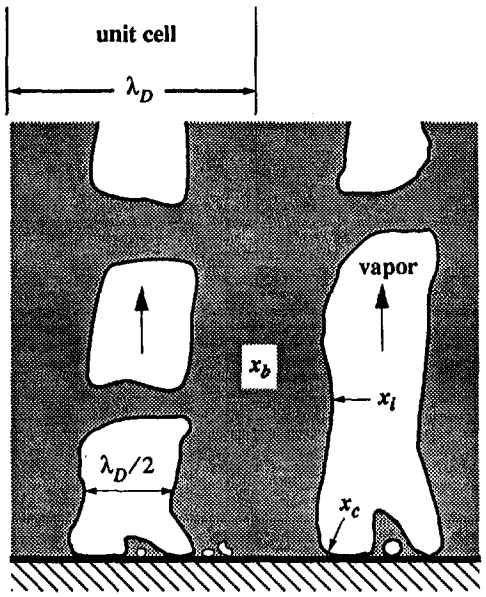

Fig. 4 Concentration variations generated as vapor slugs depart from surface

concentration of the more volatile component in the bulk will be greater than that at the liquid–vapor interface near the heated surface where rapid vaporization is occurring (see Fig. 1). The liquid at the interface has a higher local concentration of the less volatile component. When the CHF condition is reached, all the liquid reaching the surface is vaporized. Vapor produced at the heated surface is less rich in the more volatile component than that at the rest of the liquid–vapor interface. The concentration of the liquid being evaporated at the surface is approximately equal to the concentration in the vapor. The concentration of the more volatile component will thus vary along the liquid–vapor interface. The liquid concentration at the liquid–vapor interface near the heated surface decreases to x_c. Thus, a gradient of concentration along the interface is established where $x_c < x_i < x_b$.

In many, but not all, binary systems, the surface tension of the more volatile component is less than the surface tension of the less volatile component. If this is so, the concentration gradient above will generate a force that pulls the liquid toward the heated wall due to the gradient in surface tension. If the surface tension of the more volatile component is greater than the surface tension of the less volatile component, a force that pulls the liquid away from the heated wall will be created. Depending on the mixture, the surface tension gradients can be quite large.

If surface tension gradients caused by gradients in concentration influence the CHF condition, gradients in temperature may also be expected to influence the CHF condition. An increase in temperature always causes a decrease in surface tension. In systems where substantial wall superheats are experienced at the CHF condition, the temperature gradient from the heated surface to the bulk would always cause the surface tension to increase away from the heated surface and create a force that pulls liquid away from the heated wall. This impedance to renewal of liquid on the heated surface may be present in both pure fluids and binary mixtures. It is possible that temperature gradients on the vapor–liquid interface are smaller than concentration gradients on the vapor–liquid interface because the resistance to mass transfer is larger than the resistance to heat transfer in the liquid film. Also, surface tension is more dependent on concentration and less dependent on temperature. In a pure water system with a wall superheat of 30°C, the surface tension varies about 5 percent. The surface tension variation of pure water to a 0.1 mole fraction aqueous mixture of 2-propanol is about 68 percent. These two points make it reasonable to expect the effect of concentration gradients may have a greater effect on surface tension gradients than temperature gradients have on surface tension gradients. The following model development is based on modifying a pure component CHF model, which does not explicitly incorporate the effect of surface tension gradients but does predict the pure fluid CHF condition. Since dependence of surface tension gradients caused by temperature gradients must already be accounted for in previous hydrodynamic theory, only the added dependence on concentration gradients in a binary mixture will be considered in this study.

When surface tension gradients exist on the liquid–vapor interface (see Fig. 5), at any instant, the associated available energy to return liquid to the surface per unit cell is approximately given by

$$\Delta\psi_{r,\sigma} = \frac{\partial\sigma}{\partial x}(x_i - x_c)\left(\pi\frac{\lambda_D}{2}\right)\lambda_D \tag{7}$$

Equation (7) estimates the mean interfacial perimeter of the vapor column as $\pi\lambda_D/2$ and the mean distance from the surface along the interface as λ_D. The total available energy is equal to the sum of the contribution from the body forces and the surface tension forces. Therefore,

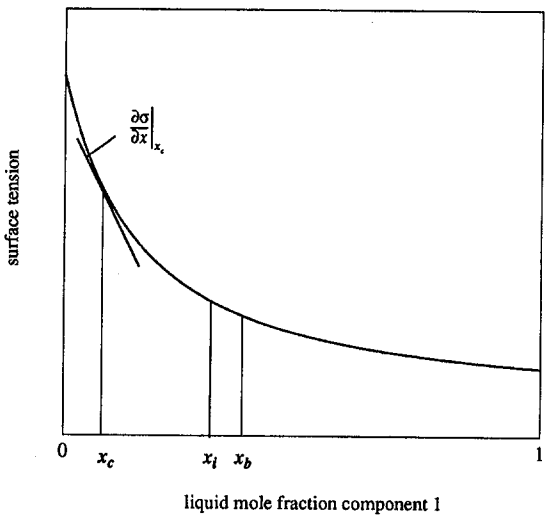

Fig. 5 Schematic surface tension diagram for a binary mixture

$$\Delta\psi_r = \Delta\psi_{r,f} + \Delta\psi_{r,\sigma} \tag{8}$$

$$\Delta\psi_r = \frac{\pi}{32}(\rho_l - \rho_v)\lambda_D^4 g + \frac{\pi}{2}\frac{\partial\sigma}{\partial x}(x_i - x_c)\lambda_D^2 \tag{9}$$

For pure fluids,

$$(\rho_l - \rho_v)g = \frac{32\Delta\psi_r}{\pi\lambda_D^4} \tag{10}$$

and the CHF is given by

$$q''_{m,Zuber} = \frac{\pi}{24}\rho_v h_{lv}\left[\frac{32\sigma\Delta\psi_r/(\pi\lambda_D^4)}{\rho_v^2}\right]^{1/4} \tag{11}$$

For the binary mixture, by analog it is therefore logical to replace $\Delta\psi_r$ in Eq. (11) to include the surface tension contribution, and arrive at the following expression for the CHF for a binary mixture:

$$q''_{m,\mathrm{MC}} = q''_{m,Zuber}\left[1 + \frac{4}{3\pi^2}\frac{1}{\sigma}\frac{\partial\sigma}{\partial x}(x_i - x_c)\right]^{1/4} \tag{12}$$

The concentration difference $(x_i - x_c)$ cannot be determined quantitatively. As shown by Hovestreijdt (1963), due to the depletion of the more volatile component, $(x_i - x_c)$ is proportional to the difference in concentration between the liquid and the vapor produced $(y_b - x_b)$. This is because the greater the volatility difference, $(y_b - x_b)$, the greater the depletion of the more volatile fluid (decrease in x_c) and an increase in $(x_i - x_c)$. Combining the coefficient $4/3\pi^2$ into a constant of proportionality, Eq. (12) can be rewritten into a more general form:

$$q''_{m,\mathrm{MC}} = q''_{m,Zuber}\left[1 + c_m\left(\frac{1}{\sigma}\right)\frac{\partial\sigma}{\partial x}(y_b - x_b)\right]^{1/4} \tag{13}$$

Equation (13) applies to saturated pool boiling near bodies with smooth surfaces of infinite extent. To obtain generality, Eq. (13) should be modified by replacing $q''_{m,Zuber}$ with an alternative correlation that applies to the specific configuration and geometry of interest. A more general form of Eq. (13) is thus provided by replacing $q''_{m,Zuber}$ by $q''_{m,sf}$:

$$q''_{m,\mathrm{MC}} = q''_{m,sf}\left[1 + c_m\left(\frac{1}{\sigma}\right)\frac{\partial\sigma}{\partial x}(y_b - x_b)\right]^{1/4} \tag{14}$$

where $q''_{m,sf}$ is the single-fluid CHF correlation correcting for

geometry and configuration. For example, in the study of Reddy and Lienhard (1989), $q''_{m,sf} = q''_{m,SL}$. Note that for pure fluids, the quantity $(y_b - x_b)$ goes to zero and the contribution of surface tension gradient effects vanishes.

The hydrodynamic model of CHF proposed by Haramura and Katto (1983) may also be modified to incorporate the effects of surface tension gradients. In their model, a thin stable liquid layer including vapor stems forms on the heated surface, feeding large slugs of vapor. The thickness of this liquid film must be sufficiently small that the vapor stems are not Helmholtz unstable. The large slugs restrict liquid from most of the liquid film. It is postulated that the CHF condition is attained when the liquid film under the vapor slugs evaporates completely during the time interval needed for the bubble to grow large enough to escape. Since the interval between bubbles seems to be accurately predicted by the Taylor instability based on arguments of previous studies, Haramura and Katto (1983) chose the unit heated area participating in the growth of one vapor slug to be λ_D^2. Their model becomes

$$q''_{m,HK} = q''_{m,Zuber} \frac{24}{\pi} \left(\frac{\pi^4}{2^{11}3^2}\right)^{1/16} \left(\frac{A_v}{A_w}\right)^{5/8} \left(1 - \frac{A_v}{A_w}\right)^{5/16} \times \left[\left(\frac{\rho_l}{\rho_v} + 1\right) \Big/ \left(\frac{11}{16}\frac{\rho_l}{\rho_v} + 1\right)^{3/5}\right]^{5/16} \quad (15)$$

which becomes identical to the Zuber (1959) model with a different coefficient. Haramura and Katto (1983) postulate $q''_{m,HK} = q''_{m,Zuber}$, $A_v/A_w \ll 1$, and $\rho_v/\rho_l \ll 1$ to simplify their coefficient. Performing these assumptions, they found

$$\frac{A_v}{A_w} = 0.0584(\rho_v/\rho_l)^{0.2} \quad (16)$$

Both the Zuber (1959) model and the Haramura and Katto (1983) model characterize the geometry of the vapor slugs by λ_D. For this reason, the length scales chosen for the liquid restoring forces is the same for both models. In a mixture, body forces and the surface tension gradients created on the vapor–liquid interface would control the inflow or outflow of liquid to the thin liquid film. The visual observations of the boiling activity close to CHF was virtually identical for both pure fluids and binary mixtures in that a large vapor slug was produced over an evaporating liquid film. Areas of dry spots were generated on the heated surface (Fig. 4). An evaporating liquid film was observed. Small vapor stems were too small to observe or did not exist.

The Haramura and Katto (1983) model applies directly to the surface tension gradient model by substituting Eqs. (15) and (16) for $q''_{m,Zuber}$ in Eq. (11). The simplification provided by Eq. (16) still holds reasonably well for the binary mixtures considered in this study. Using mixture properties, the constant coefficient determined by Haramura and Katto (1983) never differed more than 18 percent of Zuber's constant coefficient. Therefore, the simplification of Eq. (16) applies to the binary mixture CHF model.

Experimental Apparatus

Figure 6 shows the experimental test section and system used in this investigation. Details of the experiment are provided in McGillis (1993). The copper test section was machined to accommodate two cartridge heaters in the bottom end. The top half of the copper piece was milled to provide a long 1.27 × 1.27 cm square section. Within this section, 0.8 mm holes were drilled to the center to hold thermocouple wires. The copper and thermocouples were then cast in a low viscosity epoxy. The main body of the pool boiling container was made with 2.5 cm I.D. tubing. In order to examine boiling at pressures below 10 kPa, various experimental designs were considered.

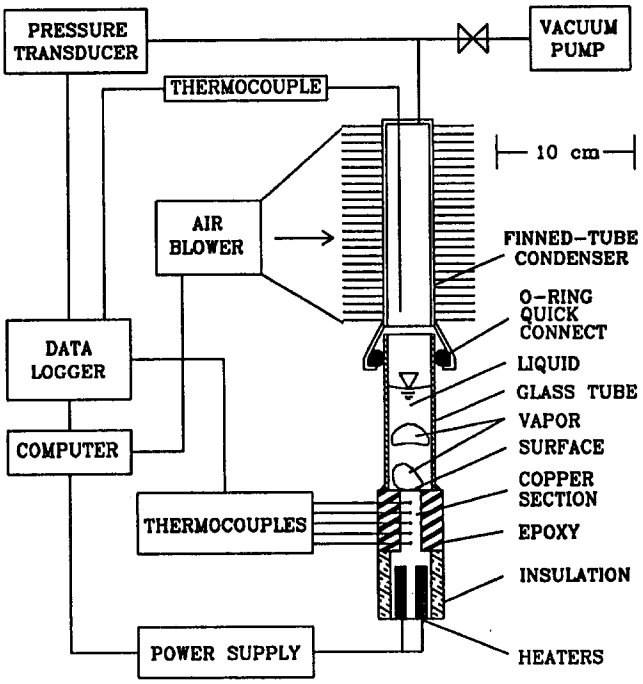

Fig. 6 Schematic diagram of testing system used in pool boiling experiments

A datalogger recorded the temperatures and system pressure, with a sampling rate of up to 1 kHz. A linear fit of the measured temperature gradient in the copper section was used to calculate the test section heat flux and the heated surface temperature. Experiments and two-dimensional numerical analyses indicate that the heat losses from the test section were less than 6 percent, and that the average heat flux at the boiling surface, q'', could be determined within 3 percent. Experimental uncertainties in the pressure and differential temperature measurements were 0.1 kPa and 0.1°C, respectively.

Steady state for the entire experiment was determined by monitoring the temperature changes with time via the datalogger and computer. When a particular surface was extended to the CHF condition, the final, highest heat flux for which the system reached steady state for nucleate boiling was used as the CHF data point.

Data presented in this paper were measured with a stationary liquid pool height of 7.1 cm. The pressures investigated ranged from 2 to 101 kPa. Heat flux levels off the 1.27 × 1.27 cm surface were as high as 200 W/cm^2.

Experiment Results and Comparisons to Theory

The mixture CHF conditions experimentally observed in this study are not monotonic with concentration. As seen in Figs. 7 and 8, small additions of the alcohol increased the CHF condition above the CHF condition of pure water. Higher concentrations of the alcohol began decreasing the CHF condition to that of the pure alcohol. Figure 9 shows CHF data for an ethylene glycol/water mixture. Small additions of ethylene glycol to water decrease the CHF condition from that of pure water. Small additions of water to ethylene glycol decrease the CHF condition from that of pure ethylene glycol. The alcohol/water binary mixtures are positive mixtures. The ethylene glycol/water mixture is a negative mixture. A positive mixture is one where the more volatile component has a lower surface tension than the surface tension of the less volatile component. A negative mixture is one where the more volatile component has a higher surface tension than the surface tension of the less volatile component.

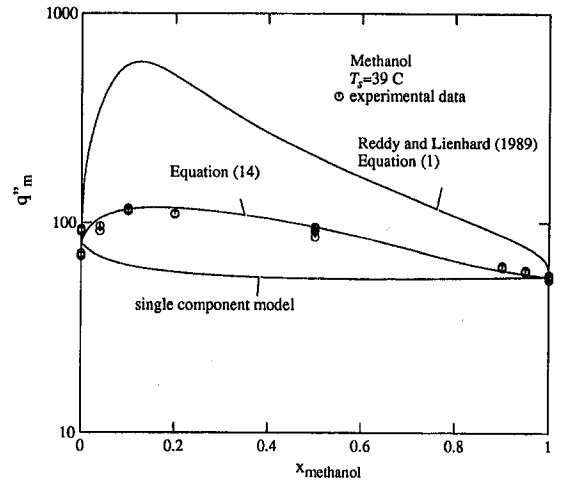

Fig. 7 Critical heat flux for methanol/water mixture. Comparisons made to: (1) single: component correlation using mixture properties, (2) Reddy and Lienhard mixture correlation, and (3) surface tension model.

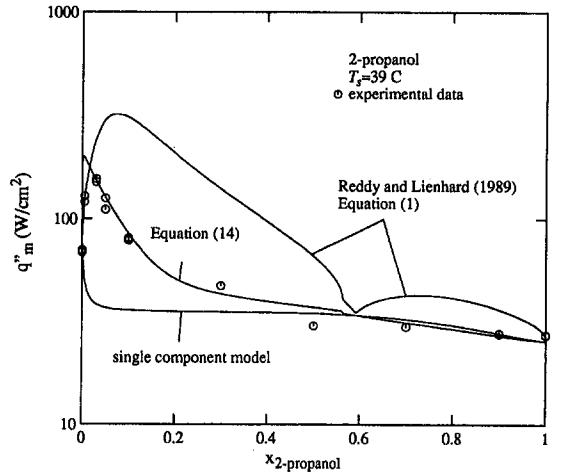

Fig. 8 Critical heat flux for 2-propanol/water mixture. Comparisons made to: (1) single-component correlation using mixture properties, (2) Reddy and Lienhard mixture correlation, and (3) surface tension model.

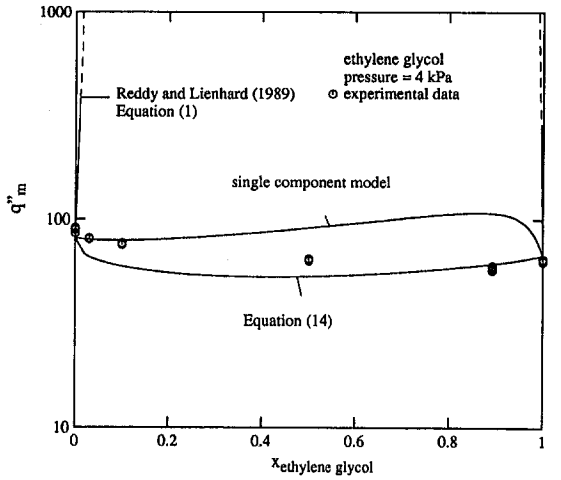

Fig. 9 Critical heat flux for ethylene glycol/water mixture. Comparisons made to: (1) single-component correlation using mixture properties, (2) Reddy and Lienhard mixture correlation, and (3) surface tension model.

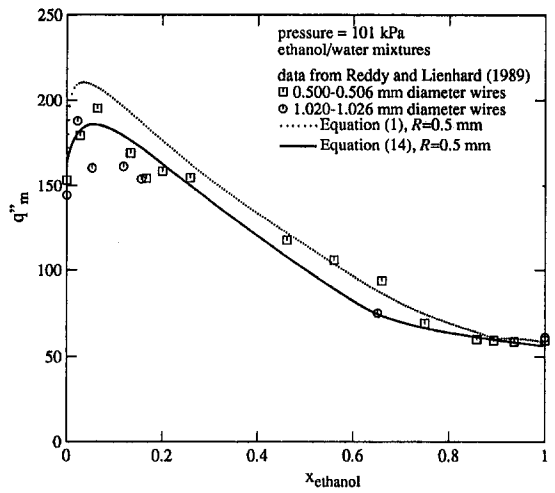

Fig. 10 Comparison of data of Reddy and Lienhard (1989) with critical heat flux models

This was also observed in the experiments of Reddy and Lienhard (1989) for ethanol/water mixtures. Their CHF data for small heated wires in a ethanol/water mixture are shown in Fig. 10. Equation (14) is plotted against experimental data in Figs. 7–10. The constant of proportionality in Eq. (14), c_m, was set to 1.14 to provide a better agreement to experimental data. There is very good agreement between Eq. (14) and experimental data.

The surface tension gradient model is compared to experimental data of this study and to the data of Reddy and Lienhard (1989). The correlation of Reddy and Lienhard (1989) will correctly predict the trends for positive mixtures because the variation of $\partial T/\partial x|_{x_b}$ with x_b is very similar to the variation of $\partial\sigma/\partial x|_x$ with x_b. However, large deviations exist between the correlation of Reddy and Lienhard and the data obtained in this study. This is largely because the data of this study are taken at subatmospheric pressure. The vapor density at subatmospheric pressure is much lower than the vapor density at atmospheric pressure. The consequence of a low vapor density is a high Ja_e and thus a high prediction of the CHF. As can be seen in Fig. 10, the surface tension gradient CHF model (Eq. (14)) accurately predicts the ethanol/water mixture data of Reddy and Lienhard (1989) at atmospheric pressures. The surface tension gradient model has the effect of pressure inherently incorporated.

As demonstrated in Fig. 9, the CHF for some mixtures cannot be modeled by a correlation based on subcooling. Water is the less volatile component in an ethylene glycol/water mixture. This means that when vapor is formed, the liquid–vapor interface will have a higher concentration of ethylene glycol. The interface, rich in ethylene glycol, will have a much higher saturation temperature and be effectively subcooled to the surrounding liquid. If, as in the case in the Reddy–Lienhard (1989) model, effective subcooling dictates the mixture CHF, the CHF for a ethylene glycol/water mixture would be very much higher than either pure component CHF. However, for this mixture, the measured CHF value is observed to match the surface tension gradient model well.

Conclusions

Methanol/water, 2-propanol/water, and ethylene glycol/water mixture CHF data were measured over the full range of concentration. In the alcohol/water mixtures, small additions of the alcohol to water increase the CHF condition above that of the pure water. Higher concentrations of the alcohol begin decreasing the CHF condition to that of the pure alcohol. In

the ethylene glycol/water mixture, small additions of ethylene glycol decreased the CHF condition above that of pure water. To account for geometry and configuration effects, previously derived single component predictions for the CHF from a small horizontal surface in a finite pool at subatmospheric pressures are used with accurate phase equilibrium and mixture properties.

Correlations based on effective subcooling fail to predict the CHF condition accurately for the mixtures and operating conditions considered in this study. Models based on subcooling predict the opposite effect for the ethylene glycol/water mixture. Our results suggest the influence of the Marangoni effect is the principle cause of the CHF variation for boiling of liquid mixtures. The surface tension gradient model developed provides a more consistent prediction than any model based on subcooling. Good agreement is found between the surface tension gradient model developed in this investigation and experimental data for different fluid combinations and configurations of this study and others.

Acknowledgments

The authors thank J. Fitch for support and encouraging discussions of this work. We also thank him for his assistance in all aspects of the experimental work. This research was supported by Digital Equipment Corporation's Western Research Laboratory, Palo Alto, CA.

References

Bonilla, C. F., and Perry, C. W., 1941, "Heat Transmission to Boiling Binary Liquid Mixtures," *Chemical Engineering Progresses Symposium Series,* Vol. 37, pp. 685–705.

Haramura, Y., and Katto, Y., 1983, "A New Hydrodynamic Model of Critical Heat Flux, Applicable Widely to Both Pool and Forced Convection Boiling on Submerged Bodies in Saturated Liquids," *International Journal of Heat and Mass Transfer,* Vol. 26, pp. 389–399.

Hovestreijdt, J., 1963, "The Influence of the Surface Tension Difference on the Boiling of Mixtures," *Chemical Engineering Science,* Vol. 18, pp. 631–639.

Kutateladze, S. S., Bobrovich, G. I., Gogonin, I., Mamontova, N. N., and Moskvichova, V. M., 1966, "The Critical Heat Flux at the Pool Boiling of Some Binary Liquid Mixtures," *Proceedings at the 3rd International Heat Transfer Conference,* Chicago, Vol. 3, pp. 149–159.

Matorin, A. S., 1973, "Correlation of Experimental Data on Heat Transfer Crisis in Pool Boiling of Pure Liquids and Binary Mixtures," *Heat Transfer—Soviet Research,* Vol. 5, No. 1, pp. 85–89.

McEligot, D. M., 1964, "Generalized Peak Heat Flux for Dilute Binary Mixtures," *AIChE Journal,* Vol. 10, No. 1, pp. 130–131.

McGillis, W. R., 1993, "Boiling From Localized Heat Sources in Pure and Binary Fluid Systems," Ph.D. dissertation, University of California—Berkeley.

Prausnitz, J. M., Lichtenthaler, R. N., and Gomes de Azevedo, E., 1986, *Molecular Thermodynamics of Fluid-Phase Equilibria,* 2nd ed., Prentice-Hall, New Jersey.

Prausnitz, J. M., 1992–1993, *Conversations and Class Notes—Molecular Thermodynamics of Fluid-Phase Equilibria,* Department of Chemical Engineering, University of California, Berkeley.

Reddy, R. P., and Lienhard, J. H., 1989, "The Peak Boiling Heat Flux in Saturated Ethanol–Water Mixtures," ASME JOURNAL OF HEAT TRANSFER, Vol. 111, pp. 480–486.

Reid, R. C., Prausnitz, J. M., and Poling, B. E., 1987, *The Properties of Gases & Liquids,* 4th ed., McGraw-Hill, New York.

Sun, K. H., and Lienhard, J. H., 1970, "The Peak Pool Boiling Heat Flux on Horizontal Cylinders," *International Journal of Heat and Mass Transfer,* Vol. 13, pp. 1425–1439.

Thome, J. R., and Shock, A. W., 1984, "Boiling of Multicomponent Liquid Mixtures," *Advances in Heat Transfer,* Academic Press, Inc., New York, Vol. 16, pp. 59–156.

Van Stralen, S. J. D., 1956, "Heat Transfer to Boiling Binary Liquid Mixtures at Atmospheric and Subatmospheric Pressures," *Chemical Engineering Science,* Vol. 5, pp. 290–296.

Van Stralen, S. J. D., and Sluyter, W. M., 1969, "Investigations on the Critical Heat Flux of Pure Liquids and Mixtures Under Various Conditions," *International Journal of Heat and Mass Transfer,* Vol. 12, pp. 1353–1384.

Zuber, N., 1959, "Hydrodynamic Aspects of Boiling Heat Transfer," AEC Report No. AECU-4439, Physics and Mathematics.

Bubble Behavior and Mean Diameter in Subcooled Flow Boiling

O. Zeitoun
Lecturer, Department of Mechanical Engineering,
Alexandria University,
Alexandria, Egypt

M. Shoukri
Professor,
Mechanical Engineering Department,
McMaster University,
Hamilton, Ontario, L8S 4L7, Canada
Mem. ASME

Bubble behavior and mean bubble diameter in subcooled upward flow boiling in a vertical annular channel were investigated under low pressure and mass flux conditions. A high-speed video system was used to visualize the subcooled flow boiling phenomenon. The high-speed photographic results indicated that, contrary to the common understanding, bubbles tend to detach from the heating surface upstream of the net vapor generation point. Digital image processing technique was used to measure the mean bubble diameter along the subcooled flow boiling region. Data on the axial area-averaged void fraction distributions were also obtained using a single-beam gamma densitometer. Effects of the liquid subcooling, applied heat flux, and mass flux on the mean bubble size were investigated. A correlation for the mean bubble diameter as a function of the local subcooling, heat flux, and mass flux was obtained.

1 Introduction

One of the most important thermal nonequilibrium two-phase flow phenomena is that of forced convective subcooled boiling. The enormous surface heat flux that can be achieved without using high heating surface temperature is the main advantage of the nucleate boiling regime. Subcooled flow boiling is encountered in many applications: nuclear reactors, boilers, refrigeration systems, and heat exchangers.

The subcooled flow boiling along a heated channel is commonly divided, as introduced by Griffith et al. (1958), into two regions: a highly subcooled region, where the void fraction is very low, and a slightly subcooled region, where the void fraction increases significantly. The transition between these two regions is called the net vapor generation (NVG), or the onset of significant void (OSV), point. The NVG point was related directly, or indirectly, to bubble behavior. The highly subcooled region is also commonly called the wall voidage region, implying that the vapor bubbles are located at the wall since the liquid bulk is highly subcooled. Understanding the local flow field at the NVG point is important since it marks the location at which significant increase in void fraction along the boiling channel is encountered. Griffith et al. (1958) speculated that this transition point is reached when the heating surface is fully covered with attached bubbles. Others, including Bowring (1962), Levy (1967), Rogers et al. (1987), Rogers and Li (1992), and Lee and Bankoff (1992), associated the NVG point with the first bubble detachment from the heating wall. In another approach, Dix (1970) and Serizawa (1979) attributed the NVG phenomenon to bubble ejection from a bubbly layer in the vicinity of the heating surface. A detailed review of available NVG models and correlations was presented by Zeitoun and Shoukri (1995).

Until recently, most research efforts in this area focused on high-pressure flow boiling, because of its relevance to power reactors, and lacked detailed information on local bubble behavior and size along the boiling channel. Recently, Bibeau (1993), Shoukri et al. (1991), Stangl and Mayinger (1990), Dimmick and Selander (1990), Bibeau and Salcudean (1990), and Rogers et al. (1987) reported void fraction measurements in low pressure subcooled flow boiling. They found that the void fraction profile upstream of the NVG point tended to be flat and formed a plateau longer than that associated with the high-pressure case.

The present work is driven by the need to understand the physical phenomena associated with low-pressure subcooled flow boiling and the need for information on bubble size, velocity, and interfacial area for numerical modeling of subcooled flow boiling in low-pressure pool-type reactors.

2 Experimental Arrangements

2.1 Experimental Facility. A schematic of the test loop is presented in Fig. 1. The low-pressure circulating loop consisted mainly of a holding tank, in which distilled-degassed water temperature was controlled by an immersed electric heater and a cooling coil, a circulating pump, a preheater, and the test section. The test section contains a heated section, where vapor bubbles are formed, followed by an unheated section, where the vapor bubbles are condensed. The water at the test section outlet was pumped back to the holding tank where its temperature was regulated. A detailed description of the facility used in this study was reported by Zeitoun (1994) and Zeitoun et al. (1994).

The test section was a vertical concentric annular test section. The inner tube, which had a 12.7 mm outside diameter, consisted of three axial sections. The middle section of the inner tube was a 30.6-cm-long, thin-walled stainless-steel tube (0.25 mm thick) that was electrically heated. This heated section was preceded by a 34-cm-long, thick-walled copper tube, and followed by another that is 50 cm long. The entire inner tube was connected to a 55 kW DC power supply. Accordingly, heat was generated uniformly in the middle section of the inner tube. The outer tube was a 25.4 mm inner diameter plexiglass tube that permitted visual observation. The flow that entered the annulus developed through the first unheated section of the annular test section. Voids, which were generated in the heated section, collapsed in the downstream unheated section. This arrangement was found to be convenient to examine vapor generation and condensation separately. The present study was carried out in the heated section to investigate bubble behavior and size in subcooled flow boiling. A square cross-sectional plexiglass shield was put around the outer tube and filled with water during photography to reduce light reflection and refrac-

Contributed by the Heat Transfer Division for publication in the JOURNAL OF HEAT TRANSFER. Manuscript received by the Heat Transfer Division March 1995; revision received October 1995. Keywords: Boiling, Multiphase Flows, Phase-Change Phenomena. Associate Technical Editor: R. A. Nelson, Jr.

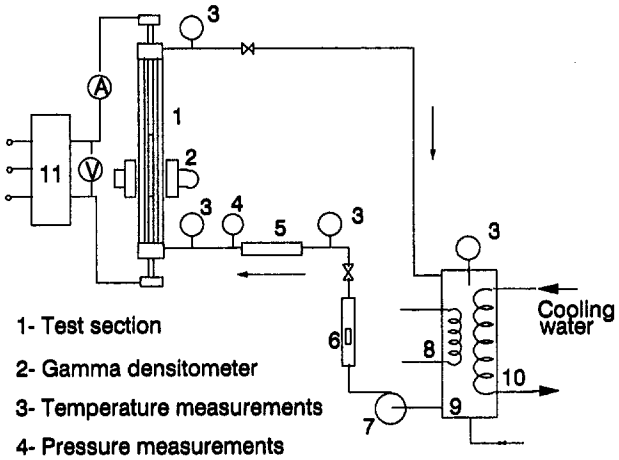

Fig. 1 Test loop

tion. Any minor change in the inlet temperature to the heating region was compensated for by readjusting the preheater.

2.2 Measurements and Instrumentation. Experiments were carried out at different levels of mass flux, heat flux, and inlet subcooling. The test conditions are listed in Table 1. A high-speed video system was used to collect visual information to study bubble behavior upstream, near, and downstream of the NVG point. A digital image processing technique was used to analyze the high-speed video information and to measure bubble size distributions along the subcooled boiling region. The measurements and instrumentation used are discussed here briefly. More details were reported by Zeitoun (1994) and Zeitoun et al. (1994).

The high-speed video system, Kodak Ektapro EM Motion Analyzer, was used to visualize the flow at 2 cm intervals along the subcooled flow boiling region. The camera and the light sources were mounted on a traversing table to enable the flow along the test section to be visualized at the same locations where the void fractions were measured. Two procedures were followed to collect the visual information. In the first procedure, the camera was focused on the annular gap where it was found appropriate to investigate bubble detachment, sliding, and ejection. In the second procedure, the camera was focused on the heater surface itself. This procedure was found convenient to examine bubble population density, bubble interactions, and bubble size along the heating surface. Digital image processing technology was used to measure bubble size. Measured distances in the field of view were estimated to be accurate within ± 0.05 mm.

A single beam gamma densitometer was used for void fraction measurements. It consisted of a 75 mCi Cobalt 57 sealed line source and a cubic NaI (T1) scintillator. As shown by Zeitoun (1994) and Zeitoun et al. (1994), static calibration showed that the void fraction measurements were accurate within ± 4 percent in the range of $0.02 < \alpha < 0.3$. The estimated maximum absolute error did not exceed 0.015.

The location of the NVG point was identified from the measured axial void fraction profile by fitting the void fraction data, downstream of the onset of nucleate boiling, with a straight line. The point at which the profile deviated from the straight-line fit was considered to be the NVG point. The procedure used for determining the NVG point, and the uncertainties associated with it, were discussed in detail by Zeitoun (1994) and Zeitoun and Shoukri (1995). It was shown that the uncertainty in determining the NVG location was ± 2 cm.

Other measurements included the flow rate, using a bank of rotameters with an estimated error of ± 2 percent, test section inlet and outlet temperature using calibrated platinum resistance temperature detectors, as well as the liquid subcooling along the test section using J-type calibrated thermocouples. The uncertainties in the temperature and pressure measurements were estimated by Zeitoun (1994) to be ± 0.2°C and ± 1 kPa, respectively.

3 Bubble Behavior

3.1 Background. It is well accepted that a bubble is generally initiated from a small gas-filled cavity or crack on a solid surface, when the heating surface is heated to a sufficiently high temperature. Many theories have been established to describe the bubble growth process in nucleate pool boiling. Fewer studies focused on bubble dynamics in flow nucleate boiling. Koumoutsos et al. (1968) and Zeng et al. (1993b) investigated bubble departure in horizontal flow boiling, while Gunther (1951), Abdelmessih et al. (1972), Akiyama and Tachibana (1974), Cooper et al. (1983), Bibeau (1993), and Bibeau and Salcudean (1994) reported experimental investigations of bubble dynamics in vertical upward flow boiling. Ünal (1976) and Meister (1979) carried out theoretical analysis of bubble growth and collapse in highly subcooled flow boiling. They considered that the bubble grew and collapsed while attached to the heating surface.

In the case of subcooled flow boiling, there are two types of bubble detachment from the heating surface. As the bubble grows on a heating surface, it reaches a certain size when it starts to slide along the heating surface (parallel detachment) and the growth continues until it leaves the surface (normal detachment, ejection, or lift off). High-speed photographic results reported by Bibeau (1993), for subcooled flow boiling at low pressures, showed that parallel detachment occurred very early after nucleation. It also showed that the bubble continued

Nomenclature

A = flow area, m^2
a_b = bubble surface area, m^2
A_b = mean bubble surface area, m^2
Bo = boiling number = q/Gh_{fg}
C_p = liquid specific heat, J/kg K
D_h = channel hydraulic diameter, m
D_s = mean Sauter bubble diameter, m
G = mass flux, kg/m^2 s
g = gravitational acceleration, m/s^2
h_{fg} = latent heat, J/kg
Ja = Jakob number based on liquid subcooling = $\rho_l C_p (T_s - T_l)/\rho_g h_{fg}$
P_h = heated perimeter, m
q = applied heat flux, W/m^2
Re = flow Reynolds number = GD_h/μ
T = temperature, °C
v_b = bubble volume, m^3
V_b = average bubble volume, m^3
z = axial location in z direction, m
Z_d = axial location of the NVG point, m
α = area-averaged void fraction
μ = liquid viscosity, Pa s
ρ = density, kg/m^3
σ = surface tension, N/m
$\Theta = T_s - T$, °C
$\Delta\rho = \rho_l - \rho_g$, kg/m^3

Subscripts

g = vapour
in = inlet
l = liquid
s = saturation
w = wall

Table 1 Test conditions

Run No.	q kW/m²	G kg/m²s	P bar	θ_{in} °C
B1	286.68	156.15	1.37	14.9
B2	286.5	258.16	1.22	11.6
B3	487.88	252.78	1.17	16.6
B4	478.44	152.5	1.19	24.7
B5	508.0	264.34	1.5	16.8
B6	496.5	151.4	1.56	21.7
B7	705.5	411.7	1.5	22.5
B8	596.0	263.8	1.2	20.1
B9	593.2	152.6	1.22	31.1
B10	603.24	403.0	1.68	19.1

growing while sliding along the heating surface until it reached a maximum size, after which the bubble size decreased as the condensation rate exceeded the evaporation. The normal detachment occurred during bubble condensation and sliding along the heating surface. The bubble collapsed completely as it moved through the subcooled bulk. The normal detachment of a bubble was seen as the phenomenon that determines the end of the evaporating process associated with this bubble.

Bubbles detach in two directions due to the forces acting on them. Modeling these forces is a very difficult task because of the link between these forces and the thermal bubble growth-collapse process. Formulation of these forces was investigated for pool boiling by Beer et al. (1977) and Zeng et al. (1993a) and for forced flow boiling along a horizontal surface by Koumoutsos et al. (1968) and Zeng et al. (1993b). For upward flow boiling, the forces acting in the axial direction are buoyancy, drag, surface tension, and inertia of the surrounding liquid. Forces acting in the normal direction are surface tension, excess pressure force, capillary pressure force, lift, drag, and the inertia of the surrounding liquid.

3.2 Visual Observations. Some visual observations derived from the high-speed photography are presented. Figure 2 shows typical bubble growth-collapse photographs along the subcooled flow boiling region for run B4 (see Table 1). In this figure, the heater edge appears at the right side of the image and the wall of the plexiglass tube and a 1 mm reference tube appear at the left side. The measured axial void fraction profiles for this run are shown in Fig. 5. The photographs also show the change of the average bubble size and population upstream, near, and downstream of the NVG point. Some individual bubbles are identified to show the bubble cycle as it nucleates, grows, and slides along the heating surface, detaches, and collapses in the subcooled liquid bulk.

Upstream of the NVG point, the photographs show that after nucleation, the bubbles grow while attached to, or slowly sliding along, the heating surface until they lift off. After detachment, the bubbles condense very rapidly in the subcooled bulk. The photographs confirm that bubbles consistently detach from the heating surface upstream of the NVG point and accordingly, at least under the present test conditions, bubble detachment is not the cause of the NVG phenomenon. Moreover, the concept of a bubbly layer from which a bubble ejected to mark the occurrence of NVG (Dix, 1970; Serizawa, 1979) cannot be supported by the present observations. The reason can be attributed to the relatively large bubbles observed under this low-pressure flow boiling condition. The bubbles may be contained in a relatively large envelope along the heating section, as compared to the high-pressure case, and this envelope may become thicker due to the decrease in subcooling along the heated section. For high pressure and high mass flow rate, where the bubbles tend to be very small, the bubbly layer may be encountered. The present observations are in agreement with recent low-pressure results of Bibeau (1993) and the earlier observations of Jain et al. (1980) for flow boiling of refrigerant R-113.

The effect of the decreasing subcooling along the heated section on the bubble size and period, i.e., growth-collapse time, can also be demonstrated by Fig. 2, where three bubbles at three different elevations, below, near, and after the NVG point are identified. The first is at z = 3 cm, where the void fraction and the subcooling were 3 percent and 22.6°C, respectively. The second is at z = 13 cm, where the void fraction and subcooling were 3 percent and 14.8°C, respectively. The third is at z = 23 cm, where the void fraction and subcooling were 8 percent and 7°C, respectively. Analyzing these photographs showed that the maximum bubble diameter measured was: 1.0 mm at z = 3 cm, 2.25 cm at z = 13 cm, and 3.25 mm at z = 23 cm and the bubble total growth-collapse time was 7, 11, and 22 ms, respectively. Of significance here is the trend, rather than the exact values, because of the sensitivity of the nucleation process to nucleation site size and bubble interaction. The effect of the subcooling will be investigated in detail during the analysis of the mean bubble size.

In the second flow visualization method, the high-speed video camera was focused on the heater surface itself. This procedure was found convenient to examine bubble population density, bubble interactions, and bubble size along the heating surface. Figure 3 shows typical bubble behavior along the test section for run number B3. The measured void fraction and the location of the NVG point of these runs are shown in Fig. 5. As shown in the photographs, the bubble size increased as the subcooling decreased along the test section. The main reason for the size increase along the heating section is the decrease in the condensation at the subcooled water–bubble interface. In subcooled boiling, the bubble grows on the heating surface under two opposing mechanisms: evaporation at the heating surface and at the superheated liquid–bubble interface and condensation at

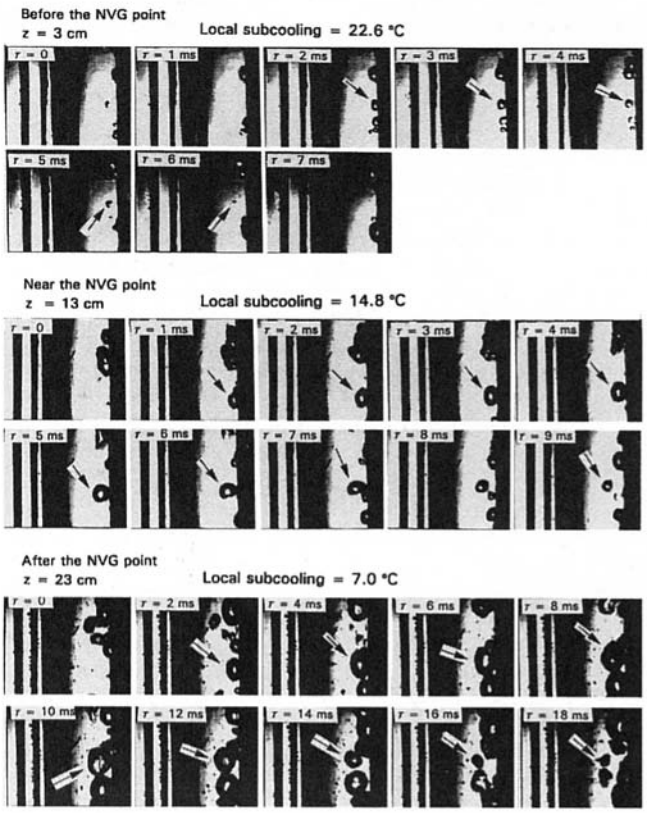

Fig. 2 Bubble growth–collapse cycle before, near, and after the NVG point (q = 478.4 kW/m, G = 152.5 kg/m²s, initial subcooling = 24.7°C, and Z_d = 17 cm)

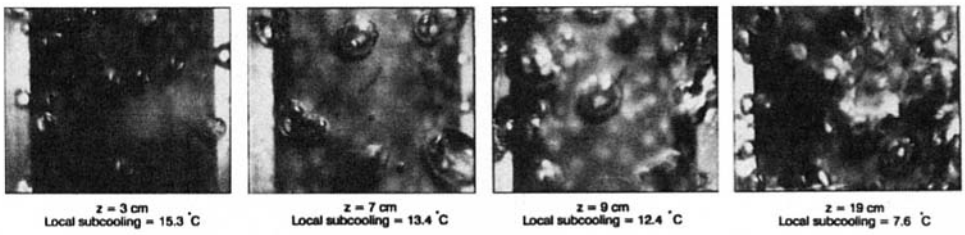

Fig. 3 Bubble behavior along subcooled flow boiling region for run No. B3 (q = 487.9 kW/m^2, G = 252.8 kg/m^{2}s, initial subcooling = 16.6°C, and Z_d = 10 cm)

the subcooled water–vapor interface. The final bubble size and life duration are mainly dependent on the relative importance of these mechanisms.

Two distinct regions were observed along the heating section, which can be seen in Fig. 3. In the region before the NVG point (Z_d = 10 cm), the bubbles behave as individual bubbles, or discrete bubbles. Bubble interaction or coalescence is not a major mechanism in this region. Bubble coalescence intensifies in the region after the NVG point and is caused by the increase in bubble size and bubble growth–collapse period. This is clearly associated with reduction in the relative importance of condensation at the bubble interface due to the decrease in liquid subcooling. As the bubble coalescence intensifies in the downstream of the NVG point, bigger bubbles are formed. The increase in bubble size decreases the interfacial area concentration, for a given void fraction, causing a reduction in the condensation rate per unit volume of the channel. Consequently, the relative effect of condensation is reduced and noticeable increase of void fraction is observed along the channel. Near the end of the heater, the coalescence intensifies significantly and the flow regime changes from bubbly flow to churn flow.

4 Bubble Size in Subcooled Flow Boiling

4.1 Background. One of the parameters required to estimate the interfacial transport of mass, momentum, and energy is the bubble size, or interfacial area concentration. Despite the importance of the bubble size in two-fluid formulation of subcooled flow boiling, no measurement was reported in the literature for mean bubble diameter in subcooled flow boiling. A few investigators—Gunther (1951), Abdelmessih et al. (1972), and Bibeau (1993)—reported measurements of bubble growth–collapse history in subcooled flow boiling. Ünal (1976) and Meister (1979) theoretically investigated the bubble growth–collapse in subcooled flow boiling. Ünal (1976) analyzed the growth and collapse of an attached hemispherical bubble. The bubble grew on the heating surface under the influence of microlayer evaporation beneath the bubble base and the condensation at the curved surface. The detachment effects were excluded from the analysis as it was assumed that the bubble remained attached to the heating surface during the growth–collapse cycle. This will, in fact, cause a longer collapse time due to the continuous evaporation at the wall. Ünal's analysis yielded an equation for the maximum bubble size, i.e., the upper limit for bubble diameter. Another correlation for maximum bubble size was given by Farajisarir (1993) as reported by Bibeau (1993). However, models for maximum bubble size are not readily applicable for estimating the interfacial transport phenomena.

A number of models and correlations are also available for bubble size at detachment, e.g., Levy (1967) and Serizawa (1979) among others. Although important in studying bubble dynamics, they cannot be used directly to estimate the mean interfacial parameters. In formulating a two-fluid model for subcooled flow boiling, there is a need to estimate the mean bubble diameter in subcooled flow boiling.

4.2 Mean Bubble Diameter Measurements. The high-speed video and digital image processing systems were used to obtain data on bubble size in subcooled flow boiling at 2 cm intervals along the heated section for the ten experimental runs listed in Table 1. The digital image processing technique was used to analyze the high-speed photographic images stored on the video tape, to measure the bubble size. The volume, and the surface area of each bubble, were calculated by measuring two diameters. The measured diameters were the maximum diameter and that perpendicular to the maximum diameter. The cross-sectional area was assumed to be an ellipse and the two measured diameters were considered the maximum and minimum dimensions of that ellipse. The bubble volume and surface area were calculated by rotating this cross section around the maximum diameter. It was endeavored to measure the maximum number of bubbles from each frame. When the two measured diameters were almost equal, the procedure reduces to estimating the surface area and volume of a sphere.

At each axial location, a total of about 350 bubbles were analyzed. The bubble volume v_b and surface area a_b were calculated as discussed above. The average bubble surface area and volume at each location were calculated as follows:

$$A_b = \frac{1}{n_b}\sum_{j=1}^{n_b} a_{b_j} \tag{1}$$

$$V_b = \frac{1}{n_b}\sum_{j=1}^{n_b} v_{b_j} \tag{2}$$

where n_b is the number of bubbles measured. The mean Sauter bubble diameter at any given axial location was defined by:

$$D_s = \frac{6.0V_b}{A_b} \tag{3}$$

Given the area-averaged void fraction, the bubble mean diameter calculated by this procedure can be used directly to estimate parameters such as the interfacial area concentration and bubble density number. Zeitoun (1994) estimated the uncertainty in determining the bubble diameter to be in the range of ±6 percent.

4.3 Data Analysis. Since the objective of this work was to obtain the average bubble diameter relevant to the various interfacial parameters, e.g., area concentration, heat transfer, etc., which are required for two-fluid modeling, the sample used included all bubbles present in the field of view, i.e., detached and attached to the wall. Typical mean Sauter bubble diameter distribution along the test section is shown in Fig. 4. The location of the NVG point, determined from the void fraction profiles, is superimposed on the figure. As expected, the bubble diameter increased along the test section due to the reduction in liquid subcooling. The bubble diameter appears to increase at a higher rate in the region downstream of the NVG point. This was caused by two factors: the decrease in the subcooling, and consequently the condensation rate, and bubble coalescence.

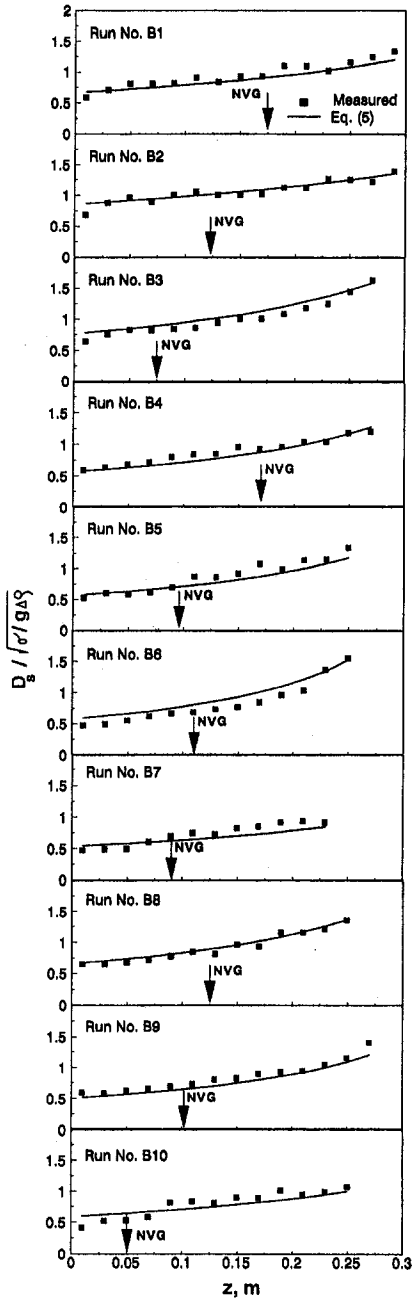

Fig. 4 Measured mean Sauter bubble diameter

It is important to note the similarity between the bubble size and the measured void fraction in the region before, and after, the NVG point. Both D_s^3 and the void fraction were plotted along the heated section, as shown in Fig. 5. The interesting finding, based on these figures, is the strong link between bubble size and void fraction. The parameter D_s^3 and the void fraction show similar trends before and after the NVG point. The rate of increase of both along the test section appears to increase at the point of NVG. The bubble size and void fraction measurements can be used to estimate the mean bubble number density. The present data showed that shortly after nucleation started, the bubble number density remained almost constant along the test section, which is supported by Figs. 2 and 3. This observation suggests that the void growth is caused by bubble size increase. In fact, the bubble number density tended to decrease near the exit of the heated section where bubble coalescence became more dominant.

To examine the effect of mass and heat flux on the bubble size, the measured mean bubble diameter was plotted versus Jakob number (subcooling). The local subcooling was obtained by interpolation between the four liquid subcooling measurements taken along the heated section. It was interesting to note that the local subcooling was in agreement with the values calculated by a simple heat balance:

$$\theta_l = \theta_{in} - \frac{qP_hz}{AGC_p} \tag{4}$$

In subcooled flow boiling almost all the wall heat flux is used to heat up the liquid either directly or indirectly through vapor condensation. The effect of the mass flux is shown in Fig. 6 while the effect of heat flux is shown in Fig. 7. As shown, increasing the mass flux decreases the bubble size, in the high Jakob number region before the NVG point. As the subcooling

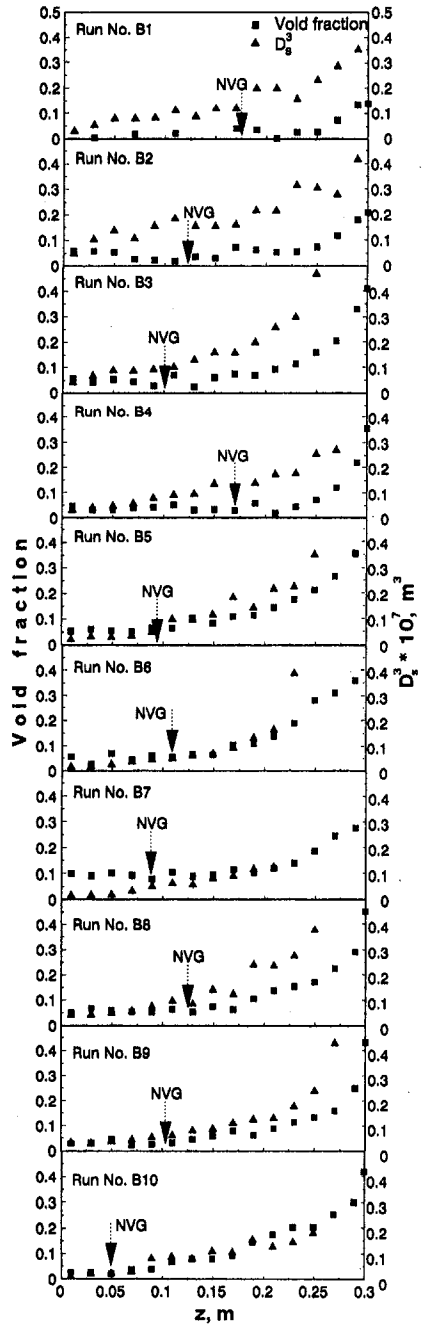

Fig. 5 Relation between bubble size and void fraction

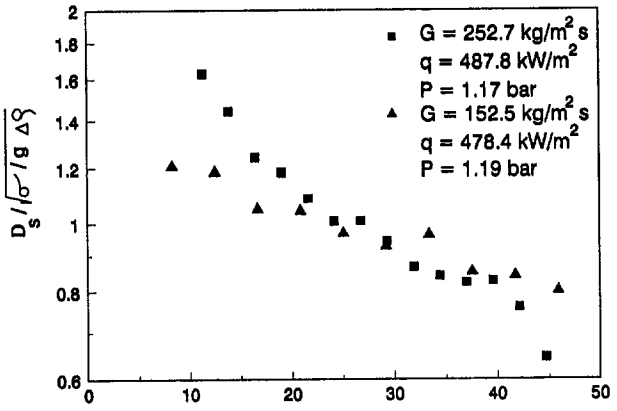

Fig. 6 Effect of mass flux on mean bubble diameter

decreases, i.e., the Jakob number decreases, the above trend is reversed, i.e., increasing the mass flux tends to increase the bubble size. In this low Jakob number region, where the bubble number density is high, increasing the mass flux increases the bubble absolute velocity, which enhances bubble coalescence. Increasing the heat flux, as shown in Fig. 7, tends to increase the bubble size. This may be caused by the increase in the driving force of the bubble growth process, i.e., the wall superheat.

Zeitoun (1994) showed that although available correlations for maximum bubble diameter should be considered as the upper limit for the mean diameters measured in the present work, Ünal's model (1976) underpredicted the present data. Farajisair's correlation, as reported by Bibeau (1993), was consistent with the present data, i.e., it consistently predicted higher diameters.

4.4 Proposed Correlation. Many methods were tried to correlate the present data of the mean bubble diameter. In these analyses, a dimensionless form with the correct limits was considered. It was found appropriate to correlate the present data by the following formula:

$$\frac{D_s}{\sqrt{\sigma/g\Delta\rho}} = \frac{0.0683(\rho_l/\rho_g)^{1.326}}{\mathrm{Re}^{0.324}\left(\mathrm{Ja} + \dfrac{149.2(\rho_l/\rho_g)^{1.326}}{\mathrm{Bo}^{0.487}\,\mathrm{Re}^{1.6}}\right)} \qquad (5)$$

The comparison between the present data and the proposed correlation is shown in Fig. 8. This correlation has a correlation coefficient of 90 percent and is capable of predicting the present data within ±15 percent. The mean bubble diameters, calculated from the Eq. (5), are imposed on Fig. 4. It should be noted that although Eq. (5) is based on dimensional analysis, its current form was only verified based on low-pressure subcooled boiling of water. Further verification work is needed to validate its use for other fluids and at higher pressures.

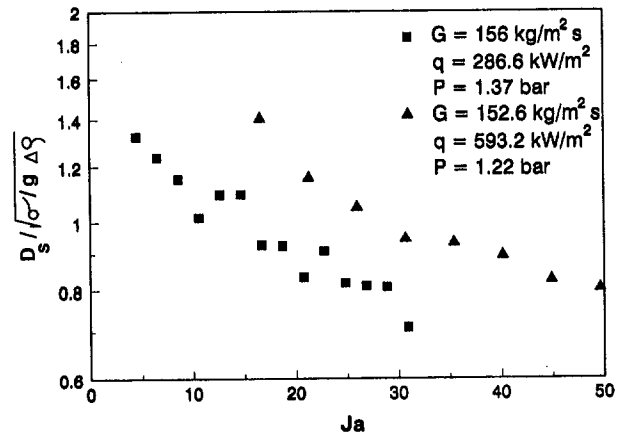

Fig. 7 Effect of applied heat flux on mean bubble diameter

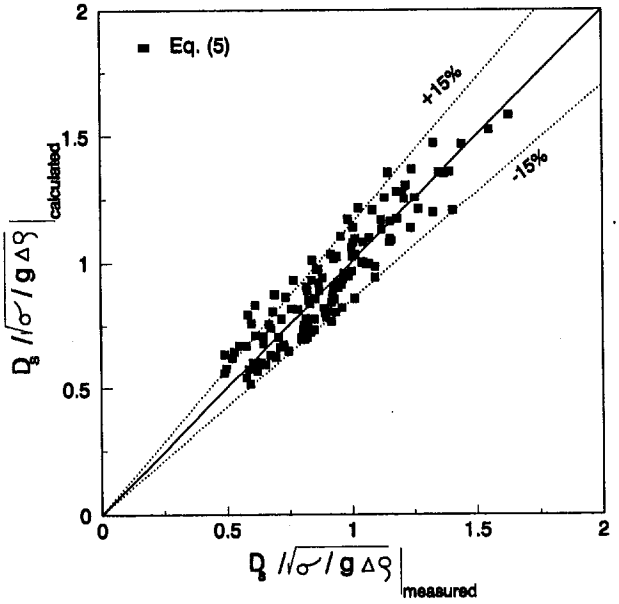

Fig. 8 Comparison between proposed correlation and measured mean bubble diameter

5 Conclusions

An experimental investigation into the bubble behavior in low-pressure subcooled flow boiling in a vertical annulus was undertaken. Using a high-speed video camera, bubble behavior was examined for different levels of mass flux, heat flux, and inlet subcooling. The high-speed photographic results confirmed the fact that the bubble departure was not the reason for the NVG phenomenon. It was found that the bubble growth–collapse cycle is similar, regarding parallel and normal detachment, along the subcooled boiling regions, i.e., upstream and downstream of the NVG point. However, the mean bubble size, and life duration, increased as the subcooling was decreased. The bubble coalescence was intensified downstream of the NVG point. The increase in bubble size due to decrease in condensation and bubble coalescence was the main reason for the significant increase in void fraction along the heated channel. Effects of local subcooling, mass flux, and heat flux on the mean bubble diameter were investigated. A new correlation for the mean bubble diameter, in terms of the flow Reynolds number, boiling number, local Jakob number, and fluid properties, was obtained. The proposed correlation has a correlation coefficient of 90 percent and can predict the present data within ±15 percent.

Acknowledgments

The work presented herein was funded by a joint grant from Atomic Energy of Canada Ltd. (AECL) and the Natural Science and Engineering Research Council (NSERC). The support and input of Dr. V. Chatoorgoon from AECL are greatly appreciated.

References

Abdelmessih, A. H., Hooper, F. C., and Nangia, S., 1972, "Flow Effects on Bubble Growth and Collapse in Surface Boiling," *Int. J. Heat Mass Transfer*, Vol. 15, pp. 115–125.

Akiyama, M., and Tachibana, F., 1974, "Motion of Vapour Bubbles in Subcooled Heated Channel," *Bulletin of the JSME*, Vol. 104, pp. 241–247.

Beer, H., Burow, P., and Best, R., 1977, "Bubble Growth, Bubble Dynamics, and Heat Transfer in Nucleate Boiling, Viewed With a Laser Interferometer," in: *Heat Transfer in Boiling,* E. Hahne and U. Grigull, ed., Hemisphere Publishing Corp., Ch. 2, pp. 21–52.

Bibeau, E. L., and Salcudean, M., 1990, "The Effect of Flow Direction on Void Growth at Low Velocities and Low Pressure," *Int. Comm. Heat Mass Transfer,* Vol. 17, pp. 19–25.

Bibeau, E. L., 1993, "Void Growth in Subcooled Flow Boiling for Circular and Finned Geometries for Low Values of Pressure and Velocity," Ph.D. Thesis, The University of British Columbia.

Bibeau, E. L., and Salcudean, M., 1994, "A Study of Bubble Ebullition in Forced Convective Subcooled Nucleate Boiling at Low Pressure," *Int. J. Heat Mass Transfer,* Vol. 37, pp. 2245–2259.

Bowring, R. W., 1962, "Physical Model Based on Bubble Detachment and Calculation of Steam Voidage in the Subcooled Region of a Heated Channel," HPR-10, Institute for Atomenergi, Halden.

Cooper, M. G., Mori, K., and Stone, C. R., 1983, "Behaviour of Vapour Bubbles Growing at a Wall With Forced Flow," *Int. J. Heat Mass Transfer,* Vol. 26, pp. 1489–1507.

Dimmick, G. R., and Selander, W. N., 1990, "A Dynamic Model for Predicting Subcooled Void: Experimental Results and Model Development," EUROTHERM Seminar #16.

Dix, G. E., 1970, "Vapour Void Fraction for Forced Convection With Subcooled Boiling at Low Flow Rates," General Electric Report No. NEDO-10491.

Griffith, P., Clark, J. A., and Rohsenow, W. M., 1958, "Void Volumes in Subcooled Boiling," ASME Paper No. 58-HT-19.

Gunther, F. C., 1951, "Photographic Study of Surface-Boiling Heat Transfer to Water With Forced Convection," *Transaction of ASME,* Vol. 73, pp. 115–123.

Jain, P. K., Nourmohammadi, K., and Roy, R. P., 1980, "A Study of Forced Convective Subcooled Boiling in Heated Annular Channels," *Nuc. Eng. and Design,* Vol. 60, pp. 401–411.

Koumoutsos, N., Moissis, R., and Spyridonos, A., 1968, "A Study of Bubble Departure in Forced-Convection Boiling," ASME JOURNAL OF HEAT TRANSFER, Vol. 90, pp. 223–230.

Lee, S. C., and Bankoff, S. G., 1992, "Prediction of the Onset of Significant Void in Down Flow Subcooled Nucleate Boiling," *Two-Phase Flow and Heat Transfer,* ASME HTD-Vol. 197, pp. 93–100.

Levy, S., 1967, "Forced Convection Subcooled Boiling: Prediction of Vapour Volumetric Fraction," *Int. J. Heat Mass Transfer,* Vol. 10, pp. 951–965.

Meister, G., 1979, "Vapour Bubble Growth and Recondensation in Subcooled Boiling Flow," *Nuclear Engineering and Design,* Vol. 54, pp. 97–114.

Rogers, J. T., Salcudean, M., Abdullah, Z., McLeod, D., and Poirier, D., 1987, "The Onset of Significant Void in Up-flow Boiling of Water at Low Pressure and Low Velocities," *Int. J. Heat Mass Transfer,* Vol. 30, No. 11, pp. 2247–2260.

Rogers, J. T., and Li, J., 1992, "Prediction of the Onset of Significant Void in Flow Boiling of Water," *Fundamentals of Subcooled Flow Boiling,* ASME HTD-Vol. 217, pp. 41–52.

Serizawa, A., 1979, "A Study of Forced Convection Subcooled Flow Boiling," *Two-Phase Momentum, Heat and Mass Transfer in Chemical Processes and Energy Engineering Systems,* F. Drust, G. V. Tsiklauri, and N. H. Afgan, eds., Vol. I, pp. 231–242.

Shoukri, M., Judd, R. L., Donevski, B., and Dimmick, G. R., 1991, "Experiments on Subcooled Flow Boiling and Condensation in Vertical Annular Channels," in: *Phase-Interface Phenomena in Multiphase Flow,* G. F. Hewitt, F. Mayinger, and J. R. Rizinic, eds., Hemisphere Pub. Corp., pp. 413–422.

Stangl, G., and Mayinger, F., 1990, "Void Fraction Measurement in Subcooled Forced Convection Boiling With Refrigerant 12," *Experimental Heat Transfer,* Vol. 3, pp. 323–340.

Ünal, H. C., 1976, "Maximum Bubble Diameter, Maximum Bubble-Growth Time and Bubble-Growth Rate During the Subcooled Nucleate Flow Boiling of Water up to 17.7 MN/m^2," *Int. J. Heat Mass Transfer,* Vol. 19, pp. 643–649.

Zeitoun, O., Shoukri, M., and Chatoorgoon, V., 1994, "Measurement of Interfacial Area Concentration in Subcooled Liquid-Vapour Flow," *Nuc. Eng. and Design,* Vol. 152, pp. 243–255.

Zeitoun, O., 1994, "Subcooled Flow Boiling and Condensation," Ph.D. Thesis, McMaster University, Hamilton, Ontario, Canada.

Zeitoun, O., and Shoukri, M., 1995, "On the Net Vapour Generation Phenomenon in Low Pressure and Low Mass Flux Subcooled Flow Boiling," *Proceedings of the Engineering Foundation Conference on Convective Flow Boiling,* Banff, Canada.

Zeng, L. Z., Klausner, J. F., and Mei, R., 1993a, "A Unified Model for the Prediction of Bubble Detachment Diameters in Boiling Systems—I. Pool Boiling," *Int. J. Heat Mass Transfer,* Vol. 36, pp. 2261–2270.

Zeng, L. Z., Klausner, J. F., Bernhard, D. M., and Mei, R., 1993b, "A Unified Model for the Prediction of Bubble Detachment Diameters in Boiling Systems—II. Flow Boiling," *Int. J. Heat Mass Transfer,* Vol. 36, pp. 2271–2279.

C. N. Ammerman
Graduate Student.
Student Mem. ASME

S. M. You
Assistant Professor.
Mem. ASME

Y. S. Hong
Graduate Student.
Student Mem. ASME

Department of Mechanical and
Aerospace Engineering,
The University of Texas at Arlington,
Arlington, TX 76019-0023

Identification of Pool Boiling Heat Transfer Mechanisms From a Wire Immersed in Saturated FC-72 Using a Single-Photo/LDA Method

A unique method to determine the vapor volumetric flow rate above a heated wire utilizing a single photograph and laser-Doppler anemometry is developed and discussed. The volumetric flow rate is combined with additional analyses to determine the overall contributions to the total heat flux from four nucleate boiling heat transfer mechanisms (latent heat, natural convection, Marangoni flow, and microconvection). This method is applied to a 75-μm wire immersed in a saturated, highly wetting liquid (FC-72). Latent heat is identified as the dominant mechanism in the fully developed nucleate boiling regime.

Introduction

Four different modes of heat dissipation are generally considered to comprise the total heat removal from a boiling surface: latent heat, natural convection, Marangoni flow, and microconvection:

$$q_{\text{Tot}} = q_{LH} + q_{NC} + q_{MF} + q_{MC} \quad (1)$$

Latent heat removal takes place when liquid vaporizes and leaves the surface. Natural convection occurs when sensible energy is removed from nonnucleating portions of the heated surface due to currents established by density gradients. Marangoni flow is induced by the surface tension gradient that exists at the bubble's liquid/vapor interface while the bubble is still attached to the heated surface. Microconvection heat transfer results from sensible energy being removed by entrainment of the superheated liquid in the departing bubble's wake. Further understanding of these four mechanisms is needed in highly wetting dielectric liquids to enable the development of more accurate pool boiling heat transfer prediction models.

Previous investigators have employed various photographic techniques to enable determination of key boiling parameters such as bubble departure diameter, frequency, and nucleation site density. Several investigators have presented experimental results of these key boiling parameters and most have used them to calculate contributions to total heat flux.

McFadden and Grassmann (1962) used high-speed photography to measure departure diameter and frequency for pool boiling of liquid nitrogen. Their work focused on determining a relationship between frequency and diameter which would allow prediction of the latent heat flux. Han and Griffith (1965) used high-speed photography at 2400 frames per second to measure diameters as a function of time for bubbles growing on a wire immersed in water. They found good agreement between experiment and theory of diameter at departure.

Rallis and Jawurek (1964) measured departure diameter, frequency, and nucleation site density in saturated water by evaluating 16 successive photographic frames at a speed of 85 frames per second using a variable-speed drum camera. Frequency measurements were obtained by counting the number of bubbles leaving an isolated site over the duration of the 16 frames. Departure diameters and nucleation site densities were obtained by inspection of individual frames. They were limited to measuring only low heat fluxes, however, because of the low frame speed of their camera. They reported that latent heat and convection accounted for the total heat flux in saturated nucleate boiling. They also reported that latent heat flux approached the total heat flux at burnout.

Paul and Abdel-Khalik (1983) measured departure diameter, frequency, and active nucleation site density from a wire immersed in saturated water by evaluating approximately 1000 frames per heat flux taken with a high-speed camera operating at 6400 frames per second. Again, frequency was obtained by counting the number of bubbles leaving a site over the duration of successive frames, and departure diameter and nucleation site density were obtained by inspection. A statistical analysis was performed on their data to obtain average values of the key boiling parameters as a function of heat flux. Their results showed that the total heat flux was composed of natural convection, latent heat, and enhanced convection (microconvection). Their subsequent analysis revealed that latent heat was dominant in the nucleate boiling regime, especially near the critical heat flux (CHF).

Barthau (1992) measured departure diameter, frequency, and active site density using video images of directly reflected light from a tube immersed in R-114 at various pressures. Nucleation site density was obtained by inspection using a single video image of the heated surface magnified 200 times. Frequency and departure diameter were acquired using successive video images taken in the presence of a stroboscope. With these results, he predicted latent heat and natural convection contributions of heat transfer, and determined that latent heat played a significant role in the total heat flux.

Tong et al. (1990) performed a theoretical parametric analysis of the heat transfer from a single nucleation site for nucleate pool boiling of highly wetting dielectric liquids. They identified four thermal transport mechanisms: latent heat, natural convection, Marangoni flow, and microconvection. To perform their analysis, they applied modifications to previously developed models of departure diameter and frequency to account for the

Contributed by the Heat Transfer Division and presented at the Energy Sources Technology Conference and Exhibition, Houston, Texas, January 29–February 1, 1995. Manuscript received by the Heat Transfer Division November 1994; revision received August 1995. Keywords: Boiling, Measurement Techniques, Phase-Change Phenomena. Associate Technical Editor: V. K. Dhir.

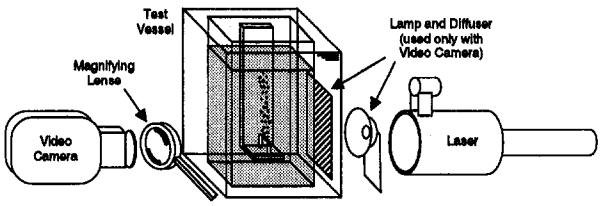

Fig. 1 Experimental setup

unique properties of highly wetting dielectric liquids (low surface tension and high wettability). For saturated FC-72 boiling from a flat surface, their results showed that microconvection was the dominant thermal transport mechanism throughout the nucleate boiling regime. In addition, they determined that the latent heat flux remained essentially constant with increasing wall superheat.

Despite their merits, the experimental methods previously listed require the interpretation of a large number of individual photographic frames at each heat flux to quantify the key boiling parameters. In addition, previous efforts to determine the boiling heat transfer mechanisms mainly employed conventional liquids. Because of the unique characteristics of highly wetting liquids, the study of Tong et al. (1990) indicates that their dominant heat transfer mechanisms may be different from conventional fluids. Therefore, the present paper has two objectives. The first is to introduce a new method that provides the capability to determine pool boiling heat transfer mechanisms by evaluating a single video image—as opposed to several hundred individual frames. This method differs from previous measurement techniques because the boiling mechanisms are determined at a location approximately two bubble diameters above the heated surface, as opposed to at the heated surface. The second objective is to evaluate the present experimental data using this method to quantify the pool boiling mechanisms for a highly wetting dielectric liquid (FC-72).

Experimental Apparatus and Procedure

The experimental setup for this study is shown in Fig. 1. The test section consisted of a 75-μm-dia platinum wire heater, mounted between two copper terminals spaced 20 mm apart. The heater was immersed in saturated FC-72 (at 1 atm), which was maintained at constant temperature with an isothermal water bath. Voltage sensors and a power supply were connected to the heater via the copper terminals. The power supply was connected in series with a standard resistor and the heater. The standard resistor, which was used to determine the current passing through the wire heater, had a resistance of 0.01 Ω accurate to ± 0.75 percent. Direct current was supplied by a power supply to the heating element. This equipment was interfaced via IEEE-488 cables and controlled by a 386 PC. Liquid temperatures were measured using copper-constantan thermocouples, which were calibrated with a precision thermometer. The wall temperature of the wire heater was calculated from its resistance via a calibration curve obtained prior to testing. Additional details on the experimental setup can be obtained from You et al. (1994).

Video imaging equipment was used to capture single-frame images of vapor bubbles above the heated wire. This system provided images at a speed of 30 frames per second. The video image was magnified by a factor of 10 using a 30-cm-focal-length lens. The camera's aperture was set to obtain a depth of field that ensured bubbles leaving the wire were in focus. High-intensity lighting (150-W projection bulb) filtered through a diffuser was used as a source of background light for the video photography. Video images were synchronized and transferred to a 386 PC, where they were digitized and analyzed by image processing software. This software enabled rapid determination of vapor characteristics above the heated wire, including the number and sizes of bubbles.

In addition to video photography, laser-Doppler anemometry (LDA) measurement techniques were used to ascertain the bubble velocity as a function of height above the heated wire. These LDA measurement techniques were previously used by O'Connor et al. (1993). The LDA equipment included a Dantec helium–neon (He–Ne) gas laser, 55X modular transmitting and receiving optics, a Bragg Cell (55×29) for beam frequency shift, and a flow velocity analyzer (FVA-58N20) software/hardware package, which provided one-dimensional velocity measurements.

The constant-temperature bath and magnetic stirrer were turned on and the test liquid was heated to saturation temperature. The test liquid was allowed to remain at saturation conditions for 3 to 4 hours to remove dissolved gases. After degassing, the magnetic stirrer was turned off and data acquisition begun. Heat flux was increased by controlling the supply voltage to the wire heater. The heat flux versus wire superheat pool boiling curve is shown in Fig. 2. The solid line indicates the single-phase natural convection correlation of Kuehn and Goldstein (1976) and compares well with the test data. Data points are shown for both increasing and decreasing heat flux. Critical heat flux occurred at 19.1 W/cm^2 at a wall superheat of 29.5°C.

Photographic and LDA Data

For this study, photographs were taken at five different heat fluxes: 1.9, 5.9, 9.1, 12.1, and 15.0 W/cm^2. The data points for both the 1.9 and the 5.9 W/cm^2 cases were obtained using decreasing heat flux. The video camera was set to its maximum shutter speed of 1/10,000th of a second, an aperture of F14, and a gain of 15 dB. Five video images were selected at random from each of the five heat fluxes for analysis. The present data reflect five-frame averages computed for each heat flux. At 1.9 W/cm^2, the wire contained only three active nucleation sites. At a heat flux of 5.9 W/cm^2, the wire was in the partially developed nucleate boiling regime (surface not fully covered with bubbles). For heat fluxes from 9.1 through 15.0 W/cm^2,

Nomenclature

C_l = specific heat, J/kg°C
CHF = critical heat flux
D_{wire} = wire diameter, mm
LDA = laser-Doppler anemometry
MA = measurement area
ΔT_{sh} = average superheat within the superheated liquid layer, °C
V_b = bubble volume, mm^3
V_{b_i} = volume of ith bubble, mm^3
$\dot{V}_g$ = vapor volumetric flow rate, mm^3/s
$\dot{V}_{sh}$ = superheated liquid volumetric flow rate, mm^3/s
f = frequency per unit length, Hz/mm
h_{lg} = latent heat of vaporization, J/kg
q = heat flux, W/cm^2
$\bar{u}_b$ = spatially averaged bubble velocity, m/s
$\bar{u}_{b_i}$ = spatially averaged velocity of ith bubble, m/s
$\bar{u}_{b_y}$ = locally averaged bubble velocity at a given height, m/s
Δt_{b_i} = time for ith bubble to traverse measurement area, s
Δx = measurement area width, mm
Δy = measurement area height, mm
δ_{99} = superheated liquid layer thickness, mm
ρ_g = vapor density, kg/m^3
ρ_l = liquid density, kg/m^3

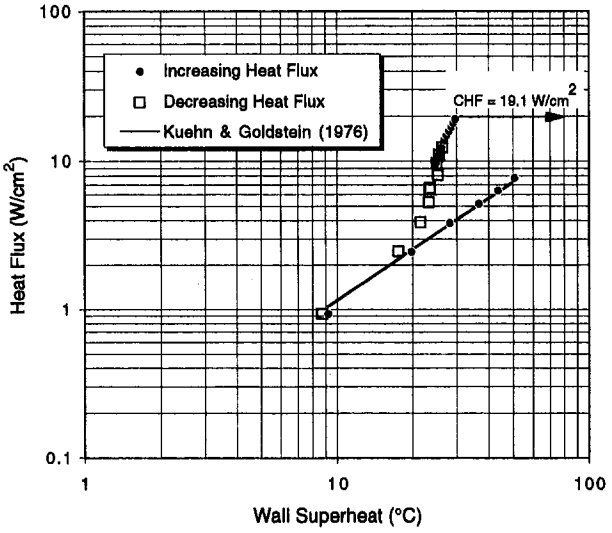

Fig. 2 Saturated FC-72 boiling curve

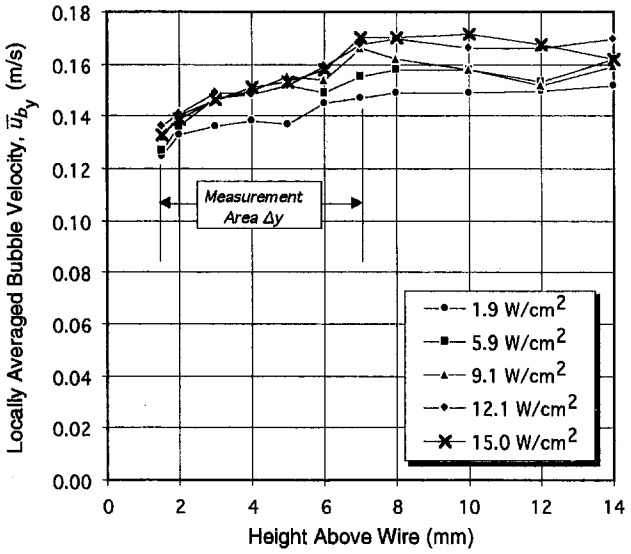

Fig. 4 Bubble velocity versus height above wire

the wire was in the fully developed nucleate boiling regime. Figure 3 is a photograph taken at 12.1 W/cm^2 and shows the wire in the fully developed nucleate boiling regime. Superimposed on the photograph in Fig. 3 is a schematic of the measurement area above the wire that was defined for this experiment. The measurement area will be discussed later in the paper.

Velocity measurements were also recorded during testing using the LDA system. Since the bubble velocity varies as a function of height above the wire, measurements were taken at several heights for each heat flux. The LDA system was used to compute an average of measured instantaneous bubble velocities at each height ($\bar{u}_{b_y}$). A plot of bubble velocity versus height above the wire for varying heat flux is shown in Fig. 4. Initially, the buoyancy force caused the bubble to accelerate upon detaching from the wire. Eventually, however, the drag force on the bubble balanced with the buoyancy force and the bubble attained a constant velocity. The spatially averaged bubble velocity within the measurement area, $\bar{u}_b$, was then calculated at each heat flux by numerically integrating the velocity versus height data (over the vertical span) and dividing by the total height. Uncertainty estimates for velocity are ±5 percent.

Vapor Volumetric Flow Rate Measurement

The single-photo method is a rapid, straightforward means of measuring the volumetric flow rate of vapor, $\dot{V}_g$, leaving a heated wire. Volumetric flow rate can be used to determine the latent heat flux component of heat dissipation from the heated surface with the following equation:

$$q_{LH} = \frac{\rho_g \dot{V}_g h_{lg}}{\pi D_{\text{wire}} \Delta x} \tag{2}$$

where ρ_g is the vapor density, h_{lg} is the latent heat of vaporization, and D_{wire} and Δx are the diameter and length of the heated wire, respectively.

In order to determine the reliability of using a single photo to measure the vapor volume, five video images were randomly chosen at each heat flux for comparison. Total vapor volume per frame was measured using the single-photo method (description of method to follow) and the single-frame uncertainty was calculated for each heat flux. At 1.9 W/cm^2, the uncertainty in using a single frame to measure vapor volume was ±12.8 percent. The rate of bubble departure from the wire at this heat flux was determined by O'Connor (1994) to be highly time dependent. At all other heat fluxes, however, the uncertainty dropped to ±3.4 percent or less, indicating that a single photo is sufficient to obtain a steady-state measurement.

A measurement area (MA) was defined within each black-and-white digitized photo using the image processor. The MA, depicted in Fig. 3, was a rectangle, 5.5-mm high (Δy) by 18-mm wide (Δx), centered above the wire. The lower edge of the MA was set 1.5 mm above the wire to ensure that bubbles would be completely detached from the wire before entering the area. The sides of the MA were set 1 mm inward from the copper posts to avoid possible effects of conduction heat loss to the posts.

Bubble edges in the photographs were defined by determining the difference between the gray level of the background versus the gray level of a bubble. Each image was divided into 255 gray-level gradations between black (gray level of zero) and white (gray level of 255). Background gray levels were obtained by averaging background values within each frame; therefore, slight errors in edge determination occurred that are included in bubble volume uncertainties.

While the shapes of the bubbles were slightly irregular, most bubbles appeared elliptical in two dimensions (Fig. 3). This was due to the initially spherical bubble being flattened between the opposing buoyancy and drag forces. Based on this flattening phenomenon, the bubble volume was determined from the two-dimensional image, as illustrated in Fig. 5. First, the image processor mathematically transformed the slightly irregular

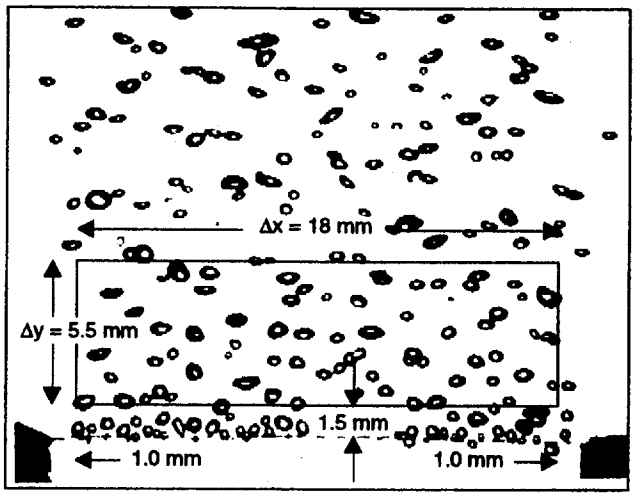

Fig. 3 Video image data for 12.1 W/cm^2 with measurement area

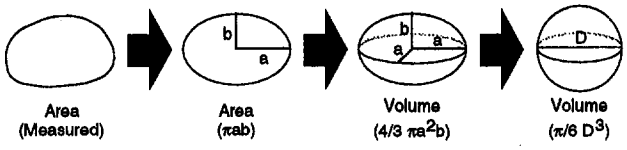

Fig. 5 Bubble volume measurement

two-dimensional bubble shape into an equivalent-area, two-dimensional ellipse with identical second moments about the center of gravity. The ellipse had semi-major and semi-minor axes of a and b, respectively. Then, based on the flattening phenomenon, the three-dimensional bubble was assumed to resemble an ellipsoid with semi-axes, a, a, and b, so that the bubble volume was calculated as

$$V_b = \tfrac{4}{3}\pi a^2 b \tag{3}$$

Finally, the spherical diameter was calculated for each bubble as shown in Fig. 5. Average bubble diameters were then computed within the MA and are shown versus heat flux in Fig. 6. The uncertainty band is also shown with the data. The open symbols in this, and subsequent plots, represent partially developed nucleate boiling, while the closed symbols represent fully developed boiling. For the small number of bubbles that happened to lie along the edge of the MA (boundary bubbles), only the portion within the MA was accounted for. Uncertainties in bubble volume measurements were estimated to be between ±8.1 and ±12.7 percent.

When each bubble's spatially averaged velocity within the MA is known, vapor volumetric flow rate can be computed for the length of the wire examined as follows:

$$\dot{V}_g = \sum \frac{V_{b_i}}{\Delta t_{b_i}} = \sum \frac{V_{b_i}\bar{u}_{b_i}}{\Delta y} \tag{4}$$

where Δt_{b_i} is the time it takes an individual bubble to travel vertically through the MA and V_{b_i} and $\bar{u}_{b_i}$ are individual bubble volume and spatially averaged velocity, respectively. Measuring individual bubble velocities during boiling was not possible; therefore, a velocity versus diameter trend was generated by correlating spatially averaged velocity versus heat flux with

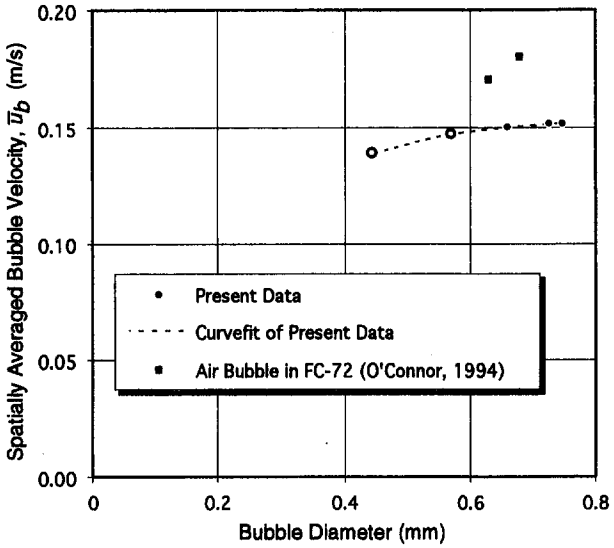

Fig. 7 Bubble velocity versus diameter

average diameter versus heat flux, as shown in Fig. 7. Velocity data taken by O'Connor (1994) for air bubbles in FC-72 are shown in Fig. 7 for comparison. The data of O'Connor are higher than the present data because they are representative of terminal velocities. The profiles over which the present data were averaged include an initial acceleration region. A curvefit of velocity versus diameter (shown in Fig. 7) was generated to enable calculation of individual bubble, spatially averaged velocities ($\bar{u}_{b_i}$) at each heat flux. These velocity values were combined with individual bubble volumes (Eq. (4)) to determine vapor volumetric flow rates. The resulting volume flow rates are shown in Fig. 8 and appear to vary linearly with heat flux.

With bubble velocities known, individual bubble frequencies can be calculated by dividing bubble velocity ($\bar{u}_{b_i}$) by vertical distance traveled (Δy). The frequency for the given length of wire examined can then be calculated as follows:

$$f = \sum \frac{\bar{u}_{b_i}}{\Delta y} \tag{5}$$

where f represents the number of bubbles leaving the 1.8 cm

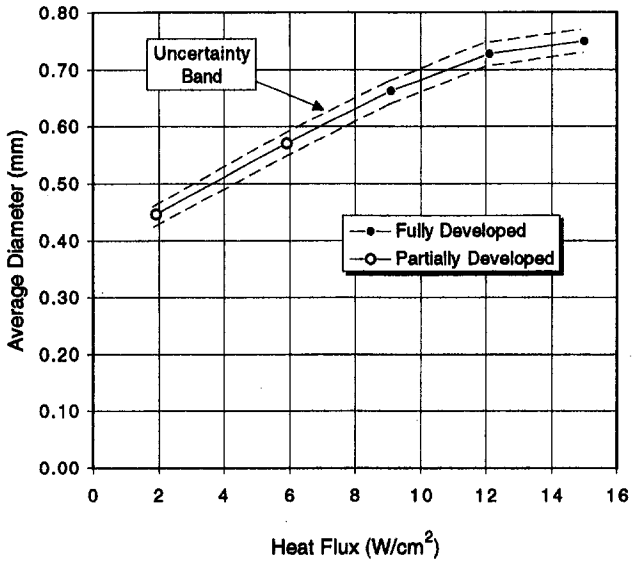

Fig. 6 Bubble diameter versus heat flux

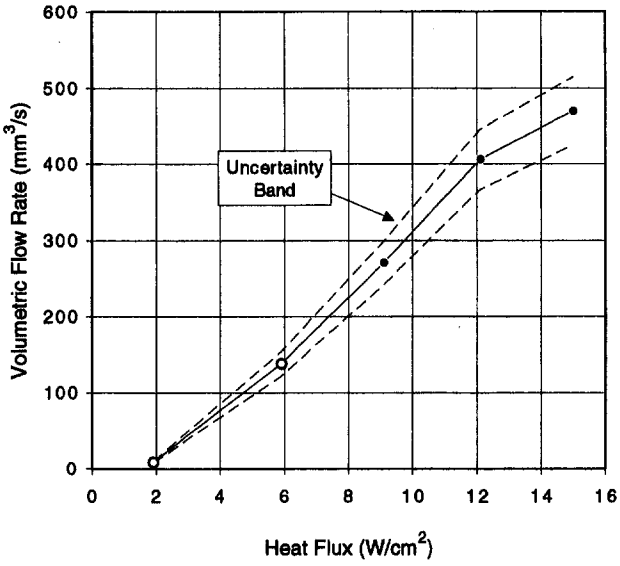

Fig. 8 Volumetric flow rate versus heat flux

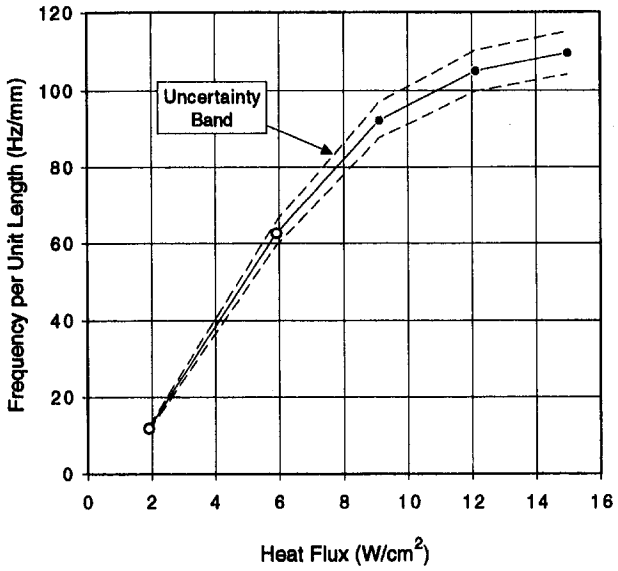

Fig. 9 Frequency per unit length versus heat flux

length of wire per second. Frequency per unit length values are shown versus heat flux in Fig. 9. Frequency increases rapidly versus heat flux in the partially developed boiling region due in part to the corresponding increase in active nucleation sites. However, the frequency then begins to level off in the fully developed region.

Bubble growth after departure (due to vaporization) and bubble agglomeration were considered as possible sources of error and were investigated. In the event of bubble growth occurring, the bubble volume, and thus the latent heat contribution, would be overpredicted. If agglomeration occurred, calculated frequency per unit length values would be lower than actual values. To investigate these phenomena, volume flow rate and frequency were measured in a region directly above the MA 7 mm high (from y = 7 to 14 mm) and 18 mm wide. Ratios were computed by dividing the volume flow rate and frequency values determined from this upper region by the corresponding values from the MA. A plot of these ratios versus heat flux is shown in Fig. 10.

The data in Fig. 10 indicate that at 1.9 W/cm^2, considerable vaporization took place after departure (which was also evident by inspection of the photos); however, no agglomeration occurred. This vaporization above the wire at 1.9 W/cm^2 was probably promoted by the relatively large amounts of superheated liquid within the plume rising from the wire due to natural convection. Since significant bubble expansion occurred, the volume flow rate at 1.9 W/cm^2 was determined by extrapolation of a least-squares linear curve fit of volume flow rate versus height to the lower edge of the MA. At heat fluxes above 1.9 W/cm^2, the volume flow rate ratio remained within ±4.5 percent of unity and therefore no corrections were made. The frequency ratio dropped approximately 5 percent at the higher heat fluxes, revealing that some agglomeration occurred. However, frequency values in the MA were assumed to be the most accurate obtainable with this method; therefore, no corrections were made to the frequency data.

Boiling Heat Transfer Mechanism Analysis

The results of the photographic and LDA investigations were used to determine the contributions of the four boiling heat transfer mechanisms that comprised the total heat dissipation above the heated wire. Calculations were performed to determine the latent heat, natural convection, Marangoni flow, and microconvection contributions. Because the lower edge of the MA was set 1.5 mm above the wire, the vapor volume measured (and hence the latent heat flux) may have been higher than the vapor volume departing the wire. This increase in vapor volume would arise from evaporation of some of the superheated liquid carried by a bubble upon departure (i.e., conversion of microconvection into latent heat). Therefore, the results from the following mechanism analysis apply to the MA—just above the surface of the wire. In order to evaluate the boiling mechanisms at the wire, a more labor-intensive method is required, as discussed in the introduction.

Latent Heat. The values of latent heat flux were calculated using Eq. (2) with the volumetric flow rates defined in Eq. (4). The vapor departing the wire was assumed to be at saturation conditions.

Natural Convection. Natural convection was assumed to occur only from nonnucleating (inactive) portions of the heated wire. The inactive wire length percentages were estimated from the photographs to be 85 and 20 percent at 1.9 W/cm^2 and 5.9 W/cm^2, respectively. Natural convection was assumed to disappear somewhere between 5.9 and 9.1 W/cm^2. After obtaining the inactive portion of the wire, the method of Kuehn and Goldstein (1976) was used to estimate the natural convection heat flux.

Superheated Liquid Layer. Both the Marangoni flow and microconvection contributions are dependent on the thickness of, and temperature distribution within, the superheated liquid layer that forms on the wire's surface between bubble departures. Therefore, a transient conduction solution (Carslaw and Jaeger, 1986) for a constant-heat-flux circular cylinder in an infinite medium was generated. To determine the elapsed time for these calculations, an estimated single-site bubble departure frequency of 45 Hz was used. This analysis resulted in a superheated liquid layer thickness of δ_{99} = 0.079 mm. The average superheat within the superheated layer was determined by numerically integrating the temperature distribution and dividing by δ_{99}. A comparison of δ_{99} with bubble size shows that the average bubble diameter is approximately 5 to 9 times greater than the superheated layer thickness.

Marangoni Flow. The contribution to total heat dissipation due to Marangoni flow at saturated conditions is usually not significant and was determined in the present study to be negligible. These results are supported by the conclusions of Jabardo (1981). Jabardo found that thermocapillary-induced flows in

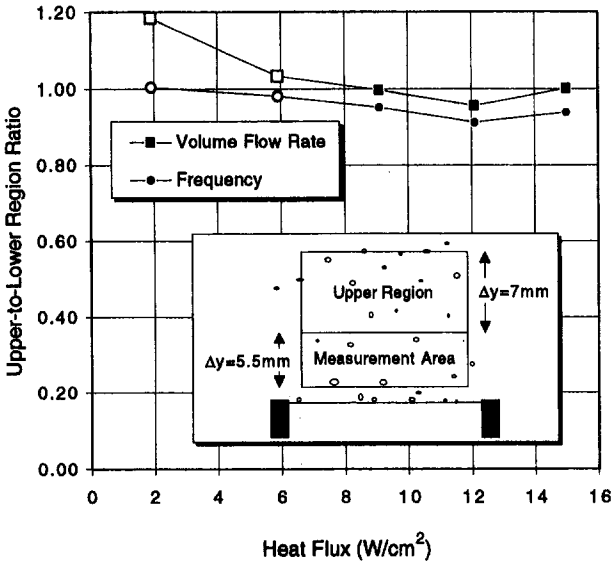

Fig. 10 Parameter ratio versus heat flux

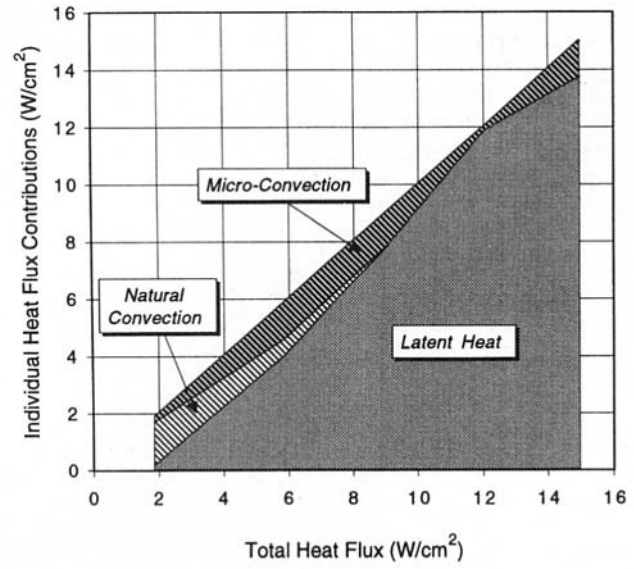

Fig. 11 Individual heat flux contributions

saturated nucleate boiling are usually not significant. Tong et al. (1990) computed theoretical Marangoni flow heat fluxes for boiling of saturated FC-72 based on surface-tension-induced jet strengths calculated by Jabardo. They also found that this contribution to overall heat flux was negligible. Thermocapillary effects could be important at low heat fluxes in gassy liquids, however. The heat transfer due to Marangoni flow, based on the calculations of Tong et al. (1990), was determined for the present study to be less than 2.5 percent of the total heat flux for all cases.

Microconvection. The microconvection contribution to overall heat dissipation is given by:

$$q_{MC} = \frac{\dot{V}_{sh}\rho_l C_l \overline{\Delta T_{sh}}}{\pi D_{\text{wire}} \Delta x} \tag{6}$$

where $\dot{V}_{sh}$ is the volumetric flow rate of the superheated liquid layer entrained in the bubble wake. The volumetric flow rate is difficult to determine, especially at higher heat fluxes where the wire is saturated with bubbles; therefore, an alternative approach was used. Since microconvection was the only remaining component to be calculated, it was derived from the previously calculated components using Eq. (1).

Heat Transfer Mechanism Results. The results of the heat transfer mechanism calculations are plotted versus total heat flux in Fig. 11. Latent heat is the dominant heat transfer mechanism throughout the boiling curve, except for the low end of the partially developed nucleate boiling region, which is dominated by natural convection. This latent heat trend agrees with observations made in previous studies using conventional liquids, such as water, but contradicts the theoretical predictions of Tong et al. (1990) for highly wetting liquids. This result is interesting because the latent heat of vaporization of water is nearly 24 times greater than that of FC-72. This similarity in the dominance of latent heat for FC-72 may be due in part to its low surface tension (85 percent less than water) and thus, a lower required bubble pressure for growth and departure.

Figure 12 shows the latent heat flux (as a percentage of total heat flux) versus heat flux (as a percentage of CHF). Shown with the present data is an uncertainty band for a 95 percent confidence level. The uncertainty in latent heat in the fully developed nucleate boiling region for the present data is less than ±10.5 percent. The latent heat increases rapidly with heat flux in the partially developed region, then flattens out and decreases slightly in the fully developed region. This decrease is probably due to uncertainty in the data as opposed to a change in boiling mechanism. Also shown in Fig. 12 are pool boiling data from Paul and Abdel-Khalik (1983) for a 300-μm-dia wire immersed in saturated water. The percent latent heat of the water data is lower than for FC-72, possibly because of the difference in surface tension of the two fluids, as discussed previously. Both sets of data approach 100 percent latent heat as they near CHF. This trend is expected since the film boiling mechanism (post-CHF) is probably all latent heat.

Conclusions

A simple, straightforward photographic/LDA method was developed and used to quantify vapor volumetric flow rate above a heated wire immersed in a highly wetting dielectric liquid (FC-72). The volumetric flow rate results were combined with additional analyses to determine the overall contributions to the total heat flux from four nucleate boiling heat transfer mechanisms (latent heat, natural convection, Marangoni flow, and microconvection). Based on the results of this investigation, the following conclusions are made:

1 For this highly wetting liquid, the latent heat contribution to total heat flux was dominant at all but the low end of the partial nucleate boiling region where natural convection was greatest. This trend agrees with results from previous experimental investigations performed with conventional liquids, but contradicts results obtained from a theoretical study performed for highly wetting liquids.

2 For FC-72, the dominance of the latent heat mechanism, in spite of FC-72's relatively low value of latent heat of vaporization, indicates that other properties (such as low surface tension) may promote the latent heat component.

3 The latent heat flux as a percent of total heat flux for the present data increased rapidly versus heat flux in the partially developed region, then leveled off in the fully developed region. The percent latent heat flux for FC-72 is greater than for water, possibly due to the surface tension difference between the two fluids.

4 The new photographic method enables the calculation of vapor volumetric flow rate using only a single video image for each heat flux. The uncertainty involved in using a single frame to measure vapor volume was determined to be within ±12.8 percent in the partial nucleate boiling region, and within ±3.4 percent for the fully developed nucleate boiling region.

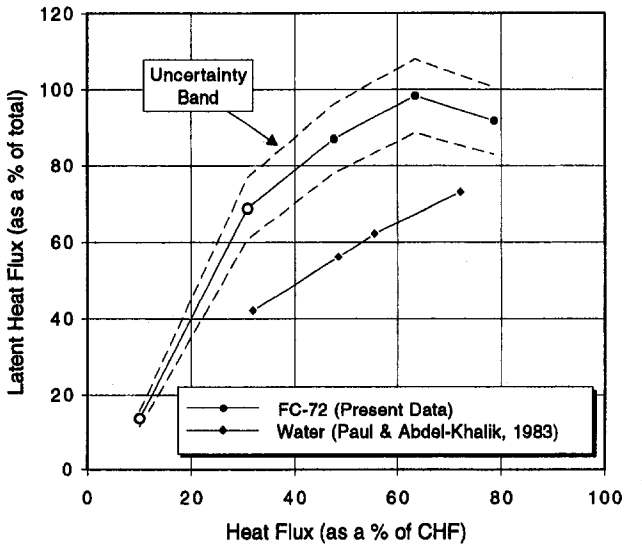

Fig. 12 Latent heat flux as a percent of total

Acknowledgments

This study was supported by the Texas Higher Education Coordinating Board; Advanced Research/Technology Program grant number 003656-101. In addition, the donation of FC-72 from the 3M Industrial Chemical Products Division is greatly appreciated.

References

Barthau, G., 1992, "Active Nucleation Site Density and Pool Boiling Heat Transfer—An Experimental Study," *International Journal of Heat and Mass Transfer,* Vol. 35, pp. 271–278.

Carslaw, H. S., and Jaeger, J. C., 1986, *Conduction of Heat in Solids,* 2nd ed., Clarendon Press, Oxford, pp. 335–339.

Han, C. Y., and Griffith, P., 1965, "The Mechanism of Heat Transfer in Nucleate Pool Boiling—Part I," *International Journal of Heat and Mass Transfer,* Vol. 8, pp. 887–904.

Jabardo, J. M. S., 1981, Ph.D. Thesis, University of Illinois at Urbana–Champaign.

Kuehn, T. H., and Goldstein, R. J., 1976, "Correlating Equations for Natural Convection Heat Transfer Between Horizontal Circular Cylinders," *International Journal of Heat and Mass Transfer,* Vol. 19, pp. 1127–1134.

McFadden, P. W., and Grassmann, P., 1962, "The Relation Between Bubble Frequency and Diameter During Nucleate Pool Boiling," *International Journal of Heat and Mass Transfer,* Vol. 5, pp. 169–173.

O'Connor, J. P., You, S. M., Hong, Y. S., and Haji-Sheikh, A., 1993, "Bubble Size, Velocity, and Frequency From a Wire Boiling in Saturated R-113," presented at the ASME 1993 Winter Annual Meeting, New Orleans, LA.

O'Connor, J. P., 1994, "Enhancement of Pool Boiling Heat Transfer in Highly Wetting Dielectric Liquids," Ph.D. Thesis, University of Texas at Arlington, Arlington, TX.

Paul, D. D., and Abdel-Khalik, S. I., 1983, "A Statistical Analysis of Saturated Nucleate Boiling Along a Heated Wire," *International Journal of Heat and Mass Transfer,* Vol. 26, pp. 509–519.

Rallis, C. J., and Jawurek, H. H., 1964, "Latent Heat Transport in Saturated Nucleate Boiling," *International Journal of Heat and Mass Transfer,* Vol. 7, pp. 1051–1068.

Tong, W., Bar-Cohen, A., and Simon, T. W., 1990, "Thermal Transport Mechanisms in Nucleate Pool Boiling of Highly-Wetting Liquids," presented at the 1990 International Heat Transfer Conference, Paper No. 1-BO-05.

You, S. M., Hong, Y. S., and O'Connor, J. P., 1994, "The Onset of Film Boiling on Small Cylinders; Local Dryout and Hydrodynamic Critical Heat Flux Mechanisms," *International Journal of Heat and Mass Transfer,* Vol. 37, No. 16, pp. 2561–2569.

Two-Phase Crossflow and Boiling Heat Transfer in Horizontal Tube Bundles

R. Dowlati[1]

M. Kawaji

Department of Chemical Engineering
and Applied Chemistry,
University of Toronto,
Toronto, Ontario, Canada M5S 1A4

A. M. C. Chan

Ontario Hydro Technologies,
800 Kipling Ave.,
Toronto, Ontario, Canada M8Z 5S4

An experimental study has been conducted to determine the void fraction, frictional pressure drop, and heat transfer coefficient for vertical two-phase crossflow of refrigerant R-113 in horizontal tube bundles under saturated flow boiling conditions. The tube bundle contained 5 × 20 tubes in a square in-line array with pitch-to-diameter ratio of 1.3. R-113 mass velocity ranged from 50 to 970 kg/m²s and test pressure from 103 to 155 kPa. The void fraction data exhibited strong mass velocity effects and were significantly less than the homogeneous and in-tube flow model predictions. They were found to be well correlated in terms of the dimensionless gas velocity, j_g^*. The two-phase friction multiplier data could be correlated well in terms of the Lockhart–Martinelli parameter. The validity of these correlations was successfully tested by predicting the total pressure drop from independent R-113 boiling experiments. The two-phase heat transfer coefficient data were found to agree well with existing pool boiling correlations, implying that nucleate boiling was the dominant heat transfer mode in the heat flux range tested.

Introduction

Heat transfer by means of shell-side boiling in horizontal multitube bundles is commonly experienced in a large variety of industrial heat exchange equipment. These include kettle reboilers, thermosyphons, and steam generators used in the chemical, process and power industries. The design of such equipment has, until recently, been primarily based on single-tube pool boiling data with various correction factors to account for the effect of neighboring tubes. However, it has become generally accepted that this empirical approach has led to overly conservative designs (Palen and Taborek, 1962; Smith, 1985; Chan and Shoukri, 1987). This is primarily due to the lack of sufficient information on local hydrodynamic and boiling characteristics in a multitube bundle.

A number of investigators have pointed out the importance of recirculation in the performance of multitube bundles (Leong and Cornwell, 1979; Palen and Yang, 1983; Fair and Klip, 1983; Jensen, 1988). Over the past years, various mechanistic models and empirical correlations have been presented to predict overall recirculation or local heat transfer under very limited conditions (Leong and Cornwell, 1979; Palen et al., 1972; Grant et al., 1983; Cornwell et al., 1980). None of these models have been proven to be generally acceptable, primarily because their application requires information on local flow conditions, which has not been available. These include information on void fraction and two-phase frictional pressure drop, which are essential in determining the recirculation rates and phasic velocities. The lack of reliable void fraction models for tube bundle crossflow has led designers and researchers to use models such as the homogeneous, in-tube, and horizontal flow models (Leong and Cornwell, 1979; Polley et al., 1980; Cornwell et al., 1980; Brisbane et al., 1980; Fair and Klip, 1983; Cornwell, 1990).

Some of the first tube bundle void fraction data were obtained in air–water experiments (Kondo and Nakajima, 1980; Schrage et al., 1988) using quick-closing valves. Dowlati et al. (1990, 1992a) performed systematic studies using various tube layouts with direct void fraction measurements in air–water flow. Their results demonstrated that the homogeneous and in-tube flow models were not capable of predicting void fraction for air–water systems, and instead proposed a void fraction correlation in terms of a dimensionless gas velocity. The new correlation was capable of predicting the slip and mass velocity effect observed in the void fraction data.

Although some experiments on forced convective boiling across horizontal tube bundles have been performed (Hwang and Yao, 1986; Hsu, 1987; Cornwell, 1990), no direct void fraction measurements have ever been made in these studies. Chan and Shoukri (1987) measured void fraction in a small tube bundle under pool boiling conditions only.

Until sophisticated multidimensional computer codes with accurate constitutive relationships needed to solve the two-phase field equations become available, investigators must rely on empirical information obtained under bundle simulated experiments. Cornwell et al. (1980) demonstrated that in the center region of a kettle reboiler, the bulk of the fluid flow was in a vertical upward direction. This indicated that a study of two-phase flow characteristics in the center region of a reboiler can be performed by using a simpler tube bundle simulating only the vertical channels of the center region of a reboiler. Circulation rate in kettle reboilers can then be obtained by a force balance between the single-phase and two-phase friction, acceleration, and static losses in the bundle, and the static head of single-phase liquid surrounding the bundle.

The work presented here is a continuation of a program to obtain new and accurate information on local two-phase flow characteristics in tube bundles. Experiments have been conducted for vertical forced-convective boiling of R-113 across a horizontal in-line tube bundle with a pitch-to-diameter ratio (P/D) of 1.3, at near-atmospheric pressures. The unique feature of the tube bundle, where oil was used for tube-side heating, allowed for accurate temperature-controlled experiments as compared to the common heat flux controlled resistance heating methods. The first known direct void fraction measurements made under convective boiling conditions in a tube bundle are presented. The data are compared with previous air–water results obtained for a similar tube bundle geometry and new correlations for bundle average void fraction and two-phase friction

[1] Present address: School of Nuclear Engineering, Purdue University, West Lafayette, IN 47907.

Contributed by the Heat Transfer Division for publication in the JOURNAL OF HEAT TRANSFER. Manuscript received by the Heat Transfer Division January 1995; revision received August 1995. Keywords: Boiling, Heat Exchangers, Multiphase Flows. Associate Technical Editor: R. A. Nelson.

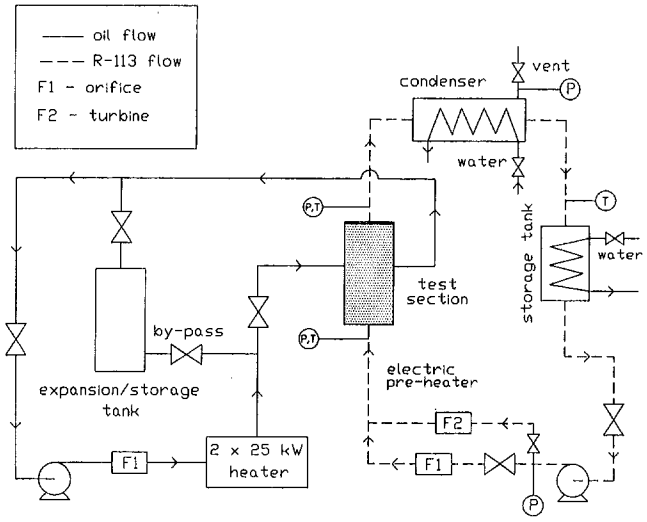

Fig. 1 Schematic of heat transfer oil and R-113 flow loops

multiplier are proposed for diabatic two-phase flow across a tube bundle. The correlations are then tested by predicting the total pressure drop in other boiling two-phase crossflow experiments. Two-phase heat transfer coefficient data are presented and comparison is made with the results of previous investigators.

Experimental Apparatus

Details of the experimental setup are given by Dowlati (1992b) and are only briefly outlined here. As shown in Fig. 1, the flow loop consisted of a high-temperature oil (Dowtherm-G) loop to heat the tube-side of the test section tube bundle, and an R-113 loop for shell-side flow boiling. The temperature of R-113 at the test section inlet was controlled with any combination of condenser, water-cooled storage tank, and electric strip preheaters.

As shown in a cross-sectional schematic of the test section in Fig. 2, the oil flowed into a vertical, rectangular inlet chamber, then was distributed through the tube-side of the tube bundle, where the tube ends were welded to a tubesheet. The oil exited the tubes into a similar rectangular exit chamber. The dimensions of the inlet and exit oil chambers were designed to achieve the best possible uniform distribution of oil flow among all tubes.

Thermocouple probes (1.6 mm O.D.) were inserted into the inlet chamber to measure the inlet oil temperature. Since the oil exit temperature from the tubes was expected to vary along the height of the bundle, due to variations in shell-side heat transfer rates, thermocouple probes were installed in the exit oil chamber. Twenty such probes were inserted approximately 6.4 mm into the exit end of the tubes at evenly spaced locations throughout the bundle. The oil exit temperatures for tubes that were not directly measured were interpolated based on the readings from the neighboring instrumented tubes.

In the shell-side loop, the R-113 piping fed vertically into an inlet rectangular channel, 79.4 mm × 100 mm in cross section, immediately upstream of the test section. The channel's inner dimensions matched those of the test section containing the tube bundle. Parallel plates were secured in the inlet channel to act as flow straighteners. Exiting the test section, the R-113 vapor–liquid mixture passed through an outlet channel of similar geometry. Thermocouple probes and pressure transducers were installed directly beneath the first row and above the last row of tubes to measure the R-113 inlet and exit conditions.

The tube bundle consisted of 100 copper tubes (5 columns by 20 rows) arranged in an in-line square array with P/D = 1.3. The tubes (12.7 mm O.D., 1.24 mm wall, and 108 mm long) were inserted into the tubesheets, leaving 80 mm of actual heated tube length in the bundle. The inner shell walls were fitted with half-round solid brass rods (12.7 mm diameter) to prevent bypass flow between the tubes and shell wall. The surfaces of the copper tubes and half-round rods were polished with grade 400 emery paper prior to installation. The outer wall of the test section was insulated to minimize heat loss.

Twenty of the tubes were equipped with thermocouples (0.5 mm O.D.) located at the center axial position of the tubes to measure outside tube wall temperature. Each thermocouple junction was positioned flush with the outside tube surface and silver-soldered in place. In 16 of these tubes, the thermocouples were positioned at the upstream (0 deg) and downstream (180 deg) positions of each tube and in the remaining five tubes an additional thermocouple was placed in the 90 deg position. The locations of the instrumented tubes were also distributed evenly throughout the bundle. The circumferential variations in the tube wall temperature were found to be less than ±0.6°C, under both single-phase and two-phase convective heat transfer conditions.

Five vertical locations on the side wall of the tube bundle, along the center axial position of the tubes, were fitted with pressure taps and connected to differential pressure transmitters to measure the pressure drop between any two taps. During

Nomenclature

A = constant, Eq. (13)
b = constant, Eq. (13)
C = constant, Eq. (11)
C_1, C_2 = coefficients, Eq. (8)
C_0 = distribution parameter, Eq. (9)
D = tube diameter, m
f = friction factor
G = mass velocity based on minimum flow area, kg/m^{2}s
g = acceleration due to gravity = 9.806 m/s^2
H = specific enthalpy, J/kg
H_{fg} = latent heat of vaporization, J/kg
h = heat transfer coefficient, W/m^{2}K
j = superficial velocity, m/s
$j_g = Gx/\rho_g$ = superficial gas velocity, m/s
j_g^* = dimensionless gas velocity, m/s
m = exponent in Blasius-type friction factor
N = number of tube rows
Nu = hD/k = Nusselt number
P = pressure, N/m^2
P/D = pitch-to-diameter ratio
Pr = $c_p\mu/k$ = Prandtl number
q'' = heat flux, W/m^2
Re = $\rho D u_{max}/\mu$ = Reynolds number
$\bar{u}_g$ = average gas velocity, m/s
V_{gj} = drift velocity, m/s
x = quality
α = void fraction
μ = dynamic viscosity, Pa-s
ρ = density, kg/m^3
ϕ^2 = two-phase friction multiplier
χ = Lockhart–Martinelli parameter

Subscripts

2ϕ = two-phase
g = gas phase only
nb = nucleate boiling
f = liquid phase only
H = homogeneous flow model
tt = turbulent regime for gas and liquid phases

Superscripts

F = friction

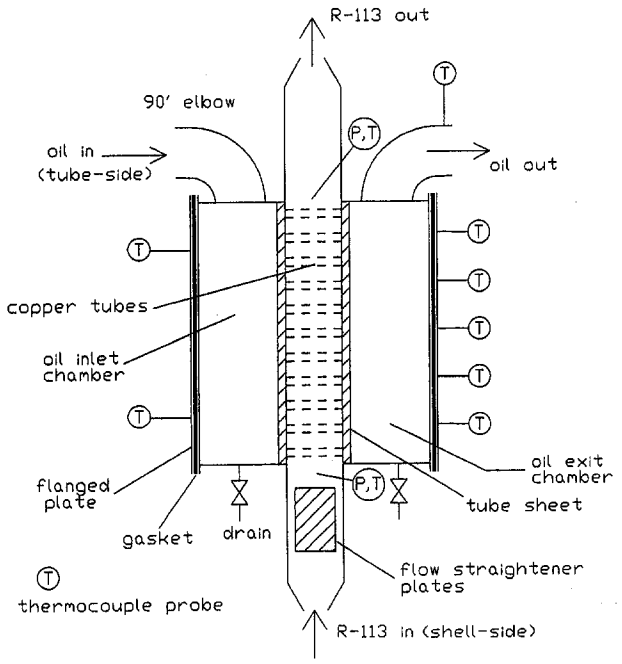

Fig. 2 Test section for crossflow boiling experiments (side view)

boiling experiments, no bubbles were observed in the transparent tubing connected to the pressure taps.

The test section was equipped with a gamma densitometer to provide void fraction measurements at rows 3, 8, 13, and 18. Each reading indicated a chordal average void fraction for the specific row. The gamma beam was collimated to yield a window with a height corresponding to the tube pitch and a width of 50.8 mm.

Data from all instruments were collected through a data acquisition and control interface board installed on an IBM-compatible PC. Prior to each experiment, the R-113 loop was heated to thoroughly degas the liquid. In each boiling experiment, R-113 entered the tube bundle as subcooled liquid, and data were collected under steady-state conditions.

The experimental test conditions are given in Table 1. The uncertainty in the data listed in Table 2 are based on standard propagation of error analysis (Kline and McClintock, 1953) and include error sources from sensor, data acquisition, and calculations.

Single-phase flow tests were initially performed to verify the experimental procedure and compare frictional pressure drop and heat transfer data with existing correlations. Tube wall temperature variations between instrumented tubes in the same row were found to be less than ±0.4°C. Further analysis of the data (Dowlati, 1992b) confirmed that the oil flow maldistribution through all tubes was less than ±5 percent, implying that the rate of heat transfer for each tube in a given row was highly similar.

Results and Discussion

Single-Phase Friction Factor and Heat Transfer. The R-113 single-phase liquid pressure drop data were used to compute the bundle friction factor, f, from

$$\Delta P_f^F = \frac{Nf[G(1-x)]^2}{2\rho_f} \tag{1}$$

where N is the number of tube rows between the pressure taps. Pressure drop measurements used to calculate the single-phase friction factor were made above the second and below the 19th tube rows, both to minimize the entrance and exit effects, and to obtain the highest possible pressure drop. Therefore, $N = 16$ was used in Eq. (1). The single-phase friction factor data showed very little scatter and were found to agree well with the correlations of Zukauskas (1972), ESDU (1979), and Hsu (1987). A Blasius-type correlation was fitted to the data as follows:

$$f = 0.811\ \mathrm{Re}^{-0.087} \tag{2a}$$

for $3500 < \mathrm{Re} < 2 \times 10^4$, and

$$f = 21.4\ \mathrm{Re}^{-0.513} \tag{2b}$$

for $700 < \mathrm{Re} < 3500$. Here the Reynolds number was based on the maximum liquid velocity and tube diameter. For greater accuracy, however, the measured single-phase pressure drop was used directly in the calculation of the two-phase friction multiplier.

Based on the relatively high thermal conductivity of the copper tubes, an assumption was made that the temperature readings at the midplane of the instrumented tubes represented an average tube wall temperature along the full length of the tube axis. Using linear interpolation between the instrumented and noninstrumented tubes, a profile of the row average tube wall temperature throughout the tube bundle was obtained.

The bulk R-113 temperature at each row was calculated from a heat balance using the average tube-side heat input, R-113 mass flow rate, and heat capacity. The single-phase heat transfer coefficient for each row was then calculated using the average tube wall temperature. The overall heat transfer coefficient for the whole bundle, computed by averaging the single-phase heat transfer coefficient for all tube rows, was found to increase with Reynolds number as expected due to the increased turbulence. The present data were fitted by the following correlation:

$$\mathrm{Nu} = 0.24\ \mathrm{Re}^{0.66}\ \mathrm{Pr}^{0.34} \tag{3}$$

with an average deviation of ±4.4 percent, and were also found to be slightly higher (5–10 percent) than the single-phase forced-convection correlations of Zukauskas (1972), ESDU (1973), and Hsu (1987).

Void Fraction. In order to ensure that the void fraction data chosen for analysis were obtained under saturated flow boiling conditions, only the void fraction data corresponding to positive equilibrium quality values were analyzed. Void fractions obtained under negative quality conditions were generally found to be below 10 percent, and never exceeded 18 percent. Zuber et al. (1966) reported void fraction values as high as 20 percent under subcooled flow boiling conditions for R-22 in a

Table 1 Experimental test conditions

Test parameters	Range
Mass Velocity	50–790 kg/m^{2}s
Quality	0–50 percent
Inlet Subcooling	3–20°C
Heat Flux	0–80 kW/m^2
Tube Wall Temp.	50–70°C
Pressure	103–155 kPa

Table 2 Uncertainties in crossflow data

Parameter	Uncertainty
G	±2%
α	±6%
T	±1%
x	±4%
$h_{1\phi}$	±4%
$h_{2\phi}$	±7%
q''	±6%

heated pipe. Assuming equilibrium conditions, the local thermodynamic quality for R-113 was calculated as

$$x = \frac{H_i - H_f}{H_{fg}} \tag{4}$$

where H_i is defined as the two-phase mixture enthalpy at row i calculated based on a local heat balance, and H_f and H_{fg} are the saturated liquid enthalpy and the latent heat of vaporization, respectively, calculated based on the local static pressure.

As is common with the analysis of in-tube flow data, the present void fraction data are plotted against the local thermodynamic quality in Fig. 3. Strong mass velocity effects are observed for the present crossflow boiling data for low to medium mass velocities. For a given value of quality, higher void fraction is generally obtained with increasing mass velocity. It is speculated that this mass velocity effect is due to the variation in the degree of momentum coupling between the two phases, possibly in different two-phase flow regimes, which in turn affects the slip ratio. For medium to high mass velocities (630–910 kg/m^2 s), there appears to be little effect of mass velocity. The data also appear to converge at both high and low vapor qualities, perhaps indicating extremes of the shear and buoyancy dominated flow regimes.

Similar observations were reported (Dowlati et al., 1990) for air–water void fraction data taken in a similar tube bundle in a transparent test section where the flow could be visually observed. However, determination of the two-phase flow regime by observation from the outside of the tube bundle was not possible in the present experiment. Recently presented two-phase flow regime maps based on direct observation (Ulbrich and Mewes, 1994) and statistical analysis of void fraction fluctuations (Noghrekar et al., 1995) have not shown consistent results for high mass velocities ($G > 400$ kg/m^2 s). Thus, at present it is not possible to determine the effect of two-phase flow regimes on the void fraction variation.

The measured void fraction data are also seen to be significantly lower than the values predicted by the homogeneous flow model evaluated at an approximately averaged pressure used in the experiment, and given by

$$\alpha_H = \frac{1}{1 + \left(\frac{1-x}{x}\right)\left(\frac{\rho_g}{\rho_f}\right)} \tag{5}$$

Overprediction by the homogeneous flow model was also reported by Dowlati et al. (1990) for air–water data. This overprediction is again attributed to the assumption of no slip between the phases in the homogeneous flow model, the validity of which depends on the degree of mixing achieved by the two phases. At low mass velocities, the effect of buoyancy is significant, especially at low qualities, and there is a considerable difference in phasic velocities. At high mass velocities and low values of quality, turbulence in the liquid phase helps in mixing the two phases and a more homogeneous mixture is obtained.

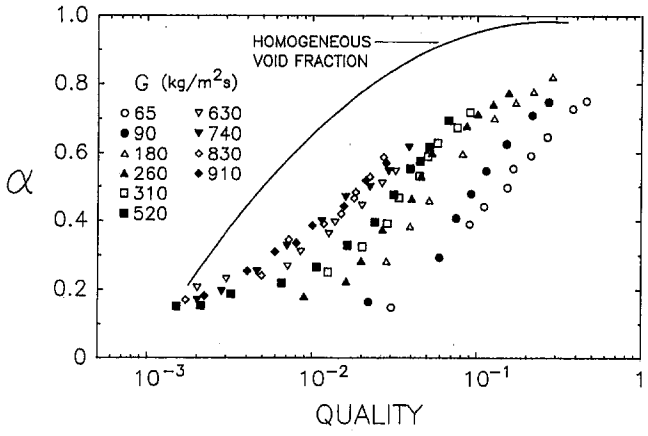

Fig. 3 Void fraction data and mass velocity effect for R-113

Compared to the air–water data obtained by Dowlati et al. (1990), the present R-113 void fraction values are found to be lower for given values of mass velocity and quality. As well, the homogeneous flow model calculated for R-113 falls below that calculated for the air–water system by a similar margin. Review of the parameters in Eq. (5) can explain the difference observed in the homogeneous flow model calculation. For the conditions used in the present experiment, the phase density ratio for R-113 is approximately four times that of air–water at atmospheric conditions. Hence, for a given quality in Eq. (5), a higher phase density ratio leads to a lower value for the predicted void fraction. With an increase in quality, the effect of the density ratio on α_H is reduced, and a similar void fraction value is obtained.

The differences observed in the void fraction data between R-113 and air–water may also be attributed to the difference in the phase density ratio between these two fluid systems. This is consistent with the variations observed in the Martinelli and Nelson (1948) void fraction correlation developed for in-tube flow. Plots of their correlation for steam–water mixture are presented by Collier (1981) for various system pressures. For a constant quality, an increase in system pressure leads to a decrease in the predicted void fraction. An increase in system pressure for a fluid system such as steam–water can also be considered equivalent to an increase in its phase density ratio.

A number of researchers have reported using in-tube void fraction models based on the well-known Lockhart–Martinelli parameter, χ, to predict void fraction in tube bundles. For turbulent gas and liquid conditions, this parameter is given by

$$\chi_{tt}^2 = \left(\frac{1-x}{x}\right)^{2-m}\left(\frac{\rho_g}{\rho_f}\right)\left(\frac{\mu_f}{\mu_g}\right)^m \tag{6}$$

where m is the exponent in the Blasius-type turbulent single-phase friction factor. With $m = 0.2$ in Eq. (6), the present R-113 void fraction data when plotted against χ_{tt} were also significantly overpredicted and showed strong mass velocity effects similar to the homogeneous void fraction model. As reported by Ishihara et al. (1979) and Dowlati et al. (1990) the choice of $m = 0.2$ results in less scatter (8 percent) than when m is allowed to vary according to the measured Reynolds number dependence of the single-phase friction factor.

The mass velocity effect also observed with χ_{tt} is not surprising, since the Lockhart–Martinelli parameter is essentially a function of the flow quality, which was shown in Fig. 3 to display a mass velocity effect. Hence, the inability to predict tube bundle void fraction using either the homogeneous or in-tube flow model has been demonstrated against the present void fraction data.

Dowlati et al. (1990) speculated that the mass velocity effect observed with the air–water void fraction data was mainly due to a balance between the gas inertia and buoyancy forces. Hence, the air–water data were found to be well correlated in terms of the dimensionless gas velocity, j_g^*, given by Wallis (1969),

$$j_g^* = \frac{\rho_g^{1/2} j_g}{\sqrt{gD(\rho_f - \rho_g)}} \tag{7}$$

The present R-113 void fraction data are shown in Fig. 4 to be also well correlated in terms of j_g^*. A correlation similar to that used by Dowlati et al. (1990, 1992a, 1992c),

$$\alpha = 1 - \frac{1}{\sqrt{1 + C_1 j_g^* + C_2 j_g^{*2}}} \tag{8}$$

is fitted to the present data using C_1 and C_2 equal to 10 and 1,

respectively, with an average deviation of ±15 percent. The mass velocity effects observed in Fig. 3 are nearly eliminated with this new correlation.

Also shown in Fig. 4 is the dashed curve representing the correlation obtained by Dowlati et al. (1992a) to best fit air–water data from various tube bundle geometries. The correlation of the present R-113 data is seen to fall below that of air–water. Although the calculation of j_g^* does take into consideration the phasic densities, this apparently is not sufficient to collapse the R-113 and air–water correlations. Since the air–water and R-113 experiments were conducted at similar mass velocities and pressures, the most prominent distinction between the two fluid systems can be considered to be the gas (vapor) phase density. This suggests that the constants in Eq. (8) may be strongly dependent on the gas density. As well, the constants may be expected to depend on other properties, such as the liquid density and surface tension, which can affect the bubble size distribution. Other fluid systems would need to be tested in order to gain further information on the physical dependence of these constants.

The present experiments did not allow for visual inspection of the R-113 crossflow boiling. However, based on flow visualization studies, Cornwell (1990) reported that the bubbles formed during R-113 boiling in a tube bundle (Cornwell and Schuller, 1982) at 101 kPa were smaller than those observed in water boiling under similar natural convection conditions. Based on a photograph provided by Cornwell (1990) the average bubble diameter for R-113 boiling appears to be in the order of 1 mm. The air bubbles in air–water experiments (Dowlati et al., 1990) were reported to be in the range of 3–5 mm in diameter. Bubble size can affect the void fraction since the rise velocity of bubbles increases with size.

Dowlati et al. (1992c) discussed the first application of the drift flux model in predicting air–water crossflow in a tube bundle. The general expression of the drift flux model in terms of the weighted mean gas velocity is given by

$$\bar{u}_g = C_0 j + \bar{V}_{gj} \tag{9}$$

where C_0 and V_{gj} are the void distribution parameter and drift velocity, respectively. The present data are plotted in Fig. 5 in terms of Eq. (9). Although not indicated in the figure, no systematic variation was observed in the data with a change in mass velocity.

Applying linear regression, the following best-fit curve was obtained with an average deviation of ±12 percent,

$$\bar{u}_g = 1.076 j + 0.85 \tag{10}$$

where $\bar{u}_g$ and j are specified in m/s. It is worth noting that to our knowledge, the drift flux model has never been tested against void fraction data from a tube bundle under boiling conditions.

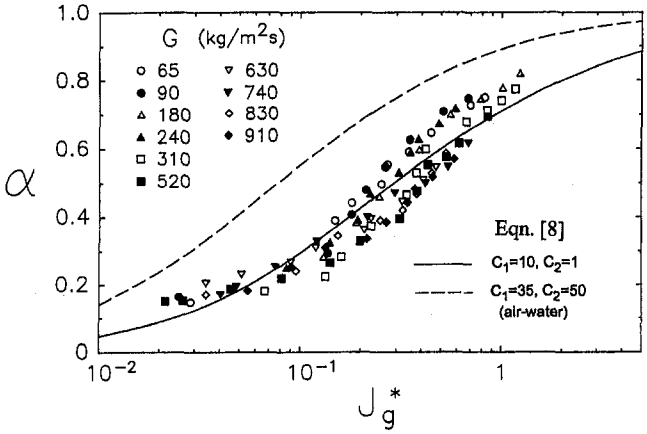

Fig. 4 Correlation of R-113 void fraction data with j_g^*

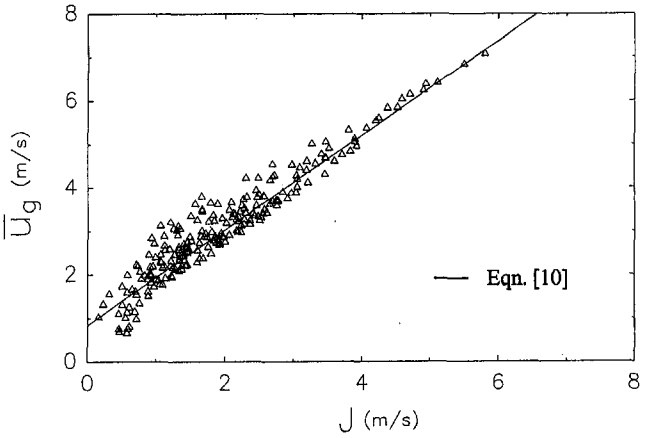

Fig. 5 Correlation of R-113 void fraction data using drift flux model

The value of C_0 in Eq. (10) is comparable to the value obtained from air–water data (1.104) (Dowlati et al., 1992c) and values reported for flows in circular tubes (1.0 to 1.3) (Nicklin et al., 1962; Zuber and Findlay, 1965; Clark et al., 1990). The slight difference in C_0 between the R-113 and air–water results is possibly due to local peaking of the void near the tube walls due to bubble nucleation, in the boiling bundle, while the bubbles are in the main stream flow in adiabatic conditions. The value of V_{gj} in Eq. (10) is higher than that found in air–water experiments (0.33 m/s) (Dowlati et al., 1992c), implying that the drift velocity of bubbles in R-113 may be higher than that for air bubbles. Presently, there are no reliable models to predict C_0 and V_{gj} in a tube bundle; hence, these two parameters also need to be obtained empirically.

At low gas velocities, the data trend in Fig. 5 appears to be changing toward a steeper slope and deviating from the best fit curve. Similar deviations have been reported for in-tube flow data, suggesting a flow regime transition. There is currently no widely accepted flow regime map for two-phase crossflow in a horizontal tube bundle; hence, the flow regimes in the present experiments cannot be further analyzed.

Due to the lack of data for other bundle geometries, it is difficult to determine the effect of pitch-to-diameter ratio on the void fraction correlations (Eqs. (8) and (9)) under actual boiling conditions. However, for air–water experiments, Dowlati et al. (1990, 1992a) reported little effect of bundle geometry on void fraction. Thus, we may also speculate the present void fraction correlations will also be applicable to different bundle geometries for R-113, but this needs to be verified in the future.

Two-Phase Friction Multiplier. The two-phase frictional pressure drop was computed for each run between the different pressure taps located on the tube bundle. Only the pressure drop data between the taps for which positive quality values were calculated were used in this analysis, in order to ensure that saturated flow boiling existed.

The procedure used to calculate the two-phase frictional pressure drop is given in detail by Dowlati (1992b). Basically, the gravitational pressure drop was estimated based on the summation of the static head terms between the pressure ports. The static head at each row was in turn calculated from the row-average void fraction value. The accelerational pressure drop was calculated from the separated flow model given by Collier (1981) using the row-average void fraction and equilibrium quality values. The gravitational and acceleration components were then subtracted from the measured total pressure drop to obtain the two-phase frictional pressure drop.

The two-phase friction multiplier is defined as the ratio of the single-phase to two-phase frictional pressure drop,

$$\phi_f^2 = \frac{\Delta P_f^F}{\Delta P_{2\phi}^F} \tag{11}$$

and is plotted against the Lockhart–Martinelli parameter in Fig. 6. As discussed earlier, a value of 0.2 was used for m in Eq. (6). The data are presented in two groups of mass velocity, $G \leq 100$ kg/m^{2}s and $G > 100$ kg/m^{2}s, and are seen to follow the same trend as suggested by the following equation given by Chisholm and Laird (1958),

$$\phi_f^2 = 1 + \frac{C}{\chi_{tt}} + \frac{1}{\chi_{tt}^2} \tag{12}$$

Using the above equation, a best-fit curve is obtained with $C = 8$. For $G \leq 100$ kg/m^{2}s, however, the data fall slightly below this curve, indicating perhaps a mass velocity effect. No mass velocity effect was observed for $G > 100$ kg/m^{2}s.

Dowlati et al. (1990) also used Eq. (12) with $C = 8$ to predict air–water data from a similar tube bundle geometry. The C-value was found to vary with tube layout, and mass velocity effects were observed for $G \leq 200$ kg/m^{2}s. A C-value of 8 was also found to best fit Eq. (12) to a large data base of Ishihara et al. (1979), although larger scatter was seen for $\chi_{tt} > 0.2$.

Pressure Drop Prediction in Crossflow Boiling. In order to test the applicability of the void fraction and two-phase friction multiplier correlations, developed in this work, the total pressure drop data from other experiments (Hsu, 1987) were analyzed.

Hsu (1987) used a 5 × 27 in-line tube bundle with $P/D = 1.3$ and 7.94 mm O.D. electrically heated tubes, to boil R-113 at elevated pressures (200–500 kPa) with varying mass velocity (50–700 kg/m^{2}s). The static pressure profile in the bundle was obtained from pressure drop measurements along the bundle.

To test the present correlations, the pressure drop between two elevations sufficiently far apart was computed from Hsu's data and compared with the predictions of the total pressure drop due to gravity, friction, and acceleration. The two-phase friction multiplier was computed from Eq. (12) with $C = 8$. Hsu's single-phase friction factor correlation was used to determine the single-phase frictional pressure drop for the prediction of the two-phase frictional pressure drop from Eq. (11). The two-phase frictional pressure drop was then numerically integrated between the two values of quality at the given elevations.

In predicting the gravitational pressure drop in Hsu's experiments, the summation procedure described by Dowlati (1992b) was used to calculate the static head between the two elevations. The row-average void fraction was evaluated from quality using the present void fraction correlation (Eq. (8)) with the constants given in Fig. 3 (i.e., $C_1 = 10$ and $C_2 = 1$). The computation of the accelerational pressure drop was performed using the separated flow model, where the row-average void fraction was evaluated using Eq. (8).

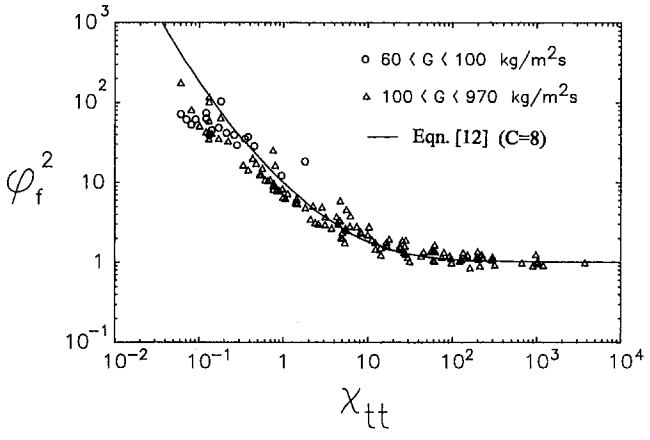

Fig. 6 Two-phase friction multiplier data with Lockhart–Martinelli parameter

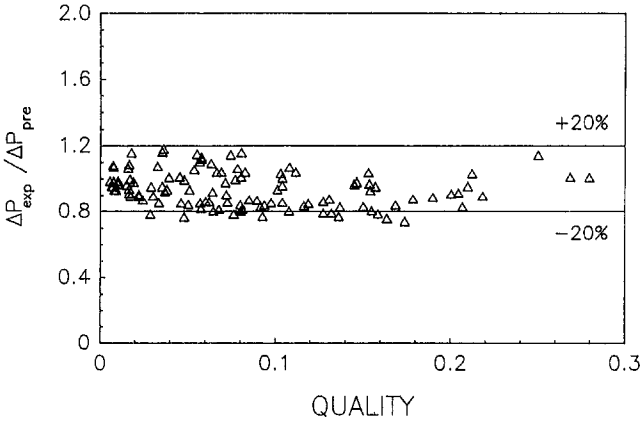

Fig. 7 Prediction of overall pressure drop data obtained by Hsu (1987)

Figure 7 shows the ratio of Hsu's experimental overall pressure drop to the predicted pressure drop based on the present correlations, plotted against the average quality between the two elevations considered. It is seen that the present correlations are successful in predicting over 90 percent of the data points considered, within ±20 percent. Thus, the present correlations can be used to predict the total pressure drop in a tube bundle geometry for R-113. For other fluids, the constants in Eqs. (8) and (12) must be obtained experimentally.

Boiling Heat Transfer. A number of researchers have presented correlations to predict the two-phase heat transfer coefficient, $h_{2\phi}$, under forced crossflow convective boiling conditions in tube bundles. Most of these are of the form similar to the Chen-type (Chen, 1966) correlation developed for in-tube flow, where single-phase convective and nucleate boiling components are summed using various multiplication factors (Cornwell et al., 1980; Hwang and Yao, 1986; Jensen and Hsu, 1987). None of these results have been shown to be generally applicable. A number of these multiplication factors have been given as functions of the void fraction; however, due to the lack of sufficient information, the homogeneous and in-tube void models have been used to estimate the void fraction. Neither of these two models can be considered to be generally applicable to crossflow in tube bundles, as demonstrated earlier in this paper. For example, Leong and Cornwell (1979) used the homogeneous model to estimate the void fraction in their two-phase heat transfer correlation. The correlation was observed to overpredict the heat transfer coefficient data in the upper region of the tube bundle. This can partially be attributed to the overprediction of the void fraction by the homogeneous flow model as demonstrated in Fig. 3.

The present $h_{2\phi}$ data are presented in Fig. 8, where nearly 200 data points were obtained in the heat flux range of 10–80 kW/m^2. Each data point reflects an averaged value for tube rows 15 to 20 where saturated boiling was considered to be well developed. As expected, the data show an increase in the rate of heat transfer with increasing heat flux. The procedure used to calculate $h_{2\phi}$ is given by Dowlati (1992b).

None of the presently available convective $h_{2\phi}$ correlations for horizontal tube bundles was successful in predicting the present data. However, shown in Fig. 8 are two nucleate boiling heat transfer correlations (Hwang and Yao, 1986; Hsu, 1987), which have been developed from R-113 pool boiling experi-

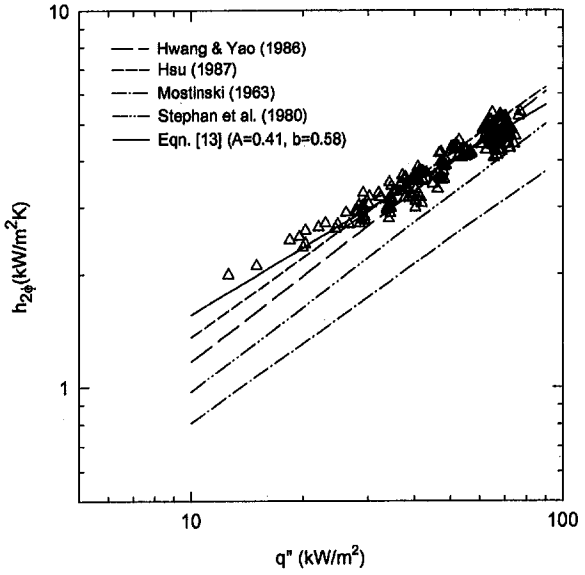

Fig. 8 Two-phase heat transfer coefficient data

ments in tube bundles. Each correlation is given as a simple function of the heat flux and can be expressed as follows:

$$h_{nb} = Aq''^{b} \tag{13}$$

where A and b are empirically determined constants. Both correlations are observed to agree well with the present data. A best-fit curve, shown in Fig. 8, was also fitted to the data for $q'' > 30$ kW/m^2 using the function given by Eq. (13) with $A = 0.41$ and $b = 0.58$, resulting in an absolute average deviation of 5 percent.

At sufficiently high values of heat flux (or wall superheat), nucleate boiling from the surface of the tubes becomes well developed and dominates any contribution from forced-convection in the rate of heat removal. The heat transfer coefficient becomes mainly a function of the heat flux (or wall superheat) similar to Eq. (13). The present boiling heat transfer data suggest this to be the case as the data follow the trend given by Eq. (13) and no mass velocity effect is observed for $q'' > 30$ kW/m^2.

Boiling heat transfer data obtained in horizontal tube bundles by Myers and Katz (1953) and Grant et al. (1983) using R-12 and by Hwang and Yao (1986) and Fujita et al. (1986) using R-113 also show convergence into a single function of the heat flux in the range of 20–100 kW/m^2, which is consistent with the present observation.

Although very few data were collected at lower heat flux values ($q'' < 30$ kW/m^2) in the present study, the few data points shown in Fig. 8 suggest a deviating trend from the pool boiling correlations. The heat transfer coefficient data appear to be "flattening out" as the dependence on the heat flux diminishes. This may be considered to be the transition region or "knee" of the boiling curve where forced-convection heat transfer becomes effective and the nucleate boiling contribution in the rate of heat removal decreases in importance. The data from Hwang and Yao (1986) for R-113 convective boiling in an in-line tube bundle also showed this transition region to be in the range of 10–30 kW/m^2. With a further reduction in heat flux, it is speculated that the heat flux dependence on nucleate boiling will be further reduced and eventually the forced convective boiling will dominate and mass velocity effects will appear as also evident from the results of Hwang and Yao (1986).

Several researchers (Brisbane et al., 1980; Grant et al., 1983; Marto and Anderson, 1991) have recommended the use of various pool boiling correlations (Mostinski, 1963; Kutateladze and Borishanski, 1966; Stephan and Abdelsalam, 1980), obtained for single horizontal tubes, in the prediction of nucleate boiling in tube bundles. In a number of cases, this was justified based on the argument that under fully developed nucleate boiling conditions, the effect of neighboring tubes can be considered negligible. Two of these correlations are shown in Fig. 11 for comparison. Both correlations are observed to underpredict the present data, suggesting that even under fully developed nucleate boiling conditions, heat transfer in a tube bundle may be considered to be higher than that from a single tube.

Conclusions

The present findings from the R-113 crossflow boiling experiments add much needed information on two-phase crossflow characteristics for improving the future design of kettle reboilers. The findings suggest that the homogeneous and in-tube void fraction models that have been commonly used in tube bundles need to be carefully reconsidered if we are to reduce the high degree of conservatism inherent in the present design methods. Application of the present void fraction and two-phase friction multiplier correlations may be very helpful in advanced kettle circulation models given by Jensen and co-workers (1988, 1991) where accurate estimation of the overall driving head and local phenomena are required.

The proposed void fraction correlation can be safely applied to fluid systems that have similar phase densities to the air–water and R-113 systems shown in this study. For fluids with highly different phase densities than air–water or R-113, the correlation may still be used to estimate the void fraction where comparison of the phase densities will indicate the conservatism in the predicted void fraction values.

The two-phase heat transfer coefficient data were shown to be correlated as a simple function of the heat flux in the range where nucleate boiling is the dominant mode of heat removal. This may lead to a great simplification in the estimation of the heat transfer performance of kettle reboilers, where presently complex models with very limited range of applicability are used. The correlation obtained in this work, however, is still empirically based and would require further verification using different fluid systems in order to be confidently used by the designers.

References

Brisbane, T. W. C., Grant, I. D. R., and Whalley, P. B., 1980, "A Prediction Method for Kettle Reboiler Performance," ASME Paper No. 80-HT-42.

Chan, A. M. C., and Shoukri, M., 1987, "Boiling Characteristics of Small Multitube Bundles," ASME JOURNAL OF HEAT TRANSFER, Vol. 109, pp. 753–760.

Chen, J. C., 1966, "A Correlation for Boiling Heat Transfer to Saturated Fluids in Convective Flow," *Ind. Eng. Chem. Process Design Dev.*, Vol. 5, No. 3, pp. 322–329.

Chisholm, D., and Laird, A. D. K. 1958, "Two-Phase Flow in Rough Tubes," *ASME Trans.*, Vol. 80, pp. 276–286.

Clark, N. N., Van Egmond, J. W., and Nebiolo, E. P., 1990, "The Drift-Flux Model Applied to Bubble Columns and Low Velocity Flows," *Int. J. Multiphase Flow*, Vol. 16, No. 2, pp. 261–279.

Collier, J. G., 1981, *Convective Boiling and Condensation*, McGraw-Hill, 2nd ed., New York.

Cornwell, K., Duffin, H. W., and Schuller, R. B., 1980, "An Experimental Study of the Effects of Fluid Flow on Boiling within a Kettle Reboiler Tube Bundle," ASME Paper No. 80-HT-45.

Cornwell, K., and Schuller, R. B., 1982, "A Study of Boiling Outside a Tube Bundle Using High Speed Photography," *Int. J. Heat Mass Transfer*, Vol. 25, No. 5, pp. 683–690.

Cornwell, K., 1990, "The Influence of Bubbly Flow on Boiling From a Tube in a Bundle," *Int. J. Heat Mass Transfer*, Vol. 33, No. 12, pp. 2579–2584.

Dowlati, R., Kawaji, M., and Chan, A. M. C., 1990, "Pitch-to-Diameter Effect on Two-Phase Flow Across an In-line Tube Bundle," *AIChE J.*, Vol. 36, No. 5, pp. 765–772.

Dowlati, R., Chan, A. M. C., and Kawaji, M., 1992a, "Hydrodynamics of Two-Phase Flow Across a Horizontal In-Line and Staggered Rod Bundle," ASME *Journal of Fluids Engineering*, Vol. 114, No. 3, pp. 450–456.

Dowlati, R., 1992b, "Hydrodynamics of Two-Phase Cross-Flow and Boiling Heat Transfer in Horizontal Tube Bundles," Ph.D. Thesis, Dept. of Chemical Eng., University of Toronto.

Dowlati, R., Kawaji, M., Chisholm, D., and Chan, A. M. C., 1992c, "Void Fraction Prediction in Two-Phase Flow Across a Tube Bundle," *AIChE J.*, Vol. 38, No. 4, pp. 619–622.

Edwards, D. P., and Jensen, M. K., 1991, "A Two-Dimensional Numerical Model of Two-Phase Heat Transfer and Fluid Flow in a Kettle Reboiler," ASME HTD-Vol. 159, New York, pp. 9–16.

ESDU, 1973, "Convective Heat Transfer During Crossflow of Fluids Over Plain Tube Banks," Engineering Sciences Data Unit, No. 73031, London.

ESDU, 1979, "Crossflow Pressure Loss Over Banks of Plain Tubes in Square and Triangular Arrays Including Effects of Flow Direction," Engineering Sciences Data Unit, No. 79034, London.

Fair, J. R., and Klip, A., 1983, "Thermal Design of Horizontal Reboilers," *Chem. Eng. Progress,* Vol. 79, No. 8, pp. 86–96.

Fujita, Y., et al., 1986, "Nucleate Boiling Heat Transfer on Horizontal Tubes in Bundles," *Proc. of 8th Int. Heat Tr. Conf.,* Paper FB02, pp. 2131–2136.

Grant, I. D. R., Cotchin, C. D., and Henry, J. A. R., 1983, "Tests on a Small Kettle Reboiler," in: *Heat Exchangers for Two-Phase Applications,* J. B. Kitto and J. M. Robertson, eds., ASME HTD-Vol. 27, New York, pp. 41–45.

Hsu, J. T., 1987, "A Parametric Study of Boiling Heat Transfer in Horizontal Tube Bundles," Ph.D. Thesis, Dept. of Mechanical Eng., Univ. of Wisconsin, Milwaukee.

Hwang, T. H., and Yao, S. C., 1986, "Forced Convective Boiling in Horizontal Tube Bundles," *Int. J. Heat Mass Transfer,* Vol. 29, No. 5, pp. 785–795.

Ishihara, K., Palen, J. W., and Taborek, J. J., 1979, "Critical Review of Correlations for Predicting Two-Phase Pressure Drop Across Tube Banks," *Heat Trans. Eng.,* Vol. 1, No. 3, pp. 1–8.

Jensen, M. K., and Hsu, J. T., 1987, "A Parametric Study of Boiling Heat Transfer in a Tube Bundle," *Proc. 2nd ASME/JSME Thermal Engineering Joint Conf.,* Vol. 3, pp. 132–140.

Jensen, M. K., 1988, "A Model for the Recirculating Flow in a Kettle Reboiler," *AIChE Symp. Ser.,* Vol. 84, No. 263, pp. 114–119.

Kline, S. J., and McClintock, F. A., 1953, "Describing Uncertainties in Single-Sample Experiments," *Mechanical Engr.,* Vol. 75, Jan., pp. 3–8.

Kondo, M., and Nakajima, K., 1980, "Experimental Investigation of Air-Water Two-Phase Upflow Across Horizontal Tube Bundles (Part I Flow Pattern and Void Fraction)," *Bulletin JSME,* Vol. 23, No. 177, pp. 385–393.

Kutateladze, S. S., and Borishanski, V. M., 1966, *A Concise Encyclopedia of Heat Transfer,* Pergamon Press, Oxford.

Leong, L. S., and Cornwell, K., 1979, "Heat Transfer Coefficients in a Reboiler Tube Bundle," *The Chemical Engineer,* No. 343, pp. 219–221.

Martinelli, R. C., and Nelson, D. B., 1948, "Prediction of Pressure Drop During Forced-Circulation Boiling of Water," *Trans. ASME,* Vol. 65, pp. 695–702.

Marto, P. J., and Anderson, C. L., 1991, "Nucleate Boiling Characteristics of R-113 in a Small Tube Bundle," *Proc. of ASME/JSME Thermal Eng. Joint Conf.,* Vol. 1, Reno, Nevada.

Mostinski, I. L., 1963, "Application of the Rule of Corresponding States for the Calculation of Heat Transfer and Critical Heat Flux," *Teploenergetika,* Vol. 4, p. 66.

Myers, J. E., and Katz, D. L., 1953, "Boiling Coefficients Outside Horizontal Tubes," *Chem. Eng. Prog. Symp. Ser.,* Vol. 49, No. 5, pp. 107–114.

Nicklin, D. J., Wilkes, J. O., and Davidson, J. F., 1962, "Two-Phase Flow in Vertical Tubes," *Trans. Inst. of Chem. Engrs.,* Vol. 40, No. 61.

Noghrekar, R., Kawaji, M., and Chan, A. M. C., 1995, "An Experimental Study of Local Two-Phase Parameters in Crossflow-Induced Vibration in Tube Bundles," *Flow Induced Vibrations,* P. W. Barman, ed., *Proc. of 6th Intl. Conf. on Flow Induced Vibration,* London, United Kingdom, Apr. 10–12.

Palen, J. W., and Taborek, J. J., 1962, "Refinery Kettle Reboilers—Proposed Method for Design and Optimization," *Chem. Engr. Prog.,* Vol. 50, No. 7, pp. 37–46.

Palen, J. W., Yarden, A., and Taborek, J. J., 1972, "Characteristics of Boiling Outside Large-Scale Horizontal Multitube Bundles," *AIChE Symp. Ser.,* Vol. 68, No. 118, pp. 50–61.

Palen, J. W., and Yang, C. C., 1983, "Circulation Boiling Model for Analysis of Kettle and Internal Reboilers," in: *Heat Exchangers for Two-Phase Applications,* J. B. Kitto and J. M. Robertson, eds., ASME HTD-Vol. 27, New York, pp. 55–61.

Polley, G. T., Ralston, T., and Grant, I. D. R., 1980, "Forced Crossflow Boiling in an Ideal In-Line Tube Bundle," ASME Paper No. 80-HT-46.

Schrage, D. S., Hsu, J. T., and Jensen, M. K., 1988, "Two-Phase Pressure Drop in Vertical Crossflow Across a Horizontal Tube Bundle," *AIChE J.,* Vol. 34, No. 1, pp. 107–115.

Smith, B., 1985, "Up-date on Shellside Two-Phase Heat Transfer," *The Chemical Engineer,* No. 414, pp. 16–19.

Stephan, K., and Abdelsalam, M., 1980, "Heat-Transfer Correlations for Natural Convection Boiling," *Int. J. Heat Mass Transfer,* Vol. 23, pp. 73–87.

Ulbrich, R., and Mewes, D., 1994, "Vertical, Upward Gas-Liquid Two-Phase Flow Across a Tube Bundle," *Int. J. Multiphase Flow,* Vol. 20, No. 2, pp. 249–272.

Wallis, G. B., 1969, *One-Dimensional Two-Phase Flow,* McGraw-Hill, New York.

Zuber, N., and Findlay, J. A., 1965, "Average Volumetric Concentration in Two-Phase Flow Systems," ASME JOURNAL OF HEAT TRANSFER, Vol. 87, pp. 453–468.

Zuber, N., Staub, F. W., and Bijwaard, G., 1966, "Vapor Void Fraction in Subcooled Boiling and in Saturated Boiling Systems," *3rd Intl. Heat Tr. Conf. Proc.,* Vol. 5, Paper No. 154, pp. 24–38.

Zukauskas, A., 1972, "Heat Transfer From Tubes in Crossflow," *Advances in Heat Transfer,* Vol. 8, pp. 93–160.

Thickness of the Liquid Film Formed by a Growing Bubble in a Narrow Gap Between Two Horizontal Plates

K. Moriyama[1]

A. Inoue

Research Laboratory for Nuclear Reactors,
Tokyo Institute of Technology,
2-12-1 O-okayama,
Meguro-ku, Tokyo 152, Japan

An experiment was performed to measure the thickness of the liquid film formed by a growing flattened bubble in a narrow gap whose width ranged from 0.1 to 0.4 mm. High-speed photographs were also taken to measure the bubble growth velocity in order to validate an investigation into the mechanism of the liquid film formation. From the experimental results, it was clarified that the liquid film thickness was controlled by the viscous boundary layer thickness or the capillary number according to whether the Bond number was greater or smaller than 2.

1 Introduction

Heat transfer enhancement due to the evaporation of thin liquid films on wall surfaces is one of the expected effects of two-phase systems in narrow channels. In such systems, the liquid film thickness is an important parameter because it controls the temperature gradient in the liquid film, and therefore, the heat flux on the wall surface.

Several investigations have been conducted on such liquid films formed by the movement of the gas–liquid interface. In the case of low Reynolds number, where movement of the interface is slow, the liquid film thickness has been correlated in terms of the capillary number ($Ca = \mu U/\sigma$), both experimentally and theoretically.

Taylor (1961) measured the thickness of the liquid film remaining on the wall when an air bubble penetrated through a glass tube (diameter 2–3 mm, length 105 mm) filled beforehand with glycerin–water solution. The results were correlated with the capillary number. His data covered a wide range of capillary numbers (Ca = 0.01–2.0). Bretherton (1961) derived a theoretical base for the capillary number dependence of the liquid film thickness. Related to parallel flat plates, Park and Homsy (1984) conducted a theoretical study and also revealed a capillary number dependence.

Further, the evaporation of the wall liquid layer has drawn attention from nucleate boiling or bubble development researchers because it has been considered to be the major mechanism producing the high heat transfer coefficient in nucleate boiling and the source of vapor supply to the growing bubbles on the wall.

Among such researchers, Katto and Yokoya (1966) estimated the liquid film thickness under a growing flattened bubble in a narrow gap, from the spreading velocity of the dry area on the wall inside the bubble. They estimated the liquid film thickness to be 3.5–11 μm as a function of the radial position inside a bubble for a 0.4 mm gap.

Cooper and Lloyd (1969) estimated the thickness of the liquid layer under a hemispherical bubble growing on a glass wall, from the transient variation of the wall surface temperature. They obtained a correlation equation based on the viscous boundary layer thickness.

Katto and Shoji (1970) studied the wall liquid film formed when an air bubble was blown into a narrow gap between two horizontal circular glass plates (diameter 30 mm, gap 0.5 mm) from the center. The gap between the two plates was filled with liquid (water or ethanol) in advance. They photographed the interference fringes inside the bubble and deduced the gradient of the liquid layer thickness. The gradient was found to be correlated with the capillary number.

Nishikawa et al. (1984) conducted a nucleate boiling experiment with a tilted heated surface. They observed heat transfer enhancement with a downward-facing heated wall in a relatively low heat flux region. They explained their observations with an analytical model in which the liquid film evaporation on the wall was considered. They also measured the thickness of wall liquid layer formed by an air bubble moving along the wall using a conductivity probe. Their measurements indicated film thickness of 40–400 μm for the wall angle 175–120 deg (horizontal downward surface: 180 deg).

Fujita et al. (1988) explained the boiling heat transfer characteristics in narrow spaces taking the liquid film evaporation into account. They measured the liquid film thickness with a method similar to Nishikawa et al., and obtained a thickness of 34 μm for the space height 2 mm and 9 μm for 0.6 mm.

Monde (1990) performed a measurement of liquid film thickness produced by an air bubble rising in a vertical rectangular duct filled with water. His measurement was based on the transient temperature variation of a thin heated material on the wall surface when a bubble passes through the duct. The results ranged from 60 to 80 μm for the duct spacing of 2 mm.

Therefore, two types of correlation have been obtained up to now: one based on the capillary number for the case of slow flow in narrow gaps or small tubes, and another based on viscous boundary layer thickness for the case of extremely rapid phenomena. Although fluid dynamics in narrow gaps have been ordinarily treated considering the viscous and surface tension forces, the effects of acceleration and boundary layer development should also be taken into account for the case of the possibly highly transient vapor bubble growth in narrow gaps. Also, liquid film thicknesses have never been measured in narrow gaps, although Katto and Shoji (1970) measured the gradient of the thickness.

In this work, experiments were conducted to measure the thickness of the thin liquid layer that is formed on the wall when a flattened bubble grows in a superheated liquid in the

[1] Present address: Severe Accident Research Laboratory, Department of Reactor Safety Research, Japan Atomic Energy Research Institute, Tokai-mura, Naka-gun, Ibaraki-ken 319-11, Japan.

Contributed by the Heat Transfer Division for publication in the JOURNAL OF HEAT TRANSFER. Manuscript received by the Heat Transfer Division December 1994; revision received July 1995. Keywords: Boiling, Evaporation, Measurement Techniques. Associate Technical Editor: R. A. Nelson, Jr.

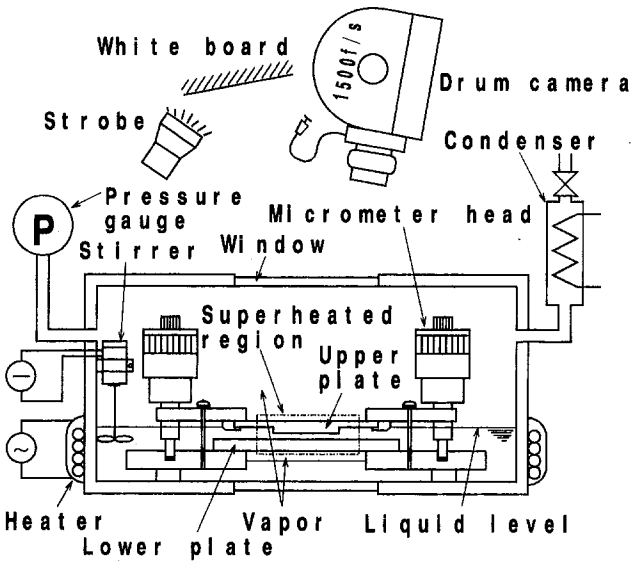

Fig. 1 Schematic diagram of experimental apparatus

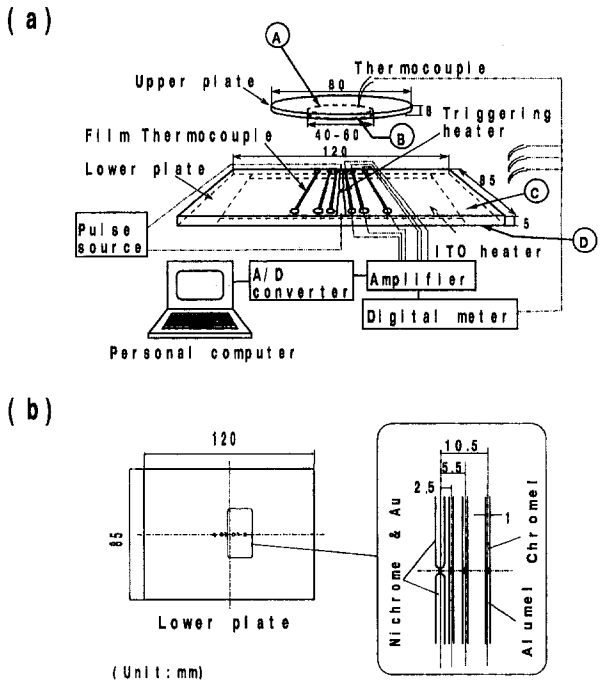

Fig. 2 (*a*) Test section and measurement system; (*b*) bubble initiation heater and vacuum-deposited thermocouples

narrow gap between two parallel glass plates. The liquid film thickness was estimated from the transient temperature variation of the wall surface, based on the assumption that the heat removed from the wall is consumed by the evaporation of the liquid film. Measurements were performed only for the liquid layer on the lower wall because of the expected symmetry and the convenience in the design of the apparatus. The results revealed the existence of two regions: one in which the liquid film thickness was correlated with the viscous boundary layer thickness on the wall, and the other in which it was correlated with the capillary number. The transition threshold between the two regions was given in terms of the Bond number.

2 Experimental Apparatus and Procedure

2.1 Apparatus. A schematic diagram of the experimental apparatus is shown in Fig. 1. The test section is contained in a cylindrical vessel of 200 mm diameter. The vessel is equipped with a heater, stirrer, pressure gage, and a condenser, for the control of system pressure and temperature. R113 was used as the test fluid.

The test section and the measurement system are illustrated in Fig. 2(*a*). The test section consists of two—upper and lower—glass plates. A bubble grows in the narrow gap between the two plates. As shown in Fig. 2(*b*), the lower glass plate is rectangular with a thickness of 5 mm, length of 120 mm, and width of 85 mm. An ITO (indium–tin oxide) layer (0.2 μm thick) is vacuum-deposited on the lower surface of the rectangular plate. On its upper surface, a trigger heater for bubble initiation at the center and chromel-alumel thermocouples for the measurement of transient temperature variation on the wall surface are also vacuum deposited. The thermocouples are positioned at 2.5, 5.5, and 10.5 mm from the center (Fig. 2*b*).

The upper plate is circular and supported by an adjustable frame, so that the gap between the upper and lower plates can be set in the range 0.1–0.4 mm arbitrarily. The lower surface of the upper plate has a central protruded region whose radius is 20 or 30 mm. The thickness of the upper plate is 8 mm at the central protruded region and 5 mm at the peripheral region. The narrow gap in question is formed between this protruded region and the upper surface of the lower plate. The radius of the protruded region, therefore, defines the inertial and viscous constraint on the liquid movement in the narrow gap induced by the bubble growth. Both surfaces of the upper and lower plates are polished to optical precision.

For convenience, let us denote the surfaces of the upper and lower plates as A, B, C, D, from top to bottom (Fig. 2*a*). The lower plate is fixed on a base plate made of stainless steal. The bubble initiation heater on surface C is supplied by a pulse power source, which provides 24 V pulse with a 0.5 ms duration. The signals from the film thermocouples are amplified (gain 1.5×10^4, 10 kHz), A/D converted (12 bit, 1 MHz), and stored in a personal computer.

A chromel-alumel thermocouple (0.02 mm dia.) is epoxied on surface A and five thermocouples are distributed around the test section, to observe the system's attainment of the saturation temperature and the uniform superheat in the test section.

Nomenclature

Bo = Bond number based on the interface acceleration = $\rho d^2 U/\sigma t_g$
Bo_g = Bond number based on gravity = $\rho d^2 g/\sigma$
Ca = capillary number = $\mu U/\sigma$
d = gap width
h_{fg} = latent heat for evaporation
Q = total heat removal for unit area of the wall surface
r = radial position
R = radius of the narrow space (protruded region of the upper plate)
t = time
t_g = time required for arrival of bubble edge at measurement point
T = temperature
U = traveling velocity of the bubble edge
We = Weber number = $\rho U^2 d/\sigma$
ΔT_{sat} = superheat
$\Delta T_{\text{sat},0}$ = initial superheat
δ = initial thickness of the liquid film
δ^* = nondimensional viscous boundary layer thickness = $\sqrt{\nu t_g}/d$
μ = dynamic viscosity
ν = kinematic viscosity
ρ = density
σ = surface tension

Table 1 Experimental conditions

Gap width	d =100, 200, 400μm
Space radius	R =20, 30mm
Thermometer position	r =2.5, 5.5, 10.5mm
Initial super heat	ΔT =1.5, 2.5, 4.5, 6.5, 8.5K
System pressure	1atm
Fluid	R113

The gap width is adjusted utilizing the micrometer built in the upper plate support. The zero point adjustment of the gap width and the parallel setting of the two plates were attained by means of a laser beam with a precision of about 5 μm.

High-speed photographs were taken to visualize the bubble growth and measure the bubble growth velocity. A drum-type camera (1500 frames per second) was used for this purpose. In order to obtain photographs of fine contrast, antireflection coatings (optical duplicated layers) were deposited on both surfaces of the observation window and the upper surface of the upper plate.

Experimental conditions are summarized in Table 1. It should be noted that, in the experimental range, the gravity-based Bond number, $Bo_g = \rho d^2 g/\sigma$, is $10^{-2} \sim 10^{-1}$, which is so small that the effect of gravity on the shape of the bubble edge can be neglected. Therefore, the bubbles should be symmetric with regard to the central plane between the upper and lower wall of the narrow gap.

2.2 Procedure. The experimental procedure is as follows. After the gap width is set and the vessel is closed, the whole system is heated to the saturation temperature (about 47°C at atmospheric pressure). Then the film heater on surface D is activated so that the upper and lower plates and the liquid layer between them are superheated. In this stage, an approximately uniform temperature distribution can be attained in the upper and lower plates as well as the liquid in the gap between them. This is because the liquid below the lower plate (adjacent to surface D) evaporates and forms several millimeters of vapor layer, which works as a thermal insulator.

After it is confirmed that all the thermocouples on surfaces A and C indicate the same prescribed superheat temperature within 0.2 K, the film heater is switched off and the pulse source is activated. It generates a trigger signal for the A/D converter to start the measurement of the temperature on surface C. Simultaneously, it provides the current for the triggering heater. Then a bubble nucleates on the triggering heater and starts to grow in the superheated liquid in the gap.

The obtained transient temperature data are used for the heat conduction analysis in the glass wall, and the initial liquid film thickness is calculated from the total heat removed from the wall. This process will be explained further in section 3.2.

2.3 Experimental Errors. The trigger heater has about 0.1 mm^2 of heating area and 1.5×10^{-4} J of total heat generation. This is so small compared with the total heat removed from the wall during bubble growth (by evaporation) that its influence on the measurement is negligible.

Although the test section experiences about a 25 K temperature change after the gap adjustment is done at room temperature with the vessel open until the system reaches saturation temperature, the gap width variation owing to thermal expansion is estimated to be about 5 μm. This is on the same order as the setting error. Therefore, the thermal expansion error was neglected.

Possible sources of error in the measurement of the liquid film thickness are (1) a time delay in the temperature signal due to the thermal diffusion in the film thermocouples, (2) a high-frequency noise, which has an amplitude of 3–10 percent of the temperature signal, (3) a low-frequency noise of the same extent (due to 50 Hz AC power supply), (4) an error due to the thermal capacity of the film thermocouples, etc. In these items, the time delay due to thermal diffusion is estimated to be on the order of 10^{-4} s and considered not significant. The high-frequency noise is removed in the integration process of the heat conduction equation and does not affect the calculated liquid film thickness. However, the low-frequency noise can cause serious problems because it has a similar frequency and amplitude to that of the temperature change signal in question. This problem was resolved by digitally processing the temperature signal to remove the 50 Hz sinusoidal wave component. The thermal capacity of the film thermocouples is approximately 3 percent compared to the latent heat of a liquid film of 1 μm, for a typical temperature change of 5 K. This is regarded as negligible.

It is difficult to estimate the final error in the liquid film thickness from the law of error propagation because of a rather complicated data reduction process including a numerical integration. The most reasonable method of error estimation is through statistical considerations. For the estimation of reliability, experiments were performed three or more times and the standard deviation of the resulting liquid film thickness was calculated for each set of conditions. The averaged relative standard deviation for all the sets of conditions was found to be 13 percent.

3 Results and Discussion

3.1 Visualization of the Bubble Growth. Figure 3 shows one of the typical high-speed photographs obtained in the case where the gap d = 0.2 mm, the upper glass plate radius R = 30 mm, and the initial superheat $\Delta T_{sat,0}$ = 6.5 K. The time interval between each frame is Δt = 0.655 ms. In the frames from 0.955 ms to 6.235 ms, a growing circular bubble appears.

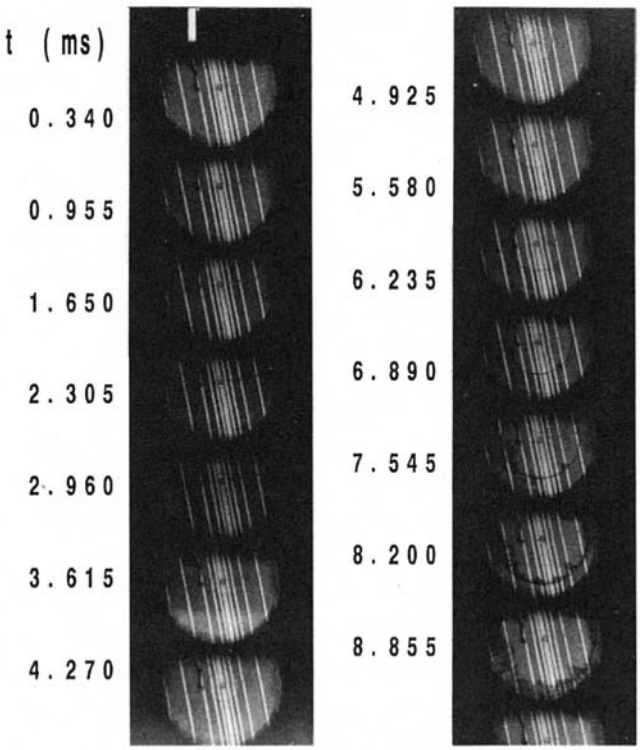

Fig. 3 High-speed photograph of the bubble growth (d = 0.2 mm, R = 30 mm, $\Delta T_{sat,0}$ = 6.5 K, Δt = 0.655 ms/frame: RUN-259)

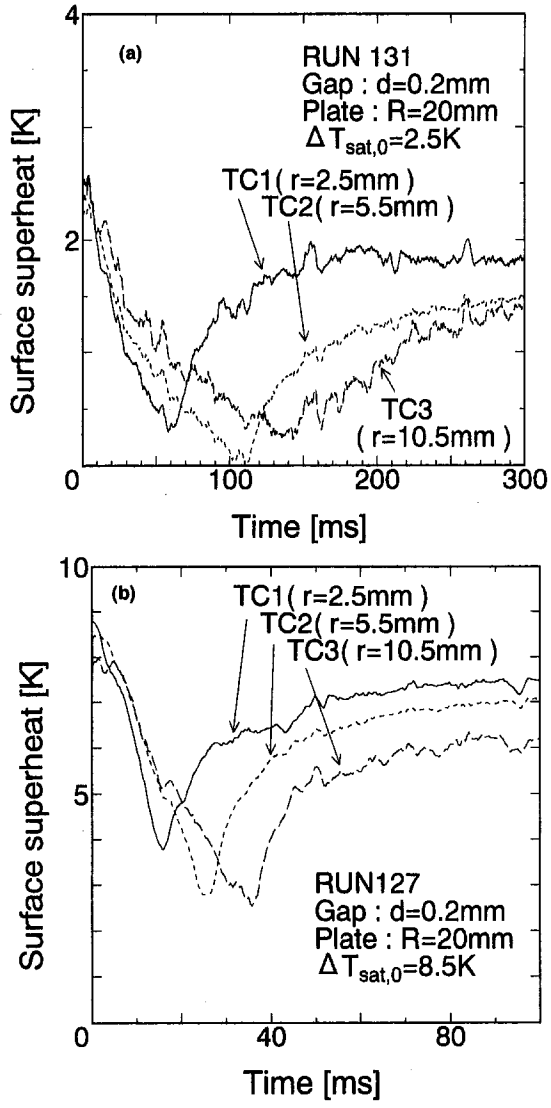

Fig. 4 Transient variation of the wall surface temperature: (*a*) $\Delta T_{sat,0}$ = 2.5 K, (*b*) $\Delta T_{sat,0}$ = 8.5 K

After the tenth frame, the circular bubble contour becomes unstable, and a ragged contour appears to grow further.

It should be noted that the liquid layer thickness discussed in this work is restricted to that in the region swept by the smooth contour. The measured film thickness in the region swept by ragged contours always revealed extensive scattering. This is probably because the fine structure of the ragged contours caused roughened liquid layers with thickness distribution finer than the spatial resolution of the thermocouples.

The velocities of the moving bubble edges were measured from the photographs, which provided primary information for a discussion of the mechanisms (Section 3.3).

3.2 Deduction of the Initial Liquid Film Thickness From the Wall Temperature Variation. Examples of transient temperature changes on the wall surface measured by the film thermocouples are shown in Fig. 4(*a*, *b*). The origin of the time axis is set at the time when the bubble initiation heater is triggered. The ordinate indicates the wall superheat relative to the system saturation temperature. The difference between Figs. 4(*a*) and 4(*b*) is in the initial superheat condition.

The wall surface temperature starts to fall several milliseconds after the bubble is initiated, reaches a minimum value, then increases and asymptotically approaches a final value, which is slightly lower than the initial superheat. The start of the wall temperature decrease is considered to coincide with the liquid film formation at the thermocouple position, and simultaneous beginning of the evaporation. Attainment of the minimum surface temperature and subsequent rapid temperature recovery imply that the liquid film has disappeared at the measurement point. Therefore, the period during which the wall temperature is decreasing is considered to be the period during which the liquid film is evaporating and being consumed.

If we assume that the liquid film is thin enough compared with the gap width, and that the effects of the flow and the sensible heat in the liquid film on the temperature change at the wall surface are negligible, the heat removed from the wall surface is the same as the heat required for the liquid film evaporation during the wall temperature decrease, i.e., the latent heat that corresponds to the initial thickness of the liquid film.

$$Q = \delta \rho h_{fg} \tag{1}$$

The amount of heat removal from the wall Q can be calculated by numerical heat conduction analysis in the wall using the measured surface temperature as the boundary condition. Hence, we can obtain the initial thickness of the liquid film, δ.

It may be worth noting that the time during which the bubble grows is typically several milliseconds, which is much shorter than the period of liquid film evaporation, say, tens or hundreds of milliseconds. Therefore, it is regarded that the liquid film is hydrodynamically formed very quickly and then evaporated over a fairly long period. The liquid film thickness measured is the thickness just after the liquid film is hydrodynamically formed.

The numerical calculation of the heat conduction equation was performed using the finite difference method with a one-dimensional (along with the vertical axis) mesh system, which simulated a 0.5-mm-deep region from the wall surface. This is considered deep compared with the thermal boundary layer, which develops in the period of interest. The number of elements in the mesh was 150, and the mesh was graded finer near the surface where a steep temperature gradient was expected. The initial condition for each case was given by the uniform superheated temperature in the corresponding experiment.

Rigorously, the thermal field that develops in the wall is not one dimensional. In particular, a significant two-dimensional effect is expected near the dryout front of the liquid film. However, the horizontal component of the heat flux through the wall surface is approximately canceled over the integration in terms of time.

The deduced initial thicknesses of the liquid film are shown in Figs. 5(*a–c*). The data in Figs. 5(*a*) and 5(*b*) are obtained at r = 2.5 mm and r = 5.5 mm from the center, respectively. It is found that the liquid film thickness has a maximum value, and that such behavior is more significant when the gap width is larger.

Cooper and Lloyd's (1969) correlation for the liquid film thickness based on the viscous boundary layer (Fig. 6*a*) has a decreasing trend in regard to the bubble growth velocity. In contrast, the model based on the capillary number (e.g., Taylor (1961), Fig. 6*b*) has an increasing trend. Intuitively, the surface tension effect in a narrow gap seems to make the liquid film thickness increase when the traveling velocity of the bubble contour becomes faster. The reason for the peaks in the present data is that the experimental conditions extend over both the two regions: one in which the liquid film thickness is controlled by the viscous boundary layer on the wall, and the other by the capillary number or other surface tension effects.

Figure 5(*c*) compares the case of different plate radii R = 20 and 30 mm. Although the plate radius should affect the viscous and inertial constraint on the bubble growth, the difference examined experimentally did not have a significant effect on the liquid film thickness.

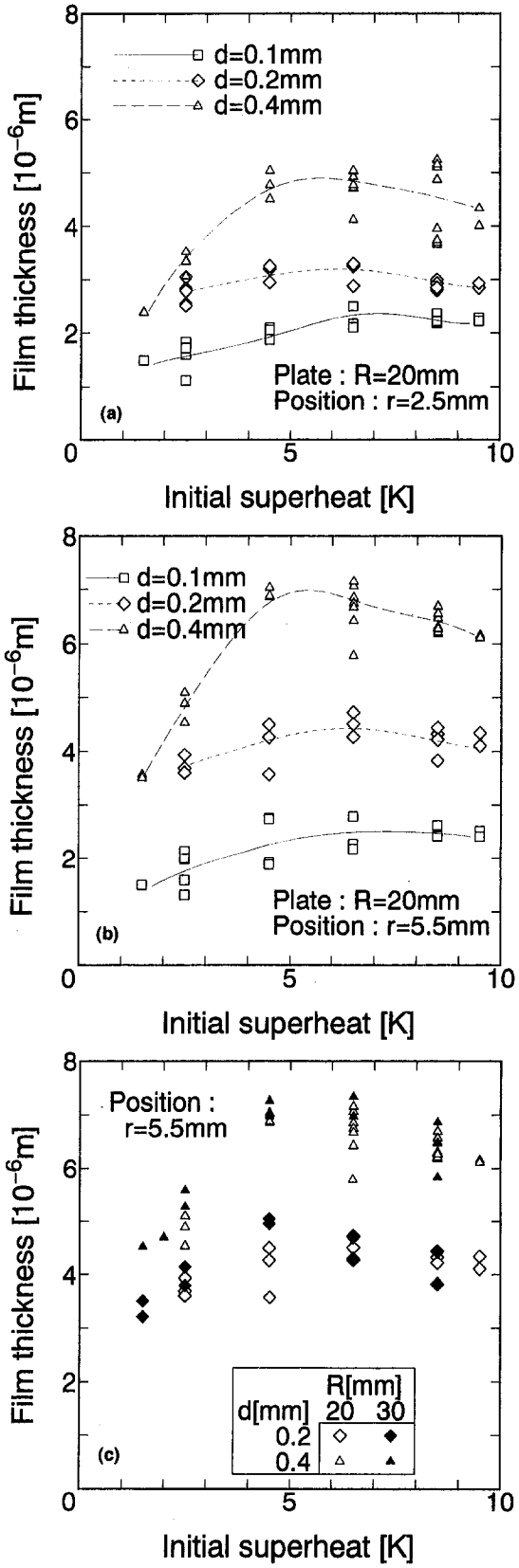

Fig. 5 Initial thickness of the liquid film: (*a*) R = 20 mm, r = 2.5 mm, (*b*) R = 20 mm, r = 5.5 mm, (*c*) effect of R (r = 5.5 mm)

3.3 Correlation of the Liquid Film Thickness Based on the Mechanisms. The traveling velocity of the bubble contour (i.e., the bubble growth velocity) is believed to play an important role in controlling the flow characteristics near the bubble contour where the liquid film is produced. Taking this point of view, we measured the bubble growth velocity using high-speed photography, and various nondimensional parameters derived from it were examined to correlate the liquid film thickness.

Some examples of the bubble growth data obtained from high-speed photographs are shown in Fig. 7. The bubble radius is approximately proportional to the square of the time during most of the bubble growth period. Such behavior was also observed by Katto and Yokoya (1966).

A surface instability phenomenon was often observed, as shown in Fig. 3. In such cases, the radii of envelopes of ragged bubble contours are plotted with filled symbols in Fig. 7 for the data after the bubble contour became unstable. These data smoothly continue from the data before the occurrence of the surface instability, and no drastic change of the trend at the transition point is found. This fact indicates that the surface area in the bubble contour was negligible compared with the area of the wall liquid film, so that the vapor required to expand the bubble was mostly supplied from the wall liquid film.

The relationship between the interface traveling velocity and the initial superheat is shown in Fig. 8. The interface traveling velocity at each thermocouple position (denoted as TC1-3 in Fig. 7) was obtained by linear fitting three or four data points around the measuring position. A narrower gap caused faster growth of the bubble. Usually it is considered that the hydrodynamics in very narrow channels can be treated as viscous and, in some cases, surface tension-driven flow. But the present experimental results reveal that the usual consideration is not sustained when a thermal effect (e.g., evaporation) is coupled.

Two figures, 5(*b*) and 8, in which the liquid film thickness and the interface traveling velocity are plotted with respect to the initial superheat, are derived from the same set of data. However, Fig. 5(*b*) shows that the liquid film thickness has a maximum variation with initial superheat, while Fig. 8 shows that the interface traveling velocity monotonically increases. This fact indicates that a transition in the controlling mechanism occurred within the range of experimental conditions.

Dependence of the liquid film thickness on several nondimensional parameters is shown in Figs. 9–11. In Figs. 9 and 10, symbols represent various combinations of geometric parameters such as the gap width, plate radius, and the measuring position. First, we examined the dependence on the thickness of the viscous boundary layer developed until the arrival of the bubble edge at a certain position, which was observed by Cooper and Lloyd (1969) for the case of hemispherical bubbles growing on a wall. In Fig. 9, the abscissa is the viscous boundary layer thickness normalized with the gap width

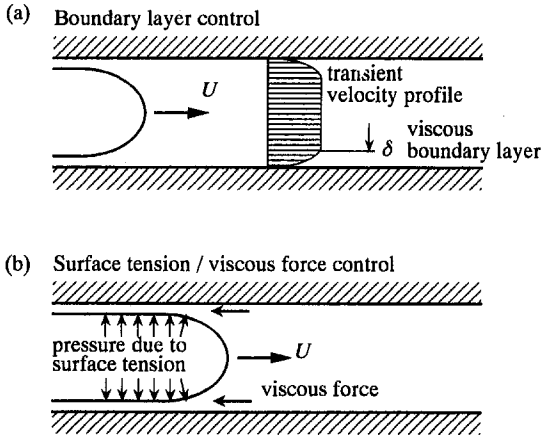

Fig. 6 Two concepts of the physics controlling the liquid film thickness

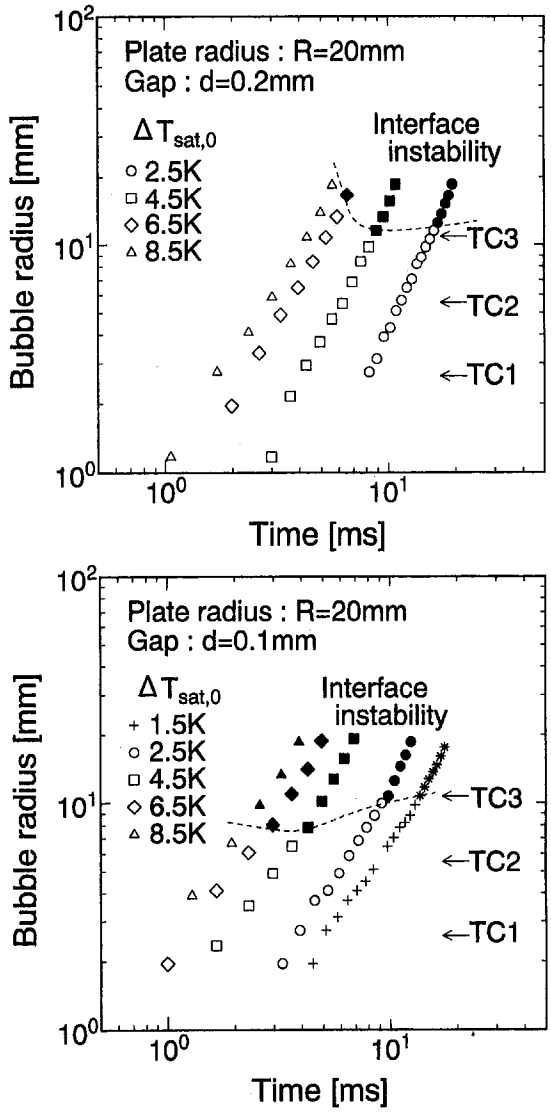

Fig. 7 Growth of bubble radius from high-speed photography

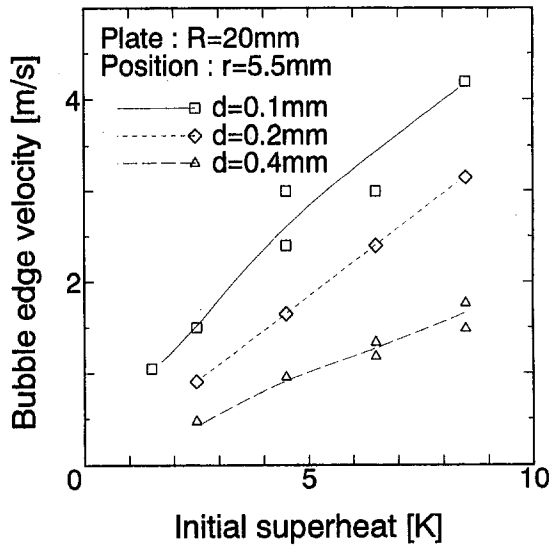

Fig. 8 Interface traveling velocity versus initial superheat (R = 20 mm, r = 5.5 mm)

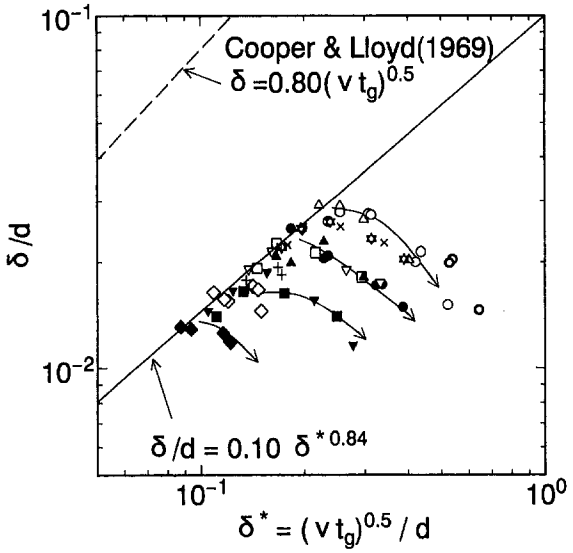

Key	R[mm]	d [mm]	r [mm]
●	20	0.1	2.5
○			5.5
⊙			10.5
■		0.2	2.5
□			5.5
×			10.5
◆		0.4	2.5
◇			5.5
+			10.5
▲	30	0.1	2.5
△			5.5
▼		0.2	2.5
▽			5.5
✡			10.5

Fig. 9 Dependence of the liquid film thickness on the viscous boundary layer thickness

$$\delta^* = \frac{\sqrt{\nu t_g}}{d}, \tag{2}$$

where t_g is the time required for the bubble edge to reach the measuring point from the bubble initiation. All the data are distributed to the right of a diagonal line described by the following equation:

$$\frac{\delta}{d} = 0.10(\delta^*)^{0.84}, \tag{3}$$

and a fairly large number of the data are found on the line. The data points that are scattered below the solid line form several arrays (arrows) with decreasing gradient for each set of the geometric parameters.

This figure can be interpreted as follows. The data on the line correspond to the condition where the liquid film thickness is controlled by the viscous boundary layer thickness. In other words, the viscous boundary layer is thin enough so that it predominantly determines the thickness of the liquid layer remaining on the wall, and the surface tension effect is excluded. When the process of the liquid film formation becomes slower, the boundary layer becomes thicker and the liquid film thickness subjects to surface tension effects which make the film thinner than that determined by the viscous boundary layer. The broken line drawn in the figure indicates Cooper and Lloyd's (1969) experimental correlation, which shows a similar gradient to the

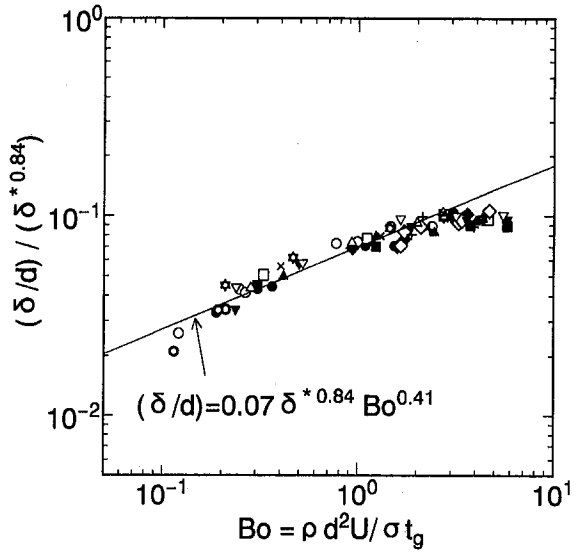

Fig. 10 Dependence of the liquid film thickness on the Bond number (key as in Fig. 9)

edge line of our data, although the absolute value is about five times larger.

In the next step, in order to examine the data scattered to the right side of the diagonal line, all the data were renormalized by dividing with $(\delta^*)^{0.84}$ and plotted again with various nondimensional parameters including capillary number ($Ca = \mu U/\sigma$), Weber number ($We = \rho U^2 d/\sigma$), and the Bond number based on the interface acceleration ($Bo = \rho d^2 \dot{U}/\sigma$). These parameters represent, respectively, the ratios of the viscous force to the surface tension force, the inertial force due to spatial velocity variation to the surface tension force, and the inertial force due to acceleration to the surface tension force.

The Bond number includes a time derivative of the interface velocity, i.e., the second derivative of the bubble radius with time. It is possible to evaluate it directly from the bubble growth data (Fig. 7), but the fluctuation due to experimental uncertainty causes significant errors in the values of the second derivatives. We overcame this problem by utilizing the fact that the bubble radius is approximately proportional to the square of the time, from which the time derivative of the interface velocity $\dot{U}$ can be replaced by U/t_g. Hence, the Bond number was redefined as $Bo = \rho d^2 U/\sigma t_g$.

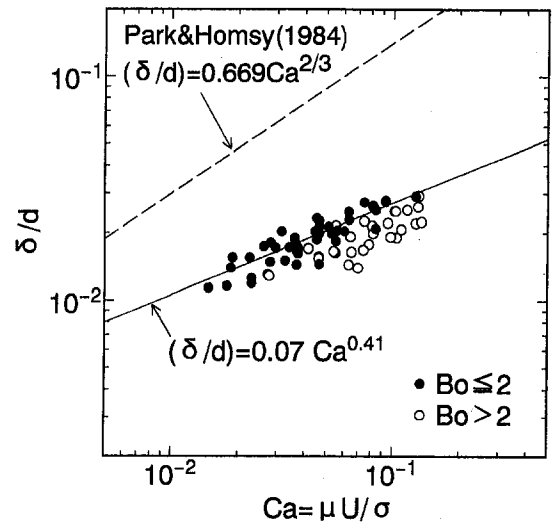

Fig. 11 Correlation of the liquid film thickness with the capillary number

It was found that the renormalized data were best correlated with the Bond number, which is shown in Fig. 10. For $Bo > 2$, no dependence on the Bond number is seen. This region consists of the data on the edge line in Fig. 9, which corresponds to the condition where the liquid film thickness is defined by the viscous boundary layer thickness. On the other hand, for $Bo \leq 2$, the dependence on the Bond number is described by the power of 0.41. In this region, the liquid film thickness is given by the following equation,

$$\frac{\delta}{d} = 0.07(\delta^*)^{0.84}\mathrm{Bo}^{0.41}. \tag{4}$$

Closer examination of Eq. (4) shows that the product of the two nondimensional parameters with their exponents can be reduced and expressed in terms of the capillary number:

$$(\delta^*)^{0.84}\mathrm{Bo}^{0.41} = \left(\frac{\nu^{0.5}t_g^{0.5}}{d}\right)^{0.84}\left(\frac{\rho d^2 U}{\sigma t_g}\right)^{0.41}$$

$$= \left(\frac{\mu^{0.42}U^{0.41}}{\sigma^{0.41}}\right)\left(\frac{t_g^{0.01}}{\rho^{0.01}d^{0.02}}\right) \simeq Ca^{0.41} \tag{5}$$

Consequently,

$$\frac{\delta}{d} = 0.07Ca^{0.41}. \tag{6}$$

The relationship of the nondimensional liquid film thickness and the capillary number is shown in Fig. 11. The data for $Bo \leq 2$ are plotted with filled symbols, which are distributed near the solid line described by Eq. (6). The other data plotted with empty symbols deviate from the line. The broken line in Fig. 11 represents Park and Homsy's (1984) theoretical correlation for $Ca \sim 0$, which gives a slightly larger gradient compared with the present correlation. According to Taylor's (1961) experiment, which dealt with liquid films in small circular tubes for a wide range of capillary number ($0.01 < Ca < 2.0$), the exponent of the capillary number decreases when the capillary number increases. Such a qualitative trend would be sustained in the present case, and the present experimental condition is considered to be in a higher range of Ca where Park and Homsy's (1984) theoretical correlation does not hold.

The experimental results are summarized as follows. When the acceleration of the bubble interface, which is represented by the Bond number, is small, the liquid film thickness is controlled by the capillary number (Eq. (6)). In contrast, when the interface acceleration is large, the liquid film thickness is controlled by the viscous boundary layer (Eq. (3)). The threshold of the two regions is given by the Bond number as $Bo = 2$.

4 Conclusion

Experiments were performed to measure the thickness of the liquid film formed on the wall surface when a flattened bubble grew in a narrow gap between two parallel glass plates. The measurement of the liquid film thickness was elaborated with transient temperature measurement on the wall surface by film thermocouples and numerical analysis of the heat conduction in the wall. Dependence of the liquid film thickness on several parameters, which were deduced from the bubble growth velocity measured by high-speed photography, was examined and it was clarified that there were two regions depending on the Bond number. The liquid film thickness was controlled by the viscous boundary layer or the capillary number according to whether the Bond number was greater or smaller than 2. This result is summarized by the following correlations:

$$\frac{\delta}{d} = \begin{cases} 0.10(\delta^*)^{0.84}, & (\mathrm{Bo} > 2) \\ 0.07\ Ca^{0.41}, & (\mathrm{Bo} \leq 2) \end{cases}$$

The present work is the first to provide experimental results that bridge the two physical regions of the liquid film formation.

Acknowledgments

This work was financially supported by the Research Fellowships of the Japan Society for the Promotion of Science for Young Scientists, 1992.

References

Bretherton, F. P., 1961, "The Motion of Long Bubbles in Tubes," *J. Fluid Mech.*, Vol. 10, p. 166.

Cooper, M. G., and Lloyd, A. J. P., 1969, "The Microlayer in Nucleate Pool Boiling," *Int. J. Heat Mass Transfer*, Vol. 12, p. 895.

Fujita, Y., Uchida, S., and Nishikawa, K., 1988, "Nucleate Boiling Heat Transfer and Critical Heat Flux in Narrow Space Between Rectangular Surfaces," *Int. J. Heat Mass Transfer*, Vol. 31, p. 229.

Katto, Y., and Yokoya, S., 1966, "Experimental Study of Nucleate Pool Boiling in Case of Making Interference-Plate Approach to the Heating Surface," *Proc. 3rd Int. Heat Transfer Conference*, Vol. 3, p. 219.

Katto, Y., and Shoji, M., 1970, "Principal Mechanism of Micro-Liquid-Layer Formation on a Solid Surface With a Growing Bubble in Nucleate Boiling," *Int. J. Heat Mass Transfer*, Vol. 13, p. 1299.

Monde, M., 1990, "Measurement of Liquid Film Thickness During Passage of Bubbles in a Vertical Rectangular Channel," ASME JOURNAL OF HEAT TRANSFER, Vol. 112, p. 255.

Nishikawa, K., Fujita, Y., Uchida, S., and Ohta, H., 1984, "Effect of Surface Configuration on Nucleate Boiling Heat Transfer," *Int. J. Heat Mass Transfer*, Vol. 27, p. 1559.

Park, C.-W., and Homsy, G. M., 1984, "Two-Phase Displacement in Hele-Shaw Cells: Theory," *J. Fluid Mech.*, Vol. 139, p. 291.

Taylor, G. I., 1961, "Deposition of a Viscous Fluid on the Wall of a Tube," *J. Fluid Mech.*, Vol. 10, p. 161.

Theoretical and Experimental Studies on the Pseudo-Dropwise Condensation of a Binary Vapor Mixture

K. Hijikata

Y. Fukasaku

O. Nakabeppu

Department of Mechano-Aerospace Engineering,
Tokyo Institute of Technology,
Meguro-ku, Tokyo 152 Japan

When a water–ethanol binary mixture condenses on a flat plate, one observes that the liquid film condensate rises locally and eventually forms many droplets on the film. Usually, filmwise condensation is expected because both substances are completely soluble in each other and they wet a copper plate well. This paper presents the droplet growth mechanism during so-called pseudo-dropwise condensation. Instability analysis is used to determine the transition from filmwise condensation to pseudo-dropwise condensation theoretically. In a stress balance at the vapor–liquid interface, the analysis considers not only the surface tension itself, but also the surface tension variation due to changes in temperature and concentration, assuming saturation conditions at the interface. Numerical results indicate that the Marangoni effect plays a more important role than the absolute value of the surface tension in pseudo-dropwise condensation. The change in surface tension with temperature is not always negative; it becomes positive for certain mixtures due to the dependence on concentration. Pseudo-dropwise condensation is only realized when surface tension increases with temperature. This analysis qualitatively predicts the critical Marangoni number experimentally observed during water–ethanol mixture condensation.

Introduction

Mixed-refrigerant condensation has been investigated for two purposes. The first is heat transfer enhancement for power generation cycles, refrigeration cycles, etc. The second is to obtain a high-performance mixed refrigerant as an alternative to CFCs for environmental reasons.

For these reasons we have investigated condensation heat transfer of vapor mixtures, especially binary vapor mixtures (Hijikata and Himeno, 1990). Through experimental investigations we found that some binary vapor mixtures form droplets or streaks in the condensation film even at a temperature difference where each pure vapor exhibits filmwise condensation. Although there is a study aimed at heat transfer enhancement by forming droplets in condensate film using an immiscible refrigerant combination (Hayashi et al., 1992), we focused on dropwise condensation of soluble refrigerant combinations. When a water–ethanol binary mixture condenses on a flat plate, one observes that the liquid condensate film rises locally and eventually forms many droplets on the film. In this paper such a condensation process is called *pseudo-dropwise condensation.*

A few experimental studies have reported pseudo-dropwise condensation phenomena (Mirkovich and Missen, 1961; Fujii et al., 1989), but no one has explained this phenomenon theoretically. We investigated experimentally the droplet formation mechanism during pseudo-dropwise condensation through microscopic observations of water–ethanol vapor mixture condensation on a horizontal plate. The condensation process was also investigated analytically using a perturbation method applied to the condensate film. It has been found that surface tension plays an important role in the droplet growth process, and dimensionless wavelength is estimated with reasonable accuracy. In addition to the droplet formation, heat transfer during pseudo-dropwise condensation on a horizontal plate has been studied and the theory has been found to agree well with experiments.

Contributed by the Heat Transfer Division for publication in the JOURNAL OF HEAT TRANSFER. Manuscript received by the Heat Transfer Division May 1995; revision received October 1995. Keywords: Condensation, Flow Instability. Associate Technical Editor: V. K. Dhir.

Experimental Apparatus

The condensation mechanism of a water–ethanol binary vapor mixture on a horizontal surface was investigated with the experimental apparatus shown in Fig. 1. The binary vapor mixture is generated with a boiler containing a suitable ratio of the two liquids. The vapor moves to the condenser section and condenses on the horizontal copper cooling wall. The cooling surface was polished with emery paper followed by polishing with a ø1.0 μm alumina particle emulsion. Thermocouples were placed on the centerline of a copper column, and the heat flux is determined from the temperature gradient. The condensing surface is viewed through a window by a CCD camera connected to a microscope. Continuous images of the condensate film are taken by an S-VHS video tape recorder and then transferred to a PC to analyze the drop formation behavior.

If the cooling surface is positioned vertically, steady condensation is observed, but droplets flow down due to gravity, which makes the process complicated. To simplify the experimental measurement, a horizontal surface is used. Since no mechanism exists for removing the condensate from a horizontal plate, the surface is periodically wiped to remove the condensate.

Observation of Dropwise Condensation

Figure 2 shows the transition of a condensate film in a water–ethanol binary system. The concentration of ethanol vapor is 25 mol%, the temperature difference between bulk vapor and the cooling wall is 11.0 K, the total vapor pressure is about 135 mmHg, and the wiping frequency is 1.38 Hz. These pictures show the time sequence of the condensed film change after a rotating wiper renewed the surface. The wiping direction in all pictures is from right to left. The time below each picture is measured from the moment when the sweeper passes the field of vision. Only a small portion of the surface is shown in the

pictures, but condensation on the whole surface was observed to be uniform, except near the edge of the copper cylinder.

Immediately after wiping, the condensate film looks flat. Then, in Fig. 2(*a*) the surface of the film becomes slightly uneven; these features become clearer in Fig. 2(*b*). Black and white regions are valleys and hills, respectively, in the film. In Fig. 2(*c*) the altitude of the valleys and the hills becomes large and it seems that the craterlike valleys are arranged in a honeycomb shape. In the lower-right portion of Figs. 2(*c*) and 2(*d*), the crater break-up is imminent and the condensation mode is changing to dropwise. Because the wiper was moved from the right to left, the progress on the right side is more advanced than on the left. In Fig. 2(*e*), many droplets have spread on the entire area of the condensate film, and are growing by coalescence. Between the droplets the film rises slightly, as shown by the small hills in Fig. 2(*f*). This state remains until the condensate is wiped again. These features of drop formation were perfectly periodic and observed repeatedly. It was also observed that drop formation began at the same point where a small scratch exists every time. Because the unevenness of the wall surface gives a strong perturbation to the film, the growth of unsteady waves always started from such points.

For comparison, ordinary dropwise condensation for pure water vapor is shown in Fig. 3. The size of the droplets is about one order of magnitude smaller than that of the water–ethanol binary mixture. For binary vapor condensation, the droplets are floating on the base liquid film, but for the water vapor condensation, they lie directly on the solid surface and do not move frequently. The comparison shows that the droplet formation mechanisms during the two condensation processes are fundamentally different between pure vapor and the binary vapor.

Experiments were also carried out by changing the inclination angle of the condensing surface and the same pseudo-dropwise condensation was observed as when the sweeper was used. This indicates that flow of liquid condensate is not essential in the droplet formation mechanism.

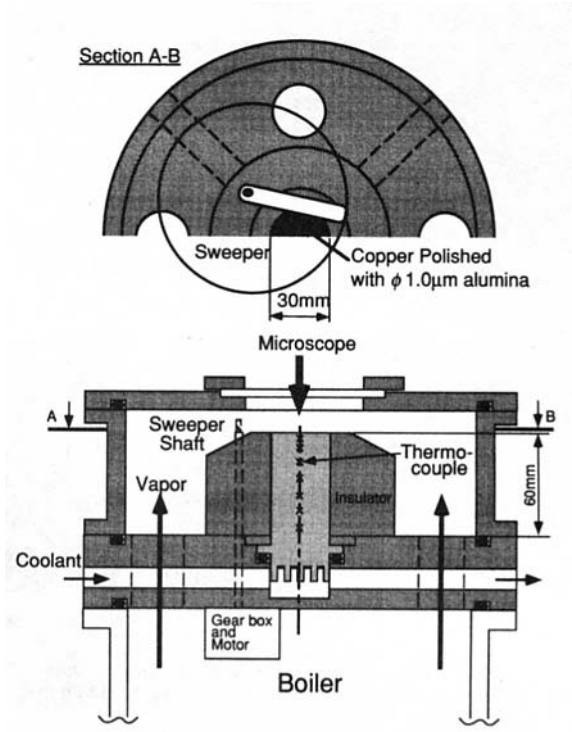

Fig. 1 Experimental apparatus

Theoretical Study

By observing the condensed liquid film, it is found that many droplets grow from small disturbances on the smooth condensate film, therefore a theoretical analysis using perturbation theory was conducted. The physical model is shown in Fig. 4. The model assumes that a binary vapor mixture of miscible liquids condenses on a infinite horizontal liquid film, whose thickness H is constant. Moreover, the analysis assumes that the velocity of the liquid film is zero, the concentration in the liquid is constant, and the temperature profile is linear due to the latent heat released by the condensation. In the analysis, the diffusion resistance in the vapor phase is assumed to be the appropriate mass transfer coefficient at the vapor–liquid interface. Under these conditions, a two-dimensional perturbation problem was solved because the two-dimensional perturbation analysis gives the same result as a three-dimensional analysis in so far as the unstable wavelength is concerned. In the analysis, the two-dimensional ordinary fundamental equations for the Newtonian fluid are used and the boundary conditions, especially at the liquid–vapor interface, play an important role.

Fundamental Equations. The following fundamental equations are used in this analysis without any simplification used in the boundary layer theory or in an analysis of thin fluid layer flow. No terms in the equations are neglected until the equations are linearized by assuming all variables are composed of basic value and perturbed value.

Continuity equation:

$$\frac{\partial u}{\partial x} + \frac{\partial v}{\partial y} = 0 \tag{1}$$

Nomenclature

c = concentration
C = integration constant
D = mass diffusivity, m^2/s
f = wiping frequency, Hz
g = gravitational acceleration, m/s^2
Ga = Galileo number
H = initial condensate film thickness, m
h = amplitude of periodic disturbance at film surface, m
h_m = mass transfer coefficient, kg/m^2 s
k = wave number, m^{-1}
K = dimensionless surface tension
L = latent heat, J/kg
Ma = Marangoni number
P = pressure, Pa
Pr = Prandtl number
Sc = Schmidt number
Sh = Sherwood number
t = time, s
T = temperature, K
u = velocity in x direction, m/s
v = velocity in y direction, m/s
x = coordinate parallel to wall, m
y = coordinate vertical to wall, m
α = proportional constant in Eq. (5), K
δ = liquid film thickness, m
κ = thermal diffusivity, m^2/s
λ = thermal conductivity, W/m·K
μ = viscosity, Pa·s
ν = kinetic viscosity, m^2/s
ρ = density, kg/m^3
σ = surface tension, N/m
ω = perturbation growth rate, s^{-1}

Subscript

0 = basic part of variable
1 = perturbed part of variable
g = vapor phase
i = interface
l = liquid phase
PD = phase diagram
s = saturation
w = cooling wall
∞ = bulk

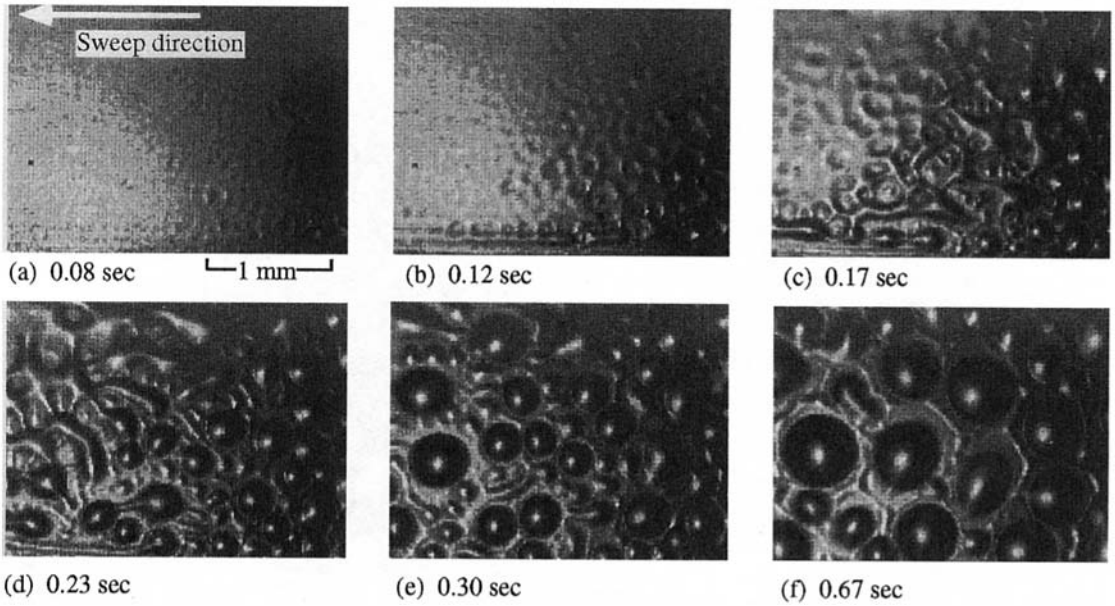

Fig. 2 Droplet formation in a condensed liquid film of a water–ethanol mixture for ethanol concentration in vapor phase, $C_{g,et.}$ = 25 mol%, wall subcool, $\Delta T = T_{sat} - T_{wall}$ = 11.0 K, total pressure, P = 135 mm Hg, and wiping frequency, f = 1.38 Hz

Momentum equations:

$$\frac{\partial u}{\partial t} + u\frac{\partial u}{\partial x} + v\frac{\partial u}{\partial y} = -\frac{1}{\rho}\frac{\partial P}{\partial x} + \nu\left(\frac{\partial^2 u}{\partial x^2} + \frac{\partial^2 u}{\partial y^2}\right) \quad (2)$$

$$\frac{\partial v}{\partial t} + u\frac{\partial v}{\partial x} + v\frac{\partial v}{\partial y} = -\frac{1}{\rho}\frac{\partial P}{\partial y} + \nu\left(\frac{\partial^2 v}{\partial x^2} + \frac{\partial^2 v}{\partial y^2}\right) - g \quad (3)$$

Energy equation:

$$\frac{\partial T}{\partial t} + u\frac{\partial T}{\partial x} + v\frac{\partial T}{\partial y} = \kappa\left(\frac{\partial^2 T}{\partial x^2} + \frac{\partial^2 T}{\partial y^2}\right) \quad (4)$$

Mass transport equation:

$$\frac{\partial c}{\partial t} + u\frac{\partial c}{\partial x} + v\frac{\partial c}{\partial y} = D\left(\frac{\partial^2 c}{\partial x^2} + \frac{\partial^2 c}{\partial y^2}\right) \quad (5)$$

Boundary Conditions. The boundary conditions are assumed as follows:

At $y = 0$ (cooling wall)

$$u = v = 0, \quad T = T_w, \quad \frac{\partial c}{\partial y} = 0 \quad (6)$$

At $y = H + h$ (vapor–liquid interface)

tangential stress balance:

$$\mu\left(\frac{\partial u}{\partial y} + \frac{\partial v}{\partial x}\right) = \frac{\partial \sigma}{\partial c}\frac{\partial c_i}{\partial x} + \frac{\partial \sigma}{\partial T}\frac{\partial T_i}{\partial x} \quad (7)$$

normal stress balance:

$$-P + 2\mu\frac{\partial v}{\partial y} = \sigma\frac{\partial^2 h}{\partial x^2} \quad (8)$$

energy balance:

$$-\lambda\frac{\partial T}{\partial y} = L \cdot h_m \cdot (c_{g\infty} - c_{gi}) = \frac{L \cdot h_m}{\alpha_g}(T_\infty - T_i) \quad (9)$$

phase equilibrium:

$$T_i = T_s + \alpha_g c_{gi}, \quad T_i = T_s + \alpha_l c_{li} \quad (10)$$

The tangential stress is generated by the surface tension change along the surface because it is a function of the concentration and the temperature. The pressure at the interface is balanced against the surface force caused by the curvature. It is assumed that heat flux at the interface is proportional to the mass transfer via diffusion in the vapor phase, which is proportional to the concentration difference between the bulk and the interface ($c_{g\infty} - c_{gi}$). The L and h_m in Eq. (9) stand for the latent heat of condensation and the mass transfer coefficient, respectively. Moreover, phase equilibrium is assumed at the interface. The condensation curve and vaporization curve in the phase diagram are assumed to be linear and expressed by Eq. (10). That is, the condensation and evaporation temperatures are linearly proportional to the concentration in the vapor and the liquid phase, thus the heat flux at the interface is expressed to be also proportional to temperature drop ($T_\infty - T_i$), as shown in Eq. (9).

Nondimensionalization. Nondimensionalization by the film thickness H, characteristic velocity ν/H, characteristic time H^2/ν, and the temperature difference $\Delta T = T_i - T_w$ gives the following dimensionless parameters:

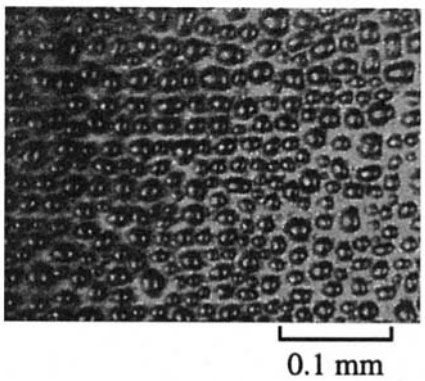

Fig. 3 Droplets of pure water condensation for ΔT = 12.8 K, P = 135 mm Hg, f = 1.82 Hz, and elapsed time = 0.47 s

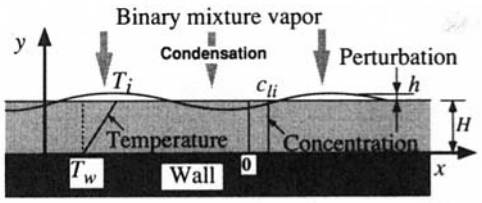

Fig. 4 Schematic diagram of condensing field

$$\mathrm{Pr} = \frac{\nu}{\kappa}, \quad \mathrm{Sc} = \frac{\nu}{D}, \quad \mathrm{Ga} = \frac{H^3 g}{\nu^2}, \quad \mathrm{Sh} = \frac{Lh_m H}{\alpha_g \lambda}$$

$$\mathrm{Ma} = \left(\frac{\partial \sigma}{\partial c}\frac{1}{\alpha_l} + \frac{\partial \sigma}{\partial T}\right)\frac{(T_\infty - T_i)\cdot H}{\kappa \mu}, \quad K = \frac{\sigma H}{\rho \nu^2} \quad (11)$$

where Pr, Sc, and Ga are Prandtl number, Schmidt number, and Galileo number, respectively. Also, Sh is the modified Sherwood number, which is the dimensionless mass transfer coefficient of the vapor phase, and Ma is the modified Marangoni number corresponding to the surface tension change due to both temperature and the concentration. The Marangoni number, Ma, is usually negative since $\partial\sigma/\partial T$ is negative for many pure liquids, but Ma can become positive for a binary mixture composed of liquids with different surface tension characteristics. A dimensionless parameter for the absolute value of surface tension is defined as K. In the following section all equations and variables are presented in dimensionless form.

Derivation of Solutions. All variables (u, v, P, c, T and h) are perturbed as follows:

$$f(x, y, t) = f_0 + f_1(y)\cdot \exp(ikx + \omega t) \quad (12)$$

where k is the x-direction wave number and ω is the perturbation growth rate. The subscripts 0 and 1 correspond to basic and perturbed terms, respectively. Since pressure, P, increases with film thickness, the perturbed term in P is expressed with $\{\mathrm{Ga}\cdot h_1 + p_1(y)\}\exp(ikx + \omega t)$, where h_1 is not a function of y, but rather a constant. A stationary liquid film is assumed as the basic state, thus the average variables have following value:

$$u_0 = v_0 = 0, \quad c_0 = c_{li}, \quad h_0 = 0 \quad (13)$$

$$T_0 = T_w + y \quad (14)$$

$$P_0 = P_g + \mathrm{Ga}(1 - y) \quad (15)$$

By substituting Eq. (12) into the fundamental equations, Eqs. (1)–(5), and neglecting higher order small terms, the differential equations for the first-order perturbed variables are obtained as follows:

$$iku_1 + \frac{dv_1}{dy} = 0 \quad (16)$$

$$\omega u_1 = -ik(\mathrm{Ga}\cdot h_1 + p_1) + \left(-k^2 u_1 + \frac{d^2 u_1}{dy^2}\right) \quad (17)$$

$$\omega v_1 = -\frac{dp_1}{dy} + \left(-k^2 v_1 + \frac{d^2 v_1}{dy^2}\right) \quad (18)$$

$$\omega T_1 + v_1 = \frac{1}{\mathrm{Pr}}\left(-k^2 T_1 + \frac{d^2 T_1}{dy^2}\right) \quad (19)$$

$$\omega c_1 = \frac{1}{\mathrm{Sc}}\left(-k^2 c_1 + \frac{d^2 c_1}{dy^2}\right) \quad (20)$$

Equation (20) indicates that the perturbed term of concentration, c_1, is independent of other variables, and only affected by v_1 and T_1 through the boundary conditions at the interface. Because Eq. (20) does not have influence on the instability analysis, c_1 is not included in the solution. The following ordinary differential equations are derived by eliminating u_1, p_1 and h_1 in Eqs. (16)–(19):

$$\left(\frac{d^2}{dy^2} - k^2\right)\left(\frac{d^2}{dy^2} - k^2 - \omega\right)v_1(y) = 0 \quad (21)$$

$$\left(\frac{d^2}{dy^2} - k^2 - \mathrm{Pr}\cdot\omega\right)T_1(y) = \mathrm{Pr}\cdot v_1(y) \quad (22)$$

General solutions of Eqs. (21) and (22) are

$$v_1(y) = C_1 e^{ky} + C_2 e^{-ky} + C_3 e^{my} + C_4 e^{-my} \quad (23)$$

$$T_1(y) = \frac{\mathrm{Pr}}{k^2 - n^2} C_1 e^{ky} + \frac{\mathrm{Pr}}{k^2 - n^2} C_2 e^{-ky} + \frac{\mathrm{Pr}}{m^2 - n^2} C_3 e^{my} + \frac{\mathrm{Pr}}{m^2 - n^2} C_4 e^{-my} + C_5 e^{ny} + C_6 e^{-ny} \quad (24)$$

where

$$m^2 = k^2 + \omega, \quad n^2 = k^2 + \mathrm{Pr}\cdot\omega \quad (25)$$

and C_1 through C_6 are integration constants. By substituting Eq. (12) into the dimensionless boundary conditions derived from Eqs. (6)–(10), the following conditions for the perturbed terms are obtained:

At y = 0:

$$v_1 = \frac{dv_1}{dy} = T_1 = 0 \quad (26)$$

At y = 1 + h (vapor–liquid interface):

$$\omega \frac{d^2 v_1}{dy^2} + k^2\left(\omega - \frac{\mathrm{Ma}}{\mathrm{Pr}}\right)v_1 - k^2\omega\frac{\mathrm{Ma}}{\mathrm{Pr}}T_1 = 0 \quad (27)$$

$$\omega\frac{d^3 v_1}{dy^3} + \omega(-3k^2 - \omega)\frac{dv_1}{dy} - k^2(\mathrm{Ga} + k^2 K)v_1 = 0 \quad (28)$$

$$\mathrm{Sh}\cdot v_1 + \omega\frac{dT_1}{dy} + \omega\mathrm{Sh}\cdot T_1 = 0 \quad (29)$$

By substituting the theoretical solutions of Eqs. (23) and (24) into these boundary conditions, the integration constants are calculated. This procedure gives the following simultaneous equations, using coefficients a_{ij}:

$$\begin{cases} a_{11}C_1 + a_{12}C_2 + a_{13}C_3 + a_{14}C_4 + a_{15}C_5 + a_{16}C_6 = 0 \\ \vdots \\ a_{61}C_1 + a_{62}C_2 + a_{63}C_3 + a_{64}C_4 + a_{65}C_5 + a_{66}C_6 = 0 \end{cases} \quad (30)$$

Equation (30) can be rewritten as follows:

$$\begin{bmatrix} a_{11} & \cdots & a_{16} \\ \vdots & \ddots & \vdots \\ a_{61} & \cdots & a_{66} \end{bmatrix}\begin{bmatrix} C_1 \\ \vdots \\ C_6 \end{bmatrix} = \begin{bmatrix} 0 \\ \vdots \\ 0 \end{bmatrix} \quad (31)$$

Because the right-hand side of Eq. (31) is zero, the following condition is necessary to obtain a nontrivial solution:

$$\begin{vmatrix} a_{11} & \cdots & a_{16} \\ \vdots & \ddots & \vdots \\ a_{61} & \cdots & a_{66} \end{vmatrix} = 0 \quad (32)$$

This equation gives the relation between the growth rate ω and the wave number k, because each coefficient a_{ij} is a function of k and ω.

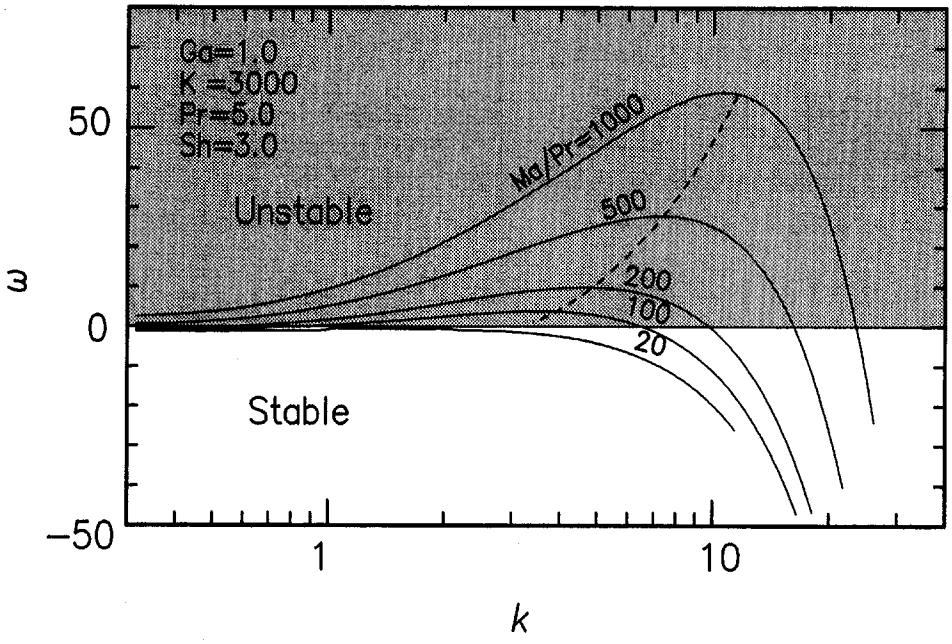

Fig. 5 Typical relation between wave number k and growth rate ω

Results and Discussion

From the numerical calculation of Eq. (32), the $k - \omega$ relation is obtained as shown in Fig. 5. From the definition of perturbed terms in Eq. (12), it is clear that the perturbation is amplified for a positive growth rate, ω, and damped for negative ω. A curve at Ma/Pr = 500 in Fig. 5, for instance, passes through both positive and negative growth rate areas. This means that only specified disturbances having particular wave numbers will grow. It is clear that the Marangoni effect (Ma/Pr) plays an important role with respect to the stability of a condensate film, because the curves largely depend on the value of Ma/Pr, and larger Ma/Pr make the condensate film more unstable.

Figure 6 shows the velocity vector profiles in the liquid and the temperature distributions at the interface for the unstable case at Ma/Pr = 200 and k = 6.2. In order to obtain the profile of v_1 and T_1, the C_2 to C_6 in Eqs. (23) and (24) were determined by assuming C_1 to be a finite value under the condition of Eq. (32). The value of u_1 is also calculated from Eq. (16) and v_1. It should be noted that the absolute values of the velocity and temperature have no meaning and only the direction and relative value are important in these figures. Although the velocity profile is similar to Marangoni convection in a channel induced by a heating wire at the liquid–gas interface, there is a large difference between the two with respect to the change in liquid layer height. For Marangoni convection in a thick liquid layer, the mass transfer due to the flow along the surface is compensated by the counterflow in the liquid layer, thus vertical motion of the interface does not appear. On the other hand, for the pseudo-dropwise condensation, where the typical film thickness is on the order of 10 to 100 μm, the counterflow is restricted by viscous forces, thus a significant height change occurs.

From Fig. 6 the mechanism of the film instability is determined. The temperature at the rising part of the interface becomes higher than that of the average value, and lower in the falling part. The higher temperature generates a higher water concentration and a lower temperature generates a higher ethanol concentration from the phase diagram of a water–ethanol binary mixture. Because the surface tension of the water is larger than that of ethanol, the thicker part of the interface has a larger surface tension than the thinner part; thus the liquid near the interface moves toward the thicker part. Consequently the liquid near the interface moves from the valley to the hill on the condensate film as shown in Fig. 6, which means the thicker parts of the film rise and thinner parts fall.

In order to see the effect of surface tension itself, the relation between the growth rate ω and the wave number k is calculated by changing the value of K. Since the stability curve does not depend on K, the surface tension itself does not influence on the condensate film stability. Using these results, the neutral stability curves are plotted versus Ma/Pr according to the wave number k as shown in Fig. 7. In the upper part of this curve, the growth rate ω is positive and film changes to a dropwise shape, but in the lower part of the curve, the condensate film is flat. This relation corresponds to that of Rayleigh number and wave number in the ordinary Bénard-cell stability problem. However, there is no minimum value of Ma/Pr in the figure, which means that no critical value of Ma/Pr for instability exists. This implies that the condensate film thickness increases with time in the experiment. Since the wave number k is nondimensionalized by the film thickness, the value of the horizontal axis in the figure increases as time elapses. Because Ma/Pr is also proportional to the film thickness H, the condensation is progressing in parallel to the line shown in Fig. 7, whose slope

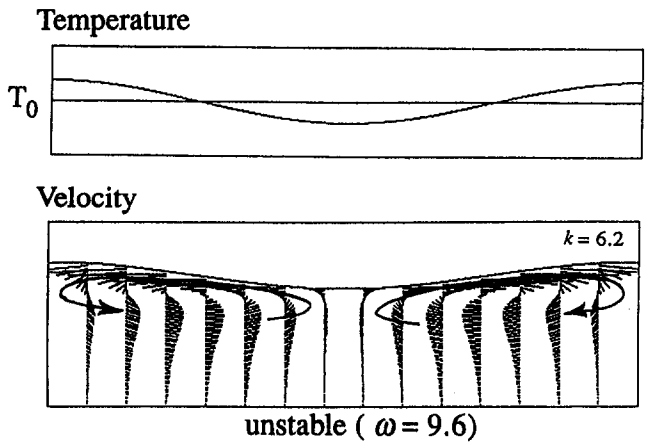

Fig. 6 Velocity profile and temperature distribution for an unstable case

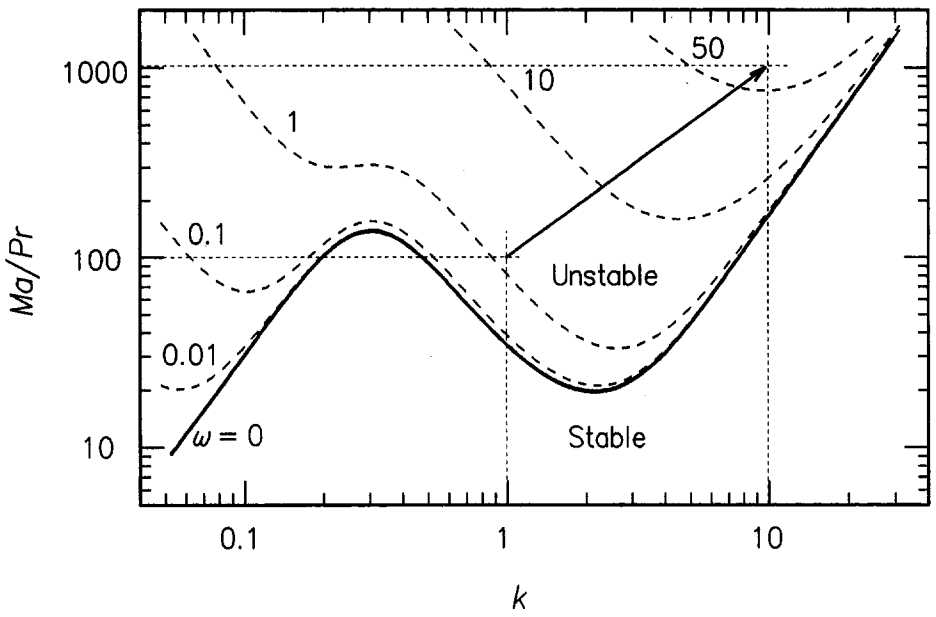

Fig. 7 Stability curves of Ma/Pr versus wave number *k*

is 45 deg. Therefore, k is transformed into $k/(\mathrm{Ma/Pr})$, to change the direction of the progress of the condensation vertical, and Fig. 7 is modified to Fig. 8. A disturbance with wave number on line A is damped because line A passes once through the unstable region, but re-enters the stable region. However, in the case of line B, a disturbance always grows as condensate film thickness increases because it is always in the unstable region.

Data plotted in the figure were experimentally obtained from the condensate film thickness immediately before the wipe. The experiments were carried out for a variety of vapor concentrations and rotation speeds of the wiper, but all the data fell on the same curve. This curve seems to coincide with the line connecting the minimum point of the constant growth rate curves. It does not correctly coincide with line B, but is very close. For example, the Sherwood number was changed from 0.7 to 0.3 during the actual case, but this is not large enough to explain this discrepancy. Since many assumptions are adopted in the analysis, the differences between the theory and the experimental data and the scatter of the data are considered satisfactory. As a conclusion, the length of the disturbance wave is constant under various experimental conditions.

Heat Transfer Characteristics

In order to see the effect of the condensation mode (dropwise of filmwise) on the heat transfer performance, the heat transfer coefficient was also measured and compared with a one-dimensional, unsteady filmwise condensation model. The governing equations of the model are as follows:

In the gas phase:

$$\frac{\partial c}{\partial t} + v_g \frac{\partial c}{\partial y} = D \frac{\partial^2 c}{\partial y^2} \tag{33}$$

In the liquid phase:

$$\frac{\partial T}{\partial t} = \kappa \frac{\partial^2 T}{\partial y^2} \tag{34}$$

where c is the concentration, T is the temperature, and v_g is the constant gas velocity. The phase equilibrium is assumed at the vapor–liquid interface. The boundary conditions including the energy balance at the interface are as follows:

In the gas phase:

$$y = \delta \quad c = c(T_i) \tag{35}$$

$$y \to \infty \quad c \to c_\infty = \text{const} \tag{36}$$

In the liquid phase:

$$y = 0 \quad T = T_w \tag{37}$$

$$y = \delta \quad T = T_i \tag{38}$$

At the interface:

$$\lambda \left.\frac{\partial T}{\partial y}\right|_{y=\delta} = L\rho_l \frac{\partial \delta}{\partial t} = L\rho_g \left(-v_g + \frac{\partial \delta}{\partial t}\right) \tag{39}$$

where L is the latent heat of condensation and δ is the condensate film thickness. The initial conditions are

$$t = 0\text{: } \delta = 0, \quad c = c_\infty (0 < y < \infty),$$

$$T = T(c_\infty)(y = 0) \tag{40}$$

When the pure-component system is considered, only the liquid phase is solved, with the assumption that the vapor–liquid boundary temperature is equal to the saturation temperature.

Figure 9 represents a modified average heat transfer coefficient of the pure vapor over one wipe period. Since the liquid film thickness, which corresponds to the amount of heat having been transferred up to the point of interest, increases with the square root of time, the heat transfer coefficient divided by the square root of the frequency is employed in Figs. 9 and 10. The calculated results (solid lines) fit the experimental data very well. The experimental condensation feature of the pure water vapor is dropwise, but the measured heat transfer coefficients are close to the calculated values of the filmwise condensation rate. The difference between the thin liquid film and the group of small droplets is not clear because the experiments are not performed under steady-state conditions, like the Nusselt filmwise condensation theory, but rather in the transient state. Moreover, the experiments on a horizontal cooling wall make the sweeping effect of the falling droplets invalid. It is therefore concluded that the heat transfer characteristics on a horizontal cooling wall with dropwise condensation can be estimated by the unsteady filmwise condensation model.

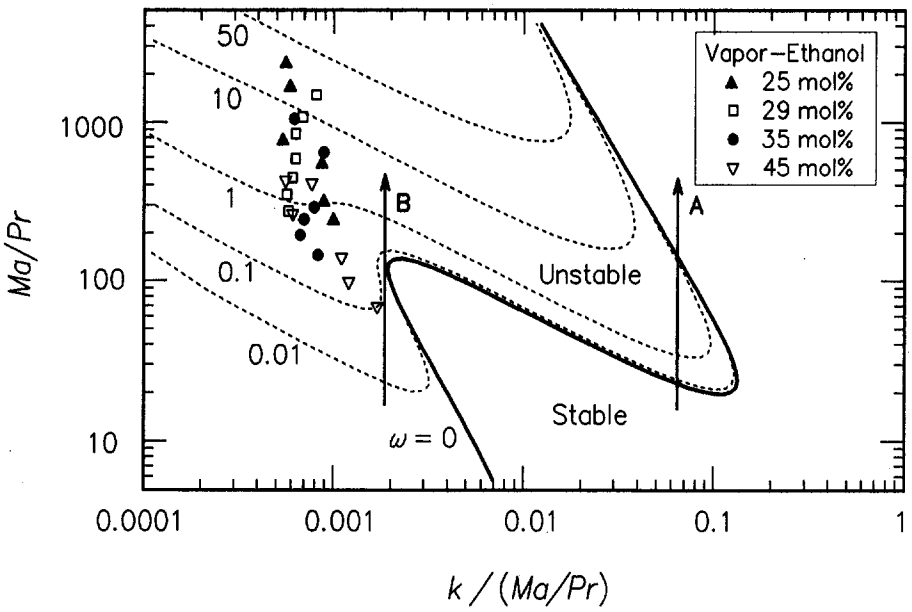

Fig. 8 Stability curves of Ma/Pr versus modified wave number $k/(Ma/Pr)$

Heat transfer coefficients of a binary vapor mixture are plotted in Fig. 10. Solid lines and dotted lines denote calculated results of the binary vapor mixture and the pure vapor, respectively. Because the initial concentration in the vapor phase is assumed to be constant, the calculation gives an overestimation of the heat transfer rate. For a vapor mixture of 55 mol%, however, the model agrees well because the concentration difference between the bulk vapor and at the liquid–vapor interface is smaller than the others. The reason high heat transfer performance of dropwise condensation does not appear in the figure is same as mentioned for the pure vapor. The ΔT_{PD}, shown in the figure is the theoretically required temperature difference for condensation, which is derived from the temperature drop between condensation and boiling curves at a concentration in the phase diagram. Minimum required temperature differences for condensation in the experiment are much higher than the theoretical value of ΔT_{PD}. The nonuniformity of the concentration in the vapor phase brings about this discrepancy. Except for these differences, measured heat transfer coefficients agree well with the theory.

Conclusions

The pseudo-dropwise condensation phenomena of the water–ethanol binary mixture was investigated and the following conclusions were obtained:

1 The droplets in the pseudo-dropwise condensation are generated by the instability of the condensing film.
2 The wavelength of this instability is explained by the theory considering the surface tension change due to the concentration and the temperature.

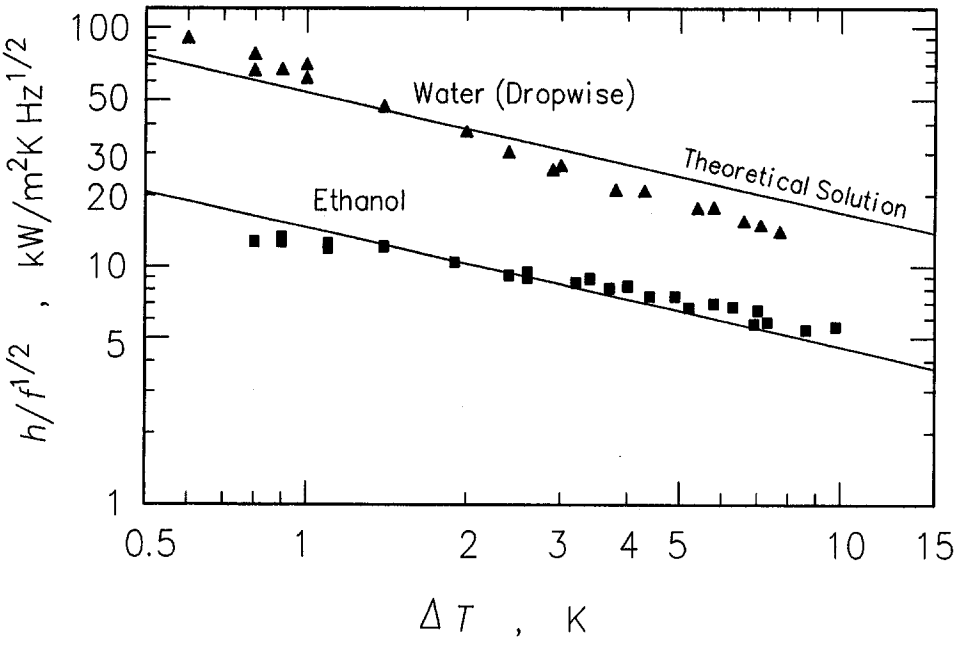

Fig. 9 Condensation heat transfer rate for pure vapor on the horizontal plate

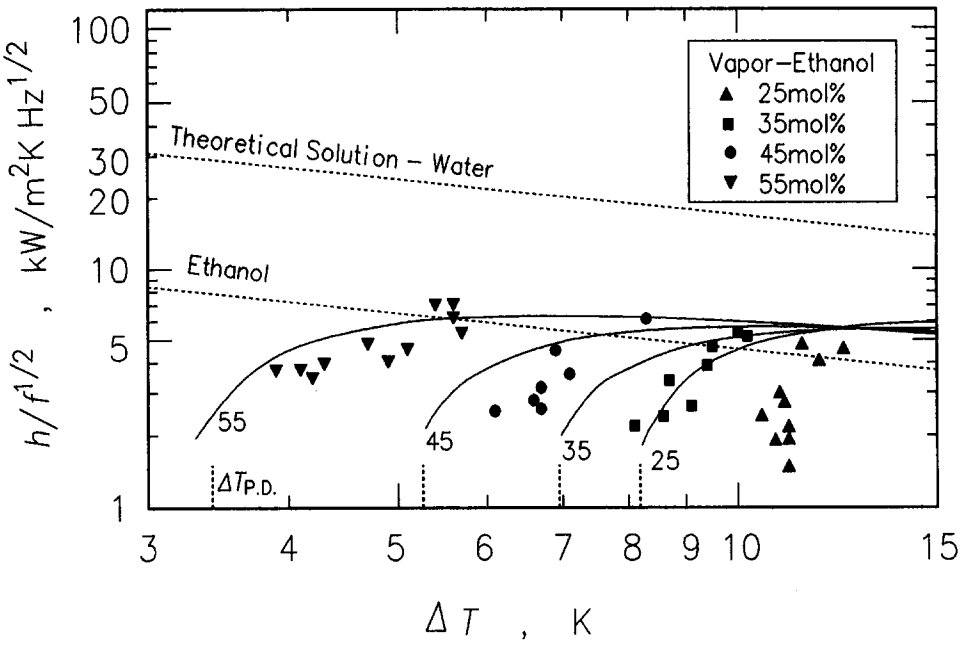

Fig. 10 Condensation heat transfer rate for binary vapor mixtures on the horizontal plate

3 The heat transfer coefficient in pseudo-dropwise condensation on a horizontal plane is nearly equal to that of unsteady filmwise condensation.

References

Fujii, T., Koyama, S., Shimizu, Y., Watabe, M., and Nakamura, Y., 1989, "Gravity Controlled Condensation of an Ethanol and Water Mixture on a Horizontal Tube," *Trans. JSME, Series B,* Vol. 55, No. 509, pp. 210–217.

Hayashi, Y., Takimoto, A., Tada, Y., and Teranishi, T., 1993, "Condensation of Binary Vapors of Immiscible Liquids," *Energy Conversion and Utilization With High Efficiency Researches Pursued by Grant-in-Aid on Priority-Area Research Supported by the Ministry of Education,* Japan, pp. 235–256.

Hijikata, K., and Himeno, N., 1990, "Condensation of Azeotropic and Non-azeotropic Binary Vapor Mixtures," *Annual Review of Heat Transfer,* Vol. III, Hemisphere Publishing Co., pp. 39–84.

Mirkovich, V. V., and Missen, R. W., 1961, "A Study of the Condensation of Binary Vapors of Miscible Liquids," *Canadian J. Chemical Engineering,* Vol. 39, pp. 86–87.

Transport Phenomena in Picoliter Size Solder Droplet Dispension

J. M. Waldvogel

D. Poulikakos[1]

Mechanical Engineering Department,
University of Illinois at Chicago,
842 W. Taylor Street,
Chicago, IL 60680

D. B. Wallace

R. Marusak

MicroFab Inc.,
1104 Summit Ave., Suite 110,
Plano, TX 75704

This paper presents a study of the fluid dynamics and heat transfer phenomena occurring during the impingement of a picoliter size liquid solder droplet upon a multilayer, composite substrate. The theoretical model, based on the Lagrangian formulation, is solved numerically with the finite element method. A deforming mesh is utilized to accurately simulate the large deformations, as well as the domain nonuniformities characteristic of the spreading process. The occurrences of droplet recoiling and mass accumulation around the deposit periphery are features of the numerical simulations and yield a nonmonotonic dependence of the maximum radius on time. The results also document the transient temperature fields developing in both the solder droplet and the substrate during the impingement process. Convection effects on the temperature field development in a deforming droplet are found to be important for the entire history of spreading. The work is directly applicable to the miniature solder droplet dispension technology for the mounting of microscopic electronic components on various substrates under development at MicroFab Inc. The results of the numerical simulations are used to explain the shape of solidified microscopic solder bumps.

Introduction

The primary motivation for the present work is the novel process of picoliter solder droplet dispension for the mounting of microelectronic components (Hayes et al., 1992). In this manufacturing process, referred to as *solder-drop-printing* herein, the shape of a solder deposit produced on a microchip is affected by the dynamics of impact and the heat removal process from the solder droplet to the microchip substrate. Solder droplets are applied directly to the bonding pads on chips in a molten state using a technique similar to ink-jet printing (Hayes et al., 1992). Solidified droplets (also called bumps) are used in the flip-chip process to bond electronic components to a substrate. In this approach, the active surface of a chip is placed in contact with a predeposited array of solder droplets. The chip/substrate assembly is then bonded in a reflow soldering oven. Partially flattened solder bump arrays have been produced in the laboratory using a trial-and-error process (Hayes et al., 1992). Precise solder bump shape prediction is crucial for the application of this technology to microelectronic component packaging.

The definition of the present study is shown in Fig. 1, which also contains a representative finite element mesh, to be discussed later in this paper. A molten solder droplet originally spherical in shape moves in the gravitational direction toward a large, horizontal, flat, multilayer, composite substrate. After the droplet impacts the substrate surface, it spreads out and is flattened. Under the appropriate conditions, the droplet may recoil due to surface tension forces, and spring back up while its lower surface remains attached to the substrate. As the droplet deforms it is cooled by the substrate and eventually solidifies. The relative time scales of the deformation and cooling processes are crucial in the determination of the ultimate droplet shape. The present study investigates the fluid dynamics and heat transfer phenomena during the *presolidification* stage of the impact process of a eutectic tin–lead solder (63 percent Sn–37 percent Pb) droplet.

The heat and fluid flow phenomena occurring during the impact of a liquid-metal droplet on a cold substrate are neither conventional, nor easy to study. The fluid dynamics describing the droplet spreading is a free surface problem with large domain deformations in the presence of surface tension. The transient heat transfer process involves convection and steep temperature gradients within a severely deforming domain, coupled with conduction in the substrate. Experimental investigation of the problem is quite challenging due to the very fast transients (on the microsecond scale) involved. Due to this difficulty, a numerical model has been developed. This model will reveal the relative importance of these process parameters: impact velocity, droplet diameter, and substrate material.

Numerical efforts targeting the fluid dynamics of the droplet impingement process initially adopted oversimplifying assumptions to facilitate solution. Harlow and Shannon (1967) neglected both viscous and surface tension effects in their modeling formulation of a liquid droplet impacting a flat plate. The "marker and cell" technique (Harlow and Welch, 1965; Frederiksen and Watts, 1981) based on a fixed grid was employed in the above-mentioned work, which pioneered the simulation efforts of the splashing process. Subsequent models (Jones, 1971) involved simplified treatments of the fluid spreading process, but incorporated provisions for phase change. Madejski (1983, 1976) circumvented the difficulties of the splashing process by simply considering an order of magnitude balance between the inertial, viscous, and surface tension effects, and reported asymptotic values of the degree of spreading of liquid-metal droplets impacting on horizontal and inclined plates. Trapaga and Szekely (1991) presented a numerical model of the droplet deformation process on a solid plate utilizing the commercially available FLOW-3D software to carry out their numerical simulations.

An important issue in the numerical simulation of the droplet impingement problem is the boundary condition at the liquid–solid–gas junction: the wetting condition at the dynamic contact

[1] Current address: Institute of Energy Technology, Swiss Federal Institute of Technology (ETH), ETH Center, CH-8092, Zurich, Switzerland.

Contributed by the Heat Transfer Division for publication in the JOURNAL OF HEAT TRANSFER. Manuscript received by the Heat Transfer Division January 1995; revision received October 1995. Keywords: Conjugate Heat Transfer, Liquid Metals, Materials Processing and Manufacturing Processes. Associate Technical Editor: A. Faghri.

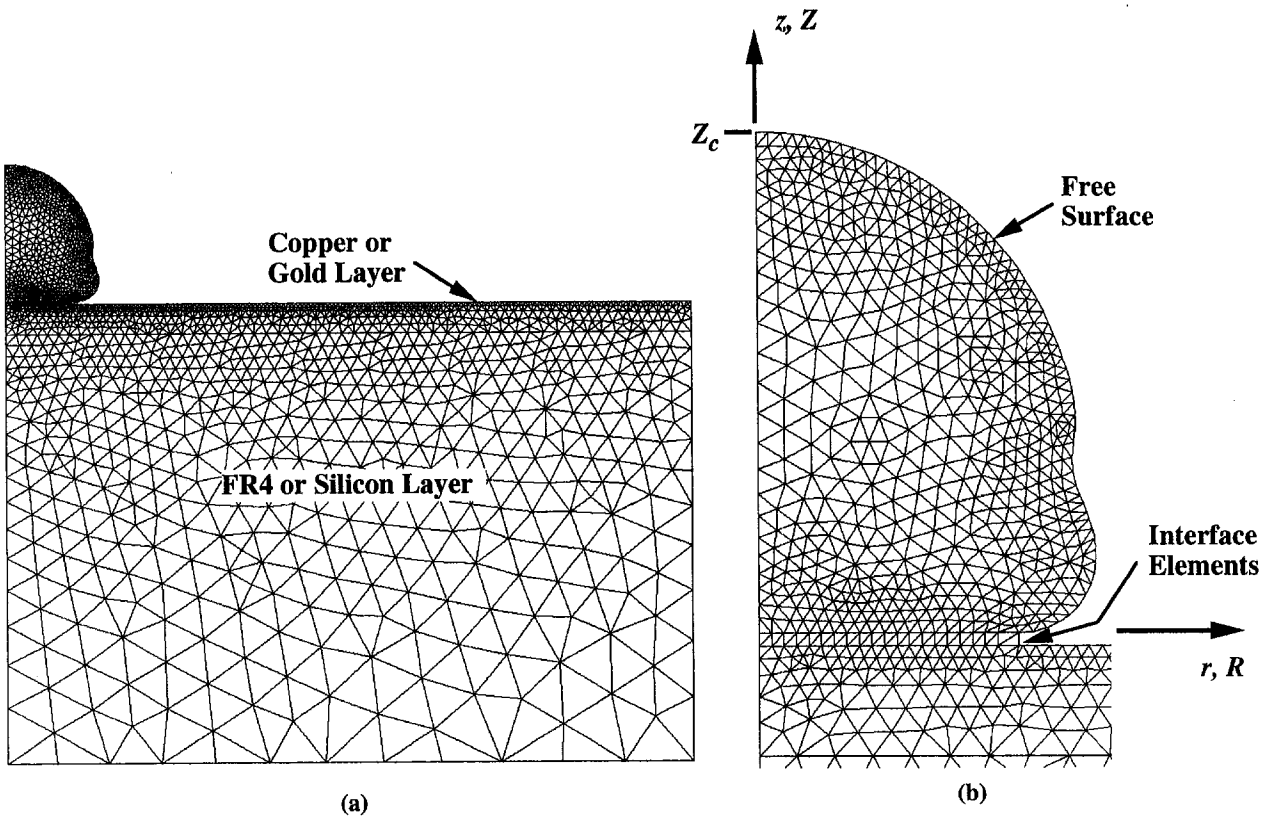

Fig. 1 Schematic of problem of interest and example finite element mesh: (*a*) entire solution domain, (*b*) droplet and interface regions

line. The relationship between contact angle and lateral velocity of the contact line has been extensively analyzed in the limit of slow motion. Haley and Miksis (1991) investigated this problem for situations where the capillary force acting at the contact line dominates the droplet spreading motion. The traditional no-slip boundary condition fails in the vicinity of the contact line because its application results in an infinite stress in that region (Huh and Scriven, 1971; Dussan, 1979). The most popular approach to circumventing this problem is the Navier slipping model discussed in detail by Dussan (1979), and Silliman and Scriven (1980). Recently, Fukai et al. (1995) demonstrated good agreement between numerical calculations and experimental data for the overall shape of a deforming droplet, including recoiling, by imposing advancing and receding contact angles determined experimentally.

Fukai et al. (1993) presented a new approach based on the finite element method to model the droplet spreading process, which accounted for the presence of inertial, viscous, gravitational, and surface tension effects. For the modeling of the splashing fluid dynamics, the present study relies on the recent work of Fukai et al. (1993). This model was extended to account for the relevant convection and conduction heat transfer

Nomenclature

c = speed of sound, m/s
C = dimensionless heat capacity
c_p = specific heat, J/kg·K
d_0 = initial diameter of droplet, m
ds = mesh density
Fr = Froude number
g = gravitational acceleration, m/s^2
h = heat transfer coefficient, W/m^2·K
H = mean surface curvature, 1/m
$\bar{H}$ = dimensionless mean surface curvature
k = thermal conductivity, W/m·K
K = dimensionless thermal conductivity
l_c = arbitrary interface layer thickness, m
L_c = dimensionless arbitrary interface layer thickness
M = Mach number
n = outward normal vector
p = droplet fluid pressure, N/m^2
P = dimensionless droplet fluid pressure
Pr = Prandtl number
r = radial coordinate, m
R = dimensionless radial coordinate
R_{max} = dimensionless maximum radius of deposit
ratio = parameter related to quality of an element based on its shape
Re = Reynolds number
s = coordinate measured along the free surface of the deforming droplet, m
t = time, s
T = temperature, K
u = radial velocity, m/s
U = dimensionless radial velocity
v = axial velocity, m/s
v_0 = droplet initial impact velocity, m/s
V = dimensionless axial velocity
We = Weber number
z = axial coordinate, m
Z = dimensionless axial coordinate
Z_c = dimensionless z-axis contact point
α = thermal diffusivity, m^2/s
γ = surface tension coefficient, N/m
Θ = dimensionless temperature
μ = viscosity, kg/s·m
ρ = density, kg/m^3
σ = stress, N/m^2
$\bar{\sigma}$ = dimensionless stress
τ = dimensionless time

Subscripts

c = contact
o = reference value
r = radial direction
z = axial direction
0 = initial
1 = droplet
2 = substrate

phenomena in the droplet and the substrate regions in a range of process parameters consistent with solder-drop-printing. Further enhancements include an improved mesh generator, contact resistance between droplet and substrate regions, and modeling of composite substrates.

Mathematical Model

The model is formulated to simulate the impact of an initially spherical, molten solder droplet on a multilayer composite substrate beginning at the instant the droplet contacts the substrate. It is based on the full Navier–Stokes equations applied to the axisymmetric coordinate system. A schematic corresponding to the mathematical model is provided in Fig. 1. Motion of the deforming free surface is accurately simulated using the Lagrangian approach (Fukai et al., 1993; Bach and Hassager, 1985). The time-dependent term is retained in the continuity equation, which becomes a pressure evolution equation by applying the artificial compressibility approach (Hirt and Nichols, 1980; Kawahara and Hirano, 1983). The governing equations in dimensionless form are

$$\frac{\partial P}{\partial \tau} + \frac{1}{M^2}\left(\frac{1}{R}\frac{\partial}{\partial R}(RU) + \frac{\partial V}{\partial Z}\right) = 0, \tag{1}$$

$$\frac{\partial U}{\partial \tau} - \frac{1}{R}\frac{\partial}{\partial R}(R\bar{\sigma}_{rr}) - \frac{\partial \bar{\sigma}_{rz}}{\partial Z} + \frac{1}{R}\bar{\sigma}_{\theta\theta} = 0 \tag{2}$$

$$\frac{\partial V}{\partial \tau} - \frac{1}{R}\frac{\partial}{\partial R}(R\bar{\sigma}_{zr}) - \frac{\partial \bar{\sigma}_{zz}}{\partial Z} + \frac{1}{Fr} = 0, \tag{3}$$

$$U = \frac{\partial R}{\partial \tau}, \tag{4}$$

$$V = \frac{\partial Z}{\partial \tau} \tag{5}$$

The dimensionless initial and boundary conditions are (see Fig. 1)

$$\tau = 0: \quad R = R_0, \quad Z = Z_0, \quad U = 0,$$

$$V = -1, \quad \text{and} \quad P = \frac{4}{We},$$

$$R = 0: \quad U = 0, \quad \frac{\partial V}{\partial R} = 0, \quad Z = 0: \quad U = V = 0 \tag{6}$$

and at the free surface (see Fig. 1)

$$\bar{\sigma}_{rr}n_r + \bar{\sigma}_{rz}n_z = -2\frac{\bar{H}}{We}n_r \quad \text{and}$$

$$\bar{\sigma}_{zr}n_r + \bar{\sigma}_{zz}n_z = -2\frac{\bar{H}}{We}n_z \tag{7}$$

The dimensionless stress tensor terms are

$$\bar{\sigma}_{rr} = -P + \frac{2}{Re}\frac{\partial U}{\partial R} \quad \bar{\sigma}_{\theta\theta} = -P + \frac{2}{Re}\frac{U}{R}$$

$$\bar{\sigma}_{rz} = \bar{\sigma}_{zr} = \frac{1}{Re}\left(\frac{\partial U}{\partial Z} + \frac{\partial V}{\partial R}\right) \quad \bar{\sigma}_{zz} = -P + \frac{2}{Re}\frac{\partial V}{\partial Z} \tag{9}$$

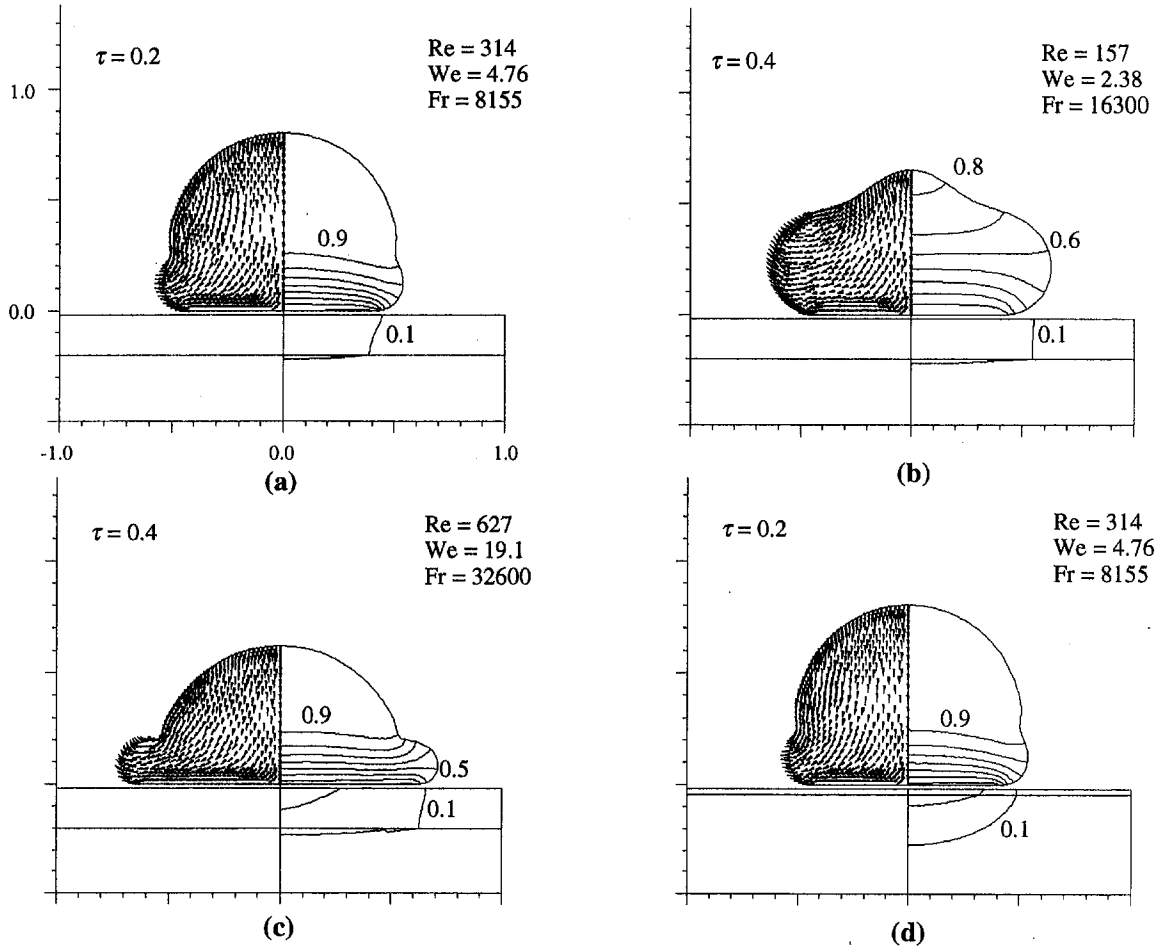

Fig. 2 Temperature and velocity distributions at $t = 5\ \mu s$, $h = 5 \times 10^7\ W/m^2 \cdot K$: (*a*) FR-4/copper, $v_0 = 2$ m/s, $d_0 = 50\ \mu m$, (*b*) FR-4/copper, $v_0 = 2$ m/s, $d_0 = 25\ \mu m$, (*c*) FR-4/copper, $v_0 = 4$ m/s, $d_0 = 50\ \mu m$, and (*d*) silicon/gold, $v_0 = 2$ m/s, $d_0 = 50\ \mu m$

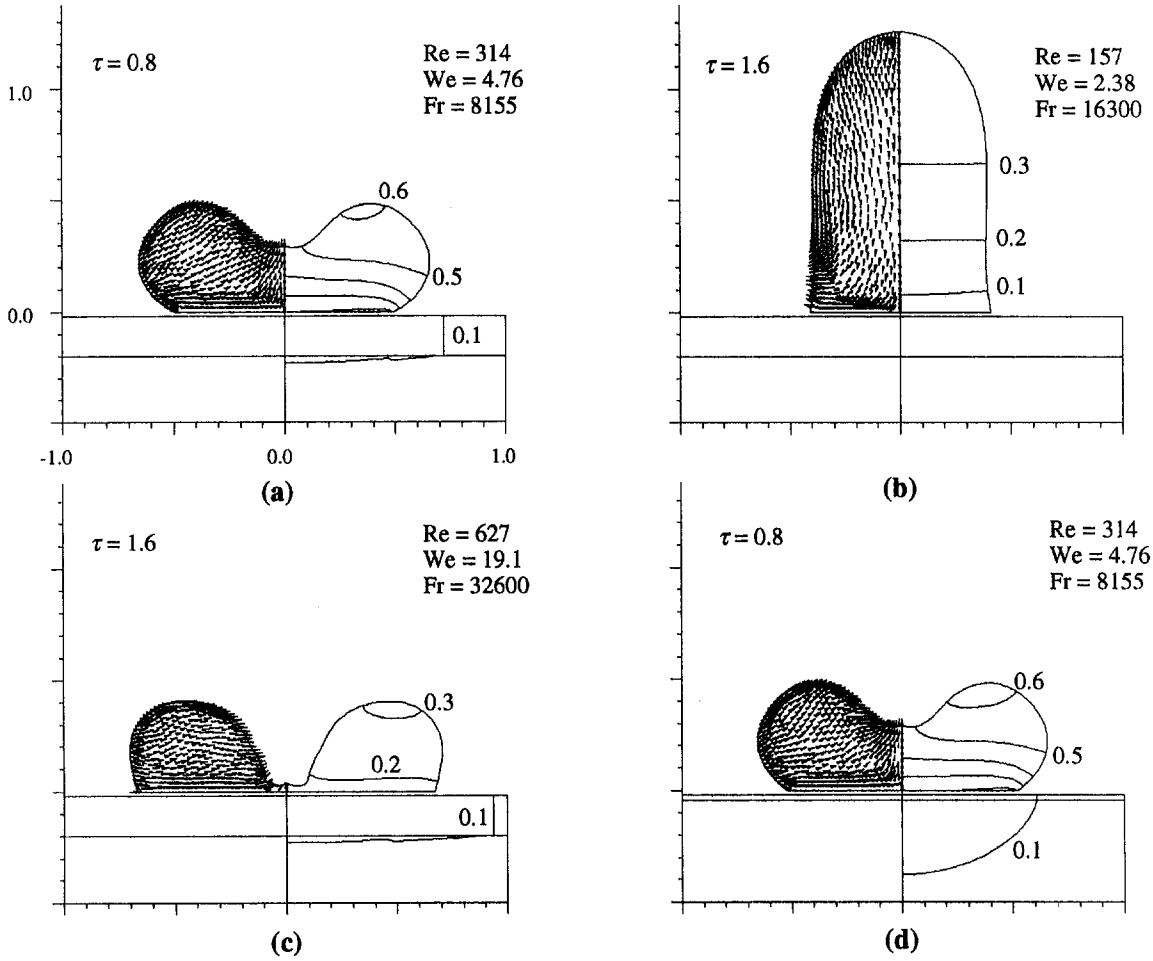

Fig. 3 Temperature and velocity distributions at $t = 20\ \mu s$, $h = 5 \times 10^7\ W/m^2 \cdot K$: (*a*) FR-4/copper, $v_0 = 2$ m/s, $d_0 = 50\ \mu m$, (*b*) FR-4/copper, $v_0 = 2$ m/s, $d_0 = 25\ \mu m$, (*c*) FR-4/copper, $v_0 = 4$ m/s, $d_0 = 50\ \mu m$, and (*d*) silicon/gold, $v_0 = 2$ m/s, $d_0 = 50\ \mu m$

The nondimensionalization was performed according to the following definitions:

$$R = \frac{r}{d_0}, \quad Z = \frac{z}{d_0}, \quad s = \frac{s}{d_0}, \quad \bar{H} = \frac{H}{1/d_0},$$

$$\tau = \frac{t}{d_0/v_0}, \quad U = \frac{u}{v_0}, \quad V = \frac{v}{v_0}, \quad P = \frac{p}{\rho_o v_0^2}, \quad \bar{\sigma}_{ij} = \frac{\sigma_{ij}}{\rho_o v_0^2} \quad (10)$$

where the mean curvature of the free surface is defined as

$$H = \frac{r^2(r'z'' - z'r'') + [(r')^2 + (z')^2]rz'}{2r^2[(r')^2 + (z')^2]^{3/2}} \quad (11)$$

The prime in Eq. (11) indicates differentiation with respect to the arc length, s. Based on the nondimensionalization scheme outlined above, the Reynolds, Weber, Froude, and Mach numbers are defined, respectively, as follows

$$\mathrm{Re} = \frac{\rho_o v_0 d_0}{\mu_o}, \quad \mathrm{We} = \frac{\rho_o v_0^2 d_0}{\gamma_o},$$

$$\mathrm{Fr} = \frac{v_0^2}{d_0 g}, \quad \text{and} \quad \mathrm{M} = \frac{v_0}{c} \quad (12)$$

The Lagrangian formulation is also used to construct the mathematical model for the conjugate heat transfer process in the droplet and the substrate. The relevant energy conservation equations, as well as the initial and boundary conditions are as follows:

Energy equation in the droplet:

$$C_1 \frac{\partial \Theta_1}{\partial \tau} - \frac{1}{\mathrm{Pr\ Re}}\left[\frac{1}{R}\frac{\partial}{\partial R}\left(K_1 R \frac{\partial \Theta_1}{\partial R}\right) + \frac{\partial}{\partial Z}\left(K_1 \frac{\partial \Theta_1}{\partial Z}\right)\right] = 0 \quad (13)$$

Energy equation in the substrate:

$$C_2 \frac{\partial \Theta_2}{\partial \tau} - \frac{1}{\mathrm{Pr\ Re}}\left[\frac{1}{R}\frac{\partial}{\partial R}\left(K_2 R \frac{\partial \Theta_2}{\partial R}\right) + \frac{\partial}{\partial Z}\left(K_2 \frac{\partial \Theta_2}{\partial Z}\right)\right] = 0 \quad (14)$$

Initial conditions in droplet and substrate regions:

$$\Theta_1(R, Z, 0) = 1, \quad \Theta_2(R, Z, 0) = 0 \quad (15)$$

Heat transfer from all exposed surfaces is neglected, and the substrate is assumed to be large, such that the following condition applies to the boundaries of both regions:

$$\frac{\partial \Theta_i}{\partial R} n_r + \frac{\partial \Theta_i}{\partial Z} n_z = 0; \quad i = 1, 2 \quad (16)$$

The nondimensionalization of temperature was carried out according to the following:

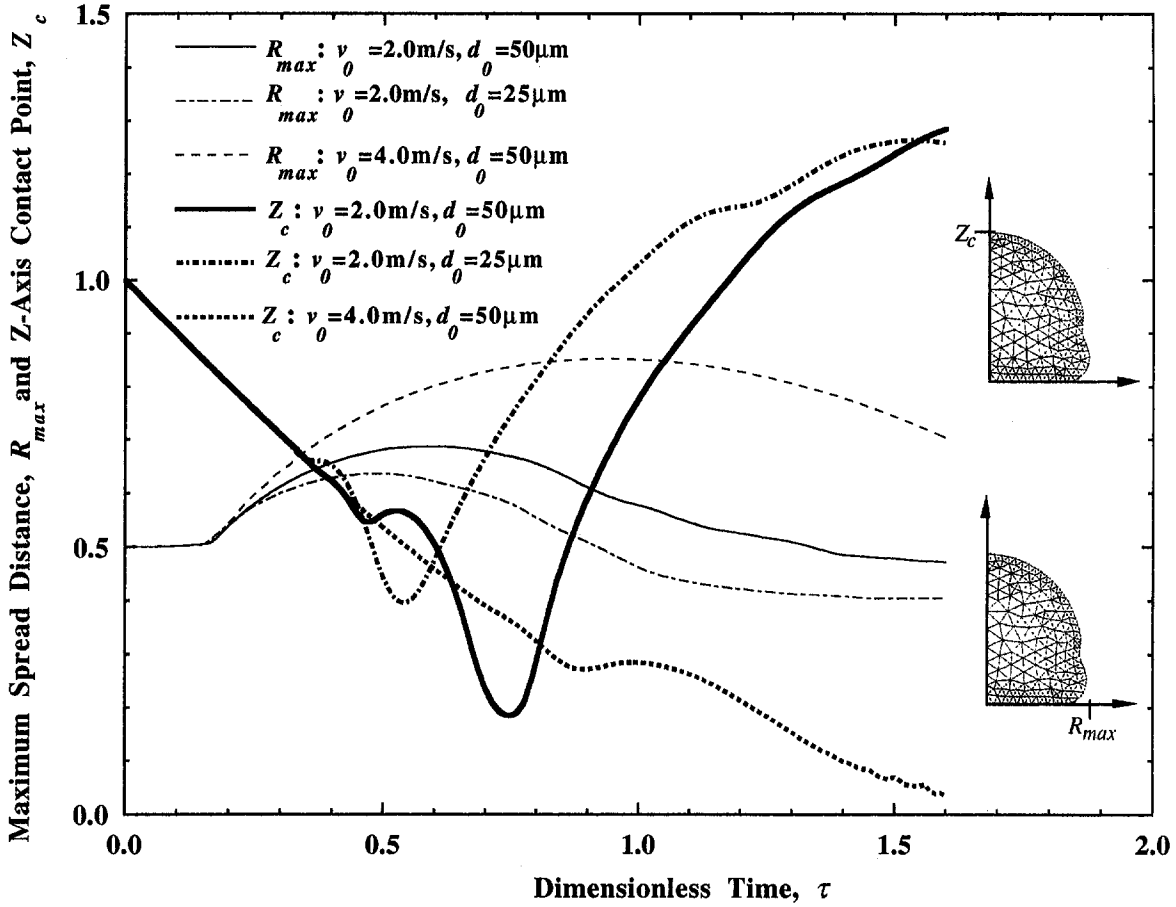

Fig. 4 Variation of maximum spread distance and z-axis contact point with time

$$\Theta_i = \frac{T_i - T_{2,0}}{T_{1,0} - T_{2,0}}; \quad i = 1, 2 \tag{17}$$

where the subscripts 0, 1, and 2 indicate initial, droplet, and substrate, respectively. The Prandtl number Pr, dimensionless heat capacity C_i, and thermal conductivity K_i are defined as

$$\mathrm{Pr} = \frac{\mu_o c_{p,o}}{k_o}, \quad C_i = \frac{\rho_i c_{p,i}}{\rho_o c_{p,o}}, \quad \text{and} \quad K_i = \frac{k_i}{k_o} \tag{18}$$

The substrates considered are constructed of layers of different materials: gold on silicon or copper on FR-4 epoxy-fiberglass printed circuit board material. Since the energy equations in the fluid and in the substrate have the same form in the Lagrangian formulation, the two regions can be combined and solved simultaneously following the same numerical procedure. Although Eq. (13) suggests a purely diffusive system, the convective energy transport within the droplet is implicit in the Lagrangian formulation.

Contact resistance between the droplet and substrate regions is modeled by a thin layer of arbitrary thickness, l_c, which attaches the two regions. To be consistent with the definition of a contact heat transfer coefficient, h_c (Wang and Matthys, 1991), this layer is assigned zero heat capacity and experiences only axial conduction. The effective layer axial thermal conductivity, $k_{zz,c}$, is related to the contact heat transfer coefficient by

$$k_{zz,c} = h_c l_c \tag{19}$$

This approach yields a mathematical model of the same form as the other regions, simplifying the numerical solution. The resulting energy equation for the layer is

$$C_c \frac{\partial \Theta}{\partial \tau} - \frac{1}{\mathrm{Pr\,Re}} \left[\frac{1}{R} \frac{\partial}{\partial R} \left(K_{rr,c} R \frac{\partial \Theta}{\partial R} \right) + \frac{\partial}{\partial Z} \left(K_{zz,c} \frac{\partial \Theta}{\partial Z} \right) \right] = 0 \tag{20}$$

where $C_c = 0$ and $K_{rr,c} = 0$. Nondimensionalization of Eq. (19) yields

$$K_{zz,c} = \frac{h_c d_o}{k_o} \frac{l_c}{d_o} = \mathrm{Bi}_c L_c \tag{21}$$

where Bi_c is the contact Biot number and L_c is the dimensionless layer thickness.

Numerical Solution

To solve the mathematical model, the computational domain was discretized with a mesh of triangular elements and solved numerically using a Galerkin finite element formulation. Quadratic and linear shape functions were used for velocity and pressure, respectively. The artificial compressibility method (Hirt and Nichols, 1980; Kawahara and Hirano, 1983) was employed to transform the continuity equation into a pressure evolution equation. This method assumes an incompressible fluid is "slightly" compressible, whereby the speed of sound is very large, but not infinite.

An implicit method was utilized for the numerical integration of the fluid mechanics equations in time, while a Crank–Nicholson scheme was used for the energy equation. The coupling of the fluid particle locations and of the conservation equa-

tions was accomplished by utilizing the technique proposed by Bach and Hassager (1985). The procedure is summarized by Fukai et al. (1993). After the solution for the velocity field at time $t + dt$ is obtained, starting with the temperature distribution at time t, the energy equation is solved in all regions simultaneously to obtain the overall temperature distribution at time $t + dt$.

As the droplet impact proceeded in time, the elements within the mesh became increasingly distorted. This distortion was quantified for each element by

$$\text{ratio} = \frac{r_1}{r_2} \tag{22}$$

where r_1 is the radius of a circle that passes through the three nodes in an element and r_2 is the radius of a circle that circumscribes an equilateral triangle with the same area as the element. To reduce solution inaccuracies due to element distortion, a new mesh was created when ratio > 1.9 for a droplet element. Once a new mesh was established, the solution variables were mapped to the new nodes via interpolation on the old mesh.

In the remeshing process, the droplet region was meshed first, then the substrate layers were each discretized in order from top to bottom such that nodes were shared along common edges. The mesh generation technique used is an advancing front method adopted from the work of Peraire et al. (1987). Once the solution domain is fully discretized, Laplacian smoothing (Field, 1988) is applied to the resulting mesh (excluding the boundary nodes) to reduce localized mesh distortions.

A sample mesh is provided in Fig. 1(a). The mesh density function was fine, $ds = 0.02$, at the free surface, and varied linearly with distance from the free surface to a maximum value of $ds = 0.06$ within the droplet. The top substrate layer was discretized such that droplet and substrate nodes formed corresponding pairs in the contact region. Elements were created in the interface region by connecting corresponding pairs of nodes (Fig. 1(b)). In the substrate region the mesh density increased linearly from the contact area to a maximum value of $ds = 0.4$ at the lower boundary of the bottom substrate layer.

A full-bandwidth solver was used to solve the nonsymmetric discretized fluid dynamics equations in the droplet domain, while a half-bandwidth solver was used to solve the symmetric discretized energy equations on the combined droplet/substrate mesh. To reduce solution times, the Cuthill–McKee algorithm (Collins, 1973) was applied to obtain optimum node numberings for the droplet mesh in the fluid dynamics calculation and for the combined droplet/substrate mesh in the heat transfer calculation.

According to Bach and Hassager (1985) one velocity and one force condition must be prescribed at the boundary node, which represents the dynamic contact line. The contact point is characterized by $v = 0$ (no penetration) and the force boundary condition expressed by Eq. (7). The formulation herein, following the approach of Bach and Hassager (1985), does not force the contact angle to assume a specific value. The assumption is made that this interfacial force is given by the equilibrium surface tension coefficients of the joining phases. Since a wetting condition is most important at the end of the spreading process, this study will focus on the initial, inertia-dominated flow. Also, for solder-drop-printing, solidification is likely to occur very quickly at the contact area, eliminating the need for a wetting condition altogether.

Results and Discussion

The numerical simulations in this study examine the effects of impact velocity, droplet diameter, and substrate material on the droplet deformation process and on the temperature distributions within the droplet and substrate regions. All parameter variations are made with respect to the following baseline condition: a 50 μm, 63 percent Sn–37 percent Pb solder droplet initially traveling at 2.0 m/s impacting a 8.9-μm-thick layer of copper on a thick layer of FR-4 epoxy–glass composite, where the contact area is characterized by an interfacial heat transfer coefficient of 5.0×10^7 W/m^2·K. Since the energy equation has been nondimensionalized, the actual values for the initial temperatures are unimportant. The following thermophysical properties were used for the molten solder droplets: surface tension coefficient $\gamma = 0.345$ N/m, density $\rho = 8218$ kg/m^3, viscosity $\mu = 0.00262$ kg/m·s, specific heat $c_p = 238$ J/kg·K, and thermal conductivity $k = 25$ W/m·K. For the substrate, the density, thermal conductivity, and specific heat used were 8933 kg/m^3, 401 W/m·K, and 385 J/kg·K for copper and 1924 kg/m^3, 0.26 W/m·K, and 1570 J/kg·K for the FR-4 material.

A detailed study was performed by Zhao (1994) to determine the temporal and spatial discretization necessary to obtain time step and grid insensitive solutions. A typical simulation was characterized by a droplet mesh of 600 nodes and 1200 elements, a substrate mesh of 1200 nodes and 2200 elements, and a time step $\Delta\tau$ of 5×10^{-4}. Implementation of the advancing front mesh generation technique represented a significant improvement over early simulations (Fukai et al., 1993) by reducing the overall problem size, while creating meshes of near optimally shaped elements with mesh refinement in the required regions. The computations were carried out on a Hewlett Packard 9000 Series 735 workstation, where a typical run required approximately 100 CPU hours to complete 2000 time steps.

The results of four simulations were chosen to demonstrate the effects of various parameter variations. The overall droplet deformation as well as the velocity and temperature distributions at time steps corresponding to $t = 5$ and 20 μs are shown in Figs. 2 and 3. In these four cases the interfacial heat transfer coefficient is set to a large value: $h_c = 5 \times 10^7$ W/m^2·K. Figures 2 and 3 depict the results of four test cases at two different instants in time to facilitate comparison among the test cases at the same instant in time or at two instants in time for any particular case. To show the results more clearly, the elements were mirrored about the z axis and plotted with the velocity distribution on the left and the temperature field on the right. Only a small portion of the substrate is shown in each figure. The droplets appear to have the same initial size in each case because the results are plotted with respect to the dimensionless coordinates, R and Z.

Numerical results for the baseline case, which corresponds to Re = 314, We = 4.76, Fr = 8155, Pr = 0.025, and $\text{Bi}_c = 1.0 \times 10^3$, are shown in Figs. 2($a$) and 3($a$). The relative importance of viscous and surface tension forces is evident as the droplet spreads to only about 1.4 times its original diameter before flow reversal (recoiling) begins. The problem is characterized by very fast transients as after only 20 μs, spreading has halted, and the bulk of the droplet has cooled to 60 percent of its initial temperature. At this extreme, mass accumulation about the periphery is apparent, and the droplet assumes a doughnut shape. It is also clear in the figures that for a high value of h_c, the spreading and cooling of the droplet occur simultaneously, which is in agreement with the findings of Trapaga and Szekely (1991). The heat conduction within the substrate is almost exclusively radial in the copper layer because the thermal diffusivity, $\alpha = k/\rho c_p$, of that material is about four orders of magnitude greater than that of the FR-4 layer, which essentially behaves as a thermal insulator in this case.

The effect of decreased droplet diameter is illustrated by comparison of cases (a) and (b) in Figs. 2 and 3. In case (b) the initial droplet diameter was reduced to 25 μm, while all other parameters remained the same as case (a). In comparison, the most striking feature of this run is that the droplet spreading stops and recoiling begins much sooner than the baseline case: by more than a factor of two. In Fig. 3(b), the smaller droplet is beginning a second downward cycle after having previously

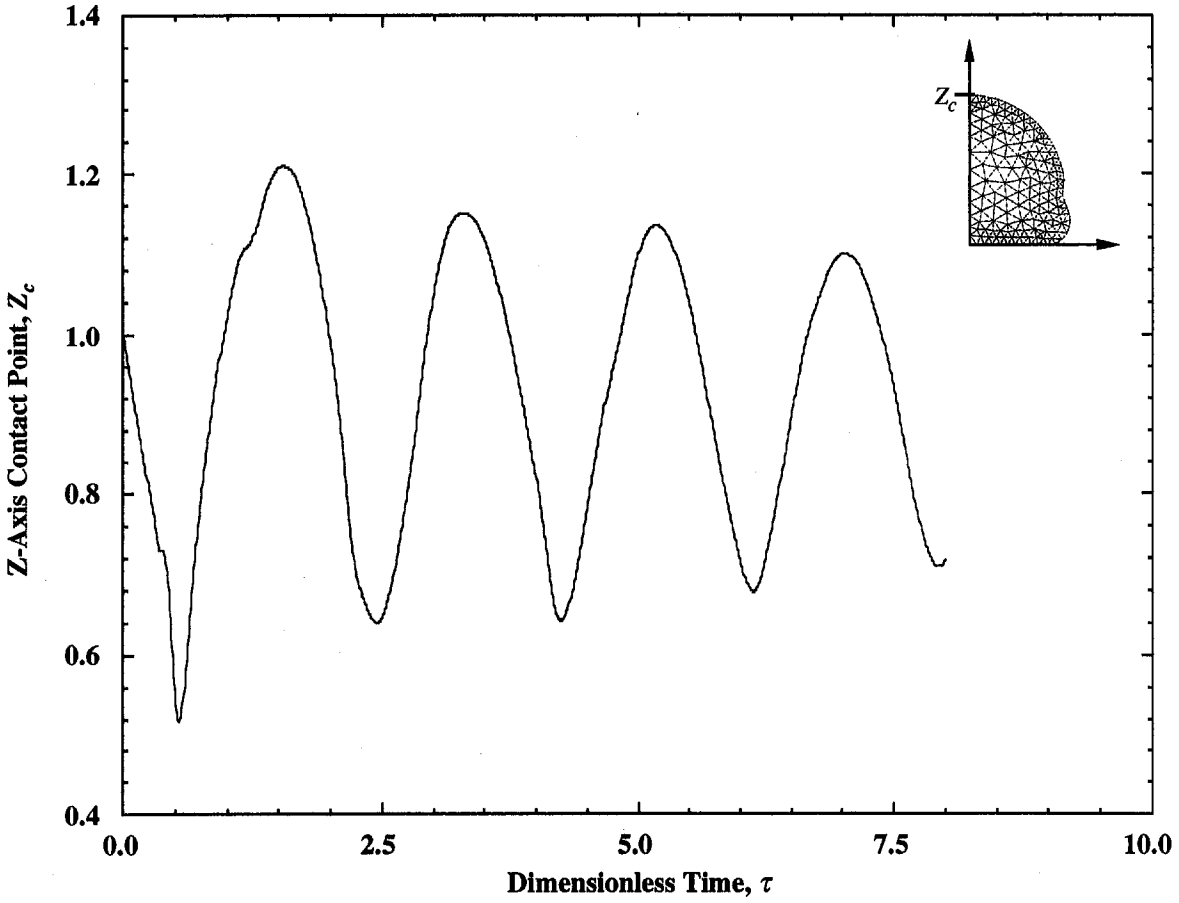

Fig. 5 The *z*-axis contact point as a function of time for v_0 = 2 m/s, d_0 = 25 μm case

flattened out (see Fig. 2(b)), and subsequently recoiled up along the z axis. Also, the droplet does not spread as far in the radial direction. Since the droplet does not deform as drastically in this case, the temperature variation within the fluid is predominantly axial.

Case (c) in Figs. 2 and 3 corresponds to an increase in the initial impact velocity to v_o = 4.0 m/s. This simulation is characterized by greater droplet deformation compared to the baseline case. Due to the greater inertial force, the droplet spreads further, and at t = 20.0 μs, fluid is almost entirely eliminated from the center. The increased fluid motion and the additional contact area between the droplet and the substrate enhance the heat transfer at the interface, which results in a more significant thermal penetration into the substrate.

In case (d), the baseline substrate was replaced by a 1.3-μm-thick layer of gold on a relatively thick slab of silicon. The density, thermal conductivity, and specific heat used were 19,300 kg/m^3, 311 W/m·K, and 131 J/kg·K for gold and 2330 kg/m^3, 105 W/m·K, and 785 J/kg·K for silicon. The fluid dynamics and interfacial thermal resistance are identical to case (a). Since the gold layer is thin and its thermal diffusivity is similar to silicon (α_{Si}/α_{Au} = 0.47), this layer has very little impact on the substrate temperature profile, which is two dimensional (see Figs. 2(d) and 3(d)). By comparing cases (a) and (d) in Figs. 2 and 3, it is clear that the droplet is cooled by the copper layer in case (a) and by the bulk of the silicon in case (d). Since the thermal diffusivity of copper is roughly twice that of silicon, the droplet cools more in case (a), but the enhanced cooling potential may have been reduced by the relatively thin layer of copper modeled. This suggests the thickness of the copper layer should be investigated as a process parameter for solder bumps deposited on FR-4.

Figure 4 shows the effect of droplet impact velocity and diameter on the maximum deposit radius and on the z-axis contact point. In this figure an increase of either the impact velocity or the droplet diameter enhances droplet deformation in both the axial and radial directions; however, increasing the velocity appears to have a more significant effect. This behavior may be explained qualitatively by examination of the Weber number, which is indicative of the ratio of inertia forces to surface tension forces, and the Reynolds number, which represents the ratio of inertia forces to viscous forces. While the Weber number depends on the second power of velocity and the first power of diameter, the Reynolds number varies linearly with both velocity and diameter. Thus, an increase of either the velocity or the diameter is indicative of greater inertia forces, which serve to enhance axial and radial deformation with respect to the retarding forces; however, a velocity increase has a more pronounced effect.

In Fig. 5 the z-axis contact point for the d_0 = 25.0 μm, v_0 = 2.0 m/s case is plotted as a function of dimensionless time for four droplet oscillations. The plot is shown to illustrate the damped oscillatory behavior that is likely to exist if solidification occurs slowly with respect to droplet dynamics. When the droplet solidifies, its latent heat is liberated, delaying the cooling of the remaining liquid in the droplet. Also, solidification is initiated in the area of contact, then propagates upward. Once this region solidifies, the wetting behavior is no longer an issue.

The accuracy of the numerical procedure was tested against the experimental results of Zhao (1994) and Zhao et al. (1996), who used holographic and photoelectric methods to measure the spreading behavior of a droplet deposited vertically on a horizontal quartz plate. Note that experimental results involving solder droplets are indeed scarce. A curve produced by the

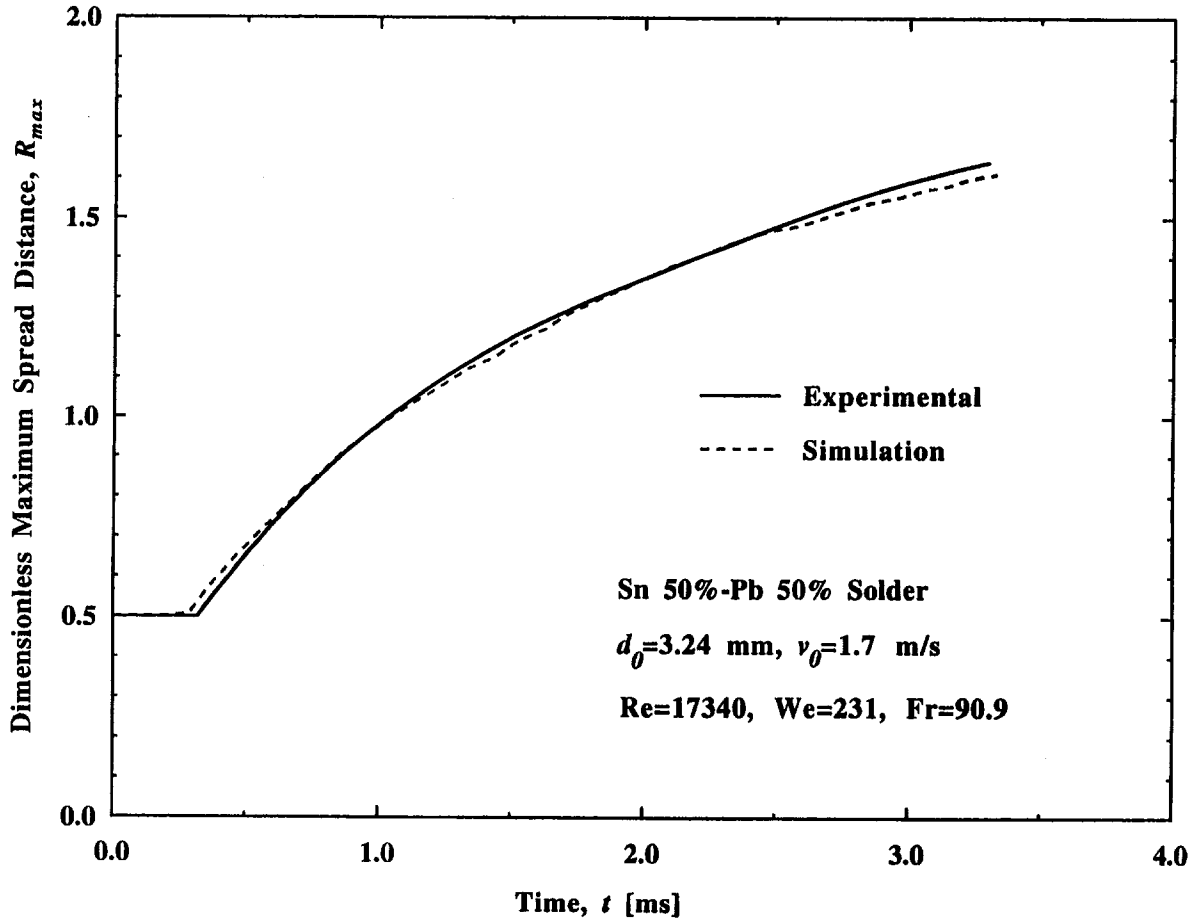

Fig. 6 Comparison of experimental and simulated maximum spread radius versus time

experiments is provided in Fig. 6 for a 3.24 mm, 50 percent Sn–50 percent Pb solder droplet impacting at 1.7 m/s. Results are also shown for a simulation for the same conditions, which differed from the experimental results by a maximum of only 3 percent.

Scanning electron micrographs are shown in Fig. 7 of single 63 percent Sn–37 percent Pb solder droplets deposited on (*a*) a 120°C gold/silicon substrate, and (*b*) a 25°C copper layer. The undesirable solder bump in Fig. 7(*b*) displays a wavy irregularity of the surface, which could be explained by the damped oscillations seen in Fig. 5. In contrast, the bump in Fig. 7(*a*) looks very much like a sessile droplet, suggesting that any oscillations in this case have subsided before the droplet has solidified. Since the freezing temperature of this solder is 183°C, it is quite reasonable to expect the droplet on the 25°C substrate to cool and solidify more quickly than the droplet on the 120°C substrate.

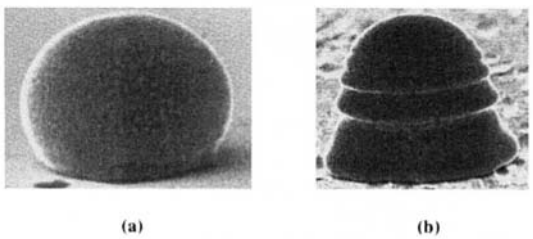

Fig. 7 Scanning electron micrographs of single solder bumps: (*a*) desirable bump geometry, (*b*) undesirable bump geometry

Conclusions

This article has presented a theoretical study of the presolidification fluid mechanics and heat transfer associated with molten solder droplets impacting a multilayer, composite substrate. This problem is of central importance to the novel manufacturing process of picoliter solder-drop-printing for the mounting of microelectronic components.

The results documented the effects of impact velocity, initial droplet diameter, and substrate thermophysical properties on the heat transfer and fluid dynamics of a deforming 63 percent Sn–37 percent Pb solder droplet. Droplet recoiling and mass accumulation around the deposit periphery yielded a nonmonotonic dependence of the maximum deposit radius on time. The droplet spreading was retarded and finally halted by the action of the surface tension and viscosity. Subsequently, flow reversal was observed and the bulk flow was directed toward the axis of symmetry.

As the impact velocity of the droplet increased, the predicted temperature distribution in a molten metal droplet exhibited an increasingly two-dimensional nature. The numerical model predicted that the heat transfer time scales were comparable to the droplet deformation time scales for low thermal contact resistance scenarios, which are expected to exist in the presolidification phase of the solder bump creation.

Finally, scanning electron micrographs of single droplets deposited on different substrates were shown. Qualitatively, distinguishing features of these solidified droplets may be explained by flow behaviors revealed in the numerical simulations. Multiple oscillations of the droplet were observed in the theoretical modeling and are likely the cause of undesirable solder bump

shapes. The relative time scales of fluid motion and solidification are key in the determination of the final bump geometry. For this reason the theoretical model will be expanded in future studies to include solidification.

Acknowledgments

Financial support for the work reported in this paper provided by MicroFab Inc. is gratefully acknowledged.

References

Bach, P., and Hassager, O., 1985, "An Algorithm for the Use of the Lagrangian Specification in Newtonian Fluid Mechanics and Application to Free-Surface Flow," *J. Fluid Mech.,* Vol. 152, pp. 173–190.

Collins, R. J., 1973, "Bandwidth Reduction by Automatic Renumbering," *Int. J. Num. Meth. Engng.,* Vol. 6, pp. 345–356.

Dussan, E. B., V, 1979, "On the Spreading of Liquids on Solid Surfaces: Static and Dynamic Contact Lines," *Annu. Rev. Fluid Mech.,* Vol. 11, pp. 371–400.

Field, D. A., 1988, "Laplacian Smoothing and Delaunay Triangulations," *Comm. Appl. Num. Meth.,* Vol. 4, pp. 709–712.

Frederiksen, C. S., and Watts, A. M., 1981, "Finite Element Method for Time-Dependent Incompressible Free Surface Flow," *J. Comp. Phys.,* Vol. 39, pp. 282–304.

Fukai, J., Zhao, Z., Poulikakos, D., Megaridis, C., and Miyatake, O., 1993, "Modeling of the Deformation of a Liquid Droplet Impinging Upon a Flat Surface," *Phys. Fluids A,* Vol. 5, pp. 2588–2599.

Fukai, J., Shiiba, Y., Miyatake, O., Poulikakos, D., Megaridis, C., and Zhao, Z., 1995, "Wetting Effects on the Spreading of a Liquid Droplet Colliding With a Flat Surface: Experiment and Modeling," *Phys. Fluids A,* Vol. 7, pp. 236–237.

Haley, P. J., and Miksis, M. J., 1991, "The Effect of the Contact Line on Droplet Spreading," *J. Fluid Mech.,* Vol. 223, pp. 57–81.

Harlow, F. H., and Welch, J. E. W., 1965, "Numerical Calculation of Time-Dependent Viscous Incompressible Flow of Fluid With Free Surface," *Phys. Fluids,* Vol. 8, pp. 2182–2189.

Harlow, F. H., and Shannon, J. P., 1967, "The Splash of a Liquid Droplet," *J. Appl. Phys.,* Vol. 38, pp. 3855–3866.

Hayes, D. J., Wallace, D. B., and Boldman, M. T., 1992, "Picoliter Solder Droplet Dispension," *ISHM '92 Proceedings,* pp. 316–321.

Hirt, C. W., and Nichols, B. D., 1980, "Adding Limited Compressibility to Incompressible Hydrocodes," *J. Comp. Phys.,* Vol. 34, pp. 390–400.

Huh, E., and Scriven, L. E., 1971, "Hydrodynamic Model of Steady Movement of a Solid/Liquid/Fluid Contact Line," *J. Colloid Interface Sci.,* Vol. 35, pp. 85–101.

Jones, H., 1971, "Cooling, Freezing, and Substrate Impact of Droplets Formed by Rotary Atomization," *J. Phys. D: Applied Physics,* Vol. 4, pp. 1657–1660.

Kawahara, M., and Hirano, H., 1983, "A Finite Element Method for High Reynolds Number Viscous Fluid Flow Using a Two Step Explicit Scheme," *Int. J. Num. Meth. Fluids,* Vol. 3, pp. 137–163.

Madejski, J., 1976, "Solidification of Droplets on a Cold Surface," *Int. J. Heat Mass Transfer,* Vol. 19, pp. 1009–1013.

Madejski, J., 1983, "Droplets on Impact With a Solid Surface," *Int. J. Heat Mass Transfer,* Vol. 26, pp. 1095–1098.

Peraire, J., Vahdati, K., Morgan, K., and Zienkiewicz, O. C., 1987, "Adaptive Remeshing for Compressible Flow Configurations," *J. Comp. Phys.,* Vol. 72, pp. 449–466.

Silliman, W. J., and Scriven, L. E., 1980, "Separating Flow Near a Static Contact: Slip at a Wall and Shape of a Free Surface," *J. Comp. Phys.,* Vol. 34, pp. 287–313.

Trapaga, G., and Szekely, J., 1991, "Mathematical Modeling of the Isothermal Impingement of Liquid Droplets in Spray Processes," *Metall. Trans. B,* Vol. 22, pp. 901–914.

Wang, G. X., and Matthys, E. F., 1991, "Modelling of Heat Transfer and Solidification During Splat Cooling: Effect of Splat Thickness and Splat/Substrate Thermal Contact," *Int. J. Rapid Solidification,* Vol. 6, pp. 141–174.

Zhao, Z., 1994, "Transport Phenomena During the Impingement of Liquid Metal Droplets on a Substrate," Ph.D Thesis, University of Illinois at Chicago, Chicago, IL.

Zhao, Z., Poulikakos, D., and Fukai, J., 1996, "Heat Transfer and Fluid Dynamics During the Collision of a Liquid Droplet on a Substrate: Part II—Experiments," *Int. J. Heat Mass Transfer,* in press.

Experimental Investigation of Interfacial Thermal Conductance for Molten Metal Solidification on a Substrate

G.-X. Wang

E. F. Matthys

Department of Mechanical and Environmental Engineering, University of California, Santa Barbara, CA 93106

Experiments have been conducted to quantify the interfacial thermal conductance between molten copper and a cold metallic substrate, and in particular to investigate the heat transfer variation as the initial liquid/solid contact becomes a solid/solid contact after nucleation. A high heat transfer coefficient during the earlier liquid cooling phase and a lower heat transfer coefficient during the subsequent solid splat cooling phase were estimated through matching of model calculations and measured temperature history of the sample. The dynamic variations in the interfacial heat transfer resulting from the solidification process were quantified for splat cooling and were found to be affected by the melt superheat, the substrate material, and the substrate surface finish.

1 Introduction

Thermal conductance at the melt/substrate interface is an important issue in many material processes, such as mold casting, strip and slab casting, splat cooling, melt-spinning, spray deposition, etc. In all these processes, the molten metal is brought in contact with a colder substrate, and the heat is transferred from the melt into this substrate. The heat transfer rate is, however, often limited by the thermal resistance at the melt/substrate interface, which results from nonperfect contact. Previous analyses (Ruhl, 1967; Wang and Matthys, 1991) confirmed that this interfacial heat transfer is one of the most important parameters controlling the melt cooling and solidification processes. It is therefore essential to understand and quantify the thermal conductance between the melt or solidified metal and the substrate during the melt spreading and cooling, melt solidification, and solid cooling phases.

Because of its importance in engineering applications, the interfacial heat transfer has been studied under various processing conditions for some time. More recently, particular attention has been paid to fast solidification processes such as in splat cooling (for example Mizukami et al., 1992; Bennett and Poulikakos, 1994; Loulou et al., 1994; Wang and Matthys, 1994; Liu et al., 1995). The dynamics of this solidification process are similar in nature to those in chill casting, strip casting, melt-spinning, etc., in that all these processes involve a thin molten metal layer put in sudden contact with a colder substrate. One anticipates, therefore, that a comprehensive study of the interfacial heat transfer during splat cooling will provide us not only with the means to develop a better understanding of the fundamentals of this thermal contact problem, but also with more accurate engineering data applicable to these other processes.

Except for the work of Mizukami et al. (1992), who used stainless steel as a working material, the previous studies used low-melting-point metals such as lead (Bennett and Poulikakos, 1994) or tin (Loulou et al., 1994; Wang and Matthys, 1994) because of their easy handling characteristics. Those low-melting-point metals, however, have physical properties that may affect the interfacial contact behavior in different ways than the high-temperature ones could. In an earlier phase of this work (Liu et al., 1995), however, we obtained some preliminary results on the interfacial heat transfer coefficient (h) for nickel (a high melting temperature material) drops impacting on various substrates.

In the present paper, we describe some new experimental results for copper splat cooling. We are now able to quantify the interfacial thermal conductance between the molten copper and various cold substrates, and also the difference in conductance between liquid/solid contact and solid/solid contact. This was made possible by the use of a fast-response pyrometer, which gives us a high-resolution temperature history of the splat top surface, especially during the initial melt cooling phase. The changes in interfacial heat transfer induced by solidification are also discussed.

2 Experimental Setup

Figure 1 shows a schematic of our free-fall splat cooling setup. (A more detailed description of the system is given elsewhere (Wang, 1995).) The two main parts of the setup are the levitation coil and the target substrate, which are enclosed in a chamber filled with an argon and helium mixture at a pressure slightly above atmospheric. The substrate is positioned underneath the levitation coil, allowing for a release height varying from 90 mm to 185 mm. Arc-melted 99.9 percent pure copper droplets of about 0.5 to 0.6 g are melted in the levitation coil and then dropped on an inclined substrate to form a thin splat.

Three metallic substrates were prepared for our experiments: copper, aluminum, and stainless steel (AISI 440C). The substrates were all machined to 76 mm × 38 mm × 12.5 mm, with the exception of the stainless steel ones, which are only 10 mm in thickness. All of the substrates were first finished with a surface grinder with a fine grit ceramic wheel (and are referred hereafter as "Ground" surfaces). In some cases, the substrates were then further polished by abrasive paper (e.g., "grit #240" surface) or bead-blasted. The beads used were of two different sizes: "coarse" beads with diameters ranging from 406 to 432 μm ("Blasted-C" surface) and "fine" beads with 89 to 150 μm diameter ("Blasted-F" surface).

The splat top surface temperature was measured by a one-color infrared pyrometer with a response time of about 1.5 ms

Contributed by the Heat Transfer Division and presented at the National Heat Transfer Conference, Portland, Oregon, August 5–9, 1995. Manuscript received by the Heat Transfer Division April 1995; revision received October 1995. Keywords: Liquid Metals, Materials Processing and Manufacturing Processes, Phase-Change Phenomena. Associate Technical Editor: T. L. Bergman.

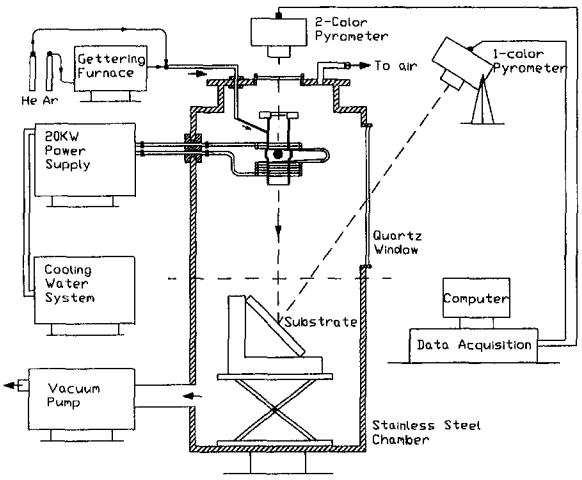

Fig. 1 Schematic of the experimental setup

and a temperature range from 1173 K to 1573 K. The pyrometer was connected to a data-acquisition system. A two-color pyrometer with a response time of about 25 ms was also used to measure the temperature of the molten copper droplet while levitating and at release. In addition, a K-type thermocouple was attached to the top substrate surface close to the location where the molten metal droplet impacts. This thermocouple was used to measure the initial substrate temperature (T_{SO}) before the molten metal impacted on the substrate. The part of the splat seen by the pyrometer was located through the pyrometer's eyepiece after each experiment. The average splat thickness (b) used in the model calculations was then calculated from numerous measurements obtained across this particular area with a micrometer fitted with a fine aluminum tip.

After each experiment, the pyrometer analog output data were converted into splat surface temperature data. Given the known splat thickness (b), the initial melt temperature upon impact (T_P), and the initial substrate temperature (T_{SO}), the temperature variation of the splat top surface can then be calculated for any interfacial heat transfer coefficient h by a splat cooling solidification model (Wang and Matthys, 1992; Liu et al., 1995). This model assumes one-dimensional heat transfer and solidification in the splat, and includes heat transfer in the substrate, which is treated as a semi-infinite body with an initially uniform temperature T_{SO}. In the present work, we excluded melt undercooling in the model, but included radiation heat loss from the top surface based on a surface emissivity value estimated from our experiments. (In the earlier phases of the process, both radiative and convective cooling at the top surface are very small (<1 percent) compared to the substrate cooling. Later, even if radiation becomes somewhat more significant (i.e., <5 percent) as the surface emissivity increases, the convection is proportionally smaller. Accordingly, convective heat transfer is neglected in this model.) By matching the top surface temperature of the splat calculated for a number of values for h with the experimental measurements through an iteration and interpolation procedure, we could then generate estimates of h for the particular experimental conditions used. More detailed descriptions of this model and of the temperature matching process used can be found in earlier articles (Liu et al., 1995; Wang, 1995).

3 Experimental Results and Discussion

The interfacial thermal conductance problem for molten copper impacting on various substrates has been studied with our experimental setup. Experience shows that regular and hole-free splats are more readily generated on some substrates than on others, presumably because of wettability issues. For example, in most cases, a fairly smooth and uniform splat can be generated on a copper substrate with various surface finishes, but it is difficult to generate good splats on stainless steel and aluminum substrates with some surface finishes. In the latter cases, either the molten droplet does not spread uniformly or the formed splats contain many small holes. The interfacial heat transfer coefficients were estimated then only for the substrate finishes giving good splats of well-defined thickness. Because of this limitation, only qualitative observations can be made at this time about the effect of substrate material and surface preparation on the interfacial heat transfer. The experimental configuration used for the data shown here was a free-fall height H of 90 mm and a 45 deg inclination of the substrate (which results in thinner and flatter splats).

3.1 Pyrometer Readings and Temperature Conversion. Figure 2 shows a typical pyrometer analog output for a copper splat cooling on a coarse-bead-blasted copper substrate ("Blasted-C" Cu). In this figure, $t = 0$ (not shown) is the time when the acquisition system was triggered; the molten copper droplet impacted on the substrate at about $t = 0.455$ s.

The entire process can be divided for simplicity into four different stages as shown by the vertical lines in the figure: Stage I from t_0 to t_1 (melt spreading); Stage II from t_1 to t_2 (liquid cooling); Stage III from t_2 to t_3 (solidification); and Stage IV after t_3 (solid cooling). The first stage corresponds to the initial impact and melt spreading process, with t_0 the approximate time when the molten droplet touches the substrate and t_1 the time at the end of the melt spreading process. (Note that the duration of this phase is indeed very consistent with our results of direct visualization of the drop impact and spreading by high-speed cameras (Trapaga et al., 1992).) The second stage covers the period from t_1 to t_2, where t_2 is the time when the pyrometer output reaches a plateau. This stage shows a fast decrease in the pyrometer's output (i.e., a fast decrease in the surface temperature), which, calculations suggest, corresponds to cooling of the splat still fully in the liquid state. The third

Nomenclature

b = thickness of the splat, μm
C_P = specific heat capacity, J/kg K
h = interfacial heat transfer coefficient, W/m^2 K
h_0 = interfacial heat transfer during melt spreading, W/m^2 K
h_1 = interfacial heat transfer coefficient in the earlier stage of splat cooling, W/m^2 K
h_2 = interfacial heat transfer coefficient during solidification, W/m^2 K
h_3 = interfacial heat transfer coefficient after solidification, W/m^2 K
H = height of droplet free fall, mm
L = latent heat of solidification, J/kg
t = time, ms or s
t_1 = transition time from h_0 to h_1, ms
t_2 = transition time from h_1 to h_2, ms
t_3 = transition time from h_2 to h_3, ms
t_N = calculated nucleation time, ms
T_{SO} = substrate initial temperature, K
T_M = equilibrium melting temperature, K
T_P = temperature of the superheated melt upon impact, K
ΔT_P = melt superheat upon impact, K
ϵ = average emissivity of the splat surface
θ = substrate inclination angle
λ = thermal conductivity, W/m K
ρ = density, kg/m^3

Subscripts

L = liquid
S = solid

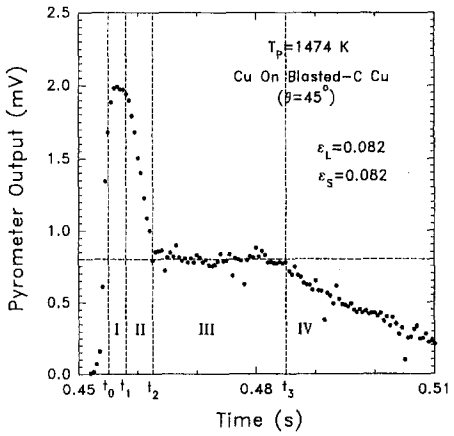

Fig. 2 Pyrometer output as a function of time for a molten copper droplet solidifying on an inclined blasted-coarse copper substrate [T_p = 1474 K, b = 190 μm, T_{SO} = 313 K, H = 90 mm, θ = 45 deg, ϵ_L = 0.082, ϵ_S = 0.082]

stage covers the plateau, which is believed to be a period of quasi-isothermal splat solidification. The end of the plateau (t_3) corresponds then to the completion of the solidification process. The last stage, stage IV, covers the solid splat cooling. (It should be noted that the division in four phases discussed above pertains to the present conditions, and may not necessarily be applicable in other cases such as for very small droplet sizes, for example, where solidification may happen fast compared to spreading.)

The plateau and absence of recalescence indicate that no significant melt undercooling exists under the present experimental conditions. Because the high thermal conductivity of copper results in small temperature gradients in the melt, the plateau in the pyrometer reading should then reflect a top surface temperature during splat solidification that remains close to the melting temperature of pure copper. Given the pyrometer output and its blackbody calibration curve, one can then determine the emissivity of the liquid copper surface at this known temperature. For these data, the emissivity of the molten copper splat surface at the melting temperature was estimated in this manner to be ϵ_L = 0.082. In addition, the constant pyrometer output during solidification suggests also that the radiative properties of the splat surface remain unchanged as the liquid surface becomes a solid surface. Accordingly, the same value was used for the emissivity of the solid splat surface.

The radiation properties of a solidifying splat surface may also vary during solidification, however, as the top surface changes from a liquid phase to a solid phase. One typical example is shown in Fig. 3 for copper splat cooling on a ground copper substrate. As shown more clearly in the inset, after a few milliseconds, the pyrometer output decreases quickly from an initial high value of about 3.0 mV to a value of 0.8 mV at 0.713 s. The decrease in the pyrometer reading then slows down and finally reaches a minimum of about 0.4 mV at 0.72 s. After that, it increases to a maximum of about 2.36 mV at 0.77 s. It remains at that level for about 10 ms and then decreases again to zero. A similar variation in pyrometer reading was also observed for a copper ingot surface (Wang, 1995), which, together with simultaneous thermocouple measurements, suggests that this large increase in pyrometer output from a minimum to a maximum is due to change in the surface emissivity rather than in temperature. If we use the same emissivity as that found in Fig. 2 for the liquid copper surface in the present case, we see that the 0.08 mV at the slowing down in pyrometer reading (at 0.713 s) corresponds precisely to the nominal melting temperature of copper. This value of emissivity used at the maximum output (3.0 mV) will also give us a temperature very close to the impact temperature of the drop, another confirmation of its validity. In other words, the event seen at 0.713 s likely corresponds to the splat top surface having reached the equilibrium melting temperature at that time (rather than the minimum at 0.717 s as one might have guessed at first). In addition, if there were undercooling, there would also not be a significant discontinuity in cooling rate at 0.713 s as seen in the graph, but rather a continuous decrease in temperature until solidification.

Our ingot solidification experiments, on the other hand, also suggest that the maximum output of the pyrometer at 0.782 s corresponds to the end of solidification, from which one can estimate the emissivity of the solid splat surface at the melting temperature: in this case, 0.238. The increase in emissivity between 0.72 and 0.77 s likely results from the progressive change from a liquid to a solid surface, which would, of course, in practice take place locally rather than all at once. The large difference between this type of signal and that shown in Fig. 2 could result from top surface contamination and nucleation as well as from variations in top surface roughness induced by variations in substrate condition.

Clearly, an adequate knowledge of the surface emissivity is essential to achieve an appropriate conversion of the pyrometer output into temperature data. For reference, it should be pointed out that very few data on high-temperature liquid and solid copper emissivities are available in the literature. We have therefore conducted extensive measurements of the emissivity of our copper splats. A more detailed description of the experimental setup and data processing can be found in Wang (1995). In all cases, the estimated liquid emissivity of copper was found to lie within the range of 0.07 to 0.085, but a broader range of 0.05 to 0.28 was found for the emissivity of the solid copper surfaces over the range of test conditions used. This large variation probably results from significant variations in the surface condition of the solidified copper.

For a given splat cooling experiment, however, a rather accurate estimate of the emissivities of both liquid and solid splat surfaces can be made directly from characteristic features of the pyrometer output curve as discussed for Figs. 2 and 3. The error in temperature conversion due to the uncertainty of surface emissivity is therefore greatly decreased. In addition, our emissivity experiments have also shown that the emissivity varies little with the temperature for either the liquid or solid surface over these ranges of temperature. The value of the emissivity estimated at the melting temperature in either liquid or solid phase can therefore be used to convert the pyrometer readings into temperature data over the whole temperature range covered in each phase, respectively. (In some cases, as seen above, the two values of emissivity may also be identical. The variation of emissivity during solidification itself has no effect on the

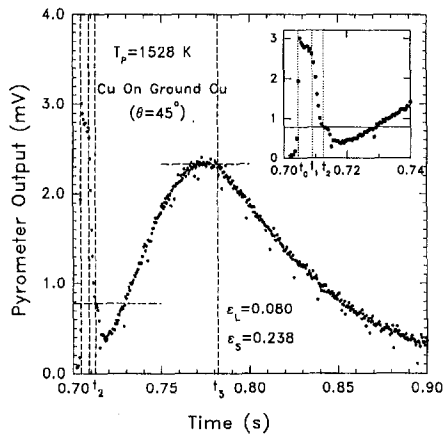

Fig. 3 Pyrometer output as a function of time for a molten copper droplet solidifying on an inclined ground copper substrate [T_p = 1528 K, b = 312 μm, T_{SO} = 315 K, H = 90 mm, θ = 45 deg, ϵ_L = 0.080, ϵ_S = 0.238]

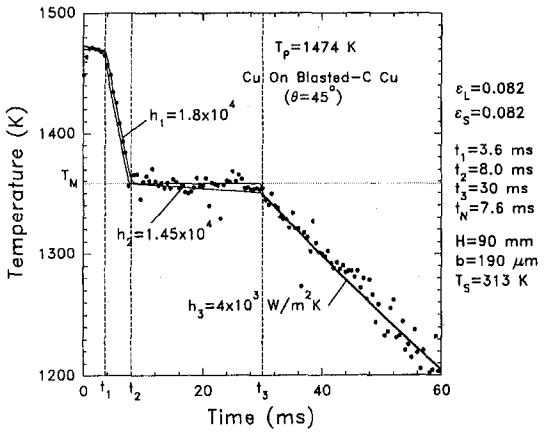

Fig. 4 Matching of calculations with converted experimental data for copper solidifying on an inclined blasted-coarse copper substrate. Solid symbols = converted experimental data; upper solid line = calculated temperature of splat top surface; lower solid line = calculated temperature of splat bottom surface [T_p = 1474 K, b = 190 μm, H = 90 mm, θ = 45 deg, T_{so} = 313 K, ϵ_L = 0.082, ϵ_S = 0.082].

calculations, though, because of the constancy in surface temperature during that phase.)

Figures 4 and 5 show the converted temperature data from Figs. 2 and 3, respectively. In the case of Fig. 4, the same emissivity (0.082) is used for both solid and liquid copper top surfaces. In the case of Fig. 5, however, different values of the emissivity for the liquid and solid phases are used: a "liquid" emissivity of 0.080 for the earlier 25 ms, and a "solid" emissivity of 0.238 for the remainder. As we see in Fig. 5, some temperature "data" (triangle symbols) below melting temperature are generated during solidification. These are an artifact of the constant values of emissivity used during this period of time, and should be disregarded. In principle, a varying emissivity should be used in this region and the converted temperature data should give a plateau at melting temperature, but we saw no purpose in artificially forcing the data to do so.

3.2 Estimation of h by Temperature Matching. The interfacial heat transfer coefficient, h, between the splat and the substrate can be determined through an iteration and interpolation procedure by matching the model calculations with the temperature data obtained from the converted pyrometer readings. (The materials properties used in the calculations are listed in Table 1.) In this study, a stepwise variation of h is used in order to simplify the estimation procedure. In agreement with the division of the process in distinct periods as discussed above for Fig. 2, we use four values of h assumed constant during each stage of splat cooling: h_0, during melt spreading (stage I, $t_0 \leq t < t_1$); h_1, during "liquid" cooling (stage II, $t_1 \leq t < t_2$); h_2, during "solidification" (stage III, $t_2 \leq t < t_3$); and h_3, during "solid" cooling (stage IV, $t_3 \leq t$).

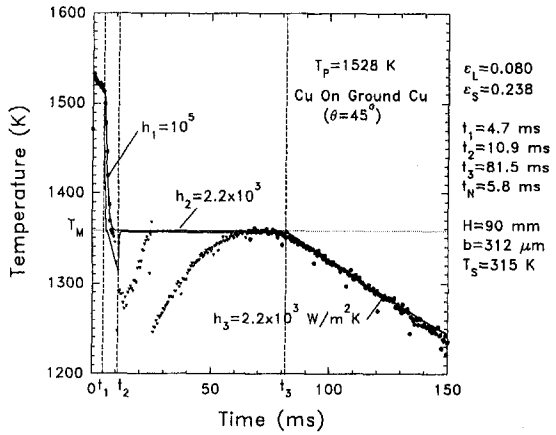

Fig. 5 Matching of calculations with converted experimental data for copper solidifying on an inclined ground copper substrate. Solid symbols = converted experimental data; upper solid line = calculated temperature of splat top surface; lower solid line = calculated temperature of splat bottom surface [T_p = 1528 K, b = 312 μm, H = 90 mm, θ = 45 deg, T_{so} = 315 K, ϵ_L = 0.080, ϵ_S = 0.238].

Table 1 Physical properties used in the calculations

	Units	Cu[1]	Cu[2]	Al[2]	SS[3]
T_m	K	1358			
L	kJ/kg	210			
C_{PL}	J/kg-K	495			
C_{PS}	J/kg-K	473	389	984	460
λ_L	W/m-K	166			
λ_S	W/m-K	334	394	238	24.2
ρ_L	kg/m^3	7940			
ρ_S	kg/m^3	8410	8900	2700	7800

1) At melting temperature and 2) at room temperature (Brandes (1983) and Metals handbook, 10th ed., Vol.2, ASM Intl., Metal Park, pp.1110-1112; p. 1143 (1990))
3) At room temperature (Metals handbook, 10th ed., Vol.1, ASM Intl., Metal Park, pp.195-199; p. 971 (1990))

In the case of Fig. 4 for copper at the initial temperature T_P = 1474 K quenched on a Blasted-C copper substrate, a rather good match between the calculations and the measurements can be obtained by choosing $h_1 = 1.8 \times 10^4$ W/m^2 K, $h_2 = 1.45 \times 10^4$ W/m^2 K, and $h_3 = 4 \times 10^3$ W/m^2 K with the transition times $t_2 = 8.0$ ms and $t_3 = 30$ ms after end of impact. These values of h_1 and h_2 are similar to those estimated by Mizukami et al. (1992) for initial stages of molten stainless steel solidification on a copper substrate. (The time scale used hereafter in the figures is with respect to end of impact.) It should also be noted that h_0, calculated to be about 800 W/m^2 K here, is of unclear validity because the one-dimensional model used is not suitable during stage I due to the varying melt thickness and the melt flow during spreading. To avoid misinterpretation, values for h_0 will therefore not be included in the figures and discussions hereafter. Note also that for very small droplets, spreading and solidification may be simultaneous and that only two parameters (a combined $h_0/h_1/h_2$ and a h_3) might then be meaningful for such a process.

The calculated temperatures of the splat top and bottom surfaces based on these values for h are also given for comparison in Fig. 4 (solid lines). Comparing these temperatures suggests that the temperature difference across the splat is very small (<10 K) during the entire process. h_1 should represent here an average interfacial heat transfer coefficient during the period of time when the splat is still liquid, and when a liquid/solid contact condition exists at the interface. This is suggested by the calculated temperature at the splat bottom surface, which is always higher than the melting temperature between t_1 and t_2. The transition from a liquid/solid contact to a solid/solid contact occurs around t_2 because the latter is very close to the calculated nucleation time (t_N = 7.6 ms). Thus h_2 should represent the average thermal conductance during splat solidification; and h_3 represents the average thermal conductance during solid splat cooling.

This division of the process in successive phases appears appropriate for most of the experiments we performed. One exception does, however, exist for copper quenched on a ground copper surface, as shown in Fig. 5. In this case, a much higher h_1 (10^5 W/m^2 K) is estimated through the temperature matching procedure. This h_1 (between t_1 and t_2) represents, however, now mostly a solid/solid contact condition because solidification is calculated to start at t_N = 5.8 ms, which is very close to t_1 = 4.7 ms. In other words, the fully liquid cooling region is too

short to be detected under these conditions. In this case, the transition time t_2 from a higher h_1 to a much lower h_2 does not correspond directly to a change from liquid/solid to solid/solid contact at the interface as shown in Fig. 4. Instead, t_2 probably corresponds to a change in the thermal contact from better to poorer, which may result from the contraction of the solidified part of the copper splat. (The poor contact could then in turn result in the top surface temperature becoming close to melting temperature.) If the thermal contact after t_2 does not change much as the splat solidifies and then cools down as a solid (i.e., $h_2 = h_3$), then t_2 can be back calculated from the total solidification time t_3, which is more easily identified on the curve. A single constant value of h from t_2 to the end of the process is indeed sufficient here for good match, suggesting no further change in thermal contact.

The uncertainty on the estimated h_1, h_2, and h_3 results primarily from the uncertainties in splat thickness b, initial melt temperature T_P, substrate temperature T_{SO}, and the temperature matching process itself, with the other parameters contributing to a smaller extent. The uncertainty on the initial melt temperature T_P, in turn, results from the uncertainty in the estimated surface emissivity ϵ. Mathematically, we can express h_1 as a function of those parameters:

$$h_1 = h_1(b, \epsilon, T_S, \text{matching process})$$

Therefore, the relative uncertainty on h_1 can be calculated by (Kline, 1985)

$$\left(\frac{P_{h_1}}{h_1}\right)^2 = \left(\frac{\partial \ln h_1}{\partial \ln b}\frac{P_b}{b}\right)^2 + \left(\frac{\partial \ln h_1}{\partial \ln \epsilon}\frac{P_\epsilon}{\epsilon}\right)^2 + \left(\frac{\partial \ln h_1}{\partial \ln T_S}\frac{P_{T_S}}{T_S}\right)^2 + \left(\frac{P_{MP}}{h_1}\right)^2$$

if the uncertainties due to bias errors in these parameters are much smaller than the uncertainties due to random errors, as is the case here. P_{h1} is the absolute uncertainty on h_1 resulting from random errors in the measured parameters and also from the matching process. P_b/b, P_ϵ/ϵ, $P_{T_{SO}}/T_{SO}$ are the relative errors on the average splat thickness, surface emissivity, and substrate temperature, which are estimated to be about 0.20 (when the splat is very rough), 0.10, and 0.05, respectively. A level of uncertainty is also introduced through manual interpolation during temperature matching between experimental and calculated data. It is represented by the term P_{MP}/h_1 and is estimated to be about 20 percent. The sensitivity coefficients, $\partial(\ln h_1)/\partial(\ln b)$, $\partial(\ln h_1)/\partial(\ln \epsilon)$, and $\partial(\ln h_1)/\partial(\ln T_{SO})$, can be estimated by model calculations and are about 3, 2, and 0, respectively. Therefore, a conservative estimate of the total uncertainty on h_1 is about 65 percent. The main contribution to this uncertainty in h_1 results from the uncertainty in splat thickness because of the large corresponding sensitivity factor. The sensitivity coefficient of h_3 with respect to b is about 1 only and its sensitivity coefficients with respect to ϵ and T_{SO} are close to zero. The uncertainty in estimated h_3 is therefore less than about 30 percent. In addition to the factors given above, the uncertainty on h_2 is also affected by the accuracy of our estimates of the solidification time, which varies from one experiment to another. The uncertainty of h_2 may therefore be either larger or smaller than that of h_1, depending on the experimental conditions. In addition, several repeatability tests have been performed. For these Cu on Cu experimental conditions, the variations in estimated h under the same experimental conditions were less than 5 percent for h_1 and 10 percent for h_2 and h_3, which are smaller than the corresponding estimated upper level of uncertainties. Our experimental results also indicate that, under these test conditions, the effect of the droplet size, the free fall distance, and the substrate inclination angle are quite small compared to the uncertainty in estimated interfacial heat transfer coefficients.

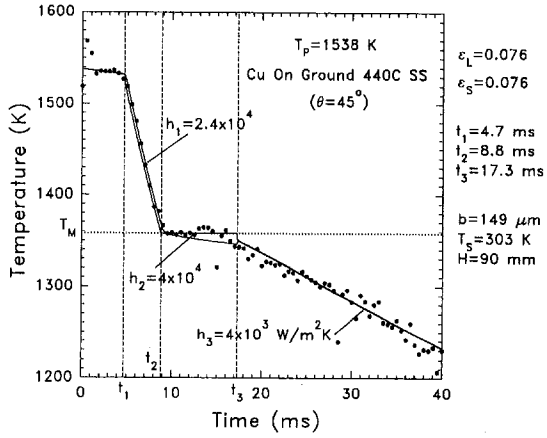

Fig. 6 Matching of calculations with converted experimental data for copper solidifying on an inclined ground stainless steel substrate. Solid symbols = converted experimental data; upper solid line = calculated temperature of splat top surface; lower solid line = calculated temperature of splat bottom surface [T_p = 1538 K, b = 149 μm, H = 90 mm, θ = 45 deg, T_{SO} = 303 K, ϵ_L = 0.076, ϵ_S = 0.076].

3.3 Variations in Thermal Contact for Copper Splat Cooling. Some interesting variations in thermal contact for copper splat cooling can be seen from comparing the values of h_1, h_2, and h_3. In the case of Fig. 4 for example, $h_1 > h_2 > h_3$. A h_3 lower than h_1 suggests a better thermal contact between the liquid splat and the substrate than that between the solid splat and the substrate, as one might expect. This transition from better to poor contact may occur primarily during the later stage of solidification in this case, because h_2 is only slightly lower than h_1 but much larger than h_3.

Four main types of variation among h_1, h_2, and h_3 during copper splat cooling have been observed in the present experiments. They are (1) $h_1 = h_2 > h_3$; (2) $h_1 > h_2 > h_3$; (3) $h_1 \gg h_2 = h_3$; and (4) $h_1 < h_2$ (with both $h_1 > h_3$ and $h_2 > h_3$). Type 1 ($h_1 = h_2 > h_3$) suggests that a good thermal contact during the initial liquid/solid cooling remains so during solidification, and that the interruption of this good thermal contact takes place at the end of solidification leading to a lower h_3. Type 2 ($h_1 > h_2 > h_3$), as shown in Fig. 4, suggests that the initial good thermal contact is degraded during solidification, which is reflected by a smaller h_2 than h_1. Type 3 ($h_1 \gg h_2 = h_3$) corresponds to the case shown in Fig. 5 with a rather high h_1. The high h_1 phase ends during the early stages of solidification. These three types of variations are not surprising, but the type 4 variation is less obvious. One example is shown in Fig. 6 for copper quenched on a ground stainless steel substrate. In this case, the estimated h_2 is higher than h_1 (4×10^4 W/m^2 K versus 2.4×10^4 W/m^2 K) and, in fact more so than one would ascribe to calculation uncertainties. A higher h_2 suggests a better solid/solid contact during solidification than the liquid/solid contact during melt cooling. Even though a higher h_2 than h_1 is observed in this case, h_3 is, as usual, much smaller than h_1.

The first three types (1, 2, and 3) of variation in h during copper splat cooling may perhaps be readily understood by considering the dynamics of the thermal contact between the splat and the substrate. At first, when the molten metal lies upon the colder substrate, one would expect good thermal contact because the fluidity of the melt allows it to "match" the shape of the substrate (with the exception of small-scale roughness and gas pockets). In addition, the high temperature of the melt may result in a good physical or chemical "bond" between the melt and substrate. Such good contact is reflected in a high h_1. This good contact would then degrade as the melt solidification

Table 2 Estimated values of h for copper on various substrates (H = 90 mm, θ = 45 deg)

Substrate		b (μm)	R_a (μm)	T_P (K)	h_1	h_2 (10^4 W/m^{2}K)	h_3	Type
Cu	Blasted-C	181	2.88	1432	1.3	1.3	0.7	1
		190		1474	1.8	1.45	0.4	2
		255		1490	2.5	2.5	0.7	1
Cu	Blasted-F	168	1.80	1424	0.9	2.4	0.9	4
		159		1473	1.3	4.0	1.5	4
		266		1523	4.6	0.75	0.3	2 or 3
Cu	Ground	371	0.29	1427	4.0	0.49	0.49	3
		314		1468	8.0	0.5	0.55	3
		312		1528	10.0	0.22	0.22	3
Al	Blasted-C	250	1.12	1423	1.2	2.2	0.33	4
		163		1470	1.4	1.8	0.15	4
		148		1508	1.7	2.1	0.23	4
SS	Ground	161	0.19	1438	1.6	1.6	0.3	1
		119		1482	1.4	8.0	0.6	4
		149		1538	2.4	4.0	0.4	4
SS	Grit #240	142	-	1428	1.05	2.75	0.55	4
		98		1528	1.4	2.0	0.15	4

is completed, as suggested by the much smaller h_3 values we obtained. The main driving force resulting in the breakage of this bond or the physical separation of splat and substrate is believed to be the stresses generated by the thermal contraction of the splat upon solidification and cooling. If the interfacial heat transfer coefficient (h_1) is not very large, the temperature difference across the splat is small because of the copper high thermal conductivity (see Fig. 4). Therefore, significant contraction occurs perhaps only after the entire splat is solidified and cooled down. This is the case for our Type 1 variation pattern. On the other hand, a significant temperature gradient may be generated in the splat if h_1 is large. In this case, the solidified portion of the splat may perhaps contract significantly before the splat is completely solidified, and may continue to do so afterwards. This contraction will result in a lower h_2 and h_3 as in the case of Type 2 variation. Finally, if h_1 is so large that a large temperature gradient will be generated quickly in the solidified splat, the breakage of the bond and contraction may occur shortly and primarily after the melt starts solidifying, with little subsequent effect. This may correspond to our Type 3 variation in h. Naturally, many other factors, such as variations in surface tension with temperature, gas contraction in interstices, roughness melt-down, etc., may also play a role, and may in particular explain why h_2 may in some cases (type 4) be greater than h_1. Such a trend is indeed not expected from a simple contraction model, and additional work will be needed to shed some light on this issue. (It may be useful to note that some previous investigations did also show a maximum in h around solidification time (Loulou et al., 1994; Wang and Matthys, 1994, for splat cooling, and Ho and Pehlke, 1985; Özişik et al., 1995, for mold casting).)

The variation of h was found to be affected by processing conditions such as melt superheat, substrate materials, and substrate surface conditions, as shown in Table 2, which summarizes the estimated values of h we obtained for some of our experiments with copper quenched on several substrates with various melt superheats. This table lists also the splat thickness (b), the surface arithmetic average roughness (R_a), and the type of variation of h observed. As can be seen, the type 4 variation of h is preponderant under the experimental configurations used, except for the ground and coarse-blasted copper substrates. A type 3 variation (much higher h_1) exists for all three superheat cases on the ground copper substrate. For the coarse-blasted copper surface, type 1 dominates.

3.4 The Effect of Melt Superheat, Substrate Material, and Substrate Surface Finish on h. Table 2 shows also the effect of the initial melt temperature, substrate materials, and substrate surface finishes on the interfacial heat transfer coefficient. As can be seen, for a given substrate surface, increasing the melt temperature T_P generally results in a moderate increase in h_1, but with no such obvious trend observed for h_2 and h_3.

The effect of the melt superheat on h_1 may be visualized more readily if the estimated h_1 is plotted as a function of the melt superheat, as shown in Fig. 7. As we see, except for the ground copper surface, most data fall in a relatively narrow band (about 10^4 to 3×10^4 W/m^2 K), and particularly so for low melt superheats. This suggests that the substrate material and the surface finish generally have a small effect on the thermal conductance for low superheat under our experimental conditions. As the melt superheat increases (for $\Delta T_P > 150$ K, say), however, the effect of the substrate material and finish on h_1 seems to become stronger. The improved thermal contact with increasing melt temperature may well be a result of the accompanying decrease in the surface tension of the liquid metal with increasing temperature. At high temperature, the melt may then penetrate more readily the roughness of the substrate and may suffer less from frequent macroscopic gas entrapment.

There is also a combined effect of the substrate material and finish on h. For example, for copper, the thermal contact is improved for the smoother ground surface over the rougher bead blasted one. For the ground stainless steel substrate, however, a much lower h_1 was estimated, which may be a result of wettability characteristics for this material pair. (These results are presented in dimensional forms to increase their readability and because the generation of meaningful nondimensional parameters will require a more complete understanding of the full physical picture of the process than is presently available. The issue of which characteristic roughness dimension to use, in particular, will have to be resolved. Systematic parametric studies on the effect of roughness on interfacial thermal conductance are underway in our laboratory and will help us resolve these issues.)

4 Conclusions

We have been able to quantify interfacial thermal conductance variations during fast solidification of a metal on a substrate. The interfacial contact during copper splat cooling is indeed a highly dynamic process. As a first approximation, a stepwise variation of the interfacial heat transfer coefficient can be estimated from the measured temperature, with three main process phases considered: h_1 (liquid cooling), h_2 (solidification), and h_3 (solid splat cooling). A higher h_1 (10^4 to 10^5 W/m^2 K) and a lower h_3 (10^3 to 10^4 W/m^2 K) were generally obtained for copper splat cooling. Depending on the processing conditions, the values estimated for h_2 (during solidification) may show different patterns, however. Four types of variation trends for h during copper splat cooling have been observed:

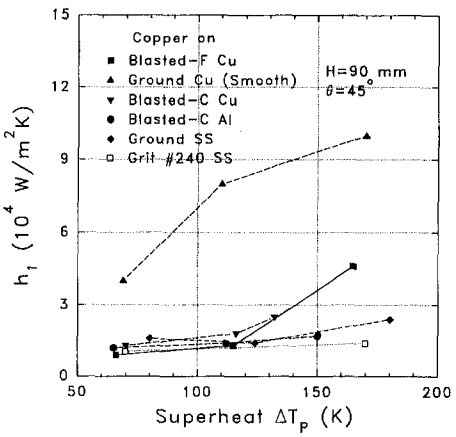

Fig. 7 Interfacial heat transfer coefficient in the "liquid" cooling region as a function of melt superheat for copper solidifying on substrates with various surface finishes [H = 90 mm, θ = 45 deg]

(*i*) $h_1 = h_2 > h_3$; (*ii*) $h_1 > h_2 > h_3$; (*iii*) $h_1 \gg h_2 = h_3$; and (*iv*) $h_1 < h_2$ (with $h_1 > h_3$ and $h_2 > h_3$); depending on the melt superheat, substrate materials, and surface conditions. Simple thermal contraction considerations could readily explain the first three types of variation of h, but not so much the fourth type—apparently the most prevalent—where the thermal contact is best during the solidification phase of the process.

Increasing the melt superheat moderately improved the thermal conductance during the initial (liquid/solid) phase of splat cooling (h_1) in general, and significantly so for the smooth copper substrate. The substrate material and the surface finish also have shown some effect on h_1.

It should be noted that the complexity of the physical mechanisms involved in the process, and of the associated experimental challenges, make it necessary to avoid overgeneralization of these results much beyond the range of conditions and parameters covered in our tests. Extensive parametric studies will have to be conducted in the future to solve this problem fully and to develop a good fundamental understanding of these issues.

Acknowledgments

We would like to acknowledge gratefully the financial support of the U.S. National Science Foundation (Grant No. DDM-8957733 to EFM), and Professor C. Levi (UCSB) for kindly making some of his equipment available to us.

References

Bennett, T., and Poulikakos, D., 1994, "Heat Transfer Aspects of Splat-Quench Solidification: Modeling and Experiment," *J. Mater. Sci.*, Vol. 29, pp. 2025–2039.

Brandes, E. A., 1983, *Smithells Metals Reference Hand Book,* 6th ed., Butterworths, United Kingdom.

Ho, K., and Pehlke, R. D., 1985, "Metal-Mold Interfacial Heat Transfer," *Metall. Trans. B,* Vol. 16B, pp. 585–594.

Kline, S. J., 1985, "The Purposes of Uncertainty Analysis," ASME *Journal of Fluids Engineering,* Vol. 107, pp. 153–160.

Liu, W., Wang, G.-X., and Matthys, E. F., 1995, "Thermal Analysis and Measurements for a Molten Metal Drop Impacting on a Substrate: Cooling, Solidification, and Heat Transfer Coefficient," *Int. J. Heat Mass Transfer,* Vol. 38, pp. 1387–1395.

Loulou, T., Artyukhin, E. A., and Bardon, J. P., 1994, "Solidification of Molten Tin Drop on a Nickel Substrate," *Heat Transfer 1994,* IChemE Pub., Brighton, United Kingdom, Vol. 4, pp. 73–78.

Mizukami, H., Suzuki, T., and Umeda, T., 1992, "Numerical Analysis for Initial Stage of Rapid Solidification of 18Cr-8Ni Stainless Steel," *Tetsu-to-Hagane,* Vol. 78, pp. 767–773.

Özişik, M. N., Bokar, J. C., Hector, L. G., Jr., Anyalebechi, P. N., and Nai, Y., 1995, "Combined Experimental/Theoretical Study of Mold Casting Interface Behavior During Directional Solidification," *Proceedings of the 1995 NSF Design and Manufacturing Grantees Conference,* SME Pub., pp. 471–472.

Ruhl, R. C., 1967, "Cooling Rates in Splat Cooling," *Mater. Sci. Engng.,* Vol. 1, pp. 313–320.

Trapaga, G., Matthys, E. F., Valencia, J. J., and Szekely, J., 1992, "Fluid Flow, Heat Transfer, and Solidification of Molten Metal Droplets Impinging on Substrate: Comparison of Numerical and Experimental Results," *Metall. Trans. B,* Vol. 23B, pp. 701–718.

Wang, G.-X., and Matthys, E. F., 1991, "Modelling of Heat Transfer and Solidification During Splat Cooling: Effect of Splat Thickness and Splat/Substrate Thermal Contact," *Int. J. Rapid Solidification,* Vol. 6, pp. 141–174.

Wang, G.-X., and Matthys, E. F., 1992, "Numerical Modelling of Phase Change and Heat Transfer During Rapid Solidification Processes: Use of Control Volume Integrals With Element Subdivision," *Int. J. Heat Mass Transfer,* Vol. 35, pp. 141–153.

Wang, G.-X., and Matthys, E. F., 1994, "Interfacial Thermal Contact During Rapid Solidification on a Substrate," *Heat Transfer 1994, Proceedings of the Tenth International Heat Transfer Conference,* IChemE Pub., Brighton, United Kingdom, Vol. 4, pp. 169–174.

Wang, G.-X., 1995, "Experimental and Numerical Study of Heat Transfer and Solidification for Molten Metal in Contact With a Cold Substrate," Ph.D. Thesis, University of California, Santa Barbara, CA.

Numerical and Experimental Investigation of Interface Bonding Via Substrate Remelting of an Impinging Molten Metal Droplet

C. H. Amon

K. S. Schmaltz

R. Merz

F. B. Prinz[1]

Department of Mechanical Engineering and Engineering Design Research Center, Carnegie Mellon University, Pittsburgh, PA 15213

A molten metal droplet landing and bonding to a solid substrate is investigated with combined analytical, numerical, and experimental techniques. This research supports a novel, thermal spray shape deposition process, referred to as microcasting, capable of rapidly manufacturing near netshape, steel objects. Metallurgical bonding between the impacting droplet and the previous deposition layer improves the strength and material property continuity between the layers, producing high-quality metal objects. A thorough understanding of the interface heat transfer process is needed to optimize the microcast object properties by minimizing the impacting droplet temperature necessary for superficial substrate remelting, while controlling substrate and deposit material cooling rates, remelt depths, and residual thermal stresses. A mixed Lagrangian–Eulerian numerical model is developed to calculate substrate remelting and temperature histories for investigating the required deposition temperatures and the effect of operating conditions on remelting. Experimental and analytical approaches are used to determine initial conditions for the numerical simulations, to verify the numerical accuracy, and to identify the resultant microstructures. Numerical results indicate that droplet to substrate conduction is the dominant heat transfer mode during remelting and solidification. Furthermore, a highly time-dependent heat transfer coefficient at the droplet/substrate interface necessitates a combined numerical model of the droplet and substrate for accurate predictions of the substrate remelting. The remelting depth and cooling rate numerical results are also verified by optical metallography, and compare well with both the analytical solution for the initial deposition period and the temperature measurements during droplet solidification.

I Introduction

Historically, thermal spray techniques have been used in the application of thin films to surfaces for corrosion, wear resistance, and thermal barriers, though more recent uses of spray processes have included forming objects from sprays (Singer, 1982). A spray deposition technique being developed at Carnegie Mellon, called microcasting, creates high-melting temperature metal objects (e.g., steel) by successively depositing material and sacrificial layers to form the desired object's shape (Merz et al., 1994). Using machining operations and sacrificial support materials (such as copper, which is removed with acid), it is possible to manufacture complex geometries possessing varied materials and composite or laminate structures; this process can generate free-form, near net-shape structures that would be difficult or impossible to create using traditional machining, casting, or spraying methods. This technique yields metastable, dense objects with rapidly solidified microstructures, dimensional accuracy, and surface finishes comparable to conventional machining. By depositing carbon or stainless steel, functional metal parts are *directly* created without postprocessing or conversion technologies required by other rapid prototyping methods; comparable spray shape deposition techniques also use low-melting temperature materials such as waxes, acrylics, and lead (Weiss et al., 1992). Figure 1 shows a stainless steel artifact, formed in a sacrificial copper support material, built to test microcasting geometric capabilities for a Carnegie Mellon consortium.

The thermal spray deposition technique modeled numerically and verified experimentally in this paper differs most significantly from traditional spray processes in the size, and consequent impact temperature, of the deposition droplets, as well as the impact velocity of the discrete droplet. With microcasting, millimeter-sized droplets free fall through a nitrogen environment, impinging the substrate surface at a rate of several droplets per second (Fig. 2); traditional wire arc or plasma spray methods propel a high-velocity mist of the order of 100 μm droplets, in a near Gaussian spray distribution. The greater droplet volume-to-surface ratio in the microcasting process yields droplet impinging temperatures several hundred degrees above the melting temperature, whereas plasma and wire arc droplets cool during droplet flight to conditions near, or below, melting. The balance sought for the microcasting impact temperature is to generate droplets that promote substrate remelting and possess good flow characteristics, and yet minimize thermally induced stresses and excessive melting of the previously deposited material. The impact temperature significantly affects the droplet/substrate interface heat transfer processes taking place during deposition, specifically, the type of bond formed between the droplet and the presolidified substrate. Whereas traditional thermal spray bonding is due to mechanical interlocking of the

[1] Current address: Department of Mechanical Engineering and Department of Materials Science & Engineering, Stanford University, Stanford, CA 94305.

Contributed by the Heat Transfer Division for publication in the JOURNAL OF HEAT TRANSFER. Manuscript received by the Heat Transfer Division February 1995; revision received August 1995. Keywords: Materials Processing and Manufacturing Processes, Modeling and Scaling, Phase-Change Phenomena. Associate Technical Editor: A. Faghri.

solidified droplets and substrate, microcasting droplets partially remelt the solid substrate to a depth of several microns, resulting in an improved metallurgical bond between the layers, and enhanced object properties.

Understanding the remelting phenomenon is the primary focus of this investigation; the optimization of microcasting requires the ability to predict remelting and to select process parameters that achieve bonding of the entire interface at minimum impinging droplet temperature. Accurate predictive capabilities are required due to the extreme thermal conditions, large spatial gradients, and rapid temporal cooling rates involved. Droplet temperature control via material feed rate, plasma power, and falling distance is required to reduce the effects of residual stresses induced by thermal gradients, to minimize the extent of substrate remelting for manufacturing purposes, and to maintain surface quality. The cooling rate of the deposited material also determines the resultant microstructure and material properties, which can differ significantly from nonsprayed values for the same material. In addition to improved material properties through the control of melting conditions and cooling rates, accurate temperature modeling is important for other manufacturing considerations, including protection of sacrificial supporting structures having lower melting temperatures than the deposited material, control of application temperatures to protect embedded electronics, and control of thermal stress-induced warping or delaminating by successive depositions as detailed by Amon et al. (1993a).

Numerical model accuracy is verified using a combination of analytical and experimental techniques. Classical Stefan melting front analytical solutions approximate the microcasting process during the initial deposition period over a range of process parameters for which droplet spreading time is much shorter than solidification time. Analytical solutions are used to predict the minimum substrate remelting conditions and the relative effects of initial droplet and substrate temperatures on remelting depth. Calorimetry and thermocouple experiments provide initial conditions for modeling, and directly verify numerical simulations of the droplet and substrate thermal histories during the cooling process. Metallurgical characterization of the microstructures indirectly measures substrate remelting depths and cooling rates for comparison with numerical predictions.

II Review of Related Research

Significant prior numerical modeling efforts for solidification have been directed toward traditional thermal sprays and casting solidification. In both situations, substrate remelting is ignored, either due to the lack of droplet superheat in traditional spraying, or because interface remelting is not desired in casting solidification. Fundamental numerical techniques to model phase-change problems have been presented (e.g., Prakash, 1990; Voller et al., 1990). Numerical modeling of traditional sprays has taken analytical approaches to solve the one-dimensional problem, assuming linear temperature profiles across the deposition layer or using Stefan problem solutions (Pawlowski, 1981; El-Kaddah et al., 1984); employed finite difference solutions to include contact resistance effects (Bewlay and Cantor, 1991); and used enthalpy energy balance to handle the discontinuities at the phase change (Griffith and Nassersharif, 1990; Mathur et al., 1989). Individual droplet models, more similar to microcasting, have also been formulated. Trapaga and Szekely (1991) initially modeled the fluid dynamics of a spreading droplet, relating splat size and spreading time to spray conditions. Trapaga et al. (1992) included droplet solidification heat transfer by modeling the substrate heat transfer with an empirically obtained constant heat transfer coefficient and conditions that do not cause substrate remelting. Methods combining analytical solidification solutions with numerical fluid flow simulations have also been employed (San Marchi et al., 1993; Liu et al., 1993). Metal droplet solidification has also been modeled using interface heat transfer coefficients to determine the heat flux into the substrate (Wang and Matthys, 1991; Bertagnolli et al., 1994; Kang et al., 1994; Bennett and Poulikakos, 1994). While a constant heat transfer coefficient between the droplet and substrate simplifies the determination of substrate heat flux, this coefficient is difficult to obtain, and, whether or not remelting occurs, interface heat transfer creates a highly time-variant heat transfer coefficient (Wang and Matthys, 1994; Amon et al., 1994b). Assuming constant material properties also simplifies the numerical effort, but microcasting properties change by a factor of two for the materials used and the range of temperatures involved.

We have developed a numerical model of the microcasting process that determines the location of the melting front, within both the deposition layer and the substrate during initial remelting, to investigate the effects of substrate remelting and metallurgical bonding (Amon et al., 1994a). The primary motivations for modeling the melting/solidification phenomena are to predict bonding conditions through substrate remelting, to predict the thickness of this remelted layer, and to aid in the selection of process parameters yielding desirable material properties. Additionally, numerical modeling provides an accurate predictive tool of the thermal deposition process to investigate the effect of operating conditions such as initial droplet and substrate temperatures on the resulting melting front migration rate, thickness of remelting, temperature distribution, and cooling rates of both the droplet and the substrate. With this knowledge, operating parameters such as power input, nozzle to substrate distance, and deposition rates can be optimized.

III Mathematical Formulation

The microcasting deposition process consists of a series of discrete molten metal droplets impinging on a presolidified substrate. Droplet solidification and cooling, and substrate heating, remelting, and cooling are governed by Fourier's heat conduction equation:

$$\rho_i(T)c_{pi}(T)\frac{\partial T_i}{\partial t} = \nabla\cdot\{k_i(T)\nabla T_i\} \qquad (1)$$

where ρ is the density, c_p is the specific heat, k is the thermal conductivity, and the subscript i corresponds to either solid or liquid regions, or differing materials. Combined convection and radiation boundary conditions are applied at the top surface of the liquid region, and constant temperature is imposed in the solid substrate region at a remote (seven droplet diameters) distance from the droplet/substrate interface. At the liquid/solid interfaces, the temperature remains at the melting point, and the heat flux balance is:

Nomenclature

c_p = specific heat, J/kg°C
D = droplet diameter, mm
k = thermal conductivity, W/m°C
L = latent heat of fusion, J/kg
n = normal direction, m
t = time, s
T = temperature, °C
X = location of melting front, mm
α = thermal diffusivity, m^2/s
β = initial condition-based constant
ρ = density, kg/m^3

Subscripts

l = liquid
lo = initial liquid temperature
m = melting temperature
s = solid
so = initial solid temperature

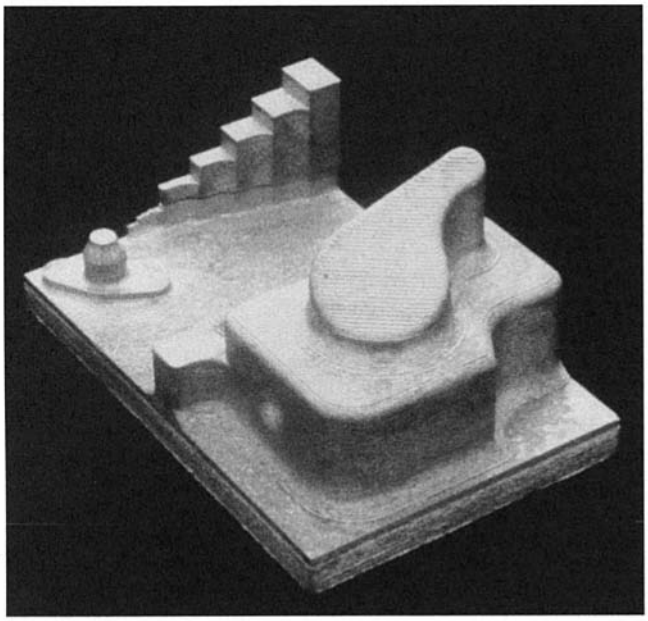

Fig. 1 A microcasting artifact

$$k_s \frac{\partial T_s}{\partial n} - k_l \frac{\partial T_l}{\partial n} = \rho L \frac{\partial X}{\partial t} \tag{2}$$

where L is the latent heat acting as either a source (solidifying) or sink (remelting) term, ρ is the density at the melting temperature, $X(t)$ is the location of the melting/solidification front, and n is the normal direction to the liquid/solid interface. Interface heat transfer resistance is not incorporated into the model due to the assumption verified by the micrographic examinations that substrate remelting creates a continuous contact between the droplet and substrate. The interface condition assumes the sharp solid to liquid transition of a pure material, occurring at the melting temperature. More precise treatment of alloy liquidus/solidus temperatures would exhibit a gradual transition to the solid state during solidification.

The dynamic effects of the droplet flattening are considered a precursor to the thermal process modeled. This allows the formulation to be uncoupled from the fluid dynamics and simplified to a heat transfer problem, because the time for a typical droplet to strike the solid surface and flatten is much shorter than the time for the droplet to solidify over the range of microcasting parameters investigated (Amon et al., 1994b). The assumption of neglecting the droplet motion is validated using Madejski's (1983) estimate of droplet spreading time, which prescribes a velocity profile and uses a lumped analysis. This applies for microcasting droplet solidification since the Biot number is sufficiently small. The spreading time is 2.6×10^{-3} seconds for a typical microcasting droplet (stainless steel material, droplet temperature of 2300°C, substrate temperature of 30°C), whereas the solidification time, including both cooling from a superheated state to the melting temperature and latent heat release, is 1.1×10^{-1} seconds. A further assumption allowing the problem to be modeled as one-dimensional is based on the height to width ratio of the impacted droplet and the even greater ratio of the remelt depth to the droplet width. This has been validated during the period of substrate remelting through the use of a three-dimensional, axis-symmetric conduction model presented in Fig. 6 (Chin et al., 1995).

The Stefan melting front problem solution of Carslaw and Jaeger (1959) provides analytical time- and position-dependent temperature profiles within the solid and liquid regions closely matching the initial phase of the microcasting deposition process. The Stefan solution assumes semi-infinite solid and liquid regions, fixed melting temperature (T_m) at the solid/liquid interface, and interface heat flux balancing latent heat release (Eq. (2)). An error function solution to Eq. (1) is found by assuming temperature-independent material properties and constant liquid and solid boundary temperatures. This analytical solution can predict temperature and melting front movement for the microcasting process until the assumed boundary conditions are invalidated by the actual finiteness of the sprayed layer and the effect of droplet surface convection and radiation.

The analytical solution also predicts the initial droplet/substrate interface temperature. Satisfying the temperature condition at the melt interface yields a melting front displacement proportional to the square root of time. Substituting temperature and melting front equations into Eq. (2) and integrating yields:

$$X(t) = \left[k_s \frac{(T_m - T_{so}) \exp\{-\beta^2\}}{\sqrt{\alpha_s}\,(1 + \operatorname{erf}(\beta))} + k_l \frac{(T_m - T_{lo}) \exp\left\{\frac{-\alpha_s \beta^2}{\alpha_l}\right\}}{\sqrt{\alpha_l}\,\operatorname{erfc}\left(\beta \sqrt{\frac{\alpha_s}{\alpha_l}}\right)} \right] \frac{2\sqrt{t}}{\rho L \sqrt{\pi}} \tag{3}$$

where β is an initial condition-dependent parameter, α is the thermal diffusivity, and t is the time. The bracketed term in Eq. (3) predicts remelting conditions for the microcasting process (Kirchner and Prinz, 1993); if negative, initial remelting is expected; otherwise no substrate remelting occurs. The required condition for interface remelting is found by setting the bracket equal to zero, and solving for T_m, which becomes an initial interface temperature at $t = 0$, rather than the melting temperature. This equation also predicts the remelting conditions required when dissimilar materials are involved, such as when sacrificial support materials are used or multimaterial layers are deposited. An example of this is given in Fig. 3, where the combination of droplet and substrate initial temperatures needed to create substrate remelting is presented for a stainless steel droplet impinging on either a copper or a stainless steel substrate. The solid line shows the combination of droplet and substrate minimum initial temperatures needed for stainless steel substrate remelting, and the dotted line shows copper substrate remelting conditions. Therefore, it is possible for a 2300°C stainless steel droplet to remelt a 100°C stainless steel substrate, but not a 100°C copper substrate. This is due to the order of magnitude difference in thermal conductivity and diffusivity values between copper and stainless steel, which makes stainless

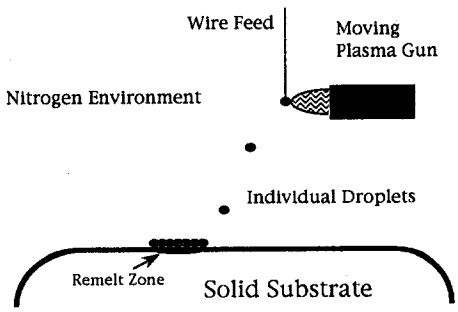

Fig. 2 Microcasting thermal deposition process; typical parameters: droplet diameter 1–4 mm, droplet splat height 0.5–1.5 mm, impact velocity 1–1.5 m/s, impact temperature 2000–2500°C, and superheat temperature 500–1000°C

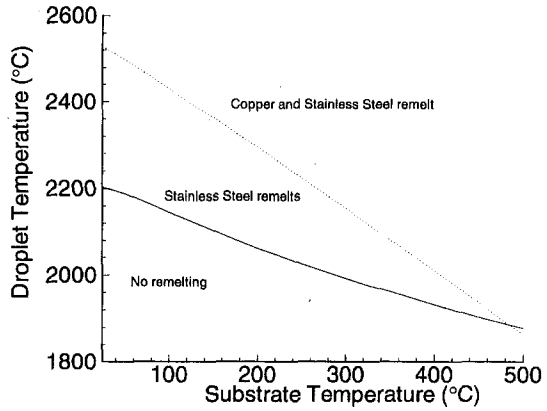

Fig. 3 Analytical calculation of impact temperatures required for substrate remelting for a stainless steel droplet impinging on a stainless steel substrate (——) or copper substrate (· · ·)

steel substrate remelting easier to achieve than copper, despite the lower melting point of copper.

IV Numerical Model and Results

The numerical formulation of the microcasting process presented in this paper employs a second-order accurate, Eulerian explicit formulation and temperature-dependent thermal properties. An explicit formulation is used for simplicity, despite the necessity of meeting numerical stability criteria, because the remelting of the microcasting process is sufficiently rapid that the small time steps required do not present a significant calculation burden, particularly for a one-dimensional model. As mentioned earlier, a one-dimensional formulation is justified on ratios of the impacted droplet width to height (*droplet* implying a layer in the one-dimensional model) and on the droplet width to remelt thickness. This assumption is validated and discussed later using multidimensional modeling results. The focus of our investigation is primarily directed toward accurate remelt determination, and secondarily toward accurate temperature history prediction throughout the entire droplet and substrate. During the period of substrate remelting, inaccuracies arising from multidimensional effects are not significant. Furthermore, the multidimensional simulations have also verified the absence of lateral temperature gradients within the liquid region, that coupled with the brevity of this solidification process, of order 0.1 second, minimize advection effects and permit the entire region to be treated as a conduction problem. Furthermore, micrographic examinations, discussed later, verify the one dimensionality of the heat flux in the droplet during solidification.

A three-point Lagrange interpolation formula at the remelting or solidification interface tracks the melting front (Crank, 1984) by using a varying mesh point corresponding to the melting front. The Lagrange formulation is used for temperature calculations with nodes preceding and following the melting point (Amon et al., 1993b). The melting front location is recalculated after each time iteration using updated temperatures and a discretized form of Eq. (2). Mesh resolution and extension into the substrate region has been varied to assure convergent solutions, to avoid excessive computation time, and to maintain lower boundary condition validity and accuracy. Theoretical numerical stability for the explicit formulation requires a maximum time step of 3×10^{-7} seconds for the typical node spacing employed; for node temperatures to converge to within 0.1 percent of previous results, time steps smaller than 1×10^{-8} seconds are required. This additional time step refinement is due to the Lagrange temperature interpolation. A mesh with 160 grid points yields a spatially convergent solution for the time period considered. Sensitivity analyses of the droplet surface convection and radiation boundary condition effects on remelting are performed because of the inaccurate knowledge of these parameters for the microcasting process. Changing the convection heat transfer coefficient (Guyer, 1989) and radiation source term values (Pawlowski, 1981) by an order of magnitude alters the temperature field by less than 1 percent during the remelting period. The fact that these boundary effects are insignificant compared to the conduction of heat into the substrate and the phase change latent heat (Amon et al., 1993b) implies that the *substrate* melting and resolidification process, which occurs on the order of 10^{-5} seconds (Fig. 4 and 5) is dominated by conductive heat transfer, with negligible surface convective and radiative effects.

Numerical simulations are presented for typical microcasting materials (low carbon steel and 300 series stainless steel), using representative, spatially uniform microcasting droplet temperature ranges of 2000–2500°C, and substrate temperature ranges of 30–500°C. The primary focus of these simulations is to examine the effect of droplet temperature and substrate temperature on remelting depth and time, as well as on cooling rates. This is done by varying either the initial droplet impact temperature or the initial substrate temperature and tracking the temporal evolution of the melting front. Results indicate that conditions permitting substrate remelting of several microns require droplet impact temperatures with significant superheat when landing on an unheated substrate; the required droplet superheating is reduced when the substrate is preheated above ambient temperatures (Amon et al., 1993b). In addition to the low carbon steel and stainless steel models, simulations are also performed with steel *droplets* landing on either zinc or copper substrates, reflecting the microcasting process involving sacrificial support substrates or multimaterial objects. Results from the steel/zinc simulation verify that the steel solidifies immediately, while the lower melting point zinc melts to a significant depth and actually vaporizes at the steel/zinc interface during this process. This supports the need to thermally protect support substrate materials having lower melting temperatures such as zinc (Amon et al., 1993b). We are presently using copper substrates as support material for the deposition of carbon or stainless steel. The need to protect the copper is eliminated due to its high thermal conductivity and relatively high melting point compared to zinc. As shown in Fig. 3, molten stainless steel can be deposited on a copper substrate without melting the copper, but does remelt the steel substrate. Conversely, molten copper can be deposited on steel without causing remelting, yet still remelt previously deposited copper (Merz, 1994).

The effect of impinging droplet temperature on substrate remelting is shown in Fig. 4, depicting the numerical melting front migration versus time for a 1 mm carbon steel droplet landing on an ambient substrate at 30°C. The positive and nega-

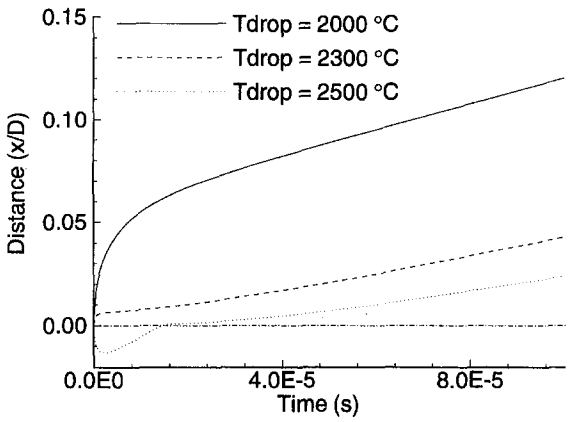

Fig. 4 Carbon steel melting front migration versus time as a function of droplet initial temperature

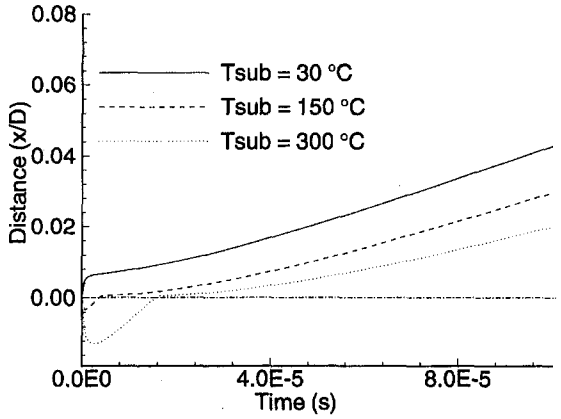

Fig. 5 Carbon steel melting front migration versus time as a function of substrate initial temperature

tive vertical axis represents the droplet and substrate regions, respectively, and is nondimensionalized by the droplet thickness. Impact temperatures below 2300°C do not achieve remelting on an ambient substrate, whereas a 2500°C droplet will cause substrate remelting. Figure 5 shows the effect of increasing substrate temperature on remelting for the same sized carbon steel droplet, increasing the substrate temperature from 30°C to 300°C while the droplet temperature remains at 2300°C. As predicted by the analytical solution, Fig. 5 indicates that a 2300°C droplet will not remelt the substrate until the substrate is heated to 150°C. In either case, initial front migration proceeds deeper into the substrate as the droplet or substrate temperature is increased. The maximum remelting front migration into the substrate changes linearly with droplet or substrate temperature, for the range of substrate temperatures explored, with a predicted remelt depth of 5–10 μm.

While the present model is aimed at resolving substrate remelting, comparisons with multidimensional, axisymmetric solidification models (Chin et al., 1995) are performed to determine the duration over which the one-dimensional simulations are valid. This is relevant to the prediction of overall droplet and substrate temperature histories, which determine the thermally induced residual stresses. Figure 6 compares the temperature evolution predicted by the one-dimensional simulations with the centerline temperature of the multidimensional simulations for a low carbon steel droplet. Comparisons are shown at a middroplet location (0.5 mm from the interface), at the original droplet/substrate interface, and within the substrate (depth of 0.5 mm). This comparison demonstrates that the one-dimensional model is valid for approximately 0.2 seconds until multidimensional heat transfer effects become important, whereas the substrate remelting occurs in about 10^{-5} seconds and the droplet midpoint solidifies in 0.14 seconds. The slope of the middroplet temperature versus time becomes first discontinuous when the middroplet reaches the melting temperature (1460°C) and, then, when the droplet has solidified completely. After this time, the heat transfer process changes from conjugate conduction/latent heat to pure conduction.

Previous numerical formulations have used an interface coefficient to determine the heat transfer from a droplet to the substrate (Trapaga et al., 1992; Bertagnolli et al., 1994; Wang and Matthys, 1991; Kang et al., 1994). This is often the best approximation for uncoupled droplet/substrate formulations, particularly when contact resistance is involved. However, during the initial remelting and resolidification phases for the microcasting process, the heat transfer coefficient decreases rapidly from 250,000 W/m^2°C to nearly half this initial value, and continues to decrease during the droplet solidification phase to approximately 50,000 W/m^2°C (Amon et al., 1994b). This variance makes it difficult to determine an accurate heat transfer coefficient at the interface between the droplet and substrate, requiring a conjugate model containing both the droplet and substrate to predict substrate remelting accurately.

V Experimental Tests and Results

To validate the numerical model, direct and indirect experimental measurements of the microcasting cooling rates, droplet impact temperatures, and substrate remelting are performed using calorimetry, thermocouple, and optical metallographic techniques. From the metallographic characterization of the interface microstructure, we determine the remelted depth for stainless steel samples, the cooling rate, and the heat flow direction. Thermocouple measurements validate the numerical temperature history predictions and provide the initial droplet temperature. Calorimetry results also verify the initial droplet temperature and quantify the range of initial temperatures available with the microcasting equipment. Comparisons between numerical and experimental results have been made for low carbon, manganese steel droplets (1.55 percent Mn, 0.84 percent Si, 0.09 percent C, 0.01 percent P) impinging on a carbon steel substrate, and 308 grade stainless steel droplets (20 percent Cr, 12 percent Ni, 2 percent Mn, 0.08 percent C) impinging on a 304 grade stainless steel substrate.

Calorimetry experiments measure average impact droplet temperatures for typical microcasting parameter settings, and also the extent that impact temperatures can be altered by changing these settings. The experiments involved depositing a series of droplets into an insulated water bath; it was necessary to compensate for the water bath temperature rise due to microcasting power source radiation, latent heat of fusion released by the solidifying steel droplets, and latent heat of vaporization of water vaporized by contact with the molten droplets. This led to uncertainties on the order of 100°C for the 1600°C to 2600°C droplet temperature ranges with both types of steel. Calorimetry temperature measurements agree with thermocouple results for similar parameter settings. Experiments varying droplet height by several centimeters (about an average value of 10 cm) will affect the impact temperature by over 100°C (Amon et al., 1994a). Manufacturability considerations limit changes possible on both the power setting and the droplet flight distance.

To verify substrate remelting, which is predicted from the numerical simulations to occur in about 10^{-5} seconds, optical metallographic characterization of a droplet/substrate cross section is performed. By sectioning the samples previously used in the thermocouple experiments, we correlate the metallographically measured remelting with experimentally measured temperatures. Both single and multiple droplet metallographic

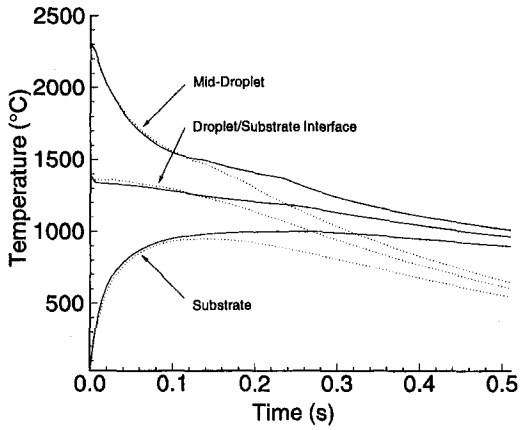

Fig. 6 Temperature profiles at middroplet, droplet/substrate interface, and substrate for carbon steel: one-dimenisonal simulations (——) and multidimensional (– –) simulations

samples were used, involving single droplets landing on ambient temperature substrates and multiple droplets landing on preheated substrates, to reflect the microcasting process more accurately. The micrographic samples were ground and polished to a mirror finish, carbon steel samples were etched with nitric acid, and stainless steel samples were etched with a stronger nitric acid/hydrochloric acid solution.

Figure 7 shows the stainless steel microstructure for a 2200°C impacting droplet temperature. The droplet contains dark regions of chromium-rich delta-ferrite microstructure and light regions of nickel-rich austenite, which are clearly different from the austenite structure of the substrate plate. A slightly darker remelted region extends 10 μm into the droplet along the droplet/substrate interface boundary. This region has the same microstructure as the droplet, but retains some indication of the austenite grain boundary of the substrate plate below. An advantage with the 300-series stainless steel material is the fact that it does not readily undergo solid state phase transformations; because the original austenite microstructure of the solid substrate plate is retained as a sharp boundary, it is possible to locate the maximum remelting point accurately. These remelting depths estimated by stainless steel metallography compare well with the depths predicted by the numerical model.

Figure 8(a) shows the droplet/interface region for a series of 2300°C carbon steel droplets impinging a substrate, preheated by the effect of previous droplets. Figures 8(b) through 8(e) show the microstructure transition from the initial droplet, through the substrate region that has experienced remelting, to the substrate region that has not undergone remelting. The droplet microstructure of austenite, Widmanstatten ferrite (lighter color fingers), and martensite is consistent with rapid solidification from a liquid state. This is also present in the remelted region of the substrate. Far from the interface, the substrate microstructure is ferrite–pearlite, shifting from coarse to fine as the droplet interface is neared (Fig. 8(d)). Where remelting has occurred (Fig. 8(c)), austenite with ferrite and martensite structure appears (Honeycombe, 1981). With carbon steel, it is not possible to locate the remelted portion of the substrate precisely because the substrate microstructure is altered both by remelting and by high-temperature (800°C) solid state transformations. The combined depth of remelting and heat effect is between 100 to 200 μm. The energy associated with solid-state phase changes of the steel is not modeled numerically since the liquid–solid latent heat transformation is over an order of magnitude greater than the austenite–ferrite transformation (Amon et al., 1994b).

Metallographic characterizations also allow the estimation of cooling rates when coupled with Cooling Transformation Diagrams, and the visualization of heat flow direction from the grain orientation. Using low carbon, manganese steel Cooling Transformation Diagrams (Boyer, 1977), the martensitic structure indicates that the droplet cools from a molten state to below 300°C in less than 1.5 seconds. The remelting zone resolidifies and cools below 300°C in less than 2 seconds to attain its microstructure. The grain direction within the droplet region indicates the predominantly unidirectional nature of conduction heat transfer at the droplet/substrate interface. The solidifying material microstructure, which aligns perpendicular to the isotherms, shows a distinct grain direction perpendicular to the substrate surface. For the stainless steel micrographs, there is also some *memory* effect during solidification, arising from the orientation of the original austenite crystals in the substrate; due to this, some of the remelted interface structure is aligned with the substrate grains. While droplet heat flow is predominantly unidirectional, the carbon steel micrographs of the substrate remelted zone indicate a definite multidimensional shape.

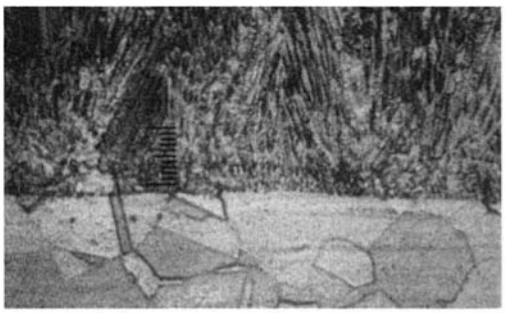

Fig. 7 Metallographic characterization of a 2200°C stainless steel droplet impacting a 30°C substrate: 500× magnification of the droplet/substrate interface (scale represents 20 μm)

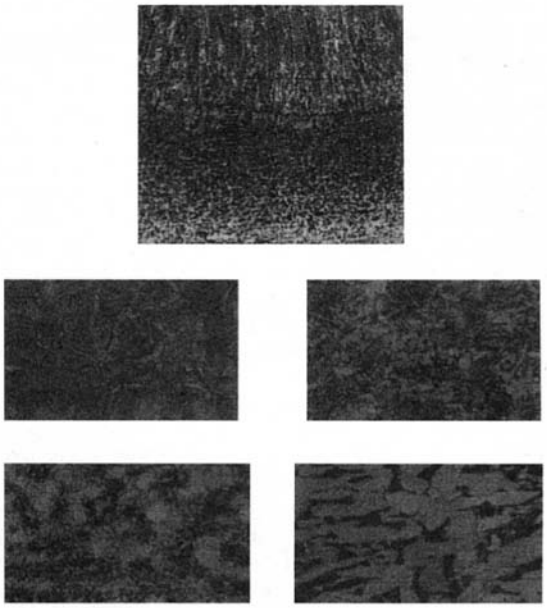

Fig. 8 Metallographic characterization of a series of 2300°C carbon steel droplets impacting a 300°C preheated substrate (scale represents 200 μm) (*a*) 50× magnification of the complete droplet/substrate interface, and 500× magnification of (*b*) droplet, (*c*) substrate remelted region, (*d*) substrate heat-affected region, and (*e*) unaffected substrate region

Thermocouple measurements at different droplet and substrate locations for the microcasting process verify actual impacting droplet conditions, provide initial condition input for the numerical simulations, and allow a comparison between numerical predictions and experimental results for temperatures beyond the valid range of the analytic solution. Microcasting droplets are landed directly onto type-C thermocouples (tungsten/rhenium, accuracy of 1 percent to measure the droplet temperature history. Temperature data are collected every 0.05 seconds on a Data Translation data acquisition system, which matches the thermocouple time constant. An individual steel droplet lands on the thermocouple to measure its impact temperature as well as the droplet cooling rate. The peak temperature of the rapidly cooling droplet is underestimated by approximately 5 percent due to the combined effects of the sampling interval, and the thermal inertia of the thermocouple. Substrate temperatures are measured by inserting type-K thermocouples (nickel/chromium, accuracy of 0.75 percent) through the substrate plate to within 1 to 4 mm of the surface and measuring the temperature of the steel substrate directly below the droplet impact.

VI Discussion

Analytical, numerical, thermocouple measurement, and metallographic evaluation techniques provide complementary results in the investigation of the microcasting process. Although

analytical solutions provide the conditions required for the onset of remelting, a numerical technique is needed to determine remelting depth, droplet solidification time, and cooling histories. Analytical and numerical results compare well during the initial 10^{-3} seconds of the deposition and substrate remelting, but comparisons with thermocouple measurements are required to validate the model's ability to predict droplet and substrate thermal histories accurately over longer times. Metallographic characterizations corroborate remelting depths and further validate the numerical cooling rate predictions. In this way, our primary objective of determining substrate remelting as a source of droplet to substrate metallurgical bonding, and our secondary goal of predicting the cooling rates relevant to the resulting microstructure, are achieved through a combined application of these methods.

The temporal evolution of the analytical and numerical temperature profiles for a 2300°C liquid carbon steel region contacting a 30°C steel substrate is compared in Fig. 9. The temperature profiles displayed are for 0.0001, 0.001, and 0.01 seconds after impact. The analytical solution compares well through 0.001 seconds; beyond this time the effect of microcasting convective and radiative boundary conditions at the top surface invalidates the analytical solution semi-infinite assumption. The substrate does not impose a limiting factor for the analytical solution during this time because it is considerably thicker than the droplet. The liquid region analytical solution differs from the numerical predictions by less than 34°C (2 percent) at 10^{-4} seconds, the maximum divergence is 11.8 percent by 10^{-3} seconds, and 15.5 percent by 10^{-2} seconds, occurring where the temperature gradient is greatest. The top liquid surface boundary condition clearly influences the comparison of analytical and numerical results, as shown by the agreement between the analytical and numerical solutions in the substrate solid region, and by the divergence in the droplet liquid region. The use of constant material properties in the analytical formulation, despite the twofold change over actual temperatures experienced, accounts for some of the difference. Analytical and numerical predictions agree well for the conditions required to commence substrate remelting, and also agree during the approximately 5 $\times 10^{-5}$ seconds duration of substrate remelting. Both methods indicate that for carbon steel substrate remelting, a 2300°C impacting droplet is necessary to remelt an ambient temperature substrate.

Thermocouple experiments using carbon and stainless steels are used for comparison with the numerical simulations at a later period of the cooling process. The model uses calorimetry results for the initial droplet temperature, an ambient temperature substrate, and a droplet *splat* height measured from cooled test samples. Figure 10 compares the numerical and thermocouple temperature histories for a carbon steel droplet and for a substrate at a depth of 2 mm. The initial droplet cooling rate predicted numerically is in good agreement with the cooling rate obtained experimentally, but at later times the predicted cooling rates are lower than the measured values. The divergence between experimental and numerical droplet results begins approximately at the solidification temperature, suggesting that thermal properties of this rapidly solidified and cooled droplet may vary from the tabulated values. However, the substrate temperature measurements and calculated values from the one-dimensional model diverge later in the cooling process. The numerical results overpredict the peak substrate temperature by 150°C compared to the experimental results as well as the timing of this peak by 0.2 to 0.4 seconds. Contact resistance between the thermocouple and substrate surface may partially explain the lower temperature of the thermocouple results, though not the time lag. The lack of multidimensional substrate cooling in the numerical model leads to both the substrate discrepancies and the droplet cooling underprediction at later times in the process. Therefore, multidimensional cooling is necessary for accurate substrate temperature predictions over longer times.

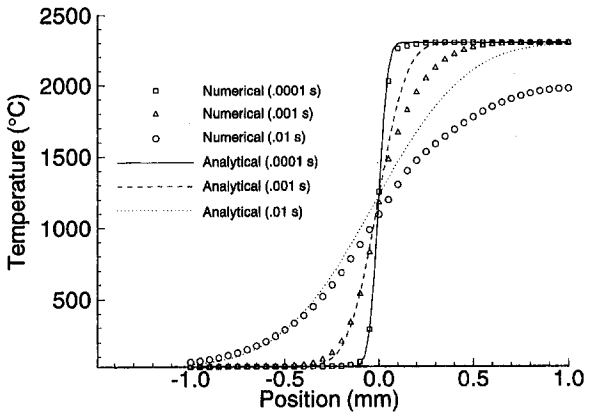

Fig. 9 Comparison of analytical and numerical temperature profiles at various times for a 2300°C carbon steel droplet impacting a 30°C substrate

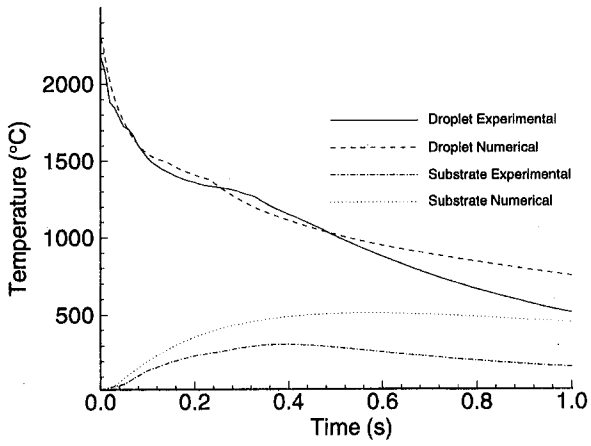

Fig. 10 Experimental and numerical temperature histories of carbon steel microcasting droplet and substrate

The cumulative results of the numerical simulations and experiments demonstrate that the remelting phenomenon of the microcasting process can be predicted accurately with a simplified heat transfer model for the range of parameters and the remelting time period investigated in this paper. This is due to the dominant effect of unidirectional conduction into the substrate during the remelting and early cooling stages of the droplet solidification process. For microcasting conditions considered in this paper, the droplet spreading time scale is much shorter than the solidification time scale, and under these conditions, the droplet first forms a quasi-equilibrium liquid layer, and then solidifies. Although the numerical model correctly predicts the occurrence of substrate remelting and the remelting depths, as verified by stainless steel metallography, a two-dimensional remelted zone is present in the carbon steel metallographic results. Both the geometry of the impacted droplet and the orientation of the steel microstructure indicate that the heat transfer in the droplet is predominantly unidirectional, and perpendicular to the substrate surface.

While the present model provides accurate results for the early time remelting phenomenon, a multidimensional model is required for the wider range of parameters available in the microcasting process and for modeling the longer term substrate cooling. A multidimensional model capturing the nonsymmetric aspects of droplets landing on previously deposited droplets is more representative of the deposition of a layer in the microcasting process. However, experiments that verify our present model can be more accurately performed than multidroplet ex-

periments. In addition, the rapid evolution of the droplet temperature necessitates the inclusion of fluid dynamics in future numerical formulations. The impacting droplet initial temperature, justified as spatially uniform based on the Biot number of a liquid metal droplet passing through a nitrogen environment, would not be uniform for a droplet simultaneously spreading and cooling across a highly conductive metal substrate. This does not reduce the accuracy of the prediction of substrate remelting and the anticipated droplet microstructure that results from the cooling rates, but does limit the ability to predict substrate operating conditions needed for thermal stress determination and for the protection of sacrificial substrate materials, as well as for predicting substrate remelting across the entire width of the impacted droplet.

VII Conclusions

Important factors in the production of high-quality microcasting objects are the creation of metallurgical bonding through substrate remelting, the control of cooling rates of both substrate and deposited material, and the minimization of residual stresses induced by temperature gradients during spray deposition. The numerical tools developed for predicting the thermal history of the microcasting spray process enable us to understand and quantify the effects that microcasting parameters have on droplet and substrate temperature evolution, remelting depths, deposition microstructures, and resulting material properties. Microcasting process conditions permit droplet spreading effects to be neglected because flattening time is an order of magnitude smaller than droplet solidification time. The heat flow in the droplet is initially unidirectional, as verified by the microstructure grain orientation, and is dominated by the heat transfer at the interface between the droplet and substrate. Examining the remelting phenomenon and cooling rates for these conditions provides an understanding of the microcasting process, renders an accurate quantitative prediction of substrate remelting and droplet solidification during the initial stages, and facilitates both analytical and numerical formulations as well as computational efforts.

The analytical solutions predict the temperatures required to promote the substrate remelting and consequent metallurgical bonding desired for the microcasting process. These results, which are also determined numerically, indicate that either an impinging steel droplet temperature of 2300°C is required to remelt about 10 μm of an ambient temperature substrate, or a lower impact temperature is sufficient to remelt a substrate preheated by several hundred degrees. The calorimetric and thermocouple experiments confirm that this 2300°C impact temperature is available with the microcasting process. Dissimilar material layers, such as copper on steel and vice versa, also achieve initial conditions that cause remelting. For the conditions investigated in this paper, numerical simulations and analytical solutions compare within 2 percent during substrate remelting and the initial stages of material deposition cooling.

Numerical temperature predictions within the droplet region are in good agreement with experimental measurements for the first 0.5 seconds, which spans the droplet solidification time of about 0.1 second. Thermocouple experiments also provide longer time cooling histories of the droplets for comparison with the numerical simulations. Although these results compare well for the initial stages of droplet cooling, at later times the numerical simulations underpredict the droplet cooling rate and overestimate the substrate temperatures due to multidimensional substrate effects. The numerical predictions of the substrate remelting and cooling rates are further verified by metallographic examination. Stainless steel metallography verifies the numerically predicted remelting depths, while the metallographic characterization of carbon steel verifies the cooling rates based upon the resulting microstructure, indicating an austenite–ferrite microstructure with martensite traces in the droplet, and a similar microstructure within the remelted substrate.

The heat transfer from the droplet to the substrate dominates the solidification and cooling processes. In addition, the heat transfer coefficient at the droplet/substrate interface is found to be strongly time dependent during substrate remelting and droplet solidification, making a conjugate treatment of the droplet and substrate necessary for accurate substrate remelting numerical modeling.

Acknowledgments

Financial support by the Advanced Research Project Agency, Grant JFBI92195, the Office of Naval Research, Grant N00014-94-1-0183 and the National Science Foundation, Grants DMI-9415001 and CTS-9311072 is gratefully acknowledged. Discussions with Prof. H. W. Paxton regarding the microstructure interpretation are also gratefully acknowledged.

References

Amon, C. H., Beuth, J. L., Kirchner, H., Merz, R., Prinz, F. B., Schmaltz, K. S., and Weiss, L. E., 1993a, "Material Issues in Layered Forming," *Proc. Solid Freeforming Fabrication Symposium,* Austin, TX, pp. 1–10.

Amon, C. H., Prinz, F. B., and Schmaltz, K. S., 1993b, "Numerical Modelling of Thermal Spray Systems," Technical Report EDRC 24-106-93, Carnegie Mellon University, Pittsburgh, PA.

Amon, C. H., Merz, R., Prinz, F. B., and Schmaltz, K. S., 1994a, "Thermal Modelling and Experimental Testing of MD* Spray Shape Deposition Processes," *Proceedings of the Tenth International Heat Transfer Conf.,* Brighton, United Kingdom, Vol. 7, pp. 321–326.

Amon, C. H., Prinz, F. B., and Schmaltz, K. S., 1994b, "Numerical Modeling and Experimental Testing of Metal Droplet Deposition Heat Transfer With Substrate Remelting as Applied to the Microcasting Deposition Process," Tech. Report EDRC 24-116-94, Carnegie Mellon University, Pittsburgh, PA.

Bennett, T., and Poulikakos, D., 1994, "Heat Transfer Aspects of Splat-Quench Solidification: Modelling and Experiment," *J. Mat. Sci.,* Vol. 29, pp. 2025–2039.

Bertagnolli, M., Marchese, M., Jacucci, G., St. Doltsinis, I., and Noelting, S., 1994, "Finite Element Thermomechanical Simulation of Droplets Impacting on a Rigid Substrate," *Proceedings, Energy Tech. Conf. and Exhib. ASME Symp. on Materials, Design and Analysis,* ETCE, New Orleans, LA.

Bewlay, B. P., and Cantor, B., 1991, "The Relationship Between Thermal History and Microstructure in Spray-Deposited Tin–Lead Alloys," *J. Mat. Res.,* Vol. 6, pp. 1433–1454.

Boyer, H. E., ed., 1977, *Atlas of Isothermal Transformation and Cooling Transformation Diagrams,* American Society for Metals, Metals Park, OH, pp. 15–39.

Carslaw, H. S., and Jaeger, J. C., 1959, *Conduction of Heat in Solids,* Clarendon Press, Oxford, pp. 282–291.

Chin, R. K., Beuth, J. L., and Amon, C. H., 1995, "Droplet-Level Thermomechanical Analysis of the Microcasting Process," Tech. Report EDRC 24-120-95, Carnegie Mellon University, Pittsburgh, PA.

Crank, J., 1984, *Free and Moving Boundary Problems,* Oxford Press, New York, pp. 1–29.

El-Kaddah, N., McKelliget, J., and Szekely, J., 1984, "Heat Transfer and Fluid Flow in Plasma Spraying," *Metall. Trans. B,* Vol. 15B, pp. 59–70.

Griffith, R., and Nassersharif, B., 1990, "Comparison of One-Dimensional Interface-Following and Enthalpy Methods for the Numerical Solution of Phase Change," *Numerical Heat Transfer,* Part B, Vol. 18, pp. 169–187.

Guyer, E. C., ed., 1989, *Hndbk. of Appl. Thermal Design,* McGraw-Hill, New York, pp. 67–72.

Honeycombe, R. W. K., 1981, *Steel Microstructure and Properties,* The MacMillan Co., London.

Kang, B., Zhao, Z., and Poulikakos, D., 1994, "Solidification of Liquid Metal Droplets Impacting Sequentially on a Solid Surface," ASME JOURNAL OF HEAT TRANSFER, Vol. 116, pp. 436–445.

Kirchner, H., and Prinz, F. B., 1993, "Adhesion of Liquid Droplet to Solid Substrates," Technical Report EDRC 24-102-93, Carnegie Mellon University, Pittsburgh, PA.

Liu, H., Lavernia, E. J., and Rangel, R. H., 1993, "Numerical Simulation of Substrate Impact and Freezing of Droplets in Plasma Spray Processes," *J. Phys. D Appl. Phys.,* Vol. 26, pp. 1900–1908.

Madejski, J., 1983, "Droplets on Impact With a Solid Surface," *Int. J. Heat Mass Transfer,* Vol. 26, pp. 1098–1102.

Mathur, P., Apelian, D., and Lawley, A., 1989, "Analysis of the Spray Deposition Process," *Acta Metallica,* Vol. 37, pp. 429–443.

Merz, R., Prinz, F. B., Ramaswami, K., Terk, M., and Weiss, L. E., 1994, "Shape Deposition Manufacturing," *Proceedings, Solid Freeform Fabrication Symposium,* Austin, TX, pp. 1–8.

Merz, R., 1994, "Shape Deposition Manufacturing," Ph.D. Thesis, Department of Electrical Engineering, Technical University of Vienna, Austria.

Pawlowski, L., 1981, "Temperature Distribution in Plasma-Sprayed Coatings," *Thin Solid Films,* Vol. 81, pp. 79–88.

Prakash, C., 1990, "Two-Phase Model for Binary Solid–Liquid Phase Change,

Part I: Governing Equations," *Numerical Heat Transfer,* Part B, Vol. 18, pp. 131–145.

San Marchi, C., Liu, H., Lavernia, E. J., Rangel, R. H., Sickinger, A., and Muehlberger, E., 1993, "Numerical Analysis of the Deformation and Solidification of a Single Droplet Impinging Onto a Flat Substrate," *J. Mat. Sci.,* Vol. 28, pp. 3313–3321.

Singer, A. R. E., 1982, "The Challenge of Spray Forming," *Powder Metall.,* Vol. 25, pp. 195–199.

Trapaga, G., and Szekely, J., 1991, "Mathematical Modeling of the Isothermal Impingement of Liquid Droplets in Spraying Processes," *Metall. Trans. B,* Vol. 22B, pp. 901–914.

Trapaga, G., Matthys, E. F., Valencia, J. J., and Szekely, J., 1992, "Fluid Flow, Heat Transfer and Solidification of Molten Droplets Impinging on Substrates: Comparison of Numerical and Experimental Results," *Metall. Trans. B,* Vol. 23B, pp. 701–718.

Voller, V. R., Swaminathan, C. R., and Thomas, B. G., 1990, "Fixed Grid Techniques for Phase Change Problems: A Review," *Intl. J. Numerical Meth. Engr.,* Vol. 30, pp. 875–898.

Wang, G.-X., and Matthys, E. F., 1991, "Modelling of Heat Transfer and Solidification During Splat Cooling: Effect of Splat Thickness and Splat/Substrate Thermal Contact," *Int. J. Rapid Solidification,* Vol. 6, pp. 141–174.

Wang, G.-X., and Matthys, E. F., 1994, "Interfacial Thermal Contact During Rapid Solidification on a Substrate," *Proc. of the Tenth Intl. Heat Transfer Conf.,* Brighton, United Kingdom, Vol. 4, pp. 169–174.

Weiss, L. E., Prinz, F. B., Adams, D. A., and Siewiorek, D. P., 1992, "Thermal Spray Shape Deposition," *J. Thermal Spray Tech.,* Vol. 1, pp. 231–238.

Infiltration and Solidification/ Remelting of a Pure Metal in a Two-Dimensional Porous Preform

X. Tong
Student Mem. ASME

J. A. Khan
Mem. ASME

Department of Mechanical Engineering,
University of South Carolina,
Columbia, SC 29208

Infiltration and solidification/remelting of a pure metal in a two-dimensional porous preform are modeled numerically. It is assumed that under the action of constant applied pressure, the flow of liquid metal through the preform is within the range of the validity of Darcy's Law. The distinguishing feature of this flow and heat transfer problem is the existence of two moving fronts: the infiltration front and the remelting front. The governing momentum and energy equations are nondimensionalized and cast into a Body-Fitted Coordinates (BFC) system to deal with the transient and irregular physical domains. The dimensionless groups that govern the infiltration and remelting processes are: the dimensionless pressure difference, the dimensionless melting temperature, the preform permeability ratio, porosity, and the geometric parameters (inlet gate size, and the preform aspect ratio). A computational code has been developed to solve the problem and is verified by using the available published results. The key parameters describing the physical phenomena, i.e., the infiltration front and remelting front evolution, the total infiltration time, and the remelting region size, are presented as a function of the operating variables for two different aspect ratios. The results can be used to optimize the infiltration processing of Metal–Matrix Composites and other related manufacturing processes.

1 Introduction

Metal–Matrix Composite (MMC) materials and components can be produced in different methods. In the powder metallurgy method, powder of metal and reinforcement material are formed into desired shapes under high pressure and high temperature. In the dispersion process, the reinforcement is stirred into molten or semi-solid metal. The powder metallurgy method is very expensive. While in the dispersion process the nonuniform distribution of reinforcement material and the chemical reaction between the reinforcement material and the molten metal may degrade the properties of the metal–matrix composites. An alternative method for fabricating fiber-reinforced metal–matrix composites is by injecting molten metal into interstices left between fibers, whiskers, or particles packed in a self-supporting preform. This process of preform infiltration has several advantages: It is relatively inexpensive, tooling is similar to casting process, it is possible to produce a net or near-net shape component that is difficult to machine, it is also possible to have a very uniform distribution of reinforcement. The molten metal (matrix) infiltrates the porous preform (reinforcement) under the action of an externally applied pressure difference. The infiltration and associated solidification and remelting phenomena determine the microstructure of the composite material (Mortensen et al., 1988). Since the fibers are usually held at a temperature significantly below the solidification temperature of the metal, some of the molten metal may solidify during the infiltration process within the interstitial spaces of the preform. The preform is held at a temperature below the melting temperature of metal matrix in order to minimize the chemical interactions between the matrix and the ceramic reinforcement. Fukunaga and Goda (1985) have proven that the formation of a layer of solid metal around the fibers can protect the fiber from chemical degradation.

In 1983 Toyota Motor Co. announced its pioneering commercialization of aluminum matrix composite diesel piston by squeeze casting (Donomoto et al., 1983). Since then a significant amount of effort has been devoted to commercialize this fabricating process for manufacturing automotive components, and considerable success has been achieved (Rohatgi, 1991; Mortensen and Koczak, 1993). A partial list of research in the area of infiltration processing of MMC includes the following: Nagata and Matsuda (1983) studied the infiltration of particles ranging in size from 37 to 3400 μm. Fukunaga and Goda (1985) investigated the infiltration of fibrous preform and verified solidification of metal around fibers. Clyne and Mason (1987) presented the critical pressure necessary for melt infiltration and the effect of pressure upon the deformation of preform. Mortensen et al. (1989) derived the general expressions for describing fluid flow and heat transfer during infiltration of fibrous preform by pure metal, and also presented an analytical (similarity) solution for the one-dimensional case. Masur et al. (1989) verified the solution by experimentally measuring the infiltration length and the temperature profile. Rohatgi et al. (1990) investigated the energetics of particle transfer during composite processing.

Infiltration of liquid (resin) in a porous preform (fiber) is also an important physical process in the manufacturing of resin–matrix composites, such as resin transfer molding (RTM), and resin film stacking/compression molding. There exist only a few published numerical stimulation of the two-dimensional mold filling process. Martin and Son (1986) used a finite-element code called POLYFLOW to model the mold filling process for fiber reinforced plastics. Coulter et al. (1987), and Coulter and Guceri (1988) developed a code called TGIMPG to model a two-dimensional resin impregnation process subjected to prescribed injection rate, and also verified

Contributed by the Heat Transfer Division for publication in the JOURNAL OF HEAT TRANSFER. Manuscript received by the Heat Transfer Division December 1994; revision received October 1995. Keywords: Materials Processing and Manufacturing Processes, Moving Boundaries, Phase-Change Phenomena. Associate Technical Editor: A. Faghri.

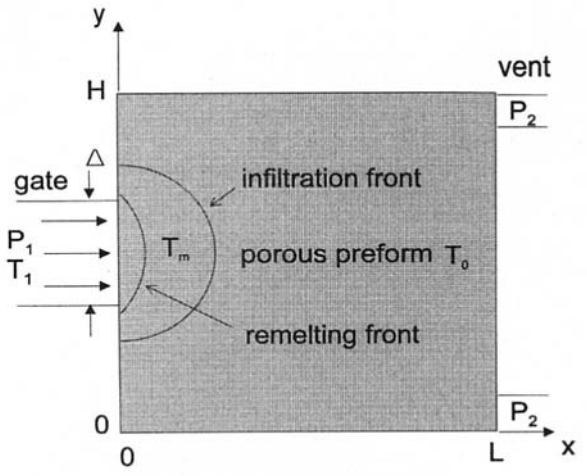

Fig. 1 Schematic of infiltration processing of metal–matrix composites

their numerical code experimentally. But in all these resin mold filling studies, only isothermal flow cases were investigated, and the possibility of phase change as would be encountered during the infiltration process of metal matrix manufacturing was not considered.

The objective of this research is to study the two-dimensional infiltration and solidification/remelting characteristics from a macroscopic point of view and try to understand the relationships between the main features describing the physical phenomenon (i.e., infiltration front, remelting front, total infiltration time, remelting region size) and the operating variables (i.e., pressure difference, temperature, permeability, porosity, and the inlet gate size). A clear understanding of these relationships is necessary to predict and design the infiltration processing of metal–matrix composites and other related manufacturing processes. To the best of the authors' knowledge this is the first study where both infiltration and heat transfer with phase change are modeled in a two-dimensional physical domain.

2 Model

2.1 Physical Domain and Basic Assumptions. The physical domain is shown schematically in Fig. 1. The gate with opening dimension Δ is assumed to be at the middle of the mold wall. The mold walls are assumed to be adiabatic. The porous preform is assumed to be homogeneous with porosity ϕ, but not necessarily isotropic; its principal permeability components are K_x, K_y, for isotropic preform $K_x = K_y$. The molten metal is driven to infiltrate the porous preform placed in the mold by an externally applied pressure difference. The inlet pressure and temperature are P_1 and T_1, respectively. The preform initial temperature is T_0.

During the infiltration process, the preform has two distinct regions: the infiltrated region and the uninfiltrated region, separated by the infiltration front. In the infiltrated region a portion of the molten charge will solidify after coming in contact with a preform that is at a temperature below the melting point. At the same time fresh superheated charge will remelt a portion of the previously solidified metal. From a heat transfer viewpoint, heat transfer occurs on two different time scales during infiltration: The first is the rapid solidification that occurs as a result of heat transfer from the molten metal to the subcooled porous preform. Only a fraction of molten metal will solidify behind the infiltration front in order to raise the preform temperature to the melting temperature. Due to fine fiber size and high thermal conductivity of matrix, the solidification process occurs very rapidly ($\sim$50 μs, Mortensen et al., 1989). While the second one occurs much slower, it results from the fact that the inlet superheated molten metal from mold gate remelts the previously solidified metal. Thus the infiltrated region has two subregions: the remelting region and the solidification region, separated by the remelting front (Fig. 1). On the time scale of infiltration, the solidification region can be considered as an isothermal region where solid and liquid metal matrix coexist.

The assumptions made to derive the governing equations are as follows:

1 The threshold pressure due to capillary effect is a constant, so the pressure difference in this paper only refers to viscous part of total pressure difference;
2 Darcy's law is valid; i.e., $\mathrm{Re}_K = UK_x^{1/2}/\nu < 1$ (Nield and Bejan, 1992). A typical infiltration velocity range for practical infiltration processing is 0.001–0.01 m/s.
3 The gravitational effects upon infiltration and solidification are neglected; it was found that the pressure difference is by far the dominant factor that drives the flow.

Nomenclature

C_p = specific heat at constant pressure
H = mold height
Δh_m = latent heat of metal matrix
$\vec{i}$, $\vec{j}$ = unit vectors in x and y directions
J = Jacobian, Eq. (20)
K_x = permeability component in x direction
K_y = permeability component in y direction
k_c = thermal conductivity of composite
L = mold length
M = dimensionless remelting front position = X/H
$\vec{n}$ = normal direction unit vector
P_1 = inlet pressure
P_2 = outlet pressure
Pr = Prandtl number, Eq. (8)
Re_K = Reynolds number based on permeability K_x
Ste = Stefan number, Eq. (8)
T_1 = melt inlet temperature
T_0 = preform initial temperature
T_m = melting temperature of pure metal
U, V = volume-averaged velocity components
$\bar{U}$, $\bar{V}$ = dimensionless velocity components, Eq. (5)
$\tilde{U}$, $\tilde{V}$ = contravariant velocity components, Eqs. (18) (19)
X = remelting front position
x, y = Cartesian coordinates
$\bar{x}$, $\bar{y}$ = dimensionless coordinates
$\hat{x}$, $\hat{y}$ = normalized coordinates
ψ = dimensionless pressure
$\Delta\psi$ = dimensionless pressure difference
ϕ = preform porosity
θ = dimensionless temperature, Eq. (7)
θ_m = dimensionless melting temperature of metal
ω = square root of permeability ratio, Eq. (6)
Δ = inlet opening size
δ = dimensionless inlet opening size = Δ/H
λ = ratio of heat capacity, Eq. (6)
ϵ = solidification volume fraction
τ = dimensionless time, Eq. (6)
σ = thermal capacity ratio of preform material to metal, Eq. (6)
ρ = density
μ = dynamic viscosity
ν = kinematic viscosity
α_c = thermal diffusivity of composite, $k_c/(\rho C_p)_m$
ξ, η = transformed coordinates
α, β, γ = geometric factors, Eqs. (14) (17)

Subscripts

c = composite
m = metal matrix
p = preform
ξ, η = derivatives with respect to ξ, η

Computational results with gravity force included produced almost identical results.

4 The pressure drop in the uninfiltrated region is negligibly small.
5 Solidification volume fraction ϵ is reasonably small (5–10 percent) such that the permeability in the solidification region can be considered approximately unchanged. The model is capable of incorporating the change in permeability.
6 Local thermal equilibrium, i.e., the preform is at the same temperature as the metal surrounding it.
7 Viscous dissipation and heat loss ahead of the infiltration front are neglected.
8 The physical properties are assumed constant. The metal density remains constant during solid/liquid phase change.

2.2 Governing Equations. The governing continuity, Darcy's law, and the energy equations in the nondimensional form are:

$$\frac{\partial \bar{U}}{\partial \bar{x}} + \frac{\partial \bar{V}}{\partial \bar{y}} = 0 \tag{1}$$

$$\bar{U} = -\frac{\partial \psi}{\partial \bar{x}}, \quad \bar{V} = -\omega^2 \frac{\partial \psi}{\partial \bar{y}} \tag{2}$$

$$\lambda \frac{\partial \theta}{\partial \tau} + \frac{\partial}{\partial \bar{x}}\left(\bar{U}\theta - \frac{1}{\mathrm{Pr}}\frac{\partial \theta}{\partial \bar{x}}\right) + \frac{\partial}{\partial \bar{y}}\left(\bar{V}\theta - \frac{1}{\mathrm{Pr}}\frac{\partial \theta}{\partial \bar{y}}\right) = 0 \tag{3}$$

The movement of the remelting front is governed by the energy conservation at the remelting front (Lim et al., 1993):

$$-\frac{\partial \theta}{\partial \bar{x}}\bigg|_{\bar{x}=M^-} + \frac{\partial M}{\partial \bar{y}}\left(\frac{\partial \theta}{\partial \bar{y}}\right)\bigg|_{\bar{x}=M^-} = \phi\,\mathrm{Pr}\,\frac{\epsilon}{\mathrm{Ste}}\frac{\partial M}{\partial \tau} \tag{4}$$

The following dimensionless variables are used in Eqs. (1)–(4):

$$\bar{x} = \frac{x}{H}, \quad \bar{y} = \frac{y}{H}, \quad \bar{U} = \frac{UH}{\nu}, \quad \bar{V} = \frac{VH}{\nu} \tag{5}$$

$$\tau = \frac{\nu t}{H^2}, \quad \omega^2 = \frac{K_y}{K_x},$$

$$\lambda = \phi + (1-\phi)\sigma, \quad \sigma = \frac{(\rho C)_p}{(\rho C_P)_m} \tag{6}$$

$$\psi = \frac{K_x(P - P_2)}{\rho \upsilon^2}, \quad \theta = \frac{T - T_0}{T_1 - T_0}, \quad \theta_m = \frac{T_m - T_0}{T_1 - T_0} \tag{7}$$

$$M = \frac{X(y,t)}{H}, \quad \mathrm{Pr} = \frac{\nu}{\alpha_c}, \quad \mathrm{Ste} = \frac{(C_P)_m(T_1 - T_0)}{\Delta h_m} \tag{8}$$

where U and V are the volume-averaged velocity (i.e., so-called "seepage velocity") components in x and y directions. $X = X(y, t)$ refers to the transient remelting front position, Δh_m the solid/liquid phase change latent heat of the metal. The aggregate thermal diffusivity α_c in the Prandtl number is evaluated by the "parallel heat conduction" model (Nield and Bejan, 1992). The boundary conditions for governing equations are:

at the inlet gate: $\psi = \Delta\psi, \quad \theta = 1$ (9a)

at the infiltration front: $\psi = 0$ (9b)

at the remelting front: $\theta = \theta_m$ (9c)

at the mold wall: $\dfrac{\partial \psi}{\partial n} = 0, \quad \dfrac{\partial \theta}{\partial n} = 0$ (9d)

where n denotes the normal direction.

An important parameter ϵ, which appears in Eq. (4), is defined as the ratio of volume of solidified metal to the total volume of metal in the solidification region. Unlike the situation for thermal energy storage application (e.g., Lim et al., 1993) where ϵ is prescribed, ϵ is unknown a priori and has to be estimated before applying Eq. (4). As mentioned in the introduction, the solidification process takes place very rapidly in the solidification region. A simple expression for estimating ϵ, which supposes that liquid metal at melting temperature is mixing adiabatically with preform at initial temperature and a fraction of metal solidifies around fibers and releases latent heat to heat up the preform to melting temperature, is given by

$$\frac{\epsilon}{\mathrm{Ste}} = \sigma\theta_m(1/\phi - 1) \tag{10}$$

In this work, however, ϵ is evaluated based on the energy conservation of the whole infiltrated region. Since the mold walls are insulated and the heat loss ahead of infiltration front is negligible (assumption 7), the total energy within the remelting region and the solidification region needs to be balanced by the energy carried in by liquid metal and the latent heat released. Only the initial value of ϵ is given by Eq. (10). The numerical result showed that ϵ is not constant during the infiltration process; it decreases slightly with infiltration process. Another feature of ϵ is that its magnitude is always proportional to Ste (Eq. (10), or energy conservation). While looking back at Eq. (4), we see that the movement of remelting front is governed by ϵ/Ste. Therefore, Stefan number plays no role explicitly! But implicitly, it is important simply because its magnitude determines the magnitude of ϵ. Assumption (5) implies that Ste is small. If Ste is so large as to make ϵ larger than or equal to 1, then infiltration will terminate, which is, of course beyond the scope of this paper. Combining Eqs. (1) and (2), and introducing new variables

$$\hat{x} = \omega\bar{x}, \quad \hat{y} = \bar{y} \tag{11}$$

we obtain the following Laplace-type pressure equation:

$$\frac{\partial^2 \psi}{\partial \hat{x}^2} + \frac{\partial^2 \psi}{\partial \hat{y}^2} = 0 \tag{12}$$

2.3 Body-Fitted Coordinate Transformation. Because both the domains, infiltrated region and remelting region, are time dependent and irregular in physical space, it is convenient to use a general curvilinear coordinate system to map these regions into squares in computational space so that the moving boundaries are immobilized. Following Thompson et al. (1974) and Karki and Patankar (1988), we introduce (ξ, η) as the transformed coordinates. The infiltrated region was mapped into a unit square in computational space by transformation $\hat{x} = \hat{x}(\xi, \eta, t)$, $\hat{y} = \hat{y}(\xi, \eta, t)$. The equations governing transformation will not be repeated here for brevity. Equation (12) takes the following form:

$$\alpha\psi_{\xi\xi} - 2\beta\psi_{\xi\eta} + \gamma\psi_{\eta\eta} = 0 \tag{13}$$

where

$$\alpha = \hat{x}_\eta^2 + \hat{y}_\eta^2, \quad \beta = \hat{x}_\xi\hat{x}_\eta + \hat{y}_\xi\hat{y}_\eta, \quad \gamma = \hat{x}_\xi^2 + \hat{y}_\xi^2 \tag{14}$$

Subscripts ξ and η denote the derivatives with respect to ξ, η. With the boundary conditions:

$$\xi = 0, \quad 0 \le \eta \le 1: \quad \psi = \Delta\psi \tag{15a}$$

$$\xi = 1, \quad 0 \le \eta \le 1: \quad \psi = 0 \tag{15b}$$

$$\eta = 0, \quad 1; \quad 0 \le \xi \le 1:$$

$$\frac{\partial \psi}{\partial n} = \vec{n} \cdot \nabla\psi = \vec{n} \cdot (\vec{i}\psi_x + \vec{j}\psi_y) = 0 \tag{15c}$$

in which ψ_x and ψ_y refer to the first derivatives of x and y.

The remelting region was similarly mapped into a unit square by introducing the transformation $\bar{x} = \bar{x}(\xi, \eta, t)$, $\bar{y} = \bar{y}(\xi, \eta, t)$. The energy equation becomes

$$\frac{\partial}{\partial \tau}(\lambda J\theta) + \frac{\partial}{\partial \xi}\left(\tilde{U}\theta - \frac{1}{\mathrm{Pr}}\frac{\alpha}{J}\frac{\partial \theta}{\partial \xi}\right) + \frac{\partial}{\partial \eta}\left(\tilde{V}\theta - \frac{1}{\mathrm{Pr}}\frac{\gamma}{J}\frac{\partial \theta}{\partial \eta}\right) = -\frac{\partial}{\partial \xi}\left(\frac{1}{\mathrm{Pr}}\frac{\beta}{J}\frac{\partial \theta}{\partial \eta}\right) - \frac{\partial}{\partial \eta}\left(\frac{1}{\mathrm{Pr}}\frac{\beta}{J}\frac{\partial \theta}{\partial \xi}\right) \quad (16)$$

where $\tilde{U}$, $\tilde{V}$ represent the relative, contravariant velocity components normal to the constant ξ- and η-coordinate lines, where

$$\alpha = \bar{x}_\eta^2 + \bar{y}_\eta^2, \quad \beta = \bar{x}_\xi \bar{x}_\eta + \bar{y}_\xi \bar{y}_\eta, \quad \gamma = \bar{x}_\xi^2 + \bar{y}_\xi^2 \quad (17)$$

$$\tilde{U} = \bar{y}_\eta(\bar{U} - \lambda \bar{x}_t) - \bar{x}_\xi(\bar{V} - \lambda \bar{y}_t) \quad (18)$$

$$\tilde{V} = \bar{x}_\xi(\bar{V} - \lambda \bar{y}_t) - \bar{y}_\eta(\bar{U} - \lambda \bar{x}_t) \quad (19)$$

$$J = \bar{x}_\xi \bar{y}_\eta - \bar{x}_\eta \bar{y}_\xi \quad (20)$$

and $\bar{y}_\eta \bar{x}_t - \bar{x}_\eta \bar{y}_t$, $\bar{x}_\xi \bar{y}_t - \bar{y}_\xi \bar{x}_t$ are called the contravariant pseudo-velocities. The boundary conditions for the energy equation are

$$\xi = 0, \quad 0 \le \eta \le 1: \quad \theta = 1 \quad (21a)$$

$$\xi = 1, \quad 0 \le \eta \le 1: \quad \theta = \theta_m \quad (21b)$$

$$\eta = 0, 1; \quad 0 \le \xi \le 1:$$

$$\frac{\partial \theta}{\partial n} = \vec{n} \cdot \nabla \theta = \vec{n} \cdot (\vec{i}\theta_x + \vec{j}\theta_y) = 0 \quad (21c)$$

The discretization of the pseudo-velocities (or mesh velocities) arising from moving grids requires careful treatment in order to satisfy global mass conservation (Kim and Kaviany, 1992).

3 Numerical Procedure

The pressure governing Eq. (13) was discretized via a finite-difference method. To avoid the singularity of pressure distribution (hence velocity profile) at the initial time and still keep the Darcy's flow model applicable, a small region near the gate was chosen to initiate the numerical simulation. This region was properly chosen such that the infiltration front and the infiltration time are independent of this small region. A rectangular region of $0.05 \times \delta$ was assumed to be the initial infiltration region. Numerical tests showed convergence of results with this choice. The line-by-line Thomas algorithm was used to solve the discretized equations. The movement of infiltration front was dealt with by applying a so-called "quasi-stationary front" approximation (Sparrow et al., 1977; Lim et al., 1993), which implies a fixed infiltrated region during each time interval, and a stepwise progression of the front. A proper choice of time step is necessary to use this approximation. A variable time step was chosen such that the center point on the infiltration front moved by 0.001 when $\bar{x} \le 0.2$, and it moved by 0.005 when $\bar{x} > 0.2$ during each time interval. The test of time step refinement showed convergence of results. In addition, the moving front was assumed to meet the mold wall orthogonally because the front is isobaric and the wall is impermeable; in other words, a slip boundary condition was used.

The energy Eq. (16) was discretized by using a control-volume-based finite-difference method. The pseudo-velocities were discretized by applying the geometric relation associated with the moving control volumes in the physical domain as suggested by Kim and Kaviany (1992). In this way the pseudo-velocities satisfy the continuity equation identically. The power law scheme proposed by Patankar (1980) was used for the convection-diffusion terms. To initiate the calculation, the initial remelting region was calculated from the ϵ given by Eq. (10) and from the known initial infiltration region. The remelting front movement was dealt with in the same way as was the infiltration front. For the present problem, a 31×31 grid was selected, which is basically a compromise between numerical accuracy and computational cost. The grids were refined from 11×11 to 41×41 grids. The refinement tests showed that 31×31 grids produced numerical results, namely, total infiltration time and remelting region size, of 3 percent accuracy (Tong, 1995).

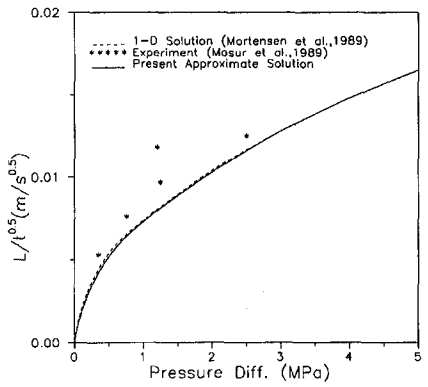

Fig. 2 Validation results for the one-dimensional infiltration process

4 Validation of the Code

The present code was validated in two steps, i.e., the code to model the infiltration of liquid metal and the code to model the heat transfer/phase change were validated separately. The infiltration code was verified with the results reported by Martin and Son (1986). They modeled a two-dimensional isothermal resin impregnation process numerically. The infiltration evolution tests showed very good agreement between the present predictions and Martin and Son's results (Tong, 1995). Moreover, we also tested a limiting case where opening size δ approaches one. In that case the two-dimensional infiltration approaches a one-dimensional case. Mortensen et al. (1989) gave a similarity solution for one-dimensional infiltration and Masur et al. (1989) verified the theory experimentally. Figure 2 shows good agreement between their result with the result from the present model for a gate dimension of $\delta = 0.9$. The coordinates in Fig. 2 were directly from Masur et al. (1989), in the one-dimensional similarity solution, the infiltration length L is found proportional to square root of time t, the proportional constant is a function of applied pressure difference Δp.

The code for the numerical solution of the energy equation was used to calculate the melting in a two-dimensional cavity filled with porous medium heated from the side. This was done because Jany and Bejan (Chap. 10, Nield and Bejan, 1992) have reported the results for the problem. Figure 3 compares

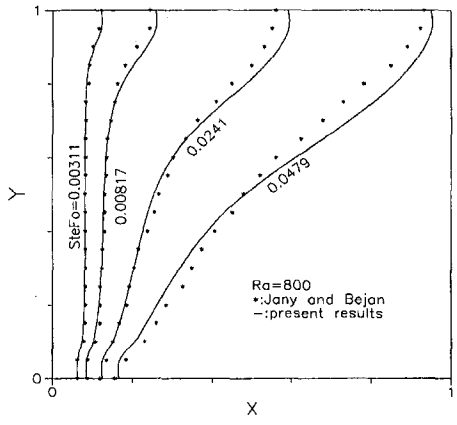

Fig. 3 Results showing melting in a two-dimensional porous medium heated from the side

Table 1 Physical properties of aluminum and SAFFIL® (Masur et al., 1989)

	ρ (Kg/m^3)	C_p (J/Kg·K)	μ (Pa·s)	k (W/m·K)	T_m (K)	Δh_m (KJ/Kg)
Al(l)	2400	1083	1.3×10^{-3}	93		
Al(s)	2700	1296			933	398
SAFFIL	3300	1213		8		

the remelting front evolution results for Ra = 800. The results from the present numerical code agree very well with the results obtained by Jany and Bejan.

5 Results and Discussion

Table 1 lists the physical properties of the pure metal and the reinforcement material used in the numerical study. These properties were chosen because they represent the properties of one of the common metal–matrix composites, i.e., the Aluminum-SAFFIL® (nominally 3-μm-dia, delta-alumina) system.

Generally, the infiltration and remelting processes are governed by the following dimensionless groups: applied pressure difference ($\Delta\psi$), melting temperature (θ_m), gate opening dimension (δ), porosity (ϕ), permeability ratio (ω), and preform aspect ratio (L/H). The magnitude of $\Delta\psi$ chosen was determined by considering real-life situations, where $\Delta p \sim 10^6$ N/m^2, $K \sim 10^{-12}$ m^2, $\nu \sim 10^{-6}$ m^2/s, $\rho \sim 10^3$/kg/m^3 $\Rightarrow \Delta\psi \sim 10^3$. The magnitude of θ_m depends not only on the superheat $T_1 - T_m$ of inlet molten metal, but also on the initial temperature difference $T_1 - T_0$ between the inlet molten metal and the preform. Lower superheat $T_1 - T_m$, or higher initial temperature $T_1 - T_0$ will result in larger θ_m; for example, $\theta_m = 1$ implies no superheat of inlet liquid metal. The following parameter ranges are studied in this paper: $\Delta\psi = 200 \sim 1500$, $\theta_m = 0.5 \sim 1.0$, $\phi = 0.3 \sim 0.8$, $\delta = 0.1 \sim 0.5$, $\omega = 0.8 \sim 1.2$, and $L/H = 1$ and 2.

Figure 4 shows a typical time evolution of the infiltration front and the remelting front in an isotropic preform ($\omega = 1$) with gate dimension $\delta = 0.1$. The dimensionless pressure difference and the preform porosity are, respectively, $\Delta\psi = 10^3$ and $\phi = 0.5$. Front locations at different time are shown in the figure. The initial front shape depends strongly on the gate dimension, and the filling behavior is similar to infiltration in a semi-infinite preform. But when the infiltration front meets the top and the bottom mold walls, the confinement of the walls make the filling behavior unidirectional. The infiltration front at this time tends to be planar. In order to show the remelting front evolution clearly, the dimensionless melting temperature was selected as $\theta_m = 0.7$, for the case shown in Fig. 4. The final remelting region size for this particular case is about 15 percent of the total infiltrated area.

The infiltration velocity decreases very rapidly with time. For a preform dimension of 1 m × 1 m, the dimensional infiltration velocity changes from $O(10^{-2}$ m/s) at the beginning to $O(10^{-3}$ m/s), which justifies the application of Darcy's law. The total infiltration time, for the particular case shown in Fig. 4, is about 17 minutes.

The temperature profile evolution in the remelting region for the same case as Fig. 4 is shown in Fig. 5. The isotherms at three times $\tau = 0.098 \times 10^{-4}$, 1.788×10^{-4}, and 5.237×10^{-4} are shown. The isotherm lines $\theta_m = 0.7$ are nothing but the remelting fronts. The isotherm lines $\theta_m = 1$ are located at the inlet gate (not shown in the figure). The main feature of the temperature profile is that temperature gradient is concentrated on the remelting side of the remelting front. This kind of temperature concentration profile has an important effect on the development of microstructure of MMCs. The existence of temperature gradient (heat flux) in the remelting region results in the columnar coarse grains, while the solidification region is featured by the equiaxed fine grains (Calhoun and Mortensen, 1992).

Figure 6 shows the effect of the pressure difference, $\Delta\psi$, on the total infiltration time τ_f. The total infiltration time is defined as the time interval from the beginning of the infiltration to the instant when the infiltration front reaches the right wall of the mold. The numerical results presented are for an isotropic preform with porosity of 0.5, aspect ratios $L/H = 1$ and 2, with three gate openings 0.1, 0.3, and 0.5. As expected, the total infiltration time τ_f decreases with the increase of $\Delta\psi$. It can be noted that at higher pressures, i.e., when $\Delta\psi > 1400$, the infiltration time decreases very slowly with increasing $\Delta\psi$. This observation implies the existence of an optimal pressure $\Delta\psi$ of below or around 1400 for practical fabrication of metal–matrix composites, since higher pressure implies higher capital costs without added benefit. The total infiltration time diminishes with increasing gate size. The curves shown by the dotted lines represent the similarity solution for one-dimensional cases (Mortensen et al., 1989). It can be observed from Fig. 6 that when the opening δ is larger than 0.5, the numerical results approach the limiting case: one-dimensional solutions, for both aspect ratios.

The effect of the preform porosity ϕ on the total infiltration time τ_f is illustrated in Fig. 7. For the two dimensionless pressure differences 200 and 1000, the total infiltration time increases linearly as ϕ increases. This is because the actual infiltration velocity (volume-averaged velocity divided by ϕ) slows down when ϕ increases. When gate opening decreases, the effect of porosity becomes more pronounced, namely, a larger slope of the straight lines in the figure. However, as observed in Fig. 6, as the dimensionless pressure difference increases, this effect becomes smaller.

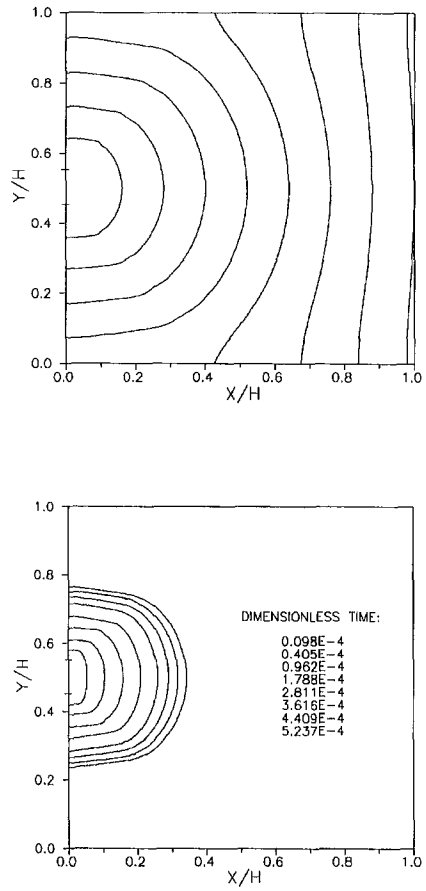

Fig. 4 Evolution of infiltration and remelting fronts: $\delta = 0.1$, $\Delta\psi = 10^3$, $\theta_m = 0.7$, $\phi = 0.5$, $\omega = 1$

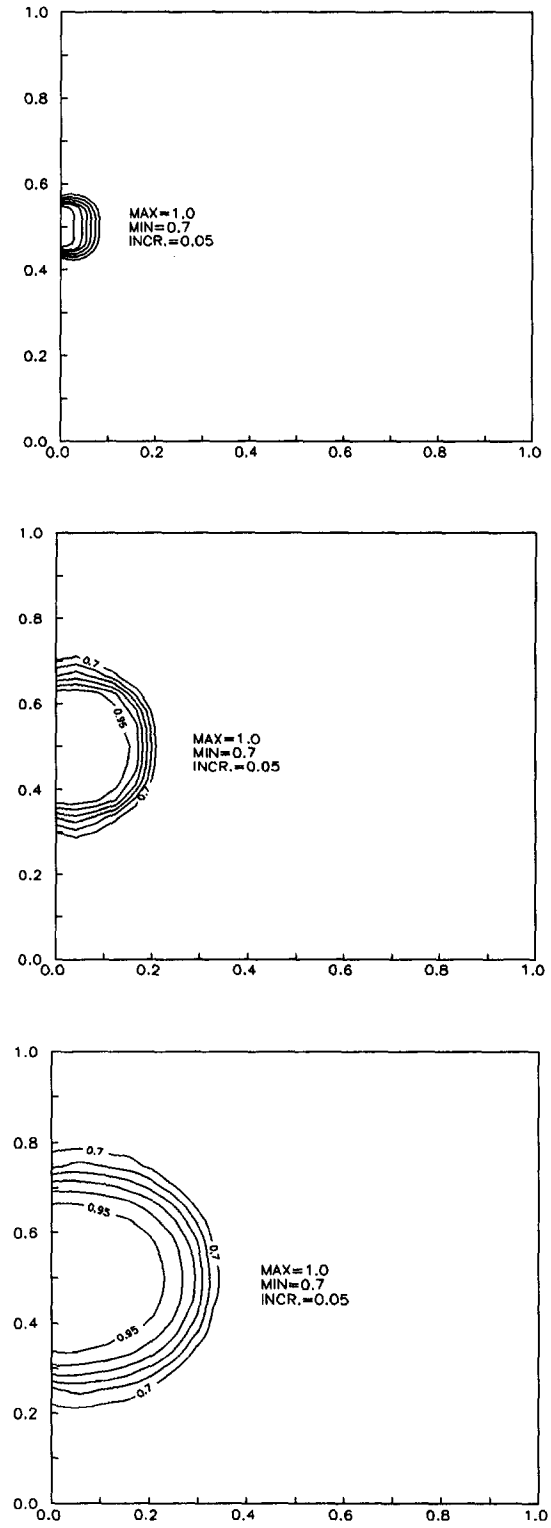

Fig. 5 Isotherm evolution within the remelting region: δ = 0.1, $\Delta\psi$ = 10^3, θ_m = 0.7, ϕ = 0.5, ω = 1

Figure 8 illustrates the effect of dimensionless melting temperature θ_m and porosity ϕ on the remelting region size. The remelting region size is defined as the area of final remelting region when the infiltration process completes. This area is normalized as a percentage of the total infiltrated area. The results show that it decreases as θ_m increases almost linearly for three different porosities of 0.3, 0.5 and 0.7. In addition, it also increases as preform porosity increases (i.e., more liquid

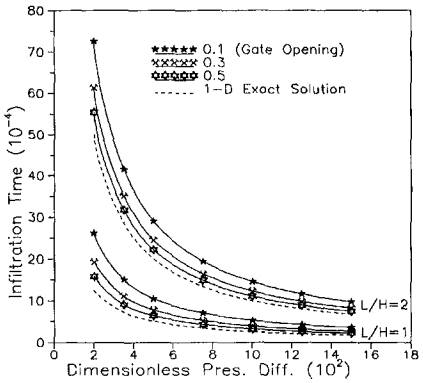

Fig. 6 Total infiltration time τ_f as a function of $\Delta\psi$ (ϕ = 0.5, ω = 1)

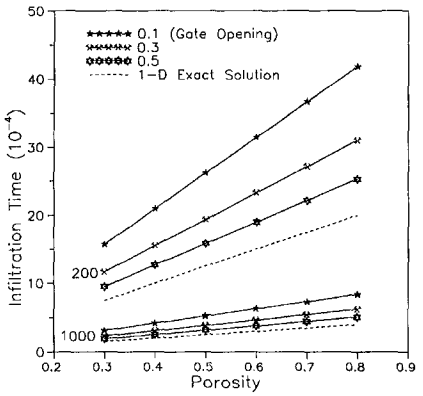

Fig. 7 Total infiltration time τ_f as a function of ϕ (ω = 1, L/H = 1)

metal needs to be filled into the preform). An interesting feature revealed by Fig. 8 is that the remelting region size is independent of the gate size δ. The reason for this is that the mold wall is adiabatic; therefore, the final remelting region size, which is a function of the total energy carried into the preform by liquid metal, is independent of the gate openings. The numerical results also show that the dimensionless pressure difference has only a minor influence on the remelting region size. As the dimensionless pressure difference decreases, the remelting region size increases slightly.

For most real-life fabrication of MMCs, it is important to note that the remelting region is usually small because of low superheat of inlet liquid metal, or high subcooled preform. For example, if preform porosity is 0.5, the inlet metal superheat is 20 K, the initial temperature difference between metal and pre-

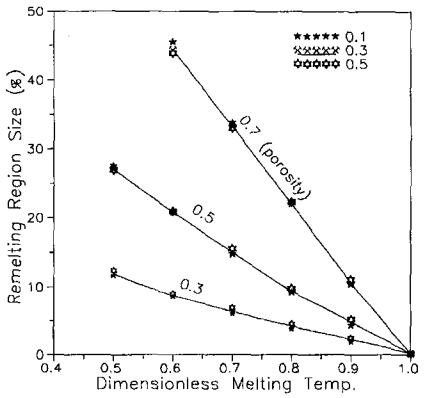

Fig. 8 Remelting region size percentage as a function of θ_m ($\Delta\psi$ = 10^3, ω = 1, L/H = 1)

form is 200 K, then $\theta_m = 0.9$, the final remelting region is only 6 percent of the total infiltrated region (see Fig. 8). Therefore, the whole infiltration region is dominated by the solidification region. If we consider the variation of K_x and K_y due to the solidification and use an appropriate permeability model to modify K_x and K_y in the solidification region, then the results given in this paper remain applicable. For example, if the externally applied pressure difference ΔP is kept fixed, then the effect of solidification is to reduce K_x and K_y, and thus reduce $\Delta\psi$, resulting in an increase in the total infiltration time.

Figure 9 shows the effect of anisotropic permeability ratio $K_y/K_x(\omega^2)$ on the total infiltration time τ_f for three different gate openings. Since we assume that $\Delta\psi(\Delta P \cdot K_x)$ is fixed for each simulation, the variation of permeability ratio implies the variation of K_y. It can be seen that the effect of ω on the infiltration time is generally weak except for the case of lower pressure difference, i.e., $\Delta\psi = 200$ and $\delta = 0.1$. The infiltration time decreases very slowly as permeability ratio increases. But the anisotropic preform has considerable influence on the shape of infiltration fronts, which are shown in Fig. 10. For the sake of comparing with Fig. 4, Fig. 10 was also based on $\Delta\psi = 1000$, $\phi = 0.5$, and $\delta = 0.1$. The infiltration front evolutions for $K_y/K_x = 0.64$ ($\omega = 0.8$), and $K_y/K_x = 1.44$ ($\omega = 1.2$) are presented. Compared with Fig. 4, the infiltration fronts are deformed and tilted according to the variation of K_y.

The numerical results also show that the effect of permeability ratio on the remelting region size is weak. The remelting region size decreases very slightly with the increase of permeability ratio. But the remelting front evolution is influenced to some degree by the variation of permeability ratio.

6 Conclusions

A numerical simulation of infiltration and solidification/remelting process of a pure metal in a two-dimensional porous preform is presented in this paper. The primary objectives, which included prediction of the total infiltration time, and the remelting region size, are accomplished. The physical variables governing the infiltration and remelting processes are nondimensionalized into several groups, and the effects of these groups on the infiltration time and the remelting region size are studied thoroughly. Based on the present numerical results, the following conclusions can be reached:

1 The infiltration and solidification processes are governed by the following dimensionless groups: $\Delta\psi$, θ_m, ϕ, ω, δ and L/H. The choice of nondimensional variables, instead of the individual physical variables, will be helpful for correlating experimental results.

2 The remelting region size strongly depends on the dimensionless melting temperature θ_m, and porosity ϕ as shown in Fig. 8, while it weakly depends on the dimensionless pressure difference $\Delta\psi$, and permeability ratio ω. The remelting region is independent of the gate size δ.

3 The total infiltration time strongly depends on the dimensionless pressure difference $\Delta\psi$, inlet gate opening δ, and aspect ratio L/H, as shown in Fig. 6.

4 The total infiltration time increases linearly with the increase of preform porosity ϕ, as shown in Fig. 7. This effect is more pronounced at lower $\Delta\psi$.

5 The anisotropy of the preform has a considerable effect on the shape of infiltration front, as shown in Fig. 10. But its effect on the total infiltration time and remelting region size is relatively weak.

6 For practical fabrication of metal matrix composites, the remelting region is usually small. The results presented in this paper can also be extended to those cases where the solidification volume fraction ϵ is so large that permeability components in the solidification region change considerably.

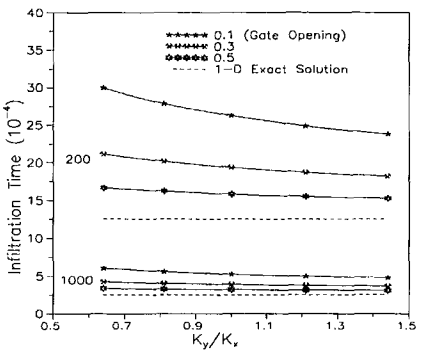

Fig. 9 Effect of $\omega^2(K_y/K_x)$ on total infiltration time τ_f ($\phi = 0.5$, $L/H = 1$)

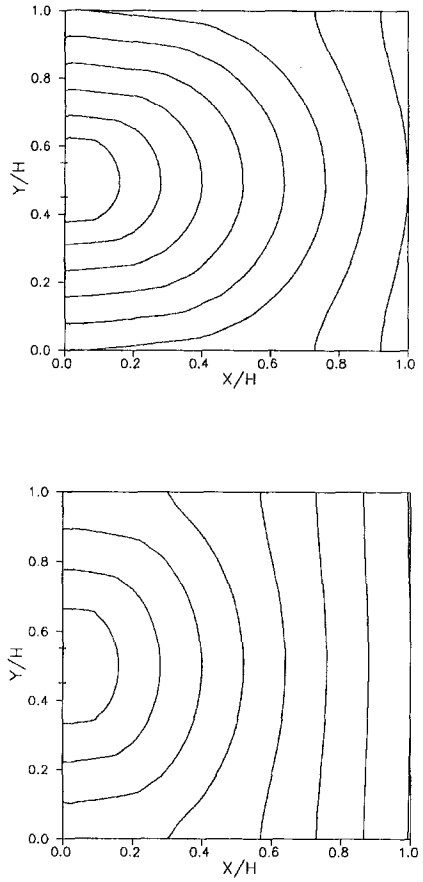

Fig. 10 Effect of ω on the infiltration front for $\omega = 0.8$ (above), 1.2 (below) ($\Delta\psi = 10^3$, $\phi = 0.5$, $L/H = 1$)

References

Calhoun, R. B., and Mortensen, A., 1992, "Infiltration of Fibrous Preform by a Pure Metal: Part IV. Morphological Stability of the Remelting Front," *Metall. Trans. A*, Vol. 23A, pp. 2291–2299.

Clyne, T. W., and Mason, J. F., 1987, "The Squeeze Infiltration Process for Fabrication of Metal-Matrix Composites," *Metall. Trans. A*, Vol. 18A, pp. 1519–1530.

Coulter, J. P., Smith, B. F., and Guceri, S. I., 1987, "Experimental and Numerical Analysis of Resin Impregnation During the Manufacturing of Composite Materials," *Proceedings of the American Society for Composites, 2nd Technical Conference*, Newark, DE, pp. 209–217.

Coulter, J. P., and Guceri, S. I., 1988, "Resin Impregnation During the Manufacturing of Composite Materials Subject to Prescribed Injection Rate," *J. of Reinforced Plastics and Composites*, Vol. 7, pp. 200–219.

Donomoto, T., Miura, N., Funatani, K., and Miyake, N., 1983, "Ceramic Fiber Reinforced Piston for High Performance in Diesel Engine," SAE Technical Paper No. 83052.

Fukunaga, H., and Goda, K., 1985, "Formation and Role of the Solidified Layer on a Fiber During the Fabrication of Fiber Reinforced Metal by the Liquid Process," *J. Jap. Institute of Metals,* Vol. 49, pp. 78–83.

Karki, K. C., and Patankar, S. V., 1988, "Calculation Procedure for Viscous Incompressible Flows in Complex Geometries," *Numerical Heat Transfer,* Vol. 14, pp. 295–307.

Kim, C. J., and Kaviany, M., 1992, "A Numerical Method for Phase-Change Problems With Convection and Diffusion," *Int. J. Heat Mass Transfer,* Vol. 35, pp. 457–467.

Lim, J. S., Fowler, A. J., and Bejan, A., 1993, "Spaces Filled With Fluid and Fibers Coated With a Phase-Change Material," ASME JOURNAL OF HEAT TRANSFER, Vol. 115, pp. 1044–1050.

Martin, G. Q., and Son, J. S., 1986, "Fluid Mechanics of Mold Filling for Fiber Reinforced Plastics," *Proceedings of the ASM/ESD Second Conference on Advanced Composites,* Dearborn, MI, pp. 149–157.

Masur, L. J., Mortensen, A., Cornie, J. A., and Flemings, M. C., 1989, "Infiltration of Fibrous Preform by a Pure Metal: Part II. Experiment," *Metall. Trans. A,* Vol. 20A, pp. 2549–2557.

Mortensen, A., Cornie, J. A., and Flemings, M. C., 1988, "Solidification Processing of Metal-Matrix Composites," *J. of Metals,* Feb., pp. 12–19.

Mortensen, A., Masur, L. J., Cornie, J. A., and Flemings, M. C., 1989, "Infiltration of Fibrous Preform by a Pure Metal: Part I. Theory," *Metall. Trans. A,* Vol. 20A, pp. 2535–2547.

Mortensen, A., and Koczak, M. J., 1993, "The Status of Metal-Matrix Composite Research and Development in Japan," *J. of Metals,* Mar., pp. 10–18.

Nagata, S., and Matsuda, K., 1983, "Pressure Casting Conditions of Metal-Hybrid Particle Composites and Their Applications," *Trans. Japan Foundry Men's Soc.,* Vol. 2, pp. 616–620.

Nield, D. A., and Bejan, A., 1992, *Convection in Porous Medium,* Springer-Verlag, New York, Chaps. 1 and 10.

Patankar, S. V., 1980, *Numerical Heat Transfer and Fluid Flow,* Hemisphere, Washington, DC.

Rohatgi, P. K., 1991, "Cast Aluminum-Matrix Composites for Automotive Applications," *J. of Metals,* Apr., pp. 10–15.

Rohatgi, P. K., Asthana, R., Yadav, R. N., and Ray, S., 1990, "Energetics of Particle Transfer From Gas to Liquid During Solidification Processing of Composites," *Metall. Trans. A,* Vol. 21A, pp. 2073–2082.

Sparrow, E. M., Patankar, S. V., and Ramadhyani, S., 1977, "Analysis of Melting in the Presence of Natural Convection in the Melt Region," ASME JOURNAL OF HEAT TRANSFER, Vol. 99, pp. 520–526.

Thompson, J. F., Thames, F. C., and Mastin, C. W., 1974, "Automatic Numerical Generation of Body-Fitted Curvilinear Coordinate System for Field Containing Any Number of Arbitrary Two-dimensional Bodies," *J. of Computational Physics,* Vol. 15, pp. 299–319.

Tong, X., 1995, "Infiltration, Solidification and Remelting of a Pure Metal in 2-D Porous Preform," MS thesis, The University of South Carolina, Columbia, SC.

The Effect of Ambient Pressure on Flame Spread Over Thin Cellulosic Fuel in a Quiescent, Microgravity Environment

S. Bhattacharjee
Department of Mechanical Engineering,
San Diego State University,
San Diego, CA 92182

R. A. Altenkirch
Department of Mechanical Engineering and
NSF Engineering Research Center for
Computational Field Simulation,
Mississippi State University,
Mississippi State, MS 39762

K. Sacksteder
NASA Lewis Research Center,
Cleveland, OH 44135

Results from recently conducted experiments on flame spread over a thin cellulosic fuel in a quiescent, microgravity environment of a 50/50 volumetric mixture of oxygen and nitrogen (oxygen mass fraction 0.53) at three different pressures—101, 152, and 203 kPa (1, 1.5, and 2.0 atm)—are analyzed. The results are compared with established theoretical results and two different computational flame spread models: one that includes gas-phase radiation, and one that does not. The spread rate behavior from experiment, i.e., an increase of spread rate with pressure, is consistent with the theoretical model that includes gas-phase radiation, and side-view photographs of the flames compare favorably with two-dimensional temperature contours produced computationally from the same model. In contrast, neither the dependence of spread rate on pressure nor the flame shape can be predicted with favorable comparison to experiment if radiation is neglected.

Introduction

The effect of ambient pressure on flame spread over thermally thin fuels in a normal-gravity environment is well known (Altenkirch and Bhattacharjee, 1990; Lastrina et al., 1971; Williams, 1976; de Ris, 1969) and can be deduced from simple scaling arguments. However, in a microgravity environment, complications arise because the conduction length scale based on a balance of upstream heat conduction and downstream convection, appropriate for flame spread into an opposing flow, becomes larger than the actual physical scale of the flame due to lack of any buoyancy-induced flow.

Consider the opposed-flow configuration depicting flame spread over a thin fuel shown in Fig. 1. In flame-fixed coordinates the oxidizer approaches with a velocity $V_r = V_f + V_g$, and the solid fuel approaches the flame with a velocity V_f, a desired unknown. Because heat transfer ahead of the flame leading edge constitutes the mechanism of flame spread, the length over which heat is transferred at the leading edge is important for scaling purposes. The balance between forward heat conduction and convection at the flame leading edge produces a thermal length scale of $L_g = \alpha_g/V_r$, also a diffusion length scale for unit Lewis number. For thin solids ($\tau \ll L_g$), gas-phase conduction is the principal forward heat transfer mechanism ahead of the flame if radiation is neglected, so L_g is the characteristic length scale for the entire problem.

The simplest model of flame spread is the thermal model in which a thin solid fuel of half-thickness τ is heated from T_∞ to a vaporization temperature T_v by conduction heat transfer from the flame to the fuel ahead of it (the preheat zone). In approximate terms, the conductive flux is $\dot{q}''_{gsc} \approx \lambda_g(T_f - T_v)/L_g$, and the length of the preheat zone is L_g, so that the total heat transfer rate is approximately $\lambda_g(T_f - T_v)$. This forward heat transfer is responsible for the sensible heating of the fuel moving at a speed V_f toward the flame, the rate of heating being $\rho_s\tau C_s V_f(T_v - T_\infty)$. Balancing these rates, $V_f \approx (\lambda_g/\tau\rho_s C_s)(T_f - T_v)/(T_v - T_\infty)$, which is similar in form to the classical solution of the flame spread problem developed by de Ris (1969). According to this expression, for fixed T_f, which for fixed $m_{ox,\infty}$ obtains for infinitely fast gas-phase kinetics, the spread rate is independent of pressure and opposing flow velocity provided the vaporization temperature, T_v, known experimentally or from correlation (Bhattacharjee et al., 1994a, b) is independent of pressure. The conduction length scale, L_g, is affected by changes in pressure and opposing flow velocity and is the length scale for heat transfer both normal and parallel to the fuel surface, so it has an effect on the size and the structure of the flame but not on V_f.

At high opposing flow velocity, however, the gas-phase kinetics can no longer be considered infinitely fast compared to the residence time of the oxidizer at the flame leading edge, and the spread rate becomes dependent on the flow velocity; this dependence has been experimentally correlated with the Damkohler number (Fernandez-Pello et al., 1981), the ratio of the characteristic residence time to the characteristic gas-phase combustion time. Although both the gas-phase residence time, $t_{res} \equiv L_g/V_r = \lambda_g/\rho_g C_g V_r^2$, and the chemical time for second-order kinetics, $t_{comb} \approx L_g^2\rho_g m_f/B_g\rho_g^2 m_f m_{ox} e^{-E_g/RT} \propto 1/\rho_g B_g$, are dependent on the ambient pressure through ρ_g, the Damkohler number is independent of pressure for forced-convective opposing flow where V_r is independent of P_∞. Therefore, the spread rate is expected to be insensitive to pressure even when gas-phase kinetics control the flame spread.

For downward flame spread over a thin fuel in a quiescent, normal-gravity environment, the characteristic opposing flow velocity created by buoyancy is $V_r \approx (g\alpha_g(T_f - T_\infty)/T_\infty)^{1/3}$ and can be high enough for the gas-phase kinetic effect to be important. The Damkohler number for this situation is proportional to $P_\infty^{2/3}$. This implies that as ambient pressure increases, the Damkohler number and the spread rate increase as well. This behavior is observed experimentally for an ambient oxygen level of 21 percent (Lastrina et al., 1971). In addition, spread rate has been correlated with a Damkohler number that includes the effect of pressure on the induced flow (Altenkirch et al., 1980).

In a microgravity environment, buoyancy being almost absent, the above-mentioned effect of the ambient pressure is almost nonexistent. Moreover, in a quiescent environment the

Contributed by the Heat Transfer Division for publication in the JOURNAL OF HEAT TRANSFER. Manuscript received by the Heat Transfer Division June 1994; revision received June 1995. Keywords: Combustion, Microgravity Heat Transfer, Radiation. Associate Technical Editor: W. L. Grosshandler.

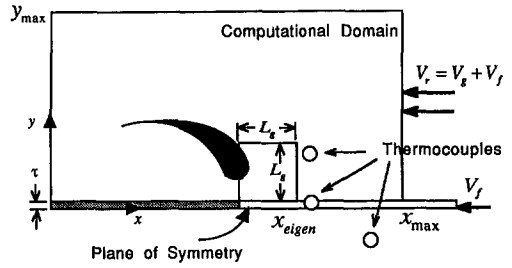

Fig. 1 Schematic of the computational domain and the relative locations of the thermocouples

Damkohler number reaches a maximum as the opposing flow velocity, with respect to the flame, reaches a minimum as $V_r \rightarrow V_f$, assuring fast chemistry. Ambient pressure, therefore, is not expected to influence the spread rate if the model developed for normal-gravity flames remains valid at microgravity. However, at low opposing flow velocity, the quiescent, microgravity configuration being the extreme case, some of the assumptions used in the normal-gravity model are no longer valid. Principal among these is the neglect of radiation.

The importance of radiation can be demonstrated through scaling arguments by comparing the time scales for radiation and conduction heat transfer (Bhattacharjee and Altenkirch, 1992). Radiation and conduction are competing parallel mechanisms for the heat transfer needed for the sensible heating of the fuel preheat zone from T_∞ to T_v. This heating must take place within the solid residence time, $t_{res,s} \equiv L_g/V_f$. The mechanism with a time scale much larger than $t_{res,s}$ clearly is unimportant.

The rate of conductive heat transfer from the gas to the solid is approximately $\lambda_g L_g(T_f - T_v)/L_g$. The heat transfer required for the sensible heating of the fuel is $L_g \rho_s \tau C_s(T_v - T_\infty)$. The conduction time scale, therefore, is: $t_{cond} \sim L_g \tau / F\alpha_s$ where $F \equiv \lambda_g(T_f - T_v)/\lambda_s(T_v - T_\infty)$. The dimensionless number FL_g/τ, the ratio of gas-phase conduction to the solid-phase forward conduction (Altenkirch and Bhattacharjee, 1990), has a value much greater than unity for thin fuels and establishes gas-phase conduction as dominant over solid-phase conduction. When the radiation time scale is large, $R_c \equiv t_{res,s}/t_{cond} = 1$ yields the heat-transfer-limited expression for V_f obtained previously. At high opposing velocity or at normal gravity, V_r is too large and hence L_g is too small for radiation, as we shall see, to have much significance. However, in the quiescent microgravity environment L_g is larger and radiation may play an important role.

To evaluate the influence of radiation on the flame, the radiation time scales should be compared with the gas-phase residence time because radiation affects the flame mostly through cooling of the gas phase (Bhattacharjee and Altenkirch, 1991). The time scale for surface radiation can be shown to be $t_{sr} = t_{res}/R_s$ where $R_s \equiv [\epsilon\sigma(T_v^4 - T_\infty^4)/\lambda_g(T_f - T_\infty)]L_g = t_{res}/t_{sr}$. And, assuming gray radiation from the gas phase with a Planck mean absorption coefficient of a_P, the time scale for gas-phase radiation is: $t_{gr} \sim t_{res}/R_g$ where $R_g \equiv [4a_P\sigma(T_f^4 - T_\infty^4)/\lambda_g(T_f - T_\infty)]L_g^2 = t_{res}/t_{gr}$ (Bhattacharjee and Altenkirch, 1992).

An increase in the ambient pressure P_∞ causes the conduction length scale L_g, and hence R_s, to decrease, thus diminishing the importance of radiation. The Planck mean absorption coefficient, a_P, on the other hand, increases with an increase in P_∞. It is, therefore, difficult to predict whether gas radiation effects will increase or decrease with an increase in P_∞ (Bhattacharjee et al., 1991).

Nomenclature

a_P = Planck mean absorption coefficient (see Table 2), m^{-1}
B_s = pre-exponential factor for pyrolysis = 7.8×10^{16} s^{-1}
B_g = pre-exponential factor for gas-phase reaction = 1.58×10^{11} $m^3/kg \cdot s$
C_g = gas specific heat = 1.465 kJ/kg·K
C_s = solid specific heat = 1.256 kJ/kg·K
E_s = pyrolysis activation energy = 2.494×10^5 kJ/kmol
E_g = combustion activation energy = 1.167×10^5 kJ/kmol
F = flame constant = $\lambda_g(T_f - T_v)/\lambda_s(T_v - T_\infty)$
f = fraction of gas-phase radiation directed to the solid surface (see Table 2)
g = acceleration due to gravity = 9.81 m/s^2
L_v^o = latent heat of vaporization = 368.45 kJ/kg
L_g = reference thermal length = α_g/V_r (see Table 2), m
L_{hd} = flame hang distance, m
L_{ph} = solid preheat length = $(T_v - T_\infty)/|dT_s/dx|_{max}$ (see Table 2), m
L_{py} = length of pyrolysis zone, m
M = molecular weight of the gas mixture, 30 kg/kmol
$m_{ox,\infty}$ = ambient oxygen mass fraction
$\dot{m}''$ = mass flux, kg/m^2
P = pressure, N/m^2
Pr = Prandtl number, variable
P_∞ = ambient pressure = 101, 152, and 203 kPa
$\dot{Q}$ = total gas radiation, W
$\dot{q}''$ = heat flux, kW/m^2
R = universal gas constant = 8.314 kJ/kmol·K
R_c = conduction number = $t_{res,s}/t_{cond}$
R_g = gas radiation number = t_{res}/t_{gr}
R_s = surface radiation number = t_{res}/t_{sr}
$R(x)$ = distribution function for gas-to-surface radiation
S = source term in the conservation equation, appropriate units
s = stoichiometric ratio of cellulose ($C_6H_{10}O_5$) combustion = 1.185
T = temperature, K
T_s = solid temperature, K
T_v = solid vaporization temperature, the first maximum after the preheat zone, K
T_∞ = ambient temperature = 298 K
t = time, s
u, v = x and y velocity, m/s
V_f = absolute value of flame spread rate, m/s
V_g = absolute value of gas velocity, m/s
V_r = reference velocity = $V_g + V_f$, m/s
V_w = blowing velocity, m/s
w = width of the sample, 0.03 m
x, y = coordinate axis, m (origin shown in Fig. 1)
x_{max} = upstream boundary location of the computational domain = $6L_g$, m
x_{min} = downstream boundary location of the computational domain = $-10L_g$, m
y_{max} = top boundary location above the fuel surface = $10L_g$, m
α, ϵ = surface absorptance and emittance, 0.5
α = reference thermal diffusivity, m^2/s
Γ = generic diffusion coefficient for ϕ
ΔH_c = heat of combustion for cellulose = 16.74 MJ/kg
λ = thermal conductivity = 0.0542 W/m·K at 750 K
μ = dynamic viscosity = 2.59×10^{-5} N/m·s at 750 K
ρ = gas density = $MP_\infty/(RT)$, kg/m^3
ρ_s = fuel density, kg/m^3
$\rho_{s,\infty}$ = 519 kg/m^3
σ = Stefan–Boltzmann constant = 5.67×10^{-8} $W/m^2 \cdot K^4$
τ = half-thickness of fuel = 0.0825 mm
ϕ = generic conserved property

Data from a computational model and experiment will be used to show that the importance of the reduction in L_g outweighs the increase in a_p, and the gas-phase radiation effect actually diminishes with an increasing ambient pressure. Computational studies (Bhattacharjee and Altenkirch, 1991, 1992) have shown that radiation, both surface and gas, acts primarily as a cooling mechanism for the flame, thereby slowing flame spread and causing the flame to shrink in size. Therefore, with an increase in P_∞ it is expected that the flame temperature, flame size, and the spread rate will all increase as radiative effects are diminished in microgravity.

Here results of three flame spread experiments conducted aboard the Space Shuttle at three different ambient pressures are compared to computational results in order to explore the strengths and weaknesses of the arguments given above concerning the importance of radiation in flame spreading and ultimately in issues of spacecraft fire safety. The numerical model and experimental data for a single pressure have been presented elsewhere (Bhattacharjee and Altenkirch, 1992). Here, we examine additional data and apply an advanced version of the model that includes radiation coupling between the gas and the solid phase to analyze and interpret the set of experiments in order to gain insight into the effect of ambient pressure on flame spread in a quiescent, microgravity environment.

Mathematical Model

Details of the mathematical model can be found elsewhere (Bhattacharjee and Altenkirch, 1992), so only a summary is presented here for completeness. The model consists of the two-dimensional, steady-state continuity, momentum, species, and energy equations in the gas and the continuity and energy equations in the solid. In addition to the unknown field variables, a boundary condition, V_f, is the desired unknown eigenvalue. The gas-phase equations can be expressed in the common form:

$$\frac{\partial}{\partial x}(\rho u\phi) + \frac{\partial}{\partial y}(\rho v\phi) = \frac{\partial}{\partial x}\left(\Gamma_\phi \frac{\partial \phi}{\partial x}\right) + \frac{\partial}{\partial y}\left(\Gamma_\phi \frac{\partial \phi}{\partial y}\right) + S_\phi \quad (1)$$

where the meanings of ϕ, Γ_ϕ, and the source term S_ϕ are given in Table 1.

Second-order Arrhenius kinetics are used for the fuel and oxygen source terms assuming a one-step, irreversible reaction. The thin-gas emission approximation is used in modeling the radiation from the gas. However, the overall mean Planck absorption coefficient is calculated from a model that ensures an overall radiation energy balance based on a more accurate solution of the radiation transport equation that accounts for total emission and absorption by CO_2 and H_2O in a nonhomogeneous medium and neglects radiation from soot and fuel vapor (Bhattacharjee and Altenkirch, 1991). The perfect gas law is used for the equation of state, and μ is allowed to vary with a square-root dependence on temperature. Boundary conditions for the gas-phase equations are (refer to Fig. 1):

Table 1 Conservation equations (see Eq. (1))

Equation	ϕ	Γ_ϕ	S_ϕ
Continuity	1	0	0
x momentum	u	μ	$-\frac{\partial P}{\partial x}$
y momentum	v	μ	$-\frac{\partial P}{\partial y}$
Fuel	m_f	μ/Pr	$-B_g\rho_g^2 m_f m_{ox} e^{-Eg/RT}$
Oxygen	m_{ox}	μ/Pr	sS_f
Nitrogen	m_n	μ/Pr	0
Energy	C_pT	μ/Pr	$\{-\Delta H_c S_f - 4a_p\sigma(T^4 - T_\infty^4)\}/C_P$

at

$$x = x_{\max}, \quad \phi = \phi_\infty (u_\infty = -V_f, v_\infty = 0)$$

at

$$x = 0, \quad \partial\phi/\partial x = 0, \quad P = P_\infty$$

at

$$y = y_{\max}, \quad \phi = \phi_\infty (\text{for all } \phi \text{ except } v)$$
$$\partial v/\partial y = 0, \quad P = P_\infty$$

at

$$y = 0, \quad u = -V_f, \quad v = V_w, \quad T = T_s$$
$$\text{and for all other } \phi\text{'s} \quad (\rho_g v\phi - \Gamma_\phi \partial\phi/\partial y)_{y=0} = I_\phi$$

where $I_\phi = \dot{m}''$ for fuel and = 0 for oxygen and nitrogen.

The interfacial quantities V_w, T_s, $\dot{m}''$ and V_f are obtained by solving the solid-phase continuity and energy equations:

Continuity:

$$\dot{m}'' = \frac{d}{dx}(\rho_s \tau V_f) \quad (2)$$

Pyrolysis:

$$\dot{m}'' = A_s \rho_s \tau e^{-E_s/RT_s} \quad (3)$$

Energy:

$$\dot{q}''_{\text{gsc}} + \alpha(\dot{q}''_{\text{gsr}} - \dot{q}''_{\text{ser}}) = -\rho_s \tau V_f C_s \frac{dT_s}{dx} + \dot{m}''[L_v^0 + (C_g - C_s)(T_s - T_\infty)] \quad (4)$$

The boundary conditions for these first-order differential equations are $T_s = T_{s,\infty}$ and $\rho_s = \rho_{s,\infty}$ at $x = x_{\max}$. The conduction flux terms from the gas to the solid, $\dot{q}''_{\text{gsc}}$, can be directly obtained from the gas-phase temperature field. The radiative term, following the simplified scheme developed by Bhattacharjee and Altenkirch (1991), is given by:

$$\dot{q}''_{\text{gsr}} = fR(x)\dot{Q}_{gr} \quad (5)$$

$$\dot{Q}_{gr} \equiv 4a_P\sigma w \iint_{\text{Comp.Domain}} (T^4 - T_\infty^4)\,dx\,dy \quad (6)$$

Nomenclature (cont.)

Subscripts/Superscripts

a = accurate
c = combustion
cond = conduction
f = fuel, flame
g = gas phase
gr = gas radiation
gsc = gas-to-surface conduction
gsr = gas-to-surface radiation
n = nitrogen
ox = oxygen
res = residence
sr = surface radiation
ser = surface-to-environment reradiation
s = solid fuel
v = vaporization
∞ = ambient condition
ϕ = pertaining to conserved variable ϕ

which can be obtained from the gas-phase temperature field if the radiation parameters f, the fraction of radiation directed to the surface, $R(x)$, the distribution of gas-to-surface radiation, and a_p are known. These parameters are obtained from the interim solution for the gas-phase field variables using advanced radiation routines and updated as the solution progresses to convergence. The parameters are obtained from a few overall quantities calculated using the accurate solution of the radiative transfer equation:

$$f \equiv \frac{\dot{Q}_{\mathrm{gsr},a}}{\dot{Q}_{gr,a}}; \quad R(x) \equiv \frac{\dot{q}'_{\mathrm{gsr},a}}{\dot{Q}_{\mathrm{gsr},a}}$$

$$a_P \equiv \frac{\dot{Q}_{gr,a}}{4\sigma w \iint_{\text{Comp.Domain}} (T^4 - T_\infty^4)\,dxdy} \tag{7}$$

The inherent three dimensionality of radiation is introduced into these parameters by considering all possible lines of sight while calculating the radiative flux at the boundary of the computational "box" from which the accurate quantities $\dot{Q}_{gr,a}$, $\dot{Q}_{gsr,a}$, and $\dot{q}'_{\mathrm{gsr},a}$ are evaluated. Although the hydrodynamic model is two dimensional, the effect of the radiative side losses from the flame is taken into account in a simplified manner by equating the width of the radiation "box" to the sample width w.

To close the formulation, one more condition is needed, which is a matching of the surface temperature distribution computed from each phase. This matching is facilitated by fixing the surface temperature, T_{eigen} ($T_\infty < T_{\mathrm{eigen}} < T_v$), at a given location, x_{eigen}, within the computational domain (see Fig. 1). It should be stressed here that the choice of T_{eigen} is arbitrary and has no effect on the solution other than to control the location of the flame leading edge with respect to the boundaries. A suitable choice of T_{eigen} and x_{eigen} assures that the flame occupies the central region of the computational domain.

The solution is started with a guessed gas-phase field, radiation parameters, and boundary conditions. After about 10 iterations of the gas-phase equations, the heat flux from the gas to the solid is computed, and the solid-phase equations are solved to obtain V_f and improved interface conditions. The process is repeated for a few cycles after which the radiation parameters, a_P, f, and $R(x)$ are computed from the gas-phase solution. The gas–solid cycle is restarted with the new radiation parameters, and the entire process is repeated until convergence is obtained for all unknown variables including the radiation parameters.

The surface radiation properties are chosen as: $\alpha = \epsilon = 0.5$ in the absence of any available measurements, and the values of the pyrolysis constants were chosen based on an extensive study (Bhattacharjee et al., 1994a, b) of the first-order Arrhenius kinetics model with regard to flame spread pyrolysis. Other properties are the same as those used before (Bhattacharjee and Altenkirch, 1991).

Experimental

A detailed discussion of the experimental techniques and apparatus, and the experimental data for 1.5 atm, has been pre-

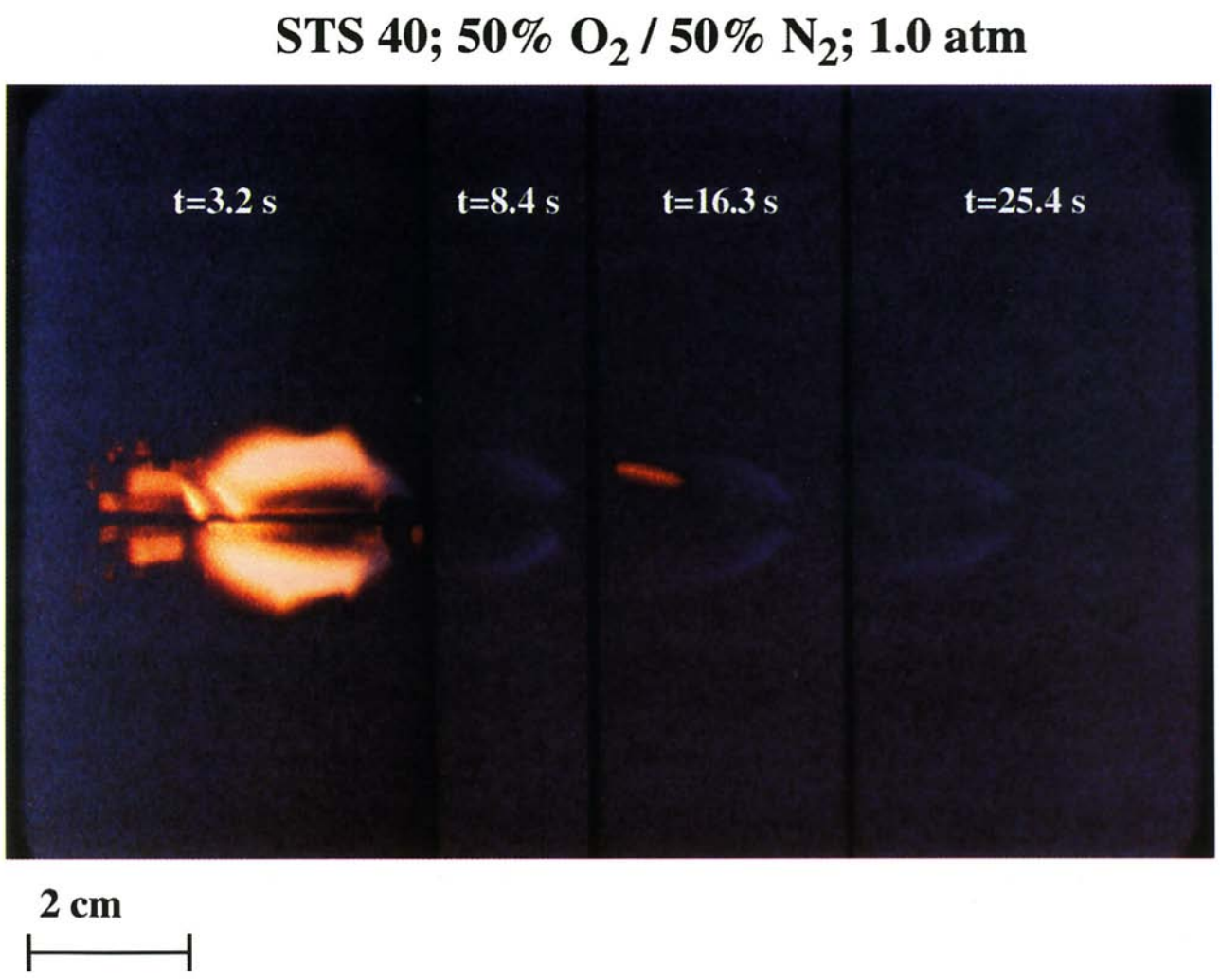

Fig. 2(*a*)

sented elsewhere (Bhattacharjee et al., 1993). The 1.5 atm data are used here as a part of a set of data in which the effects of pressure have been investigated. The experiment is conducted in a sealed chamber filled with a 50/50 (volumetric) oxygen/nitrogen mixture. The test specimen, ashless filter paper, 0.165 mm full thickness, 10 cm long, and 3 cm wide, is ignited at one end, and the resulting flame spread in the quiescent environment is filmed. Three Pt/Pt-Rh thermocouples, one imbedded in the solid and two in the gas phase (Fig. 1), record a time–temperature history as the flame moves past them.

The rate of spread of the flame leading edge, obtained by analyzing the film, is steady. The time–temperature trace from the thermocouples is mapped (Bhattacharjee et al., 1991) into $x-T$ data using this measured spread rate. These data can be used in conjunction with Eqs. (2), (3), and (4) to determine a solid density profile and a net heat flux to the solid for comparison to the complete computational model and the gas-to-surface conduction, which can be calculated from the thermocouple measurements. The implications of measurement uncertainties and thermocouple corrections, which have not been applied here, are discussed elsewhere (Bhattacharjee et al., 1993), the conclusion being that thermocouple corrections, which are difficult to determine accurately, are not particularly significant to the major findings, which are based on differences between measured temperatures.

Results and Discussion

Side-view photographs of the flames at two different ambient pressures are shown in Fig. 2(a) (1.0 atm) and Fig. 2(b) (1.5 atm). The flames, spreading from left to right in the photographs, are symmetric about the fuel surface, which is along $y = 0$. Four frames from the film are shown for each pressure. The times shown on the photographs are the times following the first appearance of a flamelike image on the film. Each flame has a blue leading edge, which for the higher pressure is followed by a long yellow zone, indicative of the presence of soot. The orange glow at the left of the third photograph in Fig. 2(a) is from a portion of a gas-phase thermocouple. The thermocouple is visible in the second photograph in Fig. 2(b).

Temperature contours computed with and without radiation in the theory are shown in Fig. 3. Only one-half of the flame is computed because the problem is symmetric about the fuel half thickness. The origin in the computed flames is the eigen location (where the surface temperature reaches a value of $T_{eigen} = 360$ K). Clearly, the experimental flame shape compares more favorably with the theoretical temperature contours when radiation is included in the model.

Without radiative loss, the maximum gas-phase temperature is about 3680 K, almost the same as the adiabatic, stoichiometric flame temperature, and remains practically unchanged with pressure. The size of the computational flame, defined by the size of

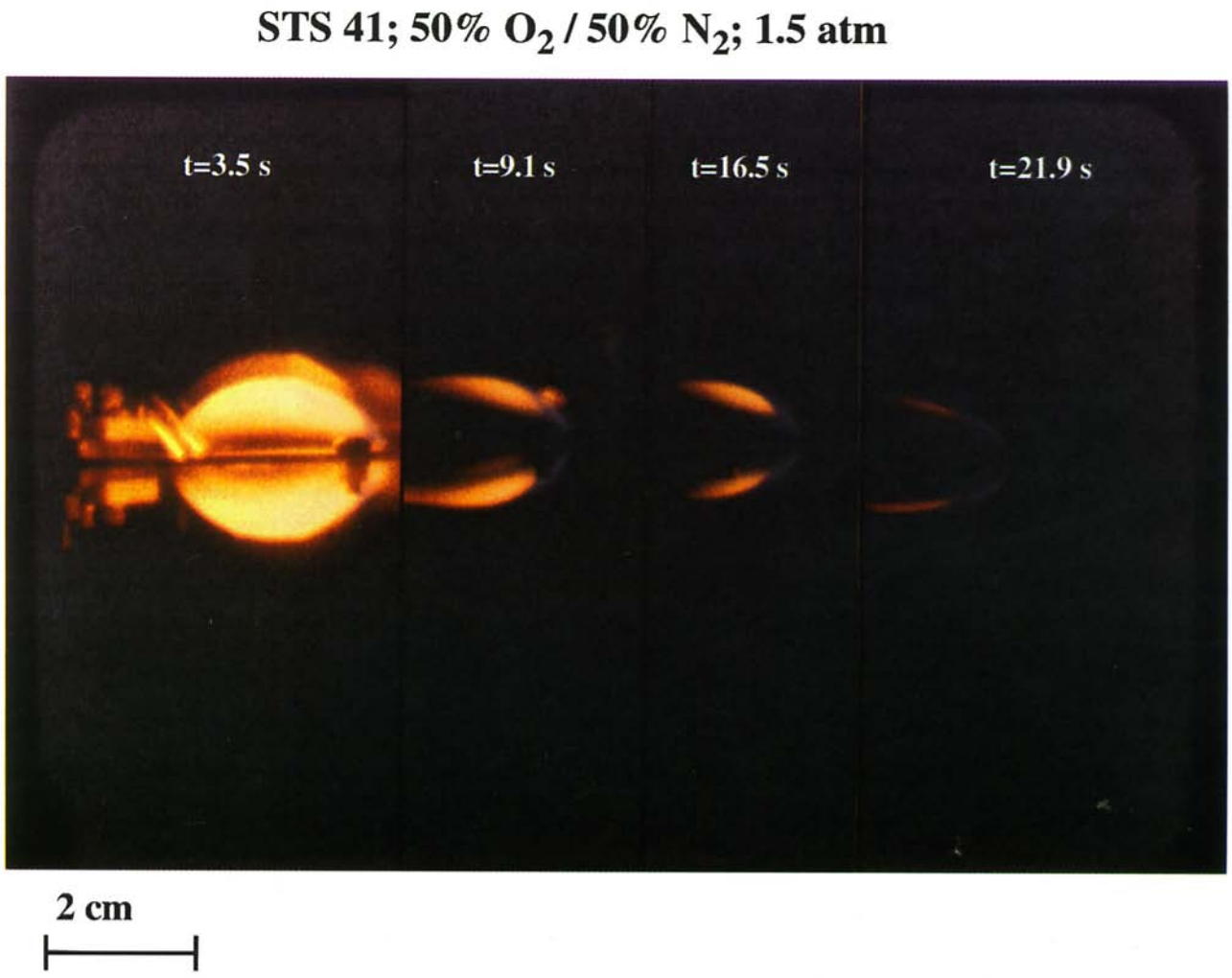

Fig. 2(*b*)

Fig. 2 Side-view photographs of the flames at: (*a*) 1.0 atm, and (*b*) 1.5 atm

the smallest (hottest) temperature contour, is too large to be contained within the domain of the plot and is unrealistic when compared with the flame size seen from the experiment (Fig. 2). As the pressure increases, the flame size in Fig. 3 decreases, and the contours become more and more closely spaced. This behavior can be explained because the length scale, L_g, is inversely proportional to P_∞. Without radiation the computed flame structure should scale with L_g. When the results in Fig. 3 without radiation are replotted in coordinates normalized by L_g, the temperature contours for the different pressures become almost identical as shown in Fig. 4. The contours are not exactly identical because the vaporization temperature depends slightly on P_∞ (Bhattacharjee et al., 1992). Because $L_g \equiv \alpha_g/V_f$ in the quiescent environment, Fig. 4 establishes the spread rate as the reference velocity of the problem if radiation is neglected.

When gas radiation is included in the theory, the peak flame temperature decreases substantially due to radiative cooling, by almost 2000 K, reducing the flame size to something more realistic. However, the hottest contour, the 1200 K line (the inner contour) in Fig. 3, grows in size as P_∞ increases. The increase in size of the computed high temperature region (which will be called the hot zone) with pressure requires some explanation.

At first the slight increase in the size of the hot zone with pressure appears counter-intuitive because L_g, the diffusion length scale, decreases with increasing P_∞ (see Table 3). In fact, the spacing between contours (Fig. 3*b*) decreases, and the low-temperature contour ($T = 1.5T_\infty$) shrinks in size with increasing pressure consistent with a reduction of L_g. But, as the length scale decreases, so does the characteristic optical depth of the flame, defined as $a_P L_g$ (see Table 2); therefore, the radiation loss can be expected to be less severe at higher pressure. Because the radiation loss affects the hottest zone of the flame the most, the high-temperature contour ($T/T_\infty = 4.0$ in Fig. 3*b*) suffers the most shrinkage at the lowest pressure. The maximum gas temperature, therefore, increases with an increase in P_∞ in Table 2. The flame size, identified with the high-temperature contours (the fuel reactivity contours follow almost the same pattern), is therefore expected to increase slightly with an increase in pressure.

The effect of pressure on flame size is not particularly evident from the visible photographs of the flame in Fig. 2; a side-view photograph at $P_\infty = 2$ atm is not available. The gas temperature recorded by the thermocouple 7 mm from the surface is shown for the three different pressures in Fig. 5, and it provides some indirect information on flame size. The temperature increases sharply at $x = 0$, the location of the peak net heat flux, reaches a peak at the flame leading edge, and then decreases before it peaks again at what will be called the flame trailing edge. The distance between these two peaks increases with increasing pressure in Fig. 5 and supports the conclusion that the size of the hot zone increases with increasing pressure. It should be mentioned here that the steady-state assumption has been used in reducing the time–temperature data from the thermocouples. Although the spread rate is very nearly steady, within 0.1 percent, the flame size in terms of the distance between the leading and the trailing edge is observed in the film to increase with time as the flame spreads.

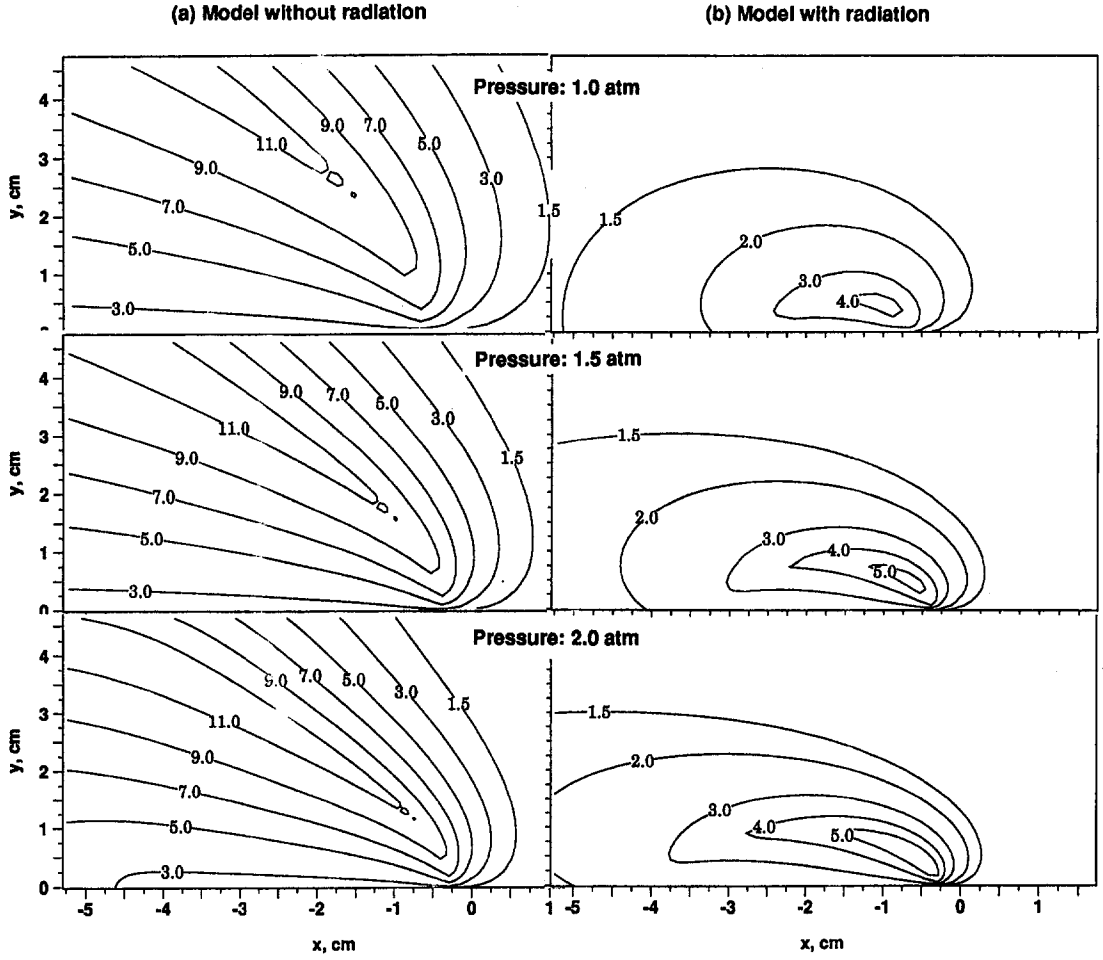

Fig. 3 Temperature contours in units of the ambient temperature 298 K at three different pressures: (a) model without radiation, (b) model with radiation

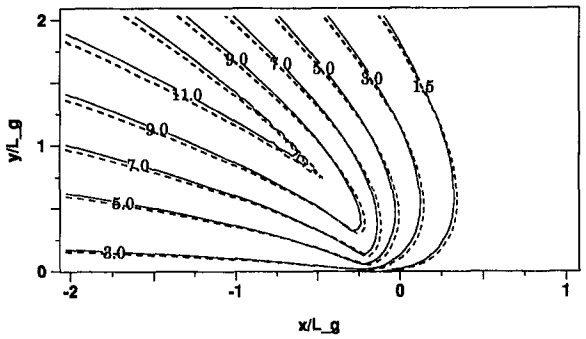

Fig. 4 Temperature contours in dimensionless space

Several important parameters from experiment and three models are summarized in Table 2. In evaluating the spread rate from the de Ris/Delichatsios formula $(V_f = (\pi/4)(\lambda_g/\tau\rho_s C_s)(T_{f,ad} - T_v)/(T_v - T_\infty)$, de Ris, 1969; Delichatsios, 1986), the vaporization temperature T_v is taken to be the maximum surface temperature near the leading edge computed from the non-radiative model. With an increase in ambient pressure, T_v increases slightly (see Table 2), as anticipated from the first-order pyrolysis kinetics (Bhattacharjee et al., 1993), which explains the slight decrease in spread rate in the de Ris and non-radiative models. Note the excellent agreement on V_f, up to one tenth of a mm/s, between the de Ris and the non-radiative model, despite the removal of a number of simplifying assumptions—negligible hang distance, Oseen flow, linearized interface conditions, infinite-rate chemistry, constant vaporization temperature, constant properties—in the latter model. This must be due to canceling effects of different physics, and the fact that λ_g used in the de Ris formula is evaluated at the reference temperature, $(T_{f,ad} + T_\infty)/2$, rather than at T_v. This choice of reference temperature was found to be "fortuitously appropriate" by Wichman and Williams (1983) in correlating the experimental data of Fernandez-Pello et al. (1981) for opposed flow flame spread over thin cellulosic fuel.

The experimental data in Table 2 clearly indicate that the spread rate increases with pressure. Similar behavior has been observed at another oxygen level (Ramachandra et al., 1995). Without radiation, the de Ris/Delichatsios formula as well as the numerical model completely fail to capture this behavior. Moreover, the predicted V_f is about three times larger than the data. When radiation is included in the model, the agreement between model and experiment improves dramatically (to within 10 percent), and the V_f versus P_∞ behavior is correctly captured.

Without radiation, the maximum gas temperature tends toward the adiabatic, stoichiometric temperature ($T_{f,ad}$ = 3908 K) in the downstream direction (see Table 2). With the inclusion of radiation in the model, T_f drops precipitously (by almost 2000 K), which must be the reason behind the dramatic decrease of V_f. With an increase in pressure the radiation parameters, a_P and f, understandably increase. However, for reasons already explained, T_f increases and T_v decreases with an increase in P_∞. Even with no radiation feedback, i.e., $f = 0$, in the model, V_f and T_f have been found to increase with P_∞. The increase in T_f with P_∞, therefore, must be responsible for the observed V_f versus P_∞ behavior. The maximum temperature, $T_{\max}$, recorded by the gas-phase thermocouple at y = 7 mm (see Fig. 1) first increases and then slightly decreases (see Table 2) with P_∞. Because the flame size changes with P_∞, $T_{\max}$ may not be a good indicator of T_f.

The surface temperature profiles at the three pressures are shown in Fig. 6. The sharp rise in surface temperature near the flame leading edge indicates the preheat zone. The surface temperature soon reaches a plateau as the pyrolysis begins with the maximum temperature defined as the vaporization temperature T_v. The pyrolysis zone follows, where the temperature is moderated by vaporization, the end of this zone being signaled by the rise in temperature of the remaining nonvolatile char.

A number of characteristic lengths of the flame, calculated from the surface temperature profiles, for the experiments and different models are expressed in terms of L_g in Table 3. Results for the de Ris model are obtained for the computational solution, which assumes nonzero flame hang distance, defined below (Bhattacharjee, 1993). In both the de Ris model and non-radiative model, the diffusion length scale is primarily controlled by the ambient pressure because the spread rate (Table 2) remains almost unchanged with pressure in these models. The sevenfold increase in L_g compared to the de Ris model for the non-radiative model is mostly due to the introduction of variable density in the model. An even larger value of L_g is calculated for the experiments and the radiative models because of smaller spread rates.

The characteristic preheat length is defined as $L_{ph} \equiv (T_v - T_\infty)/|dT_s/dx|_{\max}$, where $|dT_s/dx|_{\max}$ is the maximum temperature gradient in the preheat zone, similar to the approach taken to define the flame thickness (Kanury, 1977). An example of the dT_s/dx profile is given in Fig. 7 where the T_s profile is differentiated without any smoothing. If radiation is unimportant, solid heating takes place entirely by means of conduction; hence, L_{ph} is expected to be proportional to the gas-conduction length scale, L_g, as obtains for the de Ris and the non-radiative models. In the experimental results this proportionality is lost

Table 2 A comparison of different parameters at three different pressures

		Pressure (P_∞, atm)		
		1.0	1.5	2.0
Spread rate (V_f, mm/s)	Experiment	3.6	4.5	5.5
	Model			
	de Ris model	11.7	11.5	11.4
	No radiation	11.7	11.5	11.4
	Radiation	3.2	4.9	5.9
Maximum gas temperature* (T_f, K)	Experiment	1343	1386	1367
	Model			
	No radiation	3674	3680	1682
	Radiation	1326	1544	1751
Vaporization temperature (T_v, K)	Experiment	719	743	710
	Model			
	No radiation	749	756	761
	Radiation	728	740	749
Radiation parameters	Planck mean (a_P, m^{-1})	2.7	3.3	4.4
	Percent feedback, f	17%	29%	32%

* Maximum temperature 7 mm from the surface.

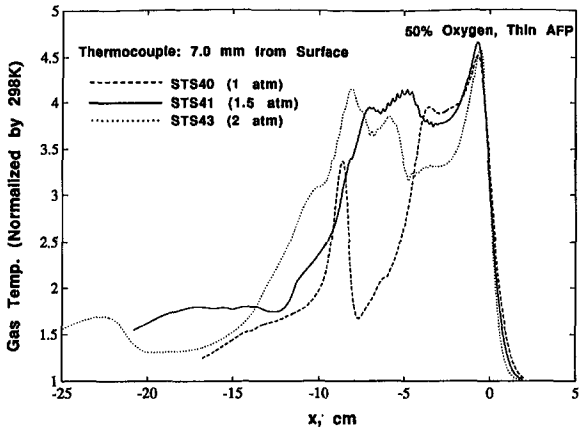

Fig. 5 Measured temperature profiles 7 mm away from the surface at three different ambient pressures

(see Table 3), and the model with radiation captures the experimental trend if not the absolute values. Because radiation acts as a net loss, a reduction in the length scale with the inclusion of radiation can be predicted from a scale analysis (Bhattacharjee et al., 1991).

As will be shown later, the x location, x_{peak}, in the preheat zone where $|dT_s/dx|_{\max}$ occurs is also the location of the peak heat flux from the gas to the solid. This location has been found to be the location of the flame leading edge for infinite-rate chemistry (Bhattacharjee, 1993). The location where pyrolysis starts is defined as the point where T_s reaches its first maximum T_v, and dT_s/dx becomes zero (see Fig. 7). The distance between this location and x_{peak} is defined as the flame hang distance, which is expressed in terms of L_g for different models and experiments in Table 3. The hang distance L_{hd} found in the computed solution of the de Ris model agrees quite well with a correlation established by Bhattacharjee et al. (1994b) that predicts a value of 0.44 L_g under all pressures. However, in the microgravity experiments as well as in the model with radiation, the hang distance increases by three times as the ambient pressure doubles from 1 to 2 atm. It should be mentioned that in the analytical solution for the de Ris spread rate (de Ris, 1969; Delichatsios, 1986) this hang distance was assumed to be zero.

The length of the pyrolysis zone, L_{py}, obtained from the T_s profiles is also listed in Table 3. A sudden change in the slope of the T_s profile is assumed to indicate the completion of the pyrolysis zone. Without radiation, according to a formula developed by Bhattacharjee et al. (1994b), the pyrolysis length, L_{py}, with the properties used in this work, is given as $L_{py} = 5.5\ L_g$ irrespective of the ambient pressure; this is in reasonable agreement with the computed values for non-radiative models. However, in the experiments and in the model with radiation, L_{py}, expressed in the units of L_g, increases dramatically with an increase in pressure (see Table 3). It should be mentioned here that the experimental values have been obtained with the steady-state assumption, which is somewhat questionable for the pyrolysis length.

At the end of the pyrolysis zone (Fig. 6), the temperature increases sharply; this is most likely due to sensible heating of the remaining nonvolatile char. The distance between the two peaks of the surface temperature, therefore, can be interpreted as the distance between the leading and the trailing edges of the gas-phase flame. The changes in temperature beyond the trailing edge of the flame (Figs. 5 and 6) are a result of unsteady glowing combustion of the remaining nonvolatile char, which is evident from the films. The films show that the surface reactions occur mostly near the edges of the sample near the sample holder. The steady-state computational model does not include any exothermic surface reaction, and so no comparison between theory and experiment can be made beyond the completion of the pyrolysis zone.

The net heat flux profiles at the three different pressures, obtained using the procedure briefly described in the experimental section and described in detail elsewhere (Bhattacharjee et al., 1993), are shown in Fig. 8. The location of the peak heat flux has been identified with the location of $|dT_s/dx|_{\max}$ for each experiment. This location, defined as the flame leading edge, is arbitrarily chosen as the origin for each flame in Figs. 5–8. In the downstream (negative x) direction, a second peak can be detected in each profile approximately at the location of the trailing edge. The positive heat flux from the gas to the solid at the trailing edge implies an endothermic process there; if burnout had occurred upstream of this location, the heat flux would be zero because of the symmetry condition. The second peak is probably caused by the trailing edge of the flame, which bends back toward the surface; limited support for this can be seen in the film, although a definitive statement is difficult to make because the flame becomes progressively fainter toward the trailing edge. The distance between these two heat flux peaks, therefore, can be taken as the flame size, which increases with increasing pressure consistent with the conclusion from the model with radiation.

Table 3 A comparison of different length scales at three different pressures

		Pressure (P_∞, atm)		
		1.0	1.5	2.0
Diffusion length scale (mm), L_g	Experiment	98.3	51.7	32.2
	Model			
	de Ris model	4.33	2.92	2.22
	No radiation	30.5	20.6	15.7
	Radiation	114.9	42.8	25.0
Preheat length, L_{ph}	Experiment	0.10 L_g	0.17 L_g	0.24 L_g
	Model			
	de Ris model	0.36 L_g	0.36 L_g	0.36 L_g
	No radiation	0.24 L_g	0.23 L_g	0.22 L_g
	Radiation	0.05 L_g	0.10 L_g	0.14 L_g
Flame hang distance, L_{hd}	Experiment	0.10 L_g	0.18 L_g	0.30 L_g
	Model			
	de Ris model	0.43 L_g	0.43 L_g	0.43 L_g
	No radiation	0.29 L_g	0.28 L_g	0.27 L_g
	Radiation	0.04 L_g	0.10 L_g	0.17 L_g
Pyrolysis length, L_{py}	Experiment	0.04 L_g	0.31 L_g	1.86 L_g
	Model			
	No radiation	2.36 L_g	2.32 L_g	2.28 L_g
	Radiation	0.37 L_g	1.10 L_g	2.50 L_g

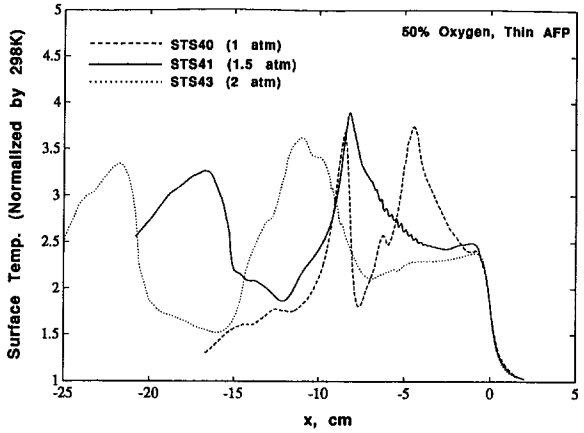

Fig. 6 Measured surface temperature profiles at three different ambient pressures

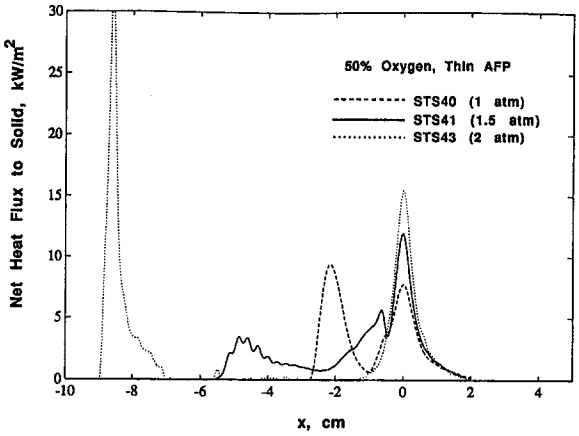

Fig. 8 Net heat flux from the gas to the solid, calculated by solving the solid-phase energy equation from the measured solid temperature

One drawback of the present model is that it does not predict the flame structure at the trailing edge of the flame properly. Several factors are responsible for this, and they have been discussed elsewhere (Bhattacharjee and Altenkirch, 1992). Because flame "reattachment" at the trailing edge has not been observed with the current steady-state model, the net heat flux from the model, shown in Fig. 8, has only one peak that corresponds to the leading edge. Despite difficulties with trailing edge prediction, the dependencies on pressure of the net heat flux and the spread rate (Table 2) seen from the model with radiation are similar to that found in the experiment. This supports the conclusion that the flame spread process in a quiescent, microgravity environment is controlled by the leading edge, as it is in other opposed-flow environments.

Conclusions

The effect of ambient pressure on flame spread over a thin cellulosic fuel in a quiescent, microgravity environment has been studied experimentally and computationally. Experiments were carried out at three different pressures aboard three different Space Shuttle missions. The model includes gas-phase radiation, including the radiation feedback from the gas to the solid. To evaluate the importance of radiation, a set of calculations in which radiation was completely neglected was also presented.

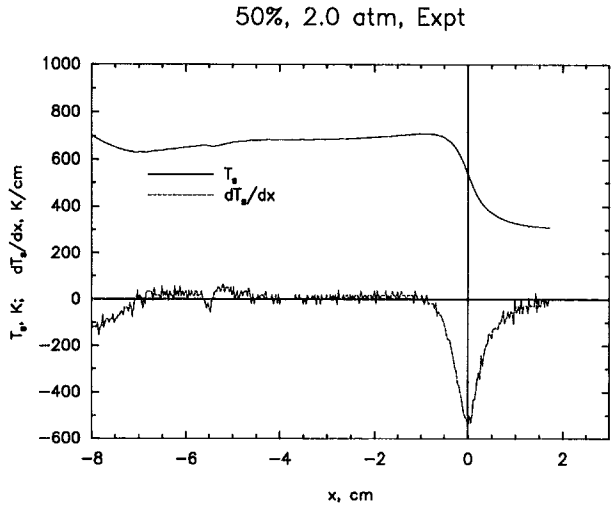

Fig. 7 Measured surface temperature and the corresponding temperature gradient for P_∞ = 2.0 atm

Data indicate that the spread rate increases with increasing pressure. This is contrary to the results expected from the model in which radiation effects are not considered, in which the spread rate is found to be almost independent of pressure. The flame, taken to correspond to the high temperature contours, scales with the diffusion length scale when radiation is neglected, is unrealistically large, and unrealistically hot. When radiation is included, the flame cools substantially and decreases in size. The effect of radiation seems to be more pronounced at lower pressures because the characteristic optical depth of the flame is larger there. Consequently, the flame is cooler and spreads more slowly at lower pressure.

The surface temperature and the gas temperature measurements, and the inferred data on the net heat flux from the gas to the solid surface are all found to be qualitatively consistent with the model including radiation near the leading edge of the flame. The dependence of flame spread rate and various length scales on pressure, which is quite different from what is seen in Earth-bound downward flame spread, is correctly predicted.

Acknowledgments

This work was supported by NASA through Contract No. NAS3-23901. We thank Sandra Olson for serving, for a period of time, as Contract Monitor and Prof. S. V. Patankar for providing to us an initial version of the gas-phase software. We gratefully acknowledge the contributions of Ralph Zavesky, John Koudelka, and the SSCE flight hardware team at the NASA-Lewis Research Center and the program support of NASA Headquarters, Microgravity Division, Office of Space Science and Applications.

References

Altenkirch, R. A., and Bhattacharjee, S., 1990, "Low Gravity Fluid Dynamics and Transport Phenomena," *Progress in Astronautics and Aeronautics,* Vol. 130, pp. 723–740.

Altenkirch, R. A., Eichhorn, R., and Shang, P. C., 1980, *Combustion and Flame,* Vol. 37, pp. 71–83.

Bhattacharjee, S., and Altenkirch, R. A., 1991, *Twenty-Third Symposium (International) on Combustion,* The Combustion Institute, Pittsburgh, PA, pp. 1627–1633.

Bhattacharjee, S., and Altenkirch, R. A., 1992, *Twenty-Fourth Symposium (International) on Combustion,* The Combustion Institute, Pittsburgh, PA, pp. 1669–1676.

Bhattacharjee, S., 1993, *Combustion and Flame,* Vol. 93, pp. 434–444.

Bhattacharjee, S., Altenkirch, R. A., and Sacksteder, K., 1993, *Combustion Science and Technology,* Vol. 91, pp. 225–231.

Bhattacharjee, S., Altenkirch, R. A., Olson, S. L., and Sotos, R. G., 1994a, ASME JOURNAL OF HEAT TRANSFER, Vol. 113, pp. 670–676.

Bhattacharjee, S., Bhaskaran, K. K., and Altenkirch, R. A., 1994b, *Combustion Science and Technology,* Vol. 100, pp. 163–183.

Bhattacharjee, S., West, J., and Dockter, S., 1995, "A Simplified Theory for de Ris Flame over Thin and Thick Fuels," *Combustion and Flame,* to appear.

de Ris, J. N., 1969, *Twelfth Symposium (International) on Combustion,* The Combustion Institute, Pittsburgh, PA, p. 241–252.

Delichatsios, M. A., 1986, *Combustion Science and Technology,* Vol. 44, pp. 257–267.

Fernandez-Pello, A. C., Ray, S. R., and Glassman, I., 1981, *Eighteenth Symposium (International) on Combustion,* The Combustion Institute, Pittsburgh, PA, pp. 579–587.

Kanury, M., 1977, *Introduction to Combustion Phenomenon,* Gordon and Breach Science Publishers, New York.

Lastrina, F. A., Magee, R. S., and McAlevy, R. F., 1971, *Thirteenth Symposium (International) on Combustion,* The Combustion Institute, Pittsburgh, PA, pp. 935–948; comments by J. N. de Ris.

Ramachandra, P. A., Altenkirch, R. A., Bhattacharjee, S., Tang, L., Sacksteder, K., and Wolverton, M. K., 1995, *Combustion and Flame,* Vol. 100, pp. 71–84.

Wichman, I. S., and Williams, F. A., 1983, *Combustion Science and Technology,* Vol. 32, pp. 91–123.

Williams, F. A., 1976, *Sixteenth Symposium (International) on Combustion,* The Combustion Institute, Pittsburgh, PA, pp. 1281–1294.

Effects of Heating Mode on Steady Axisymmetric Thermocapillary Flows in Microgravity

Y. Kamotani

A. Chang

S. Ostrach

Department of Mechanical and Aerospace Engineering, Case Western Reserve University, Cleveland, OH 44106

Steady thermocapillary flows in cylindrical containers with unit aspect ratio (radius = depth) are studied numerically and by scaling analysis in order to investigate how the velocity and thermal fields are influenced by the method of heating. Two heating modes are considered: heating by a uniform temperature cylindrical heater placed along the centerline (called the CT heating) and heating by an external radiative source (the CF heating). The steady velocity and temperature fields are computed numerically under various conditions for various Prandtl number fluids. The effects of those two types of heating on the flows are discussed. The results are also found to support the scaling laws derived herein for the characteristic velocity, length, and Nusselt number. The main thermocapillary driving force region is fixed by the heating zone area in the CF heating but it generally varies with the flow in the CT heating.

1 Introduction

Thermocapillary flow is generated by heat-induced surface tension variation along a liquid free surface. Thermocapillary flows are generated mainly by two basic heating modes. In one mode liquid is placed in an open container with differentially heated side walls to induce temperature gradients along the free surface. In the other mode a liquid free surface is subjected to a nonuniform heat flux (e.g., localized radiation heating). The former heating mode is the one considered in many earlier numerical and experimental thermocapillary flow studies. Practical examples of that heating mode are found in crystal growth systems (e.g., Czochralski growth) and many fluid systems with free surfaces in nonisothermal environments. Examples of the latter mode include welding, containerless processing (e.g., floating-zone system), and the spreading of a flame across liquid surfaces.

Thermocapillary flows tend to be overwhelmed by coexisting buoyancy-driven flows in one-g environments, but become important in microgravity. We have conducted thermocapillary flow experiments, called the Surface Tension Driven Convection Experiment (STDCE), aboard the Spacelab in 1992 (Kamotani et al., 1993, 1994), in which these two heating modes were employed to study their effects on the flows. The present work is motivated by the experiments and the main objective is to obtain the basic scaling laws for the velocity and thermal fields in order to understand better the effects of the heating mode. As in buoyancy-driven flow, the characteristic velocity of thermocapillary flow is not known a priori and the driving force is altered by the flow. Therefore, it is important to derive the velocity and length scales of the flow in each configuration. The basic configurations of the present study are those of the STDCE: an open circular container filled with liquid with a flat free surface and equipped with a cooled side wall. As illustrated in Fig. 1, the fluid is either subjected to a specified heat flux from an external heating source (called the constant flux (CF) configuration herein as in the STDCE) or heated by a cylindrical heater placed along the container centerline (called the constant temperature (CT) configuration). Although only one fluid was used in the STDCE, the present study covers a wide range of Prandtl numbers for more general use. The velocity and temperature fields are computed numerically over wide ranges of parameters and the results are then used to verify the scaling laws derived in the present analysis. Based on those results the effects of heating mode on the resulting flows are discussed.

Many investigators in the past studied steady thermocapillary flows (with or without buoyancy) numerically in rectangular cavities (e.g., Zebib et al., 1985; Bergman and Ramadhyani, 1986; Carpenter and Homsy, 1989, 1990; Keller and Bergman, 1990; Mundrane and Zebib, 1993) and in the so-called half-zone configuration (e.g., Chang and Wilcox, 1976; Fu and Ostrach, 1983), most of them in the CT heating mode. Cowley and Davis (1983), Zebib et al. (1989), and Chen (1987) determined various velocity and length scales from scaling and theoretical analyses. No numerical or scaling analyses are available for the present configurations except for our earlier work (Kamotani et al., 1993, 1994). The present work is based on the report by Chang et al. (1994).

2 Important Parameters

The important dimensionless parameters for steady thermocapillary flow both in the CT and CF configurations are: Marangoni number Ma, Prandtl number Pr, aspect ratio Ar, and heater ratio Hr. The surface tension Reynolds number $R\sigma$ = Ma/Pr is also used herein. In the CT configuration ΔT is the temperature difference between the heater and the side wall and R_h is the heater radius. In the CF configuration the imposed heat flux is assumed to have a Gaussian distribution and R_h is the location where the flux falls to e^{-2} of its maximum value. ΔT is not specified in the CF configuration but since the driving force of thermocapillary flow is directly related to ΔT, a Ma based on ΔT is used, ΔT being determined from numerical analysis. The relationship between the imposed heat flux and ΔT will be discussed later. The heat loss from the free surface is assumed to be negligible in the present analysis.

The parametric ranges studied herein are: $0.01 \leq \mathrm{Pr} \leq 100$, $Hr = 0.1$ and 0.3 in CF and $Hr = 0.1$ in CT, $Ar = 1.0$, and $\mathrm{Ma} \leq 2.0 \times 10^5$.

Contributed by the Heat Transfer Division for publication in the JOURNAL OF HEAT TRANSFER. Manuscript received by the Heat Transfer Division December 1994; revision received September 1995. Keywords: Microgravity Heat Transfer, Thermocapillary Flows. Associate Technical Editor: J. R. Lloyd.

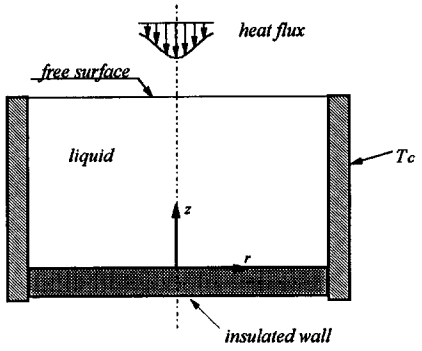

CF Configuration

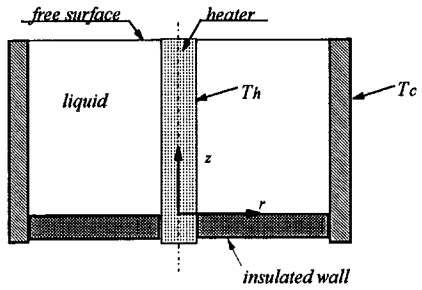

CT Configuration

Fig. 1 Schematic of two heating configurations

3 Numerical Analysis

The steady, axisymmetric, and incompressible continuity, momentum, and energy equations are solved numerically in cylindrical coordinates. The following boundary conditions are used. The no-slip condition is imposed on all solid surfaces. The shear stress along the free surface is balanced by the thermocapillary force, namely $\mu\partial u/\partial z = -\sigma_T \partial T/\partial r$. The side wall is maintained at a uniform temperature and the bottom wall is thermally insulated. In the CT configuration the heater has a uniform temperature. The amount of heat loss from the free surface is assumed to be negligible compared to the overall heat transfer rate through the bulk fluid. In the CF heating mode the free surface is subjected to a heat flux, which is distributed as $(2Q/\pi R_h^2)\exp(-2r^2/R_h^2)$ and the heat flux is absorbed at the surface. The free surface is assumed to be flat with or without fluid motion, that is, the capillary number is assumed to be much less than unity. The lengths, velocities, and stream function (in cylindrical coordinates) are made dimensionless by R, $\sigma_T\Delta T/\mu$, and $\sigma_T\Delta TR^2/\mu$, respectively. The temperature is nondimensionalized as $(T - T_c)/\Delta T$.

The numerical analysis is based on the SIMPLER algorithm of Patankar (1980). A nonuniform grid system is adopted with meshes graded toward the hot and cold walls and toward the free surface. In the CT configuration it is important to resolve the boundary layers, if they exist, along the heater length. For the conditions of Ma = 1.5×10^5, $Hr = 0.1$, and Pr = 10, the values of Nusselt number computed with three different grids, 37×31 (radial $\times$ axial), 58×51, and 80×60 with the smallest radial mesh sizes next to the heater surface of 0.001, 0.0005, and 0.0002, respectively, are 4.38, 4.30, and 4.29, respectively. With the same grids, the values of the maximum velocity along the free surface are 0.0510, 0.0533, and 0.0536, respectively, and the radial locations of the maximum velocity from the heater (Δ/R) are 0.0120, 0.0122, and 0.0123, respectively, which are determined by curve-fitting the numerically computed surface velocity distributions. Those three quantities (Nusselt number, maximum surface velocity, and its location) will be used in the later CT analysis. Based on that comparison, the finest grid used in the present analysis for the CT configuration is the 58×51 grid. In the CF configuration one needs to resolve very thin boundary layers along the free surface. For the conditions of Ma = 1.8×10^5, $Hr = 0.1$, and Pr = 20, the values of $Q/(\pi k\Delta TR_h)$ (which represents the maximum surface temperature for a given Q) with three different grids, 31×31, 58×60, and 80×80 with the smallest axial mesh sizes next to the free surface of 0.003, 0.0005, and 0.0002, respectively, are 25.2, 25.7, and 25.7, respectively. With the same grids, the values of the maximum surface velocity are 0.0753, 0.0755, and 0.0757, respectively, and their radial locations from the center (Δ/R) are 0.076, 0.090, and 0.090, respectively. The quantities $Q/(\pi k\Delta TR_h)$ and Δ/R will be used in the later CF analysis. Therefore, the finest grid used for the CF configuration is the 58×60 grid.

4 Flows in the CF Heating Mode

Typical streamline and isotherm patterns under the CF heating mode are shown in Fig. 2. The flow structure is unicellular with a relatively fast flow along the free surface (called the surface flow herein) and a weaker interior flow in the opposite

Nomenclature

Ar = aspect ratio = H/R
C = const
H = container height
Hr = heater ratio = R_h/R
k = thermal conductivity
Ma = Marangoni number = $\sigma_T\Delta TR/\mu\alpha$
Ma* = Ma based on $R_h = \sigma_T\Delta TR_h/\mu\alpha$
Nu = Nusselt number
Pr = Prandtl number = ν/α
Q = total heat transfer rate
R = container radius
R_h = heating zone radius in CF configuration and heater radius in CT configuration
$R\sigma$ = surface tension Reynolds number = $\sigma_T\Delta TR/\mu\nu$
$R\sigma^*$ = $R\sigma$ based on $R_h = \sigma_T\Delta TR_h/\mu\nu$
(r, z) = cylindrical coordinate system defined in Fig. 1
T = temperature
T_c = cold wall temperature
T_s = free surface temperature
U = characteristic velocity (= maximum surface velocity)
U^* = dimensionless characteristic velocity = $\mu U/\sigma_T\Delta T$
$U_{B,H}$ = return flow velocity near thermal boundary layer
u = velocity component in r direction
u_s^* = dimensionless free surface velocity
V = axial velocity toward heated region
α = thermal diffusivity
Δ = location of maximum surface velocity
ΔT = overall temperature drop along free surface
ΔT_H = temperature drop in Δ
δ_T = characteristic length for temperature distribution defined in Fig. 4
$\delta_{T,H}$ = thermal boundary layer along heater
δ_V = characteristic length for velocity distribution defined in Fig. 4
μ = fluid dynamic viscosity
ν = fluid kinematic viscosity
σ_T = temperature coefficient of surface tension

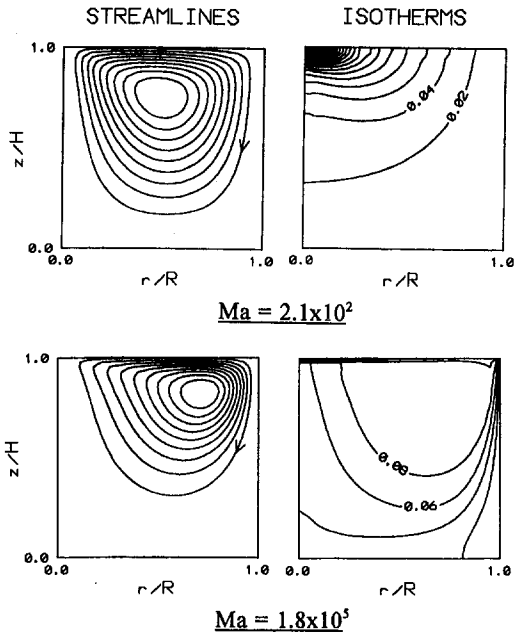

Fig. 2 Typical streamlines and isotherms in CF configuration (Pr = 20, *Hr* = 0.1)

direction (called the return flow). The numerical analysis shows that the center of the cell tends to move toward the cold wall as $R\sigma$ increases. The ratio of heating to cooling areas in the CF configuration is $Hr^2/2$ when $Ar = 1$, which is small in the present work (less than 0.05). Consequently, as Fig. 2 shows, most of the fluid remains close to the side wall temperature and sharp temperature gradients exist in and near the relatively small heated region. Since the temperature gradient along the free surface is the driving force, the flow is mainly driven in the heated region.

Figure 3 shows the surface velocity and temperature distributions for various Ma. At Ma = 210, the interior temperature distribution (Fig. 2) indicates strong conduction heat transfer and at Ma = 1.8×10^5 convection dominates. Over such a wide range of Ma the dimensionless surface temperature distribution does not change appreciably in and near the heated region. The surface velocity increases from the center up to the edge of the heated region and decreases away from that region. As seen in Fig. 3, the dimensionless peak velocity generally decreases with increasing Ma, but the radial location of the velocity peak does not vary with Ma for a given Hr. Therefore, in the ranges of Ma, Pr, and Hr studied herein, the peak location of the surface velocity depends only on Hr or the driving force region fixed by Hr. The peak velocity is considered to be the velocity scale of the flow and its magnitude is estimated in the following analysis. Note that in the present configuration even though the radial velocity starts to decrease just outside the heated region, the total volume flux of the surface flow over a circumference increases beyond that point as the streamline pattern of Fig. 2 indicates. Because of that volume flux increase, the colder interior fluid is entrained into the surface flow beyond the heated region, which prevents the surface temperature from rising outside the heated region.

Since the driving force exists mainly over R_h, the balance of surface shear and thermocapillarity in that region gives

$$U \sim \frac{\sigma_T \Delta T \delta_v}{\mu R_h} \tag{1}$$

where U represents the peak velocity and δ_V is the length scale for the radial velocity distribution in the axial direction, as illustrated in Fig. 4. If the flow is viscous dominated, δ_V scales with R_h and U then scales as

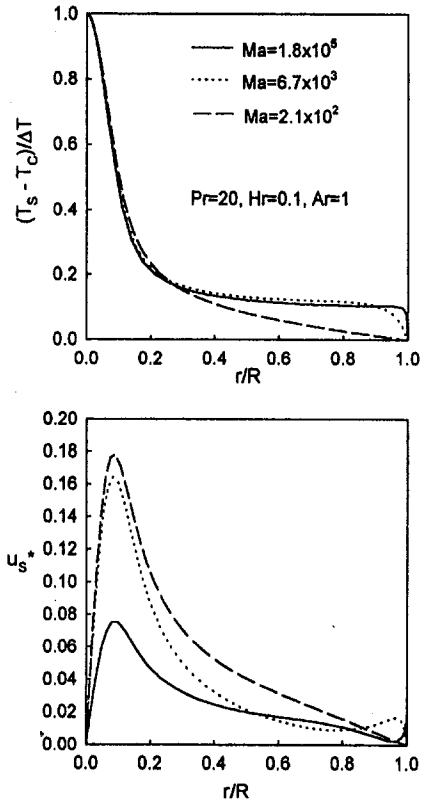

Fig. 3 Typical surface temperature and velocity distributions in CF configuration

$$U \sim \frac{\sigma_T \Delta T}{\mu} \tag{2}$$

or the dimensionless velocity U^* as

$$U^* = \frac{\mu U}{\sigma_T \Delta T} \sim \text{const} \tag{3}$$

On the other hand, if the inertia forces become important, δ_V scales with the velocity boundary layer thickness along the free surface and thus

$$\delta_V \sim \left(\frac{\nu R_h}{U}\right)^{1/2} \tag{4}$$

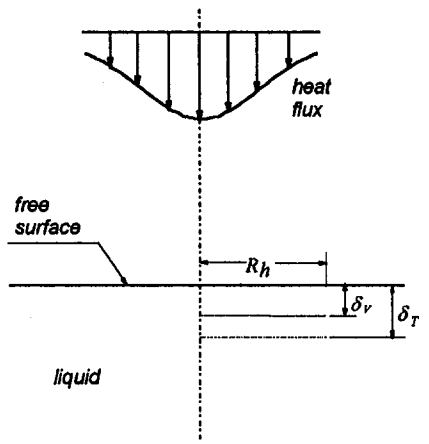

Fig. 4 Detailed illustration of heated region for CF configuration

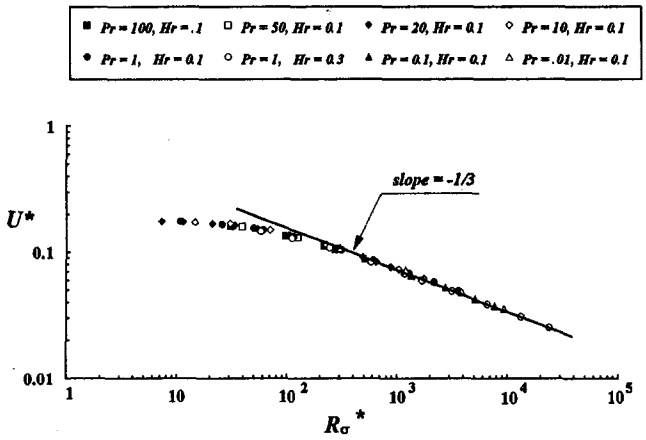

Fig. 5 Dimensionless velocity as a function of Reynolds number based on heating zone radius

From Eqs. (1) and (4) one gets

$$U^* \sim \left(\frac{\mu\nu}{\sigma_T \Delta T R_h}\right)^{1/3} = (R\sigma^*)^{-1/3} \tag{5}$$

where $R\sigma^*$ is the Reynolds number based on R_h. The results in Eqs. (3) and (5) are independent of Pr because they are valid whether or not a thermal boundary layer exists along the free surface.

The values of U^* computed under various conditions are plotted against $R\sigma^*$ in Fig. 5. For $R\sigma^*$ larger than about 200, U^* follows the scaling law of Eq. (5) and for $R\sigma^*$ less than about 10, U^* is constant in accordance with Eq. (3), the constant value being 0.176 from the numerical analysis. The results are independent of Pr.

As for the heat transfer aspect, an important problem is how to relate the total heat input Q to ΔT. Using δ_T as the characteristic length scale for the temperature distribution in the axial direction in the heated region (see Fig. 4), the balance between the heat input Q and the heat transferred to the fluid gives

$$Q \sim k \frac{\Delta T}{\delta_T} \pi R_h^2 \tag{6}$$

In obtaining Eq. (6) it is assumed that the bulk fluid temperature outside the heated region is equal to the side wall temperature, which is true in the ranges of parameters studied herein as discussed above.

If Ma is small, conduction heat transfer dominates and δ_T scales with R_h, which results in

$$\frac{Q}{\pi k \Delta T R_h} \sim \text{const} \tag{7}$$

If a temperature boundary layer exits along the free surface but there is no velocity boundary layer (large Ma, small $R\sigma$), the characteristic velocity U is given by Eq. (2) and δ_T in Eq. (6) is the thermal boundary layer thickness, which is given as

$$\delta_T \sim \left(\frac{\alpha R_h}{U}\right)^{1/2} \sim \left(\frac{\alpha R_h \mu}{\sigma_T \Delta T}\right)^{1/2} \tag{8}$$

Equation (6) then can be written as

$$\frac{Q}{\pi k \Delta T R_h} \sim \left(\frac{\sigma_T \Delta T R_h}{\mu\alpha}\right)^{1/2} = (\text{Ma}^*)^{1/2} \tag{9}$$

where Ma* is the Marangoni number based on R_h. This situation exists only for high-Pr fluids.

If both velocity and temperature boundary layers exist (large Ma and $R\sigma$), U is given by Eq. (5), but that radial velocity exists only within δ_V, so the determination of δ_T is different depending on whether δ_T is larger or smaller than δ_V or whether Pr is smaller or larger than unity. If Pr $\geq$ 1, δ_T is within δ_V so that U^* from Eq. (5) can be used within δ_T and one obtains

$$\delta_T \sim \left(\frac{\alpha R_h}{U}\right)^{1/2} \sim R_h(\text{Ma}^* U^*)^{-1/2}$$

$$\sim R_h(\text{Ma}^*)^{-1/3}\,\text{Pr}^{-1/6} \tag{10}$$

Equation (6) then becomes

$$\frac{Q}{\pi k \Delta T R_h} \sim (\text{Ma}^*)^{1/3}\,\text{Pr}^{1/6} \tag{11}$$

If Pr $<$ 1, δ_T is outside of δ_V so that one cannot use this value of U in δ_T. In that case the axial velocity V toward the heated region induced by U determines δ_T. From the balance of the volume flux toward the heated region ($R_h^2 V$) and the flux out of the region through the velocity boundary layer ($R_h \delta_V U$) one gets

$$U\delta_V \sim V R_h \tag{12}$$

and δ_T is determined by the balance of the axial conduction and convection, which gives

$$\delta_T \sim \frac{\alpha}{V} \tag{13}$$

Then from Eqs. (5), (6), (12), and (13) one obtains

$$\frac{Q}{\pi k \Delta T R_h} \sim (\text{Ma}^*)^{1/3}\,\text{Pr}^{2/3} \tag{14}$$

These expressions (Eqs. (7), (9), (11), and (14)) for the ratio $Q/\pi k \Delta T R_h$ give ΔT as a function of Q under various conditions. The ratio can also be regarded as the Nusselt number because it represents the ratio of the total heat transfer rate (Q) to the conduction heat transfer rate ($\pi k \Delta T R_h$). For Pr $>$ 1, with increasing Ma the ratio changes from Eq. (7) to Eq. (9) and then to Eq. (11), and for Pr $<$ 1, it changes from Eq. (7) to Eq. (11).

Figure 6 shows $Q/\pi k \Delta T R_h$ versus Ma* for Pr = 0.1 and Pr = 20 obtained from the numerical analysis. For Ma* less than about 10 the ratio is nearly constant. For Ma* $\to$ 0, the limiting value of the ratio is found to be 0.828. For Pr = 0.1 with increasing Ma*, the constant region is followed by the $\frac{1}{3}$-power region as predicted by Eq. (14), while for Pr = 20 there exists

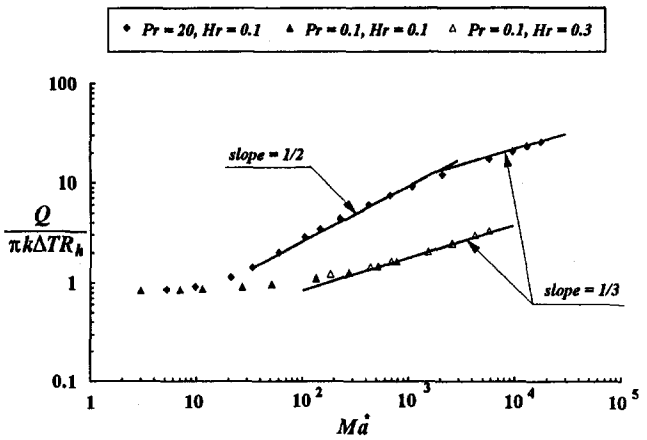

Fig. 6 Dimensionless heat transfer rate as a function of Marangoni number based on heating zone radius

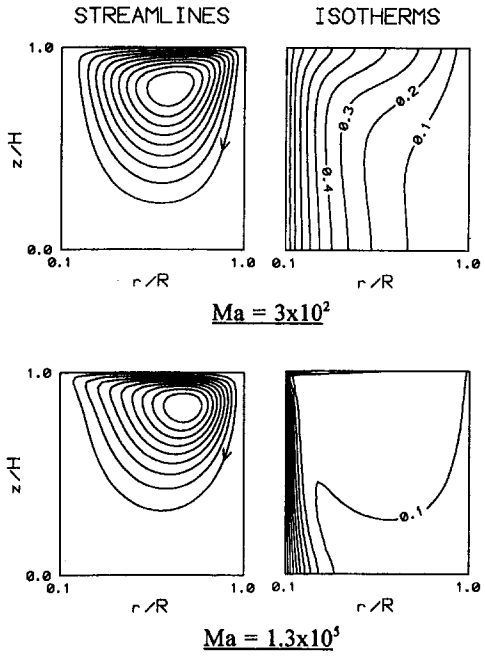

Fig. 7 Typical streamlines and isotherms in CT configuration (Pr = 20, *Hr* = 0.1)

the $\frac{1}{2}$-power region between those two regions according to Eq. (9). Figure 6 as well as the scaling analysis given above show that as long as the Ma and $R\sigma$ based on R_h are used, the dimensionless maximum velocity and heat transfer rate are independent of Hr.

5 Flows in CT Heating Mode

Typical streamlines and isotherms in the CT mode are shown in Fig. 7. The overall streamline pattern is similar to that shown in Fig. 2 for the CF heating. The ratio of the heating to cooling areas in the CT mode is Hr, compared to $Hr^2/2$ in the CF mode, so that the bulk fluid temperature is warmer in the CT heating. The fluid temperature still decreases sharply away from the heater due to the presence of a thermal boundary layer along the heater if Ma becomes large enough.

Figure 8 shows the surface temperature and velocity distributions for three values of Ma. In contrast to the CF cases (Fig. 3) the surface temperature distribution in the CT mode varies significantly with Ma, especially near the heater. The location of the surface velocity peak does not vary with Ma in the CF mode but it moves closer to the heater with increasing Ma in the CT mode. When Ma is small (300 in Fig. 8), conduction heat transfer dominates and the fluid temperature varies smoothly with radius. Consequently, the driving force is uniformly important all along the free surface and the surface velocity smoothly increases and then decreases with increasing radial position.

With increasing Ma, a thermal boundary layer develops along the heater length as convection becomes important, and the overall temperature of the bulk fluid decreases due to increased cooling effect from the cold wall, as seen in Fig. 7. The free surface temperature drops sharply near the heater because of the boundary layer. The region of large radial temperature gradient near the heater is called the hot-corner region herein. As Fig. 8 shows, outside the hot-corner region the temperature gradient is relatively small except in a very small region next to the cold wall (called the cold-corner region). As will be discussed later, since the flow is driven toward the wall in the cold region, as opposed to away from the wall in the hot corner, the driving force in the cold corner loses its effectiveness in driving the whole flow. Therefore, our focus is on the hot-corner region in the present analysis. The peak velocity location that represents the extent of the hot-corner region and the peak velocity that can be considered to be the characteristic velocity are two important quantities associated with the flow. The prediction of those quantities in the CT mode is made more complex than in the CF mode by the fact that the extent of the hot-corner region shrinks as Ma increases, as seen in Fig. 8.

For the low-Pr fluids (Pr = 0.1 and 0.01) studied herein Nu is nearly unity when Ma is less than about 1000 (Chang et al., 1994). When Nu = 1, the heat transfer is by conduction and the driving force is uniformly distributed over the entire free surface. In that situation, following the scaling analysis of Ostrach (1977), it can be shown (Chang et al., 1994) that when $R\sigma$ is small (less than about 100 in the present configuration), the length scale of the flow is R and the dimensionless velocity U^* is a constant. When $R\sigma$ is larger than about 1000, a velocity boundary layer appears along the free surface and the dimensionless velocity U^* scales with $R\sigma^{-1/3}$.

The computed values of Nu, the dimensionless peak velocity, and its radial position (distance Δ from the heater) are shown for high-Pr fluids (Pr = 10, 20, 50, and 100) in Fig. 9 in the range of $R\sigma$ less than 10^3. As Fig. 9 shows, in that range of $R\sigma$ these quantities are functions of Ma only and independent of Pr or $R\sigma$, which means that the flow is viscous dominated. The aforementioned fact that the driving force region shrinks with increasing Ma makes it possible for the viscous forces to remain important for large $R\sigma$. When Ma is less than about 100, Nu is close to unity and, as in the case of low Pr with small $R\sigma$, U^* is a constant (Fig. 9(a)).

When Ma is increased above 100, Nu increases due to increasingly important convection (Fig. 9(a)), a thermal boundary layer appears along the heater, and the length scale Δ decreases. As illustrated in Fig. 10, the free-surface temperature decreases sharply in the region where the thermal boundary layer along the heater meets the free surface, and the surface

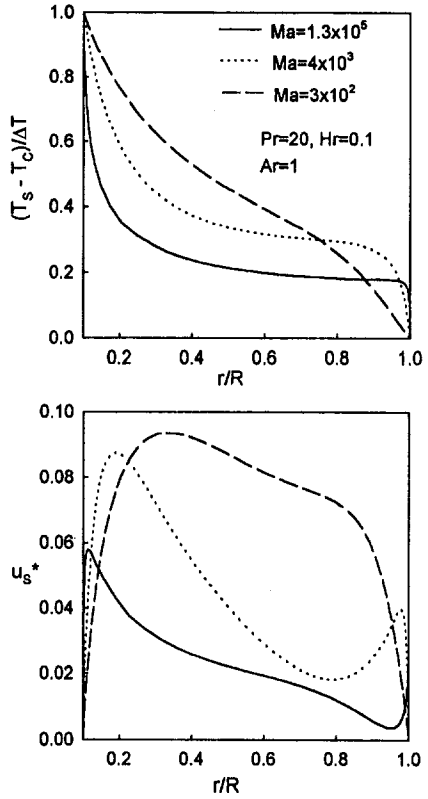

Fig. 8 Typical surface temperature and velocity distributions in CT configuration

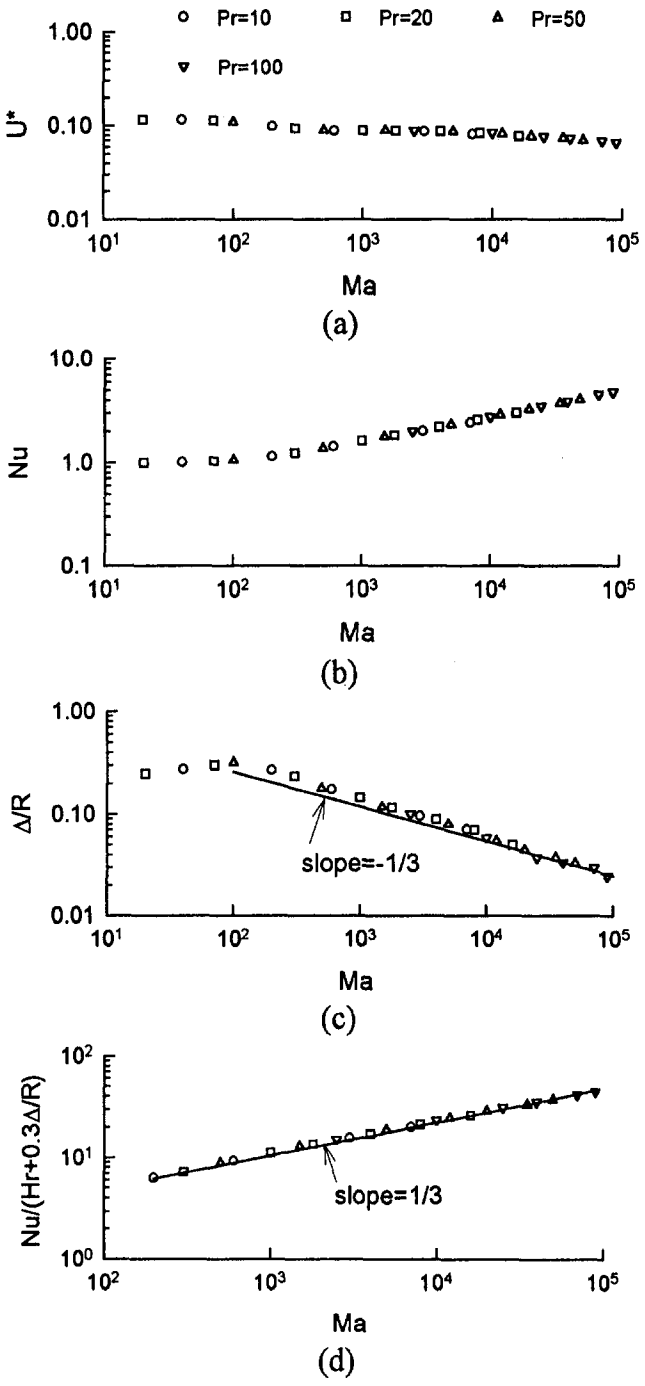

Fig. 9 Dimensionless velocity, Nusselt number, and hot corner width for high-Pr fluids in the range $R\sigma \leq 1000$

velocity increases with increasing radius up to the edge of Δ. Since the flow is viscous in the range $R\sigma < 1000$, the dimensionless velocity U^* should be constant. As Fig. 9(a) shows, U^* is nearly constant above Ma = 100 and up to Ma = 10^4. The constant value (about 0.09) is slightly different from the value for the conduction regime (0.116). Beyond Ma = 10^4, U^* decreases slightly with Ma, approximately as $\mathrm{Ma}^{-0.08}$. Since the dependence of U^* on Ma is generally weak, U^* is assumed to be constant in the present analysis.

Outside Δ the surface velocity decreases, but the velocity scale is still characterized by U since the flow is viscous. The return flow velocity also scales with U but the return flow generally slows down toward the heater except near the hot-corner region. Therefore, the return flow velocity ($U_{B,H}$) near the thermal boundary layer along most of the heater length is smaller than U and estimated proportionally as

$$U_{B,H} \sim U \frac{\delta_{T,H}}{R} \tag{15}$$

and then the thermal boundary layer thickness for $Ar = 1$ is given as

$$\frac{\delta_{T,H}}{R} \sim \left(\frac{\alpha}{U_{B,H}R}\right)^{1/2} \sim \left(\frac{1}{\mathrm{Ma}}\frac{R}{\delta_{T,H}}\right)^{1/2}$$

$$\frac{\delta_{T,H}}{R} \sim \mathrm{Ma}^{-1/3} \tag{16}$$

Since Δ is the region where the fluid temperature changes sharply, Δ should scale with the thermal boundary layer thickness (see Fig. 10), and thus $\Delta/R \sim \mathrm{Ma}^{-1/3}$. As seen in Fig. 9($c$), the scaling law is valid above about Ma = 10^3.

The total heat transfer rate from the heater to the fluid is given as $Q \sim k\Delta T(R_h + C\delta_{T,H})R/\delta_{T,H}$ for $Ar = 1$. As Fig. 9(c) shows, R_h/R and Δ/R (and $\delta_{T,H}/R$) are on the same order of magnitude in the parametric ranges studied here, so it is necessary to use the average radius of the boundary layer ($R_h + C\delta_{T,H}$) to estimate Q, constant C being of order unity. Then Nu can be expressed, for a given Hr, as

$$\mathrm{Nu} \sim \left(Hr + C\frac{\Delta}{R}\right)\mathrm{Ma}^{1/3} \tag{17}$$

where $\delta_{T,H}$ in the average radius term is replaced by Δ. As shown in Fig. 9(a), the computed results agree well with this scaling law with $C = 0.3$.

When $R\sigma$ exceeds 1000, the inertia forces become important and the dimensionless flow quantities depend not only on Ma but also on Pr or $R\sigma$ for given geometric parameters Hr and Ar. There exist both temperature and velocity boundary layers in the flow, so its analysis is more complex than the above viscous case. Due to the length limitation, the inertia case is not discussed herein and we refer to Chang et al. (1994) for a detailed discussion on that case.

As mentioned earlier, a large temperature gradient exists next to the cold wall when convection becomes important (Fig. 8), which gives rise to a velocity peak in the cold corner region. The extent of the cold corner can be determined by balancing the convection along the free surface and conduction, and Lai

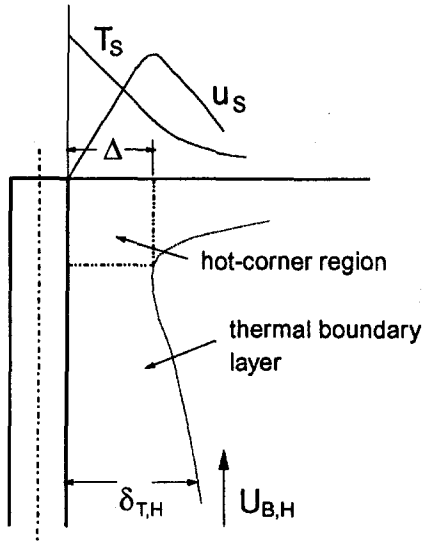

Fig. 10 Illustration showing hot corner region for viscous flow

(1984) has shown that the dimensions of the cold corner scale with Ma^{-1} for high Pr fluids. Therefore, the cold corner is a very small region when Ma is large. The fact that the cold corner is a very small region can be shown also by numerical analysis: For the conditions of $Ma = 5.4 \times 10^4$, $Pr = 20$, and $Hr = 0.1$, the numerical analysis shows that the velocity peak near the cold wall disappears only a distance of $z/H = 0.01$ away from the free surface and below that depth the velocity simply decreases monotonically toward the wall. Therefore, the total volume flux associated with the cold corner is negligibly small.

6 Summary Comparisons of CF and CT Flows

As shown above, the scaling laws and the detailed flow structure for the CF configuration are generally very different from those for the CT configuration, although the overall flow structures appear to be similar superficially. Also both cases are generally different from other configurations (e.g., rectangular cavities and half zones) mainly because of the radial spreading effect in the present cylindrical configurations with a small heating zone. In the CF case the main flow region is fixed by the heating zone area and Ma and $R\sigma$ based on R_h are the appropriate parameters. A velocity boundary layer appears in the heated region in the range $R\sigma^* > 200$ and a thermal boundary layer in the range of $Ma^* > 10$. Due to the velocity boundary layer, the dimensionless flow velocity decreases with $R\sigma^*$ and the thermal boundary layer reduces the fluid temperature for a given Q. In the CT case the main driving force region shrinks with increasing Ma in the range $Ma > 10^3$ for high-Pr fluids, which keeps the flow viscous until around $R\sigma = 1000$. Because the driving force region exists mainly in the viscous hot-corner region, the dimensionless flow velocity is generally a weak function of Ma. For low-Pr fluids ($Pr \sim 0.01$), the inertia effects become important when conduction still dominates and the main driving force exists over the entire surface, the situation similar to the CF heating with R replaced by R_h, and the dimensionless velocity decreases with increasing $R\sigma$.

Acknowledgments

This work is supported by NASA under contract No. NAS 3-25973 with Mr. A. Pline as the Project Scientist and Mr. T. Jacobson as the Project Manager.

References

Bergman, T. L., and Ramadhyani, S., 1986, "Combined Buoyancy- and Thermocapillary-Driven Convection in Open Square Cavities," *Numerical Heat Transfer,* Vol. 9, pp. 441–451.

Carpenter, B. M., and Homsy, G. M., 1989, "Combined Buoyant and Thermocapillary Flow in a Cavity," *Journal of Fluid Mechanics,* Vol. 207, pp. 121–132.

Carpenter, B. M., and Homsy, G. M., 1990, "High Marangoni Number Convection in a Square Cavity: Part II," *Physics of Fluids A,* Vol. 2, pp. 137–149.

Chang, A., Kamotani, Y., and Ostrach, S., 1994, "Scaling Analysis of Thermocapillary Flows in Cylindrical Containers," Report EMAE/TR-94-214, Department of Mechanical and Aerospace Engineering, Case Western Reserve University, Cleveland, OH.

Chang, C. E., and Wilcox, W. R., 1976, "Analysis of Surface Tension Driven Flow in Floating Zone Melting," *International Journal of Heat and Mass Transfer,* Vol. 19, pp. 355–366.

Chen, M. M., 1987, "Thermocapillary Convection in Materials Processing," *Interdisciplinary Issues in Materials Processing and Manufacturing,* ASME, Vol. 2, pp. 541–558.

Cowley, S. J., and Davis, S. H., "Viscous Thermocapillary Convection at High Marangoni Number," *Journal of Fluid Mechanics,* Vol. 135, pp. 175–188.

Fu, B. I., and Ostrach, S., 1983, "Numerical Solutions of Floating-Zone Thermocapillary Flows," *Proceedings of the 4th European Symposium on Materials Sciences Under Microgravity,* pp. 239–245.

Kamotani, Y., Ostrach, S., and Pline, A., 1993, "A Thermocapillary Convection Experiment in Microgravity," *Heat Transfer in Microgravity,* C. T. Avedesian and V. A. Arpaci, eds., ASME HTD-Vol. 269, pp. 23–30.

Kamotani, Y., Ostrach, S., and Pline, A., 1994, "Analysis of Velocity Data Taken in Surface Tension Driven Convection Experiment in Microgravity," *Physics of Fluids,* Vol. 6, pp. 3601–3609.

Keller, J. R., and Bergman, T. L., 1990, "Thermocapillary Cavity Convection in Wetting and Nonwetting Liquids," *Numerical Heat Transfer,* Vol. 18, pp. 33–49.

Lai, C.-L., 1984, "Studies of Thermocapillary Oscillation Phenomena," Ph.D. Thesis, Department of Mechanical and Aerospace Engineering, Case Western Reserve University, Cleveland, OH.

Mundrane, M., and Zebib, A., 1993, "Two- and Three-Dimensional Buoyant Thermocapillary Convection," *Physics of Fluids A,* Vol. 5, pp. 810–818.

Ostrach, S., 1977, "Motion Induced by Capillarity," *Physico-Chemical Hydrodynamics,* V. G. Levich, ed., Advanced Publication, London, Vol. 2, pp. 571–589.

Patanker, S. V., 1980, *Numerical Heat Transfer and Fluid Flow,* Hemisphere Publication.

Zebib, A., Homsy, G. M., and Meiburg, E., 1989, "High Marangoni Number Convection in a Square Cavity," *Physics of Fluids,* Vol. 28, pp. 3467–3476.

Journal of Heat Transfer

Technical Notes

This section contains shorter technical papers. These shorter papers will be subjected to the same review process as that for full papers.

Numerical Model for Quantitative Verification of Magnetic Resonance Imaging of Time-Dependent Temperature Distributions in a Phantom

C. De Wagter,[1] J. De Poorter,[2] C. Thomsen,[3] F. Ståhlberg,[3,4] Y. De Deene,[1] L. Martens,[5] and E. Achten[2]

Introduction

Hyperthermia in combination with radiation therapy has shown to be promising in the treatment of a variety of human cancers. The dosimetry and the control of the heat supply require a method of real-time thermometry. The current state of the art is to sample temperature from thermocouples, thermistors, or optical sensors placed in a few strategic locations in the patient (Shimm et al., 1988). Especially for deep-seated tumors, this invasive method has the disadvantage that it causes trauma to the patient and strongly restricts the number of measuring points. Therefore, there is a strong need for noninvasive thermometry (Cetas, 1984; Bolomey and Hawley, 1990). One of the most appealing candidates is magnetic resonance. Unlike other alternative methods (Bolomey and Hawley, 1990), NMR offers a high spatial resolution and is a clinically proven and accepted imaging modality. In addition, NMR has the advantage of supplying anatomical images during the treatment, allowing angiography studies and having the potential to study perfusion in tumors and their surroundings.

The NMR method we will consider is based on the temperature dependence of the molecular diffusion coefficient (D) of tissue water. Imaging of D is founded on the attenuation of the received NMR signal caused by the dephasing of the excited spins by their incoherent motion in a space-dependent magnetic field. In the context of hyperthermia treatment, this diffusion method was proven to be able to measure temperature within 1°C for a spatial resolution of the order of 1 cm^3, independently of depth (Le Bihan et al., 1989). It was shown later that a commercial NMR unit can be combined with a hyperthermia electromagnetic radiator (Delannoy et al., 1990).

Commonly, noninvasive thermometry methods are validated by measuring temperature in a limited number of fixed points in the phantom. We followed a different approach by implementing a numerical heat transfer model in order to achieve a threefold goal: (*i*) set up a verification procedure that considers all pixels of the entire NMR image, (*ii*) test NMR thermometry with regard to dynamic nonhomogeneous temperature behavior, and (*iii*) gage whether temperature increase induces lower signal to noise ratios.

Materials and Methods

(A) NMR Phantom Experiment. One can obtain temperature maps from diffusion images by use of the temperature dependence of the molecular diffusion coefficient D of water (Le Bihan et al., 1989)

$$D = D_0 \exp(-E_a k_B^{-1} T^{-1}) \quad (1)$$

where T is the absolute temperature, D_0 is the diffusion coefficient for $T = \infty$, and k_B is Boltzman's constant (8.616581×10^{-5} eV K^{-1}).

We constructed a phantom consisting of 51 Agarose gel contained in a 32-cm-long plexiglass cylinder of 14.2-cm inner and 15.0-cm outer diameter. A thermal conduction process was invoked in the gel by pumping hot and cold water through two parallel tubes axially embedded in the gel. The tube inner and outer diameters are 1.0 and 1.5 cm, respectively. The longitudinal extension of the cylindrical system is sufficient to assume that the induced thermal process is basically two dimensional. The phantom cross section is shown in Fig. 1. The Agarose gel is from Sigma Chemical Company (St. Louis, MO), type V High Gelling Temperature (42°C @ 1.5 percent solution). The concentration used is 1 percent. The viscosity of the gel is high enough to avoid thermally induced convective flow, even around the hot water tube. The gel was doped with a concentration of 0.1 g/l $CuSO_4$ (98 percent, Aldrich Chemical Company, Milwaukee, WI) to make the characteristic NMR time constants $T1$ and $T2$ representative for brain tissue: $T1$ = 1150 ms and $T2$ = 100 ms (@ 20°C). A considerably higher concentration of $CuSO_4$ was added to the circulating hot/cold water in order to minimize the motion artifacts.

[1] Dept. of Radiotherapy and Nuclear Medicine, University Hospital, De Pintelaan 185, B-9000 Gent, Belgium; phone: +32 9 2403014, Fax: +32 9 2403040, E-mail: carlos.dewagter@rug.ac.be.

[2] NMR Department, University Hospital, De Pintelaan 185, B-9000 Gent, Belgium.

[3] Danish Research Center of Magnetic Resonance, Hvidovre, Denmark.

[4] Dept. of Medical Radiation Physics, Lund University, Sweden.

[5] Dept. of Information Technology, Gent University, Gent, Belgium.

Contributed by the Heat Transfer Division of THE AMERICAN SOCIETY OF MECHANICAL ENGINEERS. Manuscript received by the Heat Transfer Division July 1994; revision received July 1995. Keywords: Measurement Techniques, Numerical Methods, Transient and Unsteady Heat Transfer. Associate Technical Editor: R. Viskanta.

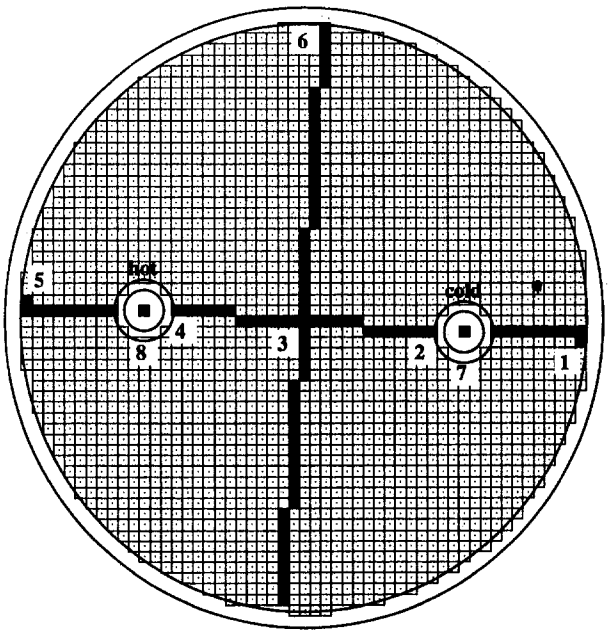

Fig. 1 Transverse cross section of the gel phantom with the cold and hot water tubes. The equidistant grid used for numerical simulation is derived from an NMR image. Pixels where thermocouples are positioned are shown in black. The gray-shaded pixels represent the line along which the temperature profiles of Fig. 5 are shown.

The cylindrical phantom was placed longitudinally in a Magnetom 1.5T SP total-body scanner (Siemens, Erlangen, Germany). The standard radiofrequency head coil and the built-in gradient system were employed. To acquire the transverse temperature images, we implemented a single spin echo sequence sensitized by pulsed magnetic field gradients. We used a 10-mm slice thickness, a (128 × 128) acquisition matrix, which is reduced to a (64 × 64) format by spatial averaging, a field of view of 17 cm, and a repetition time of 1000 ms. The echo time was optimized for maximum NMR signal following the method outlined by Thomsen et al. (1987). The resulting optimal value was 117 ms. Diffusion images were calculated from two images diffusion weighted by different z-gradients. The acquisition time was 4.5 min per diffusion image.

(B) Heat Transfer Model. The temperature T at each coordinate $\mathbf{r}$ and time t is governed by the heat conduction equation:

$$\rho(\mathbf{r})c(\mathbf{r})\frac{\partial}{\partial t}T(\mathbf{r}, t) = \nabla\cdot(k(\mathbf{r})\nabla T(\mathbf{r}, t)) \tag{2}$$

where ∇ is the spatial differential operator and ρ, c, k are the gel density, specific heat, and thermal conductivity, respectively. In previous work (De Wagter, 1986) Eq. (2) was solved numerically for hyperthermia application in two-dimensional space following a "volume integral method" and using polygonal cells. Accordingly, the phantom cross section of Fig. 1 is partitioned into a uniform grid of square cells that coincide with the NMR image pixels. Integrating both sides of Eq. (2) over each cell n, with area $S_n = S$, leads to

$$\iint_{S_n}\rho c\frac{\partial}{\partial t}T(\mathbf{r}, t)dS = \oint_{l_n} k\frac{\partial}{\partial t}T(\mathbf{r}, t)dl,$$

$$n = 1, \ldots, N. \tag{3}$$

After discretization of this expression, where l_n is the outline of area S_n and $\partial/\partial n$ denotes differentiation in the direction of the outward normal from cell n, we obtain for each nonboundary cell n, surrounded by cells $n_1, n_2, \ldots, n_4$, the following difference equation:

$$S\rho c\frac{\partial}{\partial t}\mathbf{T}_n(t) \simeq \sum_{i=1}^{4} k(\mathbf{T}_{n_i}(t) - \mathbf{T}_n(t)), \tag{4}$$

where the temperature in each cell n is denoted by $\mathbf{T}_n$, being the nth element of vector $\mathbf{T}$.

The boundary conditions are described by Newton's Law (Carslaw and Jaeger, 1959)

$$-k\frac{\partial}{\partial n}T(\mathbf{r}, t) = (T(\mathbf{r}, t) - T_0(t))H \tag{5}$$

where H is the local thermal transfer coefficient, and T_0 is the ambient temperature or the temperature of the hot/cold water. In our experiment, T_0 changes rapidly at t_0 from initial phantom temperature to the actual circulating water temperature. If side i of cell n forms part of the boundary, the corresponding term in summation (4) has to be replaced by

$$\iota\frac{T_0(t) - \mathbf{T}_n(t)}{\frac{1}{H} + \frac{\iota}{2k}}$$

where ι is the side length of each cell.

System (4) of coupled first-order differential equations is in matrix form given by

$$\frac{\partial}{\partial t}\mathbf{T}(t) = A\mathbf{T}(t) + \mathbf{f}(t). \tag{7}$$

A is a real $(N \times N)$ matrix and vector $\mathbf{f}(t)$ contains the source functions $\mathbf{f}_n(t)$ of each cell n. In this problem without volume heat sources, $\mathbf{f}_n(t)$ is different from zero only in the boundary cells:

$$\mathbf{f}_n(t) = \sum_i \frac{\iota\left(\frac{T_0(t)}{\frac{1}{H} + \frac{\iota}{2k}}\right)}{S\rho c} \tag{8}$$

where the summation applies over the number of boundary sides. If $\mathbf{f}$ is constant in time since t_0, then the general solution of Eq. (7) at $t \geq t_0$ can be expressed in the matrix form

$$\mathbf{T}(t) = \mathrm{EXP}((t - t_0)A)\mathbf{T}(t_0) + A^{-1}(\mathrm{EXP}((t - t_0)A) - I)\mathbf{f}. \tag{9}$$

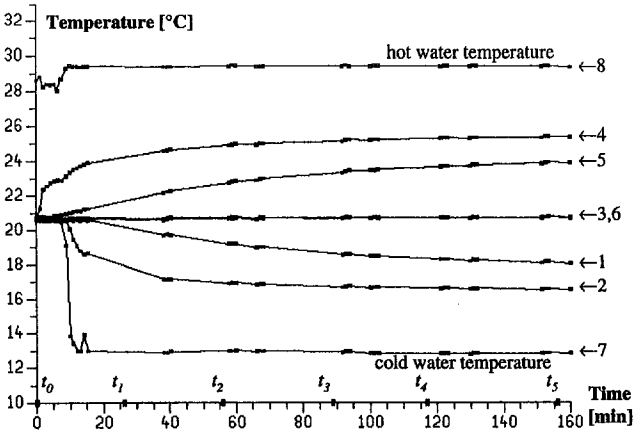

Fig. 2 Thermocouple measurements, represented by dots linearly interconnected, as a function of time. $t_0, t_1, \ldots, t_5$ are the NMR measuring time instants. No measurements were executed during the NMR acquisitions themselves, because this would give unreliable data.

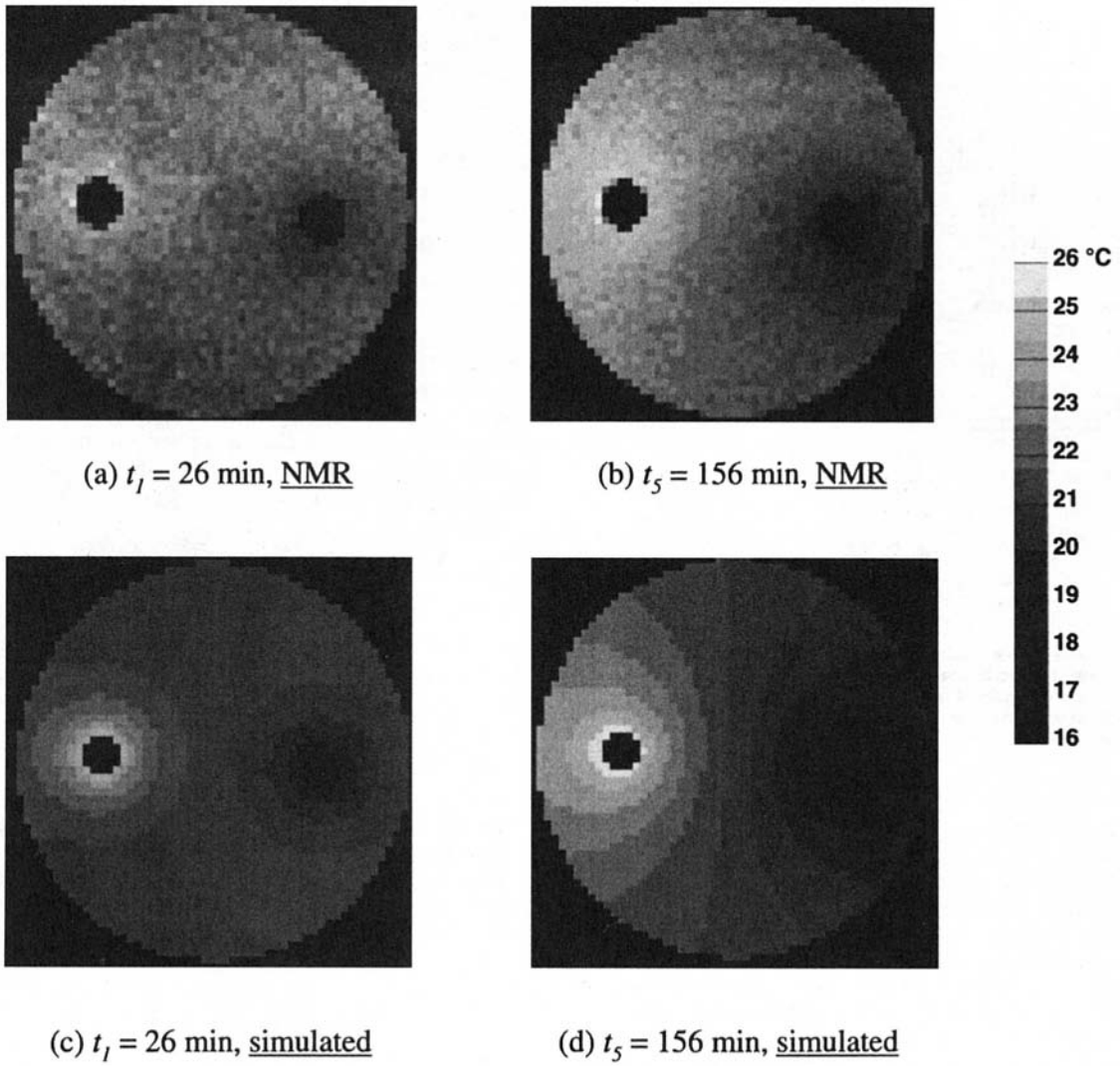

Fig. 3 Temperature maps obtained by NMR and numerical simulation. The black coloring of the water tubes is due to the heavy doping of the water in order to avoid motion artifacts, and should not be interpreted in terms of temperature.

I is the identity matrix and EXP stands for the exponential matrix function. The function EXP is computed from the eigenvalues and eigenvectors of A making use of the sparse nature of A (De Wagter, 1986). It is worthwhile to notice from Eq. (9) that, dissimilar from the finite time difference techniques, the computing time is independent of the physical heating time $(t - t_0)$, since the thermal problem is solved analytically with respect to the time variable. The eigenvector calculation has to be performed only once for a given cross section and thermal characteristics.

The cross section of the cylindrical phantom is discretized from an NMR image by selecting the pixels that exceed a predefined noise threshold. The resulting mathematical grid (Fig. 1) contains 2213 cells out of the total number of $64 \times 64 = 4096$ image pixels. A field of view of 17 cm and a slice thickness of 1 cm result in an elementary volume of $(0.27\ \text{cm})^2 \times 1\ \text{cm} = 0.073\ \text{cm}^3$. The thermal properties of the water-based gel are taken to be those of water at 20°C (*CRC Handbook of Chemistry and Physics,* 1983): $\rho c = 4.2 \times 10^6\ \text{J m}^{-3}\ \text{K}^{-1}$, $k = 0.6\ \text{W m}^{-1}\ \text{K}^{-1}$. Between the gel and the circulating hot/cold water, of which the temperature is assumed constant in each tube, a thermal transfer coefficient H_i was introduced to represent the cylindrical wall. This assumption is feasible since the wall is relative thin (2.5 mm) and the specific heat of the plexiglass $(\rho c = 1.8 \times 10^6\ \text{J m}^{-3}\ \text{K}^{-1})$ is rather low in comparison with that of the gel $(\rho c = 4.2 \times 10^6\ \text{J m}^{-3}\ \text{K}^{-1})$. So, H_i is computed by applying the following equation for the hollow cylinder (Carslaw and Jaeger, p. 189, 1959):

$$H_i = \frac{k_{\text{plexi}}}{r_o \ln\left(\frac{r_o}{r_i}\right)} \tag{10}$$

where r_i and r_o are the inner and outer diameter of the cylindrical plexiglass wall and k_{plexi} is its thermal conductivity. For the thermal conductivity k_{plexi}, the value provided by the plexiglass (Ispaglas) manufacturer was used: $k_{\text{plexi}} = 0.186\ \text{W m}^{-1}\ \text{K}^{-1}$. Introducing further $r_i = 5.0$ mm and $r_o = 7.5$ mm in Eq. (10) gives $H_i = 61.2\ \text{W m}^{-2}\ \text{K}^{-1}$.

The thermal transfer coefficient between gel and ambient air, H_o, was calculated in the following way. The part comprising the heat transfer through the outer cylindrical wall, is, in analogy with Eq. (10), represented by:

$$H^* = \frac{k_{\text{plexi}}}{r_i \ln\left(\frac{r_o}{r_i}\right)} \tag{11}$$

The second part represents the heat transferred by radiation

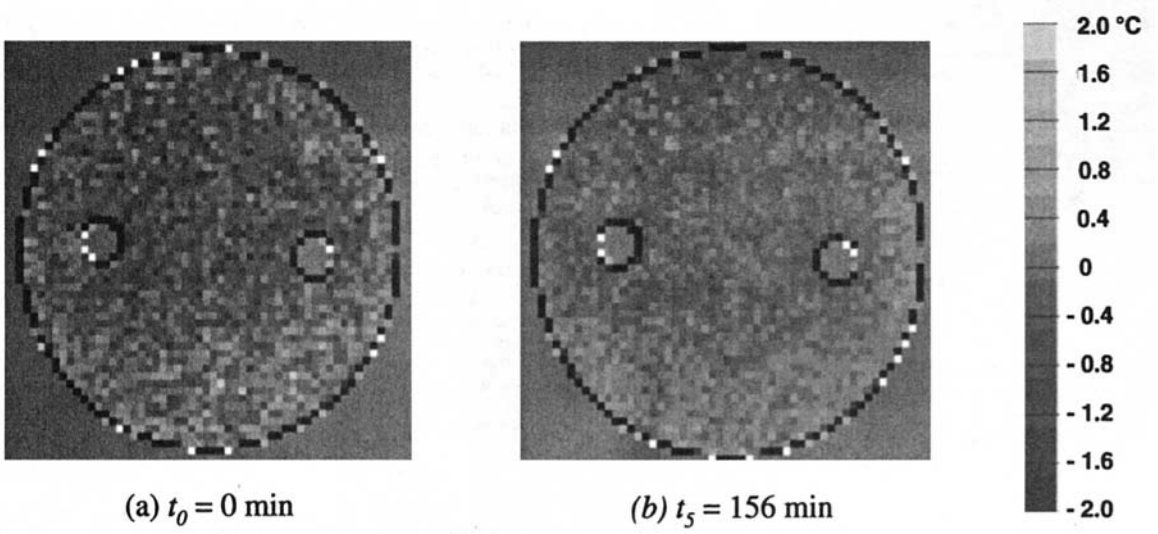

Fig. 4 Temperature difference (NMR-measured minus -simulated) maps at t_0 = 0 min and t_5 = 156 min.

from the outer cylinder wall toward the surroundings—being the ambient air, head coil, and scanner inside cover. The corresponding transfer coefficient in case of an ambient temperature of 21°C is, according to Carslaw and Jaeger (p. 21, 1959), approximately given by

$$H_r = 5.84 \times E \ [\text{W m}^{-2} \text{K}^{-1}] \tag{12}$$

E is the emissivity of the plexiglass surface, for which the typical value for glass is taken: $E = 0.8$ (Carslaw and Jaeger, p. 21, 1959). Substituting k_{plexi}, $r_i = 71$ mm, $r_o = 75$ mm, and E in Eqs. (11) and (12), gives respectively: $H^* = 47.8$ W m^{-2} K^{-1} and $H_r = 4.67$ W m^{-2} K^{-1}. Finally, the total H_o is obtained from (Carslaw and Jaeger, p. 189, 1959)

$$\frac{1}{H_o} = \frac{1}{H^*} + \frac{r_i}{r_o}\frac{1}{H_r} \tag{13}$$

resulting in $H_o = 4.47$ W m^{-2} K^{-1}. We neglected the heat loss due to natural air convection around the phantom. Our arguments are the following ones: the head coil considerably hampers natural convection and, for the modest phantom boundary temperatures, the heat transfer by even unhindered convection is lower than the transfer by radiation (Carslaw and Jaeger, p. 21, Eq. (13), 1959). In addition, the "patient" cooling system was deliberately switched off during the phantom experiment.

The quite rough Cartesian discretization of the circular tubes and outer phantom boundary (Fig. 1) has been validated on a phantom that contained only one tube in the center but which had, for the remainder, the same dimensions and contained the same gel (De Poorter et al., 1994). The one-tube phantom, as it will be designated further, was modeled both in (*i*) a Cartesian coordinate system that comprised an identical discretization of the tube, and (*ii*) a polar coordinate system that allowed a perfect matching of the boundaries. Transient and steady-state temperature distributions produced by both methods have been compared. This analysis showed that, for the specific case considered, the boundary conditions are modeled satisfyingly by the Cartesian discretization of Fig. 1 in combination with the values taken for H_i and H_o. Also the heat transfer model itself was verified on the same one-tube phantom using thermocouples. The striking agreement found justifies the use of the temperature distributions produced by the heat transfer model as a reference for the quantitative verification of the NMR thermometry method.

(C) Verification of NMR Thermometry. The verification is done by comparing the NMR-measured images with the computed temperature distributions. Two figures of merit are considered: the Root Mean Square Deviation (RMSD) and the Mean Deviation (MD), defined as

$$\text{RMSD} = \sqrt{\frac{\sum_{i=1}^{N^*} (T_{\text{meas},i} - T_{\text{simul},i})^2}{N^*}}; \qquad \text{MD} = \frac{\sum_{i=1}^{N^*} (T_{\text{meas},i} - T_{\text{simul},i})}{N^*} \tag{14}$$

where $T_{\text{meas},i}$ is the NMR-measured temperature in the ith image pixel, $T_{\text{simul},i}$ is calculated for the ith pixel, and N^* is the number of nonboundary pixels in the mathematical phantom model. The reason why the $(N - N^*)$ boundary pixels are excluded is that the corresponding boundary volume elements might not be completely contained in the actual phantom.

In order to determine the gel parameters D_0 and E_a in Eq. (1), temperature is measured invasively by using Chromel-Alumel (NiCr-Ni) thermocouples (cf. Results section). The computer-controlled data acquisition unit was placed in the NMR computer room. The thermocouple wires and the hot/cold water pipes were lead through the cut-off holes of the Faraday cage, where the thermocouple leads were low-pass filtered by capacitors connected in shunt to the electrical ground. In order to avoid artifacts caused by the ferromagnetic Ni, the thermocouples were placed in a transverse plane parallel to the imaging plane separated by a distance of about 5 cm. Hereby, we rely on the fact that the temperature distributions are independent of the longitudinal coordinate.

Results

The phantom was initially at 20.5°C. The hot and cold water temperatures were 29.3°C and 12.8°C, respectively, while the ambient air was at 21.0°C. The thermocouple measuring results are shown in Fig. 2 as a function of time for the locations shown in Fig. 1. Supplementary thermocouples were used to measure the circulating hot and cold water temperatures. As apparent from Fig. 2, the cold and hot water circulation did not start simultaneously at t_0 due to some air bubbles that blocked the cold water circuit during the first 9 min. The effect of this delay on the further thermal experiment has been neglected.

At $t_0 = 0$ min, $t_1 = 26$ min, $t_2 = 56$ min, $t_3 = 89$ min, $t_4 = 117$ min, and $t_5 = 156$ min an NMR measuring sequence was started. From (*i*) the molecular diffusion coefficient D measured in each thermocouple location, and (*ii*) the average of the before

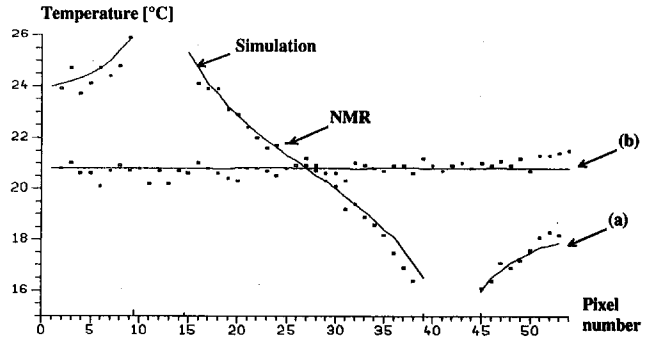

Fig. 5 Temperature profile at t_5 = 156 min along (*a*) the horizontal pixel row and (*b*) the vertical pixel column as indicated in Fig. 1. Comparison between the simulations (solid curve) and the NMR measurements (dots). The number of phantom pixels is 43 in (*a*) and 54 in (*b*).

and after NMR acquisition thermocouple read-outs, we obtained $D_0 = 9.338 \times 10^{-6}$ m^2 s^{-1} and $E_a = 0.2142$ eV by using a linear regression of ln (D) versus T^{-1} according to Eq. (1). A correlation coefficient of 0.88 was found. At 20°C there holds for D and its relative temperature sensitivity

$$D = 1.93\ 10^{-9}\ \text{m}^2\ \text{s}^{-1};$$

$$\frac{1}{D}\frac{\partial D}{\partial T} = \frac{1}{T^2}\frac{E_a}{k} = 2.9 \text{ percent } °\text{C}^{-1}, \quad (15)$$

where T is the absolute temperature. The temperature images NMR-measured at t_1 = 26 min and t_5 = 156 min are displayed in Fig. 3, where they are compared with the numerically simulated images. The temperature distribution, initially being fairly well focused at t_1, is already spread out considerably at t_5. Figure 4 displays the difference maps (NMR-measured minus -simulated) at the start and the end of the experiment.

Discussion and Conclusions

The temperature fields in Fig. 3 embody an interesting region with pronounced thermal gradients. Figure 5 shows the temperature profiles calculated and NMR-measured at t = 156 min along the pixel row and column indicated in Fig. 1. We notice that the NMR data allow us to reconstruct fairly well the subtle hyperbolic-sine-like profile between the hot and cold-water tubes.

The time course of the Root Mean Square Deviation (RMSD) and the Mean Deviation (MD) of the NMR-measured temperature maps from the simulated ones is plotted in Fig. 6. The RMSD principally involves both the systematic deviation and the noise contribution. The low absolute values of MD reveal that the RMSD is predominantly due to the noise in the diffusion image. The same conclusion can be made when observing the difference images Fig. 4(*a*) and 4(*b*). The RMSD curve confirms that it is possible to measure the time-dependent temperature distributions within 0.7°C RMSD for a spatial resolution of 0.073 cm^3. The RMSD does not increase during the thermal excitation, demonstrating the stability of the NMR method and its capability to follow the thermal transients considered. This confirms the method's potential for hyperthermic cancer therapy monitoring.

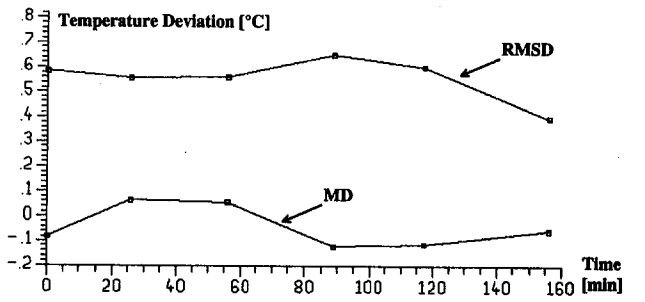

Fig. 6 Deviation of the NMR-measured from the simulated temperature maps during thermal excitation of the phantom in terms of Root Mean Square Deviation (RMSD) and Mean Deviation (MD). The dots indicate the NMR measuring time points. The linear interpolation between the dots is to pronounce possible trends.

References

Bolomey, J. C., and Hawley, M. S., 1990, "Noninvasive Control of Hyperthermia," in: M. Gautherie, ed., *Methods of Hyperthermia Control,* Springer-Verlag, Paris, pp. 35–111.

Carslaw, H. S., and Jaeger, J. C., 1959, *Conduction of Heat in Solids,* Oxford University Press, Oxford, United Kingdom.

Cetas, T. C., 1984, "Will Thermometric Tomography Become Practical for Hyperthermia Treatment Monitoring?" *Cancer Research,* Vol. 44, pp. 4805–4808.

CRC Handbook of Chemistry and Physics, 1983, 62nd ed., CRC Press, Boca Raton, FL.

Delannoy, J., Le Bihan, D., Hoult, D. I., and Levin, R. L., 1990, "Hyperthermia System Combined With a Magnetic Resonance Imaging Unit," *Medical Physics,* Vol. 17, pp. 855–860.

De Poorter, J., De Wagter, C., De Deene, Y., Thomsen, C., Ståhlberg, F., and Achten, E., 1994, "The Proton-Resonance-Frequency-Shift Method Compared With Molecular Diffusion for Quantitative Measurement of Two-Dimensional Time-Dependent Temperature Distributions in a Phantom," *Journal of Magnetic Resonance,* Series B, Vol. 103, pp. 234–241.

De Wagter, C., 1986, "Optimization of Simulated Two-Dimensional Temperature Distributions Induced by Multiple Electromagnetic Applicators," *IEEE Trans. Microwave Theory Tech.,* Vol. MTT-34, pp. 589–596.

Le Bihan, D., Delannoy, J., and Levin, R. L., 1989, "Temperature Mapping With MR Imaging of Molecular Diffusion: Application to Hyperthermia," *Radiology,* Vol. 171, pp. 853–857.

Shimm, D. S., Hynynen, K. H., Anhalt, D. P., Roemer, R. B., and Cassady, J. R., 1988, "Scanned Focussed Ultrasound Hyperthermia: Initial Clinical Results," *Int. J. Radiation Oncology Biology Physics,* Vol. 15, pp. 1203–1208.

Thomsen, C., Henriksen, O., and Ring, P., 1987, "In Vivo Measurement of Water Self Diffusion in the Human Brain by Magnetic Resonance Imaging," *Acta Radiologica,* Vol. 28, pp. 353–361.

Elastoplastic Constriction Resistance Model for Sphere-Flat Contacts

M. R. Sridhar[1,2] and M. M. Yovanovich[1,3]

Introduction

In a typical sphere-flat interface contact, heat transfer occurs through the solid contact as well as the gap. Heat transfer through natural convection and radiation across the gap has been found to be negligible for microelectronics and other tribological applications. It is also known that the coupling between solid conduction and gap conduction at the contact is weak. To simplify the analysis, heat transfer across the gap is neglected. This is achieved experimentally by working in a vacuum environment. Hence this study will examine a single sphere-flat contact at different loads in vacuum (i.e., only solid heat transfer). The purpose of this paper is to develop a model to predict accurately the constriction resistances for interfaces that have

[1] Microelectronics Heat Transfer Laboratory, Department of Mechanical Engineering, University of Waterloo, Waterloo, Ontario, Canada N2L 3G1.

[2] Postdoctoral Fellow; Assoc. Mem. ASME.

[3] Professor and Director; Fellow ASME.

Contributed by the Heat Transfer Division of THE AMERICAN SOCIETY OF MECHANICAL ENGINEERS. Manuscript received by the Heat Transfer Division May 1994; revision received November 1994. Keywords: Conduction, Electronic Equipment, Thermal Packaging. Associate Technical Editor: L. S. Fletcher.

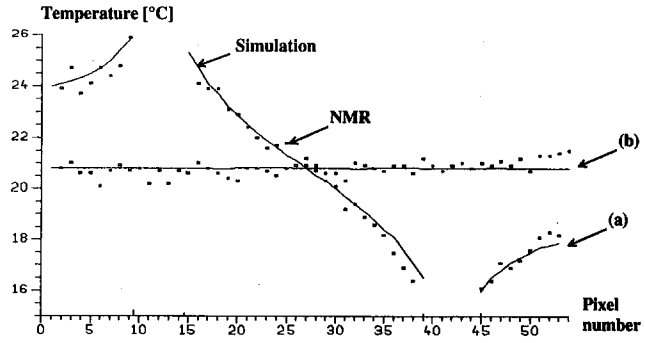

Fig. 5 Temperature profile at t_5 = 156 min along (*a*) the horizontal pixel row and (*b*) the vertical pixel column as indicated in Fig. 1. Comparison between the simulations (solid curve) and the NMR measurements (dots). The number of phantom pixels is 43 in (*a*) and 54 in (*b*).

and after NMR acquisition thermocouple read-outs, we obtained $D_0 = 9.338 \times 10^{-6}$ m^2 s^{-1} and $E_a = 0.2142$ eV by using a linear regression of ln (D) versus T^{-1} according to Eq. (1). A correlation coefficient of 0.88 was found. At 20°C there holds for D and its relative temperature sensitivity

$$D = 1.93\ 10^{-9}\ \text{m}^2\ \text{s}^{-1};$$

$$\frac{1}{D}\frac{\partial D}{\partial T} = \frac{1}{T^2}\frac{E_a}{k} = 2.9 \text{ percent } °\text{C}^{-1}, \quad (15)$$

where T is the absolute temperature. The temperature images NMR-measured at t_1 = 26 min and t_5 = 156 min are displayed in Fig. 3, where they are compared with the numerically simulated images. The temperature distribution, initially being fairly well focused at t_1, is already spread out considerably at t_5. Figure 4 displays the difference maps (NMR-measured minus -simulated) at the start and the end of the experiment.

Discussion and Conclusions

The temperature fields in Fig. 3 embody an interesting region with pronounced thermal gradients. Figure 5 shows the temperature profiles calculated and NMR-measured at t = 156 min along the pixel row and column indicated in Fig. 1. We notice that the NMR data allow us to reconstruct fairly well the subtle hyperbolic-sine-like profile between the hot and cold-water tubes.

The time course of the Root Mean Square Deviation (RMSD) and the Mean Deviation (MD) of the NMR-measured temperature maps from the simulated ones is plotted in Fig. 6. The RMSD principally involves both the systematic deviation and the noise contribution. The low absolute values of MD reveal that the RMSD is predominantly due to the noise in the diffusion image. The same conclusion can be made when observing the difference images Fig. 4(*a*) and 4(*b*). The RMSD curve confirms that it is possible to measure the time-dependent temperature distributions within 0.7°C RMSD for a spatial resolution of 0.073 cm^3. The RMSD does not increase during the thermal excitation, demonstrating the stability of the NMR method and its capability to follow the thermal transients considered. This confirms the method's potential for hyperthermic cancer therapy monitoring.

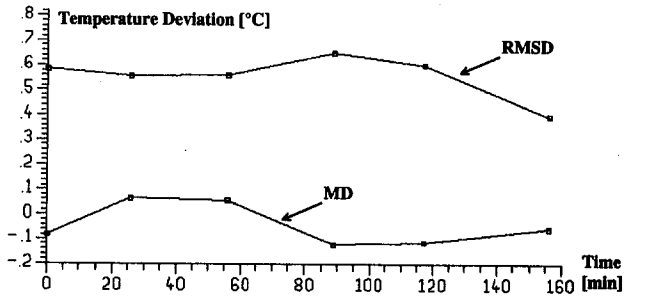

Fig. 6 Deviation of the NMR-measured from the simulated temperature maps during thermal excitation of the phantom in terms of Root Mean Square Deviation (RMSD) and Mean Deviation (MD). The dots indicate the NMR measuring time points. The linear interpolation between the dots is to pronounce possible trends.

References

Bolomey, J. C., and Hawley, M. S., 1990, "Noninvasive Control of Hyperthermia," in: M. Gautherie, ed., *Methods of Hyperthermia Control,* Springer-Verlag, Paris, pp. 35–111.

Carslaw, H. S., and Jaeger, J. C., 1959, *Conduction of Heat in Solids,* Oxford University Press, Oxford, United Kingdom.

Cetas, T. C., 1984, "Will Thermometric Tomography Become Practical for Hyperthermia Treatment Monitoring?" *Cancer Research,* Vol. 44, pp. 4805–4808.

CRC Handbook of Chemistry and Physics, 1983, 62nd ed., CRC Press, Boca Raton, FL.

Delannoy, J., Le Bihan, D., Hoult, D. I., and Levin, R. L., 1990, "Hyperthermia System Combined With a Magnetic Resonance Imaging Unit," *Medical Physics,* Vol. 17, pp. 855–860.

De Poorter, J., De Wagter, C., De Deene, Y., Thomsen, C., Ståhlberg, F., and Achten, E., 1994, "The Proton-Resonance-Frequency-Shift Method Compared With Molecular Diffusion for Quantitative Measurement of Two-Dimensional Time-Dependent Temperature Distributions in a Phantom," *Journal of Magnetic Resonance,* Series B, Vol. 103, pp. 234–241.

De Wagter, C., 1986, "Optimization of Simulated Two-Dimensional Temperature Distributions Induced by Multiple Electromagnetic Applicators," *IEEE Trans. Microwave Theory Tech.,* Vol. MTT-34, pp. 589–596.

Le Bihan, D., Delannoy, J., and Levin, R. L., 1989, "Temperature Mapping With MR Imaging of Molecular Diffusion: Application to Hyperthermia," *Radiology,* Vol. 171, pp. 853–857.

Shimm, D. S., Hynynen, K. H., Anhalt, D. P., Roemer, R. B., and Cassady, J. R., 1988, "Scanned Focussed Ultrasound Hyperthermia: Initial Clinical Results," *Int. J. Radiation Oncology Biology Physics,* Vol. 15, pp. 1203–1208.

Thomsen, C., Henriksen, O., and Ring, P., 1987, "In Vivo Measurement of Water Self Diffusion in the Human Brain by Magnetic Resonance Imaging," *Acta Radiologica,* Vol. 28, pp. 353–361.

Elastoplastic Constriction Resistance Model for Sphere-Flat Contacts

M. R. Sridhar[1,2] and M. M. Yovanovich[1,3]

Introduction

In a typical sphere-flat interface contact, heat transfer occurs through the solid contact as well as the gap. Heat transfer through natural convection and radiation across the gap has been found to be negligible for microelectronics and other tribological applications. It is also known that the coupling between solid conduction and gap conduction at the contact is weak. To simplify the analysis, heat transfer across the gap is neglected. This is achieved experimentally by working in a vacuum environment. Hence this study will examine a single sphere-flat contact at different loads in vacuum (i.e., only solid heat transfer). The purpose of this paper is to develop a model to predict accurately the constriction resistances for interfaces that have

[1] Microelectronics Heat Transfer Laboratory, Department of Mechanical Engineering, University of Waterloo, Waterloo, Ontario, Canada N2L 3G1.

[2] Postdoctoral Fellow; Assoc. Mem. ASME.

[3] Professor and Director; Fellow ASME.

Contributed by the Heat Transfer Division of THE AMERICAN SOCIETY OF MECHANICAL ENGINEERS. Manuscript received by the Heat Transfer Division May 1994; revision received November 1994. Keywords: Conduction, Electronic Equipment, Thermal Packaging. Associate Technical Editor: L. S. Fletcher.

been loaded beyond the elastic regime, i.e., to the elastoplastic and fully plastic regimes.

Review of Constriction Resistance Model

In the complete model the contacting bodies are assumed to be smooth or with negligible roughness. It is also assumed that heat flowing between idealized bodies must flow through the solid contact area. The constriction and the subsequent spreading of heat flow lines give rise to thermal constriction resistance, defined as the temperature difference across the contact divided by the total heat flow rate through the contact. The constriction resistance model can be divided into two parts: (i) thermal model and (ii) deformation model.

The theoretical thermal constriction resistance for a sphere-flat contact is given by Cooper et al. (1969):

$$R_{cT} = \frac{(1 - a/b)^{1.5}}{2k_s a} \tag{1}$$

where k_s is harmonic mean thermal conductivity given by: $k_s = (2k_A k_B)/(k_A + k_B)$, b is the flux tube radius, and the subscripts A and B refer to the sphere and flat, respectively. The constriction resistance model, Eq. (1), requires a deformation model to predict the circular contact radius a. Once the contact radius has been predicted by the deformation model, Eq. (1) can be used to predict the thermal contact resistance.

The contact deformation can be elastic, elastoplastic, or fully plastic depending upon the normal load $\tilde{F}$ applied. Three types of deformation model are available in the literature.

Deformation Models

1 Elastic Model of Hertz. A sphere in contact with a flat produces a circular contact, which can be predicted using the Hertz elastic model. The Hertz contact radius "a" in terms of load $\tilde{F}$, geometry β, and equivalent elastic modulus E' is given by (see Johnson, 1985): $a_e = [(3\tilde{F}\beta)/(4E')]^{1/3}$, where $\beta \equiv$ radius of the sphere, and the equivalent elastic modulus: $E' = [(1 - \nu_A^2)/E_A + (1 - \nu_B^2)/E_B]^{-1}$. The subscripts A and B refer to the sphere and flat, respectively.

2 Geometric Plastic Model. This model assumes that the sphere and the flat interact geometrically under fully plastic deformation. Hence the contact radius in terms of load $\tilde{F}$ and uniaxial tensile flow stress S_f of the softer material in contact is given by: $a_p = [\tilde{F}/(C_{p,a}\pi S_f)]^{1/2}$, where $C_{p,a} \equiv H_{p,a}/S_f = 2.76$, the plastic constraint factor (Sridhar, 1994), and $H_{p,a} = \tilde{F}/(\pi a_p^2)$, *where* $H_{p,a}$ is normal indentation hardness.

The ratio of hardness $H_{p,a}$, to the flow stress S_f under fully plastic deformation is a constant for real strain hardening materials, provided the appropriate value of flow stress S_f is used (see Tabor, 1951). The Hertz elastic and the geometric plastic models are inadequate to predict experimental results that lie in the elastoplastic regime.

3 Elastoplastic Model. The expression for the elastoplastic hardness was obtained by Sridhar (1994) by "patching" or "blending" the two asymptotic solutions (i.e., elastic and plastic). The technique was first introduced into convection heat transfer by Churchill and Usagi (1972). Before developing the actual model, one needs to define a dimensionless contact strain that makes the model independent of geometric and material properties. The dimensionless contact strain first presented in the paper by Johnson (1970) can be defined as: $\epsilon^*_{c,d} = E'/S_f \cdot a/\beta$, where the subscripts c and d refer to the contact and type of deformation, respectively.

We assume that the relative elastoplastic contact strain $\epsilon^*_{c,ep}$ can be related to the two asymptotic results valid for pure elastic contact $\epsilon^*_{c,e}$ and for fully plastic flow $\epsilon^*_{c,p}$ in the following blended form:

$$\epsilon^*_{c,ep} = [(\epsilon^*_{c,e})^n + (\epsilon^*_{c,p})^n]^{1/n} \tag{2}$$

where the index n is called the "blending" parameter, which is to be determined from analysis, experimental results, or numerical results. After substitution for the elastic and fully plastic solutions, one obtains the explicit relationships for the models based on the contact radius and contact displacement:

$$(\epsilon^*_{c,a})_{ep} = \left[\left(\frac{3}{4} \cdot \frac{\tilde{F}}{\left(\frac{S_f}{E'}\right)^2 \beta^2 S_f} \right)^{n/3} + \left(\frac{1}{\pi C_{p,a}} \cdot \frac{\tilde{F}}{\left(\frac{S_f}{E'}\right)^2 \beta^2 S_f} \right)^{n/2} \right]^{1/n} \tag{3}$$

where the constraint parameter is chosen to be $C_{p,a} = 2.76$ (see Sridhar, 1994). The first term on the right-hand side is the elastic solution and the second term is the fully plastic solution. They both depend on the normal load $\tilde{F}$ and the sphere radius β but to different powers, i.e., $n/3$ and $n/2$ for the elastic and plastic limits, respectively. The physical parameters are E', $C_{p,a}$, and S_f.

In order to compare the explicit elastoplastic model based on contact size or displacement with experimental data, one needs to cast Eq. (3) into a dimensionless form. We can define the dimensionless load as follows: $F^*_a = \tilde{F}/F_{c,a}$, where $F_{c,a}$ is the critical load given by the following expression: $F_{c,a} = 366.7\,(S_f/E')^2 \cdot \beta^2 \cdot S_f$. At the critical load $F_{c,a}$ (see Sridhar, 1994) the elastic and plastic theories predict the same value for the contact radius. Substituting for $\tilde{F}$ in terms of F^*_a in Eq. (3), we have:

$$(\epsilon^*_{c,a})_{ep} = [(275\,F^*_a)^{n/3} + (42.3\,F^*_a)^{n/2}]^{1/n} \tag{4}$$

With a value of $n = 5$, the Tabor (1951) mild-steel data compare quite well with the explicit model, which is based on contact radius. Its ability to predict data within the elastoplastic regime is quite good with percent difference of -2.1 percent near the critical load (i.e., $F^*_a = 1$). It is known from Churchill and Usagi (1972) that the value of n is most sensitive to experimental or computed values at or near $F^*_a = 1$. This model is insensitive to small variations to n (see Churchill and Usagi, 1972) and an integral value can be chosen without serious error. In this case, $n = 5$ is the closest integral value that predicts the Tabor (1951) data with the least error. The model is recast into a convenient form:

$$\left(\frac{a}{\beta}\right)_{ep} = \left[\left(\frac{3\tilde{F}}{4\beta^2 E'} \right)^{5/3} + \left(\frac{\tilde{F}}{2.76\pi\beta^2 S_f} \right)^{5/2} \right]^{1/5} \tag{5}$$

Results and Discussion

Previously performed thermal contact resistance experiments of Kitscha (1982), Fisher (1985), and Fisher and Yovanovich (1989) will be utilized for comparison with theoretical predictions.

Equations (1) and (5) constitute a complete elastoplastic constriction resistance model. Most of the thermophysical (k_s, E') and geometric parameters (β, b) are known beforehand and are constants for a particular experimental set. The only unknown parameter is the uniaxial tensile flow stress S_f.

It is clear from Tabor's work (1951) that flow stress "S_f" is not a constant for a real strain hardening material; it varies with increasing contact strain under plastic deformation. In the present set of experiments, uniaxial tensile flow stress S_f is not available. Fisher and Yovanovich (1989) calculated the flow stress from a bulk hardness test using Tabor's (1951) empirical relationship between hardness and flow stress given by: $S_f = H_B/$

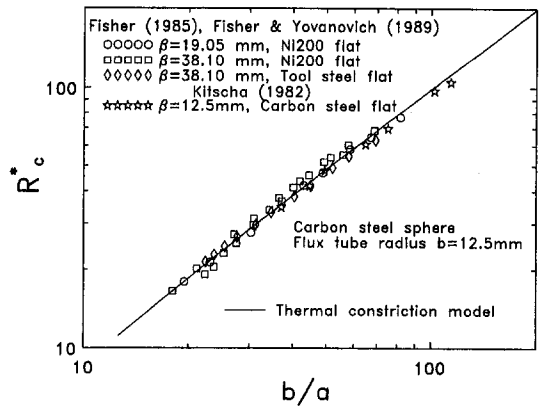

Fig. 1 Dimensionless constriction resistance and all data versus b/a

C_p, where $H_B \equiv$ bulk hardness. This is a good approximation provided both the bulk hardness test and experiments are performed approximately at the same contact strain (a/β). But this is not possible for the present set of experiments. To avoid the problem of not using an appropriate value of flow stress, a technique was developed to calculate S_f. The present method assumes that the flow stress S_f is a constant for a particular experimental set. This is a reasonable assumption since most of the present experimental data (from Fisher, 1985) lie in the elastic and the elastoplastic regimes. Hence, the value of flow stress, which is a constant for an experimental set, would be more or less close to the yield stress of the softer material in contact.

Procedure to Calculate Appropriate Flow Stress S_f. The first step would be to input values of experimental resistance R_{cE} (at maximum load $\tilde{F}_{\max}$), harmonic mean thermal conductivity k_s, equivalent elastic modulus E', and geometric properties b and β for a particular data set. With this information the contact radius can be calculated solving Eq. (1) using *Mathematica* (Wolfram, 1988–91) or any other numerical root-finding technique. It should be noted that the theoretical resistance R_{cT} in Eq. (1) is replaced with the experimental value R_{cE} at $\tilde{F}_{\max}$. Then the contact strain (a/β) at $\tilde{F}_{\max}$ for that data set can be computed. This contact strain can be in the elastic, elastoplastic, or fully plastic regimes. In order to predict a realistic value of S_f, one must make sure that a significant amount of plastic deformation has occurred at this particular load $\tilde{F}_{\max}$. To confirm this the contact strain calculated from the experimental constriction resistance is then compared with the contact strain predicted by the Hertz elastic model given by:

$$\left(\frac{a}{\beta}\right)_e = \left(\frac{3\tilde{F}}{4\beta^2 E'}\right)^{1/3} \tag{6}$$

It should also be confirmed that the calculated value of contact strain should be outside the experimental uncertainty of elastic deformation, since it is predicted from an experimental constriction resistance. This is done by comparing the computed contact strain (a/β) with 1.15 $(a/\beta)_e$ instead of just $(a/\beta)_e$. The factor 1.15 is used since the uncertainty of the computed contact strain (a/β) is of the order of ±13.4 percent. This is the root mean square of the uncertainties in the experimental resistance R_{cE} (±8 percent), harmonic mean conductivity k_s (±4 percent), and the radius of curvature β (±10 percent). If the calculated value of contact strain is greater than 1.15 $(a/\beta)_e$, then the flow stress of the softer material in contact can be determined using the following relationship:

$$S_f = \frac{\tilde{F}_{\max}}{2.76\pi\beta^2\left[\left(\frac{a}{\beta}\right)_{ep}^{n} - \left(\frac{3\tilde{F}_{\max}}{4\beta^2 E'}\right)^{n/3}\right]^{2/n}} \tag{7}$$

If the calculated value of contact strain is less than 1.15 $(a/\beta)_e$ then the procedure recommends using a value of ∞ for the flow stress S_f. This value of flow stress reduces the elastoplastic model to the Hertz elastic model, Eq. (6).

Comparison of Elastoplastic Model With Experiments. The dimensionless contact resistance can be defined as:

$$R_c^* = 2bk_sR_c = \frac{(1 - a/b)^{1.5}}{a/b} \tag{8}$$

Figure 1 shows a comparison between the proposed elastoplastic constriction model and data from Fisher (1985), Fisher and Yovanovich (1989), and Kitscha (1982) for a plot of dimensionless constriction resistance R_c^* versus the parameter b/a, which is inversely related to the applied load $\tilde{F}$. The model is independent of the type of deformation and is a plot of Eq. (8). Data reduction involved the determination of contact radius a using the elastoplastic deformation model. In Fig. 2 the lighest load data points can be seen at the top end and the highest load data at the lower end.

The advantage of defining a dimensionless constriction resistance can be seen in Fig. 1. Irrespective of the type of deformation, thermophysical properties, geometries, and materials used, all data sets can be plotted on one graph. The experimental data include two data sets from (*i*) Fisher (1985) where deformation was elastoplastic, two more from (*ii*) Fisher (1985) and Fisher and Yovanovich (1989) where deformation was fully elastic, and one from (*iii*) Kitscha (1982) where deformation was fully elastic. It is seen that the data points lie close to the model, they fall on either side, and the comparison is very good with an overall rms error of 4.5 percent.

The yield/flow stress S_f (206 and 194 MPa) determined for two data sets from Fisher (1985) is obtained from thermal contact resistance data. There was a need to validate these values independently from another source. It was not possible to perform tensile tests on Fisher (1985) specimens as they were not long enough. However, Brinell hardness tests were performed on Fisher (1985) Ni200 specimens at six different loads. Figure 2 shows the comparison of yield/flow stress S_f calculated from these two different sources for Ni200 on the same plot. It is assumed that the yield/flow stress calculated from thermal data is close to the 0.2 percent yield strength of the material. The flow strain ϵ_f was determined using the procedure developed by Sridhar (1994). There seems to be a good correlation (Fig. 2) of trends for S_f calculated from two different sources. It should be noted that the lowest load available on the Brinell

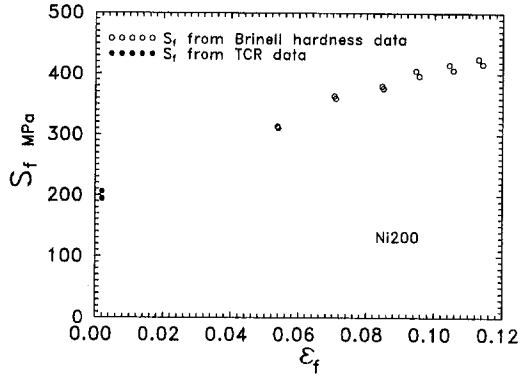

Fig. 2 Comparison of yield/flow stress for Fisher (1985) Ni200 specimens obtained from two different sources

hardness tester is only 500 kgf and S_f determined at this load corresponds to a flow strain ϵ_f, which is much higher than the 0.2 percent yield strain of the material.

Summary and Conclusions

The thermal constriction resistance model in conjunction with the elastoplastic deformation model is very versatile and can predict experimental results in any deformation regime with good accuracy.

The problem of not using an appropriate value of flow stress in the elastoplastic deformation model has been addressed here and the proposed technique to compute the flow stress seems to work quite well with the experimental data sets. In future it is suggested that an uniaxial tensile test be performed on the softer material in contact so that the appropriate value of flow stress can be obtained from it and used in the elastoplastic deformation model.

Acknowledgments

The authors acknowledge the support of the Natural Science and Engineering Research Council of Canada under grant No. A7445.

References

Churchill, S. W., and Usagi, R., 1972, "A General Expression for the Correlations of Rates and Other Phenomena," *AIChE Journal,* Vol. 18, pp. 1121–1132.

Cooper, M. G., Mikic, B. B., and Yovanovich, M. M., 1969, "Thermal Contact Conductance," *Int. J. Heat Mass Transfer,* Vol. 12, pp. 279–300.

Fisher, N. J., 1985, "Analytical and Experimental Studies of the Thermal Contact Resistance of Sphere/Layered Flat Contacts," M.A.Sc. Thesis, University of Waterloo, Canada.

Fisher, N. J., and Yovanovich, M. M., 1989, "Thermal Constriction Resistance of Sphere/Layered Flat Contacts: Theory and Experiment," ASME JOURNAL OF HEAT TRANSFER, Vol. 111, pp. 249–256.

Johnson, K. L., 1970, "The Correlation of Indentation Experiments," *Journal of Mechanics and Physics of Solids,* Vol. 18, pp. 115–126.

Johnson, K. L., 1985, *Contact Mechanics,* Cambridge University Press, Cambridge, United Kingdom.

Kitscha, W., 1982, "Thermal Resistance of Sphere-Flat Contacts," M.A.Sc. Thesis, University of Waterloo, Canada.

Sridhar, M. R., 1994, "Elastoplastic Contact Models for Sphere-Flat and Conforming Rough Surface Applications," Ph.D. Thesis, University of Waterloo, Canada.

Tabor, D., 1951, *The Hardness of Metals,* Oxford University Press, London.

Wolfram, S., 1988–91, *A System for Doing Mathematics by Computer,* Version 2.0 for DOS, Wolfram Research, Inc., Champaign, IL.

Fully Developed Laminar Fluid Flow and Heat Transfer in an Eccentric Annulus With an Axially Moving Core

T. Shigechi,[1] S. Momoki,[1] and Y. Lee[2]

Nomenclature

c = constant, Eq. (1)
e = eccentricity, see Fig. 1
E = $[\alpha^2/(\alpha^2 - 1)] - [1/\ln \alpha^2]$
f = friction factor
h = heat transfer coefficient
k = thermal conductivity
Nu = Nusselt number
p = pressure
q = heat flux
R = radius
Re = Reynolds number = $u_m 2(R_o - R_i)/\nu$
S = c/R_o
T = temperature
u = axial velocity
U = velocity of the moving core
U^* = relative velocity = U/u_m
(x, y) = Cartesian coordinates
z = axial coordinate
α = radius ratio = R_i/R_o
ϵ = dimensionless eccentricity = $e/(R_o - R_i)$
θ = $T/[q_i(R_o - R_i)/k]$
μ, ν = dynamic and kinematic viscosities
(ξ, η) = bipolar coordinates
ρ = density
τ = wall shear stress
ϕ = angle, peripheral

Superscript

$\bar{}$ = peripherally averaged

Subscripts

b = bulk
cr = critical
i, o = inner and outer walls
ii = Case A: constant heat flux at the inner wall with the outer insulated
max = maximum
oo = Case B: constant heat flux at the outer wall with the inner insulated

Introduction

Problems involving fluid flow and heat transfer with a moving core of solid body or fluid in an annular geometry can be found in many engineering/industrial processes. In our previous studies, we presented the solutions on the problems of fully developed *turbulent* fluid flow and heat transfer in an annulus with a moving core of solid body or fluid (Shigechi et al., 1990; Lee and Shigechi, 1992), and developed and developing *laminar* fluid flow and heat transfer (Shigechi and Lee, 1991; Shigechi et al., 1993) in a concentric annulus with a moving core.

The eccentricity of the core in an annular geometry may arise from design constraints or as a result of manufacturing inaccuracies, operational malfunctioning, or deformation in service from the normally concentric configuration. The fully developed laminar fluid flow and heat transfer in an eccentric annulus with a *stationary* core have been extensively studied analytically or numerically (Piercy et al., 1933; Heyda, 1959; Redberger and Charles, 1962; Snyder, 1963; Snyder and Goldstein, 1965; Jonsson and Sparrow, 1965; Tiedt, 1966, 1967; Cheng and Hwang, 1968; Trombetta, 1971; Suzuki et al., 1990).

Reported in the present paper are an exact solution for the fluid flow and numerical solutions by a finite difference method for the heat transfer between a fully developed laminar fluid flow and an axially moving core in an *eccentric* annular geometry.

Analysis

The mathematical development of the analysis is rather complex but straightforward. The assumptions used in the analysis are:

[1] Dept. of Mech. Systems Eng., Nagasaki University, Nagasaki, Japan, 852.
[2] Dept. of Mech. Eng., University of Ottawa, Ottawa, Canada, K1N 6N5.

Contributed by the Heat Transfer Division of THE AMERICAN SOCIETY OF MECHANICAL ENGINEERS. Manuscript received by the Heat Transfer Division November 1994; revision received May 1995. Keywords: Environmental Heat Transfer, Materials Processing and Manufacturing Processes, Moving Boundaries. Associate Technical Editor: Y. Bayazitoglu.

hardness tester is only 500 kgf and S_f determined at this load corresponds to a flow strain ϵ_f, which is much higher than the 0.2 percent yield strain of the material.

Summary and Conclusions

The thermal constriction resistance model in conjunction with the elastoplastic deformation model is very versatile and can predict experimental results in any deformation regime with good accuracy.

The problem of not using an appropriate value of flow stress in the elastoplastic deformation model has been addressed here and the proposed technique to compute the flow stress seems to work quite well with the experimental data sets. In future it is suggested that an uniaxial tensile test be performed on the softer material in contact so that the appropriate value of flow stress can be obtained from it and used in the elastoplastic deformation model.

Acknowledgments

The authors acknowledge the support of the Natural Science and Engineering Research Council of Canada under grant No. A7445.

References

Churchill, S. W., and Usagi, R., 1972, "A General Expression for the Correlations of Rates and Other Phenomena," *AIChE Journal,* Vol. 18, pp. 1121–1132.

Cooper, M. G., Mikic, B. B., and Yovanovich, M. M., 1969, "Thermal Contact Conductance," *Int. J. Heat Mass Transfer,* Vol. 12, pp. 279–300.

Fisher, N. J., 1985, "Analytical and Experimental Studies of the Thermal Contact Resistance of Sphere/Layered Flat Contacts," M.A.Sc. Thesis, University of Waterloo, Canada.

Fisher, N. J., and Yovanovich, M. M., 1989, "Thermal Constriction Resistance of Sphere/Layered Flat Contacts: Theory and Experiment," ASME JOURNAL OF HEAT TRANSFER, Vol. 111, pp. 249–256.

Johnson, K. L., 1970, "The Correlation of Indentation Experiments," *Journal of Mechanics and Physics of Solids,* Vol. 18, pp. 115–126.

Johnson, K. L., 1985, *Contact Mechanics,* Cambridge University Press, Cambridge, United Kingdom.

Kitscha, W., 1982, "Thermal Resistance of Sphere-Flat Contacts," M.A.Sc. Thesis, University of Waterloo, Canada.

Sridhar, M. R., 1994, "Elastoplastic Contact Models for Sphere-Flat and Conforming Rough Surface Applications," Ph.D. Thesis, University of Waterloo, Canada.

Tabor, D., 1951, *The Hardness of Metals,* Oxford University Press, London.

Wolfram, S., 1988–91, *A System for Doing Mathematics by Computer,* Version 2.0 for DOS, Wolfram Research, Inc., Champaign, IL.

Fully Developed Laminar Fluid Flow and Heat Transfer in an Eccentric Annulus With an Axially Moving Core

T. Shigechi,[1] S. Momoki,[1] and Y. Lee[2]

Nomenclature

c = constant, Eq. (1)
e = eccentricity, see Fig. 1
E = $[\alpha^2/(\alpha^2 - 1)] - [1/\ln \alpha^2]$
f = friction factor
h = heat transfer coefficient
k = thermal conductivity
Nu = Nusselt number
p = pressure
q = heat flux
R = radius
Re = Reynolds number = $u_m 2(R_o - R_i)/\nu$
S = c/R_o
T = temperature
u = axial velocity
U = velocity of the moving core
U^* = relative velocity = U/u_m
(x, y) = Cartesian coordinates
z = axial coordinate
α = radius ratio = R_i/R_o
ϵ = dimensionless eccentricity = $e/(R_o - R_i)$
θ = $T/[q_i(R_o - R_i)/k]$
μ, ν = dynamic and kinematic viscosities
(ξ, η) = bipolar coordinates
ρ = density
τ = wall shear stress
ϕ = angle, peripheral

Superscript

$\bar{}$ = peripherally averaged

Subscripts

b = bulk
cr = critical
i, o = inner and outer walls
ii = Case A: constant heat flux at the inner wall with the outer insulated
max = maximum
oo = Case B: constant heat flux at the outer wall with the inner insulated

Introduction

Problems involving fluid flow and heat transfer with a moving core of solid body or fluid in an annular geometry can be found in many engineering/industrial processes. In our previous studies, we presented the solutions on the problems of fully developed *turbulent* fluid flow and heat transfer in an annulus with a moving core of solid body or fluid (Shigechi et al., 1990; Lee and Shigechi, 1992), and developed and developing *laminar* fluid flow and heat transfer (Shigechi and Lee, 1991; Shigechi et al., 1993) in a concentric annulus with a moving core.

The eccentricity of the core in an annular geometry may arise from design constraints or as a result of manufacturing inaccuracies, operational malfunctioning, or deformation in service from the normally concentric configuration. The fully developed laminar fluid flow and heat transfer in an eccentric annulus with a *stationary* core have been extensively studied analytically or numerically (Piercy et al., 1933; Heyda, 1959; Redberger and Charles, 1962; Snyder, 1963; Snyder and Goldstein, 1965; Jonsson and Sparrow, 1965; Tiedt, 1966, 1967; Cheng and Hwang, 1968; Trombetta, 1971; Suzuki et al., 1990).

Reported in the present paper are an exact solution for the fluid flow and numerical solutions by a finite difference method for the heat transfer between a fully developed laminar fluid flow and an axially moving core in an *eccentric* annular geometry.

Analysis

The mathematical development of the analysis is rather complex but straightforward. The assumptions used in the analysis are:

[1] Dept. of Mech. Systems Eng., Nagasaki University, Nagasaki, Japan, 852.
[2] Dept. of Mech. Eng., University of Ottawa, Ottawa, Canada, K1N 6N5.

Contributed by the Heat Transfer Division of THE AMERICAN SOCIETY OF MECHANICAL ENGINEERS. Manuscript received by the Heat Transfer Division November 1994; revision received May 1995. Keywords: Environmental Heat Transfer, Materials Processing and Manufacturing Processes, Moving Boundaries. Associate Technical Editor: Y. Bayazitoglu.

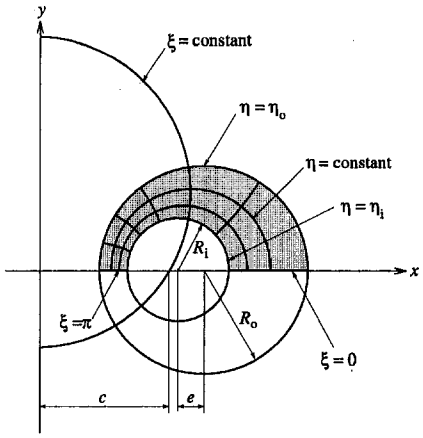

Fig. 1 Bipolar coordinate system, (ξ, η)

1 The flow is incompressible and Newtonian with constant physical properties.
2 The flow is steady and laminar, and fully developed, hydrodynamically and thermally.
3 The inner core tube is moving at a constant velocity.
4 The body forces, viscous dissipation, and axial heat conduction are neglected.

Fluid Flow. The coordinate system most suitable for the geometry of an eccentric annulus is the *bipolar coordinate* system (ξ, η) [see Fig. 1]. The transformation between the Cartesian and bipolar coordinates systems is (Margenau, 1953):

$$x + iy = ic \cot\left(\frac{\xi + i\eta}{2}\right) \tag{1}$$

where c is a constant (see Fig. 1) and $i = \sqrt{-1}$. The curve ξ = const is a circle whose center is the point (0, c cot ξ) and the curve η = const is a circle whose center is the point (c coth η, 0) and the radius is c/sinh η. The inner and outer wall surfaces of the eccentric annulus are represented by the curves of constant η, designated η_i and η_o, respectively.

Basic Equations. The governing momentum equation in the bipolar coordinate system is:

$$\frac{\partial^2 u}{\partial \xi^2} + \frac{\partial^2 u}{\partial \eta^2} = \frac{1}{\mu}\frac{dp}{dz}\frac{c^2}{(\cosh \eta - \cos \xi)^2} \tag{2}$$

The boundary conditions are:

$$u = U \quad \text{at} \quad \eta = \eta_i \quad (0 \le \xi \le \pi)$$
$$u = 0 \quad \text{at} \quad \eta = \eta_o \quad (0 \le \xi \le \pi)$$
$$\frac{\partial u}{\partial \xi} = 0 \quad \text{at} \quad \xi = 0, \pi \quad (\eta_o \le \eta \le \eta_i) \tag{3}$$

Velocity Distribution. The exact solution for Eq. (2) with the boundary conditions, Eq. (3) is:

$$u = \frac{R_o^2}{4\mu}\left(-\frac{dp}{dz}\right) g(\xi, \eta) + \frac{(\eta - \eta_o)}{(\eta_i - \eta_o)} U$$

$$(0 \le \xi \le \pi, \eta_o \le \eta \le \eta_i) \tag{4}$$

where

$$g(\xi, \eta) = 2(1 - \alpha)\,\epsilon\, S \times \left[\frac{(\eta_i - \eta)}{(\eta_i - \eta_o)} - \frac{(\coth \eta - \coth \eta_i)}{(\coth \eta_o - \coth \eta_i)}\frac{\sinh \eta}{(\cosh \eta - \cos \xi)} + 2\sum_{n=1}^{\infty} e^{-n\eta_o}\frac{\sinh n(\eta_i - \eta)}{\sinh (\eta_i - \eta_o)}\cos n\xi\right] \tag{5}$$

The technique used to obtain Eq. (4) is "the method of separation of variables," which was also employed by El-Saden (1961) and Snyder and Goldstein (1965).

From the definition, the average velocity, u_m, is:

$$u_m = \frac{1}{\pi(R_o^2 - R_i^2)}\iint_A u dA = \frac{2S^2}{\pi(1 - \alpha^2)}\int_{\eta_o}^{\eta_i}\int_0^{\pi}\frac{u}{(\cosh \eta - \cos \xi)^2} d\xi d\eta = \frac{R_o^2}{8\mu}\left(-\frac{dp}{dz}\right) M^* + E^* U \tag{6}$$

where

$$M^* = 1 + \alpha^2 - \left[\frac{1 - \alpha}{1 + \alpha}\right] 4\epsilon^2 S^2 \left[\frac{1}{\eta_i - \eta_o} + 2\sum_{n=1}^{\infty}\frac{n e^{-n(\eta_i + \eta_o)}}{\sinh n(\eta_i - \eta_o)}\right] \quad (\text{for } 0 < \alpha < 1) \tag{7}$$

and

$$E^* = \left[\frac{\alpha^2}{\alpha^2 - 1}\right] + \left[\frac{\epsilon S}{1 + \alpha}\right]\frac{1}{(\eta_i - \eta_o)} \quad (\text{for } 0 < \alpha < 1) \tag{8}$$

Friction Factor. From the definition of the local shear stresses at the inner and outer wall surfaces, and the average wall shear, we obtain the friction factor, f, from Eq. (6) as:

$$f = \frac{\bar{\tau}}{\frac{1}{2}\rho u_m^2} = \frac{16}{\text{Re}}\frac{(1 - \alpha)^2}{M^*}(1 - E^* U^*) \tag{9}$$

Heat Transfer. The two fundamental solutions obtained in the study are:

Case A: constant heat flux at the inner wall with the outer insulated, and

Case B: constant heat flux at the outer wall with the inner insulated.

Basic Equations. The governing energy equation in the bipolar coordinate system is:

$$\frac{\partial^2 \theta}{\partial \xi^2} + \frac{\partial^2 \theta}{\partial \eta^2} = \frac{S^2}{(\cosh \eta - \cos \xi)^2}\frac{2F}{(1 + \alpha)(1 - \alpha)^2}\left(\frac{u}{u_m}\right) \tag{10}$$

where $F = \alpha$ for Case A and $F = 1$ for Case B.

Boundary Conditions. At $\xi = 0$ and $\xi = \pi$ for $\eta_o \le \eta \le \eta_i$, from the conditions of symmetry on temperature:

$$\left.\frac{\partial\theta}{\partial\xi}\right|_{0,\pi} = 0 \quad (\eta_o \le \eta \le \eta_i) \tag{11}$$

From the heating conditions at $\eta = \eta_i$ and $\eta = \eta_o$ for $0 \le \xi \le \pi$,

Case A: With $\theta \equiv T/[q_i(R_o - R_i)/k]$ in Eq. (10),

$$\left.\frac{\partial\theta}{\partial\eta}\right|_{\eta_i} = \frac{S}{(\cosh\eta_i - \cos\xi)}\frac{1}{(1-\alpha)}, \quad \left.\frac{\partial\theta}{\partial\eta}\right|_{\eta_o} = 0 \tag{12}$$

Case B: With $\theta \equiv T/[q_o(R_o - R_i)/k]$ in Eq. (10),

$$\left.\frac{\partial\theta}{\partial\eta}\right|_{\eta_i} = 0, \quad \left.\frac{\partial\theta}{\partial\eta}\right|_{\eta_o} = -\frac{S}{(\cosh\eta_o - \cos\xi)}\frac{1}{(1-\alpha)} \tag{13}$$

The dimensionless bulk temperature, θ_b, for both cases A and B, can be expressed as:

$$\theta_b = \frac{2S^2}{\pi(1-\alpha^2)}\int_{\eta_o}^{\eta_i}\int_0^{\pi}\frac{(u/u_m)\theta}{(\cosh\eta - \cos\xi)^2}\,d\xi d\eta \tag{14}$$

Nusselt Number. The local Nusselt numbers, Nu_{ii} and Nu_{oo}, are defined as:

$$\mathrm{Nu}_{jj} \equiv 2/(\theta_{jj} - \theta_{bj}) \tag{15}$$

where $j = i$ for Case A and $j = o$ for Case B, and the local heat transfer coefficients, h_{ii} and h_{oo}, are defined as:

$$h_{jj} \equiv q_j/(T_{jj} - T_{bj}) \tag{16}$$

The peripherally averaged Nusselt numbers on the inner and outer walls, $\overline{\mathrm{Nu}_{ii}}$ and $\overline{\mathrm{Nu}_{oo}}$, are calculated as:

$$\overline{\mathrm{Nu}_{jj}} \equiv 2/(\overline{\theta_{jj}} - \theta_{bj}) \tag{17}$$

where

$$\overline{\theta_{jj}} = \frac{1}{\pi}\int_0^{\pi}\theta_{jj}\,d\phi_j \tag{18}$$

Numerical Calculation. The elliptic partial differential equation, Eq. (10), with Eqs. (11) to (13), is numerically solved by a finite difference method. The Successive Over-Relaxation (SOR) method is used as the iterative procedure (Gerald and Wheatley, 1984). A total of 80×160 grid points was uniformly allocated in the bipolar coordinate plane (ξ, η), which gave an excellent agreement with Trombetta's numerical results for the case with a stationary core, i.e., $U^* = 0$ (Shah and London, 1978) and this confirmed the accuracy of our calculation. The integrations in Eqs. (14) and (18) are carried out by the trapezoidal rule and the accuracy of the numerical calculation was estimated to be in the order of 10^{-3} for the Nusselt number.

The ranges of parameters considered are:
The radius ratio:

$$0 < \alpha < 1$$

The eccentricity:

$$0 \le \epsilon < 1$$

The relative velocity:

$$-\infty \le U^* \le U^*_{cr} = 1/E$$

Results and Discussion

Only a very limited number of cases for fluid flow and heat transfer will be discussed. The further details of the results are given in the reference by Shigechi et al. (1994).

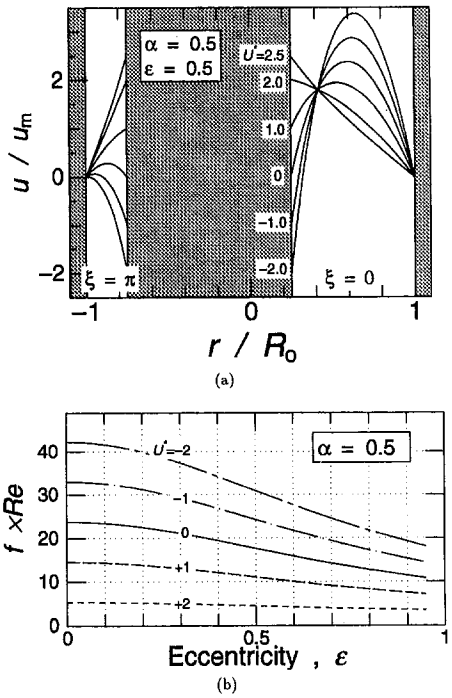

Fig. 2 Velocity profiles and friction factors

Fluid Flow. The predicted velocity profiles at $\xi = 0$ and $\xi = \pi$ (i.e., the planes of symmetry) across an eccentric annular duct with a moving core for the case of $\alpha = 0.5$ and $\epsilon = 0.5$ at the various values of U^* are shown in Fig. 2(*a*). For a concentric annulus, it was noted that for a given value of α, all velocity profiles go through a fixed single point, regardless of the value of U^*. For eccentric annuli, it was noted that the single point seems to appear only for values of $\epsilon < 0.5$ in the narrowest gap ($\xi = \pi$), and to move toward the outer wall with increasing value of ϵ, accompanied by a decrease in the value of u/u_m. For larger values of ϵ (> 0.5), the single point disappears on the outer wall, which implies that the fluid flow is only governed by the shear flow induced by the moving core.

The predicted friction factors for the case of $\alpha = 0.5$ shown in Fig. 2(*b*) illustrate the effects of ϵ and U^* on $f \cdot \mathrm{Re}$. The effect of the eccentricity is that, for all the values of ϵ, the normalized value of $f/f_{\epsilon=0}$ is always less than unity. The effect of U^* is that for $U^* < 0$, the value of $(f \cdot \mathrm{Re})/(f \cdot \mathrm{Re})_{U^*=0}$ at a given value of ϵ is always greater than unity, whereas it is always less than unity for $U^* > 0$. This is similar to those observed for the case of concentric annuli (Shigechi and Lee, 1991). For all values of ϵ, the effect of U^* is greatest at $\alpha = 1$ (i.e., parallel plates flow) and diminishes at $\alpha \to 0$. This is because with decreasing value of α, the role of the shear stress of the moving core surface on the overall pressure drop becomes less important. The study clearly demonstrates that the effect of ϵ is to reduce the friction for all the values of U^* studied. This is because with decreasing value of ϵ, the role of the shear stress of the moving core surface on the overall pressure drop becomes less important.

Heat Transfer. Representative nondimensional temperature profiles in terms of $(\theta - \theta_b)$ at $\xi = 0$ and $\xi = \pi$ in an eccentric annulus ($\alpha = 0.5$ and $\epsilon = 0.5$) with the moving core for Cases A and B are shown in Fig. 3(*a*). Shown also in the figure are the numerical values of the difference between the peripherally averaged wall temperature, $\overline{\theta}_j$, on the inner or outer wall and θ_b, defined by Eqs. (18) and (14), respectively, and the difference between the maximum wall temperature, $\theta_{j,\max}$ on the inner or outer wall and θ_b. The constant heat flux boundary conditions preclude the absolute temperature, and the Nusselt

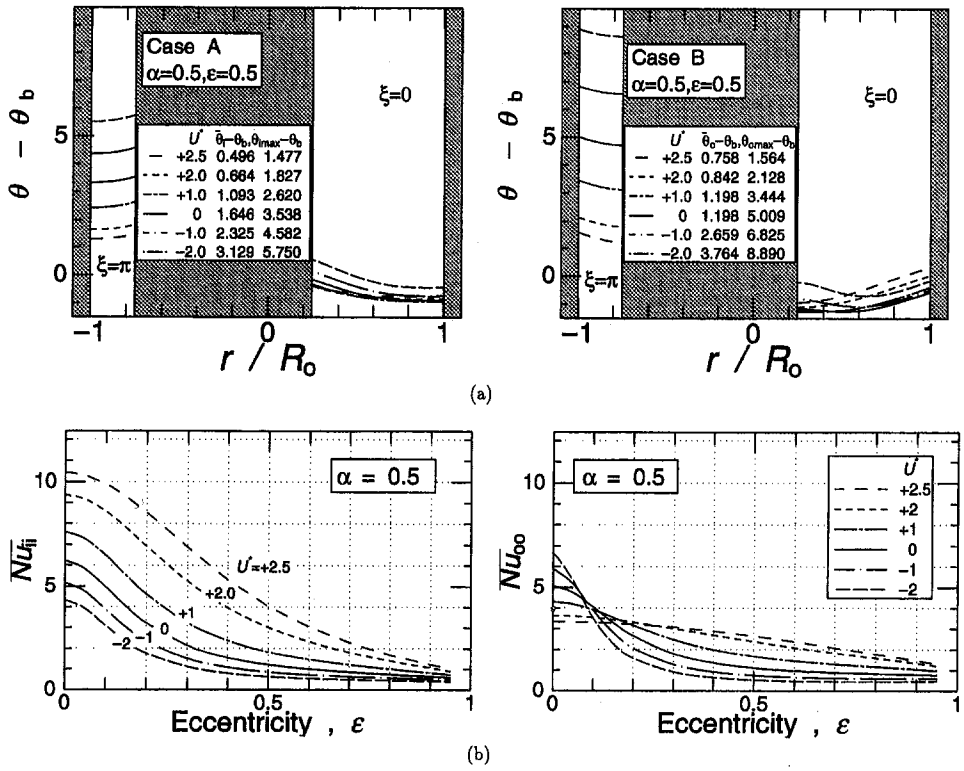

Fig. 3 Temperature profiles and Nusselt numbers

numbers are defined by Eq. (17) with "temperature difference" based on the dimensionless bulk temperature, Eq. (14). Therefore, the absolute temperature itself is not required in the numerical calculations.

The maximum wall temperatures, $(\theta_i - \theta_b)$, and $(\theta_o - \theta_b)$, appear at the narrowest gaps, i.e., the point $(\xi = \pi, \eta = \eta_i)$ for Case A, and at the point $(\xi = \pi, \eta = \eta_o)$ for Case B, respectively, which was expected. It was seen that with an increase in ϵ, for $U^* < 0$, the minimum value of the fluid temperature increases at the narrowest gap $(\xi = \pi)$, and the peripheral nonuniformity of the wall temperature is increased for both Cases A and B, and for $U^* < 0$, the minimum value of $(\theta - \theta_b)$ exits in the widest gap $(\xi = 0)$ for Case B.

The effects of ϵ and U^* (-2 to $+2.5$) on the peripherally averaged Nusselt numbers, $\overline{\mathrm{Nu}}_{jj}$, for both Cases A and B are shown in Fig. 3(*b*), for the case of $\alpha = 0.5$ as an example. It was seen for $0 < \alpha < 1.0$ that an increase ϵ is to decrease $\overline{\mathrm{Nu}}_{jj}$ for both Cases A and B, and that the effect becomes more significant as ϵ approaches 0, for the larger values of α. While an increase in U^* is to increase $\overline{\mathrm{Nu}}_{ii}$ for Case A, for Case B, this is only true for limited values of ϵ, and as ϵ approaches 0 (concentric annuli), $\overline{\mathrm{Nu}}_{oo}$ decreases with increasing U^*. It was also noted that the ratio of the average Nusselt number of an eccentric annulus to that of an concentric annulus, $\overline{\mathrm{Nu}}_{jj}/\overline{\mathrm{Nu}}_{jj(\epsilon=0)}$, decreases with increasing ϵ, and that ϵ has relatively higher effect on $\overline{\mathrm{Nu}}_{jj}/\overline{\mathrm{Nu}}_{jj(\epsilon=0)}$ for the eccentric annuli with large values of α. It was also seen that for both Cases A and B, U^* affects $\overline{\mathrm{Nu}}_{jj}/\overline{\mathrm{Nu}}_{jj(\epsilon=0)}$ more than for the case of an annulus with stationary core ($U^* = 0$) for $U^* > 0$, and always less for $U^* < 0$.

Concluding Remarks

The study showed that for equal conditions:

1 The peripheral nonuniformities of fluid velocity, wall shear stress, and temperature distribution are significantly increased with increasing eccentricity; and

2 For both Cases A and B, the ratios $f/f_{\epsilon=0}$ and $\overline{\mathrm{Nu}}_{jj}/\overline{\mathrm{Nu}}_{jj(\epsilon=0)}$ are always greater than those for the case of the annulus with a stationary core ($U^* = 0$) for $U^* > 0$ and always less for $U^* < 0$.

References

Cheng, K. C., and Hwang, G. J., 1968, "Laminar Forced Convection in Eccentric Annuli," *AIChE J.*, Vol. 14, pp. 510–512.

El-Saden, M. R., 1961, "Heat Conduction in an Eccentrically Hollow, Infinitely Long Cylinder With Internal Heat Generation," ASME JOURNAL OF HEAT TRANSFER, Vol. 83, pp. 510–512.

Gerald, C. F., and Wheatley, P. O., 1984, *Applied Numerical Analysis,* 3rd ed., Addison-Wesley Pub. Co.

Heyda, J. F., 1959, "A Green's Function Solution for the Case of Laminar Incompressible Flow Between Non-concentric Circular Cylinders," *J. Franklin Inst.*, Vol. 267, pp. 25–34.

Jonsson, V. K., and Sparrow, E. M., 1965, "Results of Laminar Flow Analysis and Turbulent Flow Experiments for Eccentric Annular Ducts," *AIChE J.*, Vol. 11, pp. 1143–1145.

Lee, Y., and Shigechi, T., 1992, "Heat Transfer in Concentric Annuli With Moving Cores—Fully Developed Turbulent Flow With Arbitrarily Prescribed Heat Flux," *Int. J. Heat Mass Transfer,* Vol. 35, pp. 3488–3493.

Margenau, H., 1953, *The Mathematics for Physics and Chemistry,* van Nostrand, New York.

Piercy, N. A. V., Hooper, M. S., and Winny, H. F., 1933, "Viscous Flow Through Pipes With Cores," *Phil. Mag.*, Ser. 7, Vol. 15, pp. 647–676.

Press, W. H., Flannery, B. P., Teukolsky, S. A., and Vetterling, W. T., 1989, *Numerical Recipes,* Cambridge Univ. Press, Cambridge, United Kingdom, pp. 652–659.

Redberger, P. J., and Charles, M. E., 1962, "Axial Laminar Flow in a Circular Pipe Containing a Fixed Eccentric Core," *Can. J. Chem. Eng.*, Vol. 40, pp. 148–151.

Shah, R. K., and London, A. L., 1978, "Laminar Flow Forced Convection in Ducts," *Advances in Heat Transfer,* Supplement 1, Academic Press, New York, pp. 322–340.

Shigechi, T., Kawae, N., and Lee, Y., 1990, "Turbulent Fluid Flow and Heat Transfer in Concentric Annuli With Moving Cores," *Int. J. Heat Mass Transfer,* Vol. 33, pp. 2029–2037.

Shigechi, T., and Lee, Y., 1991, "An Analysis on Fully Developed Laminar Fluid Flow and Heat Transfer in Concentric Annuli With Moving Cores," *Int. J. Heat Mass Transfer,* Vol. 34, pp. 2593–2601.

Shigechi, T., Araki, K., and Lee, Y., 1993, "Laminar Heat Transfer in the Thermal Entrance Regions of Concentric Annuli With Moving Heated Cores," ASME JOURNAL OF HEAT TRANSFER, Vol. 115, pp. 1061–1064.

Shigechi, T., Momoki, S., and Lee, Y., 1994, "Fully Developed Laminar Flow and Heat Transfer in Eccentric Annuli With Axially Moving Cores," *Fundamentals of Heat Transfer in Forced Convection,* ASME HTD-Vol. 285, pp. 75–84.

Snyder, W. T., 1963, "An Analysis of Slug Flow Heat Transfer in an Eccentric Annulus," *AIChE J.,* Vol. 9, pp. 503–506.

Snyder, W. T., and Goldstein, G. A., 1965, "An Analysis of Fully Developed Laminar Flow in an Eccentric Annulus," *AIChE J.,* Vol. 11, pp. 462–466.

Suzuki, K., Szmyd, J. S., and Ohtsuka, H., 1990, "Laminar Forced Convection Heat Transfer in Eccentric Annuli" [in Japanese], *Trans. JSME(B),* Vol. 56, pp. 3445–3450.

Tiedt, W., 1966, 1967, "Berechnung des laminaren und turbulenten Reibungswiderstandes konzentrischer und exzentrischer Rignspalte," *Chemiker-Ztg./Chem. Apparatur,* Vol. 90, pp. 813–821; Vol. 91, pp. 17–25.

Trombetta, M. L., 1971, "Laminar Forced Convection in Eccentric Annuli," *Int. J. Heat Mass Transfer,* Vol. 14, pp. 1161–1173.

Heat Transfer Enhancement by Longitudinal Vortices in a Fin-Tube Heat Exchanger Element With Flat Tubes

A. Valencia,[1] M. Fiebig,[2] and N. K. Mitra[2]

Introduction

In a fin-tube heat exchanger, fins enlarge the heat transfer area and thereby reduce the gas side (i.e., fin side) thermal resistance. The structure of the gas flow is complex. It consists of horseshoe vortices in the stagnation area and flow separation in the wake of the tubes. The horseshoe vortices introduce additional mixing of the fluid and thus increase strongly the fin heat transfer in the stagnation area. The two prongs of the horseshoe are longitudinal vortices, which induce transverse velocity components in the flow. The traces of these vortices on the fin should show some increase in heat transfer. The fin heat transfer in the tube wake is low.

The strength and hence the beneficial effects of the horseshoe vortex increase with the width of the bluff body. However, the size of the wake with poor heat transfer and the pressure loss also increase.

One can reduce the wake size by using, instead of round tubes, flat or elliptical tubes with their major axes parallel to the main flow direction. The heat transfer deterioration in the wake will be smaller for a flat tube of the same cross section as for a round tube. The heat transfer enhancement due to the horseshoe vortex in the stagnation area will also be smaller. However, the real gain will appear in the smaller pressure loss due to the smaller wake for the flat tube than for the round tube.

The potential for reduction of the gas side thermal resistance by increasing the fin area is limited by increasing cost and diminishing fin efficiency. For further reduction of the thermal resistance, the heat transfer coefficients need to be augmented. This can be achieved by longitudinal vortices, which can be generated by wing-type vortex generators; see Tiggelbeck et al. (1994). These vortices enhance mixing of fluids close to and far from the fin and thereby increase heat transfer.

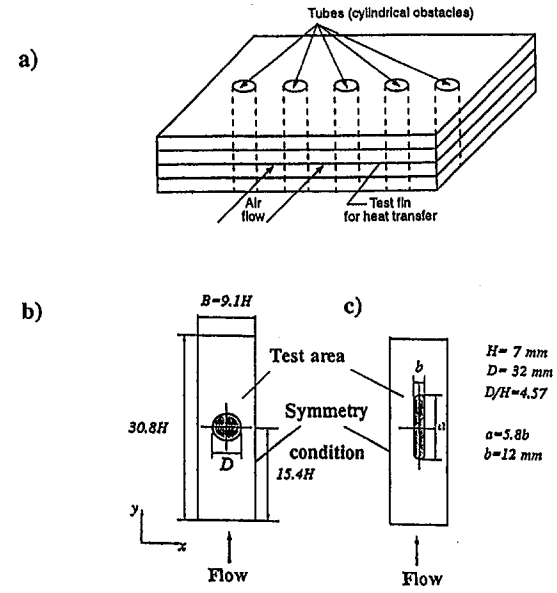

Fig. 1 Schematics of fin-tube heat exchanger with round and flat tubes

It is shown in experimental investigations by Fiebig et al. (1991) and Tiggelbeck et al. (1994) and predicted in numerical simulations by Fiebig et al. (1989) that longitudinal vortices can increase the heat transfer by several hundred percent locally and by more than 60 percent globally for flows in channels without tubes.

Fiebig et al. (1990) investigated the influence of longitudinal vortex generators (delta winglet pair) on heat transfer and drag of a fin-tube element with a round tube and found that both the location of the delta winglet pair and the angle of attack have strong influences on heat transfer. The optimum location is in the tube wake and the best angle of attack is 45 deg. The present work extends the previous investigations to flat tubes. We consider an element of a heat exchanger with one row of flat tubes (as in an automobile radiator) and investigate exemplarily the influence of delta winglets on heat transfer. Following the previous investigations, the angle of attack is kept at 45 deg (optimum for circular tubes) and only the positions of the winglets have been varied. For a proper understanding of the influence of vortices on local convective heat transfer, coefficients must be known. They have been measured by transient liquid crystal thermography. As a reference geometry, heat transfer on a fin of a round tube-fin element was also measured.

The present investigation is a preliminary study with the objective of finding a suitable location for vortex generators for a fin-tube element with a flat tube. The experience gained from this study has already been applied to the more complex geometry of a fin-tube matrix consisting of rows of 5 × 3 flat and round tubes; see Fiebig et al. (1994).

Experimental Methods and Facilities

The experimental investigations have been carried out in a small wind tunnel; see Tiggelbeck et al. (1994). The fin-tube models consist of five parallel plates representing the fins and one row of five tubes (or cylindrical obstacles) facing the flow; see Fig. 1(*a*). Flow between the fins is in a rectangular channel around cylindrical obstacles. The local convective heat transfer coefficient, h, has been deduced from transient liquid crystal thermography (LCT) on the midportion of the central fin; see Figs. 1(*b*) and 1(*c*) for the planview of the test areas with round and flat tubes. The cross-sectional areas of the tubes are identical. The width of the flat tube is 62.5 percent of the round tube. Other tubes in the row guarantee symmetry on sides. In

[1] Engineer, Universidad de Chile.

[2] Professor, Institut für Thermo- und Fluiddynamik, Ruhr-Universität Bochum, 44780 Bochum, Federal Republic of Germany; Mem ASME.

Contributed by the Heat Transfer Division of THE AMERICAN SOCIETY OF MECHANICAL ENGINEERS. Manuscript received by the Heat Transfer Division February 1994; revision received April 1995. Keywords: Finned Surfaces, Forced Convection, Heat Exchangers. Associate Technical Editor: T. W. Simon.

Shigechi, T., Momoki, S., and Lee, Y., 1994, "Fully Developed Laminar Flow and Heat Transfer in Eccentric Annuli With Axially Moving Cores," *Fundamentals of Heat Transfer in Forced Convection,* ASME HTD-Vol. 285, pp. 75–84.

Snyder, W. T., 1963, "An Analysis of Slug Flow Heat Transfer in an Eccentric Annulus," *AIChE J.,* Vol. 9, pp. 503–506.

Snyder, W. T., and Goldstein, G. A., 1965, "An Analysis of Fully Developed Laminar Flow in an Eccentric Annulus," *AIChE J.,* Vol. 11, pp. 462–466.

Suzuki, K., Szmyd, J. S., and Ohtsuka, H., 1990, "Laminar Forced Convection Heat Transfer in Eccentric Annuli" [in Japanese], *Trans. JSME(B),* Vol. 56, pp. 3445–3450.

Tiedt, W., 1966, 1967, "Berechnung des laminaren und turbulenten Reibungswiderstandes konzentrischer und exzentrischer Rignspalte," *Chemiker-Ztg./Chem. Apparatur,* Vol. 90, pp. 813–821; Vol. 91, pp. 17–25.

Trombetta, M. L., 1971, "Laminar Forced Convection in Eccentric Annuli," *Int. J. Heat Mass Transfer,* Vol. 14, pp. 1161–1173.

Heat Transfer Enhancement by Longitudinal Vortices in a Fin-Tube Heat Exchanger Element With Flat Tubes

A. Valencia,[1] M. Fiebig,[2] and N. K. Mitra[2]

Introduction

In a fin-tube heat exchanger, fins enlarge the heat transfer area and thereby reduce the gas side (i.e., fin side) thermal resistance. The structure of the gas flow is complex. It consists of horseshoe vortices in the stagnation area and flow separation in the wake of the tubes. The horseshoe vortices introduce additional mixing of the fluid and thus increase strongly the fin heat transfer in the stagnation area. The two prongs of the horseshoe are longitudinal vortices, which induce transverse velocity components in the flow. The traces of these vortices on the fin should show some increase in heat transfer. The fin heat transfer in the tube wake is low.

The strength and hence the beneficial effects of the horseshoe vortex increase with the width of the bluff body. However, the size of the wake with poor heat transfer and the pressure loss also increase.

One can reduce the wake size by using, instead of round tubes, flat or elliptical tubes with their major axes parallel to the main flow direction. The heat transfer deterioration in the wake will be smaller for a flat tube of the same cross section as for a round tube. The heat transfer enhancement due to the horseshoe vortex in the stagnation area will also be smaller. However, the real gain will appear in the smaller pressure loss due to the smaller wake for the flat tube than for the round tube.

The potential for reduction of the gas side thermal resistance by increasing the fin area is limited by increasing cost and diminishing fin efficiency. For further reduction of the thermal resistance, the heat transfer coefficients need to be augmented. This can be achieved by longitudinal vortices, which can be generated by wing-type vortex generators; see Tiggelbeck et al. (1994). These vortices enhance mixing of fluids close to and far from the fin and thereby increase heat transfer.

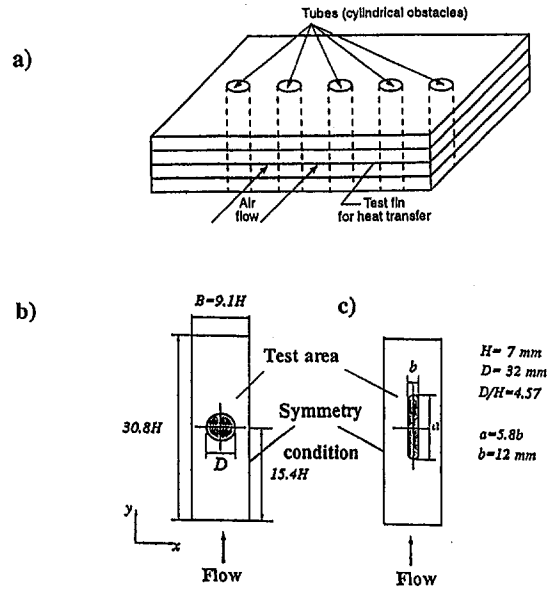

Fig. 1 Schematics of fin-tube heat exchanger with round and flat tubes

It is shown in experimental investigations by Fiebig et al. (1991) and Tiggelbeck et al. (1994) and predicted in numerical simulations by Fiebig et al. (1989) that longitudinal vortices can increase the heat transfer by several hundred percent locally and by more than 60 percent globally for flows in channels without tubes.

Fiebig et al. (1990) investigated the influence of longitudinal vortex generators (delta winglet pair) on heat transfer and drag of a fin-tube element with a round tube and found that both the location of the delta winglet pair and the angle of attack have strong influences on heat transfer. The optimum location is in the tube wake and the best angle of attack is 45 deg. The present work extends the previous investigations to flat tubes. We consider an element of a heat exchanger with one row of flat tubes (as in an automobile radiator) and investigate exemplarily the influence of delta winglets on heat transfer. Following the previous investigations, the angle of attack is kept at 45 deg (optimum for circular tubes) and only the positions of the winglets have been varied. For a proper understanding of the influence of vortices on local convective heat transfer, coefficients must be known. They have been measured by transient liquid crystal thermography. As a reference geometry, heat transfer on a fin of a round tube-fin element was also measured.

The present investigation is a preliminary study with the objective of finding a suitable location for vortex generators for a fin-tube element with a flat tube. The experience gained from this study has already been applied to the more complex geometry of a fin-tube matrix consisting of rows of 5 × 3 flat and round tubes; see Fiebig et al. (1994).

Experimental Methods and Facilities

The experimental investigations have been carried out in a small wind tunnel; see Tiggelbeck et al. (1994). The fin-tube models consist of five parallel plates representing the fins and one row of five tubes (or cylindrical obstacles) facing the flow; see Fig. 1(*a*). Flow between the fins is in a rectangular channel around cylindrical obstacles. The local convective heat transfer coefficient, h, has been deduced from transient liquid crystal thermography (LCT) on the midportion of the central fin; see Figs. 1(*b*) and 1(*c*) for the planview of the test areas with round and flat tubes. The cross-sectional areas of the tubes are identical. The width of the flat tube is 62.5 percent of the round tube. Other tubes in the row guarantee symmetry on sides. In

[1] Engineer, Universidad de Chile.

[2] Professor, Institut für Thermo- und Fluiddynamik, Ruhr-Universität Bochum, 44780 Bochum, Federal Republic of Germany; Mem ASME.

Contributed by the Heat Transfer Division of THE AMERICAN SOCIETY OF MECHANICAL ENGINEERS. Manuscript received by the Heat Transfer Division February 1994; revision received April 1995. Keywords: Finned Surfaces, Forced Convection, Heat Exchangers. Associate Technical Editor: T. W. Simon.

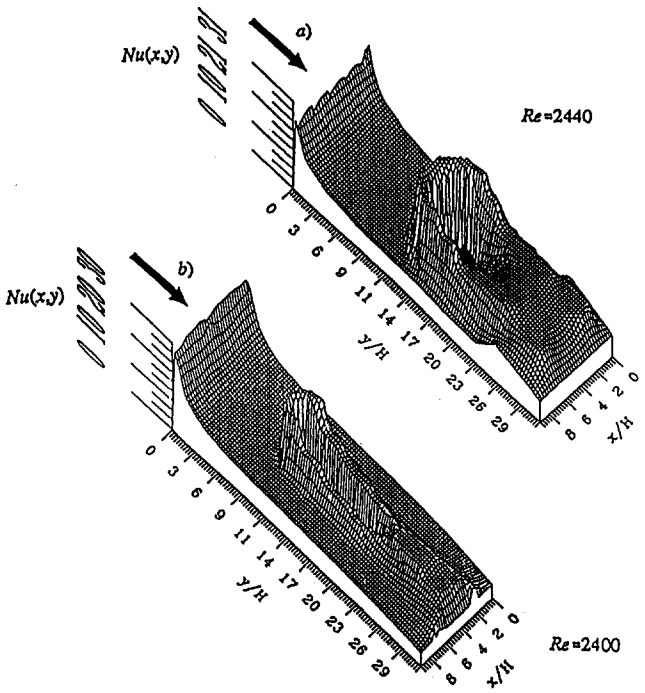

Fig. 2 Local Nusselt number contours on the test area: (*a*) round tube, (*b*) flat tube

LCT the test model covered with a thin layer of thermochromic liquid crystal is suddenly inserted into the wind tunnel test section with an established steady flow of heated air at a temperature T_a = 42°C. The transient heating of the model from room temperature T_{f0} = 22°C produces a color change of LCT. The illumination of the model with an argon–neon laser (514 nm) shows only green lines, corresponding to the T_f = 30.8°C isotherm. Temporal development (photos) of this isotherm and the heating time are used to deduce the local heat transfer coefficient, h, from the energy balance on the fin element by using the following formula:

$$h = \frac{\rho c_v \delta}{2t} \ln\left[\frac{T_a - T_{f0}}{T_a - T_f}\right] \quad (1)$$

where ρ, c_v, and δ are density, specific heat, and thickness of the fin and t is the time for an elemental area of the fin to heat from T_{f0} to T_f.

From the measured heat transfer coefficient, the local Nusselt number is defined as Nu = hH/k where H is the fin spacing and k is the heat conductivity of air. The accuracy of the temperature measurement (tested by thermocouple) is ±0.2°C. This gives a root sum square accuracy (see Moffat, 1987) of 5.8 percent for Nu.

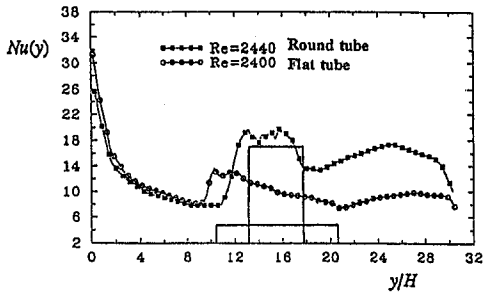

Fig. 3 Cross average fin Nusselt number Nu(*y*) for round and flat tubes

Table 1 Average Nusselt numbers on the plate, Nu, and the apparent friction factors, *f*, for round and flat tubes

Geometry	Re	f	Nu
Round tube	2440	0.0300	14.0
Flat tube	2440	0.0157	10.6

Static pressure difference Δp across the model is measured by a pressure gage (MKS Baratron). In the range of velocity of this investigation (7 m/s), Δp is of the order of 1 torr. The accuracy, as claimed by the manufacturer, is better than 1 percent. From Δp we computed the apparent friction factor $f = \Delta pH/\rho U^2 L$, where U is the average velocity, L is the model length, and ρ is the density. Pressure variation across the cross section has been neglected. U has been measured by a normed orifice meter. The accuracy tested by hot-wire measurement of axial mean velocity is better than 5 percent. The flow Reynolds number, Re, is UH/ν, where ν is the dynamic viscosity of air. Tiggelbeck et al. (1994) or Fiebig et al. (1994) can be consulted for the details of wind tunnel and experimental technique.

Results and Discussion

Heat Exchanger Element With One Tube. Figure 2 shows the local Nusselt numbers Nu (x, y) on the test fin for Reynolds number Re = 2440. Nu is large at the leading edge and decreases in the flow direction, as is typical of the entry flow in a channel. In front of the tube, Nu jumps up again due to the horseshoe vortex, which is stronger for round than for flat tubes. The area influenced by the horseshoe vortex is larger for the round tube than for the flat tube. The peak in front of the round tube is nearly 20 percent higher than the peak in front of the flat tube. On the sides one notices the two prongs of the horseshoe vortex which develop as longitudinal vortices. The decrease of Nu in the wake is also noticeable. This decrease is larger for the round tube than for the flat tube.

Figure 3 compares the spanwise-averaged Nusselt number, Nu (y), for the round and flat tubes on the test plate. The Nu (y) distributions are practically identical up to a length of y/H = 8.5 for both round and flat tubes. The peak in the stagnation area is 12 for the flat tube and 22 for the round tube. Even the drop in Nu (y) in the wake is not so severe for the round tube; Nu (y) is 14 compared to 8 for the flat tube. The results of Nu in the wake of Figs. 2 and 3 are not conflicting. The sharp drop of the local Nu (x, y) directly behind the local round tube is more than compensated by the local increase in the Nu (x, y) on the trace of the prongs of the horseshoe vortex which has developed into longitudinal vortices. Similar vortices for the flat tube are weak.

Table 1 compares the average Nusselt numbers and the apparent friction factors. The round tube gives nearly a 40 percent larger Nusselt number for a 100 percent larger friction factor, compared to the flat tube.

Heat Exchanger Element With a Flat Tube and a Pair of Winglets. For heat transfer augmentation by mounting longitudinal vortex generators (delta winglet pair), the important

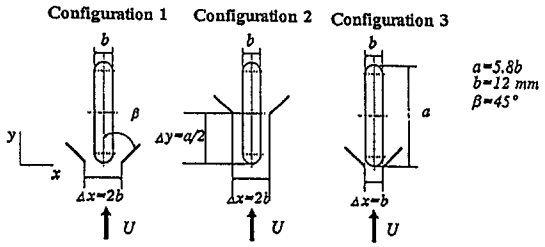

Fig. 4 Location of delta winglets

Table 2 Average Nusselt number, Nu, and the apparent friction factor for the flat tube with three arrangements of vortex generators

Configuration	Re	f	Nu
I: Δx=2b,Δy=0	2380	0.0214	15.7
II: Δx=2b,Δy=a/2	2360	0.0201	15.6
III: Δx=b,Δy=0	2360	0.0216	13.5

parameter is the location for the vortex generators. For the round tube, the vortex generators should be placed in the wake; see Fiebig et al. (1990).

For a flat tube, the wake is small. Neither the reduction of Nu in the wake nor the increase in Nu in the stagnation area are dramatic. So the vortex generators should be used either to strengthen the horseshoe vortices or to increase heat transfer on the fin near the rear part of the tube. In this work three exemplary geometric configurations have been chosen; see Fig. 4. In configuration I the VGs block the fluid in order to generate stronger horseshoe vortices. Furthermore, the VGs themselves generate longitudinal vortices, which should run parallel to the horseshoe vortices. It should be noted that the choice of $\Delta x = 2b$ is arbitrary. In configuration II the vortex generators influence only the fin near the rear part of the tube. Configuration III tries to strengthen the horseshoe vortices directly.

Figure 5 compares the spanwise-averaged Nusselt number Nu (y) on the plate for the three configurations and the case without VGs. Except for the shift in the peaks, configurations I and II give similar results. Configuration III gives the worst result.

Table 2 compares the global results of average Nu on the plate and the apparent friction factor f. With regard to the heat transfer, configurations I and II give identical average Nu, which is nearly 50 percent larger than for the case without vortex generator. The friction factor for the configuration II is nearly 6 percent less than that of configuration I. Configuration III gives the largest friction factor with the smallest Nusselt number. The friction factor increases by roughly 36 percent.

For round tubes with vortex generators, Fiebig et al. (1990) reported that for the optimum location of vortex generators in the wake ($\Delta x = 0.6\ D$, $\Delta y = 0.8\ D$, where D is tube diameter) the enhancement in average Nu is nearly 15 percent at Re = 2400. This gives practically the same Nu for both round and flat tubes, with vortex generators. The pressure loss was not measured by Fiebig et al. (1990). Even if we assume that the pressure loss does not increase with vortex generators for round tubes, the pressure loss for a flat tube with vortex generators will be still nearly 50 percent less than for a round tube.

Conclusion

A fin-tube element with a flat tube gives smaller Nu and friction factor than the element with a round tube. Longitudinal vortices generated by a pair of mounted delta winglets can substantially improve the performance of the element with a flat tube. However, the performance depends on the vortex generator location. Of the three locations tested here, the best location can increase heat transfer by 50 percent and pressure loss by 36 percent. With vortex generators, flat tubes can give a superior performance to the round tubes with or without vortex generators, since heat transfer in both cases are the same but the pressure loss is much less for flat tubes. The results presented here are only for one Reynolds number; however, their qualitative character is expected to persist at other Re.

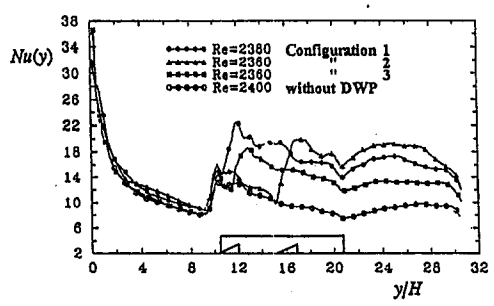

Fig. 5 Influence of delta winglet position on the span-average Nusselt number Nu(y) for flat tube

Acknowledgments

This work has been supported by the Deutsche Forschungsgemeinschaft.

References

Fiebig, M., Brockmeier, U., Mitra, N. K., and Güntermann, T., 1989, "Structure of Velocity and Temperature Fields in Laminar Channel Flows With Longitudinal Vortex Generators," *Numerical Heat Transfer*, Part A, Vol. 15, pp. 281–302.

Fiebig, M., Mitra, N. K., and Dong, Y., 1990, "Simultaneous Heat Transfer Enhancement and Flow Loss Reduction on Fin-Tubes," *Proc. 9 Int. Heat Transfer Conf.*, Jerusalem, Hemisphere, Vol. 4, pp. 51–56.

Fiebig, M., Kallweit, P., Mitra, N. K., and Tiggelbeck, S., 1991, "Heat Transfer Enhancement and Drag by Longitudinal Vortex Generators in Channel Flows," *Experimental Thermal and Fluid Science*, Vol. 4, pp. 103–114.

Fiebig, M., Valencia, A., and Mitra, N. K., 1994, "Local Heat Transfer and Flow Losses in Fin-and-Tube Heat Exchangers With Vortex Generators: A Comparison of Round and Flat Tubes," *Experimental Thermal and Fluid Science*, Vol. 8, pp. 35–45.

Moffat, R. J., 1988, "Describing the Uncertainties in Experimental Results," *EFT Science*, Vol. 1, pp. 3–17.

Tiggelbeck, St., Mitra, N. K., and Fiebig, M., 1994, "Comparison of Wing-Type Vortex Generators for Heat Transfer Enhancement in Channel Flows," ASME JOURNAL OF HEAT TRANSFER, Vol. 116, No. 4, pp. 880–885.

Heat (Mass) Transfer in a Serpentine Channel With Right-Angled Turns

J. M. Choi,[1] N. K. Anand,[1] S. C. Lau,[1] and R. T. Kukreja[1]

Introduction

Heat transfer in a two-dimensional serpentine channel is studied experimentally via the naphthalene sublimation technique and the heat/mass transfer analogy. The test section is a wide channel with staggered rectangular blockages that are affixed to the two principal walls, forcing the flow through the channel to make consecutive abrupt right-angled turns. The distribution of the local transfer coefficient, the variation of the regionally averaged transfer coefficient, and the distribution of the static pressure in the test channel are determined to examine the development of the flow near the entrance of the channel and to determine whether a periodically developed condition may be attained downstream of an entrance length. The detailed distribution of the local transfer coefficient is also used to identify flow impingement, separation, and reattachment as the flow negotiates the right-angled turns. Correlations are obtained to

[1] Dept. of Mech. Engr., Texas A&M University, College Station, TX 77843-3123.

Contributed by the Heat Transfer Division of THE AMERICAN SOCIETY OF MECHANICAL ENGINEERS. Manuscript received by the Heat Transfer Division January 1995; revision received July 1995. Keywords: Augmentation and Enhancement, Electronic Equipment, Forced Convection. Associate Technical Editor: T. W. Simon.

Table 2 Average Nusselt number, Nu, and the apparent friction factor for the flat tube with three arrangements of vortex generators

Configuration	Re	f	Nu
I: Δx=2b,Δy=0	2380	0.0214	15.7
II: Δx=2b,Δy=a/2	2360	0.0201	15.6
III: Δx=b,Δy=0	2360	0.0216	13.5

parameter is the location for the vortex generators. For the round tube, the vortex generators should be placed in the wake; see Fiebig et al. (1990).

For a flat tube, the wake is small. Neither the reduction of Nu in the wake nor the increase in Nu in the stagnation area are dramatic. So the vortex generators should be used either to strengthen the horseshoe vortices or to increase heat transfer on the fin near the rear part of the tube. In this work three exemplary geometric configurations have been chosen; see Fig. 4. In configuration I the VGs block the fluid in order to generate stronger horseshoe vortices. Furthermore, the VGs themselves generate longitudinal vortices, which should run parallel to the horseshoe vortices. It should be noted that the choice of $\Delta x = 2b$ is arbitrary. In configuration II the vortex generators influence only the fin near the rear part of the tube. Configuration III tries to strengthen the horseshoe vortices directly.

Figure 5 compares the spanwise-averaged Nusselt number Nu (y) on the plate for the three configurations and the case without VGs. Except for the shift in the peaks, configurations I and II give similar results. Configuration III gives the worst result.

Table 2 compares the global results of average Nu on the plate and the apparent friction factor f. With regard to the heat transfer, configurations I and II give identical average Nu, which is nearly 50 percent larger than for the case without vortex generator. The friction factor for the configuration II is nearly 6 percent less than that of configuration I. Configuration III gives the largest friction factor with the smallest Nusselt number. The friction factor increases by roughly 36 percent.

For round tubes with vortex generators, Fiebig et al. (1990) reported that for the optimum location of vortex generators in the wake ($\Delta x = 0.6\ D$, $\Delta y = 0.8\ D$, where D is tube diameter) the enhancement in average Nu is nearly 15 percent at Re = 2400. This gives practically the same Nu for both round and flat tubes, with vortex generators. The pressure loss was not measured by Fiebig et al. (1990). Even if we assume that the pressure loss does not increase with vortex generators for round tubes, the pressure loss for a flat tube with vortex generators will be still nearly 50 percent less than for a round tube.

Conclusion

A fin-tube element with a flat tube gives smaller Nu and friction factor than the element with a round tube. Longitudinal vortices generated by a pair of mounted delta winglets can substantially improve the performance of the element with a flat tube. However, the performance depends on the vortex generator location. Of the three locations tested here, the best location can increase heat transfer by 50 percent and pressure loss by 36 percent. With vortex generators, flat tubes can give a superior performance to the round tubes with or without vortex generators, since heat transfer in both cases are the same but the pressure loss is much less for flat tubes. The results presented here are only for one Reynolds number; however, their qualitative character is expected to persist at other Re.

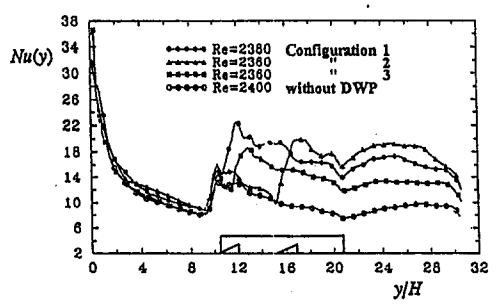

Fig. 5 Influence of delta winglet position on the span-average Nusselt number Nu(y) for flat tube

Acknowledgments

This work has been supported by the Deutsche Forschungsgemeinschaft.

References

Fiebig, M., Brockmeier, U., Mitra, N. K., and Güntermann, T., 1989, "Structure of Velocity and Temperature Fields in Laminar Channel Flows With Longitudinal Vortex Generators," *Numerical Heat Transfer*, Part A, Vol. 15, pp. 281–302.

Fiebig, M., Mitra, N. K., and Dong, Y., 1990, "Simultaneous Heat Transfer Enhancement and Flow Loss Reduction on Fin-Tubes," *Proc. 9 Int. Heat Transfer Conf.*, Jerusalem, Hemisphere, Vol. 4, pp. 51–56.

Fiebig, M., Kallweit, P., Mitra, N. K., and Tiggelbeck, S., 1991, "Heat Transfer Enhancement and Drag by Longitudinal Vortex Generators in Channel Flows," *Experimental Thermal and Fluid Science*, Vol. 4, pp. 103–114.

Fiebig, M., Valencia, A., and Mitra, N. K., 1994, "Local Heat Transfer and Flow Losses in Fin-and-Tube Heat Exchangers With Vortex Generators: A Comparison of Round and Flat Tubes," *Experimental Thermal and Fluid Science*, Vol. 8, pp. 35–45.

Moffat, R. J., 1988, "Describing the Uncertainties in Experimental Results," *EFT Science*, Vol. 1, pp. 3–17.

Tiggelbeck, St., Mitra, N. K., and Fiebig, M., 1994, "Comparison of Wing-Type Vortex Generators for Heat Transfer Enhancement in Channel Flows," ASME JOURNAL OF HEAT TRANSFER, Vol. 116, No. 4, pp. 880–885.

Heat (Mass) Transfer in a Serpentine Channel With Right-Angled Turns

J. M. Choi,[1] N. K. Anand,[1] S. C. Lau,[1] and R. T. Kukreja[1]

Introduction

Heat transfer in a two-dimensional serpentine channel is studied experimentally via the naphthalene sublimation technique and the heat/mass transfer analogy. The test section is a wide channel with staggered rectangular blockages that are affixed to the two principal walls, forcing the flow through the channel to make consecutive abrupt right-angled turns. The distribution of the local transfer coefficient, the variation of the regionally averaged transfer coefficient, and the distribution of the static pressure in the test channel are determined to examine the development of the flow near the entrance of the channel and to determine whether a periodically developed condition may be attained downstream of an entrance length. The detailed distribution of the local transfer coefficient is also used to identify flow impingement, separation, and reattachment as the flow negotiates the right-angled turns. Correlations are obtained to

[1] Dept. of Mech. Engr., Texas A&M University, College Station, TX 77843-3123.

Contributed by the Heat Transfer Division of THE AMERICAN SOCIETY OF MECHANICAL ENGINEERS. Manuscript received by the Heat Transfer Division January 1995; revision received July 1995. Keywords: Augmentation and Enhancement, Electronic Equipment, Forced Convection. Associate Technical Editor: T. W. Simon.

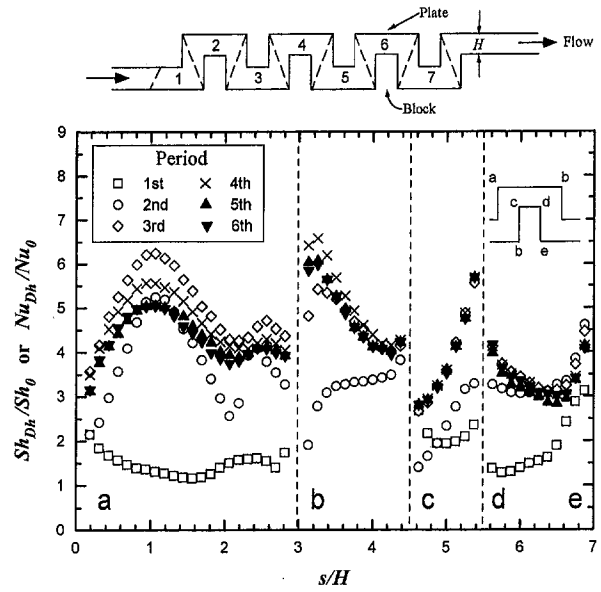

Fig. 1 Local normalized transfer coefficient distributions, Re_{Dh} = 32,940

give the effect of the periodically interrupted flow in a serpentine channel on the thermal performance: overall transfer coefficient and pressure drop. The results should enable better understanding of highly complex turbulent flow fields, and may also help design heat exchangers with enhanced surfaces and validate numerical codes.

Experimental Apparatus

For the mass transfer experiment, the aluminum test channel is an assembly of seven plates and eight blocks affixed alternately onto two base plates to form a "two-dimensional" serpentine flow passage with right-angled turns (see top of Fig. 1). The height and the width of the flow passage are 1.27 cm and 22.9 cm, respectively, giving the flow passage an aspect ratio (height/width) of 1:18. The cross-sectional dimensions of each block are 1.5 (height) by 1.0 times the channel height, while the spacing between two adjacent blocks, separated by a plate, is 1.5 times the channel height. The plates and the blocks are cassettes with cutouts that may be filled with naphthalene by casting, such that all surfaces in the flow passage that are exposed to air flow during an experiment are covered with naphthalene.

During an experiment, conditioned room air at 22°C is drawn with a blower through a 22.9-cm-long straight entrance channel that has the same cross section as the test channel before the air passes through the test channel. The air mass flow rate is determined with an orifice flow meter along with a manometer.

The regional mass transfer is measured with an electronic balance, and the local mass transfer distribution with a computer-controlled system that consists of an electronic depth gage, a coordinate table, and stepper motors.

For the pressure measurement experiment, the aluminum cassettes are replaced with wooden plates and blocks of the same dimensions. The static pressure distribution is determined with seven taps that are installed in the middle of the seven plates, along with a manometer.

Data Reduction

The regional Sherwood number is a dimensionless regional mass transfer coefficient that is defined as $\overline{Sh}_{Dh} = [\{\bar{m}''/(\rho_s - \rho_b)\}(D_h/\sigma)]$, where $\bar{m}''$ is the regionally averaged mass flux, ρ_s is the vapor density on the naphthalene surface, ρ_b is the bulk vapor density of naphthalene in the air flow at the region of interest, D_h is the hydraulic diameter of the test channel, and σ is the naphthalene/air diffusion coefficient. The mass flux is evaluated from the measured rate of mass transfer from the surfaces of a plate or a block to the flowing air and the mass transfer area. The vapor density on the naphthalene surface is based on a vapor pressure–temperature relation for naphthalene and the ideal gas equation of state, and the bulk vapor density is calculated from the cumulative mass of naphthalene vapor in the flowing air at the region of interest and the air volumetric flow rate.

The local Sherwood number, Sh_{Dh}, at a measurement point, is a dimensionless local mass transfer coefficient that is based on the local mass flux and the bulk vapor density of naphthalene in the air flow, at the measurement point.

The regional Sherwood number, $\overline{Sh}_{Dh}$, is determined separately for each plate and for each block, while the local Sherwood number, Sh_{Dh}, is obtained on the surfaces of the plates and the blocks as a function of a streamwise coordinate along the test channel. Both regional and local Sherwood numbers are normalized with the corresponding Sherwood number for fully developed turbulent flow in a straight channel, Sh_0, based on the Dittus–Boelter correlation.

The Moody friction factor, f, is defined as $(-)$ the axial pressure gradient in the test channel, $-dp/ds$, times the hydraulic diameter, over the dynamic pressure based on the average flow velocity in the channel. The friction factor is compared with that for turbulent flow in a straight tube, f_0.

Experimental mass transfer and pressure drop data are obtained for Reynolds numbers ranging from 11,000 to 33,000. Only selected results are presented and discussed here. Readers are referred to Choi (1993) for additional experimental results and corresponding numerical results for periodically developed flow in serpentine channels from a finite volume analysis.

The maximum uncertainties for the overall Sherwood number, the local Sherwood number, the Reynolds number, and the friction factor are found to be ±7.5, ±9.7, ±5.9, and ±11.9 percent, respectively. The details of the uncertainty analysis are given in Appendix G of Choi (1993).

Results and Discussion

Local Heat/Mass Transfer. The variation of the normalized local Sherwood number, Sh_{Dh}/Sh_0, with a normalized streamwise coordinate, s/H, along the test channel surfaces over each period, for $Re_{Dh} \approx 33{,}000$ is presented in Fig. 1. According to the heat and mass transfer analogy, the corresponding local heat transfer enhancement or Nusselt number ratio, Nu_{Dh}/Nu_0, may be obtained from the Sh_{Dh}/Sh_0 distribution.

The Sh_{Dh}/Sh_0 distributions on corresponding surfaces in the first two periods from the channel entrance are very different from one another. The decrease of Sh_{Dh}/Sh_0 along surface $a-b$ in the first period is the result of boundary layer development. Downstream of the second period, the differences between the distributions over consecutive periods diminish, while the shapes of distributions become very similar. It is evident that the differences between the Sh_{Dh}/Sh_0 distributions on corresponding surfaces in the fifth and sixth periods are well within the estimated experimental uncertainty. Thus, it appears that the Sh_{Dh}/Sh_0 distribution over a period repeats itself downstream of the fifth period and the flow may be considered periodically developed.

The continually increasing value of Sh_{Dh}/Sh_0 in the periodically developed distribution on surface $c-d$ suggests that the flow separates at the upstream corner at point c and never reattaches on surface $c-d$. The turning of the flow around the downstream corner at point d causes the Sh_{Dh}/Sh_0 value to be high near the corner. The distribution on surface $d-e$ is typical of a surface being washed by a recirculating flow that occurs as the flow separates at the corner at point d and reattaches on surface

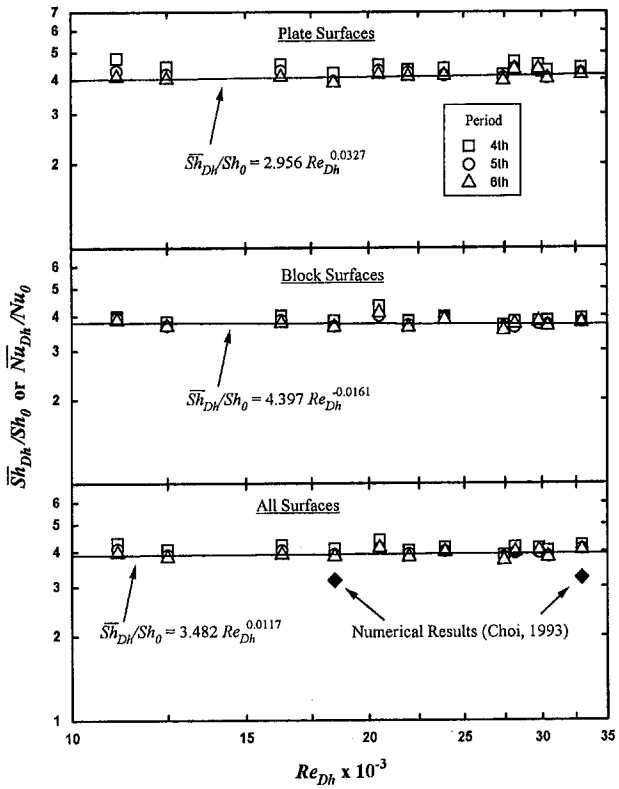

Fig. 2 Regional normalized transfer coefficient as a function of Reynolds number

$a-b$. As a result of the flow reattachment, the value of Sh_{Dh}/Sh_0 is large at $s/H \approx 1.0$ in the distribution on surface $a-b$. A peak at $s/H \approx 3.25$ in the distributions on surface $b-c$, where the Sh_{Dh}/Sh_0 value is the highest, and the second peak at $s/H \approx 2.5$ in the Sh_{Dh}/Sh_0 distributions on surface $a-b$ are believed to be caused by the flow being forced back toward surface $a-b$ after impinging onto surface $b-c$. The distribution on surface $a-b$ also suggests that there may be a second small recirculation region trapped by a larger one at corner b.

Regional and Overall Heat/Mass Transfer. Figure 2 shows the heat/mass transfer enhancement as a function of the flow Reynolds number. The values of the normalized average Sherwood number, $\overline{Sh}_{Dh}/Sh_0$, for surface $a-b$ (plate surface), surface $b-c-d-e$ (block surface), and all surfaces over the fourth, fifth, and sixth periods, are presented separately. The variations of the $\overline{Sh}_{Dh}/Sh_0-Re_{Dh}$ distributions over the fifth and sixth periods are relatively small, again indicating that the flow becomes periodically developed within a rather short distance from the channel entrance. The periodically developed value of $\overline{Sh}_{Dh}/Sh_0$ for surface $a-b$, surface $b-c-d-e$, and all surfaces over a period are all weak functions of Re_{Dh}, with values of about 4.08, 3.75, and 3.91, respectively. The values of $\overline{Sh}_{Dh}/Sh_0$ for the fourth period are slightly higher than those for the fifth and sixth periods, and the values for surface $a-b$ are generally higher than those for surface $b-c-d-e$ (that is, the average plate surface transfer coefficient is higher).

Plots of the streamwise distribution of $\overline{Sh}_{Dh}/Sh_0$, which are not presented here, show $\overline{Sh}_{Dh}/Sh_0$ increases with distance from the channel entrance, reaches a maximum at the fourth or third period (for the block or plate surface, respectively), then decreases and levels off to a constant value at the fifth through the seventh periods. The periodically developed values of $\overline{Sh}_{Dh}/Sh_0$ on surface $a-b$ (block surface) and on surface $b-c-d-e$ are typically about 2 to 6 percent and 8 to 17 percent lower than the corresponding peak values, respectively.

Pressure Results. Pressure results are obtained for Re_{Dh} between 18,000 and 32,000. The friction factor distributions along the channel show very large values between the second and third periods and almost constant values downstream of the third period. The peak friction factor values are about twice the periodic developed values, which are about 1.02 ± 0.03. Compared with the corresponding friction factors from an available correlation for fully developed turbulent flow in a straight tube, the friction factors in the serpentine channel are 36.4 to 45.5 times higher. The large pressure drops in the serpentine channel are the results of dynamic head losses during flow impingement and re-acceleration. Thus, the relative overall thermal performance of the serpentine channel being considered, in terms of $[(\overline{Sh}_{Dh}/Sh_0)/(f/f_0)^{1/3}]$, is about 1.14 ± 0.04.

Conclusions

Based on the local and regional heat/mass transfer and pressure drops obtained for turbulent flow through a serpentine channel, the flow and heat/mass transfer may be considered periodic downstream of the fifth period. The significant heat transfer enhancement is offset by the large pressure drop in the channel or pumping power requirement.

Acknowledgments

This research was supported in part by the Texas State Energy Research in Application Program, the Texas Center for Energy and Mineral Resources, and the NASA Center for Space Power.

References

Choi, J. M., 1993, "Heat Transfer in a Serpentine Channel With a Series of Right-Angle Turns," Ph.D. Dissertation, Texas A&M University, College Station, TX.

The Criterion for Turbulent Combined Forced and Natural Convection in a Vertical Flow System

T. Inagaki[1]

Nomenclature

f = friction factor
Gr = Grashof number
Gr* = modified Grashof number
$Gr/(Re^{3.0}\ Pr^{0.5})$ = governing parameter under constant temperature
$Gr^*/(Nu\ Re^{3.0}\ Pr^{0.5})$ = governing parameter under constant heat flux
Nu = Nusselt number
Nu_f = Nusselt number without buoyancy
Pr = Prandtl number
q_w = wall heat flux, W/m^2
Re = Reynolds number
T_w = wall temperature

[1] Research Associate, Department of Mechanical Engineering, University of Ibaraki, 12-1 Nakanarusawa 4 Chome, Hitachi, Ibaraki, 316 Japan.

Contributed by the Heat Transfer Division of THE AMERICAN SOCIETY OF MECHANICAL ENGINEERS. Manuscript received by the Heat Transfer Division August 1994; revision received February 1995. Keywords: Forced Convection, Mixed Convection, Natural Convection. Associate Technical Editor: Y. Jaluria.

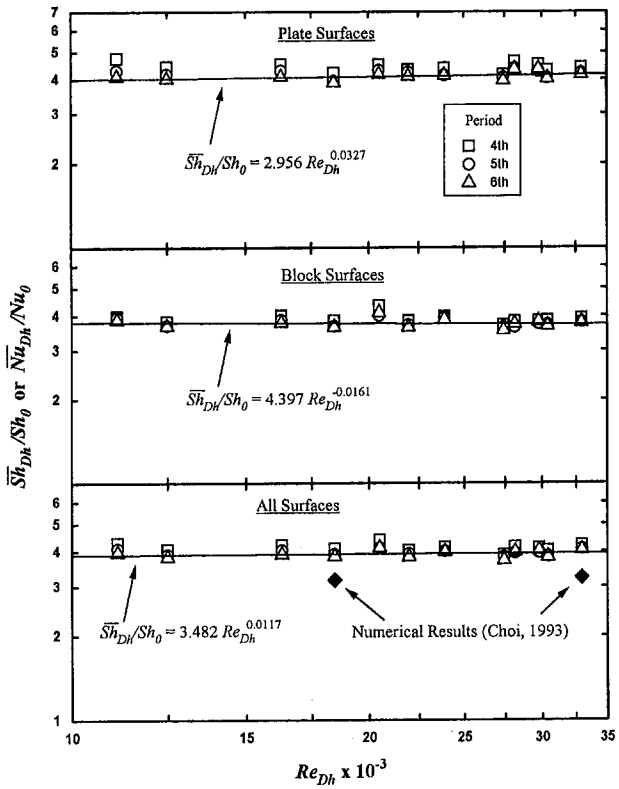

Fig. 2 Regional normalized transfer coefficient as a function of Reynolds number

$a-b$. As a result of the flow reattachment, the value of Sh_{Dh}/Sh_0 is large at $s/H \approx 1.0$ in the distribution on surface $a-b$. A peak at $s/H \approx 3.25$ in the distributions on surface $b-c$, where the Sh_{Dh}/Sh_0 value is the highest, and the second peak at $s/H \approx 2.5$ in the Sh_{Dh}/Sh_0 distributions on surface $a-b$ are believed to be caused by the flow being forced back toward surface $a-b$ after impinging onto surface $b-c$. The distribution on surface $a-b$ also suggests that there may be a second small recirculation region trapped by a larger one at corner b.

Regional and Overall Heat/Mass Transfer. Figure 2 shows the heat/mass transfer enhancement as a function of the flow Reynolds number. The values of the normalized average Sherwood number, $\overline{Sh}_{Dh}/Sh_0$, for surface $a-b$ (plate surface), surface $b-c-d-e$ (block surface), and all surfaces over the fourth, fifth, and sixth periods, are presented separately. The variations of the $\overline{Sh}_{Dh}/Sh_0-Re_{Dh}$ distributions over the fifth and sixth periods are relatively small, again indicating that the flow becomes periodically developed within a rather short distance from the channel entrance. The periodically developed value of $\overline{Sh}_{Dh}/Sh_0$ for surface $a-b$, surface $b-c-d-e$, and all surfaces over a period are all weak functions of Re_{Dh}, with values of about 4.08, 3.75, and 3.91, respectively. The values of $\overline{Sh}_{Dh}/Sh_0$ for the fourth period are slightly higher than those for the fifth and sixth periods, and the values for surface $a-b$ are generally higher than those for surface $b-c-d-e$ (that is, the average plate surface transfer coefficient is higher).

Plots of the streamwise distribution of $\overline{Sh}_{Dh}/Sh_0$, which are not presented here, show $\overline{Sh}_{Dh}/Sh_0$ increases with distance from the channel entrance, reaches a maximum at the fourth or third period (for the block or plate surface, respectively), then decreases and levels off to a constant value at the fifth through the seventh periods. The periodically developed values of $\overline{Sh}_{Dh}/Sh_0$ on surface $a-b$ (block surface) and on surface $b-c-d-e$ are typically about 2 to 6 percent and 8 to 17 percent lower than the corresponding peak values, respectively.

Pressure Results. Pressure results are obtained for Re_{Dh} between 18,000 and 32,000. The friction factor distributions along the channel show very large values between the second and third periods and almost constant values downstream of the third period. The peak friction factor values are about twice the periodic developed values, which are about 1.02 ± 0.03. Compared with the corresponding friction factors from an available correlation for fully developed turbulent flow in a straight tube, the friction factors in the serpentine channel are 36.4 to 45.5 times higher. The large pressure drops in the serpentine channel are the results of dynamic head losses during flow impingement and re-acceleration. Thus, the relative overall thermal performance of the serpentine channel being considered, in terms of $[(\overline{Sh}_{Dh}/Sh_0)/(f/f_0)^{1/3}]$, is about 1.14 ± 0.04.

Conclusions

Based on the local and regional heat/mass transfer and pressure drops obtained for turbulent flow through a serpentine channel, the flow and heat/mass transfer may be considered periodic downstream of the fifth period. The significant heat transfer enhancement is offset by the large pressure drop in the channel or pumping power requirement.

Acknowledgments

This research was supported in part by the Texas State Energy Research in Application Program, the Texas Center for Energy and Mineral Resources, and the NASA Center for Space Power.

References

Choi, J. M., 1993, "Heat Transfer in a Serpentine Channel With a Series of Right-Angle Turns," Ph.D. Dissertation, Texas A&M University, College Station, TX.

The Criterion for Turbulent Combined Forced and Natural Convection in a Vertical Flow System

T. Inagaki[1]

Nomenclature

f = friction factor
Gr = Grashof number
Gr* = modified Grashof number
$Gr/(Re^{3.0}\ Pr^{0.5})$ = governing parameter under constant temperature
$Gr^*/(Nu\ Re^{3.0}\ Pr^{0.5})$ = governing parameter under constant heat flux
Nu = Nusselt number
Nu_f = Nusselt number without buoyancy
Pr = Prandtl number
q_w = wall heat flux, W/m^2
Re = Reynolds number
T_w = wall temperature

[1] Research Associate, Department of Mechanical Engineering, University of Ibaraki, 12-1 Nakanarusawa 4 Chome, Hitachi, Ibaraki, 316 Japan.

Contributed by the Heat Transfer Division of THE AMERICAN SOCIETY OF MECHANICAL ENGINEERS. Manuscript received by the Heat Transfer Division August 1994; revision received February 1995. Keywords: Forced Convection, Mixed Convection, Natural Convection. Associate Technical Editor: Y. Jaluria.

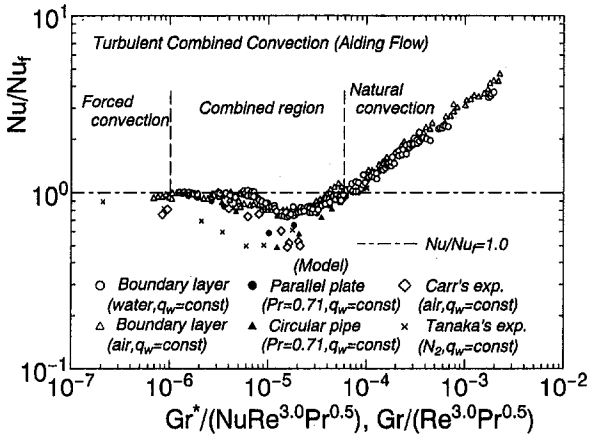

Fig. 1 Turbulent heat transfer with combined forced and natural convection of a vertical flow system (aiding flow)

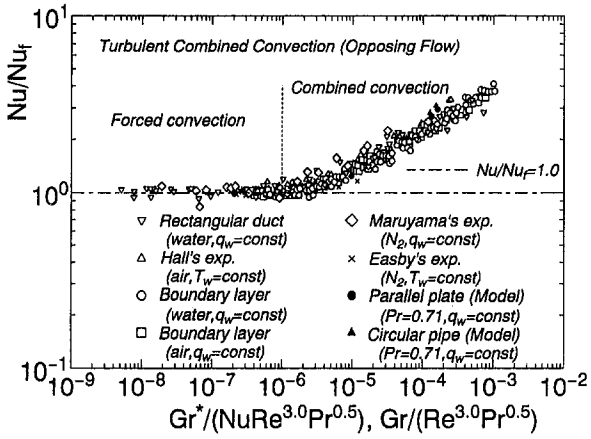

Fig. 2 Turbulent heat transfer with combined forced and natural convection of a vertical flow system (opposing flow)

1 Introduction

Buoyancy generated by a local temperature difference plays a significant role in forced convection with heat transfer on the earth, where gravity is not negligible anywhere. All heat transfer problems related to forced convection are therefore counted as combining forced and natural convection in a broad sense. We say that heat transfer by forced convection is one of the limiting cases of heat transfer with combined forced and natural convection. However, the buoyant force is negligibly small as a general rule, as compared with the inertia force in the region of forced convection. On the contrary, we say that heat transfer by natural convection is the other limiting case when natural convection is combined with forced convection. The buoyant force becomes marked as compared with the inertia force in the region of natural convection. We can apply several existing correlations for convective heat transfer when buoyancy is extremely small or large. It is therefore important to clarify the application limit of these correlations in estimating many engineering problems. The clarification of the influence of buoyant operating direction on heat transfer is also important.

Therefore, the author classified the flow region with combined forced and natural convection using various empirical heat transfer data in a vertical flow system, where buoyancy becomes significant. The characteristic behavior of turbulent combined convection will appear noticeably in a vertical flow system. Furthermore, the classification was estimated with the aid of the numerical heat transfer data simulated by the two-equation turbulence model. Several existing empirical and numerical investigations for various working fluids, heating and flow conditions will be useful in discussing the classification. The author discusses the criterion standard of the turbulent combined convection region under various flow conditions, which are the constant heat flux condition, constant wall temperature condition, internal flow, external flow, aiding flow, opposing flow, and so on. The present work was performed under fully developed flow conditions.

2 Heat Transfer and Criterion Standard

The Nusselt numbers, Nu, were normalized by Nu_f for turbulent forced convection under the same Reynolds number, Re, and were plotted in terms of nondimensional quantity, $Gr^*/(Nu\,Re^{3.0}\,Pr^{0.5})$ or $Gr/(Re^{3.0}\,Pr^{0.5})$, in Fig. 1 for aiding flow and in Fig. 2 for opposing flow. The ordinate, Nu/Nu_f, illustrates the reduction and enhancement ratios of heat transfer. The abscissa stands for the ratio of buoyant force to inertia force. The dashed-and-dotted line illustrates the heat transfer without buoyancy. We say that heat transfer and fluid flow are controlled only by the inertia force when $Nu/Nu_f = 1.0$. The author defined Nu_f as follows for individual flow conditions:

⟨for external flow⟩

$$Nu_f = \frac{0.0296\,Re^{0.8}\,Pr}{[1 + 1.54\,Re^{-0.1}\,Pr^{-0.25}(Pr - 1)]} \text{ (Katto, 1981)} \quad (1)$$

⟨for internal flow⟩

$$Nu_f = \frac{(f/2)(Re - 1000)\,Pr}{1 + 12.7\sqrt{f/2}(Pr^{2/3} - 1)} \quad (3000 < Re < 10^6,\ 0.5 < Pr < 2000) \text{ (Gnielinski, 1976)}$$

$$f = 0.079/Re^{0.25} \text{ (for circular pipe flow)},$$

$$f = 0.073/Re^{0.25} \text{ (for duct flow)} \quad (2)$$

The length scales in the nondimensional quantities are presented in Table 1 for individual flowing geometries.

These data were acquired experimentally and numerically under fully developed flow condition for various flowing geometries. The data for boundary layer and duct flows were quoted from the author's experiments (1987, 1990, 1991, 1992). Nu based on Carr's data were calculated by assuming the near wall temperature gradient. The word "Model" in these figures means the simulated results using the two-equation turbulence model proposed by Kawamura (1979). The author predicted turbulent heat transfer by adding Boussinesq-approximated buoyant term to the governing equations. The open and closed symbols present the empirical and numerical heat transfer data for aiding and opposing flows, respectively.

It is obvious that Nu values for aiding flow decrease compared with those of forced convection in a range of abscissa. The reduction rate of heat transfer for internal flow is more remarkable than that of external flow. This is due to that the energy to generate near-wall turbulent production is always supplied from the outer region of the boundary layer, where the low-temperature and high-velocity fluid flows. On the contrary, Nu values for opposing flow increase with increasing buoyancy. It is obvious from these figures that we can unify heat transfer under various flow conditions using a nondimensional quantity, $Gr^*/(Nu\,Re^{3.0}\,Pr^{0.5})$ or $Gr/(Re^{3.0}\,Pr^{0.5})$.

Table 1 Length scale of nondimensional quantities

	boundary layer	pipe flow	duct flow	parallel plate
length scale (L)	distance from a leading edge	diameter	hydraulic diameter	hydraulic diameter
Nusselt number Nuf	equation (1)	equation (2)	equation (2)	equation (2)

The author defined the combined convection regions where heat transfer coefficients are not consistent with those of forced convection without buoyancy. The regions are therefore classified as follows by applying the definition:

$$1.0 \times 10^{-6} < \frac{\mathrm{Gr}^*}{(\mathrm{Nu}\ \mathrm{Re}^{3.0}\ \mathrm{Pr}^{0.5})},$$

$$\frac{\mathrm{Gr}}{(\mathrm{Re}^{3.0}\ \mathrm{Pr}^{0.5})} < 6.0 \times 10^{-5} \quad \text{(aiding flow)} \quad (3)$$

$$1.0 \times 10^{-6} < \frac{\mathrm{Gr}^*}{(\mathrm{Nu}\ \mathrm{Re}^{3.0}\ \mathrm{Pr}^{0.5})},$$

$$\frac{\mathrm{Gr}}{(\mathrm{Re}^{3.0}\ \mathrm{Pr}^{0.5})} \quad \text{(opposing flow)} \quad (4)$$

In particular, the author interprets the region, $1.0 \times 10^{-6} < \mathrm{Gr}^*/(\mathrm{Nu}\ \mathrm{Re}^{3.0}\ \mathrm{Pr}^{0.5})$ or $\mathrm{Gr}/(\mathrm{Re}^{3.0}\ \mathrm{Pr}^{0.5}) < 6.0 \times 10^{-5}$, where the heat transfer coefficients are reduced compared with those of forced convection under the same Re, as the combined convection region of aiding flow in a narrow sense. On the other hand, the heat transfer coefficients of opposing flow increase with increasing buoyancy when $\mathrm{Gr}^*/(\mathrm{Nu}\ \mathrm{Re}^{3.0}\ \mathrm{Pr}^{0.5})$ or $\mathrm{Gr}/(\mathrm{Re}^{3.0}\ \mathrm{Pr}^{0.5}) > 1.0 \times 10^{-6}$.

3 Concluding Remarks

The boundary between forced and combined convection regions has been classified, but it is also important to classify the boundary between combined and natural convection regions, because natural convection is the other limiting case of combined convection in a broad sense. However, its criteria have not yet been obvious owing to various complex flow conditions. The criteria, including both boundaries, will be important in the future.

References

Carr, A. D., Conner, M. A., and Buhr, H. O., 1973, "Velocity, Temperature and Turbulence Measurements in Air for Pipe Flow With Combined Free and Forced Convection," ASME JOURNAL OF HEAT TRANSFER, Vol. 95, pp. 445–452.

Easby, J. P., 1978, "The Effect of Buoyancy on Flow and Heat Transfer for a Gas Passing Down a Vertical Pipe at Low Turbulent Reynolds Numbers," *Int. J. Heat Mass Transfer,* Vol. 21, pp. 791–801.

Gnielinski, V., 1976, "New Equations for Heat and Mass Transfer in Turbulent Pipe and Channel Flow," *Int. Chem. Engrs.,* Vol. 16-2, p. 359.

Hall, W. B., and Price, P. H., 1970, "Mixed Forced and Free Convection From a Vertical Heated Pipe to Air," *Proc. 4th Int. Heat Transfer Conference,* Vol. 3, NC. 3.3.

Inagaki, T., and Kitamura, K., 1990, "Turbulent Heat Transfer With Combined Forced and Natural Convection Along a Vertical Flat Plate (The Effect of Prandtl Number)," *Heat Transfer Japanese Research,* Vol. 19-2, pp. 70–80.

Inagaki, T., and Kitamura, K., 1991, "Turbulent Heat Transfer With Combined Forced and Natural Convection Along a Vertical Flat Plate (Opposing Flow)," *Heat Transfer Japanese Research,* Vol. 20-3, pp. 203–216.

Inagaki, T., and Komori, K., 1992, "Heat Transfer of Turbulent Combined Convection in a Vertical Rectangular Duct (Opposing Flow)," *Heat Transfer Japanese Research,* Vol. 21-5, pp. 483–491.

Katto, Y., 1981, *Dennetsu Gairon (Outline of Heat Transfer),* Yokendo, Tokyo [in Japanese].

Kawamura, H., 1979, "Numerical Prediction of Uniformly Heated Gas Flow Using Two-Equation Turbulence Model," *Trans. Japan Soc. Mech. Engrs.,* Series B, Vol. 45-395, pp. 1038–1046.

Kitamura, K., and Inagaki, T., 1987, "Turbulent Heat and Momentum Transfer of Combined Forced and Natural Convection Along a Vertical Flat Plate—Aiding Flow," *Int. J. Heat Mass Transfer,* Vol. 30, pp. 21–41.

Maruyama, S., Iwasaki, Y., and Tanaka, H., 1989, "Combined Forced and Natural Convection Heat Transfer for Downward Flow in a Uniformly Heated Vertical Pipe," *Proc. 26th National Heat Transfer Symposium of Japan,* B244, pp. 436–438.

Tanaka, H., Maruyama, S., and Hatano, S., 1987, "Combined Forced and Natural Convection Heat Transfer for Upward Flow in a Uniformly Heated Vertical Pipe," *Int. J. Heat Mass Transfer,* Vol. 30, pp. 165–174.

Natural Convection in a Cubic Enclosure in the Presence of a Horizontal Magnetic Field

P. S. Lykoudis[1]

Introduction

Natural convection in finite aspect ratio cells is a popular area of investigation because of several important applications. Some of them are related to manufacturing processes involving electrically conducting fluids. When an external magnetic field is applied, it is possible to suppress the convective mechanism at will, and thus obtain solid geometries of greater purity. A review on this subject can be found in Ozoe and Okada (1989).

The purpose of this work is to investigate natural convection in a cubic enclosure in the presence of a magnetic field transverse to the induced flow. Two of the opposing vertical surfaces are kept at constant temperatures T_h and T_c whereas all others are insulated. This problem has been analyzed numerically by Ozoe and Okada (1989) and experimentally with gallium by Okada and Ozoe (1992). They have correlated their heat transfer data with the following empirical equation:

$$\overline{\mathrm{Nu}} \equiv \frac{\mathrm{Nu}_B - 1}{\mathrm{Nu}_0 - 1} = 1 - \left[1 + \left(\frac{0.57\ \mathrm{Gr}^{1/3}}{\mathrm{M}}\right)^{3.19}\right]^{-1/1.76} \quad (1)$$

Here Nu_B and Nu_0 are the Nusselt numbers in the presence and absence of the magnetic field B. The symbols M and Gr are the Hartmann and Grashof numbers. All nondimensional numbers cited in the paper containing a characteristic length are based on the distance between the hot and cold wall. Note in Eq. (1) that for high magnetic field, $\mathrm{Nu}_{B\to\infty} = 1$ as it should. As shown in Fig. 1, taken from Okada and Ozoe (1992) Eq. (1) is in excellent agreement with the data.

Okada and Ozoe (1992) have tried to correlate $\overline{\mathrm{Nu}}$ with the $\mathrm{Ly} = (\mathrm{M}/\mathrm{Gr}^{1/4})^2$ nondimensional number, but they show conclusively that the combination $\mathrm{M}/\mathrm{Gr}^{1/3}$ is superior. They argue, correctly, that the Ly number had emerged from an infinite flat plate geometry and for this reason it was not the correct parameter for an enclosure. They furthermore argue that the nondimensional ratio $\mathrm{M}/\mathrm{Gr}^{1/3}$ is successful because it emerges from a particular nondimensionalization of the vorticity equation. This argument leads to inconsistency because if true, once a nondimensionalization is chosen, solutions of the emerging differential equations for the Nusselt number would be correlated with the same grouping for all geometries and boundary conditions. As an example $\overline{\mathrm{Nu}}$ calculated for the case of an infinite flat plate, following the Okada and Ozoe (1992) nondimensionalization, would correlate with $\mathrm{M}/\mathrm{Gr}^{1/3}$ rather than the correct grouping $\mathrm{Ly} = (\mathrm{M}/\mathrm{Gr}^{1/4})^2$.

One hardly needs to emphasize how difficult it is to study theoretically heat transfer problems involving liquid metals, because of their well-known peculiarities, augmented in the case of enclosures by three-dimensional effects. However, when a magnetic field is present, the convective mechanism is efficiently suppressed, a fact that allows simplifying assumptions that make the problem tractable.

[1] School of Nuclear Engineering, Purdue University, West Lafayette, IN 47907.

Contributed by the Heat Transfer Division of THE AMERICAN SOCIETY OF MECHANICAL ENGINEERS. Manuscript received by the Heat Transfer Division February 1995; revision received April 1995. Keywords: Enclosure Flows, Liquid Metals, Natural Convection. Associate Technical Editor: J. R. Lloyd.

The author defined the combined convection regions where heat transfer coefficients are not consistent with those of forced convection without buoyancy. The regions are therefore classified as follows by applying the definition:

$$1.0 \times 10^{-6} < \frac{\mathrm{Gr}^*}{(\mathrm{Nu}\ \mathrm{Re}^{3.0}\ \mathrm{Pr}^{0.5})},$$

$$\frac{\mathrm{Gr}}{(\mathrm{Re}^{3.0}\ \mathrm{Pr}^{0.5})} < 6.0 \times 10^{-5} \quad \text{(aiding flow)} \quad (3)$$

$$1.0 \times 10^{-6} < \frac{\mathrm{Gr}^*}{(\mathrm{Nu}\ \mathrm{Re}^{3.0}\ \mathrm{Pr}^{0.5})},$$

$$\frac{\mathrm{Gr}}{(\mathrm{Re}^{3.0}\ \mathrm{Pr}^{0.5})} \quad \text{(opposing flow)} \quad (4)$$

In particular, the author interprets the region, $1.0 \times 10^{-6} < \mathrm{Gr}^*/(\mathrm{Nu}\ \mathrm{Re}^{3.0}\ \mathrm{Pr}^{0.5})$ or $\mathrm{Gr}/(\mathrm{Re}^{3.0}\ \mathrm{Pr}^{0.5}) < 6.0 \times 10^{-5}$, where the heat transfer coefficients are reduced compared with those of forced convection under the same Re, as the combined convection region of aiding flow in a narrow sense. On the other hand, the heat transfer coefficients of opposing flow increase with increasing buoyancy when $\mathrm{Gr}^*/(\mathrm{Nu}\ \mathrm{Re}^{3.0}\ \mathrm{Pr}^{0.5})$ or $\mathrm{Gr}/(\mathrm{Re}^{3.0}\ \mathrm{Pr}^{0.5}) > 1.0 \times 10^{-6}$.

3 Concluding Remarks

The boundary between forced and combined convection regions has been classified, but it is also important to classify the boundary between combined and natural convection regions, because natural convection is the other limiting case of combined convection in a broad sense. However, its criteria have not yet been obvious owing to various complex flow conditions. The criteria, including both boundaries, will be important in the future.

References

Carr, A. D., Conner, M. A., and Buhr, H. O., 1973, "Velocity, Temperature and Turbulence Measurements in Air for Pipe Flow With Combined Free and Forced Convection," ASME JOURNAL OF HEAT TRANSFER, Vol. 95, pp. 445–452.

Easby, J. P., 1978, "The Effect of Buoyancy on Flow and Heat Transfer for a Gas Passing Down a Vertical Pipe at Low Turbulent Reynolds Numbers," *Int. J. Heat Mass Transfer,* Vol. 21, pp. 791–801.

Gnielinski, V., 1976, "New Equations for Heat and Mass Transfer in Turbulent Pipe and Channel Flow," *Int. Chem. Engrs.,* Vol. 16-2, p. 359.

Hall, W. B., and Price, P. H., 1970, "Mixed Forced and Free Convection From a Vertical Heated Pipe to Air," *Proc. 4th Int. Heat Transfer Conference,* Vol. 3, NC. 3.3.

Inagaki, T., and Kitamura, K., 1990, "Turbulent Heat Transfer With Combined Forced and Natural Convection Along a Vertical Flat Plate (The Effect of Prandtl Number)," *Heat Transfer Japanese Research,* Vol. 19-2, pp. 70–80.

Inagaki, T., and Kitamura, K., 1991, "Turbulent Heat Transfer With Combined Forced and Natural Convection Along a Vertical Flat Plate (Opposing Flow)," *Heat Transfer Japanese Research,* Vol. 20-3, pp. 203–216.

Inagaki, T., and Komori, K., 1992, "Heat Transfer of Turbulent Combined Convection in a Vertical Rectangular Duct (Opposing Flow)," *Heat Transfer Japanese Research,* Vol. 21-5, pp. 483–491.

Katto, Y., 1981, *Dennetsu Gairon (Outline of Heat Transfer),* Yokendo, Tokyo [in Japanese].

Kawamura, H., 1979, "Numerical Prediction of Uniformly Heated Gas Flow Using Two-Equation Turbulence Model," *Trans. Japan Soc. Mech. Engrs.,* Series B, Vol. 45-395, pp. 1038–1046.

Kitamura, K., and Inagaki, T., 1987, "Turbulent Heat and Momentum Transfer of Combined Forced and Natural Convection Along a Vertical Flat Plate—Aiding Flow," *Int. J. Heat Mass Transfer,* Vol. 30, pp. 21–41.

Maruyama, S., Iwasaki, Y., and Tanaka, H., 1989, "Combined Forced and Natural Convection Heat Transfer for Downward Flow in a Uniformly Heated Vertical Pipe," *Proc. 26th National Heat Transfer Symposium of Japan,* B244, pp. 436–438.

Tanaka, H., Maruyama, S., and Hatano, S., 1987, "Combined Forced and Natural Convection Heat Transfer for Upward Flow in a Uniformly Heated Vertical Pipe," *Int. J. Heat Mass Transfer,* Vol. 30, pp. 165–174.

Natural Convection in a Cubic Enclosure in the Presence of a Horizontal Magnetic Field

P. S. Lykoudis[1]

Introduction

Natural convection in finite aspect ratio cells is a popular area of investigation because of several important applications. Some of them are related to manufacturing processes involving electrically conducting fluids. When an external magnetic field is applied, it is possible to suppress the convective mechanism at will, and thus obtain solid geometries of greater purity. A review on this subject can be found in Ozoe and Okada (1989).

The purpose of this work is to investigate natural convection in a cubic enclosure in the presence of a magnetic field transverse to the induced flow. Two of the opposing vertical surfaces are kept at constant temperatures T_h and T_c whereas all others are insulated. This problem has been analyzed numerically by Ozoe and Okada (1989) and experimentally with gallium by Okada and Ozoe (1992). They have correlated their heat transfer data with the following empirical equation:

$$\overline{\mathrm{Nu}} \equiv \frac{\mathrm{Nu}_B - 1}{\mathrm{Nu}_0 - 1} = 1 - \left[1 + \left(\frac{0.57\ \mathrm{Gr}^{1/3}}{\mathrm{M}}\right)^{3.19}\right]^{-1/1.76} \quad (1)$$

Here Nu_B and Nu_0 are the Nusselt numbers in the presence and absence of the magnetic field B. The symbols M and Gr are the Hartmann and Grashof numbers. All nondimensional numbers cited in the paper containing a characteristic length are based on the distance between the hot and cold wall. Note in Eq. (1) that for high magnetic field, $\mathrm{Nu}_{B\to\infty} = 1$ as it should. As shown in Fig. 1, taken from Okada and Ozoe (1992) Eq. (1) is in excellent agreement with the data.

Okada and Ozoe (1992) have tried to correlate $\overline{\mathrm{Nu}}$ with the $\mathrm{Ly} = (\mathrm{M}/\mathrm{Gr}^{1/4})^2$ nondimensional number, but they show conclusively that the combination $\mathrm{M}/\mathrm{Gr}^{1/3}$ is superior. They argue, correctly, that the Ly number had emerged from an infinite flat plate geometry and for this reason it was not the correct parameter for an enclosure. They furthermore argue that the nondimensional ratio $\mathrm{M}/\mathrm{Gr}^{1/3}$ is successful because it emerges from a particular nondimensionalization of the vorticity equation. This argument leads to inconsistency because if true, once a nondimensionalization is chosen, solutions of the emerging differential equations for the Nusselt number would be correlated with the same grouping for all geometries and boundary conditions. As an example $\overline{\mathrm{Nu}}$ calculated for the case of an infinite flat plate, following the Okada and Ozoe (1992) nondimensionalization, would correlate with $\mathrm{M}/\mathrm{Gr}^{1/3}$ rather than the correct grouping $\mathrm{Ly} = (\mathrm{M}/\mathrm{Gr}^{1/4})^2$.

One hardly needs to emphasize how difficult it is to study theoretically heat transfer problems involving liquid metals, because of their well-known peculiarities, augmented in the case of enclosures by three-dimensional effects. However, when a magnetic field is present, the convective mechanism is efficiently suppressed, a fact that allows simplifying assumptions that make the problem tractable.

[1] School of Nuclear Engineering, Purdue University, West Lafayette, IN 47907.

Contributed by the Heat Transfer Division of THE AMERICAN SOCIETY OF MECHANICAL ENGINEERS. Manuscript received by the Heat Transfer Division February 1995; revision received April 1995. Keywords: Enclosure Flows, Liquid Metals, Natural Convection. Associate Technical Editor: J. R. Lloyd.

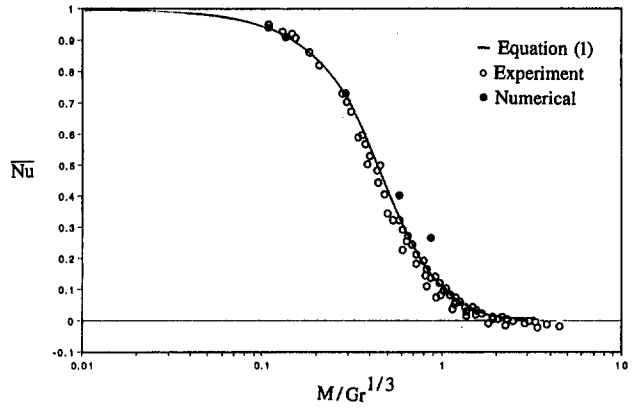

Fig. 1 Comparison of the experimental data of Okada and Ozoe (1992) with their empirical Eq. (1) in terms of the parameter $M/Gr^{1/3}$

Analysis

In the case of an infinite vertical flat plate immersed in a bath of infinite extent, the thermal and momentum boundary layers grow side by side, uninhibited by the presence of an opposite wall. On the other hand, the vertically induced flow in a natural convection cell turns horizontally in the proximity of the top and bottom surfaces, forming a circular pattern. When steady state is reached the core of the cell is stratified so that a conduction heat flux is created in the vertical direction. A proper condition needs to be satisfied to guarantee the adiabatic condition at the top and bottom surfaces. Details for the solution of this problem can be found in Gill (1966) and Bejan (1979). In this note we shall handle the problem by reducing the finite aspect ratio problem of a convection cell to the infinite vertical flat plate geometry using the "Method of Average Magnitude Analysis" as introduced in Lykoudis (1994).

Consider in Fig. 2 the geometry and thermal conditions of the problem at hand. Figure 2(b) depicts a thermal circuit equivalent to Fig. 2(a) with the help of a length X in the x direction such that the heat flux Q_X conducted normal to the hot wall through the height X is equal to the heat Q_H conducted normal to H, and Q_L normal to the direction x. We set the condition:

$$Q_X = Q_H + Q_L \tag{2a}$$

where:

$$Q_X \approx k\frac{(\Delta T)_y}{\delta}\cdot X, \quad Q_H \approx k\frac{(\Delta T)_y}{\delta}\cdot H,$$

$$Q_L \approx k\frac{(\Delta T)_x}{X}\cdot L \tag{2b}$$

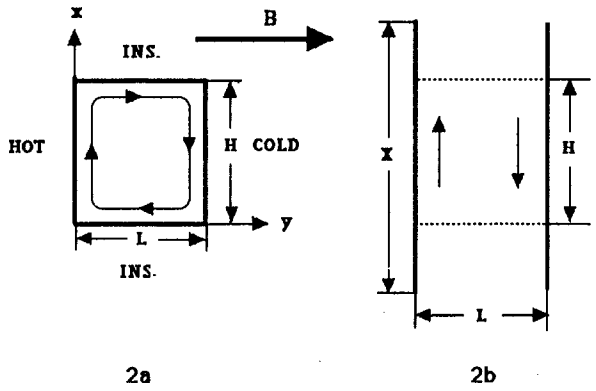

Fig. 2 Schematic and thermal equivalent of a cubic enclosure heated from the side of the plane xz and cooled on the opposite side. All other sides are insulated. The magnetic field is constant and transverse to the heated and cooled walls.

We now write the "Average Magnitude" equation of conservation of energy in terms of the length X:

$$U\frac{(\Delta T)_x}{X} \approx \alpha\frac{(\Delta T)_y}{\delta^2} \tag{3}$$

Here δ is the boundary layer thickness. For the calculation of the buoyant force we assume the Boussinesq approximation, and for the ponderomotive, we assume that the induced electric currents close in themselves, so that the electric field as measured in the laboratory is zero. Furthermore, for low magnetic Reynolds numbers, the external field is not distorted. The result of all these reasonable assumptions for the problem at hand is that the retarding ponderomotive force per unit volume equals $-\sigma uB^2$. In terms of the length X, the "average magnitude" equation of conservation of momentum in the direction x with unit weight coefficients is:

$$\frac{U^2}{X} \approx g\beta(T_h - T_a) - \nu\frac{U^2}{X} - \frac{\sigma UB^2}{\rho} \tag{4}$$

In the above T_a is the arithmetic mean of the hot and cold temperatures and U the average velocity. Equations (2), (3), and (4) form a system for the three unknowns of the problem X, U, and δ.

We solve this system of equations as follows: We eliminate U between the energy and momentum Eqs. (3) and (4), and we solve the resulting equation for X, which we then substitute in the auxiliary Eq. (2). We define the Nusselt number to be proportional to L/δ. The end result is the following:

$$\frac{\mathrm{Ra}}{\mathrm{Nu}^4\left(1+\frac{1}{\mathrm{Pr}}+\frac{\mathrm{M}^2}{\mathrm{Nu}^2}\right)} \approx \mathrm{Nu}^3\left(1+\frac{1}{\mathrm{Pr}}+\frac{\mathrm{M}^2}{\mathrm{Nu}^2}\right)+\frac{H}{L} \tag{5}$$

Let us now find solutions for different cases.

The Infinite Flat Plate Immersed in an Infinite Bath in the Presence of a Horizontal Magnetic Field

Here H/L dominates the right-hand side of Eq. (5). The resulting equation is a quadratic in terms of Nu^2. We obtain the result:

$$\mathrm{Nu}_{\mathrm{inf.plate}_{B\to\infty}} \propto \left[\frac{\mathrm{Bo}^{1/2}}{\mathrm{Ly}+(\mathrm{Ly}^2+1+\mathrm{Pr})^{1/2}}\right]^{1/2} \tag{6}$$

In Lykoudis (1994), where the weight coefficients are maintained in the equations of conservation and properly evaluated, the end result for liquid metals in terms of $\overline{\mathrm{Nu}}$ is:

$$\overline{\mathrm{Nu}}_{\mathrm{Inf.Plate}} \cong \left[\frac{(4/3)^{1/4}}{\mathrm{Ly}+(\mathrm{Ly}^2+4/3)^{1/2}}\right]^{1/2} \tag{7}$$

The Cubic Cell in the Presence of a Weak Magnetic Field

In this case the term H/L is negligible and Eq. (5) becomes:

$$\mathrm{Ra} \approx \mathrm{Nu}^{7/2}\left(1+\frac{1}{\mathrm{Pr}}+\frac{\mathrm{M}^2}{\mathrm{Nu}^2}\right) \tag{8}$$

In the special case of zero field the result is:

$$\mathrm{Nu}_{B=0} \approx \left(\frac{\mathrm{Bo}}{1+\mathrm{Pr}}\right)^{2/7} \tag{9}$$

In the above Bo is the familiar Boussinesq number defined as the product $\mathrm{Gr}\cdot\mathrm{Pr}^2$. Equation (9) is a well-known result, ob-

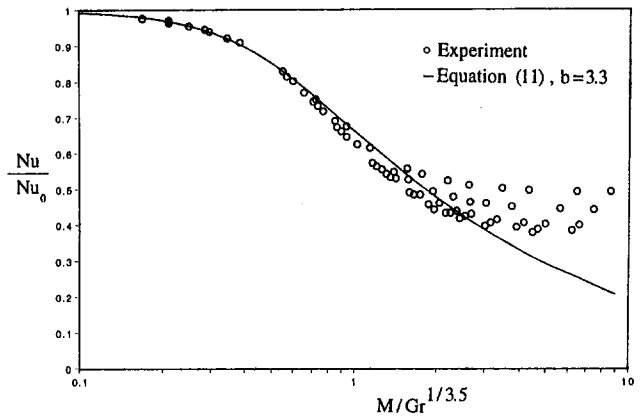

Fig. 3 Comparison of the experimental and numerical data of Okada and Ozoe (1992) with Eq. (11) derived for weak magnetic fields in terms of the parameter $M/Gr^{1/3.5}$

tained here with the help of the auxiliary length X. A correlation for this case has been derived in Lykoudis (1994) tested with numerical and experimental findings, including the ones for gallium of Okada and Ozoe (1992). This equation is:

$$\mathrm{Nu}_{B=0} \cong \frac{0.18\ \mathrm{Bo}^{2/7}}{[\mathrm{Pr}^{1/4} + 0.001^{1/4}]^{8/7}} \tag{10}$$

When $M \neq 0$, Eq. (8) is transcendental in terms of the Nusselt number. Since we are looking for solutions for small M, we substitute for Nu^2 in the denominator of the third term inside the parentheses of (8) the expression for zero magnetic field (9). Solving then for Nu and dividing by Nu_0 we find:

$$\frac{\mathrm{Nu}}{\mathrm{Nu}_0} \approx \frac{1}{\left\{1 + \left[\left(\frac{a_1}{1 + a_2\mathrm{Pr}}\right)^{1/2} \frac{\mathrm{M}}{\mathrm{Gr}^{1/3.5}}\right]^2\right\}^{2/7}}$$

$$= \frac{1}{\left\{1 + \left(b\,\frac{\mathrm{M}}{\mathrm{Gr}^{1/3.5}}\right)^2\right\}^{2/7}} \tag{11}$$

In Eq. (11) the two constants a have been introduced to represent the combination of weight coefficients that will be determined for best fit from experimental data. In Fig. 3 we plot Eq. (11) with the quantity b that multiplies $M/Gr^{1/3.5}$ equal to 3.3. The fit with the data is good for values up to about $M/Gr^{1/3.5}$ equal to 1, but poor beyond this point. As will be shown in the next section, the physics of the problem changes for stronger magnetic fields.

The Cubic Cell in the Presence of a Strong Magnetic Field

In the presence of a strong magnetic field, we expect the buoyant convection to be suppressed by the magnetic field, and at the same time also the stratification. We set $Q_L = 0$ in Eq. (2a). In the limit of a high field the cell will look very nearly like a solid block. In such a case the term Q_H in Eq. (2b) can be approximated with $Q_H \approx k(T_h - T_c/2)/(L/2) \cdot H$. Taking $Q_X \approx k(T_h - T_c/2)/\delta \cdot X$ it follows that: $X \approx 2\delta(H/L)$.

In the energy Eq. (3) we set: $(\Delta T)_y \approx (T_h - T_c)/2$, $(\Delta T)_x \approx T_h - (T_h + T_c)/2 \approx (T_h - T_c)/2$. The momentum equation is now written by neglecting the inertia force so that the buoyant force is counterbalanced by the ponderomotive force. Solving the system of Eqs. (2)–(4) as before we find:

$$\mathrm{Nu}_{B\to\infty} \approx \frac{1}{8}\left(\frac{\mathrm{Bo}^{1/2}}{\mathrm{Ly}}\right) \tag{12}$$

Here, the Nusselt number falls off with the first power of $Ly/Bo^{1/2}$ compared with the square of this parameter for the case of the infinite flat plate as indicated by Eq. (6). Using the definition of $\overline{Nu}$ of Eq. (1) and the results (10) and (12) we have:

$$\overline{\mathrm{Nu}} \cong \frac{1}{1 + c\left[(\mathrm{Pr}^{1/4} + 0.001^{1/4})^{-8/7}\left(\frac{\mathrm{Ly}}{\mathrm{Bo}^{3/14}}\right)\right]} \tag{13}$$

with $c = 1.44$.

Comparison of Results With Experimental Data and Discussion

To compare Eq. (13) with the gallium data of Okada and Ozoe (1992) we need to take $Pr = 0.024$. Using the definitions of Ly and Bo we derive from (13),

$$\overline{\mathrm{Nu}} \cong \frac{1}{1 + d\left(\frac{\mathrm{M}}{\mathrm{Gr}^{1/2.8}}\right)^2} \tag{14}$$

with $d = 13.51$. In order to obtain the best fit with the experimental data we treat the constant d as a free parameter and we make use of the NFIT software package,[2] a least-square method. The value thus determined is 13.15 rather than 13.51. The closeness of the two values for d is fortuitous. In the energy equation if we had assumed $(\Delta T)_x \approx T_h - T_c$ instead of $(T_h - T_c)/2$, the model's value for the constant $d = 13.51$ would be off by a factor of 2. Equation (14) is plotted in Fig. 4 along with the data of Okada and Ozoe (1992). The agreement of Eq. (14) with the experiment is good even for the weak magnetic fields for which nevertheless Eq. (11) is superior. Strictly speaking, since Eq. (14) has been derived for the case of a strong magnetic field, it would have been appropriate to determine d using the data for $M/Gr^{1/2.8}$ greater than about 0.6. Such a choice would not be wise because the experimental $\overline{Nu}$ numbers reported by Okada and Ozoe (1992) at high magnetic fields are negative, and therefore physically not possible. The negative values should be attributed to the higher experimental error in the absence of convection as the conduction limit is approached. In the same figure we also show the numerical results of Ozoe and Okada (1989) along with another curve with $d = 9.00$. This curve fits

[2] NFIT Version 1.0 by Island Products.

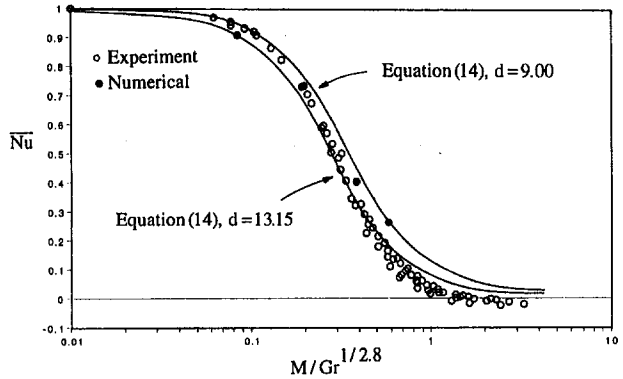

Fig. 4 Comparison of the experimental and numerical data of Okada and Ozoe (1992) with Eq. (14) in terms of the parameter $M/Gr^{1/2.8}$

well the numerical data and also the experimental points at low magnetic fields for which the experimental error as reported in Okada and Ozoe (1992) is small.

Conclusions and Recommendations

We can obtain a universal plot for all liquid metal data by plotting $\overline{Nu}$ versus the expression in brackets in the denominator of Eq. (13). Instead of $c = 1.44$ we should take the value $c = 1.40$ for best fit of the gallium data:

$$\overline{Nu} \cong \frac{1}{1 + 1.40\left[Pr^{1/4} + 0.001^{1/4})^{-8/7}\left(\frac{Ly}{Bo^{3/14}}\right)\right]} \quad (15)$$

If one wishes to favor the few numerical data, the constant 1.40 needs to change to the value of 0.96, which corresponds to $d = 9.00$.

To the extent that the strong magnetic field solution via the definition of $\overline{Nu}$ has yielded a satisfactory correlation even for the weak field range, it is best to take advantage of the simplicity of Eq. (15) and accept it for both weak and strong magnetic fields. More experimental data are needed with another liquid metal so that the dependence of $\overline{Nu}$ on the Prandtl number as found in this paper in Eq. (14) can be tested.

To bring these results into closer context with those of Okada and Ozoe (1992) we note that the dominant nondimensional grouping $Ly/Bo^{3/14}$ in Eq. (14) is equivalent to $(M/Gr^{1/2.8})^2 \cdot Pr^{-3/7}$. For a given Prandtl number, one can argue that it is not all that much different from the one used by Okada and Ozoe (1992) where the root of Gr was 3 rather than 2.8. The gain is that Eq. (15) provides both the functional relationship for $\overline{Nu}$, and the Prandtl number dependence. A functional relationship derived from first principles is a safer guide for correlation of available experimental data, providing at the same time more confidence for extrapolations where data do not exist or are hard to obtain.

One final remark: In terms of $\overline{Nu}$, for an infinite plate, the experimental data are correlated with the nondimensional number Ly, that is with the combination $M/Gr^{1/4}$. For a cell in the presence of a weak magnetic field from Eq. (11), the relevant parameter is $M/Gr^{1/3.5}$. For a strong magnetic field the parameter changes to $M/Gr^{1/2.8}$. This sequence from the fourth to the 3.5 and 2.8 roots of the Gr number explains perhaps why Takada and Ozoe's (1992) choice of the combination $M/Gr^{1/3}$ does on the average a good job in correlating their experimental data for all magnetic field strengths. It should be mentioned however that the cohesiveness of the correlations is due to a great extent to the use of the definition $\overline{Nu} \equiv (Nu_B - 1)/(Nu_0 - 1)$ as already shown many years ago by Lykoudis and Dunn (1973) in the context of a different MHD problem.

With the availability of good numerical techniques, no need is perceived by many investigators to use simple approximate arguments to find closed-form solutions. Yet even with complicated geometries, integral methods provide insights as to the correct nondimensional numbers. In particular when the conservation equations are converted to algebraic equations with the "method of average magnitude analysis," the correct nondimensional numbers can be determined, along with a satisfactory functional relation for the prediction of the Nusselt number. Of course it will be naïve to think that simple integral arguments contain all the intricacies of an actual situation with complicated secondary flows. For this reason the experimental data are the final arbiters.

Acknowledgments

The author is grateful to Professor Hiroyuki Ozoe for providing him with the computer output of all of his experimental data.

References

Bejan, A., 1979, "Note on Gill's Solution for Free Convection in a Vertical Enclosure," *J. Fluid Mech.*, Vol. 90, pp. 561–568.

Gill, A. E., 1966, "The Boundary Layer Regime for Convection in a Rectangular Cavity," *J. Fluid Mech.*, Vol. 26, pp. 515–536.

Lykoudis, P. S., 1962, "Natural Convection of an Electrically Conducting Fluid in the Presence of a Magnetic Field," *Int. J. Heat Mass Transfer*, Vol. 5, pp. 23–34.

Lykoudis, P. S., and Dunn, P. F., 1973, "MagnetoFluidMechanic Heat Transfer From Hot Film Probes," *Int. J. Heat Mass Transfer*, Vol. 16, pp. 1493–1452.

Lykoudis, P. S., 1995, "Introduction to the Method of Average Magnitude Analysis and Application to Natural Convection in Cavities," ASME JOURNAL OF HEAT TRANSFER, Vol. 117, pp. 604–610.

Okada, K., and Ozoe, H., 1992, "Experimental Heat Transfer Rates of Natural Convection in Molten Gallium Suppressed Under an External Magnetic Field in Either the *X*, *Y*, or *Z* Direction," ASME JOURNAL OF HEAT TRANSFER, Vol. 114, pp. 107–114.

Ozoe, H., and Okada, K., 1989, "The Effect of the Direction of the External Magnetic Field on the Three-Dimensional Natural Convection in a Cubical Enclosure," *Int. J. Heat Mass Transfer*, Vol. 32, No. 10, pp. 1939–1954.

Two-Flux and Diffusion Methods for Radiative Transfer in Composite Layers

C. M. Spuckler[1] and R. Siegel[2]

Nomenclature

a = absorption coefficient of material in layer, m^{-1}
CON = integration constant, W/m; $\tilde{CON} = CON/D\sigma T_{g1}^4$
c_0 = speed of electromagnetic propagation, m/s
D = thickness of each layer in composite, m
G = flux quantity $= 2(q_r^+ + q_r^-)$, W/m^2; $\tilde{G} = G/\sigma T_{g1}^4$
GS, GL = values of G in spectral bands at small and large frequencies
h_1, h_2 = heat transfer coefficients at boundaries, W/m^2K; $H = h/\sigma T_{g1}^3$
k = thermal conductivity, W/mK; $N = k/\sigma T_{g1}^3 D$
K = extinction coefficient $= a + \sigma_s$, m^{-1}
n = refractive index of a layer
q = heat flux, W/m^2; $\tilde{q} = q/\sigma T_{g1}^4$
q_r^+, q_r^- = isotropic radiative fluxes in $+x$ and $-x$ directions (Fig. 1), W/m^2
q_{r1}^0, q_{r2}^0 = externally incident radiation fluxes at boundaries, W/m^2; $\tilde{q}_r^0 = q_r^0/\sigma T_{g1}^4$
qS, qL = radiative flux in bands with small and large frequencies
T = absolute temperature, K; $t = T/T_{g1}$
T_{g1}, T_{g2} = gas temperatures on two sides of composite, K
T_{s1} = temperature of hot surroundings
x = coordinate in a layer, m; $X = x/D$
κ = optical coordinate in a layer Kx; $\kappa_D = KD$
ν = frequency of radiation; ν_c = cutoff frequency
ρ = diffuse reflectivity of interface
σ = Stefan–Boltzmann constant, W/m^2K^4
σ_s = scattering coefficient in a layer, m^{-1}; $\Omega = \sigma_s/K$

[1] Internal Fluid Mechanics Division, NASA Lewis Research Center, Cleveland, OH 44135.

[2] Research Academy, NASA Lewis Research Center, Cleveland, OH 44135.

Contributed by the Heat Transfer Division of THE AMERICAN SOCIETY OF MECHANICAL ENGINEERS. Manuscript received by the Heat Transfer Division September 1994; revision received June 1995. Keywords: Radiation, Radiation Interactions. Associate Technical Editor: M. F. Modest.

well the numerical data and also the experimental points at low magnetic fields for which the experimental error as reported in Okada and Ozoe (1992) is small.

Conclusions and Recommendations

We can obtain a universal plot for all liquid metal data by plotting $\overline{Nu}$ versus the expression in brackets in the denominator of Eq. (13). Instead of $c = 1.44$ we should take the value $c = 1.40$ for best fit of the gallium data:

$$\overline{Nu} \cong \frac{1}{1 + 1.40\left[\mathrm{Pr}^{1/4} + 0.001^{1/4}\right)^{-8/7}\left(\frac{\mathrm{Ly}}{\mathrm{Bo}^{3/14}}\right)\Bigg]} \quad (15)$$

If one wishes to favor the few numerical data, the constant 1.40 needs to change to the value of 0.96, which corresponds to $d = 9.00$.

To the extent that the strong magnetic field solution via the definition of $\overline{Nu}$ has yielded a satisfactory correlation even for the weak field range, it is best to take advantage of the simplicity of Eq. (15) and accept it for both weak and strong magnetic fields. More experimental data are needed with another liquid metal so that the dependence of $\overline{Nu}$ on the Prandtl number as found in this paper in Eq. (14) can be tested.

To bring these results into closer context with those of Okada and Ozoe (1992) we note that the dominant nondimensional grouping $\mathrm{Ly/Bo}^{3/14}$ in Eq. (14) is equivalent to $(\mathrm{M/Gr}^{1/2.8})^2 \cdot \mathrm{Pr}^{-3/7}$. For a given Prandtl number, one can argue that it is not all that much different from the one used by Okada and Ozoe (1992) where the root of Gr was 3 rather than 2.8. The gain is that Eq. (15) provides both the functional relationship for $\overline{Nu}$, and the Prandtl number dependence. A functional relationship derived from first principles is a safer guide for correlation of available experimental data, providing at the same time more confidence for extrapolations where data do not exist or are hard to obtain.

One final remark: In terms of $\overline{Nu}$, for an infinite plate, the experimental data are correlated with the nondimensional number Ly, that is with the combination $\mathrm{M/Gr}^{1/4}$. For a cell in the presence of a weak magnetic field from Eq. (11), the relevant parameter is $\mathrm{M/Gr}^{1/3.5}$. For a strong magnetic field the parameter changes to $\mathrm{M/Gr}^{1/2.8}$. This sequence from the fourth to the 3.5 and 2.8 roots of the Gr number explains perhaps why Takada and Ozoe's (1992) choice of the combination $\mathrm{M/Gr}^{1/3}$ does on the average a good job in correlating their experimental data for all magnetic field strengths. It should be mentioned however that the cohesiveness of the correlations is due to a great extent to the use of the definition $\overline{Nu} \equiv (\mathrm{Nu}_B - 1)/(\mathrm{Nu}_0 - 1)$ as already shown many years ago by Lykoudis and Dunn (1973) in the context of a different MHD problem.

With the availability of good numerical techniques, no need is perceived by many investigators to use simple approximate arguments to find closed-form solutions. Yet even with complicated geometries, integral methods provide insights as to the correct nondimensional numbers. In particular when the conservation equations are converted to algebraic equations with the "method of average magnitude analysis," the correct nondimensional numbers can be determined, along with a satisfactory functional relation for the prediction of the Nusselt number. Of course it will be naïve to think that simple integral arguments contain all the intricacies of an actual situation with complicated secondary flows. For this reason the experimental data are the final arbiters.

Acknowledgments

The author is grateful to Professor Hiroyuki Ozoe for providing him with the computer output of all of his experimental data.

References

Bejan, A., 1979, "Note on Gill's Solution for Free Convection in a Vertical Enclosure," *J. Fluid Mech.*, Vol. 90, pp. 561–568.

Gill, A. E., 1966, "The Boundary Layer Regime for Convection in a Rectangular Cavity," *J. Fluid Mech.*, Vol. 26, pp. 515–536.

Lykoudis, P. S., 1962, "Natural Convection of an Electrically Conducting Fluid in the Presence of a Magnetic Field," *Int. J. Heat Mass Transfer*, Vol. 5, pp. 23–34.

Lykoudis, P. S., and Dunn, P. F., 1973, "MagnetoFluidMechanic Heat Transfer From Hot Film Probes," *Int. J. Heat Mass Transfer*, Vol. 16, pp. 1493–1452.

Lykoudis, P. S., 1995, "Introduction to the Method of Average Magnitude Analysis and Application to Natural Convection in Cavities," ASME JOURNAL OF HEAT TRANSFER, Vol. 117, pp. 604–610.

Okada, K., and Ozoe, H., 1992, "Experimental Heat Transfer Rates of Natural Convection in Molten Gallium Suppressed Under an External Magnetic Field in Either the *X*, *Y*, or *Z* Direction," ASME JOURNAL OF HEAT TRANSFER, Vol. 114, pp. 107–114.

Ozoe, H., and Okada, K., 1989, "The Effect of the Direction of the External Magnetic Field on the Three-Dimensional Natural Convection in a Cubical Enclosure," *Int. J. Heat Mass Transfer*, Vol. 32, No. 10, pp. 1939–1954.

Two-Flux and Diffusion Methods for Radiative Transfer in Composite Layers

C. M. Spuckler[1] and R. Siegel[2]

Nomenclature

a = absorption coefficient of material in layer, m^{-1}
CON = integration constant, W/m; $\tilde{\mathrm{CON}} = \mathrm{CON}/D\sigma T_{g1}^4$
c_0 = speed of electromagnetic propagation, m/s
D = thickness of each layer in composite, m
G = flux quantity $= 2(q_r^+ + q_r^-)$, $\mathrm{W/m}^2$; $\tilde{G} = G/\sigma T_{g1}^4$
GS, GL = values of G in spectral bands at small and large frequencies
h_1, h_2 = heat transfer coefficients at boundaries, $\mathrm{W/m}^2\mathrm{K}$; $H = h/\sigma T_{g1}^3$
k = thermal conductivity, W/mK; $N = k/\sigma T_{g1}^3 D$
K = extinction coefficient $= a + \sigma_s$, m^{-1}
n = refractive index of a layer
q = heat flux, $\mathrm{W/m}^2$; $\tilde{q} = q/\sigma T_{g1}^4$
q_r^+, q_r^- = isotropic radiative fluxes in $+x$ and $-x$ directions (Fig. 1), $\mathrm{W/m}^2$
q_{r1}^0, q_{r2}^0 = externally incident radiation fluxes at boundaries, $\mathrm{W/m}^2$; $\tilde{q}_r^0 = q_r^0/\sigma T_{g1}^4$
qS, qL = radiative flux in bands with small and large frequencies
T = absolute temperature, K; $t = T/T_{g1}$
T_{g1}, T_{g2} = gas temperatures on two sides of composite, K
T_{s1} = temperature of hot surroundings
x = coordinate in a layer, m; $X = x/D$
κ = optical coordinate in a layer Kx; $\kappa_D = KD$
ν = frequency of radiation; ν_c = cutoff frequency
ρ = diffuse reflectivity of interface
σ = Stefan–Boltzmann constant, $\mathrm{W/m}^2\mathrm{K}^4$
σ_s = scattering coefficient in a layer, m^{-1}; $\Omega = \sigma_s/K$

[1] Internal Fluid Mechanics Division, NASA Lewis Research Center, Cleveland, OH 44135.

[2] Research Academy, NASA Lewis Research Center, Cleveland, OH 44135.

Contributed by the Heat Transfer Division of THE AMERICAN SOCIETY OF MECHANICAL ENGINEERS. Manuscript received by the Heat Transfer Division September 1994; revision received June 1995. Keywords: Radiation, Radiation Interactions. Associate Technical Editor: M. F. Modest.

Subscripts

$a, b \ldots h$ = the interfaces of a three-layer composite (Fig. 1)
r = radiative
tot = total heat flux by combined conduction and radiation

Introduction

The development of ceramic materials for high-temperature use is critical for advanced aircraft engines. Some ceramics are partially transparent to radiant energy so in high-temperature surroundings radiant penetration provides internal heating. At elevated temperatures, radiant emission can be large within materials with high refractive indices since internal emission depends on n^2. It must be determined how large radiative effects are, and whether partial transparency can help equalize temperatures to reduce thermal stresses and reduce maximum internal temperatures.

There is extensive literature on radiative transfer in plane layers originating from the theory to study radiation in stellar and the earth's atmospheres. As a result, many investigations have been for gases where the refractive index is close to one. Higher refractive indices are involved in predicting heat treating and cooling of glass plates (Gardon, 1958). In Spuckler and Siegel (1994a), temperature distributions and heat flows in composite layers with high refractive indices are predicted numerically using the radiative transfer equations coupled with heat conduction. Each exterior boundary is heated by radiation and convection, and diffuse interface reflections are included.

The formulation and solution of the exact spectral radiative transfer equations including scattering are rather complicated; hence it is desirable to develop more convenient approximate methods if they will yield accurate results. The two-flux equations (Siddall, 1972; Siegel and Howell, 1992) were shown by Tremante and Malpica (1994) to give accurate results for a gray layer with $n = 1$ between boundaries with specified temperatures. Two-flux and diffusion solutions, and combinations of the two for single layers with optically thin and thick spectral bands, were derived by Siegel and Spuckler (1994) for materials with $n > 1$ and with heating conditions so the boundary temperatures were determined during the solution. Flamant et al. (1988) derived two-flux solutions using two bands for a packed bed consisting of two layers of particles. In the present work approximate analyses are made for multilayer composites. The two-flux method is found convenient for layers with optical thicknesses less than about 20. It is joined with the diffusion solution when there is an adjacent optically thick layer. This yields excellent results for two-band spectral calculations in composite layers, including an optically thick layer and isotropic scattering.

Analysis

Two-Flux Method for Radiative Transfer in a Composite of Gray Layers. A composite of semitransparent isotropically scattering layers has convection and incident radiation at each boundary. To develop the two-flux method a composite of three layers with different refractive indices is considered (Fig. 1). The resulting two-flux relations provide a foundation to analyze a larger number of layers with banded spectral properties. Results are validated by comparison with numerical solutions of the radiative transfer equations. The external boundaries and interfaces between layers are assumed diffuse.

The Two-Flux and Energy Equations. The two-flux equations used here correspond to the Milne–Eddington approximation (Siddall, 1972; Siegel and Howell, 1992). A flux quantity G, and the net radiative flux q_r in the x direction, are given by

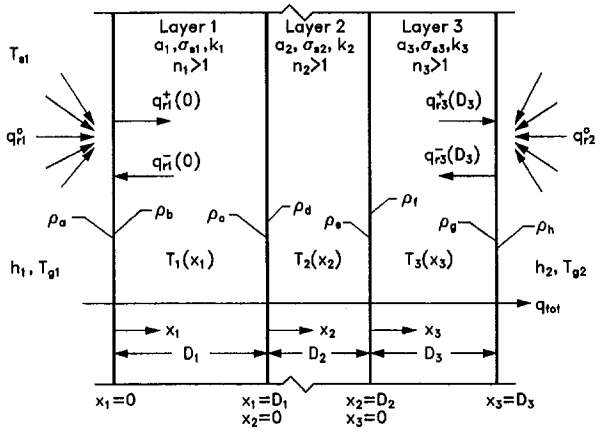

Fig. 1 Geometry and coordinate system for two-flux analysis in a composite of three absorbing, emitting, and scattering semitransparent layers

$G = 2(q_r^+ + q_r^-)$ and $q_r = q_r^+ - q_r^-$ so that $q_r^+ = (1/2)(G/2 + q_r)$ and $q_r^- = (1/2)(G/2 - q_r)$. The two-flux equations are

$$\frac{1}{K}\frac{dq_r}{dx} = (1 - \Omega)[4n^2\sigma T^4(x) - G(x)]; \qquad (1a)$$

$$\frac{1}{K}\frac{dG}{dx} = -3q_r(x) \qquad (1b)$$

For steady-state conditions the heat flow by combined conduction and radiation is constant so,

$$q_{tot} = -k\frac{dT(x)}{dx} + q_r(x) \qquad (2)$$

Equations (1a, b) and (2), subject to boundary and interface conditions, are to be solved for $q_r(x)$, $G(x)$, and $T(x)$.

The $q_r(x)$ in Eq. (2) is eliminated by using Eq. (1b), and the resulting equation is integrated over x in each layer to yield

$$k_jT_j(x_j) = -q_{tot}x_j - \frac{G_j(x_j)}{3K_j} + \mathrm{CON}_j \quad j = 1, 2, 3 \qquad (3)$$

Evaluating Eq. (3) at $x_j = 0$ and $x_j = D_j$ relates q_{tot} and CON_j to the boundary values of T_j and G_j

$$\mathrm{CON}_j = k_jT_j(0) + \frac{G_j(0)}{3K_j}; \qquad (4a)$$

$$q_{tot}D_j = -k_jT_j(D_j) - \frac{G_j(D_j)}{3K_j} + \mathrm{CON}_j \quad j = 1, 2, 3 \qquad (4b)$$

Equations (1a, b) integrated with respect to x_j are used later,

$$q_{rj}(x_j) = q_{rj}(0) + K_j(1 - \Omega_j)\int_0^{x_j}[4n_j^2\sigma T_j^4(x_j^*) - G_j(x_j^*)]dx_j^* \quad j = 1, 2, 3 \qquad (5)$$

$$G_j(x_j) = G_j(0) - 3K_j\int_0^{x_j} q_{rj}(x_j^*)dx_j^* \quad j = 1, 2, 3 \qquad (6)$$

Conditions at External Boundaries. Since a surface does not have any volume for absorption or emission, convection is balanced only by internal heat conduction at each external boundary. Since q_{tot} is constant across the entire composite, it can be expressed at each external boundary as the sum of external convection (which is equal to internal conduction) and internal radiation,

$$q_{tot} = h_1[T_{g1} - T_1(0)] + q_{r1}(0); \quad (7a)$$

$$q_{tot} = h_2[T_3(D_3) - T_{g2}] + q_{r3}(D_3) \quad (7b)$$

At each external boundary the internal radiative flux directed into the layer is,

$$q_{r1}^{+}(0) = (1 - \rho_a)q_{r1}^{0} + \rho_b q_{r1}^{-}(0); \quad (8a)$$

$$q_{r3}^{-}(D_3) = (1 - \rho_h)q_{r2}^{0} + \rho_g q_{r3}^{+}(D_3) \quad (8b)$$

The relations before Eq. (1) are used to eliminate q_{r1}^{+} and q_{r3}^{-} from Eqs. (8a, b) to obtain $G_1(0)$ and $G_3(D_3)$ in terms of the radiative fluxes $q_{r1}(0)$ and $q_{r3}(D_3)$,

$$G_1(0) = 4\frac{1 - \rho_a}{1 - \rho_b}q_{r1}^{0} - 2\frac{1 + \rho_b}{1 - \rho_b}q_{r1}(0); \quad (9a)$$

$$G_3(D_3) = 4\frac{1 - \rho_h}{1 - \rho_g}q_{r2}^{0} + 2\frac{1 + \rho_g}{1 - \rho_g}q_{r3}(D_3) \quad (9b)$$

Relations at Internal Interfaces. At the interface $x_1 = D_1$ ($x_2 = 0$) the q^{+} and q^{-} are related by $q_{r1}^{-}(D_1) = (1 - \rho_d)q_{r2}^{-}(0) + \rho_c q_{r1}^{+}(D_1)$ and there is continuity of radiative flux and temperature so that $q_{r1}(D_1) = q_{r2}(0)$ and $T_1(D_1) = T_2(0)$. By eliminating q^{+} and q^{-} from the interface relation in terms of G and q_r there is obtained for a typical interface,

$$G_2(0) = \frac{1 - \rho_c}{1 - \rho_d}G_1(D_1) - 2\frac{\rho_c + \rho_d}{1 - \rho_d}q_{r1}(D_1) \quad (10)$$

Relations for Additional Quantities. A relation for q_{tot} is now developed. Equation (3) is solved for T_j in each layer at the internal interfaces. Then continuity of temperature is applied to yield at the interfaces,

$$-q_{tot}\frac{D_j}{k_j} - \frac{1}{3}\frac{G_j(D_j)}{k_j K_j} + \frac{CON_j}{k_j} = -\frac{1}{3}\frac{G_{j+1}(0)}{k_{j+1}K_{j+1}} + \frac{CON_{j+1}}{k_{j+1}} \quad j = 1, 2 \quad (11)$$

Equation (11) is written for $j = 1$ and 2, and the two equations are added to eliminate CON_2. Equation (4a) for $j = 1$ and Eq. (4b) for $j = 3$ are respectively combined with Eqs. (7a, b) to eliminate the unknown $T_1(0)$ and $T_3(D_3)$. The resulting two equations are combined with Eq. (11) to eliminate CON_1 and CON_3 and the expression is solved for q_{tot},

$$q_{tot} = \left(\frac{1}{h_1} + \sum_{j=1}^{3}\frac{D_j}{k_j} + \frac{1}{h_2}\right)^{-1}\left\{\sum_{j=1}^{3}\left[\frac{G_j(0) - G_j(D_j)}{3k_j K_j}\right] + T_{g1} - T_{g2} + \frac{q_{r1}(0)}{h_1} + \frac{q_{r3}(D_3)}{h_2}\right\} \quad (12)$$

To obtain the integration constants, Eqs. (4a) and (7a) are combined to eliminate $T_1(0)$ to obtain

$$CON_1 = k_1\left[T_{g1} + \frac{q_{r1}(0) - q_{tot}}{h_1}\right] + \frac{G_1(0)}{3K_1} \quad (13a)$$

Similarly CON_3 and CON_2 are obtained as,

$$CON_3 = q_{tot}D_3 + k_3\left[T_{g2} + \frac{q_{tot} - q_{r3}(D_3)}{h_2}\right] + \frac{G_3(D_3)}{3K_3}; \quad (13b)$$

$$CON_2 = \frac{k_2}{k_1}(CON_1 - q_{tot}D_1) + \frac{k_2}{3}\left[\frac{G_2(0)}{k_2K_2} - \frac{G_1(D_1)}{k_1K_1}\right] \quad (13c)$$

The previous relations are solved for $T_j(x_j)$ and q_{tot} by iteration as in Spuckler and Siegel (1994b).

Two-Flux Method for Two Spectral Bands in Each Layer of a Two-Layer Composite. A two-band calculation in each layer illustrates the spectral application of the two-flux method. S and L designate bands with small and large frequencies. For a quantity such as $G(x, \nu)$ the band notation is $GS(x) = \int_0^{\nu_c} G(x, \nu)d\nu$ and $GL(x) = \int_{\nu_c}^{\infty} G(x, \nu)d\nu$. For a two-band calculation each of Eqs. (9) has a part for each frequency range. For example, Eq. (9a) gives in the small frequency range,

$$\tilde{G}S_1(0) = 4\frac{1 - \rho_a}{1 - \rho_b}\tilde{q}S_{r1}^{0} - 2\frac{1 + \rho_b}{1 - \rho_b}\tilde{q}S_{r1}(0) \quad (14)$$

where the ρ are independent of ν. Similar relations are written for $\tilde{G}L_1(0)$, $\tilde{G}S_2(1)$, and $\tilde{G}L_2(1)$. Equation (12) contains a contribution from each band, so for a two-band two-layer composite

$$q_{tot} = \left(\frac{1}{H_1} + \sum_{j=1}^{2}\frac{1}{N_j} + \frac{1}{H_2}\right)^{-1} \times \left\{\sum_{j=1}^{2}\left[\frac{\tilde{G}S_j(0) - \tilde{G}S_j(1)}{3N_j\kappa_{D_jS}} + \frac{\tilde{G}L_j(0) - \tilde{G}L_j(1)}{3N_j\kappa_{D_jL}}\right] + 1 - t_{g2} + \frac{\tilde{q}S_{r1}(0) + \tilde{q}L_{r1}(0)}{H_1} + \frac{\tilde{q}S_{r2}(1) + \tilde{q}L_{r2}(1)}{H_2}\right\} \quad (15)$$

This also occurs in Eq. (3) for the temperature distribution,

$$t_j(X_j) = \frac{1}{N_j}\left[-\frac{\tilde{G}S_j(X_j)}{3\kappa_{D_jS}} - \frac{\tilde{G}L_j(X_j)}{3\kappa_{D_jL}} - \tilde{q}_{tot}X_j + \tilde{CON}_j\right] \quad j = 1, 2 \quad (16)$$

Equation (5) for the radiative flux is written for each band in each layer. For small frequencies,

$$\tilde{q}S_{rj}(X_j) = \tilde{q}S_{rj}(0) + \kappa_{D_jS}(1 - \Omega_{Sj})\int_0^{X_j}[4n_j^2t_j^4(X_j)FS(X_j) - \tilde{G}S_j(X_j)]dX_j \quad j = 1, 2 \quad (17)$$

The $\tilde{q}L_{rj}(X_j)$ for the large-frequency band is similar. $FS(X_j)$ is the fraction of blackbody emission in the small-frequency range corresponding to the temperature $T_j(x_j) = t_j(X_j)T_{g1}$.

The change in $\tilde{G}$ across the internal interface is written for each band. For example, for the small frequency range, from Eq. (10)

$$\tilde{G}S_2(0) = \frac{1 - \rho_c}{1 - \rho_d}\tilde{G}S_1(1) - 2\frac{\rho_c + \rho_d}{1 - \rho_d}\tilde{q}S_{r1}(1) \quad (18)$$

The integration constant from Eq. (13a) for layer 1 is (similarly for layer 2),

$$\tilde{CON}_1 = N_1\left[1 + \frac{\tilde{q}S_{r1}(0) + \tilde{q}L_{r1}(0) - \tilde{q}_{tot}}{H_1}\right] + \frac{\tilde{G}S_1(0)}{3\kappa_{D_1S}} + \frac{\tilde{G}L_1(0)}{3\kappa_{D_1L}} \quad (19)$$

The solution by iteration follows the same steps as for gray layers except that calculations are required in each band (see Spuckler and Siegel, 1994b).

Two-Layer Solution Using Two-Flux Method in Layer 1 and Diffusion in Layer 2. When the optical thickness of a layer is large, the diffusion method is very useful. A two-layer geometry is considered with $\kappa_D < 20$ in each band of layer 1,

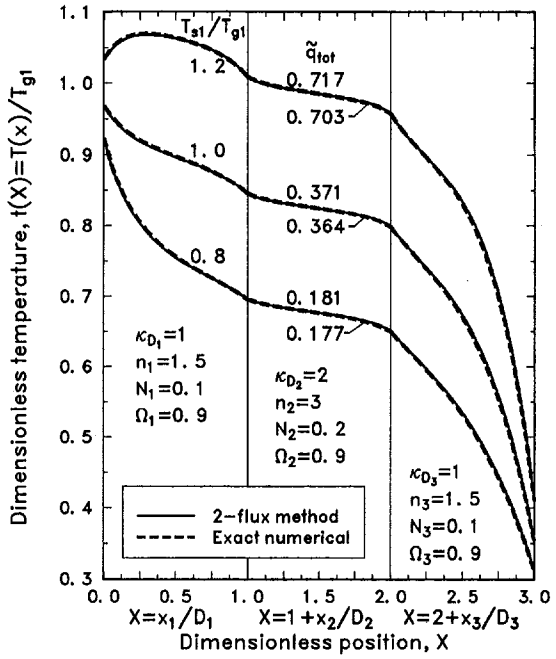

Fig. 2 Comparisons of two-flux results with exact numerical solutions for a composite of three gray layers with scattering: $n_1 = n_3 = 1.5$, $n_2 = 3$, $\tilde{q}^0_{r1} = 0.8^4$, 1, and 1.2^4, $\tilde{q}^0_{r2} = 0.25^4$, $t_{g1} = 1$, $t_{g2} = 0.25$, $H_1 = H_2 = 1$, $N_1 = N_3 = 0.1$, $N_2 = 0.2$, $\Omega_1 = \Omega_2 = \Omega_3 = 0.9$

and with a larger κ_D in layer 2. The two-flux method is used in layer 1 coupled with diffusion in layer 2, which is gray.

The first step in the iterative solution is to use Eq. (14) to calculate $\tilde{G}S_1(0)$ (and similarly $\tilde{G}L_1(0)$) at the outer boundary of layer 1 for each band. For layer 2, $\tilde{q}^-_{r1}(1) = (1 - \rho_c)n_1^2 t_2^4(0) + \rho_c \tilde{q}^+_{r1}(1)$. The relations before Eq. (1) are used to eliminate $\tilde{q}^-$ and $\tilde{q}^+$ to give $\tilde{G}S_1(1)$ as (similarly for $\tilde{G}L_1(1)$),

$$\tilde{G}S_1(1) = 4n_1^2 t_2^4(0) FS[t_2(0)T_{g1}] + 2\frac{1+\rho_c}{1-\rho_c}\tilde{q}S_1(1) \quad (20)$$

where FS is the blackbody fraction that depends on ν_c. The $t_2(0)$ at the interface is to be determined.

Three simultaneous equations are now developed. In a similar manner to Eq. (15), for layer 1,

$$\tilde{q}_{\text{tot}} = \left(\frac{1}{H_1} + \frac{1}{N_1}\right)^{-1}\left[\frac{\tilde{G}S_1(0) - \tilde{G}S_1(1)}{3N_1\kappa_{D_1 S}} + \frac{\tilde{G}L_1(0) - \tilde{G}L_1(1)}{3N_1\kappa_{D_1 L}} + \frac{\tilde{q}S_1(0) + \tilde{q}L_1(0)}{H_1} + 1 - t_2(0)\right] \quad (21a)$$

Combined conduction and radiative diffusion in the second layer gives a relation for $\tilde{q}_{\text{tot}}$ as in Siegel and Spuckler (1994),

$$\tilde{q}_{\text{tot}} = N_2[t_2(0) - t_2(1)] + \frac{4n_2^2}{3\kappa_{D_2}}[t_2^4(0) - t_2^4(1)] \quad (21b)$$

The energy balance at the exterior boundary of layer 2 gives,

$$\tilde{q}_{\text{tot}} = H_2[t_2(1) - t_{g2}] + (1 - \rho_e)n_2^2[t_2^4(1) - \tilde{q}^0_{r2}] \quad (21c)$$

Using Eq. (20) and the similar relation for $\tilde{G}L_1$ as constraints, Eqs. (21a, b, c) are solved simultaneously for $t_2(0)$, $t_2(1)$, and $\tilde{q}_{\text{tot}}$. The temperature distribution in layer 2 is then calculated by solving a local form of Eq. (21b) for $t_2(X_2)$,

$$t_2(X_2) - t_2(1) + \frac{4n_2^2}{3N_2\kappa_{D_2}}[t_2^4(X_2) - t_2^4(1)] = \frac{\tilde{q}_{\text{tot}}(1 - X_2)}{N_2} \quad (22)$$

Results and Discussion

Two-Flux Results for a Composite of Three Gray Layers. Figure 2 shows results for a composite of three gray scattering layers. For validation the results are compared with "exact" numerical solutions using Spuckler and Siegel (1994a) extended to three layers. For $T_{s1}/T_{g1} = 1.2$ the absorption of radiation, combined with the removal of heat by convection at the boundaries, provides a maximum temperature in layer 1. For $T_{s1}/T_{g1} = 1.0$ the gradient is reversed at the hot surface because of cooling by radiation and conduction through the composite to the environment outside of the third layer. For $T_{s1}/T_{g1} = 0.8$ there is radiative cooling at the hot side. The two-flux method yields excellent temperature predictions, and $\tilde{q}_{\text{tot}}$ is predicted within a few percent of those from the exact transfer equations.

Two-Flux Results for a Two-Layer Composite With Two Spectral Bands in Each Layer. In Fig. 3 the absorption coefficient has two bands in each layer: for small ν, $\nu/c_0T_{g1} < 1/4000$, $a_{1S}D_1 = 5$, and $a_{2S}D_2 = 10$, while for large ν, $\nu/c_0T_{g1} > 1/4000$, $a_{1L}D_1 = 0.1$, and $a_{2L}D_2 = 0.2$. The cutoff frequency $\nu_c = c_0T_{g1}/4000$ divides the blackbody spectrum at T_{g1} into approximately two equal parts. By comparison with numerical solutions, the spectral two-flux method in two layers yields excellent results. The effects of varying the hot surrounding temperature are similar to Fig. 2. Comparison with the opaque limit shows that internal radiation has a substantial effect on the temperature distributions.

Two-Layer Composite: Two-Flux Method in Layer 1, Diffusion in Layer 2. To test the two-flux and diffusion solution spectrally, the first layer in Fig. 4 has the same spectral bands

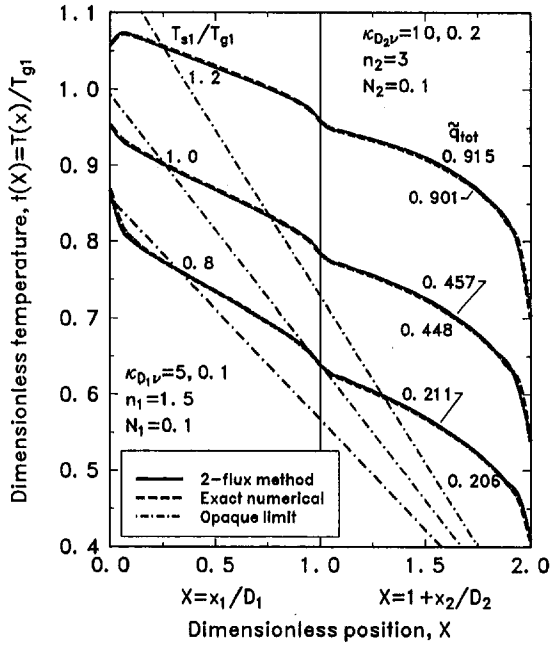

Fig. 3 Comparisons with numerical solutions of two-flux results in a two-layer composite, each layer with two spectral bands. Optical thickness of bands in order of increasing frequency: $a_{1S}D_1 = 5$, $a_{1L}D_1 = 0.1$, $a_{2S}D_2 = 10$, $a_{2L}D_2 = 0.2$, $\nu_c/c_0T_{g1} = 1/4000$; $n_1 = 1.5$, $n_2 = 3$, $\tilde{q}^0_{r1} = 0.8^4$, 1 and 1.2^4, $\tilde{q}^0_{r2} = 0.25^4$, $t_{g1} = 1$, $t_{g2} = 0.25$, $H_1 = H_2 = 1$, $N_1 = N_2 = 0.1$.

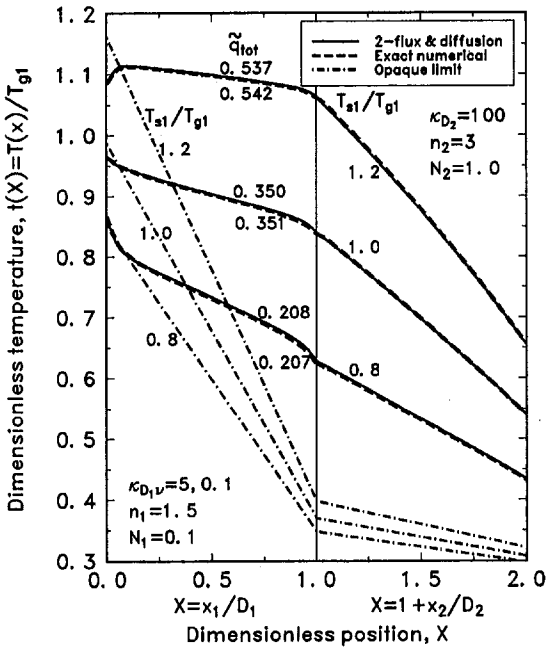

Fig. 4 Comparisons of numerical solutions with approximate temperature distributions from combined two-flux and diffusion method for two-layers: $n_1 = 1.5$, $n_2 = 3$, $\tilde{q}^0_{r1} = 0.8^4$, 1, and 1.2^4, $\tilde{q}^0_{r2} = 0.25^4$, $t_{g1} = 1$, $t_{g2} = 0.25$, $H_1 = H_2 = 1$, $N_1 = 0.1$, $N_2 = 1$. Layer 1 has two bands: $a_{1S}D_1 = 5$, $a_{1L}D_1 = 0.1$ with $\nu_c/c_0T_{g1} = 1/4000$; layer 2 is gray: $a_2D_2 = 100$.

and properties as for Fig. 3, and $a_2D_2 = 100$. For the large optical thickness in layer 2, radiative transmission is diminished and conduction has an important effect so the profiles in the second layer tend to be linear. The two-flux and diffusion results are in excellent agreement with the numerical solutions. This, and the ability of the iterative solutions to converge reasonably well, shows that the two-flux method can be used with good convergence in layers that are not too optically thick ($\kappa_D < \sim 20$), and the solution joined to the diffusion method in an adjacent optically thick layer. The opaque limits show that internal radiation has a large effect even with an optically thick substrate.

Conclusions

Temperature distributions and heat fluxes are predicted in composite semitransparent layers heated or cooled on both sides by radiation and convection. Two approximate methods were used for performing spectral calculations, and the results were validated by comparison with "exact" numerical solutions of the radiative transfer equations. The composite layers have refractive indices larger than one, and isotropic scattering is included. The two-flux method for multilayer composites gave good agreement with numerical solutions for the conditions considered. For a composite with an optically thick layer, the theory was developed to use the diffusion method and join it to the two-flux method in an adjacent layer. Convergence is improved over using the two-flux method in the optically thick layer.

When the hot surroundings are at a different temperature than the gas on the hot side, large temperature gradients can occur near the hot boundary that can cause thermal stresses. If the surroundings are at a higher temperature than the gas on the hot side, the maximum temperature can be within the material rather than at the surface. This is important if the material is operating near its upper temperature limit for adequate strength.

References

Flamant, G., Menigault, T., and Schwander, D., 1988, "Combined Heat Transfer in a Semitransparent Multilayer Packed Bed," ASME JOURNAL OF HEAT TRANSFER, Vol. 110, pp. 463–467.

Gardon, R., 1958, "Calculation of Temperature Distributions in Glass Plates Undergoing Heat-Treatment," *Journal of the American Ceramic Society,* Vol. 41, pp. 200–209.

Siddall, R. G., 1972, "Flux Methods for the Analysis of Radiant Heat Transfer," *Proceedings of the Fourth Symposium on Flames and Industry,* The British Flame Research Committee and The Institute of Fuel, Paper No. 16, pp. 169–177.

Siegel, R., and Howell, J. R., 1992, *Thermal Radiation Heat Transfer,* 3rd ed., Hemisphere, Washington, DC.

Siegel, R., and Spuckler, C. M., 1994, "Approximate Solution Methods for Spectral Radiative Transfer in High Refractive Index Layers," *International Journal of Heat and Mass Transfer,* Vol. 37, Suppl. 1, pp. 403–413.

Spuckler, C. M., and Siegel, R., 1994a, "Refractive Index and Scattering Effects on Radiation in a Semitransparent Laminated Layer," *Journal of Thermophysics and Heat Transfer,* Vol. 8, pp. 193–201.

Spuckler, C. M., and Siegel, R., 1994b, "Two-Flux and Diffusion Methods for Radiative Transfer in Composite Layers," *Heat Transfer With Combined Modes,* ASME HTD-Vol. 299, D. E. Beasley and K. D. Cole, eds., pp. 41–49.

Tremante, A., and Malpica, F., 1994, "Contribution of Thermal Radiation to the Temperature Profile of Ceramic Composite Materials," ASME *Journal of Engineering for Gas Turbines and Power,* Vol. 116, pp. 583–586.

Natural Convection in L Corners With Surface Radiation and Conduction

C. Balaji[1,2] and S. P. Venkateshan[1,3]

Nomenclature

A = aspect ratio = H/d
d = width of the horizontal leg of the L corner, m
H = height of the vertical leg of the L corner, m
k = thermal conductivity, W/mK
N_{RC} = radiation convection interaction parameter = $\sigma T_B^4 d/[k_f(T_B - T_\infty)]$
Nu_C = convective Nusselt number based on H, $-A\,\partial\phi/\partial Y|_{Y=0}$ on the vertical leg; $-A\,\partial\phi/\partial X|_{X=0}$ on the horizontal leg.
Nu_R = radiation Nusselt number = $\varepsilon N_{RC} q_R$
Pr = Prandtl number
q_R = radiative heat flux nondimensionalized with respect to σT_B^4
Ra_H = Rayleigh number based on H
t = thickness of the vertical leg of the L corner
T = temperature, K
x = vertical coordinate, m
X = nondimensional vertical coordinate = x/d
y = horizontal coordinate, m
Y = nondimensional horizontal coordinate = y/d
ε = total hemispherical emissivity of all surfaces
γ = thermal conductance parameter = $(k_f d)/(k_s t)$
ϕ = nondimensional temperature = $(T - T_\infty)/(T_B - T_\infty)$
σ = Stefan–Boltzmann constant = 5.67×10^{-8} W/m^{2}K^4

Subscripts

B = pertains to the horizontal leg of the L corner
C = convective

[1] Heat Transfer and Thermal Power Laboratory, Department of Mechanical Engineering, Indian Institute of Technology, Madras 600 036, India.
[2] Formerly Research Scholar and presently Lecturer, Regional Engineering College, Tiruchirapalli-620 015.
[3] Professor.

Contributed by the Heat Transfer Division of THE AMERICAN SOCIETY OF MECHANICAL ENGINEERS. Manuscript received by the Heat Transfer Division December 1994; revision received June 1995. Keywords: Conjugate Heat Transfer, Natural Convection, Radiation Interactions. Associate Technical Editor: Y. Jaluria.

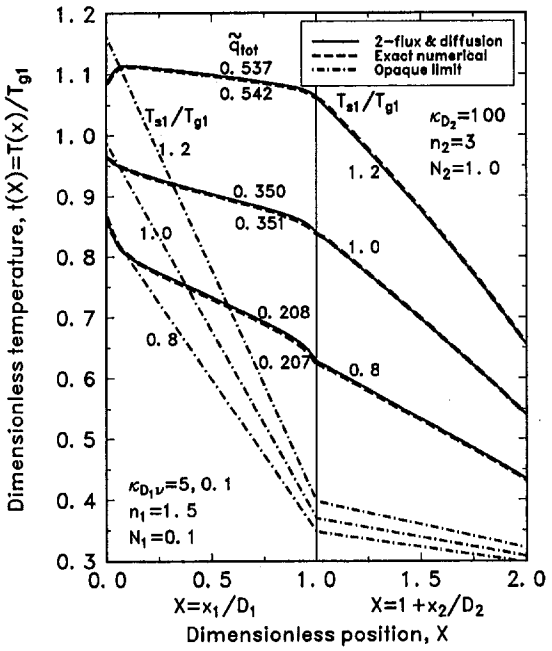

Fig. 4 Comparisons of numerical solutions with approximate temperature distributions from combined two-flux and diffusion method for two-layers: $n_1 = 1.5$, $n_2 = 3$, $\tilde{q}^0_{r1} = 0.8^4$, 1, and 1.2^4, $\tilde{q}^0_{r2} = 0.25^4$, $t_{g1} = 1$, $t_{g2} = 0.25$, $H_1 = H_2 = 1$, $N_1 = 0.1$, $N_2 = 1$. Layer 1 has two bands: $a_{1S}D_1 = 5$, $a_{1L}D_1 = 0.1$ with $\nu_c/c_0T_{g1} = 1/4000$; layer 2 is gray: $a_2D_2 = 100$.

and properties as for Fig. 3, and $a_2D_2 = 100$. For the large optical thickness in layer 2, radiative transmission is diminished and conduction has an important effect so the profiles in the second layer tend to be linear. The two-flux and diffusion results are in excellent agreement with the numerical solutions. This, and the ability of the iterative solutions to converge reasonably well, shows that the two-flux method can be used with good convergence in layers that are not too optically thick ($\kappa_D < \sim 20$), and the solution joined to the diffusion method in an adjacent optically thick layer. The opaque limits show that internal radiation has a large effect even with an optically thick substrate.

Conclusions

Temperature distributions and heat fluxes are predicted in composite semitransparent layers heated or cooled on both sides by radiation and convection. Two approximate methods were used for performing spectral calculations, and the results were validated by comparison with "exact" numerical solutions of the radiative transfer equations. The composite layers have refractive indices larger than one, and isotropic scattering is included. The two-flux method for multilayer composites gave good agreement with numerical solutions for the conditions considered. For a composite with an optically thick layer, the theory was developed to use the diffusion method and join it to the two-flux method in an adjacent layer. Convergence is improved over using the two-flux method in the optically thick layer.

When the hot surroundings are at a different temperature than the gas on the hot side, large temperature gradients can occur near the hot boundary that can cause thermal stresses. If the surroundings are at a higher temperature than the gas on the hot side, the maximum temperature can be within the material rather than at the surface. This is important if the material is operating near its upper temperature limit for adequate strength.

References

Flamant, G., Menigault, T., and Schwander, D., 1988, "Combined Heat Transfer in a Semitransparent Multilayer Packed Bed," ASME JOURNAL OF HEAT TRANSFER, Vol. 110, pp. 463–467.

Gardon, R., 1958, "Calculation of Temperature Distributions in Glass Plates Undergoing Heat-Treatment," *Journal of the American Ceramic Society,* Vol. 41, pp. 200–209.

Siddall, R. G., 1972, "Flux Methods for the Analysis of Radiant Heat Transfer," *Proceedings of the Fourth Symposium on Flames and Industry,* The British Flame Research Committee and The Institute of Fuel, Paper No. 16, pp. 169–177.

Siegel, R., and Howell, J. R., 1992, *Thermal Radiation Heat Transfer,* 3rd ed., Hemisphere, Washington, DC.

Siegel, R., and Spuckler, C. M., 1994, "Approximate Solution Methods for Spectral Radiative Transfer in High Refractive Index Layers," *International Journal of Heat and Mass Transfer,* Vol. 37, Suppl. 1, pp. 403–413.

Spuckler, C. M., and Siegel, R., 1994a, "Refractive Index and Scattering Effects on Radiation in a Semitransparent Laminated Layer," *Journal of Thermophysics and Heat Transfer,* Vol. 8, pp. 193–201.

Spuckler, C. M., and Siegel, R., 1994b, "Two-Flux and Diffusion Methods for Radiative Transfer in Composite Layers," *Heat Transfer With Combined Modes,* ASME HTD-Vol. 299, D. E. Beasley and K. D. Cole, eds., pp. 41–49.

Tremante, A., and Malpica, F., 1994, "Contribution of Thermal Radiation to the Temperature Profile of Ceramic Composite Materials," ASME *Journal of Engineering for Gas Turbines and Power,* Vol. 116, pp. 583–586.

Natural Convection in L Corners With Surface Radiation and Conduction

C. Balaji[1,2] and S. P. Venkateshan[1,3]

Nomenclature

A = aspect ratio = H/d
d = width of the horizontal leg of the L corner, m
H = height of the vertical leg of the L corner, m
k = thermal conductivity, W/mK
N_{RC} = radiation convection interaction parameter = $\sigma T_B^4 d/[k_f(T_B - T_\infty)]$
Nu_C = convective Nusselt number based on H, $-A\,\partial\phi/\partial Y|_{Y=0}$ on the vertical leg; $-A\,\partial\phi/\partial X|_{X=0}$ on the horizontal leg.
Nu_R = radiation Nusselt number = $\varepsilon N_{RC} q_R$
Pr = Prandtl number
q_R = radiative heat flux nondimensionalized with respect to σT_B^4
Ra_H = Rayleigh number based on H
t = thickness of the vertical leg of the L corner
T = temperature, K
x = vertical coordinate, m
X = nondimensional vertical coordinate = x/d
y = horizontal coordinate, m
Y = nondimensional horizontal coordinate = y/d
ε = total hemispherical emissivity of all surfaces
γ = thermal conductance parameter = $(k_f d)/(k_s t)$
ϕ = nondimensional temperature = $(T - T_\infty)/(T_B - T_\infty)$
σ = Stefan–Boltzmann constant = 5.67×10^{-8} W/m^{2}K^4

Subscripts

B = pertains to the horizontal leg of the L corner
C = convective

[1] Heat Transfer and Thermal Power Laboratory, Department of Mechanical Engineering, Indian Institute of Technology, Madras 600 036, India.
[2] Formerly Research Scholar and presently Lecturer, Regional Engineering College, Tiruchirapalli-620 015.
[3] Professor.

Contributed by the Heat Transfer Division of THE AMERICAN SOCIETY OF MECHANICAL ENGINEERS. Manuscript received by the Heat Transfer Division December 1994; revision received June 1995. Keywords: Conjugate Heat Transfer, Natural Convection, Radiation Interactions. Associate Technical Editor: Y. Jaluria.

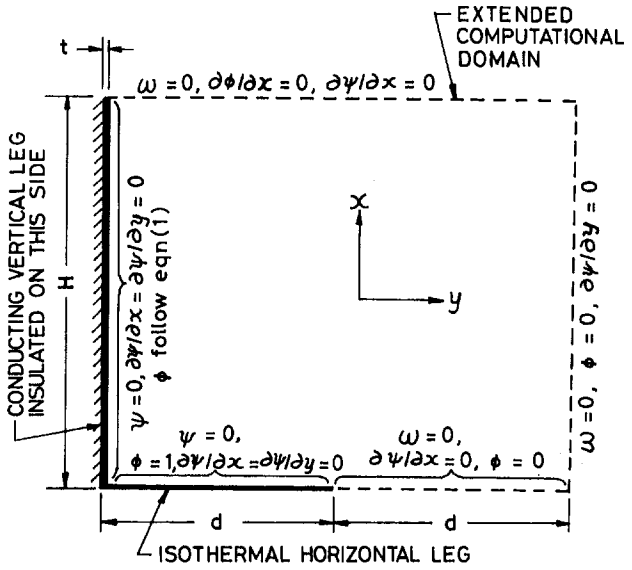

Fig. 1 Schematic of the geometry of the L-shaped corner with the boundary conditions specified at all the boundaries

f = pertaining to the fluid
R = radiative
S = pertaining to the wall material
∞ = ambient

Superscript

$^-$ = signifies the space-averaged value

1 Introduction

Natural convection in enclosed spaces has attracted attention because of its many applications, such as in cooling of electronic equipment and packages. An L corner is an example of a partially enclosed space (Fig. 1). In its most general form, the vertical leg forms a nonisothermal surface whose temperature variation is determined by an interplay of conduction within it and free convection and radiation from the surface. The problem is one of conjugate nature and hence is complex.

The L corner has been studied, in its less general forms, previously by several authors. van Leeuwan et al. (1971) studied a downward-facing L corner (the vertical leg of the L is mounted below the horizontal leg of the L) by anemometry and showed that the "chimney effect" was manifested as an increase in the velocity near the corner, compared to that at the top of a free-standing vertical surface, under similar conditions. Rodigheiro and de Socio (1983) performed experiments in air for the case of an L corner with adiabatic horizontal leg and isothermal vertical leg. Later Angirasa and Mahajan (1993) studied the same case, in its two-dimensional form, by a numerical method based on finite differences. Investigations in related areas like the interaction of natural convection wakes from two line heat sources was considered by Jaluria (1985). Free convection from three-dimensional corners was studied by Riley and Poots (1972) and Kim and Kim (1988) using the method of matched asymptotic expansions. Kim et al. (1991) extended the earlier work of Kim and Kim to corners whose angle was different from 90 deg. In all these references radiation has been ignored.

However, Rammohan Rao (1992) studied the performance of a single fin experimentally, including the effect of surface radiation. Experiments were limited to short depths of the fin and base and hence the flow was expected to be three dimensional. A problem of related interest, the combined conduction, convection, and radiation in a closed cavity, was studied by Kim and Viskanta (1985). The present study is a two-dimensional counterpart of the work of Rammohan Rao (1992) and is more general than the earlier works in this genre.

2 Mathematical Formulation

The details of the problem geometry and the boundary conditions are given in Fig. 1. The vertical wall (the vertical leg) is of finite thermal conductivity and loses heat by free convection and radiation from one face while the other face is insulated. The horizontal leg (the base) is at a uniform temperature T_B while the ambient is at a lower temperature T_∞. Under the Boussinesq approximation, the governing equations for steady, two-dimensional, laminar, incompressible, constant property fluid flow in the vorticity-stream function form are available in earlier works (as for example Balaji and Venkateshan, 1993). Flow boundary conditions on the open boundaries have been discussed by Roache (1982) and Angirasa and Mahajan (1993). The extended computational domain shown in Fig. 1 was essential to mitigate the effect of the boundary conditions that are specified at the free boundaries in an approximate way.

The thermal conditions along the hot nonisothermal vertical leg introduces conjugateness to the problem. Making a fin-type analysis for the thin vertical leg subject to a one-dimensional temperature field in the x direction, the following nondimensional equation results:

$$\frac{\partial^2 \phi}{\partial X^2} = -\gamma \frac{\partial \phi}{\partial Y} + \varepsilon \gamma N_{RC} q_R \qquad (1)$$

The dimensionless thermal conductivity parameter γ is the ratio of fluid conductance to the solid conductance. For $\varepsilon = 0$ and $\gamma \to 0$, the solid conductance far exceeds the fluid conductance and the wall tends to become isothermal. For $\varepsilon = 0$ and $\gamma \to \infty$ the wall becomes an adiabatic wall. Only when γ is finite is the conjugate nature of the wall manifest. Additionally when $\varepsilon \neq 0$ there is interaction among the three modes of heat transfer.

3 Method of Solution

The governing equations subject to the boundary conditions were solved using a finite volume method based on Gosman et al. (1969). Upwinding was used for the convective terms to ensure numerical stability and convergence. A 61×61 uniform grid was used with the horizontal domain extended to a distance equal to the width of the horizontal leg. Radiation was handled by the standard radiosity irradiation method with the needed view factors evaluated by the crossed string method (Hottel and Sarofim, 1967). Details of the procedure are available elsewhere (Balaji, 1994). The iterations were continued until the temperatures at all 3721 nodes converged to better than 0.1 percent, thus guaranteeing the convergence of Nusselt numbers to within 1.5 percent.

4 Results and Discussion

Preliminaries. For validating the code used in the present study, the problem of an L-shaped corner with isothermal vertical leg and adiabatic horizontal leg was solved for a few representative Rayleigh numbers, with $\varepsilon = 0$. The heat transfer from the vertical leg correlated as $\overline{\mathrm{Nu}}_C = 0.293\ \mathrm{Ra}_H^{0.291}$. This result is compared with the experimental results of Rodighiero and de Socio (1983) as well as the numerical results of Angirasa and Mahajan (1993). The agreement among the results can be termed very good (Fig. 2).

In order to choose the number of grids, a grid dependence study was made for the conjugate problem (but with no radiation) for a typical set of parameters given by $\mathrm{Ra}_H = 2 \times 10^6$, $\mathrm{Pr} = 0.71$, and $\gamma = 0.005$. Results of this study, shown in Table 1, indicate that 61×61 grid pattern is adequate. All calculations reported here were, hence, based on a 61×61 grid system.

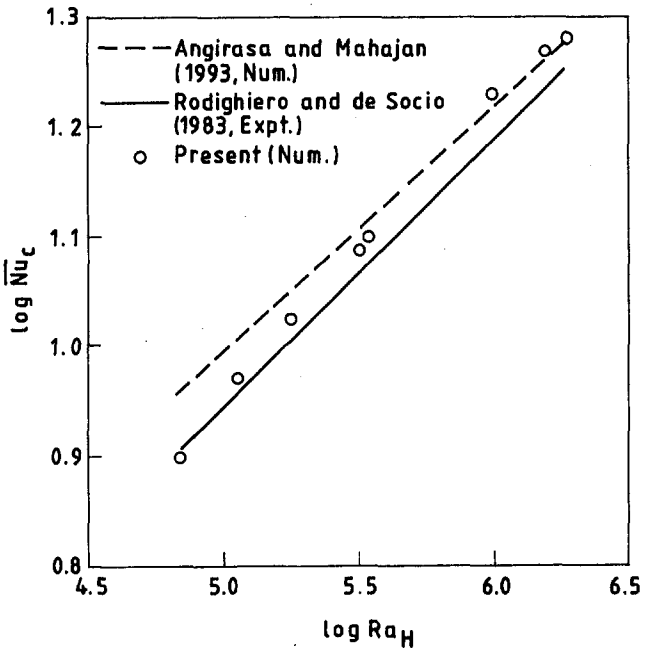

Fig. 2 Comparison of the present numerical results with the previous experimental as well as numerical results for an L corner with isothermal vertical leg and an adiabatic horizontal leg, in the absence of radiation

Flow and Heat Transfer Characteristics. Calculations were performed to cover the range of parameters shown in Table 2. The γ value range covers the commonly used wall materials like aluminum, brass, and steel when the thickness ranges between 0.5 and 1.5 mm. The fluid is air, with Pr = 0.71.

Typical results for the case with no radiation are presented first. Figure 3 shows the temperature and Nusselt number distributions along the vertical leg for two different γ values. It is seen that the average Nusselt number, as expected, decreases with an increase in γ. The temperature variation is also, as expected, more severe when γ is increased. Typically, the Nusselt number shows a peak at around $H/3$ above the horizontal leg. Such a peak was observed in the experiments of Rammohan Rao (1992) also. Since the boundary layer starts growing from the edge of the horizontal leg itself, the Nusselt number attains a low value at the corner between the horizontal and vertical legs. At points beyond the peak (i.e., for $x > H/3$) the Nusselt number variation is akin to that over a vertical surface. The temperature at the tip of the vertical leg could be smaller by as much as 20°C compared to the temperature of the horizontal leg. Hence the coupled analysis undertaken here is indeed necessary to bring out all the features.

Turning attention to the case where radiation also is important, Fig. 4 compares the Nusselt number distribution on the vertical leg for the case of a black wall with that of a wall without radiation. It is apparent that the radiation interaction is not very severe for this problem, even though the radiation contribution to heat transfer itself is very significant. Typically, when $Ra_H = 4 \times 10^6$, $\varepsilon = 1$, $T_R = 0.8$, and $\gamma = 0.035$, the ratio of radiation heat transfer to the total heat transfer (for the vertical leg as well as the horizontal leg of the L) is 0.49.

Table 1 Results of the grid dependence study: $\gamma = 0.005$, $Ra_H = 2 \times 10^6$, Pr = 0.71, $\epsilon = 0$

Grid	$\overline{Nu}_C$
41 × 41	15.10
51 × 51	14.92
61 × 61	14.66
71 × 71	14.70

Table 2 Range of parameters used in the present study

$0.005 \le \gamma \le 0.035$
$5 \times 10^5 \le Ra_H \le 5 \times 10^7$
$1 \le A \le 2$
Pr = 0.71, held constant

Streamline patterns (not presented here because of space limitations) show that there is a significant amount of entrainment of the fluid from the bottom, which is open beyond the horizontal leg. Thus the extended domain used in the present study is essential to include this feature. In the earlier work of Angirasa and Mahajan (1993), with the horizontal wall adiabatic, the entrainment from below was not very significant for similar aspect ratios (1-2 in the present study).

Correlations. Based on detailed calculations for the range of parameters given in Table 2, heat transfer results have been cast in the form of useful correlations. Separate correlations are given for the vertical and the horizontal legs, and, in turn, for the convective and radiative heat transfer rates.

Vertical Leg

$$\overline{Nu}_C = 0.226 Ra_H^{0.291}(1 - 8.03\gamma) \times (1 + \varepsilon)^{-0.202}[N_{RC}/(N_{RC} + 1)]^{-1.06} \quad (2)$$

$$\overline{Nu}_R = 0.516\varepsilon^{0.841}(1 - T_R^4)^{0.672} N_{RC}^{0.872} A^{0.889}(\gamma + 1)^{-2.56} \quad (3)$$

Horizontal Leg (Base)

$$\overline{Nu}_C = 0.586 Ra_H^{0.204}\gamma^{-0.001} \quad (4)$$

$$\overline{Nu}_R = 0.336\varepsilon^{0.813}(1 - T_R^4)^{0.966} N_{RC}^{0.998} A^{0.954}(\gamma + 1)^{0.528} \quad (5)$$

These correlations, when plotted on a parity plot, showed the maximum deviation to be limited to about ±4 percent. The presence of radiation and thermal conductivity parameters in the convective Nusselt number correlations indicate interaction between radiation, conduction, and convection. However, radiation is affected to a significant extent by wall conduction and not by convection. The parameter γ brings in the effect of the temperature variation along the vertical leg. As γ increases, the Nusselt number tends to decrease, as expected. The convective heat transfer from the horizontal leg is not significantly affected

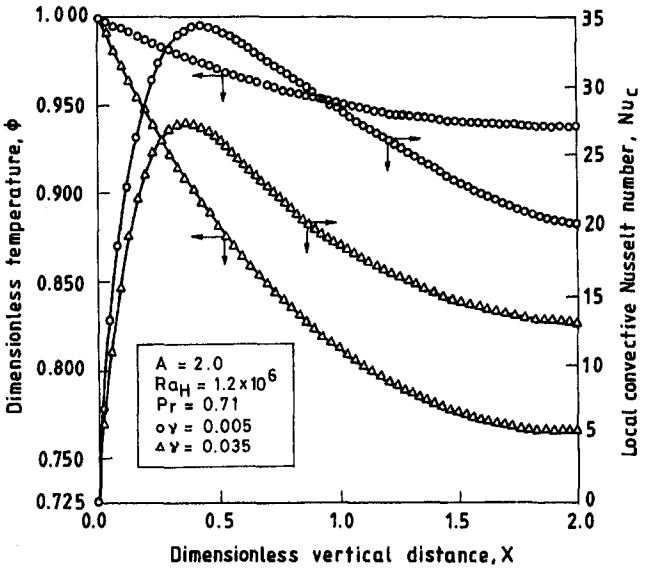

Fig. 3 Temperature and convective Nusselt number distributions over the vertical leg for no radiation and two wall materials ($t = 7.5 \times 10^{-4}$ m, $\varepsilon = 0$)

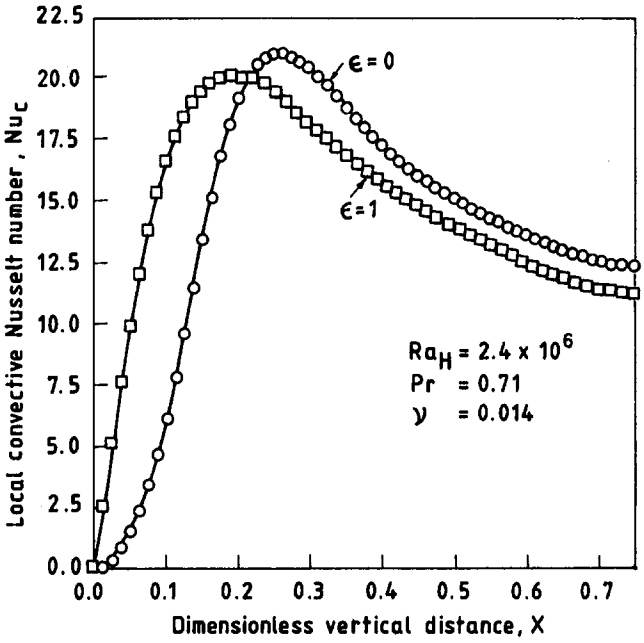

Fig. 4 Convective Nusselt number distributions over the vertical leg compared for $\epsilon = 0$ and $\epsilon = 1$

by γ since it is specified to be isothermal. The effect of γ on convective heat transfer from the vertical leg is quite severe, with a drop of 28 percent in Nu_C occurring when γ changes from the lowest to the highest value used here. In the radiative heat transfer correlations the N_{RC} as well as $(1 - T_R^4)$ terms have an exponent close to unity in the case of the isothermal horizontal leg. The aspect ratio does not affect the convective heat transfer in an explicit way. Since N_{RC} involves d and both Ra_H and $\overline{Nu}_C$ are based on H, the aspect ratio is implicitly present in the correlations for convective heat transfer. However, radiation heat transfer has an explicit dependence on A, as expected.

5 Conclusions

A numerical investigation of conjugate natural convection in L corners has been carried out. Correlations have been presented for the convective and radiative heat transfer rates based on a large number of calculations. The effect of finite thermal conductivity of the vertical leg has been explicitly brought out. The heat transfer from the horizontal isothermal leg is not affected by the thermal conductivity of the vertical leg. Comparisons with experiments show that the two-dimensional model is quite adequate to explain the results.

References

Angirasa, D., and Mahajan, R. L., 1993, "Natural Convection From L-Shaped Corners With Adiabatic and Cold Isothermal Horizontal Walls," ASME JOURNAL OF HEAT TRANSFER, Vol. 115, pp. 149–157.

Balaji, C., and Venkateshan, S. P., 1993, "Interaction of Surface Radiation With Free Convection in a Square Cavity," *Int. J Heat and Fluid Flow,* Vol. 14, pp. 260–267.

Balaji, C., 1994, "Laminar Free Convection With Conduction and Surface Radiation in Open and Closed Cavities," Ph.D. Thesis, Department of Mechanical Engineering, Indian Institute of Technology, Madras, India.

Gosman, A. D., Pun, W. M., Runchal, A. K., Spalding, D. B., and Wolfshtein, M., 1969, *Heat and Mass Transfer in Recirculating Flows,* Academic Press, London.

Hottel, H. C., and Sarofim, A. F., 1967, *Radiative Heat Transfer,* McGraw-Hill, New York.

Jaluria, Y., 1985, "Interaction of Natural Convection Wakes Arising From Thermal Sources on a Vertical Surface," ASME JOURNAL OF HEAT TRANSFER, Vol. 107, pp. 883–892.

Kim, D. M., and Viskanta, R., 1985, "Effect of Wall Conduction on Natural Convection Heat Transfer in a Square Enclosure," ASME JOURNAL OF HEAT TRANSFER, Vol. 107, pp. 139–146.

Kim, M. H., and Kim, M. U., 1988, "Natural Convection Near a Rectangular Corner," *Int. J Heat Mass Transfer,* Vol. 31, pp. 1357–1364.

Kim, M. H., Kim, M. U., and Choi, D. H., 1991, "Natural Convection Near a Vertical Corner of an Arbitrary Angle," *Int. J. Heat Mass Transfer,* Vol. 34, pp. 1327–1336.

Rammohan Rao, V., 1992, "Interferometric Study of Interaction Between Radiation and Free Convection in Fins and Fin Arrays," Ph.D. thesis, Department of Mechanical Engineering, Indian Institute of Technology, Madras, India.

Riley, D. S., and Poots, G., 1972, "Thermal Convection in a Heated Vertical Corner," *Quart. J. Mech. Appl. Math.,* Vol. 25, pp. 401–421.

Roache, P. J., 1982, *Computational Fluid Dynamics,* Hermosa, Albuquerque, NM.

Rodigheiro, C., and de Socio, L. M., 1983, "Some Aspects of Natural Convection in a Corner," ASME JOURNAL OF HEAT TRANSFER, Vol. 105, pp. 212–214.

van Leeuwan, J. H., Looman, C., and Schenk, J., 1971, "Experimental Study of Velocity and Temperature Distributions for Free Convection in a Corner," *Int. J. Heat Mass Transfer,* Vol. 14, pp. 561–564.

Radiative Heat Transfer Calculations in Three-Dimensional Complex Geometries

W. M. G. Malalasekera[1,2] and E. H. James[1]

Introduction

Many practical situations involving radiative heat transfer occur where the geometry is quite complex. Such examples include building configurations, complex furnaces, combustion chambers in internal combustion engines, gas turbine and pulse combustion systems, and many others. These geometries are invariably of irregular shape and require the adoption of radiative heat transfer techniques that are suitable for the modeling of such three-dimensional complex geometries.

The Discrete Transfer Method of Lockwood and Shah (1981) was originally developed for cylindrical and Cartesian geometries. It is a flexible method and has been shown to provide accurate results in these situations (Lockwood and Shah, 1981; Carvalho et al., 1991). Since the method is based on a ray-tracing technique, it is independent of the coordinate system and is applicable therefore in the nonorthogonal grid systems used to model complex geometries. Malalasekera and Lockwood (1991) used the Discrete Transfer Method in conjunction with a cell-blocking procedure based on Cartesian coordinates to model combustion and radiative heat transfer in a complex three-dimensional tunnel geometry. Additionally, Meng et al. (1993) have illustrated the application of the Discrete Transfer Method to two-dimensional irregular geometries using a finite element formulation. Although the generality of the method has been well noted previously (Lockwood and Shah, 1981; Carvalho et al., 1991), its application in three-dimensional, general, complex geometries involving emitting/absorbing media has not been reported to the authors' knowledge. This technical note describes how this may be achieved in nonorthogonal grid systems. It is particularly appropriate and advantageous since the same mesh can be used for the radiative heat transfer calculations as that which could be used if Computational Fluid Dynamics (CFD) methods based on nonorthogonal, body-fitted

[1] Department of Mechanical Engineering, Loughborough University of Technology, Loughborough, Leicestershire LE11 3TU, United Kingdom.

[2] Mem. ASME.

Contributed by the Heat Transfer Division of THE AMERICAN SOCIETY OF MECHANICAL ENGINEERS. Manuscript received by the Heat Transfer Division February 1995; revision received August 1995. Keywords: Furnaces and Combustors, Numerical Methods, Radiation. Associate Technical Editor: M. F. Modest.

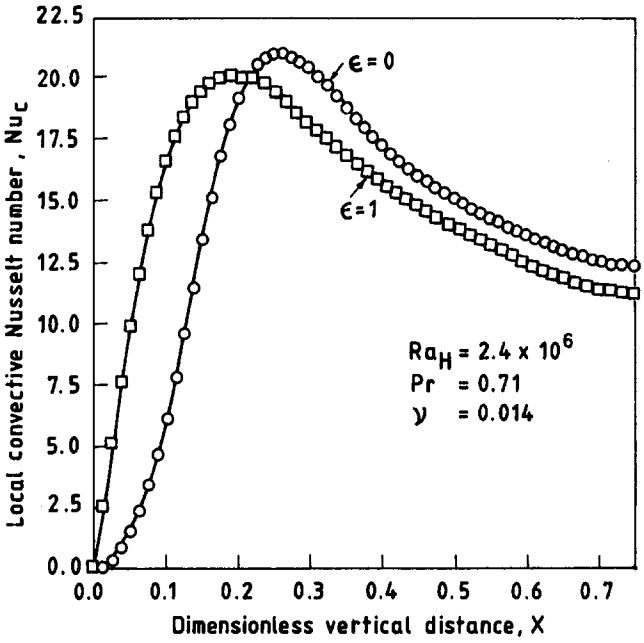

Fig. 4 Convective Nusselt number distributions over the vertical leg compared for $\epsilon = 0$ and $\epsilon = 1$

by γ since it is specified to be isothermal. The effect of γ on convective heat transfer from the vertical leg is quite severe, with a drop of 28 percent in Nu_C occurring when γ changes from the lowest to the highest value used here. In the radiative heat transfer correlations the N_{RC} as well as $(1 - T_R^4)$ terms have an exponent close to unity in the case of the isothermal horizontal leg. The aspect ratio does not affect the convective heat transfer in an explicit way. Since N_{RC} involves d and both Ra_H and $\overline{Nu}_C$ are based on H, the aspect ratio is implicitly present in the correlations for convective heat transfer. However, radiation heat transfer has an explicit dependence on A, as expected.

5 Conclusions

A numerical investigation of conjugate natural convection in L corners has been carried out. Correlations have been presented for the convective and radiative heat transfer rates based on a large number of calculations. The effect of finite thermal conductivity of the vertical leg has been explicitly brought out. The heat transfer from the horizontal isothermal leg is not affected by the thermal conductivity of the vertical leg. Comparisons with experiments show that the two-dimensional model is quite adequate to explain the results.

References

Angirasa, D., and Mahajan, R. L., 1993, "Natural Convection From L-Shaped Corners With Adiabatic and Cold Isothermal Horizontal Walls," ASME JOURNAL OF HEAT TRANSFER, Vol. 115, pp. 149–157.

Balaji, C., and Venkateshan, S. P., 1993, "Interaction of Surface Radiation With Free Convection in a Square Cavity," *Int. J Heat and Fluid Flow,* Vol. 14, pp. 260–267.

Balaji, C., 1994, "Laminar Free Convection With Conduction and Surface Radiation in Open and Closed Cavities," Ph.D. Thesis, Department of Mechanical Engineering, Indian Institute of Technology, Madras, India.

Gosman, A. D., Pun, W. M., Runchal, A. K., Spalding, D. B., and Wolfshtein, M., 1969, *Heat and Mass Transfer in Recirculating Flows,* Academic Press, London.

Hottel, H. C., and Sarofim, A. F., 1967, *Radiative Heat Transfer,* McGraw-Hill, New York.

Jaluria, Y., 1985, "Interaction of Natural Convection Wakes Arising From Thermal Sources on a Vertical Surface," ASME JOURNAL OF HEAT TRANSFER, Vol. 107, pp. 883–892.

Kim, D. M., and Viskanta, R., 1985, "Effect of Wall Conduction on Natural Convection Heat Transfer in a Square Enclosure," ASME JOURNAL OF HEAT TRANSFER, Vol. 107, pp. 139–146.

Kim, M. H., and Kim, M. U., 1988, "Natural Convection Near a Rectangular Corner," *Int. J Heat Mass Transfer,* Vol. 31, pp. 1357–1364.

Kim, M. H., Kim, M. U., and Choi, D. H., 1991, "Natural Convection Near a Vertical Corner of an Arbitrary Angle," *Int. J. Heat Mass Transfer,* Vol. 34, pp. 1327–1336.

Rammohan Rao, V., 1992, "Interferometric Study of Interaction Between Radiation and Free Convection in Fins and Fin Arrays," Ph.D. thesis, Department of Mechanical Engineering, Indian Institute of Technology, Madras, India.

Riley, D. S., and Poots, G., 1972, "Thermal Convection in a Heated Vertical Corner," *Quart. J. Mech. Appl. Math.,* Vol. 25, pp. 401–421.

Roache, P. J., 1982, *Computational Fluid Dynamics,* Hermosa, Albuquerque, NM.

Rodigheiro, C., and de Socio, L. M., 1983, "Some Aspects of Natural Convection in a Corner," ASME JOURNAL OF HEAT TRANSFER, Vol. 105, pp. 212–214.

van Leeuwan, J. H., Looman, C., and Schenk, J., 1971, "Experimental Study of Velocity and Temperature Distributions for Free Convection in a Corner," *Int. J. Heat Mass Transfer,* Vol. 14, pp. 561–564.

Radiative Heat Transfer Calculations in Three-Dimensional Complex Geometries

W. M. G. Malalasekera[1,2] and E. H. James[1]

Introduction

Many practical situations involving radiative heat transfer occur where the geometry is quite complex. Such examples include building configurations, complex furnaces, combustion chambers in internal combustion engines, gas turbine and pulse combustion systems, and many others. These geometries are invariably of irregular shape and require the adoption of radiative heat transfer techniques that are suitable for the modeling of such three-dimensional complex geometries.

The Discrete Transfer Method of Lockwood and Shah (1981) was originally developed for cylindrical and Cartesian geometries. It is a flexible method and has been shown to provide accurate results in these situations (Lockwood and Shah, 1981; Carvalho et al., 1991). Since the method is based on a ray-tracing technique, it is independent of the coordinate system and is applicable therefore in the nonorthogonal grid systems used to model complex geometries. Malalasekera and Lockwood (1991) used the Discrete Transfer Method in conjunction with a cell-blocking procedure based on Cartesian coordinates to model combustion and radiative heat transfer in a complex three-dimensional tunnel geometry. Additionally, Meng et al. (1993) have illustrated the application of the Discrete Transfer Method to two-dimensional irregular geometries using a finite element formulation. Although the generality of the method has been well noted previously (Lockwood and Shah, 1981; Carvalho et al., 1991), its application in three-dimensional, general, complex geometries involving emitting/absorbing media has not been reported to the authors' knowledge. This technical note describes how this may be achieved in nonorthogonal grid systems. It is particularly appropriate and advantageous since the same mesh can be used for the radiative heat transfer calculations as that which could be used if Computational Fluid Dynamics (CFD) methods based on nonorthogonal, body-fitted

[1] Department of Mechanical Engineering, Loughborough University of Technology, Loughborough, Leicestershire LE11 3TU, United Kingdom.

[2] Mem. ASME.

Contributed by the Heat Transfer Division of THE AMERICAN SOCIETY OF MECHANICAL ENGINEERS. Manuscript received by the Heat Transfer Division February 1995; revision received August 1995. Keywords: Furnaces and Combustors, Numerical Methods, Radiation. Associate Technical Editor: M. F. Modest.

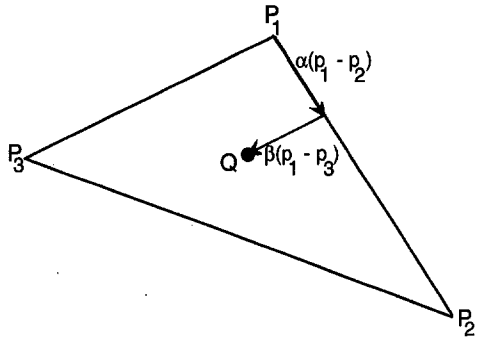

Fig. 1 Parametric representation of the point Q

coordinates systems were to be applied simultaneously to predict flow and heat transfer in such complex geometric situations.

Discrete Transfer Method

General Features. Thermal radiation is governed by the fundamental transfer equation (Lockwood and Shah, 1981):

$$\frac{dI}{ds} = -(K_g + K_s)I + \frac{K_g E_g}{\pi} + K_s\left\{\frac{1}{4\pi}\int p(\Omega, \Omega')I(\Omega')d\Omega'\right\} \quad (1)$$

where I is the radiation intensity in the direction Ω, s is distance in that direction, E_g is the black body emissive power of gas, K_g is the absorption coefficient, K_s is the scattering coefficient, and $p(\Omega, \Omega')$ is the probability of radiation traveling in the direction Ω' being scattered into the direction Ω.

We may define:

$$E' \equiv \frac{K_g(E_g/\pi) + (K_s/4\pi)\int_{4\pi} p(\Omega, \Omega')I(\Omega')d\Omega'}{K_g + K_s} \quad (2)$$

and

$$s' \equiv (K_g + K_s)s \quad (3)$$

so that substitution into Eq. (1) then gives

$$\frac{dI}{ds'} = -I + E' \quad (4)$$

Integration of Eq. (4) over the ray path across a specified control volume gives

$$I_{n+1} = E'(1 - e^{-\delta s'}) + I_n e^{-\delta s'} \quad (5)$$

where n and $n + 1$ designate successive locations separated by $\delta s \equiv \delta s'/(K_g + K_s)$. E' is presumed constant over this interval. The Discrete Transfer Method is based on a ray tracing procedure. The directions of the rays are specified in advance and the rays can be defined by azimuthal angles θ and ϕ at the wall locations. They are traced through the control volumes until a wall is reached. Equation (5) is used to calculate the resultant intensity due to the surrounding surfaces and the emitting/absorbing media along chosen rays converging to selected points on wall boundaries.

Ray Polygon Intersection Algorithm. The derivation of the method described above is independent of the orientation and location of the wall cells or control volumes. The intersecting point of a ray and a control volume face can be found by solving the vector equations of the plane (control volume face) and the line (the ray). Researchers working in the computer graphics field (Glassner, 1990; Arvo, 1991) have developed a number of techniques that are potentially useful for radiation ray tracing calculational purposes. The method described below (from Badouel, 1991) was found to be fast and computationally economical for determining whether the intersection point lies inside or outside the control volume face. Hence, it has been used for all the calculations presented in this paper. The polygon, defining the face, is divided into triangles. For a quadrilateral mesh, a face is divided into two triangles. One triangle at a time is considered in the algorithm. The point Q (see Fig. 1) is given by

$$(\mathbf{p}_1 - \mathbf{q}) = \alpha(\mathbf{p}_1 - \mathbf{p}_2) + \beta(\mathbf{p}_1 - \mathbf{p}_3) \quad (6)$$

The point Q will be inside a triangle if

$$\alpha \geq 0, \beta \geq 0, \quad \text{and} \quad \alpha + \beta \leq 1 \quad (7)$$

A unique solution exists for this system given by Eq. (6). To reduce the system, the polygon can be projected to one of the primary planes, either xy, xz, or yz. If the polygon is perpendicular to one of these planes, its projection onto the plane will be a single line. To avoid this problem, and to make sure that the projection is as large as possible, the dominant axis of the normal vector is found and the plane perpendicular to that axis is used. This is conducted as set out by Snyder and Barr (1987). Equation (6) then reduces to

$$\begin{cases} u_1 = \alpha u_2 + \beta u_3 \\ v_1 = \alpha v_2 + \beta v_3 \end{cases} \quad (8)$$

where u_1, u_2, u_3 and v_1, v_2 and v_3 are projections onto the primary plane (see Badouel, 1991). This set can be easily solved to obtain the values of α and β. The values of α and β determine whether the point of intersection is inside or outside the triangle according to condition (7). In general, the fourth vertex need not be co-planar with other vertices as the algorithm uses two triangles to represent a face. See Malalasekera and James (1995) for further details.

Illustrative Examples, Results, and Discussion

Case 1: Validation Test Case. The test case considered by Chui et al. (1993) is used here to validate the present Discrete Transfer Method. The geometry is a cylindrical enclosure, 6 m long and 2 m in diameter, with black walls at a constant temperature of 500 K. The medium is absorbing, emitting, and nonscattering and has a uniform absorption coefficient K_a. The temperature field inside has a specified temperature distribution as shown in Fig. 2. Chui et al. (1993) have provided the exact

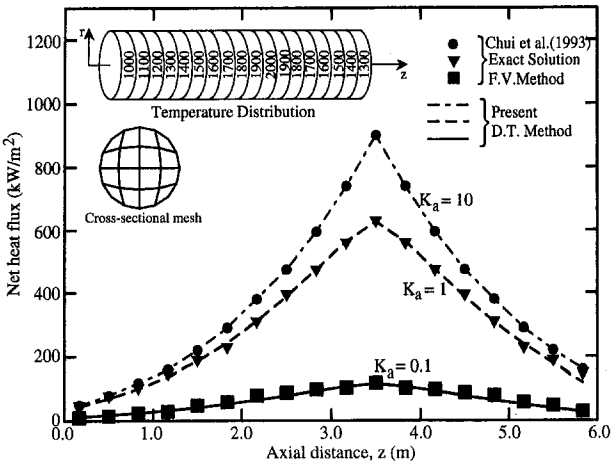

Fig. 2 Net heat flux along the cylindrical wall; comparison with exact and F.V. solutions of Chui et al. (1993)

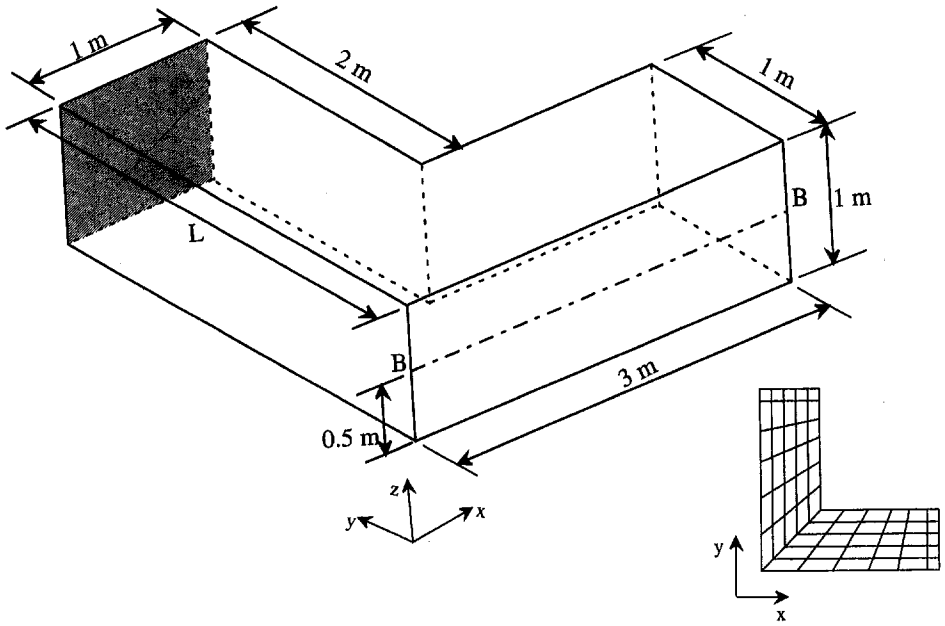

Fig. 3 The L-shaped geometry and the mesh used (Case 2)

solution for net heat flux along the cylindrical wall and their calculations, using the Control Volume Method, also closely resemble the exact solution. In the present calculation, the geometry is treated as a fully three-dimensional object so that the body-fitted treatment presented in this paper could be validated. A nonorthogonal mesh (shown in Fig. 2) was used to represent the cylindrical cross section and a uniform grid was incorporated in the axial (z) direction. The mesh representation is therefore truly three-dimensional and, for the calculation, an overall grid of $5 \times 5 \times 18$ was used to calculate the net heat flux to the cylindrical wall. The results obtained using 16×16 rays per wall point are shown on Fig. 2 for three absorption coefficients K_a = 10, 1, and 0.1 m^{-1}. As can be seen from Fig. 2, in all three cases the present results agree very well with the exact solution and the finite volume solution of Chui et al. (1993). The maximum error was only 3 percent close to the right-hand side of the geometry for the case K = 1 m^{-1}. The solution of Chui et al. (1993) was reproduced here by digitizing the relevant figure from their paper. This could incur an error of about 1 percent in the exact solution. The encouraging agreement seen in this case illustrates the accuracy of the present method using Discrete Transfer Method calculations for a nonorthogonal body fitted mesh system.

Case 2: Radiative Heat Transfer in an L-Shaped Geometry With Emitting/Absorbing Media. Here, we have considered a three-dimensional, L-shaped geometry with emitting, absorbing, and nonscattering media inside at a temperature of 1000 K. The dimensions of the geometry are shown in Fig. 3 with all walls considered to be black at 500 K. A body-fitted grid arrangement (also shown in Fig. 3) was used to discretize the L-section. No cell blocking was required in the calculations so that computer storage was utilized fully by the present method and the grid efficiently utilized in the calculation. The predicted net heat flux on the line B–B (marked on Fig. 3) is depicted in Fig. 4 for K_a values of 10, 5, 2, 1, and 0.5 m^{-1}. For high K_a's, the effects of the wall geometry seem to be less significant. This example illustrates how the present DT method can be used in an arbitrary shaped geometry with emitting/absorbing media to calculate radiative heat transfer. The method can also be used to investigate geometric and shading effects on heat transfer. Such illustrative examples are reported by Malalasekera and James (1995) to which the reader is referred for further details.

Assessment of Computer Times. The results presented in validation case 1 were calculated using 16×16 rays per wall point. The calculation took 244 cpu seconds on a HP 750 computer. To investigate the sensitivity to the internal mesh distribution, alternative meshes (not shown here in the interest of brevity) were also used to recalculate the results. No difference was observed when the results were compared with the previous mesh. Table 1 shows the computer times required for the same test case but with a different number of rays per point. It can be seen that an increase in the number of rays can lead to high computational overheads. In the authors' experience, 16×16 rays per point give results that are acceptable when compared with the accuracy of the exact solution.

Concluding Remarks

This study has shown how the Discrete Transfer Method can be applied to arbitrary shaped, three-dimensional complex geometries. Since the method is based on a body-fitted grid system, all geometric details can be accurately incorporated and the technique can be easily used in simultaneous CFD calculation procedures, which are based on body-fitted methodology

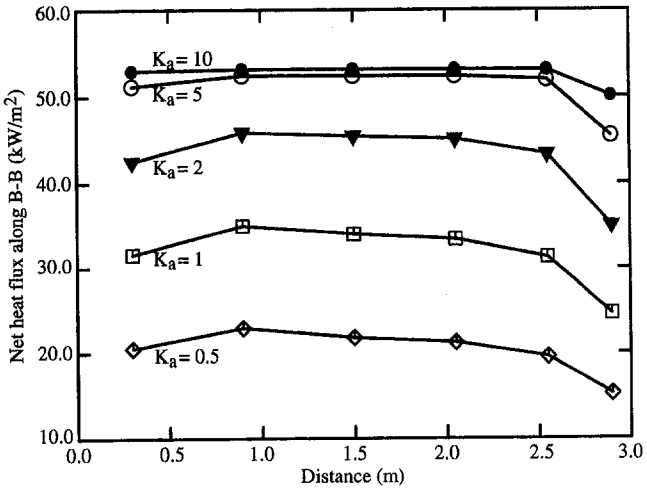

Fig. 4 Net heat flux along line B–B shown in Fig. 3

Table 1

$N_\theta \times N_\phi$	4 × 4	8 × 8	16 × 16	32 × 32	64 × 64	128 × 128
CPU, s	26	73	244	2870	14473	58779

in order to calculate heat transfer in combusting situations. In such calculations, the same mesh can be shared by both the CFD and the radiation calculation procedures, ensuring that no interpolations are required for energy source terms. The method has been shown to produce accurate results in a benchmark calculation. An illustrative example has been presented to show its flexibility and generality in dealing with a complex geometry such an L-shaped geometry. One disadvantage of the method, however, is that when the actual dimensions are large, a large number of rays per wall point is required to capture thermal details of the surfaces and volumes involved. Nevertheless, the Discrete Transfer Method is very conducive for the prediction of radiative heat transfer in complex combustion chambers, including gas turbine combustors, complex I.C. engines, etc. It can also be used to calculate solar radiation effects within building geometries, greenhouses, and various other thermal environments.

References

Arvo, J., ed., 1991, *Graphics Gems II,* Academic Press, New York.

Badouel, D., 1991, "An Efficient Ray-Polygon Intersection," in: *Graphics Gems II,* J. Arvo, ed., Academic Press, New York.

Carvalho, M. de G., Farias, T., and Fontes, P., 1991, "Predicting Radiative Heat Transfer in Absorbing, Emitting, and Scattering Media Using the Discrete Transfer Method," ASME FED-Vol. 160, pp. 17–26.

Chui, E. H., Hughes, P. M. J., and Raithby, G. D., 1993, "Implementation of the Finite Volume Method for Calculating Radiative Transfer in a Pulverised Fuel Flame," *Combust. Sci. and Tech.,* Vol. 92, pp. 225–242.

Glassner, A. S., ed., 1990, *Graphics Gems,* Academic Press, New York.

Lockwood, F. C., and Shah, N. G., 1981, "A New Radiation Solution Method for Incorporation in General Combustion Prediction Procedures," *Eighteenth Symposium (International) on Combustion,* The Combustion Institute, pp. 1405–1414.

Malalasekera, W. M. G., and Lockwood, F. C., 1991, "Computer Simulation of the King's Cross Fire: Effect of Radiative Heat Transfer on Fire Spread," *Proc. Inst. Mech. Engineers,* Vol. 205, Part C, pp. 201–208.

Malalasekera, W. M. G., and James, E. H., 1995, "Calculation of Radiative Heat Transfer in Three-Dimensional Complex Geometries," presented at the session on "Fundamentals of Radiation," 1995 ASME National Heat Transfer Conference, Portland, OR, ASME HTD-Vol. 315, pp. 53–61.

Meng, F. L., McKenty, F., and Camarero, R., 1993, "Radiative Heat Transfer by the Discrete Transfer Method Using an Unstructured Mesh," ASME HTD-Vol. 244, pp. 55–66.

Snyder, J. M., and Barr, A. H., 1987, "Ray Tracing Complex Models Containing Surface Tessellations," *ACM Computer Graphics,* Vol. 21(4).

Parametric Study of Radiative Heat Transfer in Arrays of Fixed Discrete Surfaces

Z. I. Antoniak,[1,2] B. J. Palmer,[1] M. K. Drost,[1] and J. R. Welty[3]

Nomenclature

- A = array absorptance
- D = packing factor, or fraction (linear) of array row filled with elements; relative element size (width)
- D = fraction of radiation absorbed and reflected by an array consisting of a single row
- n = number of rows in array
- R = array reflectance
- T = array transmittance
- α = absorptivity of array element surface
- β = angle between incident photon and normal to array row, rad
- γ = angle between incident photon and array row ($= \pi/2 - \beta$), rad
- ρ = reflectivity of array element surface
- τ = transmissivity of array element surface

Subscripts

- n = number of rows in array
- D = a specific value (0.5 or 0.2), defined as above

Introduction

Radiation impinging on arrays, and the ensuing radiative transfer in and through arrays, are common phenomena. The objective of the present work was to study array radiative transfer in detail by means of the MCLITE code, and to develop correlations that capture the influence of various array parameters.

Arrays of regular geometric objects with fixed surfaces typify the heat exchangers that are in everyday service in numerous industries. Most often the objects, or elements, are cylindrical, have large length/diameter ratios, and may be bare or finned. Portions of typical arrays of fixed, discrete objects are shown in Figs. 1–3. Aside from proprietary codes, a heat exchanger designer has little to assist him in evaluating absorption and scattering of radiation by an array. Textbooks (Siegel and Howell, 1992) and handbooks (Stultz and Kitto, 1992) offer simplified charts and figures that predict absorption of radiant energy by arrays of tubes. Various analytic approaches that all employ numerous assumptions in order to make the radiative problem tractable are in the open literature.

MCLITE simulates monochromatic radiation impinging on a two-dimensional array of fixed discrete surfaces that form

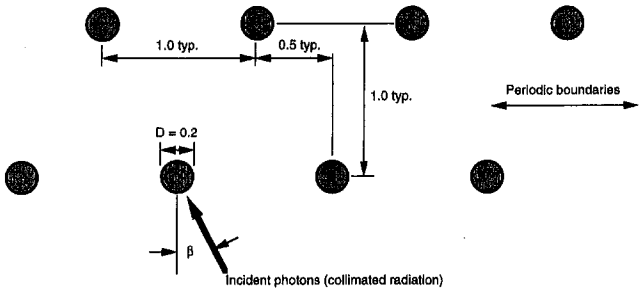

Fig. 1(*a*) Array of 0.2 diameter cylinders

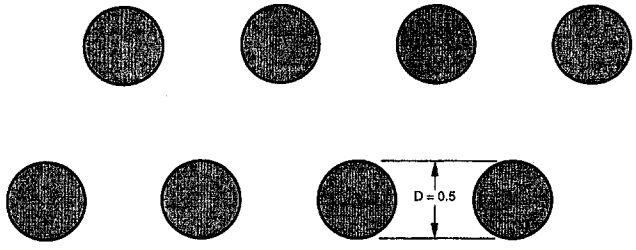

Fig. 1(*b*) Array of 0.5 diameter cylinders

[1] Pacific Northwest Laboratory, Richland, WA 99352.

[2] Senior Development Engineer.

[3] Oregon State University, Corvallis, OR 97331.

Contributed by the Heat Transfer Division of THE AMERICAN SOCIETY OF MECHANICAL ENGINEERS. Manuscript received by the Heat Transfer Division March 1995; revision received October 1995. Keywords: Heat Exchangers, Radiation, Solar Energy. Associate Technical Editor: M. F. Modest.

Table 1

$N_\theta \times N_\phi$	4 × 4	8 × 8	16 × 16	32 × 32	64 × 64	128 × 128
CPU, s	26	73	244	2870	14473	58779

in order to calculate heat transfer in combusting situations. In such calculations, the same mesh can be shared by both the CFD and the radiation calculation procedures, ensuring that no interpolations are required for energy source terms. The method has been shown to produce accurate results in a benchmark calculation. An illustrative example has been presented to show its flexibility and generality in dealing with a complex geometry such an L-shaped geometry. One disadvantage of the method, however, is that when the actual dimensions are large, a large number of rays per wall point is required to capture thermal details of the surfaces and volumes involved. Nevertheless, the Discrete Transfer Method is very conducive for the prediction of radiative heat transfer in complex combustion chambers, including gas turbine combustors, complex I.C. engines, etc. It can also be used to calculate solar radiation effects within building geometries, greenhouses, and various other thermal environments.

References

Arvo, J., ed., 1991, *Graphics Gems II,* Academic Press, New York.

Badouel, D., 1991, "An Efficient Ray-Polygon Intersection," in: *Graphics Gems II,* J. Arvo, ed., Academic Press, New York.

Carvalho, M. de G., Farias, T., and Fontes, P., 1991, "Predicting Radiative Heat Transfer in Absorbing, Emitting, and Scattering Media Using the Discrete Transfer Method," ASME FED-Vol. 160, pp. 17–26.

Chui, E. H., Hughes, P. M. J., and Raithby, G. D., 1993, "Implementation of the Finite Volume Method for Calculating Radiative Transfer in a Pulverised Fuel Flame," *Combust. Sci. and Tech.,* Vol. 92, pp. 225–242.

Glassner, A. S., ed., 1990, *Graphics Gems,* Academic Press, New York.

Lockwood, F. C., and Shah, N. G., 1981, "A New Radiation Solution Method for Incorporation in General Combustion Prediction Procedures," *Eighteenth Symposium (International) on Combustion,* The Combustion Institute, pp. 1405–1414.

Malalasekera, W. M. G., and Lockwood, F. C., 1991, "Computer Simulation of the King's Cross Fire: Effect of Radiative Heat Transfer on Fire Spread," *Proc. Inst. Mech. Engineers,* Vol. 205, Part C, pp. 201–208.

Malalasekera, W. M. G., and James, E. H., 1995, "Calculation of Radiative Heat Transfer in Three-Dimensional Complex Geometries," presented at the session on "Fundamentals of Radiation," 1995 ASME National Heat Transfer Conference, Portland, OR, ASME HTD-Vol. 315, pp. 53–61.

Meng, F. L., McKenty, F., and Camarero, R., 1993, "Radiative Heat Transfer by the Discrete Transfer Method Using an Unstructured Mesh," ASME HTD-Vol. 244, pp. 55–66.

Snyder, J. M., and Barr, A. H., 1987, "Ray Tracing Complex Models Containing Surface Tessellations," *ACM Computer Graphics,* Vol. 21(4).

Parametric Study of Radiative Heat Transfer in Arrays of Fixed Discrete Surfaces

Z. I. Antoniak,[1,2] B. J. Palmer,[1] M. K. Drost,[1] and J. R. Welty[3]

Nomenclature

- A = array absorptance
- D = packing factor, or fraction (linear) of array row filled with elements; relative element size (width)
- D = fraction of radiation absorbed and reflected by an array consisting of a single row
- n = number of rows in array
- R = array reflectance
- T = array transmittance
- α = absorptivity of array element surface
- β = angle between incident photon and normal to array row, rad
- γ = angle between incident photon and array row ($= \pi/2 - \beta$), rad
- ρ = reflectivity of array element surface
- τ = transmissivity of array element surface

Subscripts

- n = number of rows in array
- D = a specific value (0.5 or 0.2), defined as above

Introduction

Radiation impinging on arrays, and the ensuing radiative transfer in and through arrays, are common phenomena. The objective of the present work was to study array radiative transfer in detail by means of the MCLITE code, and to develop correlations that capture the influence of various array parameters.

Arrays of regular geometric objects with fixed surfaces typify the heat exchangers that are in everyday service in numerous industries. Most often the objects, or elements, are cylindrical, have large length/diameter ratios, and may be bare or finned. Portions of typical arrays of fixed, discrete objects are shown in Figs. 1–3. Aside from proprietary codes, a heat exchanger designer has little to assist him in evaluating absorption and scattering of radiation by an array. Textbooks (Siegel and Howell, 1992) and handbooks (Stultz and Kitto, 1992) offer simplified charts and figures that predict absorption of radiant energy by arrays of tubes. Various analytic approaches that all employ numerous assumptions in order to make the radiative problem tractable are in the open literature.

MCLITE simulates monochromatic radiation impinging on a two-dimensional array of fixed discrete surfaces that form

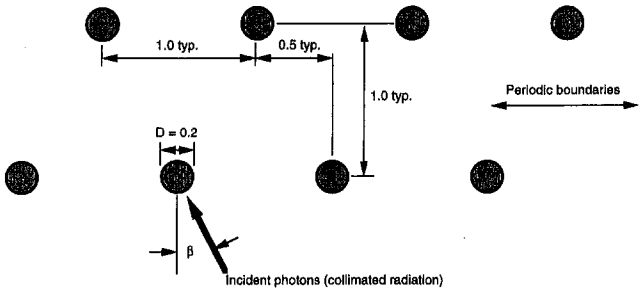

Fig. 1(*a*) Array of 0.2 diameter cylinders

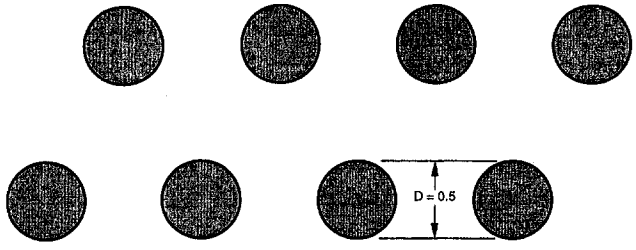

Fig. 1(*b*) Array of 0.5 diameter cylinders

[1] Pacific Northwest Laboratory, Richland, WA 99352.

[2] Senior Development Engineer.

[3] Oregon State University, Corvallis, OR 97331.

Contributed by the Heat Transfer Division of THE AMERICAN SOCIETY OF MECHANICAL ENGINEERS. Manuscript received by the Heat Transfer Division March 1995; revision received October 1995. Keywords: Heat Exchangers, Radiation, Solar Energy. Associate Technical Editor: M. F. Modest.

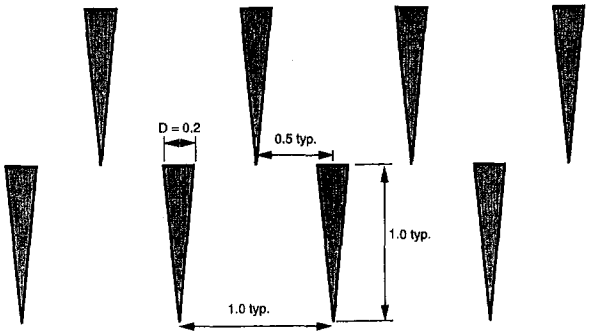

Fig. 2(*a*) Array of 0.2 wide wedges

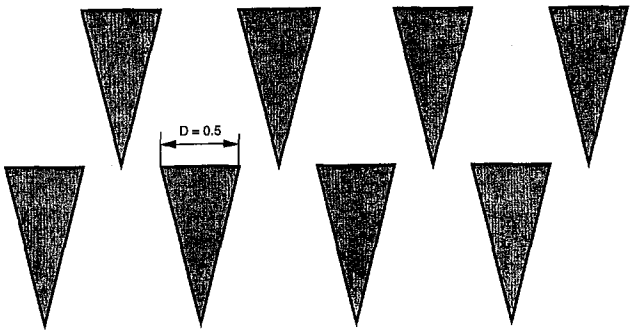

Fig. 2(*b*) Array of 0.5 wide wedges

elements. It utilizes a Monte Carlo algorithm with an original scheme for tracking cell-to-cell photon transport that optimizes the computation and greatly reduces computation time. The code has been documented by Palmer et al. (1995). MCLITE has been exercised in a parametric study of radiative transfer in arrays of regular objects; code results will be compared against experiments performed at Oregon State University in a future paper.

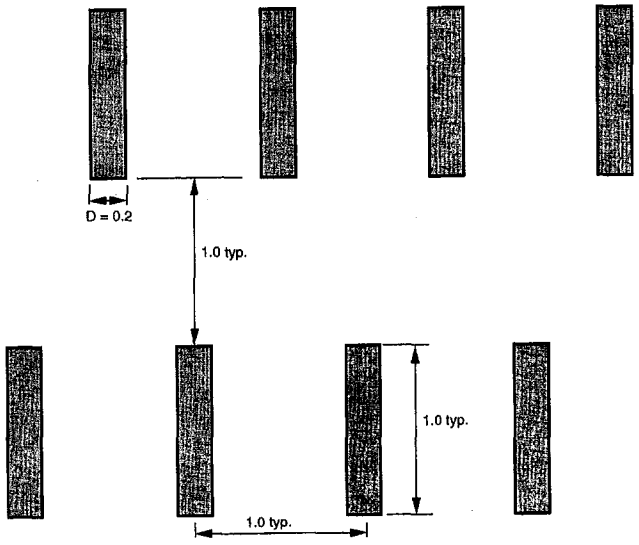

Fig. 3(*a*) Array of 0.2 wide rectangles

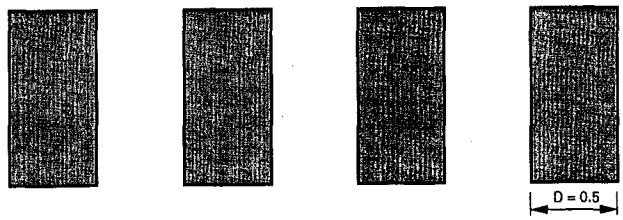

Fig. 3(*b*) Array of 0.5 wide rectangles (only a single row is shown)

Table 1 Key simulation parameters

Element Geometry	α, Surface Absorptivity	ρ, Surface Reflectivity	Incident Radiation	D, Packing Factor	Array Geometry
Cylinder	0.5; 0.8	0.5; 0.2	Diffuse; collimated	0.7[a]; 0.5; 0.3[a]; 0.2	Triangular pitch; parallel rows
Wedge	0.5; 0.8	0.5; 0.2	Diffuse; collimated	0.5; 0.2	Triangular pitch
Rectangle	0.5; 0.8	0.5; 0.2	Diffuse; collimated	0.5; 0.2	Triangular pitch

a) Not discussed here

Parametric Study

The parametric study had two goals: to evaluate the relative importance of array features in determining radiative transport, and to establish correlations that would capture the essentials of array performance. The parameters examined were object geometry and absorptivity, array depth, and array geometry. Both diffuse and collimated beam incident radiation were modeled. Approximately 280 MCLITE simulations were run, with defining parameters as specified in Table 1.

Correlations

The simulation results indicated that radiative transfer is highly dependent on all the parameters except array geometry. An adaptation of a ray-tracing method (Siegel and Howell, 1992, pp. 376–384, 928, 931) of tracking radiation proved to be capable of matching the data from MCLITE runs with reasonable accuracy. The correlations developed with this method are provided below to assist a heat exchanger designer in evaluating preliminary concepts.

Diffuse Radiation

The correlations of Table 2 provide a means for calculating the transmittance and reflectance of an array consisting of n uniform rows of geometric elements. Each of these correlations generally takes advantage of the results of a MCLITE run for an array consisting of a single row to determine the factor D, which equals the amount of radiation absorbed and reflected by that row. Thus $1-D$ represents the radiation that has passed through the first row and can interact with subsequent rows. The two values of D shown correspond to element widths D of 0.5 and 0.2. For a cylinder, the magnitude of D is only somewhat larger than the diameter D; for the other shapes, its magnitude is significantly larger than the element width D. Note that for an array of cylinders, it is possible to use the cylinder diameter directly in calculating the reflectance. Also note that when the number of rows exceeds 5, the array transmittance (for the rows > 5) decreases exponentially as predicted by Bouguer's law (Siegel and Howell, 1992, pp. 521–529; Born and Wolf, 1977).

Table 2 Correlations for diffuse radiation

Element Geometry	Transmittance of array with n rows (for n > 1; $T_1 = 1-D_0$)	D_0	Reflectance of array with n rows
Cylinder	$T_n = (1-D_0)^n [1+(1-\alpha)D_0]$, for $n \le 5$ $= T_5 \exp(-n/10)$, for $n>5$	$D_{0.5} = .622$ $D_{0.2} = .265$	$R_n = (1-\alpha)D_0 [1+\sum_{i=2}^{n}(1-D_0)^{2(i-1)}]$, where D = diameter (D)
Wedge	$T_n = (1-D_0)^k [1+(1-\alpha)D_0]$, where $k = 1.28n^{0.51}$, for $n \le 5$ $= T_5 \exp(-n/10)$, for $n>5$	$D_{0.5} = .723$ $D_{0.2} = .530$	$R_n = 0.5(1-\alpha)D_0 [1+\sum_{i=2}^{n}(1-D_0)^{2(i-1)}]$, where D_0 = from this table
Rectangle	$T_n = (1-D_0)^k [1+(1-\alpha)D_0]$, where $k = 1.28n^{0.51}$, for $n \le 5$ $= T_5 \exp(-n/10)$, for $n>5$	$D_{0.5} = .845$ $D_{0.2} = .644$	$R = 0.6(1-\alpha)D_0 [1+\sum_{i=2}^{n}(1-D_0)^{2(i-1)}]$, where D_0 = from this table

Table 3 Correlations for collimated radiation

Element Geometry	Transmittance of array with n rows (for n > 1; $T_1 = 1-D_0$)	D_0	Reflectance of array with n rows
Cylinder	$T_n = (1-D_0)^{1.4n}\,[1+(1-\alpha)D_0]$	$1-D_{0.5} = -0.66\gamma^2+1.68\gamma-0.57$ $1-D_{0.2} = -0.45\gamma^2+1.06\gamma+0.18$	$R_{0.5} = 2\rho(0.29+0.041\beta)$ $R_{0.2} = 2\rho(0.26+0.040\beta)$
Wedge	$T_n = (1-D_0)^k\,[1+(1-\alpha)D_0]$, where $k = 1.28n^{0.61}$ (for $\beta = 0.25$, $T_n = D\text{-}\beta(n-1)$)	$1-D_{0.5} = 0.93\gamma-0.70$ $1-D_{0.2} = 0.99\gamma^3-1.47\gamma^2+0.79\gamma-0.029$	$R_{0.5} = 2\rho(0.10+0.226\beta)$ $R_{0.2} = 2\rho(0.05+0.183\beta)$
Rectangle	$T_n = (1-D_0)^k\,[1+(1-\alpha)D_0]$, where $k = 1.28n^{0.61}$ (for $\beta = 0.25$, $T_n = D_0\text{-}0.016(n-1)$)	$1-D_{0.2} = 1.00\gamma^3-1.62\gamma^2+0.89\gamma-0.073$	$R_{0.2} = 2\rho(0.13+0.153\beta)$

Increasing the space between rows had no effect on the results. Also, the geometric arrangement of the elements appears to have a negligible effect on the transmittance through an array. Changing the triangular pitch of cylinders (two rows, with D = 0.5) to an orthogonal row/column arrangement changed the transmittance by <1 percent. Agreement between the correlations and MCLITE results is good, typically within <10 percent, and should be acceptable for engineering or parametric study.

Collimated Radiation

The correlations developed for collimated radiation are only partially satisfactory. Certainly the case of streaming (when β = 0.5 rad, for all elements, and also when β = 1.0 rad for the D = 0.2 cylinders) cannot be subsumed into a single correlation. For normal incidence (β = 0 rad), the array transmittance T of both cylinders and rectangles is about equal to 1-D for a single row, and 1-2D for two rows, and remains essentially unchanged with additional rows. For wedges, this relation is about 1-0.5D and 1-D, respectively. The array reflectance R also reaches an asymptotic value with only several rows (for all angles of incidence); therefore, the correlations shown in Table 3 are for this asymptote.

In general, agreement is fair, typically within about 20 percent, and should be acceptable for parametric study. Results are less sensitive to array depth than for diffuse radiation, because most of the radiative interaction takes place in the first few rows of an array.

Conclusions

The parameter space for study of radiative transfer in and through arrays of regular elements is extremely large. The present study has developed a number of correlations, based on MCLITE code results for simple geometric elements. These correlations can guide a designer of heat exchangers in optimizing performance. When the incident radiation is diffuse, these correlations are fairly accurate. When the incident radiation is collimated, and strikes the array at some arbitrary angle, the correlations are less accurate. For detailed analysis of heat exchanger performance there is no substitute for exercising a code such as MCLITE.

References

Born, M., and Wolf, E., 1975, *Principles of Optics,* 5th ed., Pergamon Press, Oxford, United Kingdom.

Palmer, B. J., Drost, M. K., and Welty, J. R., 1995, "Monte Carlo Simulation of Radiative Heat Transfer in Arrays of Fixed Discrete Surfaces Using Cell-to-Cell Photon Transport," *Int. J. Heat Mass Transfer,* in press.

Siegel, R., and Howell, J. H., 1992, *Thermal Radiation Heat Transfer,* 3rd ed., Hemisphere Publishing Corporation, Washington, DC.

Stultz, S. C., and Kitto, J. B., eds., 1992, *Steam: Its Generation and Use,* Babcock & Wilcox Company, Barberton, OH, Chap. 4.

Experimental Study of Convective Boiling in a Porous Medium: Temperature Field Analysis

F. Topin,[1] O. Rahli,[1] L. Tadrist,[1] and J. Pantaloni[1]

I Introduction

During the last two decades, a great deal of research has been carried out on porous media. This field has gone through a rapid acceleration owing to widespread concern about issues such as energy conservation and environmental pollution. The areas of application include insulation for buildings and equipment, energy storage and recovery, geothermal storage, nuclear waste disposal, chemical reactor design, and the storage of heat-generating substances.

Boiling in porous media differs from that observed in open containers, yet few experimental studies have been carried out on this field despite their practical and theoretical interest. Most previous studies have focused primarily on boiling of a stagnant liquid. It was not until the 80s that serious efforts were made to develop numerical models for these media, due to considerable progress in computing techniques. Most previous studies have been one dimensional, dealing mainly with problems of thermal migration or phase change without forced flow (Torrance, 1983; Udell, 1983, 1985).

Experiments by Sondergeld and Turcotte (1977) and Bau and Torrance (1982) have shown that the liquid regime temperature profile can be either conductive or convective. Liquid and vapor counter percolation carries heat across the two-phase zone (the liquid evaporates at the heating surface and the vapor condenses at the boundary between the liquid zone and two-phase zone). Experimental studies suggest that the thermal convection in the liquid region can occur either before or after the onset of boiling. Experiments on visualization (Sondergeld and Turcotte, 1978) reveal that the streamlines of the liquid region penetrate the two-phase zone after the onset of convection.

Schubert and Strauss (1977) noted that convection can also be caused by an unstable phase-change mechanism. If steam and water are in thermal equilibrium, thermal disturbances will cause pressure variations which, in turn, will tend to move the fluid against the frictional resistance of the medium. In accordance with the law of mass conservation, horizontal expansion must be accompanied by vertical contraction, implying that the phase change will occur so that vertical forces remain balanced.

In 1982, Naik and Dhir started looking into the temperature and pressure evolutions of a coolant that evaporates as it flows through a bed of steel spheres ($\varnothing$ = 590–4763 μm) volumically heated by induction. A theoretical model was then developed for the temperature profile in the two-phase liquid zone. Vapor channels were observed in the porous layers of the bed ($\varnothing$ < 1600 μm) and semi-empirical models were suggested as models of the pressure drop in the two-phase zone.

The purpose of the present study is to gain a better understanding of boiling mechanisms in porous media with forced flow. The heat transfer and boiling of a liquid in a porous

[1] Institut Universitaire des Systèmes Thermiques Industriels (I.U.S.T.I.), Laboratoire des Systèmes Energétiques et Transferts Thermiques: UMR 139, Université de Provence—Centre de St Jerome—Case 162, Av. Escadrille Normandie Niemen 13397 Marseille Cedex 20—France.

Contributed by the Heat Transfer Division of The American Society of Mechanical Engineers. Manuscript received by the Heat Transfer Division July 1994; revision received August 1995. Keywords: Boiling, Multiphase, Flows, Porous Media. Associate Technical Editor: V. K. Dhir.

Table 3 Correlations for collimated radiation

Element Geometry	Transmittance of array with n rows (for n > 1; $T_1 = 1-D_0$)	D_0	Reflectance of array with n rows
Cylinder	$T_n = (1-D_0)^{1.4n}\,[1+(1-\alpha)D_0]$	$1-D_{0.5} = -0.66\gamma^2+1.68\gamma-0.57$ $1-D_{0.2} = -0.45\gamma^2+1.06\gamma+0.18$	$R_{0.5} = 2\rho(0.29+0.041\beta)$ $R_{0.2} = 2\rho(0.26+0.040\beta)$
Wedge	$T_n = (1-D_0)^k\,[1+(1-\alpha)D_0]$, where $k = 1.28n^{0.81}$ (for $\beta = 0.25$, $T_n = D\text{-}\beta(n-1)$)	$1-D_{0.5} = 0.93\gamma-0.70$ $1-D_{0.2} = 0.99\gamma^3-1.47\gamma^2+0.79\gamma-0.029$	$R_{0.5} = 2\rho(0.10+0.226\beta)$ $R_{0.2} = 2\rho(0.05+0.183\beta)$
Rectangle	$T_n = (1-D_0)^k\,[1+(1-\alpha)D_0]$, where $k = 1.28n^{0.81}$ (for $\beta = 0.25$, $T_n = D_0\text{-}0.016(n-1)$)	$1-D_{0.2} = 1.00\gamma^3-1.62\gamma^2+0.89\gamma-0.073$	$R_{0.2} = 2\rho(0.13+0.153\beta)$

Increasing the space between rows had no effect on the results. Also, the geometric arrangement of the elements appears to have a negligible effect on the transmittance through an array. Changing the triangular pitch of cylinders (two rows, with D = 0.5) to an orthogonal row/column arrangement changed the transmittance by <1 percent. Agreement between the correlations and MCLITE results is good, typically within <10 percent, and should be acceptable for engineering or parametric study.

Collimated Radiation

The correlations developed for collimated radiation are only partially satisfactory. Certainly the case of streaming (when β = 0.5 rad, for all elements, and also when β = 1.0 rad for the D = 0.2 cylinders) cannot be subsumed into a single correlation. For normal incidence (β = 0 rad), the array transmittance T of both cylinders and rectangles is about equal to 1-D for a single row, and 1-2D for two rows, and remains essentially unchanged with additional rows. For wedges, this relation is about 1-0.5D and 1-D, respectively. The array reflectance R also reaches an asymptotic value with only several rows (for all angles of incidence); therefore, the correlations shown in Table 3 are for this asymptote.

In general, agreement is fair, typically within about 20 percent, and should be acceptable for parametric study. Results are less sensitive to array depth than for diffuse radiation, because most of the radiative interaction takes place in the first few rows of an array.

Conclusions

The parameter space for study of radiative transfer in and through arrays of regular elements is extremely large. The present study has developed a number of correlations, based on MCLITE code results for simple geometric elements. These correlations can guide a designer of heat exchangers in optimizing performance. When the incident radiation is diffuse, these correlations are fairly accurate. When the incident radiation is collimated, and strikes the array at some arbitrary angle, the correlations are less accurate. For detailed analysis of heat exchanger performance there is no substitute for exercising a code such as MCLITE.

References

Born, M., and Wolf, E., 1975, *Principles of Optics,* 5th ed., Pergamon Press, Oxford, United Kingdom.

Palmer, B. J., Drost, M. K., and Welty, J. R., 1995, "Monte Carlo Simulation of Radiative Heat Transfer in Arrays of Fixed Discrete Surfaces Using Cell-to-Cell Photon Transport," *Int. J. Heat Mass Transfer,* in press.

Siegel, R., and Howell, J. H., 1992, *Thermal Radiation Heat Transfer,* 3rd ed., Hemisphere Publishing Corporation, Washington, DC.

Stultz, S. C., and Kitto, J. B., eds., 1992, *Steam: Its Generation and Use,* Babcock & Wilcox Company, Barberton, OH, Chap. 4.

Experimental Study of Convective Boiling in a Porous Medium: Temperature Field Analysis

F. Topin,[1] O. Rahli,[1] L. Tadrist,[1] and J. Pantaloni[1]

I Introduction

During the last two decades, a great deal of research has been carried out on porous media. This field has gone through a rapid acceleration owing to widespread concern about issues such as energy conservation and environmental pollution. The areas of application include insulation for buildings and equipment, energy storage and recovery, geothermal storage, nuclear waste disposal, chemical reactor design, and the storage of heat-generating substances.

Boiling in porous media differs from that observed in open containers, yet few experimental studies have been carried out on this field despite their practical and theoretical interest. Most previous studies have focused primarily on boiling of a stagnant liquid. It was not until the 80s that serious efforts were made to develop numerical models for these media, due to considerable progress in computing techniques. Most previous studies have been one dimensional, dealing mainly with problems of thermal migration or phase change without forced flow (Torrance, 1983; Udell, 1983, 1985).

Experiments by Sondergeld and Turcotte (1977) and Bau and Torrance (1982) have shown that the liquid regime temperature profile can be either conductive or convective. Liquid and vapor counter percolation carries heat across the two-phase zone (the liquid evaporates at the heating surface and the vapor condenses at the boundary between the liquid zone and two-phase zone). Experimental studies suggest that the thermal convection in the liquid region can occur either before or after the onset of boiling. Experiments on visualization (Sondergeld and Turcotte, 1978) reveal that the streamlines of the liquid region penetrate the two-phase zone after the onset of convection.

Schubert and Strauss (1977) noted that convection can also be caused by an unstable phase-change mechanism. If steam and water are in thermal equilibrium, thermal disturbances will cause pressure variations which, in turn, will tend to move the fluid against the frictional resistance of the medium. In accordance with the law of mass conservation, horizontal expansion must be accompanied by vertical contraction, implying that the phase change will occur so that vertical forces remain balanced.

In 1982, Naik and Dhir started looking into the temperature and pressure evolutions of a coolant that evaporates as it flows through a bed of steel spheres ($\varnothing$ = 590–4763 μm) volumically heated by induction. A theoretical model was then developed for the temperature profile in the two-phase liquid zone. Vapor channels were observed in the porous layers of the bed ($\varnothing$ < 1600 μm) and semi-empirical models were suggested as models of the pressure drop in the two-phase zone.

The purpose of the present study is to gain a better understanding of boiling mechanisms in porous media with forced flow. The heat transfer and boiling of a liquid in a porous

[1] Institut Universitaire des Systèmes Thermiques Industriels (I.U.S.T.I.), Laboratoire des Systèmes Energétiques et Transferts Thermiques: UMR 139, Université de Provence—Centre de St Jerome—Case 162, Av. Escadrille Normandie Niemen 13397 Marseille Cedex 20—France.

Contributed by the Heat Transfer Division of The American Society of Mechanical Engineers. Manuscript received by the Heat Transfer Division July 1994; revision received August 1995. Keywords: Boiling, Multiphase, Flows, Porous Media. Associate Technical Editor: V. K. Dhir.

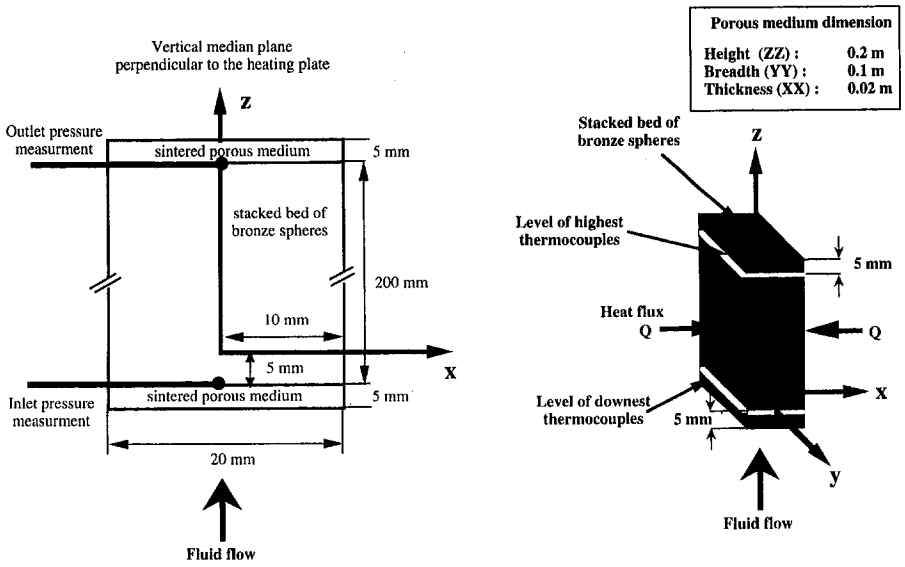

Fig. 1 Schematic diagram of the experimental apparatus to measure the temperature field and pressure drop in a porous medium. Position of the axis, dimensions of the porous medium.

medium were studied using a vertical parallelepiped box filled with stacked spheres and heated on both sides, with the fluid flowing from bottom to top within which temperature and pressure parameters were analyzed.

II Materials and Methods

The porous medium used was composed of small bronze spheres ($\varnothing$ = 140–160 μm) held inside a parallelepiped fluoride plastic (PVDF) enclosure with a low thickness-to-width ratio. The stacked spheres were held inside the enclosure by sintered consolidations formed of identical spheres and fitted on both ends of the column. The large heating surfaces were formed of bronze plates screwed into the PVDF box and an O-joint to seal the box. The bronze plates were heated by electrical resistances embedded in a ceramic block. Copper plates were inserted between the heaters and the bronze plates to ensure an even temperature distribution across the large surfaces. The entire enclosure is insulated with compressed asbestos (Fig. 1). The energy balance is checked for each experiment. The overall losses were found to be negligible (<3 percent) and the heat flux is indeed transferred to the fluid. The liquid (i.e., *n*-pentane) flows through the sintered porous media and then vertically from bottom to top. The average velocity of the liquid, effective heat flux, and temperature at the inlet were all monitored and held constant during the experiments.

Inlet and outlet pressure values were recorded using two pressure sensors. The temperature values within the porous medium were measured using 130 thermo-electrical sensors (chromel-alumel: $\varnothing$ = 0.8 mm) arranged for an optimal coverage of the enclosed volume and connected to a data-acquisition system. Local temperature measurements and polynomial interpolation functions along the vertical and horizontal axes were then used to represent the isotherms and/or the temperature field throughout the entire volume (Cioulachtjian et al., 1990).

The origin of the coordinate axes is placed at the center of the median plane perpendicular to the heating plates located 5 mm above the inlet sintered consolidation (i.e., at the same height as the lowest thermocouples: Fig. 1). Once all noncondensable substances have been eliminated from the porous medium, the liquid flow is maintained at constant temperature and velocity for approximately two hours. When the desired temperature has been reached throughout the column, the lateral plates are heated using electrical resistances whose heat flux is maintained constant. Temperature, pressure, and flow values are recorded during the whole experiment (i.e., five hours).

III Experimental Results

A series of experiments were carried out using an effective heat flux ranging from 2000 to 10,000 W/m^2 and liquid flow rates ranging from 0.55 to 3.33 cm^3/s. The temperature field for the porous medium can be determined at any moment for given heat flux and flow conditions. In all situations, a stationary regime was obtained after a waiting period ranging from 1 to 3 hours (this span of time is proportionally shorter when the power-to-flow ratio is weak). Previous studies have confirmed the two-dimensional nature of such phenomena (Rahli et al., 1992); thus only those results for the median plane perpendicular to the heating plates are presented in this paper.

III.1 Description of the Temperature Field. When there is no phase change of the liquid, the temperature increases rapidly in the inlet zone and then more slowly toward the outlet of the column. When phase change does occur, the behavior remains roughly unchanged in the inlet zone. It is followed by a zone with decreasing temperatures and then by another zone in which the temperature increases once again, if the heat flux is high enough.

Figure 2 shows the temperature profiles along the XX axis for stationary conditions at different heights (Z). The profiles show a more or less pronounced "U" shape, depending on the state of the fluid in the column. These profiles reveal different types of behavior: single-phase liquid and vapor zones having high-amplitude profiles, and the two-phase zone a relatively flat profile. At the inlet, the temperature profile is flat. In the liquid zone, the temperature increases considerably along the XX axis between the central axis and the wall ($[T_w - T_c] \approx 20$°C, Z = 1 cm); the difference in temperature values between the wall and the central axis decreases considerably as a function of the distance Z. In the two-phase zone, a nearly flat profile is observed ($[T_w - T_c] \approx 2$°C, $6 \leq Z \leq 11$ cm). The profile starts to drop again in the single-phase zone as it approaches the outlet ($[T_w - T_c] \approx 10$°C).

When no boiling occurs, the velocity and pressure profiles are obtained directly for the entire porous medium applying Darcy's law to inlet and outlet pressure readings. When a phase change does occur, determining the pressure and velocity fields

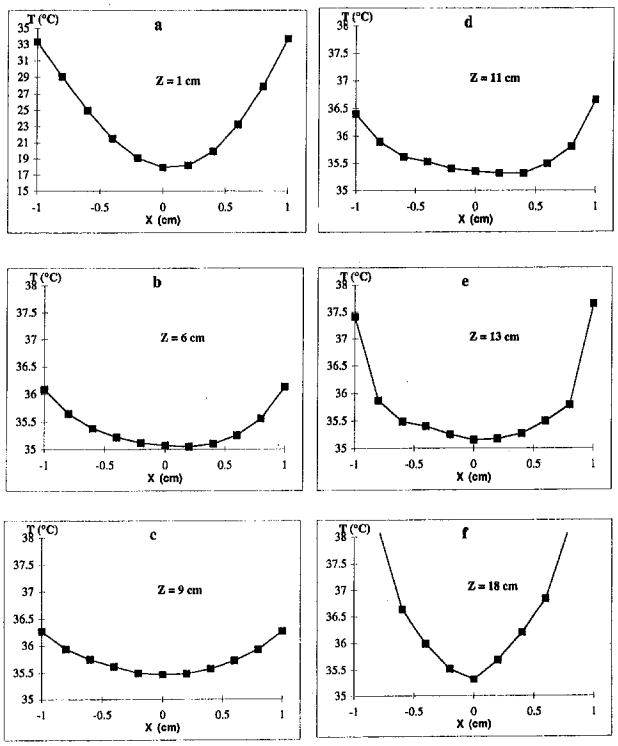

Fig. 2 Temperature profiles along the horizontal *XX* axis in the median plane perpendicular to the heating plates for several values of *Z* at stationary regime. Liquid: *n*-pentane ($U = 0.69\ 10^{-3}$ m/s); heat flux applied to the plates: 5000 W/m^2.

requires the identification of zone boundaries and of their spatial and temporal evolution. Two different approaches may be used to identify these boundaries:

- one based on the use of the experimental temperature field,
- the other relying on pressure and thermodynamic data.

III.2 Identification of Zone Boundaries Using the Temperature Fields. The longitudinal temperature profiles for the different abscissa ($X = -1$, -0.8, -0.6, -0.4, -0.2, 0, 0.2, 0.4, 0.6, 0.8, 1 cm relative to the median axis) are given in Fig. 3 at the stationary regime. The temperature profiles are nearly symmetric in relation to the median plane (parallel to the heating plates [$X = 0$]). For this reason the profiles are represented in pairs. The profiles for the different abscissa present roughly the same shape. Three distinct zones defined by the distance Z are clearly visible:

- A section with increasing values. This is the liquid zone Z_l, in which the temperature increases continuously from the inlet and shows an asymptotic tendency.
- A section with decreasing values, corresponding to the two-phase zone Z_d. The beginning of the zone corresponds to the maximum profile at the liquid front and the end to a sharp change in slope, the local minimum temperature at the vapor front.
- A third section with increasing values once again. This is the single-phase vapor zone Z_v. This zone is not always present, depending on the experimental conditions.

The two-phase zone Z_d increases in size as one moves toward the central axis of the column. This can be attributed to the decrease in heat flux moving away from the heating plates. The flux at the walls is used up for the phase change and is then transported along the Z axis. As a result, the flux decreases from the walls toward the central axis. So does the temperature. It decreases more and more sharply in the two-phase zone, most probably as a result of flow effects.

Figure 4 shows the evolution over time of the temperature profiles along the central axis [$X = 0$] for a given experimental flow rate and heat flux conditions. Depending on the flow rate and the heat flux, a stationary regime was obtained with or without phase change and with or without superheating. The different zones tended to keep a similar behavior when experimental conditions were changed. The detailed representation shows a decreasing temperature profile in the two-phase zone at different moments. This behavior is roughly the same regardless of the presence or absence of a vapor zone. The two-phase zone decreases in length and temperature until a stationary regime is reached. Along the central axis, the temperature decrease between the liquid front and the vapor front is found to vary under different experimental conditions, and the length of the two-phase zone is proportional to the flow rate.

The heat flux entering the two-phase zone is used up for the phase change. Flow effects cause a pressure drop, which in turn induces a temperature decrease, allowing the fluid to remain saturated (P_{sat}, T_{sat}). This phenomenon causes saturation variations, which lead to an increased pressure drop, which lasts until a single-phase vapor zone is reached. The shape of the profiles is largely affected by the combined influence of different phenomena, especially in the two-phase zone where the pressure and temperature profiles are imposed by combined flow and thermal effects.

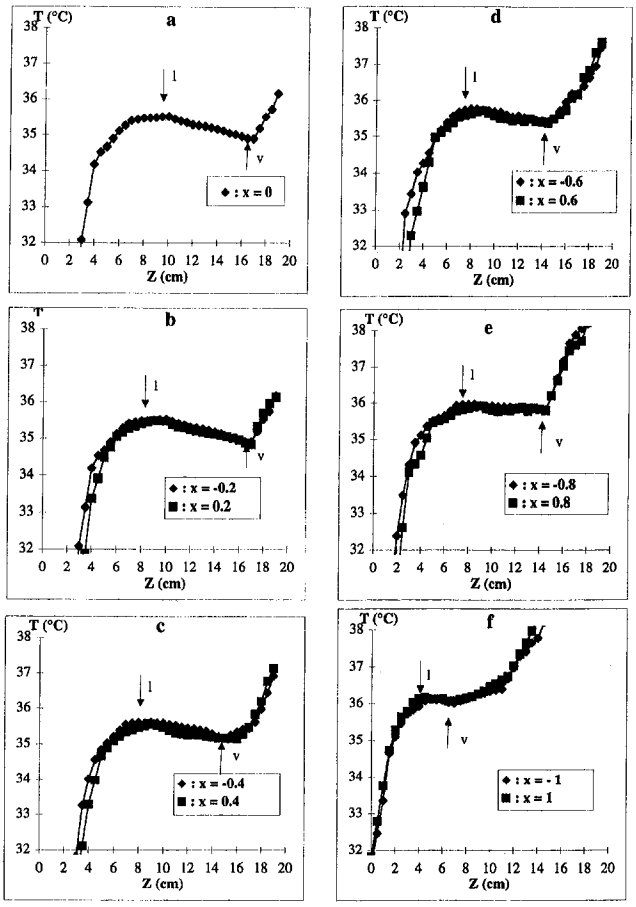

Fig. 3 Temperature profiles along vertical *ZZ* axis. These profiles are plotted in pairs (points equidistant to the centerline). On each curve, the ◇ symbol corresponds to the profile with negative abscissa and the □ symbol to those with positive abscissa. The boundaries of the different zones are marked by the arrows: \l for the liquid-two-phase front and /v for the two-phase-vapor limit. Liquid: *n*-pentane ($U = 0.69\ 10^{-3}$ m/s); heat flux applied to the plates: 5000 W/m^2.

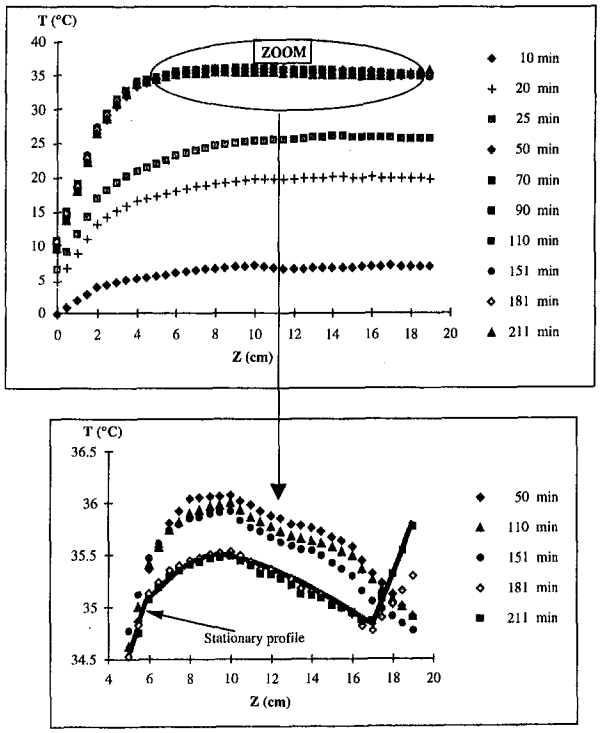

Fig. 4 Temporal evolution of the temperature profiles on the centerline along the vertical *ZZ* axis. Global view and detailed view around saturation temperature values. Liquid: *n*-pentane ($U = 0.69\ 10^{-3}$ m/s); heat flux applied to the plates: 5000 W/m^2.

V Conclusion

The experimental analysis based on the evaluation of temperature over space and time revealed three distinct zones, corresponding to the different states of the fluid:

- a liquid zone Z_l near the column inlet,
- a two-phase zone Z_d,
- a vapor zone Z_v near the outlet.

The temperature in the two-phase zone is seen to decrease, forming an N-shaped curve (), probably resulting from combined flow and phase-change effects. The boundaries of the zones were determined with great precision using the temperature fields.

References

Bau, H., and Torrance, K. E., 1982, "Boiling in Low-Permeability Porous Materials," *Int. J. Heat Mass Transfer,* Vol. 25, pp. 45–55.

Cioulachtjian, S., Tadrist, L., Santini, R., Occelli, R., and Pantaloni, J., 1990, "Etude des transferts de chaleur dans un milieu poreux. Cas d'un Liquide en Ecoulement," *Rev. Gen. Therm. Fr.,* No. 338, pp. 85–90.

Naik, A. S., and Dhir, V. K., 1982, "Forced Flow Evaporating Cooling of a Volumetrical Heated Porous Layer," *Int. J. Heat Mass Transfer,* Vol. 25, No. 4, pp. 541–552.

Rahli, O., Cioulachtjian, S., Tadrist, L., and Santini, 1992, "Boiling in Porous Media—An Experimental and Numerical Analysis," *Proceedings of the International Symposium ECOS'92; On Efficiency, Costs, Optimization and Simulation of Energy Systems.* Zaragoza, Spain, June 15–18, pp. 515–520.

Schubert, G., and Strauss, J. M., 1977, "Two-Phase Convection in a Porous Medium," *J. Geophys. Res.,* Vol. 82, pp. 3411–3421.

Sondergeld, C. H., and Turcotte, D. L., 1977, "An Experimental Study of Two-Phase Convection in a Porous Medium With Applications to Geological Problems," *J. Geophys. Res.,* Vol. 82, pp. 2045–2053.

Sondergeld, C. H., and Turcotte, D. L., 1978, "Flow Visualisation Studies of Two-Phase Convection in a Porous Medium With Applications to Geological Problems," *Pure Appl. Geophys.,* Vol. 117, pp. 321–330.

Torrance, K. E., 1983, "Boiling in Porous Media," *ASME/JSME Thermal Engineering Joint Conference Proceedings,* Y. Mori and W.-J. Yang, eds., Vol. 1, pp. 593–606.

Udell, K. S., 1983, "Heat Transfer in Porous Media Heated From Above With Evaporation, Condensation, and Capillary Effects," ASME JOURNAL OF HEAT TRANSFER, Vol. 105.

Udell, K. S., 1985, "Heat Transfer in Porous Media Considering Phase Change and Capillarity—The Heat Pipe Effect," *Int. J. Heat Mass Transfer,* Vol. 28, No. 2, pp. 485–495.

Electrohydrodynamically Enhanced Heat Transfer in Pool Boiling

J. Seyed-Yagoobi,[1] C. A. Geppert,[1] and L. M. Geppert[1]

Background

The concept of electrohydrodynamic (EHD) enhancement of boiling has been researched actively only recently (e.g., Kawahira et al., 1990; Ogata et al., 1992; Karayiannis et al., 1993; Ogata and Yabe, 1993a, 1993b; Singh et al., 1993). The main objective of this study was to investigate and measure accurately the effect of electric field presence (using various electrode designs) on the pool boiling heat transfer of R-123 refrigerant, a new ozone-friendly substitute for R-11. An experimental apparatus was designed and built. The evaporator consisted of an electrically heated smooth tube in a horizontal configuration. The details of the experimental setup and results can be found from Geppert et al. (1995).

To clarify the effects of an electric field on pool boiling, different mechanisms of electrically induced liquid and vapor motion must be explained. The electric body force density acting on the molecules of a dielectric fluid in the presence of an electric field consists of three terms (Melcher, 1981):

$$\vec{f}_e = q\vec{E} - \frac{1}{2}\vec{E}^2\nabla\epsilon + \frac{1}{2}\nabla\left(\vec{E}^2\left(\frac{\partial\epsilon}{\partial\rho}\right)\rho\right) \qquad (1)$$

where q, E, ϵ, and ρ are the electric charge density, electric field strength, fluid electric permittivity, and fluid density, respectively. The three terms in Eq. (1) stand for three different kinds of force densities acting on the liquid. The first term represents the *Coulomb force,* which is the acting force on the free charges in an electric field. The Coulomb force is negligible in this study due to the lack of free charges in the fluid (the current measured is on the order of μA). The second term stands for the *dielectrophoretic force,* which is created by a local change of the permittivity in an electric field. A change in the permittivity occurs, for example, at the interface of a vapor bubble with a liquid. The third term is called the *electrostriction term.* The electrostriction force occurs primarily when a nonuniform electric field is applied on a dielectric fluid. The dielectrophoretic force and the electrostriction force are both forces that act on polarized charges and are both defined as *polarization forces.*

In the present study, an electric field was applied on a pool-boiling configuration. Heat transfer data were taken in the convection regime and in the nucleate boiling regime. In the convection regime, the electric forces act only on liquid; this EHD effect on heat transfer is called the *electroconvection effect.* In the boiling regime, vapor bubbles are present and the electric forces act on the liquid and on the bubbles. The effect of the

[1] Department of Mechanical Engineering, Texas A&M University, College Station, TX 77843-3123.

Contributed by the Heat Transfer Division of THE AMERICAN SOCIETY OF MECHANICAL ENGINEERS. Manuscript received by the Heat Transfer Division November 1994; revision received June 1995. Keywords: Augmentation and Enhancement, Boiling, Phase-Change Phenomena. Associate Technical Editor: V. K. Dhir.

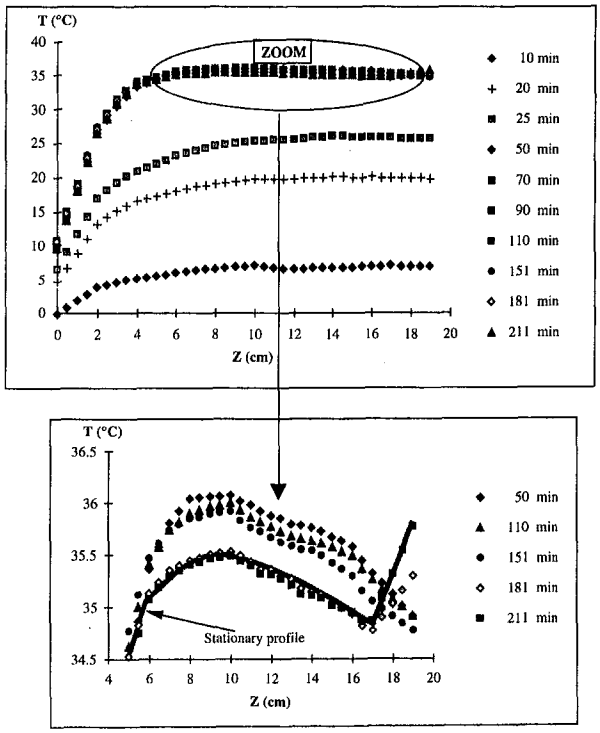

Fig. 4 Temporal evolution of the temperature profiles on the centerline along the vertical ZZ axis. Global view and detailed view around saturation temperature values. Liquid: *n*-pentane ($U = 0.69\ 10^{-3}$ m/s); heat flux applied to the plates: 5000 W/m^2.

V Conclusion

The experimental analysis based on the evaluation of temperature over space and time revealed three distinct zones, corresponding to the different states of the fluid:

- a liquid zone Z_l near the column inlet,
- a two-phase zone Z_d,
- a vapor zone Z_v near the outlet.

The temperature in the two-phase zone is seen to decrease, forming an N-shaped curve (⌇), probably resulting from combined flow and phase-change effects. The boundaries of the zones were determined with great precision using the temperature fields.

References

Bau, H., and Torrance, K. E., 1982, "Boiling in Low-Permeability Porous Materials," *Int. J. Heat Mass Transfer,* Vol. 25, pp. 45–55.

Cioulachtjian, S., Tadrist, L., Santini, R., Occelli, R., and Pantaloni, J., 1990, "Etude des transferts de chaleur dans un milieu poreux. Cas d'un Liquide en Ecoulement," *Rev. Gen. Therm. Fr.,* No. 338, pp. 85–90.

Naik, A. S., and Dhir, V. K., 1982, "Forced Flow Evaporating Cooling of a Volumetrical Heated Porous Layer," *Int. J. Heat Mass Transfer,* Vol. 25, No. 4, pp. 541–552.

Rahli, O., Cioulachtjian, S., Tadrist, L., and Santini, 1992, "Boiling in Porous Media—An Experimental and Numerical Analysis," *Proceedings of the International Symposium ECOS'92; On Efficiency, Costs, Optimization and Simulation of Energy Systems.* Zaragoza, Spain, June 15–18, pp. 515–520.

Schubert, G., and Strauss, J. M., 1977, "Two-Phase Convection in a Porous Medium," *J. Geophys. Res.,* Vol. 82, pp. 3411–3421.

Sondergeld, C. H., and Turcotte, D. L., 1977, "An Experimental Study of Two-Phase Convection in a Porous Medium With Applications to Geological Problems," *J. Geophys. Res.,* Vol. 82, pp. 2045–2053.

Sondergeld, C. H., and Turcotte, D. L., 1978, "Flow Visualisation Studies of Two-Phase Convection in a Porous Medium With Applications to Geological Problems," *Pure Appl. Geophys.,* Vol. 117, pp. 321–330.

Torrance, K. E., 1983, "Boiling in Porous Media," *ASME/JSME Thermal Engineering Joint Conference Proceedings,* Y. Mori and W.-J. Yang, eds., Vol. 1, pp. 593–606.

Udell, K. S., 1983, "Heat Transfer in Porous Media Heated From Above With Evaporation, Condensation, and Capillary Effects," ASME JOURNAL OF HEAT TRANSFER, Vol. 105.

Udell, K. S., 1985, "Heat Transfer in Porous Media Considering Phase Change and Capillarity—The Heat Pipe Effect," *Int. J. Heat Mass Transfer,* Vol. 28, No. 2, pp. 485–495.

Electrohydrodynamically Enhanced Heat Transfer in Pool Boiling

J. Seyed-Yagoobi,[1] C. A. Geppert,[1] and L. M. Geppert[1]

Background

The concept of electrohydrodynamic (EHD) enhancement of boiling has been researched actively only recently (e.g., Kawahira et al., 1990; Ogata et al., 1992; Karayiannis et al., 1993; Ogata and Yabe, 1993a, 1993b; Singh et al., 1993). The main objective of this study was to investigate and measure accurately the effect of electric field presence (using various electrode designs) on the pool boiling heat transfer of R-123 refrigerant, a new ozone-friendly substitute for R-11. An experimental apparatus was designed and built. The evaporator consisted of an electrically heated smooth tube in a horizontal configuration. The details of the experimental setup and results can be found from Geppert et al. (1995).

To clarify the effects of an electric field on pool boiling, different mechanisms of electrically induced liquid and vapor motion must be explained. The electric body force density acting on the molecules of a dielectric fluid in the presence of an electric field consists of three terms (Melcher, 1981):

$$\vec{f}_e = q\vec{E} - \frac{1}{2}\vec{E}^2\nabla\epsilon + \frac{1}{2}\nabla\left(\vec{E}^2\left(\frac{\partial\epsilon}{\partial\rho}\right)\rho\right) \qquad (1)$$

where q, E, ϵ, and ρ are the electric charge density, electric field strength, fluid electric permittivity, and fluid density, respectively. The three terms in Eq. (1) stand for three different kinds of force densities acting on the liquid. The first term represents the *Coulomb force,* which is the acting force on the free charges in an electric field. The Coulomb force is negligible in this study due to the lack of free charges in the fluid (the current measured is on the order of μA). The second term stands for the *dielectrophoretic force,* which is created by a local change of the permittivity in an electric field. A change in the permittivity occurs, for example, at the interface of a vapor bubble with a liquid. The third term is called the *electrostriction term.* The electrostriction force occurs primarily when a nonuniform electric field is applied on a dielectric fluid. The dielectrophoretic force and the electrostriction force are both forces that act on polarized charges and are both defined as *polarization forces.*

In the present study, an electric field was applied on a pool-boiling configuration. Heat transfer data were taken in the convection regime and in the nucleate boiling regime. In the convection regime, the electric forces act only on liquid; this EHD effect on heat transfer is called the *electroconvection effect.* In the boiling regime, vapor bubbles are present and the electric forces act on the liquid and on the bubbles. The effect of the

[1] Department of Mechanical Engineering, Texas A&M University, College Station, TX 77843-3123.

Contributed by the Heat Transfer Division of THE AMERICAN SOCIETY OF MECHANICAL ENGINEERS. Manuscript received by the Heat Transfer Division November 1994; revision received June 1995. Keywords: Augmentation and Enhancement, Boiling, Phase-Change Phenomena. Associate Technical Editor: V. K. Dhir.

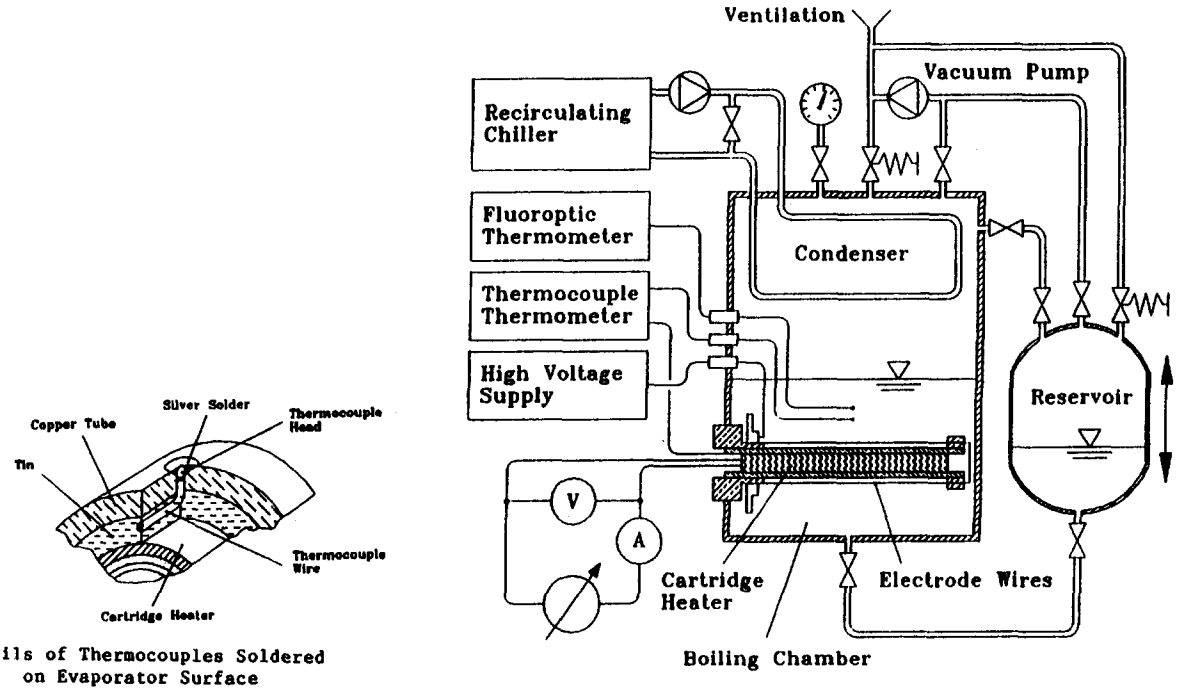

Fig. 1 Schematic of experimental setup

electric field on a vapor bubble is called the *interfacial EHD effect.* The interfacial EHD effect is involved as soon as bubbles occur in the boiling process.

Experimental Setup

The single-tube pool boiling apparatus (see Fig. 1) consists of a rectangular stainless steel chamber, which houses a condenser in the upper half and an evaporator in the lower half. A large sight glass in the lower front of the chamber allows for the observation of the experiments. The apparatus is well insulated and it stands in a ventilation chamber. The refrigerant is stored in an external can, which can be raised or lowered. In this way, the boiling chamber can be filled easily by gravity force without bringing air into contact with the refrigerant and without using a pump.

The condenser is a helically bent plain copper tube with an outer diameter of 9.5 mm and a length of 4.65 m. An external cooling system pumps cold water into the condenser tube. The evaporator consists of a single horizontal copper tube. The tube has a diameter of 2.65 cm and a heated length of 19 cm. The wall is relatively thick (3 mm) so that the thermocouples can be embedded in the tube surface. The tube surface is smooth and is polished with a 600 polish paper before every experiment. The tube is heated by an inserted cartridge heater with a maximum power output of 2000 W. The gap between the heater and the tube is filled with tin. The power input can be adjusted by a variable autotransformer. The voltage and the current are measured and give the actual power input.

There are two copper-constantan thermocouples and one fluoroptic cable to measure the temperature of the pool. The fluoroptic measurement system is of special value for use in high electric fields. In such environments, the electrically conducting leads of thermocouples could cause errors in reading temperature. A total of eight copper-constantan thermocouples (Type Omega, special limits of error) are soldered into little craters on the evaporator tube surface at the two cross sections located in the center and 18 mm to the left end of the tube. In both cross sections the thermocouples are installed in an angle of 90 deg around the tube starting from the top. The welded head of each thermocouple is sitting in this crater and touches the surface. The center of the head sits about 0.4 mm under the surface. To avoid disturbances by the electric field, the thermocouple wires are guided through the inside of the heater tube within the gap between the copper tube and the cartridge heater.

The boiling tube has a support mechanism to clamp electrode wires above the heated surface. In previous references, the wires are held in their position by small teflon rings on the heater surface. This causes a heat accumulation and a different local heat transfer. Several different electrode designs were considered in this study. The first two designs reported here were used to investigate the fundamental behavior of the boiling process in a high electric field (see Fig. 2). The distance of the electrodes to the heater surface in all cases was equal to 3.2 mm.

The first design was a construction out of eight straight stainless steel wires along the heater tube. Compared to former experiments, these wires were relatively thick (1.7 mm in diame-

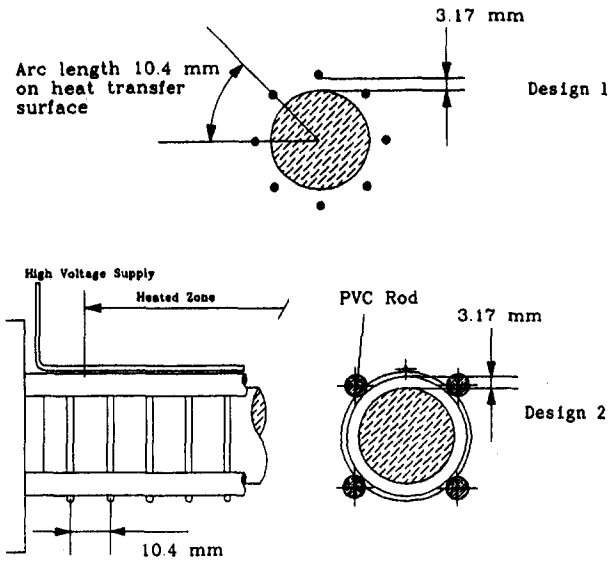

Fig. 2 Electrode designs

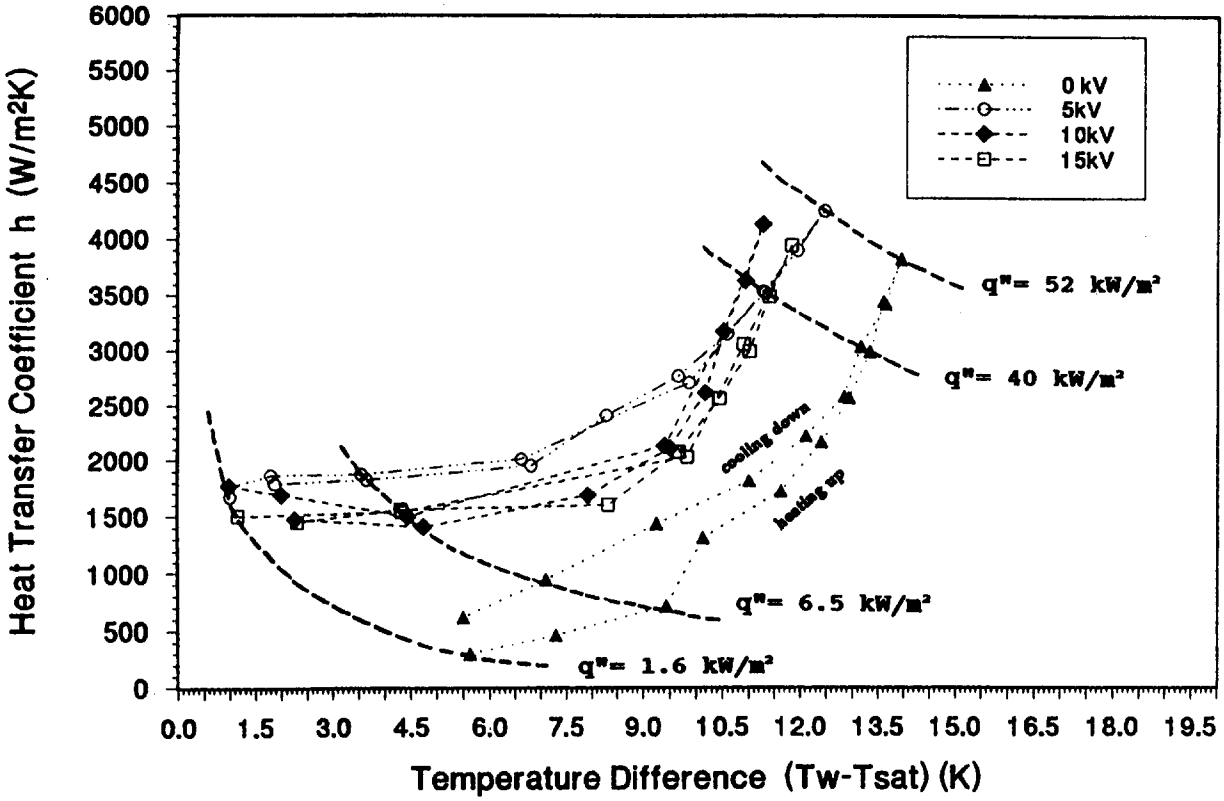

Fig. 3 Boiling curves of design 1 for different electrode voltages

ter) to avoid any electric discharge. To compare the influence of an electric field caused by parallel wires to the electric field caused by wires around the tube, the second design consisted out of 20 stainless steel rings (1.7 mm in diameter). The wire rings were held in their position by four rods of polyvinyl chloride. The spacing of the eight straight wires of the first design was defined by the arc length between the two angular positions of the electrodes. This arc length was 10.4 mm. Using this distance for the electrode rings implied a higher total wire length over the heated surface. The total wire length of the rings was 1.27 times the total wire length of the straight wires. The two selected electrode designs, straight wires and wire rings, allowed the study of very basic and fundamental electrode configurations.

At the beginning of every experiment, all gases were evacuated from the system by establishing a vacuum of 0.8 bar. During an experiment, the pressure and the saturation temperature (in a range of ± 0.1°C) were kept constant. The experiments were made at atmospheric pressure. The steady-state temperatures of the pool and the heater tube were recorded each time when the power of the evaporator was increased by 50 W. Data were taken during heating up and cooling down. Before every experiment, the base conditions without electric field had to be confirmed. Then, data were taken at 5, 10, and 15 kV. The evaporator tube was always grounded and the electrodes had a positive voltage. The electric conductivity of R-123 at 25°C was measured to be 1.0×10^{-8} S/m throughout the experiments.

Results

Figure 3 shows the average heat transfer coefficient as a function of the wall superheat for the electrode design 1. Due to the electrostriction force in this heterogeneous electric field, a voltage at the electrodes caused high turbulence in the liquid around the wires. At a heat flux of 1.6 kW/m^2, the average convective heat transfer at a voltage of 10 kV was about 4.6 times higher than without an electric field. Without the electric field presence, the onset of boiling occurred at a heat flux of about 6.5 kW/m^2 corresponding to 9.5°C wall superheat. At a voltage of 5 kV, the onset of boiling appeared first at a heat flux of 10 kW/m^2 (wall superheat of approximately 6.5°C). At higher voltages, the onset of boiling came even later. This boiling suppression was observed in all former EHD boiling experiments. The apparent reason for this is the strong turbulence of the liquid caused by the electrostriction force, which results in a high convective heat transfer.

The polarization forces pushed rising bubbles away from the high electric field around the electrode wires. The bubbles created at the bottom of the tube were held under the tube by flanking wires. The wires at the side of the heater pushed these rising bubbles back, acting against their buoyancy force. At higher voltages (10 kV to 15 kV) and a heat flux above 15 kW/m^2, a static vapor line of accumulated bubbles was held between the three bottom wires by the dielectrophoretic force. Kawahira et al. (1990) and previous researchers interpreted this effect as a "bubble growth on the electrode wires." This is the cause of the lower heat transfer coefficients at 10 and 15 kV compared to 5 kV. These results are of course dependent upon the electric field distribution and intensity, which in turn are dependent on the electrode spacing, distance from the heated surface, and the fluid electric properties. The fluid thermal properties also affect the electric field since the electric properties are temperature dependent.

The experiments using wire rings (design 2) as electrodes proved that it is possible to enhance the average heat transfer coefficient significantly at high heat fluxes by applying an electric field (See Fig. 4). Even the boiling curves of EHD enhanced experiments diverged from the normal boiling curve. At a heat flux of 1.6 kW/m^2 and a voltage of 10 kV, the heat transfer coefficient was 3.4 times higher than the coefficient without voltage (this is a smaller enhancement than the one with design

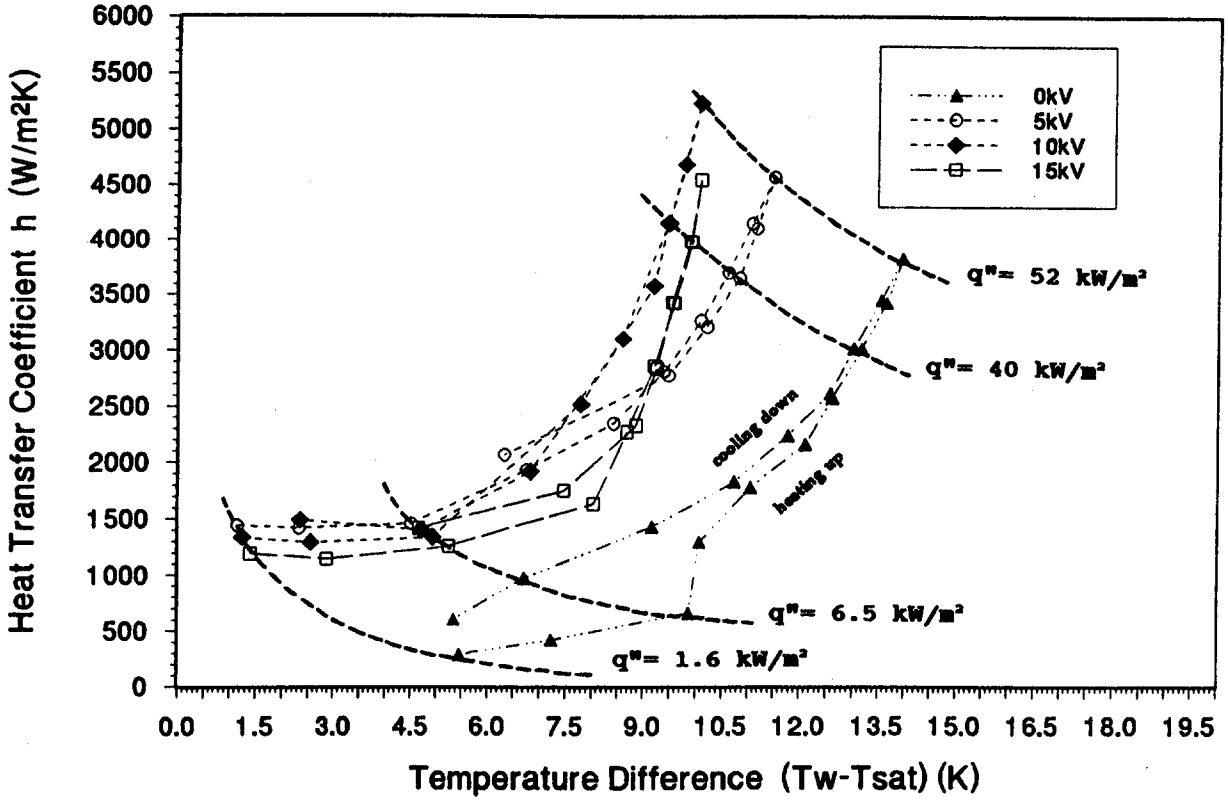

Fig. 4 Boiling curves of design 2 for different electrode voltages

1). At a heat flux of 52 kW/m^2 and the same voltage, the heat transfer coefficient was 38 percent higher than without an electric field. The enhancements achieved at the higher heat fluxes are larger with design 2 than with design 1. The onset of boiling with electrode rings at 0 kV occurred at a heat flux of about 6.5 kW/m^2 with a wall superheat of 10°C, which is a half a degree higher than the previous design. There were no vapor accumulations at high heat fluxes. The liquid area around the electrode rings maintained the liquid flow to the heat transfer.

All references have implied that the higher the voltage, the higher the enhancement of the heat transfer coefficient. The results of our experiments, however, imply that the best results were achieved at 5 to 10 kV range. This is because of two reasons. First, below 5 kV, the turbulence generated due to the electrostriction force is small. Second, at high voltages (above 10 kV), the dielectrophoretic forces are large, pushing the bubbles away from the electrodes. This effectively results in restricting the path available for the bubbles to depart.

An interesting phenomenon was observed during a boiling experiment with contaminated freon. The freon was contaminated by approximately 1 percent ethanol by weight. Figure 5 shows the resulting boiling curve using the electrode design 1 at different voltages. Especially at an electrode voltage of 15 kV, homogeneous nucleation occurred between the electrode wires and the heat transfer surface. This nucleation was a transient process in which large bubbles grew suddenly within the liquid, even when there was almost no wall superheat. This quick and sudden growth of bubbles occurred also when the heater was turned off, provided that the liquid was at saturation temperature. Bubbles produced at the bottom part of the evaporator coagulated and were constantly held by the dielectrophoretic force.

As in experiments with clean refrigerant at higher heat fluxes, the coagulated bubbles formed a vapor lines between the straight wires along the heated tube. These vapor lines first appeared at voltages between 5 and 10 kV and enhanced the heat transfer significantly at low heat fluxes of 3.3 kW/m^2 by facilitating the vaporization of the liquid microlayer. At an electrode voltage of 15 kV and a heat flux of 3.3 kW/m^2, the heat transfer coefficient was 12.6 times higher than without an electric field. At a higher heat flux, the heat transfer at the bottom of the tube dropped strongly because the two vapor lines coagulated and covered the bottom part of the tube with a vapor blanket. The boiling curve first rose when the freon started boiling on the top part of the evaporator.

Ogata and Yabe (1993a, 1993b) observed this phenomenon during boiling a mixture of R-11 and 2 percent ethanol by weight. Significant heat transfer enhancements at low heat fluxes were achieved. This phenomenon was interpreted as a bubble growth on the electrode wires. Ogata and Yabe suggested that this effect is due to a shortening of the electrical relaxation time when mixing ethanol in R-11. Another reason for this sudden homogeneous nucleation could be due to a decrease in the surface tension of R-123 because of the presence of ethanol. This results in a homogeneous nucleation with a smaller critical radius of vapor embryo.

The EHD power consumption for all the experiments conducted was on the order of 0.1 percent of the heat transfer power in the evaporator. Generally, the electrode rings of design 2 had the lowest power consumption despite its overall electrode length being larger than in the first design. Additionally, the heat transfer enhancement at larger heat flux levels was highest using the second design. In this study, all boiling curves that were taken at an electrode voltage higher than 2 kV had practically negligible hysteresis loop.

The uncertainties in the voltage, current, and temperature measurements were below ±0.1 percent, ±0.3 percent, and ±0.4°C. The accuracy uncertainty in the heat transfer coefficient value was approximately ±55 W/m^{2}K at a high heat flux value of 52 kW/m^2. The calculated precision uncertainties corre-

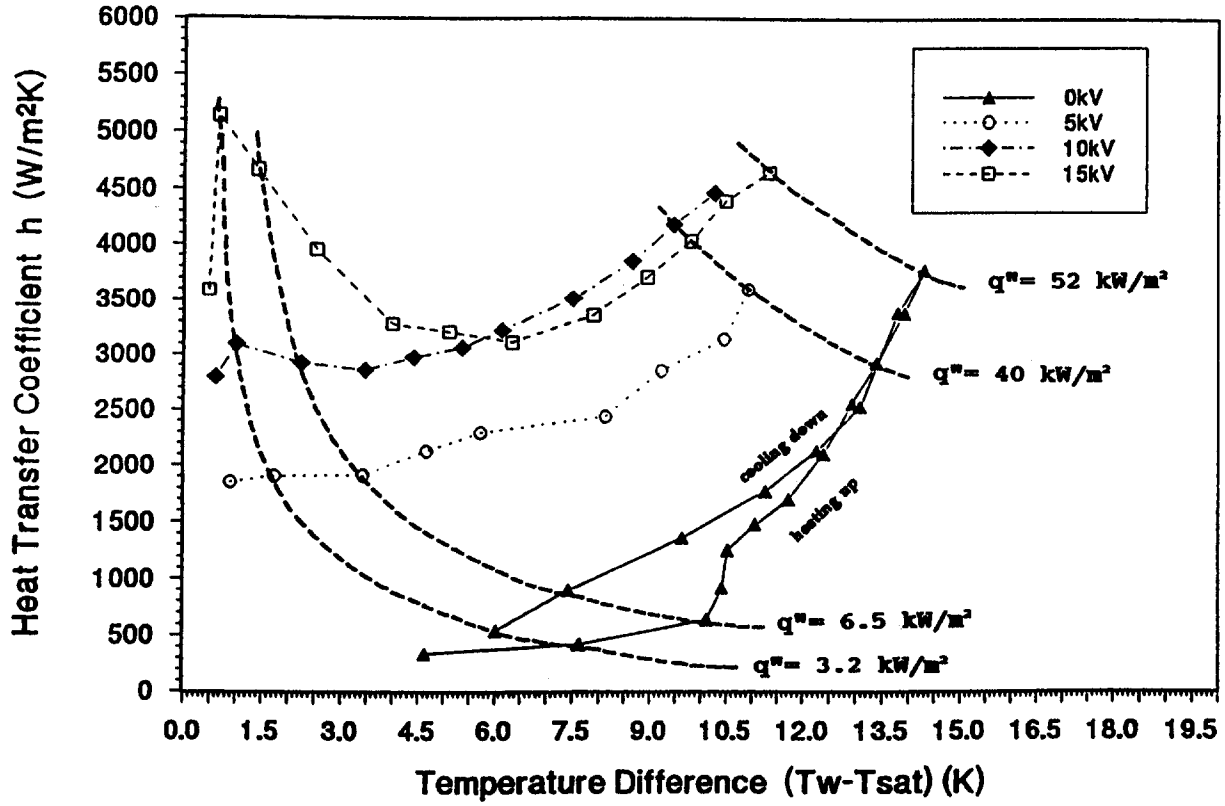

Fig. 5 Boiling curves of design 1 for different electrode voltages in contaminated freon

sponded to approximately 2 percent of the heat transfer coefficient over the whole heat flux range.

Acknowledgments

This research was partially supported by the NASA Johnson Space Center and the Texas A&M University Drying Research Center. The refrigerant was provided by DuPont.

References

Geppert, C. A., Geppert, L. M., and Seyed-Yagoobi, J., 1995, "Electrohydrodynamically Enhanced Heat Transfer in Pool Boiling," *Basic Aspects of Two Phase Flow and Heat Transfer,* ASME HTD-Vol. 308, pp. 69–76.

Karayiannis, T. G., Al-Dadah, R. K., James, R. W., and Allen, P. H. G., 1993, "Electrohydrodynamic Boiling Heat Transfer Enhancement in Heat Exchangers," ASME Paper No. 93-WA/HT-41.

Kawahira, H., Kubo, J., Yokoyama, T., and Ogata, J., 1990, "The Effect of an Electric Field on Boiling Heat Transfer of Refrigerant-11—Boiling on a Single Tube," *IEEE Transactions on Industry Applications,* Vol. 26, No. 2, pp. 359–365.

Melcher, J. R., 1981, *Continuum Electromechanics,* Massachusetts Institute of Technology Press, Cambridge, MA, p. 3–18.

Ogata, J., Iwafuji, Y., Shimada, Y., and Yamazaki, T., 1992, "Boiling Heat Transfer Enhancement in Tube-Bundle Evaporators Utilizing Electric Field Effects," Paper No. BA-92-5-2, *ASHRAE Transactions:* Symposia, Vol. 98, pp. 435–444.

Ogata, J., and Yabe, A., 1993a, "Basic Study on the Enhancement of Nucleate Boiling Heat Transfer by Applying Electric Fields," *Int. J. Heat Mass Transfer,* Vol. 36, No. 3, pp. 775–782.

Ogata, J., and Yabe, A., 1993b, "Augmentation of Boiling Heat Transfer by Utilizing the EHD Effect—EHD Behaviour of Boiling Bubbles and Heat Transfer Characteristics," *Int. J. Heat Mass Transfer,* Vol. 36, No. 3, pp. 783–791.

Singh, A., Kumar, A., Dessiatoun, S., Faani, M. A., Ohadi, M. M., and Ansari, A. I., 1993, "Compound EHD-Enhanced Pool Boiling of R-123 in a Liquid-to-Refrigerant Heat Exchanger," ASME Paper No. 93-WA/HT-40.

Experimental Examination of Forced-Convection Subcooled Nucleate Boiling and Its Application in Microgravity

T. C. Wang,[1] T. J. Snyder,[1] and J. N. Chung[2]

[1] Graduate Student, School of Mechanical and Materials Engineering, Washington State University, Pullman, WA 99164-2920; Student Mem. ASME.

[2] Professor, School of Mechanical and Materials Engineering, Washington State University, Pullman, WA 99164-2920; Mem. ASME.

Contributed by the Heat Transfer Division of THE AMERICAN SOCIETY OF MECHANICAL ENGINEERS. Manuscript received by the Heat Transfer Division February 1995; revision received October 1995. Keywords: Boiling, Microgravity Heat Transfer, Phase-Change Phenomena. Associate Technical Editor: V. K. Dhir.

Introduction

Forced-convection subcooled nucleate boiling has been recognized as one of the most efficient heat transfer mechanisms (Tsung-Chang and Bankoff, 1990; Bankoff, 1994). Many fundamental investigations were found in the literature concerning the basic mechanisms of forced-convection boiling that are responsible for the enhancements in heat transfer coefficient over the single-phase forced-convection heat transfer. The main question is, "Why does the nucleation and formation of bubbles improve the heat transfer so drastically?" However, the theories have been divided. Gunther and Kreith (1950) suggested that turbulent mixing or microconvection between growing and collapsing bubbles is the mechanism responsible for the enhancement. The second theory (Bankoff, 1959, 1961) is based on the latent heat transport where condensation at the cap of the bubble and evaporation from the surrounding microlayer are suggested as the key transport mechanisms of latent heat.

Recently Tsung-Chang and Bankoff (1990) re-examined the latent heat transport theory. They proposed that "sliding" of

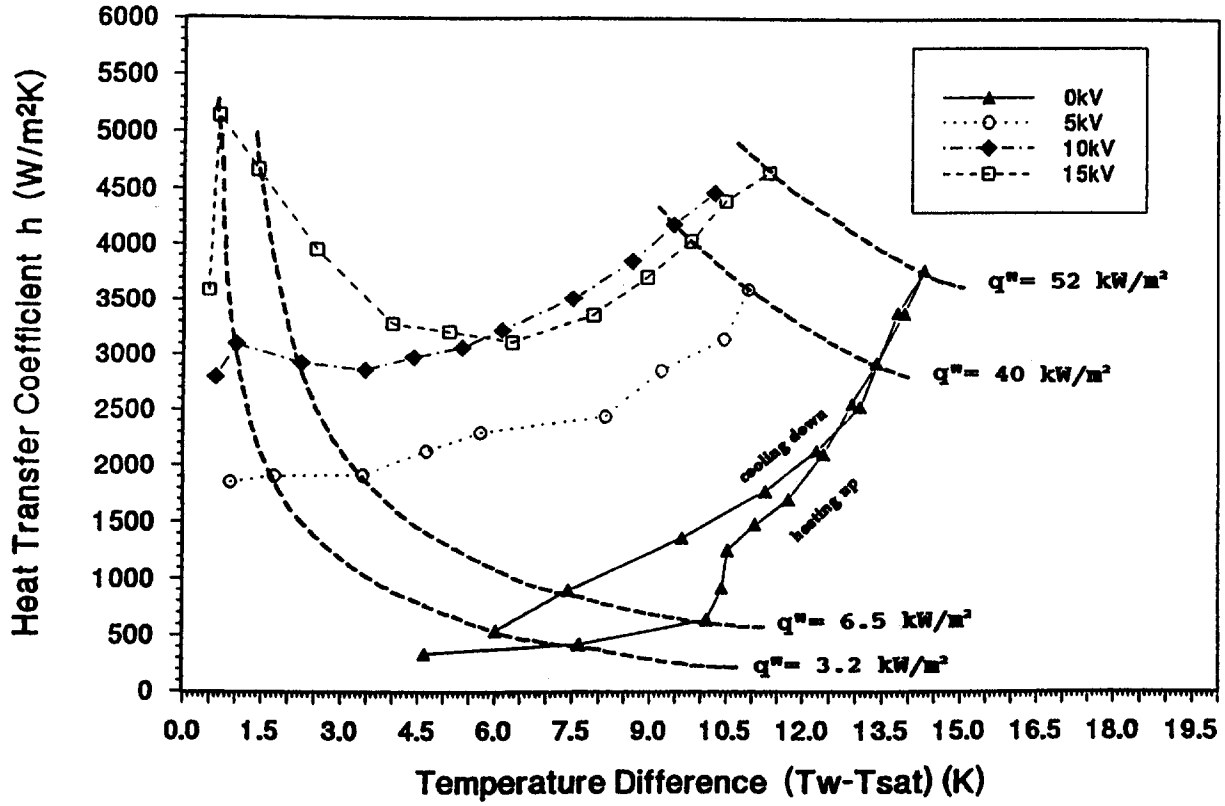

Fig. 5 Boiling curves of design 1 for different electrode voltages in contaminated freon

sponded to approximately 2 percent of the heat transfer coefficient over the whole heat flux range.

Acknowledgments

This research was partially supported by the NASA Johnson Space Center and the Texas A&M University Drying Research Center. The refrigerant was provided by DuPont.

References

Geppert, C. A., Geppert, L. M., and Seyed-Yagoobi, J., 1995, "Electrohydrodynamically Enhanced Heat Transfer in Pool Boiling," *Basic Aspects of Two Phase Flow and Heat Transfer,* ASME HTD-Vol. 308, pp. 69–76.

Karayiannis, T. G., Al-Dadah, R. K., James, R. W., and Allen, P. H. G., 1993, "Electrohydrodynamic Boiling Heat Transfer Enhancement in Heat Exchangers," ASME Paper No. 93-WA/HT-41.

Kawahira, H., Kubo, J., Yokoyama, T., and Ogata, J., 1990, "The Effect of an Electric Field on Boiling Heat Transfer of Refrigerant-11—Boiling on a Single Tube," *IEEE Transactions on Industry Applications,* Vol. 26, No. 2, pp. 359–365.

Melcher, J. R., 1981, *Continuum Electromechanics,* Massachusetts Institute of Technology Press, Cambridge, MA, p. 3–18.

Ogata, J., Iwafuji, Y., Shimada, Y., and Yamazaki, T., 1992, "Boiling Heat Transfer Enhancement in Tube-Bundle Evaporators Utilizing Electric Field Effects," Paper No. BA-92-5-2, *ASHRAE Transactions:* Symposia, Vol. 98, pp. 435–444.

Ogata, J., and Yabe, A., 1993a, "Basic Study on the Enhancement of Nucleate Boiling Heat Transfer by Applying Electric Fields," *Int. J. Heat Mass Transfer,* Vol. 36, No. 3, pp. 775–782.

Ogata, J., and Yabe, A., 1993b, "Augmentation of Boiling Heat Transfer by Utilizing the EHD Effect—EHD Behaviour of Boiling Bubbles and Heat Transfer Characteristics," *Int. J. Heat Mass Transfer,* Vol. 36, No. 3, pp. 783–791.

Singh, A., Kumar, A., Dessiatoun, S., Faani, M. A., Ohadi, M. M., and Ansari, A. I., 1993, "Compound EHD-Enhanced Pool Boiling of R-123 in a Liquid-to-Refrigerant Heat Exchanger," ASME Paper No. 93-WA/HT-40.

Experimental Examination of Forced-Convection Subcooled Nucleate Boiling and Its Application in Microgravity

T. C. Wang,[1] T. J. Snyder,[1] and J. N. Chung[2]

[1] Graduate Student, School of Mechanical and Materials Engineering, Washington State University, Pullman, WA 99164-2920; Student Mem. ASME.

[2] Professor, School of Mechanical and Materials Engineering, Washington State University, Pullman, WA 99164-2920; Mem. ASME.

Contributed by the Heat Transfer Division of THE AMERICAN SOCIETY OF MECHANICAL ENGINEERS. Manuscript received by the Heat Transfer Division February 1995; revision received October 1995. Keywords: Boiling, Microgravity Heat Transfer, Phase-Change Phenomena. Associate Technical Editor: V. K. Dhir.

Introduction

Forced-convection subcooled nucleate boiling has been recognized as one of the most efficient heat transfer mechanisms (Tsung-Chang and Bankoff, 1990; Bankoff, 1994). Many fundamental investigations were found in the literature concerning the basic mechanisms of forced-convection boiling that are responsible for the enhancements in heat transfer coefficient over the single-phase forced-convection heat transfer. The main question is, "Why does the nucleation and formation of bubbles improve the heat transfer so drastically?" However, the theories have been divided. Gunther and Kreith (1950) suggested that turbulent mixing or microconvection between growing and collapsing bubbles is the mechanism responsible for the enhancement. The second theory (Bankoff, 1959, 1961) is based on the latent heat transport where condensation at the cap of the bubble and evaporation from the surrounding microlayer are suggested as the key transport mechanisms of latent heat.

Recently Tsung-Chang and Bankoff (1990) re-examined the latent heat transport theory. They proposed that "sliding" of

bubbles on the heater surface would result in the augmentation of microlayer evaporation beneath the bubble by a factor of two or possibly more over a stationary bubble. Cooper et al. (1983) experimentally demonstrated a sliding single bubble due to forced flow under microgravity. Only a single bubble was studied; therefore, it did not offer any information for forced-convective microgravity boiling heat transfer. The first objective of this note is to verify the Tsung-Chang and Bankoff "sliding bubble" model in a carefully designed experiment. In highly subcooled and high-velocity forced-convection nucleate boiling, bubbles grow, slide, and collapse on the heater surface; therefore, buoyancy is of minimum reliance. In order to obviate the masking effect of buoyancy, our experiment was performed under low-velocity and microgravity conditions such that the physical phenomenon was more clearly recorded by our experimental system. Because subcooled forced-convection nucleate boiling has a minimum reliance on gravity, Bankoff (1994) recently has suggested its application in space. The second objective of this paper is, therefore, to study the feasibility of this highly effective heat transfer mechanism in a microgravity environment.

Experiment

The flow boiling apparatus consists of a pump, preheater, boiling test section, condenser, lighting, and video and data acquisition system. Owing to the limited space available in the drop box, the capacity of the pump was restricted. As a result, the maximum pump capacity was employed in our experiment to provide the maximum convection effect. This maximum pump capacity maintained a single-phase mean velocity of 7.7 $\pm$ 0.1 cm/s over the heater surface. Due to the physical limitations, the experimental system was open to the atmosphere. The bulk fluid temperature in the experiment was conveniently set to approximately room temperature. This resulted in a relatively constant subcooling of 17 $\pm$ 2°C for our experiment. Variations in the system pressure due to the transient gravity field during the drop resulted in about 1°C difference in the calculated superheat and were neglected. Therefore, in our case, T_{sat}(nominal) was defined as 45°C—the saturation temperature for the ambient pressure of 93.1 kPa. Spectrophotometric grade Freon-113 (1,1,2 trichlorotrifluoroethane 99+ percent) was chosen as the test fluid. Because of the high solubility of dissolved gases in Freon-113 a typical degassing procedure was followed, which involved boiling the fluid prior to an experiment (3M Manual, 1992). Data acquisition was performed at 100 Hz for 500 scans: Three seconds were recorded before the release to obtain the 1g data, and two seconds of data recorded after the release, which captured the microgravity portion and the deceleration. Microgravity was achieved in a 0.6-second drop tower outlined by Snyder (1993). A semitransparent, 400-Å-thick gold-film heater (2.54 cm $\times$ 2.54 cm) similar to that described by Oker and Merte (1981) was built and used in the experiment. Heater calibration was performed based on the procedure reported by Oker and Merte (1981). This heater design allowed us to maintain a relatively constant heat flux during the experiment and also provided the average surface temperature. The minimum heat flux used in our experiment was 2.88 $\times$ 10^4 W/m^2 and was chosen because this heat flux level was the highest heat flux that could maintain a pattern of individual bubbles on the heater surface during microgravity for the 7.7 cm/s flow. The uncertainty in the heater resistance, surface temperature, and heat flux are $\pm$0.00148 ohms, $\pm$1.16°C, and $\pm$380 W/m^2, respectively. This resulted in an uncertainty in heat transfer coefficient of $\pm$96 W/m^2 K.

Results and Discussion

The Heat Transfer Coefficient. The heat transfer coefficient was calculated according to the following definition:

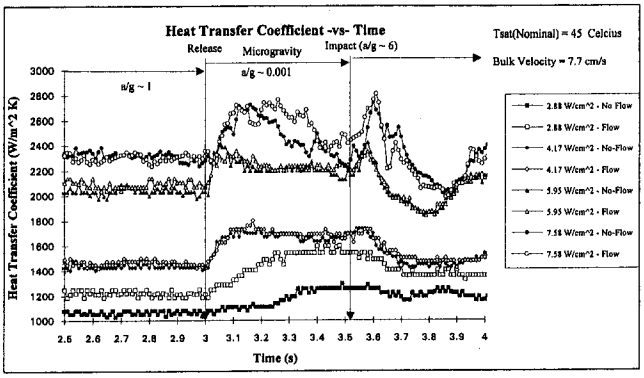

Fig. 1 Heat transfer coefficient for pool and forced-convection boiling of R-113

$$q'' = h(T_s - T_{sat}) \quad (1)$$

where q'' is the heat flux from the heater surface, h is the heat transfer coefficient, T_s is the mean heater surface temperature, and T_{sat} is the nominal saturation temperature, which is the saturation temperature corresponding to system pressure. The subcooling is not reflected in the definition of the heat transfer coefficient owing to the past experience that subcooling has been found a relatively weak parameter, especially in nucleate boiling (Carey, 1992). The heat transfer to the boiling fluid was assumed to be equal to the electrical power supplied to the heater because for a polycarbonate substrate (as used in our heater design) the heat loss from the nonwetted surface of the substrate is 3 percent or less (Wang, 1993). The maximum change in heat flux was found to be approximately $\pm$ 0.35 percent and therefore the heat flux on the heater surface was assumed constant. Thus, any changes in the boiling heat transfer process were reflected by the changes in the mean heater surface temperature. While the spatial temperature variation is not known, changes in the mean quantities provided an indication of the general condition of the heater surface. For example, enhancements or reductions in heat transfer efficiency, believed to be caused from increased microlayer evaporation or the formation of dry spots on the heater surface, could be reflected by changes in the mean surface temperature (or heat transfer coefficient) as compared to the average values measured in normal gravity, and the initial values encountered when transitioning to microgravity.

Figure 1 shows the heat transfer coefficient plot for all four heat fluxes under pool and forced-convection boiling. The first arrow in the graph indicating "release" represents the moment at which the experiment was released and microgravity started. The second arrow indicates when the experimental rig hit the airbag and microgravity ended. The heat transfer coefficients are invariably higher during microgravity for both pool and flow boiling except at the highest heat flux. The present findings for the case of pool boiling are in good agreement (both quantitative and qualitative) with some previously published results (Merte et al., 1993), which showed that nucleate pool boiling heat transfer is enhanced as the buoyancy normal to the heater surface is reduced (including microgravity) and that it is degraded as the buoyancy normal to the heater surface is increased. The next result is the sharp decline in the heat transfer coefficient during microgravity for the highest heat flux case (7.58 $\times$ 10^4 W/m^2). The forced flow only delayed the drop in heat transfer coefficient. The drop in the heat transfer coefficient is thought to have been caused by the drying-up of some portion of the heater surface due to the formation of vapor slugs, which stuck to the surface. The forced flow lost its effectiveness when the vapor agglomerates grew to a certain size and this will be further verified later in the flow visualization study. The last important finding is on the effectiveness of the forced flow.

Owing to the fact that the forced velocity is constant in all the cases, it is apparent that the forced convection is only effective for the lowest heat flux case (2.88×10^4 W/m^2), whereas for the other cases the differences in heat transfer coefficient are negligible between pool and forced convection boiling. For the lowest heat flux, the differences in heat transfer coefficient grew even larger during microgravity, which is believed to be due to the ability of the flow to prevent the formation of vapor agglomerates and to maintain single and sliding bubbles. For the other cases, the heating is so high that the bubbles merge into vapor slugs before the flow can move them. The flow visualization, presented later, will also confirm the above-suggested mechanism for the forced-convection boiling.

In an effort to examine further the forced-convection effects in a microgravity environment, the percentage increase in heat transfer coefficients under forced-convection over those of 1g pool boiling have been evaluated. Under 1g, the forced flow made a difference only for the lowest heat flux case. Approximately 15 percent increase in the heat transfer coefficient was measured for the heat flux of 2.88×10^4 W/m^2. Most of the increase was certainly due to increased convection; however, some single and sliding bubbles were observed for the 1g case. During microgravity, both the forced-convection and pool boiling heat transfer coefficients are 10 to 20 percent higher than those of 1g pool boiling for the three higher heat fluxes. For the lowest heat flux case, the forced-convection heat transfer coefficient enjoyed a 45 percent increase over the 1g pool boiling. We attribute this sizable increase in heat transfer coefficient to the sliding individual bubbles on the heater surface according to the numerical model of Tsung-Chang and Bankoff (1990) who predicted that at least a factor of two in the increase of microlayer evaporation for a sliding bubble. Again, more discussion of the sliding bubbles is given later in the visualization section.

For the heat transfer results in Fig. 1, it is reassuring to note that they are well represented by the Rohsenow correlation for nucleate boiling given in the following form by Mills (1992),

$$\mathrm{Nu} = \frac{\mathrm{Ja}^2}{C_{nb}^3 \, \mathrm{Pr}_l^m} \tag{2}$$

In this equation Nu is the Nusselt number, Ja is the Jakob number, and Pr_l is the Prandtl number of the boiling fluid. The empirical constants m and C_{nb} for our data are 4.1 and 0.0075, respectively. Rohsenow suggested for all organic fluids m = 4.1, while Mills (1992) only gave C_{nb} = 0.0068 for scored copper and C_{nb} = 0.008 for polished stainless steel. Therefore, our gold-film surface acts approximately between a copper surface and a stainless steel surface in the nucleate boiling regime.

Simplified Numerical Modeling. A transient one-dimensional numerical model was developed for the following two objectives: (1) to check whether the surface temperature measured is indeed the mean surface temperature, (2) to make sure that the assumption of negligible heat loss through the unwetted surface of the polycarbonate is valid. The governing equations and the solution method are detailed by Wang (1993). The calculated and measured surface temperatures were in reasonable agreement. Based on the close agreement, we conclude that the simplified model is a reasonable approach for the transient microgravity boiling simulation. Therefore, the measured surface temperature does represent the mean value and the heat loss through the unwetted portion is 3 percent or less of the total heat flux based on the numerical result, which is negligible.

Visualization Study. To compliment the measured data, a set of video recordings are presented to provide the physical understanding. Under normal gravity the addition of the forced flow simply swept the bubbles along the flow direction. The effect of forced flow is negligible because of the low velocity in the current study except for the lowest heat flux case. For the

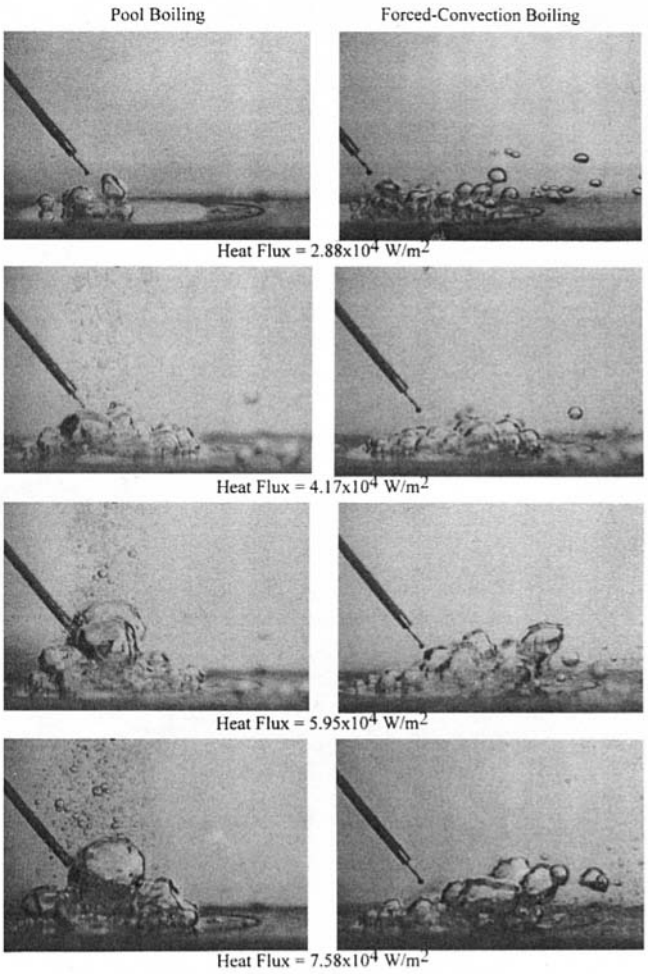

Fig. 2 Comparisons of pool and forced-convection boiling bubble dynamics

case of microgravity, Fig. 2 provides a side-by-side comparison between pool and forced-convection boiling flow patterns in the vicinity of the heater surface for heat fluxes ranging from 2.88×10^4 to 7.58×10^4 W/m^2. We found the following general trends after examining the visualization figures. During microgravity pool boiling, the bubbles did not rise off the heater surface, and as a result, they coalesced to form what might be called "vapor agglomerates." These large bubbles of various shapes have very rough surfaces and tend to cover up the heater surface, which appeared to cause some portions of the surface to become unwetted during the trailing portion of microgravity. The drying-up of the surface due to vapor agglomerates contributed to the drop in heat transfer coefficient for the heat flux of 7.58×10^4 W/cm^2, as discussed above. Therefore, under microgravity the bubble swarm of terrestrial boiling was, in general, replaced by bubble slugs and chunks. The average size of the bubbles was seen to increase with the heat fluxes. For all the cases except the lowest heat flux case we found that immediately around the large bubbles there were swarms of smaller bubbles, which were nucleating and detaching from the heater surface. The smaller bubbles appeared to coalesce with the larger bubbles. When a smaller bubble coalesced with a larger bubble, the surface where the smaller bubble originated was left wet and this transport mechanism sustained the nucleate boiling process locally. If a small bubble nucleated away from a large bubble, and could not coalesce, then it could form a large bubble itself as other smaller bubbles coalesced with it. This mechanism is consistent with previously published results (Siegel, 1967) and appears to be the driving mechanism control-

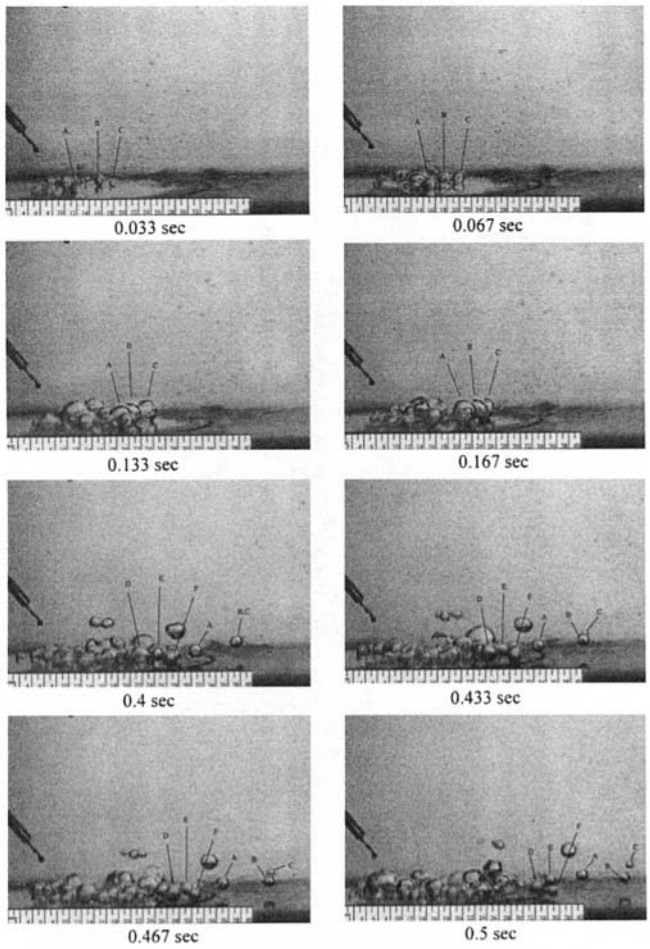

Fig. 3 Tracking of individual sliding bubbles, 2.88 × 10^4 W/m^2

ling the bubble dynamics for pool boiling in microgravity for the conditions of this study. While these effects were dominant during pool boiling, they could also be seen during the forced flow cases for the higher heat flux runs.

The second finding is concerned with the differences between pool and forced convection boiling under microgravity. With forced flows, the bubbles experienced a shear force along the flow direction. In the absence of gravity, the bubble dynamics depends on the balance between the drag due to the forced flow and the surface tension. The surface tension force would prevail if the contact area between the bubble and the heater surface is larger than the bubble frontal surface area experiencing the forced flow, otherwise the drag force would dominate. For the former, a hemispherical bubble would tend to stick to the surface while a spherical bubble, which belongs to the latter case, would most likely slide on the heater surface. Based on the visualization photographs, we found that for medium to high heat fluxes, the coalesced vapor agglomerates tend to form hemispherical or dome shapes with large base areas as a result of rapid vapor generation. Therefore at medium and high heat fluxes ($4-7 \times 10^4$ W/m^2) in the vicinity of the heater surface, the surface tension dominated, which left the forced flow with negligible effects on the bubble dynamics and heat transfer. The heat transfer coefficients presented previously also support this conclusion. The noticeable difference between pool and forced-convection boiling for medium to high heat fluxes is found at the top of the vapor agglomerates. Some vapor was sheared off in the forced convection case while the vapor agglomerates grew tall and were relatively symmetric under the pool boiling case.

For the lowest heat flux case under microgravity as shown in Fig. 2, the two-phase pattern of the forced-convection boiling was fundamentally different from that of the pool boiling. Owing to the low heating rate, the bubbles did not have any opportunity to coalesce and form vapor agglomerates, which resulted in the dominance of the flow drag over the surface tension. Basically, it was found that the bubbles are spherical and most of them are isolated from another. Based on our image analysis, the average individual bubble size was calculated at 1 to 2 mm while those of vapor chunks were on the order of 1 cm and up.

Strong evidence was found that the isolated spherical bubbles were "sliding" on the heater surface. Figure 3 is specially marked to demonstrate the "sliding" phenomenon. In order to obtain quantitative results, we marked the individual bubbles and tracked their movements on the heater surface. The sliding velocities of bubbles A–C were measured by digitizing the images and tracking the centroid of the bubble with image analysis software. As shown in Fig. 4, the patterns of bubble velocities are quite consistent among the three bubbles tracked in the analysis. The velocities of the individual bubbles fluctuated at relatively large amplitudes between 25 and 90 percent of the free-stream velocity during the first half of the transient when sliding on the heater surface. After detachment from the heater surface their velocities appeared to converge to between 80 and 90 percent of the free-stream velocity and could actually be larger than the mean velocity (presumably due to the sudden release from the heater surface and the larger bubble boundary resulting in an increased void fraction and therefore a reduced flow area). This result appears to be in agreement with that of Gunther (1951). For forced-convection nucleate boiling in water, Gunther (1951) indicated that the bubbles were sliding at 80 percent of the free-stream velocity of 1.7 m/s. As shown in Fig. 3, the bubbles grew in size from the beginning of microgravity until the tops of the bubbles reached the subcooled liquid (approximately $t = 0.167$ second for this case). After that, the sizes of the bubbles were found nearly constant due to the balance between condensation on the bubble cap and vaporization from the microlayer. The finding of this nearly constant bubble size also contributes to the verification of the latent heat transport mechanism (Bankoff, 1959, 1961).

It is our conclusion that the significantly higher heat transfer coefficient for forced-convection boiling than that for pool boiling in microgravity for the lowest heat flux is apparently due to the combination of the prevention of vapor agglomerate formation by the flow and the sliding of individual spherical bubbles. The current experimental results also help verify the mathematical model of Tsung-Chang and Bankoff (1990) that the sliding of bubbles in highly subcooled forced-convection nucleate boiling strongly augments the heat transfer through microlayer evaporation.

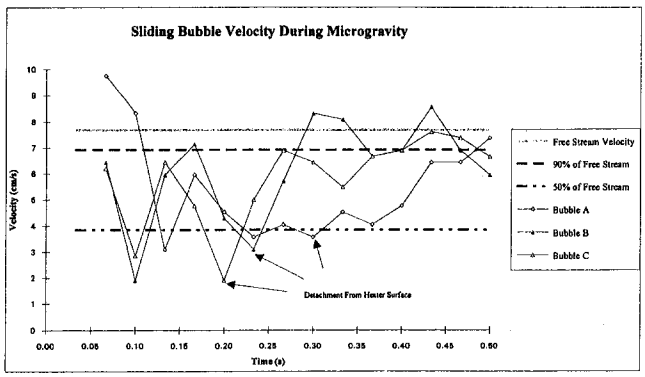

Fig. 4 Sliding bubble velocity

Implications to Space Application. Based on the measured heat transfer coefficient data and the flow visualization, it is reasonable to suggest that for a given heat flux, if the forced-flow field is strong enough to prevent bubble agglomeration and to maintain single and sliding bubbles, subcooled forced-convection nucleate boiling would be a feasible and efficient heat transfer mechanism in microgravity. Bankoff (1994) recently suggested that since subcooled forced-convection nucleate boiling is one of the most efficient heat transfer mechanisms and has a minimum reliance on gravity, it be adapted for space applications. We believe that the current paper has provided a solid support for Bankoff's idea.

Acknowledgments

This work was supported by NASA Grant No. NAG3-1387. The authors gratefully acknowledge the interest and support of Dr. Fran Chiaramonte of the NASA Lewis Research Center.

References

Bankoff, S. G., 1959, "On the Mechanism of Subcooled Nucleate Boiling," Jet Prop. Lab. Memo 30-38.

Bankoff, S. G., 1961, "On the Mechanism of Subcooled Nucleate Boiling, Parts 1 and 2," *Chem. Eng. Progr. Symposium Series*, No. 32, Vol. 57, pp. 156–163; 164–172.

Bankoff, S. G., 1994, "Future Directions in Two-Phase Flow and Heat Transfer in Space," keynote paper, *Proceedings of Second Microgravity Fluid Physics Conference*, pp. 3–11.

Carey, V. P., 1992, *Liquid–Vapor Phase-Change Phenomena*, Taylor and Francis, Bristol, PA.

Cooper, M. G., Mori, K., and Stone, C. R., 1983, "Behaviour of Vapor Bubbles Growing at a Wall With Forced Flow," *Int. J. Heat Mass Transfer*, Vol. 26, No. 10, pp. 1489–1507.

Gunther, F. C., and Kreith, F., 1950, "Photographic Study of Bubble Formation in Heat Transfer to Subcooled Water," Jet Propulsion Laboratory, Pasadena, CA, Progress Report No. 4-75.

Gunther, F. C., 1951, "Photographic Study of Surface-Boiling Heat Transfer to Water With Forced Convection," *Trans. ASME*, Vol. 73, pp. 115–124.

Merte, H. Jr., Lee, H. S., and Ervin, J. S., 1993, "Transient Nucleate Pool Boiling in Microgravity—Some Initial Results," *Int. Symp. Microgravity Science and Applications*, Paper J-5.

Mills, A. F., 1992, *Heat Transfer*, Irwin, Homeward, IL.

Oker, E., and Merte, H. Jr., 1981, "Semi-transparent Gold Film as Simultaneous Surface Heater and Resistance Thermometer for Nucleate Boiling Studies," ASME JOURNAL OF HEAT TRANSFER, Vol. 103, pp. 65–68.

Siegel, R., 1967, "Effects of Reduced Gravity on Heat Transfer," *Advances in Heat Transfer*, Vol. 4, pp. 143–228.

Snyder, T. J., 1993, "WSU 2.1 Second Microgravity Drop Tower, Design, Construction, and Performance," MS Thesis, Department of Mechanical and Materials Engineering, Washington State University.

Tsung-Chang, G., and Bankoff, S. G., 1990, "On the Mechanism of Forced-Convection Subcooled Nucleate Boiling," ASME JOURNAL OF HEAT TRANSFER, Vol. 112, pp. 213–218.

Wang, T.-C., 1993, "Transient Effects of Microgravity on Pool and Low Velocity Flow Boiling Heat Transfer," M.S. Thesis, Department of Mechanical and Materials Engineering, Washington State University.

3M Company, 1992, *Product Manual for Fluorinert Liquids*.

Critical Heat Flux in Forced Convective Subcooled Boiling With Multiple Impinging Jets

M. Monde[1] and Y. Mitsutake[1]

Nomenclature

C = constant defined by Eq. (3)
c_p = specific heat of liquid
d = diameter of an impinging jet
H_{fg} = latent heat of evaporation
Ja = Jakob number = $(\rho_l/\rho_v)(c_p\Delta T_{sub}/H_{fg})$
L = two times of maximum distance (Fig. 2)
q_{co} = critical heat flux for saturated boiling
q_c = critical heat flux for subcooled boiling
ΔT_{sub} = subcooling temperature of jet = $T_{sat} - T_{liq}$
u = velocity of a liquid jet at the nozzle exit
ρ_l = density of saturated liquid
ρ_v = density of saturated vapor
σ = surface tension

1 Introduction

In the past two decades, the critical heat flux in saturated convective boiling with an impinging jet and multiple jets has been studied rather extensively (Katto and Yokoya, 1988; Sharan and Lienhard, 1985; Monde and Inoue, 1991; Monde, 1991). The characteristics of the CHF were clarified and then generalized correlations, which are applicable for the CHF within a wide experimental range, had been proposed, for example, by Monde (1991). More recently, Monde et al. (1994) measured critical heat flux during forced convective subcooled boiling with an impinging jet within an experimental range as listed in Table 1 and have derived a generalized correlation (1), yielding the CHF for the subcooled jet well based upon Eq. (2) for the saturated jet with an accuracy as given by a mean average ($E = \Sigma\,((q_{exp} - q_{cal})/q_{exp})/n$) of −0.06 percent, a mean deviation of 12.4 percent, and a standard deviation of 15.2 percent. The total number of the subcooled and saturated CHF data is 271.

$$\frac{q_c}{q_{co}} = \frac{1 + \sqrt{1 + 4C\mathrm{Ja}}}{2}, \quad \mathrm{Ja} = \left(\frac{\rho_l}{\rho_v}\right)\left(\frac{c_p\Delta T_{sub}}{H_{fg}}\right) \tag{1}$$

where

$$\frac{q_{co}}{\rho_v H_{fg} u} = 0.221\left(\frac{\rho_l}{\rho_v}\right)^{0.645} \times \left(\frac{2\sigma}{\rho_l u^2 (L-d)}\right)^{0.343} (1 + L/d)^{-0.364} \tag{2}$$

$$C = \frac{0.95(d/L)^2(1 + L/d)^{0.364}}{(\rho_l/\rho_v)^{0.43}(2\sigma/\rho_l u^2(L-d))^{0.343}} \tag{3}$$

Monde and Inoue (1991) show that Eq. (2) is also applicable for the CHF for multiple impinging jets when a maximum flow length in the domain controlled by one jet is employed as a

Table 1 Experimental range in which Eq. (1) is derived

Test liquid	Water	R113	R22
L [mm]		40, 60	
d [mm]		2	
u [m/s]	5 - 16	4.2 - 18.4	6.6 - 33.9
ΔT_{sub} [K]	0 - 113	0 - 80	0 - 30
P [bar]	1, 3	1 - 5	16 - 25
ρ_l/ρ_v	658 - 1605	40.1 - 202	8.8 - 16.1
Ja	0 - 240	0 - 30	0 - 3.1

[1] Department of Mechanical Engineering, Saga University, 1 Honjo Saga, Japan 840.

Contributed by the Heat Transfer Division of THE AMERICAN SOCIETY OF MECHANICAL ENGINEERS. Manuscript received by the Heat Transfer Division July 1994; revision received December 1994. Keywords: Boiling, Jets, Phase-Change Phenomena. Associate Technical Editor: R. A. Nelson, Jr.

Implications to Space Application. Based on the measured heat transfer coefficient data and the flow visualization, it is reasonable to suggest that for a given heat flux, if the forced-flow field is strong enough to prevent bubble agglomeration and to maintain single and sliding bubbles, subcooled forced-convection nucleate boiling would be a feasible and efficient heat transfer mechanism in microgravity. Bankoff (1994) recently suggested that since subcooled forced-convection nucleate boiling is one of the most efficient heat transfer mechanisms and has a minimum reliance on gravity, it be adapted for space applications. We believe that the current paper has provided a solid support for Bankoff's idea.

Acknowledgments

This work was supported by NASA Grant No. NAG3-1387. The authors gratefully acknowledge the interest and support of Dr. Fran Chiaramonte of the NASA Lewis Research Center.

References

Bankoff, S. G., 1959, "On the Mechanism of Subcooled Nucleate Boiling," Jet Prop. Lab. Memo 30-38.

Bankoff, S. G., 1961, "On the Mechanism of Subcooled Nucleate Boiling, Parts 1 and 2," *Chem. Eng. Progr. Symposium Series*, No. 32, Vol. 57, pp. 156–163; 164–172.

Bankoff, S. G., 1994, "Future Directions in Two-Phase Flow and Heat Transfer in Space," keynote paper, *Proceedings of Second Microgravity Fluid Physics Conference*, pp. 3–11.

Carey, V. P., 1992, *Liquid–Vapor Phase-Change Phenomena*, Taylor and Francis, Bristol, PA.

Cooper, M. G., Mori, K., and Stone, C. R., 1983, "Behaviour of Vapor Bubbles Growing at a Wall With Forced Flow," *Int. J. Heat Mass Transfer*, Vol. 26, No. 10, pp. 1489–1507.

Gunther, F. C., and Kreith, F., 1950, "Photographic Study of Bubble Formation in Heat Transfer to Subcooled Water," Jet Propulsion Laboratory, Pasadena, CA, Progress Report No. 4-75.

Gunther, F. C., 1951, "Photographic Study of Surface-Boiling Heat Transfer to Water With Forced Convection," *Trans. ASME*, Vol. 73, pp. 115–124.

Merte, H. Jr., Lee, H. S., and Ervin, J. S., 1993, "Transient Nucleate Pool Boiling in Microgravity—Some Initial Results," *Int. Symp. Microgravity Science and Applications*, Paper J-5.

Mills, A. F., 1992, *Heat Transfer*, Irwin, Homeward, IL.

Oker, E., and Merte, H. Jr., 1981, "Semi-transparent Gold Film as Simultaneous Surface Heater and Resistance Thermometer for Nucleate Boiling Studies," ASME JOURNAL OF HEAT TRANSFER, Vol. 103, pp. 65–68.

Siegel, R., 1967, "Effects of Reduced Gravity on Heat Transfer," *Advances in Heat Transfer*, Vol. 4, pp. 143–228.

Snyder, T. J., 1993, "WSU 2.1 Second Microgravity Drop Tower, Design, Construction, and Performance," MS Thesis, Department of Mechanical and Materials Engineering, Washington State University.

Tsung-Chang, G., and Bankoff, S. G., 1990, "On the Mechanism of Forced-Convection Subcooled Nucleate Boiling," ASME JOURNAL OF HEAT TRANSFER, Vol. 112, pp. 213–218.

Wang, T.-C., 1993, "Transient Effects of Microgravity on Pool and Low Velocity Flow Boiling Heat Transfer," M.S. Thesis, Department of Mechanical and Materials Engineering, Washington State University.

3M Company, 1992, *Product Manual for Fluorinert Liquids*.

Critical Heat Flux in Forced Convective Subcooled Boiling With Multiple Impinging Jets

M. Monde[1] and Y. Mitsutake[1]

Nomenclature

C = constant defined by Eq. (3)
c_p = specific heat of liquid
d = diameter of an impinging jet
H_{fg} = latent heat of evaporation
Ja = Jakob number = $(\rho_l/\rho_v)(c_p\Delta T_{sub}/H_{fg})$
L = two times of maximum distance (Fig. 2)
q_{co} = critical heat flux for saturated boiling
q_c = critical heat flux for subcooled boiling
ΔT_{sub} = subcooling temperature of jet = $T_{sat} - T_{liq}$
u = velocity of a liquid jet at the nozzle exit
ρ_l = density of saturated liquid
ρ_v = density of saturated vapor
σ = surface tension

1 Introduction

In the past two decades, the critical heat flux in saturated convective boiling with an impinging jet and multiple jets has been studied rather extensively (Katto and Yokoya, 1988; Sharan and Lienhard, 1985; Monde and Inoue, 1991; Monde, 1991). The characteristics of the CHF were clarified and then generalized correlations, which are applicable for the CHF within a wide experimental range, had been proposed, for example, by Monde (1991). More recently, Monde et al. (1994) measured critical heat flux during forced convective subcooled boiling with an impinging jet within an experimental range as listed in Table 1 and have derived a generalized correlation (1), yielding the CHF for the subcooled jet well based upon Eq. (2) for the saturated jet with an accuracy as given by a mean average ($E = \Sigma\,((q_{exp} - q_{cal})/q_{exp})/n$) of −0.06 percent, a mean deviation of 12.4 percent, and a standard deviation of 15.2 percent. The total number of the subcooled and saturated CHF data is 271.

$$\frac{q_c}{q_{co}} = \frac{1 + \sqrt{1 + 4C\mathrm{Ja}}}{2}, \quad \mathrm{Ja} = \left(\frac{\rho_l}{\rho_v}\right)\left(\frac{c_p\Delta T_{sub}}{H_{fg}}\right) \tag{1}$$

where

$$\frac{q_{co}}{\rho_v H_{fg} u} = 0.221\left(\frac{\rho_l}{\rho_v}\right)^{0.645} \times \left(\frac{2\sigma}{\rho_l u^2 (L-d)}\right)^{0.343} (1 + L/d)^{-0.364} \tag{2}$$

$$C = \frac{0.95(d/L)^2(1 + L/d)^{0.364}}{(\rho_l/\rho_v)^{0.43}(2\sigma/\rho_l u^2(L-d))^{0.343}} \tag{3}$$

Monde and Inoue (1991) show that Eq. (2) is also applicable for the CHF for multiple impinging jets when a maximum flow length in the domain controlled by one jet is employed as a

Table 1 Experimental range in which Eq. (1) is derived

Test liquid	Water	R113	R22
L [mm]		40, 60	
d [mm]		2	
u [m/s]	5 - 16	4.2 - 18.4	6.6 - 33.9
ΔT_{sub} [K]	0 - 113	0 - 80	0 - 30
P [bar]	1, 3	1 - 5	16 - 25
ρ_l/ρ_v	658 - 1605	40.1 - 202	8.8 - 16.1
Ja	0 - 240	0 - 30	0 - 3.1

[1] Department of Mechanical Engineering, Saga University, 1 Honjo Saga, Japan 840.

Contributed by the Heat Transfer Division of THE AMERICAN SOCIETY OF MECHANICAL ENGINEERS. Manuscript received by the Heat Transfer Division July 1994; revision received December 1994. Keywords: Boiling, Jets, Phase-Change Phenomena. Associate Technical Editor: R. A. Nelson, Jr.

Table 2 Present experimental range

Test liquid	Water
N	2, 4
L [mm]	45.1, 46.5
d [mm]	2
u [m/s]	5 - 25
ΔT_{sub} [K]	0 - 80
P [bar]	1, 3
ρ_l/ρ_v	658 - 1605
Ja	0 - 170

characteristic length. In addition, they suggest that Eq. (2) can be applied to the CHF for the jet impinging on any configuration other than a disk, if a maximum flow length is chosen appropriately.

In the present study, the CHF for the multiple impinging jets is measured for water at pressures of 0.1 and 0.3 MPa, over an experimental range given in Table 2. In light of Eq. (1) predicting the effect of subcooling on the CHF well and Eq. (2) being applicable for the CHF of the saturated liquid supplied by not only a single jet but also multiple jets, the authors have discussed the applicability of Eq. (1) to the CHF of subcooled liquid with multiple impinging jets.

2 Experimental Apparatus and Procedure

2.1 Experimental Apparatus. The experimental apparatus is the same as that in the former experiment (Monde et al., 1994) except that a nozzle with multiple jets is employed in place of one with a single jet and the width of the heated surface is enlarged from 10 mm to 15 mm. Therefore, only the part changed and the arrangement of the impinging jets will be briefly described here.

Figure 1 shows the arrangement of the jets impinging on the heated surface for $N = 2$ and 4. In the hatched area, the length of $L/2$ corresponds to the maximum flow length, which is controlled by one jet (see Fig. 2). The test liquid flows out through two or four holes of inner diameter $d = 2$ mm, and impinges on the heated surface vertically. According to a calibration of mass flow rate done before the experiment, mean velocity at the nozzle exit for $N = 2$ and 4, u can be determined within an error of 3–5 percent from the pressure difference between the inlet and outlet of the nozzle measured by means of a differential pressure transducer. In addition to this, the calibration shows that there is little difference between the mass flow rates discharged through each hole.

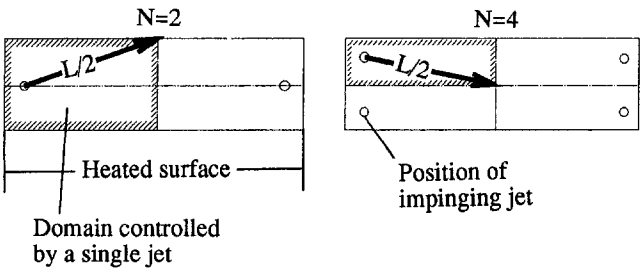

Fig. 1 Geometric arrangement of impinging jets on the heated surface

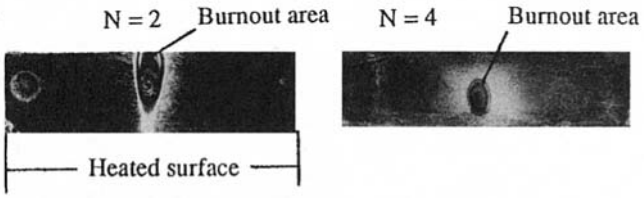

Fig. 2 Burnout of the heated surface

2.2 Procedure of Experiment and Measuring CHF. The jet velocity, the liquid temperature, and the system pressure are first fixed at each designated value. Then, the electric power to the heated surface is automatically increased at a time interval of about 3 minutes in increments that are less than 4 percent of each preceding heat flux. Finally a point is reached where the heated surface temperature runs away to burn out. The CHF is determined with an uncertainty of 0 to 4 percent. The heated surface temperature is monitored and it becomes stable within a time interval of 3 minutes after the increase in the electric power.

3 Experimental Results and Discussion

3.1 Variation of Fluid Behavior With Increase in Heat Flux. When one focuses on the domain controlled by each jet, the variation of the flow due to an increase in heat flux seems to be similar to that observed in the single jet (Monde et al., 1994) except for the interference between radial flows formed on the heated surface after the impingement of jet. Therefore, the flow situation based on a visual observation is briefly described here and will be divided into subcooled and saturated regions. In the subcooled region, after impingement of the jet, the liquid film flows radially over the heated surface. Weak boiling appears along the heated surface, but the surface is soon cooled down by the subcooled liquid. In the saturated region, most of the liquid flowing over the heated surface is splashed out as droplets, but residual liquid still remains as a very thin liquid film totally covering the heated surface and insuring heat transfer from the heated surface due to its evaporation. With increasing heat flux, the saturation region gradually extends from the outer region of the heated surface toward the center and the interference at the boundary fades due to the increase of the splashed droplets.

Finally, it may be necessary to emphasize that near the CHF point, the flow features of both multiple jets and single jet become totally similar in the domain controlled by the single jet.

3.2 Burnout of Stainless Steel Foil Due to Occurrence of CHF. Figure 2 shows representative photographs of the heated surface for both $N = 2$ and 4 when the electric power is shut down immediately after the occurrence of the CHF.

Comparing the CHF point in the heated surface and the domain (see the hatched area in Fig. 1), we may notice that the CHF takes place at the point farthest from the position of the impinging jet within the domain. The same evidence is observed in the cases not only of saturated boiling with multiple jets and a single jet but also of the subcooled boiling with a single jet. The variation of the flow aspect when increasing heat flux up to the CHF and the point of the CHF occurrence may allow us to conclude that the CHF phenomena are not different in the case of the multiple jets versus the single jet, provided that the heated surface can be divided into a subdivision where the liquid flow formed on the heated surface after impingement of the jet is influenced only by that jet.

3.3 Effect of Velocity and Subcooling on CHF. Figure 3 represents the CHF for water at a pressure of 0.1 MPa, plotted against the jet velocity at a different subcooling up to $\Delta T_{sub} =$

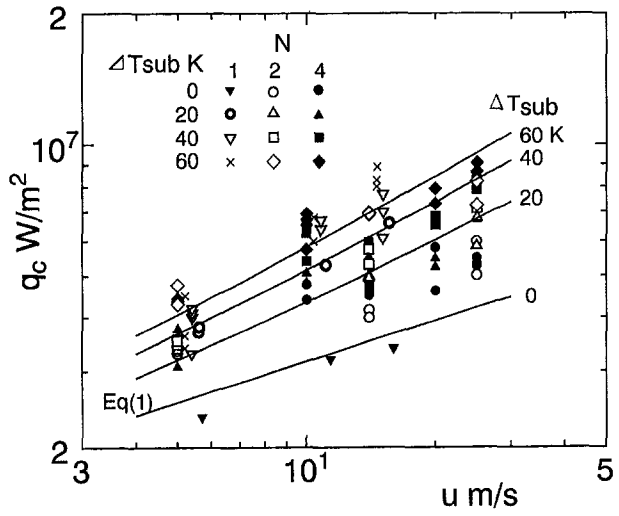

Fig. 3 Relationship between CHF and jet velocity for water at 0.1 MPa

60 K. A straight line in Fig. 3, for reference, is the CHF, which is calculated for the corresponding subcooling level from Eq. (1).

Figure 3 shows that an effect of subcooling on the CHF at the same subcooling level depends on the jet velocity, that is the CHF at the same subcooling level is enhanced with an increase in the velocity as shown by the slope of the line for the same subcooling predicted by Eq. (1), which becomes sharper with an increase in subcooling level. Incidentally, the CHF data for $\Delta T_{sub} = 0$ K are about 20–30 percent higher than those predicted by Eq. (1). The reason is not known.

The dependence of the CHF on subcooling and jet velocity may be understood easily from the change of the flow aspect and the CHF point when increasing heat flux to the CHF point.

4 Comparison of CHF Data With Eq. (1)

Figure 4 shows a relationship between the CHF data and the values predicted by Eq. (1), which are plotted against the subcooling level. It shows that the CHF data are in good agreement with the predicted values. In addition, 85 percent of the CHF data for the subcooled liquid can be predicted with an accuracy of ±20 percent while 96 percent of the data fall within a range of ±30 percent. Finally, for all the 121 CHF data points, we find a mean average of −1.85 percent, mean deviation of 11.5 percent, and standard deviation of 16.0 percent.

Comparing accuracies of predicting the CHF data for both cases of the single jet and multiple jets, one notices that both CHFs are identically predicted with the same accuracy by Eq. (1).

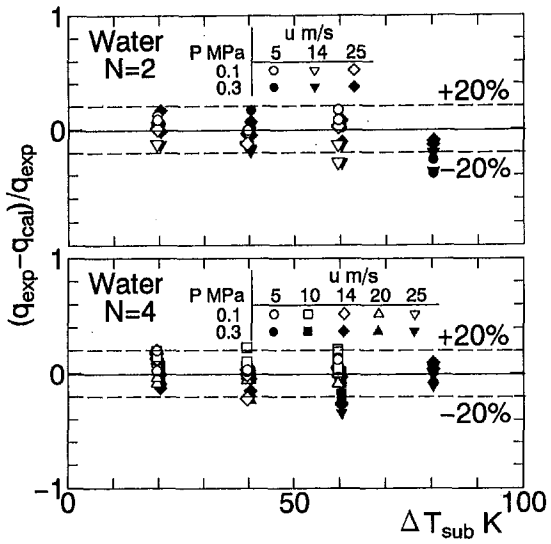

Fig. 4 Comparison of CHF data with Eq. (1)

5 Conclusions

Critical heat flux with multiple circular impinging jets has been measured by employing water at a subcooling up to ΔT_{sub} = 80 K and velocity of 5 to 25 m/s.

1 Characteristics of CHF for both the single jet and multiple jets are similar, when focusing on the region controlled by each individual jet.
2 Equation (1) can predict the CHF data not only for the multiple jets but also for the single jet with the same accuracy.

References

Katto, Y., and Yokoya, S., 1988, "Critical Heat Flux on a Disk Heater Cooled by a Circular Jet of Saturated Liquid Impinging at the Center," *Int. J. Heat Mass Transfer*, Vol. 31, No. 2, pp. 219–227.

Monde, M., and Inoue, T., 1991, "Critical Heat Flux in Saturated Forced Convective Boiling on a Heated Disk With Multiple Impinging Jets," ASME JOURNAL OF HEAT TRANSFER, Vol. 113, pp. 722–727.

Monde, M., 1991, "Critical Heat Flux in Saturated Forced Convective Boiling on a Heated Disk With One or Multiple Impinging Jets," *Trends in Heat, Mass & Momentum Transfer*, Vol. 1, pp. 33–44.

Monde, M., Kitajima, K., Inoue, T., and Mitsutake, Y., 1994, "Critical Heat Flux in a Forced Convective Subcooled Boiling With an Impinging Jet," *Heat Transfer 1994*, Vol. 7, (in press).

Sharan, A., and Lienhard, J. H., 1985, "On Predicting Burnout in the Jet-Disk Configuration," ASME JOURNAL OF HEAT TRANSFER, Vol. 107, pp. 398–401.

Effect of Fog Formation on Turbulent Vapor Condensation With Noncondensable Gases

H. J. H. Brouwers[1]

Nomenclature

c = molar density, mole m^{-3}
c_p = molar specific heat, J mole^{-1} K^{-1}
$\mathbb{D}$ = diffusion coefficient, m^2 s^{-1}
D = tube diameter, m
F = saturation line
h_{fg} = latent heat of condensation, J mole^{-1}
k = thermal conductivity, W m^{-1} K^{-1}
L = tube length, m
Le = Lewis number
l = characteristic length, m
M = mass of one kmole of substance, kg mole^{-1}
Nu = Nusselt number
P = pressure, Pa
Pr = Prandtl number
q = heat flux, W m^{-2}
Re = Reynolds number
Sc = Schmidt number

[1] University of Twente, Department of Civil Engineering & Management, P.O. Box 217, 7500 AE Enschede, The Netherlands.

Contributed by the Heat Transfer Division of THE AMERICAN SOCIETY OF MECHANICAL ENGINEERS. Manuscript received by the Heat Transfer Division November 1994; revision received April 1995. Keywords: Condensation, Heat Exchangers, Multiphase Flows. Associate Technical Editor: R. A. Nelson, Jr.

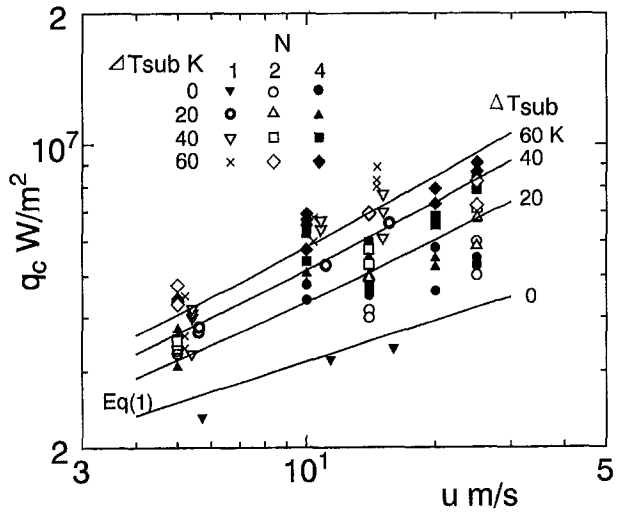

Fig. 3 Relationship between CHF and jet velocity for water at 0.1 MPa

60 K. A straight line in Fig. 3, for reference, is the CHF, which is calculated for the corresponding subcooling level from Eq. (1).

Figure 3 shows that an effect of subcooling on the CHF at the same subcooling level depends on the jet velocity, that is the CHF at the same subcooling level is enhanced with an increase in the velocity as shown by the slope of the line for the same subcooling predicted by Eq. (1), which becomes sharper with an increase in subcooling level. Incidentally, the CHF data for $\Delta T_{sub} = 0$ K are about 20–30 percent higher than those predicted by Eq. (1). The reason is not known.

The dependence of the CHF on subcooling and jet velocity may be understood easily from the change of the flow aspect and the CHF point when increasing heat flux to the CHF point.

4 Comparison of CHF Data With Eq. (1)

Figure 4 shows a relationship between the CHF data and the values predicted by Eq. (1), which are plotted against the subcooling level. It shows that the CHF data are in good agreement with the predicted values. In addition, 85 percent of the CHF data for the subcooled liquid can be predicted with an accuracy of ±20 percent while 96 percent of the data fall within a range of ±30 percent. Finally, for all the 121 CHF data points, we find a mean average of −1.85 percent, mean deviation of 11.5 percent, and standard deviation of 16.0 percent.

Comparing accuracies of predicting the CHF data for both cases of the single jet and multiple jets, one notices that both CHFs are identically predicted with the same accuracy by Eq. (1).

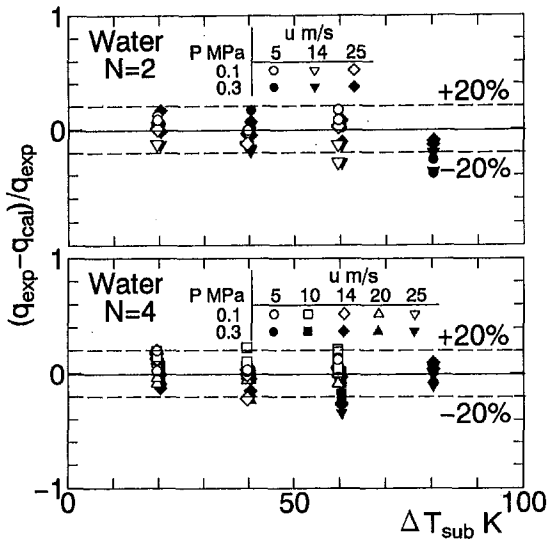

Fig. 4 Comparison of CHF data with Eq. (1)

5 Conclusions

Critical heat flux with multiple circular impinging jets has been measured by employing water at a subcooling up to ΔT_{sub} = 80 K and velocity of 5 to 25 m/s.

1 Characteristics of CHF for both the single jet and multiple jets are similar, when focusing on the region controlled by each individual jet.
2 Equation (1) can predict the CHF data not only for the multiple jets but also for the single jet with the same accuracy.

References

Katto, Y., and Yokoya, S., 1988, "Critical Heat Flux on a Disk Heater Cooled by a Circular Jet of Saturated Liquid Impinging at the Center," *Int. J. Heat Mass Transfer*, Vol. 31, No. 2, pp. 219–227.

Monde, M., and Inoue, T., 1991, "Critical Heat Flux in Saturated Forced Convective Boiling on a Heated Disk With Multiple Impinging Jets," ASME JOURNAL OF HEAT TRANSFER, Vol. 113, pp. 722–727.

Monde, M., 1991, "Critical Heat Flux in Saturated Forced Convective Boiling on a Heated Disk With One or Multiple Impinging Jets," *Trends in Heat, Mass & Momentum Transfer*, Vol. 1, pp. 33–44.

Monde, M., Kitajima, K., Inoue, T., and Mitsutake, Y., 1994, "Critical Heat Flux in a Forced Convective Subcooled Boiling With an Impinging Jet," *Heat Transfer 1994*, Vol. 7, (in press).

Sharan, A., and Lienhard, J. H., 1985, "On Predicting Burnout in the Jet-Disk Configuration," ASME JOURNAL OF HEAT TRANSFER, Vol. 107, pp. 398–401.

Effect of Fog Formation on Turbulent Vapor Condensation With Noncondensable Gases

H. J. H. Brouwers[1]

Nomenclature

c = molar density, mole m^{-3}
c_p = molar specific heat, J mole^{-1} K^{-1}
$\mathbb{D}$ = diffusion coefficient, m^2 s^{-1}
D = tube diameter, m
F = saturation line
h_{fg} = latent heat of condensation, J mole^{-1}
k = thermal conductivity, W m^{-1} K^{-1}
L = tube length, m
Le = Lewis number
l = characteristic length, m
M = mass of one kmole of substance, kg mole^{-1}
Nu = Nusselt number
P = pressure, Pa
Pr = Prandtl number
q = heat flux, W m^{-2}
Re = Reynolds number
Sc = Schmidt number

[1] University of Twente, Department of Civil Engineering & Management, P.O. Box 217, 7500 AE Enschede, The Netherlands.

Contributed by the Heat Transfer Division of THE AMERICAN SOCIETY OF MECHANICAL ENGINEERS. Manuscript received by the Heat Transfer Division November 1994; revision received April 1995. Keywords: Condensation, Heat Exchangers, Multiphase Flows. Associate Technical Editor: R. A. Nelson, Jr.

Sh = Sherwood number
T = absolute temperature, K
x = mole fraction
θ = correction factor

Subscripts

b = bulk
c = diffusional
f = fog formation
g = noncondensables
i = condensate/gas interface
l = neutral (without suction and without fog formation)
s = sensible
tot = total
t = thermal
v = vapor

Superscripts

mf = including mass transfer (suction) and fog formation

Introduction

In a recent paper, Peterson et al. (1993) analyzed the turbulent vapor condensation in tubes and on plates in the presence of noncondensables. Experiments were furthermore performed with mixtures of a noncondensable gas and steam. A parameter $C_s/C_c = 7$ was introduced to match the experimental results and the theoretical model. This parameter was attributed to mist formation, as this process enhances sensible heat transfer and reduces condensation heat transfer in a condenser. Employing the model of Brouwers (1992), it will be demonstrated that the major part of this parameter can be derived from a basic consideration of combined heat and mass transfer. These transfer rates are affected by both fog formation and suction (i.e., vapor diffusion induced velocity).

Heat and Mass Transfer Model

First, the sensible heat transfer between gas mixture and condensate is discussed. The actual Nusselt number, Nu^{mf}, in case of suction and fog formation can be obtained by multiplying the neutral (i.e., zero mass flux and no fog) Nusselt number Nu_l by two correction factors (Brouwers, 1992)

$$\mathrm{Nu}^{mf} = \mathrm{Nu}_l \theta_t \theta_{tf} \tag{1}$$

with θ_t as correction factor for the effect of mass transfer (suction/blowing) on heat transfer (Brouwers, 1991), commonly referred to as the Ackermann correction:

$$\theta_t = \frac{\dfrac{c_{pv}\,\mathrm{Sh}_l}{c_p\,\mathrm{Le}\,\mathrm{Nu}_l} \ln\left(\dfrac{1 - x_{vb}}{1 - x_{vi}}\right)}{\exp\left(\dfrac{c_{pv}\,\mathrm{Sh}_l}{c_p\,\mathrm{Le}\,\mathrm{Nu}_l} \ln\left(\dfrac{1 - x_{vb}}{1 - x_{vi}}\right) - 1\right)} \tag{2}$$

and the fog correction factor as

$$\theta_{tf} = \frac{1 + \dfrac{h_{fg}}{c_p}\dfrac{1}{\mathrm{Le}}\dfrac{x_{vb} - x_{vi}}{T_b - T_i}\dfrac{\mathrm{Sh}_l}{\mathrm{Nu}_l}}{1 + \dfrac{h_{fg}}{c_p}\dfrac{1}{\mathrm{Le}}\left.\dfrac{dF}{dT}\right|_{T_i}} \tag{3}$$

$F(T)$ represents the saturation line of water vapor, or $P_v(T)/P_{\mathrm{tot}}$ (in Eq. (7) of Peterson et al. (1993), P_i should read P_t). The mixture's specific molar heat c_p follows from $(1 - x_{vb})c_{pg} + x_{vb}c_{pv}$ and $\mathrm{Le} = k/c\mathbb{D}c_p$. The sensible heat transfer from mixture to condensate then follows from

$$q_s'' = \frac{\mathrm{Nu}^{mf}k}{1}(T_b - T_i) = \frac{\mathrm{Nu}_l k}{1}\theta_{tf}\theta_t(T_b - T_i) \tag{4}$$

Peterson et al. (1993) obtained a similar expression for the heat transfer, only $\theta_t\theta_{tf}$ was omitted (i.e., Nu^{mf} was set equal to Nu_l).

Now attention is focused on mass transfer by vapor diffusion to the condensate. The actual Sherwood number follows from multiplying the neutral Sherwood number by two correction factors

$$\mathrm{Sh}^{mf} = \mathrm{Sh}_l\theta_c\theta_{cf} \tag{5}$$

with θ_c as correction factor for the effect of mass transfer (suction/blowing) on mass transfer (Brouwers, 1991),

$$\theta_c = \frac{\ln\left[1 - \dfrac{x_{vb} - x_{vi}}{1 - x_{vi}}\right]}{-\dfrac{x_{vb} - x_{vi}}{1 - x_{vi}}} \tag{6}$$

and the fog correction factor

$$\theta_{cf} = \frac{1 + \left[\dfrac{h_{fg}}{c_p}\dfrac{1}{\mathrm{Le}}\dfrac{x_{vb} - x_{vi}}{T_b - T_i}\dfrac{\mathrm{Sh}_l}{\mathrm{Nu}_l}\right]^{-1}}{1 + \left[\dfrac{h_{fg}}{c_p}\dfrac{1}{\mathrm{Le}}\left.\dfrac{dF}{dT}\right|_{T_i}\right]^{-1}} \tag{7}$$

The latent heat transfer from mixture to condensate then reads

$$q_c'' = h_{fg}\frac{\mathrm{Sh}^{mf}c\mathbb{D}M_v}{1}\left(\frac{x_{vb} - x_{vi}}{1 - x_{vi}}\right)$$

$$= h_{fg}\frac{\mathrm{Sh}_l c\mathbb{D}M_v}{1}\theta_{cf}\theta_c\left(\frac{x_{vb} - x_{vi}}{1 - x_{vi}}\right) \tag{8}$$

Peterson et al. (1993) also used Eq. (8), including θ_c (suction), but without θ_{cf}. For turbulent flow in a tube they found an enhancement of Sh_l by a factor of 1.2, which they grant to suction and ripples. But Peterson et al. (1993) did actually include suction in their description of mass transfer. This can be verified by combining the two last factors on the right-hand side of Eq. (8) and applying Eq. (6). So, this enhancement of 20 percent can be attributed to ripples only.[2] It should be noted that this effect affects Sh_l and Nu_l to the same extent, so that it cannot be a reason for C_s/C_c being unequal to unity.

Equations (3) and (7) contain fog correction factors in mole fraction notation. Originally, the correction factors of Brouwers (1992) are based on an analysis with mass fraction notation. It can be easily verified that the same analysis with mole fraction notation will result in Eqs. (3) and (7).

For both turbulent vapor condensation in tubes and condensation on walls, the ratio of neutral Nusselt and Sherwood numbers can be expressed as

$$\frac{\mathrm{Sh}_l}{\mathrm{Nu}_l} = \mathrm{Le}^n \tag{9}$$

Peterson et al. (1993) mention $n = 0.35$ for forced convective turbulent flow in tubes and $n = 0.33$ for turbulent free convec-

[2] A part of this enhancement can also be attributed to entry effects. From Burmeister (1983) it follows that the Nusselt and Sherwood numbers are enhanced by a factor of $(1 + C\,D/L)$ for $\mathrm{Pr} \approx 1$ and $\mathrm{Sc} \approx 1$, with C ranging from 1.4 to 7, and $L/D \approx 24$ for the experiments by Peterson et al. (1993). Even for $C = 1.4$, a transfer augmention of 6 percent is obtained.

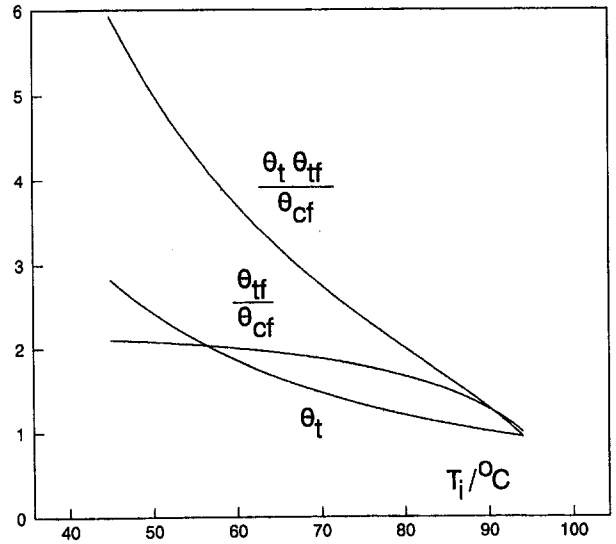

Fig. 1 Correction factors for fog formation and suction for mixtures of water vapor and air with T_b = 94°C, $x_{vb} = F(T_b)$ = 0.804, and various interface temperatures T_i

tion along vertical plates. Combining Eqs. (1), (5), and (9) yields a ratio for the actual Sherwood and Nusselt numbers

$$\frac{\mathrm{Sh}^{mf}}{\mathrm{Nu}^{mf}} = \frac{\theta_c \theta_{cf}}{\theta_t \theta_{tf}} \mathrm{Le}^n \tag{10}$$

The analysis of Peterson et al. (1993), however, yields a ratio

$$\frac{\mathrm{Sh}^{mf}}{\mathrm{Nu}^{mf}} = \frac{C_c \theta_c}{C_s} \mathrm{Le}^n \tag{11}$$

Without fog formation and suction, Peterson et al. (1993) confirmed that $C_s/C_c = 1$, which is the result of the common analogy of heat and mass transfer. Due to fog formation, they put forward a C_s/C_c unequal to unity (the exact condition for and presence of fog formation will be verified later in this note). From Eqs. (10) and (11) it can be concluded that Peterson et al. (1993): (1) included θ_c, but not the Ackermann correction θ_t. This neglect is not allowed as both θ_c and θ_t are of the same order of magnitude since Le $\approx$ 1, $\mathrm{Nu}_l \approx \mathrm{Sh}_l$, and $c_{pv} \approx c_{pg} \approx c_p$ (θ_c and θ_t are equal if $k\,\mathrm{Nu}_l = c\mathbb{D}c_{pv}\,\mathrm{Sh}_l$); (2) corrected the effects of both fog formation and θ_t via $C_s/C_c = 7$. According to the analogy of heat and mass transfer this ratio should be equal to unity.

On the basis of Eqs. (10) and (11) it can be seen that

$$\frac{C_s}{C_c} = \frac{\theta_t \theta_{tf}}{\theta_{cf}} = \theta_t \mathrm{Le}^n \frac{x_{vb} - x_{vi}}{T_b - T_i} \left[\left. \frac{dF}{dT} \right|_{T_i} \right]^{-1} \tag{12}$$

whereby Eqs. (3), (7), and (9) have been inserted.

Model Application and Results

Now it is interesting to compute the right-hand side of Eq. (12) and verify whether this ratio approximates the value of 7. To this end, computations have been performed with $P_v(T)/[\mathrm{bar}] = \exp(11.6834 - 3816.44/(227.02 + T/[°\mathrm{C}]))$, taken from Reid et al. (1977), P_{tot} = 1.01325 bar (= 1 atm), T_b = 94°C, $x_{vb} = F(T_b)$ = 0.804, Le = 0.85, n = 0.34, c_{pv} = 34 kJ/kmole K, c_{pg} = 29 kJ/kmole K. The interface properties (T_i, $x_{vi} = F(T_i)$) ranged from (45°C, 0.094) to (94°C, 0.804). In Fig. 1 the computed θ_t, θ_{tf}/θ_{cf}, and $\theta_t\theta_{tf}/\theta_{cf}$ are depicted versus T_i.

One can see that the correction factors deviate more from unity for smaller T_i, i.e., larger differences between bulk and interface properties. This would be expected as θ_t increases with larger difference between x_{vb} and x_{vi}, θ_t (and θ_c) tends to unity as x_{vb} tends to x_{vi}. Both θ_{tf} and θ_{cf} also deviate more from unity if the distance between (T_i, x_{vi}) and (T_b, x_{vb}), both situated on the saturation line, is increased and hence, the ratio of $(x_{vb} - x_{vi})/(T_b - T_i)$ and $dF/dT|$ in T_i is also increased (Brouwers, 1992). Furthermore, it can be seen that θ_t and θ_{tf}/θ_{cf} are of the same order of magnitude and contribute equally to their product. Figure 1 reveals that $\theta_t\theta_{tf}/\theta_{cf}$ tends to a value of 6, which corresponds closely to the general correlation value of 7 found by Peterson et al. (1993). This result yields the important conclusion that the factor found by these authors can be derived from known correction factors. Brouwers (1992) already demonstrated the applicability of these fog correction factors to laminar free and forced convective flow. Here then, the usefulness to turbulent free and forced convective flow is confirmed. Consequently, the film model approach can be recommended for future condenser computations.

For the remaining small difference between $\theta_t\theta_{tf}/\theta_{cf}$ and C_s/C_c of Peterson et al. (1993), besides common measurement uncertainties, a number of reasons is conceivable. For instance, they: (1) introduced an alternative description of heat transfer by replacing the bulk temperature by the saturation temperature. Although this approach is reasonable for saturated mixtures, it remains an approximate description; (2) replaced the saturation line by the Clausius–Clapeyron equation. This approach is allowed only in a narrow temperature and vapor pressure range; (3) did not account for the effect of fog formation on energy and vapor mass balances in the direction of flow. Including fog formation results in alternative incremental balances for the bulk temperature and vapor mole fraction in flow direction (Brouwers, 1992).

Furthermore, it should be noted that the film model as such, which is used in this note, also constitutes an approximate approach of heat and mass transfer. Brouwers (1992) found a discrepancy of about 4 percent between the laminar boundary layer model and the fog film model.

Finally, it should be proved that fog is really formed under all studied circumstances. To this end, the tangency condition can be employed (Brouwers, 1991, 1992), which predicts fog formation in a condenser if

$$\left. \frac{dF}{dT} \right|_{T_i} < \frac{\theta_c}{\theta_t} \frac{\mathrm{Sh}_l}{\mathrm{Nu}_l} \frac{x_{vb} - x_{vi}}{T_b - T_i} = \frac{\theta_c}{\theta_t} \mathrm{Le}^n \frac{x_{vb} - x_{vi}}{T_b - T_i} \tag{13}$$

where Eq. (9) has been substituted. This tangency condition has been verified for all situations pertaining to Fig. 1, yielding that this inequality is fulfilled for $T_i \leq$ 88.1°C ($x_{vi} \leq$ 0.644). This implies that fog formation takes place for $T_i \leq$ 88.1°C; thus the resulting θ_{tf}/θ_{cf} and $\theta_t\theta_{tf}/\theta_{cf}$ of Fig. 1 are valid in the range 45°C $\leq T_i \leq$ 88.1°C. To achieve sufficiently large heat transfer rates, it is expected that T_i was much smaller than 88.1°C for the experiments performed by Peterson et al. (1993). The observed fog formation is therefore in agreement with the fog formation predicted by the tangency condition for 45°C $\leq T_i \leq$ 88.1°C.

References

Brouwers, H. J. H., 1991, "An Improved Tangency Condition for Fog Formation in Cooler-Condensers," *International Journal of Heat and Mass Transfer*, Vol. 34, pp. 2387–2394.

Brouwers, H. J. H., 1992, "A Film Model for Heat and Mass Transfer With Fog Formation," *Chemical Engineering Science*, Vol. 47, pp. 3023–3036.

Burmeister, L. C., 1983, *Convective Heat Transfer*, Wiley, New York, p. 490.

Peterson, P. F., Schrock, V. E., and Kageyama, T., 1993, "Diffusion Layer Theory for Turbulent Vapor Condensation With Noncondensable Gases," ASME JOURNAL OF HEAT TRANSFER, Vol. 115, pp. 998–1003.

Reid, R. C., Prausnitz, J. M., and Sherwood, T. K., 1977, *The Properties of Gases and Liquids*, 3rd ed., McGraw-Hill, New York, pp. 629, 632.

Evaporative Cooling of Fibers by a Low-Reynolds-Number Crossflow

V. Simon [1]

Nomenclature

a = radius of the fiber, m
$B_1 \ldots B_6$ = parameters, defined in Eqs. (13) and (14)
c = mass fraction
c_p = specific heat at constant pressure, J kg^{-1} K^{-1}
C = normalized concentration
D = binary diffusion coefficient, m^2 s^{-1}
$\mathbf{e}_x$, $\mathbf{e}_z$ = normal unit vectors in the x, z directions, respectively
$h^V - h^L$ = heat of evaporation, J kg^{-1}
K_0 = modified Bessel function of the second kind and zeroth order
l, L = length, length of air gap, respectively, m
Pr = Prandtl number = ν^V/κ^V
r = radial coordinate = $(x^2 + y^2)^{1/2}$, m
R = gas constant of water vapor, J kg^{-1} K^{-1}
Re = Reynolds number = $2U_\infty a/\nu^V$
Sc = Schmidt number = ν^V/D^V
T, T_F = temperature, mean temperature of the fiber, respectively, K
$\mathbf{u}$ = velocity, m s^{-1}
U_F, U_∞ = downward and horizontal velocity of the fiber, respectively, m s^{-1}
u, v, w = velocity components in the x, y, z directions, respectively, m s^{-1}
x, y, z = coordinates (see Fig. 1), m
Z = dimensionless axial coordinate, defined in Eq. (11)
γ = 0.5772 Euler's constant
δ, δ_∞ = boundary layer thickness, viscous length, respectively, m
Θ = normalized temperature
κ = thermal diffusivity, m^2 s^{-1}
λ = thermal conductivity, W m^{-1} K^{-1}
ν = kinematic viscosity, m^2 s^{-1}
ρ = mass density, kg m^{-3}
φ = angle between $\mathbf{e}_r$ and $\mathbf{e}_x$

Subscripts

w = at the fiber surface
∞ = at infinity
0 = at the spinneret

Superscripts

L = in the liquid phase
V = in the gaseous or vapor phase

Introduction

In many industrial processes heat transfer on continuously drawn cylinders, threads, or sheets of material occurs somewhere along the production line. Examples of these processes include coating, hot rolling, continuous casting, or the formation of fibers and films. Knowledge about the heat transfer to continuous surfaces is of importance, because either the object has to be cooled below a given temperature, or because the motion of the object can be controlled by varying its viscosity through temperature (Simon, 1995). There is a large body of literature on heat transfer to surfaces moving through a stagnant fluid, and cases considered include simple convection (Crane, 1974), conjugate convection and conduction (Kuiken, 1975), buoyancy effects on horizontal and vertical sheets (Moutsoglu and Chen, 1980), natural and mixed convection (Karwe and Jaluria, 1988), and conjugate mixed convection and conduction (Kang et al., 1991). Heat transfer on continuous surfaces moving in a concurrent or countercurrent free stream has been studied for isothermal surfaces (Bianchi and Viskanta, 1993) as well as for surfaces loosing heat to their environment (Kang and Jaluria, 1992; Roy Choudhury and Jaluria, 1994). Forced convective cooling of fiber bundles by an air flow past them has been analyzed by Bach (1993).

Recently, another cooling mechanism, namely evaporative cooling, has been found to be relevant in the context of fiber formation during air-gap wet spinning (Simon, 1994a). In this process, the spinning solution is extruded through a spinneret hole as a hot liquid. The fiber is first drawn through an air gap, then it is led through a coagulation bath, and finally, it is collected on a wind-up roll. Fibers that are produced by this process are composed of cellulose, solvent, and water, and the solidification of the fiber is caused by the diffusional exchange of solvent and water in the coagulation bath. In this paper attention is focused on the temperature of these fibers as they move through the air gap. In the air gap, the water that is contained within the fiber evaporates at the fiber surface and this contributes to the cooling of the fiber. In his analysis, Simon (1994a) has considered the convective and evaporative cooling of a fiber that moves through still air. He compared his results to experimental data and found a fairly good agreement. Here, this idea is carried one step further and consideration is given to forced fiber cooling by a horizontal crossflow. Specifically, this paper deals with a continuous circular fiber exposed to a low-Reynolds-number crossflow. A large-Reynolds-number crossflow will exert strong horizontal forces on the fiber and bend it sideways; this is, of course, undesirable. It is shown that for typical spinning conditions, the coupling between the boundary layer produced by the fiber's downward motion and the horizontal flow is weak and the former type of flow can be neglected with respect to the latter. This suggests the adoption of Oseen's approximation to model the convective heat and mass transfer by the horizontal crossflow.

Problem Formulation and Simplification

The analysis is restricted to a circular fiber of constant radius a that issues through an orifice at $z = 0$ and moves vertically downward with velocity $\mathbf{u} = U_F \cdot \mathbf{e}_z$. The fluid at large distances from the fiber flows horizontally with velocity $\mathbf{u} = U_\infty \cdot \mathbf{e}_x$. The physical situation is sketched in Fig. 1. The flow is assumed to be steady, laminar, and incompressible. All physical properties are taken to be constant.

In general, a complex flow pattern will develop in which the fluid is dragged along with the fiber and is simultaneously blown past it. This type of flow is fully three dimensional and a comprehensive analysis is difficult. In order to simplify the problem, we first consider separately the physical effects of a continuously moving fiber and an air flow past it.

In the absence of any crossflow ($U_\infty = 0$), the fluid in the immediate neighborhood of the fiber is set into motion by it and accelerated downward. In this case, frictional forces are balanced by a downward momentum transport within a boundary layer of radial extent $\delta_F(z) \propto (\nu^V z/U_F)^{1/2}$ (Sakiadis, 1961). This type of flow is never independent of z, because more and more fluid is set into motion with increasing axial distance.

[1] Stiftstr. 46, D-45470 Mülheim a.d. Ruhr, Federal Republic of Germany; Assoc. Mem. ASME.

Contributed by the Heat Transfer Division of THE AMERICAN SOCIETY OF MECHANICAL ENGINEERS. Manuscript received by the Heat Transfer Division December 1994; revision received July 1995. Keywords: Forced Convection, Mass Transfer, Materials Processing and Manufacturing Processes. Associate Technical Editor: Y. Jaluria.

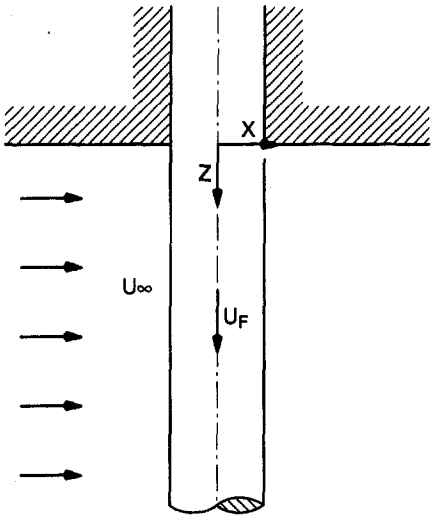

Fig. 1 Sketch of the physical situation and coordinate system

The presence of the horizontal crossflow introduces another length scale, namely the viscous length $\delta_\infty \propto \nu^V/U_\infty$. This is a rough measure of the radial distance over which frictional forces are balanced by a horizontal momentum transport. This type of flow is independent of axial position. The present analysis is restricted to those cases, in which the viscous length ν^V/U_∞ is very much larger than the fiber radius, i.e., to low-Reynolds-number crossflow: $\mathrm{Re} \equiv 2U_\infty a/\nu^V \ll 1$.

Now consider the combined effects of a moving fiber and an air flow past it. Close to the orifice, the boundary layer thickness δ_F will be much smaller than the viscous length δ_∞. Therefore, the vertical velocity component will change rapidly over the small distance δ_F, and the flow will be dominated by the boundary layer flow that is produced by the downward moving fiber. As one moves along the fiber axis, the boundary layer grows and as δ_F is comparable to δ_∞, a complex three-dimensional interaction between the boundary layer type flow and the horizontal crossflow evolves. At even larger distances, the boundary layer has grown to such an extent that a large portion of the fluid adjacent to the fiber moves downward with almost uniform velocity U_F. Therefore, the changes of the vertical velocity component are small, and they invoke neither large frictional forces nor large accelerations. The horizontal velocity components, on the other hand, are always forced to zero on the fiber surface, while they are maintained at the value U_∞ at large radial distances. Therefore, their radial changes are the source of viscous forces, and these are balanced by a horizontal momentum transport. As a result, the flow at large axial distances is dominated by the air flow past the fiber. In other words: No matter how small U_∞ may be, there will always be an axial distance l such that for $z > l$ the flow is purely two dimensional and is that produced by U_∞. A rough estimate for l may be obtained by equating δ_F and δ_∞, which yields $l/L \propto (\nu^V U_F)/(U_\infty^2 L)$, where L is the length of the air gap. In fiber spinning, typical values are $l/L = O(10^{-2})$. The quantity $(\nu^V U_F)/(U_\infty^2 L)$ may also be interpreted as the ratio of downward convection to horizontal convection, since $w\partial/\partial z \propto U_F/L$ whereas $u\partial/\partial x \propto U_\infty^2/\nu^V$. If, therefore, $(\nu^V U_F)/(U_\infty^2 L) \ll 1$, it is admissible to set $\mathbf{u}\cdot\nabla \doteq U_\infty \mathbf{e}_x \cdot \nabla$. This is Oseen's approximation, which will be used in the sequel of the paper.

To simplify the analysis further, it is assumed that the water concentration is constant within the fiber and that the temperature is constant over the cross section of the fiber. The conditions that must be met if these assumptions are to be valid are derived from the conditions of continuity of mass and heat fluxes at the fiber surface (Simon, 1994b). It is found that if $\mathrm{ReSc}(D^L L/U_F a^2)^{1/2}(\rho^V D^V(1 - c_w^L))/(\rho^L D^L(1 - c_w^V)) \ll 1$, it is admissible to neglect the change of concentration within the fiber, and if $\mathrm{RePr}\lambda^V/\lambda^L \ll 1$ and $\mathrm{RePr}(\lambda^V/\lambda^L)((h^V - h^L)(c_w^V - c_\infty^V))/(c_p^V(T_w - T_\infty)(1 - c_w^V)) \ll 1$, it is admissible to neglect the change of temperature over the cross section of the fiber. For typical spinning conditions, $\mathrm{ReSc}(D^L L/U_F a^2)^{1/2}(\rho^V D^V(1 - c_w^L))/(\rho^L D^L(1 - c_w^V)) = O(10^{-2})$, $\mathrm{RePr}\lambda^V/\lambda^L = O(10^{-2})$, and $\mathrm{RePr}(\lambda^V/\lambda^L)((h^V - h^L)(c_w^V - c_\infty^V))/(c_p^V(T_w - T_\infty)(1 - c_w^V)) = O(10^{-2})$, whence the assumptions given above provide a useful and valid simplification.

Governing Equations and Their Solution

In the low-Reynolds-number limit, a uniformly valid approximation for convective heat and mass transfer in the surroundings of the fiber is given by Oseen's approximation

$$U_\infty \frac{\partial T}{\partial x} = \frac{\kappa^V}{r}\frac{\partial}{\partial r}\left(r\frac{\partial T}{\partial r}\right), \tag{1}$$

and

$$U_\infty \frac{\partial c}{\partial x} = \frac{D^V}{r}\frac{\partial}{\partial r}\left(r\frac{\partial c}{\partial r}\right), \tag{2}$$

where axial conduction and diffusion have been neglected because $a/L \ll 1$. Equations (1) and (2) adequately describe the temperature and concentration fields at large radial distances, but introduce an error of order $O(\mathrm{RePr})$ and $O(\mathrm{ReSc})$, respectively, near the fiber. An integral energy balance for the fiber yields

$$\rho^L U_F a^2 c_p^L \pi \frac{dT_F}{dz} = a\lambda^V \int_0^{2\pi} \frac{\partial T(a)}{\partial r}\, d\varphi + a(h^V - h^L)\frac{\rho^V D^V}{1 - c^V(a)} \int_0^{2\pi} \frac{\partial c^V(a)}{\partial r}\, d\varphi. \tag{3}$$

The initial and boundary conditions that supplement these equations are

$$T = T_F = T_0, \quad c^V = c_0^V(T_0) \quad \text{at} \quad z = 0, \quad r = a, \tag{4}$$

$$T = T_F(z), \quad c^V = c_w^V(T_F(z)) \quad \text{at} \quad z \geq 0, \quad r = a, \tag{5}$$

and

$$T = T_\infty, \quad c^V = c_\infty^V \quad \text{at} \quad z \geq 0, \quad r \to \infty. \tag{6}$$

The temperature dependence of the saturation concentration is given by

$$c^V(T) = c_0^V \exp\left(\frac{(h^V - h^L)}{RT_0}\left(1 - \frac{T_0}{T}\right)\right), \tag{7}$$

where it has been assumed that the environment of the fiber, being a binary mixture of water vapor and air, behaves like an ideal mixture of ideal gases, and the saturation pressure of pure water vapor is given by the Clausius–Clapeyron equation. In the fiber, the cellulose acts as an inert matrix that does not influence thermodynamic equilibrium. Therefore, the fiber behaves like a real mixture of two substances (solvent and water), and the concentration of water vapor at the fiber surface $c^V(r = a)$ (and hence c_0^V) is proportional to the water content within the fiber and to the activity coefficient of the mixture. The activity coefficient is itself a function of water concentration and (like the water concentration) is always less than one. Therefore, the saturation concentration of water vapor at the fiber surface is much lower than that pertaining to pure water and can fall below the value c_∞^V at infinity, even if $T_F > T_\infty$. Details of the derivation of thermodynamic equilibrium for this particular case are given by Simon (1994b), where the explicit dependence of c_0^V on the activity coefficient is also shown.

The energy balance Eq. (3) simply states that the fiber temperature will change in response to a conductive and convective

heat transport or a convective enthalpy transport through the fiber surface. Depending on the values of T_0, T_∞, c_0^V, and c_∞^V, the sign of the convective heat and enthalpy transport terms may be either positive or negative and thus lead to either cooling or heating of the fiber. In most cases, however, $T_0 > T_\infty$ and $c_0^V > c_\infty^V$, and the driving temperature and concentration differences will be greater than zero. In this case, both terms on the right-hand side of Eq. (3) will have the same sign and both will lead to cooling of the fiber. With increasing axial distance, however, the temperature will decrease and subsequently the saturation concentration on the fiber surface drops. Eventually, $c_w^V = c^V(a) = c_\infty^V$ at some axial distance from the orifice, and the mass flux of water vapor vanishes. At even greater distances, $c_w^V = c^V(a) < c_\infty^V$, and the mass flux of water vapor is directed from the surrounding to the fiber. As the vapor condenses on the fiber surface, the heat of evaporation is released and transferred to the fiber. In this case, the terms on the right-hand side of Eq. (3) will have opposite signs: The first term will lead to cooling by convection and the second term will lead to heating by condensation. The ultimate fiber temperature exceeds the temperature of the surrounding air and is determined by the balance between heat removal by convection and heat supply by condensation.

Note that Eqs. (1) and (2) for heat and mass transfer in the fluid are decoupled and can be solved independently of Eq. (3) because they depend on z only parametrically through their boundary values $T(a) = T_F(z)$ and $c^V(a) = c_w^V(z)$. The reason for this decoupling is the adoption of Oseen's approximation, i.e., the neglect of downward as compared to horizontal convection. Solutions to Eqs. (1) and (2) that satisfy the boundary conditions at infinity exactly and those at the fiber surface to lowest order in (Re·Pr) and (Re·Sc), are (Bach, 1993)

$$\frac{T - T_\infty}{T_F - T_\infty} = -\frac{1}{\ln(\mathrm{PrRe}/8) + \gamma} \exp\left(\frac{\mathrm{Pr}U_\infty x}{2\nu^V}\right) K_0\left(\frac{\mathrm{Pr}U_\infty r}{2\nu^V}\right), \quad (8)$$

and

$$\frac{c^V - c_\infty^V}{c_w^V - c_\infty^V} = -\frac{1}{\ln(\mathrm{ScRe}/8) + \gamma} \exp\left(\frac{\mathrm{Sc}U_\infty x}{2\nu^V}\right) K_0\left(\frac{\mathrm{Sc}U_\infty r}{2\nu^V}\right). \quad (9)$$

Inserting Eqs. (8) and (9) into Eq. (3), carrying out the integrations and rearranging terms yields

$$\frac{d\Theta}{dZ} = -\Theta - \frac{\ln(\mathrm{PrRe}/8) + \gamma}{\ln(\mathrm{ScRe}/8) + \gamma} \frac{\mathrm{Pr}}{\mathrm{Sc}} \frac{B_1 C(\Theta)}{B_2 - C(\Theta)}, \quad (10)$$

with

$$\Theta = \frac{T_F - T_\infty}{T_0 - T_\infty}, \quad C = \frac{c_w^V - c_\infty^V}{c_0^V - c_\infty^V},$$

$$\text{and} \quad Z = 2\frac{\nu^V z}{U_F a^2} \frac{\rho^V c_p^V}{\rho^L c_p^L} \frac{B_6}{\mathrm{Pr}}. \quad (11)$$

Equation (7) transforms to

$$C(\Theta) = \exp\left(\frac{B_5(\Theta - 1)}{\Theta + B_4}\right)(1 + B_3) - B_3, \quad (12)$$

and the dimensionless parameters are given by

$$B_1 = \frac{(h^V - h^L)}{c_p^V(T_0 - T_\infty)}, \quad B_2 = \frac{1 - c_\infty^V}{c_0^V - c_\infty^V}, \quad B_3 = \frac{c_\infty^V}{c_0^V - c_\infty^V} \quad (13)$$

$$B_4 = \frac{T_\infty}{T_0 - T_\infty}, \quad B_5 = \frac{(h^V - h^L)}{RT_0}, \quad (14)$$

Table 1 Dimensionless parameters for the temperature profile shown in Fig. 2

Re = 0.1	Sc = 0.61
Pr = 0.7	B_1 = 30.77
B_2 = 31.35	B_3 = 0.369
B_4 = 3.973	B_5 = 13.41

$$B_6 = \frac{-1}{\ln(\mathrm{RePr}/8) + \gamma}.$$

Results and Discussion

Equation (10) was solved numerically using a fourth-order Runge–Kutta–Merson method. The implementation used a double precision routine of The NAG Fortran Library, and the differential equation tolerance was chosen such that the error in the solution is proportional to 10^{-6}, i.e., the solution is correct to five decimal digits. All physical properties were assigned values at a mean temperature $(T_0 + T_\infty)/2$. A resulting set of dimensionless parameters, which is representative for typical spinning conditions, is collected in Table 1. The calculated fiber temperature with and without mass transfer is shown in Fig. 2. As is expected, evaporation leads to a more rapid cooling close to the spinneret, where both heat and enthalpy fluxes have the same direction. As the mass flow is reversed and vapor condenses on the fiber surface, the heat and enthalpy fluxes are opposed and neutralize each other. The final temperature $T_F(z \to \infty)$ to which the fiber can be cooled is higher than the ambient T_∞ because heat is supplied to the fiber by condensation. Unfortunately, it is not possible to compare the computed fiber temperature that accounts for mass transfer to experimental data, because neither theoretical nor experimental data are reported in the literature.

It should be noted that the final fiber temperature is nearly independent of Reynolds, Prandtl, and Schmidt numbers. This can be seen by inspection of Eq. (10), where these quantities enter through the combination $((\ln(\mathrm{PrRe}/8) + \gamma)\mathrm{Pr})/((\ln(\mathrm{ScRe}/8) + \gamma)\mathrm{Sc})$. For values of $\mathrm{Pr} = O(1)$ and $\mathrm{Sc} = O(1)$, this quantity changes between 1.14 and 1.07 for $10^{-8} < \mathrm{Re} < 1$. The physical reason for this behavior is the following: heat and mass transport are proportional to κ^V and D^V, respectively, and they are driven by gradients that are effective over radial distances of the order $O(\kappa^V/U_\infty)$ and $O(D^V/U_\infty)$, respectively. To a first approximation, therefore, the ratio of convective heat to convective mass transport is independent of Re, Pr, and Sc, and so is the final value of the fiber temperature. The

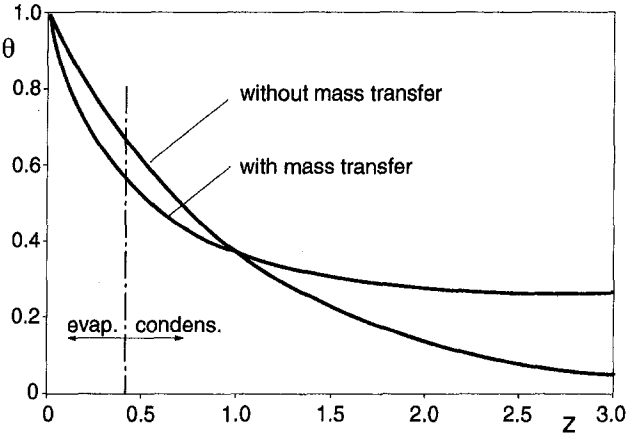

Fig. 2 Calculated fiber temperature with and without mass transfer. The chain-dotted line indicates the distance at which the mass flux of water vapor is reversed. For smaller distances water evaporates; for larger distances water vapor condenses on the fiber surface.

cooling length, however, needed to attain the final temperature is proportional to 1/Re: $z \propto \ln(\mathrm{ReSc}/8) + \gamma$.

Acknowledgments

I am grateful to Professor L. J. Crane and Dr. G. Frischmann for stimulating and helpful discussions. I am also indebted to Professor J. T. Jenkins for improvements to the English language of this paper.

References

Bach, N., 1993, "Air Flow Past a Fibre Bundle," M.S. Thesis, Trinity College, Dublin, Ireland.

Bianchi, M. V. A., and Viskanta, R., 1993, "Momentum and Heat Transfer on a Continuous Flat Surface Moving in a Parallel Counterflow Free Stream," *Wärme- und Stoffübertragung,* Vol. 29, pp. 89–94.

Crane, L. J., 1974, "Heat Transfer on Continuous Solid Surfaces," *Ing. Arch.,* Vol. 43, pp. 203–214.

Kang, B. H., Jaluria, Y., and Karwe, M. V., 1991, "Numerical Simulation of Conjugate Transport From a Continuous Moving Plate in Materials Processing," *Numerical Heat Transfer A,* Vol. 19, pp. 151–176.

Kang, B. H., and Jaluria, Y., 1992, "Numerical Study of the Fluid Flow and Heat Transfer Due to a Heated Plate Moving in a Uniform Forced Flow," *Numerical Heat Transfer A,* Vol. 22, pp. 143–165.

Karwe, M. V., and Jaluria, Y., 1988, "Fluid Flow and Mixed Convection Transport From a Moving Plate in Rolling and Extrusion Processes," ASME JOURNAL OF HEAT TRANSFER, Vol. 110, pp. 655–661.

Kuiken, H. K., 1975, "The Cooling of a Low-Heat-Resistance Cylinder Moving Through a Fluid," *Proc. R. Soc. Lond. A,* Vol. 346, pp. 23–35.

Moutsoglou, A., and Chen, T. S., 1980, "Buoyancy Effects in Boundary Layers on Inclined, Continuous, Moving Sheets," ASME JOURNAL OF HEAT TRANSFER, Vol. 102, pp. 371–373.

Roy Choudhury, S., and Jaluria, Y., 1994, "Forced Convective Heat Transfer From a Continuous, Moving Heated Cylindrical Rod in Materials Processing," ASME JOURNAL OF HEAT TRANSFER, Vol. 116, pp. 724–734.

Sakiadis, B. C., 1961, "Boundary Layer Behaviour on Continuous Solid Surfaces: III. The Boundary Layer on a Continuous Cylindrical Surface," *AIChE Journal,* Vol. 7, pp. 467–472.

Simon, V., 1994a, "Die Temperatur von Textilfasern während des Spinnprozesses," *ZAMM Z. angew. Math. Mech.,* Vol. 74(5), pp. T414–T415.

Simon, V., 1994b, "The Temperature of Fibers During Air-Gap Wet-Spinning: Cooling by Convection and Evaporation," *Int. J. Heat Mass Transfer,* Vol. 37, pp. 1133–1142.

Simon, V., 1995, "Analysis of Fiber Formation During Air-Gap Wet Spinning," *AIChE Journal,* Vol. 41, pp. 1281–1294.

Real Time Microholography for In-Situ Concentration Measurements in the Vicinity of Growing Dendrites

Y. B. Shen[1] and D. Poulikakos[2]

Nomenclature

A = constant, Eq. (1)
B = constant, Eq. (1)
c = solute concentration, wt%
d = optical path length of glass cell, m
D = species diffusivity
K = const, Eq. (1)
Le = Lewis number = α/D
n = refractive index
N = interference fringe order
T = solution temperature, °C
α = thermal diffusivity
λ = wavelength of He–Ne laser

Subscripts

1 = reference state
2 = new state

[1] Department of Mechanical Engineering, University of Illinois at Chicago, 842 West Taylor Street, Chicago, IL 60607.

[2] Department of Mechanical and Process Engineering, Institute of Energy Technology, Swiss Federal Institute of Technology (ETH) ETH Center, CH-8092 Zurich, Switzerland; Fellow ASME.

Contributed by the Heat Transfer Division of THE AMERICAN SOCIETY OF MECHANICAL ENGINEERS. Manuscript received by the Heat Transfer Division January 1995; revision received October 1995. Keywords: Materials Processing and Manufacturing Processes, Measurement Techniques, Phase-Change Phenomena. Associate Technical Editor: B. W. Webb.

1 Introduction

In the solidification of alloys and mixtures, a mixed-phase zone often exists between the solid and liquid regions. In this zone, the solid phase crystallizes, often in dendritic form, resulting in species concentration gradients. The character of the species concentration distribution is important in alloy solidification since it generates buoyancy-driven flows, which affect the final solid composition and may lead to quality problems such as macrosegregation and freckling.

In the past several years many investigations, exemplified by Incropera and co-workers (Prescott and Incropera, 1994; Prescott et al., 1994; Magirl and Incropera, 1993; Neilson and Incropera, 1991; Christenson and Incropera, 1989b) and Viskanta and co-workers (Song et al., 1993; Choi and Viskanta, 1993; Yoo and Viskanta, 1992; Viskanta, 1990; Beckermann and Viskanta, 1988) as well as references therein, focused on various aspects of the alloy solidification process from the standpoint of transport phenomena. This vivid interest has resulted in a rapidly growing literature that will not be reviewed herein, for brevity. Many of the existing studies are macroscopic, i.e., the mixed-phase region is treated as a continuum (porous medium) resulting from an averaging (often volumetric) process of the two phases.

A few investigations on transport phenomena in alloy solidification have focused on the microscopic level. For example, Copley et al. (1970) investigated the origination of freckles in casting processes, Sample and Hellawell (1984) studied the formation and prevention of solute plumes and solid channels in alloy solidification, and Sundarraj and Voller (1993) predicted numerically the characteristic size of the microstructure in a mushy zone introducing a microsegregation arm coarsening model. Bianchi and Viskanta (1994) investigated the morphology of ice crystals grown from an ammonium chloride solution. They used a novel experimental setup to determine the effects of initial composition and freezing rate on the shape of the ice crystals.

Many questions remain unanswered in the area of alloy solidification from the standpoint of materials science as well as the standpoint of transport phenomena. Two specific needs that must be addressed are the continuation of the development of accurate nonintrusive techniques for temperature and concentration measurements during the freezing process and the acquisition of a good understanding of the growth and branching of dendritic structures at the microscopic level, which leads to the formation and growth of the mixed-phase region. With reference to the former, Spatz and Poulikakos (1992) utilized two wavelength holographic interferometry to obtain local, transient heat and mass transfer coefficients at the interface between the liquid and the mixed phase regions during the freezing of an aqueous ammonium chloride mixture around a cold horizontal pipe. Because of limitations in resolution (the study was performed at the macroscopic level) and three-dimensional effects, the technique worked well only when the interface was not highly dendritic. For highly dendritic interfaces qualitative results were produced.

With reference to the latter an attempt, with some success, was made by McCay and McCay (1993) to determine the super-

cooling length, however, needed to attain the final temperature is proportional to 1/Re: $z \propto \ln(\mathrm{ReSc}/8) + \gamma$.

Acknowledgments

I am grateful to Professor L. J. Crane and Dr. G. Frischmann for stimulating and helpful discussions. I am also indebted to Professor J. T. Jenkins for improvements to the English language of this paper.

References

Bach, N., 1993, "Air Flow Past a Fibre Bundle," M.S. Thesis, Trinity College, Dublin, Ireland.

Bianchi, M. V. A., and Viskanta, R., 1993, "Momentum and Heat Transfer on a Continuous Flat Surface Moving in a Parallel Counterflow Free Stream," *Wärme- und Stoffübertragung,* Vol. 29, pp. 89–94.

Crane, L. J., 1974, "Heat Transfer on Continuous Solid Surfaces," *Ing. Arch.,* Vol. 43, pp. 203–214.

Kang, B. H., Jaluria, Y., and Karwe, M. V., 1991, "Numerical Simulation of Conjugate Transport From a Continuous Moving Plate in Materials Processing," *Numerical Heat Transfer A,* Vol. 19, pp. 151–176.

Kang, B. H., and Jaluria, Y., 1992, "Numerical Study of the Fluid Flow and Heat Transfer Due to a Heated Plate Moving in a Uniform Forced Flow," *Numerical Heat Transfer A,* Vol. 22, pp. 143–165.

Karwe, M. V., and Jaluria, Y., 1988, "Fluid Flow and Mixed Convection Transport From a Moving Plate in Rolling and Extrusion Processes," ASME JOURNAL OF HEAT TRANSFER, Vol. 110, pp. 655–661.

Kuiken, H. K., 1975, "The Cooling of a Low-Heat-Resistance Cylinder Moving Through a Fluid," *Proc. R. Soc. Lond. A,* Vol. 346, pp. 23–35.

Moutsoglou, A., and Chen, T. S., 1980, "Buoyancy Effects in Boundary Layers on Inclined, Continuous, Moving Sheets," ASME JOURNAL OF HEAT TRANSFER, Vol. 102, pp. 371–373.

Roy Choudhury, S., and Jaluria, Y., 1994, "Forced Convective Heat Transfer From a Continuous, Moving Heated Cylindrical Rod in Materials Processing," ASME JOURNAL OF HEAT TRANSFER, Vol. 116, pp. 724–734.

Sakiadis, B. C., 1961, "Boundary Layer Behaviour on Continuous Solid Surfaces: III. The Boundary Layer on a Continuous Cylindrical Surface," *AIChE Journal,* Vol. 7, pp. 467–472.

Simon, V., 1994a, "Die Temperatur von Textilfasern während des Spinnprozesses," *ZAMM Z. angew. Math. Mech.,* Vol. 74(5), pp. T414–T415.

Simon, V., 1994b, "The Temperature of Fibers During Air-Gap Wet-Spinning: Cooling by Convection and Evaporation," *Int. J. Heat Mass Transfer,* Vol. 37, pp. 1133–1142.

Simon, V., 1995, "Analysis of Fiber Formation During Air-Gap Wet Spinning," *AIChE Journal,* Vol. 41, pp. 1281–1294.

Real Time Microholography for In-Situ Concentration Measurements in the Vicinity of Growing Dendrites

Y. B. Shen[1] and D. Poulikakos[2]

Nomenclature

A = constant, Eq. (1)
B = constant, Eq. (1)
c = solute concentration, wt%
d = optical path length of glass cell, m
D = species diffusivity
K = const, Eq. (1)
Le = Lewis number = α/D
n = refractive index
N = interference fringe order
T = solution temperature, °C
α = thermal diffusivity
λ = wavelength of He–Ne laser

Subscripts

1 = reference state
2 = new state

[1] Department of Mechanical Engineering, University of Illinois at Chicago, 842 West Taylor Street, Chicago, IL 60607.

[2] Department of Mechanical and Process Engineering, Institute of Energy Technology, Swiss Federal Institute of Technology (ETH) ETH Center, CH-8092 Zurich, Switzerland; Fellow ASME.

Contributed by the Heat Transfer Division of THE AMERICAN SOCIETY OF MECHANICAL ENGINEERS. Manuscript received by the Heat Transfer Division January 1995; revision received October 1995. Keywords: Materials Processing and Manufacturing Processes, Measurement Techniques, Phase-Change Phenomena. Associate Technical Editor: B. W. Webb.

1 Introduction

In the solidification of alloys and mixtures, a mixed-phase zone often exists between the solid and liquid regions. In this zone, the solid phase crystallizes, often in dendritic form, resulting in species concentration gradients. The character of the species concentration distribution is important in alloy solidification since it generates buoyancy-driven flows, which affect the final solid composition and may lead to quality problems such as macrosegregation and freckling.

In the past several years many investigations, exemplified by Incropera and co-workers (Prescott and Incropera, 1994; Prescott et al., 1994; Magirl and Incropera, 1993; Neilson and Incropera, 1991; Christenson and Incropera, 1989b) and Viskanta and co-workers (Song et al., 1993; Choi and Viskanta, 1993; Yoo and Viskanta, 1992; Viskanta, 1990; Beckermann and Viskanta, 1988) as well as references therein, focused on various aspects of the alloy solidification process from the standpoint of transport phenomena. This vivid interest has resulted in a rapidly growing literature that will not be reviewed herein, for brevity. Many of the existing studies are macroscopic, i.e., the mixed-phase region is treated as a continuum (porous medium) resulting from an averaging (often volumetric) process of the two phases.

A few investigations on transport phenomena in alloy solidification have focused on the microscopic level. For example, Copley et al. (1970) investigated the origination of freckles in casting processes, Sample and Hellawell (1984) studied the formation and prevention of solute plumes and solid channels in alloy solidification, and Sundarraj and Voller (1993) predicted numerically the characteristic size of the microstructure in a mushy zone introducing a microsegregation arm coarsening model. Bianchi and Viskanta (1994) investigated the morphology of ice crystals grown from an ammonium chloride solution. They used a novel experimental setup to determine the effects of initial composition and freezing rate on the shape of the ice crystals.

Many questions remain unanswered in the area of alloy solidification from the standpoint of materials science as well as the standpoint of transport phenomena. Two specific needs that must be addressed are the continuation of the development of accurate nonintrusive techniques for temperature and concentration measurements during the freezing process and the acquisition of a good understanding of the growth and branching of dendritic structures at the microscopic level, which leads to the formation and growth of the mixed-phase region. With reference to the former, Spatz and Poulikakos (1992) utilized two wavelength holographic interferometry to obtain local, transient heat and mass transfer coefficients at the interface between the liquid and the mixed phase regions during the freezing of an aqueous ammonium chloride mixture around a cold horizontal pipe. Because of limitations in resolution (the study was performed at the macroscopic level) and three-dimensional effects, the technique worked well only when the interface was not highly dendritic. For highly dendritic interfaces qualitative results were produced.

With reference to the latter an attempt, with some success, was made by McCay and McCay (1993) to determine the super-

saturation at a dendrite tip interface by the central dark ground optical method. Shigematsu and Komatsu (1991) studied the growth of ionic crystals from an aqueous solution by in-situ observation using a microscope. They employed a wedge-shaped growth cell (illuminated with a monochromatic light source) with minimal thickness to suppress convection currents. This process yielded a set of parallel fringes. The fringes became distorted in the presence of a concentration gradient, which made possible the inference of concentrations. Dougherty et al. (1987) studied the growth of dendritic crystals of NH_4Br from a supersaturated solution. They found that the branches were nonperiodic at any distance from the tip with apparent variations in both phase and amplitude.

Tanaka and Sano (1992) measured nonintrusively the kinetic effect on the concentration coefficient of an ammonium chloride dendrite growing horizontally in a cell with an inclined top surface. The cell thickness was 50 μm at one end and 1 mm at the other. Because of this inclination, optical fringes were observed under monochromatic light. They found that the concentration difference between the tip and the state of equilibrium increased linearly with the tip velocity, indicating the importance of the kinetic term in the interfacial behavior of a growing dendrite. Their results contradicted the Gibbs–Thomson relationship and suggested the existence of dynamic mechanisms. Raz et al. (1989) developed an interference microscopy method that yielded useful mapping of the concentration field around a growing ammonium chloride dendrite. Their results indicated that there is a finite supersaturation of the liquid in contact with the crystal and that the rate of growth is related to this supersaturation in a highly nonlinear manner. They suggested that homogeneous nucleation theories for crystal growth of facets are applicable to the growth of these dendrites.

Kourosh et al. (1990) performed computer-based densitometry analysis to determine the transient microscopic interface morphology and two-dimensional solute concentration field for a solidifying binary mixture with a significant absorption coefficient within the visible light spectrum. Two stability theories, Mullins and Sekerka (1964) for planar interfaces and Trivedi (1985) for cellular interfaces were applied. The results indicated good agreement with the experiments for the planar interface. The theory for cellular interfaces appeared to be an efficient predictive tool as well. Bedarida (1986) used holography to determine the concentration field around regularly shaped crystals (of square and octagonal cross sections in the viewing plane). No length scale is reported in their study except for the fact that the test cell volume was large (30 cm^3). Their study underlines the potential of holography for concentration measurements in crystal growth.

The present paper reports a study that is relevant to both the needs mentioned above, for it employs a nonintrusive technique, based on real time microholography, for the measurement of the transient concentration field in the vicinity of a growing dendrite. The technique allows for the simultaneous observation of the geometric features of the dendrite during its growth and branching. To put the present paper into proper perspective with respect to earlier relevant contributions, it is worth stating that the present work is different from Bedarida's (1986) in that we use real time microholography to study *dendritic* growth and branching. They studied the growth of *regularly shaped* crystals, without branching, and the simultaneous precipitation of many tiny crystals. Additionally, it is not known what the length scale of the crystals in Bedarida's paper is. He only reported that the volume of the test cell was 30 cm^3. The volume of the test cell of the present study was 0.4 cm^3. No quantitative results are given for the one-beam interferometry in Bedarida (1986). The fringes are used only for qualitative information. Kourosh et al. (1990) do not employ holography. In addition, they are dealing with unidirectional growth of crystals. In the present paper we applied the microholography technique to dendritic growth without controlling the growth direction to test the technique in a setting resembling mushy zone formation. Next, natural convection was present in the work reported in this paper. The evolving concentration field in its presence (the cell was placed vertically and the crystals nucleated at the bottom) was studied. In the paper by Kourosh et al. (1990), the depth of the specimen chamber in the direction of the optical path of the microscope was 25 μm. This, combined with the fact that the specimen chamber was placed horizontally, eliminated natural convection currents. Finally, the technique in this paper is well suited for transparent solutions. The technique of Kourosh et al. (1990) relies on gray level calibration and is more suited for colored solutions.

2 Experimental Technique and Apparatus

Holographic interferometry is a powerful technique for the measurement of temperature and concentration fields in thermal engineering applications. No background on the technique will be given herein. A wealth of such information can be found in Vest (1979).

An aqueous ammonium chloride mixture has been chosen as the working fluid in this study. This kind of mixture is a popular choice in studies of analogs of metal solidification processes because of its low entropy of fusion, transparency, well-known properties, and the similarities in dendritic formation that exist between salt crystallization and metal solidification. The relationship between the refractive index (n), the concentration (c), and the temperature (T) of this mixture is generally expressed by a linear equation (McCay and McCay, 1993; Spatz and Poulikakos, 1992; Shigematsu and Komatsu, 1991):

$$n = K + A \times c - B \times T \tag{1}$$

where K, A, and B are constant coefficients. For the conditions of our experiments (concentration from 18.0 to 28.0 percent and temperature from 18°C to 27°C), Abbe refractometer measurements in our laboratory showed that the values of these constants are $K = 1.3385$, $A = 1.7500 \times 10^{-3}$ $(\text{wt}\%)^{-1}$ and $B = 1.2368 \times 10^{-4}$ $(°\text{C})^{-1}$, respectively. Slight differences in these values among various studies may occur due to different measurement methods and accuracy levels, as well as the fact that different studies may not be interested in exactly the same temperature and concentration ranges. Note also that as the temperature and concentration ranges widen, the linearity assumption of Eq. (1) weakens. Our relation is for a rather narrow temperature range and, as will be discussed in section 4, it was checked against data from other investigators with excellent agreement.

It can be shown (Vest, 1979) that the dependence of the index of refraction of a mixture on fringe order and wavelength is

$$(n_1(c_1, T_1) - n_0(c_0, T_0)) \times d = N \times \lambda \tag{2}$$

where the subscripts 0 and 1 denote two different states, d is the optical path length of the cell ($d = 1$ mm in our study), λ is the wavelength of the laser light ($\lambda = 632.8$ nm for the He–Ne laser employed in this study) and N is the fringe order number counted from the interferometric image. Combining Eqs. (1) and (2)

$$c_1 = c_0 + \left[N \times \frac{\lambda}{d} + B \times (T_1 - T_0) \right] \Big/ A \tag{3}$$

If the temperature and concentration of a "reference" state, denoted by the subscript 0, are known, the concentration of any other state, denoted by the subscript 1, can be obtained from Eq. (3) if the temperature of this new state is known. As will be explained below, this is indeed the case in the present experiments.

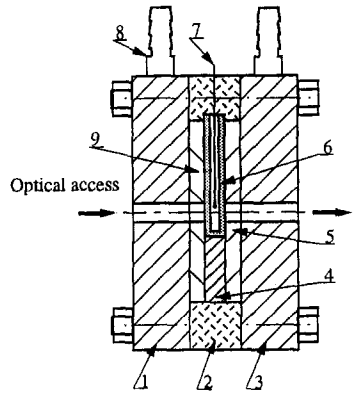

1) Heat Exchanger (Sink)
2) Insulation Foam
3) Heat Exchanger (Sink)
4) Aluminum Spacer
5) Thermoelectric (Peltier) Cooling Plate
6) Glass Cell
7) Thermocouple
8) Hose Connector for Cooling Water
9) Thermoelectric (Peltier) Cooling Plate

Fig. 1 Schematic of the temperature-controlled dendrite growth apparatus

A schematic of the cross section of the temperature-controlled dendrite growth apparatus is shown in Fig. 1. The glass cell, which has an optical depth of 1 mm and volume of 0.4 mL, contained the aqueous solution of NH_4Cl of known initial concentration. A *K*-type microscopic thermocouple with wire diameter of 50 μm was inserted in the cell to monitor the temperature of the solution as well as to calibrate the magnification rate of optical system. The measured temperature was read and recorded by an HP 3421A data acquisition system. The glass cell was sealed with silicone sealant and sandwiched between two thermoelectric (Peltier) cooling plates. The thermoelectric cooling plates were special ordered with a 4-mm-dia hole at their center to allow for optical access. The dendritic growth was initiated at a seed crystal placed at the center of the bottom of the cell and monitored in the region above the crystal, accessed optically through the aforementioned holes in the Peltier plates. These plates were operated with an HP6012B DC power supply. Heat sinks were attached on the hot sides of the thermoelectric plates to dissipate heat. Thermal compound was pasted between all the contacting surfaces to decrease thermal contact resistance. Constant-temperature cooling water, provided by a Neslab RTE-110 precision refrigerator/circulator, run continuously through the heat sinks to avoid burnout of the thermoelectric plates. This assembly provided effective thermal control and assured spatial isothermality within the glass cell.

The isothermality was tested through a series of side experiments in which the thermocouple was placed in a host of locations in the cell always indicating the same temperature. In addition, no fringes were observed in the precrystallization stages of the experiments during the cooling process (since the concentration of the solution prior to crystallization was uniform, the presence of fringes would indicate spatial temperature gradients). When solidification starts, small temperature gradients will appear in the system. Equation (1) shows that the effect of concentration gradients on the refractive index is approximately 14 times larger than that of the temperature gradients. In addition, the temperature fluctuations recorded by the thermocouple during the freezing process are very small (less than 0.2°C). Raz et al. (1989), in their study of dendritic growth of crystals from ammonium chloride, estimated the temperature difference between the interface and the bulk fluid to be approximately 0.15°C. We calculated that a 0.15°C temperature difference yields a fringe order number of 0.029. No fringes are formed with such small temperature differences. Hence, it is appropriate to neglect the effect of the temperature effect on the refractive index in the present experiment and to proceed with single wavelength interferometry.

The apparatus was installed on a vibration-isolation optical bench containing the optical set up of the real-time microholography technique shown in Fig. 2. A laser beam emitted by a 20 mW He–Ne laser was split into a reference and an object beam by a cubic beamsplitter. The reference beam was expanded, filtered, and collimated. The object beam was attenuated by a variable beam attenuator before illuminating the test cell through its access holes. After passing through the test cell, a 10X microscope objective lens received the light and formed a magnified image on the holographic plate. This plate was installed in a holder contained inside a tank that allowed for in-situ (without removal) development after the fabrication of the hologram.

To begin an experiment, the solution in the cell was allowed to stabilize for days to yield a homogeneous concentration in the cell. The initial conditions were chosen such that the mixture was close to saturation at room temperature in order to maintain the seed crystal prior to cooling. One hologram was first fabricated under the conditions of room temperature and the known initial concentration. Then, the holographic plate was developed, fixed, and rinsed in-situ, in the tank described above (Fig. 2). Subsequently, the holographic plate was illuminated by the same reference beam. The recorded image was thus reconstructed.

Next, the power of the two thermoelectric plates was turned on and the mixture in the cell was cooled down. In the process, the solution became supersaturated and unstable. Dendritic crystallization was initiated at a nucleation site at the bottom of the cell. This region was continuously illuminated by the object beam. As a result, the real magnified image of the dendrites together with the surrounding solution and the fringes (formed because of the interference between the object and the reference beams) appeared on the holographic plate. This image evolved with time due to the transient nature of the phenomenon. In real time holography, the fringes travel through the observation area as the concentration changes (the solidification progresses). The fringes are numbered in order of appearance since the initiation of the cooling. The fringe orders so obtained are used for the calculation of the concentration.

A CCD camera and a video recording system was utilized to record these events in real time (Fig. 2). The images of the fringes were processed with a Macintosh Quadra 800 computer equipped with the Image Analyst (Automatrix Inc.) software. No effort was made (deliberately) to induce the growth of the dendrites in a symmetric manner. Since this is a random event in large-scale applications, we elected to investigate the effectiveness of the technique under conditions of random growth. It is worth acknowledging that experiments with controlled dendritic growth will be beneficial to a better basic understanding of mixture solidification. However, this was not the focus of this paper. We used the technique on dendrites growing arbitrarily (without controlling the growth direction) from a single nucleation site (seed crystal). At the end of each experiment we removed the thermoelectric coolers and observed that in all cases no dendrites were growing from the top or the sides.

3 Results and Discussion

Figure 3 shows a sequence of frames depicting the growth of a single dendrite. The dark regions (streaks) in the liquid are the fringes. The integers (for example "1" on the fringe of Figs. 3(*a*, *b*) and "2" on the fringe of Figs. 3(*c*, *d*)) represent the fringe order (Vest, 1979) from the initiation of the experiment. The concentrations of the regions covered by the

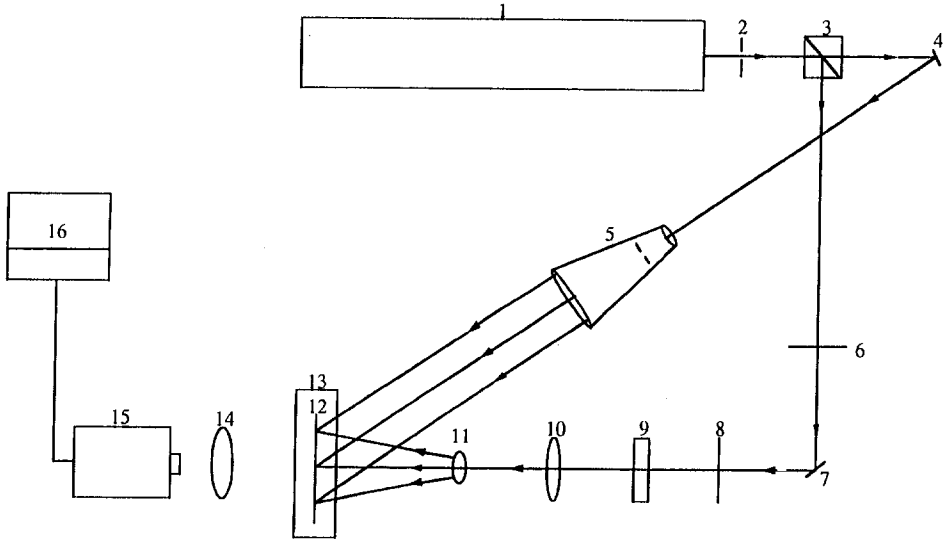

1) He - Ne Laser
2) Shutter
3) Cubic Beam Splitter
4) Mirror
5) Bean Expander with Filter
6) Beam Attenuator
7) Mirror
8) Continuous Beam Attenuator
9) Test Cell
10) Lens
11) Microscopic Objective
12) Holographic Plate
13) Developing Tank
14) Image Lens
15) Video Recorder & Monitor

Fig. 2 Schematic of the optical setup for the in-situ microholographic interferometry

dark fringes and the light regions between the fringes, calculated from Eq. (3), are also shown in the photographs. The initial temperature of the mixture for this experiment was T_0 = 22.78°C and the initial concentration c_0 = 27.56 percent (weight percentage). The value of the Lewis number in our experiments was Le = 60, which also aids the isothermality condition in the cell discussed earlier. The mixture was cooled down to 19.55°C in less than one minute and maintained at this temperature thereafter. The concentration was obtained directly from Eq. (3) for a given fringe order number. An error analysis is discussed at

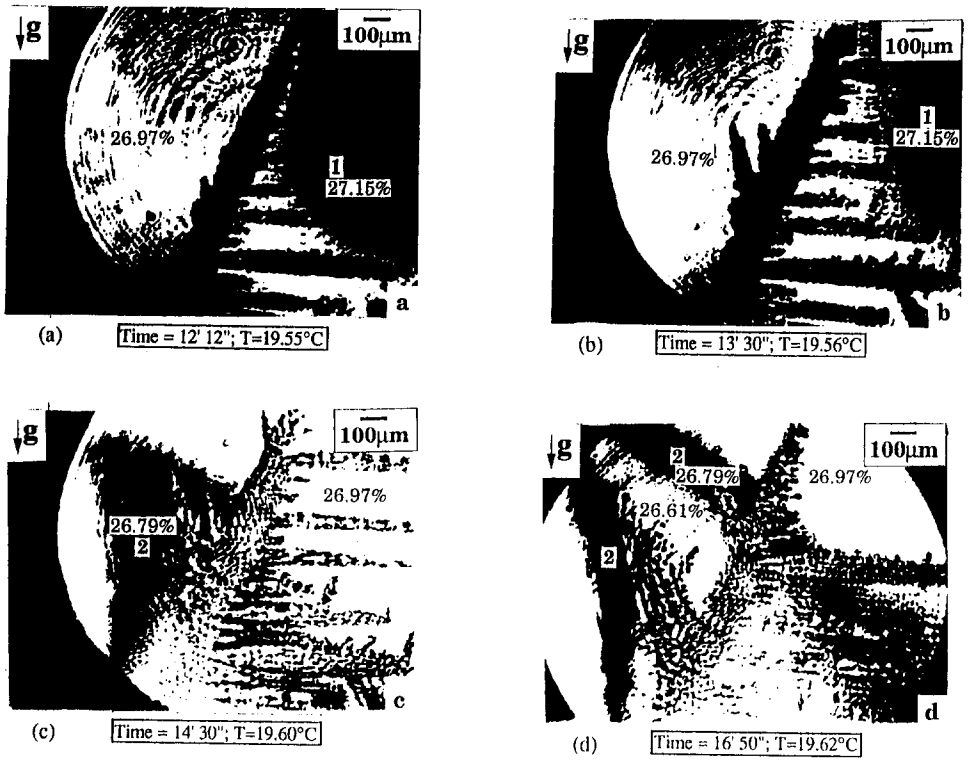

Fig. 3 Selected frames of concentration distributions around a growing dendrite of initial temperature T_0 = 22.78°C, and initial concentration c_0 = 27.56 percent

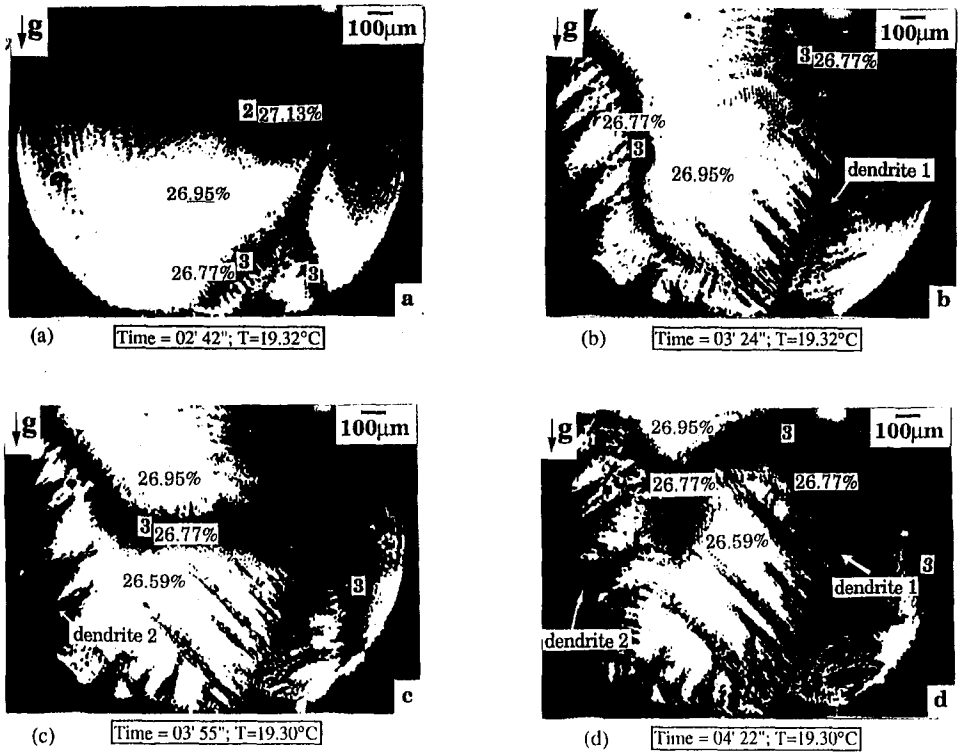

Fig. 4 Selected frames of concentration distributions around growing dendrites of initial temperature T_0 = 23.90°C, and initial concentration c_0 = 28.00 percent

the end of the paper. Bedarida (1986) states that concentration measurements with holographic interferometry can be made with a precision $\Delta c/c = 0.00001$. We performed an uncertainty analysis according to the principles of Coleman and Steel (1989) and found that the uncertainty in concentration differences in the present study was of the order of 0.0002 wt%.

Figures 3(a–d) show the concentration field during the growth and side branching of a dendrite. Higher concentration locally causes faster growth of the dendrite in that region. To this end, in Fig. 3(a) the dendrite arms grow faster on the right side than on the left side of the dendrite. On the other hand, the growth of the arms in this area results in depletion of salt and decrease in the local solute concentration in the liquid region. In Fig. 3(b) the concentration in the region of the newly grown arms changed from 27.15 to 26.97 percent.

In Fig. 3(c), the growth of the dendrite has reduced the concentration of most of the surrounding region to 26.97 percent. The beginning of the formation of a second dark fringe is also visible on the left side of the dendrite. This fringe has advanced in Fig. 3(d), which shows the existence of three distinct concentration regions in the vicinity of the dendrite. Comparing Figs. 3(b) and 3(d), one observes that the two distinct arms on the left side of the dendrite in Fig. 3(b) have grown and merged. In summary, Fig. 3 exemplifies the strong relationship between the dendritic growth and the concentration field in the liquid region in the dendrite vicinity.

Figure 4 focuses on the region between two growing dendrites. The initial conditions of the experiment illustrated in this figure are: T_0 = 23.90°C, c_0 = 28.00 percent. The mixture was cooled down to 19.30°C. Higher initial concentration and undercooling (compared to Fig. 3) caused faster dendrite growth. As mentioned earlier, no directional control on the dendritic growth was imposed in the present study. Generally, one dendrite was formed first and, as time progressed, it branched out and other dendrites were created. Sometimes, more than one dendritic branch grew simultaneously after nucleation. This behavior was observed more at higher cooling rates. As two dendrites grew together in Fig. 4, the concentration in the region between them decreased. Growth of side arms reduced the local solute concentration in the bottom region between the dendrites gradually from 26.95 percent in Fig. 4(b) to 26.59 percent in Fig. 4(d). It is worth noting that the lower concentration, less dense regions are located under the more dense heavier regions (Figs. 4(c, d)). This unstable concentration distribution at the local level drives a convection flow within the mixed-phase region as observed earlier in macroscopic studies of alloy solidification (see for example, Spatz and Poulikakos, 1992, Christenson and Incropera, 1989a). This kind of convective flow often develops in the form of plumes responsible for the formation of channels in the mixed-phase region.

In Fig. 5 the growth of the tip regions of a group of interweaving dendrites is shown. The initial condition for this experiment was T_0 = 23.27°C, c_0 = 27.56 percent. The cooling rate was increased and the mixture was cooled down to 18.08°C. As the group of dendrites grows (Figs. 5(a–d)), an unstable concentration distribution develops in the liquid in their vicinity. Interestingly, the concentration field is mainly affected by the entire group of dendrites rather than individual dendrites, i.e., the constant concentration dark fringe right over the tips of the dendrites is "pushed up" by the entire group rather than being "wrapped" around individual tips. This is a direct result of the close spacing of the dendritic arms, as well as the presence of convection in the system, which facilitates mixing in the interdendritic spaces. At a macroscopic level this result indicates that it is possible at times to have a rather smooth concentration variation directly over a group of sharp tips of dendrites. It is worth clarifying that the absence of wrapping of the fringes should be viewed within the context of the accuracy of the measurements. For measurements with more significant figures, or in the absence of convection, it is possible that isoconcentration lines can be observed to wrap around the dendrites (Kourosh et al., 1990). Note that such wrapping is also observed in

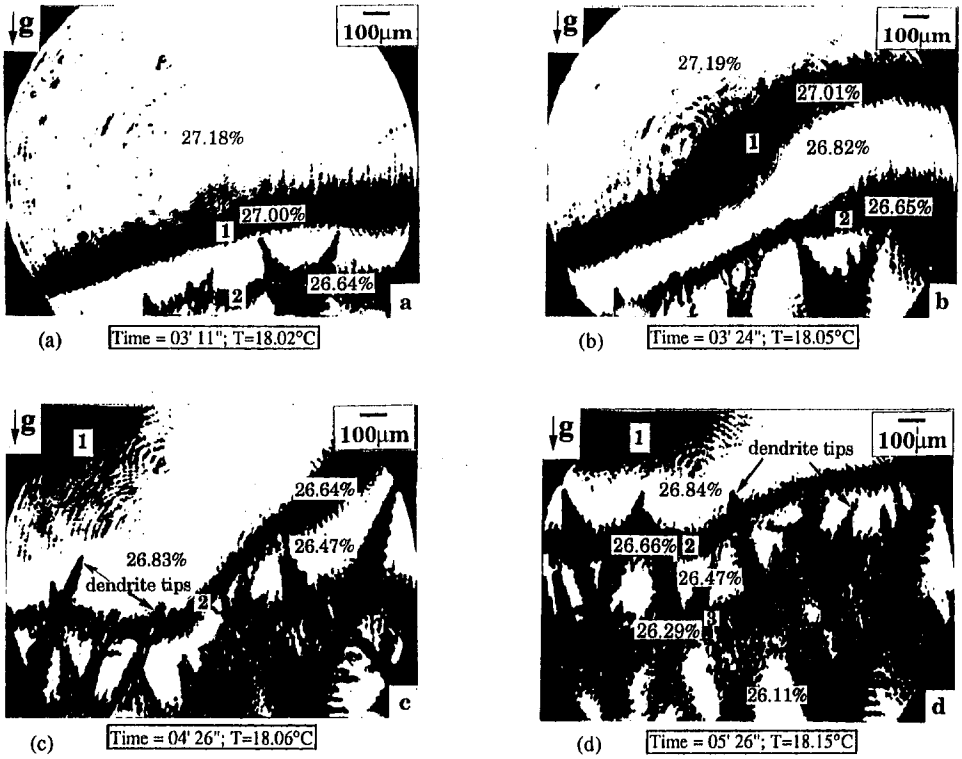

Fig. 5 Selected frames of concentration distributions around growing dendrites of initial temperature T_0 = 23.27°C, and initial concentration c_0 = 27.56 percent

the present work in the case of a single dendrite (Figs. 3(*c*, *d*) and 4(*a*)).

The results in Figs. 4 and 5 seem to support the explanation of Neilson and Incropera (1991) on the formation of channels in the mushy zone. Based on their numerical results, these authors argued that instabilities of the concentration field near the liquidus are responsible for the formation of the channels. The regions shown in Figs. 4 and 5 are near the liquidus and clearly illustrate the unstable nature of the concentration field. In addition, the bending and the wavy nature of the isoconcentration lines (fringes) as time progresses (Figs. 4(*b*, *c*, *d*), and Figs. 5(*b*, *c*, *d*)) seems to indicate the development of upward moving plumes of light interdendritic fluid, which contribute to the creation of channels in the mushy zone. Note that the fringe of order unity in Fig. 5(*d*) is severely bent but has moved practically out of the field of view. The issue of channel formation in the mushy zone deserves careful scrutiny and will be the focus of a future study.

Before closing this section it is worth clarifying that for the results presented in this paper the typical length of the dendrites is of the order of several hundred microns (similar to the cell thickness). At the same time, the width and the height of the cell (10 mm and 35 mm, respectively) are much larger than both the thickness of the cell and the size of the dendrites. This aids the two-dimensional growth of the concentration field. The reason a cell thickness of 1 mm was selected is related to the fact that the presence of buoyancy-driven convection was desirable. We wanted to demonstrate the effectiveness of the technique in the presence of convection. Earlier studies have focused on diffusion-dominated growth, and deliberately utilized very thin cells (about 50 μm thickness or less placed horizontally) to eliminate convection. In addition, the thickness of the cell was chosen with consideration to requirements in the optical path length to yield measurements with acceptable sensitivity. Qualitative comparisons between our results and the results of McCay and McCay (1993) who performed macroscopic measurements (12 mm cell thickness) for vertical growth, in the presence of natural convection showed good agreement.

4 Error Statement

The major contributions to the experimental error come from the temperature measurements and the refractive index equation (Eq. (1)). The error range of the type *K* miniature thermocouple employed in experiment was estimated by measuring the temperature of an ice–water mixture and was found to be 0.05°C. Special care was taken in carrying out the temperature measurements. The water and ice mixture was made by using distilled and degassed water. The mixture was placed within a well-insulated vessel and was stirred regularly to assure consistency and uniformity during the time that the experiments were performed. Note that the duration of each experiment was short (of the order of a few minutes), which made the heat interaction with the environment indeed negligible, in view of the above provisions.

To estimate the error associated with the refractive index, the values calculated from Eq. (1) were compared with data of Wolf et al. (1975–76), Raz et al. (1989), and Timmermans (1960). It was found that the maximum deviation was less than 0.05 percent. The error because of the wavelength difference between the Abbe refractometer measurements (sodium light source, λ = 589.3 nm) and the dendrite growth experiments (He-Ne laser, λ = 623.8 nm), was estimated to be less than 0.1 percent. The uncertainty in the value of initial concentration is less than 0.1 percent. The error in the cell thickness (optical path length) was assumed to be 0.1 percent. Taking these primary errors into account, the uncertainty in the reported solute concentration values was estimated to be less than 0.3 percent.

5 Conclusions

A real time microholography technique was presented for the determination of concentration fields in the vicinity of single,

or small groups of dendrites, in the presence of buoyancy-driven convection. The relationship between dendritic growth and the concentration field in the vicinity of the dendrites was demonstrated. It was also shown that the concentration distribution directly next to a group of sharp dendritic tips may be smoother (within a certain accuracy level) than the structure of the interface itself. The results also seem to support the explanation of Neilson and Incropera (1991) that instabilities of the concentration field near the liquidus are responsible for the formation of channels in the mushy zone, although detailed future experiments are needed to further underpin this claim. It is believed that the technique has very good potential for use in microscopic crystallization studies in the presence of flow that will aid the development of accurate macroscopic predictive models.

References

Beckermann, C., and Viskanta, R., 1988, "Double-Diffusive Convection During Dendritic Solidification of a Binary Mixture," *PhysicoChemical Hydrodynamics,* Vol. 10, pp. 195–213.

Bedarida, F., 1986, "Developments of Holographic Interferometry Applied to Crystal Growth From Solution," *Journal of Crystal Growth,* Vol. 79, pp. 43–49.

Bianchi, M. V. A., and Viskanta, R., 1994, "On the Morphology of Ice Crystals Grown From Ammonium Chloride Solutions," presented at the International Mechanical Engineering Congress and Exposition, Chicago, IL, Nov. 6–11.

Christenson, M. S., and Incropera, F. P., 1989a, "Experiments on Solidification of an Aqueous Sodium Carbonate Solution in a Horizontal Cylindrical Cavity," ASME JOURNAL OF HEAT TRANSFER, Vol. 111, pp. 998–1005.

Christenson, M. S., and Incropera, F. P., 1989b, "Solidification of an Aqueous Ammonium Chloride Solution in a Rectangular Cavity—I. Experimental Study," *International Journal of Heat and Mass Transfer,* Vol. 32, pp. 47–68.

Choi, J., and Viskanta, R., 1993, "Freezing of Aqueous Sodium Chloride Solution Saturated Packed Bed From a Vertical Wall of a Rectangular Cavity," *International Journal of Heat and Mass Transfer,* Vol. 36, pp. 2805–2813.

Coleman, H. W., and Steel, H. G., 1989, *Experimentation and Uncertainty Analysis for Engineers,* Wiley, New York.

Copley, S. M., Giamei, A. F., Johnson, S. M., and Hornbecker, M. F., 1970, "The Origin of Freckles in Unidirectionally Solidified Castings," *Metallurgical Transactions,* Vol. 1, pp. 2193–2204.

Dougherty, A., Kaplan, P. D., and Gollub, J. P., 1987, "Development of Side Branching in Dendritic Crystal Growth," *Physical Review Letters,* Vol. 58, pp. 1652–1655.

Kourosh, S., Diller, K. R., and Crawford, M. E., 1990, "Microscopic Study of Coupled Heat and Mass Transport During Unidirectional Solidification of Binary Solutions—II. Mass Transfer Analysis," *International Journal of Heat and Mass Transfer,* Vol. 33, pp. 39–53.

Magirl, C. S., and Incropera, F. P., 1993, "Flow and Morphological Conditions Associated With Unidirectional Solidification of Aqueous Ammonium Chloride," ASME JOURNAL OF HEAT TRANSFER, Vol. 115, pp. 1036–1043.

McCay, M. H., and McCay, T. D., 1993, "The Measurement of Transient Dendrite Tip Interface Supersaturation in NH_4Cl–H_2O Using Optical Techniques," *Journal of Crystal Growth,* Vol. 126, pp. 223–228.

Mullins, W. W., and Sekerka, R. F., 1964, "Stability of a Planar Interface During Solidification of a Dilute Binary Alloy," *J. Appl. Phys.,* Vol. 35, pp. 444–451.

Neilson, D. G., and Incropera, F. P., 1991, "Unidirectional Solidification of a Binary Alloy and the Effects of Induced Fluid Motion," *International Journal of Heat and Mass Transfer,* Vol. 34, pp. 1717–1732.

Prescott, P. J., and Incropera, F. P., 1994, "Convective Transport Phenomena and Macrosegregation During Solidification of a Binary Metal Alloy: I—Numerical Predictions," ASME JOURNAL OF HEAT TRANSFER, Vol. 116, pp. 735–741.

Prescott, P. J., Incropera, F. P., and Gaskell, D. R., 1994, "Convective Transport Phenomena and Macrosegregation During Solidification of a Binary Metal Alloy: II—Experiments and Comparisons With Numerical Predictions," ASME JOURNAL OF HEAT TRANSFER, Vol. 116, pp. 742–749.

Raz, E., Lipson, S. G., and Polturak, E., 1989, "Dendritic Growth of Ammonium Chloride Crystals: Measurements of the Concentration Field and a Proposed Nucleation Model for Growth," *Physical Review A,* Vol. 40, pp. 1088–1095.

Sample, A. K., and Hellawell, A., 1984, "The Mechanisms of Formation and Prevention of Channel Segregation During Alloy Solidification," *Metallurgical Transactions A,* Vol. 15, pp. 2163–2173.

Shigematsu, K., and Komatsu, H., 1991, "Growth of Ionic Crystals From Concentrated Aqueous Solutions—Hypothesis of Cation Dehydration and Insertion to Growing Interfaces," *Japanese Journal of Applied Physics,* Vol. 30, pp. 1779–1786.

Song, M., Choi, J., and Viskanta, R., 1993, "Upward Solidification of a Binary Solution Saturated Porous Medium," *International Journal of Heat and Mass Transfer,* Vol. 36, pp. 3687–3695.

Spatz, T. L., and Poulikakos, D., 1992, "A Two-Wavelength Holographic Interferometry Study on the Solidification of a Binary Alloy Around a Horizontal Pipe," ASME JOURNAL OF HEAT TRANSFER, Vol. 114, pp. 998–1010.

Sundarraj, S., and Voller, V. R., 1993, "The Binary Alloy Problem in an Expanding Domain: the Microsegregation Problem," *International Journal of Heat and Mass Transfer,* Vol. 36, pp. 713–723.

Tanaka, A., and Sano, M., 1992, "Measurement of the Kinetic Effect on the Concentration Field of a Growing Dendrite," *Journal of Crystal Growth,* Vol. 125, pp. 59–64.

Timmermans, J., 1960, *The Physicochemical Constants of Binary Systems,* Interscience, New York, p. 590.

Trivedi, R., 1985, "Theory of Dendritic Growth Under Rapid Solidification Conditions," *J. Crystal Growth,* Vol. 73, pp. 289–303.

Vest, C. M., 1979, *Holographic Interferometry,* 1st ed., Wiley, New York.

Viskanta, R., 1990, "Mathematical Modelling of Transport Processes During Solidification of Binary System," *JSME International Journal,* Series II, Vol. 33, pp. 409–423.

Yoo, H., and Viskanta, R., 1992, "Effect of Anisotropic Permeability on the Transport Process During Solidification of a Binary Mixture," *International Journal of Heat and Mass Transfer,* Vol. 35, pp. 2335–2346.

Wolf, A. V., Brown, M. G., and Prentiss, P. G., 1975–1976, "Concentrative Properties of Aqueous Solutions: Conversion Tables," *Handbook of Chemistry and Physics,* 56th ed., Weast, R. C., ed., pp. D-221–D-222.

An Analytical Method to Determine the Liquid Film Thickness Produced by Gas Atomized Sprays

J. Yang,[1,4] L. C. Chow,[2,4] and M. R. Pais[3,4]

Nomenclature

a = constant, s^{-1}
C = constant, $m^{-1}\ s^{-1}$
D = diameter of nozzle, m
h = film thickness, m
H = height of nozzle over surface, m
p = pressure, Pa
q = liquid volume flux, $m^3/m^2/s$
r = radius, m
Re = Reynolds number
u, w = radial and axial velocities, m/s
U = centerline velocity, m/s
z = axial coordinate, m
μ = dynamic viscosity, Pa.s
ν = kinematic viscosity, m^2/s
ρ = density, kg/m^3
τ = shear stress, Pa

Subscripts

D = diameter at nozzle exit
g = gas region
h = film thickness
l = liquid region
o = stagnation

Introduction

Currently, methods developed in the field of high-heat-flux thermal management invariably take advantage of the phase-

[1] Doctoral Student.
[2] Professor.
[3] Associate Research Professor.
[4] Department of Mechanical Engineering, University of Kentucky, Lexington, KY 40506.

Contributed by the Heat Transfer Division of THE AMERICAN SOCIETY OF MECHANICAL ENGINEERS. Manuscript received by the Heat Transfer Division October 1994; revision received July 1995. Keywords: Sprays/Droplets, Thin Film Flow. Associate Technical Editor: A. Faghri.

or small groups of dendrites, in the presence of buoyancy-driven convection. The relationship between dendritic growth and the concentration field in the vicinity of the dendrites was demonstrated. It was also shown that the concentration distribution directly next to a group of sharp dendritic tips may be smoother (within a certain accuracy level) than the structure of the interface itself. The results also seem to support the explanation of Neilson and Incropera (1991) that instabilities of the concentration field near the liquidus are responsible for the formation of channels in the mushy zone, although detailed future experiments are needed to further underpin this claim. It is believed that the technique has very good potential for use in microscopic crystallization studies in the presence of flow that will aid the development of accurate macroscopic predictive models.

References

Beckermann, C., and Viskanta, R., 1988, "Double-Diffusive Convection During Dendritic Solidification of a Binary Mixture," *PhysicoChemical Hydrodynamics,* Vol. 10, pp. 195–213.

Bedarida, F., 1986, "Developments of Holographic Interferometry Applied to Crystal Growth From Solution," *Journal of Crystal Growth,* Vol. 79, pp. 43–49.

Bianchi, M. V. A., and Viskanta, R., 1994, "On the Morphology of Ice Crystals Grown From Ammonium Chloride Solutions," presented at the International Mechanical Engineering Congress and Exposition, Chicago, IL, Nov. 6–11.

Christenson, M. S., and Incropera, F. P., 1989a, "Experiments on Solidification of an Aqueous Sodium Carbonate Solution in a Horizontal Cylindrical Cavity," ASME JOURNAL OF HEAT TRANSFER, Vol. 111, pp. 998–1005.

Christenson, M. S., and Incropera, F. P., 1989b, "Solidification of an Aqueous Ammonium Chloride Solution in a Rectangular Cavity—I. Experimental Study," *International Journal of Heat and Mass Transfer,* Vol. 32, pp. 47–68.

Choi, J., and Viskanta, R., 1993, "Freezing of Aqueous Sodium Chloride Solution Saturated Packed Bed From a Vertical Wall of a Rectangular Cavity," *International Journal of Heat and Mass Transfer,* Vol. 36, pp. 2805–2813.

Coleman, H. W., and Steel, H. G., 1989, *Experimentation and Uncertainty Analysis for Engineers,* Wiley, New York.

Copley, S. M., Giamei, A. F., Johnson, S. M., and Hornbecker, M. F., 1970, "The Origin of Freckles in Unidirectionally Solidified Castings," *Metallurgical Transactions,* Vol. 1, pp. 2193–2204.

Dougherty, A., Kaplan, P. D., and Gollub, J. P., 1987, "Development of Side Branching in Dendritic Crystal Growth," *Physical Review Letters,* Vol. 58, pp. 1652–1655.

Kourosh, S., Diller, K. R., and Crawford, M. E., 1990, "Microscopic Study of Coupled Heat and Mass Transport During Unidirectional Solidification of Binary Solutions—II. Mass Transfer Analysis," *International Journal of Heat and Mass Transfer,* Vol. 33, pp. 39–53.

Magirl, C. S., and Incropera, F. P., 1993, "Flow and Morphological Conditions Associated With Unidirectional Solidification of Aqueous Ammonium Chloride," ASME JOURNAL OF HEAT TRANSFER, Vol. 115, pp. 1036–1043.

McCay, M. H., and McCay, T. D., 1993, "The Measurement of Transient Dendrite Tip Interface Supersaturation in NH_4Cl–H_2O Using Optical Techniques," *Journal of Crystal Growth,* Vol. 126, pp. 223–228.

Mullins, W. W., and Sekerka, R. F., 1964, "Stability of a Planar Interface During Solidification of a Dilute Binary Alloy," *J. Appl. Phys.,* Vol. 35, pp. 444–451.

Neilson, D. G., and Incropera, F. P., 1991, "Unidirectional Solidification of a Binary Alloy and the Effects of Induced Fluid Motion," *International Journal of Heat and Mass Transfer,* Vol. 34, pp. 1717–1732.

Prescott, P. J., and Incropera, F. P., 1994, "Convective Transport Phenomena and Macrosegregation During Solidification of a Binary Metal Alloy: I—Numerical Predictions," ASME JOURNAL OF HEAT TRANSFER, Vol. 116, pp. 735–741.

Prescott, P. J., Incropera, F. P., and Gaskell, D. R., 1994, "Convective Transport Phenomena and Macrosegregation During Solidification of a Binary Metal Alloy: II—Experiments and Comparisons With Numerical Predictions," ASME JOURNAL OF HEAT TRANSFER, Vol. 116, pp. 742–749.

Raz, E., Lipson, S. G., and Polturak, E., 1989, "Dendritic Growth of Ammonium Chloride Crystals: Measurements of the Concentration Field and a Proposed Nucleation Model for Growth," *Physical Review A,* Vol. 40, pp. 1088–1095.

Sample, A. K., and Hellawell, A., 1984, "The Mechanisms of Formation and Prevention of Channel Segregation During Alloy Solidification," *Metallurgical Transactions A,* Vol. 15, pp. 2163–2173.

Shigematsu, K., and Komatsu, H., 1991, "Growth of Ionic Crystals From Concentrated Aqueous Solutions—Hypothesis of Cation Dehydration and Insertion to Growing Interfaces," *Japanese Journal of Applied Physics,* Vol. 30, pp. 1779–1786.

Song, M., Choi, J., and Viskanta, R., 1993, "Upward Solidification of a Binary Solution Saturated Porous Medium," *International Journal of Heat and Mass Transfer,* Vol. 36, pp. 3687–3695.

Spatz, T. L., and Poulikakos, D., 1992, "A Two-Wavelength Holographic Interferometry Study on the Solidification of a Binary Alloy Around a Horizontal Pipe," ASME JOURNAL OF HEAT TRANSFER, Vol. 114, pp. 998–1010.

Sundarraj, S., and Voller, V. R., 1993, "The Binary Alloy Problem in an Expanding Domain: the Microsegregation Problem," *International Journal of Heat and Mass Transfer,* Vol. 36, pp. 713–723.

Tanaka, A., and Sano, M., 1992, "Measurement of the Kinetic Effect on the Concentration Field of a Growing Dendrite," *Journal of Crystal Growth,* Vol. 125, pp. 59–64.

Timmermans, J., 1960, *The Physicochemical Constants of Binary Systems,* Interscience, New York, p. 590.

Trivedi, R., 1985, "Theory of Dendritic Growth Under Rapid Solidification Conditions," *J. Crystal Growth,* Vol. 73, pp. 289–303.

Vest, C. M., 1979, *Holographic Interferometry,* 1st ed., Wiley, New York.

Viskanta, R., 1990, "Mathematical Modelling of Transport Processes During Solidification of Binary System," *JSME International Journal,* Series II, Vol. 33, pp. 409–423.

Yoo, H., and Viskanta, R., 1992, "Effect of Anisotropic Permeability on the Transport Process During Solidification of a Binary Mixture," *International Journal of Heat and Mass Transfer,* Vol. 35, pp. 2335–2346.

Wolf, A. V., Brown, M. G., and Prentiss, P. G., 1975–1976, "Concentrative Properties of Aqueous Solutions: Conversion Tables," *Handbook of Chemistry and Physics,* 56th ed., Weast, R. C., ed., pp. D-221–D-222.

An Analytical Method to Determine the Liquid Film Thickness Produced by Gas Atomized Sprays

J. Yang,[1,4] L. C. Chow,[2,4] and M. R. Pais[3,4]

Nomenclature

a = constant, s^{-1}
C = constant, $m^{-1}\ s^{-1}$
D = diameter of nozzle, m
h = film thickness, m
H = height of nozzle over surface, m
p = pressure, Pa
q = liquid volume flux, $m^3/m^2/s$
r = radius, m
Re = Reynolds number
u, w = radial and axial velocities, m/s
U = centerline velocity, m/s
z = axial coordinate, m
μ = dynamic viscosity, Pa.s
ν = kinematic viscosity, m^2/s
ρ = density, kg/m^3
τ = shear stress, Pa

Subscripts

D = diameter at nozzle exit
g = gas region
h = film thickness
l = liquid region
o = stagnation

Introduction

Currently, methods developed in the field of high-heat-flux thermal management invariably take advantage of the phase-

[1] Doctoral Student.
[2] Professor.
[3] Associate Research Professor.
[4] Department of Mechanical Engineering, University of Kentucky, Lexington, KY 40506.

Contributed by the Heat Transfer Division of THE AMERICAN SOCIETY OF MECHANICAL ENGINEERS. Manuscript received by the Heat Transfer Division October 1994; revision received July 1995. Keywords: Sprays/Droplets, Thin Film Flow. Associate Technical Editor: A. Faghri.

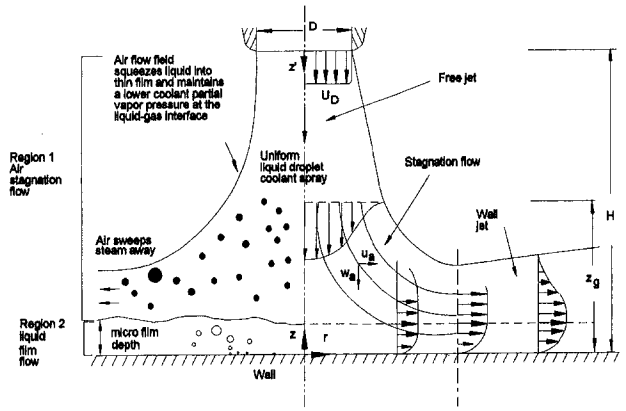

Fig. 1 Secondary gas assisted spray cooling flow field

change properties of coolants to remove heat. This is because the heat removal capability through latent heat can be an order of magnitude or more than the sensible heat removal capability. In addition, the superheat of the surface above that of the liquid is considerably reduced for cooling with phase change as opposed to single-phase cooling for the same heat flux. Examples of phase-change cooling are spray cooling (Chow et al., 1989; Sehmbey et al., 1992; Pais et al., 1989), jet impingement cooling (Katto and Yokoya, 1988; Pais et al., 1993), flow boiling (Galloway and Mudawar, 1993), etc.

The ability of spray cooling to enhance heat transfer rates greatly with temperature mitigation is largely attributed to the thermophysical phenomena occurring within the thin film of liquid deposited on the surface (Yang, 1993; Mesler et al., 1993). In gas atomized spray impingement the drops having a relatively higher inertia deviate from the air streamlines to strike directly against the hot surface. A drop on impinging the surface forms a flat disk, whose thickness can be much lower than the diameter of the drop (Chandra and Avedisian, 1991). Simultaneously, the gas stagnation flow field spreads the droplets/disks further, through shear and the pressure subjected on the film, to form a thin film on the surface.

A number of studies exist that present the effect of surface material properties (Sehmbey et al., 1992), roughness (Pais et al., 1992), droplet size and velocity (Tilton, 1989; Yang, 1993), degree of superheat and mass flow rate of both the coolant and the secondary atomizing gas (Yang, 1993) on spray cooling. A very thin liquid film assists in enhancing heat transfer by conduction through the liquid and evaporation at the surface. Second, it assists in the early bubble departure through droplet–bubble impact. Third, secondary nucleation sites generated by the spray are within the vicinity of the hot surface, enhancing heat transfer through bubble growth at these sites (Mesler et al., 1993). Techniques to measure liquid film thickness have been developed (Yang et al., 1992a; Yang, 1993) but these are complex and equipment intensive. Methods for predicting liquid film thickness in spray impingement based on knowledge of the flow field do not exist. Hence, this endeavor presents an analytical method to determine the thickness of a liquid film deposited on a flat surface by a spray under the influence of a secondary gas stagnation flow field.

Simplified Theory

The flow pattern in spray cooling shown in Fig. 1 can be simplified and considered as a two-layer model. The top layer is assumed to be one of an air stagnation flow field created by an axisymmetric jet impinging normally on a flat plate. At the top of the bottom layer, a uniform spray is impinging on the liquid film with the liquid flowing radially outward. Droplet size, velocity, and number distributions obtained using a noninvasive phase-Doppler laser technique (Yang, 1993; Tilton, 1989) indicate that in the region of interest within the flow field the distribution is approximately flat. The liquid film flow is assumed to be driven by the superjacent gas stagnation flow. Any prior droplet momentum is expended within the film and the mechanics of droplet impingement are assumed not to affect the overall liquid film flow significantly. Even though the droplet velocities are high (Yang, 1993), the average film velocity is low, with $\mathrm{Re}_h < 1$. This very low value for the Reynolds number along with the thin liquid film (approximately two to three times the diameter of the droplets) and the shear of the external air stagnation flow damps out the energy of the drops. Hence, turbulence will exist within the film only momentarily, at the instant and in the region of droplet impingement (Schlichting, 1980). It should be noted that the liquid flow rate is extremely low at 1 liter/hr/cm^2. The flow patterns of these two layers are analyzed as follows.

Top Layer: Air Stagnation Flow

The flow pattern of a normally impinging axisymmetric jet can be subdivided into three characteristic regions: the free jet region, the stagnation flow region, and the region of radial flow outside the stagnation zone, also called the wall-jet region. The velocity field of the impinging jet is shown schematically in Fig. 1. The air stream on exiting the nozzle has a nearly rectangular velocity profile. As the air jet traverses the external ambient (the air jet is really submerged in an external air ambient) its boundary spreads and widens by an intensive exchange of momentum with the quiescent air surroundings. For sufficient length of the free jet (approximately the length for which the centerline pressure head has fallen to 95 percent of its maximum value), the velocity distribution approaches a bell shape, which can be described approximately by a Gaussian distribution (Martin, 1977). The effects of the stagnation flow are experienced in the near vicinity of the surface, the limiting distance being z_g (1.2 times the nozzle diameter in the axial direction) (Martin, 1977). In this region, the vertical velocity component is decelerated and transformed into an accelerated horizontal one. Analytical solutions for the idealized limiting case of the infinitely extended axisymmetric laminar stagnation flow are provided by White (1974) and Schlichting (1980). It is a typical boundary layer flow, the influence of viscosity being restricted to a thin layer near the interface. The pressure distribution of the flow field can be written as (Schlichting, 1980):

$$p_g = p_0 - \tfrac{1}{2}\rho_g a^2 (r^2 + f(z)) \tag{1}$$

The velocity components of stagnation flow outside this boundary layer are given by (Martin, 1977)

$$u = arF'(\eta); \quad w = -2az;$$

$$a \approx \left(\frac{U_D}{D}\right)\left(1.04 - 0.034\,\frac{H}{D}\right); \quad \eta = z\sqrt{\frac{a}{\nu_g}} \tag{2}$$

Here, Martin (1977) determined that for an axisymmetric nozzle the value of a can be approximated in terms of H and U_D; see Fig. 1. Here a is a constant, i.e., the velocity components are linearly proportional to the distance from the stagnation point. Due to the finite diameter of the jet and the exchange of momentum with its quiescent air ambient the air jet spreads out, taking up an approximately conical profile; see Fig. 1. On impingement with the surface the free jet decelerates into a stagnation flow, which transforms into an accelerated wall jet flow. In this experiment because the heater size was small (10 mm × 10 mm), it only came under the influence of the cone of the jet, i.e., the wall jet was beyond the outer edge of the

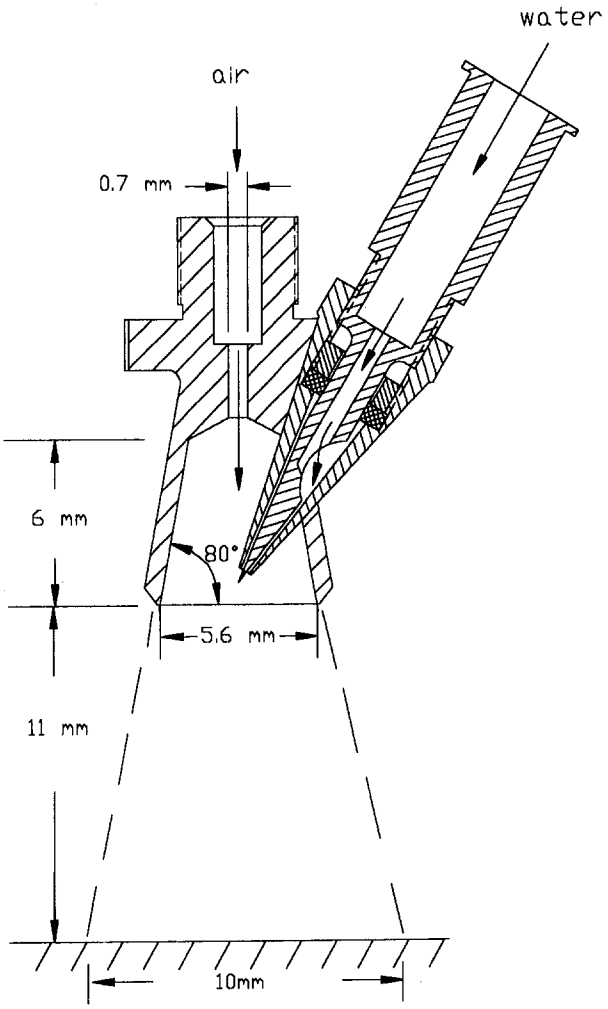

Fig. 2 Nozzle design

heater surface. Hence, only the stagnation flow region is considered in this analysis.

Bottom Layer: Liquid Film Flow

At the liquid–air interface the shear is given by, i.e.,

$$\tau = \mu_l \left.\frac{\partial u}{\partial z}\right|_l = \mu_g \left.\frac{\partial u}{\partial z}\right|_g \tag{3}$$

The velocity of the liquid film is negligible compared to that of the air at the liquid–air interface. Hence, the shear stress exerted by the air stagnation on the liquid film can be approximated by the shear stress imposed by the air on a stationary solid surface, i.e., using Eq. (2) in Eq. (3),

$$\left.\frac{\partial u}{\partial z}\right|_l = 1.312 \sqrt{\frac{a^3 \mu_g \rho_g}{\mu_l^2}}\, r = Cr;$$

$$F''(0) = 1.312 \text{ (White, 1974)} \tag{4}$$

Because the liquid film is very thin, the pressure variation in the normal direction will be negligible. The pressure distribution in the liquid film is impressed by the superjacent air stagnation flow field and depends only on r (Yang, 1993), i.e.,

$$p_l = p_l(r) \tag{5}$$

with boundary conditions:

$$u_l = w_l = 0 \quad \text{at} \quad z = 0 \tag{6}$$

and interface conditions:

$$\frac{\partial u_l}{\partial z} = Cr; \quad p_l = p_g \quad \text{at} \quad z = h(r) \tag{7}$$

Here, $h(r)$ is the local liquid film thickness or depth. Yang et al. (1992a), using a Fresnel diffraction technique, determined that the depth of the liquid film is of the order of 140 μm and flows at a low velocity such that $\mathrm{Re}_h < 1$. Hence, the inertia forces can be neglected with respect to the viscous forces, and the momentum equation is

$$0 = -\frac{\partial p_l}{\partial r} + \mu_l \frac{\partial^2 u_l}{\partial z^2} \tag{8}$$

By integrating Eq. (8) twice and applying these boundary and interface conditions, the velocity can be written as

$$u_l = \frac{\rho_g}{\mu_l} r a^2 z\left(h - \frac{z}{2}\right) + Crz \tag{9}$$

Referring to Fig. 1, it is assumed that liquid is uniformly supplied over the whole heater surface at a constant volume flux q. Droplet size, velocity, and number distributions obtained using a noninvasive phase-Doppler laser technique (Yang, 1993; Tilton, 1989) indicate that in the region of interest within the flow field, the distribution is approximately flat. Applying the continuity condition within the thin film we get

$$2\pi r \int_0^{h(r)} u_l dz = \pi r^2 q \tag{10}$$

Substituting Eq. (9) into Eq. (10), the liquid film thickness h is expressed in the form

$$q = \frac{2}{3}\frac{\rho_g}{\mu_l} a^2 h^3 + 1.312 \sqrt{\frac{a^3 \mu_g \rho_g}{\mu_l^2}}\, h^2 \tag{11}$$

It is noted from this equation that h is not a function of r.

Experimental Results and Discussion

The thickness and topography of a liquid film deposited on a surface by a droplet spray were measured using Fresnel diffraction and holographic methods by Yang et al. (1992a). Experiments using a holographic technique (Yang et al., 1992a) indicate that the liquid film produced by an air atomizing nozzle is superficially very flat and that the change in flatness is less than 1 μm. Here, the term flatness is associated with the topography of the top of the liquid film. Equation (11) confirms that indeed the liquid film thickness h remains constant, i.e., it does not depend on the radial coordinate r.

For any particular type of nozzle, the constant a can be determined from experiment. However, using Eq. (2), Fig. 2, and

Table 1 Comparison of film thickness measurement and prediction

Air pressure p_g, flow rate (Pais et al., 1989), kPa, m^3/h	Liquid volume flux q, liter/h/cm^2	Numerical h, Eq. (11), μm	Experimental h (Yang et al., 1992a), μm $\pm$ 15 μm
240, 0.584	1	91	85
240, 0.584	2	123	137

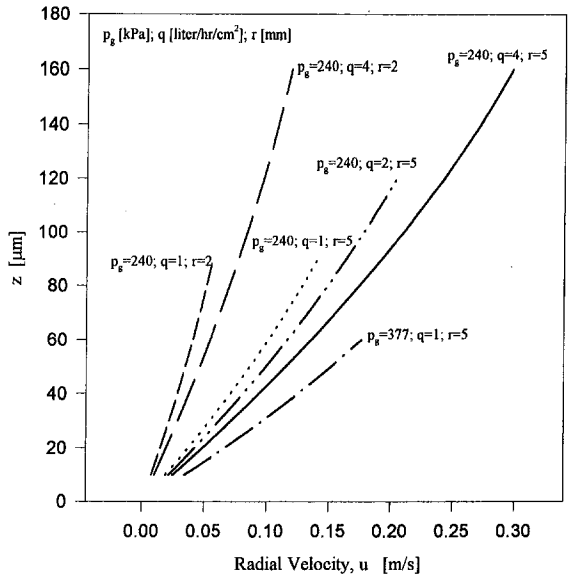

Fig. 3 Variation of velocity distribution with radial position, gas and liquid flow rate

data from Table 1, an approximate value of the constant a can be calculated to be about 1151 and 1754 s^{-1} at $p_g = 240$ and 377 kPa, respectively. Table 1 provides a comparison of the experimentally determined film thicknesses and those calculated using Eq. (11). The uncertainty in the liquid film thickness or depth (Fresnel diffraction technique, Yang, 1992a) from experimental measurements is ± 15 μm.

Based on this constant a, velocity distributions $u_l(z)$ (Eq. (9)) in the liquid film and the film thickness h (Eq. (11)) can be calculated. Figure 3 illustrates the film thickness and velocity distribution as a function of volume flux q, air pressure p_g, and radial position r. It is noted that as the liquid flows downstream (from $r = 2$ mm to $r = 5$ mm) the film velocity increases significantly, but the absolute value is still very low compared to the velocity of the drop (30 m/s, Yang et al., 1992b). It is also evident that when the air pressure increases, the liquid velocity increases and the film thickness decreases. If the liquid flow rate increases both the liquid velocity and the liquid film thickness increase. Note that the maximum value of z gives the film thickness h.

Conclusion

An analytical method for calculating the film thickness and velocity distribution within a liquid film deposited on a surface by gas-atomized droplet impingement is presented. The analysis assumes that the external pressure due to the secondary gas atomizing flow is superimposed on the film. The analysis results in a simple relation for film thickness based on easily measured flow field parameters. Good agreement is noted when the model is compared with experimental results.

Acknowledgments

This work was funded by the Aero Propulsion and Power Directorate, Wright Laboratory, Wright-Patterson Air Force Base, Ohio.

References

Chow, L. C., Tilton, D. E., and Pais, M. R., 1989, "High Power Density Spray Cooling," WRDC-TR-89-2082, Wright Laboratory, OH.

Chandra, S., and Avedisian, C. T., 1991, "On the Collision of a Droplet With a Solid Surface," *Proc. R. Soc. Lond.*, pp. 15–41.

Galloway, J. E., and Mudawar, I., 1993, "CHF Mechanism in Flow Boiling From a Short Heated Wall—II; Theoretical CHF Model," *Int. J. Heat Mass Transfer*, Vol. 36, No. 10, pp. 2527–2540.

Katto, Y., and Yokoya, S., 1988, "Critical Heat Flux on a Disk Heater Cooled by a Circular Jet of Saturated Liquid Impinging at the Center," *Int. J. Heat Mass Transfer*, Vol. 31, No. 2, pp. 219–227.

Martin, H., 1977, "Heat and Mass Transfer Between Impinging Gas Jets and Solid Surfaces," *Advances in Heat Transfer*, Vol. 13, pp. 1–60.

Mesler, R., Pais, M. R., Chow, L. C., and Mahefkey, E. T., 1993, "Discussions on Surface Roughness and Its Effects on the Heat Transfer Mechanism in Spray Cooling," ASME JOURNAL OF HEAT TRANSFER, Vol. 115, pp. 1083–1085.

Pais, M. R., Tilton, D. E., Chow, L. C., and Mahefkey, E. T., 1989, "High Heat Flux, Low Superheat Evaporative Spray Cooling," Paper No. AIAA-89-0241.

Pais, M. R., Chow, L. C., and Mahefkey, E. T., 1992, "Surface Roughness and Its Effect on the Heat Transfer Mechanism in Spray Cooling," ASME JOURNAL OF HEAT TRANSFER, Vol. 114, pp. 211–219.

Pais, M. R., Chow, L. C., and Mahefkey, E. T., 1993, "Multiple Jet Impingement Cooling," *J. Thermophysics Heat Transfer*, Vol. 7, No. 3, pp. 435–440.

Schlichting, H., 1980, *Boundary Layer Theory*, Chaps. 2 & 5, 6th ed., McGraw-Hill, New York.

Sehmbey, M. S., Pais, M. R., and Chow, L. C.; 1992, "Effect of Surface Material Properties and Surface Characteristics in Evaporative Spray Cooling," *J. Thermophysics Heat Transfer*, Vol. 6, No. 3, pp. 505–512.

Tilton, D. E., 1989, "Spray Cooling," PhD Dissertation, University of Kentucky, Lexington, KY.

White, F. M., 1974, *Viscous Fluid Flow*, Chap. 3, McGraw-Hill.

Yang, J., Chow, L. C., and Pais, M. R., 1992a, "Liquid Film Thickness and Topography Determination Using Fresnel Diffraction and Holography," *Experimental Heat Transfer*, Vol. 5, pp. 239–252.

Yang, J., Pais, M. R., and Chow, L. C., 1992b, "High Heat Flux Spray Cooling," *Proceedings of the SPIE*, Invited Paper, High Heat Flux Engineering, SPIE Vol. 1739, San Diego, CA, pp. 29–40.

Yang, J., 1993, "Spray Cooling With an Air Atomizing Nozzle," PhD Dissertation, Dept. of Mechanical Engineering, University of Kentucky, Lexington, KY.

Modeling of the Transient Heat Transfer Across a Heat Transfer Tube in a Bubbling Fluidized Bed

A. I. Karamavruç,[1] N. N. Clark,[1] and G. Ganser[2]

Nomenclature

c = thermal heat capacity, J/kg · K
k = conductivity of the tube material, W/mK
n = integer summation index
r, r_p = radial coordinate, m; radius of the interface location between zones **A** and **B**, m
T, T_W, T_B = temperature, K; measured outside tube wall temperature, K; temperature in zone **B**, K
T_{1D}, T_{2D} = temperature in 1*D*, temperature in 2*D*, K
t^* = dimensionless time
t = time, s
U_f, U_{mf} = fluidization velocity, m/s; minimum fluidization velocity, m/s
x^* = dimensionless coordinates in x direction
x = Cartesian coordinate locally in radial direction, m
α = thermal diffusivity, m^2/s

[1] Department of Mechanical and Aerospace Engineering, West Virginia University, Morgantown, WV 26506-6106.

[2] Department of Mathematics, West Virginia University, Morgantown, WV 26506-6310.

Contributed by the Heat Transfer Division of THE AMERICAN SOCIETY OF MECHANICAL ENGINEERS. Manuscript received by the Heat Transfer Division April 1995; revision received October 1995. Keywords: Conduction, Heat Exchangers, Transient and Unsteady Heat Transfer. Associate Technical Editor: R. Viskanta.

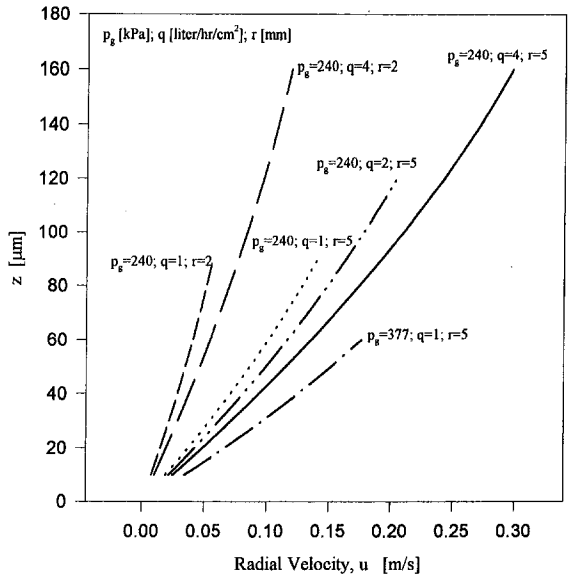

Fig. 3 Variation of velocity distribution with radial position, gas and liquid flow rate

data from Table 1, an approximate value of the constant a can be calculated to be about 1151 and 1754 s^{-1} at $p_g = 240$ and 377 kPa, respectively. Table 1 provides a comparison of the experimentally determined film thicknesses and those calculated using Eq. (11). The uncertainty in the liquid film thickness or depth (Fresnel diffraction technique, Yang, 1992a) from experimental measurements is ± 15 μm.

Based on this constant a, velocity distributions $u_l(z)$ (Eq. (9)) in the liquid film and the film thickness h (Eq. (11)) can be calculated. Figure 3 illustrates the film thickness and velocity distribution as a function of volume flux q, air pressure p_g, and radial position r. It is noted that as the liquid flows downstream (from $r = 2$ mm to $r = 5$ mm) the film velocity increases significantly, but the absolute value is still very low compared to the velocity of the drop (30 m/s, Yang et al., 1992b). It is also evident that when the air pressure increases, the liquid velocity increases and the film thickness decreases. If the liquid flow rate increases both the liquid velocity and the liquid film thickness increase. Note that the maximum value of z gives the film thickness h.

Conclusion

An analytical method for calculating the film thickness and velocity distribution within a liquid film deposited on a surface by gas-atomized droplet impingement is presented. The analysis assumes that the external pressure due to the secondary gas atomizing flow is superimposed on the film. The analysis results in a simple relation for film thickness based on easily measured flow field parameters. Good agreement is noted when the model is compared with experimental results.

Acknowledgments

This work was funded by the Aero Propulsion and Power Directorate, Wright Laboratory, Wright-Patterson Air Force Base, Ohio.

References

Chow, L. C., Tilton, D. E., and Pais, M. R., 1989, "High Power Density Spray Cooling," WRDC-TR-89-2082, Wright Laboratory, OH.

Chandra, S., and Avedisian, C. T., 1991, "On the Collision of a Droplet With a Solid Surface," *Proc. R. Soc. Lond.*, pp. 15--41.

Galloway, J. E., and Mudawar, I., 1993, "CHF Mechanism in Flow Boiling From a Short Heated Wall—II; Theoretical CHF Model," *Int. J. Heat Mass Transfer*, Vol. 36, No. 10, pp. 2527–2540.

Katto, Y., and Yokoya, S., 1988, "Critical Heat Flux on a Disk Heater Cooled by a Circular Jet of Saturated Liquid Impinging at the Center," *Int. J. Heat Mass Transfer*, Vol. 31, No. 2, pp. 219–227.

Martin, H., 1977, "Heat and Mass Transfer Between Impinging Gas Jets and Solid Surfaces," *Advances in Heat Transfer*, Vol. 13, pp. 1–60.

Mesler, R., Pais, M. R., Chow, L. C., and Mahefkey, E. T., 1993, "Discussions on Surface Roughness and Its Effects on the Heat Transfer Mechanism in Spray Cooling," ASME JOURNAL OF HEAT TRANSFER, Vol. 115, pp. 1083–1085.

Pais, M. R., Tilton, D. E., Chow, L. C., and Mahefkey, E. T., 1989, "High Heat Flux, Low Superheat Evaporative Spray Cooling," Paper No. AIAA-89-0241.

Pais, M. R., Chow, L. C., and Mahefkey, E. T., 1992, "Surface Roughness and Its Effect on the Heat Transfer Mechanism in Spray Cooling," ASME JOURNAL OF HEAT TRANSFER, Vol. 114, pp. 211–219.

Pais, M. R., Chow, L. C., and Mahefkey, E. T., 1993, "Multiple Jet Impingement Cooling," *J. Thermophysics Heat Transfer*, Vol. 7, No. 3, pp. 435–440.

Schlichting, H., 1980, *Boundary Layer Theory*, Chaps. 2 & 5, 6th ed., McGraw-Hill, New York.

Sehmbey, M. S., Pais, M. R., and Chow, L. C.; 1992, "Effect of Surface Material Properties and Surface Characteristics in Evaporative Spray Cooling," *J. Thermophysics Heat Transfer*, Vol. 6, No. 3, pp. 505–512.

Tilton, D. E., 1989, "Spray Cooling," PhD Dissertation, University of Kentucky, Lexington, KY.

White, F. M., 1974, *Viscous Fluid Flow*, Chap. 3, McGraw-Hill.

Yang, J., Chow, L. C., and Pais, M. R., 1992a, "Liquid Film Thickness and Topography Determination Using Fresnel Diffraction and Holography," *Experimental Heat Transfer*, Vol. 5, pp. 239–252.

Yang, J., Pais, M. R., and Chow, L. C., 1992b, "High Heat Flux Spray Cooling," *Proceedings of the SPIE*, Invited Paper, High Heat Flux Engineering, SPIE Vol. 1739, San Diego, CA, pp. 29–40.

Yang, J., 1993, "Spray Cooling With an Air Atomizing Nozzle," PhD Dissertation, Dept. of Mechanical Engineering, University of Kentucky, Lexington, KY.

Modeling of the Transient Heat Transfer Across a Heat Transfer Tube in a Bubbling Fluidized Bed

A. I. Karamavruç,[1] N. N. Clark,[1] and G. Ganser[2]

Nomenclature

c = thermal heat capacity, J/kg · K
k = conductivity of the tube material, W/mK
n = integer summation index
r, r_p = radial coordinate, m; radius of the interface location between zones **A** and **B**, m
T, T_W, T_B = temperature, K; measured outside tube wall temperature, K; temperature in zone **B**, K
T_{1D}, T_{2D} = temperature in 1*D*, temperature in 2*D*, K
t^* = dimensionless time
t = time, s
U_f, U_{mf} = fluidization velocity, m/s; minimum fluidization velocity, m/s
x^* = dimensionless coordinates in x direction
x = Cartesian coordinate locally in radial direction, m
α = thermal diffusivity, m^2/s

[1] Department of Mechanical and Aerospace Engineering, West Virginia University, Morgantown, WV 26506-6106.

[2] Department of Mathematics, West Virginia University, Morgantown, WV 26506-6310.

Contributed by the Heat Transfer Division of THE AMERICAN SOCIETY OF MECHANICAL ENGINEERS. Manuscript received by the Heat Transfer Division April 1995; revision received October 1995. Keywords: Conduction, Heat Exchangers, Transient and Unsteady Heat Transfer. Associate Technical Editor: R. Viskanta.

η = dimensionless coordinate in radial direction
θ, θ' = circumferential coordinate, rad; dummy variable in circumferential integration, rad
ξ = dimensionless coordinate in circumferential direction
ρ = density, kg/m^3
τ = dummy variable

Introduction

Heat transfer studies involving time-dependent boundary conditions are relevant to a wide range of engineering applications. Unfortunately, the derivations of analytical solutions for many complicated heat transfer phenomena prove intractable so that numerical solutions must be used. However, some difficult transient conduction problems can be tackled by making some rational simplifying assumptions. This paper is concerned with transient heat transfer through the wall of a tube immersed in a fluid bed. The study arose from the need to interpret data from an experimental tube instrumented on the surface with local, fast responding thermocouples (Mancuso and Diller, 1991; Rosiczkowsky and Hollworth, 1991). Recent related studies include those of George (1993), Rottger and Renz (1994), Katoh et al. (1991), and Karamavruç et al. (1994a) that were used to relate transient heat transfer to bed hydrodynamics.

A horizontal heat transfer tube, with inside and outside radii of 1.27 and 2.54 cm, was placed in a cold bubbling fluidized bed and heated internally by a flow of boiling water. The temperature data at the outside tube wall were measured by installing fast responding thermocouples around the heat transfer tube. The thermocouples were installed on only one side of the heat transfer tube with a separation of $\pi/4$, namely at $\theta = 0$, $\pi/4$, $\pi/2$, $3\pi/4$, and π, with $\theta = 0$ at the top. A detailed description of the experimental setup and instrumentation has been given by McKain et al. (1993), Sunderesan (1994), and Sunderesan and Clark (1995). These authors have both discussed the relationship between heat transfer and bed hydrodynamics, and have provided error analysis for the thermocouple signals.

Temperature Curves Within the Heat Transfer Tube Wall

Temperature data on the surface of the heat transfer tube were measured by using sand particles with an average size of 0.483 mm as fluidization material. The particles were fluidized at a velocity of 0.15 m/s, which was 1.18 times the minimum velocity and was lightly bubbling. The inside of the tube and the bed temperatures were approximately 373 K and 308 K, respectively.

Using these data, the transient two-dimensional heat conduction equation was solved in radial coordinates via the numerical approach (Karamavruç et al., 1994a). Figure 1 shows the temperature curves within the tube wall located $\theta = \pi/2$ between 13.9 s and 14.16 s. Each curve was plotted with a time interval of $\Delta t = (\frac{1}{120})$ s. Figure 1 indicates two different zones within the tube wall with respect to temperature fluctuations, namely zone **A** where the temperature curves do not change appreciably (steady state zone), and zone **B** where the temperature curves change with time (unsteady state zone). Zone **B** was enlarged, in Fig. 1, to show the transient temperature curves near the outside tube wall. The observations of several data runs evaluated for a long period of time (Karamavruç and Clark, 1995) have also showed a similar two-zone model of heat transfer behavior within the wall of the horizontal heat transfer tube immersed in the bubbling fluidized bed.

Modeling of the Heat Transfer in the Tube

According to the observations of heat conduction within the heat transfer tube wall, as was shown in Fig. 1, the tube wall

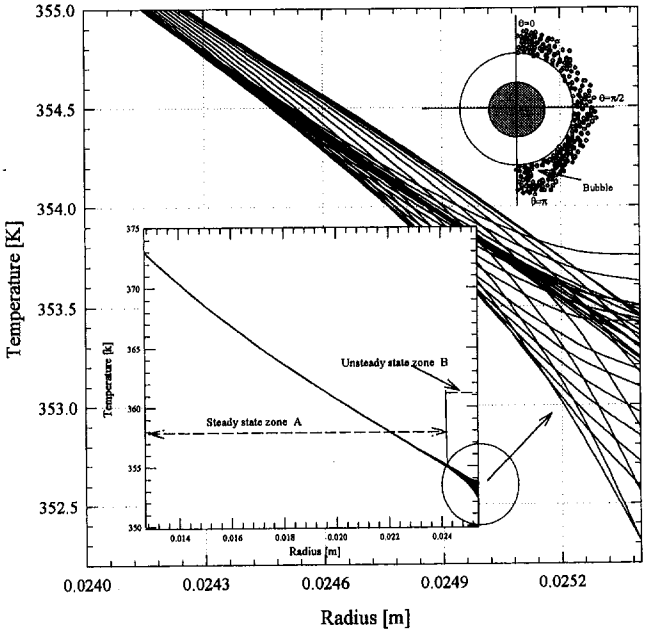

Fig. 1 Temperature curves across the tube wall between 13.9 s and 14.6 s at every 1/120 s (fluidization material = sand particles, particle size ≅ 0.483 mm, $U^* = U_f/U_{mf} = 1.18$, $U_{mf} = 0.15$ m/s, $T_f = 373$ K, $T_b = 308$ K)

can be divided into the two zones: The temperature distributions are steady in zone **A**, but unsteady in zone **B** (this zone is also called penetration depth). Further simplifications in zone **B** are possible as shown below.

Order of Magnitude Analysis for the Boundary Zone Near to Surface

Expressing the equations in dimensionless form provides a basis for making rational simplifications. The general two-dimensional unsteady heat conduction equation in cylindrical coordinates for zone **B** can be written as

$$\rho c \frac{\partial T_B}{\partial t} = k\left(\frac{\partial^2 T_B}{\partial r^2} + \frac{1}{r}\frac{\partial T_B}{\partial r} + \frac{1}{r^2}\frac{\partial^2 T_B}{\partial \theta^2}\right) \tag{1}$$

The subscript **B** refers to zone **B**. Equation (1) can be nondimensionalized by using the following dimensionless variables:

$$T^* = \frac{T_B - T_p}{\langle T_W(r_o, \theta, t)\rangle - T_p}; \quad \eta = \frac{r - r_p}{\Gamma};$$
$$\xi = \frac{\theta}{\theta_o}; \quad t^* = \frac{\alpha t}{\Gamma^2}; \quad \Gamma \le r \tag{2}$$

where η and ξ are the dimensionless coordinates. Γ (the thickness of zone **B**) is the reference length in the radial direction and θ_o is the reference angle ($\theta_o = 180$ deg) in the circumferential direction. T_p is the temperature at location r_p, and $\langle T_W(r_o, \theta, t)\rangle$ is the average temperature at the outside of the tube wall. The subscript p refers to the interface location between zones **A** and **B** and the subscript o refers to the outside boundary of the heat transfer tube. By substituting the dimensionless quantities into Eq. (1), the heat conduction equation becomes

$$\frac{\partial T^*}{\partial t^*} = \frac{\partial^2 T^*}{\partial \eta^2} + \frac{1}{\left(\frac{r_p}{\Gamma} + \eta\right)}\frac{\partial T^*}{\partial \eta}$$
$$+ \frac{1}{\left(\frac{r_p^2}{\Gamma^2} + \frac{2r_p\eta}{\Gamma} + \eta^2\right)\theta_o^2}\left[\frac{\partial^2 T^*}{\partial \xi^2}\right] \tag{3}$$

Due to the small thickness of zone **B**, Γ, compared with the circumference of the tube $r_o\theta_o$, the third term on the right-hand side of Eq. (3) can be neglected. The second term on the right-hand side is also negligible compared with the first term on the right-hand side, because, except for the small value of the factor $((r_p/\Gamma) + \eta)^{-1}$, the first derivative of dimensionless temperature ($\partial T^*/\partial\eta$) compared with the second derivative of the temperature ($\partial^2 T^*/\partial\eta^2$) with respect to η is very small. The evaluation of the real data confirmed also that the first derivative of dimensionless temperature was approximately 40 times smaller than the second derivative of the dimensionless temperature.

Evaluation of the Model

The simplifications made, as shown above, indicate that in zone **B**, there is negligible heat transfer in the circumferential direction and that the heat transfer can be modeled in Cartesian coordinates with x then substituted for r and T_{1D} for T_B. The boundary conditions for this unsteady zone **B** will be steady at x_1 and unsteady (from measurements) at x_2. The boundary condition at x_1 will be provided from the solution of steady-state zone **A**. Therefore the one-dimensional transient solution will be coupled with two-dimensional steady-state solutions via the boundary condition at the interface (x_1) between the zones **A** and **B**.

Solution to Two-Dimensional Steady Heat Conduction Equation in Zone A

The steady temperature distribution in zone A is the solution to

$$\frac{\partial^2 T_{2D}}{\partial r^2} + \frac{1}{r}\frac{\partial T_{2D}}{\partial r} + \frac{1}{r^2}\frac{\partial^2 T_{2D}}{\partial \theta^2} = 0 \tag{4}$$

with

$$T_{2D}(r, \theta) = T_i - T(r, \theta); \quad T_{2D}(r_i, \theta) = 0;$$
$$T_{2D}(r_o, \theta) = T_i - \langle T_W(r_o, \theta)\rangle \tag{5}$$

$$\frac{1}{r}\frac{\partial T_{2D}}{\partial \theta}\bigg|_{\theta=0} = 0; \quad \frac{1}{r}\frac{\partial T_{2D}}{\partial \theta}\bigg|_{\theta=\pi} = 0 \tag{6}$$

where the subscript i refers to the inside boundary of the heat transfer tube. This problem can be solved by the separation of variables. Karamavruç and Clark (1995) showed that the solution to Eq. (4) is

$$T_{2D}(r, \theta) = \frac{\int_0^\pi (T_i - \langle T_W(r_o, \theta')\rangle)d\theta'}{\pi\left(1 - \dfrac{\ln(r_o)}{\ln(r_i)}\right)}$$

$$\times\left(1 - \frac{\ln(r)}{\ln(r_i)}\right) + \frac{2}{\pi}\sum_{n=1}^{\infty}\frac{\left[\left(\dfrac{r}{r_i}\right)^n - \left(\dfrac{r}{r_i}\right)^{-n}\right]}{\left[\left(\dfrac{r_o}{r_i}\right)^n - \left(\dfrac{r_o}{r_i}\right)^{-n}\right]}$$

$$\times \cos(n\theta)\int_0^\pi (T_i - \langle T_W(r_o, \theta')\rangle)\cos(n\theta')d\theta' \tag{7}$$

where θ' is a dummy variable and refers to the locations around the heat transfer tube. The boundary condition, $\langle T_W(r_o, \theta')\rangle$, was provided from the time-averaged temperature at various locations around the tube. A third-order polynomial function was fitted to the average experimental data to approximate true values between the measurement locations around the horizontal tube. The convergence of the solution is strongly dependent on the integral in the second term at the right-hand side of Eq. (7). The convergence of the series is faster, if the integrand contains more points (or, in other words, if the integrand is smooth). Further discussion concerning the convergence of Eq. (7) has been presented by Karamavruç and Clark (1995).

Solution to the One-Dimensional Unsteady Heat Conduction Equation in Zone B

The heat conduction equation that describes zone B can be written as

$$\frac{\partial T^*_{1D}}{\partial t^*} = \frac{\partial^2 T^*_{1D}}{\partial x^{*2}} \tag{8}$$

$$T^*_{1D}(x^*_1, t^*) = 0 \tag{9}$$

$$T^*_{1D}(x^*_2, t^*) = \frac{T_W(x_2, t) - T_{2D}(r_p, \theta)}{\langle T_W(x_2, t)\rangle - T_{2D}(r_p, \theta)} = T^*_W(t^*) \tag{10}$$

$$T^*_{1D}(x^*, 0) = 0 \tag{11}$$

where the dimensionless variables are

$$T^*_{1D}(x^*, t^*) = \frac{T(x, t) - T_{2D}(r_p, \theta)}{\langle T_W(x_2, t)\rangle - T_{2D}(r_p, \theta)};$$

$$x^* = \frac{x - x_1}{\Gamma}; \quad t^* = \frac{\alpha t}{\Gamma^2} \tag{12}$$

and where $\langle T_W(x_2, t)\rangle$ is the time-averaged quantity of the measured instantaneous data $T_W(x_2, t)$ on the surface of the instrumented tube, $T_{2D}(r_p, \theta)$ is the constant temperature value at the radius r_p, which is provided from the steady-state solution in zone **A**, and Γ is the thickness of the penetration depth (zone **B**). The boundary condition shown in Eq. (10) is nonhomogenous, due to time dependency. This problem can be solved by using Duhamel's theorem (Myer, 1987; Arpaci, 1966): This seeks a fundamental solution to the problem, which is the response of a linear homogeneous system to a unit step input with a zero initial condition. This fundamental solution is then applied to the linear nonhomogeneous system by summing the system response at every time step. The solution to Eq. (8) is

$$T^*_{1D}(x^*, t^*) = -\sum_{n=1}^{\infty} 2\lambda_n(-1)^n \sin(\lambda_n x^*)\int_{\tau=0}^{t^*} T^*_W(\tau)e^{\lambda_n^2(\tau - t^*)}d\tau \tag{13}$$

This Eq. (13) is the dimensionless temperature response of a linear system to any input of $T^*_W(\tau)$. The convergence of the solution depends strongly on the function $T^*_W(\tau)$, which is the dimensionless boundary condition measured instantaneously as discrete data points at the outside of the heat transfer tube.

Results of Unsteady State Solution

The method described in this paper has been verified through comparisons with experimental instantaneous heat transfer coefficients data processed using a customary computational conduction model. The calculation of heat transfer coefficient requires the temperature gradient at the wall, according to Fourier's cooling law. Due to the discontinuity at the outside of the tube wall, it was not possible to evaluate the temperature gradients at the surface of the tube surface analytically. Therefore the temperature gradient at the wall was calculated numerically

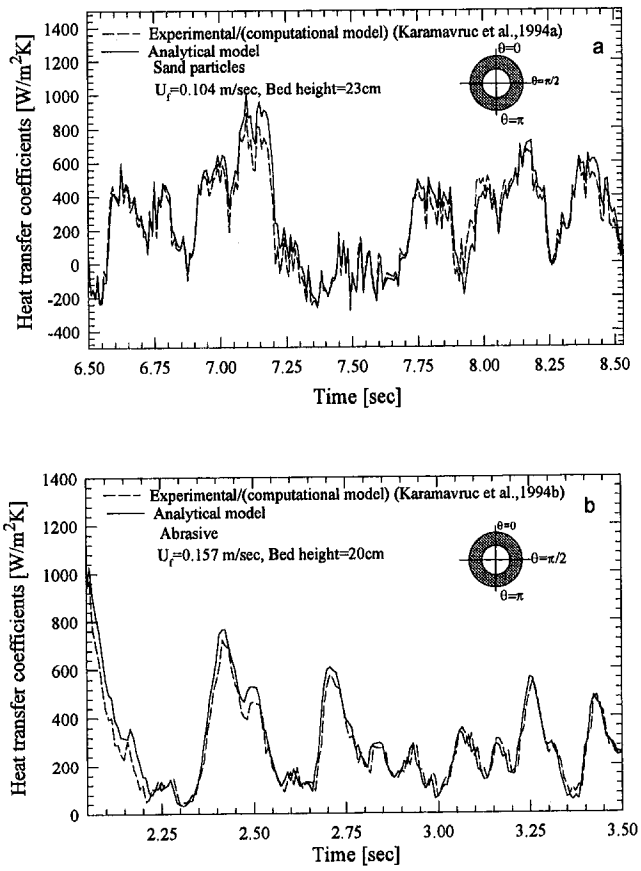

Fig. 2 Comparisons between the transient heat transfer coefficients obtained using analytical model and experimental result processed using computational heat conduction model: (*a*) fluidization material = sand, particle size ≅ 0.35 mm, U_f = 0.104 m/s, T_i = 357 K, T_b = 304.2 K, location on the tube = $\pi/2$; (*b*) fluidization material = abrasives, particle size ≅ 0.535 mm, U_f = 0.157 m/s, T_i = 373 K, T_b = 297 K, location on the tube = $\pi/2$

using a three point formula (parabolic approach). Figure 2(*a*) shows a comparison between the transient heat transfer coefficients obtained using experimental results presented by Karamavruç et al. (1994a) and the analytical model. The sand particles were run at a bed height of 23 cm with a fluidization velocity of 0.104 m/s. The mean particle diameter was 0.35 mm. Another comparison between our model and the experimental data published by Karamavruç et al. (1994b) is shown in Fig. 2(*b*). For this case, the bed particles were abrasives with a mean size of 0.535 mm and a bed height of 20 cm with an air fluidization velocity of 0.157 m/s. Both of these comparisons made on the side ($\theta = \pi/2$) of the heat transfer tube agree with each other. However, small discrepancies were observed at the peaks between experimental (processed using numerical approach) data and analytical models.

The analytical method presented in this paper is an effective concept for interpreting the experimental data around a horizontal heat transfer tube. The results obtained by analytical approach are more accurate then the numerical approach and relatively easy to calculate. However, due to the polynomial interpolation, this method becomes very time consuming for a long time series. Therefore, according to the authors' experience, the numerical method is preferable if long time calculations are required.

Acknowledgments

The authors are grateful to the National Science Foundation for support under grant #CTS 897146 and to Prof. Eric Johnson for his suggestions on the heat conduction problem across a heat transfer tube wall.

References

Arpaci, V. S., 1966, *Conduction Heat Transfer,* Addison-Wesley, MA.

George, G. H., 1993, "Instantaneous Heat Transfer Coefficients and Related Frequency Spectra for a Horizontal Cylinder in a High Temperature Fluidized Bed," *Int. J. Heat Mass Transfer,* Vol. 36, p. 337.

Katoh, Y., Miyamoto, M., and Kohno, A., 1991, "The Study on Unsteady Heat Transfer Around a Horizontal Heated Tube Surface in a Fluidized Bed," *Proc. Int. Conf. on Multiphase Flows,* Tsukuba, Vol. 1, p. 317.

Karamavruç, A. I., and Clark, N. N., 1995, "A Correction Factor for One Dimensional Heat Transfer Coefficients Around a Horizontal Tube in Fluidized Bed," *Powder Technology,* Vol. 86, p. 209.

Karamavruç, A. I., Clark, N. N., and McKain, D. L., 1994a, "Deduction of Fluid Bed Heat Transfer Coefficients Using One and Two Dimensional Analyses," *Powder Technology,* Vol. 80, p. 83.

Karamavruç, A. I., Sunderesan, S., and Clark, N. N., 1994b, "Transient Bed-to-Tube Heat Transfer: New Data Obtained Using Two Dimensional Analysis," *Powder and Bulk Solids Conference/Exhibition,* Chicago, IL, p. 413.

Mancuso, T., and Diller, T. E., 1991, "Time-Resolved Heat Flux Measurements in Unsteady Flow," *Fund. Exp. Meas. in Heat Transfer,* ASME HTD-Vol. 179, p. 67.

McKain, D. L., Clark, N. N., Karamavruç, A. I., and Turton, R., 1993, "Measurement of Time-Varying Local Heat Transfer Coefficients in a Bubbling Bed," *Proceedings of ASME 5th International Sym. on Gas-Solid Flows,* Washington, DC.

Myer, G. E., 1987, *Analytical Methods in Conduction Heat Transfer,* Genium Publ. Co., Schenectady, NY.

Rosiczkowsky, J., and Hollworth, B., 1991, "Local and Instantaneous Heat Transfer From an Isothermal Cylinder in a Cross Flow," *Fund. Exp. Meas. in Heat Transfer,* ASME HTD-Vol. 179, p. 49.

Rottger, H. K., and Renz, U., 1994, "Measurements of Instantaneous Local Heat Transfer Coefficients Around a Tube Immersed in a High Temperature Fluidized Bed," *Proc. 10th Int. Heat Transfer Conference,* Brighton, Vol. 2, p. 285.

Sunderesan, S. R., 1994, "Measurement of Local Instantaneous Heat Transfer Coefficients and Pressure Fluctuations in a Gas Fluidized Bed," M. S. Thesis, Mechanical and Aerospace Eng. Dept., West Virginia University.

Sunderesan, S. R., and Clark, N. N., 1995, "Local Heat Transfer Coefficients on the Circumference of a Tube in a Gas Fluidized Bed," *Int. J. Multiphase Flow,* Vol. 21, p. 1003.

Enhanced Flat Miniature Axially Grooved Heat Pipe[1]

D. Khrustalev[2] and A. Faghri[2]

Nomenclature

C = const
D_h = hydraulic diameter, m
f = friction coefficient
h_{fg} = latent heat of vaporization, J/kg
h = heat transfer coefficient, W/(m^2-K)
K = curvature, 1/m
k = thermal conductivity, W/(m-K)
L = length, m
L_1 = half-width of the top of the fin, m
N = total number of grooves
$\acute{n}$ = number of active sites per square centimeter
Q = axial heat flow through the heat pipe cross section, W

[1] This work was completed at Wright State University, Dayton, OH.

[2] Department of Mechanical Engineering, University of Connecticut, Storrs, CT 06269-3139.

Contributed by the Heat Transfer Division of THE AMERICAN SOCIETY OF MECHANICAL ENGINEERS. Manuscript received by the Heat Transfer Division January 1995; revision received April 1995. Keywords: Augmentation and Enhancement, Electronic Equipment, Heat Pipes and Thermosyphons. Associate Technical Editor: R. Viskanta.

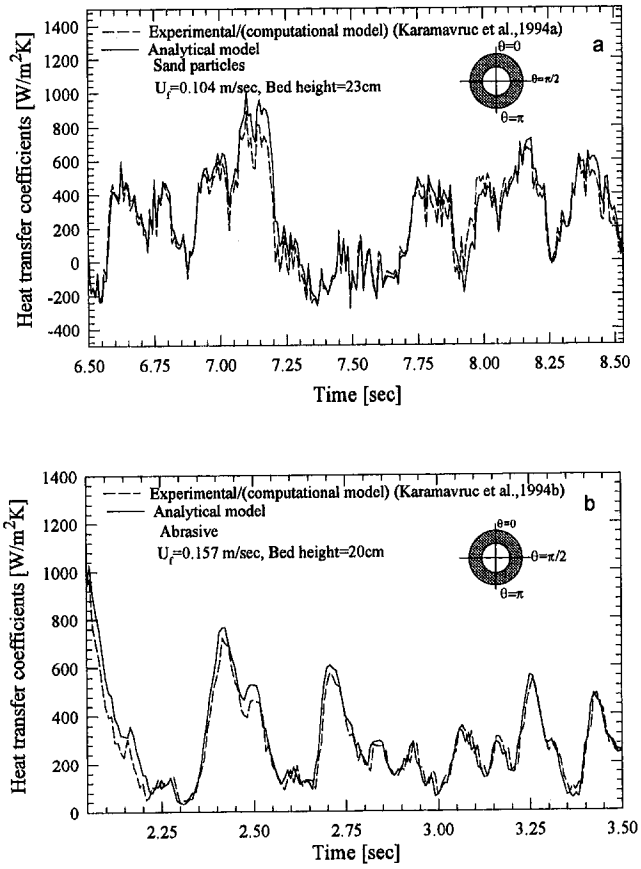

Fig. 2 Comparisons between the transient heat transfer coefficients obtained using analytical model and experimental result processed using computational heat conduction model: (*a*) fluidization material = sand, particle size ≅ 0.35 mm, U_f = 0.104 m/s, T_i = 357 K, T_b = 304.2 K, location on the tube = $\pi/2$; (*b*) fluidization material = abrasives, particle size ≅ 0.535 mm, U_f = 0.157 m/s, T_i = 373 K, T_b = 297 K, location on the tube = $\pi/2$

using a three point formula (parabolic approach). Figure 2(*a*) shows a comparison between the transient heat transfer coefficients obtained using experimental results presented by Karamavruç et al. (1994a) and the analytical model. The sand particles were run at a bed height of 23 cm with a fluidization velocity of 0.104 m/s. The mean particle diameter was 0.35 mm. Another comparison between our model and the experimental data published by Karamavruç et al. (1994b) is shown in Fig. 2(*b*). For this case, the bed particles were abrasives with a mean size of 0.535 mm and a bed height of 20 cm with an air fluidization velocity of 0.157 m/s. Both of these comparisons made on the side ($\theta = \pi/2$) of the heat transfer tube agree with each other. However, small discrepancies were observed at the peaks between experimental (processed using numerical approach) data and analytical models.

The analytical method presented in this paper is an effective concept for interpreting the experimental data around a horizontal heat transfer tube. The results obtained by analytical approach are more accurate then the numerical approach and relatively easy to calculate. However, due to the polynomial interpolation, this method becomes very time consuming for a long time series. Therefore, according to the authors' experience, the numerical method is preferable if long time calculations are required.

Acknowledgments

The authors are grateful to the National Science Foundation for support under grant #CTS 897146 and to Prof. Eric Johnson for his suggestions on the heat conduction problem across a heat transfer tube wall.

References

Arpaci, V. S., 1966, *Conduction Heat Transfer,* Addison-Wesley, MA.

George, G. H., 1993, "Instantaneous Heat Transfer Coefficients and Related Frequency Spectra for a Horizontal Cylinder in a High Temperature Fluidized Bed," *Int. J. Heat Mass Transfer,* Vol. 36, p. 337.

Katoh, Y., Miyamoto, M., and Kohno, A., 1991, "The Study on Unsteady Heat Transfer Around a Horizontal Heated Tube Surface in a Fluidized Bed," *Proc. Int. Conf. on Multiphase Flows,* Tsukuba, Vol. 1, p. 317.

Karamavruç, A. I., and Clark, N. N., 1995, "A Correction Factor for One Dimensional Heat Transfer Coefficients Around a Horizontal Tube in Fluidized Bed," *Powder Technology,* Vol. 86, p. 209.

Karamavruç, A. I., Clark, N. N., and McKain, D. L., 1994a, "Deduction of Fluid Bed Heat Transfer Coefficients Using One and Two Dimensional Analyses," *Powder Technology,* Vol. 80, p. 83.

Karamavruç, A. I., Sunderesan, S., and Clark, N. N., 1994b, "Transient Bed-to-Tube Heat Transfer: New Data Obtained Using Two Dimensional Analysis," *Powder and Bulk Solids Conference/Exhibition,* Chicago, IL, p. 413.

Mancuso, T., and Diller, T. E., 1991, "Time-Resolved Heat Flux Measurements in Unsteady Flow," *Fund. Exp. Meas. in Heat Transfer,* ASME HTD-Vol. 179, p. 67.

McKain, D. L., Clark, N. N., Karamavruç, A. I., and Turton, R., 1993, "Measurement of Time-Varying Local Heat Transfer Coefficients in a Bubbling Bed," *Proceedings of ASME 5th International Sym. on Gas-Solid Flows,* Washington, DC.

Myer, G. E., 1987, *Analytical Methods in Conduction Heat Transfer,* Genium Publ. Co., Schenectady, NY.

Rosiczkowsky, J., and Hollworth, B., 1991, "Local and Instantaneous Heat Transfer From an Isothermal Cylinder in a Cross Flow," *Fund. Exp. Meas. in Heat Transfer,* ASME HTD-Vol. 179, p. 49.

Rottger, H. K., and Renz, U., 1994, "Measurements of Instantaneous Local Heat Transfer Coefficients Around a Tube Immersed in a High Temperature Fluidized Bed," *Proc. 10th Int. Heat Transfer Conference,* Brighton, Vol. 2, p. 285.

Sunderesan, S. R., 1994, "Measurement of Local Instantaneous Heat Transfer Coefficients and Pressure Fluctuations in a Gas Fluidized Bed," M. S. Thesis, Mechanical and Aerospace Eng. Dept., West Virginia University.

Sunderesan, S. R., and Clark, N. N., 1995, "Local Heat Transfer Coefficients on the Circumference of a Tube in a Gas Fluidized Bed," *Int. J. Multiphase Flow,* Vol. 21, p. 1003.

Enhanced Flat Miniature Axially Grooved Heat Pipe[1]

D. Khrustalev[2] and A. Faghri[2]

Nomenclature

C = const
D_h = hydraulic diameter, m
f = friction coefficient
h_{fg} = latent heat of vaporization, J/kg
h = heat transfer coefficient, W/(m^2-K)
K = curvature, 1/m
k = thermal conductivity, W/(m-K)
L = length, m
L_1 = half-width of the top of the fin, m
N = total number of grooves
$\acute{n}$ = number of active sites per square centimeter
Q = axial heat flow through the heat pipe cross section, W

[1] This work was completed at Wright State University, Dayton, OH.

[2] Department of Mechanical Engineering, University of Connecticut, Storrs, CT 06269-3139.

Contributed by the Heat Transfer Division of THE AMERICAN SOCIETY OF MECHANICAL ENGINEERS. Manuscript received by the Heat Transfer Division January 1995; revision received April 1995. Keywords: Augmentation and Enhancement, Electronic Equipment, Heat Pipes and Thermosyphons. Associate Technical Editor: R. Viskanta.

q = heat flux, W/m^2
R_m = radius of the meniscus curvature, m
Re = $\bar{w}D_h/\nu$ = axial Reynolds number
T = temperature, K
t_w = wall thickness, m
t_g = groove depth, m
t_p = thickness of the porous layer, m
$\bar{w}$ = mean axial velocity, m/s
W = half-width of a groove outlet, m
z = axial coordinate, m
θ_0 = minimum wetting contact angle
ν = kinematic viscosity, m^2/s
ρ = density, kg/m^3
σ = surface tension, N/m
φ = inclination angle from horizontal

Subscripts

a = adiabatic
b = bottom of a groove
c = condenser
e = evaporator
l = liquid
max = maximum
men = meniscus
min = minimum
p = porous
v = vapor
w = wall

Introduction

To remove high heat fluxes from electronic and optical components, it has been proposed to use flat miniature axially grooved heat pipes (Plesch et al., 1991; Faghri, 1995). In an axially grooved heat pipe (AGHP), the maximum heat flux in the evaporator is restricted by the longitudinal fluid transport limitation (or capillary limit) and by the boiling limitation. These limitations should be taken into account during the design and optimization of an AGHP with the aim to make it capable of operating with high heat fluxes in the evaporator. This objective can be reached by the proper choice of the grooved surface geometry (Frank, 1967) and/or by special enhancements such as ivadizing (Grote et al., 1986), which is the deposition of a porous structure on top of the lands between the grooves. The main purpose of the present paper is to predict the maximum heat transfer capability of the proposed flat miniature copper–water heat pipe with the grooved-ivadized structure. Predictions of the capillary and boiling limitations have been made in the same manner as Khrustalev et al. (1994) and Khrustalev and Faghri (1994) with some modifications accounting for the presence of the porous layer, as explained in the following sections.

Heat Pipe Configurations

The prototype heat pipe considered here is the AGHP investigated experimentally by Plesch et al. (1991). The cross sections of the heat pipe are shown in Figs. 1(a) and 1(b) and its characteristic dimensions are represented in Table 1. The casing material was copper and the working fluid was pure water. The heaters were situated at both sides of the evaporator with the overall heated surface 2.56 cm^2.

In order to consider the enhanced AGHP modeled in this paper, some experimental results of Grote et al. (1986) and Khrustalev et al. (1987) should be mentioned first. In the experiment by Grote et al. (1986), an aluminum plate was machined with rectangular grooves (W = 0.0635 mm, t_g = 0.64 mm, L_1 = 0.06465 mm) and then enhanced by an inexpensive process called ivadizing. During ivadizing, aluminum was vapor-deposited onto the surface, forming a slightly porous coating on the top of the lands between the grooves (t_p = 0.15 mm, W_p = 0.02 mm, Fig. 1(c)). Tests of this enhanced plate with R-11 showed an improvement in the evaporative heat transfer coefficient by a factor of four compared to the surface with plain grooves. A copper heat pipe with a similar combined porous structure was tested by Khrustalev et al. (1987). The porous copper coating was deposited on the inner surface of a tube with longitudinal rectangular grooves (W = 0.37 mm, t_g = 0.46 mm, L_1 = 0.43 mm), serving as a cathode in the process of cathodic deposition from solution. A significant increase (about three to four times for acetone) in the evaporative heat transfer coefficient was registered due to the presence of the porous coating. In both papers, it was mentioned that the enhanced surfaces had a larger capillary pumping ability than that with plain grooves. Since the increase of the evaporative heat transfer coefficient means a decrease in the liquid superheat in the evaporator, which is crucial for the onset of nucleate boiling, the described enhanced surfaces are very promising for high heat flux heat pipes. Therefore, the enhanced heat pipe with the same characteristics as the prototype by Plesch et al. (1991) is considered in this study, except that a porous coating was added on the land area between the grooves with t_p = 0.15 mm and W_p = 0.02 mm (Fig. 1(c)). The maximum heat flow rates restricted by capillary and boiling limitations were predicted for both heat pipes and compared.

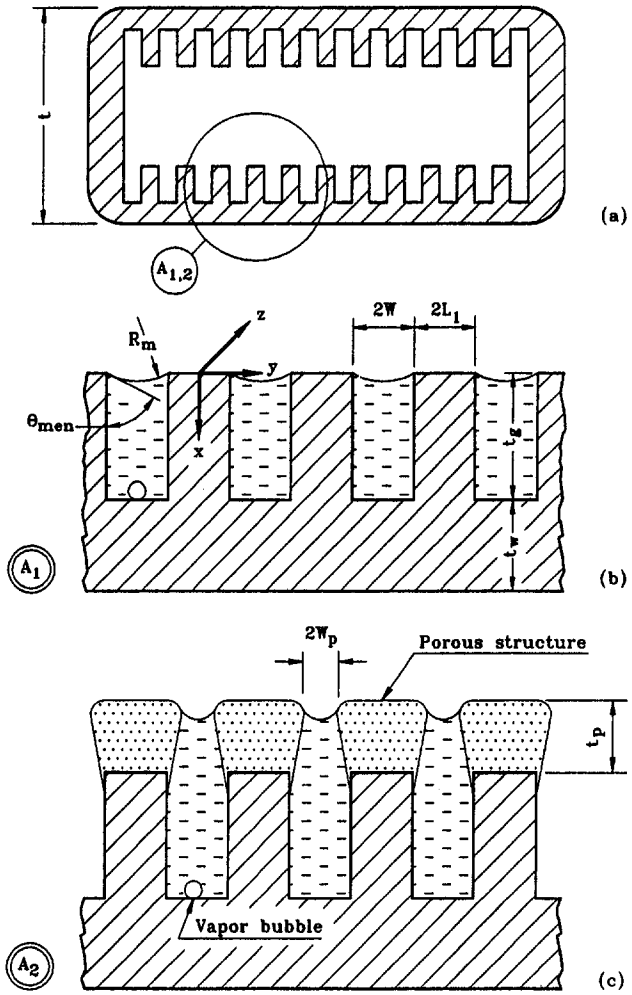

Fig. 1 Flat miniature axially grooved heat pipe cross sections

Table 1 Characteristic dimensions of the prototype AGHP

W	t_g	L_1	t	t_w	L_e	L_a	L_c	N
0.06 mm	0.24 mm	0.02 mm	2 mm	0.22 mm	20 mm	80 mm	20 mm	80

Boiling Limitation in AGHPs

Nucleation within the wick is undesirable for wicked heat pipe operation because the bubbles can obstruct the liquid circulation and cause hot spots on the evaporator walls, and/or oscillatory heat pipe performance (Faghri, 1995). Thus, for heat pipe design optimization, it is necessary to predict the value of the heat flux that initiates vapor bubble formation in the working liquid. This task can be subdivided into two parts:

1 Estimation of the critical superheat of the liquid in the wick, $(T_{b,l} - T_v)$, that causes generation of vapor bubbles at the wall–wick interface.

2 Computation of the heat transfer coefficient in the evaporator, $\bar{h}_{e,b}$, for the situation when no boiling occurs in the liquid, which relates the values of the heat flux, q_e, and the temperature drop across the wick, $(T_{b,l} - T_v)$.

Critical Liquid Superheat. The process of bubble formation depends upon the solid surface microrelief, wetting contact angles, and liquid properties. Since theoretical prediction of the superheat that causes boiling is difficult, empirical correlations should be involved in the analysis.

Lorenz et al. (1974) obtained experimental data for boiling of four different liquids on a copper surface with a #240 (sandpaper) finish. In the experiment mentioned, the number of active bubble formation sites per square centimeter ($\acute{n}$), which increased rapidly with superheat, was determined by visual counting at different superheat values. Experimental results by Lorenz et al. (1974) can be approximated by the following equation:

$$\acute{n} = C_1 - C_2\left[\frac{h_{fg}(T_{b,l} - T_v)\rho_v}{2\sigma T_v} + \frac{1}{R_m}\right]^{-1} \quad (1)$$

where for water $C_1 = 77$, $C_2 = 19 \times 10^6$, and $1 \le \acute{n} \le 6$, and for R-113, methanol, and benzene $C_1 = 39.6$, $C_2 = 19.6 \times 10^6$, and $0.5 \le \acute{n} \le 10$. Note that the vapor bubble embryo diameter is much smaller than the groove width; therefore, this correlation obtained for planar surfaces can be used in the present analysis to predict the incipience of boiling. For a known superheat, $(T_{b,l} - T_v)$, Eq. (1) indicates whether boiling occurs ($\acute{n} \ge 0$) at a given point along the evaporator length, which is characterized by the local radius of curvature of the meniscus, R_m. The values of the heat flux and superheat are related as follows:

$$q_e = \bar{h}_{e,b}(T_{b,l} - T_v) \quad (2)$$

where $\bar{h}_{e,b}$ is the local effective heat transfer coefficient between the bottom of a groove and the saturated vapor, which is generally dependent on the value of R_m at this location.

Heat Transfer Coefficient. The effective evaporative coefficient of heat transfer for the heat pipe with plain grooves was calculated in the same manner as used by Khrustalev and Faghri (1994). The heat transfer during evaporation was considered by accounting for the effects of heat conduction through thin liquid films and the metallic fin, interfacial thermal resistance, disjoining pressure, and surface roughness. The values of $\bar{h}_{e,b}$ were calculated for every point along the axial direction in the evaporator of the modeled AGHPs for a given heat load Q_a, and Eq. (1) was used with the corresponding R_m to predict the onset of nucleate boiling ($\acute{n} = 1$).

The heat transfer coefficient of the enhanced AGHP, $\bar{h}_{e,b}$, was estimated as follows: The three main thermal resistances that have the most important influence on the heat transfer in the evaporator of the enhanced AGHP (Fig. 1(*c*)) are those associated with the heat conduction in the fin between grooves, heat conduction in the porous layer, and evaporation from the porous surface wetted with liquid ($1/h_p$). This can be expressed by

$$\bar{h}_{e,b} = \left[\frac{t_g}{k_w}\frac{W + L_1}{L_1} + \frac{t_p}{k_p}\frac{W + L_1}{L_1 + 0.5(W - W_p)} + \frac{W + L_1}{(W - W_p + L_1)h_p}\right]^{-1} \quad (3)$$

Heat transfer during the evaporation of water from a porous surface was considered in the same manner as Solov'ev and Kovalev (1984). The predicted values of h_p were extremely high, especially for small pore sizes, R_p. For example, for $R_p = 20$ μm, $T_v = 100$°C, and $\theta_0 = 33°$ (Stepanov et al., 1977) h_p exceeded 500,000 W/(m^2-K). Thus, the heat transfer coefficient $h_{e,b}$ was estimated by Eq. (3), where the impact of the last term was small in comparison with those of the two other terms.

Capillary Limitation and Fluid Circulation

The mathematical model of the fluid circulation in AGHPs is given in detail by Khrustalev et al. (1994). Some distinguishing features of the model related to the considered enhanced AGHP should be mentioned here. The expression for the friction factor for liquid flow along capillary grooves affected by the vapor flow, originally obtained by Schneider and DeVos (1980) for rectangular grooves, was used for the prototype AGHP because of its reliability and accuracy. Accounting for the liquid–vapor interaction is important for the prototype AGHP because the liquid–vapor interface is a significant part of the perimeter of the liquid cross section. However, for the enhanced AGHP, for the case when $W_p \ll W$ considered in the present paper, the liquid–vapor interface is a comparatively small portion of the perimeter. Therefore, the friction factor for the liquid flow along the capillary channel of the enhanced AGHP was defined using the following equation (Shah and Bhatti, 1987):

$$(f\ \mathrm{Re}) = 24(1 - 1.3553C + 1.9467C^2 - 1.7012C^3 + 0.9564C^4 - 0.2537C^5) \quad (4)$$

where $C = 2W/(t_g + t_p)$, and the Reynolds number is based on the hydraulic diameter, which is defined accounting for the geometry of the porous layer.

The conditions for the capillary limit in the prototype AGHP used in the present analysis imply that the curvature of the meniscus is at a minimum at a single point in the condenser, and at a maximum at a single point in the evaporator with the maximum heat load.

$$\min\{K_{\mathrm{men}}(z)\} = 0 \quad (5)$$

$$\max\{K_{\mathrm{men}}(z)\} = \frac{\cos(\theta_0)}{W} \quad (6)$$

where K_{men} is the curvature of the meniscus. For the enhanced AGHP, Eq. (6) was changed to reflect the different width of the groove outlet due to the porous structure:

$$\max\{K_{\mathrm{men}}(z)\} = \frac{\cos(\theta_0)}{W_p} \quad (7)$$

For heat loads less than the maximum, only Eq. (5) was applied, which determined the value of the main meniscus radius at the evaporator end cap, R_{m0}. For the copper–water heat pipes modeled, θ_0 was set equal to 33 deg (Stepanov et al., 1977).

Results and Discussion

The numerical results for the maximum heat flow rate, $Q_{\max}$, transferred by the AGHPs modeled, are shown in Fig. 2. $Q_{\max}$ increased with the operating temperature (vapor temperature at the evaporator end cap). However, for $T_v > 100$°C, it was restricted by the boiling limitation. To validate the numerical results, obtained with an uncertainty of about ±0.2 percent, a

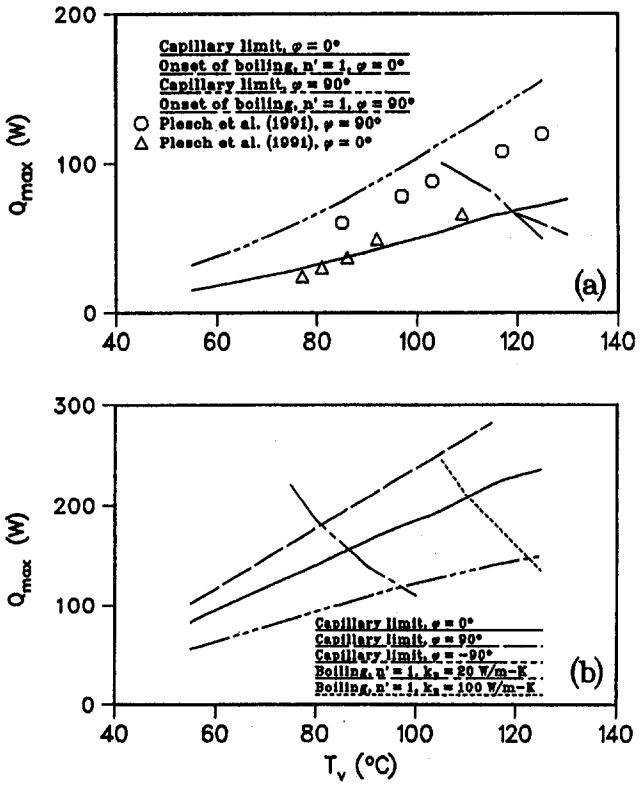

Fig. 2 Maximum heat transfer of the copper–water heat pipes versus operating temperature: (*a*) configuration of Plesch et al. (1991); (*b*) configuration of Plesch et al. (1991) plus porous coating

comparison with the two best series of the experimental data by Plesch et al. (1991) was made, as shown in Fig. 2(*a*). It should be noted that the experimental results by Plesch et al. (1991) were given versus the evaporator surface temperature, and it was not directly stated whether the data for the measured heat rate were at a maximum. The numerical predictions of the capillary limit for both the horizontal ($\varphi = 0$) and vertical ($\varphi = 90$ deg) orientations follow the experimental data. Note that a heat pipe can also work in the vertical orientation as a two-phase thermosyphon with boiling liquid in the evaporator.

For the enhanced AGHP, the maximum capillary potential, which is related to W_p (see Fig. 1), was much larger than that for the prototype AGHP because W_p was significantly smaller than W. The resulting maximum heat flow rate was also higher, and this heat pipe could effectively operate in the vertical orientation with elevated evaporator ($\varphi = -90$ deg, see Fig. 2(*b*)). In the enhanced AGHP, evaporation takes place on the surface of the porous layer where the total area of the thin film region is many times larger than that of the grooved evaporator without a porous coating. Therefore, the heat transfer coefficient and hence the maximum heat flux restricted by the boiling limit should be much larger for the enhanced AGHP provided that the thermal conductivity of the porous layer is not very low.

The prediction of the maximum heat transfer of the AGHP with a porous coating is shown in Fig. 2(*b*) where the porous layer thermal conductivity, k_p, was set equal to 20 and 100 W/(m-K). At $T_v = 110$°C, the AGHP with porous coating could operate at a heat flux of 80 W/cm^2 in the horizontal position. It is anticipated that in order to reach higher heat fluxes, more advanced heat pipe configurations should be developed.

Conclusions

The results of the numerical prediction of the enhanced flat miniature axially grooved copper–water heat pipe are summarized as follows:

1 The copper–water flat AGHP with external dimensions the same as that by Plesch et al. (1991) and with a porous coating on the lands between grooves (k_p = 100 W/(m-K)) could operate at a maximum heat flux in the evaporator of 80 W/cm^2 in the horizontal orientation at $T_v = 110$°C and about 100 W/cm^2 in the vertical orientation with elevated condenser end at $T_v = 105$°C.
2 The AGHP with a porous coating, unlike an ordinary AGHP, could effectively perform in the vertical orientation when its evaporator end was elevated.

Therefore, the enhanced AGHP with a porous coating has been found superior over the prototype AGHP with plain axial grooves. Such a heat pipe could be successfully used in thermal control systems for high heat flux electronic equipment.

References

Faghri, A., 1995, *Heat Pipe Science and Technology,* Taylor & Francis.

Frank, S., 1967, "Optimization of a Grooved Heat Pipe," *Proc. Intersociety Energy Conversion Conf.,* pp. 833–845.

Grote, M. G., Stark, J. A., and Tefft, E. C., III, 1986, "Enhanced Evaporative Surface for Two-Phase Mounting Plates," *Proc. 16th ICES Conf.,* Paper No. 860979, pp. 617–624.

Khrustalev, D. K., Grakovich, L. P., Denisevich, S. V., Yanitski, B., and Sheleg, V. K., 1987, "Heat Pipe With a Combined Capillary-Porous Structure," *J. Engineering Physics and Thermophysics,* Vol. 52, No. 4, pp. 587–592.

Khrustalev, D., Faghri, A., and Leland, J., 1994, "Thermal Analysis of Axially-Grooved Heat Pipes," *Proceedings of the Second Biennial ASME European Joint Conference on Engineering Systems, Design, and Analysis,* London, England, ASME PD-Vol. 64-1, pp. 39–54.

Khrustalev, D., and Faghri, A., 1994, "Evaporation and Condensation on Capillary-Grooved Structures of Heat Pipes," *Proceedings of 1994 Winter Annual ASME Meeting,* ASME HTD-Vol. 287, pp. 47–59.

Lorenz, J. J., Mikic, B. B., and Rohsenow, W. M., 1974, "The Effect of Surface Conditions on Boiling Characteristics," *Proc. 8th Int. Heat Transfer Conf.,* Vol. 4, pp. 35–39.

Plesch, D., Bier, W., Seidel, D., and Schubert, K., 1991, "Miniature Heat Pipes for Heat Removal From Microelectronic Circuits," in: *Micromechanical Sensors, Actuators, and Systems,* D. Cho, R. Warrington, Jr., et al., eds., ASME DCS-Vol. 32, pp. 303–313.

Schneider, G. E., and DeVos, R., 1980, "Nondimensional Analysis for the Heat Transport Capability of Axially-Grooved Heat Pipes Including Liquid/Vapor Interaction," AIAA Paper No. 80-0214.

Shah, R. K., and Bhatti, M. S., 1987, "Laminar Convective Heat Transfer in Ducts," in: *Handbook of Single Phase Convective Heat Transfer,* Kakac et al., eds., Wiley, New York.

Solov'ev, S. L., and Kovalev, S. A., 1984, "Mechanism of Evaporation of a Liquid From a Porous Surface," *Proc. 5th Int. Heat Pipe Conf.,* Tsukuba, Japan, Preprints Vol. II, pp. 77–82.

Stepanov, V. G., Volyak, L. D., and Tarlakov, Yu. V., 1977, "Wetting Contact Angles for Some Systems," *J. Engineering Physics and Thermophysics,* Vol. 32, No. 6, pp. 1000–1003.

Journal of Heat Transfer

Discussion

A Hybrid Transient Step-Heating Heat Transfer Measurement Technique Using Heater Foils and Liquid-Crystal Thermography[1]

B. Bieniasz[2] and R. Smusz.[2] We believe that we have found an error in Eq. (9) in the paper of von Wolfersdorf et al. It was carried on to Eq. (10) and has deformed the results presented in Fig. 1. That is why we feel it our duty to produce our solution for the surface temperature of semispace during the second stage of step-heating.

Heat conduction in the semispace is governed by (nomenclature here is identical to that in the paper of von Wolfersdorf et al.):

$$\rho c \frac{\partial T}{\partial t} = \lambda \frac{\partial^2 T}{\partial x^2} \quad 0 \le y < \infty. \tag{1}$$

The initial condition is represented by the known solution for the first stage of a step-heating, given by Lykov [1967, p. 183, Eq. (11)], i.e.,

$$T(y, t) - T_o = \left(\frac{q}{\alpha} + T_G - T_o\right) \left[\operatorname{erfc}\left(\frac{y}{2\lambda\sqrt{\frac{t}{k}}}\right) - \exp\left(\frac{\alpha}{\lambda} y\right) \exp\left(\alpha^2 \frac{t}{k}\right) \operatorname{erfc}\left(\frac{y}{2\lambda\sqrt{\frac{t}{k}}} + \alpha\sqrt{\frac{t}{k}}\right)\right], \tag{2}$$

taken for $t = t_u$, and with the boundary condition

$$-\lambda \frac{\partial T(y = 0, t)}{\partial y} = \epsilon q - \alpha(T_w - T_G) \quad t > t_u. \tag{3}$$

Applying Laplace's transformation yields

$$T(y, t) - T_o = \left(\frac{q}{\alpha} + T_G - T_o\right) \left[\operatorname{erfc}\left(\frac{y}{2\lambda\sqrt{\frac{t_u}{k}}}\right) - \exp\left(\frac{\alpha}{\lambda} y\right) \exp\left(\frac{\alpha^2}{k} t_u\right) \operatorname{erfc}\left(\frac{y}{2\lambda\sqrt{\frac{t_u}{k}}} + \alpha\sqrt{\frac{t_u}{k}}\right)\right]$$

$$+ - \frac{q}{\alpha}(1 - \epsilon) \left\{ \operatorname{erfc}\left(\frac{y}{2\lambda\sqrt{\frac{t - t_u}{k}}}\right) - \exp\left(\frac{\alpha}{\lambda} y\right) \times \exp\left[\alpha^2 \frac{(t - t_u)}{k}\right] \operatorname{erfc}\left(\frac{y}{2\lambda\sqrt{\frac{t - t_u}{k}}} + \alpha\sqrt{\frac{t - t_u}{k}}\right)\right\}, \tag{4}$$

which is the solution for the second stage.

Thus the specific surface-temperature solution ($y = 0$) for $t > t_u$ and $T_G = T_o$ is:

$$\alpha \frac{T_w - T_o}{q} = \epsilon - \exp\left(\frac{\alpha^2 t_u}{k}\right) \operatorname{erfc}\left(\alpha\sqrt{\frac{t_u}{k}}\right) + (1 - \epsilon) \exp\left[\frac{\alpha^2}{k}(t - t_u)\right] \operatorname{erfc}\left(\alpha\sqrt{\frac{t - t_u}{k}}\right), \tag{5}$$

which differs from Eq. (9) given by von Wolfersdorf et al.

Taking into account Eq. (2), for the first stage ($0 < t < t_u$), for $y = 0$ and $T_G = T_o$, yields

$$\alpha \frac{T_w - T_o}{q} = 1 - \exp\left(\frac{\alpha^2}{k} t\right) \operatorname{erfc}\left(\alpha\sqrt{\frac{t}{k}}\right), \tag{6}$$

which is identical to Eq. (8) in the paper of von Wolfersdorf et al.

Equalizing the right sides of Eqs. (5) and (6) for $T_w(t_1) = T_w(t_2)$, in the case of use of liquid-crystal thermography, results in:

$$1 - \exp\left(\frac{\alpha^2}{k} t_1\right) \operatorname{erfc}\left(\alpha\sqrt{\frac{t_1}{k}}\right) = \epsilon - \exp\left(\frac{\alpha^2}{k} t_u\right) \operatorname{erfc}\left(\alpha\sqrt{\frac{t_u}{k}}\right) + (1 - \epsilon) \exp\left[\frac{\alpha^2}{k}(t_2 - t_u)\right] \operatorname{erfc}\left(\alpha\sqrt{\frac{t_2 - t_u}{k}}\right), \tag{7}$$

which, in turn, differs from Eq. (10) of von Wolfersdorf et al.

The discrepancy in the surface temperature of a semispace during the second stage, calculated with the use of Eqs. (5) and (9) of von Wolfersdorf's paper, for the same data, is presented in Fig. 1. Analyzing Eq. (7) results in the conclusion that Eq. (9) in the paper of von Wolfersdorf et al. underestimates the experimental results of measurements of the heat transfer coefficient using heater foil and liquid-crystal thermography.

[1] By J. von Wolfersdorf, R. Hoecker, and T. Sattelmayer, published in the May 1993 issue of the ASME JOURNAL OF HEAT TRANSFER, Vol. 115, pp. 319–324.

[2] Thermodynamics and Aircraft Engines Department, Rzeszów University of Technology, ul. W. Pola 2, 35-959 Rzeszów, Poland.

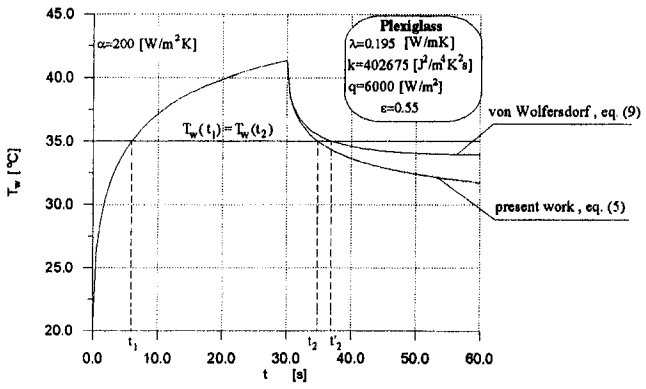

Fig. 1 Comparison of present results with those of von Wolfersdorf et al.

References

Lykov, A. V., 1967, *Teoriya menlonpovodnosmi,* Vysshaya Shkola, Moscow.

Authors' Closure

In response to the discussion of Bieniasz and Smusz, we would like to state that the proposed solution (Eq. (5)) by Bieniasz and Smusz is wrong and supposedly stems from a misinterpretation of the superposition approach (Duhamel's theorem). Equation (9) of von Wolfersdorf et al. (1993), which was taken from Carslaw and Jaeger (1959, p. 74), is correct, as will be shown here.

If we write the boundary conditions as given by von Wolfersdorf et al.,

$$-\lambda \frac{\partial T\,(y=0,\,t)}{\partial y} = q - \alpha(T_W - T_G) = \alpha\left(T_G + \frac{q}{\alpha} - T_W\right)$$

$$= \alpha(T_A - T_W) \quad 0 < t < t_u \tag{1}$$

and

$$-\lambda \frac{\partial T\,(y=0,\,t)}{\partial y} = \epsilon q - \alpha(T_W - T_G) = \alpha\left(T_G + \frac{\epsilon q}{\alpha} - T_W\right)$$

$$= \alpha(T_B - T_W) \quad t_u < t, \tag{2}$$

it is seen that the problem can be formulated as a change in equivalent driving temperature from T_A to T_B at time t_u. This is essentially the problem solved by Carslaw and Jaeger (1959, p. 74).

Using Duhamel's theorem by superposing two elemental steps in equivalent driving temperature results in (see Metzger and Larson, 1986):

$$T_W - T_0 = \sum_{i=1}^{2} U(t - \tau_i)\Delta T_{Fi} \tag{3}$$

where $U(t - \tau_i)$ is the fundamental solution:

$$U(t - \tau_i) = 1 - e^{[\alpha^2(t-\tau_i)]/k}\,\mathrm{erfc}\left(\frac{\alpha\sqrt{t - \tau_i}}{\sqrt{k}}\right) \tag{4}$$

and τ_i represents the discrete stepping time.

In the given special case one has $\Delta T_{F1} = T_A - T_0$ with $\tau_1 = 0$ and $\Delta T_{F2} = T_B - T_A$ with $\tau_2 = t_u$, which leads to:

$$T_W - T_0 = (T_A - T_0)\left(1 - e^{[\alpha^2(t-0)]/k}\,\mathrm{erfc}\left(\frac{\alpha\sqrt{t-0}}{\sqrt{k}}\right)\right)$$

$$+ (T_B - T_A)\left(1 - e^{[\alpha^2(t-t_u)]/k}\,\mathrm{erfc}\left(\frac{\alpha\sqrt{t - t_u}}{\sqrt{k}}\right)\right) \tag{5}$$

This, after rearrangement using Eqs. (1) and (2), becomes Eq. (9) of von Wolfersdorf et al. It should be noted that more than one heat step with different power input can be handled in that way.

We cannot follow the derivation by Bieniasz and Smusz; however, it is clearly seen that Eq. (5) of Bieniasz and Smusz yields wrong results for the limiting case of constant power input ($\epsilon = 1$):

$$\alpha\frac{T_W - T_0}{q} = 1 - e^{(\alpha^2 t_u)/k}\,\mathrm{erfc}\left(\frac{\alpha\sqrt{t_u}}{\sqrt{k}}\right) \tag{6}$$

which is a constant, and for the steady state ($t \to \infty$):

$$\alpha\frac{T_W - T_0}{q} = \epsilon - e^{(\alpha^2 t_u)/k}\,\mathrm{erfc}\left(\frac{\alpha\sqrt{t_u}}{\sqrt{k}}\right) \tag{7}$$

whereas our solution gives the correct answers, i.e.,

$$\alpha\frac{T_W - T_0}{q} = 1 - e^{(\alpha^2 t)/k}\,\mathrm{erfc}\left(\frac{\alpha\sqrt{t}}{\sqrt{k}}\right) \tag{8}$$

for $\epsilon = 1$ and

$$\alpha\frac{T_W - T_0}{q} = \epsilon \tag{9}$$

for the steady state.

References

Carslaw, H. S., and Jaeger, J. C., 1959, *Conduction of Heat in Solids,* 2nd ed., Oxford University Press, London.

Metzger, D. E., and Larson, D. E., 1986, "Use of Melting Point Surface Coatings for Local Convection Heat Transfer Measurements in Rectangular Channel Flows With 90-deg Turns," ASME JOURNAL OF HEAT TRANSFER, Vol. 108, pp. 48–54.

Analysis of Heat Transfer Regulation and Modification Employing Intermittently Emplaced Porous Cavities[1]

Analysis of Flow and Heat Transfer Over an External Boundary Covered With Porous Substrate[2]

F. Chen[3] and C. F. Chen.[4] Replying to the discussion of Nield (1995), Vafai and Kim (1995) attributed to us (Chen and Chen, 1992) the following equality at the interface between the liquid and porous region:

$$\mu_I\left[\frac{\partial V_y}{\partial y}\right]_I = \mu_{II}\left[\frac{\partial V_y}{\partial y}\right]_{II} \tag{1}$$

This is incorrect; we did not show nor did we imply such an equality.

In our paper, the boundary conditions for the velocity components at the interface are [Eq. (10), Chen and Chen, 1992]

[1] By K. Vafai and P. C. Huang, published in the August 1994 issue of the ASME JOURNAL OF HEAT TRANSFER, Vol. 116, pp. 604–613.

[2] By P. C. Huang and K. Vafai, published in the August 1994 issue of the ASME JOURNAL OF HEAT TRANSFER, Vol. 116, pp. 768–771.

[3] Institute of Applied Mechanics, National Taiwan University, Taipei, Taiwan 106.

[4] Department of Aerospace and Mechanical Engineering, The University of Arizona, Tucson, AZ 85721.

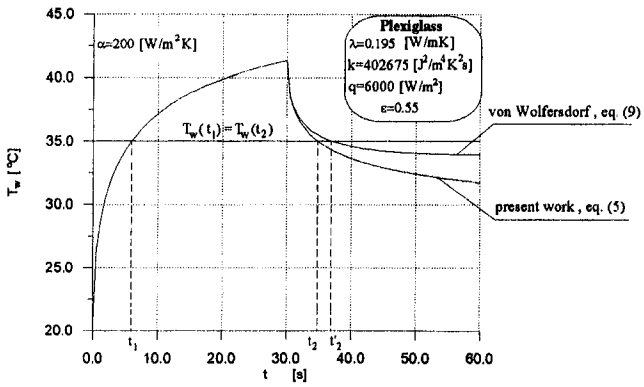

Fig. 1 Comparison of present results with those of von Wolfersdorf et al.

References

Lykov, A. V., 1967, *Teoriya menlonpovodnosmi,* Vysshaya Shkola, Moscow.

Authors' Closure

In response to the discussion of Bieniasz and Smusz, we would like to state that the proposed solution (Eq. (5)) by Bieniasz and Smusz is wrong and supposedly stems from a misinterpretation of the superposition approach (Duhamel's theorem). Equation (9) of von Wolfersdorf et al. (1993), which was taken from Carslaw and Jaeger (1959, p. 74), is correct, as will be shown here.

If we write the boundary conditions as given by von Wolfersdorf et al.,

$$-\lambda \frac{\partial T\,(y=0,\,t)}{\partial y} = q - \alpha(T_W - T_G) = \alpha\left(T_G + \frac{q}{\alpha} - T_W\right)$$

$$= \alpha(T_A - T_W) \quad 0 < t < t_u \tag{1}$$

and

$$-\lambda \frac{\partial T\,(y=0,\,t)}{\partial y} = \epsilon q - \alpha(T_W - T_G) = \alpha\left(T_G + \frac{\epsilon q}{\alpha} - T_W\right)$$

$$= \alpha(T_B - T_W) \quad t_u < t, \tag{2}$$

it is seen that the problem can be formulated as a change in equivalent driving temperature from T_A to T_B at time t_u. This is essentially the problem solved by Carslaw and Jaeger (1959, p. 74).

Using Duhamel's theorem by superposing two elemental steps in equivalent driving temperature results in (see Metzger and Larson, 1986):

$$T_W - T_0 = \sum_{i=1}^{2} U(t - \tau_i)\Delta T_{Fi} \tag{3}$$

where $U(t - \tau_i)$ is the fundamental solution:

$$U(t - \tau_i) = 1 - e^{[\alpha^2(t-\tau_i)]/k}\,\mathrm{erfc}\left(\frac{\alpha\sqrt{t - \tau_i}}{\sqrt{k}}\right) \tag{4}$$

and τ_i represents the discrete stepping time.

In the given special case one has $\Delta T_{F1} = T_A - T_0$ with $\tau_1 = 0$ and $\Delta T_{F2} = T_B - T_A$ with $\tau_2 = t_u$, which leads to:

$$T_W - T_0 = (T_A - T_0)\left(1 - e^{[\alpha^2(t-0)]/k}\,\mathrm{erfc}\left(\frac{\alpha\sqrt{t-0}}{\sqrt{k}}\right)\right)$$

$$+ (T_B - T_A)\left(1 - e^{[\alpha^2(t-t_u)]/k}\,\mathrm{erfc}\left(\frac{\alpha\sqrt{t-t_u}}{\sqrt{k}}\right)\right) \tag{5}$$

This, after rearrangement using Eqs. (1) and (2), becomes Eq. (9) of von Wolfersdorf et al. It should be noted that more than one heat step with different power input can be handled in that way.

We cannot follow the derivation by Bieniasz and Smusz; however, it is clearly seen that Eq. (5) of Bieniasz and Smusz yields wrong results for the limiting case of constant power input ($\epsilon = 1$):

$$\alpha\frac{T_W - T_0}{q} = 1 - e^{(\alpha^2 t_u)/k}\,\mathrm{erfc}\left(\frac{\alpha\sqrt{t_u}}{\sqrt{k}}\right) \tag{6}$$

which is a constant, and for the steady state ($t \to \infty$):

$$\alpha\frac{T_W - T_0}{q} = \epsilon - e^{(\alpha^2 t_u)/k}\,\mathrm{erfc}\left(\frac{\alpha\sqrt{t_u}}{\sqrt{k}}\right) \tag{7}$$

whereas our solution gives the correct answers, i.e.,

$$\alpha\frac{T_W - T_0}{q} = 1 - e^{(\alpha^2 t)/k}\,\mathrm{erfc}\left(\frac{\alpha\sqrt{t}}{\sqrt{k}}\right) \tag{8}$$

for $\epsilon = 1$ and

$$\alpha\frac{T_W - T_0}{q} = \epsilon \tag{9}$$

for the steady state.

References

Carslaw, H. S., and Jaeger, J. C., 1959, *Conduction of Heat in Solids,* 2nd ed., Oxford University Press, London.

Metzger, D. E., and Larson, D. E., 1986, "Use of Melting Point Surface Coatings for Local Convection Heat Transfer Measurements in Rectangular Channel Flows With 90-deg Turns," ASME JOURNAL OF HEAT TRANSFER, Vol. 108, pp. 48–54.

Analysis of Heat Transfer Regulation and Modification Employing Intermittently Emplaced Porous Cavities[1]

Analysis of Flow and Heat Transfer Over an External Boundary Covered With Porous Substrate[2]

F. Chen[3] and C. F. Chen.[4]

Replying to the discussion of Nield (1995), Vafai and Kim (1995) attributed to us (Chen and Chen, 1992) the following equality at the interface between the liquid and porous region:

$$\mu_I\left[\frac{\partial V_y}{\partial y}\right]_I = \mu_{II}\left[\frac{\partial V_y}{\partial y}\right]_{II} \tag{1}$$

This is incorrect; we did not show nor did we imply such an equality.

In our paper, the boundary conditions for the velocity components at the interface are [Eq. (10), Chen and Chen, 1992]

[1] By K. Vafai and P. C. Huang, published in the August 1994 issue of the ASME JOURNAL OF HEAT TRANSFER, Vol. 116, pp. 604–613.

[2] By P. C. Huang and K. Vafai, published in the August 1994 issue of the ASME JOURNAL OF HEAT TRANSFER, Vol. 116, pp. 768–771.

[3] Institute of Applied Mechanics, National Taiwan University, Taipei, Taiwan 106.

[4] Department of Aerospace and Mechanical Engineering, The University of Arizona, Tucson, AZ 85721.

$$V = V_m, \quad \mu \frac{\partial V}{\partial z} = \mu \frac{\partial V_m}{\partial z} \tag{2}$$

$$W = W_m, \quad P + 2\mu \frac{\partial W}{\partial z} = P_m + 2\mu \frac{\partial W_m}{\partial z} \tag{3}$$

in which V and W are horizontal and vertical velocity components in the y and z directions, P is the pressure, μ is the viscosity, and the subscript m denotes quantities pertaining to the porous medium. It is noted that we had chosen the "effective viscosity" in the porous medium to be equal to the fluid viscosity (Neale and Nader, 1974).

By continuity, one can show that $\partial W/\partial z = \partial W_m/\partial z$, and with μ common in both regions, one can conclude from Eq. (3) that $P = P_m$, as shown in Eq. (22) of our paper. Since in the two papers under discussion $\mu_I \neq \mu_{II}$, Eq. (1) as written is not an identity but an extra imposed boundary condition, as pointed out by Nield (1995).

References

Chen, F., and Chen, C. F., 1992, "Convection in Superposed Fluid and Porous Layers," *J. Fluid Mech.*, Vol. 234, pp. 97–119.

Neale, G., and Nader, W., 1974, "Practical Significance of Brinkman Extension of Darcy's Law: Coupled Parallel Flows Within a Channel and a Boundary Porous Medium," *Can. J. Chem. Engng.*, Vol. 52, pp. 472–478.

Nield, N. A., 1995, "Discussion," ASME JOURNAL OF HEAT TRANSFER, Vol. 117, pp. 554–555.

Vafai, K., and Kim, S. J., 1995, "Authors' Closure," ASME JOURNAL OF HEAT TRANSFER, Vol. 117, pp. 554–555.

Authors' Closure

The authors, Chen and Chen (1992), are right in that Eq. (1) is correct when the two viscosities are equal. However, a careful reading would make it very clear that the main subject of the discussion by Nield (1995) was indeed about the fact that Vafai and Huang (1994) and Huang and Vafai (1994) are setting the fluid viscosity and the effective viscosity equal, i.e., they are using the same viscosity in front of both terms in both papers. In fact, Nield (1995) had stated in the very beginning of his discussion about the works of Vafai and Huang (1994) and Huang and Vafai (1994) that, "In each of these papers the authors have modeled flow in a porous medium by a Brinkman–Forchheimer–extended Darcy equation (Eq. (5) of the first paper, Eq. (2) of the second) in which the coefficient of the Darcy term $\mathbf{v}/K$ is the same as the coefficient of the Brinkman term $\nabla^2\mathbf{v}$, and each is denoted by ν_{eff}." Therefore, the primary subject of the discussion and the closure (Vafai and Kim, 1995) is centered around the fact that our coefficient for the Darcy term $\mathbf{v}/K$ is the same as our coefficient for the Brinkman term $\nabla^2\mathbf{v}$! We use different symbols for the fluid viscosity and the effective viscosity so as to make it clear that they are usually different (also to avoid another discussion on the same point), but then we make it clear that due to lack of definitive data we always use the same value of viscosity for both when dealing with porous-fluid interfaces. We cannot emphasize this point any more strongly. It should be noted that our proof is based on facts and is independent of the material referred to by Chen and Chen (1992). We referred to their paper in our closure for the sake of brevity and as another example of the use of the type of equation that we are employing.

Furthermore, Vafai and Kim (1995) had made it extremely clear very early on that they had taken the coefficient for the Darcy term $\mathbf{v}/K$ to be the same as the coefficient for the Brinkman term $\nabla^2\mathbf{v}$ and why we had done so. In fact, in Vafai and Kim (1995) the foremost point starts with the following statement: "In general the coefficient of the Darcy term $\mathbf{v}/K$ is μ_f and the coefficient of the Brinkman term $\nabla^2\mathbf{v}$ is μ_{eff} as shown in Eq. (5) of Vafai and Kim (1990). We are well aware that there are some situations where it is important to make a distinction as shown and discussed, for example, in the works of Vafai and Kim (1990), Ettefagh et al. (1991) and Huang and Vafai (1994). But Lundgren (1972) and Neale and Nader (1974) have shown that setting the effective viscosity of the fluid-saturated porous medium equal to the fluid viscosity provides good agreement with experimental data. Hence, lacking definitive information on μ_{eff} it has become a common practice to set the effective viscosity equal to the fluid viscosity." This effective viscosity as explained by Vafai and Kim and Huang and Vafai several times is taken to be the fluid viscosity. This has always been our de-facto approach for problems dealing with the porous-fluid interface. This is similar to the work of several other investigators as cited by Vafai and Kim (1995) (which are also cited by Chen and Chen, 1992). It should be noted once again that we did not even directly use this condition when we solved our problem numerically. This is because we used a one-domain approach in terms of the vorticity–stream function–temperature formulation, which satisfies this condition indirectly. Finally, we would like to make it clear that Chen and Chen's last argument is wrong on both accounts because in the papers under discussion, as well as in Vafai and Kim (1995), $\mu_I = \mu_{II}$ as we had stated earlier. Hence we did not impose an extra boundary condition as claimed by Nield (1995).

Ironically, it appears that the effective viscosity and the fluid viscosity are not taken to be equal by Chen and Chen (1992). That is, the coefficient for the Darcy term $\mathbf{v}/K$ and the coefficient for the Brinkman term $\nabla^2\mathbf{v}$ are not set to be equal by Chen and Chen (1992). Their non-Darcian governing equation (Eq. (5)), which they have cited based on Georgiadis and Catton (1986), is actually based on the earlier work of Georgiadis and Catton (1985a, 1985b). This non-Darcian governing equation model "... is similar to the one implemented by Vafai and Tien [1] {1981} and Vafai [2] {1984} for forced boundary layer convective flow ..." (Georgiadis and Catton, 1985a, 1985b). Vafai and Tien (1981) obtained the governing momentum equation based on local volume averaging and matched asymptotic expansion. In the work of Vafai and Tien (1981), the well-established empirical information from the core region of the flow was incorporated into the analysis by using the proper matching of the inner and outer flows. This process also replaced the lost information, which is encountered as a result of the local volume averaging method. It should be noted that for this governing equation, as given by Vafai and Tien (1981), the coefficient in front of the Brinkman term $\nabla^2\mathbf{v}$ is $\Lambda_B = \mu_f/\delta$, the coefficient in front of the $\mathbf{v}$ term is $\Lambda_P = \mu_f/K$, the coefficient in front of the ∇P is unity, and the coefficient in front of the convective term (it is shown in Vafai and Tien (1981) that the advective term is negligible and the treatment for the transient part of the convective term, which is not present in Vafai and Tien (1981), is given by Vafai and Tien (1982)) is $\Lambda_I = \rho_f/\delta$. Accounting for the fact that different symbols have been used, these are the same coefficients in front of the corresponding terms of Chen and Chen (1992). Chen and Chen (1992) needed to set the effective viscosity, which refers to the coefficient in front of the Laplacian of the velocity of the fluid saturated porous medium, equal to the fluid viscosity. This point is directly and exactly consistent with the original formulation of Brinkman (1947), as displayed in his Eq. (5), that of Neale and Nader (1974), as displayed in their Eq. (1.7), as well as various other investigators. This is precisely what Vafai and Huang (1994) and Huang and Vafai (1994) have done. However, as it becomes clear in their Eqs. (16) and (17), Chen and Chen (1992) have failed to set these viscosity coefficients equal. This mistake affects the results of the analysis of Chen and Chen (1992).

Again, in both of these papers (Vafai and Huang, 1994; Huang and Vafai, 1994), and as very clearly reflected in the closure (Vafai and Kim, 1995), the coefficient for the Darcy term $\mathbf{v}/K$ is taken to be the same as the coefficient for the Brinkman term $\nabla^2\mathbf{v}$. We would like once again to reiterate that we are not trying to resolve a philosophical and complex question with respect to the physical nature of the interface. In

reality, a fluid–fluid or porous–fluid interface is significantly more complicated than what has been modeled by investigators in both fluid–fluid and porous–fluid interface modeling. Here we have adopted the traditional mathematical idealization used for both fluid–fluid and porous–fluid interfaces, i.e., representing the interface by a singular surface. Within this framework the equations used and the results obtained are correct as they stand.

We would like to thank the authors for an extension of this discussion. However, we have already discussed at length and with clarity an inapplicable point regarding a boundary condition at the interface that was never explicitly used to solve this (porous–fluid interface) problem. As such we feel that any additional discussion on this point will not be helpful to the readers of the journal.

References

Brinkman, H. C., 1947, "A Calculation of the Viscous Force Exerted by a Flowing Fluid on a Dense Swarm of Particles," *Applied Scientific Research,* Vol. A1, pp. 27–34.

Ettefagh, J., Vafai, K., and Kim, S. J., 1991, "Non-Darcian Effects in Open-Ended Cavities Filled With a Porous Medium," ASME JOURNAL OF HEAT TRANSFER, Vol. 113, pp. 747–756.

Huang, P. C., and Vafai, K., 1994, "Passive Alteration and Control of Convective Heat Transfer Utilizing Alternate Porous Cavity/Block Wafers," *International Journal of Heat and Fluid Flow,* Vol. 15, pp. 48–61.

Georgiadis, J. G., and Catton, I., 1985a, "Free Convective Motion in an Infinite Vertical Porous Slot: The Non-Darcian Regime," *Int. J. Heat Mass Transfer,* Vol. 28, pp. 2389–2392.

Georgiadis, J. G., and Catton, I., 1985b, "Free Convective Motion in an Infinite Vertical Porous Slot: The Non-Darcian Regime," ASME Paper No. 85-WA/HT-58.

Georgiadis, J. G., and Catton, I., 1986, "Prandtl Number Effect on Benard Convection in Porous Media," ASME JOURNAL OF HEAT TRANSFER, Vol. 108, pp. 284–290.

Lundgren, T. S., 1972, "Slow Flow Through Stationary Random Beds and Suspensions of Spheres," *J. Fluid Mech.,* Vol. 51, pp. 273–299.

Neale, G., and Nader, W., 1974, "Practical Significance of Brinkman's Extension of Darcy's Law Coupled Parallel Flows Within a Channel and a Bounding Porous Medium," *Can. J. Chem. Eng.,* Vol. 52, pp. 475–478.

Vafai, K., 1984, "Convective Flow and Heat Transfer in Variable-Porosity Media," *Journal of Fluid Mechanics,* Vol. 147, pp. 233–259.

Vafai, K., and Tien, C. L., 1981, "Boundary and Inertia Effects on Flow and Heat Transfer in Porous Media," *Int. J. Heat Mass Transfer,* Vol. 24, pp. 195–203.

Vafai, K., and Tien, C. L., 1982, "Boundary and Inertia Effects on Convective Mass Transfer in Porous Media," *Int. J. Heat Mass Transfer,* Vol. 25, pp. 1183–1190.

Vafai, K., and Kim, S. J., 1990, "Analysis of Surface Enhancement by a Porous Substrate," ASME JOURNAL OF HEAT TRANSFER, Vol. 112, pp. 700–706.